Transactions of the ASME®

Transactions of the ASME, Journal of Heat Transfer (ISSN 0022-1481) is published quarterly (Feb., May, Aug., Nov.) for $155 per year by The American Society of Mechanical Engineers, 345 East 47th Street, New York, NY 10017. Second class postage paid at New York, NY and additional mailing offices. POSTMASTER: Send address changes to Transactions of the ASME, Journal of Heat Transfer, c/o THE AMERICAN SOCIETY OF MECHANICAL ENGINEERS, 22 Law Drive, Box 2300, Fairfield, NJ 07007-2300.
CHANGES OF ADDRESS must be received at Society headquarters seven weeks before they are to be effective. Please send old label and new address.
PRICES: To members, $29.00, annually; to nonmembers, $155.00. Add $15.00 for postage to countries outside the United States and Canada.
STATEMENT from By-Laws. The Society shall not be responsible for statements or opinions advanced in papers or . . . printed in its publications (B7.1, para. 3).

INDEXED by Applied Mechanics Reviews and Engineering Information, Inc.

Journal of Heat Transfer

Published Quarterly by The American Society of Mechanical Engineers

VOLUME 112 • NUMBER 1 • FEBRUARY 1990

ANNOUNCEMENTS

TECHNICAL PAPERS

TECHNICAL NOTES

Porosity and Effective Thermal Conductivity of Wire Screens

Won Soon Chang
Wright Research & Development Center,
Wright-Patterson AFB, OH 45433

A simple theoretical model based on combined series and parallel conduction for the effective thermal conductivity of fluid-saturated screens has been developed. The present model has been compared with the existing correlations and experimental data available in literature, and it has been found that the model is effective in predicting thermal conductivity. The study also demonstrates that it is important to include the actual thickness of the wire screen in order to calculate the porosity accurately.

Introduction

Wire screen, commercially available in a wide variety of materials and meshes, is used extensively in such fields as aerospace, chemical product, food processing, medicine, and refrigeration and air conditioning. Because of its availability and many gages, the screen has also been found to have an application as a capillary structure in heat pipes.

In normal heat pipe operation, heat is primarily transferred across a liquid-saturated wick by conduction. Phase change occurs at the liquid–vapor interface in the heated and cooled regions (Cotter, 1965). It is thus of great importance to determine the effective thermal conductivity of the wick for designing the heat pipe.

Although the effective thermal conductivity is best evaluated by experiments, such measurements are complicated by a number of variables (mesh size, screen material, fluid, number of layers, temperature, and compression pressure) for both self-supporting and sintered screen wicks. It is therefore desirable to develop a mathematical model to arrive simply at the effective thermal conductivity with a minimum of experimental data.

Existing Correlations

A square-mesh standard wire screen, depicted in Fig. 1, has been considered in this study. It is woven plain and has equally spaced warp and shute wires of the same diameter. Screens are generally specified by manufacturers in terms of metal, mesh number, wire diameter, width of opening, percentage of open area, and weight.

The mesh number N, defined as the number of openings per unit length, linear inch or meter, is found from

$$N = 1/(d + w) \tag{1}$$

where d is the diameter of the wire and w is the width of the openings.

The porosity ϵ of porous media can be measured by a great variety of methods, as reviewed by Scheidegger (1974). For the screen it can be calculated by neglecting the degree of intermeshing between adjacent layers from (Marcus, 1972)

$$\epsilon = 1 - \pi SNd/4 \tag{2}$$

where S is a crimping factor and is approximately equal to 1.05. Equation (2) includes the crimping factor since screen wires are not simply crossed. On the other hand, ESDU (1979) suggests for single screens

$$\epsilon = 1 - \pi Nd/4 \tag{3}$$

Armour and Cannon (1968) studied various types of screens and presented for a square-mesh screen

$$\epsilon = 1 - \frac{\pi AB}{2(1+A)}\sqrt{1+\left(\frac{A}{1+A}\right)^2} \tag{4}$$

where

$$A = d/w \tag{5}$$

$$B = d/t \tag{6}$$

and t is the thickness of a layer of screen.

Neglecting free convection and radiation heat transfer, the effective thermal conductivity of fluid-saturated screen wicks may be found from the heat flux divided by the temperature gradient. The conductivity is therefore dependent upon the geometric parameters and the thermal conductivities of the solid and fluid.

For any kind of porous media, the lower and upper limits of the thermal conductivity k_e are obtained from simple heat conduction analysis by arranging the solid and fluid volumes in series and in parallel, respectively. The lower limit is

$$k_e = [\epsilon/k_f + (1-\epsilon)/k_s]^{-1} \tag{7}$$

and the upper limit is

$$k_e = \epsilon k_f + (1-\epsilon)k_s \tag{8}$$

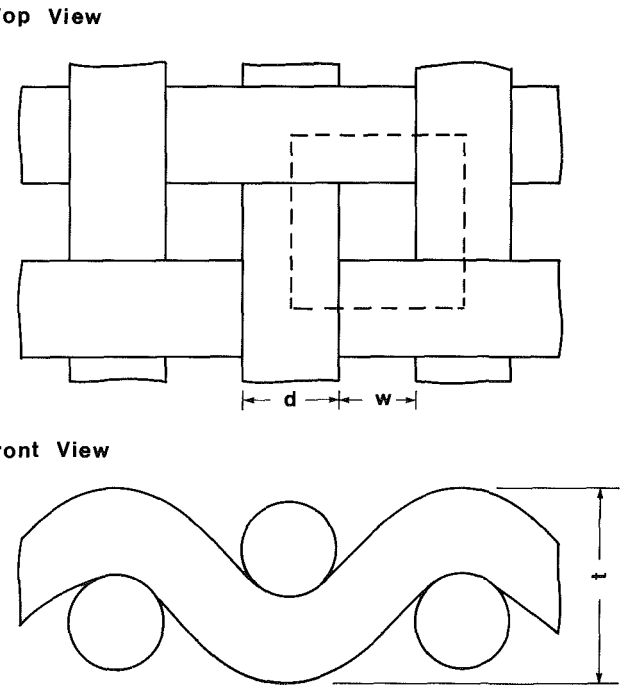

Fig. 1 Schematic of the standard wire screen

Contributed by the Heat Transfer Division and presented at the 24th ASME/AIChE National Heat Transfer Conference, Pittsburgh, Pennsylvania, August 9-12, 1987. Manuscript received by the Heat Transfer Division October 29, 1987. Keywords: Conduction, Porous Media, Thermophysical Properties.

where k_f and k_s are the thermal conductivities of the fluid and solid material. Generally, neither of these equations gives results close to the measured values.

By analyzing a square array of uniform cylinders, Rayleigh (1892) presented a series solution for the effective thermal conductivity as follows:

$$k_e/k_f = 1 - 2(1-\epsilon)[\beta + (1-\epsilon) - 0.036(1-\epsilon)^4/\beta - 0.0134(1-\epsilon)^8/\beta - \ldots]^{-1} \quad (9)$$

where

$$\beta = (k_f + k_s)/(k_f - k_s) \quad (10)$$

From equation (10) it can be seen that β becomes -1, $\pm\infty$, and 1 for $k_f << k_s$, $k_f \simeq k_s$, and $k_f >> k_s$, respectively. Since the absolute value of β is greater than or equal to 1 irrespective of the magnitude of k_f and k_s, the terms in $(1-\epsilon)^4$ and higher can be neglected in equation (9). This equation then reduces to

$$k_e = \frac{k_f[k_f + k_s - (1-\epsilon)(k_f - k_s)]}{k_f + k_s + (1-\epsilon)(k_f - k_s)} \quad (11)$$

It is from equation (11) that most heat pipe users calculate the effective thermal conductivity of liquid saturated screen wicks (Chi, 1976; ESDU, 1979; Dunn and Reay, 1982).

By measuring the thermal conductivities of sintered layers of wire screens saturated with water and air, Alexander (1972) correlated the data as

$$k_e = k_f (k_s/k_f)^{(1-\epsilon)^{0.59}} \quad (12)$$

Present Model

A unit cell model employed in this study is shown as a dashed-line region in Fig. 1. A quarter section of the region could be used in the analysis due to symmetry, but the whole section is considered for clarity.

Neglecting the effect of curvature of the wire rod, a circular cylinder of wire may be geometrically transformed to a rectangular parallelepiped of equivalent volume with the same length. If the width of the parallelepiped is αd, the height becomes $\pi d/(4\alpha)$. Here, α is an empirical constant accounting for the effects of mesh size, k_s/k_f, and contact resistance between the solid wires and also at fluid–solid interfaces, due to degree of sintering and compression pressure, on the effective thermal conductivity.

With this geometric transformation, the unit cell can be rearranged into three main sections as delineated in Fig. 2. It can be noticed that the width of opening has been changed from w to $w_o = w + d(1-\alpha)$. Because α includes the effect of contact resistance, the volumes of the solid and fluid may be lumped as shown in Fig. 3. Section 1 is for the two crossed wires, section 2 is for the single wire, and section 3 is for fluid only.

Thermal resistances in series through each section may be written as

$$R_1 = \frac{1}{k_s}\left(\frac{2\pi}{\alpha^3 d}\right) + \frac{1}{k_f}\left(\frac{4t}{\alpha^2 d^2} - \frac{2\pi}{\alpha^3 d}\right) \quad (13)$$

$$R_2 = \frac{1}{k_s}\left(\frac{\pi}{2w_o\alpha^2}\right) + \frac{1}{k_f}\left(\frac{2t}{w_o\alpha d} - \frac{\pi}{2w_o\alpha^2}\right) \quad (14)$$

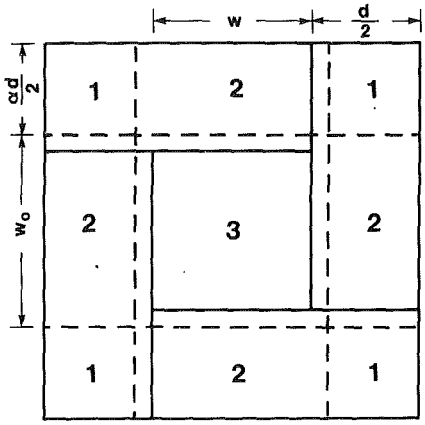

Fig. 2 Unit cell model

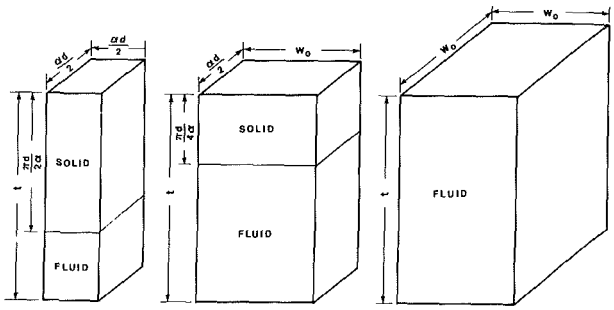

Fig. 3 Geometric model of lumped volumes of solid and fluid

$$R_3 = t/(k_f w_o^2) \quad (15)$$

From the parallel thermal circuit

$$t/[k_e(d+w)^2] = 4/R_1 + 4/R_2 + 1/R_3 \quad (16)$$

Substituting equations (13), (14), and (15) into equation (16) and rearranging yields

$$k_e = \frac{k_f}{(1+A)^2}\left\{\alpha^2 A\left[\frac{\alpha A}{\alpha - \pi B(1-k_f/k_s)/2} + \frac{2[1+A(1-\alpha)]}{\alpha - \pi B(1-k_f/k_s)/4}\right] + [1+A(1-\alpha)]^2\right\} \quad (17)$$

where $A = d/w$ and $B = d/t$ as in equation (4).

The constant α in equation (17) is geometrically ranged from the lower limit, by restricting the thickness of solid material less than t, to the upper limit, by stretching the half section of wire over the area of the top view of Fig. 2 to avoid section 3:

$$\pi d/(2t) \le \alpha \le 1 + w/d \quad (18)$$

If the base of the cross section of the parallelepiped is chosen as the wire radius, α becomes 0.5, and when the base is chosen equal to the wire diameter, α becomes 1. When the cross section of the parallelepiped is square, α becomes $\sqrt{\pi}/2$.

Equation (17) has been derived with reference to one layer

Nomenclature

A = d/w
B = d/t
d = wire diameter
k_e = effective thermal conductivity
k_f = thermal conductivity of fluid
k_s = thermal conductivity of solid
N = mesh number
R = thermal resistance
S = crimping factor
t = screen thickness
V_f = volume of fluid
w = opening width of screen
w_o = $w + d(1-\alpha)$
α = constant
β = $(k_f + k_s)/(k_f - k_s)$
ϵ = porosity

Table 1 Specifications of screens

N	d (mm)	w (mm)	t (mm)
SS 40 mesh (1.5748×10^3 m^{-1})	0.254	0.381	0.56
SS 100 mesh (3.9370×10^3 m^{-1})	0.1143	0.1397	0.23
Cu 100 mesh (3.9370×10^3 m^{-1})	0.1143	0.1397	0.27[a]
SS 150 mesh (5.8761×10^3 m^{-1})	0.06604	0.10414	0.15[b]
SS 200 mesh (7.8740×10^3 m^{-1})	0.05334	0.07366	0.12
SS 250 mesh (9.8425×10^3 m^{-1})	0.04064	0.06096	0.09662[b]
SS 400 mesh (1.5748×10^4 m^{-1})	0.0254	0.03810	0.05090[b]

[a]VanSant and Malet (1975)
[b]Armour and Cannon (1968)

Table 2 Porosity of screens

N	Measured	Eq. (2)	Eq. (3)	Eq. (4)	Eq. (22)
SS 40 mesh	0.69[a]	0.670	0.686	0.693	0.715
SS 100 mesh	0.63[a], 0.70[b]	0.629	0.647	0.629	0.649
Cu 100 mesh	0.69[b]	0.629	0.647	0.672	0.700
SS 150 mesh	0.68[a], 0.74[c]	0.680	0.695	0.712	0.732
SS 200 mesh	0.69[a]	0.654	0.670	0.682	0.707
SS 250 mesh	0.735[c]	0.670	0.686	0.715	0.735
SS 400 mesh	0.706[c]	0.670	0.686	0.662	0.686

[a]Alexander (1972)
[b]VanSant and Malet (1975)
[c]Armour and Cannon (1968)

of screen. It may also be applied to a multiple layer of screens, sintered or not, if the total thickness of the layers divided by the number of layers is used as the thickness

$$t = t_w/n \tag{19}$$

where t_w is the total thickness and n is the number of layers.

From the definition of porosity, the ratio of fluid volume to total volume

$$\epsilon = V_f/[t(d+w)^2] \tag{20}$$

where the volume of fluid V_f is

$$V_f = (\alpha d)^2[t - \pi d/(2\alpha)] + 2\alpha d w_o[t - \pi d/(4\alpha)] + t w_o^2 \tag{21}$$

Substituting equation (21) into equation (20) and rearranging results in

$$\epsilon = 1 - \pi AB/[2(1+A)] \tag{22}$$

It is seen that equation (22) does not contain the square-root term of equation (4), which is approximately 1.1 for the heat pipe screen wicks. Also, it is seen that equation (22) is identical to equation (3) if the thickness of a layer of screen is assumed to be twice the diameter, namely, $B = 1/2$. As with the effective thermal conductivity, equation (22) may be used for the multiple-layered screens with equation (19).

Comparisons and Discussion

The porosity of the screen has been calculated from the present and existing equations and compared to the experimental data from literature. Table 1 summarizes dimensions of screen mesh used. The listed thickness of the screen is the average of the readings taken at various places with a micrometer. The comparisons of the screen porosity are given in Table 2.

Since Alexander (1972) measured porosities with sintered multilayers of screen, his data in Table 2 may give smaller values than those for one layer of screen. VanSant and Malet (1975) reported the porosities of the stainless steel and copper screens of 100 mesh as 0.70 and 0.69, respectively. However, because the copper screen is thicker than the stainless steel screen with the same wire diameter and width of opening, the latter should have a lower porosity than the former. As can be seen in Table 2, the present relation, equation (22), gives good estimate of the screen porosity.

The present expression for the effective thermal conductivity, equation (17), has been compared with the measured values along with Rayleigh's and Alexander's relations, equations (11) and (12). Tables 3 and 4 show these comparisons using a stainless steel (type 304) and a copper screen of 100 mesh saturated with several different fluids at 293.15 K, respectively. The measured values with uncertainties of less than ± 5 percent are from VanSant and Malet (1975). The calculated values from Rayleigh's and Alexander's equations are tabulated with the porosities from the measured data and equations (2), (4), and (22), which are also listed in Table 2. The values of α used in calculations with the present equation are 0.5 and 1.

Tables 3 and 4 show that all the equations tend to increase the percentage of deviation from the measured values as k_s/k_f increases, with the largest error occurring with Alexander's equation. Prediction with the present model using $\alpha = 0.5$ and 1 is good when the ratio k_s/k_f ranges from 25 to 160, but is rather poor when the ratio is greater than 600.

It should be noted that an optimum value of α can be found using the measured effective thermal conductivity in equation (17). The optimum values of α for the 100 mesh screen obtained at 293.15 K are plotted in Fig. 4 as a function of k_s/k_f. For the 100 mesh screen there exist two optimum values of α when $k_s/k_f > 10$; one value when $1 < k_s/k_f < 10$; and none when $k_s/k_f < 1$.

As drawn in Fig. 4, the least-squares fit gives

$$\alpha = 0.61367 - 0.04375 \log_{10}(k_s/k_f) \tag{23}$$

for the lower values and

$$\alpha = 1.11716 - 0.07024 \log_{10}(k_s/k_f) \tag{24}$$

for the upper values. Figure 4 also includes α, which gives undefined values of k_e, shown with the open symbol, due to the two denominators of the right-hand side of equation (17); when α equals $\pi B(1 - k_f/k_s)/2$ or $\pi B(1 - k_f/k_s)/4$, equation (17) gives k_e of $\pm\infty$. An example for water and 100 mesh stainless steel screen is given in Fig. 5 to show that the model yields fairly constant values for k_e except when α is near those two critical values. Judging from Figs. 1 and 5, it seems appropriate to choose the upper values for α.

The calculated effective thermal conductivities from various equations are compared to the experimental data as a function of temperature in Fig. 6 for the stainless steel screen and Fig. 7 for the copper screen of 100 mesh. Also included in the figures is a straight line of VanSant and Malet (1975), which fits the data. It should be noted that predictions from the lower and upper limits, equations (7) and (8), are quite different from the measured values, particularly distorted at the upper limit. The two optimum values of α obtained at 293.15 K give such close results that only one line may be drawn. These values of α can of course be found at each temperature to best fit the data for the given screen. Actually, α has different optimum values depending on the temperature, k_s/k_f, and mesh number. The calculated values from the present equation with $\alpha = 0.5$ and 1

Table 3 Effective thermal conductivity of stainless steel screen at 293.15 K ($N = 100$ mesh; $k_s = 15.072$)

Fluid (k_f)	k_s/k_f	Measured k_e	ε	Rayleigh k_e	Rayleigh dev.(%)	Alexander k_e	Alexander dev.(%)	present α	present k_e	present dev.(%)
H_2O (0.598)	25.20	1.08	0.70	1.056	-2.22	1.059	-1.94	0.5	1.132	4.81
			0.629	1.222	13.15	1.212	12.22	1.0	1.138	5.37
			0.649	1.172	8.52	1.167	8.06			
CH_3OH (0.212)	71.09	0.40	0.70	0.387	-3.25	0.451	12.75	0.5	0.428	7.00
			0.629	0.451	12.75	0.539	34.75	1.0	0.421	5.25
			0.649	0.432	8.00	0.513	28.25			
CCl_3F (0.095)	158.65	0.19	0.70	0.175	-7.89	0.233	22.63	0.5	0.196	3.16
			0.629	0.205	7.89	0.288	51.58	1.0	0.191	0.53
			0.649	0.196	3.16	0.271	42.63			
Air (0.025)	602.88	0.07	0.70	0.046	-34.29	0.078	11.43	0.5	0.052	-25.71
			0.629	0.054	-22.86	0.102	45.71	1.0	0.051	-27.14
			0.649	0.052	-25.71	0.094	34.29			

* Units of k: W/m-K

Table 4 Effective thermal conductivity of copper screen at 293.15 K ($N = 100$ mesh; $k_s = 399.0$)

Fluid (k_f)	k_s/k_f	Measured k_e	ε	Rayleigh k_e	Rayleigh dev.(%)	Alexander k_e	Alexander dev.(%)	present α	present k_e	present dev.(%)
H_2O (0.598)	667.22	1.51	0.69	1.133	-24.79	1.965	30.13	0.5	1.251	-17.15
			0.629	1.300	-13.91	2.483	64.44	1.0	1.215	-19.54
			0.672	1.179	-21.92	2.105	39.40			
			0.700	1.108	-40.20	1.891	25.23			
CH_3OH (0.212)	1882.08	0.52	0.69	0.402	-22.69	0.842	61.92	0.5	0.445	-14.42
			0.629	0.462	-11.15	1.104	112.31	1.0	0.432	-16.92
			0.672	0.419	-19.42	0.912	75.38			
			0.700	0.393	-24.42	0.805	54.81			
CCl_3F (0.095)	4200.00	0.27	0.69	0.180	-33.33	0.437	61.85	0.5	0.199	-26.30
			0.629	0.207	-23.33	0.590	118.52	1.0	0.193	-28.52
			0.672	0.188	-30.37	0.477	76.67			
			0.700	0.176	-34.81	0.416	54.07			
Air (0.025)	15960.00	0.10	0.69	0.047	-53.00	0.147	47.00	0.5	0.053	-47.00
			0.629	0.054	-46.00	0.208	108.00	1.0	0.052	-48.00
			0.672	0.049	-51.00	0.163	63.00			
			0.700	0.046	-54.00	0.139	39.00			

* Units of k: W/m-K

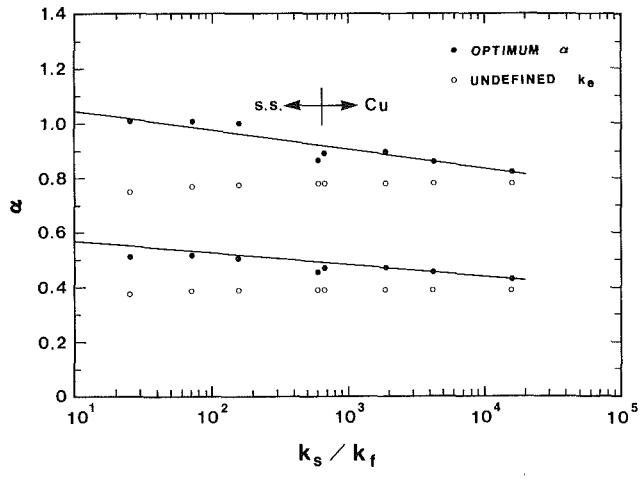

Fig. 4 Optimum values of α versus k_s/k_f ($N = 100$ mesh; $T = 293.15$ K)

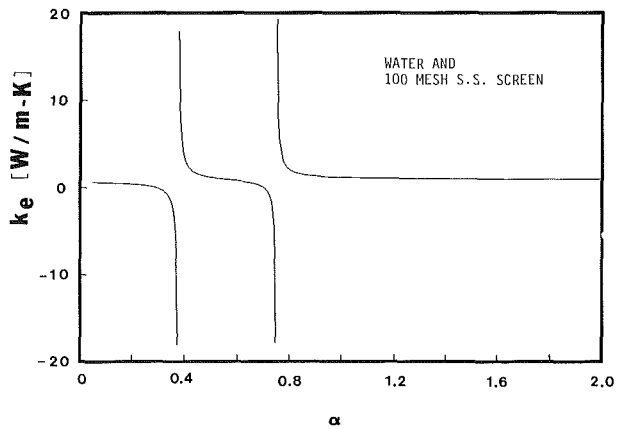

Fig. 5 Effective thermal conductivity of 100 mesh stainless steel screen saturated with water

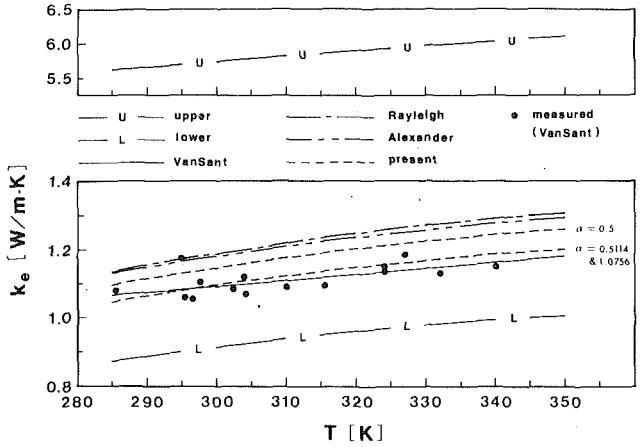

Fig. 6 Comparison of correlations for stainless steel screen saturated with water ($N = 100$ mesh; $\epsilon = 0.649$)

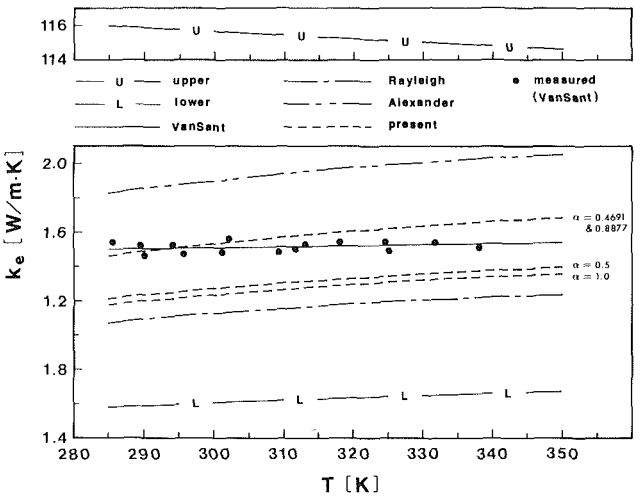

Fig. 7 Comparison of correlations for copper screen saturated with water ($N = 100$ mesh; $\epsilon = 0.7$)

give close results. For the stainless steel screen, they are so close (slightly higher with $\alpha = 1$) that only the results with $\alpha = 0.5$ are given in Fig. 6.

Figures 6 and 7 verify the suitability of the present model for predicting the effective thermal conductivity of the screen. Obviously, further study is needed to generalize the model by obtaining more experimental data. It may be valuable to validate the present model with various mesh sizes. For the present, it may be suggested to use the value of α evaluated at the design operating temperature in heat pipe application if experimental data are not available over the interested range of temperature. If none of the data are available, Fig. 4 may be used for $25 < k_s/k_f < 2 \times 10^4$.

It may be appropriate to mention that the present model works well in heat pipe applications. The present relation for the effective thermal conductivity was used in a computational model based on finite difference approximations for predicting the transient operation of the heat pipe. Detailed information on the transient numerical model of the heat pipe and its comparison to experimental data with good agreement are outlined elsewhere (Chang and Leland, 1989).

Conclusions

The comparisons between calculated and measured porosities and effective thermal conductivities show that the present model gives better accuracy than the existing equations. In dealing with analytical predictions of the effective thermal conductivity and porosity of the screen, it is important to include the actual thickness of the screen. Further experimental data on the effective thermal conductivity, especially for $k_s/k_f < 25$, are needed to generalize the present model.

References

Alexander, E. G., Jr., 1972, "Structure-Property Relationships in Heat Pipe Wicking Materials," Ph. D. Thesis, Department of Chemical Engineering, North Carolina State University, Raleigh, NC.

Armour, J. C., and Cannon, J. N., 1968, "Fluid Flow Through Woven Screens," *AIChE Journal*, Vol. 14, No. 3, pp. 415-420.

Chang, W. S., and Leland, J. E., 1989, "Finite Difference Simulation of Transient Heat Pipe Operation," AIAA Paper No. 89-0320.

Chi, S. W., 1976, *Heat Pipe Theory and Practice*, Hemisphere Publishing Corp., Washington, DC.

Cotter, T. P., 1965, "Theory of Heat Pipes," LA-3246-MS, Los Alamos Scientific Laboratory, Los Alamos, NM.

Dunn, P., and Reay, D. A., 1982, *Heat Pipes*, 3rd ed., Pergamon Press, New York, NY.

ESDU, 1979, "Heat Pipes—Properties of Common Small-Pore Wicks," Data Item No. 79013, Engineering Sciences Data Unit, London, United Kingdom.

Marcus, B. D., 1972, "Theory and Design of Variable Conductance Heat Pipes," NASA CR-2018.

Rayleigh, Lord, 1892, "On the Influence of Obstacles Arranged in Rectangular Order Upon the Properties of a Medium," *Philosophical Magazine*, Vol. LVI, pp. 481-502.

Scheidegger, A. E., 1974, *The Physics of Flow Through Porous Media*, 3rd ed., University of Toronto Press, Toronto, Canada.

VanSant, J. H., and Malet, J. R., 1975, "Thermal Conductivity of Some Heat Pipe Wicks," *Letters in Heat and Mass Transfer*, Vol. 2, pp. 199-206.

Intrinsic Thermal Stability of Anisotropic Thin-Film Superconductors

M. I. Flik[1]
Research Assistant.

C. L. Tien
UCI Distinguished Professor.
Fellow ASME

Department of Mechanical Engineering,
University of California,
Irvine, CA 92717

Intrinsic thermal stability denotes a situation where a superconductor can carry the operating current without resistance at all times after the occurrence of a localized release of thermal energy. This novel stability criterion is different from the cryogenic stability criteria for magnets and has particular relevance to thin-film superconductors. Crystals of ceramic high-temperature superconductors are likely to exhibit anisotropic thermal conductivity. The resultant anisotropy of highly oriented films of superconductors greatly influences their thermal stability. This work presents an analysis for the maximum operating current density that ensures intrinsic stability. The stability criterion depends on the amount of released energy, the Biot number, the aspect ratio, and the ratio of the thermal conductivities in the plane of the film and normal to it.

Introduction

The critical current density of a superconductor is the upper limit of the electric current it can carry without resistance at a given operating condition. The problem of thermal stability of superconductors has its root in the monotonic decrease of the critical current density with temperature. The theory of thermal stability is concerned with the prediction of the consequences of thermal disturbances for the performance and safety of superconductors. It is an engineering discipline, emerging from the need to design superconducting devices that operate safely under practical conditions.

Most previous analyses of superconductor thermal stability concerned magnet windings of multifilamentary composites, such as pancakes or internally cooled superconductors (Wilson, 1983). These studies dealt with the case where a normal zone has formed within the composite superconductor and Joule heating occurs. The cryogenic stability criteria developed for this case predict whether this normal zone grows or collapses. In superconducting composites, superconductor filaments are embedded in a metal matrix of copper or aluminum. When the filaments become normally resistive due to a thermal disturbance, the current is shared between the filaments and the matrix. The high electrical conductivity of the matrix greatly reduces the Joule heating and has a strong stabilizing effect.

In thin-film superconductors, such as for electronics applications, this metal matrix is absent. The pure superconductor is deposited as a film on a normally crystalline substrate. Hence the Joule heating following the formation of a normal zone is comparatively much higher than in composites, and indeed it appears to be very difficult to stabilize such a system cryogenically in the same way as a magnet. If a localized release of thermal energy occurs in a thin-film superconductor, then the relevant question is not whether Joule heating is compensated by heat removal, but rather whether Joule heating occurs at all. This work presents a novel criterion for *intrinsic thermal stability*, i.e., when no Joule heating occurs after a thermal disturbance.

The most widely used conventional superconductors are the A15 types and NbTi. The former, e.g., Nb_3Sn, possess a cubic crystal structure, while the latter form amorphous solution alloys. Both materials are characterized by isotropic thermal conductivity. In contrast, the new 123-phase material $YBa_2Cu_3O_7$, with a critical temperature of about 95 K, is highly anisotropic and has an orthorhombic crystal structure, as shown in Fig. 1 (Zhang et al., 1988). The *ab* plane identifies the plane of the CuO layers, and the *c* axis denotes the direction normal to them. Measurements at 150 K show that single crystals of 123 phase in the normal state have an electrical conductivity about 60 times higher in the *ab* plane than in the *c* direction. Highly oriented films at the same temperature exhibit an electrical conductivity about six times higher if the film contains the *ab* plane than in the case where it contains the *c* axis (Geballe and Hulm, 1988), and even higher levels of orientation appear feasible. Highly oriented films are desirable for high-temperature superconductor applications, because the critical current density for a single crystal is about 20 times higher parallel to the *ab* planes than normal to them (Geballe and Hulm, 1988). The critical current densities achieved with oriented films exceed those reached with bulk samples by several orders of magnitude.

Orthorhombic crystals are known to have a diagonal conductivity tensor with three different principal thermal conductivities (Nye, 1985). This basic result, together with the measured anisotropy of the electrical conductivity in the normal state, strongly indicates that highly oriented films of 123 phase have a much higher thermal conductivity in the plane of

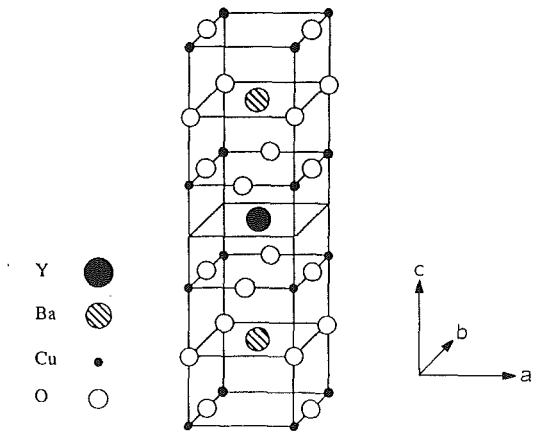

Fig. 1 The unit-cell structure of the $YBa_2Cu_3O_7$ superconductor (Zhang et al., 1988)

[1]Present address: Department of Mechanical Engineering, Massachusetts Institute of Technology, Cambridge, MA 02139.

Contributed by the Heat Transfer Division and presented at the ASME Winter Annual Meeting, Chicago, Illinois, November 29–December 2, 1988. Manuscript received by the Heat Transfer Division July 26, 1988. Keywords: Conduction, Cryogenics, Transient and Unsteady Heat Transfer.

the film than in the direction normal to it. The magnitude of the anisotropy, though, cannot be inferred from these measurements, since the electronic contribution to the thermal conductivity is only about 10 percent (Uher and Kaiser, 1987). Fisher et al. (1988) reviewed the reported measurements of the specific heat and the thermal conductivity of high-T_c superconductors. The only experiments on single crystals were performed by Graebner et al. (1988). They found that the thermal conductivity within the *ab* plane is more than five times higher than for a sintered sample, which lends support to the present argument. This difference, however, could partly be due to the absence of certain scattering mechanisms in the single crystal, and only directional measurements of the thermal conductivity on the same crystal can settle this question. However, these measurements are very difficult due to the short *c* axis of the single crystals. The $Tl_2Ba_2Ca_2Cu_3O_{10}$ superconductor with a critical temperature of about 125 K exhibits a tetragonal structure (Torardi et al., 1988), possessing different transport properties in the *ab* plane and in the *c* direction. The foregoing arguments also apply to this material.

The criterion for intrinsic thermal stability derived in this study is employed to demonstrate the effect of anisotropy on the stability of thin superconducting films. This criterion determines the maximum operating current density that ensures intrinsic stability. This current density is a function of both the magnitude of the thermal disturbance and the heat transfer coefficient at the surface and results from the solution of the Fourier equation for an anisotropic medium. This work investigates the combined influence of the ratio of the thermal conductivities parallel and normal to the film and of the aspect ratio on this stability criterion.

Thermal Stability Criteria

Stekly and Zar (1965) presented a criterion for cryogenic stability of a one-dimensional composite superconductor. They performed a balance between generation of heat by Joule heating and the heat transfer to the cryogenic coolant. If the latter exceeds the former, the composite conductor is completely stable against thermal disturbances. Maddock et al. (1969) proposed a criterion that included the effect of axial conduction and of the temperature dependence of the cryogenic heat transfer coefficient. Both of these studies considered the large-time behavior of normal zones employing steady-state analyses. Bejan and Tien (1978) removed this constraint and investigated cryogenic stability accounting for the small-time transient behavior of a normal zone. All of these three stability criteria have in common that they assume the existence of a normal zone that produces Joule heating within the composite superconductor. Then they examine the conditions under which this normal zone grows or collapses.

In contrast, intrinsic thermal stability refers to a situation where the thermal energy initially deposited diffuses to the boundary of the superconductor and is transferred to the coolant without the occurrence of Joule heating at any time. The superconductor is able to carry the operating current without resistance at all times, although its superconducting capacity is reduced due to the temperature field developed as a consequence of the heat diffusion. There are no negative effects if a composite conductor is not intrinsically stable, as long as it is cryogenically stable. On the contrary, it is indicated in the next section that, if a thin-film pure superconductor is not intrinsically stable, the ensuing Joule heating is likely to destroy the film due to the resulting high temperatures. The comparatively strong Joule heating is due to the high normal-state resistivity of superconductors, in particular the new ceramic materials. It follows that a high-temperature thin-film superconductor is either intrinsically stable for a given thermal disturbance, or it is most likely not stable at all.

Analysis

Figure 2 shows the physical model under consideration. A superconductor with rectangular cross section exchanges heat

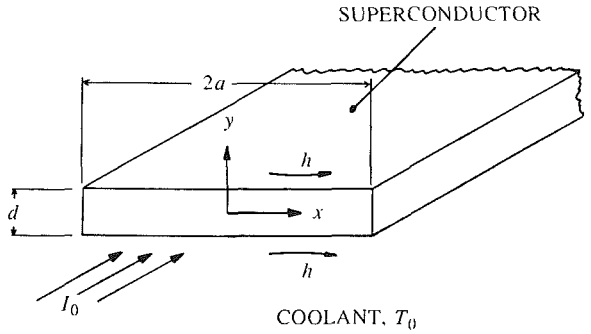

Fig. 2 Physical model of thin-film superconductor

Nomenclature

a = half-width of cross section
Bi = Biot number $= hd/2(k_xk_y)^{1/2}$
c = specific heat
d = height of cross section
e_0 = energy released as a line disturbance, per unit length
Fo = Fourier number $= \Delta\tau/(\Delta\eta)^2$
g = integrand, equation (7)
h = heat transfer coefficient
I_0 = operating current
J_c = critical current density
J_{c0} = critical current density at T_0
J_0 = operating current density $= I_0/2ad$
k = thermal conductivity
$\mathbf{K}$ = thermal conductivity tensor
M = number of nodes in the ξ direction
N = number of nodes in the η direction
r = transformed aspect ratio $= 2a(k_y/k_x)^{1/2}/d$
R = grid aspect ratio $= \Delta\eta/\Delta\xi$
t = time
T = temperature
$\bar{T}$ = average temperature of superconductor
T_c = critical temperature
T_0 = operating temperature
x = coordinate parallel to the film
y = coordinate normal to the film
ϵ_0 = dimensionless thermal disturbance $= e_0/\rho c(T_c - T_0)2ad$
η = transformed y coordinate $= 2y/d$
θ = dimensionless temperature $= (T - T_0)/(T_c - T_0)$
ξ = transformed x coordinate $= 2x(k_y/k_x)^{1/2}/d$
ρ = density
σ = normal-state resistivity of superconductor
τ = dimensionless time $= 4k_yt/d^2\rho c$
ϕ = stability parameter, equation (6)

Subscripts

m = node number in ξ direction
max = maximum value for all times t
n = node number in η direction
x = x direction
y = y direction

Superscripts

t = time step

with the surrounding coolant at a rate given by a uniform and constant heat transfer coefficient h. The electrical current I_0 flows through the superconductor normal to the xy plane. The two-dimensional analysis does not consider any temperature gradients normal to the xy plane. No magnetic field is assumed to be present, as typical for electronics applications.

The superconductor operates in steady state at a current density J_0 and at the coolant temperature T_0, which remains constant for all times. At time $t=0$, a finite amount of thermal energy e_0 is released in a line source at the origin, $x=y=0$. The line source extends to infinity normal to the xy plane. A three-dimensional analysis would allow the consideration of a release of energy in the form of a point source, which might be more realistic, but since the main purpose of this study is demonstration of the stability criterion, a two-dimensional analysis is sufficient. However, a thermal disturbance due to a sudden relaxation of a line dislocation is approximated very well by a line source. Moreover, the assumption of a line source is conservative, since in the case of a point source the heat also spreads axially and has a smaller effect in the xy plane.

Localized release of thermal energy is assumed to be a major cause of the degradation of superconducting magnets (Wilson, 1983). Little, though, is known about the physical mechanisms responsible for these disturbances. In a thin-film superconductor, these thermal disturbances will have much smaller spatial extensions than in magnets. Possible mechanisms include the sudden relaxation of dislocations and crystal defects and other spontaneous processes. The disturbance spectrum in a thin-film superconductor is likely to depend on its uniformity, purity, and epitaxy. These film properties are strongly influenced by the deposition process and the combination of film–substrate materials. A source for thermal disturbances of great technical importance is given by the absorption of radiation in superconducting films. Bolometers based on thin-film superconductors can detect very sensitively incident electromagnetic or atomic radiation (Newhouse, 1964). The powerful characterization method of low-temperature scanning electron microscopy (Huebener et al., 1988) uses the thermal disturbance induced by an absorbed electron beam to analyze local film properties.

Immediately after the occurrence of the thermal disturbance, the temperature at the boundaries is not affected by heat diffusion, and the superconductor transfers no heat to the coolant. This leads to an initial condition

$$4\int_0^{d/2}\int_0^{a}\rho c(T-T_0)dxdy=e_0 \text{ for } t\to 0 \tag{1}$$

$$T(x,y)=T_0 \text{ for } x,y\neq 0,\ t=0 \tag{2}$$

The dependence of the critical current density on the temperature is approximated by the linear relation (Wilson, 1983)

$$\frac{J_c}{J_{c0}}=\frac{T_c-T}{T_c-T_0},\qquad T_0<T<T_c \tag{3}$$

where J_{c0} is the critical current density at the operating temperature T_0. For temperatures above the critical temperature, the critical current density is zero. The critical current density is decreased in the area affected by the diffusion of the thermal energy initially deposited in the line source. Hence the diffusion of heat reduces the total current that the superconductor can carry without resistance. Figure 3 shows qualitatively that in an anisotropic medium the diffusion of thermal energy creates elliptic isotherms, the lines of constant J_c, as long as the temperature at the boundaries is not affected. This leads to the formation of three zones. The normal zone I, characterized by $T>T_c$, cannot carry any current.

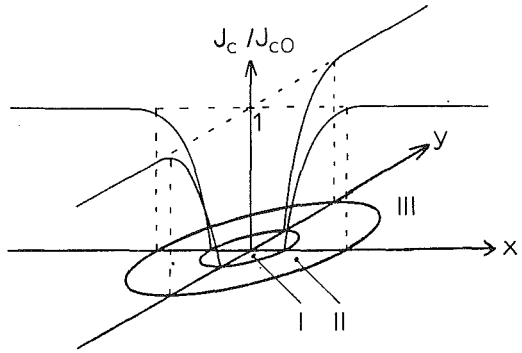

Fig. 3 Schematic distribution of critical current density after a thermal disturbance

Zone II, $T_0<T<T_c$, can accommodate a finite current, $J<J_{c0}$, and zone III, into which the heat has not yet diffused, remains at the operating condition, given by the critical current density J_{c0}. As the heat spreads, the current redistributes itself such that it makes the best use of the available distribution of the critical current density. No losses are assumed to occur due to the reorientation of current lines.

Intrinsic thermal stability denotes a situation where zones II and III together can carry the operating current I_0 at all times t after the occurrence of the thermal disturbance. The superconductor is intrinsically stable if the integral critical current density is larger than the operating current

$$4\int_0^{a}\int_0^{d/2}J_c(x,y,t)dxdy>I_0 \text{ for all } t \tag{4}$$

Dividing by the product of the cross-sectional area and J_{c0}, and using equation (3), this becomes

$$\frac{J_0}{J_{c0}}<1-\phi_{\max} \tag{5}$$

$$\phi(t)=\frac{2}{ad}\int_0^{a}\int_0^{d/2}g(\theta)dxdy \tag{6}$$

$$g(\theta)=\begin{cases}1 \text{ for } \theta\geq 1\\ \\ \theta \text{ for } \theta<1\end{cases},\qquad \theta(x,y,t)=\frac{T-T_0}{T_c-T_0} \tag{7}$$

where the subscript max indicates the maximum value for all times t. The range $\theta>1$ corresponds to zone I, $0<\theta<1$ to zone II, and $\theta=0$ prevails in zone III. At a value of $\phi_{\max}\sim 0$, the superconductor is stable carrying a large current $I_0=2adJ_{c0}$. Conversely, if $\phi_{\max}\sim 1$, then the superconductor is unstable even for very small currents I_0.

The stability parameter $\phi_{\max}$ is a measure of the maximum reduction of superconducting capacity during the thermal conduction transient. It is found from the solution of the Fourier equation

$$\nabla\cdot(\mathbf{K}\nabla T)=\rho c\frac{\partial T}{\partial t} \tag{8}$$

where $\mathbf{K}$ is the conductivity tensor and the specific heat is assumed to be constant. Most of the ceramic high-temperature superconductors possess a diagonal thermal conductivity tensor. The thermal conductivity in a highly oriented film consists of an isotropic contribution due to random orientation and an anisotropic contribution due to oriented crystals, which leads to a diagonal conductivity tensor. For Cartesian coordinates in two dimensions, equation (8) becomes

$$k_x\frac{\partial^2 T}{\partial x^2}+k_y\frac{\partial^2 T}{\partial y^2}=\rho c\frac{\partial T}{\partial t} \tag{9}$$

with the initial condition given by equations (1) and (2), and the associated boundary conditions

$$\mp k_y\left(\frac{\partial T}{\partial y}\right)_{y=\pm d/2}=h(T\Big|_{y=\pm d/2}-T_0) \tag{10}$$

$$\mp k_x\left(\frac{\partial T}{\partial x}\right)_{x=\pm a}=h(T\Big|_{x=\pm a}-T_0) \tag{11}$$

Here, k_x and k_y are assumed not to vary with temperature, which agrees with the measurements of Uher and Kaiser (1987) and Morelli et al. (1987). They showed that, although the thermal conductivity of 123 phase varies considerably below 77 K, it remains approximately constant above this temperature.

The coordinate transformation (Özişik, 1980)

$$\xi=\frac{2x}{d}\left(\frac{k_y}{k_x}\right)^{1/2},\qquad \eta=\frac{2y}{d},\qquad \tau=\frac{4k_y t}{d^2\rho c} \tag{12}$$

renders an isotropic form of the Fourier equation

$$\frac{\partial^2\theta}{\partial\xi^2}+\frac{\partial^2\theta}{\partial\eta^2}=\frac{\partial\theta}{\partial\tau} \tag{13}$$

with θ being defined in equation (7). In this coordinate system, the heat diffuses at the same rate in the ξ and η directions. The boundary conditions become

$$\mp\left(\frac{\partial\theta}{\partial\xi}\right)_{\xi=\pm r}=\mathrm{Bi}\,\theta\Big|_{\xi=\pm r} \tag{14}$$

$$\mp\left(\frac{\partial\theta}{\partial\eta}\right)_{\eta=\pm 1}=\left(\frac{k_x}{k_y}\right)^{1/2}\mathrm{Bi}\,\theta\Big|_{\eta=\pm 1} \tag{15}$$

$$\mathrm{Bi}=\frac{hd}{2(k_xk_y)^{1/2}},\qquad r=\frac{2a}{d}\left(\frac{k_y}{k_x}\right)^{1/2} \tag{16}$$

and the initial condition is transformed into

$$\int_0^r\int_0^1\theta\,d\xi\,d\eta=\epsilon_0 r \text{ for } \tau\to 0 \tag{17}$$

$$\theta(\xi,\eta,\tau=0)=0 \text{ for } \xi,\eta\neq 0 \tag{18}$$

where

$$\epsilon_0=\frac{e_0}{\rho c(T_c-T_0)2ad} \tag{19}$$

The dimensionless thermal disturbance ϵ_0 compares the amount of released energy per unit length to the sensible heat per unit length of the film associated with the difference between the critical and the operating temperatures. Recent measurements of the density (Heremans et al., 1988) and of the specific heat (Butera, 1988) of 123 phase permit an estimation of the magnitude of e_0 for a given value of ϵ_0. With liquid nitrogen as coolant, the operating temperature becomes $T_0=77$ K, and the critical temperature is $T_c=95$ K. If the film thickness is $d=4$ μm and the aspect ratio is $2a/d=100$, the measured values of $\rho=2.72\times10^3$ kg/m^3 and $c=180.2$ J/kgK imply that a value of $\epsilon_0=1$ corresponds to a line source of the strength $e_0=1.41\times10^{-8}$ J/μm. Butera (1988) also measured the latent heat of the superconducting-normal transition as 5.51 J/kg. If this latent heat is neglected, the error in the average film temperature is less than 1 percent for $\epsilon_0>0.2$.

If the integral on the left-hand side of equation (4) becomes smaller than I_0 at any time during the conduction transient, the superconductor is not intrinsically stable. In this case, the superconductor becomes normally resistant also in zones II and III. Joule heating ensues with a magnitude of $\sigma I_0^2/2ad$ per unit length, where σ is the normal-state resistivity of the superconductor. Heat is transferred to the coolant at a rate of $2h(2a+d)(\bar{T}-T_0)$ per unit length, neglecting conduction within the superconductor. The average temperature $\bar{T}$ rises to a value of $\bar{T}-T_0=\sigma I_0^2/4adh(2a+d)$ at which equilibrium is attained. Using $\sigma=10^{-2}$ Ωcm (Heremans et al., 1988), a typical value of $J_0=10^5$ A/cm^2, $h=5\times10^4$W/m^{2}K, and assuming a cross section of $2a=400$ μm, $d=4$ μm, one obtains $\bar{T}-T_0=4\times10^3$K, a very high value. This estimation indicates, as mentioned earlier, that it is unlikely that a thin-film superconductor that is not intrinsically stable can recover the superconducting state after the incipience of Joule heating.

The parameter r deserves particular attention. It is the aspect ratio of the transformed cross section, within which the heat diffuses isotropically, and describes the combined effects of the aspect ratio and of the ratio of the thermal conductivities. For $r>>1$, the transformed cross section is still very flat, and the superconductor loses heat from the wide faces while the normal zone propagates in the x direction. This influences stability favorably, since a significant amount of heat is lost before the heat diffuses far enough into the x direction to reduce the integral current density appreciably. For $r\approx1$, the transformed cross section is almost square, and the superconductor cannot lose heat before the diffusion front has reached the boundary. This influences stability adversely and leads to high values of $\phi_{\max}$. The transformed expression for the stability parameter is

$$\phi_{\max}=\left[\frac{1}{r}\int_0^r\int_0^1 g(\theta)d\xi\,d\eta\right]_{\max} \tag{20}$$

The analysis renders the maximum stable operating fraction of the critical current density, J_0/J_{c0}, as a function of four dimensionless groups. These are the released energy ϵ_0, a dimensionless heat transfer coefficient Bi, the aspect ratio $2a/d$, and the conductivity ratio k_x/k_y. Although the parameter r contains both of the latter two groups, it cannot account by itself for their influence, which agrees with the results of a dimensional analysis.

Due to the symmetry of the problem, this analysis yields identical results for a superconducting film of thickness $d/2$ with one adiabatic surface, which approximates the case of a film deposited on a substrate and directly immersed in a cryogenic coolant, as envisoned for electronics applications.

If it becomes possible to manufacture thicker oriented layers of high-temperature superconductors, then this analysis is also relevant to the strip superconductor proposed recently by Ogasawara (1987), in which a superconducting strip is sandwiched between two copper bands. Recently, Tien et al. (1988) studied this problem, analyzing the combined influence of anisotropy and different superconducting materials.

Numerical Solution

Due to symmetry, it suffices to consider the region $\xi>0$, $\eta>0$ and to prescribe adiabatic boundary conditions at the planes of symmetry. The rectangular grid is given by $\xi=(m-1/2)\Delta\xi$, $\eta=(n-1/2)\Delta\eta$, with $\Delta\xi=r/M$, $\Delta\eta=1/N$. A finite-difference scheme that is forward in time and central in space (Press et al., 1986) yields an explicit expression for the new node temperature

$$\theta^{t+1}_{m,n}=\theta^t_{m,n}[1-2\mathrm{Fo}(1+R^2)]+\mathrm{Fo}[R^2(\theta^t_{m+1,n}+\theta_{m-1,n})+\theta^t_{m,n+1}+\theta^t_{m,n-1}] \tag{21}$$

$$\mathrm{Fo}=\frac{\Delta\tau}{(\Delta\eta)^2},\qquad R=\frac{\Delta\eta}{\Delta\xi} \tag{22}$$

which leads to the numerical stability requirement

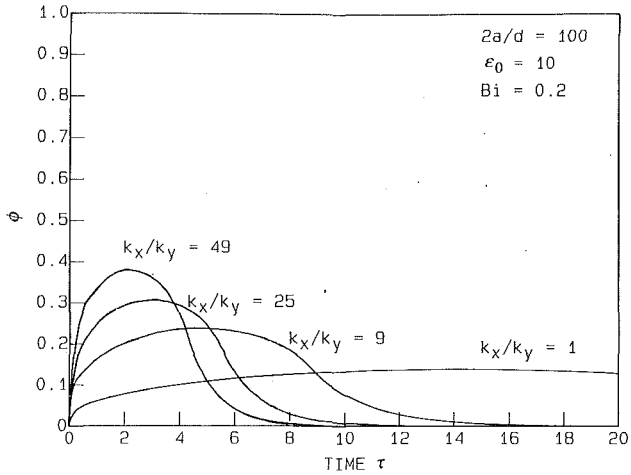

Fig. 4 Influence of anisotropy on the time dependence of ϕ

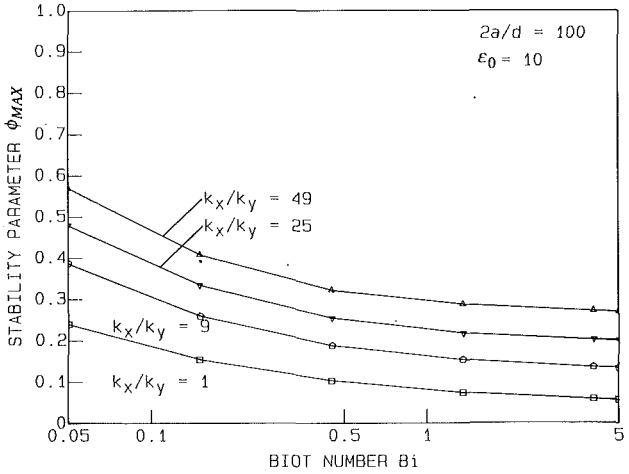

Fig. 6 Influence of anisotropy on the relation ϕ_{max} versus Bi

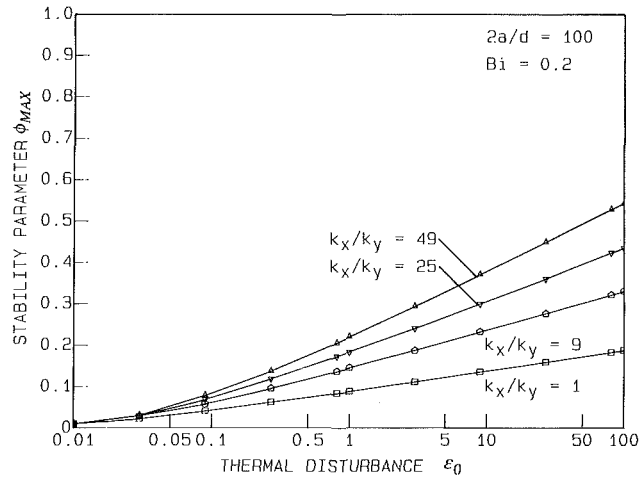

Fig. 5 Influence of anisotropy on the relation ϕ_{max} versus ϵ_0

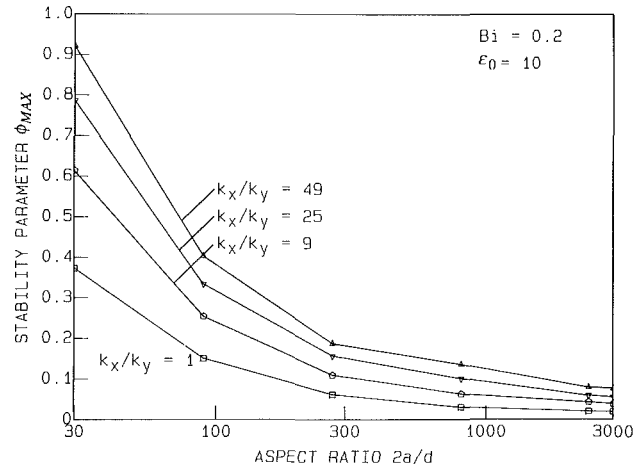

Fig. 7 Influence of anisotropy on the relation ϕ_{max} versus 2a/d

$$\mathrm{Fo} < \frac{1}{2(1+R^2)} \tag{23}$$

The boundary conditions are incorporated by introducing additional layers of material (Grigull and Sandner, 1984) to which are assigned the node numbers $m=0$, $n=0$, $m=M+1$, $n=N+1$, yielding the relations

$$\theta^t_{0,n} = \theta^t_{1,n}, \qquad \theta^t_{m,0} = \theta^t_{m,1} \tag{24}$$

$$\theta^t_{M+1,n} = \frac{2-\Delta\xi \mathrm{Bi}}{2+\Delta\xi \mathrm{Bi}}\theta^t_{M,n} \tag{25}$$

$$\theta^t_{m,N+1} = \frac{2-\Delta\eta(k_x/k_y)^{1/2}\mathrm{Bi}}{2+\Delta\eta(k_x/k_y)^{1/2}\mathrm{Bi}}\theta^t_{m,N} \tag{26}$$

The requirement that no negative terms appear in equation (21) results in three additional numerical stability requirements due to the boundary conditions. To ensure stability, the algorithm takes Fo to be 90 percent of the lowest value given by the four stability requirements.

The relation for the intrinsic stability parameter becomes

$$\phi_{\max} = \left[\frac{1}{MN}\sum_{m=1}^{M}\sum_{n=1}^{N} g^t_{m,n}\right]_{\max} \tag{27}$$

$$g^t_{m,n} = \begin{cases} 1 & \text{for } \theta^t_{m,n} \geq 1 \\ \theta^t_{m,n} & \text{for } \theta^t_{m,n} < 1 \end{cases} \tag{28}$$

To facilitate the numerical solution, the initial condition of a line source, equations (17) and (18), is approximated by a deposition of thermal energy in an area $4\Delta\xi\Delta\eta$ around the origin. The uniform temperature assumed in this small area is initially assigned to the node (1, 1)

$$\theta^0_{m,n} = \begin{cases} \dfrac{\epsilon_0 r}{\Delta\xi\Delta\eta} & \text{for } m=n=1 \\ 0 & \text{for } m\neq 1 \text{ or } n\neq 1 \end{cases} \tag{29}$$

Results and Discussion

A variable grid was used to speed up the computations. Figures 4 to 6 were produced with $R=0.1$, and Fig. 7 was generated with $R=0.1(k_x/k_y)^{1/2}$, which ensured consistency of the base-case solutions. The number of nodes in the η direction was kept constant at $N=10$. The base case for the computations was selected with $2a/d=100$ and $\epsilon_0=10$. If $(k_xk_y)^{1/2}$ is taken as a rough measure of the thermal conductivity of a bulk sample, this value can be estimated from the measurements of Morelli et al. (1987) as 0.5 W/mK. For a film of thickness $d=4$ μm and a cryogenic heat transfer coefficient of $h=5\times10^4$ W/m^{2}K, the base case Biot number becomes Bi = 0.2.

Figure 4 shows the time dependence of ϕ for different conductivity ratios k_x/k_y. If $r>>1$, then even at small times, the diffusion front reaches the boundary at $y=\pm d/2$ where

energy is transferred to the coolant. However, in the x direction the energy is confined to a narrow region around $x=0$ and does not influence the critical current density in the rest of the cross section. At very large times, most of the energy released initially has been lost across the wide faces, and the reduction of the integral critical current density is small. Hence ϕ assumes a maximum value for average times. Anisotropy strongly influences the evolution of ϕ with time. Increasing values of k_x/k_y shorten the transient and lead to higher values of the stability parameter $\phi_{\max}$, thus reducing the intrinsically stable operating fraction of the critical current density. The parameter r varies from 14 for $k_x/k_y=49$ to 100 for $k_x/k_y=1$. Clearly a higher value of r is beneficial for stability.

Figure 5 displays the influence of the conductivity ratio on the stability relation $\phi_{\max}$ versus ϵ_0. The value of ϵ_0 spans four orders of magnitude to cover a wide spectrum of thermal disturbances. Higher values of the released energy yield higher values of $\phi_{\max}$. High values of the conductivity ratio strongly increase the magnitude of the stability parameter, adversely affecting the instrinsic thermal stability.

It is seen in Fig. 6 that higher values of Bi greatly reduce $\phi_{\max}$, which is favorable for stability. Again, the strong influence of anisotropy on the intrinsic thermal stability is obvious. For large Bi, the curves indicate an asymptotic behavior. No matter how good the lateral heat transfer is, there is still a finite maximum reduction of the integral critical current density. Figure 7 shows the combined influence of the aspect ratio and the conductivity ratio on the stability parameter. High aspect ratios lead to high values of r and positively influence the stability of the superconductor, an important design consideration. For very small values of the aspect ratio, $2a/d<30$, the stability parameter $\phi_{\max}$ becomes equal to unity for high conductivity ratios, implying that in these cases the superconductor cannot carry any current in a stable manner. For $2a/d\rightarrow\infty$, $\phi_{\max}$ approaches zero, which means that the superconductor can operate at a current $I_0=J_{c0}2ad$ in a stable manner.

Concluding Remarks

The ratio of the thermal conductivities parallel and normal to the film greatly influences the intrinsic thermal stability of a thin-film superconductor. High values of this parameter are detrimental to the stability. High aspect ratios and high lateral heat transfer coefficients increase the operating fraction of the critical current density for which the superconductor is intrinsically stable. Increasing magnitudes of the released energy reduce the minimum integral critical current density and adversely affect the stability.

The criterion for intrinsic thermal stability introduced in this study is a valuable tool to transform information on the thermal disturbance spectrum into design criteria for thin-film superconductors. In applications of highly oriented films of ceramic high-temperature superconductors, the influence of anisotropic thermal conductivity on the operating performance can be substantial and must be considered. At present, there are no experimental data on the intrinsic thermal stability of thin-film superconductors. If the present criterion is applied to scanning electron microscopy of superconducting films, then it will yield stability limits for the electron beam power and the bias current. It appears feasible to verify these predictions experimentally by increasing bias current and beam power beyond these limits.

References

Bejan, A., and Tien, C. L., 1978, "Effect of Axial Conduction and Metal-Helium Heat Transfer on the Local Thermal Stability of Superconducting Composite Media," *Cryogenics*, Vol. 18, pp. 433–441.

Butera, R. A., 1988, "High-Resolution Heat Capacity of $YBa_2Cu_3O_{6.9}$ Over the Superconducting Transition Region," *Phys. Rev. B*, Vol. 37, pp. 5909–5911.

Fisher, H. E., Watson, S. K., and Cahill, D. G., 1988, "Specific Heat, Thermal Conductivity and Electrical Resistivity of High Temperature Superconductors," *Comments on Condensed Matter Physics*, Vol. 14, pp. 65–127.

Geballe, T. H., and Hulm, J. K., 1988, "Superconductivity—The State That Came in From the Cold," *Science*, Vol. 239, pp. 367–375.

Graebner, J. E., Schneemeyer, L. F., Cava, R. J., Waszczak, J. K., and Rietmann, E. A., 1988, "Thermal Conductivity of Single-Crystal and Sintered $RBa_2Cu_3O_7$ at Low Temperatures," *Mat. Res. Soc. Proc.*, Vol. 99, pp. 745–748.

Grigull, U., and Sandner, H., 1984, *Heat Conduction*, Springer-Verlag, New York.

Heremans, J., Morelli, D. T., Smith, G. W., and Strite III, S. C., 1988, "Thermal and Electronic Properties of Rare-Earth $Ba_2Cu_3O_x$ Superconductors," *Phys. Rev. B*, Vol. 37, pp. 1604–1610.

Huebener, R. P., Gross, R., and Bosch, J., 1988, "Low-Temperature Scanning Electron Microscopy for Studying Inhomogeneities in Thin-Film High-T_c Superconductors," *Z. Phys. B*, Vol. 70, pp. 425–430.

Maddock, B. J., James, G. B., and Norris, W. T., 1969, "Superconductive Composites: Heat Transfer and Steady-State Stabilization," *Cryogenics*, Vol. 9, pp. 261–273.

Morelli, D. T., Heremans, J., and Swets, D. E., 1987, "Thermal Conductivity of Superconductive Y–Ba–Cu–O," *Phys. Rev. B*, Vol. 36, pp. 3917–3919.

Newhouse, V. L., 1964, *Applied Superconductivity*, Wiley, New York.

Nye, J. F., 1985, *Physical Properties of Crystals*, Clarendon Press, Oxford, United Kingdom.

Ogasawara, T., 1987, "Feasibility Study on Large-Scale, High Current Density Superconductor by Dynamic Stabilization. Part 1: Magnetic Stability. Part 2: Stability Margin," *Cryogenics*, Vol. 27, pp. 673–681.

Özişik, M. N., 1980, *Heat Conduction*, Wiley, New York, Chap. 15.

Press, W. H., Flannery, B. P., Teukolsky, S. A., and Vetterling, W. T., 1986, *Numerical Recipes*, Cambridge University Press, Cambridge, United Kingdom.

Stekly, Z. J. J., and Zar, J. L., 1965, "Stable Superconducting Coils," *IEEE Transactions on Nuclear Science*, Vol. 12, No. 3, pp. 367–372.

Tien, C. L., Flik, M. I., and Phelan, P. E., 1989, "Mechanisms of Local Thermal Stability of High-Temperature Superconductors," *Cryogenics*, Vol. 29, pp. 602–609.

Torardi, C. C., Subramanian, M. A., Calabrese, J. C., Gopalakrishnan, J., Morrissey, K. J., Askew, T. R., Flippen, R. B., Chowdhry, U., and Sleight, A. W., 1988, "Crystal Structure of $Tl_2Ba_2Ca_2Cu_3O_{10}$, a 125 K Superconductor," *Science*, Vol. 240, pp. 631–634.

Uher, C., and Kaiser, A. B., 1987, "Thermal Transport Properties of $YBa_2Cu_3O_7$ Superconductors," *Phys. Rev. B*, Vol. 36, pp. 5680–5683.

Wilson, M. N., 1983, *Superconducting Magnets*, Clarendon Press, Oxford, United Kingdom.

Zhang, K., Bunker, G. B., Zhang, G., Zhao, Z. X., Chen, L. Q., and Huang, Y. Z., 1988, "Extended X-Ray Absorption Fine-Structure Experiment on the High-T_c Superconductor $YBa_2Cu_3O_{7-\delta}$," *Phys. Rev. B*, Vol. 37, pp. 3375–3380.

Steady-State Temperatures in an Anisotropic Strip

Zhang Xiangzhou

Department of Aircraft Engineering,
Northwestern Polytechnical University,
Xian, 710072 People's Republic of China

This article deals with the development of a rigorous solution to the steady-state temperature in an anisotropic strip. The solution is given with respect to a coordinate system (x, y), which conforms with the strip geometry but does not necessarily coincide with the principal directions of the anisotropic material. Using a partitioning–matching technique and the separation of variables method, exact expressions are obtained for temperatures in the strip under prescribed boundary temperature conditions. Numerical values of the temperatures and heat flux are provided in graphic form. Also, a discussion is presented regarding the solution method and the temperature distribution features in the heat conduction problem of an anisotropic medium.

Introduction

The ever-growing application of composite materials in engineering practice has encouraged the development of the science and engineering of heat conduction in anisotropic media since the middle of this century. This fact has been manifested in that a number of standard monographs (Carslaw and Jaeger, 1959; Ozisik, 1980) have devoted a considerable portion of their contents to the treatment of conduction of heat in anisotropic bodies. Also, many technical reports concerning the design and application aspects of the subject have appeared in various technical publications during that period. However, to form and develop a subject of heat transfer science one needs not merely theoretical foundations and application techniques but also substantial solutions to basic problems of fundamental interest. In this aspect, it seems that only a few such solutions have sporadically appeared in reference books and much more work remains to be done.

This article discusses the rigorous solution to a fundamental problem of heat conduction in anisotropic solids: to find the steady-state temperature $T(x_1, y_1)$ in an anisotropic strip depicted in Fig. 1 with prescribed temperature on its boundary. This problem can be formulated via the following equation of heat balance and boundary conditions (Ozisik, 1980):

$$k_{11}\frac{\partial^2 T}{\partial x_1^2}+2k_{12}\frac{\partial^2 T}{\partial x_1 \partial y_1}+k_{22}\frac{\partial^2 T}{\partial y_1^2}=0 \tag{1}$$

$$y_1=0, \quad |x_1|<L_1, \quad T=v_1(x_1) \tag{2a}$$

$$y_1=0, \quad |x_1|>L_1, \quad T=0 \tag{2b}$$

$$y_1=h, \quad |x_1|<L_1, \quad T=v_2(x_1) \tag{3a}$$

$$y_1=h, \quad |x_1|>L_1, \quad T=0 \tag{3b}$$

$$|x_1|\to\infty, \; T\to 0 \tag{4}$$

Two basic approaches can be used to solve the problem. In the first approach, the original rectangular coordinates as shown in Fig. 1 are transformed onto the principal axes of the anisotropic material to eliminate the cross term $\partial^2 T/\partial x_1 \partial y_1$ in equation (1). This is followed by a simple substitution used to express the transformed equation (1) by the standard form of a Laplace equation. Simultaneously the two straight boundaries of the strip become slanted to the transformed axes. Therefore, in this way, we will obtain a simpler equation of heat balance together with more complicated boundary conditions. The numerical values of the temperature can then easily be obtained by using, for instance, some universal finite element programs (Zienkiewicz, 1977) or available boundary element formulations (Wrobel and Brebbia, 1981). On the other hand, on account of the irregularity of the transformed strip geometry with respect to the coordinate axes, the reduced problem is not readily amenable to conventional analytic techniques and some approximate analytic method must be used. In either case the fundamental effect of the anisotropy on the temperature distribution may be smeared out or even distorted due both to the exotic geometry of the transformed strip and the approximation of the numerical evaluation.

In the second approach, the strip is kept parallel to the x_1 axis and the problem is solved directly from equations (1)–(4). In case an exact solution can be developed in this way, it will completely contain the basic nature of anisotropy of the problem, and how the material anisotropy affects the temperature distribution can be examined with confidence. In addition, the cross term $\partial^2 T/\partial x_1 \partial y_1$, which is the crux in solving equation (1), is very difficult to treat when one uses solution techniques conventional for solving isotropic heat conduction problems. Therefore a direct attack on this term would be of interest.

An outline of this paper is now given. Following the second approach, we solve the problem of concern with the use of a partitioning-matching technique and the separation of variables method for prescribed temperature boundary conditions. The former technique is specially devised for treating the present problem. Exact formulae for the temperatures are obtained and related numerical values of temperatures and heat flux are provided in graphic form. Finally, a discussion is presented to indicate some basic features regarding the solution method and the temperature distribution pattern and other aspects pertaining to the heat conduction problem of an anisotropic medium.

Steady-State Temperatures Under Prescribed Boundary Temperatures

Consider again the anisotropic strip shown in Fig. 1. It is

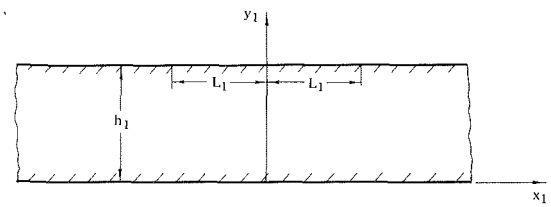

Fig. 1 The anisotropic strip

Contributed by the Heat Transfer Division for publication in the JOURNAL OF HEAT TRANSFER. Manuscript received by the Heat Transfer Division February 25, 1988; revision received June 25, 1989. Keywords: Conduction.

now required to determine the temperature of the strip subject to the basic equation (1) and the boundary conditions (2)–(4). As an essential preliminary step a basic problem specified by $v_1(x_1)=0$, $v_2(x_1)=\cos cx_1$ in boundary conditions (2*a*) and (3*a*) is in the first instance to be considered. With the substitutions $x=x_1$, $y=\sqrt{k_{11}/k_{22}}\,y_1$, $N=2k_{12}/\sqrt{k_{11}k_{22}}$, equation (1) and boundary conditions (2)–(4) are reduced to

$$\frac{\partial^2 T}{\partial x^2}+N\frac{\partial^2 T}{\partial x\partial y}+\frac{\partial^2 T}{\partial y^2}=0 \tag{5}$$

$$y=0,\quad T=0 \tag{6}$$

$$y=h,\quad T=\begin{cases}0, & x<-L, \quad (7a)\\ \cos cx, & -L<x<L, \quad (7b)\\ 0, & x>L, \quad (7c)\end{cases}$$

$$|x|\to\infty,\ T\to 0, \tag{8}$$

where $L=L_1$, $h=\sqrt{k_{11}/k_{22}}\,h_1$.

For the sake of solving the above equations, the separation of variables method is now used to write the general solution of differential equation (5) in the form

$$T(x,y)=e^{mx}p(y) \tag{9}$$

Substituting equation (9) into equation (5) results in

$$p''(y)+Nmp'(y)+m^2p(y)=0 \tag{10}$$

The above ordinary differential equation can be solved straightforwardly (Courant and Hilbert, 1953) to obtain

$$T(x,y)=e^{m(x-Ny/2)}(Ae^{imay/2}+Be^{-imay/2}), \tag{11}$$

where $a=\sqrt{4-N^2}$. Either $4-N^2>0$ or $4-N^2\le 0$ is possible in mathematical formulation; however, from physical reasoning based on irreversible thermodynamics it can be shown that (Prigogine, 1961; Ozisik, 1980)

$$k_{11}k_{22}-k_{12}^2>0$$

in addition to k_{11}, $k_{22}>0$. Therefore the case $4-N^2\le 0$ is impossible in a real physical process and only the situation where $4-N^2>0$ or $a>0$ will be considered in the further development.

By suitable choice of the constants m, A, and B, and using some basic formulae in the theory of a complex variable (Macrobert, 1954), $T(x, y)$ can be expressed by the following elementary functions such as

$$T(x,y)=e^{m(x-Ny/2)}\sin(may/2),\ e^{m(x-Ny/2)}\cos(may/2),$$
$$\sinh(may/2)\cos m(x-Ny/2),\ \ldots \tag{12}$$

and so on. These functions will be used to construct a rigorous solution to the problem.

The boundary temperature on $y=h$ is discontinuous at the points $A(-L, h)$ and $B(L, h)$. In view of this, the strip is partitioned into three regions via the interfaces AC and BD (Fig. 2). Preliminary solutions of the steady-state temperature,

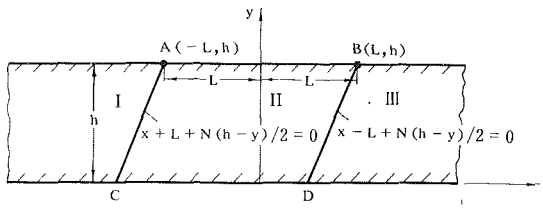

Fig. 2 The transformed and partitioned strip

which satisfy the boundary conditions of the strip, are first proposed respectively for these regions. However, since the temperature and the heat flux should be continuous across the interfaces, as a second step, the preliminary solutions are matched along AC and BD to determine the final and exact form of the steady-state temperature solution.

Partitioning of the Strip. Various curves passing through points A and B can be used as interfaces. However, the segments AC and BD are most suitable for the purpose. In fact, on these segments all elementary temperature solutions as contained in equation (12) are functions of a single variable y; therefore, the matching process can be carried out straightforwardly.

Matching on the Interfaces. Making use of the elementary solutions in equation (12), the preliminary temperature solutions can readily be proposed respectively for regions, I, II, and III as follows:

In region I,

$$T_1(x,y)=\sum_{n=1}^{\infty}A_ne^{2n\pi[x+L+N(h-y)/2]/ah}\sin(n\pi y/h)+\sum_{n=1}^{\infty}B_ne^{2n\pi[x-L+N(h-y)/2]/ah}\sin(n\pi y/h) \tag{13}$$

In region II,

$$T_{II}(x,y)=\sinh(acy/2)\cos c(x+Nh/2-Ny/2)/\sinh(ach/2)+\sum_{n=1}^{\infty}C_ne^{2n\pi[x-L+N(h-y)/2]/ah}\sin(n\pi y/h)+\sum_{n=1}^{\infty}D_ne^{-2n\pi[x+L+N(h-y)/2]/ah}\sin(n\pi y/h) \tag{14}$$

In region III,

$$T_1(x,y)=\sum_{n=1}^{\infty}A_ne^{2n\pi[x+L+N(h-y)/2]/ah}\sin(n\pi y/h)+\sum_{n=1}^{\infty}F_ne^{-2n\pi[x+L+N(h-y)/2]/ah}\sin(n\pi y/h). \tag{15}$$

Nomenclature

a_n = constant coefficient
A = constant
A_n = constant coefficient
b_n = constant coefficient
B = constant
B_n = constant coefficient
c = constant
C_n = constant coefficient
D_n = constant coefficient
E_n = constant coefficient
F_n = constant coefficient
f_x = heat flux in the x direction
f_y = heat flux in the y direction
f_z = heat flux in the z direction
h = dimension of the strip in (x, y) coordinates
h_1 = dimension of the strip in (x_1, y_1) coordinates
i = unit imaginary number
k_{ij} = component of thermal conductivity of an anisotropic solid in two-dimensional temperature problem
k'_{ij} = component of thermal conductivity of an anisotropic solid in two-dimensional heat flow problem
L = boundary temperature range in (x, y) coordinates
L_1 = boundary temperature range in (x_1, y_1) coordinates
m = real, imaginary, or complex number
$v_1(x_1)$ = boundary temperature
$v_2(x_1)$ = boundary temperature
x, y, z = rectangular coordinates
x_1, y_1 = rectangular coordinates

$T_I(x, y)$ satisfies the boundary conditions of the strip in region I (equations (6), (7*a*), and (8)), but does not necessarily satisfy the boundary conditions in regions II and III. Similar remarks apply to $T_{II}(x, y)$ and $T_{III}(x, y)$. To determine the unknown constants A_n, B_n, ... in equations (13)–(15) and to make T_I, T_{II}, and T_{III} a valid and exact temperature solution over the whole strip, matching between T_I, T_{II}, and T_{III} should be carried out along the interfaces on the basis of temperature and heat flux continuation; that is, the following conditions apply:

$$\text{on } AC \qquad T_I = T_{II} \tag{16a}$$

$$\frac{\partial T_I}{\partial x} = \frac{\partial T_{II}}{\partial x} \tag{16b}$$

$$\text{on } BD \qquad T_{II} = T_{III} \tag{17a}$$

$$\frac{\partial T_{II}}{\partial x} = \frac{\partial T_{III}}{\partial x} \tag{17b}$$

Note that in the equations (16*b*) and (17*b*) the heat flux continuation conditions have been written in a simplified form. This is due to the fact that the continuation of the temperature gradients along the AC and BD directions has already been satisfied in view of equations (16*a*) and (17*a*).

Expanding $\sinh(acy/2)$ in the following form:

$$\sinh(acy/2) = 8\pi \sinh(ach/2) \sum_{n=1}^{\infty} \frac{(-1)^{n+1} n}{(ach)^2 + (2n\pi)^2} \sin \frac{n\pi y}{h}$$

and using equations (16*a*) and (16*b*) (matching on AC), the following result is obtained:

$$B_n = C_n \tag{18a}$$

$$A_n = f_n \tag{18b}$$

$$D_n = g_n \tag{18c}$$

where

$$f_n = (-1)^{n+1} 2(2n\pi \cos cL/ah + c \sin cL)/ah(c^2 + 4n^2\pi^2/a^2h^2)$$

$$g_n = (-1)^n 2(2n\pi \cos cL/ah - c \sin cL)/ah(c^2 + 4n^2\pi^2/a^2h^2)$$

Similarly, on using equations (17*a*) and (17*b*) (matching on BD) the remaining unknowns turn out to be

$$F_n = D_n = g_n \tag{19a}$$

$$C_n = g_n \tag{19b}$$

$$E_n = f_n \tag{19c}$$

Combining the above formulae, the final, rigorous steady-state temperature solution for the strip can be written as follows:

In region I,

$$T(x, y) = \sum_{n=1}^{\infty} (f_n e^{2n\pi[x+L+N(h-y)/2]/ah} + g_n e^{2n\pi[x-L+N(h-y)/2]/ah}) \sin(n\pi y/h), \tag{20a}$$

In region II,

$$T(x, y) = \sinh(acy/2) \cos c(x + Nh/2 - Ny/2)/\sinh(ach/2) + \sum_{n=1}^{\infty} g_n (e^{2n\pi[x-L+N(h-y)/2]/ah} + e^{-2n\pi[x+L+N(h-y)/2]/ah}) \sin(n\pi y/h) \tag{20b}$$

In region III,

$$T(x, y) = \sum_{n=1}^{\infty} (f_n e^{-2n\pi[x-L+N(h-y)/2]/ah} + g_n e^{-2n\pi[x+L+N(h-y)/2]/ah}) \sin(n\pi y/h) \tag{20c}$$

Next consider the case when the boundary of the strip on $y = h$, $|x| < L$ is under the action of a prescribed temperature of the type $T(x, h) = \sin cx$, that is, when boundary condition (7*b*) is replaced by

$$y = h, \ |x| < L, \ T = \sin cx, \tag{21}$$

whereas other related equations remain unchanged. This problem can be solved with use of a procedure similar to that described above. The final results are:

In region I,

$$T(x, y) = -\sum_{n=1}^{\infty} (q_n e^{2n\pi[x-L+N(h-y)/2]/ah} + l_n e^{2n\pi[x+L+N(h-y)/2]/ah}) \sin(n\pi y/h) \tag{22a}$$

In region II,

$$T(x, y) = \sinh(acy/2) \sin c(x + Nh/2 - Ny/2)/\sinh(ach/2) + \sum_{n=1}^{\infty} q_n (e^{-2n\pi[x+L+N(h-y)/2]/ah} - e^{2n\pi[x-L+N(h-y)/2]/ah}) \sin/(n\pi y/h) \tag{22b}$$

In region III,

$$T(x, y) = \sum_{n=1}^{\infty} (q_n e^{-2n\pi[x+L+N(h-y)/2]/ah} + l_n e^{-2n\pi[x-L+N(h-y)/2]/ah}) \sin(n\pi y/h) \tag{22c}$$

where

$$q_n = (-1)^{n+1} 2(2n\pi \sin cL/ah + c \cos cL)/ah(c^2 + 4n^2\pi^2/a^2h^2)$$

$$l_n = (-1)^{n+1} 2(2n\pi \sin cL/ah - c \cos cL)/ah/c^2 + 4n^2\pi^2/a^2h^2)$$

Now consider the general case when $T(x, h)$ in equation (7*b*) stands for an arbitrary function of x. It is well known that any regular function $T(x, h)$ defined in the interval $(-L, L)$ can be expanded into a trigonometric series such as

$$T(x, h) = a_0 + \sum_{n=1}^{\infty} \left(a_n \cos \frac{n\pi x}{L} + b_n \sin \frac{n\pi x}{L}\right)$$

so that if the boundary $y = h$, $|x| < L$ is kept under a form of prescribed temperature other than $\cos cx$ or $\sin cx$, the solution can be obtained by combining solutions of type (20) and (22) by inserting $n\pi/L$ ($n = 0, 1, 2, \ldots$) for c into corresponding equations. Also, in case a certain form of prescribed temperature is assigned to the side $y = 0$ in place of $y = h$, the temperature solution can similarly be worked out following the procedure described above. The general solution for both sides $y = 0$ and $y = h$ being under prescribed temperatures can therefore be obtained by superposition.

Numerical Results and Discussion

Effective Range of the Solutions. All the solutions developed in the preceding section are based on the equation of heat balance of the form of equation (5), which applied directly to the situation when the temperature in the strip does not depend on z, that is, $\partial T/\partial z$ vanishes (Carslaw and Jaeger, 1959; Ozisik, 1980). Another case of interest is that where there is no heat flux in the z direction, that is, $f_z = 0$ holds over the strip. Under such a circumstance it is known (Carslaw and Jaeger, 1959) that the heat flux in the strip can be expressed by

$$f_x = -k'_{11} \frac{\partial T}{\partial x} - k'_{12} \frac{\partial T}{\partial y} \tag{23a}$$

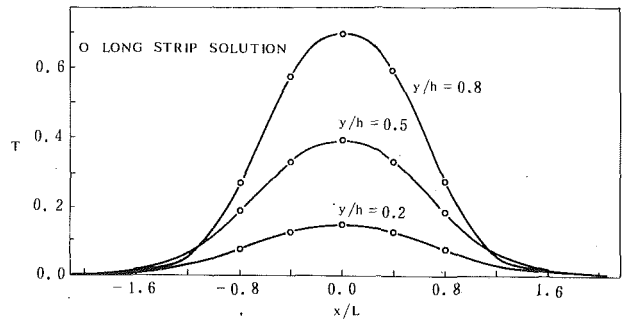

Fig. 3 Temperature distribution in longitudinal sections ($N = 0.0$, $c = \pi/2L$, $L = h = 1.0$)

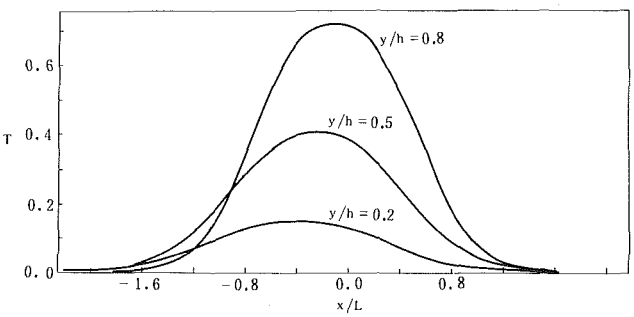

Fig. 4 Temperature distribution in longitudinal sections ($N = 1.0$, $c = \pi/2L$, $L = h = 1.0$)

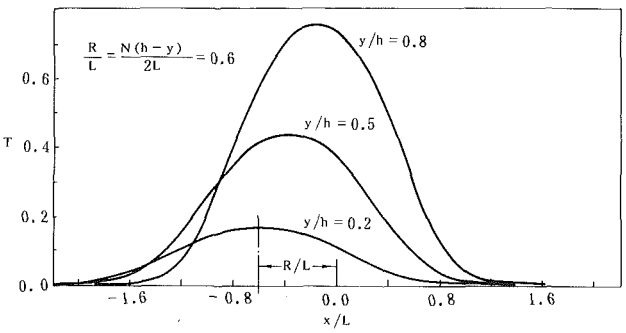

Fig. 5 Temperature distribution in longitudinal sections ($N = 1.5$, $c = \pi/2L$, $L = h = 1.0$)

$$f_y = -k'_{21}\frac{\partial T}{\partial x} - k'_{22}\frac{\partial T}{\partial y} \tag{23b}$$

and the equation of heat balance takes the following form:

$$k'_{11}\frac{\partial^2 T}{\partial x^2} + (k'_{12}+k'_{21})\frac{\partial^2 T}{\partial x \partial y} + k'_{22}\frac{\partial^2 T}{\partial y^2} = 0 \tag{24}$$

where

$$k'_{ij} = (k_{ij}k_{33} - k_{i3}k_{j3})/k_{33}, \qquad i, j = 1, 2 \tag{25}$$

Equation (24) is of the same form as that of equation (5). Besides, it is easy to see that

$$k'_{12} = k'_{21},\ k'_{11},\ k'_{22} > 0$$

on account of equation (25). Furthermore,

$$k'_{11}k'_{22} - k'^2_{12} = \frac{1}{k_{33}} \begin{vmatrix} k_{11} & k_{12} & k_{13} \\ k_{12} & k_{22} & k_{23} \\ k_{13} & k_{23} & k_{33} \end{vmatrix} > 0$$

since the above determinant is positive definite due to the fact that each of its major cofactors is positive. This gives

$$k'_{11}k'_{22} > k'^2_{12}$$

Therefore, the coefficients contained in equation (24) possess the same properties as those possessed by k_{ij}. It is then seen that the two problems are identical to each other in mathematical formulation and the solutions developed in the preceding sections can also be applied to the two-dimensional heat flow problem provided the coefficients in the preceding solutions, k_{ij} are replaced by k'_{ij} pertaining to the latter development.

Numerical Values of Temperatures. Using the exact solutions developed in the preceding section in conjunction with a microcomputer, accurate numerical data of temperatures can be obtained via a short computer program in a few minutes. In Figs. 3–5, numerical values of temperatures in the case when the boundary $y = h$, $|x| < L$ is under prescribed temperature of the type $\cos cx$, $c = \pi/2L$ are presented in graphic form for three different values of N, the principal aniostropy factor.

These numerical data have been obtained using 20 terms in the series solution (20*a*), (20*b*), and (20*c*). Comparing them with those obtained by using more (30) terms in the series shows that the data based on 20 terms have been exact to the first four significant figures. This fact manifests the good convergence behavior of the series solution.

When the strip under consideration is replaced by a strip of finite but very large length, the temperature in the central part of the strip will remain virtually unchanged. For the particular case of isotropy, the exact solution for a long strip (i.e., a narrow rectangle) is available from Carslaw and Jaeger (1959). Temperature values from the solution of Carslaw and Jaeger have been computed for a long strip of length $10L$ (see Fig. 2) and shown in Fig. 3. The agreement between the two solutions demonstrates the validity of the present solution (20*a*), (20*b*), and (20*c*).

Temperature Distribution. Figures 3–5 show the temperature distributions across the longitudinal cross sections of the strip at $y = h/5$, $h/2$, and $4h/5$, respectively. For $N = 0$, that is, the isotropic case, as expected the temperature distribution is symmetric with respect to the y axis, since both the strip geometry and the boundary temperature are symmetric to that axis. For nonvanishing values of N, this symmetry is distorted by the effect of the anisotropy of the conductive material. It can be seen that the temperature distributions are no longer symmetric to the y axis but to some other vertical lines off the y axis. An examination of equations (20*a*), (20*b*), and (20*c*) shows that the off y axis distance equals $N(h-y)/2$, as indicated for a particular case in Fig. 5.

Boundary Heat Flux Distribution. It is of interest to examine heat flux distribution on the boundaries $y = 0$, h, which can be computed from the following formula:

$$f_y = -\sqrt{k_{11}k_{22}}\left(\frac{\partial T}{\partial y} + \frac{N}{2}\frac{\partial T}{\partial x}\right) \tag{26}$$

and equations (20*a*), (20*b*), and (20*c*). The numerical result, also for the prescribed boundary temperature of type $\cos cx$ is shown in Figs. 6 and 7. Note that in Fig. 7 there are two very sharp cusps at $x = -L$ and $x = L$ on the heat flux curve, since the temperature gradient in the x direction discontinues at these points. The ordinate of the cusps is -2.066, which is not shown in the figure.

The boundary condition (8) implies that $f_x = 0$ for $|x| \to \infty$. Therefore, the sum of the heat flow on the boundaries $y = 0$ and $y = h$ must be vanishing to ensure a steady state within the strip. The heat flux distribution shown in Figs. 6 and 7 confirms such a conclusion.

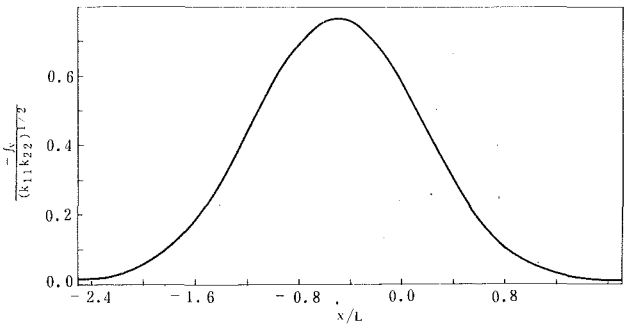

Fig. 6 Heat flux f_y on the boundary $y = 0$ ($N = 1.0$, $c = \pi/2L$, $L = h = 1.0$)

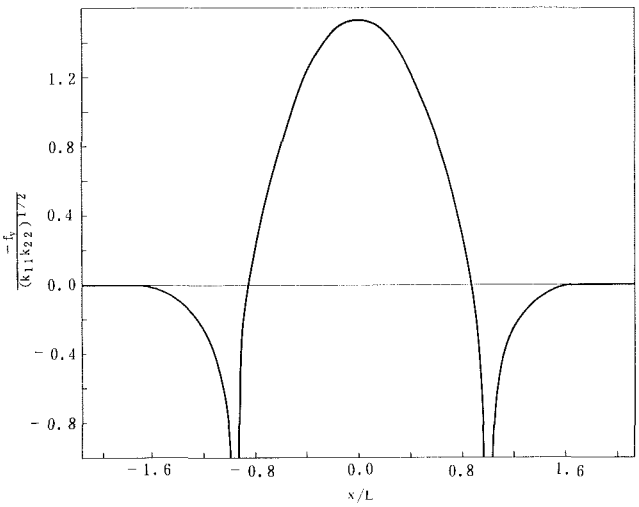

Fig. 7 Heat flux f_y on the boundary $y = h$ ($N = 1.0$, $c = \pi/2L$, $L = h = 1.0$)

Solution Method. To solve the problem of heat conduction in solids, separation of variables is a well-established method from which many classical problems of heat conduction have been developed. However, it cannot be used in a conventional manner to treat the geometry, anisotropy, and boundary conditions discussed in this paper. The partitioning–matching technique developed here effectively solved the problem. In fact, this technique extends the application range of the separation of variables method to a broader scope.

The Fourier integral transform and complex variable methods are also useful techniques for solving heat conduction problems of conductive bodies. Using these methods, steady-state temperatures in the anisotropic strip have also been worked out. The result is completely in agreement with that obtained in this paper.

Summary and Conclusions

Exact solutions are presented for steady-state temperatures in an anisotropic strip under two basic forms of prescribed temperature boundary conditions. The solutions are easy to handle in numerical computing. Solutions for other cases of boundary temperature distribution can be constructed from the basic solutions by superposition.

The solutions are obtained by the use of the separation of variables method and a partitioning–matching technique. The classical separation of variables method, in combination with the partitioning–matching technique, can be utilized to solve complicated problems in heat conduction that cannot be treated by the conventional method.

For an anisotropic strip under prescribed boundary temperatures symmetric to the y axis, the temperature in its longitudinal section ($y = y_0 = \text{const}$) will not be symmetric to the y axis, but to some other vertical lines off the y axis. The off y axis distance is found to vary linearly with y_0 for a definite anisotropic material.

It is found that the two-dimensional temperature and two-dimensional heat flow problems are identical to each other in mathematical formulation. Therefore, the solutions developed in this paper apply to both cases.

Acknowledgments

The author is grateful to Shen Kangzhi for his help in numerical computation. This work was supported in part by a grant from the State Education Commission of China.

References

Carslaw, H. S., and Jaeger, J. C., 1959, *Conduction of Heat in Solids*, Oxford University Press, London, United Kingdom.

Courant, R., and Hilbert, D., 1953, *Methods of Mathematical Physics*, Wiley, New York.

Macrobert, T. M., 1954, *Functions of a Complex Variable*, Macmillan, London, United Kingdom.

Ozisik, M. N., 1980, *Heat Conduction*, Wiley, New York.

Prigogine, I., 1961, *Thermodynamics of Irreversible Processes*, Wiley-Interscience, New York.

Wrobel, L. C., and Brebbia, C., 1981, "Boundary Elements in Thermal Problems," *Numerical Methods in Heat Transfer*, R. W. Lewis, ed., Wiley, Chichester, United Kingdom.

Zienkiewics, O. C., 1977, *Finite Element Methods*, McGraw-Hill, London, United Kingdom.

Thermal Shock Waves Induced by a Moving Crack

D. Y. Tzou
Assistant Professor,
Department of Mechanical Engineering,
University of New Mexico,
Albuquerque, NM 87131

The near-tip behavior of the thermal field around a moving crack is investigated analytically in this work. The thermal field is characterized by a thermal Mach number defined as the ratio between the linear speed v of the moving crack and the heat propagation speed C in the solid. Mathematically, $M = v/C$. In the subsonic range with $M < 1$, a detailed comparison with the thermal diffusion model is made. In the transonic and the supersonic ranges with $M \geq 1$, thermal shock waves, which separate the heat affected zone from the thermally undisturbed zone, are shown to exist in the physical domain. A swinging phenomenon for the temperature variation as a function of the thermal Mach number is found in transition from the subsonic to the supersonic ranges. Also, the r dependency of the near-tip temperature is found to be the same as that of the near-tip heat flux vector. It transits from $r^{1/2}$, r, to r^2 as the thermal Mach number transits from the subsonic, transonic, to the supersonic ranges.

Introduction

The merit of the thermal wave model (or hyperbolic theory of heat conduction) lies in its perspective in describing the thermal disturbance propagating with a finite speed in the solid. In applying such a theory, a general feature is that a distinct thermal wave front exists in the physical domain that separates, in the absence of reflecting waves, the heat-affected zone from the thermally undisturbed zone. This is a different situation from that in the thermal diffusion model where the heat propagation speed is assumed to be infinite such that the existence of a thermal agent (including heat sources or the initial/boundary conditions) at infinity can be detected right after its application.

The energy and constitutive equations in the hyperbolic theory of heat conduction are

$$-\nabla \cdot \mathbf{q} + S = \rho C_p T_{,t} \quad (\alpha/C^2)\mathbf{q}_{,t} + \mathbf{q} = -k\nabla T, \qquad (1)$$

with ρ being the density of the medium, k the thermal conductivity, C_P the heat capacity, S the body heat source, α the thermal diffusivity, and C the finite speed of heat propagation in the solid. Eliminating either temperature T or heat flux $\mathbf{q}$ from these equations, respectively, results in a field equation with flux ($\mathbf{q}$-) or temperature (T-) representations. An apparent heat source term containing the first-order derivative of S with respect to space in the $\mathbf{q}$- representation and that with respect to time in the T-representation will result.

The wave phenomena represented by equation (1) have been investigated from various physical points of view. These include, for example, a collision model established on the basis of statistical mechanics (Chester, 1963), identification of the analogy between the random walk and the diffusion processes (Weymann, 1967), modification of thermodynamics with memory (Gurtin and Pipkin, 1968), consideration of special relativity for the heat transport process (Kelley, 1968; Van Kampen, 1970), and an interpretation in terms of kinetic theory of molecules (Bobnov, 1976; Berkovsky and Bashtovoi, 1977). In these works, the limitations of the thermal diffusion model were also viewed from different angles. The mathematical structure of the field equations in the hyperbolic theroy of heat conduction was also investigated. In the absence of heat sources, propagation and reflection of thermal waves in one-dimensional media were investigated thoroughly (Boley, 1964; Baumeister and Hamill, 1969; Vick and Özişik, 1983; Özişik and Vick, 1984). Due to a complicated integral relationship between heat flux and temperature gradient in such a theory, Frankle et al. (1985) further showed that the $\mathbf{q}$-representation is more convenient to use than the T-representation for analysis involving specified heat flux conditions. A thermoelastic formulation incorporating the finite speed of heat propagation was made by Lord and Shulman (1967). Generally speaking, significant deviations between the diffusion and the wave models were found in these studies as the transient time is short or the operational temperature is low.

There is a class of problems dealing with impingement of a high-intensity energy source on the surface of a structure, which needs special consideration of the thermal wave model. For this type of problem, an extremely high temperature level is built up in the material continua adjacent to the energy source in a very short time, and the deviation between the two models is caused by the presence of large temperature gradients in the neighborhood of the heat source. Tzou (1989) showed that as the speed v of the moving heat source is equal to or faster than the heat propagation speed C in the solid, thermal shock waves will be formed in the physical domain that separate the heat affected zone from the thermally undisturbed zone. The temperature and the heat flux components (Tzou, 1988a) were shown to approach infinity in the vicinity of the thermal shock wave, which inclines an angle $\sin^{-1}$ (1/M), with M being introduced as the thermal Mach number and defined as v/C, to the trailing edge of the moving heat source. Consideration of the wave model becomes even more important if other irreversible physical processes, such as crack or void initiation in the solid, are involved in the process of heat transport. Under the application of an energy source with sufficiently high intensity (Tzou, 1988b), the local defects could be initiated in a much shorter time interval than that required for the diffusion behavior to be retrieved, and the orientation of crack initiation, for example, must be predicted according to the thermal wave model.

In the present study, we shall investigate another situation where geometric singularities are present in the physical domain, namely in the vicinity of a moving crack. We will show that as the speed of the moving crack tip is equal to or faster than that of the heat propagation in the solid, thermal shock waves will be formed in the physical domain that separate the heat-affected zone from the thermally undisturbed zone. We will also show analytically that the thermal shock angle is the same as that induced by a moving heat source. In both cases,

Contributed by the Heat Transfer Division for publication in the JOURNAL OF HEAT TRANSFER. Manuscript received by the Heat Transfer Division June 3, 1988. Keywords: Conduction.

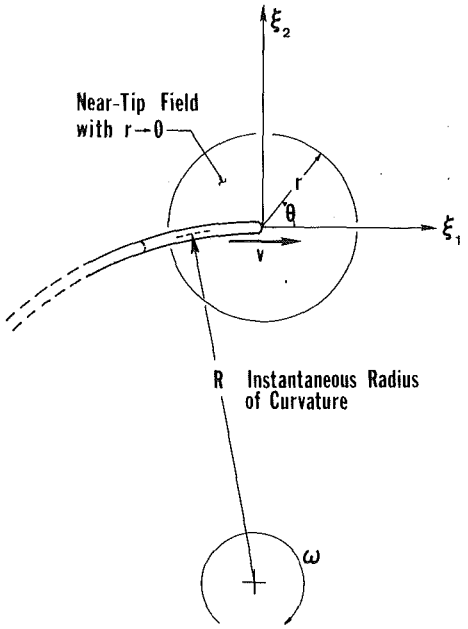

Fig. 1 Geometric configuration of a moving crack and the material coordinate system convecting with the crack tip

the angle is determined as $\sin^{-1}(1/M)$ with $M \geq 1$. In the immediate vicinity of the moving crack tip, the r-dependency of the temperature and the heat flux vector is found to be identical in the full range of the thermal Mach number. It transits respectively from $r^{1/2}$, r, to r^2 as the thermal Mach number transits from the subsonic, transonic, to the supersonic ranges. A thorough comparison with the thermal diffusion model is also made in the subsonic case with $M < 1$.

Formulation of the Problem

The T-representation of the energy equation in the thermal wave model can be obtained from equation (1) by eliminating $\mathbf{q}$

$$\alpha \nabla^2 T = (\alpha/C^2)T_{,tt} + T_{,t} \tag{1a}$$

On a moving coordinate system $\xi_i (i = 1, 2)$ such as that established at a moving heat source, Tzou (1988a, 1989) has shown that the quasi-stationary form of equation (1a) can be derived as

$$\alpha[(1-M^2)T_{,11} + T_{,22}] + 2c\alpha T_{,1} = -(Q/\rho C_p)\{S(\xi_i) - (M^2/2c)S_{,1}(\xi_i)\} \tag{1b}$$

Based upon this equation, the formation of the thermal shock wave and the thermally undisturbed zone in the physical domain for the transonic ($M = 1$)and the supersonic ($M > 1$) cases were discussed in great detail. Note also that equation (1b) changes from an elliptic, to parabolic, to a hyperbolic type as the thermal Mach number transits from the subsonic, transonic, to the supersonic regions.

Let us now consider a macrocrack propagating along a smooth but arbitrary trajectory in an infinite medium with finite speed of heat propagation, as shown in Fig. 1. The linear and angular velocities v and ω of the moving crack are assumed to be constant. In order to identify the same physical phenomenon as that induced by a moving heat source, we first establish equation (1a) on the moving coordinate system ξ_i centered at the crack tip. The terms containing derivatives with respect to time in equation (1a) must be replaced by material derivatives, i.e.,

$$T_{,t} \rightarrow T_{,t} - vT_{,1} - \omega(\xi_1 T_{,2} - \xi_2 T_{,1}) \tag{2}$$

$$T_{,tt} \rightarrow T_{,tt} - 2vT_{,t1} + v^2 T_{,11} - \omega\xi_1[T_{,t2} - (v-\omega\xi_2)T_{,12} + \omega T_{,1} - \omega\xi_1 T_{,22}] + \omega\xi_2[T_{,t1} - (v-\omega\xi_2)T_{,11} - vT_{,2} - v\xi_1 T_{,12}] + \omega[\xi_2 T_{,t1} - \xi_1 T_{,t2}] + v\omega[\xi_1 T_{,12} + T_{,2} - \xi_2 T_{,11}] \tag{3}$$

and the equation governing the temperature field observed from the moving coordinate system can be obtained by combining equations (2) and (3) with (1a). The subscripts i and t appearing in these equations denote differentiation with respect to ξ_i and t, respectively.

The resulting equation is to be solved subject to the boundary conditions specified at the crack surface and the crack line, which is instantaneously tangent to the crack trajectory and directing along the ξ_1 axis. In the immediate vicinity of a rapidly moving crack with a smooth trajectory, we may impose a symmetric condition

$$T_{,2} = 0 \text{ at } \xi_2 = 0 \text{ and } \xi_1 > 0 \tag{4}$$

Nomenclature

a_i = coefficients in the energy balance equation (5), $i = 1, 2, 3$
A, B = arbitrary constant in the eigenfunction $H(\theta)$
c = $v/2\alpha$ = a parameter used in the thermal wave equation, 1/m
C = speed of heat propagation in the solid, m/s
C_p = heat capacity, kJ/kg-°C
f, g_i = variable coefficients in the asymptotic equation of $H(\theta)$, $i = 1, 2, 3$
H = angular variation of near-tip temperature
k = thermal conductivity, W/m-°C
M = thermal Mach number defined as v/C
n = integer in the expression of eigenvalues
$\mathbf{q}, q_i$ = heat flux vector and its components in the ith direction, W/m²
Q = angular variation of near-tip heat flux components
r, θ = polar coordinates centered at the crack tip
R = instantaneous radius of curvature of the crack trajectory, m
s = exponent of r for heat flux vector
S = general heat source term, W/m²
t = physical time, s
T = temperature, °C
v = speed of the moving crack, m/s
$(\ )_D$ = Quantity in thermal diffusion model
α = thermal diffusivity, m²/s
δ = Dirac delta function
γ = transformation function on the independent variable θ
ω = angular velocity of the moving crack, rad/s
ρ = mass density, kg/m³
η = dummy variable of integrations
ξ_i = moving coordinates centered at the crack tip, m; $i = 1, 2$
∇ = gradient operator, 1/m
θ = polar angle of the moving coordinate system, deg
$(\ )_{,i}$ = $\partial/\partial\xi_i$, $i = 1, 2$
λ = eigenvalues, exponent of r for the angular variation of near-tip temperature
ζ = transformed variable from θ
Φ = transformation function on the dependent variable H
Γ = time function in the near-tip temperature distribution

to an observer standing at the moving crack tip. This concept was adopted by Williams (1952) and Achenbach and Bažant (1975) as the elastodynamic near-tip stress and displacement fields were investigated. At the surface of the crack, on the other hand, we may consider a general condition

$$a_1 T + a_2 q_2 = a_3 \text{ at } \xi_2 = 0 \text{ and } \xi_1 < 0 \tag{5}$$

which describes the energy balance across the crack surface as it propagates. The conduction mode of heat transfer lies in the second term $a_2 q_2$. In the Fourier law of heat conduction, q_2 takes the simple form of $-kT_{,2}$ and equation (5) is a Cauchy type. In the thermal wave model with finite speed of heat propagation, on the other hand, q_2 takes an integral form

$$q_2 = -(C^2 k/\alpha)\exp(-C^2 t/\alpha)\int_0^t T_{,2}\exp(C^2\eta/\alpha)d\eta \tag{5a}$$

and the condition (5) becomes an integral-differential equation. As the coefficient a_3 is equal to zero, the energy release from debonding to crack surfaces in the history of crack propagation is neglected.

In order to understand the fundamental characteristics of the near-tip solution in the vicinity of the crack tip, we will assume $a_2 = a_3 = 0$ in equation (5). As a consequence, the resulting equation implies a zero temperature at the crack surface. Equations (4) and (5) compose a mixed type boundary condition at $\xi_2 = 0$, which must be satisfied by the temperature field.

Temperature Field in the Vicinity of the Crack Tip

The field equation resulting from the combination of equations (1*a*) to (3) is a partial differential equation with variable coefficients. Obviously, a general form of the analytical solution is almost impossible to obtain. It should be noticed, however, that the near-tip solution in the problem with a crack always gives the most important information. Such a solution can not only provide characteristics of the physical quantities varying in the neighborhood of the crack tip, but also an efficient algorithm of using singular tip elements in the finite element (Tzou, 1986, for example) or the finite difference (Ju and Chen, 1987) method. In this section, therefore, we shall make an attempt to find a particular solution satisfying equations (1*a*) to (3) and boundary conditions (4) and (5) as the crack tip is closely approached. The energy equation (1*a*), with $T_{,t}$ and $T_{,tt}$ being replaced by the material derivatives (2) and (3), takes the following form:

$$\begin{aligned}
&\alpha\nabla^2 T = \alpha M^2 T_{,11} + \{(\alpha/C^2)T_{,tt} - (M^2/c)T_{,1t}\} \\
&+ \{T_{,t} - vT_{,1}\} - \omega\{\xi_1 T_{,2} - \xi_2 T_{,1}\} \\
&+ [M^2/2cR]\{\xi_2[T_{,t1} - (v-\omega\xi_2)T_{,11} - \omega T_{,2} - \omega\xi_1 T_{,12}] \\
&- \xi_1[T_{,t2} - (v-\omega\xi_2)T_{,12} + \omega T_{,1} - \omega\xi_1 T_{,22}] \\
&- (\xi_1 T_{,t2} - \xi_2 T_{,t1}) + v(T_{,2} + \xi_1 T_{,12} - \xi 2 T_{,11})\}
\end{aligned} \tag{6}$$

where a thermal Mach number M defined as v/C, in parallel to the previous study, has been introduced and c is a parameter defined as $v/2\alpha$. As the crack is stationary ($v = \omega = 0$) and the speed of heat propagation in the solid approaches infinity ($C \to \infty$), M approaches zero and equation (6) is reduced to the diffusion equation.

In the sequel a particular form of the product solution for T

$$T(r, \theta, t) = r^\lambda \Gamma(t) H(\theta) \tag{7}$$

is sought, with r and θ being the polar coordinates centered at the crack tip and $\Gamma(t)$ and $H(\theta)$ the functions governing the time and the angular dependencies of the near-tip temperature. The coordinates (r, θ) are especially useful in describing the state of the affairs in the vicinity of the crack tip. The product form of equtaion (7) is only valid as the r-dependency of the temperature field is identical along various directions approaching the crack tip. The exponent λ, although considered as yet unknown, should be an isotropic constant in this sense.

As usual, the coordinates r and θ are related to the ξ_i coordinates according to

$$T_{,1} = (\cos\theta)T_{,r} - (\sin\theta/r)T_{,\theta}, \text{ and}$$
$$T_{,2} = (\sin\theta)T_{,r} + (\cos\theta/r)T_{,\theta}, \text{ etc.,} \tag{8}$$

Substituting equations (7) and (8) into (6), the r-dependency of the terms involved in the resulting equation can be summarized as follows;

$$\begin{aligned}
&\nabla^2 T, T_{,11} \sim r^{\lambda-2}; \\
&T_{,1}, T_{,2}, T_{,t1}, \xi_2 T_{,11}, \xi_1 T_{,12}, \xi_2 T_{,11} \sim r^{\lambda-1}; \\
&T_{,t}, \xi_1 T_{,1}, \xi_2 T_{,2}, \xi_1 T_{,2}, \xi_2 T_{,1}, T_{,tt}, \xi_2 T_{,t1}, \xi_2^2 T_{,11}, \\
&\xi_1\xi_2 T_{,12}, \xi_1 T_{,t2}, \xi_2 T_{,t1}, \text{ and } \xi_1^2 T_{,22} \sim r^\lambda
\end{aligned} \tag{9}$$

Multiplying the entire equation by $r^{2-\lambda}$, then, we can see that the terms proportional to $r^{\lambda-1}$ and r^λ in equation (9) become proportional to r and r^2, respectively. As r approaches zero (0), i.e., in the immediate vicinity of the crack tip, these terms disappear and the asymptotic form of equation (6) in the (r, θ) coordinate system reduces to

$$\begin{aligned}
&(1 - M^2\sin^2\theta)H_{,\theta\theta} - [M^2(1-\lambda)\sin 2\theta]H_{,\theta} \\
&+ \lambda\{\lambda + M^2[(2-\lambda)\cos^2\theta - 1]\}H = 0
\end{aligned} \tag{10}$$

which is valid for any function of $\Gamma(t)$. The only physical parameter involved in equation (10) is the thermal Mach number M. The time independence of this equation indicates that the near-tip characteristics of H (and hence of T) are the same for a crack propagating in either transient or steady state. Also, we notice that the angular velocity ω of the moving crack with smooth trajectory is a higher order effect on the temperature distribution in the vicinity of the crack tip. These features of the near-tip solution are similar to those found for the displacement field by Achenbach and Bažant (1975). In the sequel we will present a method of variable transformation to solve equation (10). In the subsonic range with $M < 1$, the transformation reduces to that observed by Achenbach and Bažant based on the Lorentz transformation. The transformations will then be derived in a consistent fashion for the transonic and the supersonic ranges with $M \geq 1$.

Equation (10) is a second-order ordinary differential equation with variable coefficients. It has to be solved subject to the boundary conditions

$$H_{,\theta} = 0 \text{ at } \theta = 0 \text{ and } H = 0 \text{ at } \theta = \pi \tag{11}$$

resulting from equations (4) and (5) with a_2 and a_3 being equal to zero. Analytical solution for $H(\theta)$ can be found by the method of variable transformations. We first introduce a transformation on the dependent variable from H to Φ:

$$H(\theta) = (1 - M^2\sin^2\theta)^{\lambda/2}\Phi(\theta) \tag{12}$$

Substituting equation (12) into (10) renders the following equation:

$$(g_1 f)\Phi_{,\theta\theta} - (f M^2\sin 2\theta)\Phi_{,\theta} + (g_1 f_{,\theta\theta} + g_2 f_{,\theta} + g_3 f)\Phi = 0 \tag{13}$$

where

$$\begin{aligned}
&g_1 = 1 - M^2\sin^2\theta, \quad g_2 = -M^2(1-\lambda)\sin 2\theta, \\
&g_3 = \lambda\{\lambda + M^2[(2-\lambda)\cos^2\theta - 1]\}, \text{ and } f = g_1^{\lambda/2}
\end{aligned} \tag{14}$$

We now introduce another transformation on the independent variable from θ to γ to further simplify equation (13). Let us consider a general function $\gamma \equiv \gamma(\theta)$. By applying the chain rule, equation (13) can be expressed in the γ space as

$$\begin{aligned}
&\Phi_{,\gamma\gamma} + \{[(g_1 f)\gamma_{,\theta\theta} \\
&- (f M^2\sin 2\theta)\gamma_{,\theta}]/[g_1 f\gamma_{,\theta}^2]\}\Phi_{,\gamma} + \{[g_1 f_{,\theta\theta} \\
&+ g_2 f_{,\theta} + g_3 f]/[g_1 f\gamma_{,\theta}^2]\}\Phi = 0
\end{aligned} \tag{15}$$

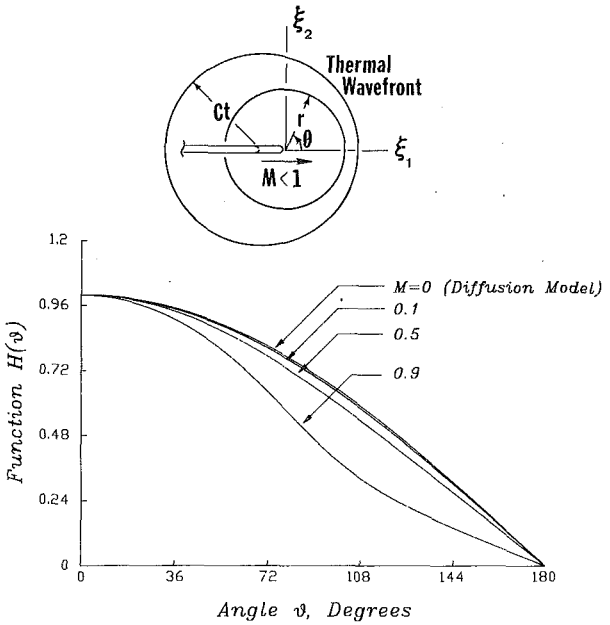

Fig. 2 Angular variations of the near-tip temperature at thermal Mach number M = 0, 0.1, 0.5, and 0.9; subsonic range with M < 1

Obviously, if we choose

$$(g_1 f)\gamma_{,\theta\theta} - (f\,M^2\sin 2\theta)\gamma_{,\theta} = 0 \tag{16}$$

the first-order derivative can be dropped from equation (15) and the resulting equation reveals the highlight of possessing a closed-form solution. Equation (16) governs the transformation γ for the independent variable θ. It strongly depends on the range of the thermal Mach number of the moving crack.

(a) Subsonic Range with M < 1. In the case of M < 1, the function $\gamma(\theta)$ satisfying equation (16) can be integrated to give

$$\gamma(\theta) = \tan^{-1}[(1-M^2)^{1/2}\tan\theta],$$

and consequently,

$$\gamma_{,\theta} = (1-M^2)^{1/2}/(1-M^2\sin^2\theta) \tag{17}$$

This is the transformation observed by Achenbach and Bažant (1975) for the out-of-plane displacement field around a moving crack tip. It is derived mathematically from equation (16) in the present approach. Substitution of (17) into (15) then yields

$$\Phi_{,\gamma\gamma} + \lambda^2\Phi = 0 \tag{18}$$

Equation (18) provides a nice feature about the angular variation of the near-tip temperature in the hyperbolic theory of heat conduction. Its simple form indeed results from the special coefficients appearing in equation (15), which is not generally the case for any second-order ordinary differential equation with variable coefficients.

The representations of the boundary condition (11) in the γ space read as

$$\Phi_{,\gamma} = 0 \text{ at } \gamma = 0 \tag{19a}$$

$$\Phi = 0 \text{ at } \gamma = \pm\pi \tag{19b}$$

Equations (18) and (19*a*, *b*) compose an eigenvalue problem for λ. A solution of (18) for Φ satisfying (19*a*) can be obtained immediately as

$$\Phi = A\cos\lambda\gamma \tag{20}$$

and from the remaining condition (19*b*), the eigen-equation for λ is thus determined:

$$\cos\lambda\pi = 0 \text{ or } \lambda = (2n+1)/2, \text{ with integer } n = 0, 1, 2, \ldots \tag{21}$$

The fundamental solution for the present problem will be investigated by taking the lowest value of λ with n being zero. As r approaches zero in the near-tip solution, we should notice that the terms of r^{λ}, with λ being shown in equation (21) but $n \neq 0$, will approach zero faster than that of $r^{1/2}$ and the fundamental solution indeed dominates the near-tip solution for the present crack problem. Substituting equation (20) into (12) and taking the inverse transformation from γ to θ according to (17), the final form of the solution for $H(\theta)$ is

$$H(\theta) = A\,[(1-M^2\sin^2\theta)^{1/2} + \cos\theta]^{1/2}/\sqrt{2}, \text{ for } M < 1 \tag{22}$$

The coefficient A in equation (18) is an arbitrary constant in the eigenvalue system, and the expression enclosed in the brackets governs the angular variation of the temperature fields in the core region.

In the subsonic range with M < 1, the angular distribution of the temperature field represented by equation (22) is well defined everywhere. There is no singularity existing in the physical domain. The expression for $H(\theta)$ in the thermal diffusion model can be retrieved by substituting 0 (zero) for M in equation (22):

$$H_D(\theta) = A\,[+\cos\theta]^{1/2}/\sqrt{2} \tag{23}$$

It should be noted, referring to equation (7), that both the thermal wave and the thermal diffusion models display a $\sqrt{r}$-temperature field in the vicinity of the crack tip. The angular variation of temperature is governed by equations (22) and (23), respectively.

For a crack moving to the right, graphic representations for $H(\theta)$ and $H_D(\theta)$ with A being unity are shown in Fig. 2. As expected, the deviation between the two models becomes significant as the thermal Mach number increases. For all the cases with M = 0 (the diffusion model), 0.1, 0.5, and 0.9, the temperature reaches its maximum at the leading edge of the moving crack at $\theta = 0$ deg. Also, the H function (and hence the temperature level) decreases as the thermal Mach number increases.

In the thermoelastic deformation with the Poisson effect in the radial direction being neglected, the quantity $T_{,\theta}$ (and hence $H_{,\theta}$) is qualitatively related to the circumferential stress component. In the subsonic case with M < 1, the slope of the function $H(\theta)$ can be obtained from the derivative of equation (22)

$$H_{,\theta} = -[A/4\sqrt{2}]\,[M^2\sin 2\theta(1-M^2\sin^2\theta)^{-1/2} + 2\sin\theta]/[(1-M^2\sin^2\theta)^{1/2} + \cos\theta]^{1/2} \tag{24}$$

As θ approaches zero and π, $H_{,\theta}$ approaches 0 and $-A(1-M^2)^{1/2}/2$, respectively. In the transition of the thermal Mach number to the transonic stage, namely $M \to 1$, $H_{,\theta}$ approaches zero at $\theta = \pi$. Note also that as M approaches zero, equation (24) reduces to that in the thermal diffusion model,

$$H_{D,\theta} = -A\sin\theta/[2\sqrt{2(1+\cos\theta)}] \tag{25}$$

which approaches 0 and $-A/2$, respectively, as θ approaches 0 and π. These results are shown in Fig. 3.

(b) Supersonic Range with M > 1. For the same crack moving to the right at a speed faster than that of the heat propagation in the solid, equation (12) can still be used, but the temperature distribution under investigation must be confined to the domain of

$$0 \le \theta \le \sin^{-1}(1/M) \text{ or } 0 \le \theta \le \tan^{-1}[1/(M^2-1)^{1/2}] \tag{26}$$

with θ being measured from the trailing edge of the moving crack, as shown in Fig. 4. For M > 1, alternatively, the transformation $\gamma(\theta)$ satisfying equation (16) takes the form of

$$\gamma(\theta) = \frac{1}{2}\ln\{[(M^2-1)^{1/2}\tan\theta + 1]/[(M^2-1)^{1/2}\tan\theta - 1]\} \text{ and } \gamma_{,\theta} = (M^2-1)^{1/2}/(1-M^2\sin^2\theta) \tag{27}$$

Substituting equation (27) into (15) then renders an equation

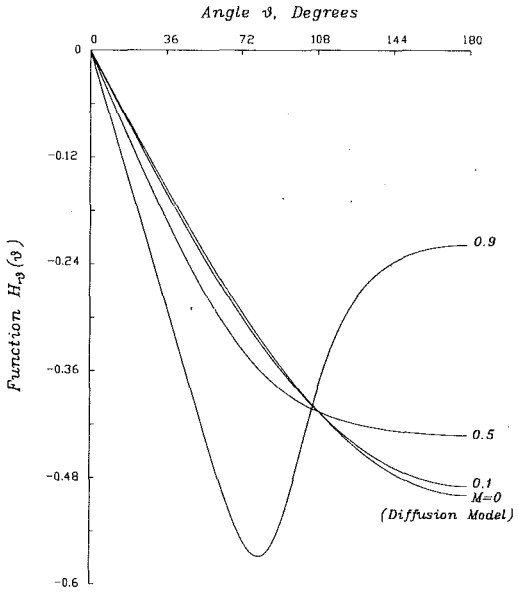

Fig. 3 Angular variations of $H_{,\theta}$ in the subsonic range with M < 1

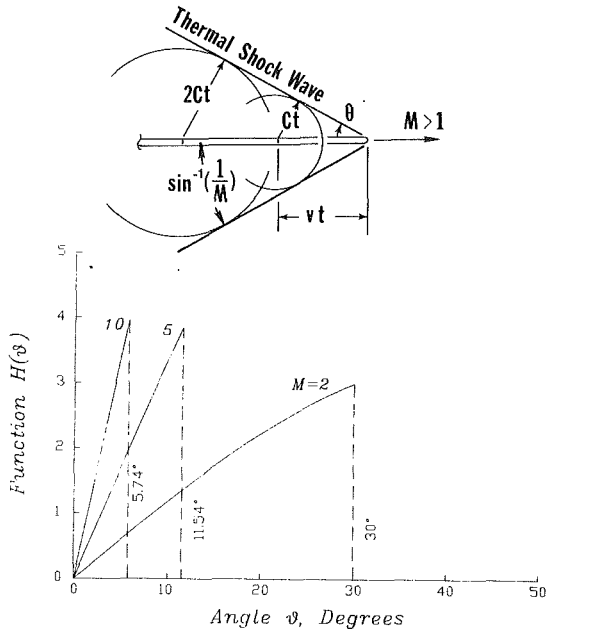

Fig. 4 Angular variations of the near-tip temperature at thermal Mach number M = 2, 5, and 10; supersonic range with M > 1

governing the Φ function (corresponding to equation (18)) in the supersonic range

$$\Phi_{,\gamma\gamma} - \lambda^2\Phi = 0 \text{ for } M > 1 \tag{28}$$

Obviously, the eigenvalue system formulated in the subsonic range with $M < 1$ is dramatically changed in the present case. We first notice that the physical domain represented by equation (26) for $M > 1$ is the same as that for the *heat-affected zone* induced by a moving heat source (Tzou, 1988a). By a similar argument, therefore, it is informative to conclude that the temperature distribution in the *heat-affected zone* is governed by equations (12), (27), and (28). The temperature stays at the initial value in the rest of the physical domain, which is defined as the *thermally undisturbed zone*. The thermal shock angle $\sin^{-1}(1/M)$ inclined to the trailing edge of the moving crack is the same as that induced by a moving heat source in the supersonic range.

Defining now a parameter ζ

$$\zeta(\theta) = [1 + (M^2 - 1)^{1/2}\tan\theta] / [1 - (M^2 - 1)^{1/2}\tan\theta] \tag{29}$$

such that from equation (27)

$$\gamma = \pm\frac{i\pi}{2} + \frac{1}{2}\ln(\zeta) \tag{30}$$

with $i = \sqrt{-1}$ and ζ being greater than zero for θ in the domain of the heat-affected zone specified by equation (26). The solution of equation (28) in terms of the variable λ can then be obtained as

$$\Phi(\zeta(\theta)) = \cos(\lambda\pi/2)\{A\exp[\lambda\ln(\zeta)/2] + B\exp[-\lambda\ln(\zeta)/2]\}$$
$$+ i\sin(\lambda\pi/2)\{A\exp[\lambda\ln(\zeta)/2] - B\exp[-\lambda\ln(\zeta)/2]\}. \tag{31}$$

Since the temperature function must be real, equation (31) gives

$$\sin(\lambda\pi/2) = 0, \text{ or } \lambda = 2n \text{ with } n = 1, 2, 3, \ldots \tag{32}$$

For a nontrivial solution, the lowest eigenvalue λ in the supersonic range is 2. This result intrinsically varies the near-tip behavior of the temperature field. In the subsonic range with $M < 1$, the r-dependency of T is $\sqrt{r}$. In the supersonic range with $M > 1$, such a dependency transits to r^2, which cannot be depicted by the thermal diffusion model. Notice also that only one boundary condition at $\theta = 0$ (the trailing edge of the moving crack), or $\zeta = 1$ and $\gamma = \pm i(\pi/2)$ according to equation (30), remains in the present case with $M > 1$:

$$\Phi = 0 \text{ at } \gamma = \pm i(\pi/2) \text{ and } \zeta = 1 \tag{33}$$

Another boundary at $\theta = \pi$ (the leading edge of the moving crack) stays in the thermally undisturbed zone and the symmetric condition $\Phi_{,\gamma} = \Phi_{,\theta} = 0$ is automatically satisfied for a uniform temperature field at the reference level. Substituting equation (31) into equation (33) renders a result of $A = -B$. The Φ function in the supersonic range is thus obtained as

$$\Phi(\zeta(\theta)) = B(\zeta - \frac{1}{\zeta}) \tag{34}$$

with B being an arbitrary constant. Combining equation (12) with $\lambda = 2$ with (34) then gives the angular distribution of the temperature field in the heat-affected zone

$$H(\theta) = B(1 - M^2\sin^2\theta)(\zeta - \frac{1}{\zeta}) \tag{35}$$

which, upon substitution of equation (29), can be expressed in terms of the variable θ

$$H(\theta) = 2B(M^2 - 1)^{1/2}\sin(2\theta) \text{ for } M > 1 \tag{36}$$

As the thermal shock wave is approached from the site in the heat-affected zone, namely $\theta \to \sin^{-1}(1/M)$, $\sin(2\theta)$ approaches $2(M^2 - 1)^{1/2}/M^2$ and we have

$$H(\theta) \to 4B(M^2 - 1)/M^2 \text{ as } \theta \to \sin^{-1}(1/M) \tag{37}$$

Equation (37) shows that the temperature remains bounded at the thermal shock wave located at $\theta = \sin^{-1}(1/M)$ with $M > 1$. It has a limit value of $4B$ as M approaches infinity. We also notice that the temperature is discontinuous but finite across the surface of the thermal shock wave. As the thermal Mach number increases, the H function represented by equation (36) (and hence the temperature level according to equation (7)) increases. Together with the result that the temperature decreases as the thermal Mach number increases in the subsonic range, this is a swinging phenomenon for the temperature field in transition of the thermal Mach number from the subsonic to the supersonic ranges. These phenomena are shown in Fig. 4 with M being 2, 5, and 10 in the supersonic range. The slope of the H function in the heat-affected zone can be obtained by a direct differentiation on equation (36)

$$H_{,\theta} = 4B(M^2 - 1)^{1/2}\cos(2\theta), \text{ with } M > 1 \tag{38}$$

(c) Transonic Stage with M = 1. As the speed of the moving crack is the same as that of the heat propagation in the solid, equation (14) reduces to the following form:

$$g_1 = \cos^2\theta,\ g_2 = (\lambda - 1)\sin 2\theta,$$
$$g_3 = \lambda[\lambda\sin^2\theta + \cos(2\theta)],\quad f = \cos^\lambda\theta \tag{39}$$

and the equation governing the Φ function becomes

$$\Phi_{,\gamma\gamma} = 0 \tag{40}$$

which possesses a solution of the form

$$\Phi(\gamma) = A\gamma + B \tag{41}$$

where, from equation (16)

$$\gamma(\theta) = \tan\theta \tag{42}$$

and similar to the supersonic case with $M > 1$, θ is measured from the trailing edge of the moving crack as shown in Fig. 5. According to equation (26), a normal shock appears at $\theta = 90$ deg in the present case with $M = 1$. The heat-affected zone consequently ranges from 0 to 90 deg measured from the crack surface. Only the boundary condition at $\theta = 0$, or $\gamma = 0$ according to equation (42), needs to be considered in this case

$$\Phi = 0 \text{ at } \gamma = 0 \tag{43}$$

From equation (41), therefore, we have $B = 0$ and A being an arbitrary constant. Determination on the value of λ at the transonic stage relies on the argument made on the *boundness* of the temperature field across the shock surface. This is a general nature obtained in the supersonic range (referring to equation (37)) and should be satisfied as the thermal Mach number approaches 1 from the supersonic site. Substituting equation (42) into (41) and the result into (12), the H function is thus obtained

$$H(\theta) = A\cos^\lambda\theta\tan\theta \text{ for } M = 1 \tag{44}$$

Obviously, the lowest value of λ must equal to 1 such that

$$H(\theta) = A\sin\theta \text{ for } M = 1 \tag{45}$$

and the angular distribution of the temperature remains bounded as θ approaches 90 deg. Again, we notice that the r-dependency of T represented in equation (7) changes from $r^{1/2}$ to r as the thermal Mach number transits from the subsonic range to the transonic stage. The graphic representation of $H(\theta)$ at $M = 1$ is shown in Fig. 5.

For the supersonic (case *b*) and the transonic (case *c*) cases with $M \geq 1$, as shown in Figs. 4 and 5, the temperature level in the heat-affected zone decays from the thermal shock wave to the trailing edge of the moving crack.

Discussion

The Temperature Gradient $\partial T/\partial r$. As the thermal Mach number transits from the subsonic, transonic, to the supersonic ranges, the r-dependency of the near-tip temperature transits from $r^{1/2}$, r, to r^2, respectively. Consequently, the temperature gradient $\partial T/\partial r$ behaves, respectively, as $r^{-1/2}$ and r in the subsonic ($M < 1$) and the supersonic ($M > 1$) ranges and is independent of r at the transonic stage with $M = 1$. The $1/\sqrt{r}$ singularity at $r = 0$ exists only for a crack propagating in the subsonic range with $M < 1$. Such a salient feature is rather interesting and the resulting thermoelastic field is expected to vary intrinsically in transition of the thermal Mach number.

The Heat Flux Vector q. The equation governing the heat flux vector $\mathbf{q}$ can be obtained similarly in the material coordinate system

$$(\alpha/C^2)[\mathbf{q}_{,t} - v\mathbf{q}_{,1} - \omega(\xi_1\mathbf{q}_{,2} - \xi_2\mathbf{q}_{,1})] + \mathbf{q} = -k\nabla T \tag{46}$$

Assuming a product form for $\mathbf{q}$

$$\mathbf{q} = \{q_r, \mathbf{q}_\theta\} = \Gamma(t)r^s\{Q_r(\theta), Q_\theta(\theta)\} \tag{47}$$

and letting r approach zero in the near-tip region, we may find that the term containing $\mathbf{q}_{,1}$ in equation (46) dominates and the asymptotic form of (46) reads as

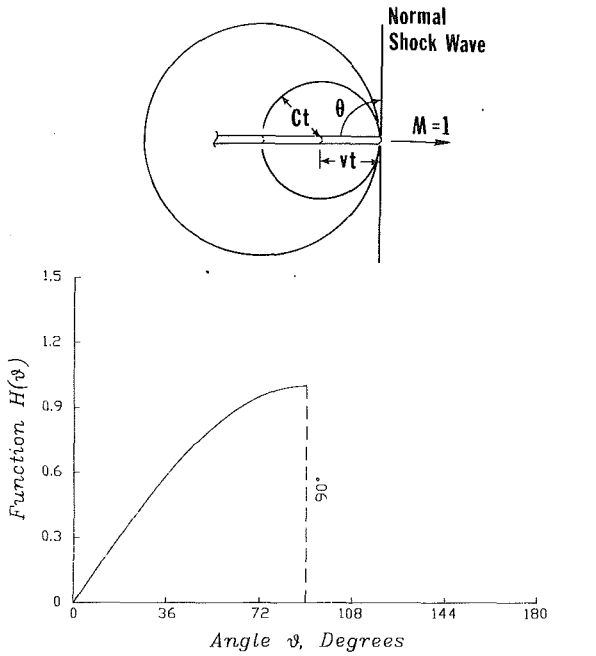

Fig. 5 **Angular variations of the near-tip temperature at the transonic stage with M = 1**

$$\mathbf{q}_{,1} = (2ck/M^2)\nabla T \tag{48}$$

From equation (8), then, we conclude that the r-dependency of the heat flux vector is the same as that of the near-tip temperature. The exponent s in equation (47) is thus 1/2, 1, and 2 in the subsonic, the transonic, and the supersonic ranges, respectively. The angular distributions of the heat flux vector are governed by

$$[-\sin(\theta)]Q_{r,\theta} + [\cos(\theta)/2]Q_r = [ck/M^2]H \tag{49}$$

$$[-\sin(\theta)]Q_{\theta,\theta} + [\cos(\theta)/2]Q_\theta = [2ck/M^2]H_{,\theta} \tag{50}$$

these distributions have a common integrating factor $\sqrt{\csc\theta}$ and the integral form of the solutions can be obtained as

$$Q_r = -[ck/M^2]\sqrt{\sin\theta}\int^\theta \{H(\eta)/\sin^{3/2}\eta\}d\eta \tag{51}$$

$$Q_\theta = -[2ck/M^2]\sqrt{\sin\theta}\int^\theta \{H_{,\eta}/\sin^{3/2}\eta\}d\eta \tag{52}$$

with the function $H(\theta)$ being the corresponding expression in the respective ranges of M, namely equation (22) for $M < 1$, (36) for $M > 1$, and (45) for $M = 1$.

For a moving crack subject to a specified heat flux at its surfaces, the energy equation with $\mathbf{q}$-representation can be used instead and the present method can be applied in a similar fashion. This is due to the similarity of the mathematical structures between the $\mathbf{q}$- and T-representations of the energy equation in the thermal wave model.

As the speed of the moving crack is high, due to the energy dissipation in the strain history especially around the crack tip, the thermal and mechanical fields may be coupled, as shown by Lord and Shulman (1967) and Tzou (1987) for instance. The temperature field in this case depends also on the deformation field in the load-time history and the results obtained in the present study do not reflect such complicated interactions.

Conclusion

The fundamental characteristics of the thermal field around a moving crack tip have been investigated analytically. The thermal Mach number M has been used successfully as the characterizing parameter. The significant findings are sum-

marized as follows: (*i*) In the subsonic range with $M<1$, the deviations from the thermal diffusion model become remarkable as the thermal Mach number increases to 0.5 and thereafter, referring to Figs. 2 and 3. (*ii*) Thermal shock waves will be formed in the physical domain as the speed of the moving crack is equal to or faster than that of the heat propagation in the solid. Measuring from the trailing edge of the moving crack, the thermal shock angle is found to be $\sin^{-1}(1/M)$ with $M \geq 1$ and the heat-affected zone is confined to the domain of $0 \leq \theta \leq \sin^{-1}(1/M)$. (*iii*) In the subsonic range with $M<1$, the temperature level around the moving crack tip is found to decrease as the thermal Mach number increases. In the transonic and the supersonic ranges with $M \geq 1$, the temperature level increases with the thermal Mach number. This is the swinging phenomenon defined in this study. (*iv*) In transition from the heat-affected zone to the thermally undisturbed zone, the temperature possesses a *finite* discontinuity across the surfaces of the thermal shock waves. It is in this sense that the thermal shock wave induced by a moving crack is *weaker* in comparison with that induced by a moving heat source. In the latter case (Tzou, 1989) the temperature approaches infinity as the thermal shock wave is closely approached. (*v*) By employing the thermal wave model, the r-dependency of the near-tip temperature is the same as that of the near-tip heat flux vector. They behave as $r^{1/2}$, r, and r^2, respectively, as the thermal Mach number transits from the subsonic, transonic, to the supersonic ranges. A further study on such a transition of the r-dependency is being made for the crack surfaces subject to a general condition specified by equation (5) with nonzero coefficients.

As global instability of a macrocrack is developed under external excitations, the crack velocity increases from a value of zero (0) to a terminating velocity approximately equal to 0.38 $\sqrt{E/\rho}\,(1-a_c/a)$, as shown by Berry (1960) and Bluhm (1969). Here $\sqrt{E/\rho}$ is the velocity of longitudinal waves in the material, a the instantaneous length of the crack, and a_c the critical crack length characterizing the brittle behavior of the crack growth. For metals, the terminating velocity is on the order of 10^3 and in the final stage of global crack instability, the crack is most likely propagating at a supersonic speed. The near-tip behavior of the thermal field summarized in (*i*) to (*v*) is important in studying the thermoelastic/plastic response of the material continua in the vicinity of the moving crack tip.

References

Achenbach, J. D., and Bažant, Z. P., 1975, "Elastodynamic Near-Tip Stress and Displacement Fields for Rapidly Propagating Cracks in Orthotropic Materials," ASME *Journal of Applied Mechanics*, Vol. 42, pp. 183–189.

Baumeister, K. J., and Hamill, T. D., 1969, "Hyperbolic Heat-Conduction Equation—A Solution for the Semi-infinite Body Problem," ASME JOURNAL OF HEAT TRANSFER, Vol. 91, pp. 543–548.

Berkovsky, B. M., and Bashtovoi, 1977, "The Finite Velocity of Heat Propagation From the Viewpoint of the Kinetic Theory," *International Journal of Heat and Mass Transfer*, Vol. 20, pp. 621–626.

Berry, J. P., 1960, "Some Kinetic Considerations of the Griffth Criterion for Fracture," *Journal of Mechanics and Physics of Solids*, Vol. 8, pp. 194–216.

Bluhm, J. I., 1969, "Fracture Arrest," in: *Fracture V*, X. X. Liebowitz, ed., Academic Press, New York, pp. 1–63.

Boley, B. A., 1964, "The Analysis of Problems of Heat Conduction and Melting," *High Temperature Structures and Materials*, Pergamon Press, New York, pp. 260–315.

Bubnov, V. A., 1976, "Wave Concepts in the Theory of Heat," *International Journal of Heat and Mass Transfer*, Vol. 19, pp. 175–184.

Chester, M., 1963, "Second Sound in Solids," *The Physical Review*, Vol. 131, pp. 2013–2015.

Frankel, J. I., Vick, B., and Ozisik, M. N., 1984, "Flux Formulation of Hyperbolic Heat Conduction," *Journal of Applied Physics*, Vol. 58, pp. 3340–3345.

Gurtin, M. E., and Pipkin, A. C., 1968, "A General Theory of Heat Conduction With Finite Wave Speeds," *Archive for Rational Mechanics and Analysis*, Vol. 31, pp. 113–126.

Ju, F. D., and Liu, J. C., 1988, "Effect of Peclet Number in Thermo-Mechanical Cracking Due to High-Speed Friction Load," ASME *Journal of Tribology*, Vol. 110, pp. 217–221.

Kelley, D. C., 1968, "Diffusion: A Relativistic Appraisal," *American Journal of Physics*, Vol. 36, pp. 585–591.

Lord, H. W., and Shulman, T., 1967, "A Generalized Dynamic Theory of Thermoelasticity," *Journal of Mechanics and Physics of Solids*, Vol. 5, pp. 299–309.

Özişik, M. N., and Vick, B., 1984, "Propagation and Reflection of Thermal Waves in a Finite Medium," *International Journal of Heat and Mass Transfer*, Vol. 27, pp. 1845–1854.

Tzou, D. Y., 1985, "Intensification of Externally Applied Magnetic Field Around a Crack in Layered Composite," *Journal of Theoretical and Applied Fracture Mechanics*, Vol. 4, pp. 191–199.

Tzou, D. Y., 1986, "Dynamic Elastic-Plastic Analysis for Crack Problems," Institute of Fracture and Solid Mechanics Technical Report, IFSM-86-140, Lehigh University, Bethlehem, PA.

Tzou, D. Y., 1987, "Kinetics of a Moving Crack: Thermal and Mechanical Interactions," Ph.D. Dissertation, Lehigh University, Bethlehem, PA.

Tzou, D. Y., 1988a, "Shock Wave Formation Around a Moving Heat Source in the Solid With Finite Speed of Heat Propagation," *International Journal of Heat and Mass Transfer*, accepted for publication.

Tzou, D. Y., 1988b, "The Effects of Thermal Shock Waves on the Crack Initiation Around a Moving Heat Source," *Journal of Engineering Fracture Mechanics*, accepted for publication.

Tzou, D. Y., 1989, "On the Thermal Shock Wave Induced by a Moving Heat Source," ASME JOURNAL OF HEAT TRANSFER, Vol. 111, pp. 232–238.

Van Kampen, N. G., 1970, "A Model for Relativistic Heat Transfer," *Physica*, Vol. 46, pp. 315–332.

Vick, B., and Özişik, M. N., 1983, "Growth and Decay of a Thermal Pulse Predicted by the Hyperbolic Heat Conduction Equation," ASME JOURNAL OF HEAT TRANSFER, Vol. 105, pp. 902–907.

Weymann, H. D., 1967, "Finite Speed of Propagation in Heat Conduction, Diffusion, and Viscous Shear Motion," *American Journal of Physics*, Vol. 35, pp. 488–496.

Williams, M. L., 1952, "Stress Singularities Resulting From Various Boundary Conditions in Angular Corners in Extension," ASME *Journal of Applied Mechanics*, Vol. 19, pp. 526–536.

Green's Function Partitioning in Galerkin-Based Integral Solution of the Diffusion Equation

A. Haji-Sheikh
Department of Mechanical Engineering,
The University of Texas at Arlington,
Arlington, TX 76019

J. V. Beck
Heat Transfer Group,
Department of Mechanical Engineering,
Michigan State University,
East Lansing, MI 48824-1226

A procedure to obtain accurate solutions for many transient conduction problems in complex geometries using a Galerkin-based integral (GBI) method is presented. The nonhomogeneous boundary conditions are accommodated by the Green's function solution technique. A Green's function obtained by the GBI method exhibits excellent large-time accuracy. It is shown that the time partitioning of the Green's function yields accurate small-time and large-time solutions. In one example, a hollow cylinder with convective inner surface and prescribed heat flux at the outer surface is considered. Only a few terms for both large-time and small-time solutions are sufficient to produce results with excellent accuracy. The methodology used for homogeneous solids is modified for application to complex heterogeneous solids.

Introduction

An accurate and rapid solution of the diffusion equation in various solids is possible with the Galerkin-based integral (GBI) method. The Green's function derived using this method has excellent large-time accuracy for various applications (Haji-Sheikh and Lakshminarayanan, 1987; Haji-Sheikh, 1988). However, because it uses a finite number of functions to construct a solution, its accuracy at very small times is usually insufficient. The partitioning of the Green's function solution into large-time and small-time solutions (Beck and Keltner, 1985) provides the desired accuracy over the entire time domain. The small-time Green's function is insensitive to the complexity of the boundaries and boundary conditions; therefore, it can accommodate complex problems at earlier stages of the transient process.

The large-time solution is analogous to the exact solution, but uses a finite number of terms. The eigenvalues in the Green's function are computed using Ritz–Galerkin minimum residual methods; hence, the large-time solution can also accommodate complex boundaries and various boundary conditions.

The partitioned Green's function solution is applied to simple problems and its accuracy is compared with that of the exact solution. Furthermore, consideration is extended to situations where a solid is heterogeneous and there is a finite contact conductance between different materials. The solution functions (basis functions) used in the Green's function solution are selected to satisfy prescribed temperature or heat flux at the boundary, or convective boundary conditions. In addition, for heterogeneous solids, the basis functions also satisfy the continuity of heat flux at the material boundaries. When the contact conductance is finite, the solution functions presented in this paper are modified to permit a temperature jump at the material boundaries.

The analytical derivation presented in this paper applies to the diffusion equation in complex heterogeneous geometries. Simple geometries are selected to demonstrate the mathematical steps and to discuss the accuracy of the results. The analytical solutions, even for simple geometries such as hollow cylinders, are cumbersome, and the numerical computations using the exact solution require the skills of specialists. The time-partitioning procedure described in this paper yields accurate solutions for many complex problems. Also, the GBI method is useful for the study of thermal conduction in one-dimensional geometries, e. g., cylinders, spheres, etc. For one-dimensional bodies, a two-term solution is accurate to a fraction of one percent. This is particularly interesting because the eigenvalues can be computed directly without using a numerical procedure. In transient conduction, the Green's functions in some regular multidimensional bodies are the products of one-dimensional Green's functions.

Green's Function Solution

The diffusion equation in three-dimensional space can be written as

$$\nabla \cdot [k \nabla T(\mathbf{r}, t)] + g(\mathbf{r}, t) = \rho(\mathbf{r}) c_p(\mathbf{r}) \partial T(\mathbf{r}, t)/\partial t \tag{1}$$

where ρ, c_p, and k are position-dependent properties. A generalized solution using the Green's function in a region with position-dependence properties (Haji-Sheikh, 1988; Haji-Sheikh and Lakshminarayanan, 1987) is

$$\rho(\mathbf{r}) c_p(\mathbf{r}) T(\mathbf{r}, t) = \int_{V'} \rho(\mathbf{r}') c_p(\mathbf{r}') G \Big|_{\tau=0} T_o(\mathbf{r}') dV'$$

$$+ \int_{\tau=0}^{t} d\tau \int_{V'} g(\mathbf{r}', \tau) G dV'$$

$$+ \int_{\tau=0}^{t} d\tau \int_{S'} k [G \partial T/\partial n - T \partial G/\partial n]_{S'} dS' \tag{2}$$

where $\mathbf{r}$ is the position vector used for convenience of formulation, $k = k(S')$. Equation (2) is called the Green's function solution equation. The standard Green's function $G(\mathbf{r}, t \,|\mathbf{r}', \tau)$, available from Ozisik (1980), is defined as the temperature effect at $(\mathbf{r}, t)$ in a solid with homogeneous boundary conditions; this effect is caused by an impulsive point heat source located at $\mathbf{r}'$ and released at time τ. However, the Green's function in equation (2) is $G(\mathbf{r}', t \,|\mathbf{r}, \tau)$, given by Haji-Sheikh (1988)

$$G = G(\mathbf{r}', -\tau \,|\mathbf{r}, -t) = G(\mathbf{r}', t \,|\mathbf{r}, \tau)$$
$$= \rho(\mathbf{r}) c_p(\mathbf{r}) G(\mathbf{r}, t \,|\mathbf{r}', \tau)/\rho(\mathbf{r}') c_p(\mathbf{r}')$$

$$= \sum_{n=1}^{N} \rho(\mathbf{r}) c_p(\mathbf{r}) F_n(\mathbf{r}) \sum_{i=1}^{N} \exp[-\gamma_n (t-\tau)] p_{ni} f_i(\mathbf{r}') \tag{3}$$

where

$$F_n(\mathbf{r}) = \sum_{j=1}^{N} d_{nj} f_j(\mathbf{r}) \tag{4}$$

Contributed by the Heat Transfer Division and presented at the ASME National Heat Transfer Conference, Houston, Texas, July 24–27, 1988. Manuscript received by the Heat Transfer Division August 31, 1988. Keywords: Conduction, Transient and Unsteady Heat Transfer.

The coefficient d_{nj} is the eigenvector corresponding to the eigenvalue γ_n and $f_j(\mathbf{r})$ is the basis function. The effect of the boundary conditions on the temperature solution is included in the value of the basis functions. Numerical values of γ_n and d_{nj} are obtainable from the following matrix relation (Haji-Sheikh, 1986; Haji-Sheikh and Mashena, 1987):

$$(\mathbf{A}+\gamma_n\mathbf{B})\mathbf{d}_n=0 \tag{5}$$

The matrices **A** and **B** have elements

$$a_{ij}=\int_V f_i\nabla\cdot(k\nabla f_j)dV \tag{6a}$$

$$b_{ij}=\int_V \rho c_p f_i f_j dV \tag{6b}$$

where $i=1, 2, 3, \ldots, N$; $j=1, 2, 3, \ldots, N$; and $\mathbf{d}_n$ is the eigenvector corresponding to eigenvalue γ_n with elements d_{n1}, $d_{n2}, \ldots, d_{nN}$.

The last term in equation (2) contains the contribution due to nonhomogeneity of the boundary conditions. The convergence of equation (2) near and at the surfaces is slow for nonhomogeneous boundary conditions. For example, when the surface temperature is prescribed, the term $f(\mathbf{r})$ in the Green's function, equations (3) and (4), takes the value of zero after $\partial G/\partial n$ is computed over S'.

Alternative Green's Function Solution

The alternative formulation of the Green's function solution improves the convergence of the temperature solution. This formulation is possible if one defines a differentiable function that satisfies the nonhomogeneous boundary conditions. When the surface temperature is prescribed, it is usually not difficult to construct a function that satisfies the boundary conditions. For example, consider a solid located between two arbitrary nonintersecting surfaces $r_1=r_1(\theta, z)$ and $r_2=r_2(\theta, z)$ with temperatures on the respective surfaces of $T_1=T_1(r_1, \theta, z, t)$ and $T_2=T_2(r_2, \theta, z, t)$. An auxiliary equation that satisfies the boundary conditions is

$$T^*=(T_2-T_1)\frac{\ln(r/r_1)}{\ln(r_2/r_1)}+T_1 \tag{7}$$

or

$$T^*=(T_2-T_1)\frac{r-r_1}{r_2-r_1}+T_1 \tag{8}$$

The function for T^* given by equations (7) and (8) need not satisfy the Laplace equation.

It is possible to derive an equation that satisfies the boundary conditions of the first, second, or third kinds at each boundary of a simple geometry. Except when the heat flux is prescribed at both surfaces, the following relation can be selected:

$$T^*=c_1u_p+c_2 \tag{9}$$

where u_p takes the value of x in Cartesian coordinates and $\ln(r)$ or $-1/r$ in radial cylindrical or spherical coordinates, respectively. Except when the heat flux is prescribed on both surfaces, the constants c_1 and c_2 can be determined by applying the appropriate boundary conditions. However, when the heat flux on both surfaces is given, the constant c_2 in equation (9) should be replaced by, for example c_2r^2 before calculating c_1 and c_2. Although there are numerous conduction problems for which a T^* can be computed, it is impossible or cumbersome to find this function for many problems, e.g., locally varying heat flux and heat transfer coefficients in multidimensional bodies, volumetric energy sources, etc. In the absence of a suitable T^*, the partitioning of the Green's function discussed in the next section is a logical approach.

An alternative Green's function solution can be derived when the function T^* is available. A function $f^*(\mathbf{r}', \tau)$ is then defined so that

$$f^*(\mathbf{r}', \tau)=\nabla_o\cdot[k\nabla_o T^*(\mathbf{r}', \tau)] \tag{10}$$

If $f^*(\mathbf{r}', \tau)$ is zero then $T^*(\mathbf{r}', \tau)$ is the quasi-steady solution. Replacing the diffusion equation with equation (10) and following standard procedures (Ozisik, 1980) used in the derivation of the Green's function solution, one obtains

$$\int_{\tau=0}^{t}d\tau\int_S k[G\partial T^*/\partial n-T^*\partial G/\partial n]_{S'}dS'=C(\mathbf{r})T^*+$$

$$\int_V C(\mathbf{r})[\int_{\tau=0}^{t}T^*(\partial G/\partial\tau)d\tau)dV'+\int_{\tau=0}^{t}d\tau\int_V Gf^*dV' \tag{11}$$

where $C(\mathbf{r})=\rho(\mathbf{r})c_p(\mathbf{r})$. The left side of this equation is exactly the same as the last term in equation (2). After integrating the

Nomenclature

a = geometric dimension
a_{ij} = element of matrix **A**, equation (6*a*)
A = matrix
b = geometric dimension
b_{ij} = element of matrix **B**, equation (6*b*)
B = matrix
c = geometric dimension
c_p = specific heat
d_{nj} = coefficients, equation (4)
$\mathbf{d}_n$ = eigenvector with elements d_{nj}
D = matrix with element d_{nj}
e_{ij} = elements of matrix **E**
E = transpose of matrix **B**•**D**
$\mathbf{f}_j$ = basis functions
$f_{j,1}$ = basis function f_j in region 1
$f_{j,2}$ = basis function f_j in region 2
f^* = function defined in equation (10)
F_n = eigenfunction
g = heat generation per unit time and unit volume
G = Green's function = $G(\mathbf{r}', t \mid \mathbf{r}, \tau)$
H = contact function
i, j, k = indices
k = thermal conductivity
k_1 = thermal conductivity in region 1
k_2 = thermal conductivity in region 2
L = slab thickness
n = index
N = number of eigenvalues
p_{ni} = element of matrix **P**
P = inverse of matrix **B**•**D** transposed
q_j = kdf_j/dx
r = radial coordinate
$\mathbf{r}$ = position vector
$\mathbf{r}'$ = position vector, dummy variable
S = surface
t = time
T = temperature
T_o = initial temperature distribution
T_s = surface temperature
T^* = auxiliary or quasi-steady solution
U = conductance function
V = volume
x, y, z = Cartesian coordinates
α = thermal diffusivity
α_1 = thermal diffusivity in region 1
α_2 = thermal diffusivity in region 2
β_j = coefficients
γ_n = eigenvalues
δ_j = coefficients
ϵ = criterion
η_j = coefficients
ρ = density
τ = time, dummy variable
ϕ = boundary function

Table 1 Comparison of $T(0.5L, t)$ using the alternative Green's function solution and exact solution or a slab

$\frac{\alpha t}{L^2}$	GBI Solution		Exact Solution	
	N = 2	N = 3	N = 10	N = 30
0.1	0.00330	0.00362	0.00362	0.00365
0.2	0.01443	0.01459	0.01458	0.01459
0.5	0.05888	0.05889	0.05888	0.05889
1	0.13566	0.13566	0.13565	0.13566
2	0.27766	0.27765	0.27764	0.27765
3	0.39248	0.39246	0.39245	0.39246
4	0.46888	0.46886	0.46885	0.46886
5	0.49938	0.49936	0.49936	0.49936
6	0.48098	0.48098	0.48098	0.48098

second term on the right side of equation (11) by parts and then eliminating the surface integral in equation (2), the following equation is obtained:

$$C(\mathbf{r})T(\mathbf{r}, t) = C(\mathbf{r})T^*(\mathbf{r}, t) + \int_{\tau=0}^{t} d\tau \int_V G[g(\mathbf{r}', \tau)$$

$$- C(\mathbf{r}')\partial T^*(\mathbf{r}', \tau)/\partial\tau]dV' + \int_V C(\mathbf{r}')G|_{\tau=0}[T_o(\mathbf{r}')$$

$$- T^*(\mathbf{r}', 0)]dV' + \int_{\tau=0}^{t} d\tau \int_V Gf^* dV' \qquad (12)$$

This equation is called the alternative Green's function solution equation. Unlike equation (2), there is no singularity at the surface of the body; therefore, one should expect a faster convergence of the solution. This improvement in the convergence behavior of both the integral and exact solution is demonstrated through the following numerical example.

Example 1: Consider a slab whose thickness is L and which is initially at zero temperature. The boundary condition at $x=0$ remains at zero temperature, while the temperature at $x=L$ changes according to the relation $T=T_o^*$ sin (ωt). The fast-converging exact solution, using Duhamel's theorem, is available is the literature (Ozisik, 1980, p. 203, equation 5-50). The alternative form of the Green's function solution, equation (12), after selecting $T^* = T_o^*(x/L)$ sin (ωt), is

$$T/T_o^* = (x/L)\sin(\omega t) - \int_0^t d\tau \frac{1}{L}\int_0^L \omega x' G \cos(\omega\tau)dx' \qquad (13a)$$

A set of basis functions that unconditionally vanishes on both surfaces, $x=0$ and $x=L$, is $f_j=(L-x)x^j$ for $j=1, 2, \ldots, N$.

The numerical values of the temperature at $x=L/2$ when $L^2\omega/\pi/10$ using the Green's function, equation (3), are computed at various times and presented in Table 1. The data are then compared with the exact series solution

$$T/T_o^* = (x/L)\sin(\omega t) + \frac{2\omega}{\pi}\sum_{n=1}^{\partial}\frac{(-1)^n}{n}\sin(n\pi x/L)$$

$$\times \frac{\alpha(n\pi/L)^2[\cos(\omega t) - \exp[-(n\pi/L)^2\alpha t]] + \omega\sin(\omega t)}{\alpha^2(n\pi/L)^4 + \omega^2} \qquad (13b)$$

At this point, it should be mentioned that the fast-converging form of the exact solution, equation (13*b*), using the Duhamel's theorem is the same as the equation (13*a*) when using the exact value of the Green's function. Table 1 shows that only three basis functions are needed to get an accurate solution. In fact, a GBI solution using $N=3$ yields a more accurate solution than the first 10 terms of the exact solution. Even for $N=2$, the solution closely agrees with the exact solution when $\alpha t/L^2$ is larger than 0.2.

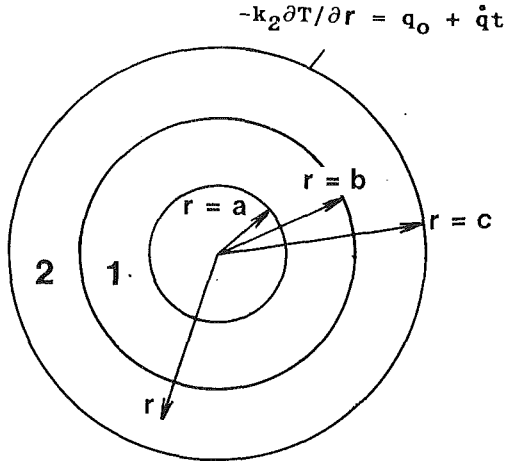

Fig. 1 Two-layer cylindrical body

Partitioning of the Green's Function Solution

The alternative formulation of the Green's function solution, equation (12), is an effective tool only if an auxiliary function T^* can be constructed with ease. For many applications, one must seek a solution using the generalized form of the Green's function, equation (2). However, there is a singularity at the surface associated with this Green's function solution that makes the series convergence unacceptably slow. This difficulty can be circumvented by using a different Green's function when $t-\tau$ is small, called the small-time Green's function. Notice that small values of $t-\tau$ are involved, rather than small t values. As a consequence, the small-time Green's function is used for large as well as small values of t. The small-time Green's function near a surface is relatively insensitive to conditions away from that surface.

A simple geometry is selected to facilitate this presentation. The problem of a hollow cylinder is considered with a heat flux boundary condition at $r=c$, the outer radius. The cylinder is composed of two materials, as shown in Fig. 1. The boundary condition at $r=a$ is for convection and the initial temperature is zero. This problem is described by

$$\frac{1}{r}\frac{\partial}{\partial r}\left[kr\frac{\partial T}{\partial r}\right] = \rho c_p \frac{\partial T}{\partial t} \qquad (14)$$

where

$$k = k_1 \text{ and } \rho c_p = (\rho c_p)_1 \text{ for } a < r < b \qquad (15a)$$

$$k = k_2 \text{ and } \rho c_p = (\rho c_p)_2 \text{ for } b < r < c \qquad (15b)$$

$$-k_1\frac{\partial T}{\partial r} + hT = 0 \quad \text{at } r=a, \quad k_2\frac{\partial T}{\partial r} = -q(t) \quad \text{at } r=c \qquad (16)$$

$$T(r, 0) = 0 \qquad (17)$$

Notice that there is only one nonzero condition in the boundary conditions and that the differential equation is homogeneous.

The solution to this problem, using equation (2), is given by

$$\rho(r)c_p(r)T(r, t) = \int_{\pi=0}^{t} d\tau \int_{S'} k(S')G(\partial T/\partial n)|_{S'=c}dS' \qquad (18a)$$

$$= -\int_{\pi=0}^{t} G(r, t\,|c, \tau)q(\tau)2\pi c d\tau \qquad (18b)$$

The attention is now focused on an expression for T at $r=c$

$$(\rho c_p)_2 T(c, t) = -\int_{\tau=0}^{t} G(c, t\,|c, \tau)q(\tau)2\pi c d\tau \qquad (19)$$

The Green's function partitioning concept is (Beck et al., 1988)

$$(\rho c_p)_2 T(c, t) = -\left[\int_{\tau=0}^{t-\Delta t} G^L(c, t\,|c, \tau) q(\tau) 2\pi c d\tau \right. \quad (19)$$

$$\left. + \int_{\tau=t-\Delta t}^{t} G^S(c, t\,|c, \tau) q(\tau) 2\pi c d\tau \right] \quad (20)$$

where Δt is chosen such that the value of $\alpha_2 \Delta t/c^2$ is small enough so that the presence of material 1 is not noted. The method of selecting the value of Δt is discussed later. The notation $G^S(\cdot)$ denotes a small-time Green's function and $G^L(\cdot)$ a large-time Green's function. Actually, the large-time expression is valid for all times if $\Delta t \to 0$ but the convergence is for the $G^L(\cdot)$ integral. If the above partitioning is employed for $\Delta t \neq 0$, the number of required terms for the $G^L(\cdot)$ integral can be greatly reduced compared to that without time partitioning. Hence, time partitioning improves convergence for both small and large values of t.

The small-time integral in equation (20) is now considered for the case of the heat flux $q(t)$ varying linearly with time

$$q(t) = q_o + \dot{q}t \quad (21)$$

The small-time Green's function for the RO2 case (Beck et al., 1988) evaluated at $r = r' = c$ is

$$G^S(c, t\,|c, \tau) = \frac{1}{2\pi c^2} \frac{c}{[\pi\alpha_2(t-\tau)]^{1/2}} + \frac{1}{2} + \frac{3}{4}\left[\frac{\alpha_2(t-\tau)}{\pi c^2}\right]^{1/2} + \frac{3}{8}\frac{\alpha_2(t-\tau)}{c^2} \quad (22)$$

where $G^S(\cdot)$ in equation (22) stands for $G^S_{RO2}(\cdot)$ in Beck et al. (1988). The notation RO2 denotes a solid cylinder with a gradient condition (condition of the second kind) at the outer radius. If the cylinder is an annulus as shown in Fig. 1, then equation (22) is valid to 0.1 percent if

$$\frac{\alpha_2(t-\tau)}{(c-b)^2} \leq 0.04 \quad (23)$$

and the constant 0.04 can be increased to 0.14 as $(c-b)/c$ approaches 1. For the $q(t)$ given by equation (21), the small-time integral (the *second* one) in equation (20) is

$$I^S = \int_{\tau=t-\Delta t}^{t} G^S(c, t\,|c, \tau)[q_o + \dot{q}\tau] 2\pi c d\tau$$

$$= \int_{u=0}^{\Delta t} G^S(c, u\,|c, 0)[q_o + (t-u)\dot{q}] 2\pi c du \quad (24)$$

where $u = t - \tau$ and $du = -d\tau$. Notice that the integral over u involves small values of $\alpha_2 u/c^2$.

The integration of equation (24) and $G^S(\cdot)$ given by equation (22) results in

$$I^S = -2(q_o + \dot{q}t)\left[\frac{\Delta t}{\pi\alpha_2}\right]^{1/2}\left[1 + \frac{1}{4}(\pi\Delta t^+)^{1/2} + \frac{1}{4}\Delta t^+ + \frac{3\pi^{1/2}}{32}(\Delta t^+)^{3/2}\right] + \frac{2(\Delta t)^{3/2}}{3(\pi\alpha)^{1/2}}\dot{q}\left[1 + \frac{3}{8}(\pi\Delta t^+)^{1/2} + \frac{9}{20}\Delta t^+ + \frac{3\pi^{1/2}}{16}(\Delta t^+)^{3/2}\right] \quad (25)$$

where Δt^+ is defined by

$$\Delta t^+ = \alpha_2 \Delta t/c^2 \quad (26)$$

The last term inside the first brackets in equation (25) is less than 0.001 for Δt^+ values less than 0.033. For the condition given by equation (23), fewer terms are needed in equation (25) because Δt^+ is even smaller than 0.033.

The plane wall case denoted X32 (see Beck, 1988, for notation) is now considered; it is described by

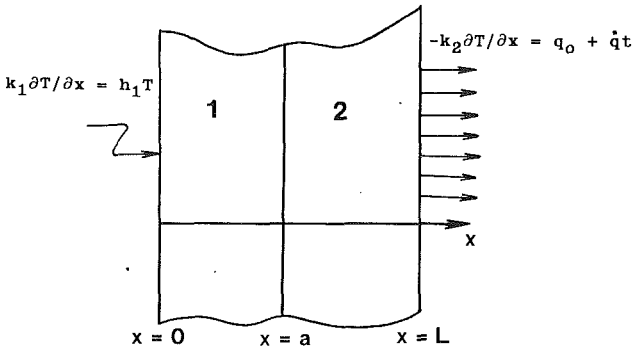

Fig. 2 Two-layer slab

$$\frac{\partial}{\partial x}\left[k(x)\frac{\partial T}{\partial x}\right] = \rho(x)c_p(x)\frac{\partial T}{\partial t} \quad (27)$$

where

$$k = k_1 \text{ and } \rho c_p = (\rho c_p)_1 \text{ for } 0 < x < a \quad (28a)$$

$$k = k_2 \text{ and } \rho c_p = (\rho c_p)_2 \text{ for } a < x < L \quad (28b)$$

$$-k_1\frac{\partial T}{\partial x} + hT = 0 \quad \text{at } x = 0, \quad k_2\frac{\partial T}{\partial x} = -q(t) \quad \text{at } x = L \quad (29)$$

$$T(x, 0) = 0 \quad (30)$$

The detailed geometric descriptions and the boundary conditions are given in Fig. 2.

Equation (18*b*), after the volume element $2\pi dr$ is replaced by $1 \cdot dx$, applies in the form

$$\rho(x)c_p(x)T(x, t) = -\int_{\tau=0}^{t} G(x, t\,|L, \tau) q(\tau) d\tau \quad (31)$$

Again, considering the point $x = L$ and using time partitioning yields

$$(\rho c_p)_2 T(L, t) = -\left\{\int_{\tau=0}^{t-\Delta t} G^L(L, t\,|L, \tau) q(\tau) d\tau + \int_{\tau=t-\Delta t}^{t} G^S(L, t\,|L, \tau) q(\tau) d\tau\right\} \quad (32)$$

where $\alpha_2 \Delta t/(L-a)^2$ is less than 0.14. If a goes to zero, the small-time Green's function $G^S(\cdot)$ for this case is the simple expression

$$G^S(L, t\,|L, \tau) = [\pi\alpha_2(t-\tau)]^{-1/2} \quad (33)$$

If the second integral in equation (24) for $\tau = t - \Delta t$ to t is called I^S, the result for $q(\tau)$ given by equation (21) is

$$I^S = -2(q_o + \dot{q}t)\left[\frac{\Delta t}{\pi\alpha_2}\right]^{1/2} + \frac{2(\Delta t)^{3/2}}{3(\pi\alpha)^{1/2}}\dot{q} \quad (34)$$

which actually contains the first term in each of the two bracketed expressions in equation (25). The other terms in equation (25) are for the curvature of the cylinder. Equation (34) is a remarkably simple expression and its use will greatly reduce the number of terms needed in the large-time expression. The large-time Green's functions in this study are given by equation (3). The next two numerical examples illustrate that the partitioning can greatly improve the accuracy of the GBI method, even for a small number of basis functions.

Example 2: A homogeneous hollow cylinder with inner radius $a = c/2$, where c is the outer radius, satisfies the boundary conditions given by equation (16). Furthermore, it is assumed that $T(r, 0) = 0$. The boundary condition at $r = a$ is convective and $h_1 a/k_1$ is selected equal to 1. The heat flux $q(t)$ at $r = c$ is given by equation (21) with $q_o = 0$ so that q varies

Table 2 Results of dimensionless surface temperature, $-kT/(a^3\dot{q}/\alpha)$, calculations at $r/a = 2$ for Example 2

Time $\alpha t/a^2$	N = 2		N = 3		N = 5		N = 7			Exact Series (first 14000 terms)
	AGFS*	PGFS**	AGFS*	PGFS**	AGFS*	PGFS*	AGFS*	GFS+	PGFS**	
0.01	0.001372	0.000765	0.000945	0.000765	0.000773	0.000765	0.000765	0.000608	0.000765	0.000765
0.02	0.003072	0.002179	0.002365	0.002179	0.002179	0.002179	0.002179	0.001870	0.002179	0.002179
0.05	0.009945	0.007840	0.008850	0.008740	0.008738	0.008740	0.008740	0.007973	0.008740	0.008739
0.1	0.026438	0.025135	0.025163	0.025135	0.025135	0.025137	0.025136	0.023607	0.025136	0.025134
0.2	0.074303	0.072923	0.072825	0.072902	0.072871	0.072870	0.072872	0.069817	0.072870	0.072868
0.5	0.30721	0.30574	0.30505	0.30554	0.30518	0.30517	0.30518	0.29755	0.30518	0.30517
1	0.93291	0.93117	0.92977	0.93100	0.93000	0.92998	0.93001	0.91475	0.93000	0.92999
2	2.8434	2.8406	2.8389	2.8417	2.8393	2.8392	2.8393	2.8088	2.8393	2.8392
5	11.243	11.235	11.237	11.245	11.237	11.237	11.237	11.161	11.237	11.237
10	27.715	27.696	27.708	27.724	27.709	27.709	27.709	27.557	27.709	27.709

\+ Green's Function Solution, equation (2)
* Alternate Green's Function Solution, equation (12)
** Partitioned Green's Function Solution, equation (20)

linearly with t. The temperature at $r=c$ is to be found as a function of time. Equation (25) already provides the small-time solution and the large-time solution must be prepared using equations (2) and (3). First, it is necessary to introduce a set of basis functions f_j; a general set of basis functions that satisfies the homogeneous convective conditions $k_1 df_j/dz = h_1 f_j$ at $z=a$ and $-k_2 df_j/dz - h_2 f_j$ at $z=c$ is

$$f_j = (\delta_j z^2 + \beta_j z + \eta_j) z^{j-1}; \text{ for } j = 1, 2, \ldots, N \qquad (35)$$

The coefficients δ_j, β_j, fand η_j are found by solving the two simultaneous equations coming from the two convective boundary conditions and using equation (35) for f_j. Because one of the coefficients δ_j, β_j, or η_j can be selected arbitrarily, the coefficient δ_j is set equal to the determinant of the coefficients in the two simultaneous equations; the solutions are

$$\delta_j = a(j - aB_1)(j - 1 - cB_2) - c(j - cB_2)(j - 1 - aB_1) \qquad (36a)$$

$$\beta_j = a^2(aB_1 - j - 1)(j - 1 - cB_2) - c^2(cB_2 - j - 1)(j - 1 - aB_1) \qquad (36b)$$

$$\eta_j = ac^2(j - aB_1)(cB_2 - j - 1) - ca^2(j - cB_2)(aB_1 - j - 1) \qquad (36c)$$

The parameters B_1 and B_2 appearing in equations (36*a*), (36*b*), and (36*c*) are h_1/k_1 and h_2/k_2, respectively. Equation (35) holds for any one-dimensional conduction problem in a finite domain; that is, r replaces z in cylindrical or spherical coordinates. For the example under consideration $h_1 = h$, $h_2 = 0$, and $c = 2a$. The coefficients δ_j, β_j, and η_j then become

$$\delta_j = a[(j - B_1)(j - 1) - 2j(j - 1 - B_1)] \qquad (37a)$$

$$\beta_j = a^2[(B_1 - j - 1)(j - 1) + 4(j + 1)(j - 1 - B_1)] \qquad (37b)$$

$$\eta_j = a^3[-4(j - B_1)(j + 1) - 2j(B_1 - j - 1)] \qquad (37c)$$

In special cases when $a=0$ or both B_1 and a are equal to zero, the coefficients δ_j, β_j, and η_j must be modified. Also, modifications are necessary when B_1, B_2, or both are infinite. The values of δ_j, β_j, and η_j for special cases can be obtained using a similar procedure. Once δ_j, β_j, and η_j are available, equations (6*a*) and (6*b*) yield the values of a_{ij} and b_{ij}. The integrations leading to the values of a_{ij} and b_{ij} are in the Appendix. The eigenvalues and the eigenvectors are computed using equation (5). After computing the p_{ni}'s, as described earlier, the Green's function is obtained using equation (3). When $N=1$, $\gamma_1 = -a_{11}/b_{11}$, $d_{11} = 1$, and $p_{11} = 1/b_{11}$. Similar expressions can be provided for $N=2$. When N is larger, it is preferable to calculate these quantities numerically.

Table 2 compares the accuracy of different temperature solutions at the surface $r=c$ for the case of $h_1 a/k = 1$. The dimensionless temperature quantity $kT/(a^3\dot{q}/\alpha)$ is displayed versus the dimensionless time $\alpha t/a^2$ for several solution methods. Results for the GBI method with $N=2$, 3, 5, and 7 are shown. Also given are values for the exact solution using 14,000 terms; all these terms were required to obtain the accuracy shown. The 14,000 terms resulted from the $G^L(\cdot)$ integral being evaluated at $\tau = t$, which gives a steady or quasi-steady term; it was not the consequence of t being large.

Three integral solutions are presented in Table 2. The first case for each N is the alternative Green's function solution (AGFS) and is found using equation (12), with the Green's function given by equations (3)–(6) (see also equations (35)–(37)). The solution gives very accurate results for $\alpha t/a^2 = 0.02$ and larger, and for $N=5$ and larger; the $N=3$ values at $\alpha t/a^2 = 0.01$ are 24 percent too large. The Green's function solution (GFS) is obtained using equation (2) and only given for $N=7$. For the GFS solution, however, the errors start at -20 percent and persist with 1.6 percent error at $\alpha t/a^2 = 1.0$. The GFS solution for $N<7$, not shown here, had even larger errors. The last integral solution is called the partitioned Green's function solution (PGFS); it gives virtually the same results for $N=2$, 3, 5, and 7 for all the times. This suggests that the use of time partitioning in the GBI method permits very efficient and accurate solutions. The results of a partitioned solution, using equation (20), are virtually the same as an alternative Green's function solution when $N=7$. It is important to note that the time partitioning is needed to obtain these benefits for large as well as small times.

When the exact solution was partitioned, seven eigenvalues produced values identical to those reported for the time-partitioned GBI solution for $N=7$. In Example 1, it was demonstrated that the accuracy of the results of the alternative Green's function solution, Table 1, agrees with the exact solution. The alternative Green's function solution when $N=7$ is slightly different from the results when $N=5$; see Table 2. The alternative Green's function solution, when available, generally provides accurate solutions except when time is very small.

As discussed earlier, the alternative Green's function solution requires an auxiliary equation, which is always available for one-dimensional geometries. However, in multidimensional and complex geometries, this auxiliary equation is either unavailable or difficult to obtain. The partitioning of the Green's function to obtain an accurate solution is an attractive alternative in this case. It is shown in Table 2 that the partitioning of the Green's function provides accuracy comparable to the alternative Green's function solution at "large" time and superior accuracy at "small" time.

Table 3 is prepared to show the numerical values of the Green's functions used in Table 2. The values of the Green's function using the GBI method agree well with the exact values when $N \geq 5$ and the $\alpha(t-\tau)/(c-a)^2 > 0.04$. Table 3 suggests using the small-time solution when $\alpha(t-\tau)/(c-a)^2 < 0.12$. This latter number is used for the time parti-

Table 3 Values of the Green's functions G(c, t |c, τ) for the GBI method, exact, and small-time solutions

$\frac{\alpha(t-\tau)}{(c-a)^2}$	Galerkin-Based Integral (GBI) Method				Small-Time Solution	Exact Solution
	N = 2	N = 3	N = 5	N = 7		
0.01	0.26457	0.38672	0.49460	0.47371	0.46974	0.46975
0.02	0.24802	0.32655	0.34709	0.33841	0.33862	0.33863
0.05	0.20838	0.22820	0.22280	0.22275	0.22275	0.22277
0.1	0.16600	0.16691	0.16495	0.16498	0.16491	0.16499
0.2	0.12670	0.12632	0.12588	0.12588	0.12480	0.12588
0.5	0.096912	0.097070	0.097042	0.097042	0.091206	0.097042
1	0.075063	0.075199	0.075185	0.075184	0.076939	0.075184
2	0.045402	0.045485	0.045477	0.045477	-	0.045477
5	0.010047	0.010066	0.010064	0.010064	-	0.010064

tioning of the GBI solution results appearing in Table 2 when $N=2$ and 3. A time-partitioned GBI solution can result in an accurate solution even when $N=2$. The computation of the large-time solution can be done manually for such a small N value.

The computed surface temperature, when $N=2$ and utilizing the time partitioning criterion of 0.12 instead of 0.04, is nearly the same as the entries for $N=7$ for $0<\alpha t/a^2<0.1$. When the dimensionless times are 0.2, 0.5, 1, 2, 5, and 10, the temperatures are 0.072923, 0.30574, 0.93117, 2.8406, 11.235, and 27.696. The respective errors are 0.08, 0.19, 0.12, 0.05, 0.02, and 0.05 percent. The error is generally less than 0.1 percent except for the errors of 0.19 and 0.12 percent at dimensionless times of 0.5 and 1. This is of particular interest because time partitioning greatly increases the accuracy of the GBI method. For many problems, $N=2$ provides sufficient accuracy, yet the computation is simple enough for manual computation. When N is larger, there are excellent computer programs available that provide the eigenvalues and the eigenvectors, e. g., the Jacobi method (Carnahan et al., 1969).

Heterogeneous Solids

The derivation of the Green's function solution, equation (2), or the alternative Green's function solution, equation (12), permits the computation of temperature distribution in heterogeneous bodies. Although the partitioning procedure described earlier is for layered cylinders or plates, it can be generalized for other geometries. The only difference between solutions for homogeneous and heterogeneous solids is the selection of a set of basis functions. A method of finding a set of basis functions is introduced that satisfies the boundary conditions and perfect or imperfect contact relations between adjacent materials. The basis functions are then used to solve a numerical example.

Let the subscript e identify an inclusion of different material enclosed in the main body and m denote the main domain. The basis function $f_{j,m}$, which satisfies the boundary conditions of the main body, is selected ignoring the inclusion; therefore, f_j is f_{jm} in the main body. However, the basis function should be modified as it crosses the boundary of the inclusion. The formulation of the basis functions in the absence of contact conductance is given by Haji-Sheikh (1988). Here, the formulation is modified to include the effect of finite contact conductance as

$$f_j = f_{j,m}; \text{ in the main domain} \tag{38a}$$

and

$$f_j = f_{j,m} + U + \phi_e H; \text{ in the } e\text{th inclusion} \tag{38b}$$

for $j=1, 2, \ldots, N$. The continuity condition that $k_m(\partial f_j/\partial n)_m = k_e(\partial f_j/\partial n)_e$ and the jump condition $f_{j,e} = f_{j,m} - (k_m/C)(\partial f_{j,m}/\partial n)$ at the boundary of the inclusion ($\phi_e = 0$ surface is different for different inclusions) permit the calculation of U and H as

$$U = -(k_m/C)(\partial f_{j,m}/\partial n)\,|_{\phi_e=0} \tag{38c}$$

$$H = [(\nabla f_{j,m} \cdot \nabla \varphi_e)\,|_{\phi_e=0}(k_m/k_e - 1) - \nabla U \cdot \nabla \varphi_e]\,|_{\phi_e=0}/[(\nabla \phi_e \cdot \nabla \phi_e)\,|_{\phi_e=0}] \tag{38d}$$

where C is the contact conductance. A linear combination of the basis function f_j satisfies the continuity of heat flux, $k_m(\partial T/\partial n)_m = k_e(\partial T/\partial n)_e$, and temperature jump, $T_e = T_m - (k_m/C)(\partial T_{j,m}/\partial n)$, on the boundary of inclusion e. When the inclusion has other boundaries in addition to the $\phi_e = 0$ surface, modification to the values of U and H is necessary as discussed in Example 3.

Example 3: To illustrate the method for accommodating the contribution of contact conductance, consider two plates; plate 1 (or e) when $0<x<1$, and plate 2 (or m) when $1<x<L$. When calculating a_{ij} from equation (6*a*), the function f_j suffers a step change at and along the contact surface. The derivatives of f_j at $x=a$ are singular, and the value of the volume integral over the singularity zone is zero. The integral given in equation (6*a*) for this example is

$$a_{ij} = \int_0^L f_i \frac{d}{dx}\left(k\frac{df_j}{dx}\right)dx = \int_0^{a-\epsilon} f_{i,e}\frac{d}{dx}\left(k\frac{df_{j,e}}{dx}\right)dx + \int_{a-\epsilon}^{a+\epsilon} f_i \frac{d}{dx}\left(k\frac{df_j}{dx}\right)dx + \int_{a+\epsilon}^{L} f_{i,m}\frac{d}{dx}\left(k\frac{df_{j,m}}{dx}\right)dx \tag{39}$$

As $\epsilon \to 0$, the first and third integrals become the integration of equation (6*a*) over regions m and e; the integration over the singular zone is ignored. The second term on the right side of equation (39), which represents the value of the volume integral over the singular zone of contact, can be integrated by parts

$$\int_{a-\epsilon}^{a-\epsilon} f_i \frac{d}{dx}\left(k\frac{df_j}{dx}\right)dx = f_i(k df_j/dx)\Big|_{a-\epsilon}^{a+\epsilon} - \int_{a-\epsilon}^{a+\epsilon} k(df_i/dx)(df_j/dx)dx = \lim_{\epsilon\to 0}\{q_j[(f_{i,m}(a+\epsilon) - f_{i,e}(a-\epsilon)] - q_j[(f_{i,m}(a+\epsilon) - f_{i,e}(a-\epsilon)]\} = 0;$$

$$q_j = k_m \partial f_j/\partial x = k_e \partial f_j/\partial x = \text{const} \tag{40}$$

The above derivation is for one-dimensional conduction and can be extended to include multidimensional bodies.

When f_j or its normal derivative on the external surface is zero, it is possible to express equation (6*a*) as

$$a_{ij} = -\int_V k \nabla f_i \cdot \nabla f_j dV \tag{41}$$

If this equation is utilized to compute a_{ij}, the value of the integral over the contact zone, where the derivatives of f_j are singular, is not zero and should be evaluated.

The composite slab under consideration has homogeneous boundary conditions

$$-k_m \partial T/\partial x = hT \text{ at } x = L \text{ and when } t>0 \tag{42a}$$

and

$$\partial T/\partial x = 0 \text{ at } x = 0 \text{ and when } t>0 \tag{42b}$$

the basis functions are

$$f_{j,m} = (\delta_j - x^2)x^{2(j-1)}; \quad 1<x<R_m \tag{43a}$$

$$f_{j,e} = (\delta_j - x^2)x^{2(j-1)} + C_j + (1-x^2)H; \; 0<x<1 \tag{43b}$$

where $\delta_j = L^2(L + 2jk_m/h)/[L + 2(j-1)k_m/h]$. The value of $C_j = -2(k_m/h_c)[j - (j-1)\delta_j]$ is computed so that the equation $f_{j,e} = f_{j,m} - (k_m/h_c)(\partial f_{j,m}/\partial x)$ at $x=1$ is satisfied, where h_c is the contact conductance. The continuity of heat flux at $x=1$

yields $H=(k_m/k_e-1)[j-(j-1)\delta_j]$. Except for the additional constant C_j, the basis functions are similar to those used for concentric cylinders. Apart from the stated difference in the volume element, the remaining analytical steps are identical to those described in Example 2. The solution when $N=2$, $a=1$, $L=2$, $k_m=1$, $k_e=2$, $h/k_m=1$, $h_c/k_m=1$, $\rho_m c_{pm}=1$, and $\rho_e c_{pe}=1$ is

$$T/T_o=0.15048F_1(x)\exp(-1.5407t)+0.006762F_2(x)\exp(-11.449t) \quad (44)$$

where

$$F_1(x)=f_1-0.040305f_2 \quad (45a)$$

$$F_2(x)=f_1+20.999f_2 \quad (45b)$$

When $x\le a$ (here $a=1$), that is, in region e (region 1 in Fig. 3), the functions $f_{1,e}$ and $f_{2,e}$ represent the f_1 and f_2 functions. However, when $x\ge a$, that is, in region m (region 2 in Fig. 3), the functions f_1 and f_2 are replaced by $f_{1,m}$ and $f_{2,m}$ functions. At $x=a=1$, it can be seen that $f_{1,e}=f_{1,m}+C_1$ and $f_{2,e}=f_{2,m}+C_2$.

When the boundary condition at $x=0$ is convective, C_j must also satisfy the convective condition at $x=0$. In addition, the coefficient $(1-x^2)$ that multiplies H should be replaced by a function that becomes 0 when $x=1$ and satisfies the convective condition at $x=0$. The computer program developed for calculation of one-dimensional transient conduction in two-layer materials can equally accommodate cylindrical and spherical bodies with various boundary conditions; however, due to space limitations other examples are not included.

Conclusion

The time partitioning discussed in this paper provides accurate solutions for both simple and complex problems. The time-partitioning procedure for heterogeneous solids is straightforward; hence, no examples are given to avoid redundancy. The method has many advantages that are described below. Generally, for one-dimensional problems, a two-term solution provides results accurate enough for most applications. The methodology, especially for one-dimensional bodies, is universal and a single computer program (Beck et al., 1989) can be used for different-shaped bodies with different boundary conditions. This is a unique feature that is not shared by the exact solution. A computer program prepared using the GBI method yields results almost instantaneously. The time-partitioned GBI method has flexibility, accuracy, and computational speed, which are the features of an efficient computational method.

Acknowledgments

The first author acknowledges the support of the 1988 CRAY Sponsored University Research and Development Grant Program, and the Department of Mechanical Engineering, University of Texas at Arlington. The second author appreciates the support of the State of Michigan through the REF program, administered through The Composites, Materials, and Structures Center.

References

Beck, J. V., and Litkouhi, B., 1989, "Heat Conduction Numbering System for Basic Geometries," *Int. J. of Heat and Mass Transfer*, Vol. 31, pp. 505–515.

Beck, J. V., Cole, K. D., Haji-Sheikh, A., and Litkouhi, G., 1989, *Green's Functions for Transient Heat Conduction*, book under preparation.

Beck, J. V., and Keltner, N. R., 1987, "Green's Function Partitioning Procedure Applied to Foil Heat Flux Gages," ASME JOURNAL OF HEAT TRANSFER, Vol. 109, pp. 274–280.

Carnahan, B., Luther, H. A., and Wilkes, J. O., 1969, *Applied Numerical Methods*, Wiley, New York, p. 255.

Haji-Sheikh, A., 1986, "On Solution of Parabolic Partial Differential Equations Using Galerkin Functions," *Integral Methods in Science and Engineering*, F. R. Payne et al., eds., Hemisphere Publishing Corp., Washington, DC, pp. 467–479.

Haji-Sheikh, A., 1988, "Heat Diffusion in Heterogeneous Media using Heat-Flux-Conserving Basis Functions," ASME JOURNAL OF HEAT TRANSFER, Vol. 110, pp. 276–282.

Haji-Sheikh, A., and Lakshminarayanan, R., 1987, "Integral Solution of Diffusion Equation: Part 2—Boundary Conditions of Second and Third Kinds," ASME J. OF HEAT TRANSFER, Vol. 109, pp. 557–562.

Haji-Sheikh, A., and Mashena, M., 1987, "Integral Solution of Diffusion Equation: Part 1—General Solution," ASME JOURNAL OF HEAT TRANSFER, Vol. 109, pp. 551–556.

Ozisik, M. N., 1980, *Heat Conduction*, Wiley, New York.

APPENDIX

The following indefinite integration assists the calculation of the elements of matrix **A**:

$$\int f_i(\nabla^2 f_j)z^p dz=\sum_{k=1}^{5} P_k(i,j,p)\frac{z^{i+j+p+2-k}}{i+j+p+2-k} \quad (A1)$$

where $p=0$, 1, or 2 for slabs, cylinders, or spheres, and

$$P_1(i,j,p)=\delta_i\delta_j(j+1)(j+p)$$

$$P_2(i,j,p)=\beta_i\delta_j(j+1)(j+p)+\beta_j\delta_i(j+p-1)j$$

$$P_3(i,j,p)=\eta_i\delta_j(j+1)(j+p)+\beta_i\beta_j(j+p-1)j+\eta_j\delta_i(j+p-2)(j-1)$$

$$P_4(i,j,p)=\eta_i\beta_j(j+p-1)j+\eta_j\beta_i(j-1)(j+p-2)$$

$$P_5(i,j,p)=\eta_i\eta_j(j-1)(j+p-2)$$

Note that when "$p=0$ and $j=1$," P_4 is zero. Also, when "$j=1$" or "$j=2-p$," the term containing P_5 is zero. The coefficients δ, β, and η are given by equations (36*a–c*).

Similarly, the following equation assists the calculation of the elements of matrix **B**:

$$\int f_i f_j z^p dz=\sum_{k=1}^{5} Q_k(i,j)\frac{z^{i+j+p+4-k}}{i+j+p+4-k} \quad (A2)$$

where $Q_1(i,j)=\delta_i\delta_j$, $Q_2(i,j)=\beta_i\delta_j+\beta_j\delta_i$, $Q_3(i,j)=\eta_i\delta_j+\beta_i\beta_j+\eta_j\delta_i$, $Q_4(i,j)=\beta_i\eta_j+\beta_j\eta_i$, and $Q_5=\eta_i\eta_j$.

A Comparison of Two Test Methods for Determining Transfer Function Coefficients for a Wall Using a Calibrated Hot Box

D. M. Burch

B. A. Licitra

R. R. Zarr

National Institute of Standards and Technology, Gaithersburg, MD 20899

This paper experimentally verifies and compares two dynamic test methods for a calibrated hot box to characterize the transient thermal performance of complex walls. In these methods, a wall specimen is sandwiched between the two conditioning chambers of a calibrated hot box. The exterior surface of the wall specimen is subjected to a time-varying excitation function in air temperature. At the interior surface, the air temperature is maintained steady, and the heat transfer response is measured. Conduction transfer function coefficients that relate the measured heat transfer response to the excitation function are derived. The two dynamic test methods were applied to an insulated hollow concrete block wall that contained significant thermal bridges and lateral heat flows. Empirical transfer function coefficients derived by the test methods predicted with good agreement the heat transfer response of this wall specimen when its exterior surface was subjected to excitation functions that differed markedly from those used to derive the coefficients.

Introduction

Computer programs are widely used to perform hourly building energy simulation analyses. Building designers, architects, and building owners use these computer programs to size HVAC equipment, to predict peak demands, or to predict annual energy costs. Moreover, such programs are used to minimize annual energy costs by investigating tradeoffs in the envelope design, selection of HVAC systems and equipment, and by analyzing various methods of building operation.

Most of these computer programs use one-dimensional analytical transfer function coefficients (TFCs) to account for time-dependent heat transfer through opaque portions of the building envelope. However, the components of a building envelope usually contain a significant number of thermal bridges, lateral heat flows, and thermal anomalies that are not accounted for by the analytical TFCs. The presence of thermal bridges and anomalies increases the heat transmission in walls of office buildings by as much as 10–21 percent (Grot et al., 1985).

The National Institute of Standards and Technology (NIST) recently developed a "curve-fitting method" (Burch et al., 1988) and a "fast ramp method" (Burch et al., 1987a) for using calibrated and guarded hot boxes to determine experimentally TFCs for a wall specimen. Many of the concepts for the fast ramp method are based upon Stephenson et al. (1988). The two methods have been verified for a "simple" masonry wall (Burch et al., 1987a, 1988). Here, the term "simple" is used to denote a wall consisting of homogeneous layers without thermal bridges, lateral heat flows, or thermal anomalies. In this paper, the applicability of these two methods to "complex" walls containing significant thermal bridges and lateral heat flows is investigated.

Procedure for Dynamic Testing

For a dynamic test, a wall specimen is installed in 3.0×4.6 m support frame and sandwiched between the metering and climatic chambers of a calibrated hot box (CHB) as shown in Fig. 1. Uniform streams of conditioned air may be delivered to either the top or bottom of vertical plenums formed between a baffle and opposite sides of the wall specimen. A time-dependent excitation function is generated in the climatic chamber. The metering chamber is operated at a typical indoor steady temperature condition and serves as a calorimeter.

For the CHB measurements presented in this paper, the air speed was adjusted and maintained at 0.3 m/s in the metering chamber and at 1.1 m/s in the climatic chamber.

The heat transfer rate (Q_{sp}) at the interior surface of the specimen is determined at hourly time steps from the following energy balance equation:

$$Q_{sp} = Q_h + Q_{bl} - Q_{\text{inf}} - Q_{\text{box}} - Q_{fl} - Q_{\text{stor}} \quad (1)$$

All powers, heat transfer rates, and energy-storage rates in the above equation are averaged over a one-hour period to smooth out fluctuations. The terms Q_h, Q_{bl}, Q_{inf}, and Q_{box} are measured directly. The requirements of ASTM standard steady-state test method C 976 (ASTM, 1988) pertinent to dynamic testing were adhered to. The measurements are

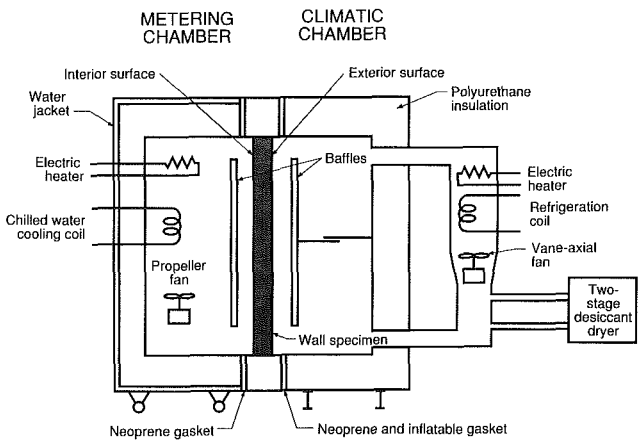

Fig. 1 Schematic cross section of the calibrated hot box

Contributed by the Heat Transfer Division for publication in the JOURNAL OF HEAT TRANSFER. Manuscript received by the Heat Transfer Division June 16, 1988; revision received June 19, 1988. Keywords: Building Heat Transfer, Measurement Techniques, Transient and Unsteady Heat Transfer.

described in the next section; the determination of Q_{fl} and Q_{stor} is described below.

The heat transfer rate (Q_{fl}) that flanks the wall specimen and passes through the specimen support frame was predicted using a time-dependent finite-difference model described by Burch et al. (1987b). The flanking heat transfer rate generally comprises less than 7 percent of the net power delivered to the metering chamber.

The total energy-storage rate (Q_{stor}) within the metering chamber (excluding the inside surface of the wall specimen) was predicted using transfer function equations derived from a series of calibration tests described by Burch et al. (1987b).

The foregoing procedure has been shown to yield closure of the energy balance for the metering chamber for a simple masonry wall under dynamic conditions within an uncertainty of ±4 percent (Burch et al., 1987b).

Calibrated Hot Box Measurements

The direct current powers delivered to the heater and blower were determined by taking the product of the measured d-c current and voltage supplied to each device. Each current was obtained by measuring the voltage drop across a precision shunt resistor. Voltages were measured using a digital voltmeter that was part of the data acquisition equipment. The measurement uncertainty of these d-c powers was less than 0.1 percent.

During CHB measurements, the pressure within the climatic chamber is maintained in slight suction with respect to the metering chamber. This prevents cold air from the climatic chamber infiltrating into the metering chamber, thereby disturbing its energy balance. Air exchange rates for the metering chamber were measured using a tracer-gas technique described by Zarr et al. (1987). The energy-transfer rate due to air exchange was determined by taking the product of the mass rate of air exchange and the difference in enthalpy between the air in the metering chamber and the laboratory. Air exchange rates were generally quite small (i.e., typically less than 0.05 volume changes per hour), resulting in Q_{inf} less than 0.5 W. In the analysis of a dynamic test, the air exchange rate was treated as constant. The heat transfer rate at the interior walls of the metering chamber (Q_{box}) was measured using an array of 28 heat flux transducers installed at various locations under the reinforced fiberglass plastic skin of the metering chamber.

The air temperature was measured in a plane 75 mm in front of the inside specimen surface (in the metering chamber) and in a plane 75 mm from the outside specimen surface (in the climatic chamber). Each of these measurements was accomplished using a thermopile consisting of 40 pairs of thermocouple junctions between grid points in the plane and a uniform temperature reference junction. The air temperature measurements are believed to have been accurate to within an uncertainty of 0.05°C. Further information on the measurements is given by Zarr et al. (1987).

Description of Wall Specimen

The wall specimen was constructed from nominal 0.20-m-thick rectangular hollow concrete blocks with insulation inserts installed within a portion of the cores. Schematics of a concrete block, an insulation insert, and a cross section of an insulated block are given in Fig. 2. The concrete used for the blocks was a lightweight aggregate having a dry density of 1350 kg/m^3. Within each block, a portion of the web was omitted for receiving the insulation insert and reducing the thermal bridging of the web. The insulation insert contained two embedded reflective air spaces. In addition, the exterior surface of the insulation insert contained a reflective surface that formed a third reflective air space between the face shell and the insulation insert.

The transient heat transfer rate through this wall specimen would be very difficult to predict using an analytical model because the heat transfer rate through the concrete is multidimensional and because of the presence of embedded reflective air spaces. Transient predictions could be accomplished using a finite-difference or finite-element model, but considerable effort would be required to generate the nodal equations.

Empirical Transfer Function Coefficients From the Curve-Fitting Method

The four-harmonic diurnal temperature cycle and the sol-air diurnal temperature cycle shown in Fig. 3 were generated in the climatic chamber of the CHB. The four-harmonic diurnal temperature cycle consists of the sum of a fundamental 24-hour sine wave and three harmonics each having reduced amplitude. Each of these periodic wave forms was repeated in the climatic chamber until a steady-periodic rate of heat transfer occurred in the wall specimen, after which 120 hours

Nomenclature

A = surface area of wall specimen, m^2
m = slope of ramp function, °C/h
n = index of summation
N = number of poles
Q_{bl} = power delivered by the blower, W
Q_{box} = heat transfer rate at inside walls of metering chamber, W
Q_f = final specimen heat transfer rate, W
Q_{fl} = flanking heat transfer rate, W
Q_h = power delivered by the electric heater, W
Q_i = initial specimen heat transfer rate, W
Q_{inf} = energy-transfer rate due to air exchange, W
Q_{sp} = specimen heat transfer rate, W
Q_{stor} = total energy-storage rate within the metering chamber, W
QG = rate of specimen heat gain, W
t = elapsed time, h
TI = air temperature in metering chamber, °C
TO = air temperature in climatic chamber, °C
U = thermal transmittance, W/m^2•°C
V = change in air temperature in climatic chamber, °C
y_i = response factors at outside surface, W/m^2•°C
Y_i = transfer function coefficients at outside surface, W/m^2•°C
β_n^2 = poles, h^{-1}
γ_n = residues at poles, h
γ_o = sum of residues, h
δ = duration of ramp, h
Δ = time interval of the analysis, h
λ = past-history transfer function coefficient
υ = transient solution, W
υ_r = residual transient solution, W
υ_1 = first exponential term of transient solution, W

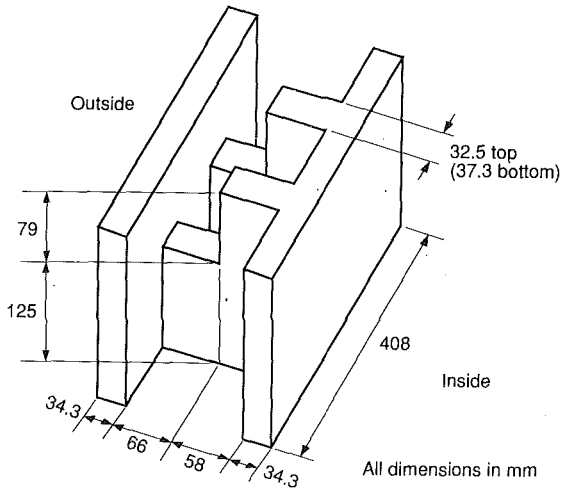

Fig. 2(A) Isometric view of block without insulation insert

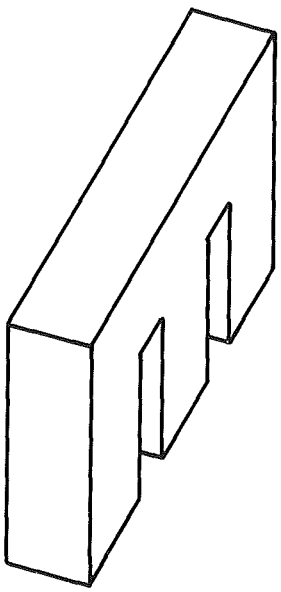

Fig. 2(B) Isometric view of insulation insert

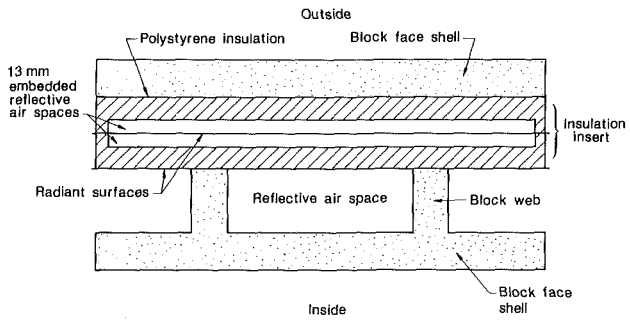

Fig. 2(C) Top view of block with insulation insert installed

Fig. 2 Hollow concrete block with partial-size insulation insert

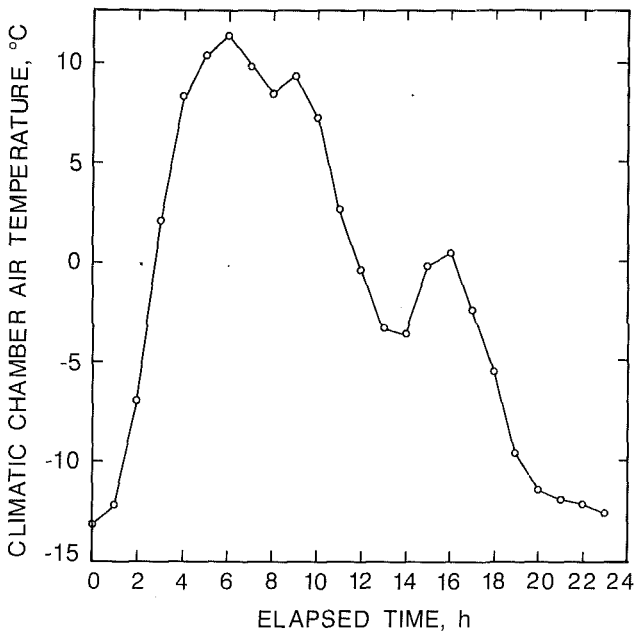

Fig. 3(A) Four-harmonic test

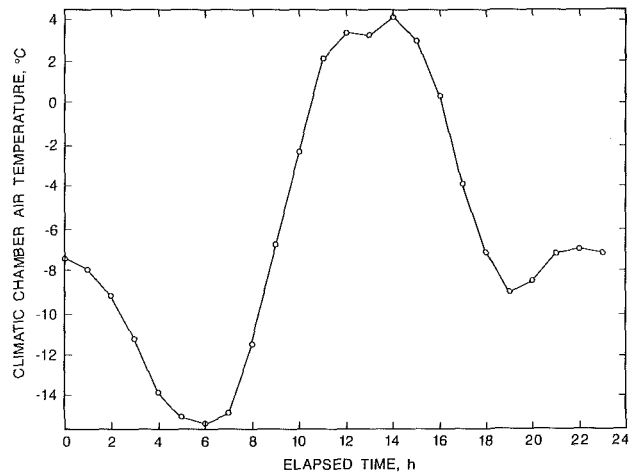

Fig. 3(B) Sol-air test

Fig. 3 Excitation functions for the diurnal cycle tests

of data were collected for analysis. The resulting specimen heat transfer rate is given in Fig. 4 for each of the excitation functions.

In the curve-fitting method, it is assumed that the specimen heat transfer rate ($Q_{sp,t}$), the air temperature in a plane at the inside surface of the specimen (TI_t), and the air temperature in a plane at the outside surface (TO_t) are related by the transfer function equation

$$\frac{Q_{sp,t}}{A} = U\cdot(1-\lambda)\cdot TI_t - Y_0\cdot TO_t - Y_1\cdot TO_{t-\Delta} - Y_2\cdot TO_{t-2\Delta} + \ldots + \lambda\cdot\frac{Q_{sp,t-\Delta}}{A} \quad (2)$$

Here the Y coefficients are outside surface TFCs, λ is a past-history TFC, sometimes called the common ratio, and Δ is the time interval for the analysis. From transfer function theory (Hittle, 1981), it can be shown that the thermal transmittance is given by

$$U_y = \frac{\sum_{n=1}^{N} Y_n}{1-\lambda} \quad (3)$$

For each of the excitation functions, the method of least squares was applied to equation (2) to yield empirical TFCs that minimized the sum of the squares of the deviations between the measured and curve-fitted results. Separate curve fits were obtained for increasing numbers of Y coefficients. As

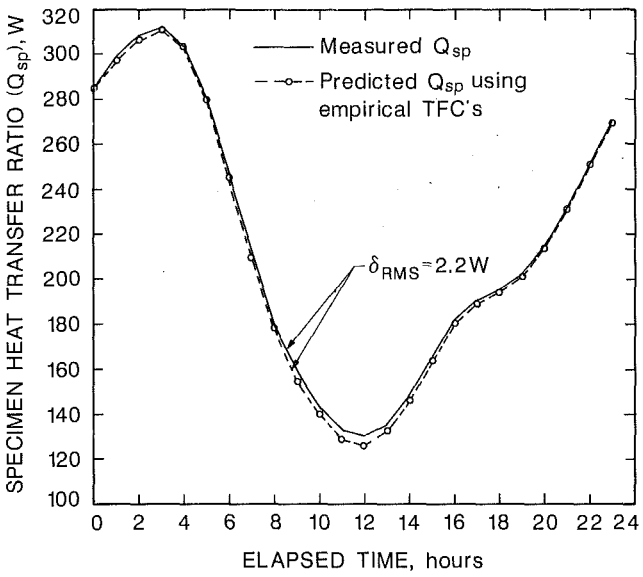

Fig. 4(*A*) Four-harmonic test

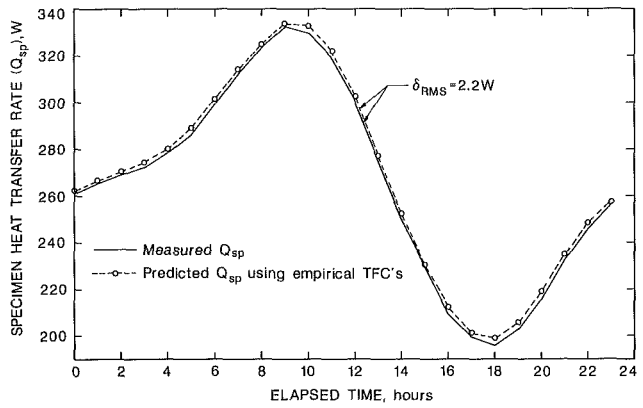

Fig. 4(*B*) Sol-air test

Fig. 4 Curve fit of specimen heat transfer rate for the diurnal cycle tests

Table 1 Empirical TFCs from curve-fitting method

TFC	Four-harmonic test	Sol-air test
U*	0.7423	0.7488
Y_o	0.0217	0.0024
Y_1	−0.0231	0.0283
Y_2	0.1598	0.1038
Y_3	0.0005	0.0321
Y_4	0.0664	0.0323
Y_5	−0.0210	0.0124
Y_6	0.0221	--
λ	0.7138	0.7353

*The U and Y TFCs are in W/m^2•°C and λ is dimensionless.

the number of Y coefficients increased, U_y approached U, and subsequently diverged. An optimum number of Y coefficients was deemed to exist when the termination criteria (CRIT) defined by

$$\text{CRIT} = 1 - U/U_y \tag{4}$$

reached a minimum value. The inclusion of more than one past-history TFC always resulted in a less satisfactory curve fit. Further information on curve fitting of TFCs is given by Seem and Hancock (1986).

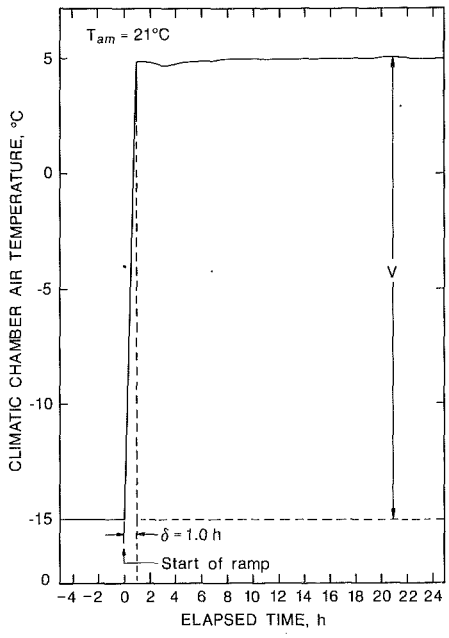

Fig. 5(*A*) Excitation function

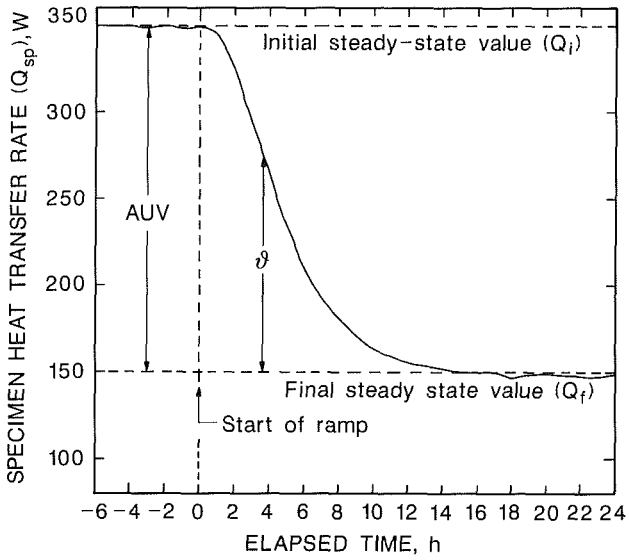

Fig. 5(*B*) Specimen heat transfer response

Fig. 5 Fast ramp method

Empirical TFCs derived for each of the excitation functions are summarized in Table 1. Note that the two sets of Y TFCs differed markedly from each other. Each of the sets of TFCs was used in equation (2) to predict the excitation function from which they were derived, in order to determine how good each set of TFCs fit the data. The root-mean-square (rms) difference between the predicted and measured specimen heat transfer rate for each of the two excitation functions was less than ±2.2 W (see Fig. 4), indicating a good curve fit in each case.

Empirical Transfer Function Coefficients by the Fast Ramp Method

Excitation Function and Heat Transfer Response. A steady air temperature of −15°C was initially maintained in the climatic chamber, while the metering chamber was maintained at 21°C. After a steady-state specimen heat transfer rate was established, the air temperature in the climatic

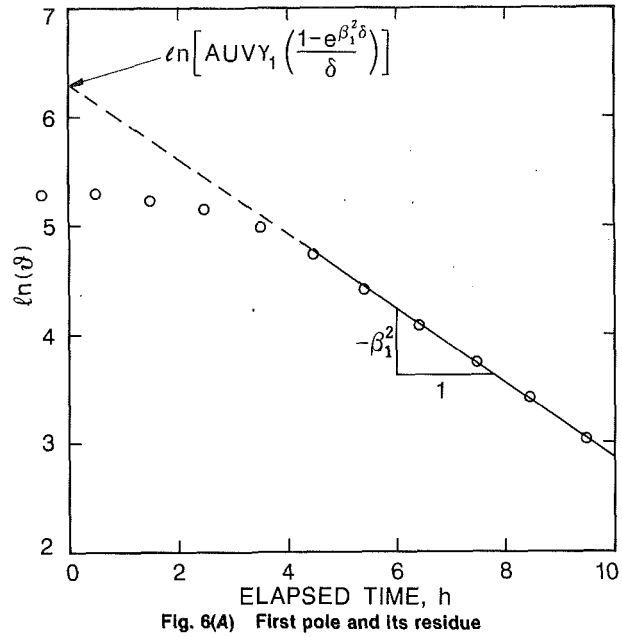

Fig. 6(A) First pole and its residue

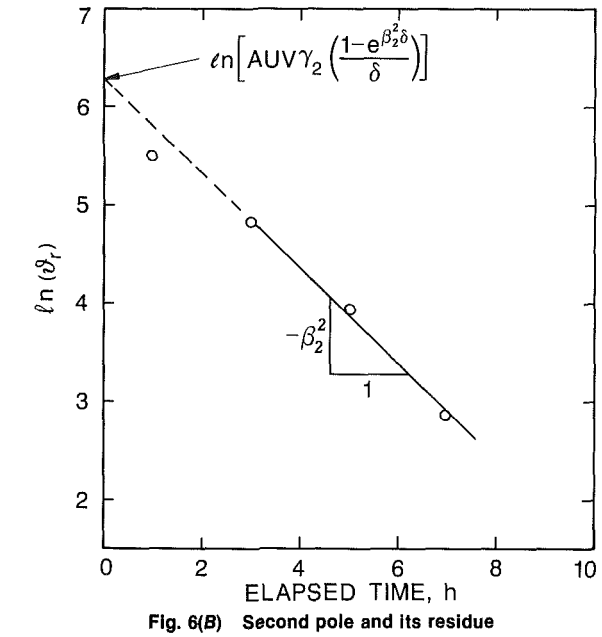

Fig. 6(B) Second pole and its residue

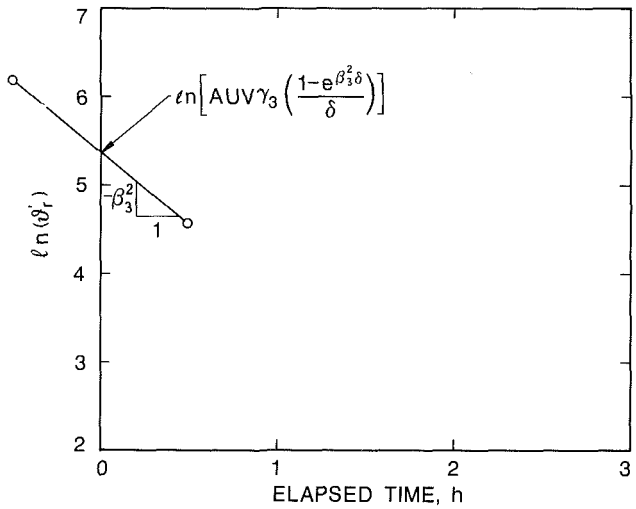

Fig. 6(C) Third pole and its residue

Fig. 6 Analysis of poles and residues

chamber was suddenly ramped to a final temperature level of 5°C. This final temperature level was maintained until a new steady-state specimen heat transfer rate was attained. The duration of the ramp (δ) was 1.0 h, and the difference (V) between the temperature levels was 20°C. This excitation function is shown in Fig. 5(A).

The measured specimen heat transfer response for the above excitation function is given in Fig. 5(B). The difference between the initial (Q_i) and the final (Q_f) specimen heat transfer rate is equal to the product of the thermal transmittance (U), temperature difference (V), and the surface area (A). Therefore, the thermal transmittance (U) of the wall may be determined by the relation

$$U=(Q_i-Q_f)/(A\cdot V) \tag{5}$$

Here the thermal transmittance is assumed to be a constant value independent of temperature.

The specimen heat transfer rate (Q_{sp}) shown in Fig. 5(B) occurring in response to the fast ramp excitation function is given by the relation

$$Q_{sp}-Q_i=A\cdot U\cdot V\left[1-\sum_{n=1}^{N}\gamma_n\left(\frac{1-e^{\beta_n^2\delta}}{\delta}\right)e^{-\beta_n^2 t}\right] \tag{6}$$

The first term ($A\cdot U\cdot V$) is the steady-state solution. The second term is the transient solution (υ) labeled in the specimen heat transfer response given in Fig. 5(B). The coefficients β_n^2 and γ_n are poles and residues, respectively.

Analysis of Poles and Residues. The transient solution (υ) may be expanded

$$\upsilon=A\cdot U\cdot V\left[\gamma_1\left(\frac{1-e^{\beta_1^2\delta}}{\delta}\right)e^{-\beta_1^2 t}+\gamma_2\left(\frac{1-e^{\beta_2^2\delta}}{\delta}\right)e^{-\beta_2^2 t}+\gamma_3\left(\frac{1-e^{\beta_3^2\delta}}{\delta}\right)e^{-\beta_3^2 t}+\ldots\right] \tag{7}$$

The second, third, and higher order terms contribute significantly to the transient solution only during an initial period of the transient response. After this initial period, the transient solution becomes

$$\upsilon\approx\upsilon_1=A\cdot U\cdot V\cdot\gamma_1\left(\frac{1-e^{\beta_1^2\delta}}{\delta}\right)e^{-\beta_1^2 t}\ \text{for } t \text{ large} \tag{8}$$

Taking the natural logarithm of equation (8) gives

$$\ln(\upsilon)\approx\ln\left[A\cdot U\cdot V\cdot\gamma_1\left(\frac{1-e^{\beta_1^2\delta}}{\delta}\right)\right]-\beta_1^2 t \tag{9}$$

Measured hourly values of $\ln(\upsilon)$ were plotted as a function of elapsed time (t) in Fig. 6(A). Values of $\ln(\upsilon)$ were plotted on the half hour because the values were time averaged over hourly intervals. Note that for t large, $\ln(\upsilon)$ follows a linear relationship. A least-squares fit of data along the linear portion of the data was obtained. From equation (9), the negative slope of this straight line is equal to the first pole (β_1^2) and the intercept (y_o) is given by

$$y_o=A\cdot U\cdot V\cdot\gamma_1\left(\frac{1-e^{\beta_1^2\delta}}{\delta}\right) \tag{10}$$

The first residue (γ_1) was determined from the above equation.

After the first pole (β_1^2) and its residue (γ_1) were determined,

Table 2 Summary of thermal transmittance, poles, and residues for fast ramp method

Thermal transmittance (U), W/m^2•°C	0.7348
Poles, h^{-1}	
β_1^2	0.3393
β_2^2	0.9785
β_3^2	1.6280
Residues, h	
γ_1	6.6329
γ_2	−1.7061
γ_3	0.2647

the first exponential term of equation (7) was subtracted to give the residual transient solution (v_r), or

$$v_r = A \cdot U \cdot V\left[\gamma_2\left(\frac{1-e^{\beta_2^2\delta}}{\delta}\right)e^{-\beta_2^2 t} + \gamma_3\left(\frac{1-e^{\beta_3^2\delta}}{\delta}\right)e^{-\beta_3^2 t} + \ldots\right] \tag{11}$$

The residual transient solution (v_r) was analyzed in a fashion similar to that used on v to obtain the second pole (β_2^2) and its residue (γ_2) as shown in Fig. 6(B).

Sufficient transient data were present in the heat transfer response to permit the above procedure to be repeated a third time to yield a third pole (β_3^2) and its residue (γ_3). The analysis for the third pole and its residue is given in Fig. 6(C).

The thermal transmittance (U) and the poles (β_n^2) and residues (γ_n) obtained from the above procedure are summarized in Table 2.

Stephenson et al. (1988) have shown that the poles and residues must also satisfy the relation

$$\sum_{n=1}^{N} \gamma_n \beta_n^2 = 1 \tag{12}$$

This equation is a good check on the validity of the empirical poles and residues. For the results of Table 2, the left side of equation (12) is equal to 1.012, which is very nearly equal to 1.

Procedure for Obtaining Transfer Function Coefficients. From the above thermal transmittance, poles, and residues, the rate of heat gain (QG) at the inside surface of the wall specimen exposed to a ramp excitation function at its outside surface is given by

$$QG = A \cdot U \cdot m\left[t - \gamma_o + \sum_{n=1}^{N} \gamma_n e^{-\beta_n^2 t}\right] \tag{13}$$

Here m is the slope of the ramp excitation function, and γ_o is the sum of the residues, or

$$\gamma_o = \sum_{n=1}^{N} \gamma_n \tag{14}$$

Response factors are the values of the rate of heat gain (QG) at the inside surface that occur in response to a triangular-pulse excitation function at the outside surface. A triangular-pulse excitation function may be formed by summing three ramp excitation functions with proper slope (m) and time delay as shown in Fig. 7(A). By superimposing three ramp solutions, each of the general form of equation (13), the following expressions for response factors (y_i) were obtained:

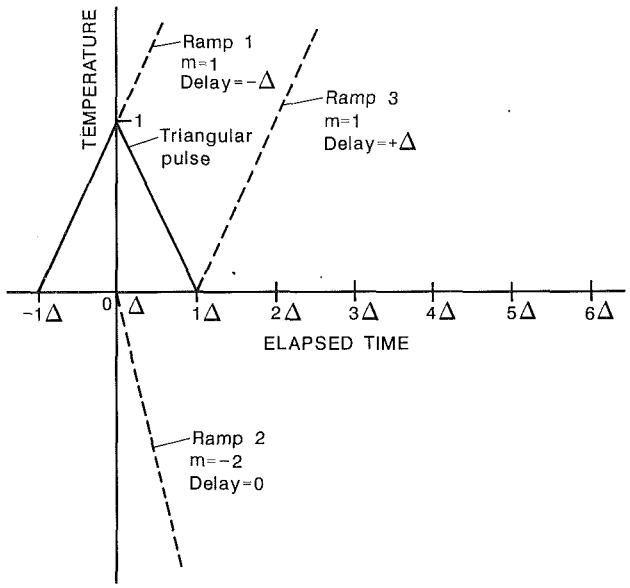

Fig. 7(A) Summing three ramp functions to form a triangular pulse

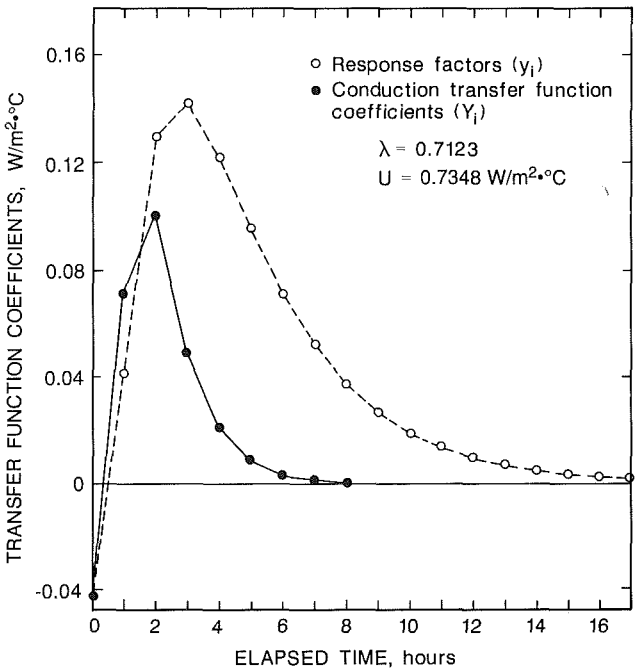

Fig. 7(B) Transfer function coefficients as a function of elapsed time

Fig. 7 Procedure for obtaining transfer function coefficients

$$y_o = \frac{U}{\Delta}\left[\Delta - \gamma_o + \sum_{n=1}^{N} \gamma_n e^{-\beta_n^2 \Delta}\right]$$

$$y_1 = \frac{U}{\Delta}\left[\gamma_o + \sum_{n=1}^{N} \gamma_n e^{-\beta_n^2 \Delta}\left(e^{-\beta_n^2 \Delta} - 2\right)\right]$$

$$y_i = \frac{2U}{\Delta}\sum_{n=1}^{N} \gamma_n e^{-i\beta_n^2 \Delta}\left[\left(\cosh(\beta_n^2 \Delta) - 1\right]\right. \qquad \text{for } i \geq 2 \tag{15}$$

The thermal transmittance (U), poles (β_n^2), and residues (γ_n) given in Table 2 were substituted into the above equation to obtain the response factors plotted in Fig. 7(B).

Table 3 Empirical TFCs* by fast ramp method

U	0.7350
Y_0	−0.0414
Y_1	0.0698
Y_2	0.0995
Y_3	0.0490
Y_4	0.0207
Y_5	0.0082
Y_6	0.0032
Y_7	0.0012
.	.
.	.
.	.
λ	0.7123

*The U and Y TFCs are in $W/m^2 \cdot °C$ and λ is dimensionless.

First-order transfer function coefficients (TFCs) were obtained by applying the recursive relations

$$Y_o = y_o$$

$$Y_i = y_i - \lambda \cdot y_{i-1} \qquad \text{for } i \geq 1 \tag{16}$$

Here λ is the common ratio defined by the relation

$$\lambda = e^{-\beta_1^2 \cdot \Delta} \tag{17}$$

Here β_1^2 is the first pole and Δ is the time interval for the analysis (i.e., 1 hr). The resulting TFCs are

$$Y_o = \frac{U}{\Delta}\left[\Delta - \gamma_o + \sum_{n=1}^{N} \gamma_n e^{-\beta_n^2 \Delta}\right]$$

$$Y_1 = \frac{U}{\Delta}\left[\gamma_o + e^{-\beta_1^2 \Delta}(\gamma_o - \Delta) + \sum_{n=1}^{N} \gamma_n e^{-\beta_n^2 \Delta}(e^{-\beta_n^2 \Delta} - 2 - e^{-\beta_1^2 \Delta})\right]$$

$$Y_2 = \frac{U}{\Delta}\left\{-e^{-\beta_1^2 \Delta}\gamma_0 + \sum_{n=1}^{N} \gamma_n [2e^{-2\beta_n^2 \Delta}(\cosh(\beta_n^2 \Delta) - 1) + e^{-\Delta(\beta_n^2 + \beta_1^2)}(e^{-\beta_n^2 \Delta} - 2)]\right\}$$

$$Y_i = \frac{2U}{\Delta} \sum_{n=2}^{N} \gamma_n e^{-i\beta_n^2 \Delta} [\cosh(\beta_n^2 \Delta) - 1] [1 - e^{\Delta(\beta_n^2 - \beta_1^2)}] \qquad \text{for } i \geq 3 \tag{18}$$

The thermal transmittance (U), poles (β_n^2), and residues (γ_n) given in Table 2 were substituted into equation (18) to give the TFCs plotted in Fig. 7(B) and summarized in Table 3.

Note that the first TFC at the outside surface is a small negative value. Transfer function theory indicates that this value should be positive. This departure from theory is an artifact of the propagation of experimental uncertainty into the higher order poles and residues. However, this experimental uncertainty does not significantly affect the predicted diurnal performance of the wall specimen as shown later in the paper.

Using Empirical TFCs to Predict Specimen Heat Transfer Rate for Different Excitation Functions

The empirical TFCs derived by the curve-fitting method (Table 1) and the fast ramp method (Table 3) were used in equation (2) to predict the specimen heat transfer rate for the four-harmonic test (Fig. 4A) and the sol-air test (Fig. 4B). For the curve-fitting results, the empirical TFCs used to predict each of the wall responses were obtained by curve fitting the specimen heat transfer rate for the other diurnal test. Comparisons of the measured and predicted specimen heat transfer rate for the two tests are given in Fig. 8.

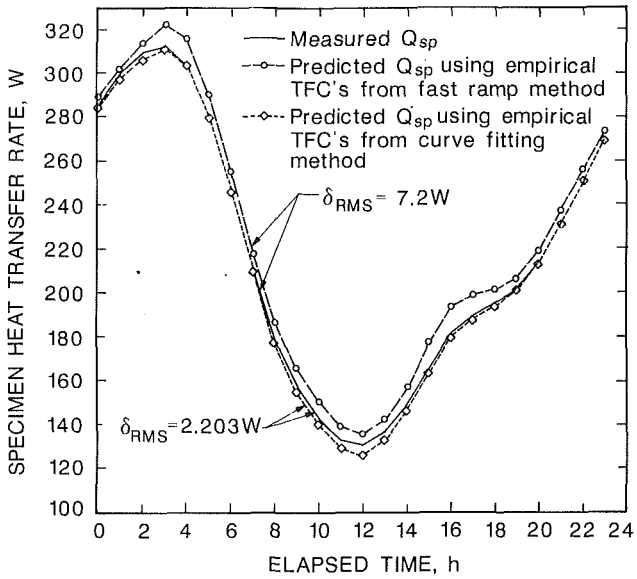

Fig. 8(A) Four-harmonic test

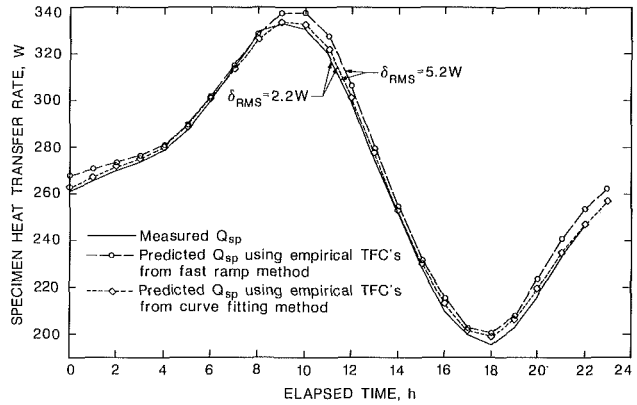

Fig. 8(B) Sol-air test

Fig. 8 Comparison of measured and empirically predicted specimen heat transfer rate

For the four-harmonic test (Fig. 8A), the empirical TFCs from the curve-fitting method predicted the measured specimen heat transfer rate within a root-mean-square (rms) difference of 2.2 W, while those from the fast ramp method predicted the wall response within 7.2 W. At a mean specimen heat transfer rate of 220 W, these rms differences represent percentage differences of 1 and 3.3 percent for the curve-fitting and fast ramp methods, respectively. For the sol-air test (Fig. 8B), the rms difference was 2.2 W for the curve fitting method and 5.2 W for the fast ramp method. At a mean specimen heat transfer rate of 260 W, these rms differences represent percentage differences of 0.8 and 2 percent for the curve-fitting and fast ramp methods, respectively. In all cases, the empirical TFCs track the measured responses very closely, and therefore appear to account for the thermal bridges and lateral heat flows present in the wall specimen.

A factor contributing to the lesser agreement for the fast ramp method is the three-pole approximation used to represent the infinite series in equation (7). Higher-order poles and

residues may affect the initial transient response, which in turn will affect the first few TFCs.

The above agreement is considered to be very good in view of the fact that the energy balance of the metering chamber has previously been shown to be uncertain by about 4 percent under dynamic conditions (Burch et al., 1987b).

Summary and Conclusion

Two dynamic test methods, called the curve fitting and fast ramp methods, for calibrated and guarded hot boxes were applied to an insulated hollow concrete block wall that contained significant thermal bridges and lateral heat flows. Empirical transfer function coefficients derived by the curve-fitting method predicted the measured specimen heat transfer response for two different diurnal temperature cycles within 1 percent, while those derived by the fast ramp method predicted the results within 3.3 percent. The empirical transfer function coefficients appeared to account for the thermal bridges and lateral heat flows present in the wall specimen.

Acknowledgments

The authors thank the U.S. Department of Energy for sponsoring this research, and the National Concrete Masonry Association for constructing the wall specimen.

References

ASTM, 1988, "Thermal Performance of Building Assemblies by Means of a Calibrated Hot Box," *1988 Annual Book of ASTM Standards*, Standard Method of Test C 976-82, Vol. 04.06, pp. 464–480.

Burch, D. M., Zarr, R. R., and Licitra, B. A., 1987a, "A Dynamic Test Method for Determining Transfer-Function Coefficients for a Wall Specimen Using a Calibrated Hot Box," presented at the ASTM Conference on Insulation Materials, Testing and Applications, Bal Harbour, FL.

Burch, D. M., Zarr, R. R., Faison, T. K., Licitra, B. A., and Arnold, C. E., 1987b, "A Procedure for Measuring the Dynamic Thermal Performance of Wall Specimens Using a Calibrated Hot Box," *ASHRAE Transactions*, Vol. 93, Part 2.

Burch, D. M., Zarr, R. R., and Licitra, B. A., 1988, "A Method for Characterizing the Dynamic Performance of Wall Specimens Using A Calibrated Hot Box," *ASHRAE Transactions*, Vol. 94, Pt. 1.

Grot, R. A., Persily, A. K., Chang, Y. M., Fang, J. B., Weber, S., and Galowin, L. S., 1985, "Evaluation of the Thermal Integrity of Building Envelopes of Eight Federal Office Buildings," NBSIR 85-3147, National Institute of Standards and Technology.

Hittle, D. C., 1981, "Calculating Building Heating and Cooling Loads Using the Frequency Response of Multilayered Slabs," Technical Manuscript E-169, Construction Engineering Research Laboratory.

Seem, J., and Hancock, E., 1986, "A Method for Characterizing the Thermal Performance of a Solar Storage Wall From Measured Data," *Proceedings of ASHRAE/DOE/BTECC Conference on Thermal Performance of the Exterior Envelopes of Buildings III*, ASHRAE SP 49, pp. 1304–1315.

Stephenson, D. G., Ouyang, K., and Brown, W. C., 1988, "A Procedure for Deriving Thermal Transfer Functions for Walls From Hot-Box Test Results," Internal Report No. 568, National Research Council of Canada, Ottawa, Canada.

Zarr, R. R., Burch, D. M., Faison, T. K., Arnold, C. E., and O'Connell, M. E., 1987, "Calibration of the NBS Calibrated Hot Box," *Journal of Testing and Evaluation*, Vol. 15, No. 3, pp. 167–177.

Response of Rotary Regenerators to Step Changes in Mass Rates

F. E. Romie
Palos Verdes Estates, CA 90274

Rotary regenerator exit gas temperature responses to step changes in mass flow rates are presented. When the step change is the same for both gases the responses are shown to have a decaying oscillation to the final values of the exit gas temperatures. The source of the oscillations is explained. The responses are found by dividing the regenerator into pie-shaped segments and approximating the area-mean gas temperature leaving a segment as the temperature of the gas leaving a small regenerator located on the central radius of the segment.

Introduction

Data on the transient response of rotary counterflow regenerators are required for control purposes, particularly in the case of regenerative gas turbine applications, in which the regenerator serves as the regenerative heat exchanger. A recent paper (Romie, 1988) treats the response of the rotary regenerator to step changes of its gas inlet temperatures. The purpose of this paper is to find the regenerator exit gas temperature responses to step changes in mass flow rates of either or both gases. The governing equations are linear and homogeneous but have coefficients that change stepwise at time zero and are thus not constant. Therefore temperature responses to step excitations cannot be used to find responses to arbitrary time variations of the mass rates. Use of the usual methods of linear analysis will lead to erroneous results. Even so, the response to a step excitation is important because it gives a measure of the duration and nature of the transient following a flow disturbance. A glance at the figures will show that the transient is not simple.

Willmott and Burns (1977) treat the response of single stationary regenerators to step changes of either inlet temperatures or mass flow rates. Burns and Willmott (1978) extend their earlier work to consideration of responses to simultaneous step changes of both inlet temperatures and mass rates.

The regenerator analyzed is defined by the following idealizations: (1) Both before and after the step change in mass rates, the fluid capacitance rates $(wc)_a$ and $(wc)_b$ are uniform and constant, as are the thermal conductances $(hA)_a$ and $(hA)_b$, for heat transfer between the fluids and the matrix. Values before and after the step are, in general, different. (2) No heat is conducted in the matrix in the direction of fluid flow but the matrix material offers no resistance (locally) to heat flow in the direction normal to fluid flow. (3) The ratios of the thermal capacitances of the fluids contained at any instant in the matrix to the thermal capacitance of the containing matrix are negligibly small and are treated as zero. This latter idealization means, in effect, that the two fluids must be gases and that transit times for gas particles to flow through the matrix must be negligibly small compared to t_a and t_b. (The sum $t_a + t_b$ is the time for one revolution of the regenerator, which can be in the form of a disk or drum.)

The dimensionless time variable used is $\theta = (wc)_{af}t/(WC)_t$, which can be interpreted as the ratio of the thermal capacitance of the mass of gas that has passed through region a (Fig. 1) since initiation of the step excitation to the thermal capacitance of the entire disk.

Either of two sets of four parameters are in use to characterize a regenerator. The first set introduced, by Hausen (1929), is Λ_a, Λ_b, Π_a, Π_b and is more suited to writing the governing equations. The second set, introduced by Coppage and London (1953), is Ntu, C^*, C_r^*, $(hA)^*$ and is commonly used to characterize the rotary regenerator. In this paper the reciprocal C_{rr}^* of C_r^* will be used primarily because the change in θ for a complete disk revolution is C_{rr}^*. Either set of four parameters can, of course, be translated into the other, as indicated in Table 1. A fifth parameter required only for transient responses is the seal angle α (Fig. 1). Nine parameters are thus required to describe the general response of the rotary regenerator to step changes in mass rates: the seal angle α, four characterizing parameters prior to the step, designated by the subscript o, and four characterizing parameters following the step, designated by the subscript f.

The convention is adopted that the subscript a is assigned such that the parameter $C_o^* = (wc)_{ao}/(wc)_{bo}$ is not greater than unity. If τ_c is the temperature of the colder gas with inlet temperature τ_{cin} and τ_h is the temperature of the hotter gas with inlet temperature τ_{hin} then $\tau_a = (\tau_c - \tau_{\text{cin}})/(\tau_{\text{hin}} - \tau_{\text{cin}})$, $\tau_b = (\tau_h - \tau_{\text{cin}})/(\tau_{\text{hin}} - \tau_{\text{cin}})$ and $T = (T_m - \tau_{\text{cin}})/(\tau_{\text{hin}} - \tau_{\text{cin}})$ where T_m is the matrix temperature. An alternate set can be used: $\tau_a = (\tau_h - \tau_{\text{hin}})/(\tau_{\text{cin}} - \tau_{\text{hin}})$, $\tau_b = (\tau_c - \tau_{\text{hin}})/(\tau_{\text{cin}} - \tau_{\text{hin}})$, and $T = (T_m - \tau_{\text{hin}})/(\tau_{\text{cin}} - \tau_{\text{hin}})$. Thus τ_a represents the temperature of the colder or hotter gas as appropriate. In either case the matrix inlet values of τ_a and τ_b are zero and unity, respectively. The temperature variables τ_a, τ_b, and T will be referred to as temperatures.

The following basic equations used in the transient analysis have been presented by Romie and Baclic (1988). The functions F_n and G_n (Romie, 1987) are briefly described in the appendix. At time $t = 0$ let the temperature distribution of a (sta-

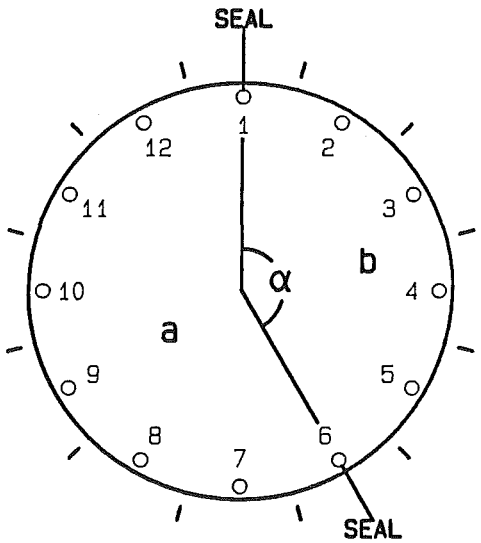

Fig. 1 Schematic of disk showing numbered small regenerators, stationary seals, and position marks; rotation is clockwise

Contributed by the Heat Transfer Division for publication in the JOURNAL OF HEAT TRANSFER. Manuscript received by the Heat Transfer Division November 23, 1988. Keywords: Heat Exchangers, Transient and Unsteady Heat Transfer.

Table 1 Parameter equivalents; *A* = stationary regenerator; *B* = rotary regenerator

		A	B
Ntu	$\frac{\Lambda_a}{1+(hA)^*}$	same	same
C^*	$\frac{\Pi_a\Lambda_b}{\Pi_b\Lambda_a}$	$\frac{(wct)_a}{(wct)_b}$	$\frac{(wc)_a}{(wc)_b}$
C^*_{rr}	$\frac{\Pi_a}{\Lambda_a}$	$\frac{(wct)_a}{WC}$	$\frac{(wc)_a t_t}{(WC)_t}$
$(hA)^*$	$\frac{\Pi_a}{\Pi_b}$	$\frac{(hAt)_a}{(hAt)_b}$	$\frac{(hA)_a}{(hA)_b}$

For stationary regenerators:

$$(WC)_a = (WC)_b = WC$$

For rotary regenerators:

$$\frac{t_a}{(WC)_a} = \frac{t_b}{(WC)_b} = \frac{t_t}{(WC)_t}$$

tionary) matrix be expressed as an Nth degree polynomial of $\Lambda_a y$

$$T_a(0, y) = \sum_{n=0}^{N} A_n(\Lambda_a y)^n/n! \tag{1}$$

Then the exit ($y = 1$) temperature of gas a, which enters ($y = 0$) at zero temperature, will be

$$\tau_a(\frac{t}{t_a}, 1) = \sum_{n=0}^{N} A_n G_n(\Pi_a \frac{t}{t_a}, \Lambda_a) \tag{2}$$

and the matrix temperature distribution will be

$$T_a(\frac{t}{t_a}, y) = \sum_{n=0}^{N} A_n F_n(\Pi_a \frac{t}{t_a}, \Lambda_a y) \tag{3}$$

Let the initial matrix temperature be expressed as an Nth degree polynomial of $(1-y)\Lambda_b$

$$T_b(0, y) = 1 - \sum_{n=0}^{N} B_n(\Lambda_b(1-y))^n/n! \tag{4}$$

Then the exit ($y = 0$) temperature of gas b, which enters ($y = 1$) at unity temperature, will be

$$\tau_b(\frac{t}{t_b}, 0) = 1 - \sum_{n=0}^{N} B_n G_n(\Pi_b \frac{t}{t_b}, \Lambda_b) \tag{5}$$

and the matrix temperature distribution will be

$$T_b(\frac{t}{t_b}, y) = 1 - \sum_{n=0}^{N} B_n F_n(\Pi_b \frac{t}{t_b}, \Lambda_b(1-y)) \tag{6}$$

In these equations, time t can have any positive value.

Solution Method

To find the solution for the transient, the disk is divided into N_t equal pie-shaped segments. The area-mean exiting gas temperature for a segment is approximated as the temperature of the gas leaving an elementally small regenerator (*SR*) located on the center radius of the segment. Figure 1 shows the *SR* located at the ends of the central radii but the radial location is arbitrary. Stationary position marks separated by the angle $360/N_t$ are shown outside the disk rim. The dimensionless time for an *SR* to rotate from one position mark to the next is $\Delta\theta = C^*_{rrf}/N_t$. When the *SR* are at the position marks ($\theta = \frac{1}{2}\Delta\theta, 1\frac{1}{2}\Delta\theta, 2\frac{1}{2}\Delta\theta, \ldots$), region a contains N_a complete segments and region b contains N_b complete segments ($N_a + N_b = N_t$). At these times the exit temperature of gas a is computed as the sum of the temperatures of the gas leaving the *SR* in region a divided by N_a and, similarly, the exit temperature of gas b is the sum of the gas temperatures leaving the *SR* in region b divided by N_b. The transient response is thus found by computing, at the position marks, the gas exit temperatures for the N_t *SR*'s as they rotate about the axis.

Nomenclature

A_n = coefficients
B_n = coefficients
$B_{a,b}(\theta)$ = defined in equations (30) and (31)
C^* = defined in Table 1
C^*_r = $1/C^*_{rr}$
C^*_{rr} = defined in Table 1
$F_n(\ )$ = function, see Appendix
$G_n(\ )$ = function, see Appendix
hA = thermal conductance, W/K
hA^* = defined in Table 1
k = index (number of successive integrations)
$M_{a,b}$ = $(wc)_{af}/(wc)_{ao}$, $(wc)_{bf}/(wc)_{bo}$, $M = M_a = M_b$
N = polynomial degree, equations (1), (4)
N_a = number of disk segments in region a
N_b = number of disk segments in region b
N_t = total number of disk segments
Ntu = defined in Table 1
t = time from initiation of step, s
t' = time from passing a seal (for *SR* $t' = t$ until first seal is passed), s
t_a = time for point on disk to rotate through region a (Fig. 1), s
t_b = time for point on disk to rotate through region b (Fig. 1), s
t_t = time for complete disk revolution, s
$T_{a,b}$ = defined in text
T_m = disk temperature, K
$(wc)_{a,b}$ = capacitance rate of gas, W/K
$(WC)_{a,b}$ = thermal capacitance of disk in regions a and b (Fig. 1), J/K
$(WC)_t$ = thermal capacitance of entire disk, J/K
y = fractional distance through disk, measured from gas a entrance plane
α = seal angle subtending area through which gas b flows, deg.
$\Delta\theta$ = C^*_{rrf}/N_t
$\epsilon_{a,b,o}$ = exit value of $\tau_{a,b}$ prior to step
$\epsilon_{a,b,f}$ = exit value of $\tau_{a,b}$ following step as $\theta \to \infty$
θ = $(wc)_{af}t/(WC)_t$
$\Lambda_{a,b}$ = $(hA)_a/(wc)_a$, $(hA)_b/(wc)_b$
$\pi_{a,b}$ = $(hA)_a t_a/(WC)_a$, $(hA)_b t_b/(WC)_b$
$\tau_{a,b}$ = defined in text
τ_{cin} = inlet temperature of colder gas, K
τ_{hin} = inlet temperature of hotter gas, K

Subscripts

a = denotes quantities associated with gas having lesser capacitance rate prior to step
b = denotes quantities associated with other gas
f = denotes quantities following step
o = denotes quantities prior to step

The seal angle α is 360 N_b/N_t so that, for example, with $\alpha = 150$ deg the minimum number for N_t is 12 giving $N_a = 5$ and $N_b = 7$; N_a and N_b must be integers.

The steady-state temperature distribution of the disk prior to the step is required to start calculations. In region a (Fig. 1)

$$T_{ao}\left(\frac{t'}{t_a}, y\right) = \sum_{n=0}^{N} A_{no} F_n\left(\Pi_{ao}\frac{t'}{t_a}, \Lambda_{ao} y\right) \tag{7}$$

and in region b

$$T_{bo}\left(\frac{t'}{t_b}, y\right) = 1 - \sum_{n=0}^{N} B_{no} F_n\left(\Pi_{bo}\frac{t'}{t_b}, \Lambda_{bo}(1-y)\right) \tag{8}$$

The matrix temperature given by these equations can be interpreted in two ways. To an observer riding on the disk, for example with an SR, t' is the time elapsed since passing a seal and the matrix temperature varies with t' and y. To a fixed observer the disk temperature is time-invariant and t'/t_a and t'/t_b define, in effect, the angular position relative to the last seal passed. At any given angle the temperature varies with y only. For an SR, t' is always the time elasped since passing a seal unless, in the following equations, the SR has not passed a seal since initiation of the step excitation, in which case $t' = t$, where t is always the elapsed time since the step. The "angular" position of, for example, $SR4$ at $t = 0$ is $3/N_b$ (Fig. 1).

The $2(N+1)$ coefficients A_{no} and B_{no} of equations (7) and (8) are determined by requiring that the matrix temperature distributions immediately on the two sides of a seal be equal and are evaluated by solving $2(N+1)$ simultaneous equations found with use of the Successive Integral Method (SIM) described by Romie and Baclic (1988). (Derivation of the two following SIM equations is indicated by equations (23)-(26).) A first set of $N+1$ equations is

$$\sum_{n=0}^{N}\left\{A_{no}F_{n+k}(\Pi_{ao}, \Lambda_{ao})k!/\Lambda_{ao}^{k} + B_{no}\left(\frac{k}{k+n}\right)\Lambda_{bo}^{n}/n!\right\} = 1 \tag{9}$$

$$k = 1, 2, \ldots, N+1$$

The second set of $(N+1)$ equations is

$$\sum_{n=0}^{N}\left\{A_{no}\left(\frac{k}{k+n}\right)\Lambda_{ao}^{n}/n! + B_{no}F_{n+k}(\Pi_{bo}, \Lambda_{bo})k!/\Lambda_{bo}^{k}\right\} = 1 \tag{10}$$

$$k = 1, 2, \ldots, N+1$$

Each of these two equations for each value of k produces a row in a $2(N+1)\times 2(N+1)$ array and, cumulatively, a $2(N+1)$ unit vector. Solution of the system gives the $2(N+1)$ values of A_{no} and B_{no}.

Before proceeding with the transient response, it is convenient at this point to calculate the rotary regenerator gas exit temperatures prior to the step and the final ($\theta \to \infty$) gas exit temperatures. The gas a exit temperature, ϵ_{ao}, prior to the step excitation is, due to the choice of variables and the convention adopted for assignment of subscript a, the thermal effectiveness of the regenerator prior to the step. With the same values of the four characterizing parameters the effectiveness is the same for rotary and stationary regenerators for which an equation given by Romie and Baclic (1988) is

$$\epsilon_{ao} = (1/\Pi_{ao})\sum_{n=0}^{N} A_{no}\left(\Lambda_{ao}^{n+1}/(n+1)! - F_{n+1}(\Pi_{ao}, \Lambda_{ao})\right) \tag{11}$$

The gas b exit temperature, ϵ_{bo}, is given by an overall energy balance of the regenerator

$$\epsilon_{bo} = 1 - C_o^* \epsilon_{ao} \tag{12}$$

The final ($\theta \to \infty$) exit gas temperatures, ϵ_{af} and ϵ_{bf}, are found by changing the subscript o to f in equations (9), (10), (11), and (12). The final thermal effectiveness is ϵ_{af} unless $C_f^* > 1$ in which case it is ϵ_{af}/C_f^*.

The details of computing the transient will be illustrated by following $SR4$ (Fig. 1) as it rotates past the position marks. Figure 1 shows the SR at their positions at $\theta = 0$. The temperature distribution of $SR4$ just prior to the step is

$$T_{b4} = 1 - \sum_{n=0}^{N} B_{no} F_n(\Pi_{bo} 3/N_b, \Lambda_{bo}(1-y)) \tag{13}$$

The temperature distribution just after the step is unchanged but must be expressed (see equation (4)) in the form

$$T_{b4} = 1 - \sum_{n=0}^{N} B_{nf}(\Lambda_{bf}(1-y))^n/n! \tag{14}$$

Thus

$$\sum_{n=0}^{N} B_{nf}(\Lambda_{bf}(1-y))^n/n! = \sum_{n=0}^{N} B_{no} F_n(\Pi_{bo} 3/N_b, \Lambda_{bo}(1-y)) \tag{15}$$

The $N+1$ unknown coefficients B_{nf} are found using SIM. The basis of SIM is that if two functions are equal over an interval ($y = 0$ to 1 in this case) then their successive integrals over the interval will be equal. Making the substitution $\eta' = 1 - y$ and integrating the left and right sides of equation (15) k times from $\eta' = 0$ to η and then setting $\eta = 1$ gives the $N+1$ equations required to find the $N+1$ values of B_{nf}

$$\sum_{n=0}^{N} B_{nf}\Lambda_{bf}^{k}/(n+k)! = \sum_{n=0}^{N} B_{no} F_{n+k}(\Pi_{bo} 3/N_b, \Lambda_{bo})/\Lambda_{bo}^{k} \tag{16}$$

$$k = 1, 2, \ldots, N+1$$

The integrations use the integral (Romie, 1987)

$$\int_0^v F_n(u, z)dz = F_{n+1}(u, v), \; n \geq 0 \tag{17}$$

For each value of k the left-hand side gives a row ($n = 0$ to N) in an $(N+1)\times(N+1)$ array and the right side the corresponding entry in an $(N+1)$ column vector. Solution of the system gives the $N+1$ coefficients B_{nf}.

From this point on the analysis parallels that used to find the transient response to step changes of inlet temperatures (Romie, 1988).

At time $\theta = {}^1/_2\Delta\theta$ ($t' = {}^1/_2 t_b/N_b$) the exit gas temperature is

$$\tau_{b4}\left(\frac{1}{2}\Delta\theta\right) = 1 - \sum_{n=0}^{N} B_{nf} G_n\left(\frac{1}{2}\Pi_{bf}/N_b, \Lambda_{bf}\right) \tag{19}$$

At time $\theta = 1{}^1/_2\Delta\theta$ ($t' = 1{}^1/_2 t_b/N_b$) the exit gas temperature is

$$\tau_{b4}(1{}^1/_2\Delta\theta) = 1 - \sum_{n=0}^{N} B_{nf} G_n(1{}^1/_2\Pi_{bf}/N_b, \Lambda_{bf}) \tag{20}$$

At time $\theta = 2\Delta\theta$ ($t' = 2t_b/N_b$) $SR4$ reaches the seal with a matrix temperature distribution

$$T_{b4}(2\Delta\theta) = 1 - \sum_{n=0}^{N} B_{nf} F_n(\Pi_{bf} 2/N_b, \Lambda_{bf}(1-y)) \tag{21}$$

The unchanged matrix temperature distribution just on the other side of the seal must be expressed in the form (see equation (3))

$$T_{a4} = \sum_{n=0}^{N} A_{nf}(\Lambda_{af} y)^n/n! \tag{22}$$

Thus

$$\sum_{n=0}^{N} A_{nf}(\Lambda_{af} y)^n/n! = 1 - \sum_{n=0}^{N} B_{nf} F_n(\Pi_{bf} 2/N_b, \Lambda_{bf}(1-y)) \tag{23}$$

The new set of coefficients A_{nf} is found using SIM. Making the substitution $\eta' = 1 - y$ and integrating both sides k times ($\eta' = 0$ to η) and then setting $\eta = 1$ gives

$$\sum_{n=0}^{N} A_{nf}\Lambda_{af}^{n} \sum_{j=1}^{k} \frac{(-1)^{j-1}}{(n+j)!(k-j)!} = \frac{1}{k!} - \sum_{n=0}^{N} B_{nf}F_{n+k}(\Pi_{bf}2/N_b,\ \Lambda_{bf})/\Lambda_{bf}^{k} \tag{24}$$

Using the equality

$$\sum_{j=1}^{k} \frac{(-1)^{j-1}k!}{(n+j)!(k-j)!} = \left(\frac{k}{n+k}\right)/n! \tag{25}$$

gives the SIM equation (which has the form of equation (10))

$$\sum_{n=0}^{N} A_{nf}\left(\frac{k}{k+n}\right)\Lambda_{af}^{n}/n! = 1 - \sum_{n=0}^{N} B_{nf}F_{n+k}(\Pi_{bf}2/N_b,\ \Lambda_{bf})k!/\Lambda_{bf}^{k} \tag{26}$$

$$k = 1, 2, \ldots, N+1$$

The $N+1$ values of the new coefficients A_{nf} are found as described following equation (17).

At time $\theta = 2^{1}/_{2}\Delta\theta$ ($t' = {}^{1}/_{2}t_a/N_a$) the exiting gas temperature is

$$\tau_{a4}(2^{1}/_{2}\Delta\theta) = \sum_{n=0}^{N} A_{nf}G_n(\Pi_{af}/(2N_a),\ \Lambda_{af}) \tag{27}$$

and so on until at $\theta = 9\Delta\theta$ ($t' = t_a$) $SR4$ rotates past the other seal. The SIM equation to find the new set of B_{bf} coefficients is

$$\sum_{n=0}^{N} B_{nf}\left(\frac{k}{k+n}\right)\Lambda_{b}^{n}/n! = 1 - \sum_{n=0}^{N} A_{nf}F_{n+k}(\Pi_{af},\ \Lambda_{af})k!/\Lambda_{af}^{k} \tag{28}$$

$$k = 1, 2, \ldots, N+1$$

At $\theta = 9^{1}/_{2}\Delta\theta$ ($t' = {}^{1}/_{2}t_b/N_b$) the exit gas temperature is

$$\tau_{b4}(9^{1}/_{2}\Delta\theta) = 1 - \sum_{n=0}^{N} B_{nf}G_n(\Pi_{bf}/(2N_b),\ \Lambda_{bf}) \tag{29}$$

and so on to the next (bottom) seal, which is reached at $\theta = 14\Delta\theta$ ($t' = t_b$).

The transient response is essentially completed when $\theta = 2^{1}/_{2}$, which means that the N_t SR's are followed for $2^{1}/_{2}/C_{rrf}^{*}$ revolutions of the disk.

Results and Discussion

To this point no relationship between the initial and final characterizing parameters has been defined. For many potential rotary regenerator applications, for example, the heat exchanger for the regenerative gas turbine, it seems reasonable to consider that the fractional mass rate changes will be the same for both gases and will occur simultaneously. For such applications the flows in the regenerator matrix are typically laminar and the conductances (hA) are independent of the mass rates. Thus defining $M_a = (wc)_{af}/(wc)_{ao}$ and $M_b = (wc)_{bf}/(wc)_{bo}$ gives, with $M_a = M_b = M$, $\Lambda_{af} = \Lambda_{ao}/M$, $\Lambda_{bf} = \Lambda_{bo}/M$, $\Pi_{af} = \Pi_{ao}$, $\Pi_{bf} = \Pi_{bo}$ or, using the Ntu set, $\mathrm{Ntu}_f = \mathrm{Ntu}_o/M$, $C_f^{*} = C_o^{*}$, $C_{rrf}^{*} = MC_{rro}^{*}$, and $hA_f^{*} = hA_o^{*}$. Figures 2 through 6 have been prepared using these relations. The seal angle is 180 deg unless otherwise indicated.

The responses are normalized by defining variables $B_a(\theta)$ and $B_b(\theta)$, which vary from zero just prior to the step to a final value of unity. For gas a

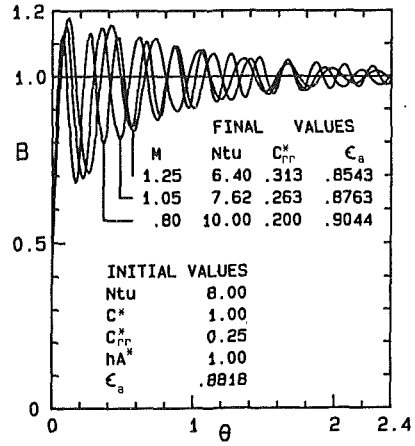

Fig. 2 Responses for three magnitudes of the step excitation

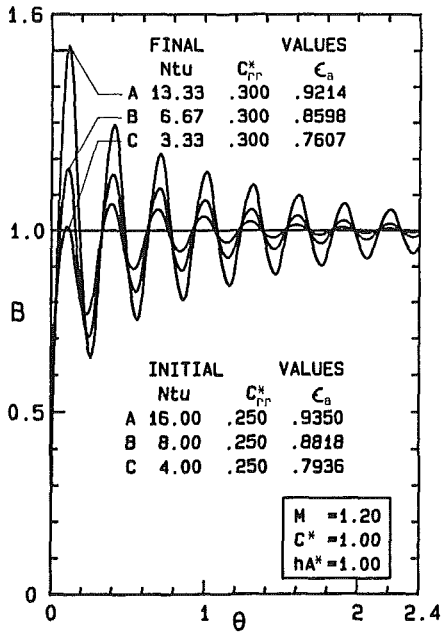

Fig. 3 Responses for three initial values of Ntu

$$B_a(\theta) = \frac{\tau_a(\theta) - \epsilon_{ao}}{\epsilon_{af} - \epsilon_{ao}} \tag{30}$$

and, for gas b,

$$B_b(\theta) = \frac{\tau_b(\theta) - \epsilon_{bo}}{\epsilon_{bf} - \epsilon_{bo}} \tag{31}$$

For a symmetric regenerator ($C_o^{*} = C_f^{*} = 1$ and $hA_o^{*} = hA_f^{*} = 1$) $B_a(\theta) = B_b(\theta)$, $\epsilon_{bo} = 1 - \epsilon_{ao}$, and $\epsilon_{bf} = 1 - \epsilon_{af}$.

Figure 2 shows $B(\theta)$ for a symmetric regenerator for three magnitudes (M) of the step change in mass rates. The unanticipated oscillations of the responses have a period of C_{rrf}^{*}, which is different for the three cases but always corresponds to one revolution of the disk. The amplitudes of the $B(\theta)$ oscillations are not very different even though $M = 0.8$ corresponds to a 20 percent reduction of the mass rates and $M = 1.25$ to a 25 percent increase.

Figure 3 shows the influence of the initial value of Ntu on the responses of a symmetric regenerator for an excitation of $M = 1.2$. The time (θ) required to attain a new equilibrium state increases with increasing Ntu, as was observed for stationary regenerators by Willmott and Burns (1977).

For a numerical example using case B of Fig. 3, suppose that gas a enters with $\tau_{cin} = 400$ K and gas b with $\tau_{hin} = 700$ K.

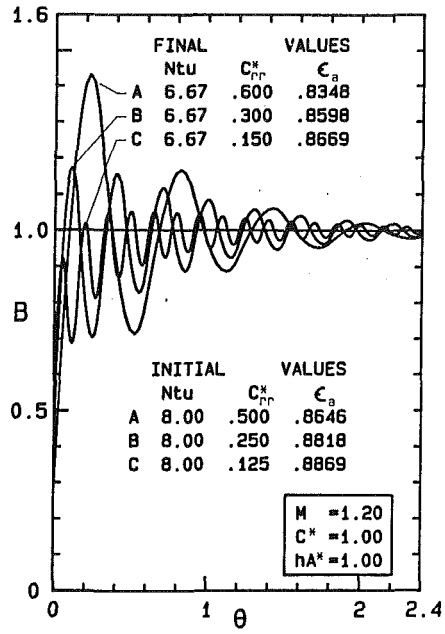

Fig. 4 Responses for three initial values of C^*_{rr}

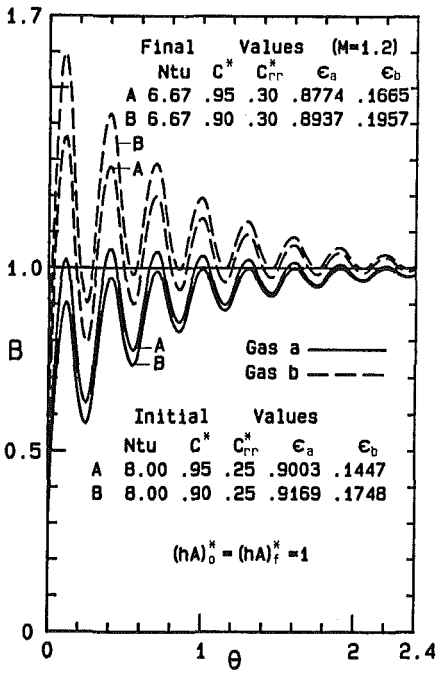

Fig. 5 Responses for two initial values of C^*

Then variation of $B(\theta)$ from 0 to 1 corresponds to an exit temperature change of 300 (0.8598-0.8818) = −6.6 K for gas a and +6.6 K for gas b. The maximum value of $B(\theta)$ corresponds to −7.7 K and the minimum (at $\theta \cong 0.24$) to −4.7 K for gas a. Although not discernible, the value of $B(\theta)$ at $\theta = 0$ (just after the step) is not zero but has a value of 0.427, which corresponds to an initial step of −2.8 K for gas a.

Figure 4 shows the influence of the initial value of C^*_{rr} on the responses for a symmetric regenerator. As C^*_{rr} becomes smaller the response more rapidly attains its final value. Figure 5 shows, with $M = 1.2$, the effect on the response when the initial (and final) values of C^* are 0.95 and 0.9. For $C^* = 1$ see Fig. 3.

Figures 6, 7, and 8 show responses for the same regenerator. The responses shown by the thicker lines on Fig. 6 are for a 10 percent ($M = 1.1$) increase in the mass rates of both gases.

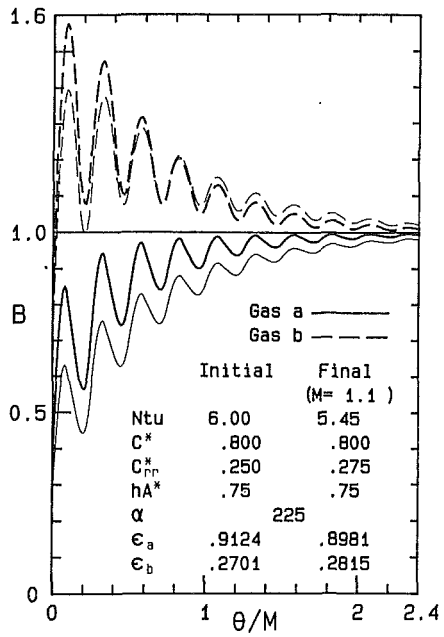

Fig. 6 Responses (thicker lines) with $M = 1.1$ for both gases

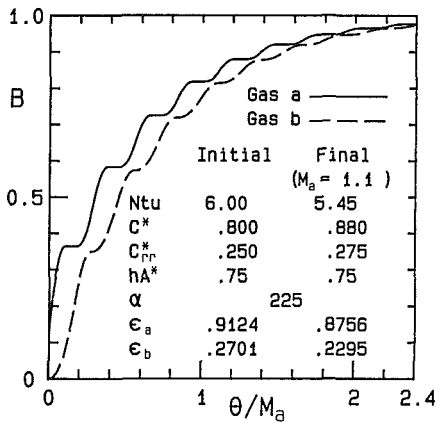

Fig. 7 Responses with $M_a = 1.1$ ($M_b = 1$)

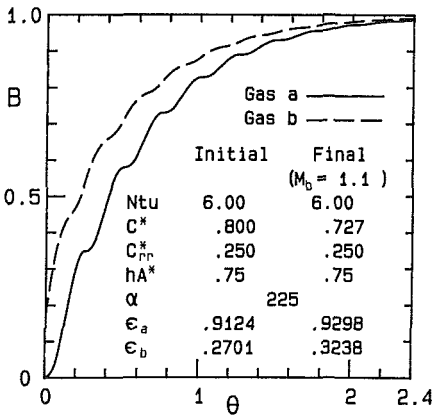

Fig. 8 Responses with $M_b = 1.1$ ($M_a = 1$)

Figures 7 and 8 show responses for, respectively, a 10 percent mass rate increase of gas a only and gas b only. The time variable for the three figures has been adjusted to be $\theta' = t(wc)_{ao}/(WC)_t$ so that a given value of t always corresponds to the same abscissa value. Linear analysis would permit superposition of the responses $(\tau_a(\theta') - \epsilon_{ao})_7$ and $(\tau_a(\theta') - \epsilon_{ao})_8$ to find the response when the mass rate of both

gases, as in Fig. 6, is increased by 10 percent. (The subscripts 7 and 8 refer to the data used to plot responses in Figs. 7 and 8.) The predicted value of $B_a(\theta')$ would then be

$$B_a(\theta') = \frac{(\tau_a(\theta') - \epsilon_{ao})_7 + (\tau_a(\theta') - \epsilon_{ao})_8}{(\epsilon_{af} - \epsilon_{ao})_7 + (\epsilon_{af} - \epsilon_{ao})_8}$$

with a similar equation for $B_b(\theta')$. The thinner lines on Fig. 6 show responses predicted using this approach. The agreement is fairly good considering that linear analysis is not mathematically justified, as has been noted in the introduction.

The flats shown on Fig. 7 for the response of gas a begin once each revolution at times $\theta_m = \alpha C^*_{rrf}/360 + mC^*_{rrf}$ ($m = 0, 1, 2, \ldots$) and have a duration of $\delta\theta = C^*_{rrf}(\alpha/180 - 1)$. The same phenomenon has been noted (Romie, 1988) for responses to step changes of gas inlet temperatures. The explanation is that once each revolution region a (Fig. 1 with $\alpha = 225$ deg) contains, for a time $\delta\theta$, only the portion of the disk that has passed the seal with the same temperature distribution. During this time the matrix temperature of the disk in region a is time invariant (to a fixed observer) and thus the gas a exit temperature is also time invariant. (For a seal angle of 180 deg the duration of the flat is zero but the slope of the response is zero at times θ_m.) These flats and the associated bumps shown by the other responses in Figs. 7 and 8 afford, as demonstrated by the thinner lines on Fig. 6, an explanation for the oscillatory nature of the responses observed when the mass rates of both gases are stepped.

Concluding Remarks

It is emphasized that the analytical method presented requires only values for the four parameters both prior to and following the step: The relationships among initial and final values can be arbitrarily assigned. For example, the method can be used to find responses to step changes in rotation rate, in which case only the value of C^*_{rr} is different before and after the step.

For turbulent flows $(hA)_f/(hA)_o = ((wc)_f/(wc)_o)^n$ where n is typically 0.8 or less. For turbulent flows it is easy to show that the temperature changes of the gases are much less than would be the case with laminar flows.

The value of N used was 3 ; larger values produced no change in results. The values of N_a and N_b were both 10 for Figs. 2 to 5 and 9 and 15 for Figs. 6 to 8. These large values were chosen to produce smooth plots and were not required by accuracy considerations. The ϵ values have four-place accuracy.

References

Burns, A., and Willmott, A. J., 1978, "Transient Performance of Periodic Flow Regenerators," *International Journal of Heat and Mass Transfer*, Vol. 21, pp. 623-627.

Coppage, J. E., and London, A. L., 1953, "The Periodic-Flow Regenerator—A Summary of Design Theory," *Transactions of the ASME*, Vol. 75, pp. 779-787.

Hausen, H., 1929, "Uber die Theorie des Warmeaustausches in Regeneratoren," *Zeitschrift für Angewandte Mathematik und Mechanik*, Vol. 9, pp. 173-200.

Romie, F. E., 1987, "Two Functions Used in the Analysis of Crossflow Exchangers, Regenerators and Related Equipment," ASME JOURNAL OF HEAT TRANSFER, Vol. 109, pp. 518-521.

Romie, F. E., 1988, "Transient Response of Rotary Regenerators," ASME JOURNAL OF HEAT TRANSFER, Vol. 110, pp. 836-840.

Romie, F. E., and Baclic, B. S., 1988, "Methods for Rapid Calculation of the Operation of Asymmetric Counterflow Regenerators," ASME JOURNAL OF HEAT TRANSFER, Vol. 110, pp. 785-788.

Willmott, A. J., and Burns, A., 1977, "Transient Performance of Periodic-Flow Regenerators," *International Journal of Heat and Mass Transfer*, Vol. 20, pp. 753-761.

APPENDIX

The functions $F_n(u, v)$ and $G_n(u, v)$ satisfy two first-order partial differential equations

$$-\frac{\partial F_n(u, v)}{\partial u} = F_n - G_n = \frac{\partial G_n(u, v)}{\partial v} \tag{A1}$$

For $n \geq 0$, $F_n(0, v) = v^n/n!$ and $G_n(u, 0) = 0$. Numerical values for F_n, G_n, $n = 0, 1, 2 \ldots$ can be found by evaluating just three functions and then using two recurrence equations. The three functions are

$$F_{-1}(u, v) = \exp(-u - v)\left(\frac{u}{v}\right)^{1/2} I_1(2\sqrt{uv}) \tag{A2}$$

$$G_{-1}(u, v) = \exp(-u - v) I_0(2\sqrt{uv}) \tag{A3}$$

$$G_0(u, v) = \exp(-u - v) \sum_{r=0}^{\infty} \left(\frac{v}{u}\right)^{\frac{r+1}{2}} I_{r+1}(2\sqrt{uv}) \tag{A4}$$

I_r is the modified Bessel function of the first kind, rth order, and u and v are positive. Power series expansions of these three functions are given by Romie (1987, 1988). The two recurrence equations are

$$F_n(u, v) = G_n(u, v) + G_{n-1}(u, v), \quad \pm \text{integer } n \tag{A5}$$

$$G_{n+1}(u, v) = \frac{1}{n+1}[(v - u - 1 - 2n)G_n + (2v - n)G_{n-1} + vG_{n-2}], \quad n \geq 0 \tag{A6}$$

Performance of a Heat Exchanger Based on Enhanced Heat Diffusion in Fluids by Oscillation: Analysis

M. Kaviany
Department of Mechanical Engineering and Applied Mechanics,
The University of Michigan,
Ann Arbor, MI 48109

Fluid flow and heat transfer in capillary tubes (Stokes' boundary-layer thickness nearly equal to the tube radius), subject to oscillatory flow from two reservoirs maintained at different temperatures, has been analyzed. Extension of existing analysis has been made by allowing for finite wall thickness and estimating the viscous dissipation. For a bundle of tubes connected to reservoirs of finite volume, analysis is also made of the oscillatory motion in the reservoirs (assuming a piston-type displacement within the reservoirs). The effects of various fluid and tube parameters on the heat transfer in a single tube are examined. The pathlines followed by fluid particles show that the extent of interaction between the fluid exiting the bundle and the fluid in the reservoirs (or the heat transfer surfaces in the reservoirs) depends strongly on the radial position of the exiting fluid particles. In a follow-up paper, these predictions are compared with some experimental results.

1 Introduction

For an oscillatory fluid flow over a rigid surface, the influence of the surface no-slip condition penetrates a distance $(2\nu/\omega)^{1/2}$ into the fluid. If the oscillating fluid has a lower specific enthalpy in one-half of a period than in the other half (e.g., fluid arriving from a cold reservoir, followed by fluid arriving from a hot reservoir), then the heat diffusion into and out of this penetration (or Stokes') layer results in a net transfer of heat between the higher and lower enthalpy fluids. This heat transfer is further enhanced if the rigid surface (part of a wall with a finite thickness) has a nonzero thermal diffusivity, due to the added heat storage/release capability of the wall.

This phenomenon was initially observed and explained by Chatwin (1975), Watson (1983), Joshi et al. (1983), and Kurzweg and Jaeger (1986) for the enhanced diffusion of contaminants in gases and for the diffusion of heat by Kurzweg and Zhao (1984) and Kurzweg (1985a, 1985b, 1986).

For the enhancement of oxygen gas diffusion in a nitrogen gas, good agreement has been found between the predictions and the experimental results (Kurzweg and Jaeger, 1986). Presently, experimental verification of the enhanced thermal diffusion is limited to the transient heat transfer experiment performed by Kurzweg and Zhao (1984), where relatively good agreement between experimental and predicted results was found. Kurzweg and Zhao's results show that since there is no net fluid flow, oscillation of the fluid occupying the capillary tubes (the radius of each tube is just large enough to contain only the Stokes' layer) connecting a hot reservoir to a cold reservoir enhances heat diffusion between the two reservoirs. Their steady-state predictions are based on the assumption that a constant, time-averaged, nonzero temperature gradient is always present. By neglecting the axial molecular diffusion along the wall and in the fluid, except for the time-averaged temperature gradient, and assuming a fully developed velocity profile, the energy and momentum equations become linear and lend themselves to closed-form solutions. It is also assumed that fluid entering the capillary tubes has a constant, uniform temperature (during each half of a cycle). Mean parameter analysis (average over cross section) (Gredeon, 1986) of the problem has led to more useful relationships for the friction factor, but in general the results are not in agreement with the exact solutions. Transition to turbulence has been discussed by Grassmann and Tuma (1979).

In the following, the available predictions also extend to circular tubes with a finite wall thickness, and results are obtained for the entire range of frequencies used in the experiment. An analysis of the fluid dynamics in the reservoir is also made.

2 Analysis of Fluid Flow and Heat Transfer in Tubes

Based on the assumptions of a fully developed velocity field and constant properties and by neglecting the axial molecular heat diffusion in the tube wall and in the fluid, the governing

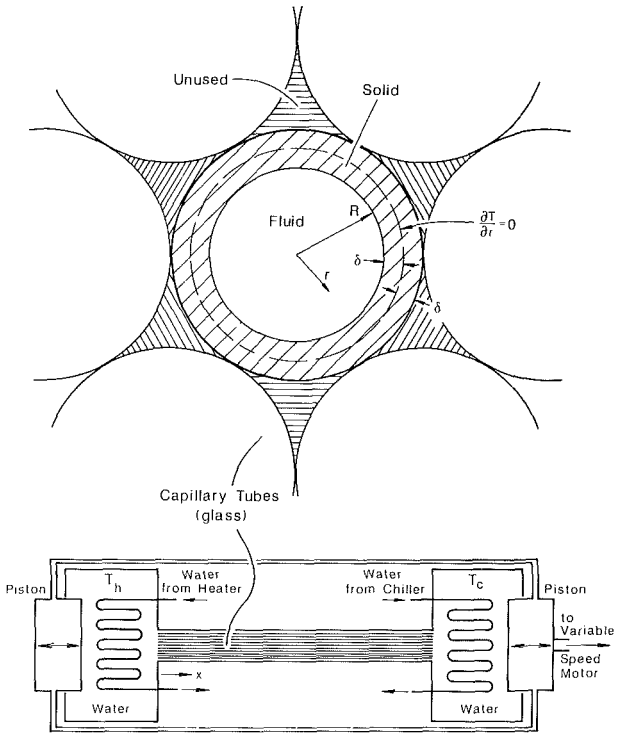

Fig. 1 Schematic of the heat exchanger; the ideal packing of the capillary tubes is also shown

Contributed by the Heat Transfer Division for publication in the JOURNAL OF HEAT TRANSFER. Manuscript received by the Heat Transfer Division October 18, 1988. Keywords: Augmentation and Enhancement, Forced Convection, Heat Exchangers.

equations for the velocity and temperature field of the system shown in Fig. 1 are

$$u_t = P_{x,\max}\cos(t) + \alpha^{-2}(u_{rr} + r^{-1}u_r) \tag{1}$$

$$T_t + u\,\bar{T}_x = (\alpha^2\mathrm{Pr})^{-1}(T_{rr} + r^{-1}T_r) + \mathrm{Ec}\alpha^{-2}u_r^2 \qquad 0 \le r \le 1 \tag{2}$$

$$T_t = (\sigma\alpha^2\mathrm{Pr})^{-1}(T_{rr} + r^{-1}T_r) \qquad 1 \le r \le 1+\Delta \tag{3}$$

where the variables have been nondimensionalized using the tube radius R for the length, the angular frequency ω for time, $\rho_f R^2\omega^2$ for pressure, and $\bar{T}_h^* - \bar{T}_c^* = \Delta T^*$ for the temperature. For quantities that appear in both dimensionless and dimensional forms, the dimensional quantities are shown with asterisks. The variables are defined in the nomenclature and the choice of the variables is explained by Chatwin (1975), Kurzweg (1985a), and Kaviany (1986). The boundary conditions for equations (1)–(3) are

$$u(1, t) = u_r(0, t) = 0$$

$$T_f(1, t) = T_s(1, t),\ \mu T_{r,f}(1, t) = T_{r,s}(1, t)$$

$$T_{r,f}(0, t) = T_{r,s}(1+\Delta, t) = 0$$

The dimensionless average displacement of the fluid (along the tube axis) over half the period is called the tidal displacement and is given by

$$\Delta x = 2\left|\int_{-\pi/2}^{\pi/2}\int_0^1 u\, r\, dr\, dt\right| \tag{4}$$

This is twice the cross-section-averaged oscillation amplitude a. The dimensionless tidal volume ΔV is $\pi\Delta x$.

The effective thermal diffusivity is defined as

$$\frac{\kappa_e}{R^2\omega} = -\frac{1}{\pi}\int_0^{2\pi}\int_0^1 \mathrm{Real}\,(u)\ \mathrm{Real}\,(T)\ r\, dr\, dt \tag{5}$$

and the average dimensionless work done per unit time (per tube) is

$$W = \frac{l}{2\pi}\int_0^{2\pi}\int_0^1 u\, P_{x,\max}\cos t\, r dr dt \tag{6}$$

The solution for the velocity field is available (Chatwin, 1975; Schlichting 1979; Arpaci and Larson, 1984) and is

$$u = iu_c\left[\frac{I_o(i^{1/2}\alpha r)}{I_o(i^{1/2}\alpha)} - 1\right]e^{it} = iu_c F e^{it} \tag{7}$$

where u_c is the dimensionless characteristic velocity equal to $p^*_{x,\max}/\rho_f R\omega^2$, $I_o(i^{1/2}z) = \mathrm{ber}(z) + i\,\mathrm{bei}(z)$, ber and bei are the Kelvin functions (Oliver, 1972), and $i = (-1)^{1/2}$. The solution to the temperature field for $\mathrm{Ec} \approx 0$ and Pr not equal to unity is

$$T_f = \bar{T}_x x + \bar{T}_x\theta(r, t)$$

$$T_f = \bar{T}_x x + \bar{T}_x\left\{\frac{u_c}{1-\mathrm{Pr}} + \frac{\mathrm{Pr}\,u_c}{1-\mathrm{Pr}}\left[\frac{I_o(i^{1/2}\alpha r)}{I_o(i^{1/2}\alpha)} - 1\right] + C_1\, I_o(i^{1/2}\alpha\mathrm{Pr}^{1/2}r)\right\}e^{it} = \bar{T}_x(x + g_f e^{it}) \tag{8}$$

$$T_s = \bar{T}_x x + \bar{T}_x\{C_2\, I_o[i^{1/2}\alpha(\sigma\mathrm{Pr})^{1/2}r] + C_3\, K_o[i^{1/2}\alpha(\sigma\mathrm{Pr})^{1/2}r]\}e^{it} \tag{9}$$

where

$$C_1 = \frac{C_2 I_o[i^{1/2}\alpha(\sigma\mathrm{Pr})^{1/2}] + C_3 K_o[i^{1/2}\alpha(\sigma\mathrm{Pr})^{1/2}] - u_c(1-\mathrm{Pr})^{-1}}{I_o(i^{1/2}\alpha\mathrm{Pr}^{1/2})}$$

$$C_3 = -C_2\,\frac{I_o'[i^{1/2}(\sigma\mathrm{Pr})^{1/2}(1+\Delta)]}{K_o'[i^{1/2}(\sigma\mathrm{Pr})^{1/2}(1+\Delta)]}$$

Nomenclature

A = cross-sectional area of the capillary tube bundle, m^2
a = amplitude of displacement $= \Delta x^*/2$, m
c = specific heat, J/kg-K
Ec = Eckert number $= R^2\omega^2/c_f\Delta T^*$
f = frequency, Hz
F = spatial component of velocity
g = spatial component of the fluctuating temperature, m
h = heat transfer coefficient $= q''^*/\Delta T^*$, W/m^2-K
k = thermal conductivity, W/m-K
L = length of tube, m
L_r = length of reservoir, m
l = L/R
$\dot{m}$ = mass flow rate, kg/s
N = number of tubes
p = pressure, N/m^2
$p_{x,\max}$ = maximum pressure gradient, N/m^3
Pe_c = Peclet number $= 2u_cR/\kappa_f$
Pr = Prandtl number $= \nu/\kappa_f$
q = heat transfer per unit area, W/m^2
Q = heat flow rate, W
r = radial coordinate axis, m
R = inner radius of tube, m
R_r = radius of reservoir, m
R_1 = radius of capillary bundle, m
Re = reservoir Reynolds number $= u^*_{\max,1}R_r/\nu$
R_p = piston radius, m
Re_c = Reynolds number $= 2u_cR/\nu$
T = temperature, K
t = time, s
$\bar{T}_x$ = time-averaged temperature gradient, K/m
u_c = characteristic velocity $= p_{x,\max}/(\rho_f R\omega^2)$, m/s
u, v = velocity components in x and r directions, m/s
$u_{\max,1}$ = maximum inlet velocity, m/s
$u_{\max,2}$ = maximum outlet velocity, m/s
x = axial coordinate axis, m
α = Womersley or Stokes number $= R\omega^{1/2}/\nu^{1/2}$
Δ = δ/R
Δ_p = piston displacement, m
ΔT = $\bar{T}_h - \bar{T}_c$, K
ΔT_c = temperature drop in the cold loop, K
ΔT_h = temperature drop in the hot loop, K
δ = half wall thickness, m
ϵ = porosity
ϵ_c = porosity correction
η = efficiency, defined in equation (13)
θ = fluctuating component of temperature, m
κ = thermal diffusivity, m^2/s
μ = k_f/k_s
ν = kinematic viscosity, m^2/s
ξ = defined in equation (18)
ρ = density, kg/m^3
σ = thermal diffusivity ratio $= \kappa_f/\kappa_\sigma$
τ = period
ψ = stream function
ω = frequency, rad/s; also vorticity

Superscripts

$\bar{}$ = time averaged
* = quantity is dimensional (whenever a quantity appears in both dimensional and dimensionless forms)

Subscripts

c = cold
e = effective
f = fluid
h = hot
max = peak
r, t, x = derivatives with respect to r and x
s = solid

$$C_2 = \frac{\dfrac{\mu \mathrm{Pr}}{1-\mathrm{Pr}} u_c \alpha \dfrac{I_o'(i^{1/2}\alpha)}{I_o(i^{1/2}\alpha)} - \dfrac{\mu \alpha \mathrm{Pr}^{1/2} I_o'(i^{1/2}\alpha \mathrm{Pr}^{1/2})}{I_o(i^{1/2}\alpha \mathrm{Pr}^{1/2})} \dfrac{u_c}{1-\mathrm{Pr}}}{-\mu \alpha \mathrm{Pr}^{1/2} \dfrac{I_o'(i^{1/2}\alpha \mathrm{Pr}^{1/2})}{I_o(i^{1/2}\alpha \mathrm{Pr}^{1/2})} \left\{ I_o[i^{1/2}\alpha(\sigma \mathrm{Pr})^{1/2}] - K_o[i^{1/2}\alpha(\sigma \mathrm{Pr})^{1/2}] \right.}$$

$$\left. \times \frac{I_o'[i^{1/2}\alpha(\sigma \mathrm{Pr})^{1/2}(1+\Delta)]}{K_o'[i^{1/2}\alpha(\sigma \mathrm{Pr})^{1/2}(1+\Delta)]} \right\}$$

$$+ \alpha(\sigma \mathrm{Pr})^{1/2} \left\{ I_o'[i^{1/2}\alpha(\sigma \mathrm{Pr})^{1/2}] \right.$$

$$\left. - K_o'[i^{1/2}\alpha(\sigma \mathrm{Pr})^{1/2}] \frac{I_o'[i^{1/2}\alpha(\sigma \mathrm{Pr})^{1/2}(1+\Delta)]}{K_o'[i^{1/2}\alpha(\sigma \mathrm{Pr})^{1/2}(1+\Delta)]} \right\}$$

where

$$I_o'(i^{1/2}z) = \mathrm{ber}'(z) + i\,\mathrm{bei}'(z),$$

$$K_o(i^{1/2}z) = \mathrm{ker}(z) + i\,\mathrm{kei}(z)$$

$$K_o'(i^{1/2}z) = \mathrm{ker}'(z) + i\,\mathrm{kei}'(z)$$

are also given by Oliver (1972) and are available as computer library subroutines (IMSL). An estimate of the temperature rise per cycle due to the viscous dissipation can be obtained using equations (2) and (3) and the solution to the velocity field. This is done by adding equations (2) and (3) and then integrating the resulting equation between $0<r<1+\Delta$ and $0<t<2\pi$, applying the boundary conditions at $r=1$ and $r=1+\Delta$, and finally dividing by 2π. The result is

$$\Delta T_{\mathrm{diss}} = \frac{1}{\pi} \int_0^{2\pi} \int_0^1 u_c^2 \mathrm{Ec} \times \left\{ \mathrm{Real}\left[\frac{I_o'(i^{1/2}\alpha r)}{I_o(i^{1/2}\alpha)} e^{it} \right] \right\}^2 r\, dr\, dt \tag{10}$$

The rate of the viscous dissipation for the bundle is

$$Q^*_{\mathrm{diss}} = \rho c_p N \pi R^2 L \Delta T_{\mathrm{diss}} \Delta T^* f \tag{10a}$$

In terms of the functions F and g_f defined in equations (7) and (8), the volume displacement, the effective diffusivity, and the work per unit time are (Watson, 1983)

$$\Delta V = 4\pi \left| \int_0^1 i F r\, dr \right| \tag{4a}$$

$$\frac{\kappa_e}{R^2 \omega} = -\frac{1}{2} \int_0^1 (\bar{F}g + F\bar{g}) r\, dr \tag{5a}$$

$$W = \frac{i u_c^2 l}{4} \int_0^1 [(F-1) - (\overline{F-1})] r\, dr \tag{6a}$$

where bars indicate complex conjugate quantities.

The required pressure gradient $p^*_{x,\max}$ needed for a given Δ^*_x and f is obtained from integration of equations (4) or (4a) and the result given by Watson (1983) is

$$p_{x,\max} = \frac{\Delta x^* \rho_f \nu_f^2 \alpha^2}{2R^4} \left[\frac{B_1(\alpha)}{B_3(\alpha)} \right]^{1/2}$$

where

$$B_1(\alpha) = \frac{\alpha^3 B(\alpha)}{B'(\alpha)}$$

$$B(\alpha) = \mathrm{ber}^2(\alpha) + \mathrm{bei}^2(\alpha)$$

$$B_3(\alpha) = \frac{\alpha^2 B(\alpha) + B'(\alpha) - \alpha B''(\alpha) - \alpha^2 B'''(\alpha)}{\alpha^4 B'(\alpha)}$$

The derivatives of $B(\alpha)$ are found from Watson (1983)

$$B(\alpha) = \sum_{n=0}^{\infty} \frac{(1/2\ \alpha)^{4n}}{(n!)^2 (2n)!}$$

The heat transfer per unit area is

$$q = \epsilon \frac{\kappa_e}{R^2 \omega} \bar{T}_x \text{ or } q^* = \epsilon \rho_f c_f \kappa_e \bar{T}^*_x = \epsilon \rho_f c_f \kappa_e \frac{\bar{T}^*_h - \bar{T}^*_c}{L} \tag{11}$$

where the porosity ϵ is based on the ideal packing shown in Fig. 1 (where the unused interstitial volume is also shown) and is the volume fraction used by the moving fluid, i.e.,

$$\epsilon = \left(\frac{1}{1+4\Delta^2+4\Delta} \right) \left(\frac{\pi}{3^{1/2}2} \right) \tag{12}$$

An efficiency based on the ratio of heat transfer to the work done is defined as

$$\eta = Q/W \tag{13}$$

Estimates on the entrance length and the effect of the axial conduction in the fluid can be made using the available steady-state results along with a Reynolds and Peclet numbers defined as

$$\mathrm{Re}_c = \frac{2u_c^* R}{\nu} = 2u_c \alpha^2, \qquad \mathrm{Pe}_c = 2\mathrm{Pr} u_c \alpha^2$$

Based on the available results, these effects are not significant. The required integration of the above equations has been performed numerically using the trapezoidal rule and progressively decreasing the spatial and temporal steps until convergence was found. Comparisons were made for those predicted quantities that have also appeared in the analysis of Watson (1983) and complete agreement has been found.

3 Analysis of Fluid Flow in Reservoirs

An attempt has been made to estimate the extent of the interaction between the fluid exiting the tubes and entering the reservoirs, and the fluid in the reservoirs. This was done by solving the momentum equation (vorticity–stream function formulation) for a laminar and axisymmetric flow with time periodic flow boundary conditions. The nonuniformity in the velocity distribution across each capillary tube has been neglected. The presence of the coils inside the reservoirs has not been accounted for in this study. It must be mentioned that the flow within the reservoirs may not be laminar and this estimation of the flow field is only an approximation. However, it will in part explain the lack of radial temperature uniformity at the bundle ends. The pathline followed by the particles exiting the bundle and then traveling through one of the reservoirs is then computed. The dimensionless governing equations for the transient, laminar, incompressible, constant properties and axisymmetric flow field considered is given by the vorticity–stream function formulation as (Fig. 2 gives a schematic of the problem considered)

$$\omega_t + (v\omega)_r + (u\omega)_x = \mathrm{Re}^{-1}[r^{-1}(r\omega)_r]_r + \mathrm{Re}^{-1}\omega_{xx} \tag{14}$$

$$(r^{-1}\psi_r)_r + r^{-1}\psi_{xx} = \omega \tag{15}$$

$$u = -r^{-1}\psi_r \tag{16}$$

$$v = r^{-1}\psi_x \tag{17}$$

where the reservoir radius, R_r, and the maximum velocity at $z=0$, i.e., $u^*_{\max,1}$, are used to scale the variables. The dimensionless variables are $t = t^* u^*_{\max,1} R_r^{-1}$, $r = r^* R_r^{-1}$, $u = u^*/u^*_{\max,1}$, and $\mathrm{Re} = u^*_{\max,1} R_r \nu^{-1}$. The choice of R_r as the length scale is made because the bundle radius is varied while R_r is kept constant. As was mentioned before, whenever the quantities appear in dimensional and dimensionless forms, an asterisk indicates that the quality is dimensional. For a maximum fluid

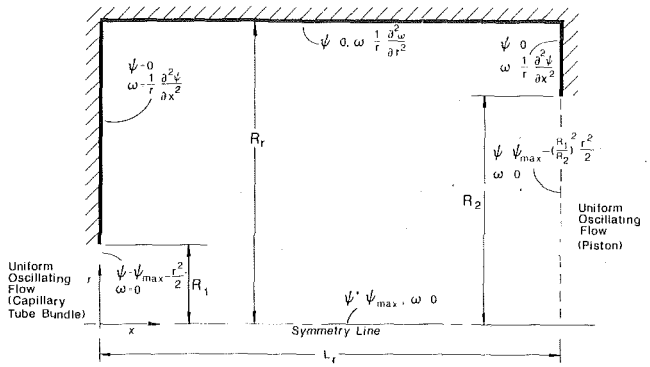

Fig. 2 Schematic of the reservoir showing the boundary conditions

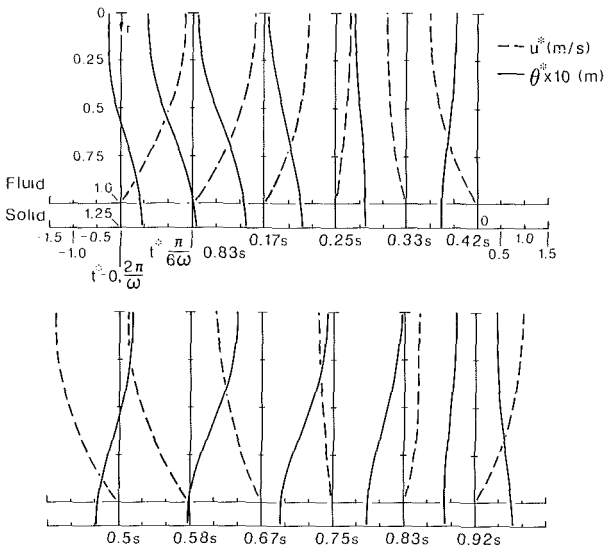

Fig. 3 Distributions of the velocity and temperature at several elapsed times for $f = 1$ Hz

displacement in the bundle, a, and a peak velocity that is nearly twice the average velocity, this peak velocity is

$$u^*_{\max,1} = 4af$$

and the dimensionless period is

$$\tau = f^{-1}\, u^*_{\max,1} R_r^{-1} = 4aR_r^{-1}$$

The velocity of flow entering the reservoir is in phase with the piston velocity (piston motion has been modeled by a periodic boundary condition at $x = L_r/R_r$ where L_r is the length of the reservoir).

Figure 2 gives the coordinate system used and the boundary conditions applied to equations (14) and (15). These boundary conditions are

$u = \cos(2\pi\tau^{-1}t)$ at $x = 0$, $0 < r < R_1/R_r$

$u = (R_1/R_2)^2 \cos(2\pi\tau^{-1}t)$ at $x = L_r/R_r$, $0 < r < R_2/R_r$

$\psi = 0$ on the reservoir wall

$\psi = \psi_{\max}$ on the centerline

where $\psi_{\max} = \int_0^{R_1} r\,dr = (R_1/R_r)^2$. The instantaneous particle positions for particles starting at $z = 0$ and $r = r_o$ are given in terms of the r and z components of the positions

$$r = r_o + \int_{t_o}^{t} v\,dt$$

$$x = \int_{t_o}^{t} u\,dt$$

and the pathline at t is the trace of this position up to time t.

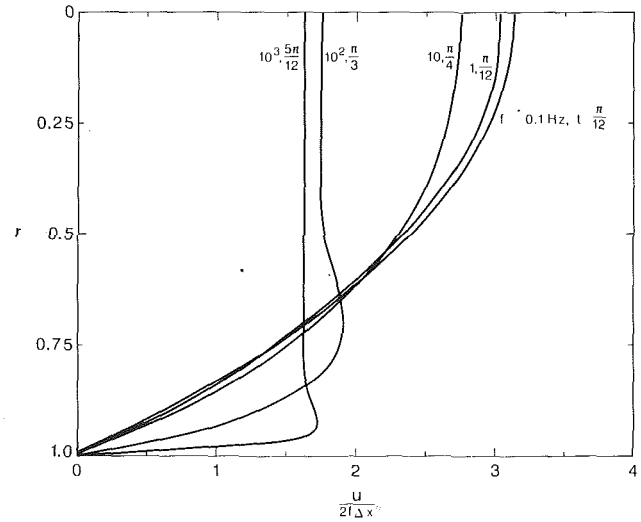

Fig. 4 Velocity distribution for several frequencies and at elapsed times associated with maximum centerline velocity

Approximate solutions to the above-posed transient equations were found using the finite-difference approximations given by Torrance (1968). These are the fully explicit forms for time, second-order difference forms for space, and the upwind scheme. For $L_r/R_r = 1.5$, a 41×61 mesh was used. The standard convergence test of reducing the mesh size until the solution no longer changes substantially was applied and this mesh net was found accurate and economical. The difference between the path lines obtained using a 61×91 and those for the 41×61 mesh was less than 2 percent (in terms of the maximum deviation of the r and z locations).

The integration started by setting $\omega = \psi = 0$ at $t = 0$. The results became periodic (quasi-steady) after one to three cycles, depending on Re. The pathlines were determined after quasi-steady solutions were found.

4 Results and Discussion

4.1 Predictions of Heat Transfer. For the system considered other than the fluid properties and tube material and dimensions, the two independently chosen parameters are Δx^* and f. The former is taken to be that fraction of the total length of the tubes given by the inequality $\Delta x^* < L/3$.

Velocitiy and Temperature Distributions. Figure 3 shows the distributions of the velocity and the fluctuating component of the temperature (given in dimensions of m and multiplied by the temperature gradient, $(\bar{T}^*_h - \bar{T}^*_c)/L$, to obtain the unit of temperature); water is the fluid (properties evaluated at 60°C, i.e., Pr = 3.0), and the tubes are glass with $\Delta x^* = 20$ cm, R = 0.4 mm, and $f = 1$ Hz. Heat flows first toward and then away from the walls as time elapses; then this process is repeated.

Location of Maximum Velocity. At relatively low frequencies the velocity profile is similar to that of steady-state Poiseuille flow, but due to the quasi-steadiness the mean velocity constantly changes. As the frequency increases, the flow in the middle portion of the tube becomes nearly uniform. Figure 4 shows this trend for the system in Fig. 3. The velocity is normalized with respect to $2f\Delta x^*$, which is the average velocity for traveling the distance $\Delta x^*/2$ in one-fourth the period. The elapsed time is chosen to correspond with the occurrence of the maximum centerline velocity. The results show that for low frequencies, the centerline velocity can be higher than three times this average velocity. Therefore,

$$\frac{\Delta x^*}{2} \le \frac{L}{\beta} \text{ where } \beta \simeq 3 \qquad (18)$$

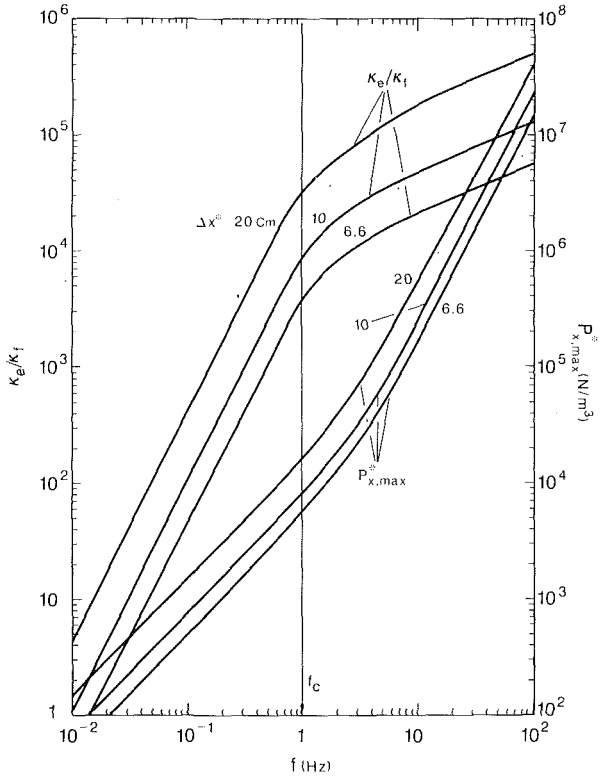

Fig. 5 Effect of displacement and frequency on the effective thermal diffusivity and the required pressure gradient

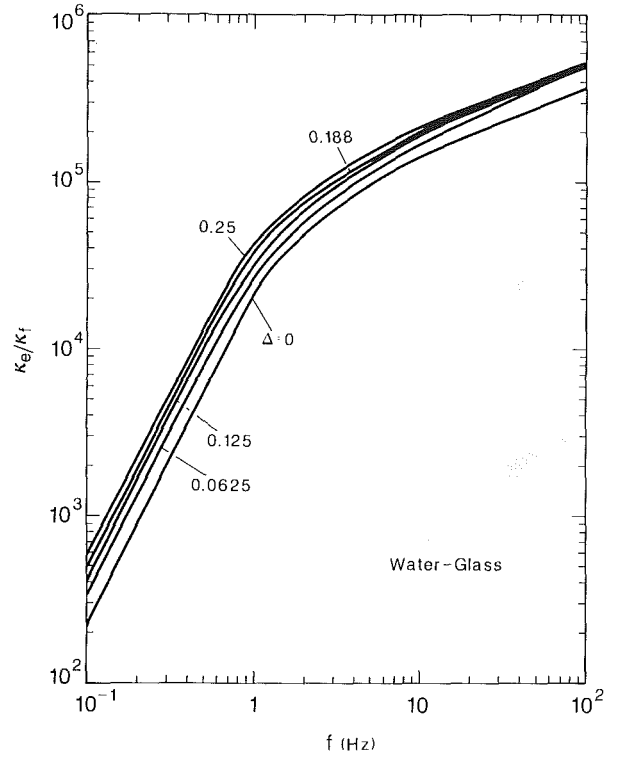

Fig. 6 Effect of wall thickness and frequency on effective thermal diffusivity

Choosing β to be less than three causes mixing between the fluids of the two reservoirs.

Influence of Displacement. For a given system, the required pressure gradient, $p^*_{x,\max}$, increases as f increases. However, the increase is more substantial for frequencies

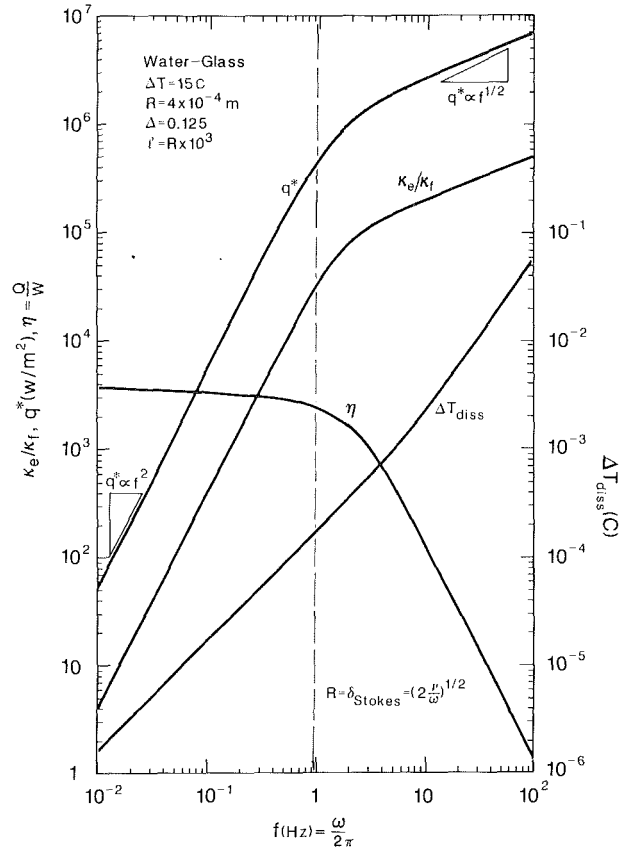

Fig. 7 Variations in the effective thermal diffusivity, the efficiency, the heat flux, and the temperature rise due to the viscous dissipation, with respect to frequency. The experimental results are also shown with symbols. Water properties are evaluated at 60°C (Pr = 3).

higher than that associated with the Stokes' layer thickness equal to R, i.e., $f \leq \nu/\pi R^2 = f_c$, where the entire cross section is made of boundary layers (no near uniform velocity zone present). Figure 5 shows the required pressure gradient for the system in Fig. 4 and for $\Delta x^* = 20$, 10, and 6.6 cm. The ratio of the enhanced heat diffusion coefficient to the fluid molecular diffusion coefficient is also shown. For the properties evaluated at 60°C, the optimum frequency is about 1 Hz.

Tube Wall Thickness. For a semi-infinite slab, the heat diffusion penetration depth decreases with the square root of the period of oscillation. Therefore, it is expected that as the frequency increases, the contribution of the tube wall to the heat storage release mechanism gradually vanishes. Figure 6 shows this trend for the system in Fig. 3.

Efficiency. As the frequency increases, the required pressure gradient increases; for frequencies larger than f_c the required pressure gradient may be excessive. Figure 7 shows that the efficiency of the system, as defined by equation (13), decreases rather abruptly as $f > f_c$. The temperature rise per cycle due to viscous dissipation, as determined from equation (10), is also shown and is generally negligible (except for high Prandtl numbers, Kaviany, 1986). The heat transfer per unit area, as given by equation (11), is also given for the parameters listed in the caption and $\Delta x = l/2$. For $f \leq f_c$, the effective thermal diffusivity is proportional to f^2 and the efficiency is nearly constant. For $f > f_c$ the performance deteriorates as the efficiency drops monotonically; for $f \gg f_c$ the heat flux and effective thermal diffusivity become proportional to $f^{1/2}$. These asymptotes have also been observed by Watson (1975) and Kurzweg (1985).

Other Fluids. Since the thermal boundary layer is thicker

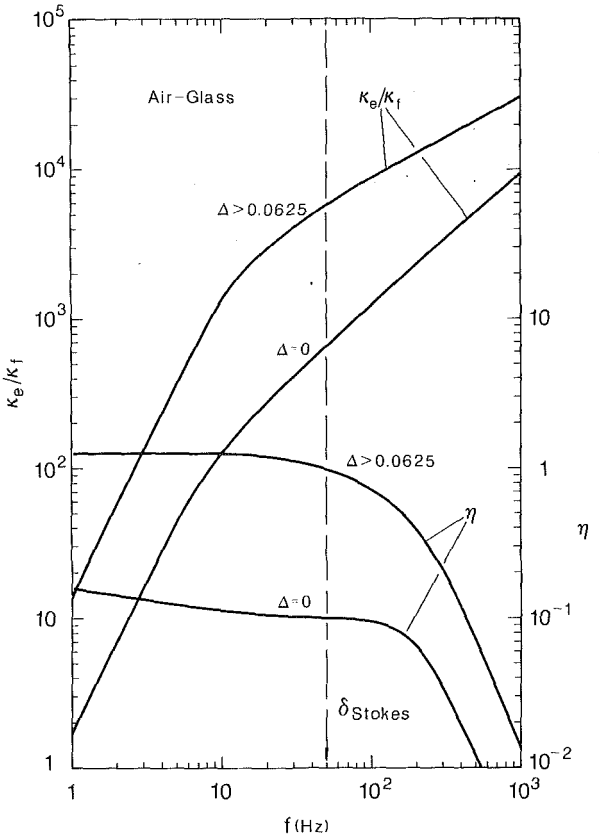

Fig. 8 Variation in the effective thermal diffusivity with respect to tube wall thickness and frequency, with air as the fluid

for gases, the optimum frequency would be larger than that for water when gases are used as the working fluid. The results for air at 60°C (Pr = 0.71) are shown in Fig. 8. Note that since the heat penetrates faster into air (larger thermal diffusivity), the tube wall plays a much more substantial role in the heat storage–release process. For water this contribution is about 35 percent of the total, but for air it dominates the contribution.

4.2 Prediction of Fluid Flow in Reservoirs. In order to simulate the conditions of the heat exchanger closely, the parameters chosen are $a = 15$ cm, $R = 6$ cm, $\nu = 10^{-6}$ m^2/s, $0.1 \le f \le 10$ Hz, $1/4 \le R_1/R_r \le 1/2$, and $1/4 \le R_2/R_r \le 3/4$. This leads to $4 \times 10^3 < \mathrm{Re} < 4 \times 10^5$ and $\tau = 10$. Figures 9(a) and 9(b) show typical constant stream-function contours for the time intervals of one up to the end of a period, i.e., $\tau = 10$. Figure 12(a) is for $R_1/R_r = 1/4$, $R_2/R_r = 3/4$, and $f = 1$ Hz; and Fig. 9(b) represents $R_1/R_r = R_2/R_1 = 1/4$ and $f = 1$ Hz. At $t = 0$, $n\tau$ ($n = 0, 1, 2, \ldots,$) the inlet fluid velocity and the piston velocity are maximum. As the velocities at $z = 0$ and $z = L_r/R_r$ decrease, the accelerating fluid that has left the entrance must decelerate. This results in a recirculation of the high-inertia core. The recirculation in Fig. 9(b) is more pronounced because of the smaller exit orifice. Throughout the cycle these accelerations/decelerations cause the formation of vortices, which grow and decay and are then replaced with others of the opposite directions. Figure 10 shows the pathlines for the existing reservoir geometry $R_1/R_r = 1/4$, $R_2/R_r = 3/4$. The pathlines are for three cycles starting at $t_o = n\tau + 7.5$, i.e., when the entering fluid is at the velocity of zero, but is accelerating (i.e., $2\pi t/\tau = 2\pi n + 3\pi/2$) to $t = (3+n)\tau + 7.5$. The results show that for lower frequencies the entering particles at a radial location closer to the centerline will not return during these three cycles, while those farther away from the centerline will return without inter-

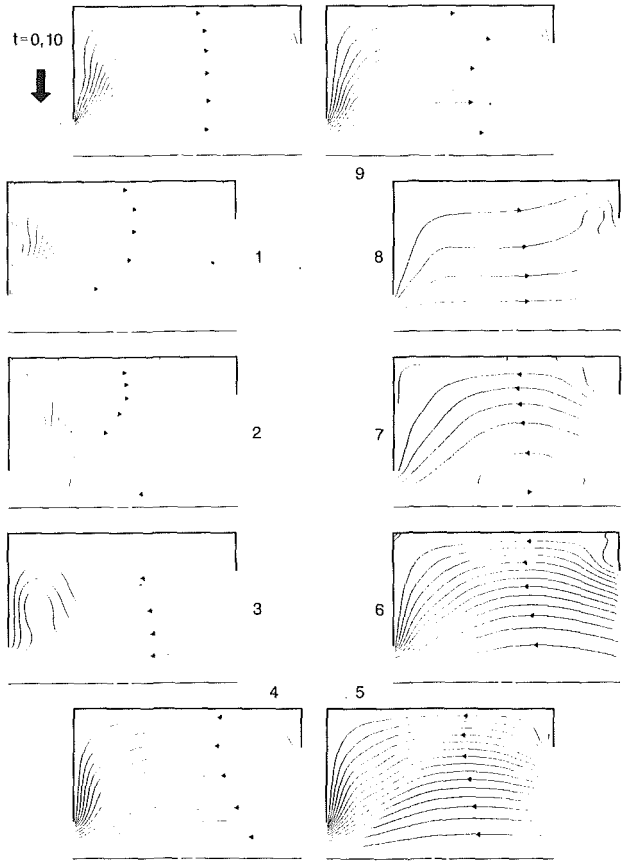

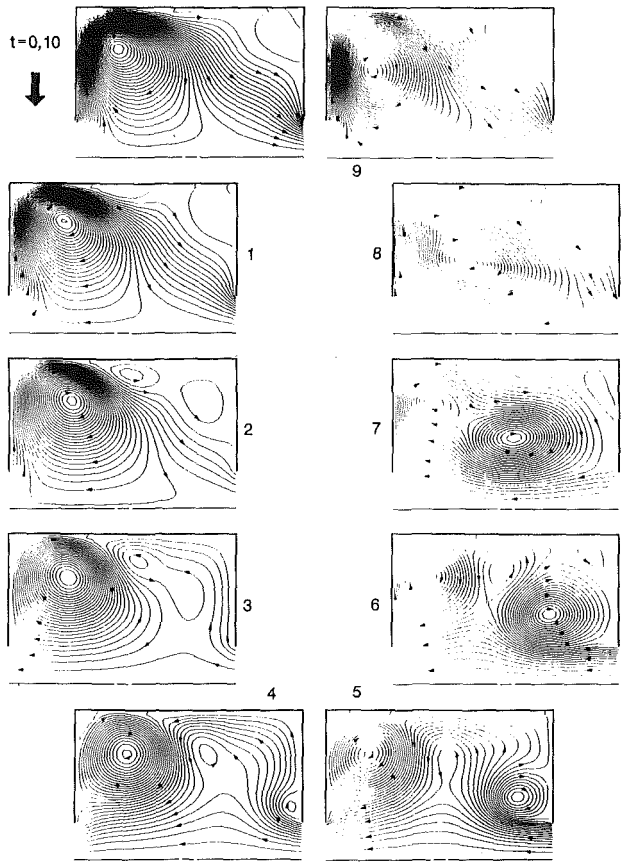

Fig. 9 Contours of constant stream function, for (a) $R_1/R_r = 1/4$, $R_2/R_r = 3/4$, and (b) $R_1/R_r = R_2/R_r = 1/4$; the frequency is 1 Hz

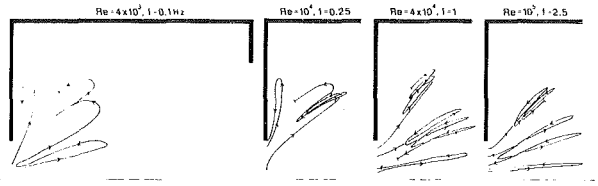

Fig. 10 Pathlines for the reservoir geometry of $R_1/R_r = 1/4$, $R_2/R_r = 3/4$, and various frequencies

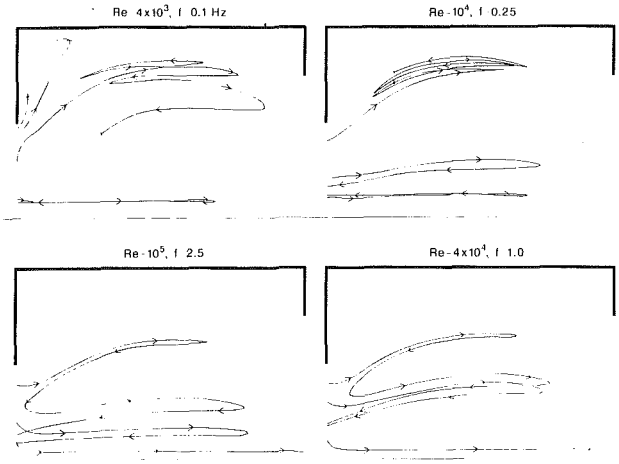

Fig. 11 Same as Fig. 5 except $R_1/R_r = 1/2$

acting substantially with the fluid in the reservoir. At higher frequencies the opposite takes place.

5 Summary

The tube bundle acts as a heat pipe in transferring the heat from the hot to the cold reservoir. The behavior of each tube is idealized and treated analytically. The bundle-reservoir interaction, where most of resistance to the heat flow may exist, has also been idealized and treated numerically.

(*a*) The results show that the performance of the heat exchanger deteriorates as the thermal boundary layer becomes smaller than the tube radius.

(*b*) The viscous dissipation is generally negligible for water as the fluid.

(*c*) Subject to the assumptions of negligible buoyancy effects, no disturbances due to the presence of the internal coils, and uniform inlet and outlet velocities, the pathlines of the fluid particles entering the reservoirs of an existing heat exchanger have been determined. The results show that depending on the initial radial position, the interaction with the fluid in the reservoirs is substantially different, and this depends on the frequency and the reservoir geometry. The larger the ratio R_r/R_1, the stronger the vortices are near the inlet and outlet; therefore, the extent of this interaction is less. The limited experimental results regarding the velocity and temperature distributions in the reservoirs and near the bundle ends support the numerical predications.

Alternatives to heat removal/supply from the handle ends have not been considered. The bundle end-reservoir thermal resistance can be reduced by proper management of fluid dynamics and heat transfer surface area in the reservoirs.

References

Arpaci, V. S., and Larson, P. S., 1984, *Convection Heat Transfer*, Prentice-Hall, Englewood Cliffs, NJ, pp. 425-458.

Chatwin, P. C., 1975, "On the Longitudinal Dispersion of Passive Contaminant in Oscillatory Flows in Tubes," *J. Fluid Mech.*, Vol. 71, pp. 513-527.

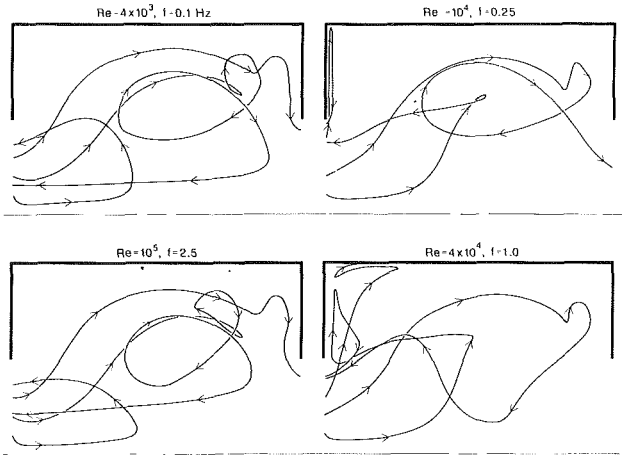

Fig. 12 Same as Fig. 5 except $R_1/R_r = R_2/R_r = 1/2$

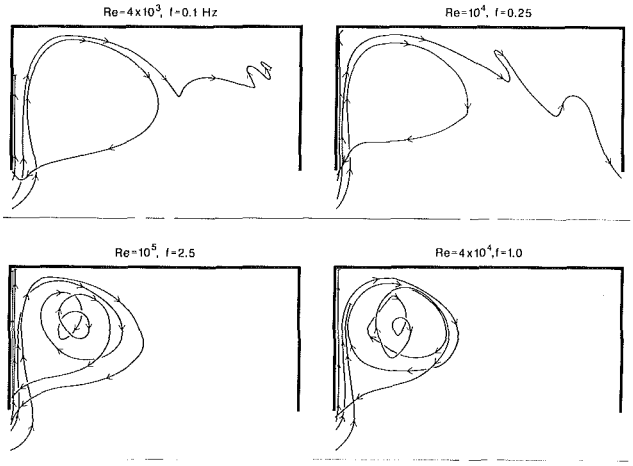

Fig. 13 Same as Fig. 6 except for $R_1/R_r = R_2/R_r = 1/4$

Gedeon, D., 1986, "Mean-Parameter Modeling of Oscillating Flow," ASME JOURNAL OF HEAT TRANSFER, Vol. 108, pp. 513-518.

Grassmann, P., and Tuma, M., 1979, "Critical Reynolds Number for Oscillating and Pulsating Tube Flow" (in German), *Thermo-Fluid Dyn.*, Vol. 12, pp. 203-209.

Joshi, C. H., Kamm, R. D., Drazen, J. M., and Slutsky, A. S., 1983, "An Experimental Study of Gas Exchange in Laminar Oscillatory Flows," *J. Fluid Mech.*, Vol. 133, pp. 245-254.

Kaviany, M., 1986, "Some Aspects of Heat Diffusion in Fluids by Oscillation," *Int. J. Heat Mass Transfer*, Vol. 29, pp. 2002-2006.

Kurzweg, U. H., and Zhao, L. de, 1984, "Heat Transfer by High Frequency Oscillations: A New Hydrodynamic Technique for Achieving Large Effective Thermal Conductivities," *Phys. Fluids*, Vol. 27, pp. 2624-2627.

Kurzweg, U. H., 1985a, "Enhanced Heat Conduction in Fluids Subjected to Sinusoidal Oscillations," ASME JOURNAL OF HEAT TRANSFER, Vol. 107, pp. 459-462.

Kurzweg, U. H., 1985b, "Enhanced Heat Conduction in Oscillatory Viscous Flows Within Parallel-Plate Channels," *J. Fluid Mech.*, Vol. 156, pp. 291-300.

Kurzweg, U. H., 1986, "Temporal and Spatial Distribution of Heat Flux in Oscillating Flow Subjected to an Axial Temperature Gradient," *Int. J. Heat Mass Transfer*, Vol. 29, pp. 1969-1977.

Kurzweg, U. H., and Jaeger, M. J., 1986, "Tuning Effect in Enhanced Gas Dispersion Under Oscillatory Conditions," *Phys. Fluids*, Vol. 29, pp. 1324-1326.

Oliver, F. W. J., 1972, "Bessel Functions of Integer Order," in: *Handbook of Mathematical Functions*, M. Abramowitz and X. Stegun, eds., p. 379.

Torrance, K. E., 1968, "Comparison of Finite-Difference Computations of Natural Convection," *Journal of Research NBS-B*, Vol. 728, pp. 281-301.

Schlichting, H., 1979, *Boundary-Layer Theory*, 7th ed., McGraw-Hill, New York.

Watson, E. J., 1983, "Diffusion in Oscillatory Pipe Flow," *J. Fluid Mech.*, Vol. 133, pp. 233-244.

Performance of a Heat Exchanger Based on Enhanced Heat Diffusion in Fluids by Oscillation: Experiment

M. Kaviany

M. Reckker

Department of Mechanical Engineering and Applied Mechanics,
The University of Michigan,
Ann Arbor, MI 48109

The results of a study on the performance of a heat exchanger that takes advantage of enhanced heat diffusion in oscillated fluids are presented. In this heat exchanger, the fluid occupies a bundle of capillary tubes that connects two reservoirs at different temperatures; a piston in each reservoir drives the oscillation. The experimental findings are compared with predictions based on the assumptions that (a) a capillary tube does not exchange heat with the neighboring tubes, (b) the pressure in the reservoirs undergoes an ideal sinusoidal motion, and (c) each reservoir has an infinite heat capacity such that the fluid entering the tubes is at a constant temperature. Good agreement has been found between the actual performance of the heat exchanger and the idealized analysis for low and high frequencies. However, around the frequency corresponding to optimum performance, i.e., where the thermal boundary layers occupy the entire cross section of the capillary tubes, agreement is only fair. The measurements show that there is a temperature variation across the bundle and that the fluid entering the tubes has a nonsteady temperature due to weak, nonuniform mixing within the reservoirs (therefore, a spatial/temporal average was taken). This lateral and temporal variation in the temperature distribution appears to be the leading cause of the difference between the experimental and predicted results. As with any heat pipe, the reduction in the resistance to heat flow in the pipe must be accompanied by a similar ease of heat flow to and away from the ends of the pipe. Therefore, the reservoir fluid dynamics is of paramount importance in these heat exchangers. Some numerical modeling of the fluid flow in the reservoirs, as well as some velocity measurements (using a laser-Doppler anemometer), are also presented.

1 Introduction

The ideal performance of a single tube has been given in the preceding paper (Kaviany, 1990). As was mentioned there, the only verification of enhanced heat diffusion by fluid oscillation has been in a transient experiment.

In order to (*a*) observe the steady-state behavior of such a heat exchange, (*b*) evaluate the validity of the assumptions mentioned above, and (*c*) examine the extent of heat exchange within each of the reservoirs, the following experiment is performed.

The nomenclature and the relevant references are given in the preceding paper (Kaviany, 1990).

2 Experiment

The apparatus consisted of (*a*) the capillary heat exchanger, consisting of the two reservoirs, the connecting bundle of capillary tubes, two pistons, and a motor; and (*b*) the supporting heat exchangers placed inside and outside the reservoirs.

2.1 Capillary Heat Exchanger. Figure 1 gives the details of the capillary heat exchanger. For convenience of disassembly the system is made of modules. The primary overall design consideration is the reduction of heat losses. The assembly consists of two reservoir modules, a test section module, and the driving motor connections. The two reservoirs are connected together by the test section module (capillary tube bundle). The fluid oscillation is controlled by pistons that are housed in cylinders located on the outer wall of each reservoir.

The entire assembly is fastened to a 2.54-cm (1-in.) plywood base, which in turn is fastened to the table top. The test section consists of glass capillary tubes encased by a plexiglass tube. The glass tubes are standard soda lime 1 mm o.d., 0.8 mm i.d., and are 427 mm long. These tubes were purchased as redrawn tubing from Fredrich & Dimmock (Millville, NJ). The plexiglass tube has an inner radius of 2.54 cm (1 in.) and a wall thickness of 0.635 cm (0.25 in.). The interstitial area between the tubes was filled with epoxy. This was done by fusing the ends of all the tubes with a torch and then submerging the ends of the bundle into a 1-in. epoxy bath. After curing, the ends were cut so that only the interstitial area was blocked with epoxy.

Each reservoir consists of three components. The reservoir is a 12.7-cm i.d., 13.97-cm o.d., and 13.02-cm-long plexiglass cylinder closed on each end by a phenolic (Garolite) plate (low thermal conductivity). The end plates are 1.59 cm G-11 phenolic (purchased from McMasters, Chicago, IL) with machined O-ring grooves. The end plates are fastened together with a threaded stainless steel rod.

The driving apparatus consists of two pistons, two cylinders, and a connecting harness. The pistons are Ford 2300 series aluminum automobile pistons. They are both 9.53 cm (3.75 in.) in diameter and each has a 2.54-cm (1-in.) phenolic head plate (to reduce heat loss through the piston). The cylinder is stainless steel with a 0.635-cm (0.25-in.) thick wall. A plexiglass flange is epoxied to the cylinder for connection to the reservoir. The piston uses an O-ring and a teflon glide-ring

Contributed by the Heat Transfer Division for publication in the JOURNAL OF HEAT TRANSFER. Manuscript received by the Heat Transfer Division October 18, 1988. Keywords: Augmentation and Enhancement, Forced Convection, Heat Exchangers.

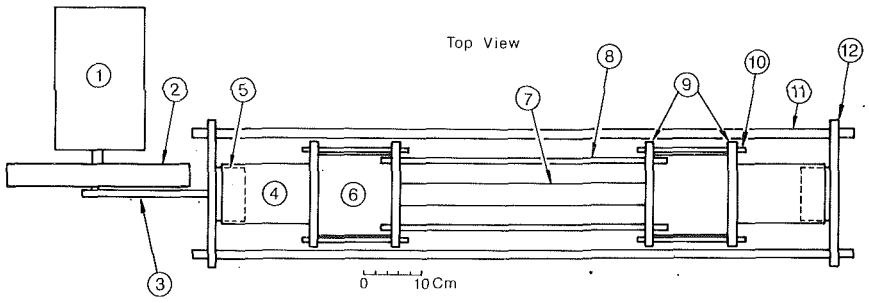

① Variable Speed Motor–3/4 HP, 50–1600 RPM

② Flywheel

③ Connecting Arm–1.27 X 5.08 X 27.94 cm (1/2 X 2 X 11 in) aluminum

④ Piston Cylinder–10.16 cm (4 in) OD, 0.318 cm (1/8 in) wall thickness stainless steel

⑤ Piston–9.53 cm (3 3/4 in) diameter aluminum

⑥ Reservoir Body–13.97 cm (5 1/2 in) OD, 0.635 cm (1/4 in) wall X 12.70 cm (5 in) long acrylic tubing

⑦ Test Section–bundle of glass capillary tubes

⑧ Reservoir Connecting Rods–1.59 cm (5/8 in) diameter, 50.80 cm (20 in) long G–10 phenolic

⑨ Reservoir End Plates–1.59 X 17.78 X 17.78 cm (5/8 X 7 X 7 in) G–11 phenolic

⑩ Reservoir Holding Rods–0.952 cm (3/8 in) diameter, 17.78 cm (7 in) long stainless steel

⑪ Piston Connecting Rods–1.91 cm (3/4 in) diameter, 121.9 cm (48 in) long aluminum

⑫ Piston Connecting Bracket–1.59 X 7.62 X 25.4 cm (5/8 X 3 X 10 in) aluminum

Fig. 1 Compounds of the capillary tube heat exchanger

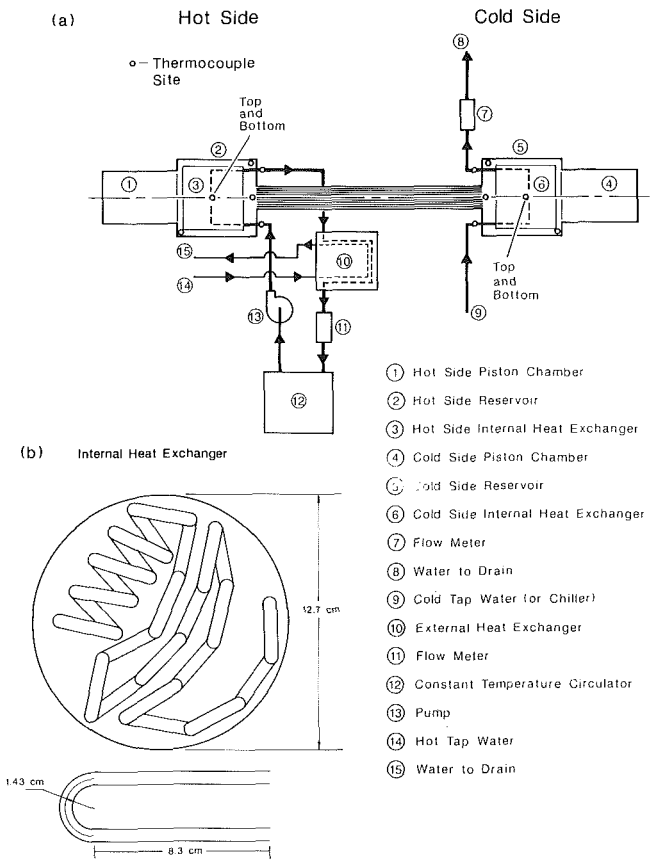

Fig. 2 Schematic of (*a*) the supporting heat exchangers and the position of the thermocouples, and (*b*) the coil heat exchangers in the reservoirs

combination manufactured by CBB Seal Company (Cleveland, OH). The back of each piston is fitted with a winged bracket that allows two 1.91-cm (0.75-in.) aluminum rods to connect the two pistons together. Aluminum was used for the connecting harness to reduce the moving mass. The powering unit is a variable speed a-c motor. The motor has a rating of 0.75 hp and has an electric clutch allowing for variable speed. A flywheel is attached to the shaft. This flywheel has a variable offset pin that regulates the amount of displacement by the pistons. This pin is connected to the pistons through an aluminum connecting arm.

2.2 Supporting Heat Exchangers. Figure 2(*a*) gives a schematic of the system, the supporting heat exchangers, and the position of the thermocouples; Fig. 2(*b*) shows the arrangement of the copper tubes in one of the reservoirs. The copper tube in each reservoir (i.d. = 0.635 cm, o.d. = 0.787 cm) has a total length of 3.27 m.

The external heat exchanger (item 10 in Fig. 2(*a*)) is a coiled copper tubular heat exchanger of 4.57 m with an outer tube of 3.81 cm i.d. (o.d. = 4.06 cm) and an inner tube of 2.22 cm i.d. (o.d. = 2.43 cm) manufactured by Turbutec (Windsor, CT). This heat exchanger was necessary for the high heat flux experiments. The constant temperature circulator has a 1 kW heating capacity.

2.3 Operation. Two of the major problems that arise when operating at relatively high speeds are cavitation and vibration. These were circumvented by keeping the water in the reservoirs under pressure and fastening the entire assembly to a steel beam permanently embedded in the laboratory wall. By keeping the system under high pressure through connection to a tank partially filled with water and under high pressure (via air supply from a compressor; approximately 1.7×10^5 N/m^2 of gage pressure), the small leakages through the piston seals are outward and therefore do not result in air entering the capillary heat exchanger.

In order to avoid entrapment of air bubbles in the capillary tubes, the capillary heat exchange was vacuumed before filling it with water from below (by placing it vertically). This proved to reduce the entrapment significantly, although a few air pockets were observed in the capillary tubes. The temperature of the hot and cold reservoirs cannot be assigned a priori; they depend on the inlet temperature and flow rate of the water flowing into each of the internal heat exchangers. For a given combination of frequency, inlet temperatures, and flow rates, the other temperatures attain magnitudes such that

$$Q^* = (\dot{m}c)_c \Delta T_c^* = (\dot{m}c)_h \Delta T_h^* = \epsilon A \kappa_e \rho_f c_f \left(\frac{\bar{T}_h^* - \bar{T}_c^*}{L} \right) \quad (1)$$

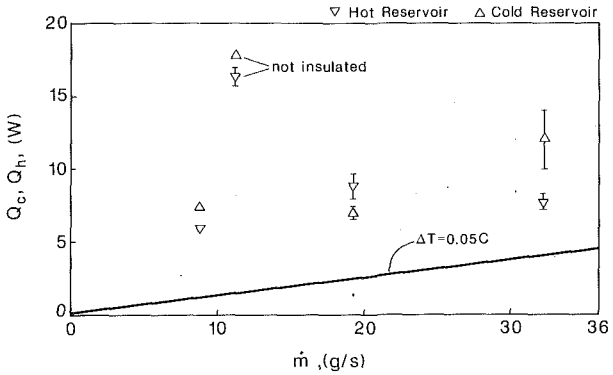

Fig. 3 Calibration with no piston motion

where the subscripts c and h refer to the internal coil heat exchangers in the cold and hot reservoirs, respectively. Flow mixers were placed in the lines in order to ensure that bulk temperatures were recorded. In placing the capillary tubes inside the 2.54-cm i.d. plexiglass tube the ideal packing shown was not obtained: only 519 tubes (instead of 585 for a perfect packing with $\epsilon = 0.58$) were placed in the tube. In addition 11 of these tubes were accidently plugged during filling of the interstitial area by an adhesive. Therefore, a total of 508 tubes were considered in the calculation of piston displacement. Therefore, a porosity correction ϵ_c equal to 585/508 was used in comparing the experimental and predicted results. The piston volume displacement is equal to the volume displacement of the fluid in the capillary tubes, and since Δx^* is twice the displacement aptitude

$$\Delta V_p^* = A_p \Delta_p = N \Delta V^*/2 = N\pi R^2 \Delta x^*/2 \tag{2}$$

and since the velocity profile in the tubes is not uniform, Δx^* (and consequently Δ_p) should be chosen such that the displacement of the fluid at the centerline does not result in the exchange of fluid between the two reservoirs (i.e., net flow). The ratio of the maximum to average velocity is greater than unity; therefore, it is necessary to ensure that

$$L \geq \beta \Delta x^*/2 = \beta \frac{\Delta_p}{N} \left(\frac{R_p}{R}\right)^2 \tag{3}$$

where β is $u_{\max}/u_{\text{ave}}$ and u_{ave} is based on the distance $\Delta x^*/2$ traveled in 1/4 the period, i.e., $u_{\text{ave}} = 2f\Delta x^*$. Note that if mixing of the two fluids occupying the reservoirs were allowed, then an ideal heat transfer based on displacement of the volume of $A_p\Delta_p$ of the fluid over the period of $1/f$ with a temperature change of $(T_h - T_c)$ gives

$$Q_{\text{mix}}^* = A_p \Delta_p \rho_f c_f f(\bar{T}_h^* - \bar{T}_c^*) \tag{4}$$

The ratio of this heat transfer to the heat transfer by enhanced diffusion is

$$\xi = \frac{Q_{\text{mix}}^*}{Q^*} = \frac{A_p \Delta_p L f}{\epsilon A \kappa_e} \tag{5}$$

It is very important that there be no net flow in the capillary heat exchangers, because ξ can easily take on values greater than one. Therefore, if inequality (3) is not satisfied, the heat transfer due to mixing may be mistakenly taken as enhanced diffusion effects.

In order to eliminate the problem associated with uncertainty about the volume of the air pocket trapped in the few tubes, in addition to measuring the piston displacement for each run the total fluid displacement was measured before and after by freezing one of the pistons in one of the reservoirs and connecting that reservoir to a water column. Then the water displacement in this column (i.d. = 2.32 cm) was measured. The piston displacement and column height measurements were in good agreement.

2.4 Calibration

No Motion. For no piston motion, the heat transfer occurs by (*a*) conduction through the capillary bundle (including the plexiglass casing), the rods (phenolic) connecting the two reservoirs, and the phenolic support to the plywood base, and (*b*) natural convection from the reservoirs.

The conduction heat loss through the bundle is

$$Q_b^* = \frac{\Delta T^*}{L}(k_w A_w + k_g A_g + k_{pg} A_{pg}) \tag{6}$$

where w stands for water, g for glass, and pg for plexiglass. For $k_w = 0.6$, $k_g = 1.07$, $k_{pg} = 0.25$ (W/m-K), and $\Delta T^* = 25°C$, we have $Q_b^* = 0.036$ W. This small amount of heat flow rate cannot be measured with the instruments used. The other conduction heat losses are also very small due to small thermal conductivities and temperature differences.

When the reservoirs are kept above and below the ambient temperature, the natural convection heat transfer is from the hot reservoir to the ambient air and from the air to the cold reservoir. The reservoirs rest on a flat piece of plywood, a situation that may be idealized as a semicylinder insulated at the bottom (plywood is about 2 in. thick) with its surface at ΔT_c^* and ΔT_h^*, below and above the ambient temperature, respectively. The velocity field for the cold section is dissimilar to that in the hot section because of the lack of symmetry in the direction of gravity. However, attempts have been made to make ΔT_c equal to ΔT_h and, therefore, nearly balance the heat loss by the heat gained. The heat loss by natural convection via the hot reservoir (through the fiberglass insulation covering the reservoir) was estimated by measuring the temperature at the surface of the insulation and using correlations for natural convection from cylinders. For the measured $\Delta T^* = 6°C$, the heat transfer coefficient was 2.2 W/m-K and the heat loss from the upper half was estimated as 3.1 W. The heat gained by the cold reservoir is expected to be nearly the same.

Figure 3 shows the measured heat loss through the hot reservoir and heat gain through the cold reservoir. The measured heat transfer rates are larger than those estimated. This could be due to the conduction heat transfer through the plywood. However, after leaving the system running for 10 h, a temperature stratification still exists in each of the reservoirs (recorded through thermocouples placed in various locations) that does not appear to reach steady state. Since the heat capacity of each reservoir is 1.45×10^4 J/°C and the measured heat transfer rates are about 8 W, then one hour of heat flow results in 2°C changes in the reservoir temperature (if all the heat is converted to sensible heat in an adiabatic process.) Therefore, the results of the calibration should be considered as a qualitative assurance that the heat losses of the insulated system with no piston motion are less than approximately 15 W.

Viscous Dissipation. The primary friction heat sources are the piston moving against the cylinder and the viscous dissipation in the fluid. In an effort to quantify the combined heat produced by these sources, the following runs were made:

(*a*) running the system with both circulators initially set at room temperature.

(*b*) running the system with both reservoirs held at room temperature.

(*c*) running the system at various frequencies without the circulators while monitoring the temperature rise in the system.

Each of these steps provided some information. Steps (*a*) and (*b*) proved useful in confirming that indeed friction was generated, causing heat to be added to the system. Also is was learned that when the circulator temperatures are not controlled, the recirculators themselves generate heat through the viscous effects while flowing in the heat exchange loops. Step

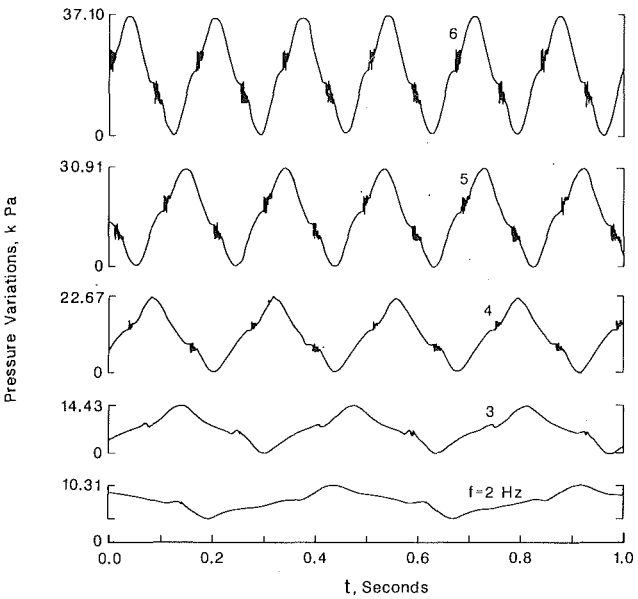

Fig. 4 Pressure variation in the reservoirs

(*c*) provided quantitative information about the two sources mentioned above (and not the circulators).

Step (*c*) was carried out for two frequencies. For 2 Hz, the temperature rise was found to be 0.56 and 0.61°C/h for each reservoir. This corresponds to 2.59 and 2.78 W added to the system. At 4 Hz temperature rises of 2.79 and 2.77°C/h were measured. This corresponds to 12.72 and 12.61 W, respectively.

The rate of heat dissipated by viscous forces in the tube can be determined from the predicted temperature rise (Kaviany, 1990) as

$$Q^*_{\text{diss}} = \rho c_p N \pi R^2 L \Delta T^*_{\text{diss}} f \tag{7}$$

For $f = 2$ Hz and 4 Hz the values are 0.293 and 3.93 W, respectively. These are fractions of the measured friction heat generation rates and therefore, the piston-casing friction heat generation and the viscous dissipations inside the reservoirs should make up the balance of the measured heat generation. There are further losses associated with the sudden expansion at the exits.

2.5 Placement of Baffles in Reservoirs. As will be discussed, the temperature measurements show that fluid entering the bundle has a significant radial and temporal variation. In order to compare the experimental and predicted results, a spatial-temporal averaging was performed (details are given in the next section). This averaging of the temperature was scrutinized by intentionally charging the radial and temporal variation of temperature through placement of various baffles adjacent to the bundle ends. These baffles were plexiglass disks (5 cm diameter and 0.6 cm thickness with various circular holes drilled in them). Then, the ease of flow through these disks was varied by using various hole diameters. The disks were placed away from the bundle ends and beyond the thermocouples measuring the radial temperature distributions. The results are discussed in the next chapter.

2.6 Velocity Measurement in Reservoirs. Velocity measurements within the reservoir were made with a laser-Doppler anemometer (LDA). Details of the type of LDA system used, the modified reservoir, and the data processing, are given below.

The LDA system used for measurements was a one-component helium-neon system manufactured by DANTEC. The system consists of 55x modular optics and 55L90a counter processor with the 55N10 frequency shifter.

Measurements were carried out by the optical arrangement and seeding technique. The optics were arranged in the backscatter mode. This mode has a less intense signal, but allowed easier traversing within the reservoir (across the tube bundle end). As described before, the reservoir is made of a large plexiglass tube cylinder (12.7 cm), and the capillary bundle has an inner diameter of 2.54 cm. A square flat glass window (3.81 cm on each side and 0.63-cm thickness) was placed in the reservoir tube adjacent to the capillary bundle end and the laser beams entered the reservoir through this window. This was done to minimize beam crossing and measuring volume location errors caused by the curved surface. Since the difference in the index of refraction between air and glass and glass and water resulted in distortion of the radial location in the reservoir, the distance traveled on the LDA traverse was calibrated against the distance between the reservoir wall and the centerline of the capillary bundle and a linear relationship was assumed. The ratio of the traversing optics distance to traversing measuring volume distance was measured to be 1.36. The analytical valve was computed from (Durst et al., 1981)

$$y = \left[y' + d\left(1 - \frac{\cos a_1}{\left[\left(\frac{n_2}{n_1} \right)^2 - \sin^2 a_1 \right]^{1/2}} \right) \right]$$

$$\frac{1}{\cos a_1} \left[\left(\frac{n_3}{n_1} \right)^2 - \sin^2 a_1 \right]^{1/2}$$

where y' is the traversing distance of optical bench (mm), y is the measuring volume traversing distance (mm), d is the thickness of the glass (6.35 mm), n_1 is the index of refraction of air (1.0), n_2 is the index of refraction of glass (1.57), n_3 is the index of refraction of water at 26°C (1.33), and a_1 is the beam incident angle (3.23 deg), which results in a ratio nearly the same as that measured. A compromise was made on the laser bean spacing. The spacing was chosen to be 35 mm (using a 310 mm focal length lens), which allowed measurements to be taken 6 mm from the end of the bundle and kept the length of the measuring volume perpendicular to the flow, down to 2.76 mm. The coil heat exchangers were removed from the reservoirs since they did not allow for passage of the beams. Portions of the interior of the reservoir were painted black to help eliminate stray reflections and decrease the noise level of the measurement signal. The measurement period was triggered by the output of a pressure transducer housed in one of the reservoirs.

The other important element in the measurement setup is seeding. Due to the nature of the oscillating flow, seeding particles had to be selected carefully. The particles had to be small enough to follow the flow accurately and large enough to give a good signal-to-noise ratio. The concentration of particles had to be large enough to permit data rates of approximately 1 kHz so the oscillating flow could be adequately sampled. After various attempts with seedings such as milk and latex spheres, aluminum dust provided the qualities sought. The use of aluminum dust was made possible by the short amount of time needed for the measurements. After longer periods of time, the aluminum dust had a tendency to oxidize in the water, thus reducing the data rate significantly.

Data processing takes place in two separate sections. The first and most important area is the counter processor. The Dantec 55L90a counter processor takes an analog measuring signal and outputs a validated digital signal. The counter module is reset under certain circumstances to help minimize errors, e.g., oversized particles, particles passing out of the measurement plane. The 55L90a reduces these errors by passing only "valid" signals. Two registers record the time a parti-

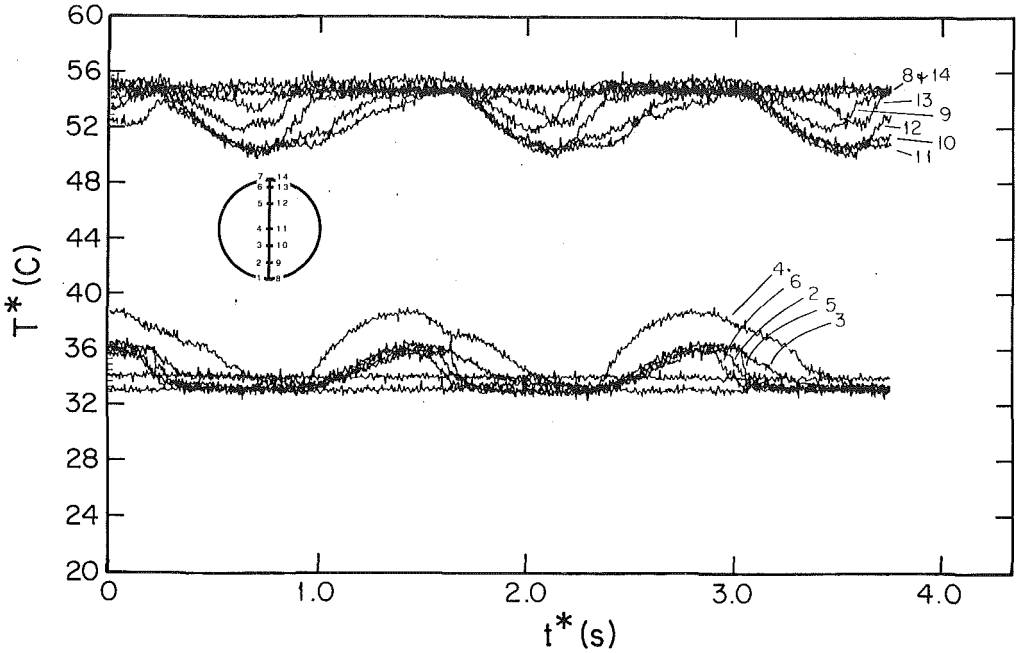

Fig. 5 Spontaneous temperature in the cold and hot reservoirs in the vicinity of the capillary tube bundle, with respect to time; temperatures are not recorded simultaneously.

cle takes to pass through a given number of fringes. The times per fringe are then compared and must be within a given percentage of each to be considered "valid" and passed on to the digital output. Upon leaving the counter, the second phase of processing takes place. The digital value for passage time (the time required for a particle to pass eight fringes) is then read into a Hewlett Packard model 310. The passage times are read and stored in blocks of ten readings. Each block is labeled with the time it was stored. Each block of ten passage times is converted to one average velocity. The averaged velocities are then plotted with respect to the labeled time.

3 Comparison of Experimental and Predicted Results

Pressure Variation in the Reservoir. Figure 4 shows the temporal variation of the pressure in one of the reservoirs for three different frequencies. The presence of other harmonics appears to be due to the clutch slippage in the variable speed motor. Note that slight, nonideal decreases in the pressure do not result in the flow reversal, because the other reservoir is at a lower pressure during the pressure rise in this reservoir.

Temperature Variation at the Bundle Ends. Figure 5 shows the temperature variations measured by thermocouples placed axially about 3 mm from each end and radially (as shown in the insets). It is clear that there is not only radial variation in the temperature but that these variations do not remain constant with respect to time. This is because the fluid particles leaving the capillary tubes follow significantly different paths depending on their radial location and therefore have different intensities of interaction with the heat exchangers.

The average temperature difference across the bundle, ΔT^*_{exp}, was found by (*a*) averaging each temperature reading over three cycles, (*b*) taking the weighted-area average of those temperatures on each side, and (*c*) taking the difference, i.e.,

$$\bar{T}^*_{c,i} = \frac{f}{3}\int_0^{3/f} T^*_{c,i}\,dt \tag{8a}$$

$$\bar{T}^*_c = \sum_{i=1}^{n} \bar{T}^*_{c,i} A_i / A_t \tag{8b}$$

$$\Delta T^*_{\text{exp}} = \bar{T}^*_h - \bar{T}^*_c \tag{8c}$$

(An asterisk indicates that the quantity is dimensional.) Since the only fluid temperature during the inflow periods is of interest, in principle the temperature should be averaged using the velocity as the weighting factor. This is being considered.

Axial Velocity in Reservoirs. Using the measurement technique described above, the spontaneous axial velocity was measured at various radial locations and for two different axial locations. Due to the rather small angle between the beams, the measuring volume was relatively large (2.8 mm); yet the beam intersection could be moved only as close as 6 mm from the bundle end. With this measurement volume, the velocity nonuniformity in the jets emerging from each capillary tube could not be resolved. Figure 6 shows the spontaneous axial velocity variation for $f = 0.73$ and 2 Hz. Figures 6(*a*) and 6(*b*) show the results for $f = 0.73$. The average axial velocity for various radial locations are also shown in these figures. At $r^* = 0$ (centerline), the average velocity is larger than zero, indicating that the outward flow is more intense than the inward flow. This is because the outward flowing jet (emerging from the bundle) contains a zone of high velocities near the center, while near its edges the jet is flared (due to entrainment by the reservoir fluid). The inflow is more uniform. Then, as the radial distance increases beyond the radius of the bundle, the average velocity becomes negative. At $r^* = 12.6$ mm, which is nearly equal to the bundle radius, there is a rather substantial reduction in the axial velocity (compared to that at the smaller radial location), which supports the measured spontaneous temperature at this location. The measured results (Fig. 5) show that at $r^* = R_b$ (thermocouples number 1, 7, 8, and 14) there is the least amount of change in the temperature. The measurements were taken at about 3 mm from the bundle ends. The results for $f = 2$ Hz (Figs. 6(*c*) and 6(*d*)) show similar results but the magnitude of velocities are higher because of the higher frequency.

Comparison With the Predicted Results. Table 1 gives the results for two displacements (approximately $L/3$ and $L/6$) and for no baffle. Due to the rather large force acting on the heat exchanger and the consequent deformations, frequencies

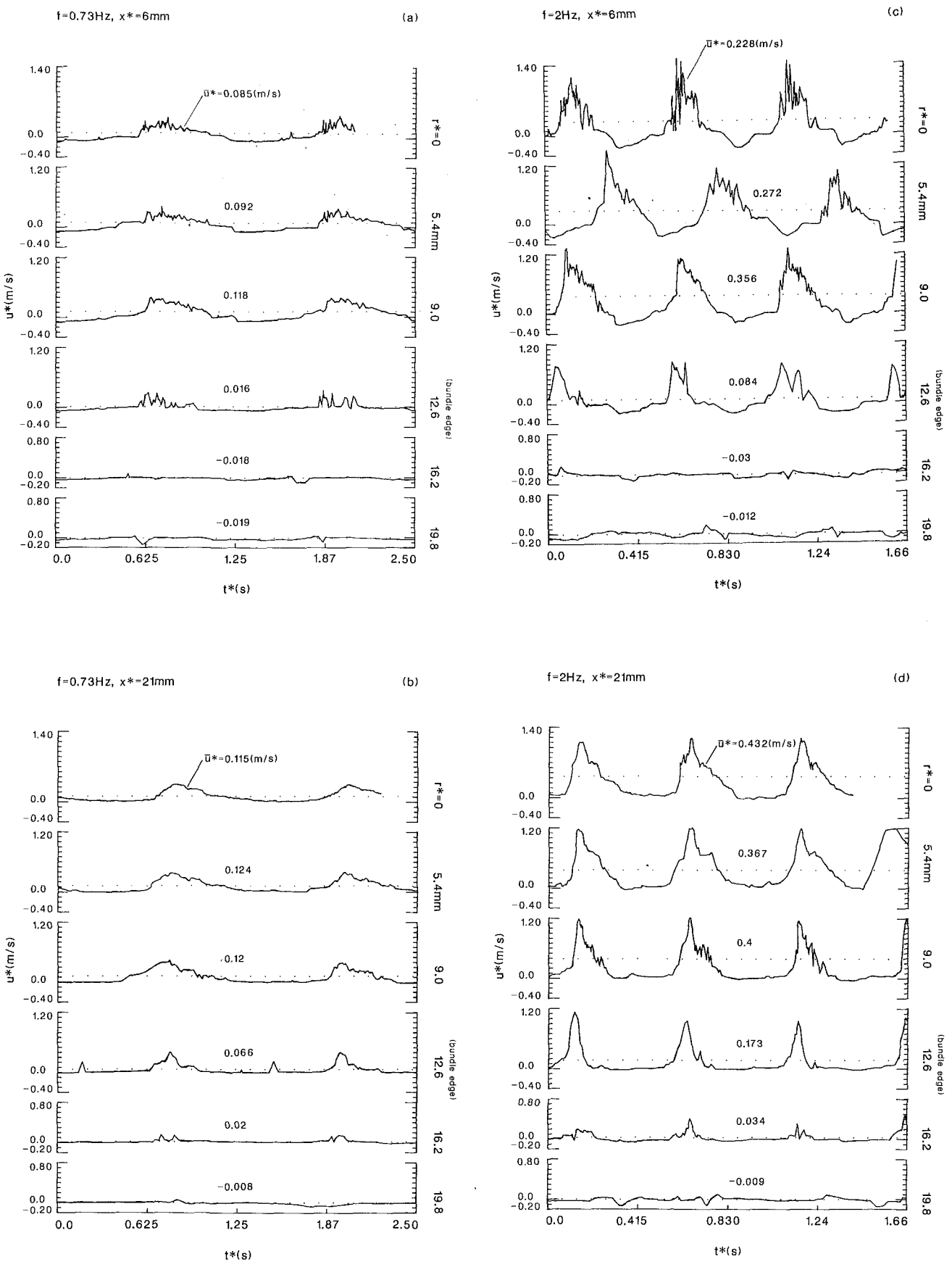

Fig. 6 Spontaneous axial velocity at various radial locations: (*a*) $f \approx 0.73$ Hz and $x^* = 6$ mm, (*b*) $f = 0.73$, $x^* = 21$, (*c*) $f = 2$, $x^* = 6$, and (*d*) $f = 2$, $x^* = 21$

Table 1 Experimental conditions (no baffles)

a	f	ΔT_c^*	ΔT_H^*	$Q_c^* - Q_h^*$	Q^*	ΔT_{exp}^*	$\bar{q}^* \times 10^{-5}$	$\bar{h} \times 10^{-4}$	$\kappa_e \times 10^3$	$\frac{\kappa_e}{\omega \Delta x^{*2}}$
mm	Hz	C	C	W	W	C	$\frac{W}{m^2}$	$\frac{W}{m^2\text{-C}}$	$\frac{m^2}{s}$	
72.55	0.60	0.275	0.358	-12.0	44.60	24.9	0.6093	0.244	0.717	9.38
72.55	0.80	0.47	0.52	- 8.32	70.90	24.01	0.9948	0.414	1.171	11.49
72.55	1.01	0.61	0.67	- 9.2	91.04	23.66	1.311	0.554	1.544	12.00
72.55	1.62	1.06	1.09	- 5.45	152.88	22.52	2.315	1.028	2.724	13.21
72.55	2.0	1.39	1.42	- 7.78	198.85	21.62	3.134	1.449	3.689	14.49
72.55	2.98	1.88	1.87	- 0.86	264.07	21.13	4.260	2.016	5.013	13.21
72.55	4.0	2.57	2.53	- 1.21	360.9	19.89	6.184	3.110	7.28	14.29
72.55	6.0	3.6	3.39	19.74	494.73	18.82	8.962	4.761	10.55	13.81
72.55	8.1	4.66	4.3	37.42	634.18	16.25	13.30	8.182	15.65	15.18
72.55	10.25	4.23	3.87	33.25	570.31	18.72	10.39	5.55	12.22	9.36
147.89	0.52	0.894	1.04	-12.18	125.3	22.21	1.924	0.866	2.264	8.617
147.89	0.80	1.62	1.67	0.45	211.35	19.61	3.675	1.874	4.326	10.62
147.89	1.07	2.27	2.32	6.1	296.4	17.72	5.704	3.22	6.72	12.33
147.89	1.60	3.35	3.37	10.44	431.99	15.58	9.448	6.062	11.12	13.65
147.89	1.90	3.55	3.77	14.80	490.14	15.26	10.945	7.171	12.88	13.31
147.89	2.10	4.1	4.18	16.64	537.96	14.37	12.75	8.872	15.01	14.03
147.89	2.10	4.11	4.19	16.61	539.26	14.36	12.80	8.91	15.06	14.08
147.89	3.0	5.28	5.26	29.49	681.15	13.02	17.83	13.69	20.98	13.73
147.89	4.0	6.47	6.36	46.93	828.81	10.70	26.39	24.67	31.07	15.25
147.89	5.87	7.15	6.77	59.75	979.5	8.40	39.73	47.27	46.76	15.64
147.89	7.25	8.39	7.80	91.0	1139.6	9.56	40.61	42.44	47.79	12.94
147.89	8.42	8.72	8.47	87.0	1116.1	7.8	48.81	62.63	57.46	13.4
147.89	9.83	8.24	7.51	110.0	1108.7	8.36	45.18	54.01	53.18	10.62

N = 508, L = 42.7 cm, R_p = 4.76 cm, R = 0.8mm, δ = 0.05mm

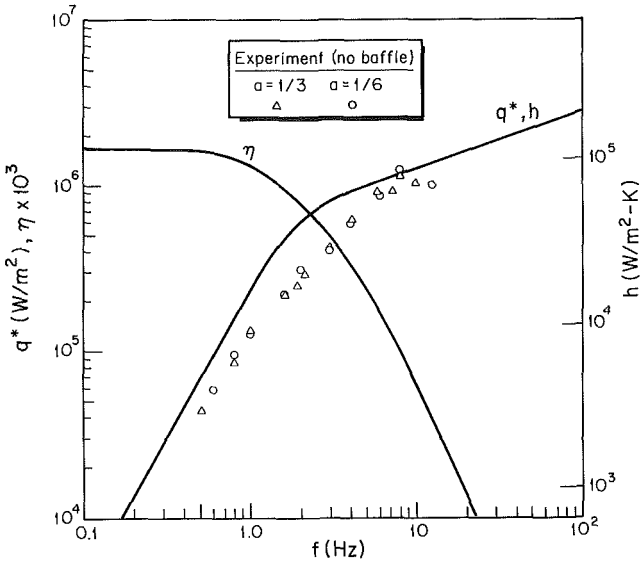

Fig. 7 Comparison of the experimental and predicted results for $\Delta x = \ell/3$

above 10 Hz were not attempted for the period of time needed to ensure steady-state behavior. The maximum difference between the heat flow rate found by the energy balance on the hot reservoir and the cold reservoir was about 10 percent. The largest difference, at $f = 9.83$ Hz and $a = 147.9$ mm, cannot be readily explained. The outputs of the thermocouples were checked against single thermocouples placed at the entrance and exit of the heat exchangers, and complete agreement was found. Enough time was allowed to ensure that the flow rates and heat transfer were steady (three to five hours for the first run of each displacement, and one and one-half to three hours for subsequent runs; these were found by trials including 12 hours for a single run).

In order to compare the experimental data with the predicted results (Kaviany, 1988), which are for the perfect packing condition, on the same figure, corrections were made for the parameters shown in the figure caption, namely,

$$q_c^* = \epsilon_c \frac{\Delta T^*}{\Delta T_{exp}^*} \frac{\bar{Q}^*}{A} \tag{9}$$

where $\epsilon_c = 585/508$, $A = \pi R_b$, $R_b = 1.27$ cm, $\Delta T^* = 15$°C, and ΔT_{exp}^* was the average temperature difference across the tube

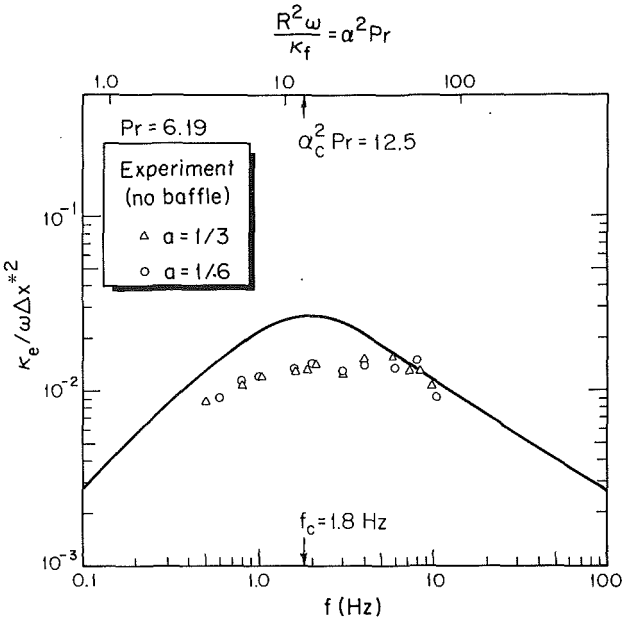

Fig. 8 Comparison of the experimental and predicted results for several displacements

bundle over a cycle. Also, since the predictions have shown that q_c^* is proportional to Δx^{*2}, the results for different Δx^* values have been compared with that for $\Delta x = l/3$.

The experimentally determined effective thermal diffusivity is given by

$$\kappa_e = \frac{L}{\Delta T_{exp}^*} \frac{1}{\rho_f c_f} \frac{\bar{Q}^*}{N} \frac{1}{\pi R^2} \tag{10}$$

The thermophysical properties for water (at 25°C) are $\rho_f = 997$ kg/m³, $\nu = 90 \times 10^{-7}$ m²/s, $k_f = 0.607$ W/m-°C, $c_f = 4180$ J/kg-°C, and for glass (soda lime), they are $\rho_s = 2530$ kg/m³, $k_s = 1.07$ W/m-°C, $c_s = 800$ J/kg-°C.

The experimental results given in Table 1 are plotted in Figs. 7 and 8, along with the predicted results; q^* is the heat transfer per unit area of the bundle cross section, and h is the heat transfer coefficient. Figure 7 shows that the experimental results are in good agreement with the predictions for the low and high-frequency ranges. However, near the frequency associated with the beginning of a significant drop in the efficiency, the agreement is only fair. This lack of close agreement is more evident in Fig. 8, where the dimensionless group $\kappa e/\omega \Delta x^{*2}$, which is a figure of merit number for this system, is predicted to have a maximum value when the thermal boundary-layer thickness nearly equals the capillary tube radius. The tube material and wall thickness, and Pr, also affect the value of α_c^2. The lack of good agreement between the predicted and experimental results can be associated with (*a*) lack of a constant temperature fluid flowing into the tubes, (*b*) lack of temperature uniformity in the radial directions (Fig. 5), (*c*) presence of some fluid motion in the interstitial areas, (*d*) lack of an ideal sinosoidal pressure variation in the reservoirs, and (*e*) lack of complete regidity of the system. These nonideal conditions are listed in what appears to be their order of importance. In general, the experimental results indicate that the effective thermal diffusivity is nearly proportionate to frequency to the first power.

In order to examine the validity of the temperature averaging given by equations (8*a–c*), the flow field (and therefore the temperature field) in the reservoirs near the bundle ends was modified by adding baffles, which faced the jets emerging from the capillary tubes (section 2.5). Figure 9 shows the geometry of the baffles and the associated average (temporal and spatial) temperature differences. The results show that, as

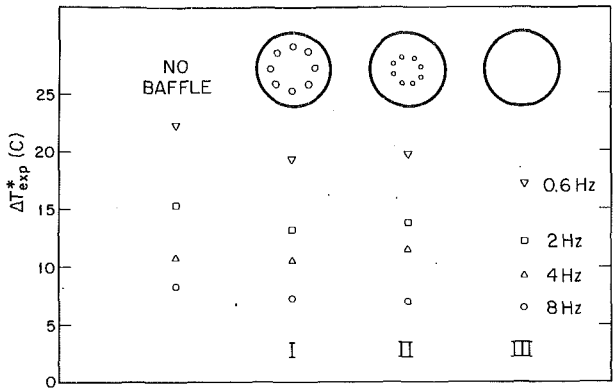

Fig. 9 Effect of the presence of baffles on the average temperature difference across the bundle

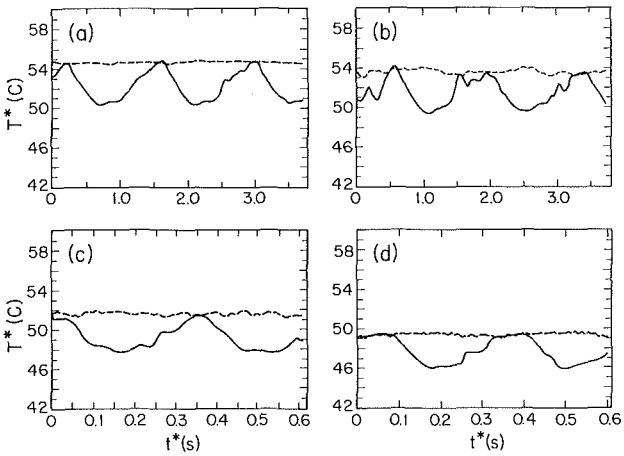

Fig. 10 Effect of the presence of baffles on the spontaneous temperature near the bundle ends

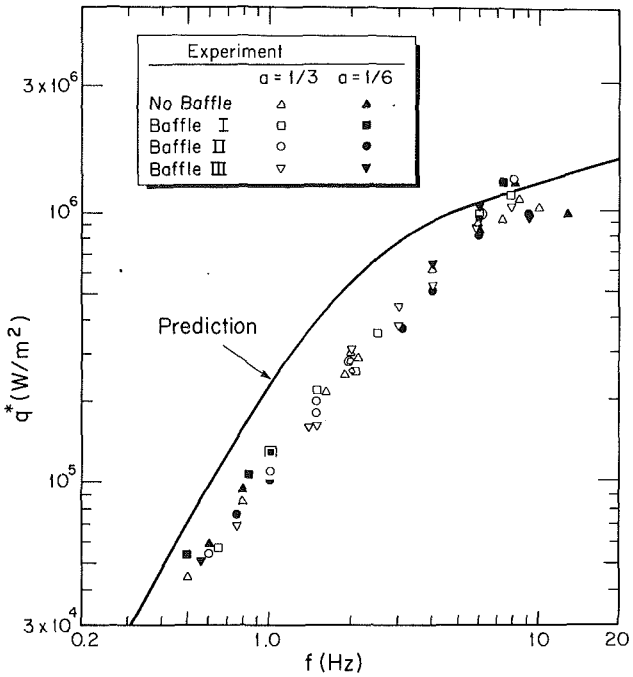

Fig. 11 Same as Fig. 8 except the results for baffles I–III are also shown

expected, the presence of the baffle creates an extra resistance to the heat flow between the two heat exchangers. This is evident through the smaller temperature drops across the capillary tubes and, therefore, smaller heat flow rates. Figure 10 shows the spontaneous temperature variations at two radial locations (see Fig. 5 for radial locations). The results indicate that both the magnitude and temporal variation of the temperature have been altered by the presence of the baffles. Finally, Fig. 11 shows the effect of the baffle on the adjusted measured heat flux. Note that in order to compare the experimental and predicted results, equation (9) has been used. Although the heat transfer rate is smaller for the cases with baffles, adjusting the temperature difference according to equation (9) corrects the heat flux is expected to be the same, if the temperature averaging of equations (*8a–c*) are appropriate. The results in Fig. 11 show that this temperature averaging is indeed appropriate.

4 Summary

The experimental results based on a cycle-averaged temperature difference across the capillary tube bundle are in relatively good agreement with the predicted results. This agreement suggests that the idealizations introduced into the analysis—such as no axial conduction, laminar, one-dimensional flow field (no end effects) and the presence of only the fundamental harmonic produced by the piston—are valid assumptions. However, the fluid dynamics and heat transfer interactions between (*a*) the flow entering the reservoirs from the capillary tubes and the fluid in the reservoirs, and (*b*) the fluid in the reservoirs and the internal heat exchangers play a significant role in the overall performance of the heat exchanger.

The performance of heat exchangers based on the enhancement of heat transfer through the tubes is strongly dependent on the removal (and supply) of heat to tube ends. This is a common problem with any heat pipe heat exchanger. Alternatives to the heat supply-removal to the heat pipe were not explored in this study.

Acknowledgments

The financial support of the National Science Foundation through grant No. CBT-86-03415 is greatly appreciated. Professor E. M. Sparrow has made valuable comments for which we are grateful.

References

Durst, F., Melling, A., and Whitelaw, J. H., 1981, *Principles and Practice of Laser-Doppler Anemometry*, 2nd ed., Academic Press, New York.

Kaviany, M., 1990, "Performance of a Heat Exchanger Based on Enhanced Heat Diffusion in Fluids by Oscillation: Analysis," ASME JOURNAL OF HEAT TRANSFER, Vol. 112, this issue.

S. A. Idem
Tennessee Technological University,
Mechanical Engineering Department,
Cookeville, TN 38505

A. M. Jacobi
The Johns Hopkins University,
Department of Mechanical Engineering,
Baltimore, MD 21218

V. W. Goldschmidt
Purdue University,
School of Mechanical Engineering,
W. Lafayette, IN 47907

Heat Transfer Characterization of a Finned-Tube Heat Exchanger (With and Without Condensation)

The effects upon the performance of an air-to-water copper finned-tube crossflow heat exchanger due to condensation on the outer surface are considered. A four-tube, two-pass heat exchanger was tested over a Reynolds number range (based on hydraulic diameter) from 400 to 1500. The coil was operated both in overall parallel and overall counterflow configurations. Convective heat and mass transfer coefficients are presented as plots of Colburn j-factor versus Reynolds number. Pressure losses are, similarly, presented as plots of the friction factor versus Reynolds number. Enhancement of sensible heat transfer due to the presence of a condensate film is also considered.

Introduction

Copper finned-tube heat exchangers are quite common in applications such as gas-fired water heaters. In instances where the incoming water temperature is sufficiently below the dew point of the products of combustion, condensation occurs on the outside of the heat exchanger, thereby affecting its performance. The analysis of such an effect is now presented. It is based primarily on wind tunnel data at Reynolds numbers (based on the hydraulic diameter of a multipass coil) on the order of 10^3. Data for condensing finned-tube crossflow heat exchangers operating in this range have not been reported in the literature. Some data, from noncondensing experiments with a similar, single-row heat exchanger, have been presented by Idem et al. (1987).

Due to the complex pattern of the fluid flow over the external surface of a typical condensing heat exchanger, the theoretical prediction of heat and mass transfer coefficients is often precluded. The combined processes of heat, mass, and momentum transfer serve to complicate the analysis. As a result, it is necessary to resort to experimentation in order to construct useful models.

A great variety of fluids and condensing flow configurations have been studied and documented in the literature. Reviews of the literature have been given by Elmahdy (1975), Webb (1980), McQuiston (1981), and most recently Marto (1986). In addition, a great resource is available in the work of Honda and Nozu (1984), on low, integral-fin tubes. However, the results being reported here are unique, in that data from high, integral-fin exchangers, which are common in application, have not been reported under these conditions. The following review is not intended to be exhaustive, but rather to provide background for the present study.

Colburn (1933) presented a general method for the correlation of forced convection heat transfer data, wherein the parameter

$$j = \left(\frac{h}{Gc_p}\right)\mathrm{Pr}^{2/3} \tag{1}$$

was plotted as a function of the Reynolds number.

Chilton and Colburn (1934) suggested that the sensible heat transfer j-factor could also be used to correlate mass transfer. The mass transfer j-factor can be defined as

$$j_h = \left(\frac{h_d}{G}\right)\mathrm{Sc}^{2/3} \tag{2}$$

In the original paper of Chilton and Colburn, additional terms were included on the right-hand side of equation (2) that accounted for the partial pressure change of the condensing components across the vapor film, but the use of equation (2) is now standard. Thus, for many configurations and for a wide range of fluids.

$$j \approx j_h \tag{3}$$

provided that the rate of mass transfer is low. The use of the Chilton–Colburn analogy, equation (3), is advantageous in the design and analysis of condensing heat exchangers, as it is often simpler to obtain heat transfer data and apply the analogy rather than measure the mass transfer directly.

Bryan (1961, 1962) presented data for heat and mass transfer for plain and finned dehumidifying coils. It was reported that for finned tubes the sensible heat transfer j-factor was greater than the mass transfer j-factor, or $j > j_h$. It was also suggested that for the finned-tube heat exchanger, the sensible heat transfer was lower during dehumidification than when dehumidification was not occurring. Experiments on a plain tube heat exchanger indicated that sensible heat transfer increased during dehumidification.

Fuks and Zernova (1970) performed tests on a tube bank with steam or a steam–air mixture. No marked quantitative variations in the intensity of mass transfer with the orientation of the flow were noted. Buglayev and Kazakov (1972) considered the flow of saturated air across a vertical tube bank with continuous fins, at different levels of specific humidity. It was found that the Nusselt number Nu and the Reynolds number Re were correlated by an equation of the form

$$\mathrm{Nu} = 0.016\,\epsilon^2\mathrm{Re}^{0.8}$$

where ϵ is the partial pressure of the steam divided by the total pressure of the mixture. At values of $\epsilon < 2$ percent, it was found that the heat transfer approaches that for dry air.

Guillory and McQuiston (1973) and McQuiston (1976) performed experiments on a parallel plate heat exchanger and observed that the sensible heat transfer j-factors were greater for a wet surface than a dry surface. It was felt that this phenomenon was due to the disturbance of the vapor boundary layer by the presence of waves or droplets in the condensate layer. Tree and Helmer (1976) observed that condensation did not affect the sensible heat transfer in the region of laminar flow in a parallel plate heat exchanger, but in the transition and fully turbulent flow region increased the sensible heat transfer noticeably.

McQuiston (1978a) and (1978b) examined the effects of fin spacing and number of tubes on the heat and mass transport

Contributed by the Heat Transfer Division for publication in the JOURNAL OF HEAT TRANSFER. Manuscript received by the Heat Transfer Division January 26, 1988; revision received July 27, 1988. Keywords: Augmentation and Enhancement, Heat Exchangers.

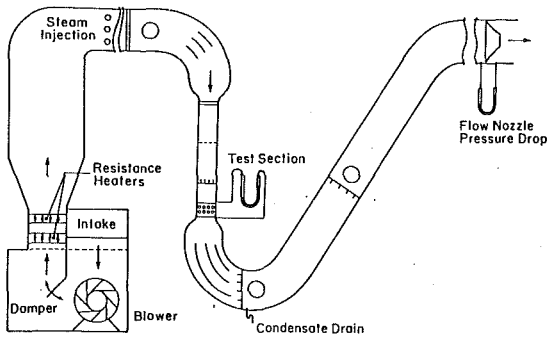

Fig. 1 Sketch of wind tunnel

of several heat exchangers with continuous plate fins. It was found that the j-factors were best correlated by applying a correction factor to the Reynolds number, given by

$$\left(\frac{A}{A_{ba}}\right)^n$$

McQuiston (1981) showed that the effect of the condensate on the sensible heat transfer j-factor or mass transfer j-factor was strongly influenced by the fin spacing.

The work now presented documents performance parameters for a finned tube heat exchanger obtained from controlled experiments in a wind tunnel.

Experimental Setup

The experimental apparatus is illustrated in Fig. 1. The desired approach air temperature at the heat exchanger face was set by adjusting the output of four of the resistance heaters. All walls downstream of the heaters were insulated with 5.1 cm (2 in.) of glass wool, while the heat exchanger was covered by 4.5 cm (1.75 in.) of styrofoam.

The humidity level in the duct was controlled by the injection of steam. A burlap evaporating screen was installed in order to prevent injection of water droplets into the air stream.

Turning vanes, a louvered mixing device located approximately 86.4 cm (34 in.) upstream of the heat exchanger, and a fibrous screen 55.9 cm (22 in.) upstream from the heat exchanger were used to obtain uniform flow conditions.

For some operating conditions, the injected steam caused condensate to form on the heat exchanger. This water was collected in the reservoir formed by the bottom elbow of the duct and accordingly measured.

The flow nozzles for measuring the flow rate of the air consisted of four spun aluminum elliptical nozzles, two of them having a 5.1 cm (2 in.) throat diameter, and the remaining two having a 10.2 cm (4 in.) throat diameter.

An independent water loop (not shown in Fig. 1) provided circulation of the water through the heat exchanger. For the data now reported, the temperature at the heat exchanger inlet was approximately 15.6°C (60°F).

An externally mounted psychrometer was used to measure the humidity ratio upstream of the heat exchanger. It was located directly behind the burlap evaporator. A sampling device, located within the duct, was used to obtain an average sample, which was circulated through the psychrometer. An air velocity of 91.4 m/min (300 ft/min) was maintained at the wet-bulb thermocouple, in order for evaporative equilibrium to be obtained.

A similar psychrometer was located downstream from the heat exchanger in the bottom elbow of the duct. By making a simple mass balance the amount of water vapor that was condensed could be deduced. As an added precaution, a third psychrometer was placed in the inclined section of the duct in order to determine whether any additional condensation was occurring on the walls of the duct, or whether re-evaporation of the condensate was taking place. This effect was found to be negligible.

Measurements of the temperature of the air stream upstream of the heat exchanger were obtained by means of a 20-thermocouple (copper-constantan) grid located 40.6 cm (16 in.) from the heat exchanger. The thermocouple junctions faced into the incoming air stream, and were positioned at least 3.8 cm (1.5 in.) away from any grid support structure so as to minimize the conduction of heat along the wires.

A similar thermocouple grid was located downstream of the heat exchanger in the bottom elbow, slightly downstream of the duct expansion from the test section, so as to prevent the condensate from wetting the thermocouple junction. Large turning vanes were placed in the lower elbow to ensure that the flow did not separate from the wall upon reaching the bend in the duct. Another thermocouple grid was also located in the inclined portion of the duct in order to measure the amount of heat loss occurring through the insulated walls. This was found to be negligible.

The temperature rise of the water in the heat exchanger was

Nomenclature

A = area, m² (ft²)
b = slope of enthalpy curve, kJ/kg•°C (Btu/lb$_m$•°F)
c_p = specific heat, kJ/kg•°C (Btu/lb$_m$•°F)
d = diameter, m (ft)
f = friction factor
G = mass flux, kg/h•m² (lb$_m$/h•ft²)
h = heat transfer coefficient, W/m²•°C (Btu/h•ft²•°F)
h_d = mass transfer coefficent, kg/h•m² (lb$_m$/h•ft²)
i_s = saturation enthalpy, kJ/kg (Btu/lb$_m$)
j = Colburn j-factor
j_h = mass transfer Colburn j-factor
k = thermal conductivity, W/m•°C (Btu/h•ft•°F)
L = characteristic length, m (ft)
N = characteristic number
Nu = Nusselt number
p = pressure, Pa (psi)
Pr = Prandtl number
Q = heat transfer rate, W (Btu/h)
r = radius, m (ft)
Re = Reynolds number
S_F = fin density, fin/m (fin/ft)
S_L = longitudinal pitch, m (ft)
S_T = transverse pitch, m (ft)
Sc = Schmidt number
Sh = Sherwood number
T = temperature, °C (°F)
U = overall heat transfer coefficient, W/m² °C (Btu/h•ft²•°F)
U_d = overall mass transfer coefficient, kg/h•ft² (lb$_m$/h•ft²)
γ = fin/total area
δ = thickness, m (ft)
η = efficiency
σ = minimum/frontal area

Subscripts

ba = bare area
f = fin
fr = frontal
H = hydraulic
i = inside
min = minimum
o = outside
pass = tube pass
r = root
t = tip
tfr = tube in front row
tube = tube
W = water

Superscripts

$'$ = per unit length
$\bar{}$ = mean

Table 1 Experimental uncertainties

Property	Uncertainty	Range
Water flow rate	±0.26 kg/min (±0.5 lbm/min)	up to 22.7 1/min (6 gpm)
Inlet water temperature	±0.1°C (±0.2°F)	0.6 to 18.3°C (33 to 65°F)
Water temperature difference	±0.6°C (±1°F)	up to 8.6°C (15.4°F)
Air temperatures	±0.3°C (±0.5°F)	21.1 to 121.1°C (70 to 250°F)
Air velocity	±0.2 m/s (±0.5 ft/s)	1.2 to 4 m/s (4 to 13 ft/s)
Humidity ratio	±0.004	0.01 to 0.08 (at inlet)
Air pressure drop	±0.003 cm (±0.001 in.) of water	up to 0.25 cm (0.1 in.)

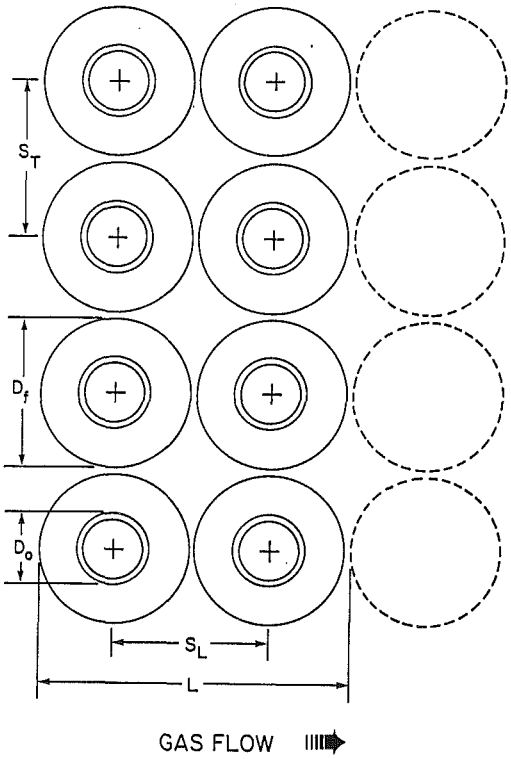

Fig. 2(a) Heat exchanger characteristic geometry

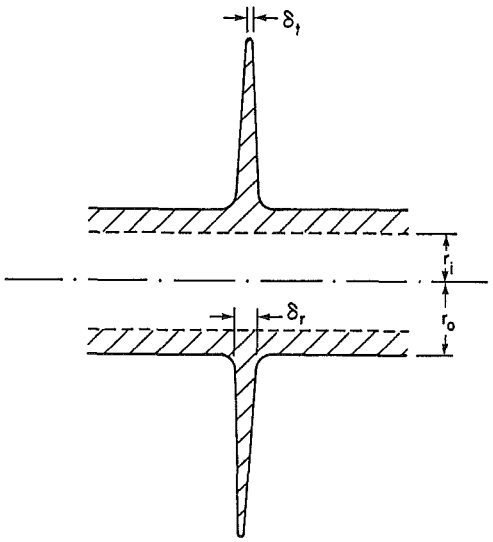

Fig. 2(b) Idealized fin geometry

measured by three copper-constantan thermocouples. The first was located in the inlet portion of the front header, the second was placed in the back header, and the third measured the temperature in the outlet portion of the front header. The thermocouples were inside oil-filled stainless steel tubes, which penetrated into the water and were sealed by epoxy.

Four nozzles were available for measuring air flow rates.

Table 2 Two-pass heat exchanger characteristic geometry

S_F, fins/m (fins/ft)	S_T, m (ft)	S_L, m (ft)	δ, m (ft)
270.1 (82.3)	0.040 (0.131)	0.039 (0.127)	0.00060 (0.00196)

d_i, m (ft)	d_o, m (ft)	d_f, m (ft)
0.016 (0.053)	0.019 (0.063)	0.039 (0.127)

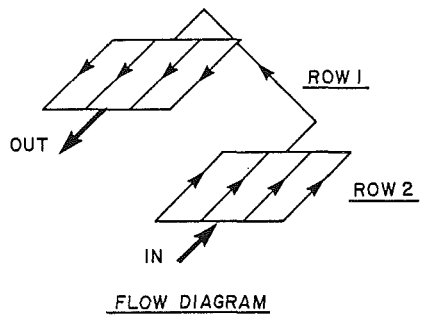

Fig. 3 Two-pass heat exchanger flow circuiting

Following Gonzalez (1982) an energy balance on the water flowing through the heat exchanger and on the air stream was used to relate the pressure drop through the flow nozzles to the mass flow rate of the air.

The flow rate of the water was measured by weighing the amount of cooling water, which was diverted into a 151.4 liter (40 gallon) capacity tank, and measuring the amount of time required.

The uncertainties in the measured properties, typically at the heat exchanger inlet, were estimated to be as in Table 1.

With the uncertainties given in Table 1, and over these ranges, the method of Kline and McClintock (1953) was employed to evaluate the uncertainties of the experimental results. For a typical case, the Colburn j-factors were found to be within 8.3 percent, and the Reynolds numbers within 8.4 percent of the reported values (refer to Idem, 1986 for details).

Test Heat Exchanger

Figure 2 shows the copper finned-tube heat exchanger that was studied in this experiment. Table 2 presents the dimensions of the coil. The four-tube two-pass crossflow heat exchanger was tested under both overall parallel and overall counterflow. Figure 3 shows the circuiting for the counterflow configuration; the water flow was split evenly among each tube in a pass.

In this study, the maximum velocity, i.e., the velocity at the minimum flow area, was used for the Reynolds number characteristic velocity, and the hydraulic diameter as a characteristic length. Hydraulic diameter is defined by

$$\frac{d_H}{L}=\frac{4A_{\min}}{A_o} \tag{4}$$

L is an equivalent flow length measured from the leading edge

of the first tube row to the leading edge of the hypothetical tube row that would follow the last tube row. This definition reduces to the conventional interpretation of hydraulic diameter for a cylindrical tube, namely the cross-sectional area divided by the wetted perimeter. Appendix A relates the hydraulic diameter to the geometry of the heat exchanger.

From it we obtain

$$\frac{d_H}{L} = 4\sigma \frac{A_{fr}}{A_o} \tag{5}$$

where A_{fr}/A_o, and hence d_H/L, is independent of both tube length and heat exchanger width (or number of tubes per pass), and hence correlations based on hydraulic diameter are also independent of these parameters.

Test Results

By the Chilton-Colburn analogy, the functional relationship $\mathrm{Nu} = \phi(\mathrm{Re}, \mathrm{Pr})$ suggested by the governing equations becomes

$$\mathrm{Nu} = C\,\mathrm{Re}^m\,\mathrm{Pr}^{1/3} \tag{6}$$

for Prandtl numbers in the range $0.5 < \mathrm{Pr} < 100$. Similarly, over the range of Schmidt numbers $0.5 < \mathrm{Sc} < 100$

$$\mathrm{Sh} = C'\,\mathrm{Re}^k\,\mathrm{Sc}^{1/3} \tag{7}$$

For the test cases, it was calculated that $\mathrm{Pr} \approx 0.7$ and $\mathrm{Sc} \approx 0.6$. Combining the definition of the Stanton number and the sensible Colburn J-factor yields

$$j = \frac{\mathrm{Nu}}{\mathrm{Re}\,\mathrm{Pr}^{1/3}} \tag{8}$$

Hence, it is apparent with equation (6) that

$$j = C\,\mathrm{Re}^{m-1} \tag{9}$$

A log-log plot of experimental data permits ready determination of the coefficients of equation (9). In an entirely analogous fashion, it can be shown that the mass transfer Colburn j-factor is given by an equation of the form

$$j_h = C'\,\mathrm{Re}^{k-1} \tag{10}$$

Determination of h and h_d is made by first determining an overall transfer coefficient from the general relationship

$$Q_k = U_k A_o \Delta K_m \tag{11}$$

where, for sensible transfer, $U_k = U_o$; ΔK_m = log mean temperature difference; and, for mass transfer, $U_k = U_d$; and ΔK_m = log mean enthalpy difference.

The overall transfer coefficient is related to the desired outside film transfer through the general relationship

$$\frac{1}{U_k} = b_k \frac{A_o}{A_i}\frac{1}{h_i} + \frac{A_o}{A_i} b_k \frac{A_o}{A_i}\frac{r_i}{k}\ln(r_o/r_i) + \frac{1}{\eta_o}\cdot\frac{1}{h_k} \tag{12}$$

where for sensible heat transfer $h_k = h_o$ and $b_k = 1$. For mass transfer $h_k = h_d$, and

$$b_k = \frac{di_s}{dT_w} \tag{13}$$

The surface efficiency η_o is given by

$$\eta_o = 1 - \frac{A_f}{A_o}(1 - \eta_f) \tag{14}$$

Here, η_f is the fin efficiency, and for the condensing case the film efficiency is calculated as per McQuiston (1975).

The water-side heat transfer coefficient h_i was determined from the correlation of Nusselt (1931)

$$\mathrm{Nu} = 0.036\,\mathrm{Re}^{0.8}\,\mathrm{Pr}^{1/3}\left(\frac{d}{L}\right)^{0.055} \tag{15}$$

Since the surface efficiency η_o depends upon h_o, an iterative determination of h_o and h_d from measured data was required.

Pressure drop data were interpreted per Idem et al. (1987) and Kays and London (1984), whereby, neglecting entrance and exit loss coefficients

$$f = \Delta p \frac{A_{\min}}{A_o}\left(\frac{2\bar{\rho}}{G^2}\right) \tag{16}$$

Results

Figures 4 through 7 present the results for the sensible heat tranfer coefficient. A least-squares curve fit to the data suggests the following correlations:

Dry, parallel flow

$$j = 0.595\,\mathrm{Re}^{-0.673} \tag{17a}$$

Wet, parallel flow

$$j = 0.306\,\mathrm{Re}^{-0.570} \tag{17b}$$

Dry, counterflow

$$j = 0.145\,\mathrm{Re}^{-0.484} \tag{17c}$$

Wet counterflow

$$j = 0.104\,\mathrm{Re}^{-0.423} \tag{17d}$$

Figures 8 and 9 present the results for the condensing mass transfer Colburn j-factor j_h. The corresponding least-squares curve fits are

Parallel flow

$$j_h = 0.126\,\mathrm{Re}^{-0.472} \tag{18a}$$

Counterflow

$$j_h = 1.212\,\mathrm{Re}^{-0.860} \tag{18b}$$

Figures 10 and 11 present results for the friction factor f. The corresponding least-squares curve fits are

Dry

$$f = 0.944\,\mathrm{Re}^{-0.517} \tag{19a}$$

Wet

$$f = 4.280\,\mathrm{Re}^{-0.722} \tag{19b}$$

Even though equations (19) do not readily demonstrate it, the differences in the two data sets are relatively small.

Conclusion

The performance of a copper finned-tube heat exchanger under the presence of outside condensation is best expressed in terms of a sensible and a mass transfer Colburn j-factor. For example, equations (17) present least-squares curve fits to sensible heat transfer coefficient data obtained from a test heat exchanger operated in either overall parallel or overall counterflow. The test conditions ranged from a completely dry outer surface to an outer surface that was completely wet due to condensation. Equations (18) present least-squares curve fits to mass transfer coefficient data obtained from a test heat exchanger operated in either overall parallel or overall counterflow for cases wherein the entire outer surface of the coil was wet due to condensation. The friction factor results presented by equations (19) characterize the pressure drop through the heat exchanger for dry or wet conditions.

Condensation slightly enhances the sensible heat transfer due to the presence of the condensate, while the total transfer is obviously increased through the latent transport that is a consequence of condensate mass transport. Presumably, the presence of the condensate affects the gas-vapor velocity pro-

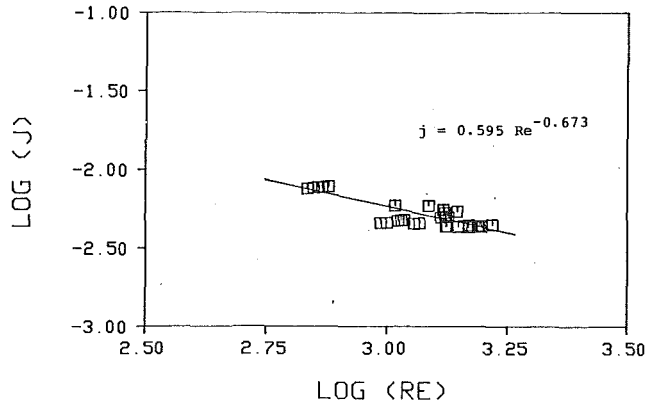

Fig. 4 *j* versus Re: sensible heat transfer coefficient dry or partially wet surface parallel flow two-pass heat exchanger (no baffles)

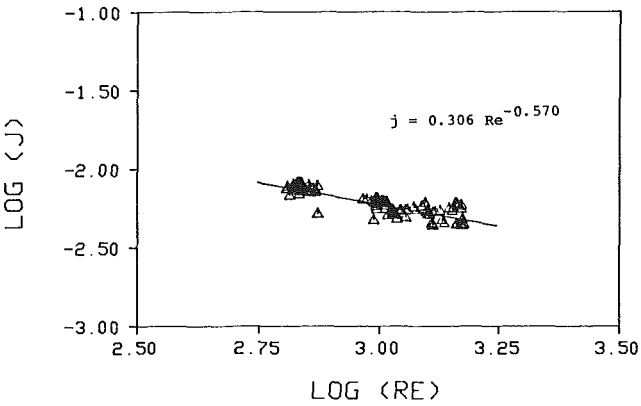

Fig. 5 *j* versus Re: sensible heat transfer coefficient wet surface parallel flow two-pass heat exchanger (no baffles)

file. Waves in the condensate film, or perhaps droplets on the fins, disturb the boundary layers by acting as surface rougheners, induce turbulence, and enhance mixing within the boundary layers. This explanation is corroborated by the increase in the friction factor for wet conditions, over dry conditions. As an example of the sensible heat transfer enhancement, at a Reynolds number of 1000 the sensible Colburn *j*-factors are increased by 4.6 percent for the parallel flow case and 9.3 percent for the counterflow case.

Consideration of Figs. 4 and 5 or 6 and 7 as well as 8 and 9 shows the effect of circuiting on the transfer coefficients (due to the influence on local temperature and degree of wetness). At a Reynolds number of 1000, the sensible Colburn *j*-factor for the parallel circuiting is about 10 percent higher for the dry case and 6 percent higher for the wet case compared to counterflow circuiting. Similarly, the mass transfer Colburn *j*-factor is about 35 percent higher for the parallel flow case.

Figures 10 and 11 illustrate the influences of circuiting and wetness on the friction factor. The behavior is consistent with the mechanisms discussed above. Friction factors are insensitive to circuiting, as expected. However, there is an increase of about 10 percent for the wet exchanger, over the dry exchanger (at a Reynolds number of 1000).

The trends for the sensible heat transfer Colburn *j*-factor are consistent with those reported in the literature for similar tests. Kays and London (1984) presented sensible *j*-factors for numerous coil geometries. The *j*-factor slopes, $m-1$ in equation (16), ranged from -0.3 to -0.6 for several two-pass, staggered, finned-tube heat exchangers operated in overall counterflow. Similarly, Gonzalez (1982) obtained a sensible *j*-factor slope of -0.547 for a single-row, eight-tube, two-pass finned-tube coil, and -0.570 for a nine-tube, staggered configuration, four-pass heat exchanger.

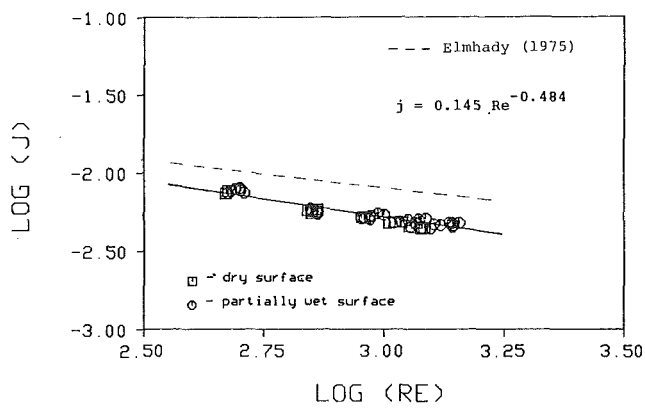

Fig. 6 *j* versus Re: sensible heat transfer coefficient dry or partially wet surface counterflow two-pass heat exchanger (no baffles)

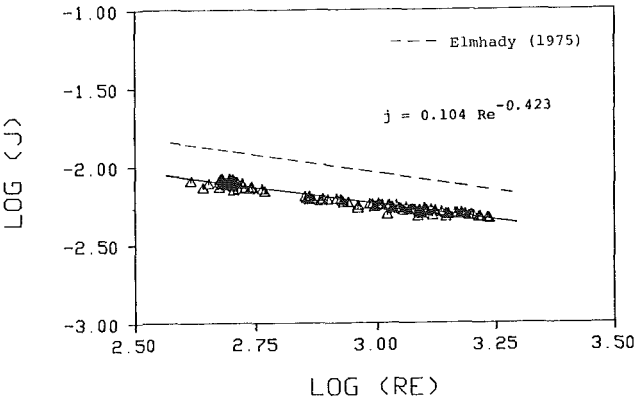

Fig. 7 *j* versus Re: sensible heat transfer coefficient wet surface counterflow two-pass heat exchanger (no baffles)

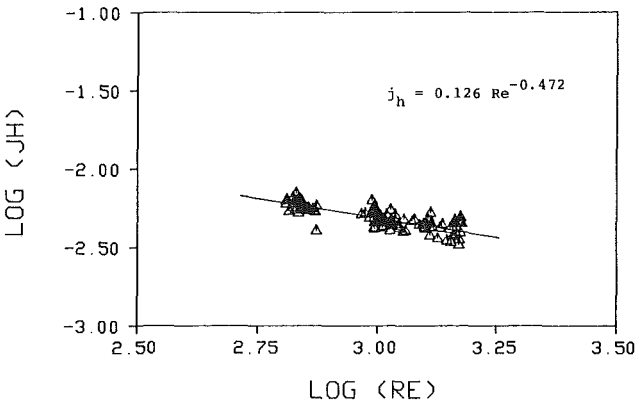

Fig. 8 j_h versus Re: mass transfer coefficient wet surface parallel flow two-pass heat exchanger (no baffles)

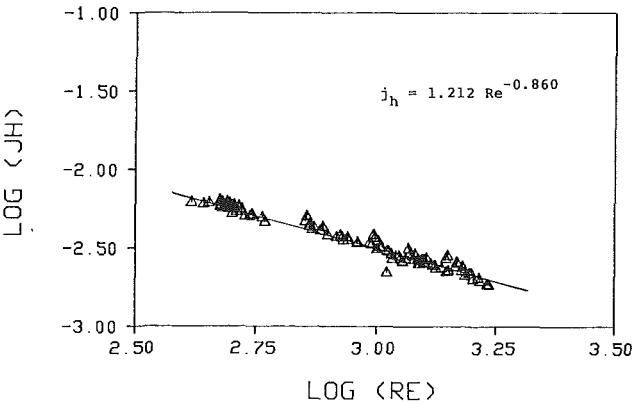

Fig. 9 j_h versus Re: mass transfer coefficient wet surface counterflow two-pass heat exchanger (no baffles)

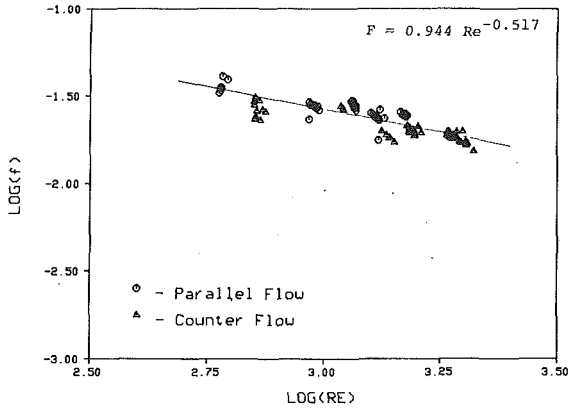

Fig. 10 Friction factor dry or partially wet surface counter and parallel flow two-pass heat exchanger (no baffles)

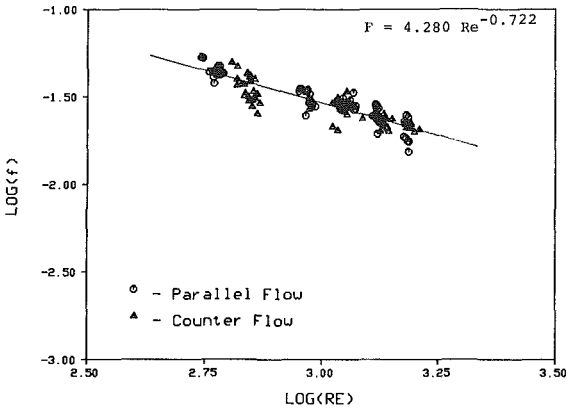

Fig. 11 Friction factor wet surface counter and parallel flow two-pass heat exchanger (no baffles)

Unfortunately, there are few appropriate correlations available for comparison to the results reported here. The work of Elmhady (1975) does provide a basis for a partial comparison. Correlations due to Elmhady are compared with the sensible Colburn j-factors in Figs. 6 and 7. While the proper trends are exhibited, Elmhady's correlations for his test heater consistently show higher values for the heat transfer in both the dry and wet cases.

The transport coefficients are presented as functions of Reynolds number based on hydraulic diameter. Hydraulic diameter is independent of both tube length and heat exchanger width (or number of tubes per pass); hence correlations based on hydraulic diameter are also independent of these parameters. The correlations presented in this paper may therefore be used to predict the performance characteristics of untested but geometrically similar heat exchangers, provided they are operated in the Reynolds number range 400 to 1500.

Acknowledgments

The work now reported is part of an overall research project sponsored by Teledyne LAARS. Their support, as well as the technical insight and sounding board provided by Mr. William Raleigh, are gratefully acknowledged. Aspects of the work were completed while the third author was hosted as a Visiting Professor by the University of British Columbia. The University also is acknowledged.

References

Buglayev, V. T., and Kazakov, V. S., 1972, "Heat Transfer From Saturated Air Flowing Across Tube Banks," *Heat Transfer—Soviet Research*, Vol. 4, pp. 1-5.

Bryan, W. L., 1961, "Heat and Mass Transfer in Dehumidifying Surface Coils," *ASHRAE Trans.*, Vol. 67, pp. 393-405.

Bryan, W. L., 1967, "Heat and Mass Transfer in Dehumidifying Extended Surface Coils," *ASHRAE Trans.*, Vol. 68, pp. 237-247.

Chilton, T. H., and Colburn, A. P., 1934, "Mass Transfer (Absorption) Coefficients," *Ind. Eng. Chem.*, Vol. 26, pp. 1183-1187.

Colburn, A. P., 1933, "A Method of Correlating Forced Convection Heat Transfer Data and a Comparison With Fluid Friction," *AIChE Trans.*, Vol. 29, pp. 174-210.

Elmhady, A. H., 1975, "Analytical and Experimental Multi-Row, Finned-Tube Heat Exchanger Performance During Cooling and Dehumidification Processes," Ph.D. Dissertation, Carleton University, Ottawa, Canada.

Fuks, S. N., and Zernova, E. P., 1970, "Heat and Mass Transfer With Condensation of Pure Steam and of Steam Containing Air, Supplied From the Side of a Tube Bank," *Thermal Eng.*, Vol. 17, pp. 84-90.

Gonzales, G. J., 1982, "Modeling and Testing of Helically Finned-Tube Cross-Flow Heat Exchangers With Baffling Surfaces, Operating of Moderately Low Reynolds Number," Master's Thesis, Purdue University, Dec.

Guillory, J. L., and McQuiston, F. C., 1973, "An Experimental Investigation of Air Dehumidification in a Parallel Plate Exchanger," *ASHRAE Trans.*, Vol. 79, pp. 146-151.

Honda, H., and Nozu, S., 1984, "A Prediction Method for Heat Transfer During Film Condensation on Horizontal Integral Finned Tubers," *Fundamentals of Phase Change Boiling and Condensation*, ASME HTD-Vol. 38, pp. 107-114.

Idem, S. A., 1986, "An Instantaneous Condensing Gas-Fired Water Heater: Modeling and Performance," Ph.D. Thesis, School of Mechanical Engineering, Purdue University, W. Lafayette, IN.

Idem, S. A., Jung, C., Gonzalez, G. J., and Goldschmidt, V. W., 1987, "Performance of Air-to-Water Copper Finned-Tube Heat Exchangers at Moderately Low Air-Side Reynolds Numbers, Including Effects of Baffles," *Int. J. Heat Mass Transfer*, Vol. 30, pp. 1733-1741.

Kays, W. M., and London, A. L., 1984, *Compact Heat Exchangers*, McGraw-Hill, New York.

Kline, S. J., and McClintock, F. A., 1953, "Describing Uncertainties in Single-Sample Experiments," *Mech. Eng.*, Vol. 75, pp. 3-8.

Marto, P. J., 1986, "Recent Progress in Enhancing Film Condensation Heat Transfer on Horizontal Tubes," *Proceedings, 8th International Heat Transfer Conference*, C. L. Tien, et al., eds., Hemisphere Publishing Corp., Washington, DC, Vol. 1, pp. 161-170.

McQuiston, F. C., 1975, "Fin Efficiency With Combined Heat and Mass Transfer," *ASHRAE Trans.*, Vol. 81, pp. 350-355.

McQuiston, F. C., 1976, "Heat Mass and Momentum Transfer in a Parallel Plate Dehumidifying Exchanger," *ASHRAE Trans.*, Vol. 82, pp. 87-106.

McQuiston, F. C., 1978a, "Heat, Mass and Momentum Transfer Data for Five Plate-Fin-Tube Heat Transfer Surfaces," *ASHRAE Trans.*, Vol. 84, pp. 266-293.

McQuiston, F. C., 1978b, "Correlation of Heat, Mass and Momentum Transport Coefficients for Plate-Fin-Tube Heat Transfer Surfaces With Staggered Tubes," *ASHRAE Trans.*, Vol. 84, pp. 294-309.

McQuiston, F. C., 1981, "Finned Tube Heat Exchangers: State of the Art for the Air Side," *ASHRAE Trans.*, Vol. 87, pp. 1077-1085.

Nusselt, W., 1931, "Der Warmeaustausch zwischen Wand und Wasser im Rohr," *Forsch. Geb. Ingenieurwes.*, Vol. 2, p. 309.

Tree, D. R., and Helmer, W. A., 1976, "Experimental Heat and Mass Transfer Data for Condensing Flow in a Parallel Plate Heat Exchanger," *ASHRAE Trans.*, Vol. 82, pp. 289-299.

Webb, R. L., 1980, "Air-Side Heat Transfer in Finned Tube Heat Exchangers," *Heat Transfer Engr.*, Vol. 1, No. 3, pp. 33-49.

APPENDIX A

Diameter to Heat Exchanger Geometry

In order to relate the hydraulic diameter to the geometry of the heat exchanger, it is necessary to consider the following definitions for a helically finned crossflow in-line heat exchanger. Referring to Fig. 2, the transverse pitch S_T is seen to be the distance between tubes normal to the direction of gas flow. Then, denoting the fin tip diameter by d_f and the fin root diameter by d_o and taking the mean film thickness to be

$$\bar{\delta}_f = \frac{\delta_r + \delta_t}{2} \tag{A1}$$

where δ_r equals the fin root thickness, and δ_t equals the fin tip thickness, yields the following definition for the ratio of minimum heat exchanger face area per unit length to the frontal area per unit length:

$$\sigma = \frac{S_T - d_o - [(d_f - d_o)\bar{\delta}_f S_F]}{S_T} \tag{A2}$$

The parameter S_F is termed the fin density, and has units of fins per unit length. The finned area per unit length is given by

$$A_f' = \pi\left[\frac{d_f^2 - d_o^2}{2} + d_f\delta_t\right]S_F \tag{A3}$$

while the total outside area per unit length is given by

$$A_o' = A_f' + \pi(1 - \delta_r S_F)d_o \tag{A4}$$

The parameter γ is the ratio of total finned area to total outside area

$$\gamma = \frac{A_f'}{A_o'} \tag{A5}$$

The heat exchanger frontal area is approximated by the relation

$$A_{fr} = L_{\text{tube}}[(N_{\text{tfr}} - 1)S_T + d_f] \tag{A6}$$

The total heat exchanger outside surface area is described by the equation

$$A_o = A_o' L_{\text{tube}} N_{\text{tfr}} N_{\text{pass}} \tag{A7}$$

where N_{pass} is the number of the tube passes. It is then readily apparent that total finned surface area is given by

$$A_f = \gamma A_o$$

Moreover, if d_i is the inner tube diameter, the total inside surface area is given by

$$A_i = \pi d_i L_{\text{tube}} N_{\text{tfr}} N_{\text{pass}} \tag{A8}$$

Finally, it is observed that the effective flow length of a multipass crossflow heat exchanger is given by

$$L = N_{\text{pass}} S_L \tag{A9}$$

Having thus described the characteristic geometry of a multipass crossflow heat exchanger, it is apparent that the hydraulic diameter may be defined as

$$d_H = \frac{4\sigma A_{fr} L}{A_o} \tag{A10}$$

Note that the ratio A_{fr} to A_o can be obtained from the relation

$$\frac{A_{fr}}{A_o} = \frac{S_T}{\pi\left[\frac{d_f^2 - d_o^2}{2} + d_f\delta_t\right]S_F + \pi(1 - \delta_r S_F)d_o} \tag{A1}$$

which is derived on a per unit length basis from the characteristic geometry of a heat exchanger tube.

G. S. H. Lock

J. D. Kirchner

Department of Mechanical Engineering,
University of Alberta,
Edmonton, Alberta, Canada

Wind-Augmented Heat Transfer in an Open Thermosyphon Tube With Large Length-Diameter Ratios

The paper reports an experimental study of the open thermosyphon tube when its heat transfer performance is augmented by the prevailing wind flowing down the inside of an insert tube concentric with the thermosyphon tube. Data are presented for the large length-diameter ratios characteristic of geotechnical applications. A flow model is developed and used to interpret these and other results. Comparisons are made with the performance of liquid-filled thermosyphons.

Introduction

As noted in a previous paper (Lock and Kirchner, 1988), the open thermosyphon tube has many potential applications, among which are its uses in a northern geotechnical context for the stabilization of soil and the production of underwater ice. Under such circumstances, the device acts as a "thermal diode": During the winter, air temperatures less than the thermosyphon tube wall temperature establish an effective natural convection system within the tube, whereas during the summer, when the air temperature is higher than the tube wall temperature, the system transmits heat downward by the relatively ineffective mechanism of conduction. This paper is concerned with winter operations.

The seminal paper of Lighthill (1953) has provided the basis for many subsequent studies of the open thermosyphon, both theoretical (Japikse, 1968; Gosman et al., 1971; Leslie and Martin, 1959) and experimental (Japikse and Winter, 1981; Martin, 1955; Martin and Cresswell, 1957). Lighthill's work revealed two flow regimes: At sufficiently high temperature differences, an annular boundary layer of heated fluid rises adjacent to the tube wall while a cool replenishing core descends about the tube axis; at lower temperature differences, the boundary layer thickness is no longer small compared with the core radius, thus creating an impeded flow regime in which heat transfer rates are not only lower than in the boundary layer regime but fall off more rapidly with a decreasing temperature difference.

Another significant feature of Lighthill's work is the suggestion (in a note added in proof) that the junction of the two flow regimes would not be marked by a smooth, gradual transition but by a region of ambivalence and uncertainty. This feature has not been reproduced numerically (Gosman et al., 1971) but has been observed in the laboratory (Martin, 1955; Bayley and Lock, 1965). When air fills the tube the inter-regime transition is marked by a chasm in the heat transfer data. This chasm is narrow and deep, and is best avoided in field applications, where the thermal properties of air (momentum and thermal diffusivity in particular) automatically ensure lower Rayleigh numbers than may be obtained when a nonmetallic liquid fills the same tube.

To overcome the intrinsic limitations of an air-filled, open thermosyphon it has been suggested by Lock and Kirchner (1988) that the prevailing wind may be harnessed to provide a superimposed forced flow. If this flow is directed down a smaller tube, concentric with the thermosyphon tube, it should be possible, at least in principle, to offset the abovementioned inefficiency and raise heat transfer rates to levels where they provide a viable alternative to liquid-filled systems. Such viability has been demonstrated by the authors but only for tubes with a length-diameter ratio of 10:1. Since many field applications would require much greater length-diameter ratios, the present paper focuses on longer tubes, and, in the light of an extended set of data, offers a suggestion for a model describing system behavior.

Experimental Considerations

The Rig. The experiments were conducted in a low-temperature wind tunnel in which the air velocity could be set in the range $10\ \text{m/s} < U_\infty < 60\ \text{m/s}$, and the air temperature could be adjusted in the range $-20°\text{C} < T < 10°\text{C}$. The thermosyphon tube was situated on the outside of the tunnel but penetrated the tunnel wall by an amount sufficient to place the wind inlet and outlets beyond the wall boundary layer. The inlet consisted of a simple extension of the insert tube on top of which was soldered a right angle fitting with the mouth facing upstream (see Fig. 1). The outlets were two 8-mm-dia holes drilled in the *sides* of the thermosyphon tube extension (not in the rear face indicated in the schematic).

To cover a practical range of average sustainable wind speeds in the field, it was decided to limit the tests to maximum wind speeds of 20 m/s. Since the tunnel velocities were limited by a minimum value of 10 m/s, the test section had to

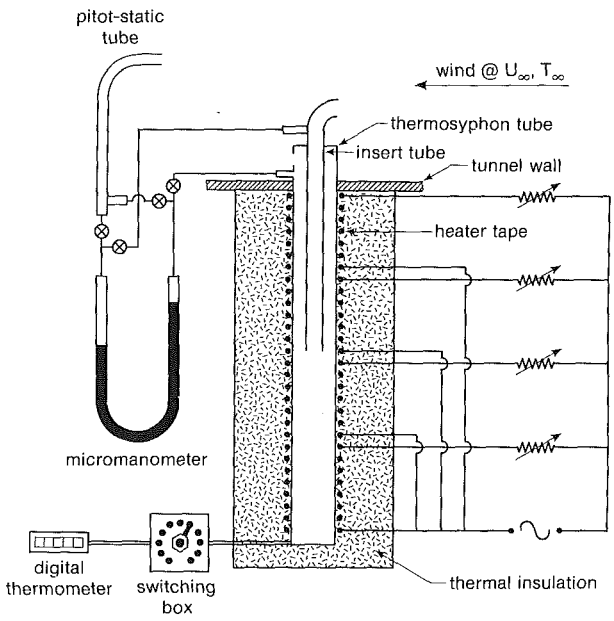

Fig. 1 Schematic of thermosyphon apparatus

Contributed by the Heat Transfer Division and presented at the 25th National Heat Transfer Conference, Houston, Texas, July 24-27, 1988. Manuscript received by the Heat Transfer Division December 21, 1987; revision received November 29, 1988. Keywords: Heat Pipes and Thermosyphons, Mixed Convection, Natural Convection.

be subdivided, with a reduced section being used to generate velocities below 10 m/s (Lock and Kirchner, 1988). This proved to be a convenient way of exposing the thermosyphon to reduced wind velocities and was considered to be a more realistic simulation of field conditions than the simpler expedient of connecting the insert tube to a compressor line.

A schematic of the rig is given in Fig. 1. The thermosyphons were made from 19.6-mm i.d. copper tubes cut to various lengths. The insert tubes were made from polycarbonate tubing of i.d. 12.7 mm and o.d. 15.9 mm. These dimensions, which were fixed throughout the experiments, ensured that the flow area inside the insert tube was roughly equal to (actually slightly greater than) the flow area within the annular space between the tubes. The relatively low thermal conductivity of the insert tube material helped minimize heat exchange between the ascending annular flow and the descending core flow.

Instrumentation and Calibration. Temperatures were measured throughout by means of thermocouples: These were attached to the outer surface of the thermosyphon tubes at intervals of 5 cm, and located in both the wind and surrounding room air. The thermocouples were connected to a multichannel switching box, which in turn was connected to a Fluke 2175A digital thermometer.

Fiberglass tape was wrapped around the thermosyphon tube, enclosing thermocouple wires and providing a layer of electrical insulation between the copper thermosyphon tube and the metal heating tape wrapped over the fiberglass tape. A thick layer of fiberglass insulation was then wrapped around the heater tape as indicated in Fig. 1.

The heater tape windings were divided into 10-cm tube lengths arranged in parallel, each separate length being connected with a variable resistance in series. This arrangement enabled the power supplied to each 10-cm length of thermosyphon tube to be varied with a certain degree of independence, thus giving flexibility in establishing an isothermal tube wall; accuracy was typically $\pm 2°C$.

A pitot-static tube connected to a Dwyer Instruments Microtector micromanometer was used to measure wind speed. A micromanometer was also used to measure the wind-driven pressure drop occurring in the thermosyphon tube, as indicated in Fig. 1. The tube pressure drop measurements were reproduced later when the thermosyphon had been removed from the tunnel and was connected to an air supply in series with a rotameter. By this means the air flow rate through the thermosyphon under simulated tunnel conditions could be determined.

The heat leakage under test conditions was determined before the tests began through a series of calibration runs in which the thermosyphon was packed with a fine-grained thermal insulation material. With the wind temperature and speed set at a number of different values, measurements of power supply ($\dot{Q}_e$) and temperature difference between the tube wall (T_w) and the ambient air (T_a) were taken. These enabled the heat leakage $\dot{Q}_e$ to be calculated during test conditions, thus making it possible to determine the net heat supply rate.

Table 1 Test schedule

Test	L/D	U_∞(m/s)	ΔP(Pa)	$\bar{U}$ (m/s)	Re
1	10	5	8.7	2.0	500
2	10	10	32	5.9	1530
3	10	20	80	11	2550
4	20	5	8.0	1.3	340*
5	20	10	37	4.9	1270
6	20	20	95	9.6	2460
7	40	5	4.2	0.67	170**
8	40	10	42	3.9	980*
9	40	20	119	7.9	1940
10	60	5	8.7	0.60	150**
11	60	10	44	2.7	690*
12	60	20	122	6.2	1600*

L_i = L/2
D = 0.0196m
d = 0.0159m

Possible fully developed:
*Annular zone
**Annular zone and entrance zone

$2.1 < \log_{10} t_D < 3.8$

Test Procedure and Schedule. Once a given thermosyphon tube had been located in the wind tunnel wall, the test procedure was as follows. The tunnel was started and the wind speed and temperature set at fixed values. While the tunnel was approaching steady-state conditions, a period which lasted about 2 h, the electrical power supply to the thermosyphon was switched on and set at some value in the anticipated range. Periodic readings of temperature were then taken until the thermosyphon had reached steady state. This period lasted at least three hours.

With steady conditions attained, the following readings were taken: gross power, wind speed, wind temperature, tube pressure drop, tube wall temperatures, and ambient temperature. These data, and the calibration data, were then used to calculate the tube Nusselt number and Rayleigh number as defined in the Nomenclature. Subsequent to the tests proper, the tube pressure drops were converted into tube Reynolds numbers using the procedure mentioned earlier.

The test schedule is shown in Table 1, from which it is evident that three wind speeds and four length-diameter ratios were used. These were chosen with a geotechnical application in mind. The actual dimensions of the insert and ther-

Nomenclature

b, c = coefficients
d = insert tube diameter
D = thermosyphon tube diameter
g = gravitational acceleration
Gz = Graetz number
h = heat transfer coefficient
k = thermal conductivity
L = tube length
m, n = exponents
Nu = Nusselt number = $\bar{h}D/k_a$
Pr = Prandtl number
P = static pressure
$\dot{Q}$ = heat flux
Ra = Rayleigh number = $\beta g(T_w - T_\infty)D^3/\nu\kappa$
Re = Reynolds number = $\bar{U}(D-d)/\nu$
T = temperature
t = RaD/L
U = air velocity
β = thermal expansion coefficient
κ = thermal diffusivity
ν = momentum diffusivity

Subscripts
a = air
D = thermosyphon tube diameter
e = entry
i = insert tube
w = wall
∞ = wind

Superscripts
$\bar{}$ = average

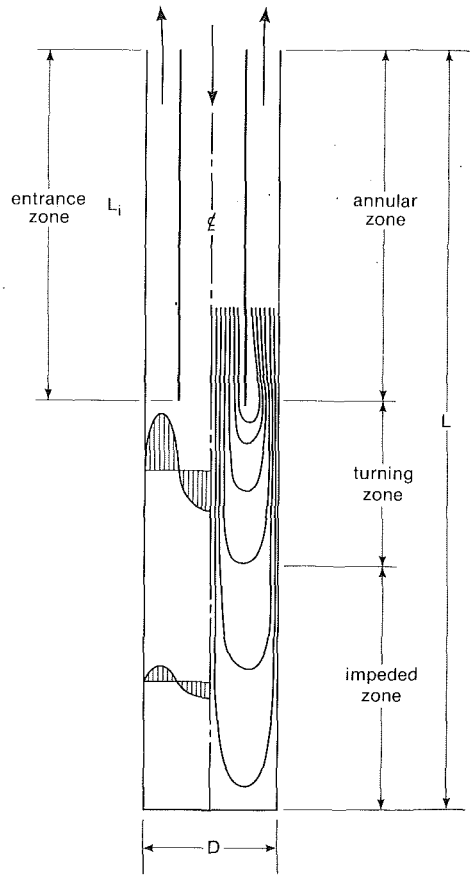

Fig. 2 Suggested flow model

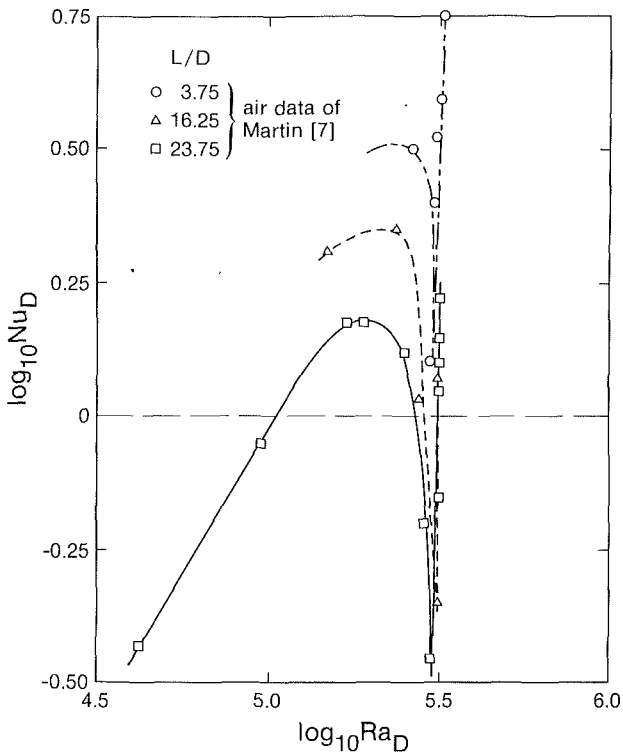

Fig. 3 Chasmic transitional behavior

mosyphon tubes were based on an attempt to minimize the physical and economic scale of the experiments while maximizing the use of similitude. Previous experience suggested that the insert tube length should be set at half the thermosyphon tube length. This length was chosen to cover the range 20–120 cm, which, together with the tube diameter, served to limit the gross power supply to under 100 W; this provided a convenient range, except at the lower end where the net and gross power were both of the order of 1 W and experimental error became unacceptable. Measurement uncertainties for the temperatures, heat supplied, heat loss, and fluid properties were used in a formal error analysis to yield the uncertainty in Nu, Ra, and t_D. Error bars are shown in Figs. 4, 5, and 6, and in the empirical correlation displayed in Fig. 10.

Discussion of Results

Flow Model. For the range of conditions covered in the experiments, the expected velocity profiles and streamline pattern are depicted in Fig. 2. This diagram suggests that the flow system may be divided into four zones:

1 Entrance Zone. Fluid moving inside the insert tube represents an entrance flow for the pure thermosyphon piece below. The insert tube flow itself may be developing or developed, thermally or hydrodynamically, depending upon the inlet condition created in the cowling. If the insert tube is not too close to the thermosyphon tube wall, and is made from an insulating material, the role of heat transfer in the entrance zone should be negligible. Ideally, the fluid emerging from the insert tube would be uniformly at the wind temperature.

2 Turning Zone. Before entering the annular space between the insert tube and the thermosyphon tube, the fluid must turn through 180 deg in an effective length, which may be expected to increase with increasing wind speed (Reynolds number).

3 Impeded Zone. For low values of Re and t_D, the space beneath the turning zone is essentially the bottom piece of a pure thermosyphon operating in the impeded regime. Free convection dominates in this zone where heat transfer rates are comparatively low.

4 Annular Zone. Upon finally leaving the turning zone, the fluid enters an annulus in which mixed convection occurs, in general. The absence of any recirculation suggests that this zone would exhibit the highest heat transfer rates of the entire system.

The transition between the turning zone and the impeded zone is not precisely defined and may in fact be a gradual merging of the two flow systems. In any event, the bottom of the turning zone represents the "mouth" of the thermosyphon system beneath. It was noted earlier that flow conditions in the mouth were unstable in the vicinity of the impeded/boundary layer regime junction. This may be seen from the original data of Martin (1955) replotted in Fig. 3 against Rayleigh number. It is immediately evident that the chasm bottoms occur at a common value of $\log_{10}Ra_D = 5.48 \pm 0.01$. This strongly suggests that the instability condition is determined by a Rayleigh number criterion; the tube length appears to be unimportant.

The thermosyphon "mouth" beneath the insert tube also gives rise to a flow instability when wind augmentation is being used, but the details are influenced by the magnitude of the wind (Lock and Kirchner, 1988). As might be expected, the instability occurs at a lower value of t_D (or Rayleigh number) as the wind speed is increased, presumably because of vorticity generated at the bottom edge of the insert tube, where the flow may become turbulent at unusually low Reynolds numbers. Also observed is a decrease in the overall effect of the instability (indicated by chasm depth) as the wind speed increases. This is to be expected from the zonal model outlined above: Increasing the forced convection effect reduces the relative importance of free convection, including any perturbations in free convection.

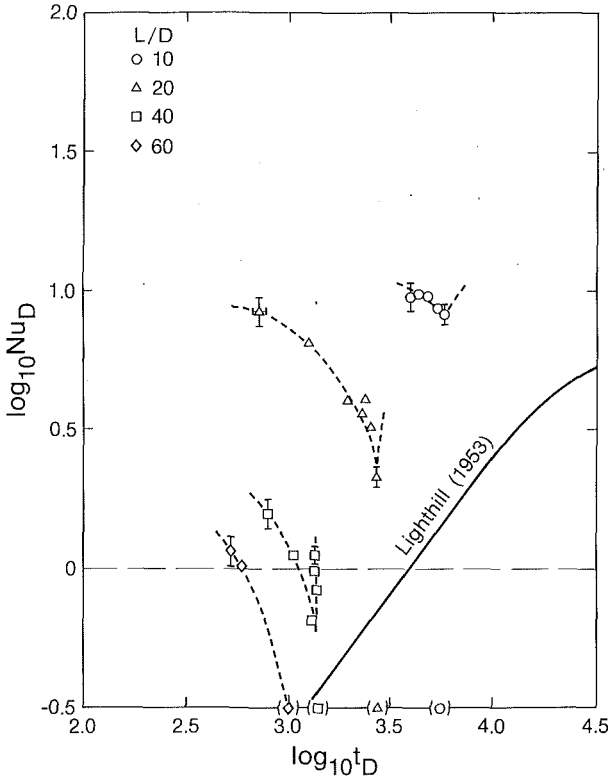

Fig. 4 Heat transfer data: $U_\infty = 5$ m/s

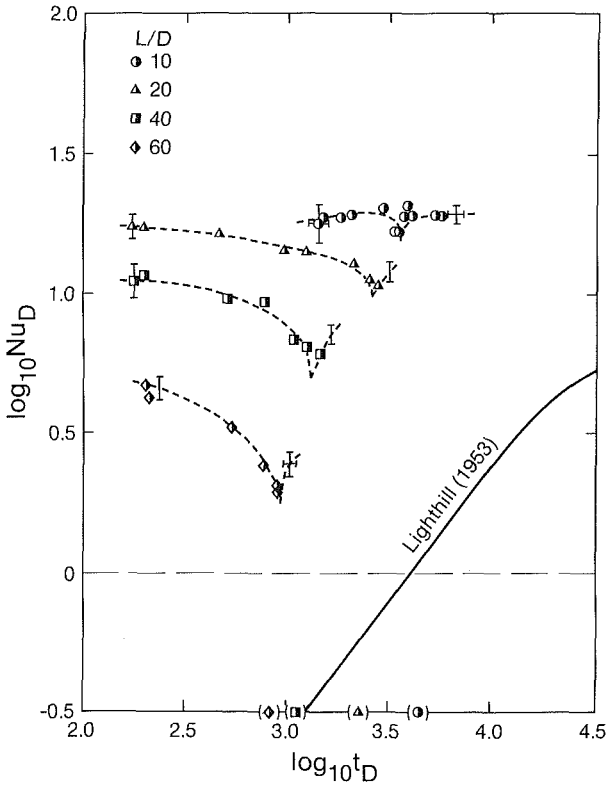

Fig. 5 Heat transfer data: $U_\infty = 10$ m/s

Before turning to consideration of the effect of wind speed and length-diameter ratio it is worth noting that the effect of the insert tube will not be considered as a variable. Previous work suggested that the insert tube has an optimum length: As $L_i \rightarrow 0$, the system assumes a two-zone form (turning and impeded), thus eliminating the high-efficiency annular zone; as

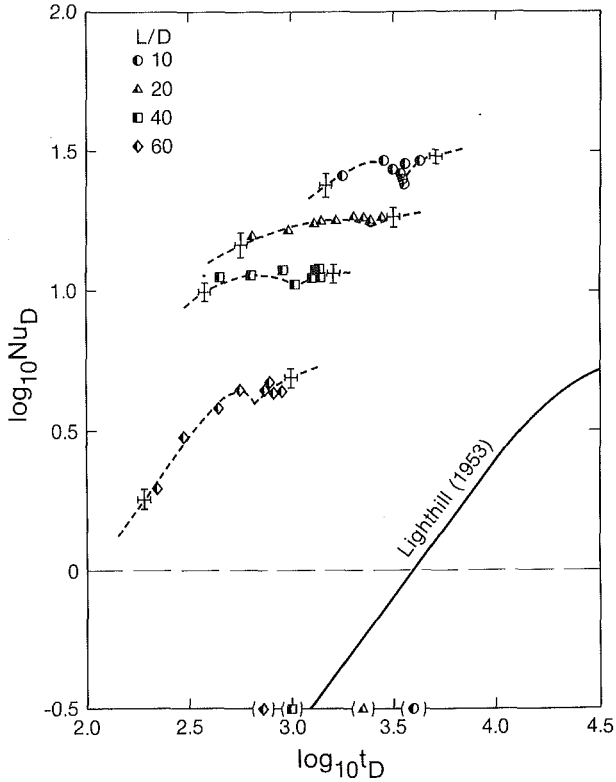

Fig. 6 Heat transfer data: $U_\infty = 20$ m/s

Table 2 Chasmic transition: log Ra and log t_D

L/D	WIND SPEED (m/s)							
	0		5		10		20	
	log Ra	log t_D	log Ra	log t_D	log Ra	log t_D	log Ra	log t_D
3.75	5.48	4.9	-		-		-	
10	-		4.75	3.75*	4.65	3.65	4.6	3.6
16.25	5.48	4.27	-		-		-	
20	-		4.75	3.45*	4.65	3.35*	4.6	3.3
23.75	5.48	4.1	-		-		-	
40	-		4.75	3.15	4.65	3.05*	4.6	3.0
60	-		4.75	3.0*	4.65	2.9*	4.6	2.8*

The zero wind speed data are Martin's [7]

*Estimated

$L_i \rightarrow L$, the viscous drag of the insert tube is maximized and the pressure drop in the turning zone would become infinite. For a thermosyphon tube with a length-diameter ratio of 10:1, the optimum was around 0.5 over the range of conditions covered. This value of L_i/L has been used in all long tube results reported here.

Effect of Length-Diameter Ratio. The effect of length-diameter ratio may be seen in Figs. 4, 5, and 6, from which it is apparent that an increase in L/D is accompanied by a decrease in heat transfer rate, as might be expected. Most of the data lie to the left of the chasm, which was not always identified by direct measurement. Martin's data suggest that the chasmic transition is marked by the Rayleigh number Ra_D,

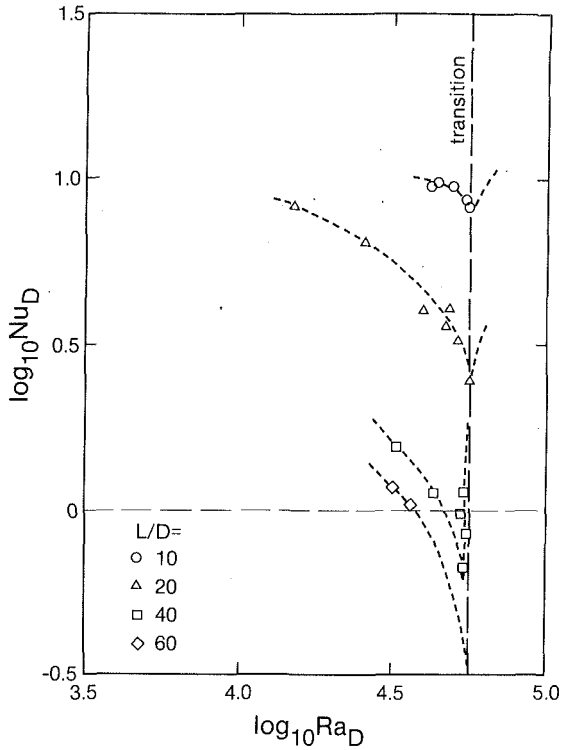

Fig. 7 Nusselt number versus Rayleigh number: 5 m/s

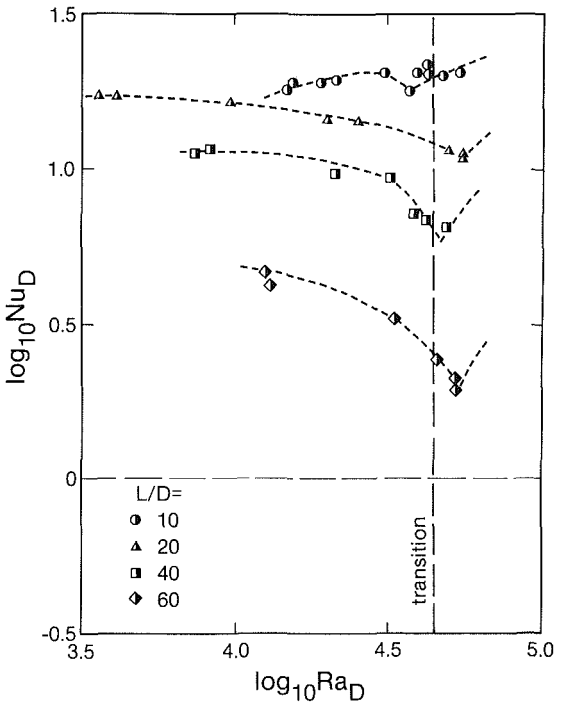

Fig. 8 Nusselt number versus Rayleigh number: 10 m/s

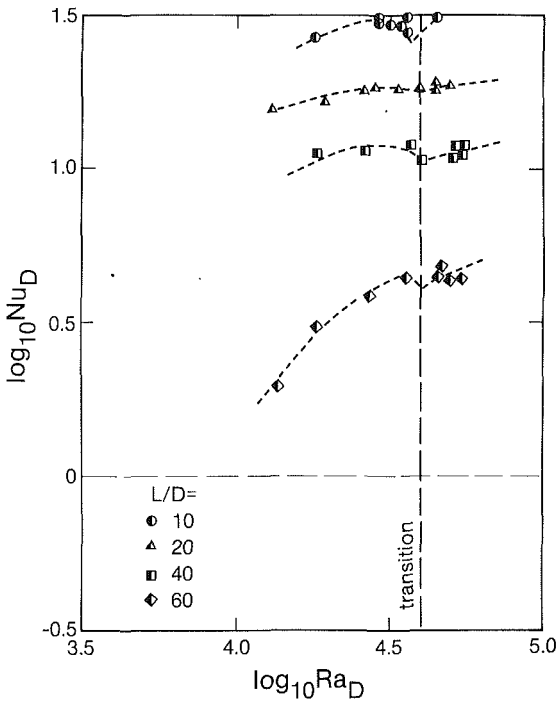

Fig. 9 Nusselt number versus Rayleigh number: 20 m/s

while our previous study indicates that the transition moves to lower values of Ra_D (or t_D) as the wind speed increases.

On the assumption that the position of the transition does not change with L/D, for any given wind speed, the data in Table 2 have been compiled from observed chasmic transitions. From these data it is evident that the transitional Rayleigh numbers are near 5.48, 4.75, 4.65, and 4.6 for wind speeds of 0, 5, 10, and 20 m/s, respectively. The corresponding transitional values of t_D are shown plotted on the horizontal axis in Figs. 4, 5, and 6. Where chasmic transitions were not actually observed, the predicted locations are believed to provide good estimates, and thus provide assistance to the designer wishing to avoid chasmic behavior.

Figures 7, 8, and 9 show the data of Figs. 4, 5, and 6 replotted against Rayleigh number. It is evident that the chasmic transitions organize the data horizontally, and leave the monotonic effect of length-diameter ratio essentially unchanged. In an attempt to correlate this effect, an expression of the form $Nu_D \alpha (D/L)^m$ was used. The results indicated that two values of m were required: above and below a transitional value of D/L corresponding to $\log_{10}(D/L) = -1.6$ to -1.5. This suggests a regime change when $L/D \simeq 40$, the explanation of which may be seen in Table 1, which shows the estimates of entry lengths (in the annular and entrance zones) found to be greater than the zone length. These were based on the simple, conventional expression giving entry length L_e equal to 0.05 multiplied by the product of the appropriate diameter and Reynolds number. For the arrangement considered here, this expression becomes

$$L_e = 0.2D\mathrm{Re}$$

and

$$L_e = 0.03D\mathrm{Re}$$

for the entrance and annular zones, respectively. Table 1 reveals that with one exception this length was exceeded for $L/D \geq 40$, especially in the annular zone.

Effect of Wind Speed. Figures 4, 5, and 6 also reveal the effect of wind speed. Table 1 indicates that the mean air velocity in the thermosyphon tube is less than the wind speed, the ratio of about 0.5 or less being attributable to drag on the insert tube and the design of the inlet and outlet. The latter could perhaps be improved under field conditions but the former is an intrinsic loss. Table 1 reveals that the ratio decreases as length-diameter ratio increases, as would be expected, and suggests that inlet and outlet conditions accounted for most of the loss in the range of tubes tested.

The wind velocity and the internal velocity may both be used to describe system performance. Wind speed is used in

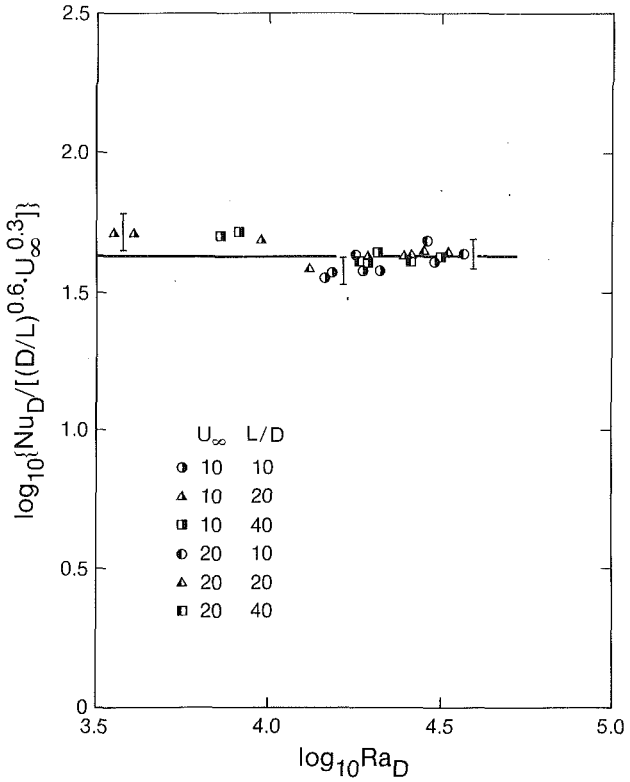

Fig. 10 Empirical correlation

Figs. 4, 5, and 6, which confirm the broad expectation that the heat transfer rate increases as the wind rises; this is not invariably true, as the $L/D=60$ data show. By comparison with the theoretical predictions of Lighthill (1953), it is evident that the forced convection effect attributable to the wind is capable of raising the heat transfer efficiency of the device above the level normally associated with impeded flow, in which $\log_{10}Nu_D \lesssim 0.8$. Only the longest tube, which had a length-diameter ratio of 60:1, failed to reach this level; nonetheless its performance improved considerably with wind speed.

It is interesting to note that it is not just the level but the shape of the curves that changes with wind speed. At the lowest wind speed tested, the Nusselt numbers decrease monotonically with increasing t_D for reasons associated with the chasm discussed earlier; it is quite likely that the same behavior occurs at a zero wind speed, only beneath Lighthill's theoretical prediction. At the highest wind speed used, the monotonicity appears to have changed sign, except in the vicinity of the chasms. An explanation of this gradual change in slope may be found in the flow model, which suggests that the initial effect of increasing the wind speed would be to increase the circulation in a mixed convection system, but would eventually lead to a laminar-turbulent transition, which would convert the turning zone into an "isothermal pool" supplying a strongly impeded free convection flow beneath; this would increase the relative role of pure free convection though not the instability associated with it: the longer $(L-L_i)$, the greater would be the effect. If the wind speed were increased far enough it is to be expected that the curves would eventually become independent of t_D, but for the range of Re and t_D covered the effect of free convection is still noticeable in the positive slopes at 20 m/s.

These changes in slope evidently create an optimum heat transfer rate, at least to the left of the chasm. Figures 5 and 6 reveal that for $t_D \lesssim 10^{2.5}$, increasing the wind speed from 10 m/s to 20 m/s actually decreases the heat transfer rate, whereas the reverse appears to be true between 5 m/s and 10 m/s. Since the effect on the annular zone would be monotonic, it must be surmised that the cause of the optimum lies in the turning and impeded zones, as suggested above.

Empirical Correlation. For the purpose of developing an empirical correlation, the wind speed is not an appropriate variable because it is not directly related to the flow details within the tube. In general, the flow field would depend upon the inlet and outlet geometry as well as on the internal geometry, represented by L_i/L and d/D. All of these variables were fixed in the experiments reported here, but the overall thermosyphon tube geometry was varied, thus destroying a direct relation between external and internal air velocities. The latter provide the better basis for a correlation.

The flow model suggests that the major contribution to heat transfer occurs in the annular zone in which the Reynolds number is appropriately defined by $Re=\bar{U}(D-d)/\nu$, where $\bar{U}$ is the mean velocity in the annulus. It is evident from Table 1 that $150<Re<2550$, and from Figs. 4, 5, and 6 that $2.2<\log_{10}t_D<3.8$. A map of the mixed convection regimes for the system studied here is not available, but the nearest vertical-tube equivalent map of Metais and Eckert (1964) indicates that the range of conditions considered covers several regimes: forced convection laminar flow, mixed convection laminar flow, mixed convection turbulent flow, and, of course, the laminar-turbulent transition for mixed convection. A similar conclusion may be drawn from the range of the parameter Ra/Re^2 using Table 1 and Figs. 4, 5, and 6. The system behavior is correspondingly complex.

An initial attempt to correlate the data in the more conventional form of Nu versus $(Gz+at^p)$ failed, and hence the simpler form

$$Nu_D \alpha (D/L)^m$$

was tried, as mentioned earlier. Using only data to the left of the chasm, it was found that the average value of m was 0.60 for $L/D \leq 40$ and 2.53 for $L/D \geq 40$. The lower range data were replotted in the form $\log_{10}Nu_D/(D/L)^m$ versus $\log_{10}Ra_D$. This revealed a residual effect of the wind, which was readily expressed in a power law form. The final result is shown in Fig. 10, from which it is evident that the empirical relation

$$Nu_D = A Re_D^n (D/L)^m$$

in which $A=A(Ra_D)$, is an adequate correlation for most design purposes providing the wind is not negligible (5 m/s or less) and the Rayleigh number lies in the range $10^{3.5}<Ra_D<10^{4.5}$ (where its effect is essentially constant). In such a range, the role of free convection is evidently smaller than that of forced convection. This may not be true for large-diameter tubes, which may exhibit Rayleigh numbers well in excess of $10^{4.5}$.

Conclusions

The principal conclusion to be drawn from the above results is that wind augmentation is very effective over a practical range of average wind speeds. With the exception of the low t_D range, the improvement in Nusselt number was about an order of magnitude, depending upon L/D and the particular choice of t_D. This establishes the fact that heat transfer rates in the wind-augmented thermosyphon may be raised to values normally associated with the more efficient boundary layer regime, even for tubes with large length-diameter ratios. In practice, where tube diameters are likely to be much greater, at least in geotechnical applications, the heat transfer rates would be higher again. The results recorded here were obtained from an impeded-regime base and are therefore likely to be conservative.

An attempt has been made to develop a model of the system. Despite the fact that data may cover laminar and turbulent flow for free, forced, and mixed convection, and despite the appearance of several forms of inter-regime transition, including the dramatic chasmic transition inherited from the pure thermosyphon, it appears that the system may be described effectively in zonal terms: an entrance zone (essentially isothermal), a turning zone (which may be the origin of the laminar-turbulent transition), an impeded regime (exhibiting low heat transfer rates), and an annular zone (exhibiting high heat transfer rates). This model provided satisfactory explanations of system behavior, in general, and of the effects of the insert tube and wind speed in particular.

The data of Martin for the pure thermosyphon, together with present and previous data for the wind-augmented thermosyphon, suggest that the clearly noticeable chasmic transition in the impeded regime is marked by a critical value of Rayleigh number (based on the tube diameter). This transitional Rayleigh number, and the corresponding value of t_D, was found to decrease with increasing wind speed, the range covered in the present experiments being about an order of magnitude. These findings provide a means of predicting the location of the chasm, and of thus avoiding the associated low heat transfer rates.

The effect of length-diameter ratio was found to be monotonic, as expected. However, it appears that the decrease in heat transfer rates associated with an increase in length-diameter ratio undergoes a transition around $L/D = 40$. For greater values of L/D the effect of L/D is much steeper. It is suggested that this transition marks the onset of fully developed flow.

The discovery that the chasm location is primarily controlled by Rayleigh number was used to organize the data. The Nu-Ra data plots thus formed were found to correlate with reasonable accuracy if simple power law forms were used for the effect of wind speed and length-diameter ratio. It is recommended that the empirical correlation thus found should not be used beyond the range of Rayleigh numbers tested here; this limitation would apply particularly to large-diameter tubes that are capable of operating well above the range covered.

Acknowledgment

This work was undertaken with a grant from the Natural Sciences and Engineering Research Council of Canada to whom we are grateful. We would also like to thank Mr. T. Nord, Mr. T. Villett, Mr. A. Muir, and the workshop staff of the Department of Mechanical Engineering at the University of Alberta.

References

Bayley, F. J., and Lock, G. S. H., 1965, "Heat Transfer Characteristics of the Closed Thermosyphon," ASME JOURNAL OF HEAT TRANSFER, Vol. 87, pp. 30-40.

Gosman, A. D., et at., 1971, "A Numerical Study of the Heat Transfer Performance of the Open Thermosyphon," *Int. J. Heat Mass Trans.*, Vol. 14, pp. 1717-1730.

Japikse, D., 1968, "Heat Transfer in Open and Closed Thermosyphons," Ph.D. thesis, Purdue University, W. Lafayette, IN.

Japikse, D., and Winter, E. R. F., 1971, "Single-Phase Transport Processes in the Open Thermosyphon," *Int. J. Heat Mass Trans.*, Vol. 14, pp. 427-441.

Leslie, F. M., and Martin, B. W., 1959, "Laminar Flow in the Open Thermosyphon With Special Reference to Small Prandtl Numbers," *J. Mech. Eng. Sci.*, Vol. 1, pp. 184-193.

Lighthill, M. J., 1953, "Theoretical Considerations on Free Convection in Tubes," *Q. J. Mech. Appl. Math.*, Vol. 6, pp. 398-439.

Lock, G. S. H., and Kirchner, J. D., 1988, "Performance of an Open, Air-Filled Thermosyphon Tube With Special Reference to Wind Augmentation," *Int. J. Heat Mass Transfer*, in press.

Martin, B. W., 1955, "Free Convection in an Open Thermosyphon With Special Reference to Turbulent Flow," *Proc. Roy. Soc.*, Vol. A230, pp. 502-530.

Martin, B. W., and Cresswell, D. J., 1957, "The Influence of Coriolis Forces on Heat Transfer in the Inclined, Open Thermosyphon," *Engineer*, London, Vol. 204, pp. 926.

P. F. Peterson
Assistant Professor,
Department of Nuclear Engineering,
University of California,
Berkeley, CA 94720
Assoc. Mem. ASME

C. L. Tien
UCI Distinguished Professor.
Department of Mechanical Engineering,
University of California,
Irvine, CA 92717
Fellow ASME

Mixed Double-Diffusive Convection in Gas-Loaded Heat Pipes

This study examines mixed double-diffusive convection in gas-loaded heat pipes and two-phase thermosyphons. The numerical simulation and experiments show that steady, laminar natural convection due to the combined effects of temperature and concentration gradients can greatly redistribute the noncondensable gas within the condenser. This change of the gas distribution, however, does not significantly alter the overall condensation heat transfer. This interesting result implies that even with natural convection present, much simpler integral models can still be applied with confidence for the design of variable-conductance heat pipes and thermosyphons.

Introduction

Under double-diffusive convection, flow is driven by buoyancy forces from two or more components diffusing at different rates. This commonly results in completely different behavior from that observed under single-component natural convection. Double-diffusive convection has been studied for a wide variety of geometries and fluid combinations, as summarized by Viskanta et al. (1985). In condensing systems containing noncondensable gases, several additional phenomenon are introduced that greatly complicate analysis, arising primarily from the nonlinear relationship between temperature and concentration at the vapor/liquid interface and from the forced convection component driven by the condensation. This study of gas-loaded heat pipes and two-phase closed thermosyphons shows how these new complications can be dealt with, and quantifies the effects of double-diffusive mixed convection on the operation of these useful heat transfer devices.

When temperature and concentration gradients cause mixed forced and natural convection in gas-loaded heat pipes and thermosyphons, the natural convection component recirculates and significantly changes the distribution of the noncondensable gas inside the condenser. Several inherent features of gas-loaded devices complicate numerical modeling and quantification of the effects of this mixed convection. Condensation, at spatially varying rates, drives the forced component of the convection. Temperature and concentration gradients in the region between the gas and the vapor drive the double-diffusive natural convection component. The low velocities in the diffusion region require the use of full elliptic equations, rather than the simpler parabolic forms that can be applied in some pipe flow evaporation and condensation problems (Lin et al., 1988). The greatest difficulties in numerical modeling arise from the complicated nature of the boundary conditions. Phase equilibrium requires a highly nonlinear relationship between the gas concentration and the temperature at the wall. Thus, at lower gas concentrations, small changes of the gas fraction at the vapor/liquid interface result in large temperature changes. This large sensitivity to the presence of gas causes an abrupt decrease of the pipe wall temperature and condensation rate to occur over a short axial distance, giving gas-loaded devices their characteristically steep axial temperature profile and clearly defined shut-off zone.

Both the nonlinear boundary conditions and the velocity field help to couple the species and momentum equations. Rohani and Tien (1973) first overcame the difficulty of the nonlinear boundary conditions by assuming a parabolic temperature profile for the three nodes next to the wall, rather than requiring that the liquid/vapor interface be impermeable to the noncondensable gas. Although they did not cite Rohani and Tien (1973) as their source, Galaktinov and Trukhanova (1985) used an identical approach and equations, with the same assumptions for the boundary conditions, except for the addition of buoyancy terms to the momentum equation and a constant-heat-flux evaporator boundary condition. Kobayashi and Matsumoto (1987) also encountered these difficulties and were forced to use experimentally measured values of the wall temperature, stream function, and vorticity as boundary conditions.

To address the difficulties with the nonlinear boundary conditions encountered by previous investigators, this study makes use of a modified formulation of the species equation to provide an initial solution for $\mathrm{Ra}=0$. This $v_g=0$ formulation uses the fact that the gas velocity v_g is small. Using this information helps to reduce the coupling through the velocity field, making it possible to solve the species equation independently from the momentum and other conservation equations. This $v_g=0$ solution provides values for the suction velocities, wall temperatures, and wall gas concentrations. The assumption that $v_g=0$ is then relaxed, and the $v_g=0$ wall values are then used as boundary conditions to solve the complete momentum, continuity, species, and energy equations. These wall values satisfy all the boundary conditions exactly, except the constraint that the vapor/liquid interface be impermeable to the noncondensable gas. The impermeability constraint is satisfied approximately by axially shifting the boundary values obtained from the $v_g=0$ solution, until the absolute flux of gas through the vapor/liquid interface is minimized.

The most interesting result obtained using this numerical model is that with steady laminar flow, the gas redistribution due to natural convection does not significantly alter total condensation heat transfer, a result confirmed by experimental tests. This implies that the simple two-dimensional integral model developed previously (Peterson and Tien, 1989) provides an excellent design tool, even when laminar natural convection exists.

Formulation

In cylindrical heat pipes, mixed convection is three-dimensional. Axial stratification of the gas and vapor results since with gravity the gas tends to flow down along one side of the pipe, while the vapor flows up along the other, as shown experimentally by Peterson and Tien (1988). However, important, fundamental questions about the effects of natural convection on performance can be answered by studying the simpler planar two-dimensional heat pipe. Figure 1 illustrates the planar geometry, where condensation occurs between two infinite flat plates. Experimental evidence suggests that the

Contributed by the Heat Transfer Division for publication in the JOURNAL OF HEAT TRANSFER. Manuscript received by the Heat Transfer Division November 14, 1988. Keywords: Double Diffusion Systems, Heat Pipes and Thermosyphons, Mixed Convection.

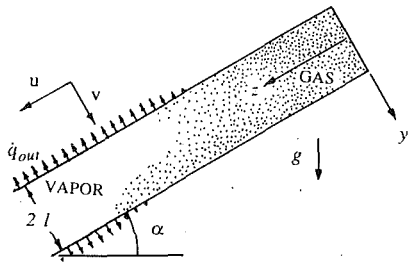

Fig. 1 Geometry for two-dimensional planar heat pipe

major finding of this numerical study, that steady laminar natural convection does not significantly alter the quantity of heat transported, can be readily applied to the three-dimensional heat pipe.

To provide results consistent with and comparable to those of the simpler integral model (Peterson and Tien, 1989), variation of the molar density with temperature is neglected in the modified species equation, and the vapor/gas mixture properties are assumed constant. In addition, axial wall conduction is neglected here. Peterson and Tien (1989) explore the effects of wall conduction in depth.

Modified Species Equation. To address the difficulties with boundary conditions, and to allow precise specification of vapor flow into the condenser, it is desirable to derive a modified form of the species equation based on molar properties, but independent of the average molar velocity. This $v_g = 0$ formulation gives values of the suction velocity, wall temperatures, and wall gas concentrations, for use as boundary conditions for the momentum, continuity, species, and energy equations. The derivation starts with the molar form of Fick's law

$$cx_g\mathbf{v}_g = cx_g\mathbf{V} - cD\nabla x_g \tag{1}$$

where $\mathbf{v}_g$ is the absolute velocity of the gas, $\mathbf{V}$ the average-molar-velocity vector, x_g the gas molar fraction, c the molar density, and D the diffusion coefficient. Continuity for the mixture requires that

$$\nabla \cdot (c\mathbf{V}) = 0 \tag{2}$$

The primary advantage derived from the use of molar quantities is now invoked. For most gas mixtures at lower or moderate pressures, the molar density c can be assumed to be constant, if variations in pressure and temperature are small. Using this, dividing equation (1) by cx_g, combining equations (1) and (2), noting that $(\nabla x_g)/x_g = \nabla \ln x_g$, and assuming that the gas remains stationary, results in the modified species equation

$$\nabla^2(\ln x_g) = 0 \tag{3}$$

Boundary conditions for the modified species equation arise from energy conservation, combined with the requirement of vapor/liquid-interface impermeability to the gas and the requirement of phase equilibrium. Assuming that conduction through the vapor and the pipe wall are negligible, an energy balance requires that the heat gained from condensation equal the heat lost via external convection. The flux of mass and latent heat to the vapor/liquid interface is related to the slope of the gas concentration through equation (1). Additionally, a phase-equilibrium expression results from application of the Clausius–Clapeyron equation. These give boundary conditions at $y = \pm l$, respectively,

$$\pm h_{fg}M_v cD\frac{\partial(\ln x_g)}{\partial y} = h(T_i^s - T_c) \tag{4}$$

$$x_g = 1 - \exp(T_*(1 - T_e^s/T_i^s)) \tag{5}$$

where T_i^s is the interface temperature, T_e^s the saturation temperature of the pure vapor, T_c the bulk cooling-medium temperature, M_v the vapor molecular weight, and h_{fg} the latent heat of evaporation. In equation (5) $T_* = (1 - T_e^s/T_c)^{-1}\ln(1 - P_c^s/P_e^s)$, where P_c^s and P_e^s are the saturation pressures at the cooling medium and evaporator temperature, respectively.

The top of the condenser is impermeable, giving the boundary condition at $z = 0$ as

$$\partial(\ln x_g)/\partial z = 0 \tag{6}$$

Use of equation (1) and $\mathbf{v}_g = 0$ allows explicit specification of the total heat load of the condenser q in terms of the slope of $\ln x_g$ at the condenser entrance, avoiding an iterative solution like that of Hijikata et al. (1984). At the entrance of the condenser, $z = z_a$, there follows

$$\partial(\ln x_g)/\partial z = q/(2lh_{fg}M_v c_e D) \tag{7}$$

noting that $\ln x_g \to -\infty$ as $z \to \infty$ since $x_g \to 0$.

Nomenclature

c = molar density, kmol/m^3
c_p = specific heat, J/kgK
$\dot{\mathbf{c}}$ = net-molar-flux vector, kmol/m^{2}s
D = mass diffusivity, m^2/s
E = diffusion parameter = $(c_e M_v D h_{fg})/(h(T_e^s - T_c)l)$
F = transformed mole fraction = $E \ln x_g$
g = gravitational acceleration, m/s^2
h = heat transfer coefficient, W/m^{2}K
h_{fg} = latent heat of vaporization, J/kg
k = thermal conductivity, W/mK
l = half distance between plates, m
L_g = gas-inventory length, equation (17), m
Le = Lewis number
M = molecular weight, kg/kmol
N_g = moles of noncondensable gas, kmol
P = absolute pressure, Pa
q = heat input to condenser, W/m
Q_q^* = length shut off to condensation, equation (18)
Ra = Rayleigh number
Sc = Schmidt number
T = absolute temperature, K
T_* = constant = $(1 - T_e^s/T_c)^{-1}\ln(1 - P_c^s/P_e^s)$
u = transverse mass velocity, m/s
v = axial mass velocity, m/s
$\mathbf{v}_g$ = gas absolute velocity vector, m/s
$\mathbf{V}$ = molar average velocity vector, m/s
x = mole fraction
y = transverse coordinate, m
z = axial coordinate, m
α = inclination angle from horizontal
θ = dimensionless temperature = $(T - T_c)/(T_e^s - T_c)$
θ_c = dimensionless temperature = $T_c/(T_e^s - T_c)$
μ = dynamic viscosity, kg/ms
ρ = mass density, kg/m^3
ω = mass fraction

Subscripts

a = condenser end
c = cooling-medium temperature
d = desired value
e = evaporator
f = flat front
F = value obtained from modified species equation
g = noncondensable gas
i = interface between vapor and liquid/wick structure
v = vapor

Superscripts

s = saturation
$*$ = nondimensional quantity

Other Conservation Equations. After boundary values from the $v_g = 0$ solution are obtained, the actual velocity field can be determined using the other conservation equations. To simplify the task of determining the velocity field, the Boussinesq approximation is invoked in the momentum equations

$$c_c M_v \left(u \frac{\partial u}{\partial z} + v \frac{\partial u}{\partial y}\right) = - \frac{\partial P}{\partial z} + \mu \left(\frac{\partial^2 u}{\partial z^2} + \frac{\partial^2 u}{\partial y^2}\right) + \rho g \sin \alpha \tag{8}$$

$$c_c M_v \left(u \frac{\partial v}{\partial z} + v \frac{\partial v}{\partial y}\right) = - \frac{\partial P}{\partial y} + \mu \left(\frac{\partial^2 v}{\partial z^2} + \frac{\partial^2 v}{\partial y^2}\right) + \rho g \cos \alpha \tag{9}$$

where P is the pressure, μ the dynamic viscosity, ρ the local density, α the pipe inclination angle, v the transverse mass-average velocity, u the axial mass-average velocity, y the transverse coordinate, and z the axial coordinate measured from the top of the condenser, as shown in Fig. 1. Total mass conservation requires

$$\frac{\partial}{\partial z}(\rho u) + \frac{\partial}{\partial y}(\rho v) = 0 \tag{10}$$

The species conservation equation is

$$\rho u \frac{\partial \omega_g}{\partial z} + \rho v \frac{\partial \omega_g}{\partial y} = D\left(\frac{\partial}{\partial z}\left(\rho \frac{\partial \omega_g}{\partial z}\right) + \frac{\partial}{\partial y}\left(\rho \frac{\partial \omega_g}{\partial y}\right)\right) \tag{11}$$

where ω_g is the gas mass fraction. Note that both the gas mass fraction and mole fraction are used in this work, depending on which is the most convenient for the particular task.

The energy equation is simplified by assuming constant thermal diffusivity

$$u \frac{\partial T}{\partial z} + v \frac{\partial T}{\partial y} = \frac{k}{\rho c_p}\left(\frac{\partial^2 T}{\partial z^2} + \frac{\partial^2 T}{\partial y^2}\right) \tag{12}$$

where T is the temperature, k the thermal conductivity, and c_p the specific heat at constant pressure.

The boundary conditions for these conservation equations are obtained from the solution of the modified species equation. The momentum boundary conditions result from the normal velocity obtained in the species-equation solution and the no-slip condition. Mass conservation uses the same normal velocity. The wall gas concentrations and temperatures obtained from the species equation solution are used as boundary conditions for species and energy, respectively. There results, at $y = \pm l$

$$\rho v = [M_v c D\, \partial(\ln x_g)/\partial y]_F, \qquad u = 0 \tag{13}$$
$$\omega_g = \omega_{g,F}, \qquad T = T_F$$

where the subscript F denotes the value obtained from the solution of the modified species equation. The top of the condenser is assumed adiabatic and impermeable, giving boundary conditions at $z = 0$,

$$u = 0, \quad v = 0, \quad \partial \omega_g/\partial z = 0, \quad dT/dz = 0 \tag{14}$$

At the entrance of the condenser a parabolic profile is assumed for the velocity, and the entering vapor is assumed to be pure at the evaporator saturation temperature, giving boundary conditions at $z = z_a$

$$\rho u = \frac{3}{4}\frac{q}{l\, h_{fg}}\left(\left(\frac{y}{l}\right)^2 - 1\right), \qquad T = T_c^s \tag{15}$$
$$\omega_g = 0, \qquad \rho v = [M_v c D\, \partial(\ln x_g)/\partial y]_F$$

The quantity of noncondensable gas in the heat pipe is

$$N_g = \int_0^\infty \int_{-l}^{l} c_g \, dy \, dz \tag{16}$$

where c_g is the local molar density of the gas. The gas inventory is related to the condenser geometry by

$$L_g = \int_0^\infty \int_{-1}^{l} (c/c_c) x_g \, d(y/l) \, d(z/l) \tag{17}$$

where L_g is the length the gas would occupy if all the gas were restricted to the top of the condenser at the cooling medium temperature. The function c/c_c is the ratio of the local molar density at the local temperature T to the total molar density at the cooling-medium temperature T_c. This function corrects for the change in the local molar density due to temperature variation. For an ideal gas, $c/c_c = T_c/T$.

Dimensionless Formulation. The following parameters are used for nondimensionalization:

$$y^* = y/l \qquad z^* = z/l \qquad v^* = vl/D \qquad u^* = ul/D$$
$$\theta = (T - T_c)/(T_e^s - T_c)$$
$$E = (c_e M_v D h_{fg})/(h(T_e^s - T_c)l) \qquad \rho^* = \rho/c_c M_v$$
$$\theta_c = T_c/(T_e^s - T_c) \qquad M^* = M_g/M_v - 1 \qquad P^* = Pl^2/c_c M_v D^2$$
$$\mathrm{Sc} = \mu/c_c M_v D \qquad \mathrm{Le} = k/c_p c_c M_v D \qquad \mathrm{Ra} = g l^3/D^2$$
$$F = E \ln x_g \qquad Q_g^* = z_a/l - q/(2lh(T_e^s - T_c))$$
$$L^*{}_g = L_g/l = N_g/2c_c l^2 \tag{18}$$

In nondimensional form, the modified species equation (3) becomes

$$\frac{\partial^2 F}{\partial z^{*2}} + \frac{\partial^2 F}{\partial y^{*2}} = 0 \tag{19}$$

The boundary conditions for the modified species equation become

at $y^* = \pm 1$

$$\pm\left(\frac{\partial F}{\partial y^*}\right) = \theta \tag{20}$$

$$\exp(F/E) = 1 - \exp\left(T_* \frac{(\theta - 1)}{(\theta + \theta_c)}\right) \tag{21}$$

at $z^* = 0$

$$dF/dz^* = 0 \tag{22}$$

at $z^* = z_a^*$

$$\partial F/\partial z^* = z_a^* - Q_{g,d}^* \tag{23}$$

where $z_a^* - Q_{g,d}^*$ is the active condenser length and corresponds to the desired heat input q through equation (18).

In nondimensional form the momentum equations become

$$u^* \frac{\partial u^*}{\partial z^*} + v^* \frac{\partial u^*}{\partial y^*} = - \frac{\partial P^*}{\partial z^*} + \mathrm{Sc}\left(\frac{\partial^2 u^*}{\partial z^{*2}} + \frac{\partial^2 u^*}{\partial y^{*2}}\right) + \mathrm{Ra} \sin \alpha \left(\frac{\theta_c}{\theta + \theta_c}\right)(1 + M^* x_g) \tag{24}$$

$$u^* \frac{\partial v^*}{\partial z^*} + v^* \frac{\partial v^*}{\partial y^*} = - \frac{\partial P^*}{\partial y^*} + \mathrm{Sc}\left(\frac{\partial^2 v^*}{\partial z^{*2}} + \frac{\partial^2 v^*}{\partial y^{*2}}\right) + \mathrm{Ra} \cos \alpha \left(\frac{\theta_c}{\theta + \theta_c}\right)(1 + M^* x_g) \tag{25}$$

Mass conservation is written

$$\frac{\partial}{\partial z^*}((1 + M^* x_g) u^*) + \frac{\partial}{\partial y^*}((1 + M^* x_g) v^*) = 0 \tag{26}$$

The species conservation equation is

$$(1+M^*x_g)\left[u^*\frac{\partial\omega_g}{\partial z^*}+v^*\frac{\partial\omega_g}{\partial y^*}\right]$$

$$=\frac{\partial}{\partial z^*}\left((1+M^*x_g)\frac{\partial\omega_g}{\partial z^*}\right)+\frac{\partial}{\partial y^*}\left((1+M^*x_g)\frac{\partial\omega_g}{\partial y^*}\right) \quad (27)$$

The energy equation is

$$u^*\frac{\partial\theta}{\partial z^*}+v^*\frac{\partial\theta}{\partial y^*}=\mathrm{Le}\left(\frac{\partial^2\theta}{\partial z^{*2}}+\frac{\partial^2\theta}{\partial y^{*2}}\right) \quad (28)$$

The boundary conditions for these conservation equations become

at $y^*=\pm 1$

$$(1+M^*x_g)v^*=[\partial(\ln F/E)/\partial y^*]_F, \qquad u^*=0 \quad (29)$$
$$\omega_g=\omega_{g,F}, \qquad \theta=\theta_F$$

at $z^*=0$

$$u^*=0, \quad v^*=0, \quad \partial\omega_g/\partial z^*=0, \quad d\theta/dz^*=0 \quad (30)$$

at $z^*=z_a^*$

$$u^*=\frac{3}{2}(z_a^*-Q_{g,d}^*)(y^{*2}-1)/E, \qquad \theta=1 \quad (31)$$
$$\omega_g=0, \qquad v^*=[\partial(F/E)/\partial y^*]_F$$

The gas-inventory length, equation (17), becomes

$$L_g^*=\int_0^\infty\int_{-1}^{1}(1+\theta/\theta_c)^{-1}\exp(F/E)dy^*dz^* \quad (32)$$

using the nondimensional ideal-gas relation for c/c_c. The length effectively shut off to condensation heat transfer by this quantity of gas is

$$Q^*{}_g=\int_0^\infty(1-0.5(\theta_{y^*=-1}+\theta_{y^*=-1}))dz^* \quad (33)$$

To verify the assumption of laminar flow, derivation of a simple form of the Reynolds number is valuable

$$\mathrm{Re}=2\rho ul/\mu=(z^*-Q_g^*)/(E\,\mathrm{Sc}) \quad (34)$$

Since E is normally of order unity (Peterson and Tien, 1989) and the nondimensional active length, $z^*-Q_g^*$, is normally small, the Reynolds number is small and well within the laminar regime as assumed here, particularly in the vicinity of the gas front.

Solution Procedure

The solution procedure uses the iterative semi-implicit routine discussed by Patankar (1980). The power-law scheme is used for the convection-diffusion formulations. The solution of the modified-species equation provides boundary conditions for the momentum and other conservation equations. The solution proceeds as follows.

1 Assuming the gas to be stationary, $v_g=0$, solve equation (19) for the distribution of F. Rather than using the method Hijikata et al. (1984), a line-by-line iterative scheme performs well. The domain is divided into axial columns of nodes. Each row is then solved explicitly using a tridiagonal matrix algorithm, assuming the node values at the neighboring rows remain constant. This method pulls information from the boundary rapidly to the center and speeds convergence. Line-by-line iteration allows use of a linearized form of the boundary conditions, which can be developed by performing a Taylor-series expansion of equation (21) around the value of the wall temperature from the previous iteration, θ_o,

$$F=F_o+(\theta-\theta_o)\left[\frac{dF}{d\theta}\right]_o \quad (35)$$

This equation, together with equation (20), relates the absolute value of F to its slope, producing a mixed boundary condition for the species equation at $y^*=\pm 1$

$$F=F_o+\left(\pm\frac{\partial F}{\partial y^*}-\theta_o\right)T_*E\frac{(\theta_o+1)}{(\theta_o+\theta_c)^2}$$
$$\left[1-\exp\left(-T_*\frac{\theta_o+1}{\theta_o+\theta_c}\right)\right]^{-1} \quad (36)$$

If the tridiagonal matrix algorithm is applied more than once at each row of nodes, iterating at a row until convergence is obtained for θ_o and then proceeding to the next row, the solution converges. After iterating through all the rows, the solution is checked to see how well it satisfies the finite-difference equations. When the maximum absolute error for any difference is less than 10^{-4}, the solution is considered to be converged.

2 Given the solution for F, the normal velocities (condensation rates) at the condenser walls are known. If a parabolic axial velocity profile is assumed, than an integral form of the mass-conservation equation can provide an initial guess for the velocity profile with no natural convection.

3 Since conduction in the vapor is neglected in the wall energy balance, the solution for F also specifies the wall temperature. Using this temperature distribution as the boundary condition, and the velocity profile obtained in the previous step, the energy equation, equation (28), can be solved for the temperature distribution using a line-by-line routine with relaxation. Likewise the species equation (27) can be solved for ω_g.

4 With the velocities given at the boundaries and a density distribution calculated from the results of step 3, the momentum and continuity equations can be solved using any desired method. Here the SIMPLER method, given by Patankar (1980), is used.

5 Steps 3 and 4 are repeated until a converged solution is obtained for $\mathrm{Ra}=0$.

6 The Rayleigh number is then increased and steps 3 and 4 are repeated until a converged solution is obtained. For this solution the absolute quantity of gas passing in and out through the boundary is calculated

$$\dot{c}_g/c=\int_0^{z_a^*}\left|(1+M^*x_g)(\omega_g v^*-\partial\omega_g/\partial y^*)\right|_{y^*=-1}$$
$$+\left|(1+M^*x_g)(\omega_g v^*-\partial\omega_g/\partial y^*)\right|_{y^*=1}dz^* \quad (37)$$

The boundary values of the velocity, temperature, and concentration are then shifted up one side and down the other by a single grid increment. Again a solution is obtained using steps 3 and 4 and the integral in equation (37) is evaluated. This shifting of the wall velocity, temperature, and concentration profiles by increments is repeated, until the minium value of the gas-flux integral is found. This is the set of boundary conditions that best satisfies the constraint that the interface be impermeable to gas.

Results

Figure 2 shows typical examples of velocity and concentration fields in a gas-loaded device, comparing numerical results for Rayleigh numbers ranging from zero to 800 to the approximate pure-diffusion result of the modified species equation. For these cases $M^*=1$, which means that the buoyancy forces due to temperature and concentration gradients augment each other and strengthen the natural convection. The velocity vectors graphically illustrate the concentration and temperature-gradient driven recirculation, which begins to occur as the Rayleigh number increases in this $\alpha=45$ deg orientation. The lighter vapor flows up across the top (left), condensing on the wall. The heavier gas/vapor mixture tends to flow down across the bottom (right). The downward flowing gas diffuses

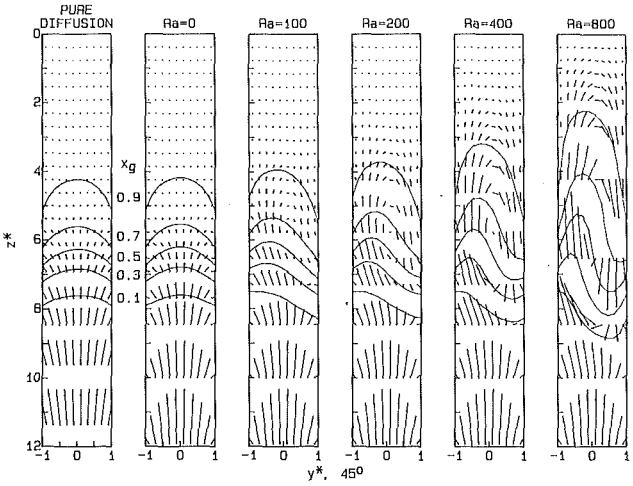

Fig. 2 Typical isoconcentration profiles and velocity vectors

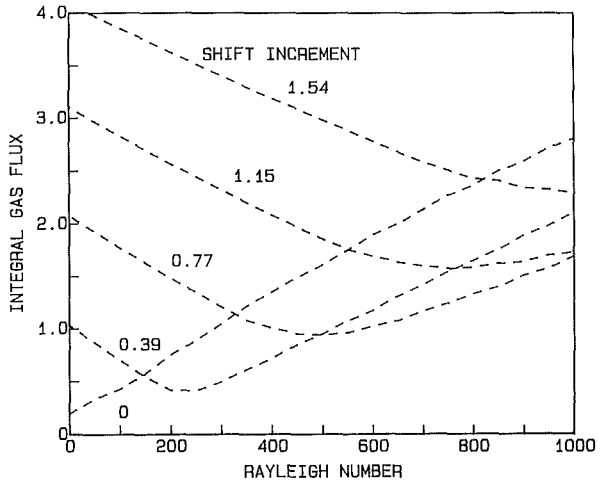

Fig. 3 Integral of absolute gas flux through the interface versus the Rayleigh number

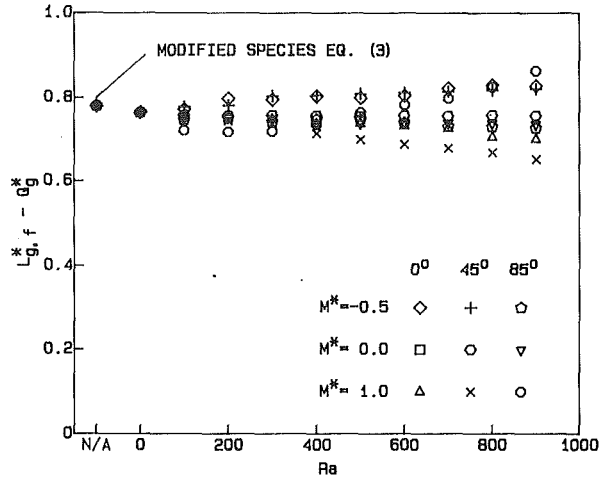

Fig. 4 Parametric study of the effect of Rayleigh number on total heat transfer

up into the rising vapor, which carries the gas back up, resulting in steady recirculation of the gas.

The modified species equation ($v_g = 0$) can be easily solved with numerical or integral techniques (Peterson and Tien, 1988), and the left side of Fig. 2 shows that the isoconcentration profiles from this simpler method match the exact numerical Ra = 0 results very closely. The modified species equation, equation (3), is identical to the potential flow equation, except the concentration gradient provides the flow driving force, rather than a pressure gradient. As with potential flow, slip exists at the boundary, giving a slug-flow velocity profile.

To satisfy approximately the constraint of gas/vapor interface impermeability to the gas species, this model axially shifts the boundary values obtained from the modified species equation. For different Rayleigh number values and shifting distances, the model predicts different absolute quantities of gas, as given by equation (37), blowing through the interface. Figure 3 illustrates how for increasing shifting increments this gas quantity reaches a minimum at increasing values of the Rayleigh number, for a typical case where $\alpha = 0$ deg and $M^* = -0.5$. These points of minimum absolute gas flux are the Rayleigh number values that best satisfy the gas impermeability constraint.

The question of greatest practical interest involves the effect of mixed convection on the total heat transfer. The parametric study summarized in Fig. 4 shows that the Rayleigh number, inclination angle, and nondimensional gas molecular weight M^* have a minimal effect on the total heat transfer. The most general way to specify the total heat transfer q, as given nondimensionally by Q_g^* (equation (18)), is by relating it to the actual quantity of gas N in the pipe using equation (18) and the very simple flat-front model, $L^*_{g,f} = L^*_g / x_{g,\max}$, where $x_{g,\max}$ is the maximum gas concentration in the shut-off region. Thus the total heat transfer q is linearly related to the difference between the length that would be shut off if there were a sharp flat front, and the actual length shut off, $L^*_{g,f} - Q^*_g$. The case shown in Fig. 2, where the gas distribution changes dramatically due to natural convection, is included in this parametric study. Even for this case the length shut off by gas changes by only slightly more than 1/10 of a pipe radius over the entire range of Rayleigh numbers.

These numerical results showing minimal overall effect on heat transfer are consistent with the experimental observations of Peterson and Tien (1988), where the orientation of a gas-loaded thermosyphon was changed from horizontal to 45 deg to vertical. Then, for the cases where only one gas species was used and under stable conditions (disturbances can occur at higher Rayleigh numbers in the vertical orientation), the total pressure was observed to vary by less than 1.0 percent, even though the gas distribution changed significantly with changing orientation. Thus both numerical and experimental results show that the three simple methods for calculating $L^*_{g,f} - Q^*_g$ presented by Peterson and Tien (1989) assuming $v_g = 0$ can be applied with good accuracy for predicting total heat transfer, even when steady, laminar natural convection occurs.

Even though this numerical model strictly applies only to planar heat pipes, its results can be compared qualitatively with the experimental measurements of Peterson and Tien (1988). The comparison given in Fig. 5 is for the helium/water system, which is interesting since the buoyancy forces due to temperature and concentration oppose each other. Noting that the experimental concentration measurements were made in an arc that did not reach the top or bottom of the cylinder, good qualitative agreement is obtained between the experimental and the corresponding numerical analysis, based on the same hydraulic diameter $l = r_i$, and on the parameter values Ra = 170, $M^* = -0.78$, $\theta_c = 6.85$, and $T^* = 17.0$. The numerically generated velocity vectors illustrate the flow patterns. For the horizontal orientation the lighter helium/water mixture flows up from the shut-off zone over the heavier water vapor. In the vertical orientation ($\alpha = 88$ deg) the system is stable with negligible natural convection.

Figure 6 illustrates the effects of different diffusion rates for heat and mass. It shows isoconcentration profiles and isotherms for a horizontal system with $M^* = 0.5$, at three dif-

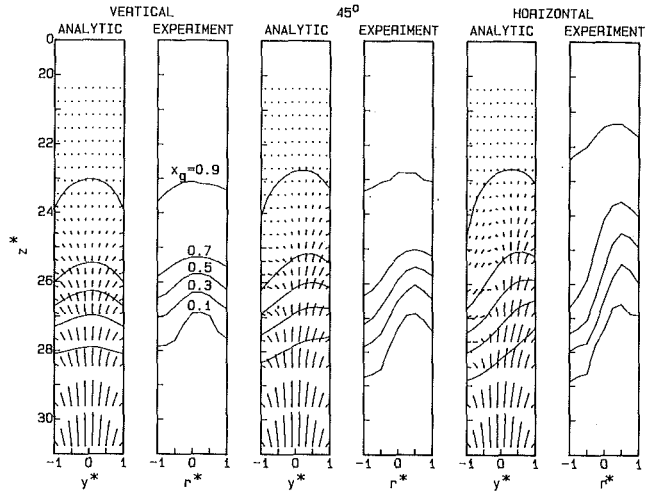

Fig. 5 Comparison of numerical (planar, with velocity vectors) and experimental (cylindrical) isoconcentration profiles for a helium/water system (right is bottom)

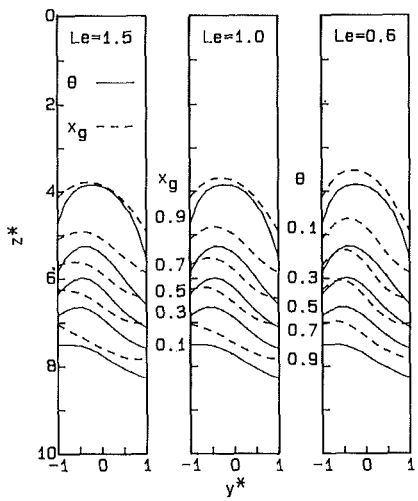

Fig. 6 Isoconcentration profiles and isotherms for different Lewis numbers (right is bottom)

ferent values of the Lewis number. The isotherm shapes are similar to those of the isoconcentration profiles. For Lewis numbers equal to or greater than one, subcooling occurs in the diffusion region. These small amounts of subcooling were also observed experimentally, quantitatively by measurements of the wet and dry-bulb temperatures and qualitatively by condensation occurring on a wet-bulb probe, as discussed by Peterson and Tien (1988). At smaller Lewis numbers some superheating of the vapor occurs.

The results presented here, unless otherwise noted, were calculated with the following parameter values: $E=1.0$, $\theta_c=5.0$, $T_*=15.0$, $\alpha=0$, $M^*=0.5$, $\mathrm{Le}=1.0$, $\mathrm{Sc}=1.0$, $Q_g^*=6.0$, and $z_a^*=15$. A 40×12 grid was used. Halving the grid increment to produce a 80×24 grid resulted in less than a 1 percent change in the integral gas value L_g^*, or a 7 percent change in $L_{gf}^*-Q_g^*$.

Conclusions

Double-diffusive natural convection due to temperature and concentration gradients can significantly redistribute the noncondensable gas in a heat pipe or thermosyphon condenser. This redistribution can be especially large when $M^*>0$ and the buoyancy forces from temperature and concentration augment each other. Both the numerical simulation of a planar heat pipe and experiments show that steady, laminar double-diffusive convection does not significantly alter the total heat transfer of gas-loaded devices, compared to the heat transfer predicted by an approximate pure diffusion model based on the modified species equation. The error from neglecting natural convection when calculating the shut-off length using this simplified pure-diffusion approach is commonly under 1/10 of a pipe radius. This means that the three simple calculation methods presented by Peterson and Tien (1989) can be applied with confidence, even when laminar natural convection exists. There are two situations where natural convection effects do become important. The first occurs at low power levels when the gas front is near the entrance of the condenser, creating a discontinuity in the boundary conditions. Then natural convection can result in "heat-leaks" since it causes the vapor to flow over or under the gas and into the condenser, when the simplified axisymmetric models would predict complete shut off. The second situation occurs when a device is instrumented to measure wall temperatures. Here the circumferential location of the temperature sensor becomes important, and ideally more than one sensor should be provided at each axial location.

Acknowledgments

The support of the National Science Foundation through Grant No. CBT 8807174 is sincerely appreciated.

References

Edwards, D. K., and Marcus, B. D., 1972, "Heat and Mass Transfer in the Vicinity of the Vapor-Gas Front in a Gas-Loaded Heat Pipe," ASME JOURNAL OF HEAT TRANSFER, Vol. 94, pp. 155-162.

Galaktionov, V. V., and Trukhanova, L. P., 1985, "Study of the Process of Heat and Mass Transfer in the Region of the Vapor-Gas Front in a Gas-Regulable Heat Pipe," *Journal of Engineering Physics*, Vol. 48, pp. 296-300.

Hijikata, K., Chen, S. J., and Tien, C. L., 1984, "Non-condensable Gas Effect on Condensation in a Two-Phase Closed Thermosyphon," *International Journal of Heat and Mass Transfer*, Vol. 27, pp. 1319-1325.

Kobayashi, Y., and Matsumoto, T., 1987, "Vapor Condensation in the Presence of Non-condensable Gas in the Gravity Assisted Thermosyphon," *Proceedings of the Sixth International Heat Pipe Conference*, Grenoble, France, May 25-29, Paper No. 3.1.1.

Lin, T. F., Chang, C. J., and Yan, W. M., 1988, "Analysis of Combined Buoyancy Effects of Thermal and Mass Diffusion on Laminar Forced Convection Heat Transfer in a Vertical Tube," ASME JOURNAL OF HEAT TRANSFER, Vol. 110, pp. 337-344.

Patankar, S. V., *Numerical Heat and Fluid Flow*, 1980, Hemisphere, Washington, DC.

Peterson, P. F., and Tien, C. L., 1988, "Gas-Concentration Measurements and Analysis for Gas-Loaded Thermosyphons," ASME JOURNAL OF HEAT TRANSFER, Vol. 110, pp. 743-747.

Peterson, P. F., and Tien, C. L., 1989, "Numerical and Analytical Solutions for Two-Dimensional Gas Distribution in Gas-Loaded Heat Pipes," ASME JOURNAL OF HEAT TRANSFER, Vol. 111, pp. 598-604.

Rohani, A. R., and Tien, C. L., 1973, "Steady Two-Dimensional Heat and Mass Transfer in the Vapor-Gas Region of a Gas-Loaded Heat Pipe," ASME JOURNAL OF HEAT TRANSFER, Vol. 95, pp. 377-382.

Viskanta, R., Bergman, T. L., and Incropera, F. P., 1985, "Double-Diffusive Natural Convection," *Natural Convection, Fundamentals and Applications*, S. Kakac, W. Aung, and R. Viskanta, eds., Hemisphere Publishing Corporation, Washington, DC, pp. 1075-1099.

Transient Heat Transfer in a Fluid Sphere Translating in an Electric Field

J. N. Chung
Mem. ASME

D. L. R. Oliver

Department of Mechanical and Materials Engineering,
Washington State University,
Pullman, WA 99164-2920

The transient heat transfer in a fluid sphere translating steadily in a dielectric medium is numerically investigated. The energy equation with velocity components of combined translation-induced and electric field-induced internal motion is integrated by the Alternating Direction Implicit (ADI) method for the entire drop interior. Creeping flow is assumed and the preponderance of the thermal resistance is assumed completely in the dispersed phase. The enhancement of heat transfer due to internal motion induced by both drop translation and the electric field is given in terms of the Nusselt number. Nusselt numbers are plotted as a function of the Fourier number, the Peclet number, and a parameter E. The parameter E represents the ratio of electric field-induced flow strength to that of translation-induced flow. In general, the heat transfer rate is approximately doubled when the flow is dominated by the electric field as compared with the case where no electric field is applied. It is suggested that for large Peclet numbers, the electric field is negligible for E less than 0.5, while the translation is unimportant for E larger than 10. For small Peclet numbers, the electric field is of minor importance for E less than 2 and the translation is insignificant for E greater than 50.

Introduction

The transport mechanisms inside a drop with hybrid internal motion, which results from the translational motion of the drop and a uniform electric field (parallel to the gravitational field), have not been completely understood. Because of the enhanced flow motion, higher transport rates have been predicted and measured in heat and mass transfer systems. Qualitative and quantitative information on the enhancement of transfer rates by an electric field will help engineers design more efficient systems that depend on interfacial exchange of momentum, heat, and mass between the continuous phase and the dispersed phase. Compact direct-contact heat exchange, spray cooling and combustion, and extraction processes are examples of such systems. A wider understanding in this area is essential. In this paper, numerical model and parametric sample solutions are provided for the heat transfer inside a drop slowly translating in a dielectric medium with a uniform electric field applied. The preponderence of the heat transfer resistance is assumed to be in the dispersed phase. This is the so-called internal problem, which is practically valid for drops of high Biot number defined by the product of the external heat transfer coefficient and the drop diameter divided by the thermal conductivity of the drop. For example, vapor bubbles rising in liquids or droplets experiencing condensation at the interface fall into this category. The relative importance of the presence of the electric field in improving convective heat transfer is indicated by a dimensionless parameter E, which represents the ratio of the maximum electric field-driven velocity to the maximum surface velocity owing to translation of the drop. Therefore

$$E=\frac{2V(1+X)}{U_\infty} \tag{1}$$

where V is the maximum interfacial velocity generated by the electric field in the absence of droplet translation. U_∞ is the steady translational velocity of the drop without an applied electric field. $U_\infty/2(1+X)$ gives the maximum drop surface velocity in the absence of an electric field for a drop in creeping motion. X is the viscosity ratio between the drop and the ambient fluid. As compared with unity, large values of E indicate that electric field-driven flow dominates, while small E implies that translation-induced internal flow is the main convective force. Most of the previous investigations related to heat transfer in a droplet assumed either that the droplet was stationary in an electric field or that it was translating in an otherwise quiescent medium. For example, Griffiths and Morrison (1979), Morrison (1977), and Oliver et al. (1985) investigated the pure electric effects and Johns and Beckmann (1966) studied the case for pure translation. We have only found the work by Chang et al. (1982) that investigated both effects. Their analysis employed boundary layer assumptions for both continuous and dispersed phases for predicting the heat transfer. But the results of Chang et al. (1982) suffer from the same problem as those of Morrison (1977) in that the boundary layer approach does not provide proper estimations for heat transfer rates except at very short values of time, i.e., before one complete lap of internal motion. In this paper, the transient energy equation with combined flow fields of translation and electric effect was solved numerically for the entire droplet interior. The validity of the boundary layer approach is also assessed in this paper using fully numerical solutions.

Theoretical Formulation

In this analysis, we consider a dielectric fluid sphere of radius R, which is translating steadily at velocity U_∞ in a uniform electric field. The droplet with a uniform initial temperature of T_0 is suddenly exposed to an ambient fluid of temperature T_∞. A transient heat transfer analysis is conducted for the interior of the droplet. The present paper deals with the transient heat transfer in the dispersed phase, which is decoupled with the continuous phase by providing the necessary conditions at the surface of the fluid sphere. The justification for only investigating the dispersed phase transport process is given as follows:

1 In many transport processes involving a fluid sphere and its surrounding fluid, the transport in the continuous phase can be considered quasi-steady relative to the dispersed phase (Sundararajan and Ayyaswamy, 1984) and the dispersed phase must always be treated as a transient process owing to the im-

Contributed by the Heat Transfer Division for publication in the JOURNAL OF HEAT TRANSFER. Manuscript received by the Heat Transfer Division November 13, 1987. Keywords: Multiphase Flows, Transient and Unsteady Heat Transfer.

permeable condition at the center of the fluid sphere. Therefore dispersed phase transport is dominant and the characteristics of the entire conjugate process rest on the dispersed phase. This paper intends to provide useful insights into the dispersed phase process similar to Prakash and Sirignano's (1978) exclusive modeling for the transient heating of a liquid droplet.

2 Another case where the current model can be applied directly is related to the heat transfer inside a condensing droplet. For this case, the Biot number is very large because of the latent heat release and therefore the surface is almost at constant temperature. The increase in droplet size is negligible owing to the large difference in density between the gaseous and the liquid phases (Chung et al., 1986). The other assumptions in the current analysis are given as follows:

1 The fluid motion is steady and in the creeping flow regime.

2 The transport properties are constant.

3 The droplet remains spherical during the transient heating.

It should be noted that for high Reynolds number flows, the core flow in the fluid sphere may be represented by the same stream function given by equation (3) with a larger strength of $A = 3U_\infty/2R^2$. As a result, many important aspects of this analysis may be applied closely for high Reynolds number cases. The schematic of the system is shown in Fig. 1(*a*).

Flow Equations. For a dielectric fluid sphere translating in another such fluid with a uniform electric field applied in the direction of the motion, the internal motion within the fluid sphere is induced by the tangential shear stresses at the interface, as shown in Fig. 1. These stresses are caused by the relative motion between the dispersed and the continuous phases and by the interaction of the charges that accumulate at the interface owing to the electric field. Based on the creeping flow assumption, the nonlinear advection term is negligible and the total flow is thus the linear combination of the pure translation solution given by Hadamard (1911) and Rybczynski (1911), and the pure electric field-driven internal flow given by Taylor (1966).

Therefore the assumptions and limitations adopted in these two papers are carried over to the current analysis and will not be repeated here. Chang et al. (1982) also used the same combined flow fields for a heat transfer analysis under high Peclet numbers with a boundary layer approach. Taylor and Acrivos (1968) investigated the drop deformation for the Hadamard-Rybczynski flow, and Stewart and Morrison (1979) conducted

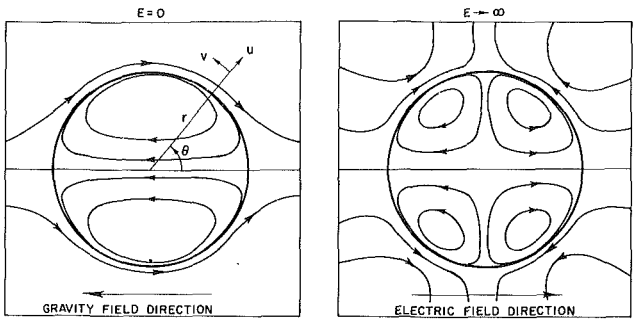

Fig. 1 Physical coordinate system and streamlines in a drop for $E = 0$ and $E \to \infty$

a similar study for the Taylor flow. Both reported that the maximum drop deformation is one order of magnitude smaller than the flow field and therefore the effect is neglible in low Reynolds number flows. Based on a creeping-flow assumption, the deformation of the drop in our problem may also be neglected, which supports the sphericity assumption made in previous sections. The stream function is

$$\hat{\psi} = \hat{\psi}_{tr} + \hat{\psi}_{el} \tag{2}$$

where

$$\hat{\psi}_{tr} = \frac{A}{2}(\hat{r}^4 - R^2\hat{r}^2)\sin^2\theta \tag{3}$$

and $\hat{r}$ is the dimensional radial coordinate.

The strength of the vortex A for the creeping flow is given by

$$A = U_\infty/2(1+X)R^2 \tag{4}$$

$$\hat{\psi}_{el} = VR^2(\hat{r}^3/R^3 - \hat{r}^5/R^5)\sin^2\theta\cos\theta \tag{5}$$

The maximum surface velocity V owing solely to the electric field is equal to

$$V = \frac{9F^2Rd_2[1-(\sigma_1 d_1)/(\sigma_2 d_2)]}{8\pi(2+\sigma_1/\sigma_2)^2 5(\mu_1+\mu_2)} \tag{6}$$

where σ and d are the electrical resistivity and dielectric constant, respectively. The subscripts 1 and 2 refer to the continuous and dispersed phases, respectively. F is the electric field strength. It is noted that because the flow induced by the electric field contributes no net drag force to the droplet (Chang et al., 1982), the steady translation velocity is unaffected by the presence of electric field-driven flows. The

Nomenclature

A = vortex strength owing to translation only
d = dielectric constant
E = ratio of maximum electric field-driven velocity to that of translation-induced velocity
F = electric field strength
k = thermal conductivity
Nu = Nusselt number defined by equation (23)
Pe = Peclet number $= U_c 2R/\alpha_2$
q'' = local heat flux at droplet surface
Q = total rate of heat transfer from the drop surface to the interior at any instant
r = dimensionless radial coordinate $= \hat{r}/R$
$\hat{r}$ = dimensional radial coordinate
R = drop radius
t = dimensional time
T = temperature
T_o = drop initial temperature
T_∞ = ambient fluid temperature
u = dimensionless radial velocity
U_c = characteristic velocity for the hybrid flow
U_∞ = drop translational velocity
v = dimensionless tangential velocity
V = maximum velocity produced by the electric field
W = Zr
X = interior-to-exterior viscosity ratio
y = normal distance from droplet surface
Z = dimensionless temperature $= (T-T_o)/(T_\infty - T_o)$
α = thermal diffusivity
θ = tangential coordinate
μ = dynamic viscosity
σ = electrical resistivity
τ = dimensionless time $= \alpha_2 t/R^2$
ψ = dimensionless stream function
$\hat{\psi}$ = dimensional stream function
Δr = dimensionless radial step size
$\Delta\theta$ = dimensionless tangential step size
$\Delta\tau$ = dimensionless time step size

Subscripts

b = bulk or average
el = induced by electric field
tr = induced by drop translation
1 = exterior phase
2 = interior phase

dimensionless stream function, $\psi = \hat{\psi}/U_c R^2$, $U_c = [2U_\infty/(1+X)+V]$, is

$$\psi = \frac{\phi}{(1+X)}[(r^4 - r^2)\sin^2\theta/4 + E(r^3 - r^5)\sin^2\theta \cos\theta/2] \quad (7)$$

$$r = \hat{r}/R,\ \phi = U_\infty/U_c, \text{ and } E = 2V(1+X)/U_\infty \quad (8)$$

The dimensionless velocity components in the droplet are given by

$$u = \frac{1}{r^2 \sin\theta}\frac{\partial\psi}{\partial\theta}$$

$$= \frac{1}{(2+E/2)}[(r^2 - 1)\cos\theta/2 + E(r - r^3)(2\cos^2\theta - \sin^2\theta)/2] \quad (9)$$

$$v = -\frac{1}{r\sin\theta}\frac{\partial\psi}{\partial r}$$

$$= \frac{1}{(2+E/2)}[(1-2r^2)\sin\theta/2 + E(5r^3 - 3r)\sin\theta\cos\theta/2] \quad (10)$$

Energy Equation. The dimensionless energy equation may be written as

$$\frac{\partial Z}{\partial\tau} + \frac{\mathrm{Pe}}{2}\left(u\frac{\partial Z}{\partial r} + \frac{v}{r}\frac{\partial Z}{\partial\theta}\right)$$

$$= \frac{1}{r^2}\frac{\partial}{\partial r}\left(r^2\frac{\partial Z}{\partial r}\right) + \frac{1}{r^2\sin\theta}\frac{\partial}{\partial\theta}\left(\sin\theta\frac{\partial Z}{\partial\theta}\right) \quad (11)$$

The dimensionless temperature Z is defined as

$$Z = \frac{T - T_o}{T_\infty - T_o} \quad (12)$$

Therefore Z will vary from 0 to 1 during the transient process. The Peclet number and dimensionless time are given by $\mathrm{Pe} = U_c 2R/\alpha_2$ and $\tau = \alpha_2 t/R^2$, where α_2 is the thermal diffusivity of the dispersed phase and t is the dimensional time.

The above energy equation is solved subject to the following boundary and initial conditions:

$$Z = 1 \quad \text{at } r = 1 \text{ and all } \theta \text{ and } \tau \quad (13)$$

$$\frac{\partial Z}{\partial\theta} = 0 \quad \text{at } \theta = 0 \text{ and } \pi/2 \text{ and all } r \text{ and } \tau \quad (14)$$

$$Z \text{ is finite} \quad \text{at } r = 0 \text{ all } \theta \text{ and } \tau \quad (15)$$

$$Z = 0 \quad \text{at } \tau = 0 \text{ all } r \text{ and } \theta \quad (16)$$

It is noted that the combination of a steady flow field and a transient temperature field is consistent because the equations for mass and momentum conservation are decoupled from the energy equation.

Method of Solution

Equation (11) along with velocity components given by equations (9) and (10) and boundary and initial conditions (equations (13)-(16)) forms a well-posed parabolic partial differential equation set. The Alternating Direction Implicit (ADI) numerical method (Ames, 1977) was considered most appropriate for the current problem. Because this method is well known, most of the details of the integration procedures are neglected here. In the ADI formulation, the radial derivatives are treated implicitly for the first-half time step, while the tangential derivatives are treated explicitly. The resulting system of equations then forms a tridiagonal matrix set. It is solved line by line along the radial direction. For the second-half time step, the tangential derivatives are treated implicitly, with the radial derivative treated explicitly. With the two symmetric boundary conditions (equation (20)), the matrix form for this second-half time step is similar to that for the radial system with the only exception being that non-tridiagonal elements are in the first and the last rows. These matrix systems are then solved by Gaussian elimination without pivoting. A variable transformation, which simplifies the energy equation, is performed before numerical integration by the ADI method. By definition

$$W = Zr \quad (17)$$

Thus the energy equation based on the new variable W becomes

$$\frac{\partial W}{\partial\tau} + \frac{\mathrm{Pe}}{2}\left[u\left(\frac{\partial W}{\partial r} - \frac{W}{r}\right) + \frac{v}{r}\frac{\partial W}{\partial\theta}\right]$$

$$= \frac{\partial^2 W}{\partial r^2} + \frac{1}{r^2\sin\theta}\frac{\partial}{\partial\theta}\left(\sin\theta\frac{\partial W}{\partial\theta}\right) \quad (18)$$

The boundary and initial conditions become

$$W(r = 1, \theta, \tau) = 1 \quad (19)$$

$$\partial W(r, \theta = 0 \text{ or } \pi/2, \tau)/\partial\tau = 0 \quad (20)$$

$$W(r = 0, \theta, \tau) = 0 \quad (21)$$

$$W(r, \theta, \tau = 0) = 0 \quad (22)$$

For convective terms, central differencing was employed, hence all spatial derivative approximations are second-order accurate. A total of 61 nodes were used for each space dimension, that is $\Delta r = 1/60$ and $\Delta\theta = \pi/60$. One run was made with a 91×91 grid system, a Peclet number of 1000, and $E = 2$, to check the precision of the spatial approximation. There were less than one percent differences in the computed Nusselt numbers and the bulk temperature (all defined in next section) between the 61×61 and the 91×91 calculations. A constant time step was employed for each run with the time step ranging between $\Delta\tau = 0.0007$ for small Peclet numbers to $\Delta\tau = 0.000025$ for $\mathrm{Pe} = 1000$.

The choice of time-step size also depends on the parameter E. The time-step size was not relaxed for large values of time because of the following two reasons: (1) at large times, numerical instabilities often occurred for large Peclet numbers, and (2) small savings in computation time were realized by not decomposing the matrices used in the implicit tangential pass. All computations were performed on a PRIME 400 computer.

Results and Discussion

Parametric investigations were performed for the heat transfer inside the fluid sphere. The results are given in terms of the Peclet number, $\mathrm{Pe} = U_c 2R/\alpha_2$, and $E = 2V(1+X)/U_\infty$, which characterizes the relative importance of the electric field to the translation of the droplet owing to gravity. The overall transfer efficiency is measured through the instantaneous time-dependent Nusselt number Nu, defined as follows:

$$\mathrm{Nu} = Q2R/4\pi R^2(T_\infty - T_b)k_2 \quad (23)$$

where Q is the total heat transfer from the interface to the droplet interior at any instant and T_b is the bulk temperature of the droplet at the same instant. It may be shown that the dimensionless bulk temperature Z_b is equal to

$$Z_b = 1.5\int_0^1\int_0^\pi Zr^2 \sin\theta d\theta dr \quad (24)$$

The Nusselt number may be written as

$$\mathrm{Nu} = \frac{(2/3)}{(1 - Z_b)}\frac{dZ_b}{d\tau} \quad (25)$$

As will be shown later, the Nusselt number as defined above

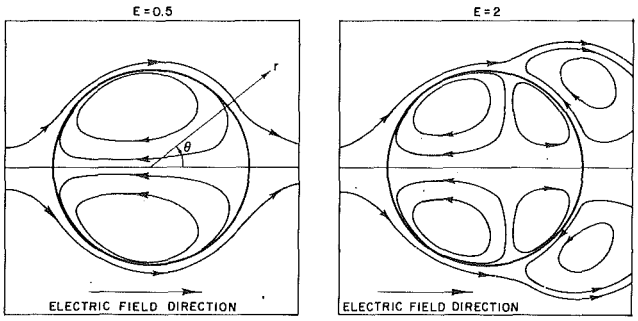

Fig. 2 Streamlines in a drop for $E = 0.5$ and $E = 2$

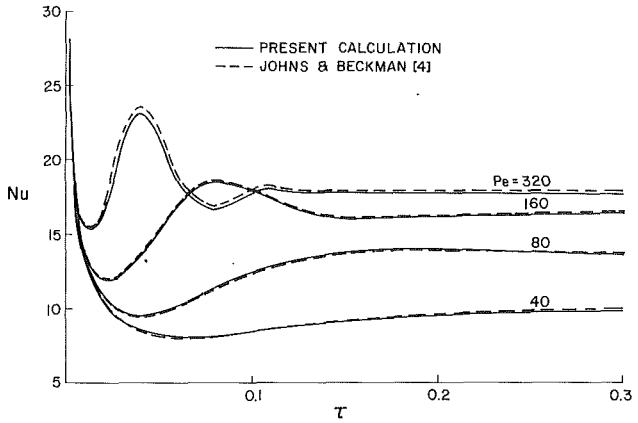

Fig. 3 Comparison of present calculations with those of Johns and Beckman (1966)

will approach asymptotic values under different conditions for large values of time ($\tau \to \infty$). For a pure translation drop, the Nusselt number will approach 17.66 asymptotically for a large time term (Kronig and Brink, 1950), and the Nusselt number approaches 30 for a pure electric field-driven flow as indicated in Oliver et al. (1985). For solid spheres or drops with no internal motion, the large-time Nusselt number is $2\pi^2/3 (= 6.58)$ (Cliff et al., 1978).

Figures 1(*a*) and 1(*b*) show, respectively, the flow streamlines inside the drop for a pure translating drop and a suspended drop in an electric field. It is noted that the electrically generated flow is more efficient than the translation-induced flow in transporting heat from the drop surface to the interior of the drop, if both have identical maximum surface velocities. This is attributed to the double torus in the suspended drop in an electric field. This also assists in explaining the higher steady-state Nusselt number for drops in an electric field.

Figures 2(*a*) and 2(*b*) show the typical hybrid flow streamlines owing to both the drop translation and the electric field. In Fig. 2(*a*) the translation-induced circulation is dominant for $E = 0.5$, and the electrically driven flow is the main flow for $E = 2$ as shown in Fig. 2(*b*). In these figures, the arrows indicate a positive flow direction.

The computer program was tested against available limiting cases for accuracy. For the case of pure translating drops, the comparison was made with the results reported by Johns and Beckmann (1966). As shown in Fig. 3, the agreement is quite satisfactory. For a pure electrically driven flow, an excellent comparison can be observed with the results reported in our earlier paper (Oliver et al., 1985).

The transient Nusselt numbers for various Peclet numbers and different E values are plotted in Figs. 4(*a*)–4(*e*). In each figure, E is held constant, so that the ratio of electrically driven flow strength to that of translation is fixed, and the effect of a varying Peclet number is shown. The Nusselt number, as expected, increases with an increase in the Peclet number. For small values of time, a very thin conduction boundary layer, next to the surface, dominates the transport process. This causes the steep drop in the Nusselt number initially as the thickness of the boundary layer increases. Then the oscillations in Nusselt number occur because of the internal circulation. Initially the circulation transports fresh fluid to the interface and causes the rise of the instantaneous Nusselt number following the initial steep drop. However, if the rate of diffusion of heat to the center of the vortex lags behind the rate of convection of the internal circulation, the circulation will start to transport warmer fluid that causes the instantaneous Nusselt number again to drop. This explains the damping oscillations in Nusselt number for higher Peclet numbers, because the Peclet number represents the ratio of the rate of convection to that of conduction. It is also clear that the frequency of the oscillation increases with the Peclet number. It is noted that the boundary layer approach by Chang et al. (1982) can only predict the steep slope in the Nusselt number at small values of τ. Their method does not address the oscillation stage.

The characteristics of the oscillations are also dependent upon the Peclet number. For large Peclet numbers, the Nusselt number oscillates at high frequencies, but reaches steady state sooner. The high frequencies result from the high heat transfer rates associated with the large Peclet numbers. The combination of high heat transfer rates and constant thermal capacity of the drop results in the short cycles.

The effects of E for a given Peclet number are shown in Figs. 5(*a*), 5(*b*), and 5(*c*). It can be observed for each Peclet number that the trends in the variation of the Nusselt number are similar for different values of E. They differ only in magnitude and frequency. This may be explained by the definition of the Peclet number where the velocity is the sum of the translation component and the electric component.

The dimensionless bulk temperatures of the drop during the transient process are shown in Figs. 6(*a*), 6(*b*), and 6(*c*). They were plotted for constant values of E and various Peclet numbers for each figure. In all of the figures the dimensionless bulk temperature is observed to decrease more rapidly at higher Peclet number. Each curve passes through three stages. The first stage is at the steepest linear drop period where conduction is the dominant mechanism in the boundary layer. The conduction boundary layer is formed because of the diffusion of heat from the drop surface toward the interior of the drop. Heat flux is basically perpendicular to the streamlines of the internal motion; consequently, conduction is the heat transfer mechanism. This phenomenon is somewhat similar to the case of transient heat conduction in a semi-infinite region where the transient heat transfer starts with a sudden increase of interface temperature. The conduction boundary layer domination in transport is further confirmed by the leading single curve, which in turn splits into three curves. The second stage is the transition period during which the internal circulation modifies the transport porcesses. The last period is the steady-state transport process.

Figure 7 presents a summary of the apparent steady-state Nusselt numbers. The steady-state Nusselt number is plotted as a function of the Peclet number and each curve is identified by a different number of E. The top curve corresponds to a suspended drop in an electric field ($E \to \infty$) and the bottom curve represents a translating drop with no electric field ($E = 0$). Both curves converge to $\mathrm{Nu} = 6.58$ as the Peclet number approaches zero, which corresponds to a solid sphere with pure conduction as the transport mechanism. For large Peclet numbers, the top curve approaches 30 asymptotically (Oliver et al., 1985) and the bottom curve approaches 17.66 asymptotically (Clift et al., 1978). All the information given in Fig. 7 was generated by our computer program. The bottom

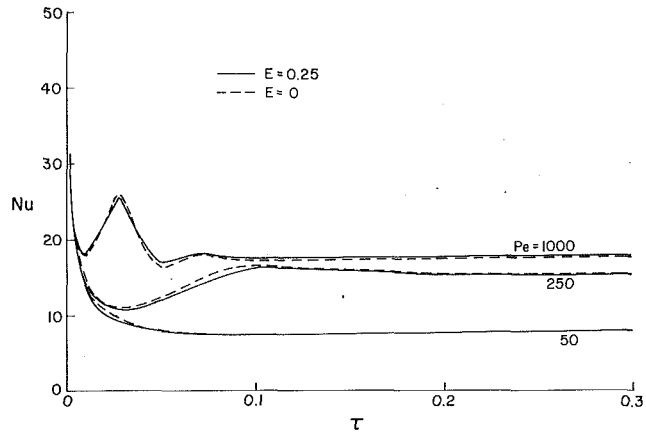

Fig. 4(*a*) Nusselt number versus dimensionless time for $E = 0.25$ and $E = 0$

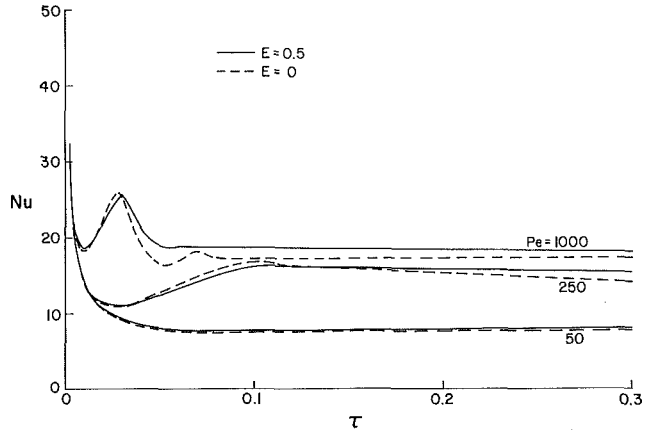

Fig. 4(*b*) Nusselt number versus dimensionless time for $E = 0.5$ and $E = 0$

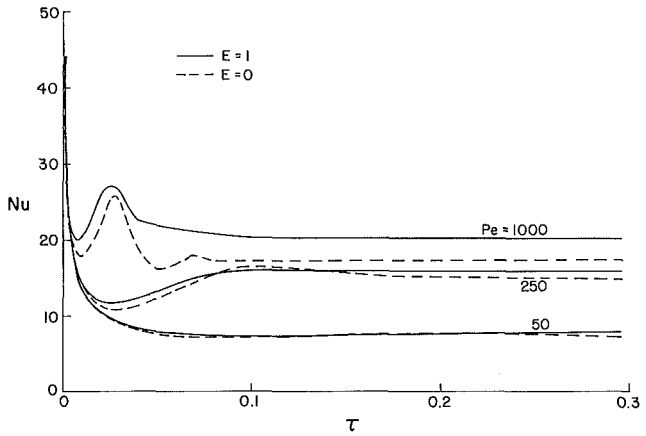

Fig. 4(c) Nusselt number versus dimensionless time for $E = 1$ and $E = 0$

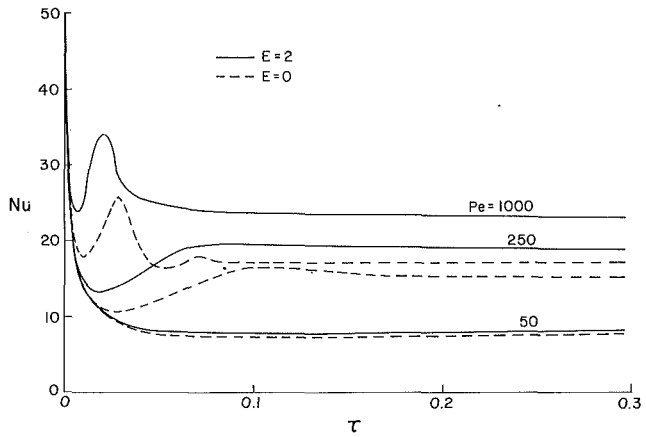

Fig. 4(*d*) Nusselt number versus dimensionless time for $E = 2$ and $E = 0$

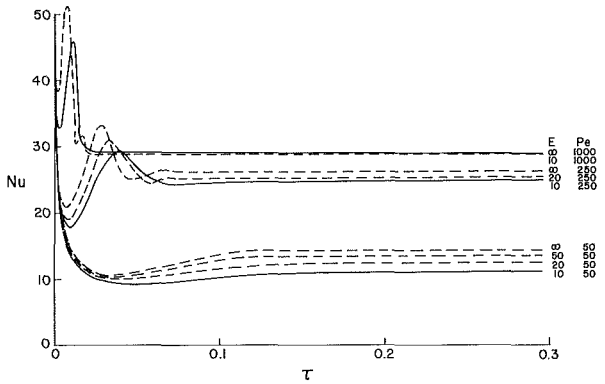

Fig. 4(*e*) Nusselt number versus dimensionless time for various E and Pe

curve in Fig. 7 agrees well with Fig. 3.17 of Clift et al. (1978), which deals with pure translation drops. From Fig. 7, at different Peclet numbers, the reader will be able to evaluate the relative importance of translation to electric field on the heat transfer in drop. For Peclet numbers on the order of 1000, the electric field is negligible for E less than 0.5, while the translation is unimportant when E is larger than 10. But for Peclet numbers around 50, the effect of the electric field is small for values of E less than 2 and the effect of translation is minor when the value of E is greater than 50. This indicates that the relative importance of translation to the electric field is strongly dependent on the Peclet number. Although the above criteria are appropriate for steady-state Nusselt numbers, the same criteria may be applied equally well to transient Nusselt numbers as subsequently explained. In Figs. 4(*a*)–4(*d*), the broken lines were plotted for pure translation drops ($E = 0$). It is still reasonable to assume that the electric field is negligible for values of E less than 0.5, for large Peclet numbers, and for E less than 2 for small Peclet numbers. In Fig. 4(*e*), the broken lines were plotted for values of E equal to 20 and 50. It is reasonable to assume that the translation effect is small for values of E less than 10, for large Peclet numbers, and for E less than 50 for small Peclet numbers.

Another interesting plot is shown in Fig. 8 for isotherm development in a fluid sphere with $\mathrm{Pe} = 250$ and $E = 2$ at three different times for $\tau = 0.05$, 0.1, and 0.15. This case is selected because a direct comparison may be made between Fig. 8 and Fig. 2(*b*). Figure 2(*b*) shows the flow field. It is very clear that the isotherm patterns are dictated by the flow structures and the isotherms show the effects of asymmetric size in flow loops.

For all of the results presented so far, a positive value of E was used. A positive value of E indicates that the electrically induced internal flow extends from the pole to the equator, while for a negative E value, the flow direction is reversed and the streamline pattern is the image of that for a positive value of E as shown in Chang et al. (1982). Several runs have been made with identical parameters except for negative values of E. In all cases investigated, the differences are negligible for both the Nusselt number and the bulk temperature.

Although this paper is written more from the point of an academic study, we still need to mention its engineering values. In engineering applications, the results presented in this paper are useful for liquid drops of relatively high Prandtl number because the Reynolds number is restricted to less than

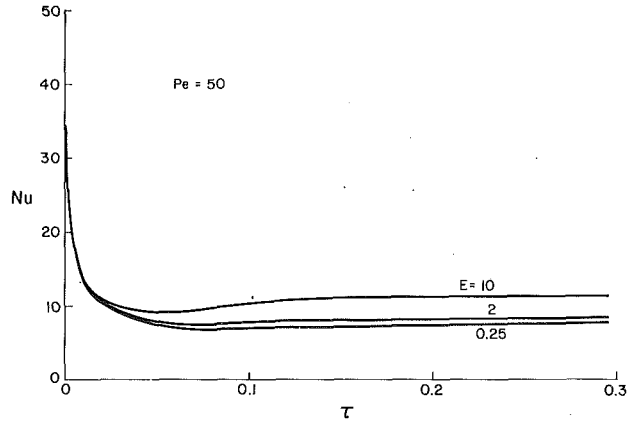

Fig. 5(*a*) Nusselt number versus dimensionless time for Pe = 50

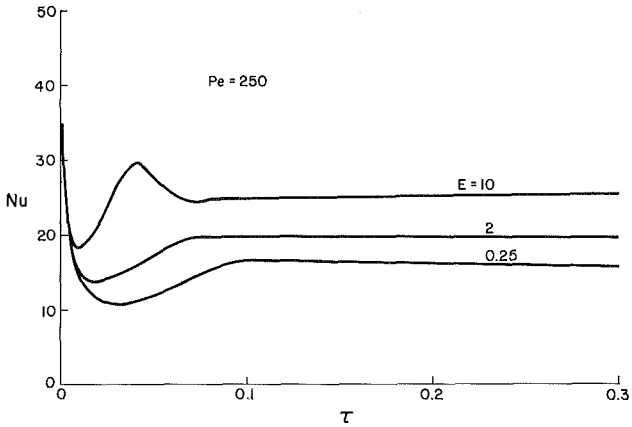

Fig. 5(*b*) Nusselt number versus dimensionless time for Pe = 250

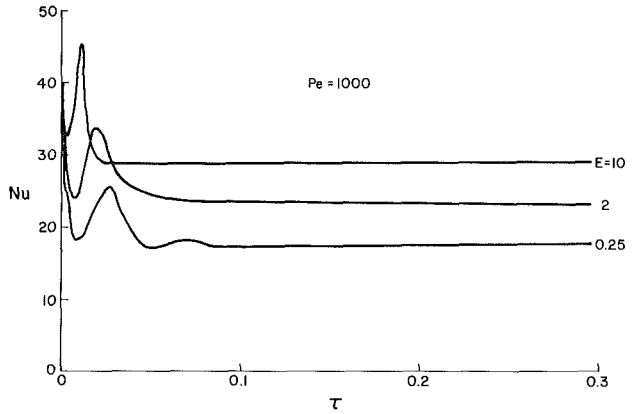

Fig. 5(*c*) Nusselt number versus dimensionless time for Pe = 1000

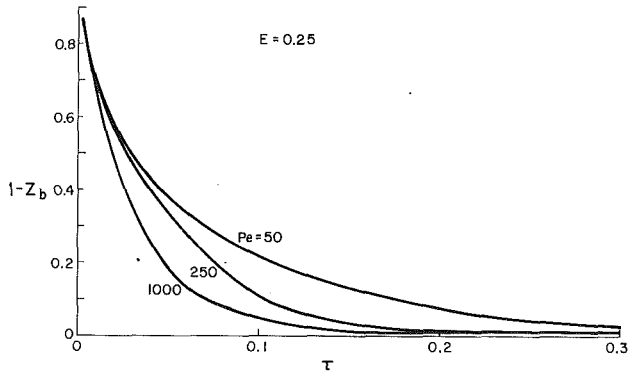

Fig. 6(*a*) Dimensionless bulk temperature versus dimensionless time for $E = 0.25$

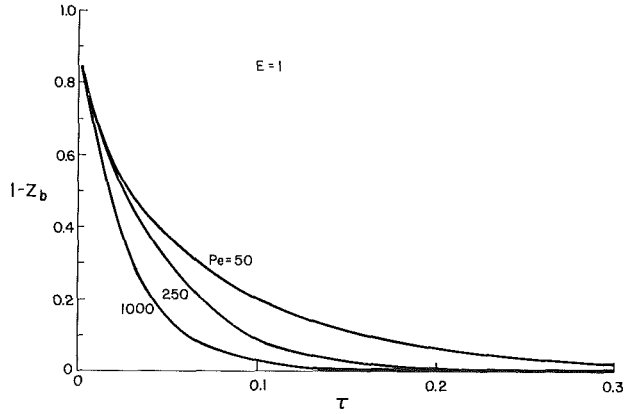

Fig. 6(*b*) Dimensionless bulk temperature versus dimensionless time for $E = 1$

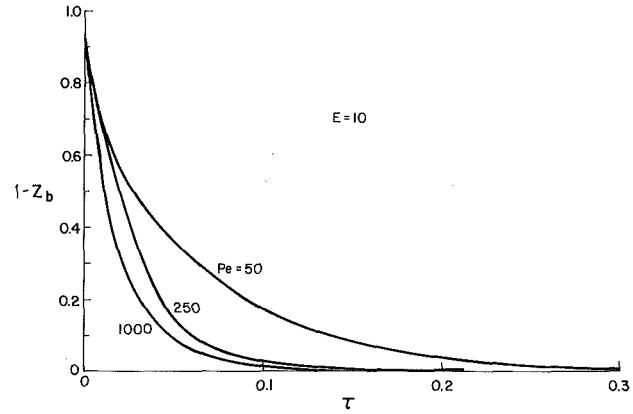

Fig. 6(*c*) Dimensionless bulk temperature versus dimensionless time for $E = 10$

unity. The Peclet number in this paper ranges from 10 to 1000; this leads to a requirement that the Prandtl number be between $0(10^2)$ and $0(10^4)$. Liquids like jet fuel ($Pr \sim 30$), butyl alcohol ($Pr \sim 100$), ethylene glycol ($Pr \sim 100$ to 500), silicon oil ($Pr \sim 200$ to 500), hydraulic fluid ($Pr \sim 500$ to 1000), glycerine ($Pr \sim 10^3$ to 10^5), and oils ($Pr \sim 10^2$ to 10^4) fall into this category. Owing to the Reynolds number limitation ($Re < 1$), the results presented in this paper are generally applicable to systems where droplets are smaller in size and move at slower speeds. High Prandtl number fluids usually have much larger kinematic viscosities that allow larger droplet sizes and high velocities. For a glycerine or oil droplet of 1000 μm diameter, the Reynolds number will remain smaller than unity if it translates at a velocity that is less than 10 cm/s because the

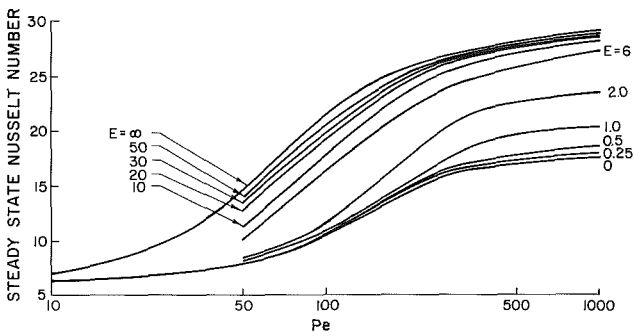

Fig. 7 Steady-state Nusselt number versus Peclet number

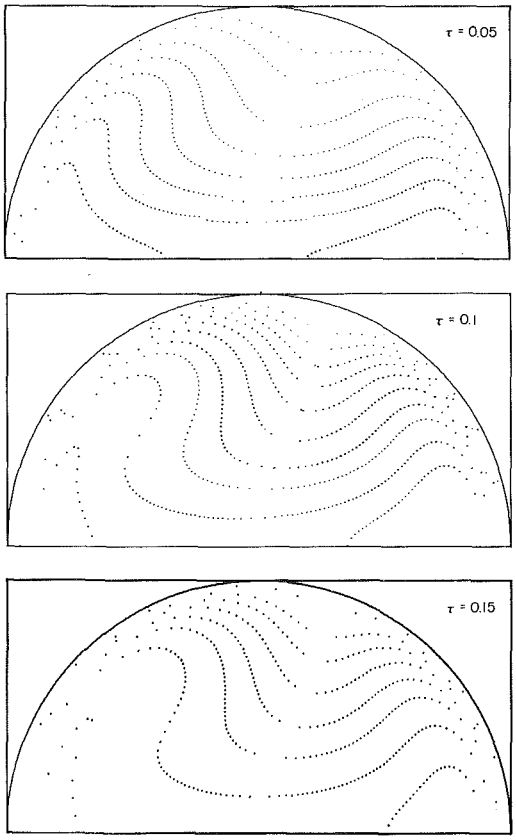

Fig. 8 Isotherm patterns at $\tau = 0.05$, 0.1, and 0.15 for Pe = 250 and $E = 2$

kinematic viscosity of the droplet is of the order of 10^{-4} m^2/s. For organic droplets of 100 μm in diameter their velocities should be lower than 10 cm/s to satisfy the Re < 1 requirement. For droplets of a given fluid, the product between the drop size and its velocity should remain unchanged for the Reynolds number to stay constant.

It should be pointed out that in general there is a lack of experimental data concerning the heat and mass transfer between a single drop and its environment, particularly for drops under the influence of an electric field. This is clearly shown in recent publications, which mainly cover the theoretical analyses without any comparison to experiments (Chow and Halat, 1969; Morrison, 1977; Griffiths and Morrison, 1979; Chang et al., 1985; Chang and Berg, 1985; Oliver et al., 1985; Nguyen and Chung, 1988). Basically this results from the high level of difficulties involved in the measurements of velocity, temperature, and concentration profiles for very small and translating drops. Future efforts should be directed to the experimental aspects of the drop transport phenomena.

Assessment of the Boundary Layer Model

Since the boundary layer approach has been adopted by many investigators to approximate the transport mechanisms inside a droplet or a bubble, it is of special interest to compare quantitatively the transport rates predicted by the boundary layer method with those predicted by the current full numerical calculations. This comparison is intended to establish the range of validity of the boundary layer model for transient transport inside the dispersed phase.

In a boundary layer approach, the energy equation (11) is rewritten in boundary layer coordinates ξ and θ as follows:

$$\frac{\partial z}{\partial \tau} + \frac{\mathrm{Pe}}{2}\left(u\frac{\partial Z}{\partial \xi} + v\frac{\partial Z}{\partial \theta}\right) = \frac{\partial^2 Z}{\partial \xi^2} \tag{26}$$

where the new variable ξ is defined as y/R and y is the normal distance from the interface. With the assumption that all transport activities are confined within this boundary layer, Chang et al. (1982) have shown that equation (26) may be transformed with similarity variables into the following set of simpler equations:

$$\frac{\partial Z}{\partial \zeta} = \frac{\partial^2 Z}{\partial \eta^2} \tag{27}$$

with

$$Z = Z(\eta, \zeta)$$
$$\eta = \xi f(\theta)$$
$$\zeta = \zeta(\theta, \tau)$$

and ζ needs to satisfy the equation

$$\frac{\partial \zeta}{\partial \tau} + \mathrm{Pe}'\,(G\cos\theta - 1)\sin\theta\frac{\partial \zeta}{\partial \theta} = \sin^4\theta(G\cos\theta - 1)^2\mathrm{Pe}' \tag{28}$$

$$\mathrm{Pe}' = u_\infty R/2\alpha_2(1+X) \text{ and } G = 2E$$

The boundary and initial conditions are

$$Z = 1, \quad \eta = 0$$
$$Z = 0, \quad \eta \to -\infty$$
$$Z = 0, \quad \zeta = 0$$
$$\zeta(\theta, \tau) = 0, \quad \tau = 0$$
$$\frac{\partial \zeta}{\partial \theta} = 0, \quad \theta = 0 \text{ and } \pi$$

The solution for equation (27) is

$$Z = \mathrm{erfc}\frac{|\eta|}{2\sqrt{|\zeta|}} \tag{29}$$

As ζ is needed in equation (29), the solution is incomplete until ζ is solved from equation (28). Chang et al. (1981) solved equation (28) numerically and noted that general closed-form solutions are impossible to obtain. Contrary to their conclusion, in this investigation the following closed-form solution for equation (28) was obtained by the method of characteristics:

$$\zeta(\theta, \tau) = \frac{G}{4}\sin^4\theta - \frac{\cos^3\theta}{3} + \cos\theta + \Phi(y) \tag{30}$$

where $y(\theta, \tau) = \epsilon^{-\mathrm{Pe}'\tau}(G\cos\theta - 1)^\alpha(\cos\theta + 1)^\beta(\cos\theta - 1)^\gamma$

$$\alpha = -\frac{G}{G^2 - 1}, \quad \beta = \frac{1}{2(G+1)}, \text{ and } \gamma = \frac{1}{2(G-1)}$$

The following equation is obtained by invoking the initial condition, $\zeta(\theta, 0) = 0$:

$$\Phi(y(\theta, 0)) = -\frac{G}{4}\sin^4\theta + \frac{\cos^3\theta}{3} - \cos\theta \tag{31}$$

The heat flux at the droplet surface is

$$q'' = \frac{k(T_\infty - T_o)}{R}\sqrt{\frac{\mathrm{Pe}'}{\pi}}\,\frac{\sin^2\theta\,|G\cos\theta - 1|}{\sqrt{|\zeta|}} \tag{32}$$

The transient heat transfer rate to the droplet then becomes

$$Q = 2\pi R\int_0^\pi q''\sin\theta d\theta$$

$$= 2\pi Rk(T_\infty - T_o)\sqrt{\frac{\mathrm{Pe}'}{\pi}}\int_0^\pi \frac{\sin^3\theta\,|G\cos\theta - 1|}{\sqrt{|\zeta|}}d\theta \tag{33}$$

A typical comparison is given in Fig. 9 to assess the validity

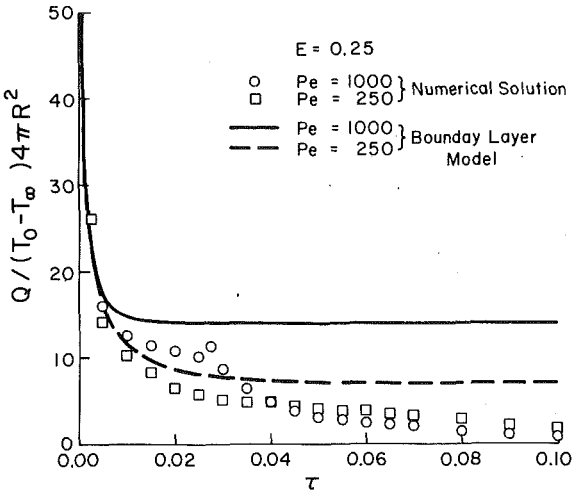

Fig. 9 Comparisons of boundary layer model with numerical solutions

of the boundary layer model. In Fig. 9, the average heat flux per unit initial temperature difference, $Q/4\pi R^2(T_\infty - T_o)$, is plotted as a function of dimensionless time τ for Peclet number of 250 and 1000, and for $E = 25$. The solid lines represent the heat transfer rates predicted by the boundary layer model, and the discrete symbols represent those predicted by the current numerical method. As indicated by the comparison, the boundary layer is only reasonably accurate during the very beginning of the transient process ($\tau < 0.01$). The boundary layer model fails to predict any internal circulation-induced oscillations in heat transfer rates as calculated by the numerical method. Therefore, the boundary layer model is strictly valid only before the internal fluid makes a complete lap of circulation. For larger values of time, the boundary layer model appears to predict asymptotically steady heat transfer rates, whereas physically there is no steady heat transfer for a droplet of finite volume.

Conclusion

The transient heat transfer inside a fluid sphere translating steadily with an electric field, applied in the same direction as that of the translation, is numerically investigated by the Alternating Direction Implicit (ADI) method. In this report, the heat transfer resistance is considered to be completely in the dispersed phase.

The transient behavior of the Nusselt number depends strongly on the Peclet number, which is defined on the basis of a characteristic velocity of combined translation and electric field. A common feature of all the transient Nusselt numbers is the initial very steep linear drop before the oscillation starts. This steep drop results from the heat transfer in the conduction boundary layer that forms next to the surface of the drop. High-frequency oscillations in the Nusselt number are typical for high Peclet number drops, but steady-state oscillations develop rather quickly. For smaller Peclet numbers, the frequency of oscillation is quite low and it takes much longer for the Nusselt number to reach steady state.

The steady-state Nusselt numbers are shown to increase with an increase in both the Peclet number and the parameter E. All the steady-state Nusselt numbers are confined between two limiting curves, i.e., the pure translating drop and a suspended drop in an electric field.

The relative importance of translation to electric field is assessed based on the Nusselt numbers. It is suggested that for large Peclet numbers, the translation is unimportant for E larger than 10, while the electric field is negligible for E smaller than 0.5. For small Pecelt numbers, the translation is of minor effect for E larger than 50 and the electric field is less important for E smaller than 2.

As compared with the numerical solutions, the boundary layer model is unable to predict any internal circulation-induced oscillations in heat transfer rates. The boundary layer model is strictly valid only before the internal fluid makes a complete lap of circulation.

It should be pointed out that all the heat transfer results and trends predicted in this paper are also valid for mass transfer to a fluid sphere under an electric field because of the analogy between heat and mass transfer.

Acknowledgments

The authors wish to thank Emeritus Professor H.A. Sorensen of Washington State University for his review and corrections on the manuscript. Assistance offered by Dr. H. D. Nguyen is appreciated. The quality of the paper was improved substantially by the efforts from all three referees.

References

Ames, W. F., 1977, *Numerical Methods for Partial Differential Equations*, Academic Press, New York.

Chang, L. S., and Berg, J. C., 1983, "Fluid Flow and Transfer Behavior of a Drop Translating in an Electric Field at Intermediate Reynolds Numbers," *Int. J. Heat Mass Transfer*, Vol. 26, pp. 823–832.

Chang, L. S., Charleson, T. E., and Berg, J. C., 1982, "Heat and Mass Transfer to a Translating Drop in an Electric Field," *Int. J. Heat Mass Transfer*, Vol. 25, pp. 1023–1030.

Chow, C. Y., and Halat, J. A., 1969, "Drag of a Sphere of Arbitrary Conductivity in a Current-Carrying Fluid," *Physics Fluids*, Vol. 12, pp. 2317–2322.

Chung, J. N., Ayyaswamy, P. S., and Sadhal, S. S., 1984, "Laminar Condensation on a Moving Drop. Part 1. Singular Perturbation Technique," *J. Fluid Mech.*, Vol. 139, pp. 105–130.

Clift, R., Grace, J. R., and Weber, M. E., 1978, *Bubbles, Drops, and Particles*, Academic Press, New York.

Griffiths, S. K., and Morrison, F. A., Jr., 1979, "Low Peclet Number and Mass Transfer From a Drop in an Electric Field," ASME JOURNAL OF HEAT TRANSFER, Vol. 101, pp. 484–488.

Hadamard, J., 1911, "Movement permanent lent d'une sphere liquide et visqueuse dans une liquide visqueux," *C. R. Acad. Sci*, Vol. 152, pp. 1735–1738.

Johns, L. E., Jr., and Beckmann, R. B., 1966, "Mechanisms of Dispersed-Phase Mass Transfer in Viscous, Single-Drop Extraction Systems," *AIChE J.*, Vol. 12, pp. 10–16.

Kronig, R., and Brink, J. C., 1950, "On the Theory of Extraction From Falling Droplets," *Appl. Sci. Res.*, Vol. A2, pp. 142–154.

Morrison, F. A., Jr., 1977, "Transient Heat and Mass Transfer to a Drop in an Electric Field," ASME JOURNAL OF HEAT TRANSFER, Vol. 99, pp. 269–273.

Nguyen, H. D., and Chung, J. N., 1988, "Translating and Evaporating Drop in an Electric Field," AIAA *J. Thermophysics and Heat Transfer*, Vol. 2, pp. 285–286.

Oliver, D. L. R., Carleson, T. E., and Chung, J. N., 1988, "Transient Heat Transfer to a Fluid Sphere Suspended in an Electric Field," *Int. J. Heat Mass Transfer*, Vol. 28, pp. 1005–1009.

Prakash, S., and Sirignano, W. A., 1978, "Liquid Fuel Droplet Heating With Internal Circulation," *Int. J. Heat Mass Transfer*, Vol. 21, pp. 885–895.

Rybczynski, W., 1911, "On the Translating Motion of a Fluid Sphere in a Viscous Medium," *Bull. Int. Acad. Pol. Sci. Maxh. Natur.*, Ser. A., pp. 40–46.

Stewart, M. B., and Morrison, F. A., 1979, "Small Reynolds Number Electrohydrodynamics Flow Around Drops and the Resulting Deformation," ASME *J. Applied Mech.*, Vol. 46, pp. 510–512.

Sundararajan, T., and Ayyaswamy, P. S., 1984, "Hydrodynamics and Heat Transfer Associated With Condensation on a Moving Drop: Solutions for Intermediate Reynolds Numbers," *J. Fluid Mech.*, Vol. 149, pp. 35–58.

Taylor, G. I., 1966, "Studies in Electrohydrodynamics, I. The Circulation Produced in a Drop by an Electric Field," *Proc. Roy. Soc.*, Vol. 291A, pp. 159–166.

Taylor, T. D., and Acrivos, A., 1964, "On the Deformation and Drag of a Falling Viscous Drop at Low Reynolds Number," *J. Fluid Mech.*, Vol. 18, pp. 466–476.

Convection From a Periodically Stretching Plane Wall

J. L. Lage

A. Bejan
Fellow ASME

Department of Mechanical Engineering and Materials Science,
Duke University,
Durham, NC 27706

This paper documents the convection heat transfer enhancement effect that is associated with the periodic (timewise and spatial) longitudinal stretching of an infinite plane wall bathed by a semi-infinite fluid reservoir. It is shown that the flow field reaches a truly periodic state, and that the temperature field does not. The time-dependent heat transfer rate is greater than the classical pure-diffusion limit only when the Reynolds number based on wall speed and wavelength is greater than 1. The enhancement effect becomes pronounced as Re increases above 10. The enhancement effect increases also as the Prandtl number increases, provided Re is greater than 1. The same conclusions apply in the case of convective mass transfer, when a concentration difference is maintained between the flexible wall and the ambient fluid.

Introduction

The functioning of living systems, and processes for the controlled production of substances that employ living systems (e.g., culture reactors), have become an important growth area for modern convection research. The two most common features of the flows that are involved in these systems are (*i*) the flexibility and stretchability of the solid walls, and (*ii*) the spatial and temporal periodicity of the flows.

The fundamental work in this area was reviewed most recently by Weaver (1988). The early research focused on the external flow problem, most notably, on the sinuous movement of microscopic organisms through a body of fluid (e.g., Taylor, 1959). Internal flows have come under scrutiny in connection with the phenomenon of peristaltic pumping (e.g., Jaffrin and Shapiro, 1971; Wilson et al., 1979; Macagno and Christensen, 1980; Ayukawa, 1981; Ohki, 1980, 1982a, 1982b), and the periodic flow through spatially varicose channels (e.g., Nishimura et al., 1987, 1988). The latter is relevant not only to the study of blood flow, but also to the convection transport characteristics of membrane oxygenators. In the two classes of problems that have been studied so far—external flows and internal flows—the wall shapes can be described as waves of finite amplitude.

In the present study we focus on another basic problem, namely the convective transport capability of a flexible wall that stretches and contracts periodically in its own plane (i.e., longitudinally). Such walls are being considered in the design of culture reactors, in which a desirable feature is the enhancement of convective transfer from the wall to the reactor (culture) fluid, without an increase in the mechanical damage suffered by the living systems that are suspended in the fluid (Weaver, 1988). The pure fluid mechanics part of the present problem was studied in the context of tubes of constant circular cross section by Ohki (1980). In what follows, we show what features of the wall stretching motion most influence the "enhancement" of the convective transport from the wall to the surrounding fluid. The analysis is presented in heat transfer terms. However, the conclusions of the study apply equally to mass transfer applications in which the stretching membranes are active components.

It is important to note also the growing interest in the fundamentals of the mechanism of heat and mass transfer enhancement due to the oscillatory motion of the fluid. It has been shown that the mass transfer rate due to a concentration gradient in a fluid is considerably greater than the pure-diffusion value when the fluid oscillates longitudinally, i.e., parallel to the imposed gradient (e.g., Chatwin, 1975; Watson, 1983). The heat transfer engineering implications of this mechanism have been explored by Kurzweg and Zhao (1984), Kurzweg (1985a, 1985b, 1986), Kaviany (1986) and Kurzweg and Chen (1988). In all these studies, the transport phenomenon is parallel to the direction of oscillatory fluid motion. Using this background, the problem that is analyzed in this paper unveils a new phenomenon in which the heat and mass transfer process and its enhancement occur in the direction normal to the oscillatory motion.

Mathematical Formulation

Consider the time-dependent flow and heat transfer in the two-dimensional configuration illustrated in Fig. 1. The base

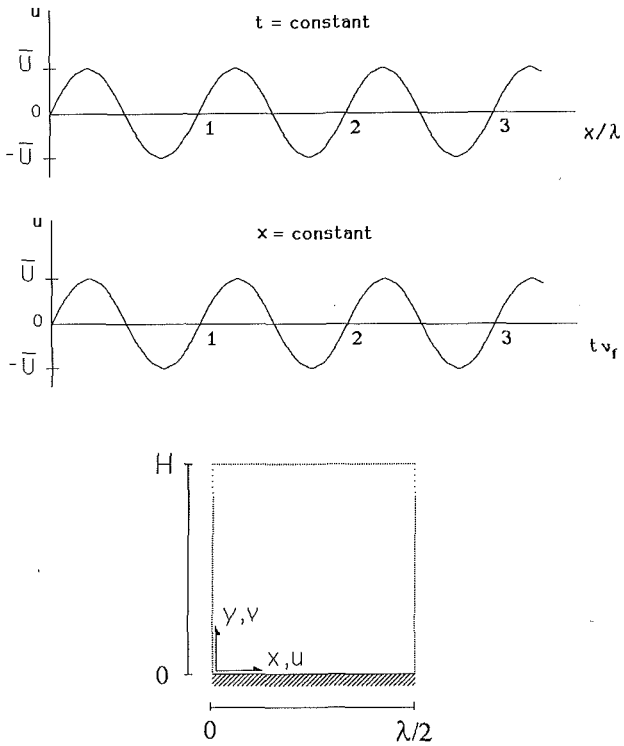

Fig. 1 Periodic surface velocity, and the half-wavelength control volume chosen for analysis

Contributed by the Heat Transfer Division for publication in the JOURNAL OF HEAT TRANSFER. Manuscript received by the Heat Transfer Division August 5, 1988. Keywords: Augmentation and Enhancement, Biotechnology, Moving Boundaries.

surface ($y = 0$) stretches and contracts periodically in its own plane. The periodicity is both spatial and temporal, and is expressed by the horizontal velocity distribution along the base

$$u(x, 0, t) = \bar{U} \sin(2\pi\nu_f t) \sin(2\pi x/\lambda) \quad (1)$$

It is shown later in equations (17) and (18) that this velocity distribution corresponds to a wall, the material points of which oscillate in the $y = 0$ plane. The material points of two adjacent wall segments of length $\lambda/2$ come together (the material contracts) during half of the cycle, and travel in opposite directions during the remaining half of the cycle.

Far above the base surface the fluid is isothermal and motionless. According to equation (1), the spatial wave described by the longitudinal movement of the surface material is stationary with respect to the semi-infinite fluid reservoir. The motion of the base surface induces a periodic flow in the fluid layers situated near the base. The question is how this periodic flow affects the transient transport of heat (or mass) from the base to the semi-infinite fluid reservoir.

With reference to the x–y system of coordinates shown in Fig. 1, the dimensionless equations for the conservation of mass, momentum, and energy in the fluid are

$$\frac{\partial U}{\partial X} + \frac{\partial V}{\partial Y} = 0 \quad (2)$$

$$\frac{\partial U}{\partial \tau} + U\frac{\partial U}{\partial X} + V\frac{\partial U}{\partial Y} = -\frac{\partial P}{\partial X} + \frac{1}{\mathrm{Re}}\left(\frac{\partial^2 U}{\partial X^2} + \frac{\partial^2 U}{\partial Y^2}\right) \quad (3)$$

$$\frac{\partial V}{\partial \tau} + U\frac{\partial V}{\partial X} + V\frac{\partial V}{\partial Y} = -\frac{\partial P}{\partial Y} + \frac{1}{\mathrm{Re}}\left(\frac{\partial^2 V}{\partial X^2} + \frac{\partial^2 V}{\partial Y^2}\right) \quad (4)$$

$$\frac{\partial T}{\partial \tau} + U\frac{\partial T}{\partial X} + V\frac{\partial T}{\partial Y} = \frac{1}{\mathrm{RePr}}\left(\frac{\partial^2 T}{\partial X^2} + \frac{\partial^2 T}{\partial Y^2}\right) \quad (5)$$

In these equations the flow is being modeled as two dimensional and incompressible, while the fluid is treated as Newtonian and with constant properties (ν, k, α). The effect of frictional heating is also being neglected. The flow field is decoupled from the temperature field: The circumstances when this assumption is valid are discussed in the closing paragraphs of this paper.

The dimensionless variables used in equations (2)–(5) are defined by

$$(X, Y) = \frac{(x, y)}{\lambda/2}, \qquad (U, V) = \frac{(u, v)}{\bar{U}} \quad (6)$$

$$\tau = \frac{\bar{U}}{\lambda/2} t, \qquad T = \frac{\bar{T} - \bar{T}_\infty}{\bar{T}_0 - \bar{T}_\infty} \quad (7)$$

$$P = \frac{p}{\rho\bar{U}^2}, \qquad \mathrm{Re} = \frac{\bar{U}\lambda/2}{\nu}, \qquad \mathrm{Pr} = \frac{\nu}{\alpha} \quad (8)$$

where (x, y), (u, v), t, p, and $\bar{T}$ are the physical (dimensional) coordinates, velocity components, time, pressure, and temperature. The velocity scale $\bar{U}$ is the amplitude of longitudinal velocity of the base, equation (1).

The dimensionless initial and base surface conditions that apply to equations (2)–(5) are

$$U = V = T = 0 \quad \text{at} \quad \tau = 0 \quad (9)$$

and

$$U = \sin(2\pi\xi\tau) \sin(\pi X),$$
$$V = 0 \text{ and} \quad (10)$$
$$T = 1, \quad \text{at} \quad Y = 0$$

The conditions that have been imposed on the remaining three boundaries of the $H \times (\lambda/2)$ domain shown in Fig. 1 are discussed in the next section. The dimensionless frequency number ξ, which appears in the first of equations (10), is defined as

$$\xi = \frac{\lambda/2}{\bar{U}} \nu_f \quad (11)$$

It is shown later in equation (17) that the degree of freedom represented by ξ accounts for the amplitude of the travel executed by one material point in the plane of the stretching wall.

Numerical Method

The problem stated in the preceding section was solved using the control volume method described by Patankar (1980). The

Nomenclature

$\bar{C}$ = concentration of species, kg/m^3
$\bar{C}_0$ = concentration of species at the wall, kg/m^3
$\bar{C}_\infty$ = concentration of species in the fluid reservoir, kg/m^3
D = mass diffusivity, m^2/s
f = friction factor, equation (12)
$j_{0,\mathrm{avg}}$ = wall averaged mass flux, kg/m^{2}s
k = thermal conductivity, W/mK
Nu = instantaneous wall-averaged Nusselt number, equation (13)
Nu_l = local instantaneous Nusselt number, equation (21)
Nu_0 = pure diffusion limit of Nu, equation (23)
$\overline{\mathrm{Nu}}$ = time-averaged Nusselt number, equation (20)
p = pressure, N/m^2
P = dimensionless pressure, equation (8)
Pr = Prandtl number, equation (8)
q_0'' = local instantaneous heat flux, W/m^2
$q_{0,\mathrm{avg}}''$ = wall averaged heat flux, W/m^2
Re = Reynolds number, equation (8)
Sh = instantaneous wall-averaged Sherwood number, equation (24)
Sh_0 = pure diffusion limit of Sh, equation (26)
t = time, s
T = dimensionless temperature, equation (7)
$\bar{T}$ = temperature, K
$\bar{T}_0$ = wall temperature, K
$\bar{T}_\infty$ = fluid reservoir temperature, K
u = longitudinal velocity, m/s
U = dimensionless longitudinal velocity, equation (6)
$\bar{U}$ = velocity of the stretching wall, m/s
v = transversal velocity, m/s
V = dimensionless transversal velocity, equation (6)
x = longitudinal coordinate, m
X = dimensionless longitudinal coordinate, equation (6)
y = transversal coordinate, m
Y = dimensionless transversal coordinate, equation (6)
α = thermal diffusivity, m^2/s
λ = wavelength of the wall stretching motion, m
ν = kinematic viscosity, m^2/s
ν_f = frequency, s^{-1}
ξ = frequency number, equation (11)
ρ = density, kg/m^3
τ = dimensionless time, equation (7)
$\tau_{0,\mathrm{avg}}$ = wall-averaged shear stress, equation (12)
Φ = heat transfer enhancement factor, equation (22)
Φ_m = mass transfer enhancement factor, equation (25)
Ψ = dimensionless streamfunction, equation (16)
$(\ )_A$ = coordinates of a material point attached to the wall

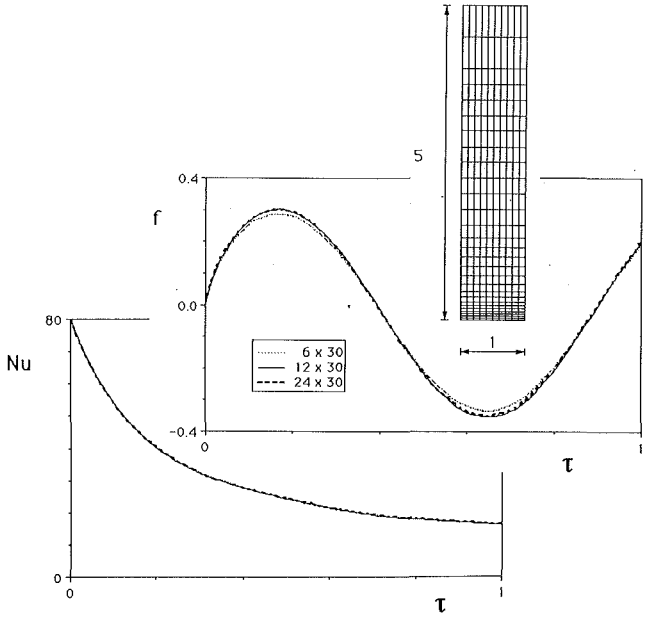

Fig. 2(*a*) The effect of the number of nodes in the longitudinal (x) direction ($\Delta\tau$ = 0.0125)

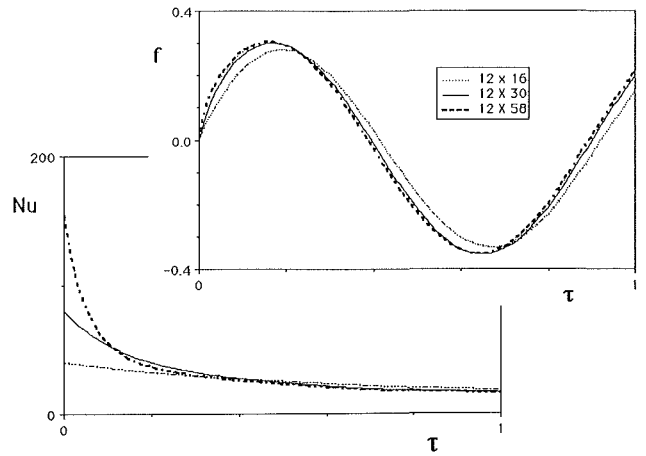

Fig. 2(*b*) The effect of the number of nodes in the transversal (y) direction ($\Delta\tau$ = 0.0125)

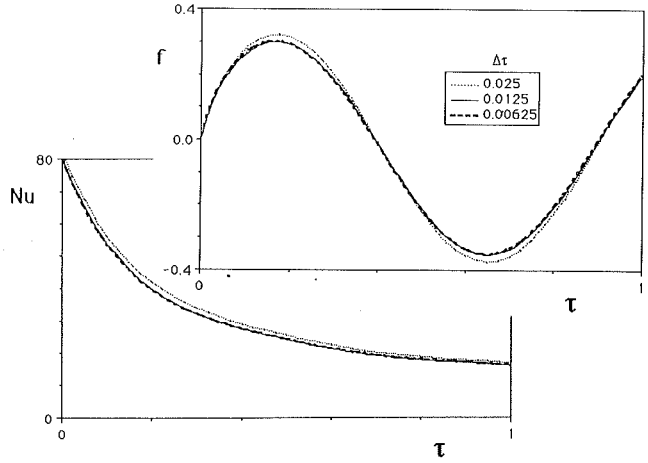

Fig. 2(*c*) The effect of the time step $\Delta\tau$ (grid = 12 × 30)

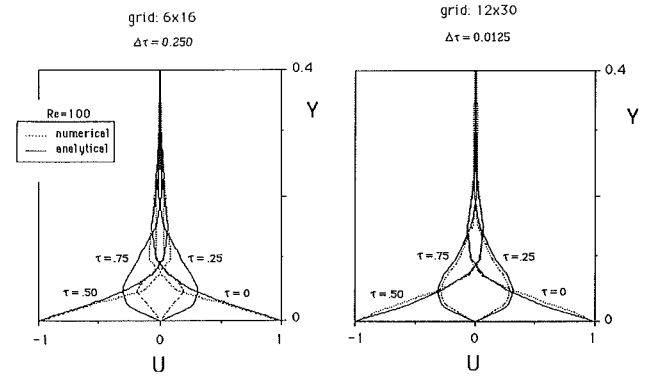

Fig. 2(*d*) Comparison with the exact solution to Stokes' oscillating plate problem

Fig. 2 Numerical accuracy tests (Re = 100, Pr = 7, ξ = 1)

method consisted of using the SIMPLE algorithm, a power-law scheme for evaluating the convection terms, and the Tri-Diagonal-Matrix-Algorithm for solving the discretized equations.

The semi-infinite reservoir was simulated by choosing a sufficiently tall (X, Y) domain, so that the far-region velocities (U, V) and temperature (T) were of the order 10^{-4} or smaller, that is, much smaller than the O(1) values that are calculated in the fluid layer situated close to the $Y = 0$ base. The upper extremity of the numerical domain was typically positioned at $Y = 5$ (see Fig. 2). This boundary was modeled as adiabatic ($\partial T/\partial Y = 0$), impermeable ($V = 0$), and zero-shear ($\partial U/\partial Y = 0$).

The spatial periodicity of the problem made it sufficient to perform the calculations only in the half-wavelength domain $0 \le X \le 1$ isolated in Fig. 1. The vertical sides of this domain are planes of symmetry; therefore, in the numerical work they were treated as adiabatic ($\partial T/\partial X = 0$), impermeable ($U = 0$), and zero-shear ($\partial V/\partial X = 0$).

The nonuniform 12 × 30 grid shown in the inset of Fig. 2(a) was chosen as a tradeoff between the computer time requirement and numerical accuracy and stability. The grid is finer near the base surface, where higher gradients of velocity and temperature are expected. The 12 × 30 grid fineness was selected based on "overall" accuracy tests of the kind illustrated in Figs. 2(a–c), where f is the friction factor averaged over the length of the base

$$f = \frac{\tau_{0,\text{avg}}}{\rho\bar{U}^2/2} = \frac{2}{\text{Re}}\int_0^1 \left(\frac{\partial U}{\partial Y}\right)_{Y=0} dX \tag{12}$$

and where Nu is the base-averaged Nusselt number

$$\text{Nu} = \frac{q''_{0,\text{avg}}\lambda/2}{k(\bar{T}_0 - \bar{T}_\infty)} = -\int_0^1 \left(\frac{\partial T}{\partial Y}\right)_{Y=0} dX \tag{13}$$

These accuracy tests were performed at the highest Reynolds number considered in this study, namely, Re = 100. The effect of grid fineness in the longitudinal direction is reported in Fig. 2(a). This figure shows that the use of 12 nodes is indeed adequate, and that the use of a finer division in the x direction leads to practically the same f and Nu results as in the case of 12 nodes.

The effect of increasing the number of control volumes distributed unevenly in the transversal (y) direction is illustrated in Fig. 2(b). The friction factor plot shows that 30 nodes are sufficient. The Nusselt number plot shows that the act of increasing the number of control volumes continues to have an effect on the $\tau \to 0$ limit of the Nu(τ) curve, because of the theoretical limit Nu = ∞ that holds at $\tau = 0$. The same plot shows that the use of 30 nodes is adequate at times greater than approximately $\tau = 0.075$. The time domain of the numerical results reported in this paper consists of τ values considerably greater than $\tau = 0.075$ (e.g., Figs. 3 and 6); therefore, 30 nodes in the vertical direction were considered sufficient.

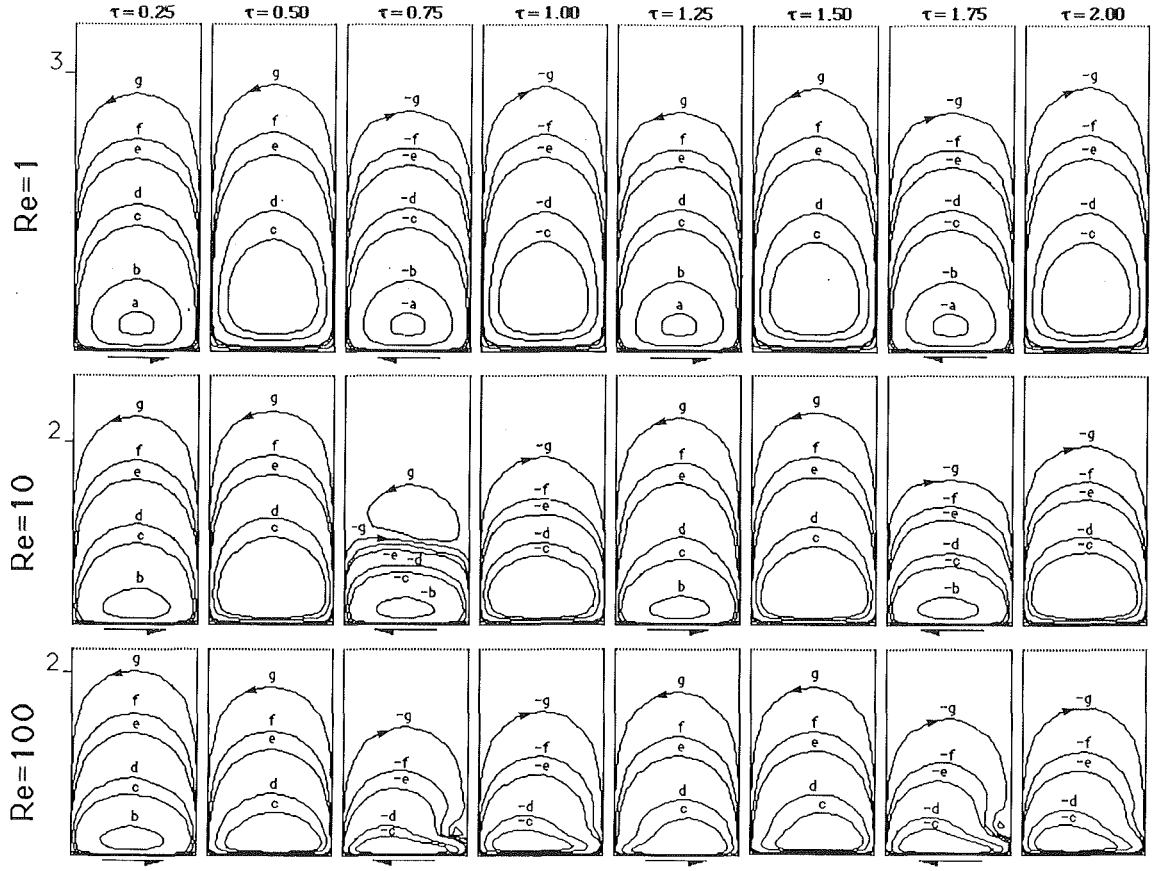

Fig. 3 The Reynolds number effect on the development of the flow pattern (ξ = 1)

The effect of the time step $\Delta\tau$ is illustrated in Fig. 2(*c*), in the case of the 12 × 30 grid that was ultimately used in the study. Both the f and Nu plots show that the use of a time step smaller than 0.0125 does not lead to significant changes in the numerical solution. The test of Fig. 2(*c*) corresponds to the frequency number $\xi = 1$. For other values of ξ, the acceptable time step varies in such a way that the product $\xi\Delta\tau$ remains constant: This choice guarantees that the velocity change between two consecutive time steps does not vary in time. Therefore the numerical solutions described next were obtained by using the time steps provided by the formula $\Delta\tau = 0.0125/\xi$.

The convergence criterion used was the max-norm, according to which the maximum local change of all parameters is to be less than 0.1 percent.This criterion guarantees a global accuracy that is at least as good as the local accuracy. Furthermore, the numerical convergence was checked at each time iteration in order to verify the performance of (and determine the optimum) relaxation factors. The most often used relaxation factors were 0.8 for the momentum equations, and 0.5 for the pressure equation. There was no need to relax the energy equation in the present problem.

The computational time needed varied from case to case. However, it was generally of the order of 40,000 CPU-seconds on a Micro VAX I microcomputer. Some of the solutions were executed on an AT&T 3B15 computer, which is twice as fast.

The numerical method and the chosen grid were tested also against the exact solution to Stokes' oscillating plate problem (Schlichting, 1978)

$$\frac{u}{\bar{U}} = \exp\left[-y\left(\frac{\pi\nu_f}{\nu}\right)^{1/2}\right]\cos\left[2\pi\nu_f t - y\left(\frac{\pi\nu_f}{\nu}\right)^{1/2}\right] \quad (14)$$

in which the velocity of the solid wall, $u(y = 0)$, is a periodic function of time, but not a function of longitudinal position. Worth keeping in mind is that the exact solution (14) is of the steady-periodic type, that is, of the type approached by the present flow field solutions (e.g., Fig. 3) only after a sufficiently large number of cycles. Therefore, in order to simulate the solution to Stokes' problem with the present numerical code, we imposed the boundary conditions

$$U = \cos(2\pi\xi\tau) \text{ and } V = 0 \quad \text{at} \quad Y = 0$$

$$\frac{\partial U}{\partial X} = 0 \quad \text{and} \quad V = 0 \quad \text{at} \quad X = 0 \quad \text{and} \quad X = 1 \quad (15)$$

$$\frac{\partial U}{\partial Y} = 0 \quad \text{and} \quad V = 0 \quad \text{at} \quad Y = 5$$

and started the calculations from the initial nonflow condition $U = V = 0$. The numerical solution obtained after ten complete cycles was compared with the exact solution (14), and the results are presented in Fig. 2(*d*). This figure shows that the agreement between the numerical and analytical solutions improves as the grid and time step become finer. The right side of the figure shows that the approximate (10-cycles) solution based on the grid and time step chosen for the present study agrees well with Stokes' steady-periodic solution.

The Flow Field

The main features of the flow induced by the periodic stretching of the base surface are illustrated in Fig. 3. The sequence of streamline patterns covers only the first two time periods of the phenomenon ($0 \le \tau \le 2$), although the actual calculations proceeded to longer times. The streamline labels are shorthand for the sequence

(*a*) $\Psi = 0.1$ (*c*) $\Psi = 0.01$ (*e*) $\Psi = 0.001$
(*b*) $\Psi = 0.05$ (*d*) $\Psi = 0.005$ (*f*) $\Psi = 0.0005$
(*g*) $\Psi = 0.0001$

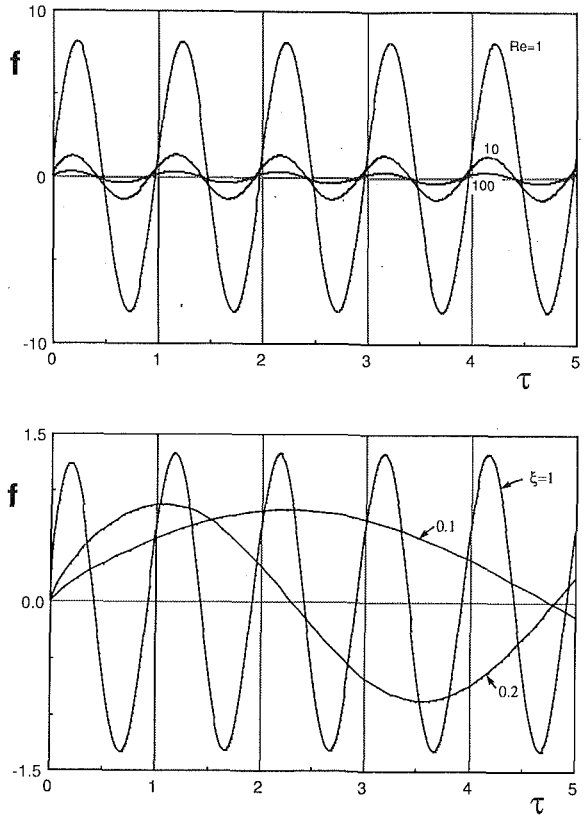

Fig. 4 Top: the Reynolds number effect on the average friction factor (ξ = 1). Bottom: the effect of the frequency number ξ on the average friction factor (Re = 10).

the dimensionless streamfunction having been defined by writing

$$U = \frac{\partial \Psi}{\partial Y}, \qquad V = -\frac{\partial \Psi}{\partial X} \tag{16}$$

Figure 3 shows that the fluid executes a quasi-periodic rolling motion that follows the rhythm dictated by the motion of the base surface. The instantaneous direction of the latter is indicated by horizontal arrows. The frames without arrows correspond to those moments when the base surface changes direction, that is, when the base velocity is zero everywhere from $X = 0$ to $X = 1$. The fluid motion is quasi-periodic because in the beginning the fluid is motionless; a truly periodic motion is achieved only after a sufficiently large number of time periods. This number increases with the Reynolds number. In the cases illustrated in Fig. 3, for example, the truly periodic motion sets in at $\tau \approx 0.75$ when Re = 1, and $\tau \approx 3.5$ when Re = 10. In the last case, Re = 100, the truly periodic motion is not observed even after five full periods.

The effect of increasing the Reynolds number can be seen by reading Fig. 3 in the vertical direction. One trend is that the eye of the roll migrates toward the base surface, which means that the flow boundary layer becomes thinner. At the same time, the far-field flow subsides gradually, i.e., the effect of the base stretching motion penetrates to smaller depths into the fluid reservoir.

Another interesting feature of the flow is the influence of fluid inertia, which becomes more visible as Re increases. It can be seen in the frame (Re = 10, τ = 0.75), in which the sense of the far-field roll lags behind that of the flat roll near the base. The fluid inertia effect is visible also in the time frames τ = 0.75 and τ = 1.75 of the bottom row (Re = 100), in which a small counterrotating roll persists outside the starting end of the base boundary layer.

The overall flow quantity that accompanies the flow development tracked in Fig. 3 is the average friction factor plotted in upper portion of Fig. 4. This quantity appears to reach its periodic state at times shorter than the bulk of the flow field. The time lag between the oscillation of f and that of the base surface increases as the Reynolds number increases.

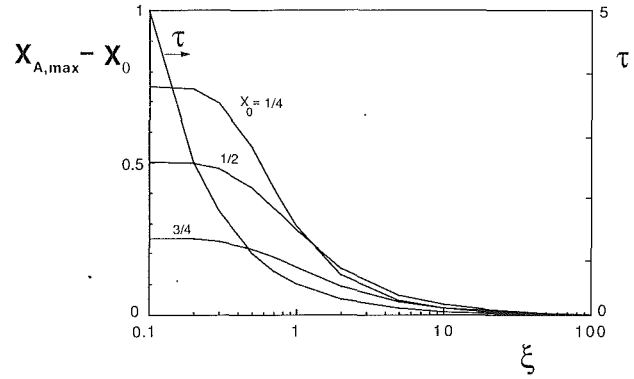

Fig. 5 The relationship between the frequency number and the maximum travel of a material point of the stretching wall

The lower graph of Fig. 4 shows the effect of the frequency number ξ on the length-averaged friction factor. The amplitude of the f oscillation decreases as the frequency number decreases.

The frequency number ξ is related to the amplitude of the periodic travel executed by a material point (A) on the base surface. Let $x_A(t)$ represent the instantaneous position of point (A), and x_0 its position at $t = 0$; in other words, $x_0 = x_A(0)$. An ordinary differential equation for $x_A(t)$ is obtained by substituting x_A in place of x, and dx_A/dt in place of u in equation (1). Integrated away from $t = 0$, and nondimensionalized according to equations (6)–(11), that equation yields

$$X_A = \frac{2}{\pi} \tan^{-1}\left\{\tan\left(\frac{\pi}{2} X_0\right) \cdot \exp\left[\frac{1-\cos(2\pi\xi\tau)}{2\xi}\right]\right\} \tag{17}$$

Equation (17) shows that point (A) moves back and forth along the base as the time τ increases. The maximum X_A value, or the rightmost position of point (A), occurs when $\xi\tau = 1/2$

$$X_{A,\max} = \frac{2}{\pi} \tan^{-1}\left[\tan\left(\frac{\pi}{2} X_0\right) \cdot \exp\left(\frac{1}{\xi}\right)\right] \tag{18}$$

Figure 5 shows the monotonic relationship that exists between the maximum travel of one material point ($X_{A,\max} - X_0$) and the frequency number. One such curve can be drawn for each X_0, that is, for each material point identified at $t = 0$ along the base. We see that frequency numbers much greater than 1 are associated with very small material-point amplitudes. In the limit of small frequency numbers, on the other hand, the amplitude of the longitudinal travel scales with the length of spatial periodicity ($\lambda/2$). The right side of Fig. 5 shows also the τ value when $X_A = X_{A,\max}$, namely $\tau = (2\xi)^{-1}$.

The Temperature Field

The development of the thermal boundary layer is illustrated in Fig. 6. In each (Re, τ) frame, the $T = 1$ isotherm coincides with the base surface; proceeding into the fluid, the temperature T decreases from one isotherm to the next in steps of 0.2. Note further that each (Re, τ) frame has been dilated in the vertical direction, in order to show more clearly the structure of the thermal boundary layer.

When the Reynolds number is of order O(1) or smaller, the temperature distribution approaches the well-known solution for pure conduction into a semi-infinite medium with instantaneous temperature change at the boundary (e.g., Grigull and Sandner, 1984)

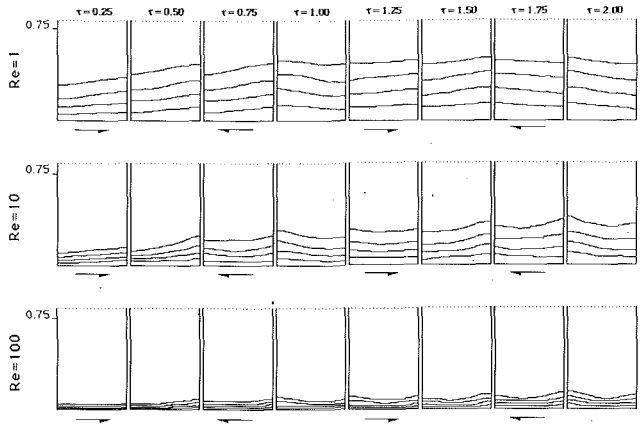

Fig. 6 The Reynolds number effect on the development of the temperature field (ξ = 1, Pr = 7)

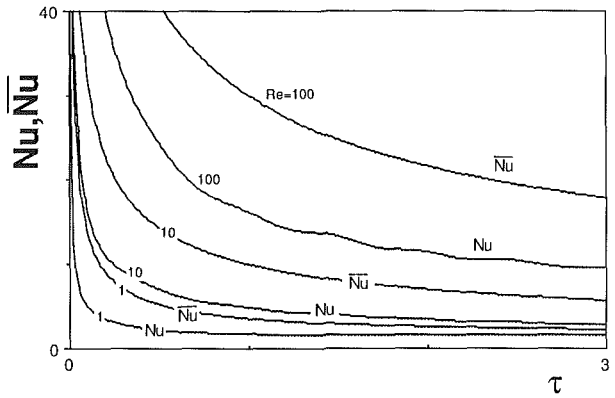

Fig. 7 The evolution of the instantaneous Nusselt number (Nu) and the time-averaged Nusselt number ($\overline{\text{Nu}}$) (ξ = 1, Pr = 7)

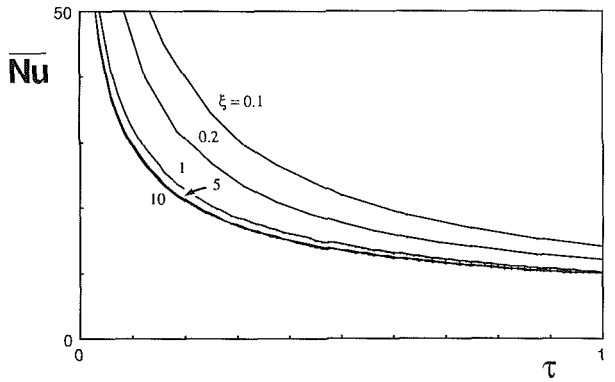

Fig. 8 The effect of the frequency number ξ on the time-averaged Nusselt number (Re = 10, Pr = 7)

$$T = \text{erfc}\left[\frac{Y}{2}\left(\frac{\text{RePr}}{\tau}\right)^{1/2}\right] \tag{19}$$

The effect of convection becomes increasingly evident as Re increases. The isotherms tilt quasi-periodically with the movement of the base surface; however, unlike the streamlines, they never reach a truly periodic state. At sufficiently large τ values, the thermal boundary layer expands beyond the region inhabited by meaningful fluid motion, and continues to swell via thermal diffusion.

The important effect of a large Reynolds number is that, in the short run, it leads to the formation of a relatively thin thermal boundary layer, especially along the middle portion of the base segment $0 < x < \lambda/2$, that is, over the patch of surface that moves the fastest. The thinning of the thermal boundary layer is reflected in the enhancement of the overall

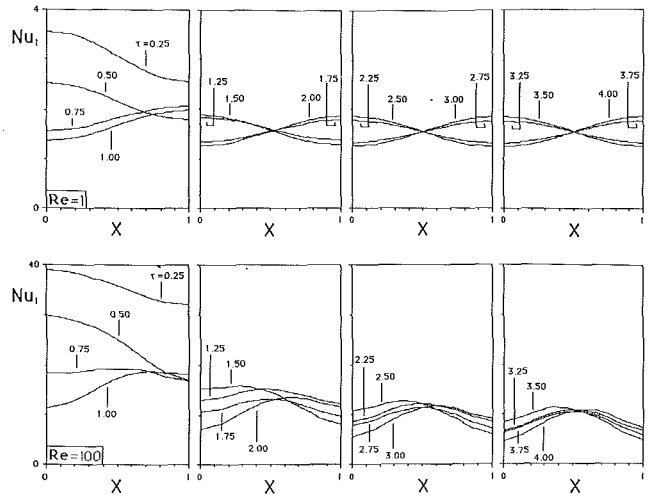

Fig. 9 Timewise and spatial variation of the local instantaneous Nusselt number (ξ = 1, Pr = 7)

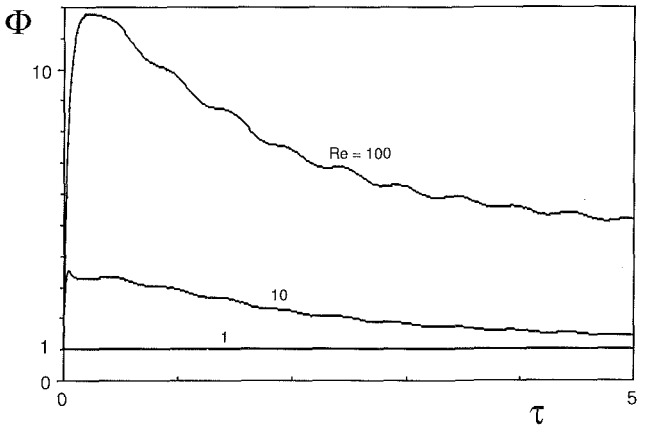

Fig. 10 The heat transfer enhancement factor Φ, and the effect of increasing the Reynolds number (ξ = 1, Pr = 7)

heat transfer rate between the base and the fluid, as will be seen shortly in Figs. 9 and 10.

Figure 7 shows the evolution of the instantaneous Nusselt number Nu defined in equation (13). Each Nu(τ) curve starts from Nu = ∞ at τ = 0, and descends to zero at sufficiently large τ values. This feature is the result of pure thermal diffusion, which sets it at sufficiently large τ values. The Nu descent is accompanied by a very slight waviness, the time period of which is the same as that of the base stretching motion. At any fixed time τ, the instantaneous heat transfer rate increases as Re increases.

Plotted on Fig. 7 are also the corresponding time-averaged Nusselt number curves, where $\overline{\text{Nu}}$ is defined as

$$\overline{\text{Nu}} = \frac{1}{\tau}\int_0^\tau \text{Nu}(\tau')d\tau' \tag{20}$$

The qualitative behavior of the $\overline{\text{Nu}}(\tau)$ curve is nearly the same as that of the instantaneous Nusselt number curve Nu(τ). One difference is that the time-averaging operation (20) removes most of the waviness from the Nu(τ) curves.

The effect of the frequency number ξ on the heat transfer rate is illustrated by means of the time-averaged $\overline{\text{Nu}}$ curves shown in Fig. 8. The Nusselt number decreases as ξ increases to values of order 5, beyond which the effect of ξ on $\overline{\text{Nu}}$ is imperceptible. This behavior is explained by the fact that the amplitude of the motion executed by the base material is very small when ξ is greater than 5 (Fig. 5).

Figure 9 shows the timewise and spatial variation of the local instantaneous Nusselt number

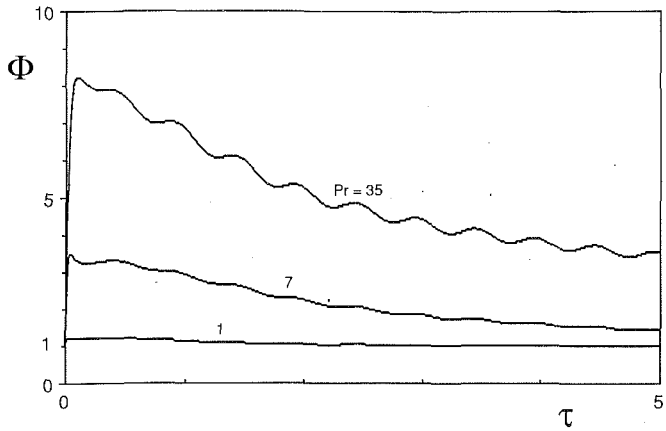

Fig. 11 The Prandtl number effect on the heat transfer enhancement factor (ξ = 1, Re = 10)

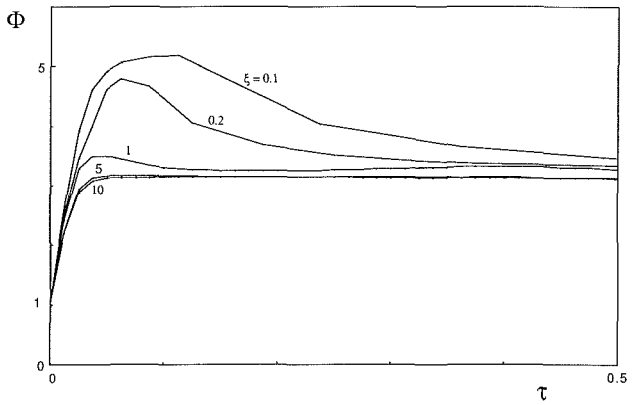

Fig. 12 The effect of the frequency number on the heat transfer enhancement factor (Re = 10, Pr = 7)

$$\mathrm{Nu}_l = \frac{q_0'' \lambda/2}{k(\bar{T}_0 - \bar{T}_\infty)} = -\left(\frac{\partial T}{\partial Y}\right)_{Y=0} \tag{21}$$

in which q_0'' (x, t) is the local and instantaneous heat flux through the $y = 0$ plane. Viewed from left to right, the four frames in each row correspond to the first four complete cycles of the base-wall motion. The local Nusselt number generally decreases as the time (τ) increases. At low Reynolds numbers (the top row in Fig. 9), the local Nusselt number tends toward a periodic state characterized by an almost constant Nu_l value at $X = 1/2$ (i.e., in the middle of the wall segment of length $\lambda/2$, Fig. 1). The Nu_l values to the left and right of the midpoint fluctuate about the midpoint constant Nu_l.

The long-time behavior of Nu_l changes as the Reynolds number increases. The fourth frame in the bottom row of Fig. 9 shows that the temporal fluctuations of the local Nusselt number are overshadowed by its longitudinal variation. The latter is characterized by an instantaneous Nu_l maximum that is always close to the midpoint of the wall segment $0 < x < \lambda/2$.

Discussion: The Enhancement of Heat or Mass Transfer

The heat transfer results discussed until now can be compared with the pure conduction limit (Re = 0), in order to evaluate the degree of heat transfer enhancement that is associated with the periodic stretching of the base surface. It is convenient to define the heat transfer enhancement factor

$$\Phi = \frac{\mathrm{Nu}}{\mathrm{Nu}_0} \tag{22}$$

for which the pure-conduction instantaneous Nusselt number (Nu_0) can be determined by combining equations (13) and (19)

$$\mathrm{Nu}_0 = \left(\frac{\mathrm{RePr}}{\pi\tau}\right)^{1/2} = \frac{\lambda/2}{(\pi\alpha t)^{1/2}}. \tag{23}$$

Figure 10 shows that the enhancement factor Φ can be considerably greater than 1, particularly during the first few cycles in the life of the heat transfer process. If the Reynolds number is of order 1 or smaller, the factor Φ is practically equal to 1 for all τ; in other words, the movement of the base has no heat transfer enhancement value. The enhancement effect becomes pronounced if Re exceeds O(10). The factor Φ is exactly equal to 1 in the beginning of the process, because before any fluid motion develops the heat transfer mechanism is that of pure conduction. The enhancement factor decreases to 1 in the limit of large τ values, when the temperature field expands via thermal diffusion beyond the layer occupied by the periodic flow.

Figure 11 illustrates the effect of the Prandtl number on the instantaneous heat transfer rate. The enhancement factor and Nu increase as Pr increases. This effect is to be expected, because higher Prandtl numbers mean thermal boundary layers that are progressively thinner relative to the near-base velocity boundary layer illustrated in Fig. 3.

Finally, Fig. 12 shows the effect of the frequency number on heat transfer enhancement factor. When ξ is smaller than 1, the factor Φ exhibits a maximum during the early part of the first period of the base-stretching motion. The peak value reached by Φ increases as ξ decreases, because in the same limit the amplitude of the base motion increases. The peak disappears when ξ becomes of order 5 or greater.

The preceding conclusions concerning the behavior of the enhancement factor Φ apply also to mass transfer applications in which a concentration difference $(\bar{C}_0 - \bar{C}_\infty)$ is maintained between the flexible wall and the neighboring fluid. The transport quantity of interest in such applications is the instantaneous wall-averaged Sherwood number

$$\mathrm{Sh} = \frac{j_{0,\mathrm{avg}} \lambda/2}{D(\bar{C}_0 - \bar{C}_\infty)} \tag{24}$$

in which $j_{0,\mathrm{avg}}$ is the wall-averaged mass flux, and D is the mass diffusivity constant. In a way that parallels the definition of Φ, equation (22), the instantaneous Sherwood number can be evaluated as the product

$$\mathrm{Sh} = \Phi_m \mathrm{Sh}_0 \tag{25}$$

in which Sh_0 represents the pure-diffusion limit, cf. equation (23),

$$\mathrm{Sh}_0 = \frac{\lambda/2}{(\pi D t)^{1/2}} \tag{26}$$

Finally, based on the analogy between mass transfer and heat transfer, the mass transfer enhancement ratio Φ_m, equation (25), assumes the same values as the Φ function displayed in Figs. 10–12, provided the Prandtl number is replaced by the Schmidt number $\mathrm{Sc} = \nu/D$.

A final observation concerns the decoupling of the flow field from the temperature field, which was recognized starting with equations (3), (4), and (5). The momentum and energy equations are truly decoupled only when the buoyancy effect due to temperature gradients is negligible, that is when the flow regime is one of forced convection. It is known that the buoyancy effect is negligible when (Lloyd and Sparrow, 1970)

$$\mathrm{Gr}^{1/2} < \mathrm{Re} \tag{27}$$

where Gr is the Grashof number based on the length scale $\lambda/2$

$$\mathrm{Gr} = \frac{g\beta\Delta T(\lambda/2)^3}{\nu^2} \tag{28}$$

and where $\Delta T = \bar{T}_0 - \bar{T}_\infty$. The inequality (27) holds for fluids with Prandtl numbers of the same order of magnitude as 1 (see, for example, Bejan, 1984, p. 144).

As a numerical example of the implications of the restriction posed by the inequality (27), consider the case where the fluid is liquid water with an average temperature of 25°C. Substituting the water property values (Bejan, 1984, p. 463) into this inequality leads to an upper bound for the permissible temperature difference scale of the problem

$$\frac{\Delta T}{1\ \text{K}} < 0.63 \left(\frac{\bar{U}}{1\ \text{cm/s}}\right)^2 / \left(\frac{\lambda/2}{1\ \text{cm}}\right) \tag{29}$$

This result shows that the buoyancy effect is indeed negligible in applications where $O(\lambda/2) \sim 1$ cm, $O(\Delta T) \sim 1$ K and where the order of magnitude of $\bar{U}$ is greater than 1 cm/s.

Acknowledgments

The support received from the National Science Foundation through Grant No. CBT-8711369 is gratefully acknowledged. J. L. Lage acknowledges with gratitude the support received from CAPES—the Brazilian Post-Graduate Education Federal Agency (Process No. 5943/87-5).

References

Ayukawa, K., 1981, "Streamlines and Pathlines in Peristaltic Flows at High Reynolds Numbers," *Bulletin of the Japanese Society of Mechanical Engineers*, Vol. 24, pp. 948–955.

Bejan, A., 1984, *Convection Heat Transfer*, Wiley, New York, pp. 144, 463.

Chatwin, P. C., 1975, "On the Longitudinal Dispersion of Passive Contaminant in Oscillatory Flow in Tubes," *J. Fluid Mechanics*, Vol. 71, pp. 513–527.

Grigull, U., and Sandner, H., 1984, *Heat Conduction*, Hemisphere, Washington, DC, p. 77.

Jaffrin, M. Y., and Shapiro, A. H., 1971, "Peristaltic Pumping," *Annual Review of Fluid Mechanics*, Vol. 3, pp. 13–36.

Kaviany, M., 1986, "Some Aspects of Enhanced Heat Diffusion in Fluids by Oscillation," *Int. J. Heat Mass Transfer*, Vol. 29, pp. 2002–2006.

Kurzweg, U. H., and de Zhao, L., 1984, "Heat Transfer by High Frequency Oscillations: A New Hydrodynamic Technique for Achieving Large Effective Thermal Conductivities," *Phys. Fluids*, Vol. 27, pp. 2624–2627.

Kurzweg, U. H., 1985a, "Enhanced Heat Conduction in Oscillating Flows Within Parallel-Plate Channels," *J. Fluid Mechanics*, Vol. 156, pp. 291–300.

Kurzweg, U. H., 1985b, "Enhanced Heat Conduction in Fluids Subjected to Sinusoidal Oscillations," ASME JOURNAL OF HEAT TRANSFER, Vol. 107, pp. 459–462.

Kurzweg, U. H., 1986, "Temporal and Spatial Distribution of Heat Flux in Oscillating Flow Subjected to an Axial Temperature Gradient," *Int. J. Heat Mass Transfer*, Vol. 29, pp. 1969–1977.

Kurzweg, U. H., and Chen, J., 1988, "Heat Transport Along an Oscillating Flat Plate," ASME JOURNAL OF HEAT TRANSFER, Vol. 110, pp. 789–790.

Lloyd, J. R., and Sparrow, E. M., 1970, "Combined Forced and Free Convection Flow on Vertical Surfaces," *Int. J. Heat Mass Transfer*, Vol. 13, pp. 434–438.

Macagno, E. O., and Christensen, J., 1980, "Fluid Mechanics of the Duodenum," *Annual Review of Fluid Mechanics*, Vol. 12, pp. 139–158.

Nishimura, T., Tarumoto, A., and Kawamura, Y., 1987, "Flow and Mass Transfer Characteristics in Wavy Channels for Oscillatory Flow," *Int. J. Heat Mass Transfer*, Vol. 30, pp. 1007–1015.

Nishimura, T., Arakawa, S., Murakami, S., and Kawamura, Y., 1988, "Oscillatory Viscous Flow in a Wavy-Walled Channel," presented at the First World Conference on Experimental Heat Transfer, Fluid Mechanics and Thermodynamics, Dubrovnik, Yugoslavia, Sept. 4–9.

Ohki, M., 1980, "Unsteady Flow in a Porous, Elastic, Circular Tube—1. The Wall Contracting or Expanding in an Axial Direction," *Bulletin of the Japanese Society of Mechanical Engineers*, Vol. 23, pp. 679–686.

Ohki, M., 1982a, "Unsteady Flow in a Porous, Elastic, Circular Tube—2. The Tube Contracting or Expanding in Radial Direction," *Bulletin of the Japanese Society of Mechanical Engineers*, Vol. 25, pp. 552–561.

Ohki, M., 1982b, "Unsteady Flow in a Porous, Elastic, Circular Tube—3. The Tube Contracting or Expanding in Axial and Radial Directions," *Bulletin of the Japanese Society of Mechanical Engineers*, Vol. 25, pp. 562–569.

Patankar, S. V., 1980, *Numerical Heat Transfer and Fluid Flow*, Hemisphere, Washington, DC.

Schlichting, H., 1978, *Boundary Layer Theory*, translated by J. Kestin, McGraw-Hill, New York, pp. 93–94.

Taylor, G. I., 1959, "Analysis of the Swimming of Microscopic Organisms," *Proceedings of the Royal Society*, Vol. A209, pp. 447–461.

Watson, E. J., 1983, "Diffusion in Oscillatory Pipe Flow," *J. Fluid Mechanics*, Vol. 133, pp. 233–244.

Weaver, M. K., 1988, "Flow of a Confined Viscous Fluid due to Deformation of a Compliant Boundary," Ph.D. Thesis, Department of Mechanical Engineering and Materials Science, Duke University, Durham, NC.

Wilson, D. E., Stearman, R. R., and Panton, R. L., 1979, "Peristaltic Pumping by a Lateral Bending Wave," ASME *Journal of Biomechanical Engineering*, Vol. 101, pp. 239–245.

Thermal Radiation in Rayleigh-Bénard Instability

J. H. Lienhard V
Department of Mechanical Engineering,
Massachusetts Institute of Technology,
Cambridge, MA 02139
Mem. ASME

Thermal radiation from finite-conductivity boundaries can strongly affect the stability of horizontally unbounded, plane fluid layers heated from below. The role of thermal radiation in plane layer instabilities is studied under the assumption that the fluid medium is transparent, as a model of infrared transfer through gas layers. The solution procedure modifies a previous formulation of the conductive boundary problem to account for the gray radiant interchange between boundaries. The nonisothermal character of the boundaries is shown to bias instability toward higher wavenumbers and to substantially increase the stability of fluid layers between radiative, nonconductive boundaries relative to layers having nonradiative boundaries. A single layer is studied first, and then a case of parallel, interacting fluid layers is considered. Critical Rayleigh numbers are presented as both tabulations and correlations. The implications for solar collector design are discussed.

1 Introduction

Wall radiation has long been believed to play a significant role in the stability of gas layers heated from below. Theoretical treatments of this problem have been rather limited, however, because radiation can only play an active role when the boundaries are of finite thermal conductivity and the instability with conductive boundary has only been fully treated in recent years. The problem of thermal instability in radiatively participating media has received considerable attention, particularly in the astrophysical literature, but in those cases boundary effects have been generally minimized.

The effects of boundary radiation can be substantial. Edwards and Sun (1971) considered sidewall radiation in thermal instability of diathermanous gases in long vertical cylinders. Their analysis adapted an existing result for conductive sidewalls by introducing an effective conductivity that incorporated the radiant exchange between elements of the sidewalls. They found that wall radiation strongly stabilizes the fluid column.

Various situations of technical interest involve thermal instability in plane air layers at relatively low temperatures. Two prominent examples are the instabilities in air layers within the cover plates of flat-plate solar collectors and the instabilities arising in various building ceiling insulation problems. In such situations, radiant emission from the boundaries is dominantly in the infrared, and the gas layer is essentially diathermanous. In this paper, I consider the effect that thermal radiation may have upon such instabilities.

Previous work on plane layer instabilities (e.g., Lienhard, 1987) has shown that boundaries of low thermal conductivity can support large temperature perturbations (hot and cold spots), which reduce the critical Rayleigh number of a fluid layer by as much as a factor of 2.5. The effect of radiation is to cool hot spots by emission and to warm cold spots by absorption; as a result, radiation stabilizes these otherwise very unstable configurations.

This paper begins with a formulation of the radiant instability for an individual layer, building upon methods introduced in the conductive-boundary stability problem. With this solution, important features of the single-layer instability are explored. Then a coupled fluid layer instability is studied, in a configuration typical of flat-plate solar collectors. The relative importance of thermal radiation in these situations is assessed, and correlations of the numerical results are given.

In a recent work, Richards and Edwards (1989) have treated a similar problem in which boundary temperature disturbances are represented by a heat transfer coefficient. That model effectively requires that the wall have no horizontal thermal diffusivity, as discussed by Lienhard (1987). Some caution is required in applying that approximation, as it can easily lead to errors that are as large as radiative effects. In this work, I consider the opposite limiting case of fully conductive walls. The relation of the two limits is also assessed.

Various other contrasts between these two studies may also be noted. Richards and Edwards allow for spectral wall radiation; the present work has been confined to gray walls. Richards and Edwards consider only rolls at onset of motion and obtain numerical solutions; the present work treats all allowable planforms and presents analytical solutions. The present formulation is valid for an arbitrary number of asymmetric layers with conductive interaction; the other allows for radiative interactions of highly symmetric fluid layers through midlayers having no horizontal diffusivity. This work and that of Richards and Edwards are thus complementary in several respects.

2 Formulation

We have assumed the medium between the plates to be transparent to infrared radiation, and, consequently, the fluid temperature profile in the quiescent state remains linear, as in the nonradiative case. Radiation is apparent only in the calculation of the heat flux at the boundaries of a given fluid layer.

The fluid stability problem thus differs from the classical problem only in the type of boundary conditions to be applied. The fluid itself, in the usual fashion, satisfies a normal mode perturbation solution (Rayleigh, 1916); for steady onset of motion, the general solution for the dimensionless normal mode amplitude of the temperature disturbance in layer i, $\Theta_i(z_i)$, was found by Pellew and Southwell (1940)

$$\Theta_i = A\cosh(qz_i) + A^*\cosh(q^*z_i) + A_0\cos(q_0z_i) + B\sinh(qz_i) + B^*\sinh(q^*z_i) + B_0\sin(q_0z_i) \quad (1)$$

where $(\ )^*$ denotes a complex conjugate, A and B are unknown constants, and

$$q_0 = a_i(\tau-1)^{1/2},\ q^2 = a_i^2\left(1+\frac{1}{2}\tau(1\pm i\sqrt{3})\right),\ \text{with } \mathrm{Ra}_i = a_i^4\tau^3 \quad (2)$$

The Rayleigh number of layer i is an eigenvalue of this equation, determined by application of the boundary conditions. An analogous analysis of the heat equation shows that the temperature perturbation in a solid boundary is given by

Contributed by the Heat Transfer Division for publication in the JOURNAL OF HEAT TRANSFER. Manuscript received by the Heat Transfer Division November 18, 1988. Keywords: Natural Convection, Radiation Interactions, Solar Energy.

$$\Theta_B(z_B) = M \cosh(a_B z_B) + N \sinh(a_B z_B) \quad (3)$$

for unknown constants M and N. More specific features of the present development appear in the usual literature.

Scaling. The nondimensionalization is based on the scales of an individual layer. In fluid layer i, temperature is scaled with its difference across the layer, ΔT_i, and length is scaled with the layer thickness, L_i. In a solid wall of finite thickness, temperature is scaled with its difference across the wall, ΔT_B, and length is scaled with the wall thickness, L_B. In a semi-infinite wall, temperature and length are scaled with the scales of the adjacent fluid layer. Wavenumbers are nondimensionalized with the length scale of the layer in which they are considered. For example, $a_i = 2\pi L_i/\lambda$ and $a_B = 2\pi L_B/\lambda$. The disturbance wavelength λ clearly has the same value in every layer.

2.1 Boundary Conditions. The fluid layer is contained between rigid walls at $z = \pm 1/2$ for which the no-slip condition applies. From this condition, one obtains (Lienhard, 1987) the following relations among the coefficients of the solution:

$$\begin{bmatrix} \cosh(q/2) & \cosh(q^*/2) \\ q\sinh(q/2) & q^*\sinh(q^*/2) \end{bmatrix} \begin{bmatrix} (q^2-a^2)A \\ (q^{*2}-a^2)A^* \end{bmatrix} = A_0(q_0^2+a^2)\begin{bmatrix} \cos(q_0/2) \\ -q_0\sin(q_0/2) \end{bmatrix} \quad (4)$$

and

$$\begin{bmatrix} \sinh(q/2) & \sinh(q^*/2) \\ q\cosh(q/2) & q^*\cosh(q^*/2) \end{bmatrix} \begin{bmatrix} (q^2-a^2)B \\ (q^{*2}-a^2)B^* \end{bmatrix} = B_0(q_0^2+a^2)\begin{bmatrix} \sin(q_0/2) \\ q_0\cos(q_0/2) \end{bmatrix} \quad (5)$$

These conditions determine A and B in terms of A_0 and B_0.

Thermal boundary conditions are the matching of fluid and solid temperature and heat flux. These conditions reduce to a matching of perturbation temperature and flux, which fixes A_0 and B_0. The difficulty encountered in the radiative problem is the calculation of the radiant perturbation.

2.2 Radiant Exchange. The perturbation to the basic temperature field renders the boundaries nonisothermal, and this perturbation radiant exchange enters the boundary condition for the stability problem. Hence, the calculation of the radiant exchange must account for the variation in surface temperature; integration is required.

Prior to calculating the radiant exchange between two gray walls, it is convenient to find the radiation incident on an element of one wall that is emitted by an opposing black wall when the temperature field experiences a small wavelike perturbation of planform $f(x,y)$. The perturbed temperature along the opposing wall (wall 2, say) is

$$T_2(x,y) = \bar{T}_2 + \tilde{T}_2 f(x,y) \quad (6)$$

for mean temperature $\bar{T}_2$ and perturbation $\tilde{T}_2$, and the linearized radiant emission at any point is thus

$$\sigma T_2^4 = \sigma(\bar{T}_2^4 + 4\bar{T}_2^3\tilde{T}_2 f(x,y)) = \sigma\bar{T}_2^4 + \Delta_2 f(x,y) \quad (7)$$

where $\Delta_2 = 4\sigma\bar{T}_2^3\tilde{T}_2$ is the amplitude of the normal mode radiative emission at wall 2.

The radiation received at an element of wall 1 may be found by integrating the differential flux received from an element of wall 2 over surface 2. The differential flux is

$$d^2q_1^- = \sigma T_2^4(r,\theta)\, dF_{d2-d1}\frac{dA_2}{dA_1} = \sigma T_2^4(r,\theta)\frac{1}{\pi(r^2+1)^2} r\,dr\,d\theta \quad (8)$$

We have introduced a polar coordinate system on surface 2 with origin above the differential element of surface 1 to facilitate the integration (see Fig. 1). Lengths have been scaled with the plate spacing L_i, leaving other variables in dimen-

Nomenclature

a_i = dimensionless wavenumber in layer $i = 2\pi L_i/\lambda$
A = midlayer to fluid layer aspect ratio $= L_B/2L_i$
A, A_0, B, B_0 = unknown coefficients of the temperature normal mode amplitude, equations, (1), (4), (5) and Appendix A
dF_{d1-d2} = view factor between a differential element of surface 1 and a differential element of surface 2
D_i = dimensionless vertical derivative in layer $i = d/dz_i$
$f(x,y)$ = dimensionless solution of the Helmholtz equation
g = gravitational body force
k, k_B = thermal conductivity of the fluid or boundary
$K_1(a)$ = modified Bessel function of first order
L_i, L_B = thickness of fluid layer i or midlayer B
N_i = radiation/conduction parameter at wall $i = 4\sigma T_i^3 L_i/k$
q, q_0, τ = see equations (1) and (2)
q_{12} = net base state radiant heat flux $= \sigma(T_1^4 - T_2^4)/(1/\epsilon_1 + 1/\epsilon_2 - 1)$
q_{bs} = net base state heat flux
q_i^- = incoming radiant heat flux at wall i
$\tilde{q}_i^+, \tilde{q}_i^-$ = outgoing/incoming radiant perturbation heat flux at black wall i
$\tilde{q}_i$ = net perturbation radiant flux leaving wall i
(r, θ) = dimensionless polar coordinates in the horizontal plane
Ra_i, Ra_c = critical Rayleigh number for layer $i = g\beta L_i^3\Delta T_i/\nu\alpha$
$T(x,y,z), \tilde{T}(x,y,z)$ = dimensional fluid temperature distribution, fluid temperature perturbation
$T_i, \bar{T}, \tilde{T}_i$ = dimensional temperature, mean (base state) temperature, and perturbation temperature of wall i

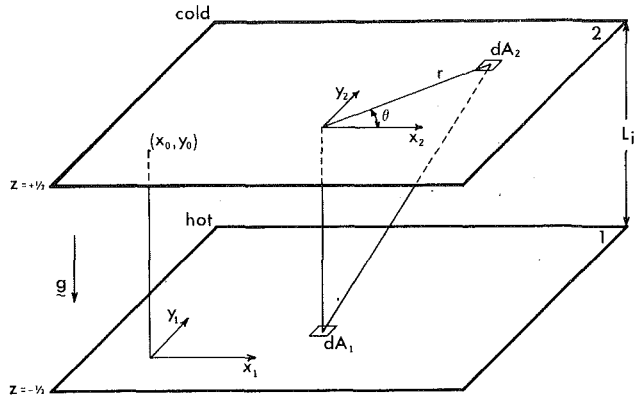

Fig. 1 Geometry and coordinate systems

sional form. This allows us to use the dimensionless planform and wavenumber of the stability analysis without becoming ensnared in additional nomenclature. The incoming flux at surface 1 is then $q_1^- = \sigma \bar{T}_2^4 + \tilde{q}_1^-$, where the radiant perturbation is given by the integral

$$\tilde{q}_1^- = \frac{\Delta_2}{\pi} \int_0^\infty \int_0^{2\pi} \frac{f(r,\theta) r dr d\theta}{(r^2+1)^2} \tag{9}$$

in which r, f, and the wavenumbers are dimensionless.

2.3 Planform at Onset. To integrate the radiative exchange over the boundaries, some assumption as to the planform at onset of motion must be introduced. The normal mode analysis shows that the planform at onset, $f(x,y)$, must satisfy the Helmholtz equation $(\partial^2 f/\partial x^2 + \partial^2 f/\partial y^2 + a^2 f = 0)$; no more specific assumptions are needed.

Experimentally the planform is most often observed to be either rolls or hexagons near onset of motion, although the presence of vertical sidewalls in most laboratory situations will influence the specific mode observed. Here we compute the radiant perturbations for a general planform, which includes those planforms as special cases. Somewhat surprisingly, the results are identical for *all* planforms. We thus show that radiant stabilization does not favor one mode of onset over any other.

Several coordinate systems are required in evaluation of the integrals (see Fig. 1): (x_1, y_1) and (x_2, y_2) are Cartesian systems on A_1 and A_2, respectively; the integrals over A_2 are most conveniently phrased in polar coordinates, (r, θ), which coincide with (x_2, y_2). The origin of the (x_1, y_1) system may be placed at the origin of planform symmetry for convenience, and the origin of the (x_2, y_2) system may be located above the point (x_1, y_1) at which the incident radiation is to be calculated. The origin of symmetry (x_0, y_0) is located in the A_2 coordinates, and it follows that (x_0, y_0) has the value $-(x_1, y_1)$.

Bisshopp (1960) has found the most general planform that has x and y periodicities characterized by a given total wavenumber a (cf. Chandrasekhar, 1961):

$$f(x, y) = C \cos\left[a\left(1 - \frac{1}{m^2}\right)^{1/2} x\right] \cos \frac{a}{m} y + \cos ay \tag{10}$$

for m an integer greater than 1, C a constant, and a the total wavenumber.[1] This equation may be recast into polar coordinates, letting $\kappa = (1 - 1/m^2)^{1/2}$

$$\begin{aligned} f(r,\theta) = \frac{C}{2}\Bigg\{ & \cos\left[ar\left(\frac{\cos\theta}{\kappa} + \frac{\sin\theta}{m}\right)\right] c_-(x_0, y_0) \\ & + \sin\left[ar\left(\frac{\cos\theta}{\kappa} - \frac{\sin\theta}{m}\right)\right] s_-(x_0, y_0) \\ & + \cos\left[ar\left(\frac{\cos\theta}{\kappa} + \frac{\sin\theta}{m}\right)\right] c_+(x_0, y_0) \\ & - \sin\left[ar\left(\frac{\cos\theta}{\kappa} + \frac{\sin\theta}{m}\right)\right] s_+(x_0, y_0) \\ & + \cos(ar\sin\theta)\cos ay_0 + \sin(ar\sin\theta)\sin ay_0 \Bigg\} \end{aligned} \tag{11}$$

[1] For rolls, $m = 1$; for hexagons, $C = 2$, $m = 2$.

Nomenclature (cont.)

$W(z)$ = dimensionless normal mode amplitude of vertical fluid velocity
(x, y, z) = dimensionless Cartesian coordinates, z vertical and increasing upward
X_i = ratio of fluid thermal conductivity to wall i conductivity
X_B = fluid to midlayer (or boundary) thermal conductivity ratio
α = midlayer temperature disturbance coupling parameter or fluid thermal diffusivity, by context
Δ_i = dimensional amplitude of normal mode radiant emission at wall $i = 4\sigma \bar{T}_i^3 \tilde{T}_i$
ΔT_i = temperature difference across layer i
ϵ_i = gray body emissivity of wall i
$\Theta_i(z)$ = dimensionless normal mode temperature disturbance amplitude in layer i
λ = dimensional disturbance wavelength
Λ_{ij} = coefficient of third-kind boundary condition, defined where used
ν = kinematic viscosity
σ = Stefan-Boltzmann constant
ψ = $aK_1(a)$
Ψ_a, Ψ_b = reflection functions defined by equations (23) and (24)
$\Im$ = imaginary part of a complex number
$\Re$ = real part of a complex number

Superscripts and Subscripts

$(\ )^*$ = complex conjugate
$(\tilde{\ })$ = a perturbation
$(\ )_B$ = quantity referred to the midlayer or boundary, or quantity nondimensionalized in midlayer or boundary scales
$(\ )_i$ = quantity referred to fluid layer i or nondimensionalized in scales of fluid layer i

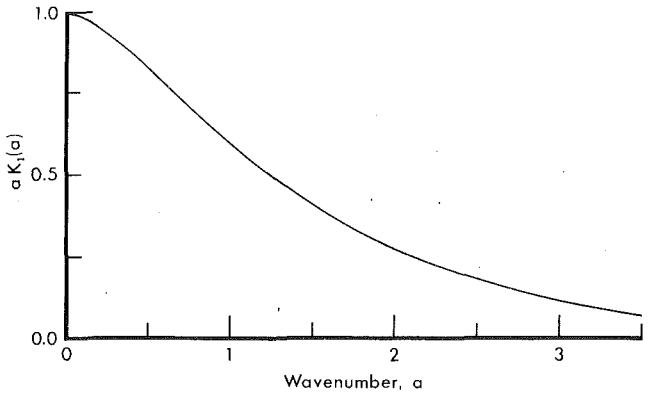

Fig. 2 Attenuation factor

where we use the notation $c_{\pm}(x_0, y_0) = \cos a(x_0/\kappa \pm y_0/m)$ and $s\pm(x_0, y_0) = \sin a(x_0/\kappa \pm y_0/m)$. With some calculation, the integral for this planform may be reduced to

$$\tilde{q}_1^-(x_1, y_1) = \frac{\Delta_2}{\pi}\left[\cos ay_0 + \frac{C}{2}(c_- + c_+)\right] \times \int_0^\infty \frac{r}{(r^2+1)^2}\int_0^{2\pi} \cos(ar \sin\theta)\, d\theta\, dr$$

$$= 2\Delta_2\left[\cos ay_0 + \frac{C}{2}(c_- + c_+)\right]\int_0^\infty \frac{rJ_0(ar)\,dr}{(r^2+1)^2} \tag{12}$$

in which we have identified the integral representation of the first kind Bessel function of order zero, J_0

$$J_0(z) = \frac{1}{\pi}\int_0^\pi \cos(z \sin\theta)\, d\theta \tag{13}$$

The remaining integral may be evaluated, so producing

$$\tilde{q}_1^-(x_1, y_1) = aK_1(a)\Delta_2 f(x_0, y_0) = aK_1(a)\Delta_2 f(x_1, y_1) \tag{14}$$

where K_1 is a modified Bessel function of first order. The result is the opposing wall perturbation radiosity multiplied by an attenuation factor dependent upon the wavenumber. Richards and Edwards (1989) also obtained this factor for a roll planform, although their result is in numerical form. (Their $S(a)$ is actually $aK_1(a)$.)

Evidently, the form of the attenuation factor is a property of the present averaging of unbounded, symmetric solutions of the Helmholtz equation.

The physical interpretation of these results relates simply to the periodic variations in radiant emission from the surface being viewed. The attenuation factor (Fig. 2) represents the reduction in net radiation incident from the surface viewed caused by increasing the spatial frequency of surface temperature variations. When the surface temperature varies rapidly (large a), the point considered receives little net perturbation transmission: The perturbation flux averages out. When the spatial variation is slow (small a), little averaging occurs because the surface as viewed is largely isothermal. Similarly, the flux received at any point depends on its location relative to the hot and cold peaks of the wavelike perturbation. At a hot peak of the wave, the radiation perturbation is greatest; at a node of the wave, the radiation perturbation is zero.

The radiative transport shows a significant dependence upon the wavenumber. Edwards and Sun (1971) were able to incorporate radiative effects into an effective wall conductivity in their study of sidewall radiation in circular cylinders, by deducing a priori the most unstable wavenumber in their horizontally bounded domain. The horizontal domain of the present problem is unbounded, and the wavenumber may vary continuously. As a result, radiation effects will influence the critical wavenumber, and the wavenumber at onset of motion cannot generally be inferred from other considerations.

2.4 Net Radiant Exchange. The boundary conditions of the stability analysis require us to know the net radiant exchange along both surfaces. For two black walls, the perturbation exchange follows directly from the preceding results:

$$\tilde{q}_1(x, y) = \tilde{q}_1^+(x, y) - \tilde{q}_1^-(x, y) = (\Delta_1 - aK_1(a)\Delta_2) f(x, y) \tag{15}$$

For gray walls, the exchange problem is complicated by reflection between the two walls. Richards and Edwards (1989) solved this problem using a radiosity-irradiation approach. Here we sketch an alternate (although longer) solution using a net-radiation method.

The radiant interchange can be expressed in terms of a pair of coupled integral equations relating the wall temperature distributions to the net heat flux *leaving* each point on the two surfaces (Siegel and Howell, 1981, §8-4.1). Upon deducting the base state radiant exchange q_{12} from those equations we obtain a similar pair of coupled equations describing the perturbation exchange

$$\frac{\tilde{q}_1(x_1, y_1)}{\epsilon_1} - (1-\epsilon_2)\int_{A_2}\frac{\tilde{q}_2(x_2, y_2)}{\epsilon_2} dF_{d1-d2} = (\Delta_1 - aK_1(a)\Delta_2) f(x_1, y_1) \tag{16}$$

$$\frac{\tilde{q}_2(x_2, y_2)}{\epsilon_2} - (1-\epsilon_1)\int_{A_1}\frac{\tilde{q}_2(x_2, y_2)}{\epsilon_2} dF_{d2-d1} = (\Delta_2 - aK_1(a)\Delta_1) f(x_2, y_2) \tag{17}$$

These equations decouple if one wall (wall 1, say) is black. In that case, $\tilde{q}_2$ is obtained directly and $\tilde{q}_1$ by a second integration

$$\tilde{q}_1(x, y) = \{\Delta_1[1-(1-\epsilon_2)(aK_1(a))^2] - \epsilon_2 aK_1(a)\Delta_2\} f(x,y) \tag{18}$$

$$\tilde{q}_2(x, y) = \epsilon_2\{\Delta_2 - aK_1(a)\Delta_1\} f(x,y) \tag{19}$$

The attenuation factor appears squared as a result of the reflection integration of $\tilde{q}_1$.

The appearance of powers of $aK_1(a)$ in the gray-black solution, deriving from the partial reflection at the gray wall, suggests that the gray-gray solution, involving an infinite sequence of such partial reflections[2], will be expressible as a power series in $aK_1(a)$. Thus, we attempt the general solution of equations (16) and (17) using the forms

$$\frac{\tilde{q}_1}{\epsilon_1} = \left(\sum_{n=1}^\infty A_n\psi^n\right) f(x, y) \text{ and } \frac{\tilde{q}_2}{\epsilon_2} = \left(\sum_{n=1}^\infty B_n\psi^n\right) f(x, y) \tag{20}$$

with $\psi = aK_1(a)$. Substituting these into equations (16) and (17) and equating coefficients of like powers of ψ, we obtain four geometric series in $(1-\epsilon_1)(1-\epsilon_2)\psi^2$, which may each be summed, producing a closed-form solution. The dimensional normal mode radiant perturbation flux leaving each wall is thus found to be

$$\tilde{q}_1 = 4\sigma\Delta T_i\{\bar{T}_1^3\Psi_a(\epsilon_1, \epsilon_2, a)\Theta_i(-1/2) - \bar{T}_2^3\Psi_b(\epsilon_1, \epsilon_2, a)\Theta_i(1/2)\} f(x, y) \tag{21}$$

[2] Recall the ray tracing derivation of the view factor for infinite parallel plates.

$$\tilde{q}_2 = 4\sigma \Delta T_i \{ -\tilde{T}_1^3 \Psi_b(\epsilon_2, \epsilon_1, a)\Theta_i(-1/2) + \tilde{T}_2^3 \Psi_a(\epsilon_2, \epsilon_1, a)\Theta_i(1/2)\} f(x, y) \quad (22)$$

where we have defined the following transfer factors

$$\Psi_a(\epsilon_1, \epsilon_2, a) = \epsilon_1 \left(1 - \frac{\epsilon_1(1-\epsilon_2)\psi^2}{1-(1-\epsilon_1)(1-\epsilon_2)\psi^2}\right) \quad (23)$$

$$\Psi_b(\epsilon_1, \epsilon_2, a) = \epsilon_1 \epsilon_2 \left(\frac{\psi}{1-(1-\epsilon_1)(1-\epsilon_2)\psi^2}\right) \quad (24)$$

These functions account for the absorption and reflection of radiation; the order of the arguments, ϵ_i, of Ψ_a must be reversed at the opposing wall. These are identical (for gray walls) to the transfer factors F_0 and F_{01}, respectively, obtained by Richards and Edwards.

2.5 Thermal Boundary Conditions. Having the general radiative boundary condition, we are now able to form the thermal boundary conditions on the normal mode amplitudes. The matching of temperatures, under the present scaling, yields

$$\Theta_i = \left(\frac{k_i}{k_B}\right)\left(\frac{L_B}{L_i}\right)\Theta_B \quad (25)$$

for walls of finite thickness, and

$$\Theta_i = \Theta_B \quad (26)$$

for semi-infinite walls. The matching of the perturbation heat flux must incorporate the radiative transfer. In physical variables, for Z the dimensional vertical coordinate,

$$-k_i \left.\frac{d\tilde{T}}{dZ}\right|_1 + \tilde{q}_1 = -k_B \left.\frac{d\tilde{T}_B}{dZ}\right|_1 \quad (27)$$

at wall one and

$$-k_i \left.\frac{d\tilde{T}}{dZ}\right|_2 = -k_B \left.\frac{d\tilde{T}_B}{dZ}\right|_2 + \tilde{q}_2 \quad (28)$$

at wall two. In nondimensional form, the conditions on the normal mode amplitudes at walls of finite thickness become

$$D_i\Theta_i(-1/2) = \left(\frac{k_B}{k_i}\right)\left(\frac{L_i}{L_B}\right)\left(\frac{\Delta T_B}{\Delta T_i}\right) D_B\Theta_{B_1}(1/2) + \left(\frac{L_i}{k_i \Delta T_i}\right)\frac{\tilde{q}_1}{f(x, y)} \quad (29)$$

$$D_i\Theta_i(1/2) = \left(\frac{k_B}{k_i}\right)\left(\frac{L_i}{L_B}\right)\left(\frac{\Delta T_B}{\Delta T_i}\right) D_B\Theta_{B_2}(-1/2) - \left(\frac{L_i}{k_i \Delta T_i}\right)\frac{\tilde{q}_2}{f(x, y)} \quad (30)$$

where the fluid and solid layer normal mode amplitudes are scaled with variables appropriate to the individual layers. For semi-infinite walls, the normal mode amplitudes are scaled with the fluid layer thickness and temperature difference

$$D_i\Theta_i(-1/2) = \left(\frac{k_B}{k_i}\right) D_B\Theta_{B_1}(0) + \left(\frac{L_i}{k_i \Delta T_i}\right)\frac{\tilde{q}_1}{f(x, y)} \quad (31)$$

$$D_i\Theta_i(1/2) = \left(\frac{k_B}{k_i}\right) D_B\Theta_{B_2}(0) - \left(\frac{L_i}{k_i \Delta T_i}\right)\frac{\tilde{q}_2}{f(x, y)} \quad (32)$$

Using methods developed in an earlier work (Lienhard, 1987), the wall temperature disturbances may be eliminated from these boundary conditions to produce a third kind condition to be applied directly to the fluid temperature disturbance at either boundary of the fluid layer. The procedure consists of using the exact solution for $\Theta_B(z)$ to eliminate $D\Theta_{B_j}$ in favor of Θ_{B_j}, which is then replaced with $\Theta_i(\mp 1/2)$. (For example, at an upper semi-infinite boundary, $D\Theta_B(0) = -a_B/(k_i/k_B)\Theta_B(0) = -a_i/(k_i/k_B)\Theta(1/2)$.) The resulting conditions have the form

$$D\Theta_i(-1/2) = \Lambda_{11}\Theta_i(-1/2) + \Lambda_{12}\Theta_i(1/2) \quad (33)$$

$$D\Theta_i(1/2) = \Lambda_{21}\Theta_i(-1/2) + \Lambda_{22}\Theta_i(1/2) \quad (34)$$

The Λ_{ij} depend on various physical parameters. Specific examples appear below.

These boundary conditions differ from the usual third kind conditions in that the temperature gradient at either wall depends upon the temperature disturbance at *both* walls. Nonetheless, these boundary conditions may be applied to close the solution with a condition on the remaining unknown coefficients of equation (1), A_0 and B_0:

$$\begin{bmatrix} \mathcal{C}_1 & \mathcal{C}_2 \\ \mathcal{C}_3 & \mathcal{C}_4 \end{bmatrix}\begin{bmatrix} A_0 \\ B_0 \end{bmatrix} = 0 \quad (35)$$

The functions $\mathcal{C}_i$ are given in Appendix A. By determining values of Ra for which the matrix $\mathcal{C}$ is nonsingular, we find the eigenvalues of the stability problem. The smallest eigenvalue is then minimized as a function of wavenumber to give the critical Rayleigh number of the configuration, Ra_c.

2.6 Models of Wall Thermal Behavior. We have taken the wall temperature to satisfy a heat conduction condition. Richards and Edwards treated instead the situation when the wall heat loss is characterized by a convective boundary condition. The difference between the two conditions has been discussed by Lienhard (1987), who found that critical Rayleigh numbers for the conditions differ significantly (differences can be as large as those produced by radiation). In particular, suppose fluid layer i to be bounded by a conductive slab (thickness L_B, conductivity k_B) whose outer side is cooled according to a convection coefficient h_i. Lienhard showed that only when

$$a_i^2\left(\frac{L_B}{L_i}\right)^2 << hL_i/k_i << 1 \quad (36)$$

may the thermal diffusivity of the slab be ignored and the fluid boundary condition represented by a Biot number, hL_i/k_i. Conversely, a slab of arbitrary thermal conductivity will behave as a semi-infinite boundary when

$$\left(a_i \frac{L_B}{L_i}\right) \geq 1.8 \quad (37)$$

In between these two limits, the boundary condition applied must account for *both* the conductive and the convective effects. In this paper, we consider the purely conductive boundary condition.

In all three circumstances, the third-kind boundary condition is wavenumber dependent. Richards and Edwards surmounted this complication with a graphic solution to be used iteratively. Here, we employ the methods developed in the previous work (1987) to facilitate direct solutions for such wavenumber-dependent conditions. Our results are both tabulated and presented as a correlation.

Direct comparison of the present work to the Richard and Edwards results is not possible because the boundary conditions are different. We avoid the tempting, but erroneous, model of a conducting boundary slab (thickness L_B, conductivity k_B) as a heat transfer coefficient $h = k_B/L_B$; this approximation neglects the *horizontal* diffusion of heat in the slab, which damps wall temperature perturbations. A conducting wall solution must account for such transverse heat conduction, as do the boundary conditions used here.

We also note that the differing wavenumber dependences of the conductive and convective boundary conditions will lead

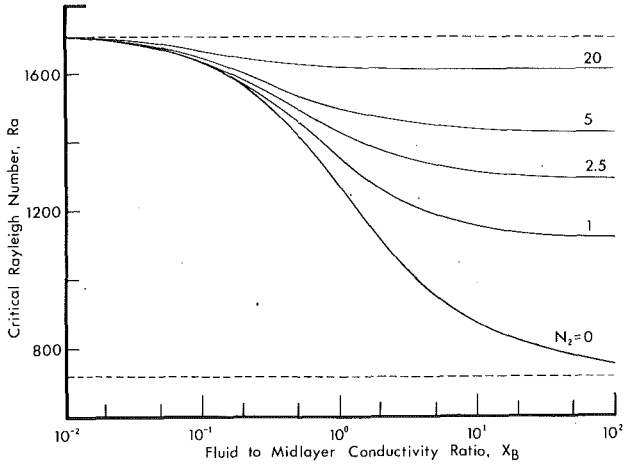

Fig. 3 Single layer with identical, conducting, black walls: $N_1/N_2 = 2$

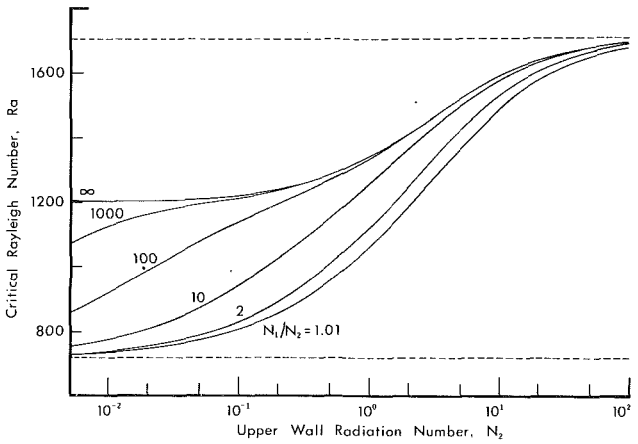

Fig. 4 Fixed heat flux limit of the single layer

Table 1 Critical Rayleigh numbers and wavenumbers for a single layer with identical, semi-infinite, conductive, black walls: $N_1/N_2 = 2$

Critical Rayleigh Number

	Fluid Layer to Wall Conductivity Ratio, X_B							
N_2	0	0.1	0.3	1.0	3.0	10.0	100.0	∞
0.0	1707.76	1628.01	1505.29	1267.47	1037.89	872.10	753.34	720.00
0.5	1707.76	1629.57	1515.34	1315.25	1150.45	1054.16	1007.02	1001.33
1.0	1707.76	1631.06	1524.27	1351.74	1222.96	1153.41	1121.09	1117.27
2.5	1707.76	1635.16	1546.14	1425.76	1350.46	1313.95	1297.86	1296.00
5.0	1707.76	1640.99	1572.11	1495.38	1454.51	1436.26	1428.51	1427.62
20.0	1707.76	1662.09	1636.92	1619.67	1613.02	1610.44	1609.41	1609.29

Critical Wavenumber

	Fluid Layer to Wall Conductivity Ratio, X_B							
N_2	0	0.1	0.3	1.0	3.0	10.0	100.0	∞
0.0	3.116	3.004	2.818	2.398	1.873	1.330	0.641	0.00
0.5	3.116	3.007	2.839	2.514	2.208	2.001	1.888	1.873
1.0	3.116	3.010	2.856	2.594	2.384	2.264	2.205	2.198
2.5	3.116	3.017	2.890	2.737	2.640	2.594	2.574	2.572
5.0	3.116	3.027	2.941	2.853	2.810	2.793	2.785	2.784
20.0	3.116	3.061	3.036	3.023	3.018	3.016	3.016	3.016

to different critical wavenumbers: The constrained variation of the Rayleigh number in the wavenumber/"Biot number" (or Λ_{ij}) space differs for the two problems, and consequently so must the critical loci. No change of variables will cause the problems to become formally identical (see Fig. 2 of Lienhard, 1987).

3 Single Layer With Conductive, Radiating Boundaries

The solution that best illustrates the radiant instability is that for a single layer with semi-infinite walls of finite thermal conductivity. Critical Rayleigh numbers have been calculated for the full range of wall conductivities and temperatures, assuming black walls of equal conductivity.

For semi-infinite boundaries of unequal conductivity and emissivity, equations (31) and (32) yield the following general boundary conditions after elimination of the wall temperature disturbances:

$$D\Theta(-1/2) = \left\{\frac{a}{X_1} + N_1 \Psi_a(\epsilon_1, \epsilon_2, a)\right\}\Theta(-1/2) - N_2 \Psi_b(\epsilon_1, \epsilon_2, a)\Theta(1/2) \quad (38)$$

$$D\Theta(1/2) = N_1 \Psi_b(\epsilon_2, \epsilon_1, a)\Theta(-1/2) - \left\{\frac{a}{X_2} + N_2 \Psi_a(\epsilon_2, \epsilon_1, a)\right\}\Theta(1/2) \quad (39)$$

Here, we have introduced the nondimensional conduction/radiation groups

$$N_1 = \frac{4\sigma \bar{T}_1^3 L}{k} \text{ and } N_2 = \frac{4\sigma \bar{T}_2^3 L}{k} \quad (40)$$

(with $N_1 > N_2$ for unstable stratification) and we have defined $X_i = k/k_i$ for k the thermal conductivity of the fluid and k_i the thermal conductivity of wall i. The terms on the right-hand sides of the boundary conditions represent the heat conducted into the walls (a/X terms) and the radiant transfer at the walls.

For brevity, we consider only the case of identical black walls of conductivity ratio $X_i = X_B$, for which the boundary conditions simplify considerably

$$D\Theta(-1/2) = \left\{\frac{a}{X_B} + N_1\right\}\Theta(-1/2) - N_2 a K_1(a)\Theta(1/2) \quad (41)$$

$$D\Theta(1/2) = N_1 a K_1(a)\Theta(-1/2) - \left\{\frac{a}{X_B} + N_2\right\}\Theta(1/2) \quad (42)$$

Typical results[3] are shown in Fig. 3. The lowest curve is the nonradiative case. As the level of radiation rises, the layer is increasingly stabilized. This stabilizing effect is greater for the less conductive walls (larger X_B). The mechanism of this stabilization is quite clear: Radiation allows hot and cold spots to be cooled or warmed, thus relieving the otherwise large and destabilizing nonuniformities of the nonconductive walls. The isothermal wall condition ($Ra_c = 1707.762$) is approached as the level of radiation becomes very large.

Radiation markedly increases the critical wavenumber in the nonconductive cases that are strongly stabilized (Table 1). This trend represents an interesting competition between the decreasing stability of less conductive boundaries and the increasingly large radiative stabilization at the small critical wavenumbers normally associated with poorly conducting boundaries.

The limiting case of boundaries of vanishing conductivity ($X_B \to \infty$) also corresponds to boundaries of fixed heat flux (since $D\Theta_B \to 0$). All radiation received at a wall is reradiated; however, the combined emission and absorption still act to reapportion heat among the hot and cold regions of the boundary. Thus, radiation maintains its stabilizing influence (Fig. 4). The usual limits ($Ra_c = 720$, 1707.762) appear at low and high levels of radiation; however, when N_1 remains very large while N_2 vanishes, a new limit is reached in which $Ra_c = 1202.17$. For that case, radiant effects are present at both walls, but the primary behavior is that of an additional mode of cooling the lower surface.

Rather than presenting a large compendium of Rayleigh numbers, we give only a limited tabulation and cover the broader range by correlating the numerical data. The form of

[3] Numerical values are accurate to the number of digits shown; errors are less than 5 ppm.

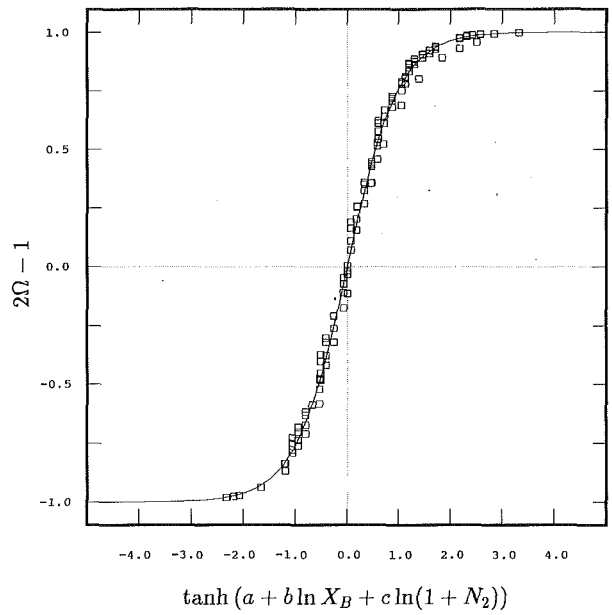

Fig. 5 Correlation of numerical critical Rayleigh numbers for a single layer with semi-infinite, black, conductive walls

the correlation is motivated by the shape of the curves in Fig. 3 and the form of the actual boundary conditions. The Rayleigh number is scaled against its maximum (1707.762) and minimum value (the latter depending on the level of radiation) and is correlated as

$$\Omega = \frac{1707.762 - \mathrm{Ra}_c}{1707.762 - \mathrm{Ra}_{\min}}$$

$$= \frac{1}{2} + \frac{1}{2} \tanh\,[a + b \ln X_B + c \ln(1 + N_2)] \tag{43}$$

The exact solutions for Ra suggest that variations of N_1/N_2 are important in determining $\mathrm{Ra}_{\min}$ but do not affect the shape of the stability boundary. Thus, that parameter is not introduced explicitly in the correlating equation. With exact values of Ra_c spanning the ranges

$$0 \le X_B \le \infty,\ 0 \le N_2 \le 20.0(\to \infty),$$

$$\text{and } 1.0 \le N_1/N_2 \le 10.0 \tag{44}$$

the constants (a, b, c) were determined by least squares to be $(-0.077472, 0.48969, 0.37331)$ to an rms error *in the Rayleigh number* of 1.1 percent and a maximum error of 5.1 percent (see Fig. 5). The ranges of X_B and N_2 cover essentially the complete variation of those parameters; the ratio N_1/N_2 was held below 10 because this covers the range of greatest interest.

In the nonconductive wall case ($X_B \to \infty$), similar considerations lead us to fit Ra_c (which is now $\mathrm{Ra}_{\min}$ in equation (43)) to the form

$$\Omega_\infty = \frac{1707.762 - \mathrm{Ra}_{\min}}{1707.762 - 720.0}$$

$$= \frac{1}{2} + \frac{1}{2} \tanh\,[e + f \ln N_2 + g \ln N_1] \tag{45}$$

Least-squares fitting of (e, f, g) over the ranges

$$0 \le N_2 \le \infty \text{ and } 1.0 \le N_1/N_2 \le 10.0 \tag{46}$$

gives $(0.27145, -0.17811, -0.20976)$ with an rms error *in the Rayleigh number* of 1.8 percent and a maximum error of 4.8 percent. The form of the fit is inadequate to represent the two-step behavior of the stability boundary, which appears at larger values of N_1/N_2. Using equations (43) and (45) for given values of X_B, N_1, and N_2, one may compute Ra_c.

These results may be applied to gas layers with thick boundaries at moderate temperatures. For common materials, the conductivity ratio X_B will always be small when a gas layer is bounded by a solid wall ($X_B < 0.5$). In this range, radiation effects are relatively unimportant, and for such thick boundaries they may almost always be ignored. However, when the boundaries are thin, the effects of finite thermal conductivity are more pronounced because larger temperature gradients can be supported. Thus, radiative effects are quite important for thin layers such as those used as stabilizing partitions in solar collectors. We consider such multilayer problems in the following section. Additional calculations (which are not presented) indicate that reducing the wall emissivity simply decreases the single-layer stability toward the nonradiative limit.

4 Two Layers Separated by a Thin Midlayer

The air gap between a flat-plate solar collector and its coverglass is often partitioned with a thin plastic film in order to reduce natural convection heat loss from the absorber plate. The stability limit of the two layers so formed is coupled by conduction through the separating midlayer (Fig. 6). This behavior has been discussed previously in the absence of thermal radiation (Catton and Lienhard, 1984; Lienhard, 1987). When thermal radiation enters the problem, the base state temperatures are altered and radiation stabilization can also occur.

In this section, we obtain stability results for such a horizontal two-layer configuration. These results are not directly applicable to the finite amplitude convection state, but may be extended to it through such procedures as the power integral method (Lienhard and Catton, 1986). These results should also characterize the finite amplitude heat transfer to the extent that a more stable geometry transfers less heat at a fixed supercritical Rayleigh number. Inclined enclosures of relatively high aspect ratio can be approximated from the horizontal results by using an appropriate effective gravity in calculating the critical Rayleigh number (Hart, 1971).

The wall temperatures satisfy the following equations, which may be solved iteratively for the unknown $\bar{T}_2$ and $\bar{T}_3$:

$$q_{bs} = \frac{k}{L}(\bar{T}_1 - \bar{T}_2) + \frac{\sigma(\bar{T}_1^4 - \bar{T}_2^4)}{1/\epsilon_1 + 1/\epsilon_2 - 1}$$

$$= \frac{k_B}{L_B}(\bar{T}_2 - \bar{T}_3)$$

$$= \frac{k}{L}(\bar{T}_3 - \bar{T}_4) + \frac{\sigma(\bar{T}_3^4 - \bar{T}_4^4)}{1/\epsilon_3 + 1/\epsilon_4 - 1} \tag{47}$$

Radiation brings the midlayer temperature closer to the temperature of the outer wall having higher radiant intensity. As a result, unstable conditions are reached in one layer first and convection in the other layer is driven via the midlayer interaction. This behavior is similar to that found by Catton and Lienhard (1984) in parallel layers of unequal height, where the thicker layer drives convection in the thinner layer.

The general two-layer boundary conditions with semi-infinite outer walls are

$$D_1\Theta_1(-1/2) = \left\{\frac{a_1}{X_1} + N_1\Psi_a(\epsilon_1, \epsilon_2, a_1)\right\}\Theta_1(-1/2)$$

$$- N_2\Psi_b(\epsilon_1, \epsilon_2, a_1)\Theta_1(1/2) \tag{48}$$

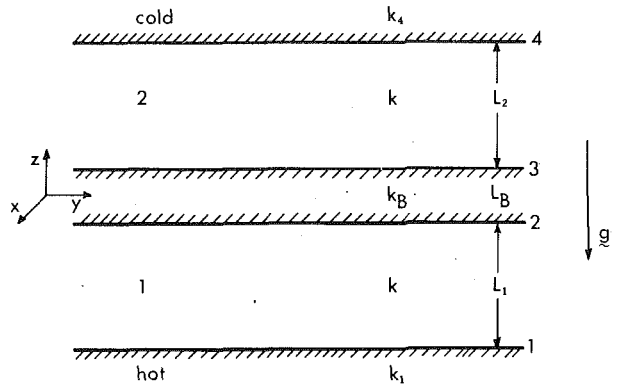

Fig. 6 Two-layer configuration

$$D_1\Theta_1(1/2)=\left\{\frac{a_1}{X_B}\left(\frac{\cosh(a_1A)-\alpha\sinh(a_1A)}{\alpha\cosh(a_1A)-\sinh(a_1A)}\right)\right.$$

$$\left.-N_2\Psi_a(\epsilon_2,\epsilon_1,a_1)\right\}\Theta_1(1/2)+N_1\Psi_b(\epsilon_2,\epsilon_1,a_1)\Theta_1(-1/2) \quad (49)$$

$$D_2\Theta_2(-1/2)=\left\{\frac{a_2}{X_B}\left(\frac{\cosh(a_2A)-\alpha\sinh(a_2A)}{\alpha\cosh(a_2A)-\sinh(a_2A)}\right)\right.$$

$$\left.-N_3\Psi_a(\epsilon_3,\epsilon_4,a_2)\right\}\Theta_2(-1/2)-N_4\Psi_b(\epsilon_3,\epsilon_4,a_2)\Theta_2(1/2) \quad (50)$$

$$D_2\Theta_2(1/2)=N_3\Psi_b(\epsilon_4,\epsilon_3,a_2)\Theta_2(-1/2)$$

$$-\left\{\frac{a_2}{X_4}+N_4\Psi_a(\epsilon_4,\epsilon_3,a_2)\right\}\Theta_2(1/2) \quad (51)$$

where $N_2=4\sigma L_1\bar{T}_3^3/k$, $N_3=4\sigma L_2\bar{T}_3^3/k$, $N_4=4\sigma L_2\bar{T}_4^3/k$, $A=L_b/2L_1$, and other terms are defined in the figure or have been defined previously. The groups N_2 and N_3 are fixed by N_1 and N_4 as part of the base state temperature profile. The parameter α represents the midlayer's conductive coupling between the two layers (Lienhard, 1987); it is iterated against a matching condition on the temperature gradients of the two layers

$$\mathrm{Ra}_1=\left(\frac{\bar{T}_1-\bar{T}_2}{\bar{T}_3-\bar{T}_4}\right)\left(\frac{L_1}{L_2}\right)^3\mathrm{Ra}_2 \quad (52)$$

For a solar collector type geometry, the simplest two-layer construction is a centered midlayer (under some circumstances, this is also the best configuration for convection suppression). The lowermost wall is liable to be highly conductive (typically copper, $X_1\approx 7\times10^{-5}$) and blackened selectively. The uppermost wall will likely be glass, which has a large conductivity in comparison to air ($X_4\approx 0.03$) and is black in the infrared. The center layer is likely to be a thin plastic film of moderate conductivity ($X_B\approx 0.1$), preferably black in the infrared.

The high conductivity of the outer bounding surfaces, in conjunction with their relatively high thickness, allows them to be treated as isothermal; the thinness of the midlayer forces consideration of conductive effects there. The top wall and the midlayer may be modeled as black. The lowermost wall, when properly designed, will be gray and of low emissivity in the infrared ($\epsilon_1\approx 0.10$). For arbitrary ϵ_1, the boundary conditions are now

$$\Theta_1(-1/2)=0 \quad (53)$$

$$D_1\Theta_1(1/2)=\left\{\frac{a_1}{X_B}\left(\frac{\cosh(a_1A)-\alpha\sinh(a_1A)}{\alpha\cosh(a_1A)-\sinh(a_1A)}\right)\right.$$

$$\left.-N_2\Psi_a(1.0,\epsilon_1,a_1)\right\}\Theta_1(1/2) \quad (54)$$

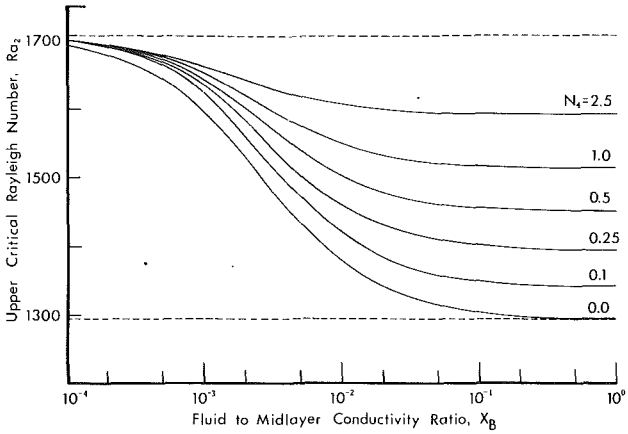

Fig. 7 Upper layer critical Rayleigh Number for $A=0.001$ and $N_1/N_4=2.0$ as a function of midlayer conductivity and radiation level

$$D_2\Theta_2(-1/2)=$$

$$\left\{\frac{a_2}{X_B}\left(\frac{\cosh(a_2A)+\alpha\sinh(a_2A)}{\alpha\cosh(a_2A)+\sinh(a_2A)}\right)+N_3\right\}\Theta_2(-1/2) \quad (55)$$

$$\Theta_2(1/2)=0 \quad (56)$$

where $a_1=a_2$. For simplicity, we focus on situations in which the bottom wall is simply black. A limited set of calculations outlines the effect of lower wall grayness.

Typical solutions are shown in Fig. 7 for a very thin midlayer ($A=0.001$). The behavior is very similar to that shown for a single layer in Fig. 3, but here radiation has a stabilizing influence at much smaller values of the conductivity ratio. The thin wall geometry has previously been found to be much more susceptible to finite conductivity effects since the boundary thinness allows greater temperature gradients to be supported; hence, radiation effects are much more pronounced at lower conductivities. For the two-layer case, in contrast to the single layer, radiation can be quite important for real materials.

Small effects of radiation on the base state temperatures result in the uneven spacing of the curves as $X_B\to 0$. Similarly, as $X_B\to\infty$, the critical Rayleigh number is slightly nonmonotonic, a small effect that we ignore for brevity. Both anomalies vanish as the radiation goes to zero.

Again, we offer a limited compilation of solutions in Table 2 while correlating a larger body of data in terms of the upper layer critical Rayleigh number

$$\Omega=\frac{1707.762-\mathrm{Ra}_c}{1707.762-\mathrm{Ra}_{\min}}$$

$$=\frac{1}{2}+\frac{1}{2}\tanh[a+b\ln X_B+c\ln(1+N_4)] \quad (57)$$

For $A=0.001$, exact values of the critical Rayleigh number spanning the ranges

$$0\le X_B\le 1.0,\quad 0\le N_4\le 2.5,\ \text{and}\ 1.0\le N_1/N_4\le 5.0 \quad (58)$$

yield the constants (a, b, c) as (2.9019, 0.50163, 0.24120) to an rms error *in the Rayleigh number* of 0.37 percent and a maximum error of 1.4 percent. Appropriate values of $\mathrm{Ra}_{\min}$ were extrapolated (to $\mathrm{Ra}_c\approx 3$) and fit as before

$$\Omega_{\min}=\frac{1707.762-\mathrm{Ra}_{\min}}{1707.762-1295.78}$$

$$=\frac{1}{2}+\frac{1}{2}\tanh[c+d\ln N_4+e\ln N_1] \quad (59)$$

A least-squares fit over the range

Table 2 Upper layer critical Rayleigh number and wavenumber for two layers with black walls and conducting midlayer: $N_1/N_4 = 2$, $A = 0.001$

Critical Rayleigh Number

	Fluid Layer to Wall Conductivity Ratio, X_B							
N_4	0	0.0003	0.001	0.003	0.01	0.03	0.1	1.0
0.0	1707.76	1668.56	1596.97	1483.85	1374.40	1325.09	1304.95	1296.71
0.1	1707.76	1683.58	1623.81	1518.53	1415.82	1369.72	1350.90	1343.23
0.25	1707.76	1686.21	1638.03	1548.95	1458.90	1418.19	1401.55	1394.30
0.50	1707.76	1687.32	1646.23	1574.99	1503.27	1470.66	1457.31	1451.83
1.00	1707.76	1688.20	1653.02	1599.76	1550.47	1528.63	1519.74	1516.01
2.50	1707.76	1689.64	1662.94	1631.77	1608.42	1599.08	1595.40	1593.64

Critical Wavenumber

	Fluid Layer to Wall Conductivity Ratio, X_B							
N_4	0	0.0003	0.001	0.003	0.01	0.03	0.1	1.0
0.0	3.116	3.038	2.898	2.708	2.590	2.562	2.554	2.552
0.1	3.116	3.060	2.921	2.737	2.630	2.605	2.599	2.597
0.25	3.116	3.070	2.957	2.788	2.690	2.667	2.662	2.660
0.50	3.116	3.074	2.985	2.852	2.772	2.752	2.747	2.746
1.00	3.116	3.077	3.008	2.923	2.873	2.86	2.858	2.857
2.50	3.116	3.082	3.039	3.004	2.990	2.987	2.987	2.987

Midlayer Coupling Parameter, α

	Fluid Layer to Wall Conductivity Ratio, X_B							
N_4	0	0.0003	0.001	0.003	0.01	0.03	0.1	1.0
0.0	∞	∞	∞	∞	∞	∞	∞	∞
0.1	∞	492.22	875.77	1177.9	772.12	335.42	111.00	11.525
0.25	∞	373.77	475.44	532.11	327.33	139.80	45.995	4.7642
0.50	∞	336.60	355.36	323.78	179.99	74.683	24.324	2.5183
1.00	∞	313.97	289.95	217.55	105.66	41.874	13.412	1.3756
2.50	∞	285.94	223.66	133.95	54.792	20.319	6.3437	0.64505

$$0 \le N_4 \le 2.5 \text{ and } 1.0 \le N_1/N_4 \le 5.0 \qquad (60)$$

gives (c, d, e) as (0.49225, 0.17771, −0.64288) to an rms error *in the Rayleigh number* of 0.78 percent and a maximum error of 1.5 percent. The values given by equation (59) intended for use with the preceding fit equation (57); they do *not* represent the limiting Rayleigh number as $X_B \to \infty$.

The above curve fits apply exactly only for $A = 0.001$. However, for small values of X_B, the parameter α becomes sufficiently large that the stability limit is characterized by the single parameter A/X_B, as was previously shown for thin midlayers in symmetric two-layer geometries (Lienhard, 1987). Hence, the critical Rayleigh number for thin midlayers of other A may be found as Ra_c for $A = 0.001$ from the correlation with X_B chosen so that A/X_B has the same value as the case of interest. For example, if we desire Ra_c for $A = 0.01$ and $X_B = 1.0$ (with $N_1 = 1.0$ and $N_4 = 0.5$), we may find it from the fit as Ra_c for $A = 0.001$ and $X_B = 0.1$ (at the same N_1 and N_4): The critical Rayleigh number for the unknown case is taken as 1457.31 from Table 2. The exact value calculated for the case of interest is 1457.11.

For $A \le 0.033$, this extrapolation procedure introduces errors of less than 1.1 percent over the entire range of X_B, N_1, and N_4 covered by equations (57) and (59). Errors decrease rapidly for thinner, more conductive midlayers and for lower levels of radiation. The extrapolation procedure provides a direct extension of the present results to other midlayer thicknesses.

Finally, we illustrate the effects of lower wall grayness for a plastic midlayer ($X_B = 0.1$) of aspect ratio $A = 0.01$, fairly common values for a solar collector partition. We vary only the radiation level and the lower wall emissivity, assuming the system to be otherwise the same as considered above (Table 3). As ϵ_1 decreases, the decreasing radiative exchange between the lower wall and the midlayer produces an increasing lower layer temperature difference. The Rayleigh numbers move in opposition, with Ra_1 decreasing and Ra_2 increasing. Consequently, control of the instability shifts from the upper layer at large ϵ_1 to the lower layer at small ϵ_1. As this change occurs, $1/\alpha$ passes from positive to negative values.[4]

[4]The parameter $\alpha = M/N$ (see equation (5)) characterizes the even/odd behavior of the temperature distribution. In all cases, onset of motion occurred for corotating cells (Lienhard and Catton, 1986) in the two layers with a predominantly even midlayer temperature distribution.

Table 3 Critical Rayleigh numbers for two layers with lowest wall gray: $N_1 = 1.0$, $N_4 = 0.5$, $A = 0.010$, and $X_B = 0.1$

ϵ_1	Ra_1	Ra_2	$\mathrm{Ra}_T \times 10^{-4}$	α	a
1.0	1300.74	1503.20	2.00	17.972	2.772
0.9	1348.27	1485.94	2.13	25.567	2.751
0.8	1393.44	1461.44	2.25	50.789	2.734
0.7	1433.49	1427.48	2.38	−53.669	2.726
0.6	1466.56	1382.84	2.49	−41.433	2.734
0.5	1491.54	1328.03	2.62	−22.032	2.754
0.4	1509.46	1265.14	2.74	−15.593	2.779
0.3	1522.06	1196.67	2.86	−12.549	2.802
0.2	1530.98	1124.74	2.98	−10.845	2.822
0.1	1537.45	1050.77	3.14	−9.7852	2.838

Table 4 Lower layer critical Rayleigh number and wavenumber for two layers with lowest wall gray: $\epsilon_1 = 0.1$, $A = 0.010$, and $X_B = 0.1$

Critical Rayleigh Number

	Upper Wall Radiation Number, N_4					
N_1/N_4	0.0	0.1	0.25	0.5	1.0	2.5
1.01	1374.38	1433.98	1486.78	1527.17	1560.62	1601.43
1.1	1374.38	1434.96	1488.08	1528.36	1561.71	1602.38
2.0	1374.38	1442.81	1498.06	1537.45	1570.13	1609.83
5.0	1374.38	1458.74	1516.34	1554.39	1586.45	1625.08

Critical Wavenumber

	Upper Wall Radiation Number, N_4					
N_1/N_4	0.0	0.1	0.25	0.5	1.0	2.5
1.01	2.590	2.631	2.714	2.812	2.897	2.983
1.1	2.590	2.633	2.717	2.815	2.899	2.985
2.0	2.590	2.646	2.741	2.838	2.918	3.000
5.0	2.590	2.673	2.787	2.880	2.952	3.022

The variation of the critical Rayleigh numbers with N_1 and N_4 for $\epsilon_1 = 0.1$ is shown in Table 4. The Rayleigh numbers are remarkably insensitive to N_1/N_4 over the range considered, but still respond strongly to N_4; the low levels of radiant exchange at the bottom wall are probably the cause of this behavior.

Table 3 also presents the *overall* Rayleigh number

$$\mathrm{Ra}_T = \left(\frac{g\beta}{\nu\alpha}\right)(L_1 + L_b + L_2)^3(\bar{T}_1 - \bar{T}_4) \qquad (61)$$

which characterizes the overall stability of a partitioned fluid layer. Overall stability *increases* as the lower wall emissivity decreases, a trend consonant with an intuitive view of the effects of lower wall grayness on the heat transfer, but in contradiction to the single-layer results. Although increasing radiant exchange raised the critical Rayleigh number of an individual fluid layer, the radiant equalization of the base state temperature differences increases overall stability as the lower wall emissivity drops. Evidently, the best two-layer solar collector design, in terms of convective or radiative top loss, is that with the lowest infrared emissivity at the absorber plate, in spite of the generally stabilizing effects of radiation found for a single fluid layer.

Two routes may be taken in determining a fluid layer's stability. The first is to regard N_1 and N_4 as being specified through a knowledge of T_1, T_4, and L_i, and then using the present data to determine whether or not convection occurs. The second route is to view only two of T_1, T_4, and L_i as being given, and to determine the value of the third parameter at which instability occurs. The latter case requires an iterative solution using the results for $\mathrm{Ra}(N_1, N_4)$: Each of Ra, N_1, and N_4 depend on two or more of T_1, T_4, and L_i.

5 Summary

The consequences of radiant heat exchange in Rayleigh–Bénard instability have been examined. Wall radiation through transparent gas layers has been incorporated into the usual boundary conditions for Bénard instability. Perturbations in the local net radiant heat transfer damp in-

stabilities, resulting in an increase in the critical Rayleigh number. The stabilization is independent of the specific planform at onset of motion, although the planform will still satisfy the Helmholtz equation.

In principle, thermal radiation may increase the critical Rayleigh number by as much as a factor of 2.5, but in practice the increase is smaller as a result of the low thermal conductivity of the gases considered. Solutions are given for a single fluid layer confined between identical, black, semi-infinite walls of finite conductivity and for a pair of fluid layers coupled by a conducting midlayer. For real materials, radiant effects are almost always negligible for a single layer confined by semi-infinite walls. For the two-layer case, however, radiant effects are substantial because the thinness of the midlayer accentuates the destabilizing effects of finite wall conductivity. The maximum overall stability for a two layer configuration is nevertheless achieved for a bottom wall of minimum infrared emissivity.

Acknowledgments

I am indebted to Professor D. K. Edwards and Professor I. Catton who originally called my attention to the possible importance of thermal radiation in Rayleigh–Bénard instability. This work was supported by the National Science Foundation under Grant No. CBT-8858288.

References

Bisshopp, F. E., 1960, "On Two-Dimensional Cell Patterns," *J. Math. Anal. Appl.*, Vol. 1, pp. 373–385.

Catton, I., and Lienhard V, J. H., 1984, "Thermal Stability of Two Fluid Layers Separated by a Solid Interlayer of Finite Thickness and Thermal Conductivity," ASME JOURNAL OF HEAT TRANSFER, Vol. 106, pp. 605–612.

Chandrasekhar, S., 1961, *Hydrodynamic and Hydromagnetic Stability*, Clarendon Press, Oxford, United Kingdom.

Edwards, D. K., and Sun, W. M., 1971, "Effect of Wall Radiation on Thermal Instability in a Vertical Cylinder," *Int. J. Heat Mass Transfer*, Vol. 14, pp. 15–18.

Hart, J. E., 1971, "Stability of the Flow in a Differentially Heated Inclined Box," *J. Fluid Mech.*, Vol. 47, pp. 547–576.

Lienhard V, J. H., 1987, "An Improved Approach to Conductive Boundary Conditions for Rayleigh-Bénard Instability," ASME JOURNAL OF HEAT TRANSFER, Vol. 109, pp. 378–387.

Lienhard V, J. H., and Catton, I., 1986, "Heat Transfer Across a Two Fluid Layer Region," ASME JOURNAL OF HEAT TRANSFER, Vol. 108, pp. 198–205.

Pellew, A., and Southwell, R. V., 1940, "On Maintained Convective Motion in a Fluid Heated From Below," *Proc. Roy. Soc. (London)*, Ser. A, Vol. 176, pp. 312–343.

Lord Rayleigh (John Wm. Strutt), 1916, "On Convection Currents in a Horizontal Layer of Fluid, When the Higher Temperature is on the Under Side," *Phil. Mag.*, Ser. 6, Vol. 32, No. 192, pp. 529–546.

Richards, R. F., and Edwards, D. K., 1989, "Effect of Boundary Radiation on Thermal Stability in Horizontal Fluid Layers," *Int. J. Heat Mass Transfer*, Vol. 32, pp. 81–86.

Siegel, R., and Howell, J. R., 1981, *Thermal Radiation Heat Transfer*, 2nd ed., Hemisphere, New York.

APPENDIX A

Generalized Third-Kind Boundary Conditions

Boundary conditions (33) and (34) applied to equation (1) produce the $\mathcal{C}_i$ indicated in the text as

$$\mathcal{C}_1 = -q_0 \sin(q_0/2) - (\Lambda_{21} + \Lambda_{22}) \cos(q_0/2) + 2\Re\left\{\frac{A}{A_0}[q \sinh(q/2) - (\Lambda_{21} + \Lambda_{22}) \cosh(q/2)]\right\} \tag{62}$$

$$\mathcal{C}_2 = q_0 \cos(q_0/2) + (\Lambda_{21} - \Lambda_{22}) \sin(q_0/2) + 2\Re\left\{\frac{B}{B_0}[q \cosh(q/2) + (\Lambda_{21} - \Lambda_{22}) \sinh(q/2)]\right\} \tag{63}$$

$$\mathcal{C}_3 = q_0 \sin(q_0/2) - (\Lambda_{11} + \Lambda_{12}) \cos(q_0/2) - 2\Re\left\{\frac{A}{A_0}[q \sinh(q/2) + (\Lambda_{11} + \Lambda_{12}) \cosh(q/2)]\right\} \tag{64}$$

$$\mathcal{C}_4 = q_0 \cos(q_0/2) + (\Lambda_{11} + \Lambda_{12}) \sin(q_0/2) + 2\Re\left\{\frac{B}{B_0}[q \cosh(q/2) + (\Lambda_{11} - \Lambda_{12}) \sinh(q/2)]\right\} \tag{65}$$

in which A/A_0 and B/B_0 may be evaluated from equations (4) and (5).

Natural Convection From Horizontal Disks and Rings

M. Sahraoui

M. Kaviany
Department of Mechanical Engineering and Applied Mechanics, University of Michigan, Ann Arbor, MI 48109

H. Marshall
Scientific Computation Group, Computing Center, University of Michigan, Ann Arbor, MI 48109

A length scale similar to the hydraulic diameter for natural convection from horizontal surfaces has been previously suggested by others. This length scale correlates the available experimental results for circular, rectangular, and triangular surfaces fairly well. Herein this length scale is used for natural convection from rings. The obtained experimental (using naphthalene sublimation) and numerical (finite-difference approximation of the governing equations for axisymmetric fields) results confirm this length scale applicability to this class of multiply connected surfaces. Relatively good agreement is found between the experimental and numerical results for small inside diameters, while for large inside diameters the agreement is fair. These numerical results correlate well with $\overline{Nu}=0.603\ Ra^{1/5}\ Pr^{0.085}$ *where the length scale is the ratio of area to perimeter of the heat transfer surface. A disk with an impermeable, adiabatic core is used numerically to explore the influence of the flow through the core on the local and average heat transfer rates. These numerical results correlate well with* $\overline{Nu}=0.561\ Ra^{1/5}\ Pr^{0.085}$. *This indicates that the lack of core flow decreases the overall heat transfer rate by 7 percent.*

1 Introduction

Natural convection from finite size, horizontal surfaces is characterized by a boundary-layer flow behavior near the edges and a stagnation-type behavior adjacent to the centerline where a plumelike flow exists. Based on these characteristics Goldstein et al. (1973) suggested that the area of active (rigorous convection) heat transfer is confined to the boundary-layer region, and therefore the length scale $L=A/P$, where A is the area and P is the perimeter of the heat transfer surface. For a disk of radius R_o this length scale is $R_o/2$.

Assuming the nearly boundary-layer flow behavior near the edge of the surface (except for the leading edge, where longitudinal diffusions are significant), Pera and Gebhart (1973a) obtained similarity solutions assuming two-dimensional, semi-infinite surfaces. These solutions are for constant surface temperature and heat flux, as well as longitudinal and slightly tilted surfaces. Their results showed that the local Nusselt number was proportional to the local Rayleigh number to the 1/5 power and a Prantdl number dependency to the power of 1/20. They also found (Pera and Gebhart, 1973b) that the onset of separation for the laminar, two-dimensional flow occurs at a local Rayleigh number of 3.6×10^5 (for horizontal surfaces and $Pr=0.7$). However, they showed that this separated flow is stable to two-dimensional disturbances.

The Pera and Gebhart results cannot be directly applied to heat transfer from finite size surfaces when the flow is no longer of boundary-layer type in the plume area. However, since most of the heat transfer takes place in the region where a nearly boundary-layer flow exists, the Rayleigh number dependency, as predicted by their treatment, is very close to that obtained when the plume area is also included. Zakerullah and Ackroyd (1979) extended the analysis to include fluid property variation and showed that the Rayleigh number dependency was increased from 1/5 to 1/4 when allowance was made for a variation of density and viscosity.

Merkin (1983), by developing inner and outer solutions, was able to approximate the influence of the plume presence on the boundary-layer flow. Robinson and Liburdy (1987) have included the entrainment effect of the plume. The last two studies show that the dependency (of the local Nusselt number) on the local Rayleigh number is a power of 1/5 away from the plume and then decreases as the center of the plume is approached.

Laboratory experiments using naphthalene sublimation (Goldstein et al., 1973) for $1<Ra<10^4$ have showed that the average Nusselt number is proportional to Ra to the 1/6 power for $Ra<200$ and 1/4 power for $Ra>200$. The electrochemical experiment of Lloyd and Moran (1974) covered $2.2\times10^4<Ra<1.6\times10^9$ and showed a transition Rayleigh number of about 10^7. Their exponents were 1/4 for laminar and 1/3 for turbulent flows. Al-Arabi and El-Riedy (1976) have measured the local Nusselt number, using a local condensation method, and have confirmed the exponent reported by Lloyd and Moran (1974), who have also found two local transition Rayleigh numbers, the first one at 2×10^5 and the second one at 3.8×10^6 (for air). Their results for the average Nusselt number show a transition Rayleigh number of 4×10^7. Table 1 summarizes these results.

In heat transfer from rings the departing plume entrains fluid from both inside and outside of the ring. Therefore, it is possible to increase the total heat transfer from a disk by removing a circular portion from its center (while keeping the outside radius and the buoyancy potential the same). As will be shown, this will indeed happen when the ratio of inside to outside diameter is relatively small. In order to examine the validity of application of the length scale A/P for buoyancy-driven flow over rings, the following experimental-numerical study was performed. The available experimental (Goldstein et al., 1973; Goldstein and Lau, 1983; Lloyd and Moran, 1974, for high Rayleigh numbers) and numerical, analytical-numerical (Zakerullah, 1979; Goldstein and Lau, 1983; Merkin, 1983; Robinson and Liburdy, 1987) results for infinite strips and disks were also used for validation of the experimental and numerical results.

For computational convenience the numerical results of this study are scaled by using R_o. The Rayleigh and Nusselt numbers based on R_o are designated by a prime (Ra′ and Nu′) while those based on L are shown as Ra and Nu.

2 Analysis

The length, time, and temperature scales used for normalization of the governing equations are R_o, R_o^2/α, and T_s-T_∞. The dimensionless governing equations for the axisymmetric fields considered are

Contributed by the Heat Transfer Division for publication in the JOURNAL OF HEAT TRANSFER. Manuscript received by the Heat Transfer Division July 21, 1988. Keywords: Mass Transfer, Natural Convection, Plumes.

Table 1 Correlations for average Nusselt number

Reference		Correlation		
Pera and Gebhart (1973) (Analytical-numerical)		$\overline{Nu}=0.656\ Ra^{1/5}Pr^{1/20}$		$0.1\le Pr\le 100$
Goldstein et al. (1973) (Experiment)		$\overline{Nu}=0.59\ Ra^{1/4}$ $\overline{Nu}=0.96\ Ra^{1/6}$	$200\le Ra\le 10^4$ $200\ge Ra;$	$Sc=2.5$
Lloyd and Moran (1974) (Experiment)		$\overline{Nu}=0.54\ Ra^{1/4}$ $\overline{Nu}=0.15\ Ra^{1/3}$	$2.2\times10^4\le Ra\le 8\times10^6$ $8\times10^6\le Ra\le 1.6\times10^9;$	$Sc=2200$
Al-Arabi and El-Riedy (1976) (Experiment)		$\overline{Nu}=0.70\ Ra^{1/4}$ $\overline{Nu}=0.155\ Ra^{1/3}$	$3.2\times10^5\le Ra\le 4\times10^7$ $4\times10^7\le Ra\le 2.5\times10^9;$	$Pr=0.72$
Zakerullah and Ackroyd (1979) (Analytical-numerical)		$\overline{Nu}=0.577\ Ra^{1/5}$		$Pr=0.72$
Goldstein and Lau (1983) (Numerical)		$\overline{Nu}=0.621\ Ra^{1/5}$		$Pr=0.7$
Robinson and Liburdy (1987) (Analytical-numerical)		$\overline{Nu}=0.602\ Ra^{1/5}$		$Pr=0.72$
This study (Numerical)	Ring	$\overline{Nu}=0.603\ Ra^{1/5}Pr^{0.085}$		$0.1\le Pr\le 10$
	disk with adiabatic core	$\overline{Nu}=0.561\ Ra^{1/5}Pr^{0.085}$		$0.1\le Pr\le 10$

$$\frac{\partial\omega}{\partial t}+\frac{\partial u\omega}{\partial r}+\frac{\partial v\omega}{\partial z}=-\mathrm{Pr}\ \mathrm{Ra}'\frac{\partial\theta}{\partial r}+\mathrm{Pr}\frac{\partial}{\partial r}\frac{1}{r}\frac{\partial r\omega}{\partial r}+\mathrm{Pr}\frac{\partial^2\omega}{\partial z^2} \quad (1)$$

$$\frac{\partial\theta}{\partial t}+\frac{1}{r}\frac{\partial ru\theta}{\partial r}+\frac{\partial v\theta}{\partial z}=\frac{1}{r}\frac{\partial}{\partial r}r\frac{\partial\theta}{\partial r}+\frac{\partial^2\theta}{\partial z^2} \quad (2)$$

$$-\omega=\frac{\partial}{\partial r}\frac{1}{r}\frac{\partial\psi}{\partial r}+\frac{1}{r}\frac{\partial^2\psi}{\partial z^2} \quad (3)$$

$$v=-\frac{1}{r}\frac{\partial\psi}{\partial r},\qquad u=\frac{1}{r}\frac{\partial\psi}{\partial z} \quad (4)$$

The initial conditions used are:

$$\psi=\omega=\theta=0 \quad (5)$$

and the boundary conditions are given in Fig. 1 The local Nusselt number (or Sherwood number) is given as

$$\mathrm{Nu}'=-\frac{\partial\theta}{\partial z}$$

on the heated surface. The average Nusselt number (or Sherwood number) is given as

$$\overline{\mathrm{Nu}}'=-\frac{2}{1-r_i^2}\int_{r_i}^{1}\frac{\partial\theta}{\partial z}\,r\,dr$$

The dimensionless total heat transfer rate is $Q=2\pi\int_{r_i}^{1}$

Nomenclature

A = area of disk or ring $=\pi(R_o^2-R_i^2)$, m^2
D = local binary mass diffusion coefficient, m^2/s
h = heat transfer coefficient, W/m^2-K
k = thermal conductivity, W/m-K
g = gravity constant
L = characteristic length $=A/P=(R_o-R_i)/2$, m
N_r, N_z = number of nodes in r and z directions
Nu = local Nusselt number based on L, hL/k
$\overline{\mathrm{Nu}}$ = average Nusselt number based on L, $\bar{h}L/k$
Nu′ = local Nusselt number based on R_o, hR_o/k
$\overline{\mathrm{Nu}}'$ = average Nusselt number based on R_o, $\bar{h}R_o/k$
P = perimeter $=2\pi(R_o+R_i)$, m
p = partial pressure of naphthalene, lb/ft^2
Q = dimensionless total heat transfer rate
Ra = Rayleigh number based on L, $g\beta(T_s-T_\infty)L^3/\nu\alpha$
Ra′ = Rayleigh number based on R_o, $g\beta(T_s-T_\infty)R_o^3/\nu\alpha$
Ra_m = mass transfer Rayleigh number $=g(\rho_s-\rho_\infty)L^3\mathrm{Sc}/\nu^2\rho_\infty$
R_o = outside radius, m
R_i = inside radius, m
r_i = dimensionless inside radius $=R_i/R_o$
r, z = dimensionless radial and axial coordinates
Sc = Schmidt number $=\nu/D$
Sh = local Sherwood number $=h_mL/D$
$\overline{\mathrm{Sh}}$ = average Sherwood number $=\bar{h}_mL/D$
t = dimensionless time
T = temperature, K
u = dimensionless velocity in r direction
v = dimensionless velocity in z direction
α = thermal diffusivity, m^2/s
β = thermal expansion coefficient, K^{-1}
δ = dimensionless disk or ring thickness
θ = dimensionless temperature $=(T-T_\infty)/(T_s-T_\infty)$
ν = kinematic viscosity, m^2/s
ρ = density kg/m^3
ψ = dimensionless stream function
ω = dimensionless vorticity

Superscripts

- = average
′ = based on R_o

Subscripts

i = inside
m = mass transfer
max = maximum
o = outside
s = surface
∞ = ambient

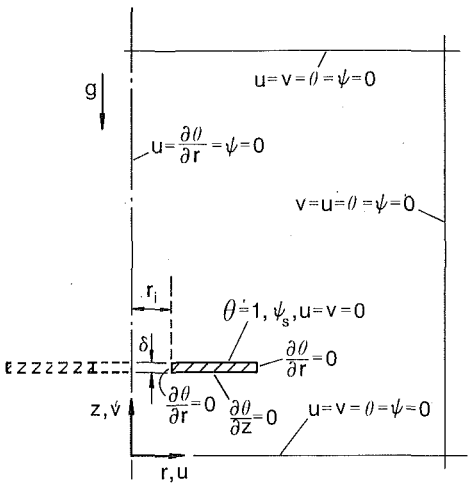

Fig. 1 Schematic of the problem, the coordinate system, and the boundary conditions

$(\partial\theta/\partial z)\, rdr$. The boundary and initial conditions for equations (1)–(4) are given in both equations (5) and Fig. 1. These equations were solved using the explicit finite-difference described by Torrance (1968) and Jaluria and Torrance (1986). The modified upwind advection scheme used here is conservative for both energy and vorticity.

Steady-state solutions were found by a false transient time integration using a variable Euler time step, following Torrance (1968). The time step computation can be outlined as follows where n is the time step, and i and j are the radial and vertical grid indices. Let a_k denote the coefficients that vary in time. Then equation (2) becomes

$$\theta^{n+1}_{i,j} = a_1\theta^n_{i+1,j} + a_2\theta^n_{i-1,j} + a_3\theta^n_{i,j} + a_4\theta^n_{i,j+1} + a_5\theta^n_{i,j-1}$$

where $a_3 = 1-(a_1+a_2+a_4+a_5)$. The coefficient a_3 is made positive by restricting the time step. This is also done for the vorticity equation. This is equivalent to imposing a hyperbolic and diffusive stability criterion to the time step choice.

Nonuniform grid nets were used with adequately fine grids placed next to the heated surface and coarser grids elsewhere. Standard convergence tests using progressively finer grids were performed. As an example, for $\mathrm{Ra}' = 72{,}000$ and $\mathrm{Pr} = 0.72$, the computed Nusselt number was 7.09 for a net of 70×90 ($N_r \times N_z$) with the finest grid sizes of $\Delta r = 0.03$ and $\Delta z = 0.02$. Nusselt number was equal to 7.18 for a net of 70×90 nodes with the finest grid sizes of $\Delta r = 0.03$ and $\Delta_z = 0.01$. As long as the thickness of the disk or ring δ was kept small no influence of δ on the heat transfer rate was found.

The size of the enclosure was also made progressively larger until the average Nusselt number no longer changed. As an example, for $\mathrm{Ra}' = 4800$, $\mathrm{Pr} = 1.95$, and $r_i = 0.54$, an enclosure of dimensions 5.6×10.4 (r and z directions) resulted in $\mathrm{Nu}' = 5.984$, while using 3.6×4.6 resulted in $\mathrm{Nu}' = 5.895$. The effect of the ring location within the enclosure was also examined and for all the results reported the effect of the enclosure on the results is less than a few percent.

The value of the stream function is a constant on the ring surface and its value is obtained by iteration and through averaging the values obtained at each node on the surface. For $r_i = 0$, the value of stream function on the surface is zero. As $\mathrm{Ra}' \to 0$, i.e., for conduction only (used for validation of the results), it was necessary to include one adiabatic grid on the inside and outside of the ring in order to avoid very large temperature gradients in these areas.

The computations were done using an IBM 3090. The vector facility of the computer was used. A typical run ($N_r \times N_z = 60\times 80$) uses 1250 cpu seconds with the initial condition of zero velocity throughout, while it takes 200 seconds of cpu when a converged solution was used as the initial condition.

3 Experiment

As applied elsewhere (Goldstein et al., 1973; Goldstein and Lau, 1983) sublimation of naphthalene was used along with the assumption of a close analogy between heat and mass transfer in order to determine the average Nusselt number (or Sherwood number) as a function of Rayleigh number. The Schmidt number for naphthalene is 1.95 (Goldstein, 1988).

3.1 Sample Preparation. This is done as described by Jones (1971). Boiling naphthalene is poured into an aluminum mold made of a base, a ring consisting of three parts, and an inner core. By varying the size of the core, naphthalene specimens with outer diameters of 11 cm and inside diameters of 0, 2, 3, 4, 5, 6, 6.5, 7, 7.5, 8, 8.5, 9, 9.5 cm were made. The surface of the base is covered by a piece of aluminum foil in order to avoid adherence of the naphthalene to the mold surface. A small amount of oil is placed between the base and the aluminum foil in order to avoid the creation of air pockets, which in turn could make the mold surface wavy. Once the mold temperature reaches the room temperature, first the outer ring is removed and with a slight heating the core is then removed. The surface aluminum foil is not removed and the exposed areas of the mold are covered by aluminum foil pieces. Prior to the experiments, the surface aluminum is removed and the specimen is hung for sublimation of the excess naphthalene that might have adhered to the remaining aluminum foil pieces.

3.2 Measurement. In order to isolate the experiment from the room air currents, an enclosure made of 7.5-cm-thick styrofoam sheets with an inside volume of 3.5 m^3 was used for the experiments. An electronic digital balance with accuracy of 0.1 mg is used for the mass measurement. A thermocouple placed near the specimen measures the ambient temperature. Initially, a thermocouple was also placed inside the naphthalene sample and slightly underneath its surface. Since the ambient and specimen temperatures were found to be very close, the specimen thermocouple was no longer used. The balance and the thermocouple were connected to a Hewlett-Packard data acquisition-processing system and then data were taken every 15 minutes. The experiments were run at night where room disturbances were minimal. The balance output drifted in the first ten to twenty hours after it was turned on. Therefore, no measurements were taken during this period. The typical amount of mass sublimated every 15 min was about 30 mg. The ambient pressure was measured using a barometer, before and after the experiment, and an arithmetic average was used.

Once all the data were acquired, the instantaneous mass transfer rate was computed by a linear curve fit (five points are used). Then, through arithmetic averaging, the average mass transfer rate was determined. The data used for the averaging were taken from those recorded between one and three hours after the start of the experiments. This assured that steady state had been reached. The data taken after three hours were not considered because of the rising naphthalene concentration in the room. In addition, the room temperature did not remain constant and on the average changed one degree centigrade every three hours.

The partial pressure of naphthalene vapor as a function of temperature was determined using the relation given in Sogin (1958). This relation is $\log_{10}(p_s) = 11.884 - (6713/T_s)$, where T_s is given in deg Rankine and p_s is in $\mathrm{lb/ft^2}$. The Schmidt number for naphthalene was taken as 1.95. The mass transfer Rayleigh number becomes $\mathrm{Ra}_m = 3.43\, g\, P_s\, L^3\, \mathrm{S_c}/(P_\infty \nu^2)$ when pressures are used instead of densities.

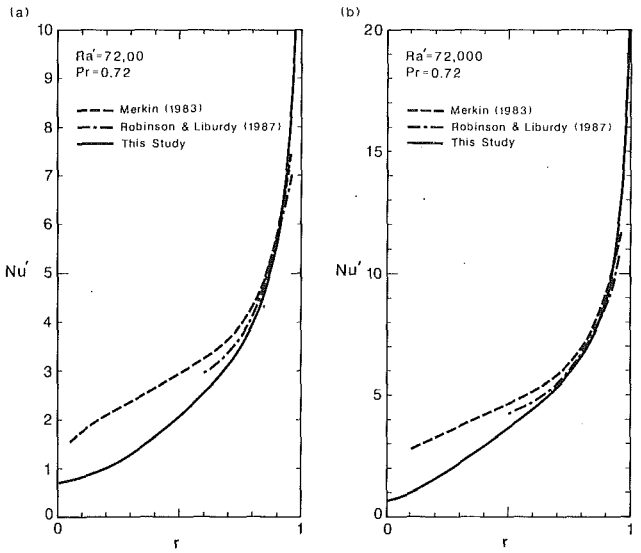

Fig. 2 Comparison between the numerical results for local Nusselt number obtained by others with those of this study

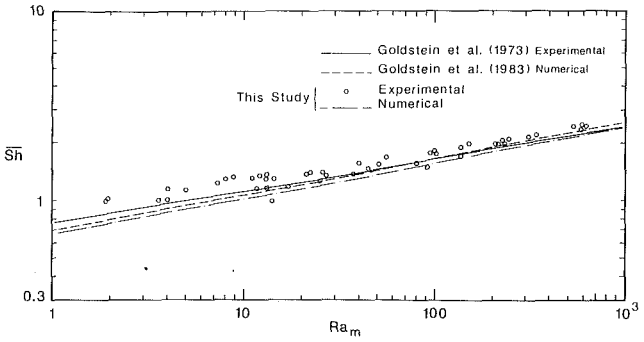

Fig. 3 Comparison between the experimental and numerical results of this study and those of others

4 Results and Discussion

4.1 Validation of Numerical Results. The analytical-numerical results of Merkin (1983) (an extension of the results obtained by Zakerullah and Ackroyd, 1979), and those of Robinson and Liburdy (1987), for the local Nusselt number, have been used for comparison with the numerical results obtained in this study. Since their treatments were in part based on boundary-layer approximations, their results are expected to be valid at relatively high Rayleigh numbers and near the disk edge. Figure 2 shows the results of these comparisons for $\mathrm{Pr}=0.72$ and $\mathrm{Ra}'=\mathrm{Gr}'\mathrm{Pr}=7200$ and 72,000. The agreement at the outer region of the disk, where their results are applicable and also where most of the heat transfer area is located, is rather good.

4.2 Comparison Between Experimental and Numerical Results. Figure 3 shows the experimental and numerical results, for the average Sherwood number, for the various rings (R_o was kept constant while R_i was changed) obtained in this study. Also shown are the experimental (circular, rectangular, and triangular surfaces) and numerical (two-dimensional flow over an infinite strip) results of Goldstein et al. (1973) and Goldstein and Lau (1983). The length scale used is $(A/P)=(R_o-R_i)/2$. While the numerical results obtained here are in relatively good agreement with their experimental and numerical results, the experimental results for the average Sherwood number are larger than those predicted. This disagreement is largest for the largest inside diameter. This could be due to the nonideal coverage of the inside and outside of the rings with the aluminum foil pieces and the resulting extra area of mass transfer. In general, the agreement between the experimental and numerical results obtained can be considered fair as they both confirm that by using the length scale (A/P) the results can be correlated fairly well.

4.3 Flow and Temperature Fields. The flow near the edges is expected to be nearly horizontal while the ascending plume is vertical. Figure 4 shows the lines of constant stream function, the velocity field, the lines of constant temperature, and the $\theta=0.7$ surface, for the various inside radii. Note that the velocity vectors are drawn with a uniform lower spatial resolution and not on the computational grid nodes. The results are for $\mathrm{Ra}'=20{,}000$ and $\mathrm{Pr}=0.72$. Only the fields near the disk or ring are shown and, as mentioned above, these fields are nearly independent of the enclosure size. The relative size of the arrowhead in the velocity field plots gives the relative magnitude of the local velocity.

The results show that as r_i increases the fluid flows through the ring and merges with the flow over the outer edge of the ring. The inside branch of the flow does turn slightly toward the outer edge but lacks the inertia and the mass flow rate required to move the plume toward the middle of the surface. The outside branch of the flow sweeps the surface and is responsible for almost the entire heat transfer from the surface (until the inside radius becomes large). With the addition of the inside branch of the flow, it is possible for the heat transfer from a ring (having the same outside radius and Ra′ as a disk) to be greater than that for the disk. This is shown in Fig. 5(*a*) and the results show that at $r_i=0.3$ the heat transfer rate reaches its maximum value.

The average Nusselt number based on R_o increased monotonically as r_i increases, indicating that the average heat transfer coefficient increases as r_i increases. This is also shown in Fig. 5(*b*) where the distribution of the dimensionless local heat transfer rate is shown for various values of r_i. Note that the local heat transfer rate at the inside edge increases as r_i increases, and as expected, reaches that of the outside edge as r_i goes to unity. This limit represents an infinite strip. Figure 5(*c*) gives the value of the stream function at the surface, which is indicative of the mass flow rate of the inner branch of the flow. As expected, as r_i is increased to values slightly above zero this flow rate is small and the viscous forces prevent the formation of strong inner flows. As r_i increases further this flow rate increases and a near-linear relationship exists for $r_i>0.2$.

An additional set of numerical experiments was undertaken to examine the effect of multiply connected surfaces. Previously, the validity of the proposed length scale has been shown for simply connected surfaces such as rectangles, triangles, etc. By obstructing the flow in the center, one can determine the relative importance of the inside branch of the flow. Figure 6 shows both stream function and temperature with and without the adiabatic core. The inflow field is changed as well as the field far from the disk. The most significant change is the flow over the left-hand part of the heat transfer area, which is due to the absence of the merging plume when the adiabatic core is present. These changes are also shown by the local Nusselt number in Fig. 5(*b*). The figure shows that the local Nusselt number at $r=r_i$ is higher for the ring. It is slightly higher inside the heat transfer area for the disk with the adiabatic core. These changes will compensate each other and only a slight decrease on average Nusselt number occurs for the disk with an adiabatic core.

4.4 Correlation. The average Nusselt number increases as the Prandtl number increases and this is shown in Fig. 7 for $\mathrm{Ra}=1250$, $r_i=0.50$, and $0.1\le\mathrm{Pr}\le 10$. The symbols show the numerical results and the line is a curve fit (least square) to the

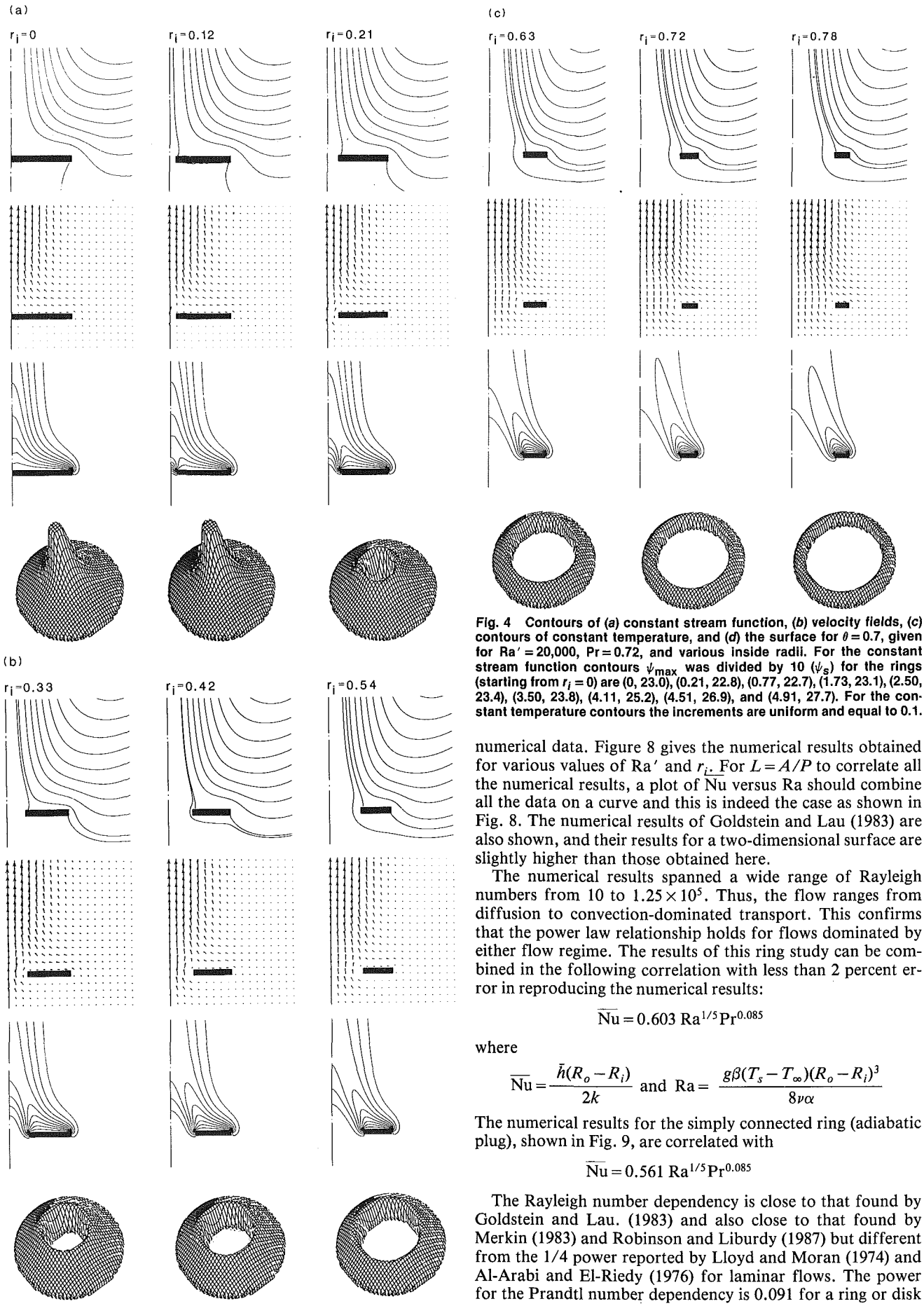

Fig. 4 Contours of (*a*) constant stream function, (*b*) velocity fields, (*c*) contours of constant temperature, and (*d*) the surface for $\theta = 0.7$, given for $Ra' = 20{,}000$, $Pr = 0.72$, and various inside radii. For the constant stream function contours ψ_{max} was divided by 10 (ψ_s) for the rings (starting from $r_i = 0$) are (0, 23.0), (0.21, 22.8), (0.77, 22.7), (1.73, 23.1), (2.50, 23.4), (3.50, 23.8), (4.11, 25.2), (4.51, 26.9), and (4.91, 27.7). For the constant temperature contours the increments are uniform and equal to 0.1.

numerical data. Figure 8 gives the numerical results obtained for various values of Ra′ and r_i. For $L = A/P$ to correlate all the numerical results, a plot of $\overline{Nu}$ versus Ra should combine all the data on a curve and this is indeed the case as shown in Fig. 8. The numerical results of Goldstein and Lau (1983) are also shown, and their results for a two-dimensional surface are slightly higher than those obtained here.

The numerical results spanned a wide range of Rayleigh numbers from 10 to 1.25×10^5. Thus, the flow ranges from diffusion to convection-dominated transport. This confirms that the power law relationship holds for flows dominated by either flow regime. The results of this ring study can be combined in the following correlation with less than 2 percent error in reproducing the numerical results:

$$\overline{Nu} = 0.603\ Ra^{1/5} Pr^{0.085}$$

where

$$\overline{Nu} = \frac{\bar{h}(R_o - R_i)}{2k} \quad \text{and} \quad Ra = \frac{g\beta(T_s - T_\infty)(R_o - R_i)^3}{8\nu\alpha}$$

The numerical results for the simply connected ring (adiabatic plug), shown in Fig. 9, are correlated with

$$\overline{Nu} = 0.561\ Ra^{1/5} Pr^{0.085}$$

The Rayleigh number dependency is close to that found by Goldstein and Lau. (1983) and also close to that found by Merkin (1983) and Robinson and Liburdy (1987) but different from the 1/4 power reported by Lloyd and Moran (1974) and Al-Arabi and El-Riedy (1976) for laminar flows. The power for the Prandtl number dependency is 0.091 for a ring or disk

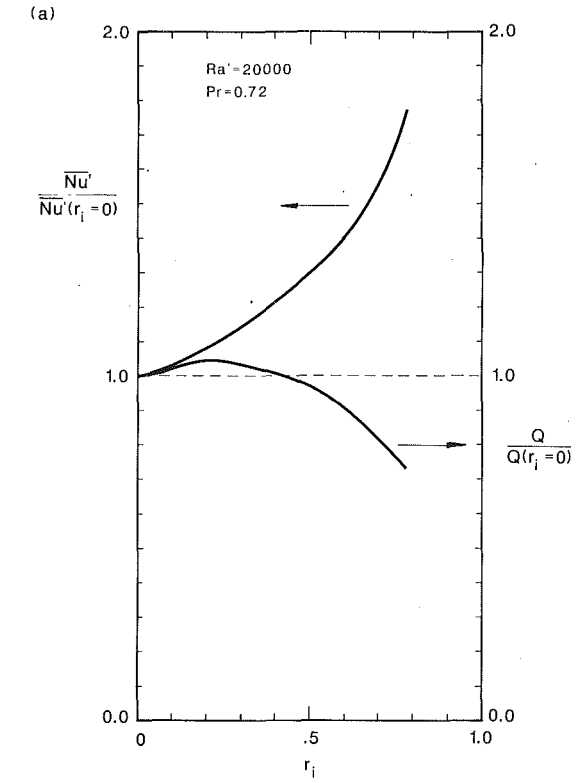

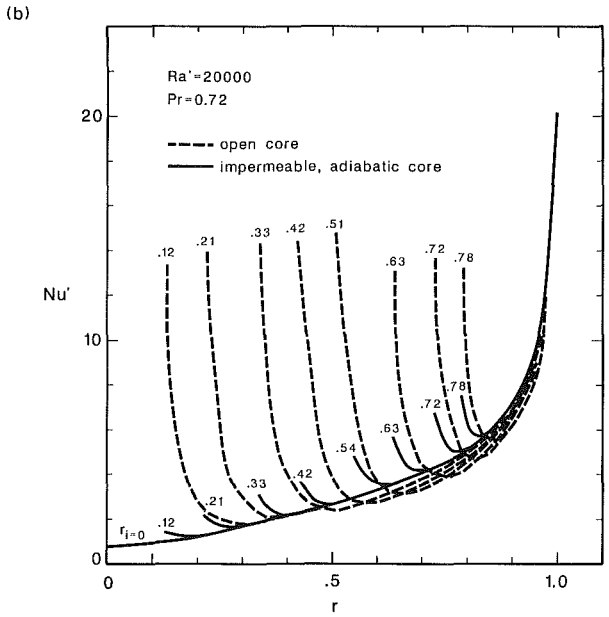

with adiabatic core and 0.08 for disk. When combined, the power is 0.085 with a 1 percent error margin. This Prandtl number dependency is larger than that suggested by Goldstein and Lau (1983), and Pera and Gebhart (1973), for two-dimensional simply connected surfaces. However, for the simply connected ring (adiabatic core) both the Rayleigh and Prandtl exponents are unchanged. The proportionality constant decreases slightly, in spite of the rather significant flow and temperature field changes.

5 Summary

The heat transfer rate from disks and rings has been studied in order to determine the influence of the inner branch of the flow on the overall heat transfer. It is shown that:

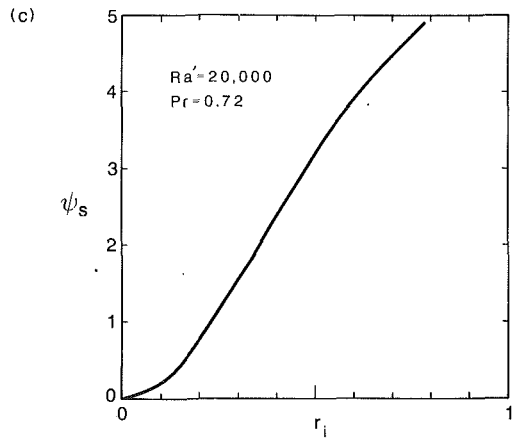

Fig. 5 *(a)* **Variation of the average Nusselt number and total heat transfer rate with respect to r_i, *(b)* variation of the distribution of local Nusselt number with respect to r_i, for ring (solid lines) and disk with impermeable adiabatic core, and *(c)* variation of the value of stream function on the surface of disk or ring.**

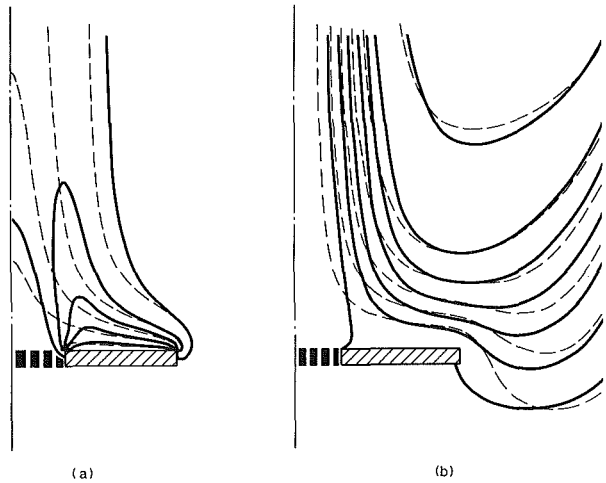

Fig. 6 *(a)* **Comparison of the isothermal lines (0.9, 0.7, 0.5, 0.3, 0.1) between the ring (solid lines) and the disk with an impermeable adiabatic core. *(b)* Comparison of the stream lines between the ring (solid lines) and disk with an impermeable adiabatic core.**

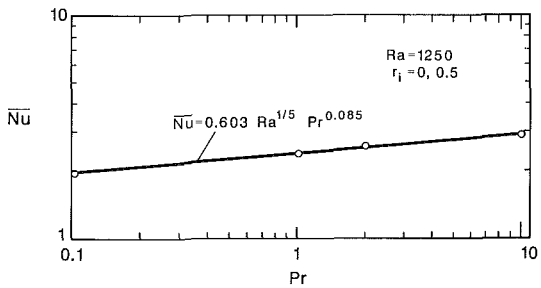

Fig. 7 Variation of average Nusselt number with respect to Prandtl number

1 For small inside radii the total heat transfer rate for the ring is larger than that for the same outside diameter disk, and

2 the previously proposed length scale, namely area divided by perimeter, correlates the data well even for such multiply connected surfaces as rings.

3 The numerical results shows that for rings with impermeable, adiabatic cores, the flow and temperature fields change considerably (relative to an unobstructed ring); however, this length scale correlates the overall heat transfer rate very well.

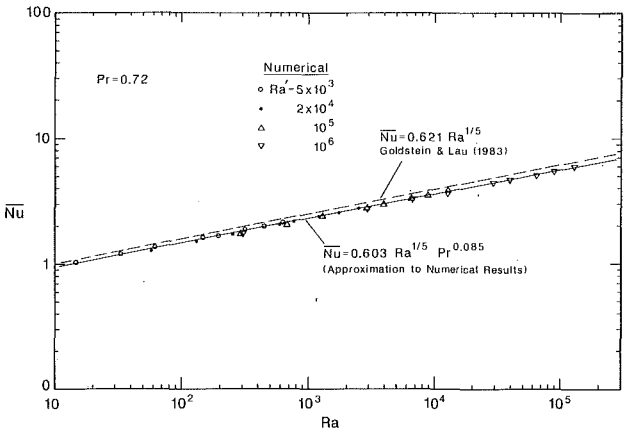

Fig. 8 Variation of average Nusselt number with respect to the Rayleigh number (Pr = 0.72), for a ring. Also shown are the correlations obtained here and by Goldstein and Lau (1983).

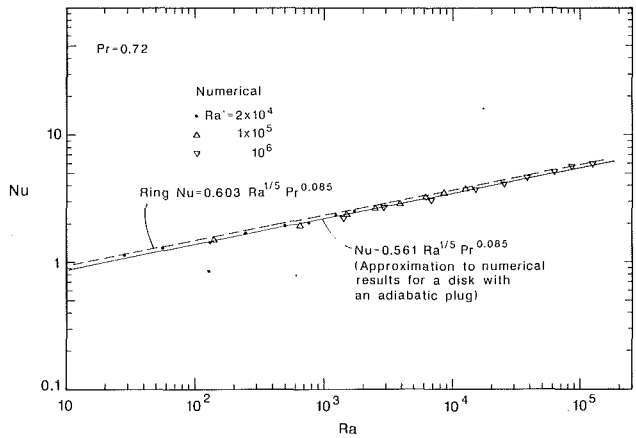

Fig. 9 Variation of the average Nusselt number with respect to the Rayleigh number (Pr = 0.72), for a disk with an impermeable, adiabatic core. Also shown are the results for a ring.

References

Al-Arabi, M., and El-Riedy, M. K., 1976, "Natural Convection Heat Transfer From Isothermal Horizontal Plates of Different Shapes," *International Journal of Heat and Mass Transfer*, Vol. 19, pp. 1399–1404.

Al-Arabi, M., and Sakr, B., 1988, "Natural Convection Heat Transfer From Inclined Isothermal Plates," *International Journal of Heat and Mass Transfer*, Vol. 31, pp. 559–566.

Goldstein, R. J., Sparrow, E. M., and Jones, D. C., 1973, "Natural Convection Mass Transfer Adjacent to Horizontal Plates," *International Journal of Heat and Mass Transfer*, Vol. 16, pp. 1025–1035.

Goldstein, R. J., and Lau, K.-S., 1983, "Laminar Natural Convection From a Horizontal Plate and the Influence of Plate-Edge Extensions," *Journal of Fluid Mechanics*, Vol. 129, pp. 55–75.

Goldstein, R. J., 1988, Private Communication.

Jaluria, Y., and Torrance, K. E., 1986, *Computational Heat Transfer*, Hemisphere Pub. Co., Washington, D.C.

Jones, D. C., 1971, "Experiments on Natural Convection Mass Transfer on Horizontal Surfaces," M.S. Thesis, Department of Mechanical Engineering, University of Minnesota, Minneapolis, MN.

Lau, K.-S., 1978, "The Effect of Edge Conditions on Laminar Natural Convection Adjacent to a Horizontal Plate," M.S. Thesis, Department of Mechanical Engineering, University of Minnesota, Minneapolis, MN.

Lloyd, J. R., and Moran, W. R., 1974, "Natural Convection Adjacent to Horizontal Surface of Various Planforms," ASME Paper No. 74-WA/HT-66.

Merkin, J. H., 1983, "Free Convection Above a Heated Horizontal Circular Disk," *Journal of Applied Mathematics Physics*, Vol. 34, pp. 596–608.

Pera, L., and Gebhart, B., 1973a, "Natural Convection Boundary-Layer Flow Over Horizontal and Slightly Inclined Surfaces," *International Journal of Heat and Mass Transfer*, Vol. 16, pp. 1131–1146.

Pera, L., and Gebhart, B., 1973b, "On the Stability of Natural Convection Boundary-Layer Flow Over Horizontal and Slightly Inclined Surfaces," *International Journal of Heat and Mass Transfer*, Vol. 16, pp. 1147–1163.

Robinson, S. B., and Liburdy, J. A., 1987, "Prediction of the Natural Convective Heat Transfer From a Horizontal Disk," ASME JOURNAL OF HEAT TRANSFER, Vol. 109, pp. 906–911.

Sogin, H. H., 1958, "Sublimation From Disks to Air Streams Flowing Normal to Their Surfaces," *Trans. ASME*, Vol. 80, pp. 61–69.

Torrance, K. E., 1968, "Comparison of Finite-Difference Computations of Natural Convection," *Journal Research National Bureau Standards*, B. Mathematical Sciences, Vol. 72B, No. 4, pp. 281–301.

Zakerullah, M., and Ackroyd, J. A. D., 1979, "Laminar Natural Convection Boundary Layers on Horizontal Circular Disks," *Journal of Applied Mathematics Physics*, Vol. 30, pp. 427–435.

Natural Convection of Cold Water in a Vertical Annulus With Constant Heat Flux on the Inner Wall

C. J. Ho
Professor.
Assoc. Mem. ASME

Y. H. Lin
Graduate Student.

Department of Mechanical Engineering,
National Cheng Kung University,
Tainan, Taiwan 70101

A numerical solution for steady laminar natural convection of cold water in a vertical annulus with a constant-heat-flux heated inner wall and an isothermally cooled outer wall is examined. Results are generated for flow in annuli with aspect ratio $0.5 \le A \le 8$, the radius ratio varying between 1.2 and 10, and the density inversion parameter ranging from -2 and 1 for $10^3 \le Ra^* \le 10^6$. The heat and fluid flow structures of cold water are vividly visualized by means of contour maps of heatlines and streamlines. The results clearly indicate that the mixed boundary conditions considered can have a significant influence on the geometric dependence of heat transfer characteristics and fluid flow structures in comparison with those reported for isothermal boundary conditions. Multicellular flow behavior of cold water can arise in a tall annulus of $A = 8$.

Introduction

The present study deals with natural convection of cold water in a vertical cylindrical annulus with a constant heat flux condition on the inner wall and an isothermally cooled outer wall, as depicted in Fig. 1. It is well known that thermally driven convection of cold water is characterized by the existence of an anomalous density–temperature relationship having a density maximum at about 4°C at atmospheric pressure. Due to the fundamental interest as well as the practical relevance in the wide variety of systems in natural occurrences and engineering applications, a number of experimental and theoretical studies have been carried out for natural convection of cold water in rectangular and horizontal annular enclosures. Comprehensive reviews of the studies involving these two configurations can be found in previous works (Inaba and Kukuda, 1984; Lin and Nansteel, 1987a; Vasseur et al., 1983). Aside from the rectangular and horizontal annular configurations, another fundamental geometry of interest for natural convection in enclosures is the vertical annulus formed by two co-axial vertical cylinders. With the exception of a recent numerical analysis by Lin and Nansteel (1987b), no earlier work on the natural convection of cold water contained in vertical annular enclosures has been reported in the literature. They found that the annulus curvature can significantly affect the density inversion phenomenon of cold water enclosed in a vertical annulus with isothermal boundary conditions on both inner and outer walls. Yet it is realized that the natural convection phenomenon in enclosures is quite sensitive to the thermal boundary conditions imposed (Ostrach, 1982). In view of the lack of information on natural convection of cold water in vertical annuli subjected to other types of thermal boundary conditions of engineering interest, additional attention in this respect is evidently needed. The present study of mixed thermal boundary conditions as described in the foregoing is primarily motivated by the problem of related interest concerning natural convective dominated melting of ice around a vertical cylinder with constant heat flux.

In the current study, the governing equations for the problem under consideration are solved numerically via a finite difference method. The primary objective is to provide numerical results to show how the mixed boundary conditions influence the heat and fluid flow structures of natural convection of cold water in a vertical annulus.

Mathematical Formulation

The dimensionless governing equations for steady axisymmetric incompressible laminar natural convection of cold water in a vertical annulus shown in Fig. 1 may be written in terms of stream function, vorticity, and temperature as follows:

$$\frac{1}{r}\frac{\partial}{\partial r}\left(\frac{\omega}{r}\frac{\partial \psi}{\partial z}\right) - \frac{1}{r}\frac{1}{\partial z}\left(\frac{\omega}{r}\frac{\partial \psi}{\partial r}\right) = \mathrm{Pr}\left[\frac{\partial^2(\omega/r)}{\partial r^2} + \frac{3}{r}\frac{\partial(\omega/r)}{\partial r} + \frac{\partial^2(\omega/r)}{\partial z^2}\right] + \mathrm{PrRa}^* \frac{1}{r}\frac{\partial}{\partial r}|\theta - \theta_m|^a \quad (1)$$

$$\frac{\partial^2 \psi}{\partial r^2} - \frac{1}{r}\frac{\partial \psi}{\partial r} + \frac{\partial^2 \psi}{\partial z^2} = -r\omega \quad (2)$$

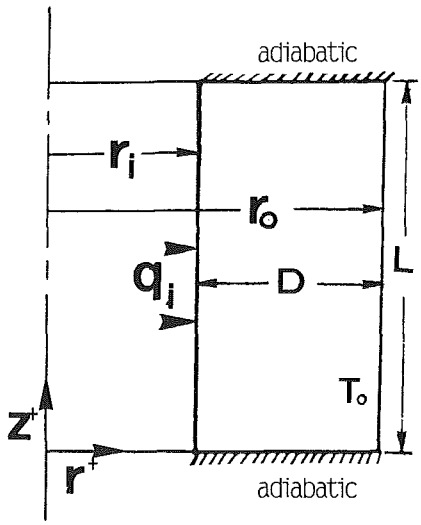

Fig. 1 Schematic view of the physical configuration

Contributed by the Heat Transfer Division for publication in the JOURNAL OF HEAT TRANSFER. Manuscript received by the Heat Transfer Division July 22, 1988. Keywords: Enclosure Flows, Natural Convection.

$$\frac{1}{r}\frac{\partial}{\partial r}\left(\theta\frac{\partial\psi}{\partial z}\right)-\frac{1}{r}\frac{\partial}{\partial z}\left(\theta\frac{\partial\psi}{\partial r}\right)$$

$$=\frac{\partial^2\theta}{\partial r^2}+\frac{1}{r}\frac{\partial\theta}{\partial r}+\frac{\partial^2\theta}{\partial z^2} \tag{3}$$

The governing equations (1)–(3) are based on the constant property model and the assumption that the density can be treated as constant except for the buoyancy term. The density–temperature relation of cold water was based on a widely used correlation proposed by Gebhart and Mollendorf (1974), which is of the form

$$\rho(T)=\rho_m(1-\text{rsp}\,|T-T_m|^a) \tag{4}$$

where $\rho_m=999.9720$ kg/m^3, rsp$=9.297173\times10^{-6}$ (°C)$^{-a}$, $T_m=4.029325$°C, $a=1.894816$. The dimensionless boundary conditions for the present system are

$$\frac{\partial\psi}{\partial r}=\frac{\partial\psi}{\partial z}=\psi=0, \quad \text{on all boundaries} \tag{5a}$$

$$\frac{\partial\theta}{\partial r}=-1 \quad \text{at } r=\frac{1}{RR-1} \tag{5b}$$

$$\theta=0, \quad \text{at } r=\frac{RR}{RR-1} \tag{5c}$$

$$\frac{\partial\theta}{\partial z}=0, \quad \text{at } z=0 \text{ or } A \tag{5d}$$

An examination of the above formulation reveals that the dimensionless parameters for the problem include a modified Rayleigh number Ra*, a radius ratio RR, an aspect ratio A, and a dimensionless temperature parameter θ_m, which characterizes the density inversion of cold water under the mixed boundary conditions. Alternatively, on the basis of the dimensionless surface temperature on the inner wall for pure conduction, a renormalized inversion parameter γ is adopted here (Vasseur et al., 1984)

$$\gamma=-2\theta_m(RR-1)/\ln RR \tag{6}$$

From equation (6), the density inversion phenomenon of cold water can only occur for negative values of γ.

Numerical Method

The dimensionless governing equations (1)–(3) and the associated boundary conditions given by equation (5) were solved by a finite difference method. The finite difference procedure adopts a quadratic upstream difference treatment for the convective terms (Leonard, 1983) and a second-order central finite differencing scheme for the other spatial derivatives. The resulting finite-difference equations for the temperature and vorticity were solved by the successive line relaxation method (Anderson et al., 1984), while a modified strongly implicit (MSI) procedure (Schneider and Zedan, 1981) was used to solve the stream function equation. An iterative solution procedure was employed here to obtain the steady-state solution of the problem considered. The convergence criteria used for all field variables $\xi(=\omega, \psi, \theta)$ are as follows:

$$\frac{|\xi_{i,j}^{n+1}-\xi_{i,j}^{n}|_{\max}}{|\xi_{i,j}^{n+1}|_{\max}}\le10^{-5}$$

where n is the index representing iteration number.

Various uniform grids that discretize the r and z directions into 35 ~ 55 by 31 ~ 71 nodal points were used for the present calculations, depending upon either the modified Rayleigh number or the aspect ratio. The adequacy of the grid size selected was established on the basis of tests for numerical accuracy on refined grids until relatively small changes in the results were obtained. For instance, a less than 2 percent change in the results for the maximum values of temperature and stream function occurred as the grid fineness changes from 55×41 to 81×61 for the case of $RR=2.6$, $A=2$, $\gamma=-2$, and Ra* $=10^6$.

Results and Discussion

The range of parameters considered in the present study is $0.5\le A\le8$, $1.2\le RR\le10$, $-2\le\gamma\le1$, and $10^3\le\text{Ra}^*\le10^6$. As a postprocessing task for the numerical results generated for the field variables (ω, ψ, θ), the concept of heat function (Kimura and Bejan, 1983) was adopted in the present study. This permits numerical heat flow visualization, displaying the heat flow paths developed in the annulus. Here a dimensionless heat function H is defined as

$$\frac{1}{r}\frac{\partial H}{\partial z}=u\theta-\frac{\partial\theta}{\partial r} \tag{7a}$$

$$-\frac{1}{r}\frac{\partial H}{\partial r}=v\theta-\frac{\partial\theta}{\partial z} \tag{7b}$$

Heat and Fluid Flow Structures. At first, the heat and fluid flow structures of cold water in the annulus will be

Nomenclature

a = exponent in the density equation
A = aspect ratio $=L/D$
D = gap width $=r_o-r_i$
g = gravitational acceleration
H = dimensionless heat function, equation (7)
k = thermal conductivity
L = annulus height
Nu = Nusselt number
Pr = Prandtl number
q_i = uniform heat flux on the inner wall
r^+ = radial coordinate
r = dimensionless radial coordinate $=r^+/D$
Ra* = modified Rayleigh number $=g\,\text{rsp}\,D^{(3+a)}q_i^a/(\nu\alpha k^a)$
r_i = radius of inner wall
r_o = radius of outer wall
RR = radius ratio $=r_o/r_i$
rsp = coefficient in density equation
T = temperature
u^+ = radial velocity
u = dimensionless radial velocity $=u^+D/\alpha$
v^+ = axial velocity
v = dimensionless axial velocity $=v^+D/\alpha$
z^+ = axial coordinate
z = dimensionless axial coordinate $=z^+/D$
α = thermal diffusivity
γ = density inversion parameter, equation (6)
θ = dimensionless temperature $=(T-T_o)k/(q_iD)$
θ_m = dimensionless temperature parameter $=(T_m-T_o)k/(q_iD)$
ν = kinematic viscosity
ρ = density
ψ^+ = stream function
ψ = dimensionless stream function $=\psi^+/\alpha D$
ω^+ = vorticity
ω = dimensionless vorticity $=\omega^+D^2/\alpha$

Subscripts

i = inner wall
m = extreme temperature
o = outer wall

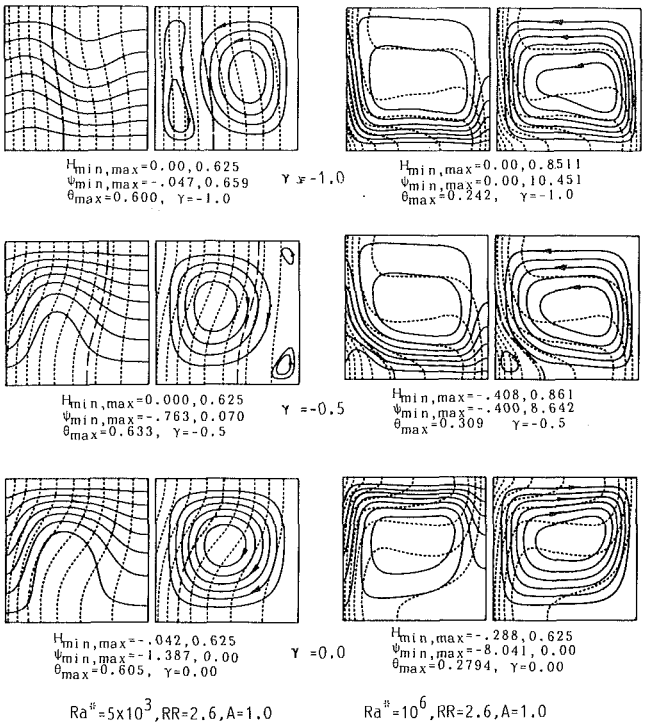

Fig. 2 Heatlines (left), streamlines (right), and isotherms (dashed lines) in a unit-aspect-ratio annulus with $RR = 2.6$ at three different inversion parameters

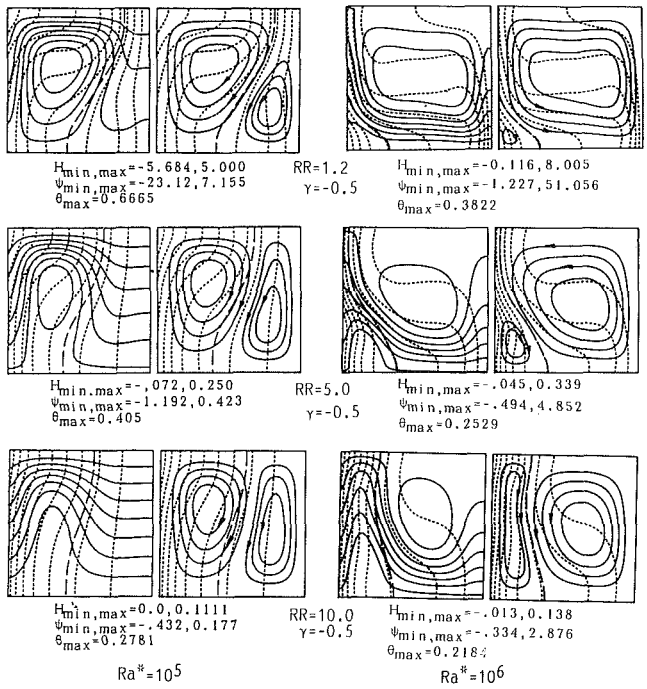

Fig. 3 Influence of radius ratio on the heat and fluid flow structures at $\gamma = -0.5$ and $A = 1$

presented by means of contour maps of heatlines and streamlines, respectively, which also overlap the isotherms (dashed lines). Furthermore, the isotherm corresponding to the density extreme (i.e., $\theta = \theta_m$), when it exists, is depicted by a heavy dashed line on the isotherm plots. In all the contour plots the heated inner wall is on the left. The increment between the contour lines is constant, except in the cases showing bicellular flow structure, for which distinctive increments are used for the streamlines in the respective flow regions.

Figure 2 is intended to illustrate the effect of the inversion parameter γ, with a fixed RR and A. For $\gamma = 0$ (i.e., $T_o = T_m$), having water of the maximum density always situated on the outer wall, the water in the annulus is expected to behave like an ordinary fluid. For it a clockwise unicellular flow structure is formed at $Ra^* = 5 \times 10^3$. As a consequence, the heatlines as well as the isotherms exhibit pseudo-conduction characteristics commonly observed for ordinary fluids; heat from the inner wall is channeled through a horizontal corridor near the ceiling of the annulus as evidenced by the clustering of heatlines there. As noted previously, the density inversion phenomenon is prone to arise for negative values of the inversion parameter only. Accordingly, with $\gamma = -0.5$ at the same Ra*, secondary counterclockwise eddies can be readily detected in both upper and lower corners of the outer wall and the main clockwise recirculation flow (inner circulation) in the annulus is markedly impeded as witnessed by the decrease of the minimum dimensionless stream function. Further, the appearance of the isotherm for the density extreme near the outer wall, as shown in Fig. 2, provides further direct evidence for the occurrence of the density inversion phenomenon. With further decrease of γ, the isotherm for the density extreme is seen to shift toward the heated inner wall and hence the effect of density inversion on the fluid flow pattern becomes more pronounced. At $\gamma = -1$ and $Ra^* = 5 \times 10^3$, as depicted in Fig. 2, the growing counterclockwise recirculation near the outer wall (outer circulation) becomes the dominant flow structure in the annulus. This change is further reflected by the heatline pattern exhibiting a slightly downward deformation.

Another important fact revealed in Fig. 2 is that with a fixed negative value of the inversion parameter in an annulus of fixed geometry, the increase of Ra* tends to promote the density inversion effect. At $Ra^* = 10^6$ with $RR = 2.6$, $A = 1$, and $\gamma = -1$, the streamlines and heatlines display a convective inversion pattern of fluid and heat flow in which the sense of the convection is simply opposite to that of the ordinary fluid as by the results for $\gamma = 0$ shown in Fig. 2. This can be ascribed to the fact that under steady-state conditions with mixed boundary conditions, the enhanced convective heat transfer across the annulus with increasing Ra* requires the surface temperature of the inner wall of constant heat flux to decrease, causing the extreme density isotherm to shift further toward the inner wall at a given negative value of the inversion parameter.

The influence of the radius ratio on the heat and fluid flows is next demonstrated in Fig. 3. One can see that increasing the radius ratio for a fixed negative value of the inversion parameter and modified Rayleigh number decreases the surface temperature of the inner wall, and hence the strength of the bicellular flow structure induced by density inversion is noticeably reduced as is the relative size difference between the inner and outer circulation. Furthermore, the intensity of convective heat flow weakens accordingly as indicated by the heatline distributions shown in Fig. 3. The foregoing for the effect of the radius ratio appears to be in contrast to that reported for an isothermally heated inner wall (Lin and Nansteel, 1987b) except for the diminishing size difference between the inner and outer cells.

In Figs. 4 and 5, the heat and fluid flow structures in the annulus of various aspect ratio for $\gamma = -0.5$ and $\gamma = -0.75$, respectively, at $RR = 2.6$ and $Ra^* = 10^5$, are exemplified. An overview of these figures indicates that the heat and fluid flow structures are affected by the aspect ratio of the annulus differently, depending upon the inversion parameter. For $\gamma = -0.5$ (Fig. 4), the increase of the aspect ratio up to 2 tends to strengthen both the inner and outer circulations. With further increase of the aspect ratio, one can notice that the outer circulation is markedly impeded while the dominant inner circulation continues to intensify. Meanwhile, the isotherm for the density extreme tends to shift inward with increasing

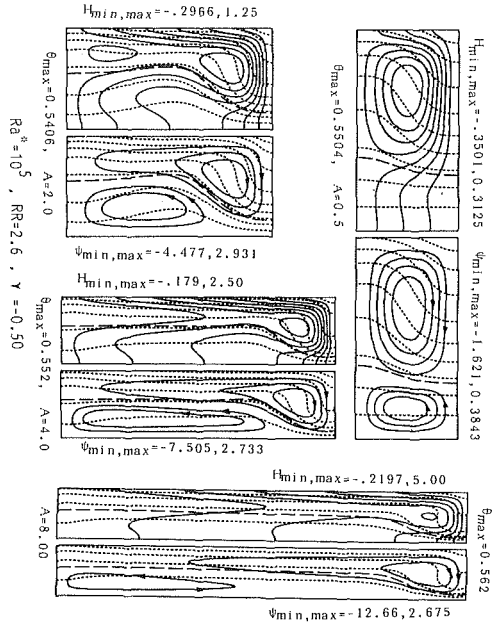

Fig. 4 Influence of aspect ratio on the heat and fluid flow structures at $RR = 2.6$, $Ra^* = 10^5$, and $\gamma = -0.5$

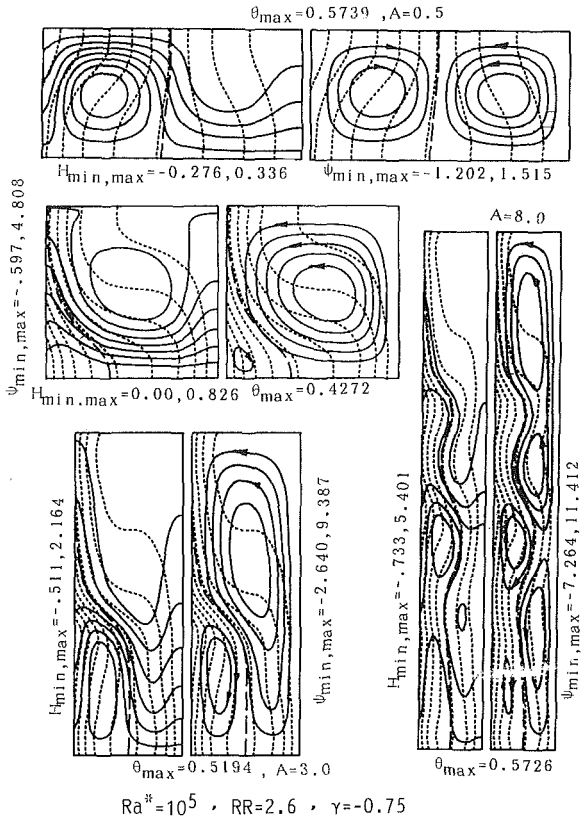

Fig. 5 Influence of aspect ratio on the heat and fluid flow structures at $RR = 2.6$, $Ra^* = 10^5$, and $\gamma = -0.75$

aspect ratio from $A = 0.5$ up to unity; but beyond that, a further increase of the aspect ratio results in no apparent shift of this isotherm, which essentially is situated midway between the inner and outer walls over much of the vertical span of the annulus when $A \geq 4$. Moreover, the heatlines in Fig. 4 reveal that in the tall annulus, heat from the inner wall is mostly carried by the dominant inner circulation toward the outer surface, even though a nearly parallel isotherm distribution is exhibited

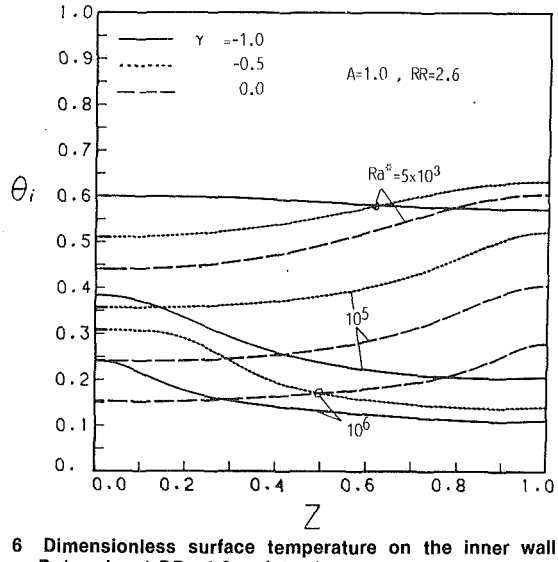

Fig. 6 Dimensionless surface temperature on the inner wall with various Ra* and γ at $RR = 2.6$ and $A = 1$

over much of the vertical span of the annulus. As for the case of $\gamma = -0.75$, a different influence of the aspect ratio is observed. In Fig. 5, the increase of aspect ratio for the shallow annulus results in an inward shift of the isotherm for the density extreme and intensified outer circulation; at $A = 1$, the heatlines and streamlines exhibiting a nearly convective inversion phenomenon can be readily detected. In the tall annulus, the increase of aspect ratio renders both the inner and outer circulations more intense, such that at $A = 8$ a splitting of eddies arises within the bicellular circulations, and hence a multicellular flow structure is formed, as is also indicated by the waviness of the isotherms in Fig. 5. It should be noted that the calculation for this case actually encountered difficulties in the satisifaction of the predetermined relative convergence criterion ($\leq 10^{-5}$); instead the solution reported here could only satisfy at most a criterion of 10^{-4}. The reason for the onset of multicellullar flow behavior at an aspect ratio much smaller than that reported for ordinary fluids (Lee et al., 1982) may follow from the fact that the bicellular structure of approximately equal strength makes the effective aspect ratio of either the inner or outer circulation considerably larger, thus provoking the multicellular flows in the annulus. Moreover, the wavy isotherms and the multicellular fluid flow lead to rather complicated heat flow paths across the annulus. Admittedly, there exits a possibility that heat and fluid flows for this case are periodic in time as well as wavy in space; a true transient numerical simulation and/or a corresponding experimental investigation are certainly needed in future work.

Surface Temperature of Inner Wall. The heat and fluid flow structures elaborated in the foregoing can be further inferred from the surface temperature of the constant-heat-flux inner wall. The dimensionless surface temperature distributions on the heated inner wall at different modified Rayleigh numbers are graphically presented in Fig. 6 for $A = 1$, $RR = 2.6$, and $\gamma = 0, -0.5, -1$. For $\gamma = 0$ and $Ra^* \geq 5 \times 10^3$, the surface temperature consistently increases from the bottom edge to the top of the inner wall, which is indicative of clockwise circulation. For negative values of the inversion parameter, the convective inversion phenomenon, as demonstrated in Fig. 2, can arise from the enhanced density inversion by the increase of Ra*. Accordingly, the surface temperature profile exhibits an adjustment from the monotonic increasing trend toward the opposite; as can be seen in Fig. 6, for $\gamma = -0.5$ with Ra* increasing up to 10^6, the surface temperature profile is inverted, decreasing along the inner wall. Further inspection of Fig. 6 reveals that the surface

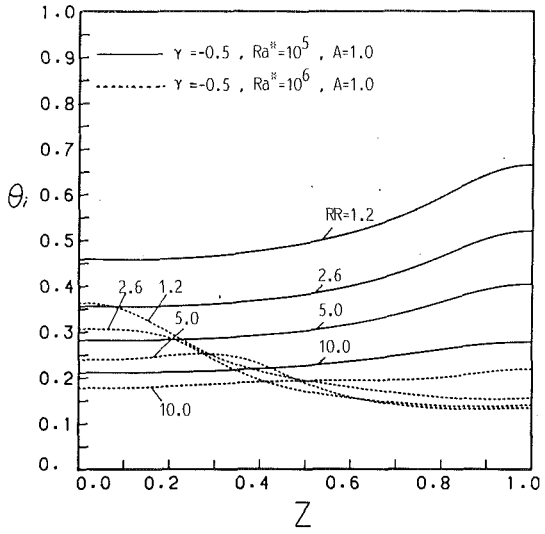

Fig. 7 Dimensionless surface temperature on the inner wall with various Ra* and *RR* at $\gamma = -0.5$ and $A = 1$

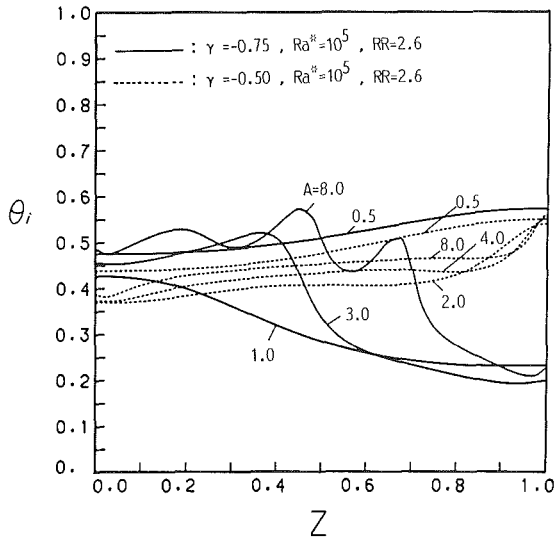

Fig. 8 Dimensionless surface temperature on the inner wall with various *A* and γ at *RR* = 2.6 and Ra* = 10^5

temperature of the inner wall decreases with increasing Ra*, indicating a higher heat transfer coefficient.

Figure 7 presents the effect of the radius ratio on the surface temperature of the inner wall in a unit-aspect-ratio annulus for $\gamma = -0.5$. In general, it can be noted that the axial variation of the surface temperature diminishes with the increase of radius ratio; at $RR = 10$, a nearly isothermal inner wall is observed. Further examination of Fig. 7 reveals that the influence of the radius ratio is a function of Ra* as well.

Next, the results for the surface temperature distributions corresponding to the cases presented in Figs. 4 and 5 are depicted in Fig. 8 to illustrate the effect of the aspect ratio. For the shallow annulus, $A = 0.5$, in contrast to that of the unit aspect ratio, the weakening convective flow results in a higher surface temperature on the inner wall. On the other end, for the tall annulus, with $\gamma = -0.5$, the surface temperature increases with increasing aspect ratio, with the exception of the region near the top edge of the inner wall, where a temperature drop occurs due to the intensified inner circulation there. As for the case of $\gamma = -0.75$, the multicellular natural convection in the tall annulus ($A \geq 3$) leads to a wavy temperature distribution along the inner wall.

Overall Heat Transfer Results. Now, attention will be turned to the results for the average heat transfer coefficient at the inner wall, which are presented by means of an average Nusselt number defined as

$$\overline{\mathrm{Nu}} = q_i D / [k(\bar{T}_i - T_o)] \tag{8}$$

Figure 9 presents the typical relationship between the average Nusselt number and the inversion parameter at various values of the other relevant parameters. As is expected, for fixed geometric parameters and modified Rayleigh number, a minimum Nusselt number occurs at a negative value of the inversion parameter between -1 and 0. It can be further seen from the figure that the variation of either the aspect ratio or the modified Rayleigh number has a marked effect on the critical value of the inversion parameter yielding the minimum heat transfer. With increasing Ra* at a fixed A, the critical value tends to shift toward zero, while the opposite is true for increased aspect ratio ($A \geq 1$) at a given Ra* ($\geq 10^4$). Comparatively, the variation of the radius ratio weakly affects the critical value of the inversion parameter for the minimum heat transfer.

Figure 10 supplemented with Fig. 9 demonstrates the influence of the aspect ratio on the average heat transfer results. It is evident that for fixed *RR* and Ra*, the average Nusselt number exhibits a maximum value at the value of the aspect ratio between 1 and 2, depending upon the inversion parameter as well as the modified Rayleigh number.

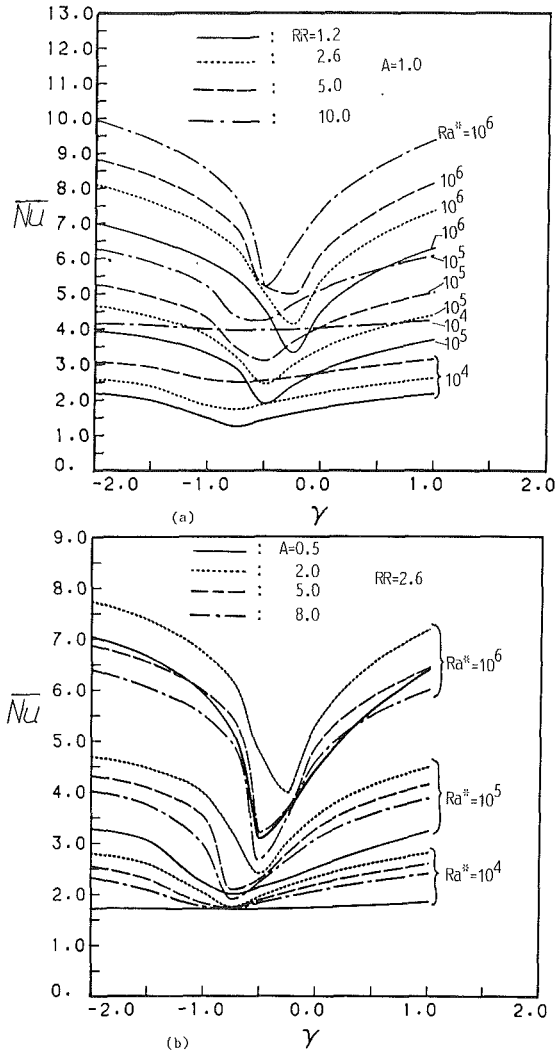

Fig. 9 Relationship of the average Nusselt number with the inversion parameter: (*a*) for different *A* and Ra* at *RR* = 2.6, (*b*) for different *RR* and Ra* at *A* = 1

Table 1 Coefficients of equation (10)

γ	C_1	C_2	C_3	C_4	C_5	C_6	Maximum development, percent	range
−2.0	0.3049	0.2255	−0.0014	−0.0015	0.2632	−0.0521	3.86	R1
−1.5	0.2603	0.2348	−0.0017	−0.0012	0.2805	−0.0837	4.98	R1
−1.0	0.2297	0.2398	−0.0003	−0.0016	0.2096	−0.0905	6.15	R2
−0.50	0.6433	0.0817	0.0021	−0.0015	0.3428	−0.0102	6.47	R3
−0.25	0.4965	0.1333	0.0002	−0.0011	0.3033	−0.0250	4.89	R1
0.00	0.3400	0.1857	−0.0010	−0.0017	0.2956	−0.0118	5.78	R1
0.50	0.3349	0.2036	−0.0013	−0.0016	0.2785	−0.0314	3.91	R1
1.00	0.3507	0.2082	−0.0014	−0.0016	0.2736	−0.0370	2.83	R1
−2.0	0.2258	0.4128	−0.0016	−0.1674	0.2502	1.8873	4.23	R4
−1.5	0.1950	0.4073	−0.0023	−0.1550	0.2798	1.7993	4.42	R4
−1.0	0.1712	0.4166	−0.0023	−0.1606	0.2534	2.0423	2.35	R5
−0.50	0.5215	0.1012	0.0014	0.0027	0.3286	0.1776	3.80	R6
−0.25	0.4013	0.2336	−0.0002	−0.0849	0.3100	1.0590	3.05	R4
0.00	0.2967	0.2953	−0.0008	−0.1036	0.2838	1.3026	4.72	R4
0.50	0.2661	0.3450	−0.0013	−0.1279	0.2699	1.5247	4.25	R4
1.00	0.2714	0.3585	−0.0013	−0.1342	0.2572	1.5579	3.55	R4

R1 : $10^4 \le Ra^* \le 10^6$, $1.2 \le RR \le 5.0$, $2.0 \le A \le 8.0$
R2 : $10^5 \le Ra^* \le 10^6$, $1.2 \le RR \le 7.0$, $2.0 \le A \le 8.0$
R3 : $10^4 \le Ra^* \le 10^5$, $1.2 \le RR \le 7.0$, $2.0 \le A \le 8.0$
R4 : $5\times10^4 \le Ra^* \le 10^6$, $1.2 \le RR \le 5.0$, $0.5 \le A \le 1.0$
R5 : $10^5 \le Ra^* \le 10^6$, $1.2 \le RR \le 5.0$, $0.75 \le A \le 1.0$
R6 : $10^4 \le Ra^* \le 10^5$, $1.2 \le RR \le 5.0$, $0.5 \le A \le 1.0$

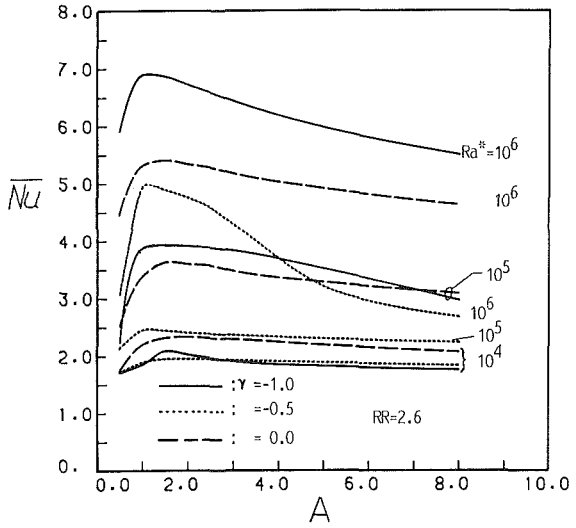

Fig. 10 Effect of aspect ratio on the average Nusselt number

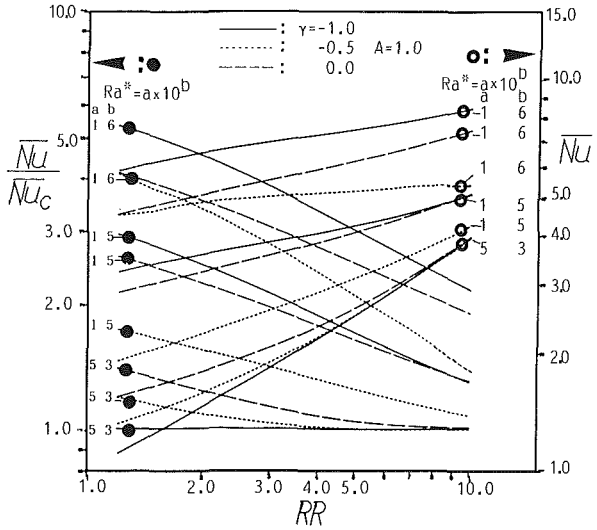

Fig. 11 Influence of radius ratio on the average heat transfer coefficient and the convective heat transfer contribution for different γ and Ra* at $A = 1$

In Fig. 11, the average Nusselt number is plotted against the radius ratio of the annulus for $A = 1$ and three different inversion parameters. The increase of radius ratio tends consistently to enhance the average heat transfer coefficient for all the cases considered in the figure. Also included in Fig. 11 are the results for the ratio of the average Nusselt number to that for pure conduction, $\overline{Nu}/\overline{Nu}_c$, in order to reflect the convective contribution to the overall heat transfer for various radius ratios. The average Nusselt number for pure conduction can be easily obtained as

$$\overline{Nu}_c = (RR-1)/\ln(RR) \tag{9}$$

The figure clearly shows that the contribution of the convective heat transfer mechanism subsides substantially with increased radius ratio, in turn signifying the increasing importance of conduction heat transfer across the annulus. For $Ra^* = 5\times10^3$, the curves for all three different inversion parameters progressively decay to unity at $RR = 10$, while a rather drastic decline with increasing radius ratio prevails for higher Ra* ($\ge 10^5$) as shown in Fig. 11. This is clearly consistent with the finding concerning the weakening convective heat and fluid flows with increasing radius ratio illustrated in Fig. 3. Moreover, the foregoing effect of radius ratio on heat transfer appears to be somewhat different from that reported for an isothermally heated inner wall (Lin and Nansteel, 1987b) in which a bunching-up of isotherms near the heated inner wall gives rise to a locally diminished heat transfer with increasing radius ratio.

Finally, the present numerical data for heat transfer coefficients in certain ranges of the governing parameters may be correlated by means of a least-square regression as

$$\overline{Nu} = C_1 Ra^{*(C_2+C_3RR+C_4A)} RR^{C_5} A^{C_6} \tag{10}$$

the values of C_i ($i = 1, \ldots, 6$) have been obtained for each inversion parameter as tabulated in Table 1. These equations further reflect the rather complicated influence of the geometric parameters on the overall heat transfer.

Concluding Remarks

Numerical results are reported for the steady laminar natural convection of cold water in a vertical annulus with

constant heat flux on the inner wall. The heat and fluid flow structures of cold water in the vertical annulus are vividly visualized by means of contour maps of heatlines and streamlines. It is found that the mixed boundary conditions considered here can have a significant influence on the geometric dependence of the heat transfer characteristics and flow structures. The maximum heat transfer takes place with a radius ratio of 2.6 for aspect ratio between 1 and 2, depending on the inversion parameter as well as the modified Rayleigh number. A multicellular flow behavior of cold water is found to arise with increasing aspect ratio up to 8 when the inner and outer circulations are approximately equal in strength. Moreover, a consistent increase of the average Nusselt number with the increase of radius ratio is observed, in contrast to that reported for an isothermal inner wall; the contribution of convective heat transfer subsides substantially as well. As commonly expected for cold water natural convection, the average Nusselt number exhibits a minimum at a negative value of the inversion parameter between -1 and 0, depending mainly on the modified Rayleigh number and the aspect ratio of the annulus. Since no experimental or analytical results are available for the problem under consideration, it is not possible to make a direct comparison of the results presented. A corresponding experimental study is apparently needed in future work.

Acknowledgments

Computer facilities were made available by National Cheng Kung University Computer Center. The helpful comments made by the reviewers are also greatly appreciated.

References

Anderson, D. A., Tannehill, J. C., and Pletcher, R. H., 1984, *Computational Fluid Mechanics and Heat Transfer*, Hemisphere Publishing Corp., Washington, DC.

Gebhart, B., and Mollendorf, J., 1974, "A New Density Relation for Pure and Saline Water," *Deep-Sea Research*, Vol. 24, pp. 831–848.

Inaba, H., and Kukuda, T., 1984, "An Experimental Study of Natural Convection in an Inclined Rectangular Cavity Filled With Water at Its Density Extreme," ASME JOURNAL OF HEAT TRANSFER, Vol. 108, pp. 109–115.

Kimura, S., and Bejan, A., 1983, "The Heatlines Visualization of Convective Heat Transfer," ASME JOURNAL OF HEAT TRANSFER, Vol. 105, pp. 916–919.

Lee, Y., Korpela, S. A., and Horne, R. N., 1982, "Structure of Multicellular Natural Convection in a Tall Vertical Annulus," *Heat Transfer—1982*, Hemisphere Publishing Corp., Washington, DC, Vol. 2, pp. 221–226.

Leonard, B. P., 1983, "A Convectively Stable Third-Order Accurate Finite-Difference Method for Steady Two-Dimensional Flow and Heat Transfer," *Numerical Properties and Methodologies in Heat Transfer*, T. M. Shih, ed., Hemisphere Publishing Corp., Washington, DC, pp. 211–226.

Lin, D. S., and Nansteel, M. W., 1987a, "Natural Convection Heat Transfer in a Square Enclosure Containing Water Near Its Density Maximum," *Int. J. Heat Mass Transfer*, Vol. 30, No. 11, pp. 2319–2329.

Lin, D. S., and Nansteel, M. W., 1987b, "Natural Convection in a Vertical Annulus Containing Water Near the Density Maximum," ASME JOURNAL OF HEAT TRANSFER, Vol. 109, pp. 899–905.

Ostrach, S., 1982, "Natural Convection Heat Transfer in Cavities and Cells," *Heat Transfer—1982*, Hemisphere Publishing Corp., Washington, DC, Vol. 1, pp. 365–379.

Schneider, G. E., and Zedan, M., 1981, "A Modified Strongly Implicit Procedure for the Numerical Solution of Field Problems," *Numerical Heat Transfer*, Vol. 4, pp. 1–19.

Vasseur, P., Robillard, L., and Chandra Shekar, B., 1983, "Natural Convection Heat Transfer of Water Within a Horizontal Cylindrical Annulus With Density Inversion Effects," ASME JOURNAL OF HEAT TRANSFER, Vol. 105, pp. 117–123.

Vasseur, P., Nguyen, T. H., and Caltagrione, J. P., and Chandra Shekar, B., 1984, "Convection in a Horizontal Annular Porous Layer With Non-linear Density Effects," *Chem. Eng. Commun.*, Vol. 26, pp. 55–71.

N. Ramachandran
USRA, NASA/MSFC,
Huntsville, AL 35812

B. F. Armaly
Fellow ASME

T. S. Chen
Fellow ASME
Department of Mechanical and Aerospace Engineering and Engineering Mechanics,
University of Missouri—Rolla,
Rolla, MO 65401

Turbulent Mixed Convection Over an Isothermal Horizontal Flat Plate

Turbulent boundary layer flow adjacent to an isothermal horizontal flat plate is analyzed for the mixed convection regime. Results are presented for both air ($Pr=0.7$) and water ($Pr=7$) flowing above the heated plate at various velocities over a range of temperature differences between the plate and the free stream. Closure of the governing, time-averaged, turbulent equations for the mean flow quantities is attained by using a modified k–ϵ model that accounts for the influence of buoyancy-induced forces on the turbulent quantities. It is found that the local surface heat flux increases with increasing buoyancy force parameter. The numerical results are in qualitative agreement with available experimental measurements.

Introduction

There are many transport processes that occur in nature and in industry, where, in addition to the natural convection flow induced by thermal gradients, there exists an externally forced flow. For some of these cases, the existing pure forced convection or pure free convection correlations fail to predict accurately the temperature and the flow fields. This mixed convection domain has been the subject of many experimental and analytical investigations in laminar boundary layer flows (see for example, Ramachandran et al., 1983, and the references cited therein). The onset of instability in mixed convection boundary layer flows has been reported by Chen and Mucoglu (1979) and Moutsoglu et al. (1981) for heated horizontal surfaces. Wang (1982) experimentally verified these instability criteria for the case of horizontal heated surfaces, using air as the flowing medium. He reported heat transfer results for upward and downward facing horizontal surfaces and concluded that the local heat transfer coefficient is strongly dependent on the free-stream velocity and on the temperature difference between the plate and the free stream. For the case of the heated plate facing upward, he established that the heat transfer rates dip slightly below the corresponding free convection values at certain free-stream velocities and temperature differences. A similar effect was observed by Hall and Prince (1970) in mixed convection along vertical surfaces and by Seiichi and Takuro (1975) for mixed convection around horiontal cylinders.

Very recently, Moharerri et al. (1988) reported experimental measurements in the transition regime of mixed convective air flow over an isothermal horizontal plate. The ranges of experimental parameters were $10^3 < \mathrm{Re}_x < 10^5$ $(0.34 < u_\infty < 0.63$ m/s) and $5\times10^6 < \mathrm{Gr}_x < 10^8$ $(10 \le \Delta T \le 30°\mathrm{C})$. Detailed velocity and temperature distributions were presented in the transitional vortex flow regime and a correlation was presented for the onset of vortex instability. Their results infer the beginning of transition from laminar to turbulent flow due to the onset of three-dimensional longitudinal vortices at $\mathrm{GR}_{x,c}/\mathrm{Re}_{x,c}^{1.5} = 100$. This value is smaller than the value of 190 for the same grouping of parameters as reported in the experimental findings of Hayashi et al. (1977) and differs substantially from the numerically predicted values of 0.447 (Moutsoglu et al., 1981). Experimental data on mixed convection from isothermal horizontal surfaces were reported by Townsend (1972) for air flow and by Imura et al. (1978) and Cheng et al. (1986) for water flow. Imura et al. (1978) have concluded that for water flow, the transition from laminar forced convection to turbulent mixed convection occurs when the parameter $\mathrm{Gr}_x/\mathrm{Re}_x^{1.5}$ lies between 100 and 300, and that for $\mathrm{Gr}_x/\mathrm{Re}_x^{1.5}$ larger than 300 the heat transfer rates become independent of the Reynolds number, which are typical of those for turbulent free convection from a horizontal surface. Their data are in the Reynolds number range of $\mathrm{Re}_x = 3.2\times10^3 - 2\times10^5$. Later Cheng et al. (1986) extended the work of Imura et al. (1978) to higher Reynolds numbers $(\mathrm{Re}_x = 2.5\times10^4 - 2.2\times10^6)$ and covered the Grashof number range of $\mathrm{Gr}_x = 2\times10^8 - 1.5\times10^{12}$. They found that for $\mathrm{Gr}_x/\mathrm{Re}_x^{1.5} > 200$, the heat transfer rate becomes higher than the turbulent free convection value. The experimental work of Townsend (1972) in air flow over a slightly heated horizontal plate involved measurements of velocity and temperature fluctuations in the boundary layer. His data showed that the mean temperature and mean velocity profiles were closely similar, implying a close analogy for the transfer coefficient of heat and momentum in the boundary layer.

A survey of the various turbulence models that have been proposed in recent years (see Launder and Spalding, 1972, 1974) reveals that the k–ϵ model of Jones and Launder (1972, 1973) has been successfully used in predicting a variety of complex turbulent flows. Others (see Armaly et al., 1986, and the references cited therein) have utilized this model for forced, natural and mixed convection. The turbulent mixed convection domain has received very little attention. Subramanian and Antonia (1981) investigated experimentally the effect of Reynolds number on turbulent boundary layer flow over a slightly heated flat plate subjected to a uniform heat flux. Chung and Sung (1984) utilized a four-equation model to investigate the buoyancy force effect in turbulent boundary layer flow over a horizontal flate plate. In their study, the flow was assumed to be turbulent from the leading edge of the plate and the buoyancy term was omitted in the mean flow momentum equation. In the present study, a modified version of the k–ϵ model is used (see Armaly et al., 1986) to analyze turbulent mixed convection in boundary layer flow along an isothermal horizontal flat plate. The objectives of the study are to utilize the modified k–ϵ model in buoyancy-affected mixed convective flow, to investigate the effect of buoyancy on the numerical developments of the transition from laminar to turbulent flow, to gain better understanding of how the various flow regimes in mixed convection develop through this model, and to compare the results with available data from experiments for flow over a heated horizontal flat plate.

Analysis

Consider an isothermal horizontal flat plate maintained at temperature T_w, above which a fluid at temperature T_∞ is flowing with velocity u_∞. Under the Boussinesq approxima-

Contributed by the Heat Transfer Division and presented at the ASME Winter Annual Meeting, Boston, Massachusetts, December 13–18, 1987. Manuscript received by the Heat Transfer Division September 24, 1987. Keywords: Mixed Convection, Numerical Methods, Turbulence.

tion, the resulting time-averaged turbulent boundary layer equations are given by (Armaly et al., 1986)

$$\frac{\partial u}{\partial x}+\frac{\partial v}{\partial y}=0 \tag{1}$$

$$u\frac{\partial u}{\partial x}+v\frac{\partial u}{\partial y}=\frac{\partial}{\partial y}\left[(\nu+\nu_t)\frac{\partial u}{\partial y}\right]+\frac{\partial}{\partial x}\int_y^\infty g\beta(T-T_\infty)dy \tag{2}$$

$$u\frac{\partial T}{\partial x}+v\frac{\partial T}{\partial y}=\frac{\partial}{\partial y}\left[\left(\frac{\nu}{\mathrm{Pr}}+\frac{\nu_t}{\sigma_T}\right)\frac{\partial T}{\partial y}\right] \tag{3}$$

$$u\frac{\partial k}{\partial x}+v\frac{\partial k}{\partial y}=\frac{\partial}{\partial y}\left[\left(\nu+\frac{\nu_t}{\sigma_k}\right)\frac{\partial k}{\partial y}\right]+\nu_t\left(\frac{\partial u}{\partial y}\right)^2 -\epsilon-2\nu\left(\frac{\partial k^{1/2}}{\partial y}\right)^2-\left|C_k g\beta\frac{\nu_t}{\sigma_T}\frac{\partial T}{\partial y}\right| \tag{4}$$

$$u\frac{\partial \epsilon}{\partial x}+v\frac{\partial \epsilon}{\partial y}=\frac{\partial}{\partial y}\left[\left(\nu+\frac{\nu_t}{\sigma_\epsilon}\right)\frac{\partial \epsilon}{\partial y}\right]+2\nu\nu_t\left(\frac{\partial^2 u}{\partial y^2}\right)^2 +C_1F_1\frac{\epsilon\nu_t}{k}\left(\frac{\partial u}{\partial y}\right)^2-C_2F_2\frac{\epsilon^2}{k}-\left|C_\epsilon\frac{\epsilon}{k}g\beta\frac{\nu_t}{\sigma_T}\frac{\partial T}{\partial y}\right| \tag{5}$$

The boundary conditions are

$$u=v=k=\epsilon=0,\quad T=T_w \text{ at } y=0$$
$$u\to u_\infty,\ T\to T_\infty,\quad k=\epsilon=0 \text{ as } y\to\infty$$
$$u=u_\infty,\quad T=T_\infty \text{ at } x=0 \tag{6}$$

The equations given above are the same as those proposed by Jones and Launder (1972, 1973), except that one extra term has been added to each of equations (4) and (5) to account for the contribution of buoyancy forces to the turbulent kinetic energy and its dissipation rate. The inclusion of these two terms, enclosed by the dashed lines, follows from an analysis similar to that done by Armaly et al. (1986) and by Lin and Churchill (1978). The last term in equation (2) represents the streamwise pressure gradient resulting from the buoyancy force. In the above equations the eddy diffusivity for momentum, ν_t, is defined as

$$\nu_t=C_\nu F_\nu k^2/\epsilon \tag{7}$$

The C's and the Prandtl numbers σ's as well as the low Reynolds number wall functions, F_1, F_2, and F_ν, cited by Lin and Churchill (1978), are used in the present analysis.

Method of Solution

The governing equations (1)–(6) were solved by a fully implicit finite difference scheme similar to the one used by Patankar and Spalding (1970). Computations were done using 100 cross-stream grid points and a forward step in x of 2–3 percent of the boundary layer thickness. For the mixed convection problem, the presence of the buoyancy force term in the momentum equation (the last term on the right-hand side of equation (2)) requires an iterative procedure in the numerical solution. A convergence criterion of 0.01 percent (the maximum difference between the velocities and the temperatures between successive iterations) was imposed in the numerical solution, giving satisfactory results that agreed to within 1 percent of the previously published solutions for the two test cases, one for laminar mixed convection (Ramachandran et al., 1983) and the other for turbulent forced convection (Jones and Launder, 1972). The solution proceeded from the laminar region to transition, and then to the turbulent regime. A procedure similar to the one described by Armaly et al. (1986) was used to trigger turbulence at some critical Reynolds and/or Grashof numbers. Turbulence calculations for air flow were initiated at the value of $\mathrm{Gr}_{x,c}=2\times10^7$ or $\mathrm{Re}_{x,c}=5\times10^4$, whichever was reached first. Thus, for the range of free-stream velocities (0.5–10 m/s) and plate-ambient temperature differences (0–100°C) investigated in this study, the Grashof number criterion is usually the first one to be met for velocities less than 10 m/s. This transition criterion also satisfied the vortex instability criterion given by Moharreri et al. (1988) as $\mathrm{Gr}_x/\mathrm{Re}_x^{1.5}=100$, for the low velocities studied. For example, for $u_\infty=0.5$ m/s and $\Delta T=25$°C the numerical transition due to the introduction of k and ϵ profiles at an upstream location is noticed at $\mathrm{Gr}_x/\mathrm{Re}_x^{1.5}\simeq113$, and for the $(u_\infty, \Delta T)$ combination of (0.75 m/s, 25°C) the transition occurs at $\mathrm{Gr}_x/\mathrm{Re}_x^{1.5}\simeq102$. This transition criterion however does not hold for the other velocity and temperature difference combinations investigated and hence indicates the dependence of transition on the magnitude of the primitive variables governing the flow. It is worthwhile recalling that the experimental results of Moharreri et al.

Nomenclature

A = Van Driest damping factor
$C_1, C_2, C_3, C_\epsilon, C_\nu$ = empirical constants
F_1, F_2, F_ν = empirical wall functions
Gr_x = local Grashof number = $g\beta(T_w-T_\infty)x^3/\nu^2$
g = gravitational acceleration
h = local heat transfer coefficient = $q_w/(T_w-T_\infty)$
J = heat transfer parameter = $\mathrm{Nu}_x\mathrm{Re}_x^{-0.8}$
k = kinetic energy of turbulence
K = thermal conductivity of fluid
L = length of the plate
Nu_x = local Nusselt number = hx/K
Pr = Prandtl number
q_w = local wall heat flux = $-K(\partial T/\partial y)_{y=0}$
Re_x = local Reynolds number = $u_\infty x/\nu$
T = fluid temperature
u, v = time-averaged velocity components in the axial (x) and normal (y) directions, respectively
x, y = axial and normal coordinates
α = thermal diffusivity of fluid
β = volumetric coefficient of thermal expansion
ϵ = dissipation rate of turbulent kinetic energy
η = pseudosimilarity variable = $(y/x)\mathrm{Re}_x^{1/2}$
ΔT = temperature difference = (T_w-T_∞)
μ = dynamic viscosity of fluid
ν = kinematic viscosity of fluid
ν_t = eddy diffusivity for momentum
ξ = buoyancy parameter = $\mathrm{Gr}_x/\mathrm{Re}_x^{5/2}$
ρ = density of fluid
$\sigma_k, \sigma_\epsilon, \sigma_T$ = turbulent Prandtl numbers

Subscripts

c = critical condition
w = condition at wall
∞ = condition at free stream

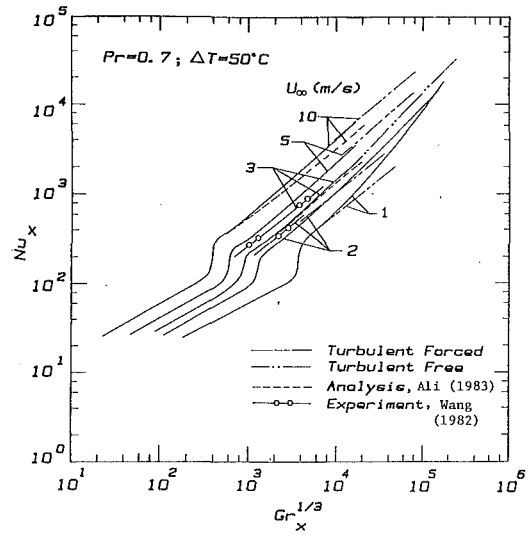

Fig. 1 Variation of Nu_x with Gr_x; Pr = 0.7

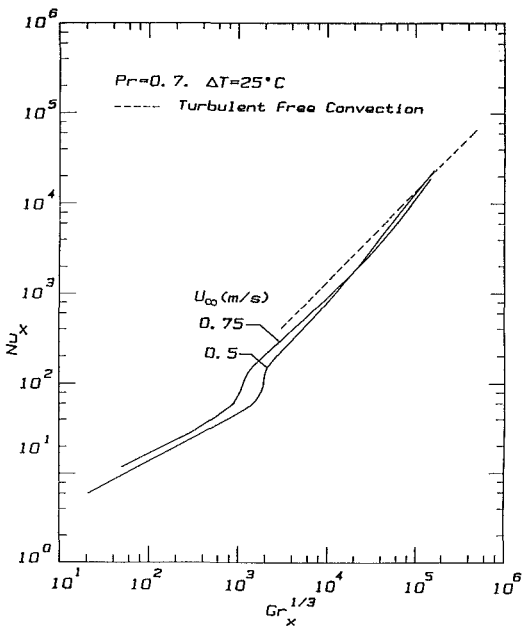

Fig. 2 Variation of Nu_x with Gr_x; Pr = 0.7

(1988) were limited to $0.34 \le u_\infty \le 0.63$ m/s and $10 \le \Delta T \le 30$°C. It should be noted, however, that in the numerical simulations the exact values of the critical Grashof and Reynolds numbers did not have a significant influence on the fully developed turbulent region. Computations were repeated by doubling the number of cross-stream points to 200, which did not cause any appreciable changes in the results at any x location.

It may be pointed out here that although the calculations proceed through the transitional regime, the model should not be expected to predict transition accurately and the results in that regime should be used with caution. But in the absence of other data they can be used to estimate the behavior of mixed convection in that regime. This point is further emphasized in the subsequent sections where the effect of buoyancy forces on the different flow regimes and on the numerical results is discussed.

Results and Discussion

Numerical solutions of the governing equations with the associated boundary conditions were obtained for a range of free-stream velocities (0.5–10 m/s) and temperature differences between the surface and the ambient (0–100°C) to cover a wide range of the mixed convection regime. The various fluid properties were evaluated at the film temperature, $T_f = (T_w + T_\infty)/2$, with the ambient being constant at 27°C. A numerical solution was started at the leading edge of the plate ($x = 0$) and carried out to $x = 30$ m. At a downstream location where either the critical Grashof number or the critical Reynolds number was reached, the starting profiles for k and ϵ were generated and the solution of the k and ϵ equations was initiated.

The mixed convection results for air flow are presented in Figs. 1 and 2, where the Nusselt number Nu_x is plotted against $Gr_x^{1/3}$ for different free-stream velocities. Results presented in Fig. 1 are for a temperature difference ΔT of 50°C. It can be seen from this figure that higher Nusselt numbers and hence higher heat transfer rates are associated with higher velocities. The introduction of the k and ϵ profiles at some critical Reynolds or Grashof numbers causes a transition at some downstream location from laminar to turbulent flow, as seen from the two figures. For a further increase in the streamwise distance x, the behavior of the flow and thermal fields is largely dependent on the free-stream velocity and the value of ΔT. For higher velocities ($u_\infty > 2$ m/s), the local Nusselt number is very nearly equal to the turbulent forced convection value. For lower free-stream velocities ($u_\infty \le 2$ m/s) the local Nusselt number is less than the natural convection value at the same Grashof number. For example, at velocities of 10 m/s and 5 m/s the local Nusselt numbers show very little departure from their respective turbulent forced convection asymptotes. On the other hand, for $u_\infty = 1$ m/s, the local Nusselt number attains the turbulent forced convection value immediately after the transition has occurred. For larger x, the local Nusselt number departs from the forced convection asymptote and tends toward the turbulent free convection value. This is in contrast to the behavior for the vertical plate geometry (Armaly et al., 1986) where the presence of a strong assisting buoyancy force tends to delay the transition from laminar to turbulent flow to a farther location downstream. Thus a clear transition from laminar to turbulent forced convection flow is seen in Fig. 1 for $u_\infty = 1$ m/s with a subsequent approach to the turbulent free convection value. The intermediate region between turbulent forced convection and fully turbulent free convection represents the turbulent mixed convection regime and the local Nusselt number in this regime lies somewhere between the turbulent forced and free convection values. Based on a 5 percent departure of the local Nusselt number results from the fully turbulent forced convection and free convection values, this mixed convection regime for $u_\infty = 1$ m/s and $\Delta T = 50$°C is given by $5.04 \times 10^3 \le Gr_x/Re_x^{1.5} \le 2.10 \times 10^5$ ($0.015 < \xi < 0.0513$). Thus, for a free-stream velocity of 1 m/s and a ΔT of 50°C, the mixed convection regime will begin at about $x = 5.5$ m and turbulent free convection characteristics will be evident at a very large x ($x = 60$ m). This range will however be different for different (u_∞, ΔT) combinations. The agreement between the present results and the experimental data of Wang (1982) is good, as shown in Fig. 1. However, the agreement with the mixing-length model results used by Ali (1983) is good only at low Grashof numbers and deteriorates at large Grashof numbers.

The behavior of the local Nusselt number is also illustrated in Fig. 2 where lower free-stream velocities are examined. The results presented are for temperature difference of 25°C and for two velocities of 0.75 and 0.5 m/s. The numerical computations were carried out to $x = 100$ m to obtain a better insight into the flow behavior. From the figure it is seen that the local Nusselt number shows the transition from laminar to turbulent flow and then approaches the turbulent free convection asymptote. The transition from laminar to turbulent flow is not delayed by the buoyancy force as is the case in the vertical

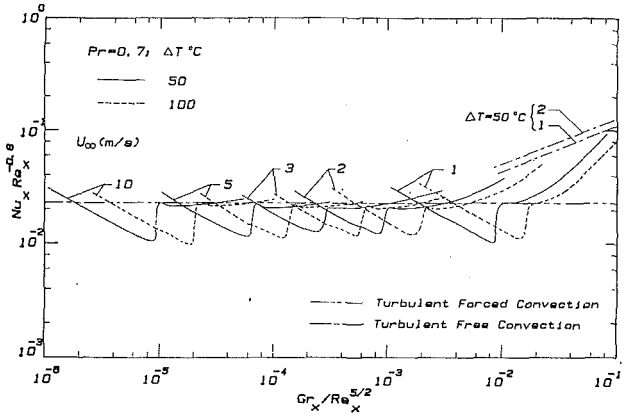

Fig. 3 Heat transfer parameter for turbulent mixed convection; Pr = 0.7

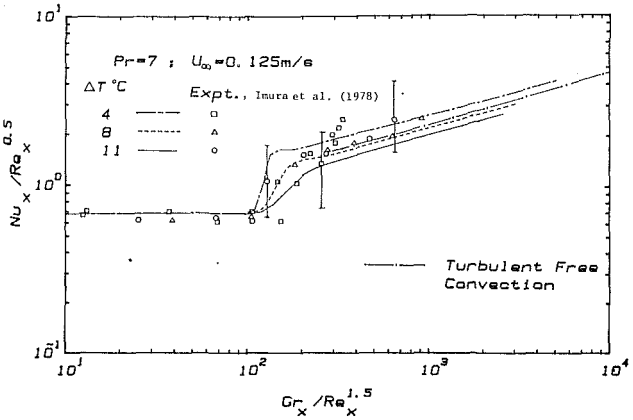

Fig. 4 Heat transfer results for turbulent mixed convection; Pr = 7

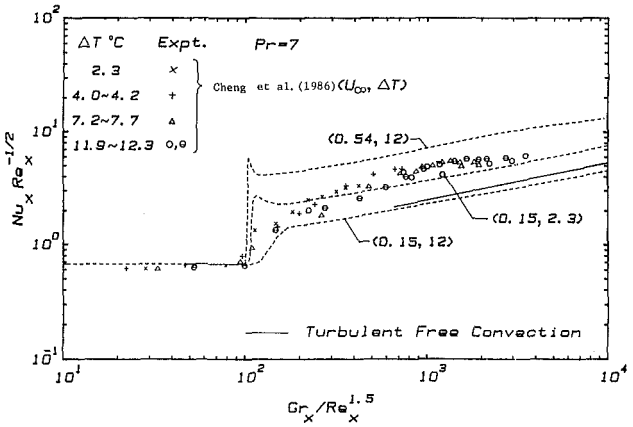

Fig. 5 Heat transfer results for turbulent mixed convection; Pr = 7

geometry (Armaly et al., 1986) where the assisting buoyancy force adds to the flow stability. In the horizontal geometry, the increasing magnitude of the buoyancy force with increasing axial distance x is in a direction normal to the flow, thus causing the flow to be inherently unstable. The flow field thus shifts from laminar mixed convection to turbulent forced convection and ultimately displays the characterisitcs of turbulent free convection. Flow with higher velocities will also display such characteristics, but at very high values of the Grashof number.

Figure 3 shows the previous results from Fig. 1 on different coordinates, $J = \mathrm{Nu}_x \mathrm{Re}_x^{-0.8}$ versus the buoyancy parameter $\xi = \mathrm{Gr}_x/\mathrm{Re}_x^{5/2}$. Local Nusselt number results are presented for ΔT of 50°C and 100°C. As can be seen from the figure, the higher velocities are associated with very small values of the buoyancy parameter and show very little departure from the turbulent forced convection asymptote after the transition from laminar to turbulent flow has occurred. The thermal buoyancy force, if any, causes a slight decrease in the heat transfer rate for the higher velocities from the fully turbulent value. It can also be seen from the figure that in the high-velocity range (3–10 m/s), the heating of the plate to a temperature of 100°C above the ambient conditions does not cause any significant departure in the heat transfer rate from the pure forced convection results. Lower velocities, on the other hand, cause a significant departure from the pure forced convection value and show an approach to the free convection limit.

Thus for the mixed convection flow regime along an isothermal horizontal surface that was examined in this study, one of the following prominent flow characteristics will be displayed:

Case 1. Laminar forced convection—laminar mixed convection—transition—turbulent forced convection. This behavior is typical of very high velocities (for example, for cases with $u_\infty > 3$ m/s and $\Delta T = 50$°C).

Case 2. Laminar forced convection—laminar mixed convection—transition—turbulent forced convection—turbulent mixed convection—turbulent free convection. This behavior is exhibited at intermediate velocities (e.g., $u_\infty = 1$–2 m/s and $\Delta T = 50$°C). The higher velocities discussed in case 1 will also show such a trend at very large x values or at smaller x values if ΔT is increased.

Case 3. Laminar forced convection—laminar mixed convection—transition—turbulent free convection. This is the representative behavior for small velocities (e.g., $u_\infty < 1$ m/s and $\Delta T = 50$°C).

Secondary interactions of these three flow characteristics in regions where the boundary layer is very thick are possible, but these are difficult to delineate precisely, and are attributed to a particular set of flow parameters, and hence are not included in any further discussion in this paper.

A comparison between the experimental data obtained by Imura et al. (1978) for water flow along a horizontal heated plate and the results obtained by the present analysis is given in Fig. 4. The numerical results were obtained for the same conditions as the experimental runs and the Prandtl number in the computations was taken as 7. Also shown in the figure are the bounds of experimental errors given by the authors and the turbulent free convection asymptote. The agreement between the analysis and the experiment is within the experimental error. In the range of parameters (Gr_x and Re_x) investigated, Imura et al. (1978) concluded that the boundary layer flow along a heated horizontal plate undergoes a transition from laminar forced convection to turbulent free convection. The numerical results also seem to indicate that kind of behavior. The aforementioned trends are similar to the flow behavior for mixed convection in low-velocity air flow.

Figure 5 shows a comparison between the present numerical results and the recent experimental results reported by Cheng et al. (1986). The turbulent free convection asymptote is also shown in the figure. The fully turbulent results for the (u_∞, ΔT) combination (0.15, 12) shown in this figure approximates the results for turbulent forced convection. The experiment was an extension of the earlier work reported by Imura et al. (1978) to higher values of Grashof and Reynolds numbers. The experimental data are seen to exhibit an appreciable departure from the turbulent free convection value. This behavior is in contrast to the heat transfer results of Imura et al. (1978), which show a qualitative agreement with the free convection asymptote. The numerical results obtained for the experimental range of velocities and temperature differences

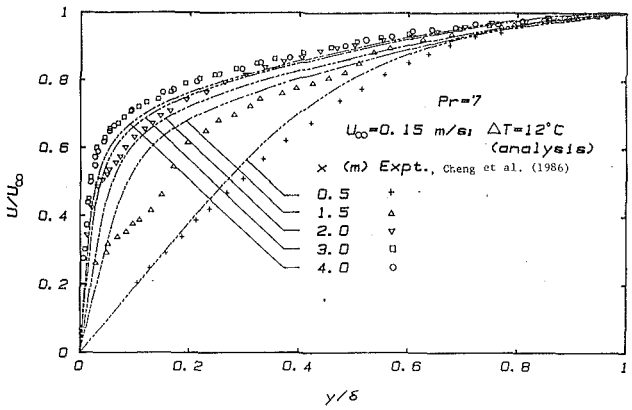

Fig. 6 Velocity profiles in turbulent mixed convection; Pr = 7

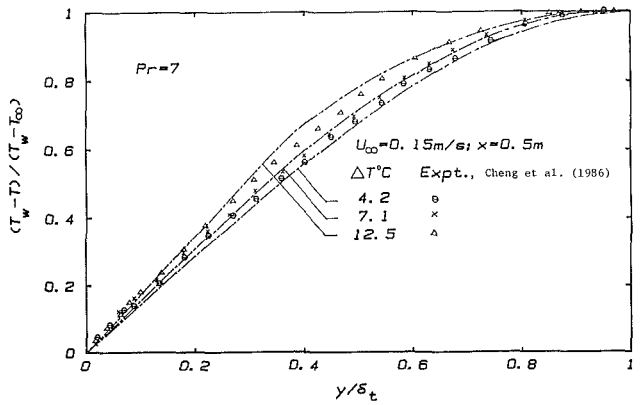

Fig. 7 Temperature profiles in turbulent mixed convection; Pr = 7

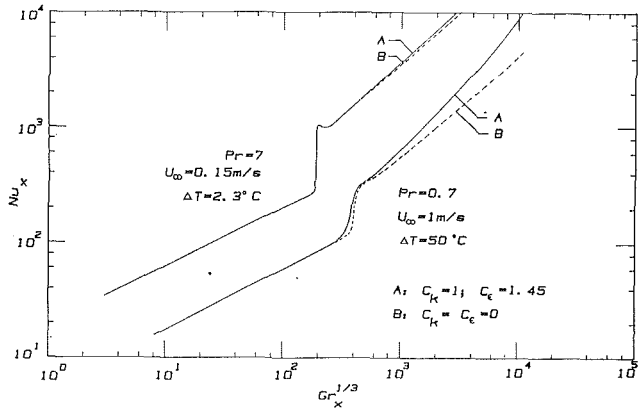

Fig. 8 Effect of buoyancy terms (k and ϵ equations) on the heat transfer results

show only a marginally good agreement with the experimental data. However, no error bounds were reported for this set of experimental data, which makes it difficult to compare directly the predicted results with the experimental data. The marginal agreement of the data with the numerical results also prompts the question of the adequacy of the treatment of buoyancy terms in the k and ϵ equations. This question will be examined further in a later section where these buoyancy terms are neglected and the two results, with and without these buoyancy terms, are compared. The predictions show a sharp overshoot in the vicinity of transition and then a rapid decay to the fully turbulent value. The overshoot is due to the rapid numerical transition from laminar to turbulent flow that is caused by introducing the starting profiles for the turbulent kinetic energy and its dissipation. As mentioned earlier, the numerical results in the transition region are based on a two-dimensional characterization of the flow field. The flows near the reattachment region and in the transition flow regime have been shown experimentally (see Imura et al., 1978, and Cheng et al., 1986) to be three dimensional in nature and hence the numerical results in that region and in that flow regime are questionable. The data presented in this figure can be thought of as being similar in characteristics to the high-velocity air flows discussed earlier. The sequence of events is: laminar forced convection—laminar mixed convection—transition—turbulent forced convection. At larger downstream locations the turbulent free convection asymptote will be approached.

The streamwise velocity distributions for water flow at different x locations are presented in Fig. 6 for the case of $u_\infty = 0.15$ m/s and $\Delta T = 12°C$. As can be seen from the figure, the numerical results compare well with the experimental data of Cheng et al. (1986). At a very small x location ($x = 0.5$ m) the flow is still laminar and displays the effect of buoyancy on what may be regarded as forced convection flow (Blasius profile). The next downstream location, $x = 1.5$ m, is in the transition region, in which turbulence has already been triggered by the introduction of k and ϵ profiles and, in the experimental setup, vortex instability has set in. A study of mixed convection instability by Moharreri et al. (1988) reveals that the flow is three dimensional in this region and thus the two-dimensional boundary-layer equations fail to yield accurate predictions in this region, as is apparent from the figure. Farther downstream at $x = 2$, 3, and 4 m, the flow is turbulent, as is evident from the fuller velocity profiles, and the numerical predictions compare well with the experimental data. The region $0.5 < x < 2$ m can be regarded as the transition regime where vortex instability prevails in the flow field. Thus, the heat transfer results from the numerical predictions in this region are at best preliminary and should be used with caution.

A comparison of the temperature distributions for $Pr = 7$ between experiments and predictions at the location $x = 0.5$ m is shown in Fig. 7 for a free-stream velocity of 0.15 m/s and three temperature differences. As can be seen, the agreement between the experiment and the predictions is good.

It was mentioned earlier that the k–ϵ model of Jones and Launder (1972, 1973) was modified to account for the effects of buoyancy on the turbulence quantities by including one term in each of the equations (4) and (5) (terms enclosed in dashed lines). In order to determine the effects of introducing buoyancy forces in the turbulence model, computations were done at a free-stream velocity of 1 m/s and a temperature difference of 50°C for air flow and for a free-stream velocity of 0.15 m/s and a temperature difference of 2.3°C for water flow, with and without the inclusion of these terms in the turbulence model. The deletion of these terms in the computations may be easily done by assigning the coefficients of these terms, $C_k = C_\epsilon = 0$. Results from such calculations (Fig. 8) show that the inclusion of these terms improves the prediction of mixed convection flows. As can be seen, the deletion of these terms leads to a decrease in the Nusselt number by about 15–20 percent for air flow at $Gr_x = 10^4$ and about 5 percent for water flow at $Gr_x = 2 \times 10^3$. This difference is due to the fact that the buoyancy forces act in a direction normal to the flow, which promotes turbulence and enhances the rate of heat transfer. As is evident from the figure, the inclusion of buoyancy terms in the k and ϵ equations shows a relatively small difference in the computed Nusselt number for $Pr = 7$. The marginal agreement between the computations and the data of Cheng et al. (1986) presented in Fig. 5 then reflects that further turbulence modeling is required for use in this particular geometry for high Prandtl numbers.

Conclusions

In this paper, mixed convection in turbulent boundary layers along an isothermal horizontal flat plate has been investigated numerically for various ranges of the free-stream velocities and temperature differences, covering a wide range of the mixed convection regime. Numerical results have been presented for both air and water flows and compared to available data from experiments. In general, the local surface heat flux increases with increasing buoyancy parameter ξ. It is also found that for higher air velocities ($u_\infty > 2$ m/s) heating the plate to temperature differences of up to 100°C does not lead to significant departures in the heat transfer rate from the pure forced convection values. Different flow situations have been considered and the sequence of events in each regime has been established. For example, for air flow with $u_\infty = 1$ m/s and $\Delta T = 50$°C, the flow starts out as laminar forced convection, undergoes transition to turbulent forced convection, and goes through the turbulent mixed convection regime before displaying turbulent free convection behavior. Similarly for water flow, for a given (u_∞, ΔT) combination, the flow field exhibits different characteristics and flow regimes. Experiments have shown that the transition region is three dimensional and the numerical results show some inadequacy of the two dimensional treatment of this region. However, the numerical results for the entire regime are in qualitative agreement with the available experimental data.

Acknowledgments

This study was supported in part by grants (MEA-83-00785 and CBT-87-04896) from the National Science Foundation.

References

Ali, M. M., 1983, "Turbulent Mixed Convection Along Vertical and Horizontal Surfaces," MS thesis, Department of Mechanical and Aerospace Engineering, University of Missouri—Rolla.

Armaly, B. F., Ramachandran, N., and Chen, T. S., 1986, "Prediction of Turbulent Mixed Convection Along an Isothermal Vertical Plate," *Proceedings of the Eighth International Heat Transfer Conference*, Vol. 3, pp. 1445–1450.

Chen, T. S., and Mucoglu, A., 1979, "Wave Instability of Mixed Convection Flow Over a Horizontal Flat Plate," *International Journal of Heat and Mass Transfer*, Vol. 22, pp. 185–196.

Cheng, K. C., Obata, T., and Gilpin, R. R., 1986, "Buoyancy Effects on Forced Convection Heat Transfer in the Transition Regime of Horizontal Boundary Layer Heated From Below," ASME Paper No. 86-WA/HT-97.

Chung, M. Y., and Sung, H. J., 1984, "Four-Equation Turbulence Model for Prediction of the Turbulent Boundary Layer Affected by Buoyancy Force Over a Flat Plate," *International Journal of Heat and Mass Transfer*, Vol. 27, pp. 2387–2395.

Hall, W. B., and Price, P. H., 1970, "Mixed Forced and Free Convection from a Vertical Heated Plate to Air," *Proceedings of the 4th International Heat Transfer Conference*, Vol. 4, Paper No. NC3.3.

Hayashi, Y., Takimoto, A., and Hori, K., 1977, "Buoyancy Effects on Forced Turbulent Convection Heat Transfer (the Case of the Horizontal Flat Plate)," *Proceedings of the JSME Symposium*, pp. 155–157.

Imura, H., Gilpin, R. R., and Cheng, K. C., 1978, "An Experimental Investigation of Heat Transfer and Buoyancy Induced Transition From Laminar Forced Convection to Turbulent Free Convection Over a Horizontal Isothermally Heated Plate," ASME JOURNAL OF HEAT TRANSFER, Vol. 100, pp. 429–434.

Jones, W. P., and Launder, B. E., 1972, "The Prediction of Laminarization With a Two-Equation Model of Turbulence," *International Journal of Heat and Mass Transfer*, Vol. 15, pp. 301–314.

Jones, W. P., and Launder, B. E., 1973, "The Calculation of Low-Reynolds-Number Phenomenon With a Two-Equation Model of Turbulence," *International Journal of Heat and Mass Transfer*, Vol. 16, pp. 1119–1130.

Lin, S. J., and Churchill, S. W., 1978, "Turbulent Free Convection From a Vertical Isothermal Plate," *Numerical Heat Transfer*, Vol. 1, pp. 129–145.

Launder, B. E., and Spalding, D. B., 1972, *Mathematical Models of Turbulence*, Academic Press, London.

Launder, B. E., and Spalding, D. B., 1974, "The Numerical Computation of Turbulent Flows," *Computer Methods in Applied Mechanics and Engineering*, Vol. 3, pp. 269–289.

Moharreri, S., Armaly, B. F., and Chen, T. S., 1988, "Measurements in the Transitional Vortex Flow Regime of Mixed Convection Above a Horizontal Heated Plate," ASME JOURNAL OF HEAT TRANSFER, Vol. 110, pp. 358–365.

Moutsoglou, A., Chen, T. S., and Cheng, K. C., 1981, "Vortex Instability of Mixed Convection Flow Over a Horizontal Flat Plate," ASME JOURNAL OF HEAT TRANSFER, Vol. 103, pp. 257–261.

Patankar, S. V., and Spalding, D. B., 1970, *Heat and Mass Transfer in Boundary Layers*, 2nd ed., Intertext Books, London.

Ramachandran, N., Armaly, B. F., and Chen, T. S., 1983, "Mixed Convection Over a Horizontal Plate," ASME JOURNAL OF HEAT TRANSFER, Vol. 105, pp. 420–423.

Seiichi, N., and Takuro, O., 1975, "Heat Transfer From a Horizontal Circular Wire at Small Reynolds and Grashof Numbers—II, Mixed Convection," *International Journal of Heat and Mass Transfer*, Vol. 18, pp. 397–413.

Subramanian, C. S., and Antonia, R. A., 1981, "Effect of Reynolds Number on a Slightly Heated Turbulent Boundary Layer," *International Journal of Heat and Mass Transfer*, Vol. 24, pp. 1833–1846.

Townsend, A. A., 1972, "Mixed Convection Over a Heated Horizontal Plane," *Journal of Fluid Mechanics*, Vol. 55, Part 2, pp. 209–227.

Wang, X. A., 1982, "An Experimental Study of Mixed, Forced, and Free Convection Heat Transfer From a Horizontal Flat Plate to Air," ASME JOURNAL OF HEAT TRANSFER, Vol. 104, pp. 139–144.

Y. Asako
Associate Professor.

H. Nakamura
Professor.
Department of Mechanical Engineering,
Tokyo Metropolitan University,
Setagaya, Tokyo, 158, Japan

M. Faghri
Professor,
Department of Mechanical Engineering
and Applied Mechanics,
University of Rhode Island,
Kingston, RI 02881

Three-Dimensional Laminar Natural Convection in a Vertical Air Slot With Hexagonal Honeycomb Core

Numerical solutions are obtained for a three-dimensional natural convection heat transfer problem in a vertical air slot with a thin hexagonal honeycomb core. The air slot is assumed to be of such dimensions that the velocity and temperature fields repeat themselves in successive enclosures. The numerical methodology is based on an algebraic coordinate transformation technique, which maps the complex cross section onto a rectangle, coupled with a calculation procedure for fully elliptic three-dimensional flows. The calculations are performed for the Rayleigh number in the range of 10^3 to 10^5, for a Prandtl number of 0.7, and for five values of the aspect ratio of the honeycomb enclosure. The average Nusselt number results for the case of a thin honeycomb core are compared with the previously obtained results for a thick honeycomb core with conduction and adiabatic side wall boundary conditions.

Introduction

A vertical air slot with a hexagonal honeycomb core is often used as an insulating wall. Inside such a slot the main mechanisms of heat transfer are natural convection and radiation. A summary of the literature on buoyancy-induced flows has recently been brought together by Gebhart et al. (1988). This review includes a chapter about natural convection in enclosures and partial enclosures. From a study of this information, it is evident that three-dimensional natural convection inside enclosures has been limited to simple geometries. This was the motivation for the present study to obtain solutions for natural convection in a complex geometry such as a vertical air slot with a hexagonal honeycomb core. This is an extension of the recent work by Asako et al. (1989) who used conduction and adiabatic side wall thermal boundary conditions. These conditions exist when the honeycomb walls are good conductors and are thick, and when they are thermally insulated, respectively. In the present study, the honeycomb walls are assumed to be poor conductors and thin such that the thermal wall boundary conditions approach the so called "no-thickness" wall boundary condition dictated by Nakamura et al. (1987).

The numerical methodology used in this study utilizes an algebraic coordinate transformation developed previously in papers by Faghri et al. (1984a), Faghri (1984b), and Faghri and Asako (1987), which maps the irregular cross section into a rectangle. This method was extended to fully three-dimensional problems by Asako et al. (1989). The numerical solutions are obtained for the "no-thickness" thermal wall boundary condition, for three values of the Rayleigh number ($Ra = 10^3$, 10^4, and 10^5), for five values of the aspect ratio ($H/L = 0.25$, 0.5, 1, 2, and 5), and for a Prandtl number of 0.7. The results are presented in the form of axial and vertical velocity profiles and average and local heat transfer coefficients and they are compared with the corresponding values for conduction and adiabatic thermal boundary conditions.

Formulation

Description of the Problem. The problem to be considered in this study is schematically depicted in Fig. 1. It involves the determination of three-dimensional heat transfer for laminar natural convection in a regular hexagonal honeycomb enclosure. If the air slot is very long in both the vertical and the horizontal directions and the honeycomb walls are thin, the velocity and temperature fields repeat themselves in successive enclosures, except at the end boundaries of the enclosure. Therefore, it is possible to solve the natural convection problem in only one honeycomb enclosure with periodic thermal boundary conditions. This enclosure is illustrated in Fig. 2. As seen in this figure, the two hexagonal end walls of the honeycomb enclosure are differentially heated to the

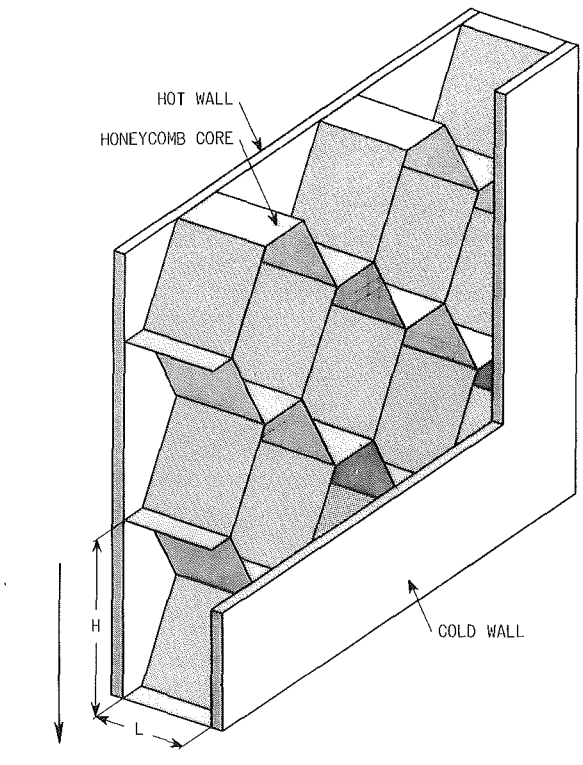

Fig. 1 Schematic diagram of a vertical air slot with honeycomb core

Contributed by the Heat Transfer Division for publication in the JOURNAL OF HEAT TRANSFER. Manuscript received by the Heat Transfer Division May 5, 1988; revision received June 25, 1989. Keywords: Enclosure Flows, Natural Convection, Numerical Methods.

uniform temperatures t_H and t_C, respectively. The geometry of the problem is specified by the height (H) and the length (L). The solution domain, with the assumption of symmetry, is confined to the right half of the honeycomb enclosure. The mathematical expression for the width of this honeycomb, $\delta(y)$, is derived in an earlier paper by Asako et al. (1989).

Conservation Equations. The governing equations to be considered are the continuity, momentum, and energy equations. Constant thermophysical properties are assumed except for the density in the buoyancy force term. The following dimensionless variables are used:

$$X=x/L,\quad Y=y/L,\quad Z=z/L,$$
$$U=u/(\nu/L),\quad V=v/(\nu/L),\quad W=w/(\nu/L),$$
$$P=p/\rho(\nu/L)^2,\quad T=(t-t_m)/(t_H-t_C) \tag{1}$$

where t_m is the average temperature of end walls and is expressed by $t_m=(t_H+t_C)/2$. Then, upon introduction of the dimensionless variables and parameters, the governing equations have the following forms:

$$\partial U/\partial X+\partial V/\partial Y+\partial W/\partial Z=0 \tag{2}$$

$$U(\partial U/\partial X)+V(\partial U/\partial Y)+W(\partial U/\partial Z)=-\partial P/\partial X+\nabla^2 U \tag{3}$$

$$U(\partial V/\partial X)+V(\partial V/\partial Y)+W(\partial V/\partial Z)=-\partial P/\partial Y+\nabla^2 V+(\mathrm{Ra/Pr})T \tag{4}$$

$$U(\partial W/\partial X)+V(\partial W/\partial Y)+W(\partial W/\partial Z)=-\partial P/\partial Z+\nabla^2 W \tag{5}$$

$$U(\partial T/\partial X)+V(\partial T/\partial Y)+W(\partial T/\partial Z)=(1/\mathrm{Pr})\nabla^2 T \tag{6}$$

where

$$\nabla^2=\partial^2/\partial X^2+\partial^2/\partial Y^2+\partial^2/\partial Z^2 \tag{7}$$

To complete the formulation of the problem, it remains to discuss the boundary conditions. These are:

$$\text{at all walls: } U=V=W=0$$

$$\text{at the symmetry plane } (X=0)\text{: } U=\partial V/\partial X=\partial W/\partial X=0 \tag{8}$$

The thermal boundary conditions on the hot and cold walls reduce to

$$\text{hot wall: } T=0.5$$
$$\text{cold wall: } T=-0.5 \tag{9}$$

The thermal boundary condition for the side walls is that of a "no-thickness" wall condition, which indicates that conduction is negligible along the walls because the walls are thin. Therefore, the heat flux through the top wall (AGLF) becomes equal to that through the bottom wall (CIJD); the heat flux through one of the upper side walls (ABHG) becomes equal to that through the lower side walls (EDJK). From the assumption of symmetry, the heat flux through the right upper wall (FEKL) becomes equal to that through the left upper wall (ABHG). The mathematical expressions for these conditions are expressed as follows:

$$T_{\mathrm{AGLF}}=T_{\mathrm{CIJD}},\quad (\partial T/\partial N)_{\mathrm{AGLF}}=-(\partial T/\partial N)_{\mathrm{CIJD}}$$
$$T_{\mathrm{FEKL}}=T_{\mathrm{EDJK}},\quad (\partial T/\partial N)_{\mathrm{EFKL}}=-(\partial T/\partial N)_{\mathrm{EDJK}} \tag{10}$$

where N is the dimensionless coordinate directed along the outward normal to the walls.

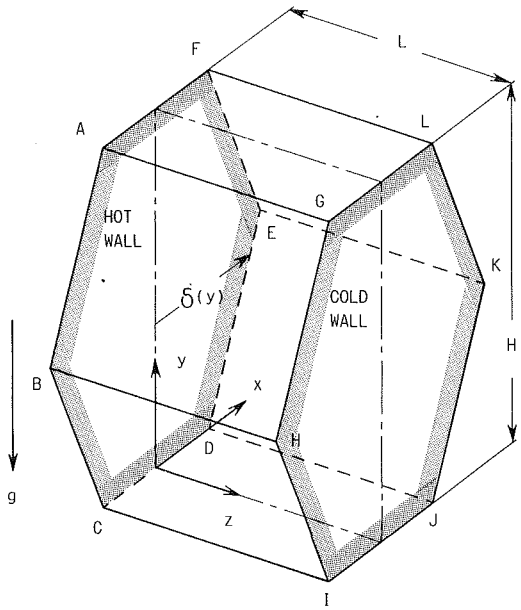

Fig. 2 Schematic diagram of a horizontal honeycomb enclosure

Analytical and Numerical Methods. A simple algebraic coordinate transformation is used that maps the hexagonal cross section onto a rectangle. Specifically, the X, Y coordinates are transformed into η, ξ coordinates by the relations

$$\eta=X/[\delta(y)/L],\quad \xi=Y \tag{11}$$

In terms of the new coordinates, the solution domain is bonded by $0<\eta<1$, $0<\xi<H/L$. The transformed equations and their discretization and solutions are documented in an earlier paper by Asako et al. (1989). The discretized procedure of the equations is based on the control volume based power-law scheme of Patankar (1981), and the discretized equations

Nomenclature

a = thermal diffusivity
Cp = specific heat of the fluid
H = height of a hexagonal honeycomb enclosure
h = local heat transfer coefficient [equation (26)]
h_m = average heat transfer coefficient [equation (27)]
k = thermal conductivity
L = axial length of a hexagonal honeycomb enclosure
Nu = local Nusselt number [equation (28)]
Nu_m = average Nusselt number [equation (29)]
Pr = Prandtl number
P = dimensionless pressure
p = pressure
Q = total heat transfer from a hot wall
q = heat flux from a hot wall
Ra = Rayleigh number = $g\beta L^3(t_H-t_C)/a\nu$
T = dimensionless temperature
t_m = averaged temperature = $(t_H+t_C)/2$
t_H = hot wall temperature
t_C = cold wall temperature
U, V = dimensionless velocity components [equation (1)]
u, v = velocity components
W = dimensionless axial velocity component [equation (1)]
w = axial velocity component
X, Y = dimensionless coordinates; $X=x/L$, $y=y/L$]
x, y = coordinates
Z = dimensionless axial coordinate = z/L
z = axial coordinate
$\delta(y)$ = half-width of a hexagonal enclosure
η = transformed coordinate = $X/\{\delta(y)/L\}$
μ = viscosity
ν = kinematic viscosity
ξ = transformed coordinate = Y
ρ = density of the fluid

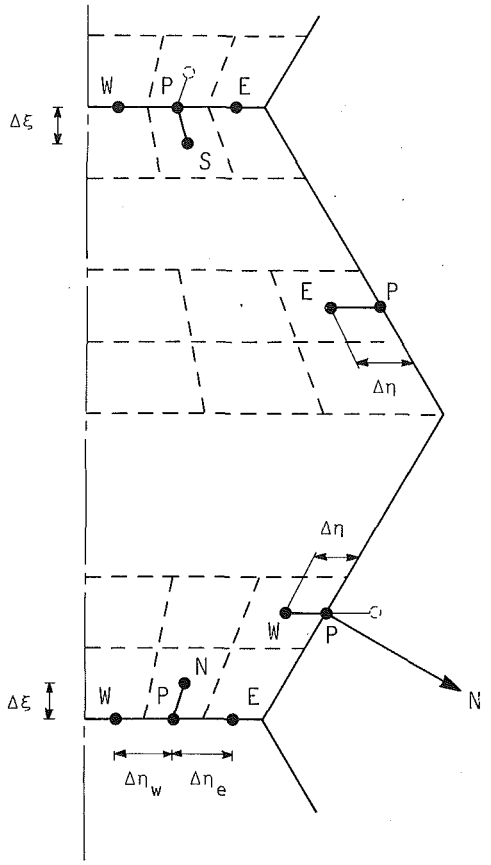

Fig. 3 Control volume cluster near boundaries

are solved by using a line-by-line method. The pressure and velocities are linked by the SIMPLE algorithm of Patankar (1980).

Attention is now focused on the discretized equations for the thermal boundary conditions and their numerical implementation. The thermal boundary conditions for the top and bottom walls, given by equation (10), are expressed as

$$(\partial T/\partial Y)_{Y=0} = (\partial T/\partial Y)_{Y=H/L} \tag{12}$$

The partial derivative $\partial/\partial Y$ in equation (12) is expressed in the transformed coordinates as

$$(\partial/\partial Y) = -\frac{\beta}{\delta/L}(\partial/\partial\eta)_\xi + (\partial/\partial\xi)_\eta \tag{13}$$

where

$$\beta = \eta d(\delta/L)/d\xi \tag{14}$$

Substituting equation (13) into equation (12) one obtains

$$\left[-\frac{\beta}{\delta/L}(\partial T/\partial\eta) + (\partial T/\partial\xi)\right]_{\xi=0} = \left[-\frac{\beta}{\delta/L}(\partial T/\partial\eta) + (\partial T/\partial\xi)\right]_{\xi=H/L} \tag{15}$$

The values of $d(\delta/L)/d\xi$ in equation (14) at $\xi = 0$ and $\xi = H/L$ are, respectively

$$[d(\delta/L)/d\xi]_{\xi=0} = 1/\sqrt{3}$$
$$[d(\delta/L)/d\xi]_{\xi=H/L} = -1/\sqrt{3} \tag{16}$$

Substituting these values into equation (15) results in

$$-\frac{2\eta}{\sqrt{3}(\delta/L)}(\partial T/\partial\eta)_{\xi=0} = (\partial T/\partial\xi)_{\xi=H/L} - (\partial T/\partial\xi)_{\xi=0} \tag{17}$$

The finite difference representation of equation (15) can be expressed in terms of the values at the five neighboring nodes shown in Fig. 3 as

$$2T_P/\Delta\xi = 2\eta(T_W - T_E)/[\sqrt{3}(\delta/L)(\Delta\eta_e + \Delta\eta_w) + (T_S + T_N)/\Delta\xi \tag{18}$$

Attention is now given to the discretized equations for the thermal boundary condition on the upper and lower side walls. The temperature gradient normal to the wall ($\partial T/\partial N$) in Fig. 3 is expressed as

$$(\partial T/\partial N) = \mathbf{N}\cdot\nabla T = [(\partial T/\partial X) - \beta(\partial T/\partial Y)]/\alpha^{1/2} \tag{19}$$

where

$$\alpha = 1 + \beta^2 \tag{20}$$

The partial derivative with respect to X is transformed to

$$\partial/\partial X = \frac{1}{(\delta/L)}(\partial/\partial\eta)_\xi \tag{21}$$

Then, equation (19) is reduced to

$$\partial T/\partial N = \alpha^{1/2}(\partial T/\partial\eta)/(\delta/L) - \beta(\partial T/\partial\xi)/\alpha^{1/2} \tag{22}$$

The thermal boundary conditions for the upper and lower side walls given by equation (10) is expressed as

$$[\alpha^{1/2}(\partial T/\partial\eta)/(\delta/L) - \beta(\partial T/\partial\xi)/\alpha^{1/2}]_{EDJK} = -[\alpha^{1/2}(\partial T/\partial\eta)/(\delta/L) - \beta(\partial T/\partial\xi)/\alpha^{1/2}]_{FEKL} \tag{23}$$

Since $(\partial T/\partial\xi)_{EDJK} = (\partial T/\partial\xi)_{FEKL}$, equation (23) can be rewritten as

$$[(\partial T/\partial\eta)/(\delta/L)]_{EDJK} = -[(\partial T/\partial\eta)/(\delta/L)]_{FEKL} \tag{24}$$

The finite difference representation of equation (24) is expressed by the values at the three neighboring nodes shown in Fig. 3 as

$$(T_P - T_W)/[\Delta\eta(\delta/L)_{EDJK}] = (T_E - T_P)/[\Delta\eta(\delta/L)_{FEKL}] \tag{25}$$

The procedure for the numerical solutions is as follows:

1 Guess the side wall temperature, i.e., the linear variation from hot to cold wall.

2 Solve the momentum and energy equations to obtain U, V, W, and T.

3 Calculate the side wall temperature to satisfy the thermal boundary conditions given by equations (18) and (25), using the temperature at interior grid points.

4 Treat the calculated wall temperatures as the new guessed values.

5 Repeat this procedure until a converged solution is obtained.

All computations were performed with $(16\times30\times22)$ grid points. These grid points are distributed in a uniform manner over the solution domain in the η, ξ, and Z coordinate directions. The effect of grid size on the Nusselt number result has already been examined and illustrated in the previous paper by Asako et al. (1989).

The convergence criterion that is used in these computations is that the value of the mass flux residuals (mass flow) divided by the total mass flow in each control volume is under 10^{-9}. The underrelaxation factors for the velocity and pressure are set to 0.5 and 0.8, respectively. About 200 to 800 iterations are required to obtain a converged solution. The number of iterations depends on the geometric parameter and the Rayleigh number. The computations for higher Rayleigh numbers require a large number of iterations.

From an examination of the governing equations (2) to (6), it can be seen that there are two parameters whose values have to be specified prior to the initiation of the numerical solutions. These are the Prandtl number Pr and the Rayleigh number Ra. In this paper, a value of 0.7 is selected for Pr, and the values chosen for the Rayleigh number are in the range from 10^3 to 10^5. Aside from Pr and Ra, there are two geometric parameters that have to be specified. These are the

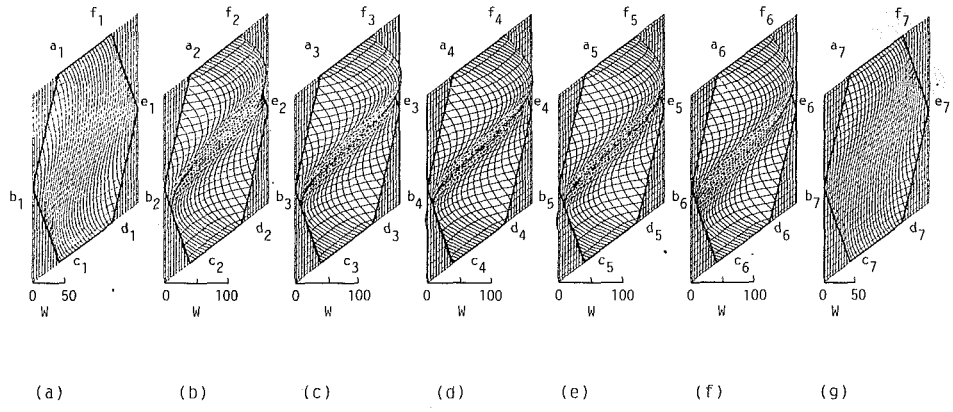

Fig. 4 Axial velocity profiles at vertical planes for $H/L = 0.5$, $Ra = 10^5$: (a) $Z = 0.05$; (b) $Z = 0.2$; (c) $Z = 0.35$; (d) $Z = 0.5$; (e) $Z = 0.65$; (f) $Z = 0.8$; (g) $Z = 0.95$

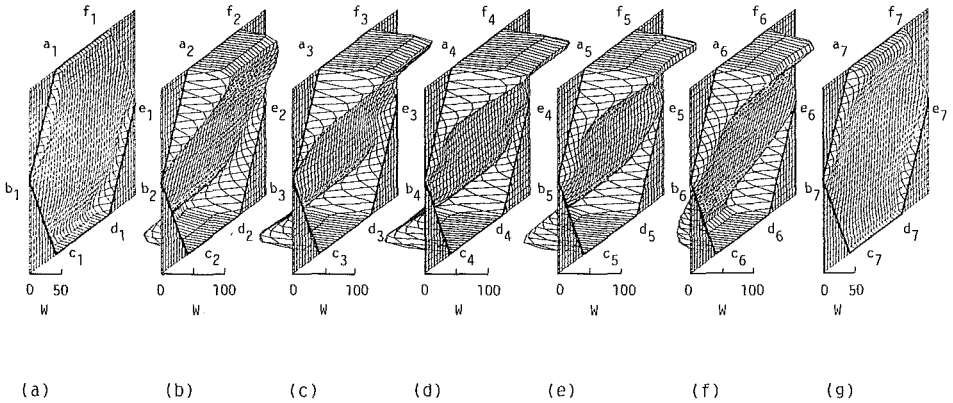

Fig. 5 Axial velocity profiles at vertical planes for $H/L = 2$, $Ra = 10^5$: (a) $Z = 0.05$; (b) $Z = 0.2$; (c) $Z = 0.35$; (d) $Z = 0.5$; (e) $Z = 0.65$; (f) $Z = 0.8$; (g) $Z = 0.95$

height (H) and the length of the enclosure (L). If L is used as a reference length, then H/L needs to be specified as geometric parameter. The selected values of H/L are 0.25, 0.5, 1, 2, and 5.

Nusselt Numbers. The local and average heat transfer coefficients on the hot wall will be defined as

$$h = q/(t_H - t_C) \tag{26}$$

$$h_m = Q/[A_H(t_H - t_C)] \tag{27}$$

where q is the local heat flux, A_H is the area of the hexagonal hot wall equal to $(3/2)H^2\tan(\pi/6)$, and Q is the total heat transfer rate from the hot wall. The Nusselt number expressions are as follows:

$$\mathrm{Nu} = h\,L/K = (\partial T/\partial Z)_H \tag{28}$$

$$\mathrm{Nu}_m = h_m L/K =$$

$$\int_0^{H/L}\int_0^1 (\partial T/\partial Z)_H(\delta/L)d\eta d\xi/[(3/2)(H/L)^2\tan(\pi/6)] \tag{29}$$

Results and Discussion

Axial Velocity Profiles. The axial velocity component W at vertical planes of $Z = 0.05$, 0.2, 0.35, 0.5, 0.65, 0.8, and 0.95 are presented in Fig. 4 for $H/L = 0.5$ and $Ra = 10^5$ and in Fig. 6 for $H/L = 2.0$ and $Ra = 10^5$. The locations of the vertical planes are speckled as shown in Fig. 5 of the earlier paper by Asako et al. (1989). The corners of the hexagonal cross section are marked with the letters a_1, b_1, . . . in the figures. Although the solution domain is confined to the right half of the enclosure, the velocity profiles of the left half of the enclosure are also presented in the figure by using the symmetry of the problem. The computations are performed in the transformed domain and the results are transformed back to the physical domain. A general-purpose solid graphic utility is used for this purpose. It is noteworthy that the grid lines in the figures do not lie on the η-ξ coordinates grid lines. The values at the graphic grid points were interpolated from the computational grid point values.

In the earlier paper by Asako et al. (1989) for the conduction and adiabatic side wall thermal conditions, it was evident that the axial velocity component profile W was classified into two types. Namely, type A refers to Fig. 4 where the fluid on the vertical symmetry line ($X = 0$) is moving faster than other locations at the same elevation. Type B refers to Fig. 5 where the velocity profile has two peaks at the same elevation. The classifications of the velocity profiles are summarized in Table 1. It is noteworthy that the thermal boundary condition on the side wall does not influence this classification.

Vertical Velocity Profiles. The vertical velocity component V at the locations $Y = (1/7)(H/L)$, $(9/28)(H/L)$, $(1/2)(H/L)$, $(19/28)(H/L)$, and $(6/7)(H/L)$ for $H/L = 2$ and $Ra = 10^5$ are presented in Fig. 6. The locations of the horizontal planes are speckled as shown in Fig. 7 of the earlier paper by Asako et al. (1989). The corners are marked with letters g_1, h_1, . . . in the figures. In the earlier paper by Asako et al. (1989), the vertical velocity profile V for the thermally con-

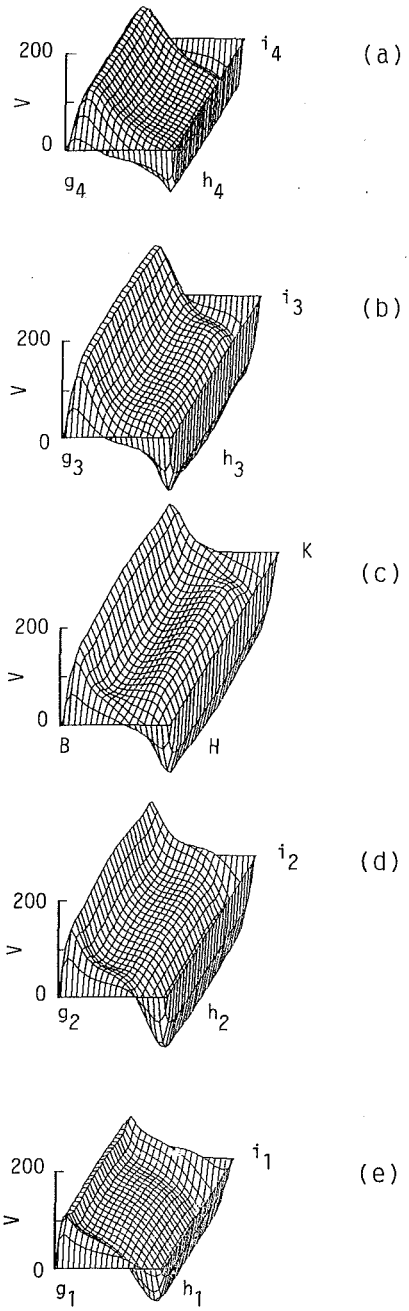

Fig. 6 Vertical velocity profiles at horizontal planes for $H/L = 2$, $Ra = 10^5$: (*a*) $Y = (6/7)\ H/L$; (*b*) $Y = (19/28)\ H/L$; (*c*) $Y = (1/2)\ H/L$; (*d*) $Z = (9/28)\ H/L$; (*e*) $Z = (1/7)\ H/L$

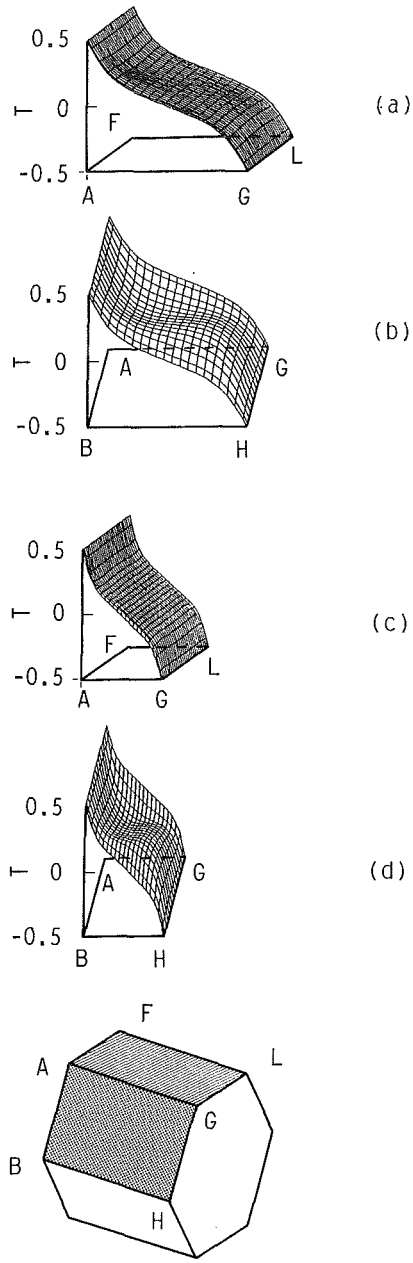

Fig. 7 Temperature profile of the side wall for $H/L = 1$ and $Ra = 10^5$: (*a*) top wall; (*b*) upper side wall; $H/L = 2$ and $Ra = 10^5$: (*c*) top wall; (*d*) upper side wall

ducting side walls had two peaks in the X direction at all horizontal planes. These peaks were formed by the converging side walls. As seen from Fig. 6, V is almost flat in the X direction at all horizontal planes for the present thermal boundary condition.

Temperature Profiles. The temperature profiles of the top wall (AGLF) and the upper side wall (ABHG) are presented in Figs. 7(*a*) and 7(*b*), respectively, for $H/L = 1$ and $Ra = 10^5$ and in Figs. 7(*c*) and 7(*d*) for $H/L = 2$ and $Ra = 10^5$. Although the results are not presented here, the temperature changes almost linearly in the Z direction as in the case of a conduction thermal boundary condition at low values of the Rayleigh number. The linear variation of the temperature profile disappears with increasing Rayleigh numbers. This tendency is accentuated at high aspect ratios. Note that the temperature of the upper side wall (ABHG) becomes equal to that of the lower side wall (BCIH).

Table 1 Classification of axial velocity profile W

	H/L				
Ra	0.25	0.5	1	2	5
10^3	A	A	A	B	B
10^4	A	A	A	B	B
10^5	A	A	A	B	B

Heat Flux Through Side Walls. The heat flux through the top of the side wall (AGLF) and the upper side wall (ABHG) are presented in Figs. 8(*a*) and 8(*b*), respectively, for $H/L = 1$

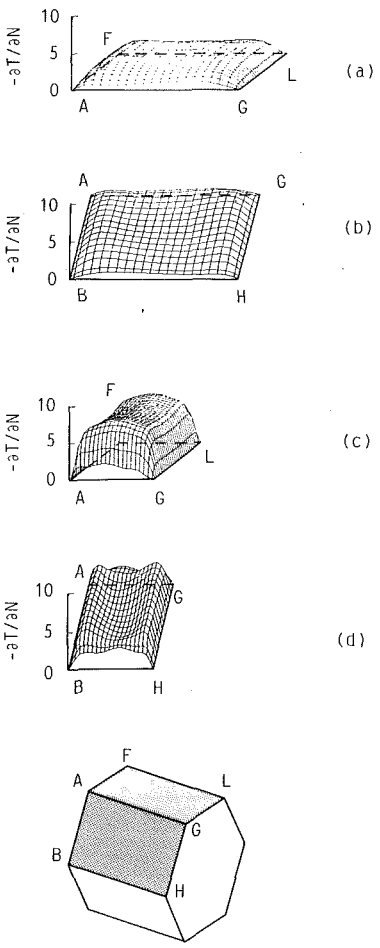

Fig. 8 Heat flow through the side wall for $H/L = 1$ and $Ra = 10^5$: (*a*) top wall (*b*) upper side wall; $H/L = 2$ and $Ra = 10^5$: (*c*) top wall; (*d*) upper side wall

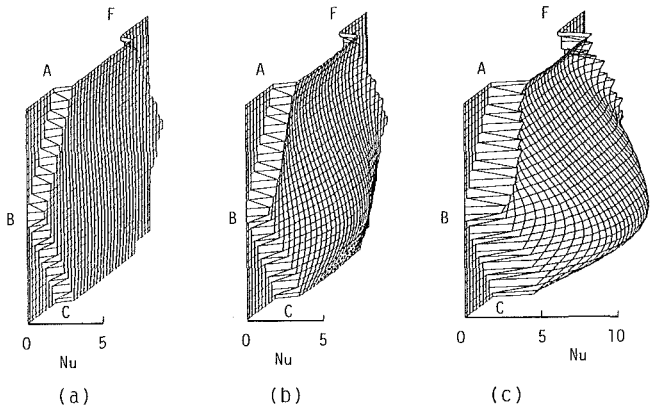

Fig. 9 Local Nusselt number on the hot wall for $H/L = 1$: (*a*) $Ra = 10^3$; (*b*) $Ra = 10^4$; (*c*) $Ra = 10^5$

and $Ra = 10^5$, and in Figs. 8(*c*) and 8(*d*) for $H/L = 2$ and $Ra = 10^5$. As seen from the figure, the dimensionless value of the heat flux, $(-\partial T/\partial N)$, takes a positive value. This indicates that the direction of the heat flow that passes through the top and the upper side walls is upward. The value of $(-\partial T/\partial N)$ increases with increasing aspect ratio.

Local Nusselt Number. The local Nusselt number on the hot wall for $H/L = 1$ and for Rayleigh numbers in the range of 10^3 to 10^5 are presented in Fig. 9. As seen from this figure, the

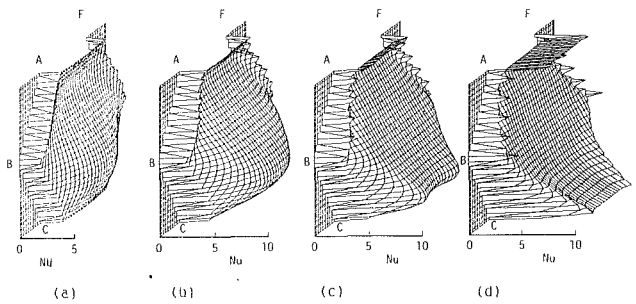

Fig. 10 Local Nusselt number on the hot wall for $Ra = 10^5$: (*a*) $H/L = 0.5$; (*b*) $H/L = 1$; (*c*) $H/L = 2$

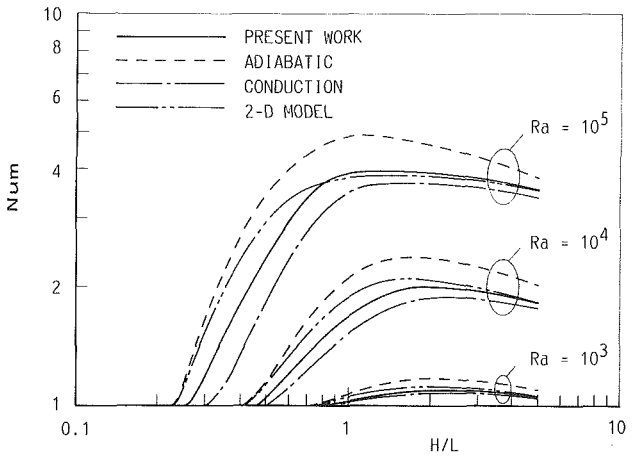

Fig. 11 Average Nusselt number Nu_m as a function of the aspect ratio H/L

local Nusselt number value approaches unity for $Ra = 10^3$. This result indicates that the heat is transferred by heat conduction at lower values of the Rayleigh number and it increases with the Rayleigh number. The local Nusselt number on the symmetry line $(X = 0)$ is the highest at the same elevation for the case of $H/L = 1$.

The local Nusselt numbers on the hot wall for $Ra = 10^5$ and for the aspect ratio in the range of 0.5 to 5 are presented in Fig. 10. The local Nusselt number values for $H/L = 0.25$ approaches unity. Therefore, the results are not presented here. Note that the local Nusselt number value has two peaks on the same horizontal level as seen in Figs. 10(*c*) and 10(*d*). This result corresponds to the presence of the two peaks in the axial velocity profile.

Average Nusselt Number. The average Nusselt numbers are plotted as a function of the aspect ratio H/L, with the Rayleigh number as a curve parameter in Fig. 11. The Nusselt numbers for conduction and adiabatic side wall conditions are also plotted in this figure. As seen from this figure, the Nusselt number for the "no-thickness" boundary condition takes a value between the values for the conduction and adiabatic wall boundary conditions. It approaches the values for the conduction wall boundary condition at low values of the Rayleigh number as is expected from the temperature profile of the side walls. As seen from the figure, the average Nusselt number for $H/L = 0.25$ is almost unity. This result indicates that the motion of the fluid in the enclosure is very slow and heat is transferred by conduction up to $Ra = 10^2$ for $H/L = 0.25$.

Although the range of the present computations covers three regimes, namely, the conduction, the intermediate, and the boundary layer regimes, it is assumed that a single correlation for the Nusselt number result can be obtained for the

whole range for most practical engineering calculations. A smooth transition from the conduction regime to the boundary layer regime is assumed. The method is based on the work by Bejan (1978). The following correlation is obtained for $10^3 < \mathrm{Ra} < 10^5$ and for $0.25 < H/L < 5$:

$$\mathrm{Nu} = 1 + \left\{ \left[\frac{\mathrm{Ra}^2 (H/L)^8}{362880} \right]^n + [0.0038\ \mathrm{Ra}^{0.6} (H/L)^{-0.175}]^n \right\}^{1/n} \tag{30}$$

The value of the exponent n is -0.32 with a maximum error of less than 11 percent for the whole range of the parameters.

The full three-dimensional computation requires extensive computer time. Therefore, it would be helpful if the average Nusselt number can be predicted from the result of a two-dimensional model. To investigate this, supplementary two-dimensional computations were performed. The two-dotted chain lines in Fig. 11 are the results for a two-dimensional rectangular enclosure of height H and horizontal length L. The two-dimensional computer code "SIMPLE" is used for the computations. Computations were performed with (30×22) grid points. The grid points were distributed in a uniform manner over the solution domain in the Y and Z directions. As seen from Fig. 11, the results of the two- and three-dimensional model agree well for higher aspect ratios. On the other hand, slight differences can be seen for the cases of $H/L = 0.5$ and 1 because of the side wall effect.

Concluding Remarks

Three-dimensional laminar natural convection heat transfer characteristics in a vertical air slot with a hexagonal honeycomb core are obtained numerically by using a coordinate transformation technique. The computations were performed for Rayleigh numbers in the range 10^3 to 10^5, for a Prandtl number of 0.7, and for five values of the aspect ratio. The main conclusions of the study are: (*a*) the temperature profile of the side wall for low values of the Rayleigh number varies linearly but deviates from the linear profile with an increase in the Rayleigh number. (*b*) The direction of the energy flow that passes through the side wall is upward. (*c*) The average Nusselt number takes on values between those of the conduction and of the adiabatic side wall thermal conditions, and a correlation of the Nusselt number results is obtained. (*d*) The average Nusselt number can sometimes be predicted by a two-dimensional model, depending on the aspect ratio and the Rayleigh number value.

References

Asako, Y., Nakamura, H., and Faghri, M., 1989, "Three-Dimensional Laminar Natural Convection in Horizontal Hexagonal Honeycomb Enclosure," *Numerical Heat Transfer*, Vol. 15, pp. 67–86.

Bejan, A., and Tien, C. L., 1978, "Laminar Natural Convection Heat Transfer in a Horizontal Cavity With Different End Temperature," ASME JOURNAL OF HEAT TRANSFER, Vol. 100, pp. 641–647.

Faghri, M., Sparrow, E. M., and Prata, A. T., 1984, "Finite Difference Solutions of Convection-Diffusion Problems in Irregular Domains Using a Nonorthogonal Coordinate Transformation," *Numerical Heat Transfer*, Vol. 7, pp. 183–209.

Faghri, M., 1984, "Slot Jet Impingement on a Cylinder," *Proceedings of the ASME/AIChE Heat Transfer Conference*, Paper No. 84-HT-7.

Faghri, M., and Asako, Y., 1987, "Numerical Determination of Heat Transfer and Pressure Drop Characteristics for a Converging-Diverging Flow Channel," ASME JOURNAL OF HEAT TRANSFER, Vol. 109, pp. 606–612.

Gebhart, B., Jaluria, Y., Mahajan, R. L., and Sammakia, B., 1988, *Buoyancy Induced Flows and Transport*, Hemisphere Publishing Corporation, Washington, DC.

Nakamura, H., Asako, Y., and Aoki, H., 1987, "Natural Convection Heat Transfer in a Vertical Air Slot Partitioned by Corrugated Plates," *Numerical Heat Transfer*, Vol. 11, pp. 77–94.

Patankar, S. V., 1980, *Numerical Heat Transfer and Fluid Flow*, McGraw-Hill, New York.

Patankar, S. V., 1981, "A Calculation Procedure for Two-Dimensional Elliptic Situations," *Numerical Heat Transfer*, Vol. 4, pp. 409–425.

Analysis of Direct-Contact Melting Under Rotation

K. Taghavi
Department of Mechanical Engineering,
University of Kentucky,
Lexington, KY 40506-0046

In this paper the phenomenon of direct melting under rotation and external pressure is considered. Rotation may be added to direct-contact melting for several purposes, including keeping the melting surface uniform or creating a centrifugal field to assist the removal of the melt. An exact analysis is presented here, which resembles that of the condensation on a rotating surface or the problem of a rotating disk in a large body of fluid. A similarity transformation is applied to reduce the full Navier-Stokes and energy equations to ordinary differential equations. A dimensionless parameter σ has emerged from the analysis, which is the ratio of the external force to the centrifugal force. As σ becomes large ($\sigma \to \infty$, no rotation), the problem becomes that of pure direct-contact melting under external force, and hence resulting in the exact formulation for such a problem. For $\sigma = 0$ (pure rotation, no external force), the formulation becomes similar to that of condensation on a rotating disk or a rotating disk in a large body of fluid. It is noted that different scaling of the problem with respect to σ is needed to obtain the solution for the wide range of $\sigma = 0 \to \infty$. A closed-form solution is obtained for the case where the film is approximated to be thin. A criterion for the validity of this approximation is given. Finally, the numerical results for the general problem are presented in terms of the Prandtl number, the Stefan number, and the force ratio σ.

Introduction

The phenomenon of melting occurs in many practical situations and is of great interest in several technical areas. Examples are thermal energy storage, nuclear reactor safety, welding, and crystal growth. In all these cases the basic phase-change phenomena are similar; however, the source of energy for melting and the mode of melt removal are different. For example, in nuclear reactor safety, a situation may arise that a solid melts by contact with a warmer liquid (Taghavi et al., 1979). In other cases the solid melts due to contact with a warmer solid (Pfann, 1958; Moallemi et al., 1986; Saito et al., 1986).

The other distinction is the mode of melt removal. For example, in most thermal energy storage cases the melt is allowed to remain near its solid and therefore presents resistance to further heat transfer and subsequent melting. In other cases gravity is used to remove the melt (e.g., Tien and Yen, 1971; Taghavi and Dhir, 1983). Buoyancy is also used for removing the melt, such as in melting or sublimation of a horizontal substrate under a heavier pool (Dhir et al., 1977; Farhadien and Baker, 1978; Taghavi, 1987).

Another method for removing the melt is using the weight of the solid or applying external pressure (Emerman and Turcotte, 1983; Moallemi and Viskanta, 1985). Finally, in the absence of gravity or in a microgravity environment, rotation can be used to create a centrifugal field for removing the liquid condensate (e.g., Sparrow and Gregg, 1959b, 1961).

Close-contact melting under external force or the weight of the solid has been investigated in a few studies such as that by Saito et al. (1986) and Moallemi et al. (1986). Both of these studies assume that the melt film is thin and that the inertia and convective terms are negligible. The result is an approximate solution for the melting rate. In addition, in these studies the varying mass of the solid (while melting) is considered and transient results are presented. Experiments performed by both investigators revealed no significant deviation from the analysis and generally verified the analytical results.

In this paper the combination of external force and rotation is included in the direct-contact melting. An exact solution is sought by invoking the technique of similarity transformation. Naturally this exact analysis will apply to the case with no rotation in its proper limit.

Analysis

In this paper the phenomenon of direct-contact melting under external force and rotation is considered. A schematic of the problem is shown in Fig. 1. A solid at its melting temperature is exposed from below to another solid acting as a heater. Since the melting temperature of the overlying solid is less than the temperature of the heater, the solid starts to melt. Subsequently, a thin layer of melt separates the heater and the melting solid. The melt flows outward radially due to the external pressure p_o (p_o includes the weight of the melting solid, if any) and the centrifugal force created by the rotating heater. The following simplifying assumptions are made:

- The term p_o includes the weight of the solid. As melting progresses, the weight changes. It is assumed that the melting process adjusts to the changing weight much faster than the weight changes. In other words, a quasi-steady assumption is

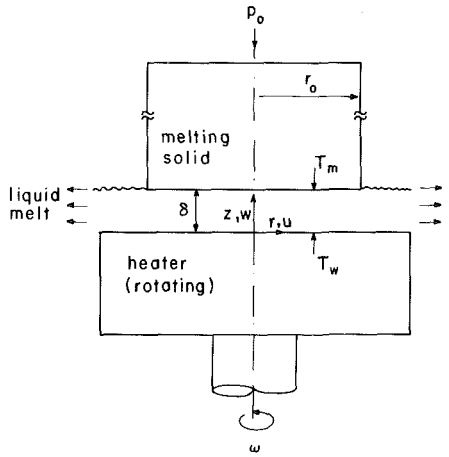

Fig. 1 Schematic of direct-contact melting under rotation

Contributed by the Heat Transfer Division for publication in the JOURNAL OF HEAT TRANSFER. Manuscript received by the Heat Transfer Division January 5, 1988; revision received June 27, 1989. Keywords: Direct-Contact Heat Transfer, Phase-Change Phenomena, Rotating Flows.

made so that at any time the corresponding value of the weight is used to obtain P_o.

- The solid is at its melting temperature T_m. If the solid is subcooled at T_{sub}, the latent heat of melting may be corrected for the sensible heating by replacing h_{sf} with h'_{sf}. This assumption is valid if the melting speed (melting rate per area/melt density) is much smaller than the speed heat is conducted into the solid and if heat loss or heat gain through the side wall of the melting solid is negligible.

$$h'_{sf} = h_{sf} + c_p(T_m - T_{sub}) \tag{1}$$

- The heater is assumed to be at a prescribed constant temperature T_w. The case where the heater thermal boundary condition is prescribed heat flux rather than a prescribed temperature is discussed later in the paper.
- The problem possesses azimuthal symmetry, i.e., $\partial/\partial\theta \equiv 0$.
- The melting solid and the heater are initially flat and horizontal. The effect of melting on the shape of the melting solid will be discussed later in the paper.
- The flow of the melt is laminar. This will be checked later in the paper.
- All solid and melt properties are assumed to be constant and independent of temperature.

The governing equations for this problem are similar to the problem of condensation on a rotating disk studied by Sparrow and Gregg (1959b), with the exceptions that the fluid pressure in the present problem changes radially due to the external pressure p_o and the boundary conditions are different. The conservation equations may be written as (all $\partial/\partial\theta$ terms are neglected)

$$\frac{1}{r}\frac{\partial}{\partial r}(ru) + \frac{\partial w}{\partial z} = 0 \tag{2}$$

$$u\frac{\partial u}{\partial r} + w\frac{\partial u}{\partial z} - \frac{v^2}{r} = -\frac{1}{\rho}\frac{\partial p}{\partial r} + \nu\left[\frac{\partial^2 u}{\partial r^2} + \frac{1}{r}\frac{\partial u}{\partial r} + \frac{\partial^2 u}{\partial z^2} - \frac{u}{r^2}\right] \tag{3}$$

$$u\frac{\partial v}{\partial r} + w\frac{\partial v}{\partial z} + \frac{uv}{r} = \nu\left[\frac{\partial^2 v}{\partial r^2} + \frac{1}{r}\frac{\partial v}{\partial r} + \frac{\partial^2 v}{\partial z^2} - \frac{v}{r^2}\right] \tag{4}$$

$$u\frac{\partial w}{\partial r} + w\frac{\partial w}{\partial z} = -\frac{1}{\rho}\frac{\partial p}{\partial z} + \nu\left[\frac{\partial^2 w}{\partial r^2} + \frac{1}{r}\frac{\partial w}{\partial r} + \frac{\partial^2 w}{\partial z^2}\right] \tag{5}$$

$$u\frac{\partial T}{\partial r} + w\frac{\partial T}{\partial z} = \alpha\left[\frac{\partial^2 T}{\partial r^2} + \frac{1}{r}\frac{\partial T}{\partial r} + \frac{\partial^2 T}{\partial z^2}\right] \tag{6}$$

The problem of condensation on a rotating disk admits a similarity solution (Sparrow and Gregg, 1959b). This similarity solution was obtained by drawing on the experience of von Karman (1921) with the problem of a rotating disk in an infinite fluid medium. Fortunately the present problem, although different from condensation on a rotating disk, still admits a similarity transformation, which will transform the governing partial differential equations to ordinary differential equations. The similarity transformation consists of

$$\eta = (\omega/\nu)^{1/2} z \tag{7}$$

$$F(\eta) = u/(r\omega),\ G(\eta) = v/(r\omega),\ H(\eta) = w/(\nu\omega)^{1/2} \tag{8}$$

$$P(\eta) = [p(r, z) - p(r, \delta)]/(\rho\nu\omega) \tag{9}$$

$$\Theta(\eta) = (T - T_w)/(T_m - T_w) \tag{10}$$

where $p(r, \delta)$ is the melt pressure at the melting surface. In arriving at the similarity variable for pressure it is assumed that

$$-\frac{1}{r}\frac{\partial p}{\partial r} = C \tag{11}$$

where C is a constant. Equation (11) is based on intuition and inspection of equation (3) in conjunction with the similarity transformation. It should be noted that the choice of the similarity variables for the present problem by no means forces a similarity transformation. The proof of the validity of this proposition is in successfully implementing the similarity transformation. This includes eliminating the r dependence from the governing equations and their boundary conditions. Evaluating equation (11) at $z = \delta$ and integrating twice yield a relation for the pressure at the melting surface.

Nomenclature

C = constant used in equation (11)
c_p = specific heat at constant pressure
F = similiarity function related to u, equation (8)
G = similiarity function related to v, equation (8)
H = similarity function related to w, equation (8)
h = heat transfer coefficient
h_{sf} = latent heat of melting
h'_{sf} = latent heat of melting corrected for sensible heating $= h_{sf} + c_p(T_m - T_{sub})$
k = thermal conductivity
Nu = Nusselt number
P = similarity function related to pressure, equation (9)
Pr = Prandtl number $= \nu/\alpha$
p = pressure
p_o = pressure equivalent to imposed force
Re = Reynolds number, equation (32)
r = radial coordinate
r_o = radius of melting solid
Ste = Stefan number $= c_p(T_w - T_m)/h_{sf}$
T = temperature
T_{sub} = subcooled temperature of melting solid
u = velocity in r direction
v = velocity in θ direction
w = velocity in z direction
z = vertical coordinate
α = thermal diffusivity
δ = liquid melt film thickness
η = similarity variable, equation (7)
η_δ = similarity variable η evaluated at $z = \delta$
Θ = similarity function related to temperature, equation (10)
θ = coordinate in azimuthal direction
ν = kinematic viscosity
ρ = mass density
σ = ratio of external to centrifugal forces, equation (20)
ω = circular frequency of rotation, radians per second

Subscripts and Superscripts

m = evaluated at melting surface
p = Nusselt number based on external force p_o
w = evaluated at heater wall
ω = Nusselt number based on circular frequency
$'$ = differentiation with respect to function's principal argument
$\bar{}$ = modified variables defined in Appendix A

$$p(r,\ \delta)=\frac{C}{2}\ (r_o^2-r^2) \tag{12}$$

To find the constant C, a force balance in the z direction is applied, which relates C to p_o

$$p_o(\pi r_o^2)=\int_0^{r_o} p(r,\ \delta)\ (2\pi r dr) \tag{13}$$

Substitution of equation (12) into (13) yields:

$$C=4p_o/r_o^2 \tag{14}$$

Equations (9), (12), and (14) may be combined to obtain a single equation for the pressure in the melt $P(\eta)$.

After applying the similarity transformation it is seen from the continuity equation that

$$H'=-2F \tag{15}$$

Subsequently all Fs are substituted from equation (15). The remaining transformed governing equations become

$$H'''=HH''-(H')^2/2+2G^2+2\sigma \tag{16}$$

$$G''=HG'-H'G \tag{17}$$

$$P'=H''-HH' \tag{18}$$

$$\Theta''=\mathrm{Pr}H\Theta' \tag{19}$$

where the parameter σ is the ratio of the external and centrifugal forces.

$$\sigma=4p_o/(\rho r_o^2\omega^2) \tag{20}$$

The appearance of equations (16) – (19) is similar to those obtained by Sparrow and Gregg (1959b) except for the term 2σ in equation (16) and the boundary conditions. The boundary conditions are

$$u=0,\quad v=r\omega,\quad w=0,\quad T=T_w \qquad \text{at } z=0 \tag{21}$$

$$u=0,\quad v=0,\quad T=T_m \qquad \text{at } z=\delta \tag{22}$$

In the transformed form, the boundary equations are

$$H'=0,\quad G=1,\quad H=0,\quad \Theta=0 \qquad \text{at } \eta=0 \tag{23}$$

$$H'=0,\quad G=0,\quad \Theta=1 \qquad \text{at } \eta=\eta_\delta \tag{24}$$

An energy balance at $z=\delta$ relates the heat conduction through the melt to the rate of melting

$$-k\left.\frac{\partial T}{\partial z}\right|_{z=\delta}\left\{1+[d\delta/dr]^2\right\}=\rho h_{sf} w(z=\delta) \tag{25}$$

Realizing that δ is not a function of r [see equation (7)] and defining a Stefan number, equation (25) may be written in terms of the similarity functions as

$$\mathrm{Ste/Pr}=[c_p(T_w-T_m)/h_{sf}]/\mathrm{Pr}=-H(\eta_\delta)/\Theta'(\eta_\delta) \tag{26}$$

The fact that equations (15)–(19) are ordinary differential equations is an indication that our similarity transformation has been successful and that the transformation and the transformed equations are consistent with the conservation laws.

Two heat transfer coefficients may be defined based on heat fluxes at the wall or at the melting surface

$$h_w=\frac{-k\left.\dfrac{\partial T}{\partial z}\right|_{z=0}}{T_w-T_m} \tag{27}$$

$$h_m=\frac{-k\left.\dfrac{\partial T}{\partial z}\right|_{z=\delta}}{T_w-T_m} \tag{28}$$

The two corresponding Nusselt numbers may be defined and related to the transformed variables as

$$\mathrm{Nu}_w^\omega=h_w(\nu/\omega)^{1/2}/k=\Theta'(0) \tag{29}$$

$$\mathrm{Nu}_m^\omega=h_m(\nu/\omega)^{1/2}/k=\Theta'(\eta_\delta) \tag{30}$$

The choice of the characteristics length $(\nu/\omega)^{1/2}$ in equations (29) and (30) is common for rotating flows (e.g., Sparrow and Gregg, 1959b). The superscript ω in equations (29) and (30) is used to signify that the characteristic length used in the Nusselt number definition is based on ω. The two different heat transfer coefficient in equations (27) and (28), h_w and h_m, are needed in order to estimate the heat flux at the wall and at the melting surface, respectively. The heat flux at the melting surface can then be used directly to estimate the melting rate, while the heat flux at the heater surface can be used to estimate the required heater power.

The above equations constitute the governing equations for rotation and direct-contact melting together. A new parameter σ is introduced such that it represents the ratio of the external force to the centrifugal force. If $\sigma=0$, the problem reduces to pure rotation and is identical to that studied by Sparrow and Gregg (1959b). If $\sigma\to\infty$, then the problem is that of no rotation. It seems from equation (16) that this case may present some numerical difficulty since $\sigma\to\infty$. However, an appropriate, new scaling in σ will resolve this problem. The newly scaled equations will then present the exact formulation for the problem of direct-contact melting under external force with no rotation. Appendix A explains this new scaling later in the paper.

It is appropriate at this point to examine the validity of the assumption that the flow is laminar. The largest Reynolds number occurs at $r=r_o$. Therefore, a Reynolds number may be defined as

$$\mathrm{Re}=\left[\frac{1}{\delta}\int_0^\delta u(r=r_o,\ z)\ dz\right]\delta/\nu \tag{31}$$

In order to maintain a laminar flow, the following criterion in terms of the similarity variables and a critical Re, say 2300, should be met:

$$\mathrm{Re}=-\frac{r_o}{4}\left(\frac{\omega}{\nu}\right)^{1/2}H(\eta_\delta)<2300 \tag{32}$$

Observations

It can be observed from the governing equations and their boundary conditions that temperature in the melt is a function of only z. This is not a result of any approximation; rather it is in the characteristic of the phenomenon under consideration. Similar behavior has been observed in rotating and stagnation problems by Schlichting (1968), Sparrow and Gregg (1959b), Squire (1938), and White (1974, p. 180).

Often in melting problems the melting rate is a function of location. This will lead to change of shape of the melting surface as melting progresses (Taghavi and Dhir, 1983). It may be observed, however, from the formulation and particularly from equations (29) and (30) that the heat transfer coefficients at the wall and at the melting surface are independent of the radial location. This in turn means that the melting rate is independent of the radial location. As a result, an initially flat surface undergoing direct-contact melting under the influence of rotation and external force will stay flat, and therefore, change of shape need not be considered.

Another ramification of a heat flux being independent of radial location is that the solution to the present problem could be directly applied to the case where the thermal boundary condition at the heater is no longer a prescribed constant surface temperature, but rather a prescribed constant heat flux. It should be mentioned, therefore, that all the analysis and results will equally apply to the case of prescribed heat flux.

Finally, the present problem is considered under the condition that the heater is rotating. A situation may arise for consideration where the melting and solid may be rotating instead. Such a problem may be formulated exactly similar to the present problem with the exception of two boundary conditions, those related to the angular velocities at the heater and melting surfaces. The two appropriate boundary conditions will be as follows:

$$G(\eta=0)=0 \text{ and } G(\eta=\eta_\delta)=1 \tag{33}$$

It can be concluded from the next section that the results are identical under the thin-film approximation for the cases of rotating heater and rotating solid. It is anticipated that the change in the boundary condition will not alter the results drastically for the general case. This will be discussed in the section on Results and Discussion.

Thin-Film Approximation

It is useful to find any limiting solution before attempting the general case. The limiting solutions are convenient, provide physical insight, and help the proper scaling of the general problem. The approximation here is that the melt film is thin and that the inertia and convective terms may be neglected. A criterion on the validity of this approximation is developed and explained in Appendix B. The governing equations become

$$H'''=2G^2+2\sigma \tag{34}$$

$$G''=0 \tag{35}$$

$$\Theta''=0 \tag{36}$$

The same boundary conditions outlined in equations (23) and (24) also apply here. Equations (34), (35), and (36) may easily be integrated analytically to obtain

$$H(\eta)=-(1/2+\sigma)\eta_\delta\eta^2/2+(1+\sigma)\eta^3/3-\eta^4/(6\eta_\delta)+\eta^5/(30\eta_\delta^2) \tag{37}$$

$$G(\eta)=1-\eta/\eta_\delta \tag{38}$$

$$\Theta(\eta)=\eta/\eta_\delta \tag{39}$$

The Stefan number may be calculated from equation (26) while using equations (37) and (39) as

$$\text{Ste/Pr}=(\sigma/6+1/20)\eta_\delta^4 \tag{40}$$

The Nusselt number may now be obtained by substituting equation (39) into equations (29) and (30) while using equation (40) to eliminate η_δ. The Nusselt number for the case of thin film is denoted hereafter by Nu_o. It should be noted that for a thin film the heat fluxes at the wall and at the melting surface are equal [since the temperature profile is approximately linear; see equation (39)] and that the subscripts w and m are not necessary to accompany Nu.

$$\text{Nu}_o^\omega=h_o(\nu/\omega)^{1/2}/k=\left[\frac{\sigma+3/10}{6\text{Ste/Pr}}\right]^{1/4} \tag{41}$$

Equation (41) is in an appropriate form for small σ. For cases of $\sigma\to\infty$, however, this equation is not adequate and new scaling and definition of Nusselt number is needed. Recognizing that $\sigma\to\infty$ is associated with $\omega\to0$, σ in equation (41) may be replaced from equation (20). This equation may then be rewritten in the limit of $\omega\to0$, while cancelling ω, as

$$\text{Nu}_o^p=\frac{h_o}{k}\left[\frac{\rho r_o^2\nu^2}{4p_o}\right]^{1/4}=\left[\frac{1+3/(10\sigma)}{6\text{Ste/Pr}}\right]^{1/4} \tag{42}$$

It should be mentioned that equation (42) offers a new version for the definition of Nusselt number, which is most useful for cases with slow or no rotation.

It will be interesting at this point to compare the results for thin melt film with those obtained by Sparrow and Gregg (1959b) and Moallemi et al. (1986). For the case with no external pressure, $\sigma=0$, equation (41) yields

$$h_o(\nu/\omega)^{1/2}/k=[\text{Pr}/(20\text{Ste})]^{1/4} \tag{43}$$

This equation is essentially identical to equation (32) of Sparrow and Gregg (1959b), except for the numerical constant, which is different. This difference is caused by the fact that the velocity boundary conditions are not identical in these two cases. At $z=\delta$, the present problem has a rigid boundary while condensation has a free surface. For the case with no rotation, $\sigma\to\infty$, equation (42) yields the following:

$$\frac{h_o}{k}\left[\frac{\rho r_o^2\nu^2}{4p_o}\right]^{1/4}=\left[\frac{\text{Pr}}{6\text{Ste}}\right]^{1/4} \tag{44}$$

Equation (44) is identical to equation (20) of Moallemi et al. (1986). Moallemi et al. did not define a Nusselt number; therefore, some manipulation is necessary to perform the comparison.

The Reynolds number criterion for maintaining a laminar flow, equation (32), may be rewritten for a thin film, while using equations (37), (40), and (41), as

$$\text{Re}=\frac{h_o r_o}{4k}\frac{\text{Ste}}{\text{Pr}}<2300 \tag{45}$$

Then equation (41) is used to eliminate h_o and k to obtain

$$\frac{r_o}{4(\nu/\omega)^{1/4}}\left[\frac{\sigma}{6}+\frac{1}{20}\right]^{1/4}\left[\frac{\text{Ste}}{\text{Pr}}\right]^{3/4}<2300 \tag{46}$$

Except for low Prandtl number metals and high Stefan numbers, most materials should yield a laminar flow.

It should be mentioned here that equations (40)–(46) apply equally to the case where the melting solid is rotating instead of the underlaying heater. This is only true for the thin-film approximation and does not hold in general.

Results and Discussion

The governing equations (16)–(19) with the boundary conditions (23) and (24) constitute a set of coupled nonlinear ordinary differential equations. These equations are solved using a Runge-Kutta subroutine (White, 1974, p. 675). Here, we are not particularly interested in the pressure distribution. The velocity and temperature profiles will not be presented here since we are mainly interested in the Nusselt number. The velocity and temperature profiles for the case of pure rotation, $p_o=0$, are available from Sparrow and Gregg (1959b).

We are, however, interested in the dependence of the heat transfer coefficients, the Nusselt numbers, and the melting rate on the dimensionless parameters involved in this problem, i.e., Ste, Pr, and σ. Our interest is especially focused on the influence of the parameter σ, which is the ratio of the pressure to the centrifugal forces. Figures 2–7 show the dependence of various Nusselt numbers on Ste, Pr, and σ. In these figures no distinction is made as to which Nusselt number is used (whether the characteristic length in Nu is based on ω or p_o). This distinction is avoided by plotting a normalized Nusselt number, Nu/Nu_o, rather than the Nusselt number. This par-

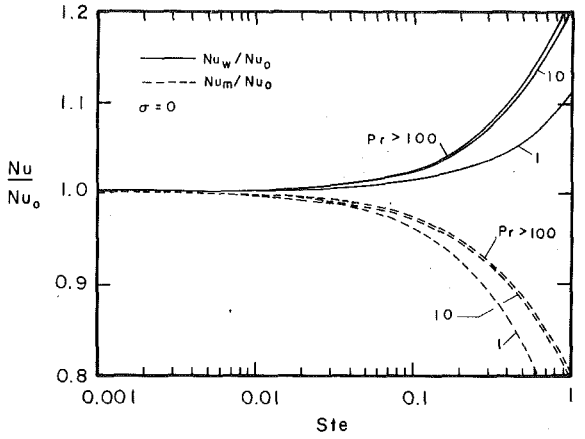

Fig. 2 Normalized Nusselt number as a function of Stefan number for various Prandtl numbers and $\sigma = 0$

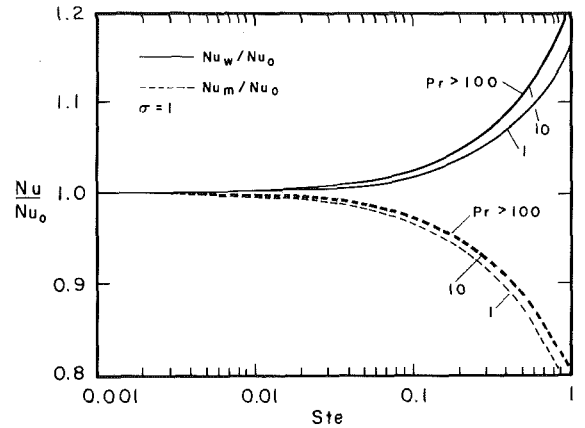

Fig. 3 Normalized Nusselt number as a function of Stefan number for various Prandtl numbers and $\sigma = 1$

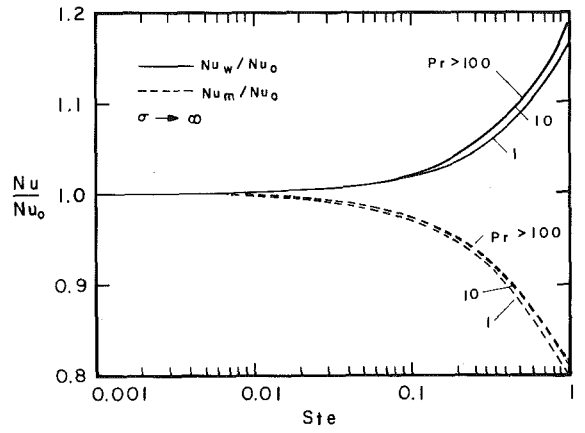

Fig. 4 Normalized Nusselt number as a function of Stefan number for various Prandtl numbers and $\sigma = \infty$

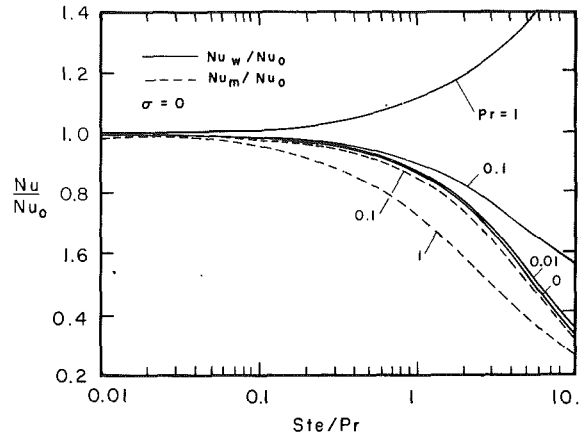

Fig. 5 Normalized Nusselt number as a function of Stefan number for various Prandtl numbers and $\sigma = 0$

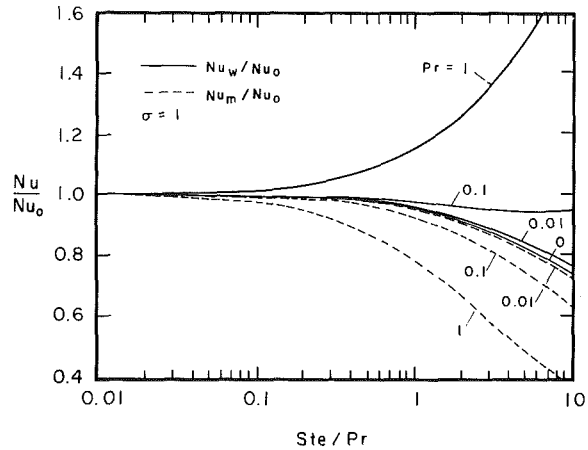

Fig. 6 Normalized Nusselt number as a function of Stefan number for various Prandtl numbers and $\sigma = 1$

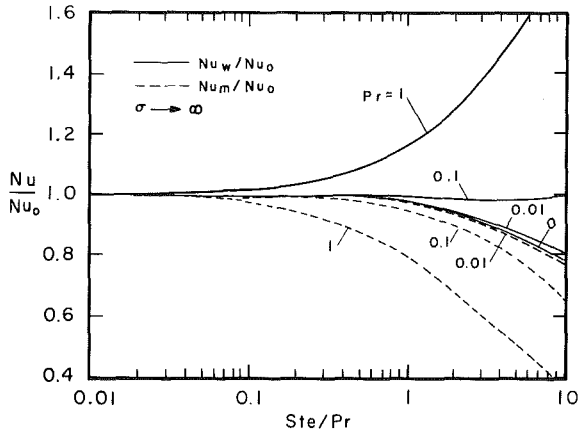

Fig. 7 Normalized Nusselt number as a function of Stefan number for various Prandtl numbers and $\sigma = \infty$

ticular normalization is chosen so that most of the Nusselt number dependencies on the dimensionless parameters will be scaled out.

Figures 2–4 show the normalized Nusselt number for high Prandtl number melts, i.e., $Pr > 1$. In these figures the parameter σ is chosen to be 0 (rotation with no external pressure), 1 (rotation and external pressure together), and ∞ (external pressure with no rotation). Two different Nusselt numbers are given, Nu_w, which is based on heat transfer at the wall, and Nu_m, which is based on heat transfer at the melting surface. The latter is directly related to the melting rate.

All normalized Nusselt numbers start at unity for small Stefan numbers. This is expected since a small Stefan number indicates a thin melt film and therefore Nu becomes equal to Nu_o. As the Stefan number is increased, Nu at the wall increases while Nu at the melting surface decreases. The principal difference between these two Nusselt numbers is caused

by the sensible heating of the melt film beyond the melting temperature. Because a small Stefan number means small difference between the wall and melting temperature, the difference between the two Nu vanishes for small Ste.

Figures 2–4 are plotted for various Pr. It is seen that the normalized Nu increases with Pr. However, it becomes bounded asymptotically as $Pr \to \infty$. This indicates that the chosen dimensionless parameters have the proper Pr scaling. It is also seen that the results for $Pr > 10$ are relatively independent of Pr for the range of the Stefan number in these figures.

Figure 2 is for pure rotation, $\sigma = 0$. Figures 3 and 4 are plotted for $\sigma = 1$ and $\sigma = \infty$. It is observed that the normalized Nu depends rather weakly on the parameter σ. It should be noted that this does not mean that the heat flux is independent of the frequency of rotation or the external pressure, as Nu_o is strongly dependent on σ; see equations (41) and (42). As the parameter σ increases the dependency of the normalized Nu on Pr becomes much weaker.

Figures 5–7 repeat similar information in Figs. 2–4 but for small Prandtl number, i.e., $Pr < 1$. These figures are plotted for $Pr = 1$, 0.1, 0.01, and 0. Unlike the earlier figures, Figs. 5–7 are plotted versus Ste/Pr. If Ste was chosen instead, the Nu would never become bounded as Pr decreases (see results by Sparrow and Gregg, 1959b). If Ste/Pr is chosen, however, the Nusselt number quickly becomes bounded asymptotically as Pr decreases (see the discussion by Seban in the paper by Sparrow and Gregg, 1959a).

Figures 2–7 indicate the error associated with neglecting the inertia and convective terms (i.e., thin-film approximation). It is seen that this error increases as Ste or Ste/Pr increases. For example, it can be seen from Fig. 2 that for $Ste = 0.2$ and $Pr = 1$ the Nusselt number at the melting surface is about 8 percent less than that obtained from the thin-film approximation. Figure 7 indicates that for $Ste = 0.1$ and $Pr = 0.01$ the Nusselt number at the melting surface is about 25 percent lower than that obtained from the thin-film approximation. Therefore, it may be concluded that while for high Prandtl numbers, $Pr > 1$, and moderate Stefan numbers, $Ste < 0.1$, the thin film approximation is reasonable, the error involved for low Prandtl numbers, $Pr < 0.1$, can be substantial.

Finally, numerical results were also obtained for the case where the melting solid is rotating instead of the heater. As expected, the changes in the results were insignificant. For example, for $\sigma = 1$ and $Ste = 1$, the difference of values of Nusselt numbers for all Prandtl numbers was less 1 percent. Therefore, Figs. 2–7 should apply equally to the case of the rotating solid. Of course this conclusion is limited to $Ste < 1$; for higher Ste (thicker melt layers), the appropriate differential equations should be solved.

Summary and Concluding Remarks

The problem of direct-contact melting under the combination of external pressure and rotation has been studied. An exact analysis is performed by adopting a similarity transformation. The following observations and conclusions are made:

- Exact analysis is performed using similarity transformation. A new dimensionless number σ is obtained, which is the ratio of the external force to the centrifugal force. In the limit of a large σ ($\sigma \to \infty$), the governing equations are reduced to those representing exact formulation of the direct-melting process under external force (no rotation).
- Although the present analysis is performed for the prescribed constant-temperature boundary conditions, the derivations and the results are equally applicable to the case with the prescribed constant heat flux boundary conditions. This is due to the characteristic of the present problem that the melt film thickness is uniform and the temperature in the melt does not depend on the radial coordinate. As a result, both the temperature and the heat flux at the heater and melting surfaces are uniform.
- The thin-film approximation yields the closed-form solutions, equations (41) and (42). Equation (41) should be used with the cases of pure rotation (no external force) while equation (42) should be used with the cases of pure external force (no rotation). When both effects are present, either equation (41) or equation (42) may be used, which would result in identical heat transfer coefficients.
- Equation (41) in the limit of $\sigma = 0$ reduces to an equation similar to that obtained by Sparrow and Gregg (1059b) for pure rotation (condensation on a rotating disk). Similarly, equation (42) in the limit of $\sigma \to \infty$ reduces to the result obtained by Moallemi et al. (1986) for the case with pure external force (no rotation).
- Different scaling of the variables with respect to σ is necessary for the cases with very large and very small force ratios.
- Different scaling of the variables with respect to Pr is necessary for the cases with very large and very small Prandtl numbers. It is seen that Ste is appropriate for cases with large Pr, while Ste/Pr is suitable for cases with small Pr.
- The present results also apply to the case where the solid is rotating rather than the heater as long as $Ste < 1$.
- A criterion is developed for the validity of thin-film approximation. For the case with no external force, $Ste/Pr \ll 12$; and for the case with no rotation, $Ste/Pr \ll 2$.

References

Dhir, V. K., Castle, J. N., and Catton, I., 1977, "Role of Taylor Instability on Sublimation of a Horizontal Slab of Dry Ice," ASME JOURNAL OF HEAT TRANSFER, Vol. 99, pp. 411–418.

Emerman, S. H., and Turcotte, D. L., 1983, "Stokes' Problem With Melting," *International Journal of Heat and Mass Transfer*, Vol. 26, pp. 1625–1630.

Farhadieh, R., and Baker, L. Jr., 1978, "Heat Transfer Phenomenology of Hydrodynamically Unstable Melting System," ASME JOURNAL OF HEAT TRANSFER, Vol. 100, pp. 305-310.

Moallemi, M. K., and Viskanta, R., 1985, "Melting Heat Transfer Around a Migrating Heat Source," ASME JOURNAL OF HEAT TRANSFER, Vol. 107, pp. 451–458.

Moallemi, M. K., Webb, B. W., and Viskanta, R., 1986, "An Experimental and Analytical Study of Close-Contact Melting," ASME JOURNAL OF HEAT TRANSFER, Vol. 108, pp. 894–899.

Pfann, W. G., 1958, *Zone Melting*, Wiley, New York.

Saito, A., Utaka, Y., and Tokihiro, Y., 1986, "Direct Contact Melting Heat Transfer on a Heated Surface," *Proceedings of the Eighth International Heat Transfer Conference*, San Francisco, CA, pp. 1805–1810.

Schlichting, H. S., 1968, *Boundary Layer Theory*, 6th ed., McGraw-Hill, New York, p. 287.

Sparrow, E. M., and Gregg, J. L., 1959a, "A Boundary-Layer Treatment of Laminar-Film Condensation," ASME JOURNAL OF HEAT TRANSFER, Vol. 81, pp. 13–18.

Sparrow, E. M., and Gregg, J. L., 1959b, "A Theory of Rotating Condensation," ASME JOURNAL OF HEAT TRANSFER, Vol. 81, pp. 113–120.

Sparrow, E. M., and Gregg, J. L., 1961, "Condensation on a Rotating Cone," ASME JOURNAL OF HEAT TRANSFER, Vol. 83, pp. 101–102.

Squire, H. B., 1938, in: *Modern Developments in Fluid Dynamics*, S. Goldstein, ed., Oxford, United Kingdom, pp. 623–627.

Taghavi, K., Dhir, V. K., and Catton, I., 1979, "Thermal and Hydrodynamic Phenomena Associated With Melting of a Horizontal Substrate Place Beneath a Heavier Immiscible Liquid," ASME JOURNAL OF HEAT TRANSFER, Vol. 101, pp. 318–325.

Taghavi, K., and Dhir, V. K., 1983, "Shape Change of an Initially Vertical Wall Undergoing Condensation-Driven Melting," ASME JOURNAL OF HEAT TRANSFER, Vol. 105, pp. 235–240.

Taghavi, K., 1987, "Melting of a Horizontal Substrate Placed Under a Heavier and Miscible Pool," *AIAA Journal of Thermophysics and Heat Transfer*, Vol. 1, No. 4, pp. 321–326.

Tien, C. L., and Yen, Y. C., 1971, "Condensation—Melting Heat Transfer," *Chemical Engineering Progress Symposium Series*, Vol. 67, No. 113, pp. 1–9.

von Karman, T., 1921, "Uber Laminare und Turbulente Reiburg," *Z. Angew. Math. Mech.*, Vol. 1, pp. 233–252.

White, F. M., 1974, *Viscous Fluid Flow*, McGraw-Hill, New York.

APPENDIX A

Proper Scaling for the Case With Large σ

The governing equations in their present form, equations (14)–(18), are not in a proper form for large σ, especially when no rotation exists and $\sigma \to \infty$. In this appendix, a new scaling in terms of the parameter σ is adopted. The following transformation is suggested:

$$\bar{\eta} = \sigma^{1/4}\eta \tag{A.1}$$

$$\bar{G}(\bar{\eta}) = \sigma^{-1/2}G(\eta) \tag{A.2}$$

$$\bar{H}(\bar{\eta}) = \sigma^{-1/4}H(\eta) \tag{A.3}$$

$$\bar{\Theta}(\bar{\eta}) = \Theta(\eta) \tag{A.4}$$

The new set of governing equation is given below:

$$\bar{H}''' = \bar{H}\bar{H}'' - (\bar{H}')^2/2 + 2\bar{G}^2 + 2 \tag{A.5}$$

$$\bar{G}'' = \bar{H}\bar{G}' - \bar{H}'\bar{G} \tag{A.6}$$

$$\bar{\Theta}'' = \mathrm{Pr}\,\bar{H}\bar{\Theta}' \tag{A.7}$$

All the homogeneous boundary conditions in equations (21) and (22) remain unchanged. The rest are transformed to

$$\bar{G}(\bar{\eta}_\delta = 0) = \sigma^{-1/2} \tag{A.8}$$

and

$$\bar{\Theta}(\bar{\eta} = \bar{\eta}_\delta) = 1 \tag{A.9}$$

The energy balance equation (24) is transformed to

$$\mathrm{Ste/Pr} = -\bar{H}(\bar{\eta}_\delta)/\bar{\Theta}'(\bar{\eta}_\delta) \tag{A.10}$$

Finally, the Nusselt numbers in equations (27) and (28) may be transformed. In doing this, however, a new characteristic length for the Nusselt number is formed. The new equations are

$$\mathrm{Nu}_w^p = \frac{h_w}{k}\left[\frac{\rho r_o^2 \nu^2}{4p_o}\right]^{1/4} = \bar{\Theta}'(0) \tag{A.11}$$

$$\mathrm{Nu}_m^p = \frac{h_m}{k}\left[\frac{\rho r_o^2 \nu^2}{4p_o}\right]^{1/4} = \bar{\Theta}'(\bar{\eta}_\delta) \tag{A.12}$$

It should be remembered that the superscript p is used here to signify that the Nusselt number is defined based on a characteristic length, which depends on p_o.

It is observed from the new transformed governing equations that these equations are manageable as $\sigma \to \infty$. In this limit the boundary condition equation (A.8) is replaced by $\bar{G}(\bar{\eta} = 0) = 0$.

APPENDIX B

Criterion for Validity of Thin-Film Approximation

Traditionally, inertia and convective terms have been neglected when the phase change parameter (Stefan number or Jakob number for melting/freezing or evaporation/condensation, respectively) is small. This assumption has often been accompanied by numerical verification. Since the film thickness is proportional to the phase change parameter, this assumption is also called the thin-film approximation.

In this appendix, a systematic approach will be adopted to obtain a criterion for the validity of the thin-film approximation. This method consists of evaluating the neglected terms by using the thin-film approximation results. Thereafter, the neglected terms will be compared to the retained terms in the governing differential equation in order to obtain a criterion.

The neglected term according to equations (16) and (34) is $HH'' - H'^2/2$. This term does not have a single value and is a function of η. For order-of-magnitude analysis, however, its value at $\eta = \eta_\delta$ is used for this analysis (the neglected term is zero at the wall). Using the approximate solution, equation (37), the neglected term is evaluated as

$$HH'' - H'^2/2 = -(\sigma/6 + 1/20)\,(\sigma + 1/6)\eta_\delta^4 \qquad \text{at } \eta = \eta_\delta \tag{B.1}$$

The parameter η_δ may be eliminated from equation (B.1) by using equation (40).

$$HH'' - H'^2/2 = -(\sigma + 1/6)\ (\mathrm{Ste/Pr}) \qquad \text{at } \eta = \eta_\delta \tag{B.2}$$

The following criterion is used for the thin-film approximation:

$$|HH'' - H'^2/2| \ll |2G^2 + 2\sigma| \tag{B.3}$$

Equation (B.3) simply states that the neglected term should be much smaller than the retained terms. The order of magnitude of the retained term may be calculated from equation (38) as (G varies from 0 to 1)

$$2G^2 + 2\sigma = 2 + 2\sigma \tag{B.4}$$

The criterion therefore becomes

$$\frac{\mathrm{Ste}}{\mathrm{Pr}} \ll \frac{2(\sigma + 1)}{\sigma + 1/6} \tag{B.5}$$

For the limits of no rotation and no external force the criterion becomes

$\mathrm{Ste/Pr} \ll 12$ for $\sigma = 0$, no external force (B.6)

$\mathrm{Ste/Pr} \ll 2$ for $\sigma \to \infty$, no rotation (B.7)

Equations (B.6) and (B.7) suggest a somewhat more relaxed criterion for the problem with no external force. This is indeed observed by comparing Figs. 5 and 7.

Mixed Convection on a Vertical Flat Plate With Transition and Separation

T. Cebeci
Professor and Chairman.

D. Broniewski
Graduate Student.

C. Joubert
Graduate Student.

O. Kural
Professor.

Aerospace Engineering Department,
California State University,
Long Beach, CA 90840

A numerical method has been developed and used to calculate the flow properties of laminar, transitional, and turbulent boundary layers on a vertical flat plate with heat transfer. The governing boundary-layer equations include a buoyancy-force term and are solved by a two-point finite-difference method due to Keller and results obtained for heating and cooling and, in the case of the laminar flows, for an isothermal surface corresponding to that of Merkin. Cooled plates with unheated sections can give rise to boundary-layer separation and reattachment and, on occasions, transition can occur within the separation bubble. Flows of this type have been examined with the inviscid–viscous interaction procedure developed by Cebeci and Stewartson and the location of transition obtained by the e^n method based on the linear stability theory for air with $Pr = 1$. Results are given in dimensionless form as a function of Reynolds number, Richardson number, and Prandtl number and quantify those parameters that give rise to separation. Consequences of the use of interaction and stability theory are examined in detail.

1.0 Introduction

Many engineering flows are subject to a combination of natural and forced convection and include heated jets and diffusion flames from a vertical pipe, which are controlled by forced convection in the initial region and by buoyancy forces far from the pipe exit. Buoyancy is also of importance in an environment where differences between land and air temperature can give rise to complicated flow patterns and in enclosures such as ventilated and heated rooms and reactor configurations. The present study was undertaken to provide results for "mixed" convection flows, which encompass laminar, transitional, and turbulent boundary layers on vertical plates with a range of heat transfer boundary conditions. For a heated plate with free-stream velocity directed vertically upward along the plate, the buoyancy forces act in the direction of the free stream, so that the fluid receives additional acceleration, and the boundary-layer profile takes on the characteristic form of natural convection flows at large distances from the origin. In the case of a cooled plate, the buoyancy forces oppose the viscous forces and exert a retarding force on the velocity, which becomes increasingly pronounced until eventually the boundary layer separates.

The prediction of buoyancy-aided flows does not pose a difficult task. That of buoyancy-opposed flows is less straightforward because the boundary-layer equations can become singular and cause the calculations to break down at a location of flow separation. This phenomenon is well known in fluid dynamics and implies that the boundary-layer properties and particularly the displacement thickness must be allowed to modify the external flow (Catherall and Mangler, 1966). Equivalently the effect of the boundary layer may be regarded as providing a blowing velocity $v_w(x)$ $(\equiv d/dx\,(u_e\delta^*)$ through the surface of the plate, thus modifying the external flow. The procedure used here and by Veldman (1981) and Cebeci et al. (1980) is to write the edge boundary conditions with $u_e^o(x)$ denoting the inviscid velocity distribution and $\delta u_e(x)$ the perturbation velocity due to viscous effects as

$$y=\delta, \qquad u_e(x)=u_e^o(x)+\delta u_e(x) \tag{1}$$

With the assumptions that the plate is thin and of an infinite extent and that the convection takes place on both sides, the perturbation velocity is computed from the Hilbert integral given by

$$\delta u_e(x)=\frac{1}{\pi}\int_0^{*\infty}\frac{v_w(x')}{x-x'}\,dx' \tag{2}$$

where * means that the finite part of the improper integral is to be used. The edge boundary condition given by equation (1) is rewritten as

$$y=\delta, \qquad u_e(x)=u_e^o+\frac{1}{\pi}\int_0^{*\infty}\frac{v_w(x')}{x-x'}\,dx' \tag{3}$$

The present contribution should be viewed in the context of previous work, including that of Oosthuizen (1974), Seibers et al. (1983), and Chen et al. (1987). Early contributions were concerned with boundary conditions, which gave rise to similar solutions and were confined to a limited range of laminar boundary-layer flows. Calculations of mixed convection turbulent flows, such as those of Oosthuizen (1974) and Chen et al. (1987), have made use of mixing-length models to obtain solutions for turbulent flows and in the latter case these encompass a range from forced to free convection. Experimental information (Seibers et al., 1983) has provided support for these results, although it is to be expected that higher-order models and some representation of temperature fluctuations will be required for strongly buoyant flows. The results of Chen et al. (1987) were obtained by solving boundary-layer equations with a form of the eddy-viscosity formulation of Cebeci and Smith (1974) and the finite-difference method of Keller (1970). The same approach is used here to obtain results that include transitional flows and, with opposed free and forced convection, a separating boundary layer and the resulting region of separated flow. The location of the onset of transition is determined by the e^n method proposed by Smith (1956) and Van Ingen (1956) and based on the solution of the Orr–Sommerfeld equation; the resulting region of transitional flow is represented by the extension to the eddy-viscosity equations of Cebeci and Smith (1974), as suggested by Chen and Thyson (1971). The extension of the boundary-layer procedure to deal with separating and reattaching flows makes use of the interaction procedure referred to above and used previously by Cebeci et al. (1986) to represent the flow over

Contributed by the Heat Transfer Division for publication in the JOURNAL OF HEAT TRANSFER. Manuscript received by the Heat Transfer Division June 7, 1988. Keywords: Flow Separation, Flow Transition, Mixed Convection.

airfoils at high angles of attack. It should be emphasized that the method described and evaluated here is intended to provide a calculation foundation that can be used subsequently with more advanced physical models such as buoyancy-driven turbulence models and stability procedures such as that of Mucoglu and Chen (1978) and Chen and Mucoglu (1979). The numerical results are expected to be reasonably accurate, especially for unit Prandtl number and for the assumed small temperature differences, and the calculated trends will certainly be correct. They can also be used to represent flows with limited regions of reverse flow, as discussed by Cebeci et al. (1986) and elsewhere, which we expect to encounter with opposed forced and free convection.

2.0 Basic Equations

The present calculations require the solution of the boundary-layer equations appropriate to laminar and turbulent flows and these are presented in the first subsection. It is also necessary to determine the location of transition and a brief description of the equations solved for this purpose is provided in the second subsection.

2.1 Boundary-Layer Equations. The boundary-layer equations for a two-dimensional incompressible laminar and turbulent flow on a vertical flat plate are well known. With the concepts of eddy viscosity ϵ_m and turbulent Prandtl number Pr_t they can be written as in Cebeci and Bradshaw (1984)

$$\frac{\partial u}{\partial x} + \frac{\partial v}{\partial y} = 0 \tag{4}$$

$$u\frac{\partial u}{\partial x} + v\frac{\partial u}{\partial y} = u_e\frac{du_e}{dx} + \nu\frac{\partial}{\partial y}\left(b\frac{\partial u}{\partial y}\right) + g\beta(T - T_e) \tag{5}$$

$$u\frac{\partial T}{\partial x} + v\frac{\partial T}{\partial y} = \frac{\nu}{\mathrm{Pr}}\frac{\partial}{\partial y}\left(c\frac{\partial T}{\partial y}\right) \tag{6}$$

Here β denotes the coefficient of thermal volumetric expansion of the fluid and is equal to T^{-1} for an ideal gas. The two parameters b and c are given by

$$b = 1 + \frac{\epsilon_m}{\nu}, \qquad c = 1 + \frac{\mathrm{Pr}}{\mathrm{Pr}_t}\frac{\epsilon_m}{\nu} \tag{7}$$

In the solution of equations (4)–(6) we consider the boundary conditions in which wall temperature is specified with no mass transfer,

$$y = 0, \qquad u = v = 0, \qquad T = T_x(x) \tag{8a}$$

$$y = \delta, \qquad u = u_e(x), \qquad T = T_e \tag{8b}$$

Here the external temperature is a prescribed constant and the wall temperature is a prescribed function of x. The latter is chosen such that the plate is either heated or cooled up to $x = x_o$ after which the wall temperature is the same as the external temperature. In this way, the surface conditions correspond to an isothermal flat plate followed by an unheated section. To avoid the possible numerical difficulties that may result from the sudden rise or drop in the wall temperature at $x = x_o$, we use an expression that allows the wall temperature to change continuously in the neighborhood of x_o. As a result, for $x \geq x_o$, we assume the wall temperature to be of the form

$$T_w(x) = \begin{cases} T_w + \dfrac{1}{2}(T_e - T_w)\left[1 - \cos\pi\left(\dfrac{x - x_o}{x_1 - x_o}\right)\right] & x_o \leq x \leq x_1 \\ T_e & x > x_1 \end{cases} \tag{9}$$

The solution of the system of equations given by equations (4)–(9) also requires expressions for eddy viscosity ϵ_m and turbulent Prandtl number Pr_t. Here we use the formulas developed by Cebeci and Smith (1974); we take Pr_t to be constant equal to 0.9 and ϵ_m to be defined by two separate expressions given by

Nomenclature

f = dimensionless stream function, equation (12)
g = gravitational acceleration
h = characteristic length $= (\nu x/u_0)^{1/2}$
l = modified mixing length, equation (11a)
L = reference length
n = disturbance amplification ratio, equation (20)
Pr = Prandtl number
Re = Reynolds number in the stability equation $= \mathrm{Re}_x^{1/2}$
Ri = Richardson number, equation (15b)
Re_L, Re_x = Reynolds numbers based on L and x, respectively; $\mathrm{Re}_L = u_o L/\nu$, $\mathrm{Re}_x = u_o x/\nu$
T = temperature
u, v = velocity components in x and y directions
u_o = free-stream velocity
$\bar{u}$ = velocity ratio $= u/u_o$
x, y = coordinates in the streamwise and normal flow directions, respectively
x_0 = length of the heated portion of the plate
$\bar{y}$ = dimensionless $y = y/h$
α = dimensionless wave number based on h
β = coefficient of thermal expansion
γ_{tr} = intermittency factor, equation (11b)
δ = boundary-layer thickness
δ^* = displacement thickness
Δ = dimensionless δ^*, equation (17)
ϵ_m = eddy viscosity, equation (10)
ζ = dimensionless $x = x/L$
η = dimensionless boundary-layer coordinate, equation (12)
θ = dimensionless temperature, equation (15a)
ν = kinematic viscosity
ρ = density
τ = shear stress
ϕ = dimensionless velocity disturbance amplitude function
ψ = stream function, equation (12)
ω = dimensionless frequency $= \omega^* h/u_e$

Superscripts

$'$ = primes denote differentiation with respect to η or $\bar{y}$

Subscripts

e = boundary-layer edge
w = wall

$$\epsilon_m = \begin{cases} l^2\left(\dfrac{\partial u}{\partial y}\right)\gamma_{tr} \\ 0.0168\left|\displaystyle\int_0^{\delta}(u_e-u)dy\right|\gamma_{tr} \end{cases} \tag{10}$$

where the modified mixing length l and the intermittency factor γ_{tr} are given by

$$l=0.4y[1-\exp(-y/A)], \qquad A=26\left(\frac{\tau}{\rho}\right)^{-1/2}_{\max}\nu \tag{11a}$$

$$\gamma_{tr}=1-\exp\left[-G(x-x_{tr})\int_{x_{tr}}^{x}\frac{dx}{u_e}\right] \tag{11b}$$

$$\eta=0 \qquad f=f'=0, \qquad \theta=\begin{cases}1 & \zeta\le\zeta_o \\ 1-\dfrac{1}{2}\left[1-\cos\pi\left(\dfrac{\zeta-\zeta_o}{\zeta_1-\zeta_o}\right)\right] & \zeta_o<\zeta<\zeta_1 \\ 0 & \zeta\ge\zeta_1\end{cases} \tag{16a}$$

Here x_{tr} is the location of the beginning of transition and the parameter G is defined by

$$G=\left(\frac{3}{C^2}\right)\frac{u_o^3}{\nu^2}\,\mathrm{Re}_{x_{tr}}^{-1.34} \tag{11c}$$

where the transition Reynolds number $\mathrm{Re}_{x_{tr}}=(u_o x/\nu)_{tr}$ and C is constant with a recommended value of 60. The extent of the transition region $\mathrm{Re}_{\Delta x}$ ($\equiv\Delta x u_o/\nu$) is related to the transition Reynolds number $\mathrm{Re}_{x_{tr}}$ by

$$\mathrm{Re}_{\Delta x}=C\mathrm{Re}_{x_{tr}}^{2/3} \tag{11d}$$

Before we solve the above set of equations, we transform them into a more convenient form with the definition of the steam function $\psi(x, y)$, which automatically satisfies the continuity equation (4) and the Falkner-Skan transformation defined by

$$\eta=\left(\frac{u_o}{\nu x}\right)^{1/2}y, \qquad \zeta=\frac{x}{L}, \qquad \psi=(u_o\nu x)^{1/2}f(\zeta,\eta) \tag{12}$$

With these relations, equations (5) and (6) can be written as

$$(bf'')'+\frac{1}{2}ff''=\pm\mathrm{Ri}\,\zeta\theta+\zeta\left(f'\frac{\partial f'}{\partial\zeta}-f''\frac{\partial f}{\partial\zeta}-w\frac{dw}{d\zeta}\right) \tag{13}$$

$$\frac{1}{\mathrm{Pr}}(c\theta')'+\frac{1}{2}f\theta'=\zeta\left(f'\frac{\partial\theta}{\partial\zeta}-\theta'\frac{\partial f}{\partial\zeta}\right) \tag{14}$$

Here, θ, f', and w represent dimensionless temperature, velocity, and external velocity as defined by

$$\theta=\frac{T-T_e}{T_w-T_e}, \qquad f'=\frac{u}{u_o}, \qquad w=\frac{u_e}{u_o} \tag{15a}$$

The parameter Ri denotes the Richardson number, which can be used to assess the importance of the buoyancy effect. It is defined by

$$\mathrm{Ri}=\frac{|T_e-T_w|}{T_e}\frac{qL}{u_o^2} \tag{15b}$$

If $\mathrm{Ri}\gg 1$, buoyancy effects are dominant over the majority of the plate and this type of flow is commonly referred to as "natural" or "free" convection flow, while buoyancy effects may largely be neglected if $\mathrm{Ri}\ll 1$. Flows with $\mathrm{Ri}\sim 1$ are referred to as "mixed" convection flows and are investigated in this paper. The $\pm$ sign in front of the $\mathrm{Ri}\zeta\theta$ term in equation (13) corresponds to heating (+) and cooling (−) wall conditions.

In the early stages of boundary-layer growth, the transformation given by equation (13) provides a valuable computational advantage since the flow is represented by the Blasius solution at $\zeta=0$ and, as a result, there is no difficulty in generating the initial conditions needed for equations (13) and (14). At small values of ζ, the flow departs slowly from flat-plate flow and allows the calculations to be performed without numerical difficulties. At larger values of ζ, the transformed equations can still be applied for either continuous unseparated laminar flow or, in the case of separation, to compute the characteristics of the separation bubble.

The wall boundary conditions for the velocity and temperature field follow from equations (3), (8), and (9), and in transformed coordinates with $u_e^o/u_o=1$, can be written as

$$\eta=\eta_e, \qquad w=1+\epsilon\int_0^{*\infty}\frac{d\Delta}{d\zeta'}\frac{d\zeta'}{\zeta-\zeta'}, \qquad \theta=0 \tag{16b}$$

where

$$\epsilon=\frac{1}{\pi\sqrt{\mathrm{Re}_L}} \qquad \Delta=(w\eta_e-f_e)\sqrt{\zeta'} \tag{17}$$

2.2 Linear Stability Equation. The prediction of the onset of transition is obtained from the e^n method, which assumes that transition occurs when a small disturbance with a critical frequency is amplified by a factor of e^n where n is commonly taken to be between 8 and 9. With velocity profiles obtained from the equations of the previous section, the Orr-Sommerfeld equation

$$\phi^{iv}-2\alpha^2\phi''-\alpha^4\phi-i\mathrm{Re}(\alpha\bar{u}-\omega)(\phi''-\alpha^2\phi)+i\mathrm{Re}\alpha\bar{u}''\phi=0 \tag{18}$$

subject to boundary conditions given by Cebeci and Bradshaw (1977)

$$y=0, \quad \phi=0, \quad \phi'=0 \tag{19a}$$

$$y=\delta, \quad (D^2-\alpha^2)\phi+(\alpha+\xi_2)(D+\alpha)\phi=0, \quad (D+\xi_2)(D^2-\alpha^2)\phi=0 \tag{19b}$$

where D denotes $d/d\bar{y}$ and

$$\xi_2^2=\alpha^2+i\mathrm{Re}(\alpha\bar{u}_e-\omega)$$

is solved and its stability properties are examined. In particular, the amplification factors n are computed as functions of x (or ζ) from the evaluation of the integral

$$n=\int_{x_s}^{x}-\alpha_i dx \tag{20}$$

for a set of specified dimensional frequencies ω^*. The solution of equations (18) and (19) begins at a Reynolds number, say Re, greater than the critical value, Re_{cr}, on the lower branch of the neutral stability curve. This provides the desired frequency at $x=x_s$, which at the subsequent x locations or Reynolds numbers allows the solution of the eigenvalue problem in which α is computed as discussed in Cebeci and Bradshaw (1977). This leads to one of the amplification curves of Fig. 1 obtained for a horizontal flat plate and given by Cebeci and Egan (1989) and the process is repeated to obtain similar amplification curves for different values of ω^*. As can be seen from Fig. 1, the envelope of the resulting curves corresponds to the maximum amplification factors from which transition is computed for a selected value of n.

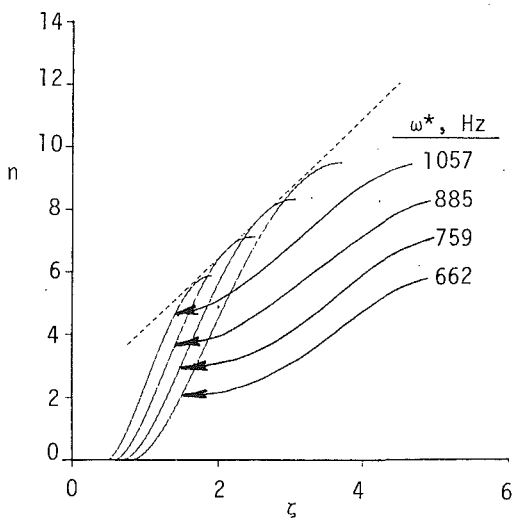

Fig. 1 Variation of the amplification factor n with different values of dimensional disturbance frequency ω^*

3.0 Solution Procedure

The solution of the equations and boundary conditions given in the previous section was obtained in the standard mode, meaning that the external velocity is given, or in the inverse mode in which case the external velocity was computed as part of the solution. In both cases, the procedure made use of Keller's two-point finite-difference scheme extensively used for the solution of parabolic partial-differential equations as discussed by Bradshaw et al. (1981). Equations (13) and (14) were written as a system of six first-order equations by defining new dependent variables and the boundary conditions, equation (16), were rewritten in terms of these new variables. Two-point finite-difference approximations were applied to this first-order system and the resulting nonlinear algebraic equations were linearized by Newton's method and solved by the block-elimination method. Further details of the procedure for the standard problem are provided by Cebeci and Bradshaw (1984) and for the inverse problem by Bradshaw et al. (1981).

As long as there is no flow separation, it was sufficient to solve the boundary-layer equations (13) and (14) with boundary conditions corresponding to those given by equation (16) with $w=1$ so that $\epsilon=0$. The pressure gradient term $dw/d\zeta$ in equation (13) was set equal to zero. The inverse mode was necessary for flows with separation, where the longitudinal-convection term of equation (13) was neglected in the separated-flow region. The two calculation procedures were arranged in a general form so that the same computer code was used with minor changes.

It should be noted that the form of Δ given by equation (17) and found in equation (16b) becomes singular as $\zeta \to 0$ and is equal to

$$1.72\sqrt{\zeta'} \qquad \text{when} \qquad \zeta' \ll 1 \tag{21}$$

However, the indefinite integral in equation (16b) is finite and equal to zero near the leading edge. To show this, we use equation (21) and write the integral in equation (16b) as

$$\int_0^{*\infty} \frac{d\zeta'}{(\zeta')^{1/2}(\zeta-\zeta')} \tag{22a}$$

or with $\zeta t=\zeta'$ as

$$\frac{1}{\zeta^{1/2}}\int_0^{*\infty} \frac{dt}{t^{1/2}(1-t)} \tag{22b}$$

The integral in equation (22b) has a solution that may be written as

$$\ln\frac{(1-t)}{1+t-2\sqrt{t}}$$

which indicates that it is equal to zero at the leading edge of the plate where $t=0$.

This singular form of Δ makes no contribution to the external velocity u_e (or w) near the leading edge but it can cause numerical difficulties to the solution procedure if the calculations are initiated close to $\zeta=0$. To avoid this, we write the integral in equation (16b) as

$$I=\int_0^{\infty}\frac{d\Delta}{\partial\zeta'}\frac{d\zeta'}{\zeta-\zeta'}=\int_0^{\infty}\frac{d(\Delta-\Delta')}{d\zeta'}\frac{d\zeta'}{\zeta-\zeta'}+\int_0^{\infty}\frac{d\Delta'}{d\zeta'}\frac{d\zeta'}{\zeta-\zeta'}=I_1+I_2 \tag{23}$$

where, with b_2 denoting a constant, and $\bar{w}$ an average velocity between two consecutive x stations,

$$\Delta'=1.72\sqrt{\zeta'}\,\frac{b_2+w\zeta'}{b_2+\zeta'} \tag{24}$$

The integral I_1 can be obtained numerically as discussed by Cebeci et al. (1986), and I_2 can be determined analytically as discussed by Broniewski (1988)

$$I_2=-1.72\pi\,\frac{b_2^{3/2}(\bar{w}-1)}{(\zeta+b_2)^2} \tag{25}$$

The resulting boundary condition in equation (16b) can then be rewritten as

$$w=1+\frac{1.72\,b_2^{3/2}(1-\bar{w})}{\sqrt{\mathrm{Re}_L}\,(\zeta+b_2)^2}+\epsilon I_1 \tag{26}$$

The solution of the Orr–Sommerfeld equation was achieved in the manner described by Cebeci and Bradshaw (1977) and in greater detail by Cebeci and Egan (1989) and Broniewski (1988). It used the same two-point finite-difference method with a novel continuation method, which was necessary to solve the eigenvalue problem in the vicinity of separation.

4.0 Results and Discussion

The results are presented in three subsections, which deal with a laminar attached flow, laminar flows with boundary-layer separation, and flows that involve transition from laminar to turbulent flow and that can involve separation. The first subsection is short and is included to demonstrate that the numerical solution method provides results that closely resemble the established values of Merkin (1969) for aided and opposed free and forced convection. The second highlights the use of interaction between inviscid and viscous flows in the determination of the onset of separation in opposed free and forced convection, the nature of the resulting separation bubble, and the range of parameters for which separation occurs. The final section considers flows that undergo transition from laminar to turbulent flow and makes use of the interactive method to obtain results for opposed-convection cases where transition occurs within a region of separated flow. The determination of the location of transition from stability theory is essential in these cases and consequences of its use are examined.

4.1 Laminar Flows. Merkin (1969) computed the development of a laminar boundary layer over a uniform temperature vertical flat plate for a Prandtl number of unity and with buoyancy forces aiding and opposing the development of the flow. For the case of heat transfer to the flow, two series solutions were devised, one for the leading-edge region and the other for the fully developed condition away from the leading edge. In the region in between, where the series were inappropriate, a numerical method was used to solve the equa-

Table 1 Comparison of computed results for a laminar flow over a cooled plate for Pr = 1.0, Ri = 0.4, $Re_L = 10^7$. The starred quantities (*) denote Merkin's results.

ζ	$\theta_w'^*$	θ_w'	$f_w''^*$	f_w''
0.00622	0.3655	0.3320	0.3635	0.3320
0.03162	0.3486	0.3285	0.3381	0.3174
0.07935	0.3230	0.3230	0.2947	0.2948
0.21247	0.3046	0.3040	0.2263	0.2273
0.28415	0.2921	0.2922	0.1852	0.1858
0.35585	0.2762	0.2769	0.1387	0.1397
0.41727	0.2569	0.2575	0.0909	0.0923
0.44800	0.2231	0.2430	0.0607	0.0626
0.46847	0.2261	0.2288	0.0399	0.0368
0.47745	0.2120	0.2173	0.0160	0.0209
0.47935	0.2059	0.2134	0.0127	0.0164

tions. Merkin used the same procedures for heat transfer from the flow with the calculations stopping at the point of boundary-layer separation. A sample of the results for Ri = ±0.4, $Re_L = 10^7$ is shown in tabular form in Table 1 for the case of cooled plate and in graphic form in Fig. 2 for the heated plate and, as can be seen, the present values of wall heat transfer parameter θ_w' and the wall shear-stress parameter f_w'' agree well with those given by Merkin. His separation point corresponded to Riζ = 0.19235, which may be compared to Riζ = 0.20592 obtained with the present method, which is likely to be more accurate since close to separation special care was taken to ensure that the grid spacing did not limit the accuracy.

4.2 Separating and Reattaching Laminar Flows. Calculations were performed for a uniformly cooled surface followed by an unheated section for Prandtl numbers in a range from 0.1 to 10. For each Prandtl number, the plate was cooled up to $\zeta = \zeta_o = 4.0$, after which the wall boundary conditions θ_w changed from 1 at 4.0 to 0 at $\zeta = \zeta_1 = 4.5$ according to the formula given in equation (16). Results are presented here for Prandtl numbers of 1 and 10 with $Re_L = 10^5$; additional results are given by Broniewski (1988).

Before we discuss the results obtained in the inverse mode with the Hilbert integral formulation, it is useful to comment on the behavior of the indefinite integral in equation (16*b*) as $\zeta \to 0$. Figure 3(*a*) shows that the inverse solutions oscillate with increasing amplitude as the starting location is moved upstream. These particular calculations were performed with a step size $\Delta\zeta = 0.02$ but the same behavior was experienced for other values. In all cases the oscillations diminish with increasing ζ but not always to an acceptable extent. A preferred solution to this problem is to make use of equation (26), which yielded the results of Fig. 3(*b*) with the standard procedure used between two ζ stations corresponding to 0 and 0.01 and the inverse procedure used thereafter. The result is not subject to oscillations and was independent to step length for values less than 0.01.

Figure 4 shows the variations of the dimensionless wall shear parameter f_w'' and heat transfer rate θ_w' for Pr = 1 and for a range of Richardson numbers Ri. As expected, the wall shear parameter drops rapidly with increasing Richardson number and with dimensionless surface distance ζ. Separation is evident for Richardson numbers greater than around 0.055 and, in all cases, the recovery to an asymptotic value is initially rapid and latterly very slow. For example, a Richardson number of 0.02 leads to a minimum value of f_w'' around 0.24 at $\zeta = 3.75$ and requires a dimensionless length of around $\zeta = 200$ to recover from its minimum value to its asymptotic value of 0.332. The corresponding distributions of wall heat flux parameter θ_w' are shown in Fig. 4(*b*) and indicate a behavior similar to that of Table 1 up to the location where the wall ceases to be cooled. As ζ increases further, θ_w' increases rapidly to a maximum value from which it decreases to an asymptotic

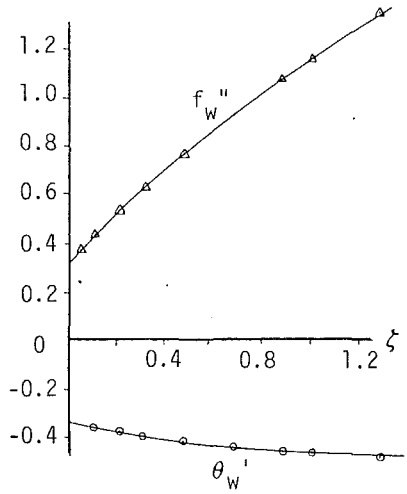

Fig. 2 Laminar flow results for the heated plate for Pr = 1.0, Ri = 0.4, $Re_L = 10^7$. Symbols denote the results of Merkin (1969).

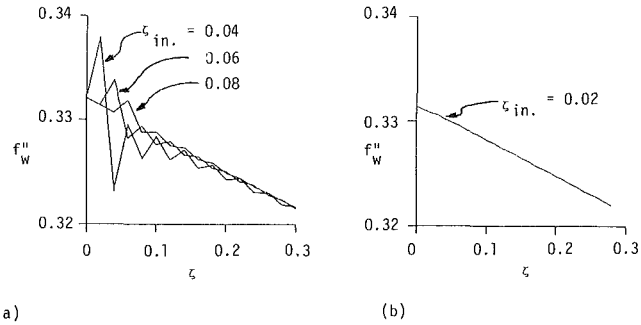

Fig. 3 Behavior of the inverse flow solutions close to the leading edge. Formulation with (*a*) equation (16*b*), (*b*) equation (26). $\zeta_{in.}$ denotes the location of the inverse flow calculations with $\Delta\zeta$ = 0.01.

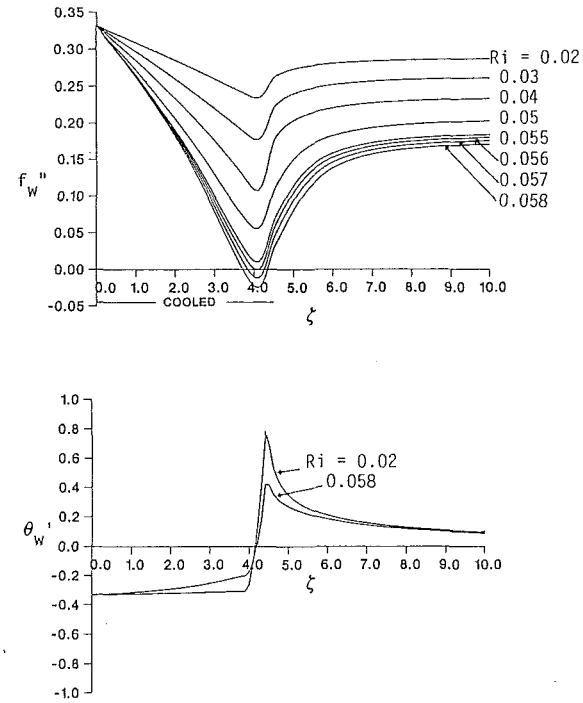

Fig. 4 Variations of dimensionless (*a*) wall shear parameter and (*b*) heat transfer rate; Pr = 1.0, $Re_L = 10^5$

value of zero, again after a distance equivalent to a value of ζ greater than 200.

Similar results, shown in Fig. 5, were obtained for a Prandtl

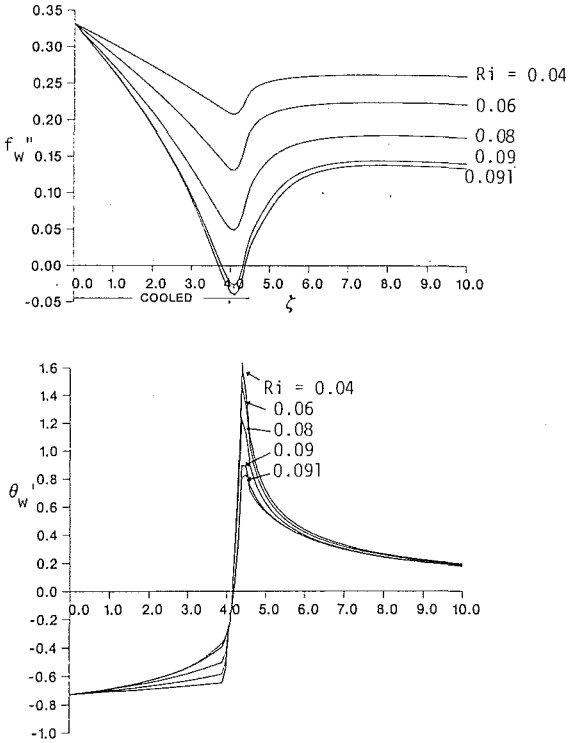

Fig. 5 Variations of dimensionless (*a*) wall shear parameter and (*b*) heat transfer rate; Pr = 10, $Re_L = 10^5$

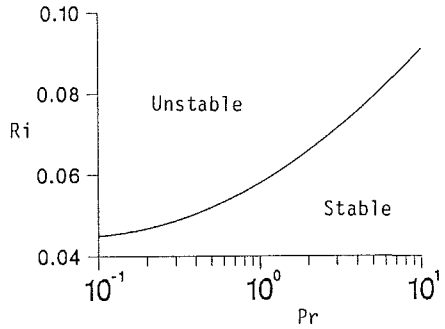

Fig. 6 Regions for which laminar flows can exist for $Re_L = 10^5$

number of 10 and in this case extend to Ri = 0.091. As expected, the values of wall shear parameter are similar for both Prandtl numbers, but the higher Prandtl number leads to heat transfer rates that are nearly twice as large. The limiting Richardson numbers of 0.058 and 0.091, corresponding to Prandtl numbers of 1 and 10, represent the lowest values for which stable solutions could be obtained. As described in the following subsection, the flows corresponding to limiting values are laminar but cannot remain laminar at lower Richardson numbers. Figure 6 shows the locus of values of Richardson number and Prandtl number for which stable laminar flow solutions could be obtained. Thus, the region indicated on the figure as unstable for $Re_L = 10^5$ requires that transition from laminar to turbulent flow be represented for solutions to exist. Similar results can be expected for other Reynolds numbers with a curve moving to the left as the Reynolds number is decreased.

4.3 Laminar, Transitional, and Turbulent Flows. The nature of the interactive boundary layer theory requires that the solutions begin at the leading edge and extend to the asymptotic region with successive sweeps on the plate to ensure that the viscous and inviscid flow equations are satisfied

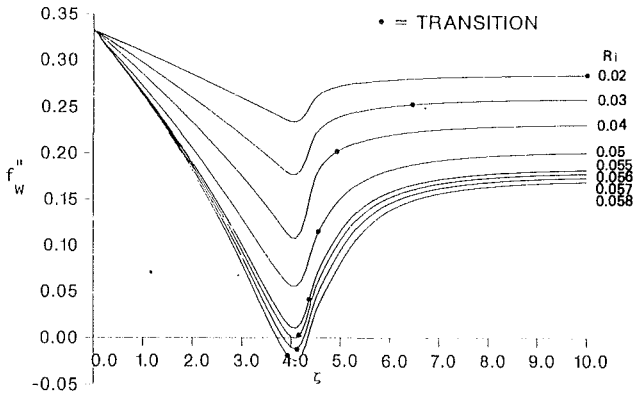

Fig. 7 Calculated locations of transition for Pr = 1.0, $Re_L = 10^5$

Table 2 Variation of transition location with calculation sweep for Ri = 0.059

Sweep	$(\zeta)_{tr}$
5	3.97113
10	3.90536
15	3.88998
20	3.8856

together with the boundary conditions. With a Prandtl number of unity, this led to the converged solutions of Fig. 4. Similar calculations at a Richardson number of 0.059 also led to flow separation but the length of the recirculation region grew with number of sweeps and the solution tended to oscillate. Figure 7 shows this unstable behavior, which is analogous to that of the laminar separation bubbles found on the leading edge of thin airfoils discussed by Cebeci et al. (1981) and Stewartson (1981). In physical terms, this numerical instability indicates that the flow is not real and transition occurs within the separated flow region as was shown by Cebeci (1989a). This conclusion is confirmed by the computed transition locations of Fig. 7 and obtained from the e^n method with $n = 9$. It is evident that the location of transition moves upstream with increasing Richardson number and occurs inside the separation bubble and close to the separation location for Ri = 0.058. Thus it can be expected that the results for values of ζ higher than those of transition will not exist for laminar flow.

The transition locations for Ri = 0.059 are shown for each sweep in Table 2 and confirm the expected tendency to move upstream toward the separation location. The implication is that the real flow is not laminar and will have a shorter recirculation region than shown in Fig. 7. It also suggests that, in common with the leading-edge separation bubbles computed at high angles of attack, there is little merit in expending effort to compute the large laminar flow bubbles that would be obtained with smaller Richardson numbers.

Figure 8 shows the results of interactive calculations for Richardson numbers of 0.058 and greater with transition computed with the e^n method and with turbulent flow assumptions beyond these locations. The calculation of transition locations involved iteration with successive laminar and turbulent calculations. It can be seen that with Ri = 0.058 and transition determined with the e^n method, there is no region of recirculating flow, in contrast to the result of Fig. 3, and the values of f''_w have increased substantially. The behavior of the heat transfer parameter is more complicated. The decrease in the value of θ'_w as ζ approaches 4, at which the boundary condition is changed, is consistent with that of Fig. 4(*b*), except that results could not be obtained at high values of Ri with laminar flow. The rapid rise in θ'_w is associated with the change in boundary condition and the subsequent decline is again similar to that for laminar flow but with a more rapid decay.

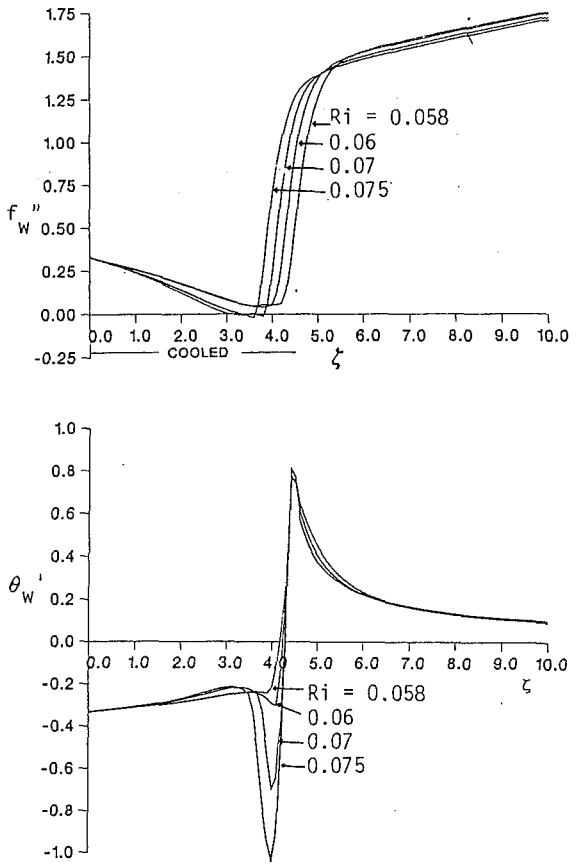

Fig. 8 Variation of dimensionless (a) wall shear parameter and (b) heat transfer rate for laminar, transitional, and turbulent flow, Pr = 1.0 $Re_L = 10^5$

The laminar flows of Fig. 4 and the laminar, transitional, and turbulent flows of Fig. 8 both show regions of recirculating flow; these tend to be smaller in the latter case. The occurrence of the onset of transition with a region of recirculating flow and the associated assumptions for the turbulence model for the transition region led to breakdown of the calculations for Ri > 0.075 for reasons similar to those encountered with the leading-edge separation bubbles of airfoils and could be removed by the assumptions described by Cebeci (1989b). As was discussed by Cebeci (1986b), the present intermittency expression was based on attached flows and is not expected to apply to flows in which transition is separation induced.

5.0 Concluding Remarks

The use of interactive boundary-layer theory is usually associated with external flows and the calculation of lift and drag. Here we have shown that it can be used for a mixed convection problem and indeed it is essential to the proper representation of convective heat transfer processes that involve flow separation. The results demonstrate that noninteractive calculations can lead to erroneous results in that the assumption of laminar flow can be made where it is physically implausible. We have shown that it is essential to perform calculations in an interacting manner, which involves determination of the transition location and the use of turbulent flow assumptions downstream of it.

The use of linear stability theory is also less common for problems of convective heat transfer but was necessary for the present mixed convection flows to determine the onset of turbulent flow. The resulting calculations are different from those of laminar flows and are extended to higher values of Richardson number.

Distributions of wall shear parameter and heat transfer rate are provided for a length Reynolds number of 10^5 and for a range of Richardson numbers and Prandtl numbers of 1 and 10. The influence of Prandtl number is greater for the heat transfer quantity. A locus is established for Richardson numbers for which stable laminar flow results can be obtained and it is argued that laminar flow cannot exist in the region of unstable solutions, and shown that the onset of transition can alter the laminar-flow results. In calculating these results, we have made use of an eddy-viscosity approach to represent turbulent diffusion and neglected temperature fluctuations and compressiblity. These simplifications are not expected to affect the calculated trends and do not influence the conclusions of the above paragraphs. The present interactive approach can readily be extended to involve higher-order turbulence models and improved stability assumptions if required.

References

Bradshaw, P., Cebeci, T., Whitelaw, J. H., 1981, *Engineering Calculation Methods for Turbulent Flows*, Academic Press, London.

Broniewski, D., 1988, "Mixed Convection With Transition and Separation," M.S. Thesis, California State University, Long Beach, CA.

Catherall, D., and Mangler, K. W., 1966, "The Integration of the Two-Dimensional Laminar Boundary-Layer Equations Past the Point of Vanishing Skin Friction," *J. Fluid Mech*, Vol. 26, pp. 163–182.

Cebeci, T., 1989a, "Numerical Instabilities in the Calculation of Laminar Separation Bubbles and Their Implications," *AIAA J.*, Vol. 27, pp. 656–658.

Cebeci, T., 1989b, "Essential Ingredients of a Method for Low-Reynolds-Number Airfoils," *AIAA J.*, Vol. 27, pp. 1680–1688.

Cebeci, T., and Bradshaw, P., 1977, *Momentum Transfer in Boundary Layers*, McGraw-Hill, New York.

Cebeci, T., and Bradshaw, P., 1984, *Physical and Computational Aspects of Convective Heat Transfer*, Springer-Verlag, New York.

Cebeci, T., Clark, R. W., Chang, K. C., Halsey, N. D., and Lee, K., 1986, "Airfoils With Separation and the Resulting Wakes," *J. Fluid Mech.*, Vol. 163, pp. 323–347.

Cebeci, T., and Egan, D. A., 1989, "Prediction of Transition Due to Isolated Roughness," *AIAA J.*, Vol. 27, pp. 870–875.

Cebeci, T., and Smith, A. M. O., 1974, *Analysis of Turbulent Boundary Layers*, Academic Press, New York.

Cebeci, T., Stewartson, K., and Williams, P. G., 1981, "Separation and Reattachment Near the Leading Edge of a Thin Airfoil at Incidence," AGARD CP 291, paper 20.

Chen, K. K., and Thyson, N. A., 1971, "Extension of Emmons' Spot Theory to Flows on Blunt Bodies," *AIAA J.*, Vol. 9, pp. 821–825.

Chen, T. S., Armaly, B. F., and Ali, M. M., 1987 "Turbulent Mixed Convection Along a Vertical Plate," ASME JOURNAL OF HEAT TRANSFER, Vol. 109, pp. 251–253.

Chen, T. S., and Mucoglu, A., 1979, "Wave Instability of Mixed Convection Flow Over a Horizontal Flat Plate," *Int. J. Heat Mass Transfer*, Vol. 22, pp. 185–196.

Keller, H. B., 1970, "A New Difference Scheme for Parabolic Problems," in: *Numerical Solution of Partial-Differential Equations*, J. Bramble, ed., Vol. II, Academic Press, New York.

Merkin, J. H., 1969, "The Effect of Buoyancy Forces on the Boundary-Layer Flow Over a Semi-infinite Vertical Flat Plate in a Uniform Freestream," *J. of Fluid Mech.*, Vol. 35, pp. 439–450.

Mucoglu, N., and Chen, T. S., 1978, "Wave Instability of Mixed Convection Flow Along a Vertical Flat Plate," *Numerical Heat Transfer*, Vol. 1, pp. 267–283.

Oosthuizen, P. H., 1974, "Turbulent Combined Convection Flow Over a Vertical Plane Surface," *Proceedings of the 5th International Heat Transfer Conference*, Vol. 3, pp. 129–133.

Seibers, D. I., Schwind, R. G., and Moffat, R. J., 1983, "Experimental Mixed Convection Heat Transfer From a Large Vertical Surface in a Horizontal Flow," Rept. No. HMT-36, Thermosciences Division, Dept. of Mechanical Engineering, Stanford University, Stanford, CA.

Smith, A. M. O., 1956, "Transition, Pressure Gradient and Stability Theory," *Proc. IX Intl. Congress Appl. Mech.*, Brussels, Vol. 4, pp. 234–244.

Stewartson, K., 1981, "D'Alembart's Paradox," *Siam Review*, Vol. 23, p. 308.

Van Ingen, J. L., 1956, "A Suggested Semi-empirical Method for the Calculation of the Boundary-Layer Transition Region," Rept. No. VTH71, VTH74, Delft, The Netherlands.

Veldman, A. E. P., 1981, "New, Quasi-Simultaneous Method to Calculate Interacting Boundary Layers," *AIAA J.*, Vol. 19, p. 79.

Mixed Thermal Convection of Power-Law Fluids Past Bodies With Uniform Fluid Injection or Suction

T.-Y. Wang

C. Kleinstreuer
Mem. ASME

Department of Mechanical and Aerospace Engineering,
N. C. State University,
Raleigh, NC 27695-7910

Steady laminar flow of power-law fluids past heated two-dimensional or axisymmetric bodies is strongly influenced by the rate of fluid mass transfer at the wall, the buoyancy force, and the characteristics of the power-law fluid. The effects of these parameters on the local skin friction group and heat transfer group are analyzed for wedges of different angles, horizontal cylinders, and spheres. The local heat transfer group, $HTG \sim Nu_x$, for wedge flows is greatly affected by the power-law viscosity index n, and by fluid withdrawal especially when the generalized Prandtl number is relatively high. Fluid suction at larger Prandtl numbers also generates high HTG values for cylinders and spheres. However, the local skin friction group, $SFG \sim c_f$, for cylinders or spheres increases with fluid injection and decreases with suction largely because of buoyancy effects.

1 Introduction

The analysis of laminar, two-dimensional or axisymmetric flow past heated or cooled bodies with porous walls is of interest in different engineering branches. Examples include boundary-layer control on airfoils, transpiration cooling of turbine blades, lubrication of ceramic machine parts, and food processing. Some of these applications involve non-Newtonian fluids, which can be approximated by the power-law viscosity model. The present study is an extension and generalization of our previous contributions, which do not include wedge flow configurations, fluid injection or suction, and the constant wall heat flux cases (Wang and Kleinstreuer, 1988a, 1988b).

In the past, researchers considered simpler systems that were solved using truncated series expansions, local similarity theory, or integral methods. Acrivos et al. (1960) were probably the first to study heat transfer in laminar boundary layer flows past external surfaces for non-Newtonian fluids with very large Prandtl numbers. Chen and Radulovic (1973) solved the nonsimilar problem of forced convection heat transfer in non-Newtonian flow past a wedge with nonisothermal surfaces in terms of an infinite set of similar solutions. Kim et al. (1983) employed a Merk-series expansion to analyze forced convection of a power-law fluid past isothermal bodies. The same problem was solved in a recent series of papers using a generalized integral method (Nakayama and Koyama, 1986; Shenoy and Nakayama, 1986; Nakayama et al., 1986). Lien et al. (1986) included fluid injection/suction in their analysis of forced convection of a Newtonian fluid past (rotating) bodies. The effect of mixed free-forced convection heat transfer was studied by Lin and Shih (1980) for power-law fluids moving along vertical plates and by Mucoglu and Chen (1977) and Chen and Mucoglu (1977) for Newtonian fluids past horizontal cylinders or spheres.

In this paper, steady laminar mixed thermal convection of power-law fluids past wedge-type or axisymmetric bodies with permeable walls is investigated. Of interest are the effects of the power-law index, the mass transfer parameter, the buoyancy parameter, the two distinct thermal boundary conditions, and the generalized Prandtl number on the local skin friction and heat transfer coefficients. Both heated and cooled body surfaces are being considered. A powerful transformation of the coupled nonlinear system equations allows an efficient and accurate solution based on an implicit finite difference scheme with Newton linearization.

2 Theory

Consider steady laminar upward boundary-layer flow of a power-law fluid past a permeable body with a surface temperature either higher or lower than the ambient temperature. Consequently, measurable buoyancy forces aid ($T_w > T$; $Z = 1$) or retard ($T_w < T$; $Z = -1$) forced convection. The resulting mixed (free-forced) convection heat transfer system can be further perturbed by wall injection or suction of non-Newtonian fluids at temperature T_w. The system is sketched in Fig. 1. The orthogonal coordinates x and y are measured from the forward stagnation point along the body surface and outward normal to the wall, respectively. Neglecting wake effects on the attached boundary layer, the governing equations, with the standard power-law viscosity model and Boussinesq assumption, are:

$$\frac{\partial}{\partial x}(r^\kappa u) + \frac{\partial}{\partial y}(r^\kappa v) = 0 \tag{1}$$

$$u\frac{\partial u}{\partial x} + v\frac{\partial u}{\partial y} = u_e\frac{du_e}{dx} + Zg\beta\,|T - T_\infty|\sin\phi$$

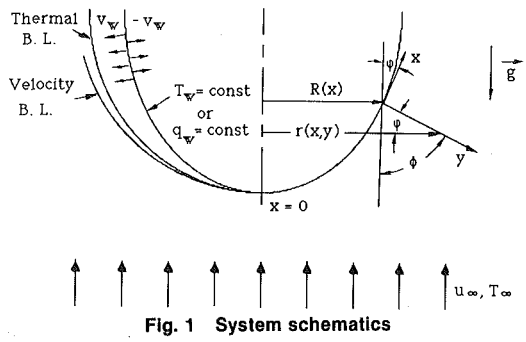

Fig. 1 System schematics

Contributed by the Heat Transfer Division and presented at the 25th National Heat Transfer Conference, Houston, Texas, July 24-27, 1988. Manuscript received by the Heat Transfer Division January 21, 1988. Keywords: Mass Transfer, Mixed Convection, Non-Newtonian Flows and Systems.

$$+\frac{K}{\rho r^{\kappa}}\frac{\partial}{\partial y}\left(r^{\kappa}\left|\frac{\partial u}{\partial y}\right|^{n-1}\frac{\partial u}{\partial y}\right) \quad (2)$$

$$u\frac{\partial T}{\partial x}+v\frac{\partial T}{\partial y}=\frac{\alpha}{r^{\kappa}}\frac{\partial}{\partial y}\left(r^{\kappa}\frac{\partial T}{\partial y}\right) \quad (3)$$

$$\psi = r^{\kappa}Lu_{\infty}\left(\frac{\xi}{\mathrm{Re}}\right)^{1/(n+1)}\left(\frac{u_{\infty}}{u_e}\right)^{(1-2n)/(n+1)}$$

$$F(\xi,\eta)-\int_0^x r^{\kappa}v_w dx \quad (6)$$

$$\theta(\xi,\eta)=\begin{cases}\dfrac{T-T_{\infty}}{T_w-T_{\infty}} & \text{for } T_w=\text{const} \quad (7a)\\[2ex] (T-T_{\infty})\left[\dfrac{q_wL}{k}\left(\dfrac{\xi}{\mathrm{Re}}\right)^{1/(n+1)}\left(\dfrac{u_e}{u_{\infty}}\right)^{(n-2)/(n+1)}\right]^{-1} & \text{for } q_w=\text{const} \quad (7b)\end{cases}$$

Here, κ is a "flow index" equal to unity in axisymmetric flow and zero in two-dimensional flow. In general, r is related to $R(x)$, the radius of the body surface, by

$$r(x,y)=R(x)+y\cos\varphi$$

where $\varphi(x)=\tan^{-1}(dR/dx)$ and $\cos\varphi=\sin\phi$. In boundary-layer flow, $R(x)$ is much larger than the boundary-layer thickness. The associated boundary conditions are

$$u=u_e(x) \text{ and } T=T_{\infty} \text{ at } y=\infty \quad (4a)$$

(*i*) For the constant wall temperature case

$$u=0,\ v=\pm v_w, \text{ and } T=T_w \text{ at } y=0 \quad (4b)$$

(*ii*) For the constant wall heat flux case

$$u=0,\ v=\pm v_w \text{ and } q_w=-k\frac{\partial T}{\partial y}\bigg|_{y=0} \text{ at } y=0 \quad (4c)$$

Based on our past experience, the following transformation parameters have been developed to reduce the x dependence and hence to facilitate the solution of this problem (cf. Kleinstreuer, 1990).

$$\xi=\frac{x}{L} \quad (5a)$$

$$\eta=\left(\frac{\mathrm{Re}}{\xi}\right)^{1/(n+1)}\left(\frac{u_e}{u_{\infty}}\right)^{(2-n)/(n+1)}\frac{y}{L} \quad (5b)$$

where Re is the generalized Reynolds number

$$\mathrm{Re}=\frac{\rho u_{\infty}^{2-n}L^n}{K} \quad (8)$$

with L being a characteristic body length. The stream function of equation (6), defined as

$$u=\frac{1}{r^{\kappa}}\frac{\partial\psi}{\partial y} \quad (9a)$$

and

$$v=-\frac{1}{r^{\kappa}}\frac{\partial\psi}{\partial x} \quad (9b)$$

automatically satisfies the continuity equation.

2.1 Constant Wall Temperature Case. The governing equations (2) and (3) together with the boundary conditions (4*a*) and (4*b*) are transformed to

$$(|F''|^{n-1}F'')'+\gamma(\xi)FF''+\Lambda(\xi)(1-F'^2)-MPD(\xi)F''$$
$$=-Z\theta\lambda_T\Omega(\xi)+\xi\left(F'\frac{\partial F'}{\partial\xi}-F''\frac{\partial F}{\partial\xi}\right) \quad (10)$$

and

$$\frac{E(\xi)}{\mathrm{Pr}}\theta''+\gamma(\xi)F\theta'-MPD(\xi)\theta'=\xi\left(F'\frac{\partial\theta}{\partial\xi}-\theta'\frac{\partial F}{\partial\xi}\right) \quad (11)$$

Nomenclature

c_f = local skin friction coefficient
F = dimensionless stream function
g = gravitational acceleration
h = local heat transfer coefficient
K = fluid consistency index for power-law fluid
k = thermal conductivity
L = characteristic length of body
MP = mass transfer parameter
Nu = local Nusselt number (based on L)
Nu_x = local Nusselt number (based on x)
n = index of power-law viscosity model
Pr = generalized Prandtl number
Re = generalized Reynolds number (based on L)
Re_x = generalized Reynolds number (based on x)
R = distance from a point on the surface to the axis of symmetry
R_c = radius of cylinder
R_s = radius of sphere
r = distance from a point in the fluid to the axis of symmetry
T = temperature
u = velocity component in x direction
v = velocity component in y direction
x = streamwise coordinate measured along surface from forward stagnation point
y = coordinate normal to surface
Z = dimensionless parameter; $Z=1$ for heated and $Z=-1$ for cooled submerged body
α = thermal diffusivity
β = thermal expansion coefficient
β^* = wedge angle
$\hat{\beta}$ = dimensionless wedge angle $=\beta^*/\pi$
η = dimensionless parameter (combined variable)
θ = dimensionless temperature
λ = buoyancy parameter
ξ = dimensionless parameter (streamwise coordinate)
ρ = density of fluid
τ = shear stress
ϕ = angle between the gravitational acceleration vector and the outward normal to the body surface
φ = angle shown in Fig. 1
ψ = stream function

Subscripts

e = boundary layer edge condition
T = constant wall temperature case
q = constant wall heat flux case
w = wall condition
∞ = ambient condition

subject to

$$F'(\xi, 0) = 0 \tag{12a}$$

$$F(\xi, 0) = 0 \tag{12b}$$

$$\theta(\xi, 0) = 1 \tag{12c}$$

and

$$F'(\xi, \infty) = 1 \tag{12d}$$

$$\theta(\xi, \infty) = 0 \tag{12e}$$

The primes in the foregoing equations denote differentiation with respect to η.

The system parameters include the generalized Prandtl number

$$\mathrm{Pr} = \frac{u_\infty L}{\alpha}\mathrm{Re}^{-2(n+1)} \tag{13a}$$

the buoyancy parameter for isothermal walls

$$\lambda_T = \mathrm{Gr}\mathrm{Re}^{-2/(2-n)} \tag{13b}$$

where

$$\mathrm{Gr} = \left(\frac{K}{\rho}\right)^{2/(n-2)} g\beta\,|T_w - T_\infty|\,L^{(2+n)/(2-n)} \tag{13c}$$

and the mass transfer parameter

$$MP = \pm\frac{v_w}{u_\infty}\mathrm{Re}^{1/(n+1)} \tag{13d}$$

The new coefficients in equation (10) and (11) are defined as

$$\Lambda(\xi) = \frac{\xi}{u_e}\frac{du_e}{d\xi} \tag{14a}$$

$$\gamma(\xi) = \begin{cases} \dfrac{1}{n+1} + \dfrac{2n-1}{n+1}\Lambda(\xi) & \text{for two-dimensional bodies} \quad (14b) \\ \dfrac{1}{n+1} + \dfrac{2n-1}{n+1}\Lambda(\xi) + \dfrac{\xi}{r}\dfrac{dr}{d\xi} & \text{for axisymmetric bodies} \quad (14c) \end{cases}$$

$$\Omega(\xi) = \frac{\xi\sin\phi}{(u_e/u_\infty)^2} \tag{14d}$$

$$D(\xi) = \xi^{n/(n+1)}\left(\frac{u_e}{u_\infty}\right)^{(1-2n)/(n+1)} \tag{14e}$$

$$E(\xi) = \left(\frac{u_e}{u_\infty}\right)^{3(1-n)/(n+1)} \xi^{(n-1)/(n+1)} \tag{14f}$$

With the definition of the local skin friction coefficient

$$c_f = \frac{2\tau_w}{\rho u_\infty^2}$$

a dimensionless skin friction group, SFG, can be formed as

$$\mathrm{SFG} \equiv \frac{1}{2}c_f\mathrm{Re}^{1/(n+1)} = \xi^{-n/(n+1)}\left(\frac{u_e}{u_\infty}\right)^{3n/(n+1)}[F''(\xi, 0)]^n \tag{15}$$

Similarly, using the Nusselt number as

$$\mathrm{Nu} = hL/k$$

a dimensionless heat transfer group can be formed as

$$\mathrm{HTG} \equiv \mathrm{NuRe}^{-1/(n+1)} = -\xi^{-1/(n+1)}\left(\frac{u_e}{u_\infty}\right)^{(2-n)/(n+1)}\theta'(\xi, 0) \tag{16}$$

For a specific problem solution, the shape of the body $R(x)$, its characteristic length L, and the outer flow distribution $u_e(x)/u_\infty$ have to be known.

2.2 Constant Wall Heat Flux Case. The uniquely transformed temperature for the thermal boundary condition $q_w = \mathrm{const}$ (cf. equation (7*b*)) causes slight changes in the transformed equations and boundary conditions when compared with the isothermal wall case. The momentum equation now reads

$$(|F''|^{n-1}F'')' + \gamma(\xi)FF'' + \Lambda(\xi)(1 - F'^2) - MPD(\xi)F''$$

$$= -Z\theta\lambda_q\Omega^*(\xi) + \xi\left(F'\frac{\partial F'}{\partial\xi} - F''\frac{\partial F}{\partial\xi}\right) \tag{17}$$

The energy equation becomes

$$\frac{E(\xi)}{\mathrm{Pr}}\theta'' + \gamma(\xi)F\theta' - N(\xi)F'\theta - MPD(\xi)\theta'$$

$$= \xi\left(F'\frac{\partial\theta}{\partial\xi} - \theta'\frac{\partial F}{\partial\xi}\right) \tag{18}$$

The corresponding boundary conditions are as simple as for the isothermal wall case because of equation (7*b*), viz.:

$$F'(\xi, 0) = 0 \tag{19a}$$

$$F(\xi, 0) = 0 \tag{19b}$$

and

$$\theta'(\xi, 0) = -1 \tag{19c}$$

$$F'(\xi, \infty) = 1 \tag{19d}$$

and

$$\theta(\xi, \infty) = 0 \tag{19e}$$

The buoyancy parameter for the constant wall heat flux case is

$$\lambda_q = \mathrm{Gr}^*\mathrm{Re}^{-(n+4)/[(n+1)(2-n)]} \tag{20a}$$

where

$$\mathrm{Gr}^* = \left(\frac{K}{\rho}\right)^{2/(n-2)} g\beta\left|\frac{q_w}{k}\right|L^{4/(2-n)} \tag{20b}$$

The new coefficients in equations (17) and (18) are

$$\Omega^*(\xi) = [\xi^{(n+2)/(n+1)}\sin\phi]\Big/\left(\frac{u_e}{u}\right)^{(n+4)/(n+1)} \tag{21a}$$

and

$$N(\xi) = \frac{1}{n+1} + \frac{n-2}{n+1}\Lambda(\xi) \tag{21b}$$

The local heat transfer group, HTG, is defined as

$$\mathrm{NuRe}^{-1/(n+1)} = \xi^{-1/(n+1)}\left(\frac{u_e}{u_\infty}\right)^{(2-n)/(n+1)}\Big/\theta(\xi, 0) \tag{22}$$

All other parameters, coefficients, and the skin friction group, SFG, are the same as given in Section 2.1.

3 Applications

In order to test the applicability of the general analysis, several thermal boundary-layer flow problems have been solved numerically using Keller's box method (Cebeci and Bradshaw, 1977). The heated or cooled bodies, i.e., Falkner-Skan wedge configurations, horizontal cylinders, and spheres, are immersed in a stream of pseudoplastics ($n<1$), Newtonian fluids ($n=1$), or dilatant fluids ($n>1$). The forced flow can be directed either upward or downward. In the latter case, the rear stagnation point becomes the origin of the orthogonal coordinate system. The momentum boundary layer is influenced by blowing or suction near the wall and by buoyancy forces, which in turn depend on the heating or cooling mode and the type of thermal boundary condition invoked. The structure of the thermal boundary layer is determined by both forced and free convection heat transfer as well as the degree and direction of wall mass transfer.

For each case study, the body shape, its characteristic length, and the outer flow distribution have to be given. The latter, i.e., u_e/u_∞, is typically independent of n, the power-law viscosity index. Results for each case study will be discussed in Section 5.

3.1 Wedge Flow. For a Falkner-Skan wedge flow configuration, $R(x)$is linear, $u_e(x)=Cx^m$, where C is a constant and $m=\hat{\beta}/(2-\hat{\beta})$ with $\hat{\beta}=\beta^*/\pi$ where β^* is the wedge angle. From the given geometry it can be deduced that $\phi=(\pi/2)(1-\hat{\beta})$. For a flat plate, $\hat{\beta}=m=0$.

Treating the two thermal boundary conditions together, certain coefficients of equations (14) and (21) can be reduced.

$$\Lambda(\xi)=m \tag{23a}$$

$$\Omega(\xi)=\xi\cos\frac{\pi\hat{\beta}}{2} \tag{23b}$$

$$D(\xi)=\xi^{n/(n+1)} \tag{23c}$$

$$E(\xi)=\xi^{(n-1)/(n+1)} \tag{23d}$$

$$\Omega^*=\xi^{(n+2)/(n+1)}\cos\frac{\pi\hat{\beta}}{2} \tag{23e}$$

With a local Reynolds number and local Nusselt number defined as

$$\mathrm{Re}_x=\frac{\rho u_e^{2-n}x^n}{K} \tag{24a}$$

$$\mathrm{Nu}_x=\frac{hx}{k} \tag{24b}$$

the skin friction group and the heat transfer group collapse to

$$\frac{1}{2}c_f\mathrm{Re}_x^{1/(n+1)}=[F''(\xi,0)]^n \tag{25}$$

and

$$\mathrm{Nu}_x/\mathrm{Re}_x^{1/(n+1)}=\begin{cases}-\theta'(\xi,0) & \text{for } T_w=\text{const} \quad (26a)\\ [\theta(\xi,0)]^{-1} & \text{for } q_w=\text{const} \quad (26b)\end{cases}$$

3.2 Horizontal Cylinder. For a cylinder, $R(x)=R_c\equiv L$, and an empirical edge velocity distribution (Shah et al., 1962)

$$\frac{u_e}{u_\infty}=0.92\frac{x}{R_c}-0.131\left(\frac{x}{R_c}\right)^3 \tag{27}$$

is assumed. From geometric considerations, $\phi=x/R_c=\xi$. Only one of the coefficients listed in Section 2 can be reduced, i.e.,

$$\Lambda(\xi)=1-0.262\xi^2/(0.92-0.131\xi^2) \tag{28}$$

3.3 Sphere. For a sphere, $R(x)=R_s\sin x/R_s$, where $R_s\equiv L$ and $\xi=x/R=\phi$. A suitable empirical outer flow expression can be found in White (1974)

$$\frac{u_e}{u_\infty}=1.5\xi-0.4371\xi^3+0.1481\xi^5-0.0423\xi^7 \tag{29}$$

The coefficients and parameters given in Section 2 remain basically the same.

4 Solution Method

The modeling equations (10) and (11) or (17) and (18) with the appropriate coefficients, for each individual case outlined in Section 3, were solved numerically using the two-point finite difference method described in Cebeci and Bradshaw (1977). The convergence criterion used was $|(\omega_i^{k+1}{}_j-\omega_{ij}^k)/\omega_{ij}^{k+1}|_{\max}<10^{-5}$, where ω^k and ω^{k+1} are the values of the kth and $(k+1)$th iteration of F, F', F'', θ, or θ'. A nonuniform mesh with a very fine grid spacing near the stagnation point was selected to obtain accurate velocity and temperature profiles. A total of 121 nodal points in the ξ direction and 144 grid points in the η direction were necessary in order to achieve mesh density independence of the results.

5 Results and Discussion

Because of the lack of experimental data sets for the present system, predictive results of reduced forms of our computer simulation model have been compared with accepted data found in the open literature.

5.1 Model Verification. Previously we reproduced (Wang and Kleinstreuer, 1988b) the SFG and HTG profiles published by Mucoglu and Chen for combined free-forced convection heat transfer of a Newtonian fluid across an impermeable, horizontal cylinder and impermeable sphere. In the same paper we presented a data table showing an excellent agreement of SFG values near the stagnation point, $\xi<0.5$, when compared with data points given by Kim et al. (1983) for forced convection of non-Newtonian fluids ($n=0.52$ and 1.6) across a horizontal, heated cylinder. However, for $\xi>0.5$ the results obtained by Kim et al. (1983) with a Merk-series expansion technique become somewhat erroneous, especially for pseudoplastics. In order to verify the accuracy of our extended computer simulation model, we compared our results with published data sets (Chen and Radulovic, 1973; Elzy and Sisson, 1967) for Newtonian wedge flow, $\hat{\beta}=1$ (Table 1).

In Table 2, our prediction for the separation angle for Newtonian flow past a sphere is compared with data compiled by White (1974). For reference purpose, the separation angles computed with the commonly used potential flow equation are included.

Table 1 Comparison of results of $\mathrm{Nu}_x\mathrm{Re}_x^{-1/(n+1)}$ for $n=1$, $\hat{\beta}=1.0$, $\lambda=0$, $MP=0$

Pr	Chen and Raduclovic (1973)	Elzy and Sisson (1967)	Present method
0.7	0.486	0.496	0.496
0.8	0.514	0.523	0.523
1.0	0.562	0.570	0.570
5.0	1.038	1.043	1.043
10.0	1.333	1.339	1.339
100.0	2.981	2.986	2.986
1000.0	6.523	6.529	6.528

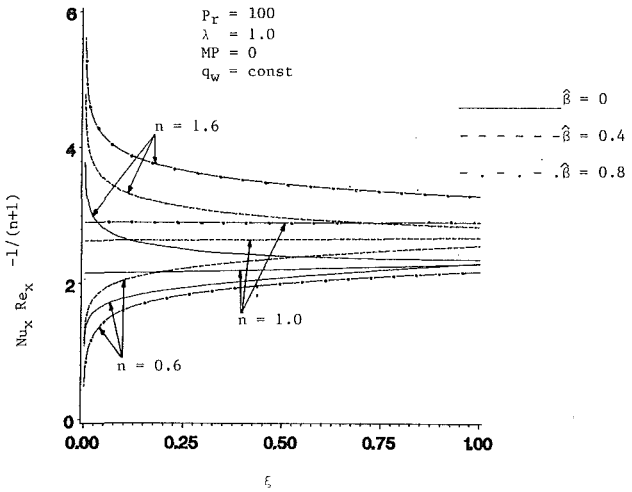

Fig. 2 Effect of wedge angle on heat transfer group for different fluids

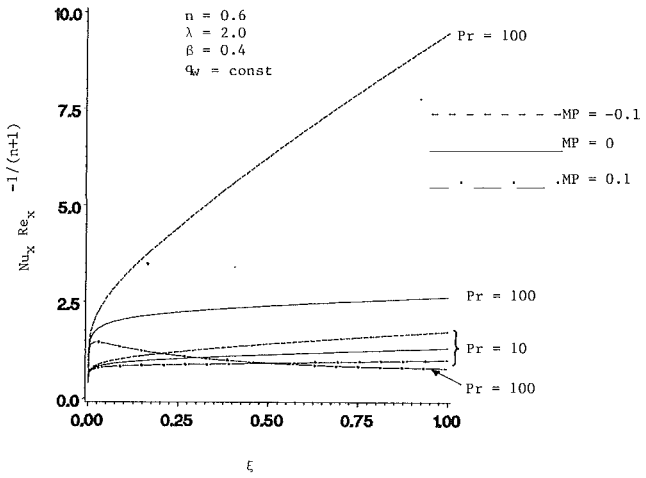

Fig. 3 Effect of mass transfer and generalized Prandtl number on HTG for pseudoplastics past a heated wedge

Table 2 Comparison of separation angles for Newtonian flow past a sphere*

Actual flow: equation (29)	
Series solution (Frossling, 1940; Scholkemeier, 1949)	79.5
Pohlhausen type (Tomotika and Imai, 1938)	84.0
Integral method (Rott and Crabtree, 1952)	81.0
Measurements (Fage, 1936)	83.0
Present method	81.9
Potential flow: $u_e/u_\infty = 1.5 \sin x/R$	
Series solution (Frossling, 1940; Scholkemeier, 1949)	109.6
Finite difference (Smith and Clutter, 1963)	105.9
Finite difference (Sheridan, 1968)	104.0
Integral method (Rott and Crabtree, 1952)	103.6
Present method	104.8

*References for Table 2 are given in White (1974)

5.2 Model Predictions. Of the numerous system parameters of interest (cf. Section 2), we concentrated on the effects of different body shapes, power-law fluids, generalized Prandtl numbers, and fluid injection/suction rates on the local heat transfer group, HTG, and the local skin friction group, SFG.

For wedge flow, a parametric sensitivity analysis showed that increases in both dimensionless wedge angle $\hat{\beta}$, and buoyancy parameter λ, result in higher SFG values for the two thermal boundary conditions. The SFG is higher for pseudoplastics than for dilatant fluids for a given λ and $\hat{\beta}$. The isothermal wall case, $T_w = \text{const}$, generates larger skin friction values than the constant wall heat flux condition, $q_w = \text{const}$, if $\lambda > 0$. When the buoyancy effect is negligible and at larger wedge angles, $\hat{\beta} > 0.8$, differences in SFG for the two thermal boundary conditions are less than 5 percent.

The local Nusselt number expressed in terms of HTG is almost independent of λ and differs strongly with the type of fluid used. Figure 2 shows the effect of the power law viscosity index n on HTG of a heated wedge ($q_w = \text{const}$) with impermeable surface and different wedge angles. The Newtonian fluid ($n = 1.0$) behavior differs, for a given $\hat{\beta}$, only slightly when compared with HTG = const for forced convection past a flat plate. These profiles are contrasted to those of a pseudoplastic ($n = 0.6$) and a dilatant fluid ($n = 1.6$). The HTG is very large near the stagnation point for power-law fluids with $n > 1.0$ and then decreases rapidly, whereas the HTG increases from very small values near $\xi = 0$ for fluids with $n < 1.0$. The effect of the wedge angle when compared with flat plate flow, $\hat{\beta} = 0$, is that the HTG of power-law fluids does not approach asymptotically Newtonian HTG values. When $\xi \to 0$, the coefficient of the highest derivative in equation (18), which ultimately determines $\text{Nu}_x \propto \xi^{(1-n)/(n+1)}[\theta(\eta = 0)]^{-1}$, as either very large for $n > 1$ or very small for $n < 1$ because the exponent in $E(\xi)/\text{Pr} \propto \xi^{2(1-n)/(n+1)}$ changes its sign when n changes from say, $n > 1$ to $n < 1$. Figure 3 depicts the effect of the mass transfer parameter, *MP*, i.e., fluid injection/suction at the wedge wall, on HTG. Pseudoplastics with higher Prandtl numbers have thinner boundary layers, which implies steeper temperature gradients or lower wall temperatures, and hence injection and especially suction of fluid at the wall influences HTG(ξ) more drastically.

Figures 4 and 5 show for horizontal cylinders with a constant wall heat flux the effect of the mass transfer parameter MP on SFG for a pseudoplastic of different Prandtl numbers. The trend of SFG(ϕ) for dilatant fluids is very similar. Fluid injection increases SFG with a dramatic impact of the generalized Prandtl number while fluid withdrawal decreases the local skin friction coefficient. Previously, the opposite trend for SFG with respect to MP was shown to be true for pure forced convection (Wang and Kleinstreuer, 1988a). Thus, the buoyancy force may reverse the impact of fluid injection/suction on SFG. For the heat transfer group (Fig. 5) injection reduces HTG(ϕ) and suction increases HTG(ϕ) when $\lambda > 0$. The reason is that suction shifts the temperature profile while pulling cooler fluid toward the cylinder surface. This results in steeper wall temperature gradients for $T_w = \text{const}$ when $\text{HTG} \sim \theta'(\eta = 0)$ or lower surface temperatures for $q_w = \text{const}$ when $\text{HTG} \sim 1/[\theta(\eta = 0)]$.

The fluid dynamics and heat transfer of a sphere subject to a constant wall heat flux (Fig. 6) are somewhat similar to those of the horizontal cylinder. Mixed thermal convection between power-law fluids and a heated or cooled sphere/horizontal cylinder for the isothermal wall case is discussed in another paper (Wang and Kleinstreuer, 1988b).

Considering spheres and cylinders, rather comprehensive correlations for local Nusselt number distributions, i.e., $\text{Nu} = \text{Nu}(x/R, \text{Re}, \text{Pr}, \lambda, n, \text{etc.})$ are being developed based on elaborate computer experiments (Kleinstreuer and Wang, 1988).

Conclusions

Mixed convection heat transfer between power-law fluids and two-dimensional or axisymmetric bodies with two distinct thermal boundary conditions are analyzed. With newly developed coordinate transformations and dimensionless groups based on scale analysis, the complexity of the governing equations plus boundary conditions has been significantly reduced. An implicit finite difference scheme has been used to

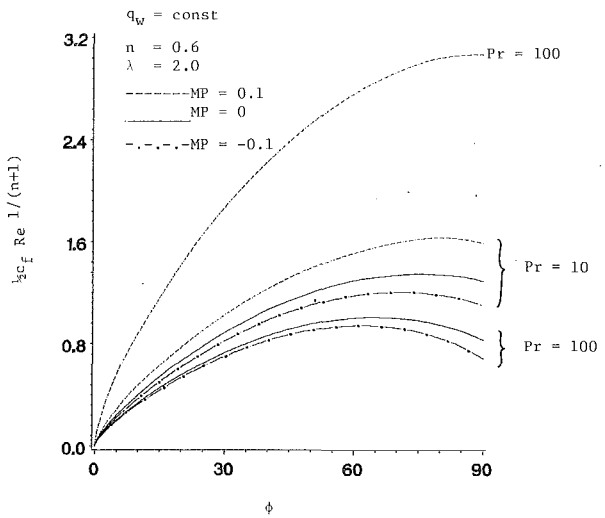

Fig. 4 Effect of mass transfer and generalized Prandtl number on SFG for pseudoplastics past a heated cylinder

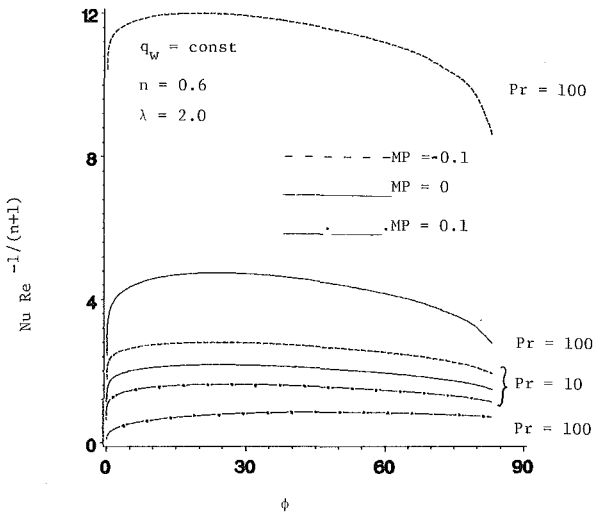

Fig. 5 Effect of mass transfer and generalized Prandtl number on HTG for pseudoplastics past a heated cylinder

provide a general, accurate, and relatively simple computer simulation model for the analysis of steady laminar thermal boundary-layer flow of power-law fluids.

Of interest are the effects of the buoyancy parameter, the power-law index, the fluid mass transfer parameter, the type of thermal boundary condition, and the generalized Prandtl number on the velocity and temperature fields as well as on the local skin friction and heat transfer coefficients. The results can be summarized as follows:

- The powerful transformation reduces the numerical work required to solve the coupled nonlinear set of equations significantly.
- The buoyancy force may shift the roles of injection/suction effects with respect to the local skin friction coefficient. This phenomenon is most evident for strong buoyancy-assisted flows away from the stagnation point.
- The generalized Prandtl number has a pronounced effect on the heat transfer group, especially in the presence of fluid withdrawal.
- The type of non-Newtonian fluid, i.e., pseudoplastic versus dilatant fluid, affects the local Nusselt number most distinctively near the stagnation point.
- The trends of SFG and HTG are very similar for the two thermal boundary conditions.

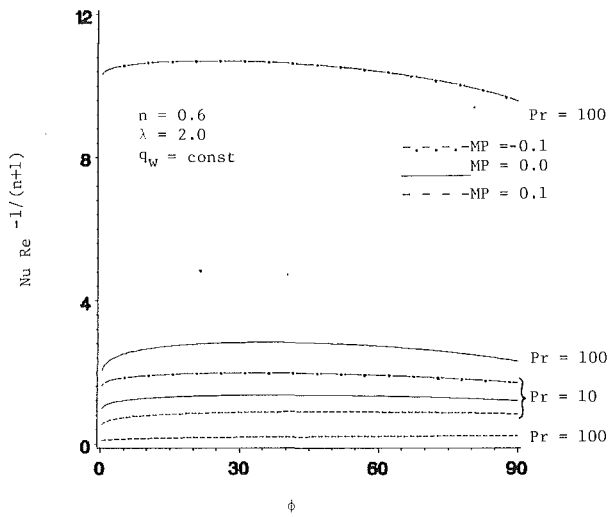

Fig. 6 Effect of mass transfer and generalized Prandtl number on HTG for pseudoplastics past a heated sphere

Acknowledgment

This research was supported in part by the Department of Energy, Basic Energy Science, Grant No. DE-FG05-87ER13728.

References

Acrivos, A., Shah, M. J., and Peterson, E. E., 1960, "Momentum and Heat Transfer in Laminar Boundary-Layer Flow of Non-Newtonian Fluids Past External Surfaces," *AIChEJ*, Vol. 6, pp. 312–317.

Cebeci, T., and Bradshaw, P., 1977, *Momentum Transfer in Boundary Layers*, Hemisphere Publishing Corp., Washington, DC.

Chen, J. L. S., and Radulovic, P. T., 1973, "Heat Transfer in Non-Newtonian Flow Past a Wedge With Non-isothermal Surfaces," ASME Journal of Heat Transfer, Vol. 95, pp. 498–504.

Chen, T. S., and Mucoglu, A., 1977, "Analysis of Mixed Forced and Free Convection About a Sphere," *Int. J. Heat Mass Transfer*, Vol. 20, pp. 867–875.

Elzy, E., and Sisson, R. M., 1967, "Tables of Similar Solutions to the Equations of Momentum, Heat and Mass Transfer in Laminar Boundary Layer Flow," Engineering Experiment Station Bulletin No. 40, Oregon State University, Corvallis, OR.

Kim, H. W., Jeng, D. R., and DeWitt, K. J., 1983, "Momentum and Heat Transfer in Power-Law Fluid Flow Over Two-Dimensional or Axisymmetric Bodies," *Int. J. Heat Mass Transfer*, Vol. 26, pp. 245–259.

Kleinstreuer, C., and Wang, T.-Y., 1988, "Mixed Thermal Convection of Power-Law Fluids Past Standard Bodies With Suction/Injection and Axisymmetric Body Rotation," *Proceedings of the 25th National Heat Transfer Conference*, Houston, TX, July 24–27, H. R. Jacobs, ed., ASME HTD-Vol. 96, Part 2, pp. 27–32.

Kleinstreuer, C., 1990, *Engineering Fluid Dynamics—An Interdisciplinary Systems Approach*, Springer-Verlag, New York, in press.

Lien, F. S., Chen, C. K., and Cleaver, J. W., 1986, "Forced Convection Over Rotating Bodies With Blowing and Section," *AIAA J.*, Vol. 24, pp. 854–856.

Lin, H. T., and Shih, Y. P., 1980, "Combined Laminar Free and Forced Convection From a Vertical Plate to Power Law Fluids," *Chem. Eng. Comm.*, Vol. 7, pp. 327–334.

Mucoglu, A., and Chen, T. S., 1977, "Analysis of Combined Forced and Free Convection Across a Horizontal Cylinder," *Canadian J. Chem. Eng.*, Vol. 55, pp. 265–271.

Nakayama, A., and Koyama, H., 1986, "An Asymptotic Expression for Forced Convection in Non-Newtonian Power-Law Fluids," *Int. J. Heat and Fluid Flow*, Vol. 7, pp. 99–101.

Nakayama, A., Shenoy, A. V., and Koyama, H., 1986, "An Analysis for Forced Convection Heat Transfer From External Surfaces to Non-Newtonian Fluids," *Wärme und Stoffübertragung*, Vol. 20, pp. 219–227.

Shah, M. J., Peterson, E. E., and Acrivos, A., 1962, "Heat Transfer From a Cylinder to Power-Law Fluid," *AIChE Jl.*, Vol. 8, pp. 542–549.

Shenoy, A. V., and Nakayama, A., 1986, "Forced Convection Heat Transfer From Axisymmetric Bodies to Non-Newtonian Fluids," *Canadian J. Chem. Eng.*, Vol. 64, pp. 680–686.

Wang, T.-Y., and Kleinstreuer, C., 1988a, "Combined Free-Forced Convection Heat Transfer Between Vertical Slender Cylinders and Power-Law Fluids," *Int. J. Heat Mass Transfer*, Vol. 31, pp. 91–98.

Wang, T.-Y., and Kleinstreuer, C., 1988b, "Analysis of Local Skin Friction and Heat Transfer Groups for Mixed Thermal Convection Across a Horizontal Cylinder or Sphere," *Int. J. Heat & Fluid Flow*, Vol. 19, No. 2, pp. 182–187.

White, F. M., 1974, *Viscous Fluid Flow*, McGraw-Hill, New York.

Non-Darcian Boundary Layer Flow and Forced Convective Heat Transfer Over a Flat Plate in a Fluid-Saturated Porous Medium

A. Nakayama

T. Kokudai

H. Koyama

Department of Energy and Mechanical Engineering, Shizuoka University, 3-5-1 Johoku, Hamamatsu, 432 Japan

The local similarity solution procedure was successfully adopted to investigate non-Darcian flow and heat transfer through a boundary layer developed over a horizontal flat plate in a highly porous medium. The full boundary layer equations, which consider the effects of convective inertia, solid boundary, and porous inertia in addition to the Darcy flow resistance, were solved using novel transformed variables deduced from a scale analysis. The results from this local similarity solution are found to be in good agreement with those obtained from a finite difference method. The effects of the convective inertia term, boundary viscous term, and porous inertia term on the velocity and temperature fields were examined in detail. Furthermore, useful asymptotic expressions for the local Nusselt number were derived in consideration of possible physical limiting conditions.

Introduction

Flow and heat transfer within porous media are of great practical interest. Applications include chemical reactors, thermal storage systems, thermal insulation, petroleum reservoirs, nuclear waste, etc. A considerable number of publications is now available for the problems of free convection in porous media. Forced convection boundary layer flow, however, has received less attention so far, in spite of its importance in many practical thermal systems, such as geothermal reservoirs, where a pressure gradient exists due to withdrawal or reinjection of fluids. In the present study, we shall focus on one of the most fundamental forced convection problems, namely, the problem of forced convection boundary layer flow over a flat plate in a fluid-saturated porous medium.

The Darcy model (which assumes proportionality between the velocity and pressure gradient) has been extensively used to investigate a number of interesting fluid and heat transfer problems associated with heated bodies embedded in fluid-saturated porous media (e.g., Wooding, 1963; Cheng, 1978; Cheng and Minkowycz, 1977). The model, however, is valid only for slow flows through porous media with low permeability. Muskat (1946) added a velocity square term (known as the Forchheimer term) to account for the porous inertia effect on the pressure drop, while Brinkman (1948) introduced a viscous diffusion term to consider the boundary frictional drag on impermeable walls.

Treating a fluid-saturated porous medium as a continuum, Vafai and Tien (1981) integrated the momentum equation for a fluid over a local control volume, and derived a volume-averaged momentum equation. This generalized momentum equation for non-Darcy flows reveals the importance of the convective inertia term for highly porous materials. Subsequently, Chen et al. (1987) evoked the boundary layer approximations and solved the generalized equation to investigate free convection from a vertical flat plate in a highly porous medium, while the corresponding forced convection problem was treated by Kaviany (1987), who employed the finite difference calculation procedure developed by Cebeci and Bradshaw (1984). Kaviany also employed the Kàrmàn–Pohlhausen integral relation and obtained useful asymptotic expressions for the local Nusselt number. He, however, dropped the Forchheimer term in his finite difference calculations.

In this paper, non-Darcian forced convection over a flat plate is treated. The aforementioned generalized momentum and energy equations in a full boundary layer form are solved using novel transformed variables deduced from a scale analysis (Bejan, 1984). The effects of the non-Darcy terms, namely, the convective inertia term, Forchheimer term (i.e., porous inertia term) and Brinkman term (i.e., boundary friction term) on the velocity and temperature fields are investigated in detail. Furthermore, asymptotic expressions for the local Nusselt number are furnished in consideration of physical limiting conditions.

Governing Equations

Using the boundary layer coordinates (x, y) shown in Fig. 1, the full set of governing equations, namely, the continuity equation, the generalized momentum equation, and the energy equation, may be written as follows (note that the boundary layer equations become invalid in the vicinity of the leading edge):

$$\frac{\partial u}{\partial x} + \frac{\partial v}{\partial y} = 0 \tag{1}$$

$$u\frac{\partial u}{\partial x} + v\frac{\partial u}{\partial y} = -\frac{\epsilon^2}{\rho}\frac{dp}{dx} + \epsilon\nu\frac{\partial^2 u}{\partial y^2} - \epsilon^2\frac{\nu}{k}u - \epsilon^2\frac{C}{\sqrt{K}}u^2 \tag{2}$$

$$u\frac{\partial T}{\partial x} + v\frac{\partial T}{\partial y} = \alpha\frac{\partial^2 T}{\partial y^2} \tag{3}$$

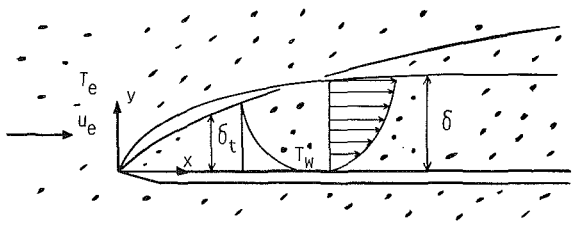

Fig. 1 Physical model and its coordinate system

Contributed by the Heat Transfer Division for publication in the JOURNAL OF HEAT TRANSFER. Manuscript received by the Heat Transfer Division March 16, 1988. Keywords: Forced Convection, Porous Media.

In the foregoing equations, u and v are the apparent (Darcian) velocity components in the x and y directions, while p and T are the local pressure and temperature; ρ and ν are the density and kinematic viscosity of the fluid; K is the permeability; ϵ, the porosity; α the effective thermal diffusivity of the porous medium; and C, an empirical constant. In the left-hand side of the momentum equation (2), the convective inertia terms are present, while the pressure gradient term, Brinkman term, Darcy term, and Forchheimer term (i.e., porous inertia term) appear in the right-hand side. Since K becomes infinite for $\epsilon = 1$, equation (2) reduces to the usual boundary layer equation for Newtonian fluids. The appropriate boundary conditions are

$$y=0: \quad u=v=0, \quad T=T_w \tag{4a, b}$$

$$y\to\infty: \quad u=u_e, \quad T=T_e \tag{4c, d}$$

where the external Darcian velocity u_e, the ambient temperature T_e and the wall temperature T_w are all constants.

Scale Analysis

We shall seek appropriate length scales implicit in the governing equations, and use them to transform the equations. Let us write the momentum equation at the boundary layer edge

$$-\frac{\epsilon^2}{\rho}\frac{dp}{dx} = \epsilon^2\left(\frac{\nu}{K}u_e + \frac{C}{\sqrt{K}}u_e^2\right) \equiv \lambda u_e^2 \tag{5a}$$

where

$$\lambda = \epsilon^2\left(1+\frac{1}{\mathrm{Re}_K}\right)\frac{C}{\sqrt{K}} \tag{5b}$$

and

$$\mathrm{Re}_K = C\sqrt{K}\,u_e/\nu \tag{5c}$$

is the Reynolds number based on the permeability. λ is related to the pressure gradient caused by the solid matrix. Obviously, λ vanishes for a flow over a flat plate without a porous medium. $1/\lambda$ may be chosen to be the streamwise length scale. The momentum equation (2) is rewritten as

$$u\frac{\partial u}{\partial x} + v\frac{\partial u}{\partial y} = \epsilon\nu\frac{\partial^2 u}{\partial y^2} - \epsilon^2\left(\frac{\nu}{K}u + \frac{C}{\sqrt{K}}u^2\right) + \lambda u_e^2 \tag{6}$$

In the boundary layer developing region, the convective inertia term is as significant as the boundary viscous term, so that

$$\epsilon\nu\frac{\partial^2 u}{\partial y^2} \sim u\frac{\partial u}{\partial x} \tag{7a}$$

Hence, the boundary layer thickness δ may be on the order of

$$\delta \sim (\epsilon\nu x/u_e)^{1/2} \tag{7b}$$

In the fully developed region, on the other hand, the convective inertia term can be neglected. Thus, the viscous term roughly balances with the pressure gradient term

$$\epsilon\nu\frac{\partial^2 u}{\partial y^2} \sim \lambda u_e^2 \tag{8a}$$

$$\delta \sim (\epsilon\nu/\lambda u_e)^{1/2} \tag{8b}$$

Hence, the viscous boundary layer thickness increases as $\delta \propto \sqrt{x}$ in the developing region, and approaches its upper bound in the fully developed region. The foregoing scale analysis can also be performed for the energy equation, and we find the thermal boundary layer thickness

$$\delta_t \sim (\alpha x/u_e)^{1/2} \tag{9}$$

Thus, the thermal boundary layer thickness grows as $\delta_t \propto \sqrt{x}$ without a bound.

The fact that the viscous boundary layer grows in a manner quite different from that of the thermal boundary layer makes it difficult to apply the usual coordinate transformations. In the following section, we shall introduce a novel transformation procedure and solve the momentum and energy equations under the local similarity assumption.

Solution to the Momentum Equation

Upon noting that the viscous boundary layer grows according to equations (7b) and (8b), we introduce the following transformed variables for the momentum equation:

$$\xi = \lambda x \tag{10a}$$

and

$$\eta = \frac{y}{x}(\mathrm{Re}_x/I)^{1/2} \tag{10b}$$

where

$$\mathrm{Re}_x = u_e\,x/\epsilon\,\nu \tag{10c}$$

and

$$I = \frac{1-e^{-\xi}}{\xi} \tag{10d}$$

The transformed streamwise coordinate $\xi = (p(0)-p(x))/\rho(u_e/\epsilon)^2$ corresponds to the pressure coefficient. The function I defined by equation (10d) yields $\eta \cong y/(\epsilon\,\nu\,x/u_e)^{1/2}$ (i.e., $I \cong 1$) for $\xi \ll 1$ and $\eta \cong y/(\epsilon\,\nu/\lambda\,u_e)^{1/2}$ (i.e., $I \cong 1/\xi$) for $\xi \gg 1$. (The function I can also be deduced from the integral procedure proposed in the study of Darcian free convective flows: Nakayama and Koyama, 1987). Re_x is the local Reynolds number based on the pore velocity u_e/ϵ.

Nomenclature

C = empirical constant for Forchheimer term
C_{fx} = local skin friction coefficient
f = dimensionless stream function
I = function to adjust the boundary layer length scale
K = permeability
Nu_x = local Nusselt number
p = pressure
Pr = Prandtl number
Re_K = Reynolds number based on the permeability
Re_x = Reynolds number based on the pore velocity
T = temperature
u, v = Darcian velocity components
x, y = boundary layer coordinates
α = effective thermal diffusivity
δ = boundary layer thickness
ϵ = porosity
ξ, η = transformed coordinates
θ = dimensionless temperature
λ = reciprocal of the streamwise length scale
ν = kinematic viscosity of the fluid
ρ = density of the fluid
ψ = stream function

Subscripts

e = external
t = thermal
x = based on x

Now, let us introduce the stream function ψ such that the continuity equation (1) is automatically satisfied

$$\psi(x, y) = \epsilon \nu (\mathrm{Re}_x I)^{1/2} f(\xi, \eta) \tag{11a}$$

Hence,

$$u = \frac{\partial \psi}{\partial y} = u_e f' \tag{11b}$$

and

$$v = -\frac{\partial \psi}{\partial x} = \frac{\epsilon \nu}{x} (\mathrm{Re}_x/I)^{1/2} \left[\frac{1}{2} e^{-\xi} (\eta f' - f) - (1 - e^{-\xi}) \frac{\partial f}{\partial \xi} \right] \tag{11c}$$

where the prime denotes differentiation with respect to η. After some manipulation, we can transform the momentum equation (2) into

$$f''' + \frac{1}{2} e^{-\xi} f f'' - (1 - e^{-\xi}) \left[\frac{f' + \mathrm{Re}_K (f')^2}{1 + \mathrm{Re}_K} - 1 \right] = (1 - e^{-\xi}) \left(f' \frac{\partial f'}{\partial \xi} - f'' \frac{\partial f}{\partial \xi} \right) \tag{12}$$

The boundary conditions, equations (4a) and (4b) can be rewritten in terms of the transformed variables as

$$\eta = 0: \quad f = f' = 0 \tag{13a}$$

$$\eta \to \infty: \quad f' = 1 \tag{13b}$$

Let us consider equation (12) for $\xi \ll 1$ (which is always the case in the entrance region)

$$f''' + \frac{1}{2} f f'' = 0 \tag{14}$$

Thus, for this case, we obtain the well-known Blasius similarity solution. On the other hand, for $\xi \gg 1$ (which can be met in a nearly developed region), equation (12) reduces to

$$f''' - \frac{f' + \mathrm{Re}_K (f')^2}{1 + \mathrm{Re}_K} + 1 = 0 \tag{15}$$

Hence, this case also permits similarity solutions. However, in general, the right-hand side terms in equation (12), which contain ξ derivatives, do not vanish. These right-hand side terms, however, are expected to be small enough for the local similarity assumption (Sparrow and Yu, 1971) to be valid. Thus, dropping them, we have

$$f''' + \frac{1}{2} e^{-\xi} f f'' - (1 - e^{-\xi}) \left[\frac{f' + \mathrm{Re}_K (f')^2}{1 + \mathrm{Re}_K} - 1 \right] = 0 \tag{16}$$

Since all coefficients can be evaluated for given ξ, we can easily integrate equation (16), and exploit any standard shooting procedure to find $f''(\xi, 0)$. The validity of this local similarity assumption will be examined by comparing the results against the nonsimilar results obtained from finite difference calculations.

Once $f''(\xi, 0)$ is found, the local skin friction coefficient C_{fx} can be evaluated from

$$C_{fx} = \epsilon \nu \frac{\partial u}{\partial y}\Big|_{y=0} \Big/ \frac{1}{2} u_e^2 = 2 f''(\xi, 0)/(\mathrm{Re}_x I)^{1/2} \tag{17}$$

$f''(\xi, 0)$ possesses the following asymptotic values:

$$f''(0, 0) = 0.332 \tag{18a}$$

$$f''(\infty, 0)\,|_{\mathrm{Re}_K = 0} = 1 \tag{18b}$$

$$f''(\infty, 0)\,|_{\mathrm{Re}_K \to \infty} = 1.155 \tag{18c}$$

The asymptotic values in equations (18a) and (18c) were obtained from numerical integrations, while equation (18b) was derived from the velocity profile function:

$$f' = 1 - e^{-\eta} \tag{19}$$

which satisfies equation (15) when $\mathrm{Re}_K = 0$.

Solution to the Energy Equation

In consideration of the proportional relationship (equation (9)) from the scale analysis, we introduce the following transformations for the energy equation:

$$T - T_e = (T_w - T_e)\theta(\xi, \eta_t) \tag{20a}$$

where

$$\eta_t = \frac{y}{x} \mathrm{Re}_x^{1/2} (= \sqrt{I}\,\eta) \tag{20b}$$

The subscript t refers to as thermal boundary layer. Thus, the energy equation and its boundary conditions can be transformed into

$$\frac{1}{\epsilon \mathrm{Pr}} \theta'' + \frac{1}{2} \sqrt{I} f \theta' = \xi \left[(\sqrt{I} f)' \frac{\partial \theta}{\partial \xi} - \theta' \frac{\partial}{\partial \xi} (\sqrt{J} f) \right] \tag{21}$$

subjected to

$$\eta = 0 \quad : \quad \theta = 1 \tag{22a}$$

$$\eta \to \infty \quad : \quad \theta = 0 \tag{22b}$$

where $\mathrm{Pr} = \nu/\alpha$ is the Prandtl number based on the effective thermal diffusivity of the fluid-saturated porous medium. The primes, here, indicate differentiation with respect to η_t (not to η).

As we did for the momentum equation, we shall consider the energy equation (21) for the case of $\xi \ll 1$. Since the right-hand-side terms can be neglected for small ξ, we have

$$\frac{1}{\epsilon \mathrm{Pr}} \theta'' + \frac{1}{2} f \theta' = 0 \tag{23}$$

Thus, for small ξ, we obtain the well-known flat plate flow solution for Newtonian fluids. (The Prandtl number, here, corresponds to the product $\epsilon \mathrm{Pr}$.) Let us further note that, in the limiting case of $\xi \gg 1$, the terms $\partial/\partial\xi$ $(f/\sqrt{I})$ and $\partial\theta/\partial\xi$ become small. The foregoing consideration of the two kinds of physical limiting condition prompts us to drop the right-hand-side terms on the basis of the local similarity approximation:

$$\frac{1}{\epsilon \mathrm{Pr}} \theta'' + \frac{1}{2} \sqrt{I} f \theta' = 0 \tag{24}$$

Equation (24) under the boundary conditions given by equations (22a) and (22b) yields the local similarity solution as follows:

$$\theta(\xi, \eta_t) = \frac{\int_{\eta_t}^{\infty} \exp\left[-\frac{1}{2} \epsilon \mathrm{Pr} \sqrt{I} \int_0^{\eta_t} f(\xi, \eta_t/\sqrt{I}) d\eta_t \right] d\eta_t}{\int_0^{\infty} \exp\left[-\frac{1}{2} \epsilon \mathrm{Pr} \sqrt{I} \int_0^{\eta_t} f(\xi, \eta_t/\sqrt{I}) d\eta_t \right] d\eta_t} \tag{25}$$

This integral expression enables us to find $\theta(\xi, \eta_t)$ by integrating the $f(\xi, \eta)$ distribution already obtained in the preceding chapter. Once the $\theta(\xi, \eta_t)$ distributions are found, the local Nusselt number of the primary concern may readily be evaluated from

$$\mathrm{Nu}_x/\mathrm{Re}_x^{1/2} = -x \frac{\partial \theta}{\partial y}\Big|_{y=0} / \mathrm{Re}_x^{1/2} = -\theta'(\xi, 0) = \left[\sqrt{I} \int_0^{\infty} \exp\left(-\frac{1}{2} \epsilon \mathrm{Pr} I \int_0^{\eta} f(\xi, \eta^*) d\eta^* \right) d\eta \right]^{-1} \tag{26}$$

By virtue of the present transformation based on the variables

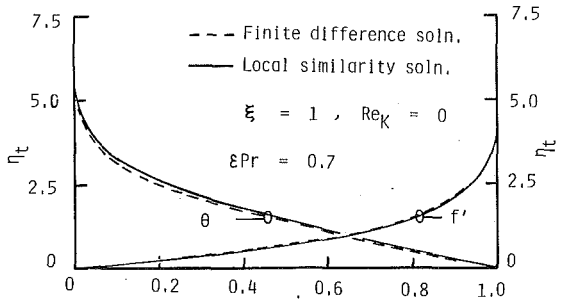

Fig. 2 Velocity and temperature profiles

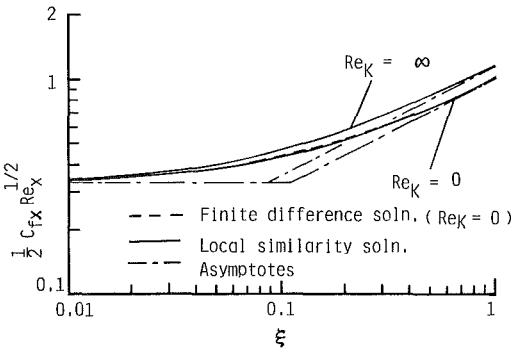

Fig. 3 Local skin friction coefficient

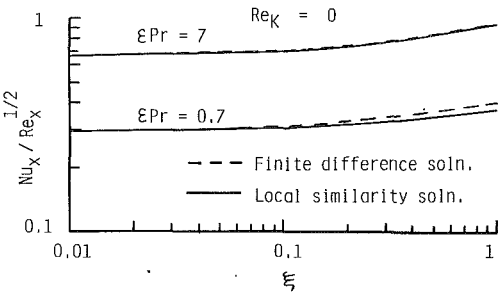

Fig. 4 Local Nusselt number

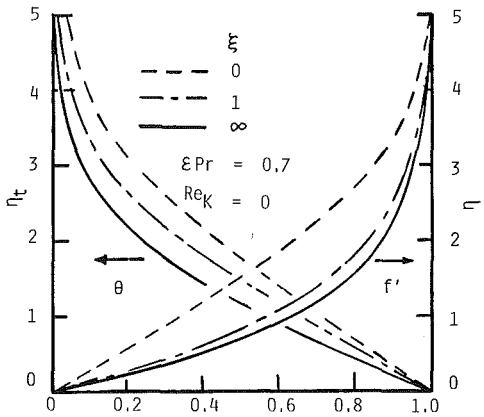

Fig. 5 Influence of the convective inertia

ξ, η, and η_t, only three parameters, namely, ξ, Re_K, and $\epsilon\mathrm{Pr}$ are required to determine the heat transfer function $\mathrm{Nu}_x/\mathrm{Re}_x^{1/2}$.

Equation (26) suggests that the heat transfer function depends strongly on the lumped parameter $\epsilon\mathrm{Pr}I$, which may well be taken as an equivalent Prandtl number for the case of porous media. When the product $\epsilon\mathrm{Pr}I$ is small, we may use the slug flow approximation, namely,

$$f'(\xi, \eta) = 1 \tag{27a}$$

Substitution of the foregoing equation into equation (26) yields

$$\theta(\xi, \eta_t) = 1 - \mathrm{erf}\left(\frac{1}{2}(\epsilon\,\mathrm{Pr})^{1/2}\eta_t\right) \tag{27b}$$

where erf( ) denotes the error function. When the product $\epsilon\,\mathrm{Pr}I$ is large, we may assume a linear velocity profile across the thin thermal boundary layer

$$f'(\xi, \eta) = f''(\xi, 0)\eta \tag{28a}$$

Hence, for this case, we have

$$\theta(\xi, \eta_t) = 1 - \frac{3}{\Gamma(1/3)}\int_0^{\zeta} e^{-\zeta^3}d\zeta\Big|_{\zeta=\left[\frac{1}{12}\frac{\epsilon\mathrm{Pr}}{\sqrt{I}}f''(\xi,0)\right]^{1/3}\eta_t} \tag{28b}$$

where $\Gamma(\ )$ is the gamma function such that $1/3\ \Gamma(1/3) = 0.893$.

Results and Discussion

Examination of the Local Similarity Solution. In Fig. 2, the results from the proposed local similarity solution are compared against the finite difference calculation results obtained by Kaviany (1987) for the case of $\mathrm{Re}_K = 0$, $\epsilon\mathrm{Pr} = 0.7$, and $\xi = 1$, in which the deviation from similarity is expected to be most significant. The ordinate variables for both θ and f' are set to η_t so that a direct comparison against Kaviany's solution is possible. A reasonable agreement between the local similarity solution and finite difference solution can be seen from the figure.

Figure 3 shows the skin friction function $1/2\ C_{fx}\,\mathrm{Re}_x^{1/2} = f''(\xi, 0)/\sqrt{I}$ in the range $0.01 \le \xi \le 1$. Kaviany's finite difference solution without the Forchheimer term (shown by the dashed line) overlaps onto the present local similarity solution for $\mathrm{Re}_K = 0$. The asymptotes given by equations (18) are also indicated in the figure. The skin friction function increases in proportion to $\xi^{1/2}$ as ξ grows big, since the wall shear stress attains a constant value in the fully developed region. The total pressure drop increases with Re_K (i.e., the ratio of the Forchheimer drag to the Darcy drag), since $-1/\rho\ dp/dx = (\nu\, u_e/K)\ (1 + \mathrm{Re}_K)$. The effect of Re_K, however, does not reflect on the skin friction function as markedly. The fully developed skin friction function for $\mathrm{Re}_K = \infty$ differs from that for $\mathrm{Re}_K = 0$ only by the factor of 1.155, as seen in equation (18c).

The local Nusselt numbers evaluated from the present local similarity solution are compared in Fig. 4 against Kaviany's numerical calculation results for the case of $\mathrm{Re}_K = 0$. The present solution and Kaviany's solution for the high Prandtl number case are almost indistinguishable.

The foregoing examination of the flow and heat transfer results substantiates the validity of the proposed local similarity assumption.

Influence of the Convective Inertia. The velocity and temperature profiles for $\xi = 0$, 1, and ∞ with $\epsilon\mathrm{Pr} = 0.7$ and $\mathrm{Re}_K = 0$ are shown in Fig. 5 to investigate the influence of the convective inertia. Since the transformed variable ξ increases with either λ (i.e., the pressure drop) or x (i.e., the streamwise distance from the leading edge), the effects of both the pressure gradient and flow development on the velocity and temperature profiles can be examined from the figure. The velocity profile changes from the Blasius profile at $\xi = 0$ to the profile given by equation (19) on increasing ξ. (Note that the ordinate variable η is proportional to y/δ in which δ increases downstream as discussed in the scale analysis.) The convective inertia appears to be significant only in the entrance region

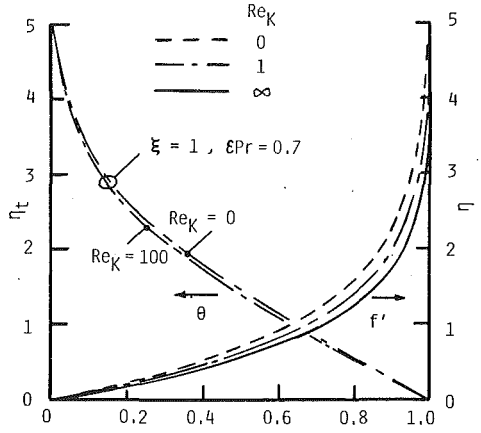

Fig. 6 Influence of the porous inertia

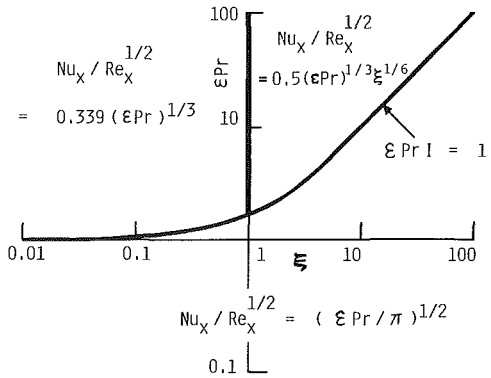

Fig. 7 Regime diagram for asymptotic formulas

where ξ is less than unity. Correspondingly, the temperature across the boundary layer alters its profile. As ξ becomes large, the temperature distribution closely follows the error function given by equation (27*b*).

Influence of the Porous Inertia. Equation (16) suggests that the influence of the porous inertia (Re_K) becomes appreciable as ξ grows large, so that equation (16) reduces to (15). The velocity profiles obtained by integrating equation (15) are plotted in Fig. 6 for $Re_K = 0$, 1, and ∞. As the drag due to the porous inertia increases with Re_K, the velocity profile becomes somewhat more uniform. The effect of Re_K on the velocity profile, however, does not seem to be significant. The analytical expression, equation (19) for $Re_K = 0$, in fact, can be a good approximation for all cases of large ξ.

The temperature profiles obtained with $\xi = 1$ and $\epsilon \mathrm{Pr} = 0.7$ are also plotted in Fig. 6 for two different values of Re_K, namely, $Re_K = 0$ and 100. This vast difference in Re_K does not reflect on the temperature profiles so markedly. The function $\theta(\xi, \eta_t)$ actually has been found quite insensitive to the porous inertia, for all ranges of ξ. The reason for this insensitivity can be explained as follows. We already know that the porous inertia effect on the dimensionless velocity profile is appreciable only in large ξ range. However, in this range, the thermal boundary layer grows so thick that the slug flow approximation holds, and hence the dimensionless temperature profile follows the error function (equation (27*b*)), irrespectively of the Re_K value. (Note that $\epsilon \mathrm{Pr}\, I = \epsilon \mathrm{Pr}(1 - e^{-\xi})/\xi \ll 1$ for $\xi \gg 1$.)

Asymptotic Expressions for the Local Nusselt Number. Kaviany (1987) employed the Kàrmàn–Pohlhausen integral relation, and derived asymptotic expressions for the local Nusselt number. However, the integral shape parameters he introduced to subdivide the regime do not seem very convenient to use. Furthermore, there is some uncertainty in the multiplicative constants of his expressions due to the approximations involved in the integral analysis of this kind.

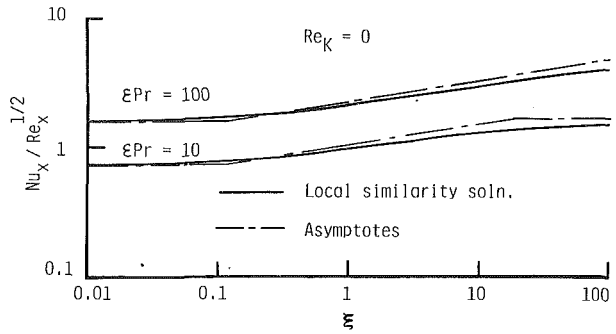

Fig. 8 Local similarity solution and its asymptotes

By virtue of the present local similarity transformation, we can easily extract asymptotic formulas from equations (27*b*), (28*b*), and (18), depending on the values of $\epsilon \mathrm{Pr} I$ and ξ.

For $\epsilon \mathrm{Pr} I \gg 1$ and $\xi \ll 1$:

$$\mathrm{Nu}_x/\mathrm{Re}_x^{1/2} = 0.339\ (\epsilon\ \mathrm{Pr})^{1/3} \tag{29a}$$

For $\epsilon \mathrm{Pr} I \gg 1$ and $\xi \gg 1$:

$$\mathrm{Nu}_x/\mathrm{Re}_x^{1/2} = \begin{cases} 0.489\ (\epsilon\ \mathrm{Pr})^{1/3}\xi^{1/6} & (\mathrm{Re}_K \ll 1) \quad (29b) \\ 0.513\ (\epsilon\ \mathrm{Pr})^{1/3}\xi^{1/6} & (\mathrm{Re}_K \gg 1) \quad (29c) \end{cases}$$

$$\cong 0.5(\epsilon\ \mathrm{Pr})^{1/3}\xi^{1/6} \tag{29d}$$

For $\epsilon \mathrm{Pr} I \ll 1$:

$$\mathrm{Nu}_x/\mathrm{Re}_x^{1/2} = (\epsilon \mathrm{Pr}/\pi)^{1/2} \tag{29e}$$

The effect of the porous inertia (Re_K) does appear on the local Nusselt number when $\epsilon\ \mathrm{Pr} I \gg 1$ and $\xi \gg 1$. The difference in the multiplicative constants, however, is so small that equation (29*d*) may be used for this regime, irrespectively of the Re_K value. Figure 7 illustrates the three regimes where the asymptotic formulas, namely, equations (29*a*), (29*d*), and (29*e*) are applicable. Equation (29*a*) turns out to be identical to the well-known high Prandtl number formula, except that the Prandtl number is replaced by the product $\epsilon \mathrm{Pr}$ to account for the porous medium. The formula can be used for the boundary layer developing region of high Prandtl number fluid. Equation (29*d*) is valid for the regime bounded by $\epsilon\ \mathrm{Pr} I > 1$ and $\xi > 1$. In this regime, the thermal boundary layer is still thin enough for the high Prandtl number approximation to be valid, while the velocity boundary layer attains its fully developed stage. The third regime bounded by $\epsilon \mathrm{Pr} I < 1$ corresponds to the slug (Darcian) flow regime, in which the low Prandtl number approximation is valid, and hence, θ is given by the error function. Vafai and Thiyagaraja (1987) and Beckermann and Viskanta (1987) studied the fully developed flow and heat transfer, corresponding to the case for $\xi \gg 1$ in our analysis. Their expressions for the low Prandtl number case appear to be identical to our asymptotic expression (29*a*). The high Prandtl number expressions derived by them under Leveque's approximation also reduce to our asymptotic expression (29*d*), except that the value 0.5384 (which is very close to ours, namely, 0.5) has been assigned to the multiplicative constant in their expressions.

In order to examine the validity of the foregoing asymptotic formulas, the heat transfer resutls based on the local similarity solution are presented in Fig. 8 along with the asymptotes given by equations (29*a*), (29*d*), and (29*e*), for $\epsilon \mathrm{Pr} = 10$ and 100. Since the asymptotic formulas provide fairly good approximations to the local similarity solutions, these formulas can be exploited for all practical estimations of local heat transfer rates.

Concluding Remarks

The full boundary layer equations were analyzed to investigate forced convection from a horizontal flat plate embedded in a fluid-saturated porous medium. The momentum equation, which includes the convective inertia term, the Forchheimer term, and the Brinkman term in addition to the Darcy term, was solved by means of the local similarity solution using novel transformed variables deduced from a scale analysis. Excellent agreement was found between the local similarity solution and the finite difference solution.

The convective inertia effect appears on the velocity and temperature profiles in the boundary layer developing region (where ξ is less than unity). In the downstream region (with large ξ), the porous inertia becomes appreciable on the velocity profile, but its effect on the temperature profile seems insignificant, since all temperature distributions for large ξ must follow the error function.

Furthermore, the asymptotic formulas for the local Nusselt number were extracted in consideration of physical limiting conditions. These asymptotic formulas can be quite useful for estimating local heat transfer rates.

References

Beckermann, C., and Viskanta, R., 1987, "Forced Convection Boundary Layer Flow and Heat Transfer Along a Flat Plate Embedded in a Porous Medium," *Int. J. Heat Mass Transfer*, Vol. 30, pp. 1547–1551.

Bejan, A., 1984, *Convective Heat Transfer*, Wiley, New York, pp. 17–20.

Brinkman, H. C., 1948, "A Calculation of the Viscous Force Exerted by a Flowing Fluid on a Dense Swarm of Particles," *Appl. Scient. Res.*, Vol. A1, p. 81.

Cebeci, T., and Bradshaw, P., 1984, *Physical and Computational Aspects of Convective Heat Transfer*, Springer-Verlag, New York, pp. 406–428.

Chen, C. K., Hung, C. I., and Cleaver, J. W., 1987, "Non-Darcian Effects on Vertical-Plate Transient Natural Convection in Porous Media With High Porosities," *Proc. 1987 ASME-JSME Thermal Eng. Joint Conf.*, Vol. 2, pp. 313–318.

Cheng, P., 1978, "Heat Transfer in Geothermal Systems," *Advances in Heat Transfer*, Vol. 14, pp. 1–105.

Cheng, P., and Minkowycz, W. J., 1977, "Free Convection About a Vertical Flat Plate Embedded in a Saturated Porous Medium With Application to Heat Transfer From a Dike," *J. Geophysics Res.*, Vol. 82, pp. 2040–2044.

Kaviany, M., 1987, "Boundary Layer Treatment of Forced Convection Heat Transfer From a Semi-infinite Flat Plate Embedded in Porous Media," ASME JOURNAL OF HEAT TRANSFER, Vol. 109, pp. 345–349.

Muskat, M., 1946, *The Flow of Homogeneous Fluids Through Porous Media*, Edwards, MI.

Nakayama, A., and Koyama, H., 1987, "Free Convective Heat Transfer Over a Non-isothermal Body of Arbitrary Shape Embedded in a Fluid-Saturated Porous Medium," ASME JOURNAL OF HEAT TRANSFER, Vol. 109, pp. 125–130.

Sparrow, E. M., and Yu, H. S., 1971, "Local Non-similarity Thermal Boundary Layer Solutions," ASME JOURNAL OF HEAT TRANSFER, Vol. 93, pp. 328–334.

Vafai, K., and Thiyagaraja, R., 1987, "Analysis of Flow and Heat Transfer at the Interface Region of a Porous Medium," *Int. J. Heat Mass Transfer*, Vol. 30, pp. 1391–1405.

Vafai, K., and Tien, C. L., 1981, "Boundary and Inertia Effects on Flow and Heat Transfer in Porous Media," *Int. J. Heat Mass Transfer*, Vol. 24, pp. 195–203.

Wooding, R. A., 1963, "Convection in a Saturated Porous Medium at Large Rayleigh Number or Peclet Number," *J. Fluid Mech.*, Vol. 15, pp. 527–544.

Investigation of High-Intensity Beam Characteristics on Welding Cavity Shape and Temperature Distribution

P. S. Wei
Professor.

T. H. Wu
Graduate Student.

Y. T. Chow
Graduate Student.

Institute of Mechanical Engineering,
National Sun Yat-Sen University,
Kaohsiung, Taiwan

A model for investigating the characteristics of a high-intensity beam on welding cavity shape and temperature distribution is developed. The beam power density is assumed to have a Gaussian distribution. The local heat transfer rate to the liquid–vapor interface depends on this distribution and on the interface contour. This contour as determined by an iterative procedure involves simultaneously satisfying the heat conduction rate into the liquid and equilibrium of the normal forces. Computed shapes of the cavity and the free surface temperature distributions agree well with experimental data. The beam energy flux distribution parameter is found to have the strongest effect on the welding process. The predicted dimensionless curve of the beam power-penetration depth parameter versus the welding velocity-thermal property parameter is also in accord with experimental results. The use of the energy flux distribution parameter instead of the fusion zone width at the workpiece surface for the welding velocity-thermal property parameter is recommended.

Introduction

During high-intensity beam (electron or laser beam) welding processes the beam creates a narrow vapor-filled cavity. A description and analysis of the penetrating process has recently been presented by Wei and Chiou (1988). Energy from the beam is absorbed in the liquid layer surrounding this cavity and transferred to the solid primarily by conduction (Wei and Giedt, 1985). Latent heat effects due to melting and evaporation have been shown to be negligibly small (Wei and Ho, 1988).

During quasi-steady state, welding cavity depth-to-width ratios of 5 to 10 or greater are commonly achieved. This type of deep penetration welding has recently been reviewed by Giedt and Tallerico (1988). Basically, two approaches have been developed. One is the application of the moving-line source solution (Rosenthal, 1941; Swift-Hook and Gick, 1973); the second is the use of a moving elliptical cylinder at the melt temperature (Tong and Giedt, 1971; Miyazaki and Giedt, 1982). Giedt and Tallerico (1988) compared these two solutions by introducing the melt isotherm into the moving-line source solution. It is interesting to find that these solutions overlap with the line source solution, agreeing with a cylindrical boundary at low welding speeds and crossing toward more elongated elliptical melt boundaries with increasing welding speed. Curves for both solutions applied to conical shaped fusion zones were also presented. Although available data fell along these curves, there was considerable scatter. In view of this a simple logarithmic relation was proposed to represent the variation of penetration with welding speed and surface fusion zone width parameter.

The scatter of experimental data for the depth of penetration may be of the order of ±30 to 40 percent or greater. Such significant errors depend on the precision in machine settings. Giedt and Tallerico (1988) modified their empirical equation to estimate the effects of beam focus coil current and focus coil to work distance. An uncertainty analysis was then used to investigate the sensitivity of errors caused by the variation of beam voltage, current, welding speed, focus coil current, and work distance. It was found that the first priority for controlling depth of penetration is the beam focus location. This essentially determines the energy flux distribution and suggests the need for a detailed investigation of the influence of the energy flux distribution in high-intensity beam welding. This was the objective of the present study.

In this study, a quasi-steady-state model accounting for three-dimensional heat flow is developed for predicting the liquid–vapor interface contours and temperature distributions in a high-intensity beam welding cavity. Effects of beam power, energy flux distribution, and welding speed variations are investigated. The importance of the beam energy flux distribution parameter is demonstrated, and the use of the parameter in controlling penetration is also proposed.

System Model and Analysis

As illustrated in Fig. 1(A), a semi-infinite workpiece is moving at a constant speed u relative to the energy beam. A quasi-steady deep and narrow vapor-filled cavity is supported by energy transfer from the beam. A cylindrical coordinate system is adopted with r, ϕ, z measured from and along the beam axis as shown in Fig. 1(B). The major assumptions made are:

1 Any horizontal cross section of the cavity is assumed to be a circle of radius $\bar{r}(z)$. This is reasonable because of the effect of surface tension.

2 The energy deposited can be considered a surface source. Since the cavity wall is very steep, electrons that reach the wall directly will have large incident angles. Most of these will be scattered after depositing some energy. Electrons that do penetrate the surface will be those that have been slowed by one or more interactions with the cavity surface. The penetration of the electron beam in the liquid layer can therefore be considered negligible.

3 The liquid surface temperature at any depth is assumed to be uniform. It is recognized that some variation must occur in order to provide a surface tension or pressure gradient (or both) to cause fluid flow. Results of Wei and Giedt (1985) in-

Contributed by the Heat Transfer Division for publication in the JOURNAL OF HEAT TRANSFER. Manuscript received by the Heat Transfer Division September 28, 1987. Keywords: Laser Processing, Materials Processing and Manufacturing Processes, Phase-Change Phenomena.

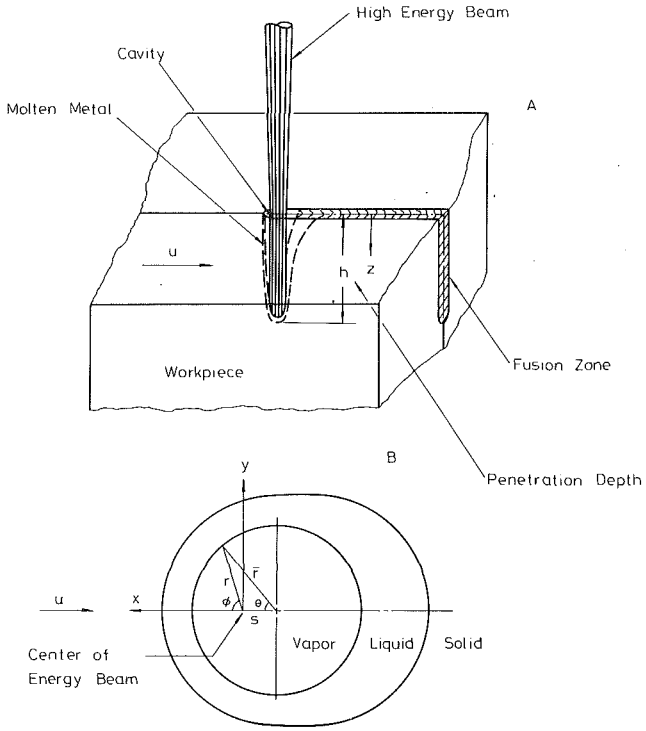

Fig. 1 Schematic sketch of (A) the high-energy beam welding process, and (B) the coordinate system

dicate that the maximum surface temperature variation of the liquid in the front of the cavity is on the order of 50 to 100°C. Such variations are small compared to liquid surface temperatures of 2000°C.

4 The radiation and the evaporation energy losses are assumed to be negligible. The radiative loss can be estimated to be only 0.2 percent of the beam power of 3 kW at a typical cavity radius of 1 mm and a cavity surface temperature of 2350 K. The evaporation rate measured by Hashimoto and Matsuda (1965a) for drilling aluminum was 6.2×10^{-7} kg/s. Hence the evaporation energy loss was approximately 0.4 percent of the beam power.

5 Heat convected by the molten metal has been shown to be negligible (Wei and Giedt, 1985). Also, the latent heat of melting is small compared to the beam power and is neglected (Wei and Ho, 1988). Thermal and physical properties are evaluated at an average temperature between the ambient and the melting temperatures.

Energy Balance at Cavity Wall. With the above assumptaions, the energy balance at the vapor-liquid interface becomes

$$\eta q \bar{r}\, d\theta\, d\bar{r} = k\,\frac{\partial T}{\partial n}\,\bar{r}\, d\theta\, dl \tag{1}$$

where the energy transfer coefficient η is assumed equal to 1. The energy flux incident on the workpiece is assumed to be described by

$$q = \frac{3Q}{\pi\sigma^2}\exp\left(-\frac{3r^2}{\sigma^2}\right) \tag{2}$$

where σ is an energy flux distribution parameter that defines the region in which 95 percent of the total heat is deposited. The following relationship between r, $\bar{r}$, s, and θ is illustrated in Fig. 1(B):

$$r^2 = \bar{r}^2 + s^2 - 2\bar{r}s\cos\theta \tag{3}$$

The local temperature gradient on the right-hand side of equation (1) can be expressed as

$$\frac{\partial T}{\partial n} = \frac{\partial T}{\partial \bar{r}}\frac{dz}{dl} - \frac{\partial T}{\partial z}\frac{d\bar{r}}{dl} \tag{4}$$

where the cavity is assumed to be axisymmetric. This will be verified later because the beam axis generally coincides with the axis of the cavity. The cavity surface temperature is assumed to be uniform at any depth z, and the temperature field is assumed to be given by the solution for a constant temperature cylinder moving in a direction perpendicular to its axis through an infinite medium (Carslaw and Jaeger, 1959; Tong and Giedt, 1971). This solution can be expressed as

$$\frac{T_c - T}{T_c - T_\infty} = 1 - \exp\left(\frac{-u\sqrt{r^2+s^2+2rs\cos\phi}\,\cos\theta}{2\alpha}\right)$$

$$\sum_{n=0}^{\infty}\xi_n\frac{I_n(A)}{K_n(A)}\cdot K_n\left(\frac{u\sqrt{r^2+s^2+2rs\cos\phi}}{2\alpha}\right)\cos n\theta \tag{5}$$

Nomenclature

A = $u\bar{r}/2\alpha$
ξ = gravitational acceleration
h = cavity depth
h_{lg} = latent heat of evaporation
I_n = modified Bessel function of the first kind and of order n
k = liquid thermal conductivity
K_n = modified Bessel function of the second kind and of order n
k_s = solid thermal conductivity
l = depthwise coordinate along cavity surface
n = normal to cavity surface toward workpiece
p, p_b = vapor pressure and boiling vapor pressure
q = beam energy flux
Q = beam power
r = polar coordinate
R = specific gas constant
R_1, R_2 = principal curvatures of cavity surface
$\bar{r}$ = cavity radius
s = distance between energy beam and center of cavity shown in Fig. 1(B)
T, T_b, T_c = temperature, boiling and constant temperature
T_m = melting temperature
T_∞ = ambient temperature
u = welding speed
w = fusion zone width at workpiece surface
x, y, z = coordinates shown in Fig. 1
α = liquid thermal diffusivity
α_s = solid thermal diffusivity
γ, γ_m = surface tension and surface tension at melting temperature; $\gamma = \gamma_m + (d\gamma/dT)(T - T_m)$, where $d\gamma/dT$ is a constant
δ = ellipse axis ratio
η = energy transfer efficiency
θ = angle shown in Fig. 1(B)
ρ = density
σ = energy flux distribution parameter
ϕ = polar coordinate shown in Fig. 1(B)

Superscripts

m = iteration number

Subscripts

i = grid number in depthwise direction on cavity surface

where $\xi_0 = 1$ and $\xi_n = 2$ if $n \geq 1$. Note that this result implies two-dimensional conduction and that the same average thermal properties apply to both the liquid and solid regions. Differentiating equation (5) yields the temperature gradient at the liquid-vapor surface at any z and θ as

$$\frac{\partial T}{\partial \bar{r}} = \frac{A(T_\infty - T)}{\bar{r}} \exp(-A\cos\theta)\left\{I_0(A)\left[\cos\theta + \frac{K_1(A)}{K_0(A)}\right] + \sum_{n=1}^{\infty} 2I_n(A)\cos n\theta\left[\cos\theta + \frac{K_{n-1}(A)}{K_n(A)} + \frac{n}{A}\right]\right\} \tag{6}$$

The required temperature gradient specified by equation (4) is obtained by substituting equation (6) for $\partial T/\partial \bar{r}$. Heat conduction in the z direction is approximated by determining a temperature gradient $\partial T/\partial z$ from values for the temperatures at adjacent locations given by equation (5). Although this is not a precise calculation, it is considered to provide an adequate accounting for the depthwise heat conduction. The analysis is therefore three-dimensional.

Finite Difference Equations. Substituting equations (2)-(4) into the heat flux equation (1) gives, in finite difference form

$$\bar{r}_{i+1} = \bar{r}_i + \frac{\partial T}{\partial \bar{r}} \frac{z_{i+1} - z_i}{\frac{3\eta Q}{\pi k \sigma^2} \exp\left(\frac{-\bar{r}_i^2 - s_i^2 + 2\bar{r}_i s_i \cos\theta}{\sigma^2/3}\right) + \frac{\partial T}{\partial z}} \tag{7}$$

where the subscript i denotes the grid number in the depthwise direction along the cavity wall. A global condition for the beam energy incident on a circular ring on the cavity wall is used and is specified by the following relation, which is obtained by integrating equation (1) from $\theta = 0$ to π and $\bar{r} = \bar{r}_i$ to $\bar{r}_{i+1}$:

$$\frac{\eta Q}{k} \exp\left(\frac{-3s_i^2}{\sigma^2}\right) \int_{\frac{\sqrt{3}\bar{r}_i}{\sigma}}^{\frac{\sqrt{3}\bar{r}_{i+1}}{\sigma}} I_0\left(\frac{2\sqrt{3}s_i}{\sigma} x\right) \exp(-x^2) x\, dx = (z_{i+1} - z_i) \int_0^{\pi} \bar{r} \frac{\partial T}{\partial \bar{r}} d\theta - \frac{\pi}{2} (\bar{r}_{i+1}^2 - \bar{r}_i^2) \frac{\partial T}{\partial z} \tag{8}$$

Force Balance at Cavity Wall. Assuming local equilibrium, cavity surface temperatures can be determined from the balance of forces normal to the vapor-liquid interface as suggested by Lankin (1978)

$$p = \gamma\left(\frac{1}{R_1} + \frac{1}{R_2}\right) + \rho g z \tag{9}$$

where the vapor pressure p can be derived from the Clausius-Clapeyron equation (e.g., Giedt, 1971). The first term on the right-hand side of equation (9) is the surface tension force, which is assumed to be a linear function of temperature; the second term is the hydrostatic pressure. Introducing the appropriate relations for these terms equation (9) becomes

$$p_b \exp\left[\frac{h_{lg}}{R}\left(\frac{1}{T_b} - \frac{1}{T_i}\right)\right] = -\left[\gamma_m + \frac{d\gamma}{dT}(T_i - T_m)\right] \frac{\frac{\partial^2 z_i}{\partial r^2} + \frac{1}{r}\frac{\partial z_i}{\partial r} + \frac{1}{r}\left(\frac{\partial z_i}{\partial r}\right)^3}{\left[1 + \left(\frac{\partial z_i}{\partial r}\right)^2\right]^{3/2}} + \rho g z_i \tag{10}$$

Solution Procedure. The mesh size required for sufficient numerical accuracy depends mainly on the beam energy. For most of the numerical experiments, a grid of 5000 nodal points in the depthwise direction ensured independence of the solution on the grid spacing. For comparisons with the experimental results, a grid of 10,000 depthwise nodal points was used. A typical nodal spacing was 0.004 cm near the top of the cavity. After the beam axis coincides with that of cavity, a grid size of 1×10^{-4} cm was chosen. Heat conduction loss was calculated by a finite difference with a radial grid size of 1×10^{-4} cm. The procedure developed for solving this problem was:

1 An initial cavity surface temperature distribution is guessed.

2 A cavity opening radius $\bar{r}_{i=0}^{(m)}$, and a distance between the energy beam and the center of the cavity opening $s_{i=0}^{(m)}$, where the iteration number $m = 1, 2, \ldots$, are guessed.

3 The cavity radius $\bar{r}_{i+1}^{(m)}$ is determined from equation (7).

4 Substituting $\bar{r}_i^{(m)}$ and $\bar{r}_{i+1}^{(m)}$ into equation (8), $s_i^{(m)}$ is modified by using the bisection method (e.g., King, 1984).

5 Steps 3 and 4 are repeated and $\bar{r}_{i+1}^{(m)}$ and $s_i^{(m)}$ are found as the relative difference between the incident energy and the heat conduction loss specified by equation (8) is less than 1×10^{-7}.

6 The calculation is continued in the depthwise direction ($i = 1, 2, \ldots$). The depth of penetration is determined as the total heat conduction loss is greater than 98 percent of the total incident energy. If the cavity radius approaches zero and the conservation of the global energy is not satisfied, initial estimations of $\bar{r}_0^{(m)}$ are changed.

7 Cavity surface temperatures are calculated from equation (10) by using the bisection method to an error limit of 10 K.

8 Steps 2 to 7 are repeated for different values of m until the depth of penetration converges to within 5 percent between the mth and $(m+1)$th iterations. The iteration number for m is usually no more than 5.

Results and Discussion

The primary welding parameters affecting the welding process are the beam power, the energy flux distribution parameter, and the welding speed. Values for these variables chosen for calculation in this study are 4.34, 6.00, and 7.66 kW for the beam power, 0.52, 0.866, and 1.212 mm for the energy flux distribution parameter, and 0.8, 1.6, and 2.4 cm/s for the welding speed, respectively. In view of the limited data available at the temperatures involved, it was decided to make initial calculations with thermal property values appropriate for aluminum.

Cavity Shape, Temperature, and Heat Flux Distributions. The shape of the cavity and the location of the energy beam incident on the cavity wall for different beam powers are shown in Fig. 2. The shape of the cavity is similar to a Gaussian distribution, which agrees with the suggestion made by Juptner et al. (1974). Increasing the beam power results in an increase of the depth of penetration. The deviation of the center of the horizontal cross section from the energy beam axis has a maximum at the cavity opening. For a beam power $Q = 7.66$ kW, the maximum is 0.035 mm, which is around 4 percent of the radius of the cavity opening, and decreases to zero near the cavity bottom. Hence it is reasonable to assume that the energy beam coincides with the axis of the cavity.

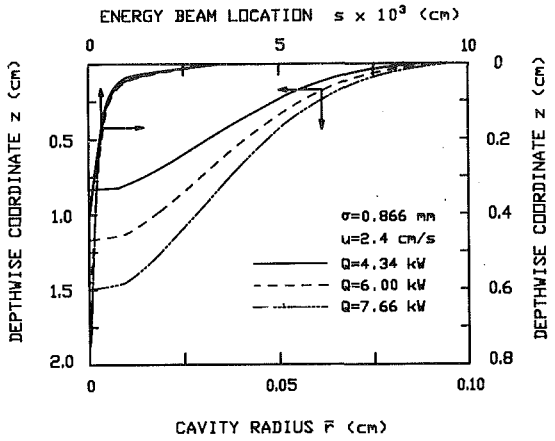

Fig. 2 Depthwise variations of cavity radius and centers of horizontal cross sections measured from energy beam for different beam powers

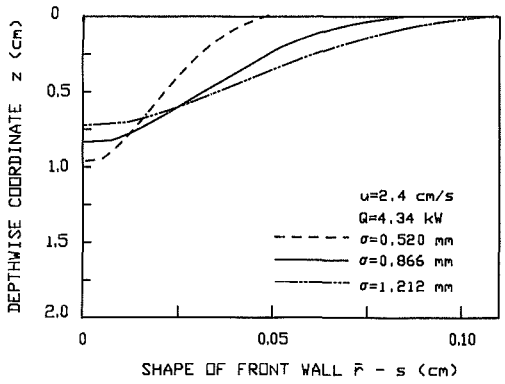

Fig. 3 Shapes of front cavity wall for different energy flux distribution parameters

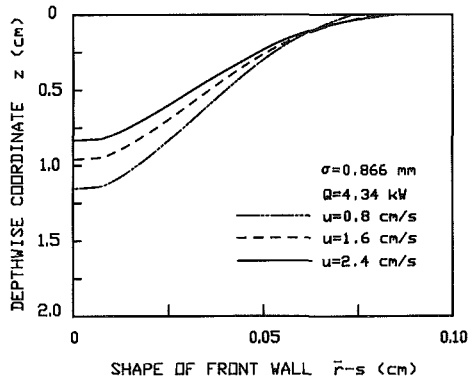

Fig. 4 Shapes of front cavity wall for different welding speeds

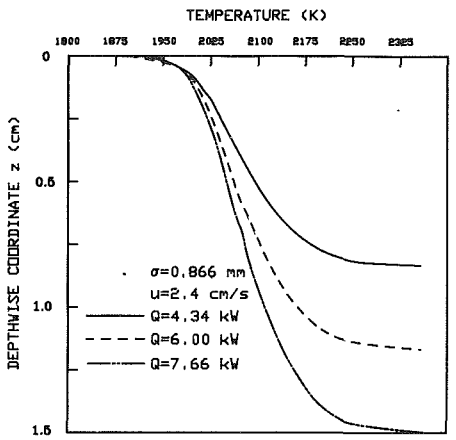

Fig. 5 Cavity temperature distributions for different beam powers

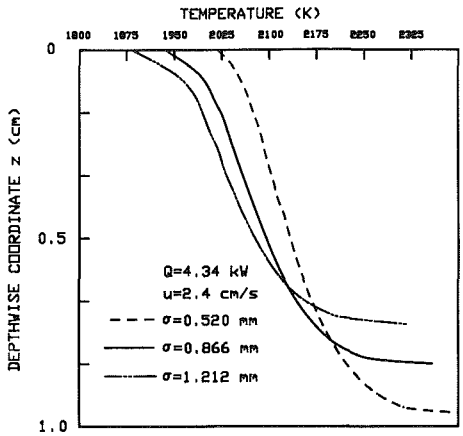

Fig. 6 Cavity temperature distributions for different energy flux distribution parameters

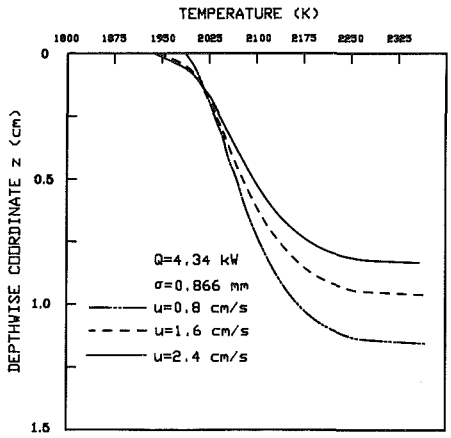

Fig. 7 Cavity temperature distributions for different welding speeds

The shape of the cavity changes significantly with the energy flux distribution as shown in Fig. 3. An increase in the energy flux distribution parameter greatly reduces the depth of penetration, whereas the cavity opening radius increases. The depth of penetration, however, is increased by decreasing the welding speed as presented in Fig. 4.

Cavity surface temperature distributions for different beam powers are shown in Fig. 5. Temperatures increase from the cavity opening to the cavity base, where a relatively constant value of around 2340 K was found. These results are in accord with experimental data obtained by Schauer et al. (1978). Temperature gradients are large near the top and bottom regions. This is attributed to the surfaces having large inclination angles; hence the incident beam energy is increased.

The effects of the energy flux distribution parameter on the cavity temperature distribution are presented in Fig. 6. Temperatures are higher for a smaller energy flux distribution parameter due to a higher incident energy density. However, the temperature gradient is reduced. Referring to Figs. 5–7, the base temperatures are found to be relatively constant with different welding conditions and agree with experimental findings (Schauer et al., 1978; Schauer and Giedt, 1978).

The heat conduction through the front and the rear walls of a cavity for different beam powers is shown in Fig. 8. The heat conduction at the front wall, where the incoming solid material is melted, is higher than that at the rear wall, and increases rapidly in the depthwise direction. Referring to Figs. 9

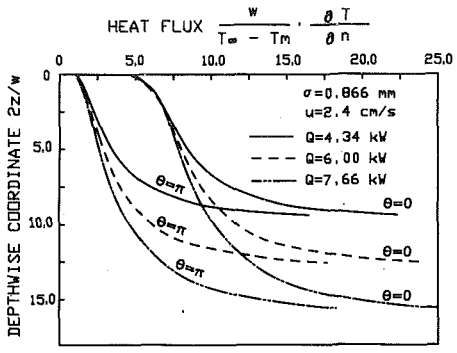

Fig. 8 Heat conduction through front and rear walls of cavity for different beam powers

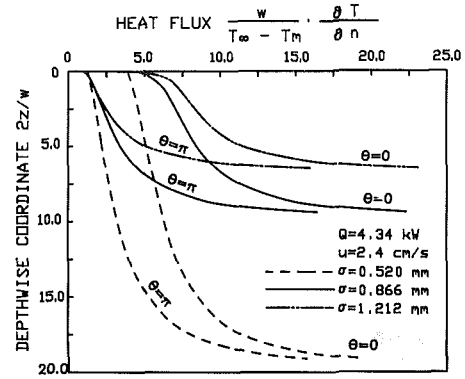

Fig. 9 Heat conduction through front and rear walls of cavity for different energy flux distribution parameters

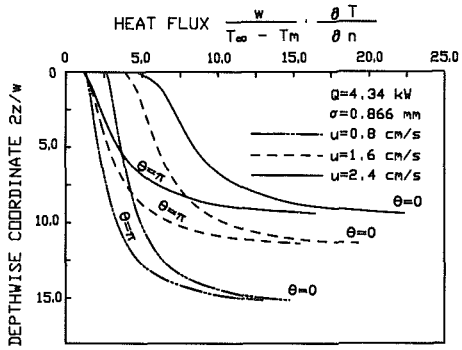

Fig. 10 Heat conduction through front and rear walls of cavity for different welding speeds

and 10, the heat conduction increases rapidly as the energy flux distribution parameter or the welding speed increases. The difference in the heat conduction at the front and the rear walls increases with the energy flux distribution parameter and the welding speed.

The predicted shape of the cavity and location of the melt isotherm are shown in Fig. 11 for $Q = 4.34$ kW, $\sigma = 1.91$ mm, and $u = 0.8$ cm/s. Only the fusion zone above the region of nonvanishing radius of the cavity is shown due to a limitation of the analytical solution. Although the fusion zone is narrower in the front region than that in the rear, it is substantially thicker than indicated in the experimental observations made by Tong and Giedt (1969) and by the predictions of Giedt and Wei (1982). The difference is attributed to the assumption of conduction heat transfer only with no accounting for fluid flow around the cavity. It is noted, however, that the liquid layer thickness predicted by the present analysis is consistent with measured cavity surface

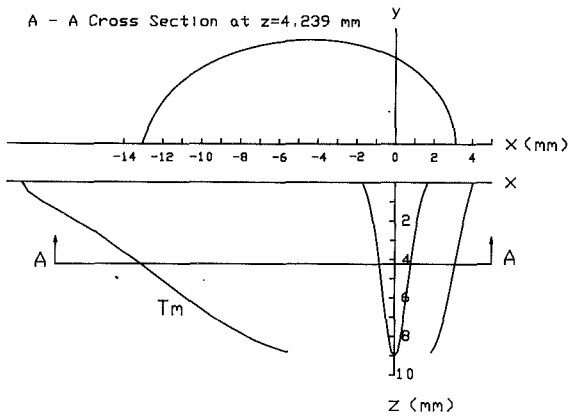

Fig. 11 Horizontal and longitudinal cross sections of fusion zone ($Q = 4.34$ kW, $\sigma = 1.91$ mm, and $u = 0.8$ cm/s)

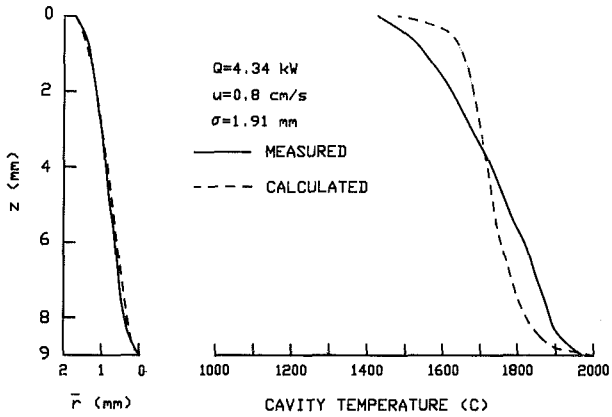

Fig. 12 Comparison between predicted and measured shapes and temperatures of a cavity

temperatures. It was pointed out by Giedt and Wei (1982) that heat transfer to the liquid-solid interface was essentially by conduction. Based on this, the liquid layer thickness shown in Fig. 11 leads to surface temperatures on the order of the experimental values.

Comparison of the predicted shape of the transverse cross section of the cavity with the fusion zone boundary measured by Schauer and Giedt (1978) is shown in Fig. 12. The two curves are in good agreement. The predicted cavity surface temperatures agree to within about 6 percent with the measured temperature distribution. The greatest difference occurs near the top, where predicted values are higher than the experimental data. It is possible that this is due to heat transfer from the outer regions of the beam having a significant vertical component or to a thinner liquid layer due to flow around the cavity. In addition, the uncertainty of the value of the beam energy flux distribution parameter used may also be responsible for the temperature differences (see Fig. 6). In order to match the experimental data, it is possible that a smaller beam energy distribution parameter is required at the bottom of the cavity and a larger energy flux distribution parameter near the top region. This implies that the heat transfer distribution along the cavity wall may be more complex than assumed.

Welding Penetration. Analyses show that the power required per unit of penetration during high-intensity beam welding is a function of the ratio of the welding speed divided by the material thermal diffusivity multiplied by a fusion zone

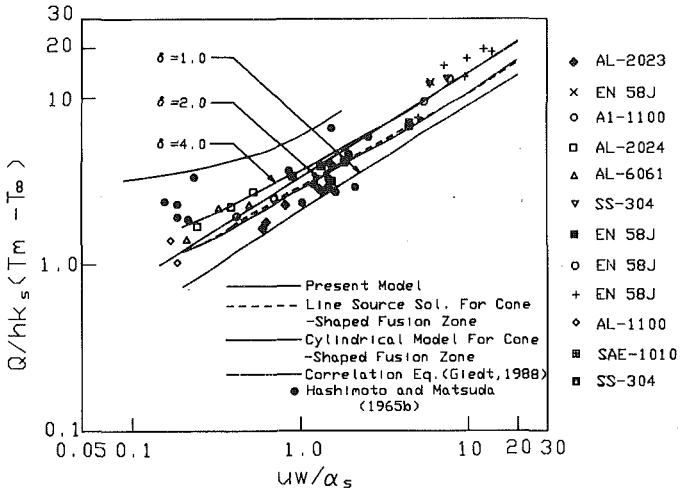

Fig. 13 Comparison between predicted and measured dimensionless relationship of the beam power-penetration depth versus fusion zone width-thermal property parameters

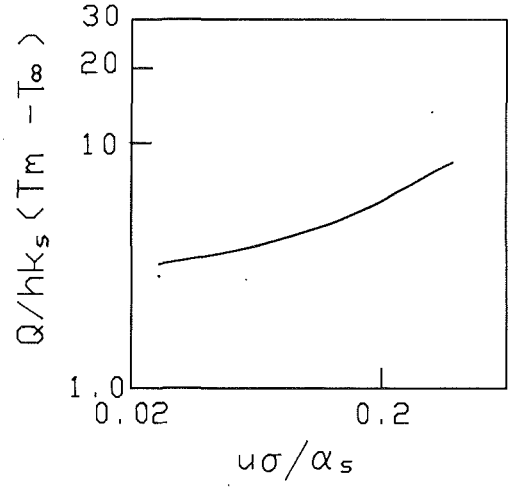

Fig. 14 Dimensionless relationship between beam power-penetration depth parameter and beam energy flux distribution-thermal property parameter

or cavity dimension. This is illustrated in Fig. 13 where the dependent variable is the dimensionless parameter $Q/hk_s(T_m - T_\infty)$ and the independent variable is uw/α_s. Here w is the width of the fusion zone at the surface as proposed by Giedt and Tallerico (1988). By assuming that the width of the fusion zone equals the cavity opening diameter, the computed results in this study is plotted. As can be seen, the penetration curve predicted by the present analysis falls around 40 percent above the correlation developed by Giedt and Tallerico (1988). In addition to the underestimation of the width of the fusion zone, a possible explanation for this is that the incident energy flux is focused after impinging on the cavity wall (see Fig. 3). Hence a larger discrepancy occurs for a small value of the fusion zone width. Since the heat conduction loss is calculated from the cavity surface temperature, which is larger than the melting temperature, the depth of penetration predicted by the present model is smaller than that predicted by the cylindrical model.

The use of the width of the fusion zone at the surface in the independent parameter in Fig. 13 was recommended by Giedt and Tallerico (1988) instead of a beam diameter, because beam dimensions are usually not known and just how the diameter is to be specified has not been established. The use of the fusion zone width, however, is inconvenient for application since the depth of penetration can not be calculated directly unless the width of the fusion zone at the surface is specified or estimated. An alternate approach is to use a beam characteristic such as the distribution parameter σ. This is specified in the present analysis and techniques are being developed for determining this parameter from beam current distribution measurements (e.g., Hicken and Giedt, 1988). Therefore, a correlation of the beam power-penetration depth parameter and welding velocity-thermal property parameter, which is nondimensionalized by the energy flux distribution parameter σ, is proposed. A curve showing the proposed relationship based on the present analysis is shown in Fig. 14. The application of this approach depends upon knowledge or measurement of the beam distribution parameter. Current developments indicate such information may become available.

Conclusions

Conclusions drawn are as follows:

1 In this study, the shape of a high-energy beam welding cavity is determined by satisfying balances of energies and normal forces at the vapor-liquid interface.

2 The effects of beam power, the energy flux distribution parameter, and the welding speed on the three-dimensional geometry of the cavity, cavity temperature, and heat transfer distributions along the cavity are investigated for the first time. Results are in agreement with available experimental data for electron beam welding.

3 The energy flux distribution parameter is found to have the strongest effect on the geometry, temperature, and heat transfer distributions in the welding cavity. The cavity base temperature is found to be essentially constant for different welding parameters.

4 Dimensionless correlation of the depth of penetration with the energy flux distribution parameter rather than the width of the fusion zone is proposed.

Acknowledgment

The authors acknowledge the interest and guidance of Professor W. H. Giedt during this study.

References

Carslaw, H. C., and Jaeger, J. C., 1959, *Conduction of Heat in Solids*, Clarendon Press, Oxford, United Kingdom, p. 390.

Giedt, W. H., 1971, *Thermophysics*, Van Nostrand Reinhold, New York, pp. 387-388.

Giedt, W. H., and Tallerico, L. N., 1988, "Prediction of Electron Beam Welding Depth of Penetration," *Welding Journal*, Vol. 67, pp. 299-s-305-s.

Giedt, W. H., and Wei, P. S., 1982, "Temperature and Velocity Distributions in the Liquid Flowing Around the Front of an Electron Beam Welding Cavity," *Proceedings, 7th International Heat Transfer Conference*, Hemisphere Publishing Corp., Washington, DC, Vol. 6, pp. 403-407.

Hashimoto, T., and Matsuda, F., 1965a, "Penetration Mechanism of Weld Beads in Electron-Beam Welding—Studies on EB Weldings No. 6," *Transactions of National Research Institute for Metals*, Vol. 7, pp. 183-185.

Hashimoto, T., and Matsuda, F., 1965b, "Effect of Welding Variables and Materials Upon Bead Shape in Electron Beam Welding," *Transactions of National Research Institute for Metals*, Vol. 7, pp. 22-35.

Hicken, G. K., and Giedt, W. H., 1988, "Variables of Weld Penetration With Electron Beam Current Profile," *69th AWS Annual Meeting*, New Orleans, pp. 20-22.

Juptner, W., Bodecker, V., and Sepold, G., 1974, "Influence of the Spatial Intensity Distribution on Deep Welding Geometry," *Electron and Ion Beam Science and Technology*, R. Bakish, ed., Proceedings of the Sixth International Conference, San Francisco, CA, Electrochemical Society, Princeton, NJ, pp. 366-376.

King, J. T., 1984, *Introduction to Numerical Computation*, McGraw-Hill, New York, pp. 42-47.

Lankin, Yu. N., 1978, "Evaluating the Temperature and Vapor Pressure in the Melted Channel During Electron-Beam Welding," *Avt. Svarka*, No. 2, pp. 16–19.

Miyazaki, T., and Giedt, W. H., 1982, "Heat Transfer From an Elliptical Cylinder Moving Through an Infinite Plate Applied to Electron Beam Welding," *International Journal of Heat and Mass Transfer*, Vol. 25, pp. 807–814.

Rosenthal, D., 1941, "Mathematical Theory of Heat Distribution During Welding and Cutting," *Welding Journal*, Vol. 20, pp. 220-s–234-s.

Schauer, D. A., and Giedt, W. H., 1978, "Prediction of Electron Beam Welding Spiking Tendency," *Welding Journal*, Vol. 57, pp. 189-s–195-s.

Schauer, D. A., Giedt, W. H., and Shintaku, S. M., 1978, "Electron Beam Welding Cavity Temperature Distributions in Pure Metals and Alloys," *Welding Journal*, Vol. 57, pp. 127-s–133-s.

Swift-Hook, D. T., and Gick, A. E. F., 1973, "Penetration Welding With Lasers," *Welding Journal*, Vol. 52, pp. 492-s–499-s.

Tong, H., and Giedt, W. H., 1969, "Radiographs of the Electron Beam Welding Cavity," *Review of Scientific Instruments*, Vol. 40, pp. 1283–1285.

Tong, H., and Giedt, W. H., 1971, "Depth of Penetration During Electron Beam Welding," ASME JOURNAL OF HEAT TRANSFER, Vol. 93, pp. 155–163.

Wei, P. S., and Chiou, L. R., 1988, "Molten Metal Flow Around the Base of a Cavity During a High-Energy Beam Penetrating Process," ASME JOURNAL OF HEAT TRANSFER, Vol. 110, pp. 918–923.

Wei, P. S., and Giedt, W. H., 1985, "Surface Tension Gradient-Driven Flow Around an Electron Beam Welding Cavity," *Welding Journal*, Vol. 64, pp. 251-s–259-s.

Wei, P. S., and Ho, J. Y., 1988, "Energy Considerations in High-Energy Beam Drilling," to appear in *International Journal of Heat and Mass Transfer*.

Effect of Oxidation and Plume Formation on Low Power Nd-Yag Laser Metal Interaction[1]

R. S. Patel
Graduate Research Assistant.
Student Mem. ASME

M. Q. Brewster
Associate Professor.
Assoc. Mem. ASME

Department of Mechanical and Industrial Engineering,
University of Illinois at Urbana-Champaign,
Urbana, IL 61801

The effect of oxide formation and plume formation on laser energy absorption by metallic targets has been studied. The change in directional-hemispherical spectral reflectance of metallic targets during single-shot Nd-Yag laser pulse irradiation was measured using an integrating sphere under controlled environments of both oxygen and argon gas. The spectral transmittance of the plume formed over the targets was also measured using a He-Ne probe laser. The metal targets studied included Al6061, Cu, 304 stainless steel, and low-carbon steel. Results obtained show that once a target is hot enough to form a vapor plume, in either argon or oxygen, absorption by the plume significantly limits the amount of laser energy available for absorption at the target surface. Prior to plume formation, the amount of laser energy absorbed by the target is determined by the target surface optical properties. Under the conditions of the present study (incident laser flux of the order of 10^6 W/cm^2 over 0.5-1.0 ms), in the case of absorbing metals ($\alpha_\lambda > 0.3$), such as stainless and low carbon steel, the intrinsic absorptivity of the metal is high enough that the effect of ambient gas (oxygen or argon) on absorptivity is insignificant. In the case of nonabsorbing metals ($\alpha_\lambda < 0.3$), such as Cu and Al6061, the intrinsic metal absorptivity is low enough that the ambient gas does have a significant effect on the target absorptivity. The formation of an oxide layer that occurs in an oxidizing environment generally has the effect of increasing the target absorptivity. The relative magnitude of the absorptivity enhancement due to oxide formation depends on the respective absorptivities of the oxide and metal. For metals that form oxides that are intrinsically absorbing in the solid state, such as Cu_2O or CuO, the enhancement in absorptivity due to oxide formation can be as much as an order of magnitude. For metals that form oxides that are intrinsically nonabsorbing in the solid state, such as MgO or Al_2O_3, the enhancement in absorptivity due to oxide formation is more modest but still significant (40 percent). The enhancement in absorptivity in the latter case (MgO or Al_2O_3) is postulated to be associated either with a thin, absorptive, transition region composed of a mixture of metal and substoichiometric solid oxide just below target surface or with the melting of the oxide at the surface.

Introduction

It has been observed by many researchers that metal surfaces show a strong decrease in reflectivity when irradiated with focused laser light. This phenomenon is well known by now but the exact mechanism is still not clear. A variety of explanations, as summarized by Von Allmen et al. (1978), includes temperature dependence of the reflection coefficient, metal-dielectric transition of the hot liquid, and the appearance of a stationary surface plasma layer just above the metal target surface. For laser power densities of the order of 10^6 to 10^7 W/cm^2 and pulses lasting several ms, it is well documented now that an absorbing, partially ionized cloud of metal vapor formed over the target surface is responsible for the observed sudden decrease in reflectance of metals subject to intense laser radiation. This cloud has been referred to by different names such as plume, laser-supported combustion (LSC) or laser-supported absorption (LSA) wave, weakly ionized plasma, and screening cloud. Early experimental evidence of the presence of a screening cloud over an aluminum target was reported by Bonch-Bruevich et al. (1973). Bergel'son et al. (1974) also reported the formation of an absorbing layer above an aluminum target surface when the target was irradiated with Nd-Yag laser pulses of 1 ms duration with power density of 10^7 W/cm^2. Rosen et al. (1982) reported the formation of an absorbing plasma over an Al2024 sample when XeF laser radiation was focused on it under vacuum. Using high-speed photography and transmittance measurements, Matsunawa et al. (1984, 1985) showed evidence of a partially transmissive plume being formed over Ti samples when irradiated by an Nd-Yag laser. The transmittance measurements of a metal vapor plume using an He-Ne probe, during laser welding of Al1100 by Peebles and Williamson (1987), also indicated 10 percent attenuation in the probe signal. Von Allmen et al. (1978) carried the work one step further by correlating target damage with the experimentally measured reflectivity of Cu samples subjected to a 1.4×10^8 W/cm^2, 1.0 μs, flat output Nd-laser pulse. It was observed that the reflectivity did not change significantly until the target surface temperature reached the vicinity of the evaporation temperature.

Since an assist gas is used during most laser-metal interaction processes for one reason or another, it also becomes important to identify the effect of the surrounding gas atmosphere on absorptivity of the metal. Although it is generally agreed by the researchers in the area of laser cutting that the use of oxygen as an assist gas increases the efficiency of the process, there are different opinions about how oxygen helps the process. It was shown experimentally in early 1969 by Asmus and Baker that the absorption of cw CO_2 laser radia-

[1]This paper appears with permission of the Laser Institute of America.

Contributed by the Heat Transfer Division and presented at the International Congress on Applications of Lasers and Electro Optics, Santa Clara, California, October 31-November 3, 1988, sponsored by the Laser Institute of America. Manuscript received by the Heat Transfer Division January 17, 1989. Keywords: Laser Processing, Radiation, Thermophysical Properties.

tion by metallic targets would increase considerably when targets were in an oxidizing environment. This effect was attributed to the growth of an oxide layer on the surface. Similar observations of an increase in absorptivity of metal in an oxidizing medium have been reported by Arzuov et al. (1976, 1978) and by Wautelet (1987). From the above-described work of different researchers, it would seem that plume formation and oxide layer formation are two important factors that affect the amount of laser energy absorbed by the metal.

Objective

The objective of the experimental study described herein is to identify the parameters affecting laser energy absorption by a metal target during low-power ($\sim 10^6$ W/cm^2) single shot Nd-Yag laser-metal interaction. Target materials were selected so as to obtain a wide variety of thermophysical properties for both the selected metals and their oxides. An effort was made experimentally and analytically to quantify the effect of oxidation on the change in the absorptivity of the metal. The directional-hemispherical spectral reflectance was measured for various metals (Al6061, Cu, 304 stainless steel, and low C steel) exposed to Nd-Yag laser pulses in a controlled atmosphere of oxygen (O_2) and argon (Ar). Spectral transmittance of the plume formed over the metallic samples was measured. To ensure that the plume did not blow away, the experiments were conducted in a slow-flowing gas environment. The target damage resulting from the laser-metal interaction was also observed under a microscope at a magnification of 50×. Theoretical estimations of temperature were obtained by using a two-dimensional model described by Duley (1976). The comparison between estimated temperature and target behavior led to some significant conclusions about the role of the metal and oxide thermophysical properties in laser metal interaction.

Experimental Arrangement

A 100-W average power multimode Nd-Yag pulsed laser (Model MS 810, J. K. Lasers, Inc.) with a "top hat" spatial profile (5 percent intensity variation across the top) has been used throughout the study. The pulse width, pulse shape, and power output of laser pulse were controlled by supplying an external voltage signal to the laser controller unit. The laser beam was focused onto the target surface using a 120 mm focal length lens. The focused beam diameter was estimated to be approximately 0.2 mm. The flux available at the focal spot was estimated to be of the order of 10^6 W/cm^2.

Four different types of pulse were used in the study. A low-power short pulse, pulse 1, was used to determine the room temperature reflectance of the target materials. A higher power pulse, pulse 2, was used to study changes in the reflectance of the target upon heating and the transmittance of the plume formed over three of the materials (Al6061, 304 stainless steel (SS), and low C steel). The energy in pulse 2 was sufficient to cause permanent damage to these three metallic samples. Due to the high reflectivity and thermal conductivity of Cu compared to other metals, the energy in pulse 2 was not sufficient to cause permanent damage in the Cu sample. A higher power, longer pulse, pulse 3 and a higher power, shorter pulse, pulse 4 were used for Cu samples. The average power per pulse was estimated by dividing the known value of energy (Joules) per pulse by the pulse width. The average powers for pulse 1, pulse 2, pulse 3, and pulse 4 were approximately 600, 700, 900, and 770 W, respectively.

Square metal samples of dimensions 1 cm × 1 cm and thickness 1/32 in. (0.79 mm) were used for reflectance measurements. Transmittance measurements were performed on samples of dimension 1 cm × 3 cm and thickness 1/32 in. (0.79 mm). Low C Steel samples were an exception with a 1/16 in. (1.5 mm) thickness. All the samples were tested in an unpolished condition, as received. As the qualitative aspects of the results were observed to be reproducible with samples in as-received condition, further characterization of the initial surface condition of the samples was not carried out. However it should be noted that surface roughness has a strong influence on reflectance. In this study the room temperature reflectance was taken as a characterization of the as-received surface condition. In addition acetone was used to remove the grease from the samples before measurement. For the room temperature measurements of reflectance, Kodak White Reflective coating #6080 was used as a reference.

Reflectance Measurements. A schematic arrangement of the reflectance measurement is shown in Fig. 1. A 2-in. (5.08-cm) diameter integrating sphere (Labsphere Inc.) was used. Provision for gas input and gas output was made by modifying the standard design of the sphere. Other openings on the sphere surface were the incident beam port, detector port, and a sample holder. It was ensured that enough flow was present to protect the inside wall of the sphere from debris generated during laser-metal interaction. The sphere was internally coated with $BaSO_4$. The samples were placed at an angle of 7 to 8 deg to the incident beam direction to avoid escape of specularly reflected energy through the incident beam port. A line filter at 1.06 μm wavelength, with band width of 5.9 nm, and a neutral density filter, with transmittance of 10^{-3}, were placed in front of the silicon photodiode detector whose rise time was 2.0 μs. The voltage signal generated by the detector was stored on a digital storage oscilloscope (Tektronix model 2023) and eventually the signal was transferred to a computer for further data reduction. The radiative energy emitted at 1.06 μm by the plume was much

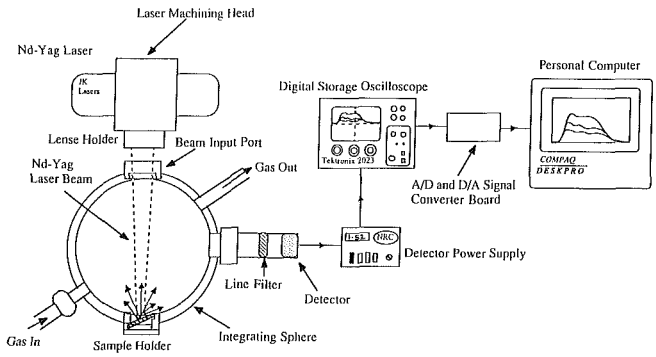

Fig. 1 Schematic arrangement for the reflectance measurements

Nomenclature

A = focused laser beam radius
J_0, J_1 = Bessel functions of the first kind
k = thermal conductivity
P = incident laser power
r, z = spatial coordinates
T = temperature
t = time
α_λ = spectral absorptivity
β = integration parameter
κ = thermal diffusivity

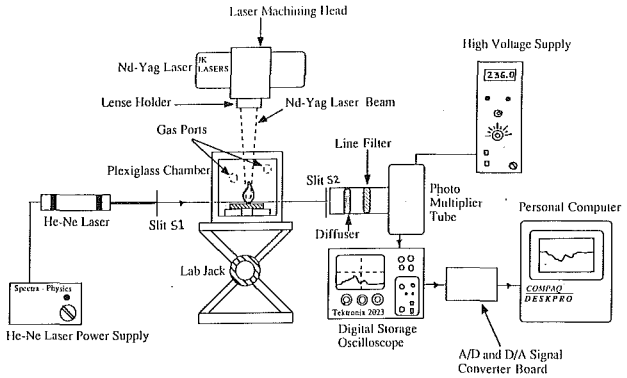

Fig. 2 Schematic arrangement for the transmittance measurements

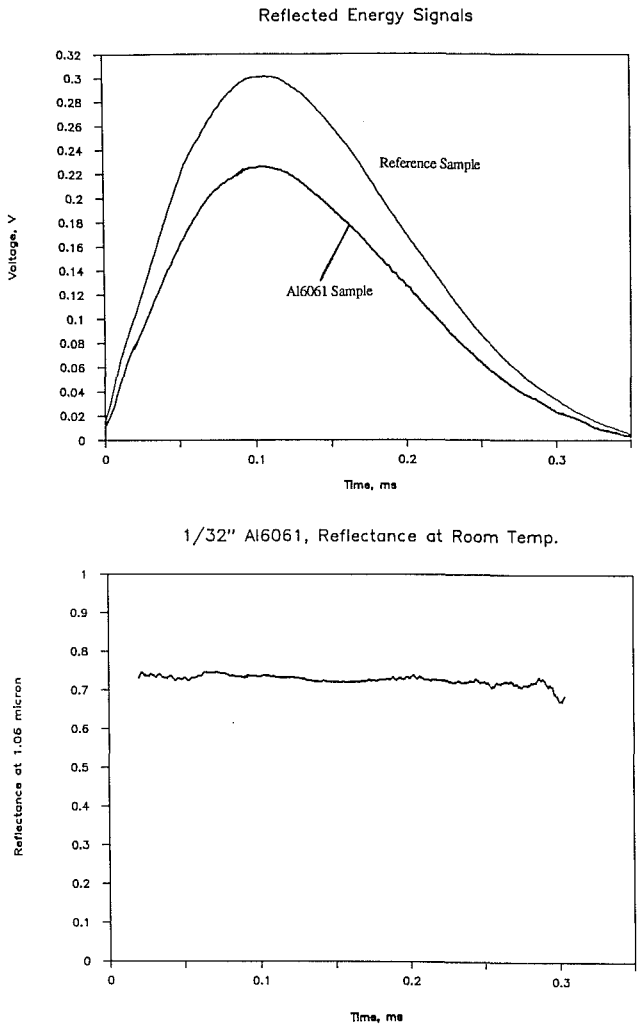

Fig. 3 Room temperature measurements of reflectance for A16061 (pulse 1): (*a*) reflected energy signal from reference and A16061 sample; (*b*) room temperature reflectance for A16061

smaller (after passing through the neutral density filter) than the reflected laser beam energy and did not affect the reflectance measurement.

Transmittance Measurements. The arrangement of the transmittance measurement is shown in Fig. 2. A metal target sample was placed inside a plexiglass chamber. The chamber allowed a controlled atmosphere (either O_2 or Ar) to be maintained. A He-Ne probe laser was passed 0.5 mm above the target surface. A slit S1 was used to reduce the probe laser width to 0.3 mm. A photomultiplier tube (PMT) along with a

Table 1 Room temperature reflectance of samples

Metal	Room temperature reflectance
A16061	0.72
Cu	0.98
304 SS	0.68
Low C Steel	0.55

632.8 nm line filter, band width of 1.2 nm, and a diffuser to spread the light over the photocathode of the PMT made up the detection system to trace the changes in transmitted probe laser energy during plume initiation. The voltage signal generated by the PMT was processed in a similar manner as described above for the reflectance measurements. A slit S2 of width 0.5 mm was placed in front of the detector to minimize the light emitted from the plume from reaching the detector. To ensure that this was the case, the experiment was run with the probe laser off. No signal was recorded on the oscilloscope, which confirmed that the emitted light from the plume was not affecting the transmittance measurements.

Results

Reflectance. The room temperature reflectance of samples was measured with pulse 1 using the arrangement shown in Fig. 1. The sample was placed far below the focal plane to ensure that excessive heating of the sample did not take place. The signal obtained for the reference and the Al6061 sample in the defocused situation is shown in Fig. 3(*a*). The reference signal represents the incident laser pulse shape. As the absolute reflectance of the reference sample at 1.06 μm was known to be 0.985 (specified by Kodak for White Reflective coating #6080), the room temperature value of reflectance for the Al6061 sample could be calculated from the ratio of the voltage signals. The reflectance value obtained is shown in Fig. 3(*b*). The fairly constant value of reflectance confirms that the laser energy at such a defocused situation was not capable of introducing any thermal effects. A similar procedure was applied for the other metal samples to find their respective room temperature reflectance. The results are summarized in Table 1.

Once the room temperature value of reflectance of samples was known, the change in reflectance during irradiation with higher power pulses was measured. The sample was first placed far below the focal plane to obtain the defocused reflected energy signal as shown in Fig. 4(*a*). The value of defocused reflected energy signal depends on the room temperature value of reflectance of the sample. The defocused reflected energy signal represents the incident laser pulse shape. The sample was then brought up to the focal plane and the reflected energy signal under the oxygen and argon atmosphere were recorded as shown in Fig. 4(*a*). The same method was applied to all the other metallic samples. The value of reflectance as a function of time was calculated from Fig. 4(*a*) as the ratio of reflected energy signal obtained at the focused situation to the signal obtained at the defocused situation, multiplied by the room temperature reflectance of the target. The calculated results of reflectance as a function of time for the Al6061 sample under an O_2 and Ar atmosphere are shown in Fig. 4(*b*). The results for Cu are shown in Figs. 5 and 6. The results of reflectance as a function of time for 304 SS and low C steel are shown in Fig. 7. Results shown in Figs. 4–7 are for one sample, but they are representative of the results obtained for several samples. Although the detailed structure of the curves obtained was obviously different for different samples due to the transient nature of the process, the important features of the curves on which the conclusions were based were reproducible. Therefore one representative curve for each metal has been presented.

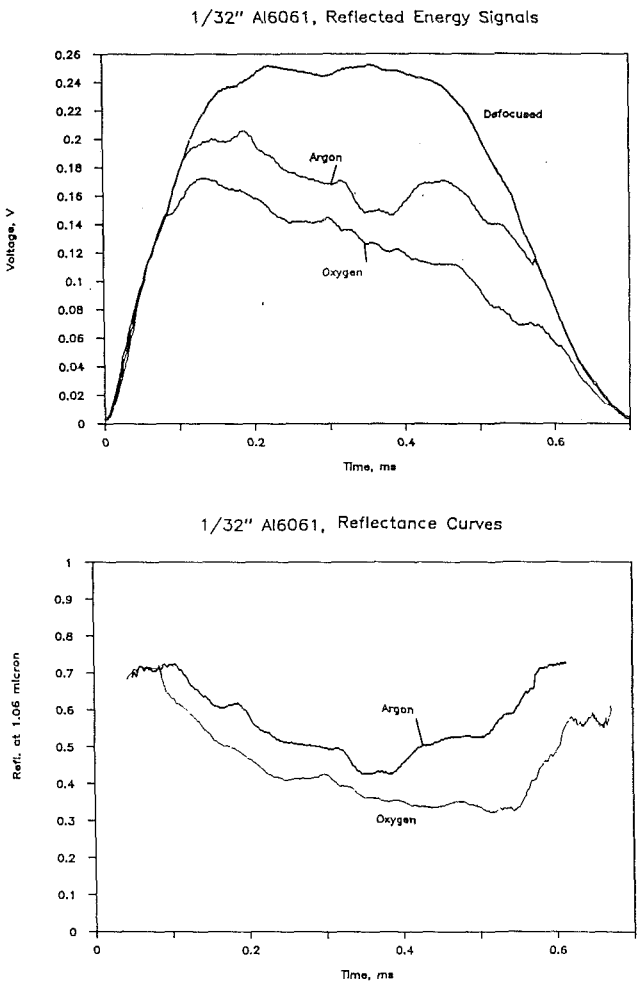

Fig. 4 Reflectance measurements for A16061 sample under O_2 and Ar atmosphere (pulse 2): (*a*) reflected energy signals and (*b*) reflectance values

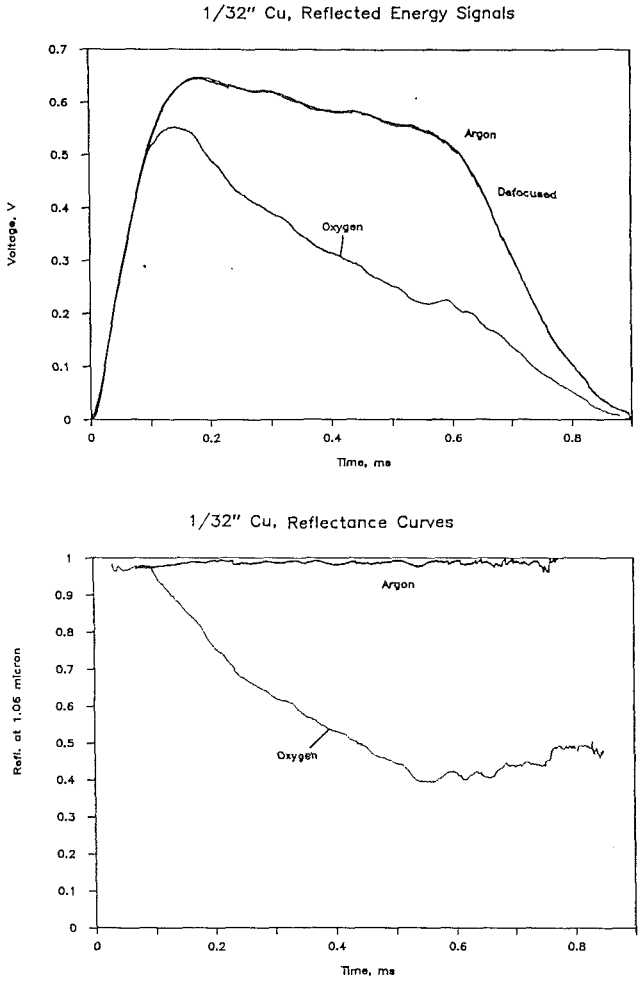

Fig. 5 Reflectance measurements for Cu sample under O_2 and Ar atmospheres (pulse 3): (*a*) reflected energy signals and (*b*) reflectance values

Plume Transmittance. For measurement of plume transmittance, the sample was placed at the focal point and the change in the He–Ne probe laser signal during plume formation was measured. The results of the plume transmittance for O_2 and Ar atmosphere for different metals are given in Figs. 8 and 9. As for reflectance, for plume transmittance results also, only one representative curve for each metal has been presented.

Estimating Surface Temperature. The time-dependent temperature history of the metal samples before the drop in reflectance occurs was estimated using a two-dimensional heat conduction model described by Duley (1976). Appendix A describes the assumptions, uncertainties, scope, and purpose associated with the model briefly. The temperature calculations were performed to support the conclusions that were reached based upon the reflectance and the plume transmittance measurements. The primary purpose of this study was not to develop a detailed theoretical model. The temperatures estimated using Duley's model were adequate for present purposes and were probably accurate to within a few hundred degrees, at least up to the point when the rapid drop in reflectance was observed.

Discussion

Before discussing the curves of reflectance for different metals under an O_2 and Ar atmosphere it is worthwhile to discuss some of the possible mechanisms that may affect the reflectance of a metal target upon irradiation with focused laser light.

When laser energy is incident upon a metallic sample, a fraction gets reflected that depends upon the reflectivity of the sample. The amount of reflected energy reaching the detector in a reflectance measurement during the early stages of the laser pulse can be changed by several different phenomena. One is a change in the absorptivity of the surface (e.g., due to oxide layer formation), which may either increase or decrease the reflected energy signal. Another is the formation of a vapor plume, which reduces the amount of reflected energy reaching the detector. So a decrease in the amount of energy reaching the detector does not necessarily mean that the absorptivity of the metal surface has increased.

Also the other phenomenon that can reduce the reflected energy reaching the detector is cavity formation. For a surface having a deep narrow cavity, the reflectivity decreases due to the internal reflections occurring within the cavity. Therefore at the end of the laser pulse if the value of reflectance returns to its starting value and a cavity was formed by the pulse, then it means that the cavity is not deep enough for multiple reflections to be prominent. But when the value of reflectance at the end of the pulse does not return to the starting value, then either an absorbing oxide layer has been formed or the damage caused by the laser pulse is sufficient for the cavity effect to be prominent, or both.

During the transmittance measurements, the transmittance of the volume above the metallic target surface decreases once

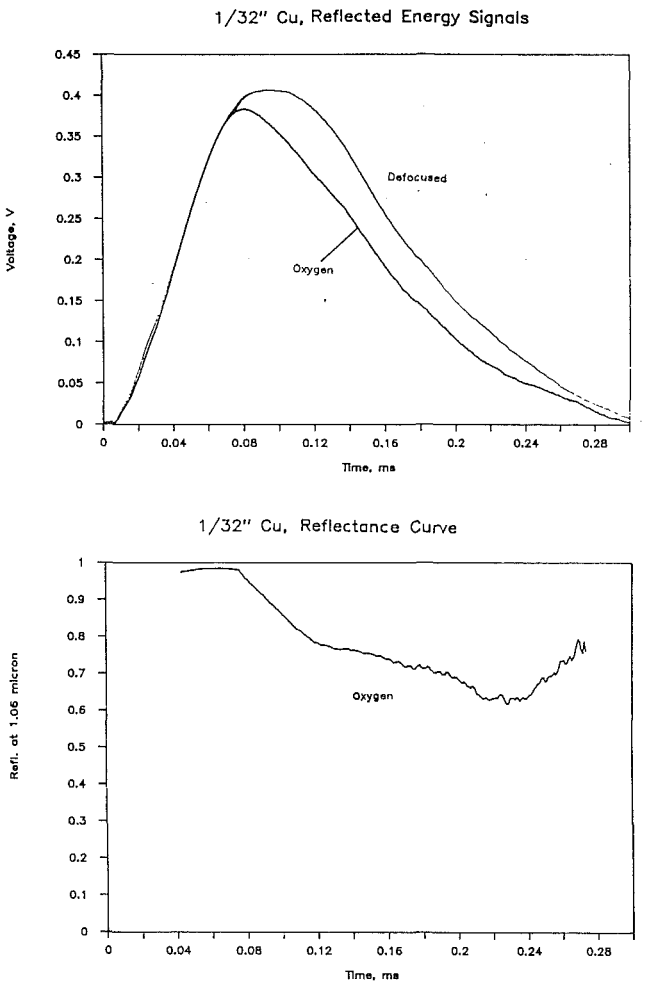

Fig. 6 Reflectance measurements for Cu sample under an O_2 atmosphere (pulse 4): (*a*) reflected energy signals and (*b*) reflectance value

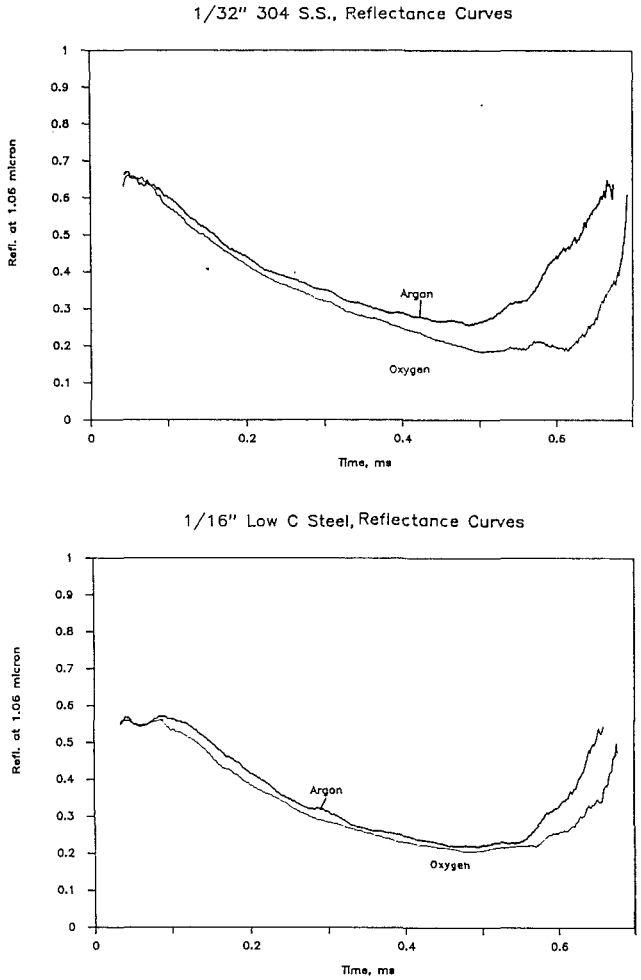

Fig. 7 Reflectance values under O_2 and Ar atmospheres (pulse 2) for (*a*) 304 stainless steel and (*b*) low-carbon steel

the absorptive plume forms. It should be mentioned that the transmittance measurements presented here indicate the drop in the transmittance in the transverse direction. The transmittance in the incident beam direction (longitudinal direction) will be further reduced because of the fact that the geometric dimension of the plume in the longitudinal direction is much larger than in the transverse direction. The photographic results of Stegman et al. (1973) support this argument.

A16061 Sample

Ar Atmosphere. From Fig. 4(*a*) it is seen that during the early stages of the pulse, the reflected energy signal for the focused situation coincides with the reflected energy signal for the defocused situation, indicating that the reflectance remains at the room temperature value of 0.72. Figure 4(*b*) shows a sudden decrease in the reflectance at 0.12 ms. It was observed that the sudden change in reflectance was related to the formation of a crater on the target. By slightly defocusing the beam it was observed that when the incident laser pulse failed to produce a crater, the drop in the reflectance was not observed. Also the theoretical model described in Appendix A estimates that the temperature reached at the center of the laser–metal interaction area at 0.12 ms after the start of the pulse would be 2447 K, which is within the vicinity of the evaporation temperature of the Al metal (2740 K). This suggests that an absorptive metal vapor plume was forming at the time the reflectance started to drop and that the crater was formed by the recoil pressure generated by the vaporizing metal. Further confirmation of the absorptive plume formation over target surface is given by the plume transmittance result shown in Fig. 8(*a*).

Further examination of the reflectance curve shows that after 0.38 ms the value of reflectance starts increasing and eventually reaches the value of room temperature reflectance at the end of the pulse. This trend is explained by the plume transmittance curve shown in Fig. 8(*a*), which indicates that the plume transmittance starts increasing around 0.25 ms. It should be noted that the zero on the time scale in the transmittance curve does not correspond to the zero in the reflectance curve, because the reflectance and transmittance are measured in two independent experiments, which were not time-correlated. But as shown in Fig. 4(*b*) the time for which the reflectance value remains below the room temperature reflectance value is about 0.48 ms and Fig. 8(*a*) shows that the absorptive plume exists over the sample for about 0.5 ms. Therefore the association of absorptive plume formation with the observed drop in the reflectance appears to be justifiable within the limits of experimental error.

O_2 Atmosphere. Figure 4(*b*) shows that the reflectance for an O_2 atmosphere also starts at the same value of 0.72 as for the Ar atmosphere case, but the decrease in reflectance occurs at 0.07 ms, which is 0.05 ms earlier than for the Ar case. As everything else between the O_2 and Ar case was kept the same, the earlier drop in reflectance is attributed to an oxide layer formation. Theoretical calculation shows that the temperature reached at 0.07 ms would be 2225 K, which is 515

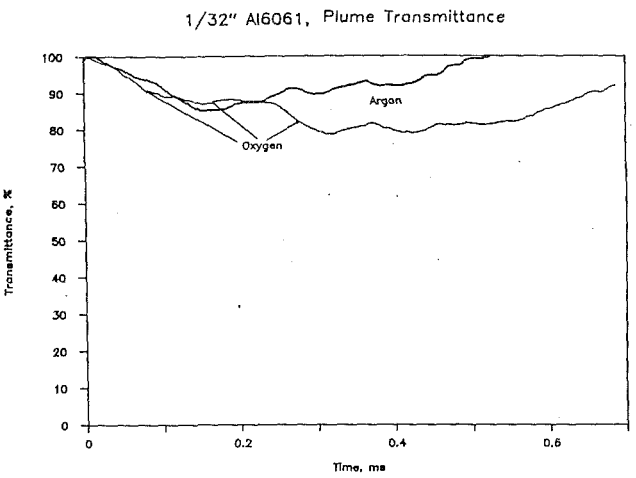

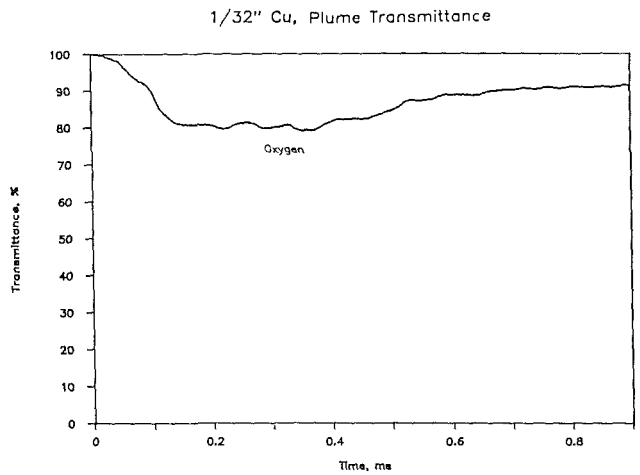

Fig. 8 Transmittance of plume formed under O_2 and Ar atmosphere for (*a*) A16061 (pulse 2) and (*b*) Cu (pulse 3)

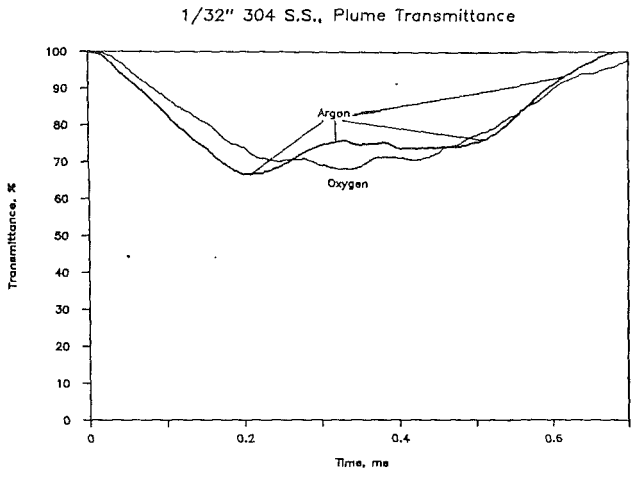

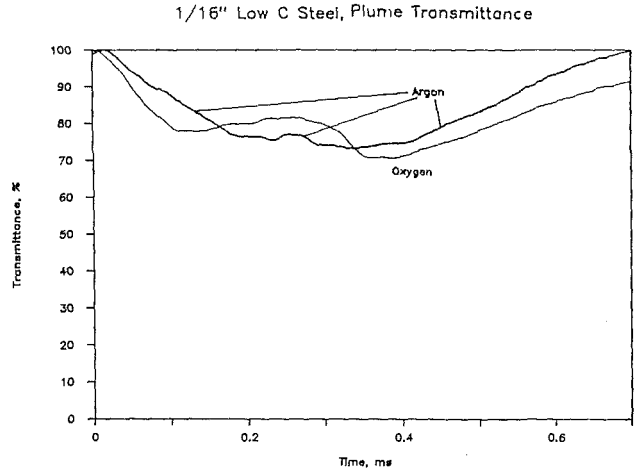

Fig. 9 Transmittance of plume formed under O_2 and Ar atmospheres for (*a*) 304 stainless steel (pulse 2) and (*b*) low C steel (pulse 2)

K below the Al metal evaporation temperature (2740 K) and 1028 K below the aluminum oxide dissociation temperature (3253 K) but is very close to the oxide melting temperature (2320 K). It is interesting in this regard to note that the absorption index of pure Al_2O_3 increases from about 10^{-6} to 10^{-3} upon melting (Parry and Brewster, 1988). Furthermore, Auger spectroscopic study of the conventionally oxidized A16061 sample, oxidized for 5 h at 813 K, shows that the oxide formed on the surface is a gray-colored magnesium oxide. Similar observation of darker magnesium oxide formation over an Al-Mg alloy has been reported by Smeltzer (1958). Even though the kinetics of oxide formation could be different under isothermal conditions and pulsed laser heating conditions, it seems likely that there is an initial increase in the absorptivity of the surface due to oxide formation, which quickly leads the surface to the dissociation temperature of the oxide. Once plume formation takes place it dominates the process. The plume transmittance result is shown in Fig. 8(*a*). The plume formed in an O_2 atmosphere is more opaque and lasts longer than the plume formed in an Ar atmosphere, indicating more absorptive species formation under the O_2 atmosphere. Whenever the probe laser beam signal in transmittance measurement failed to come back up to its starting value at the end of the laser pulse, it was observed that a lip had formed around the crater and was obstructing the probe beam.

As seen in Fig. 4(*b*), the value of reflectance does not return to the room temperature value of 0.72 at the end of the laser pulse but stays low at 0.6. This is due to the presence of an oxide layer on the crater. The effect is not the cavity effect because the crater formed in the Ar atmosphere was observed to be deeper and slightly smaller in diameter than the crater formed in an O_2 atmosphere, and as stated above the reflectance value comes back up to the room temperature value of reflectance at the end of the pulse with Ar atmosphere.

Cu Sample

Ar Atmosphere. Due to the high reflectivity of Cu (0.98), the energy in pulse 3 was not sufficient to cause any permanent damage under an Ar atmosphere. The curves in Fig. 5(*a*) show that the reflected energy signal under the Ar atmosphere at the focused situation remains almost the same as the reflected energy signal for the defocused situation. No target damage was observed under the microscope at a magnification of 50×. The temperature reached at the end of the pulse is estimated to be 417 K, which is too low to cause any melting or evaporation.

O_2 Atmosphere. Under an O_2 atmosphere, a crater was formed on the target surface and the reflected energy signal at the focused situation is shown in Fig. 5(*a*). Figure 5(*b*) shows that the value of the reflectance starts decreasing at 0.08 ms. The temperature that would be reached at this point is estimated to be 383 K, which is too low to cause any evaporation. As there is no drop in reflectance observed under an Ar atmosphere for similar conditions, the initial drop observed under the O_2 atmosphere is attributed to the change in the absorptivity of the surface due to the oxide formation. The increase in the absorptivity of the surface eventually leads to vapor formation and plume initiation, as made evident by the transmittance measurement shown in Fig. 8(*b*) and the fact

that reflectance at the end of the pulse remains at 0.52. These results are similar to those obtained for Al6061, but the effect of the oxide formation is more prominent in the Cu case because of the large difference in the absorptivity of Cu compared to the absorptivity of Cu_2O and CuO (Makino et al., 1986).

As mentioned earlier, the fact that the reflectance at the end of the pulse remains below the initial reflectance could be due to the surface oxide layer on the crater and/or due to the cavity formation. To distinguish between the two effects, a shorter pulse, pulse 4, was directed at the Cu sample under an O_2 atmosphere and the results of the reflectance measurement were as shown in Fig. 6. After the initial value of 0.98, the reflectance returned to the value of 0.8 at the end of the pulse. Due to the shorter width of pulse 4 the crater formed was shallow and small in diameter compared to the crater formed by pulse 2 on Al6061 target under the Ar atmosphere. This indicates that the cavity effect was negligible. Therefore the reflectance value of 0.8 at the end of pulse 4 was attributed to the presence of an oxide layer. This means that the reflectance value of 0.52 observed in Fig. 5(*b*) must be due to the combined effect of oxide layer and cavity formation.

304 Stainless Steel Sample. The results of the reflectance variation for 304 SS under O_2 and Ar atmospheres are shown in Fig. 7(*a*). Reflectance starts decreasing from the room temperature value after 0.04 ms in both cases. As the room temperature reflectance is 0.68 for the 304 SS sample, the evaporation temperature is reached very quickly. Theoretical calculation estimates that the temperature reached at 0.04 ms without any change in the absorption mechanism (*i.e.*, no plume formation) would be 6450 K, which is definitely in excess of the temperature required to cause evaporation and plume initiation. Oxidation seems to be playing a very small role for 304 SS samples under the conditions of the present study. The plume transmittance measurements are shown in Fig. 9(*a*).

Low C Steel Sample. The reflectance and the plume transmittance results for low C steel are shown in Figs. 7(*b*) and 9(*b*). The results are qualitatively the same as those for 304 SS. Reflectance starts decreasing from the room temperature value after 0.08 ms in both O_2 and Ar atmosphere cases. Again the low room temperature value of the reflectance (0.55) is responsible for early plume formation. The theoretical calculation estimates that the temperature reached at 0.08 ms assuming no plume formation would be 5581 K, which definitely exceeds the boiling point for Fe (3023 K). These results indicate that if the heating rate is fast, due to the high absorptivity of the metal, the boiling point of the metal would be reached very quickly and the oxide formation effects would be negligible.

Conclusions and Summary

The results for Al6061 and Cu clearly show that oxide layer formation during the early stages of irradiation increases the amount of energy absorbed by these metals. For Cu the reflectance decreases from 0.98 to as low as 0.8 due to the oxide layer formation, whereas for Al6061 the reflectance reduces from 0.72 to 0.6 due to the oxide formation. The effect of oxide formation seems to be negligible for 304 SS and low carbon steel. The plume transmittance measurements for Al6061 indicate that the plume formed under an O_2 atmosphere is more absorptive and exists for a longer time than the plume formed under an Ar atmosphere. No plume formation takes place for Cu under an Ar atmosphere but the plume formed under the O_2 atmosphere is absorptive in nature. For 304 SS and low-carbon steel the plumes formed under O_2 and Ar atmospheres are also absorptive in nature, exist for the same amount of time, and have the same degree of absorptivity.

Under the conditions of the present study the transmittance measurements show that the plumes formed over all the metals studied are absorptive in nature. Therefore it is concluded that once a plume is formed during laser-metal interaction, it significantly limits the amount of laser energy reaching the target. The reflectance measurements and temperature calculations indicate that metals (304 SS and low-carbon steel in the present case) with a relatively high value of room temperature absorptivity (>0.3) get heated very quickly to their boiling point. An oxidizing environment has negligible effect on the absorptivity of such metals because quicker evaporation of metal leads to an earlier plume formation during laser-metal interaction. Hence the laser energy coupling for a metal with a high absorptivity is controlled by the plume.

On the other hand for metals (Al6061 and Cu in the present case) with a relatively low value of room temperature absorptivity (<0.3), plume formation gets delayed in time because of slower heating rates. The absorptivity of such metals in the presence of an oxidizing environment increases due to the oxide formation. The amount of increase in absorptivity depends upon the radiative properties of the oxide relative to those of the metal. For Cu the absorptivity increases by a factor of 10 (from 0.02 to 0.2), due to the fact that Cu oxides are much more absorptive than Cu. For Al6061 the absorptivity increases by a factor of about 1.5 (from 0.28 to 0.4) due to the aluminum/magnesium oxide formation. Even though the absorptivities of solid aluminum oxide and magnesium oxide are essentially no larger than those of Al6061, it should be noted that the absorptivity of a thin, nonstoichiometric mixture of aluminum and magnesium oxide or aluminum and aluminum oxide near the surface is much greater than that of the metal alloy Al6061 or either solid oxide in pure form. Further, the absorptivity of metal oxides typically increases significantly upon melting. Thus the mechanism responsible for the enhancement of metal target absorptivity prior to plume formation may be either the nonstoichiometric transition layer between metal and oxide near the target surface or the melting of relatively stoichiometric oxide formed on the surface. In either case, the formation of an oxide layer on the surface of a poorly absorbing metal increases the laser energy absorption during laser-metal interaction. These results should prove to be useful in modeling gas-assisted laser metal processing phenomena such as laser drilling, cutting, etc.

Acknowledgments

Support for this work from the National Science Foundation (CBT86-96162) is gratefully acknowledged.

References

Arzuov, M. I., Barchukov, A. I., Bunkin, F. V., Konov, V. I., and Lyubin, A. A., 1976, "Violent Surface Oxidation of Metals and Associated Phenomena Resulting From Continuous Irradiation With CO_2 Laser Radiation," *Sov. J. Quant. Electron.*, Vol. 5, No. 8, pp. 931-935.

Arzuov, M. I., Karasev, M. E., Konov, V. I., Kostin, V. V., Metev, S. M., Silenok, A. S., and Chapliev, N. I., 1978, "Investigation of the Absorption Coefficient of Metal Targets Irradiated by Pulse-Periodic CO_2 Laser Radiation in Air," *Sov. J. Quant. Electron.*, Vol. 8, No. 7, pp. 892-897.

Asmus, J. F., and Baker, F. S., 1969, "Nonlinear Surface Phenomena Associated With Laser Beam Penetration of Metatls," *Record of the 10th Symposium on Electron, Ion, and Laser Beam Technology*, San Francisco Press Inc., May, pp. 241-246.

Bergel'son, V. I., Golub', A. P., Loseva, T. V., Nemchinov, I. V., Orlova, T. I., Popov, S. P., and Svettsov, V. V., 1974, "Appearance of a Layer Absorbing Laser Radiation Near the Surface of a Metal Target," *Sov. J. Quant. Electron.*, Vol. 4, No. 5, pp. 704-706.

Bonch-Baruevich, A. M., Balashov, E. I., Gagarin, A. P., Zakharov, A. S., Kotylev, V. N., and Kalabushkin, O. I., 1973, "Experimental Investigation of Screening in Aluminum Vapor," *JETP Lett.*, Vol. 17, pp. 241-244.

Duley, W. W., 1976, *CO_2 Lasers: Effects and Applications*, Academic Press, New York.

Makino, T., Matsuda, S., Hirata, N., and Kunitomo, T., 1986, "Measurement of Transient Behaviors in Thermal Radiation Characteristics of Materials by High-Speed Spectroscopy," *Proc. of the Eighth Int. Heat Transfer Conf.*,

Vol. 2, C. L. Tien, V. P. Carey, and J. K. Ferrell, eds., San Francisco, CA, pp. 577-582.

Matsunawa, A., and Katayama, S., 1985, "High Speed Photographic Study of Yag Laser Material Processing," *Laser Welding, Machining and Material Processing*, C. Albright, ed., ICALEO'85 Proc., L.I.A., p. 41-48.

Matsunawa, A., Yoshida, H., and Katayama, S., 1984, "Beam-Plume Interaction in Pulsed Nd-Yag Laser Processing," ICALEO-84 Proc., L.I.A., Vol. 44, pp. 35-42.

Parry, D. L., and Brewster, M. Q., 1988, "Optical Constants and Size of Propellant Combustion Aluminum Oxide (Al_2O_3) Smoke," AIAA Paper No. 88-3350, presented at the AIAA/ASME/ASEE 24th Joint Propulsion Conf., Boston, MA.

Peebles, H. C., and Williamson, R. L., 1987, "The Role of the Metal Vapor Plume in Pulsed Nd-YAG Laser Welding on Aluminum 1100," *Proc. International Conf. on Laser Advanced Materials Processing*, Osaka, Japan, printed by High Temp. Soc. of Japan, pp. 19-24.

Rosen, D. I., Mitteldorf, J., Kothandaraman, G., Pirri, A. N., and Pugh, E. R., 1982, "Coupling of Pulsed 0.35-μm Laser Radiation to Aluminum Alloys," *J. Appl. Phys.*, Vol. 53, No. 4, pp. 3190-3200.

Smeltzer, W. W., 1958, "Oxidation of an Aluminum-3 Per Cent Magnesium Alloy in the Temperature Range 200-500 C," *J. Electrochemical Soc.*, Vol. 105, No. 2, pp. 67-71.

Stegman, R. L., Schriempf, J. T., and Hettche, L. R., 1973, "Experimental Studies of Laser-Supported Absorption Waves With 5-ms Pulses of 10.6 μm Radiation," *J. Appl. Phys.*, Vol. 44, No. 8, pp. 3675-3681.

Von Allmen, M., Blaser, P., Affolter, K., and Sturmer, E., 1978, "Absorption Phenomena in Metal Drilling With Nd-lasers," *IEEE J. of Quant. Electron.*, Vol. QE-14, No. 2, pp. 85-88.

Wautelet, M., and Andrew, R., 1987, "Laser-Assisted Oxidation of Metallic Films on Insulators," *Philosophical Magazine B*, Vol. 55, No. 2, pp. 261-269.

APPENDIX A

The theoretical model described by Duley (1976) solves the time-dependent heat conduction equation. The time-dependent temperature distribution at the solid surface is obtained for applied constant power P for $t>0$, over an area πA^2, at the $z=0$ plane, of the semi-infinite region. The model assumes that the thermophysical properties of the metal are constant and independent of temperature and the laser intensity within the focused area is spatially uniform. For further details of the model, refer to Duley (1976). The solution for temperature in the (r, z) coordinate system is given as

$$T(r, z, t) = \frac{P\alpha_\lambda}{2\pi Ak}\int_0^\infty J_0(\beta r)J_1(\beta A)\left\{e^{-\beta z}\mathrm{erfc}\left[\frac{z}{2\sqrt{\kappa t}}-\beta\sqrt{\kappa t}\right]\right.$$
$$\left.-e^{\beta z}\mathrm{erfc}\left[\frac{z}{2\sqrt{\kappa t}}+\beta\sqrt{\kappa t}\right]\right\}\frac{d\beta}{\beta}$$

Table 2 Thermophysical properties of metals

Metal	k, W/cm°C	κ, cm^2/s	α_λ
Al	2.1	0.85	0.28
Cu	3.6	0.95	0.02
304 SS	0.21	0.065	0.32
Fe (Low C Steel)	0.6	0.1	0.45

The principal sources of uncertainty in using this simple analysis are:

1 Nonconstant thermophysical properties
2 Negligible vapor phase absorption
3 Laser power and beam diameter estimations

The uncertainty associated with (1) is difficult to estimate due to the limited data available. The values of thermophysical properties, averaged over the temperature range (room temperature to melting temperature of the metal) obtained from Duley (1976) are listed in Table 2. The use of room temperature value of absorptivity for calculations is reasonable because the temperature calculations are performed only up until the significant drop in the reflectance is observed, and as indicated by the reflectance measurements the value of absorptivity during these period is close to the room temperature value of absorptivity.

The error introduced by (2) has been avoided by applying the model only up until significant vaporization occurs as indicated by a rapid drop in reflectance and transmittance. When the calculated temperature clearly exceeded the boiling or dissociation temperature, that was taken as an indication that plume formation had occurred and the calculated temperature was recognized as representing an unrealistic overprediction.

The error introduced by (3) can be avoided by carrying out very accurate measurements of the laser power and beam diameter, but as stated earlier the temperature calculations in the present study are performed to support the conclusions that are based primarily upon the reflectance and plume transmittance measurements. The temperature values obtained using the estimated values of laser power and beam diameter are accurate to within a few hundred degrees, which is sufficient for the present purposes.

Dependent Absorption and Extinction of Radiation by Small Particles

S. Kumar[1]

C. L. Tien
A. Martin Berlin Professor.
Fellow ASME

Department of Mechanical Engineering,
University of California,
Berkeley, CA 94720

This study presents an analytical model to evaluate the dependent absorption and extinction characteristics of dense particulate systems. Simple expressions are obtained by considering statistical averages based on the random character of the particulate medium. Departure from the assumption of independent scattering and absorption of radiation originates from two mechanisms: perturbation of the internal field of each particle by the presence of other particles, and coherent addition (i.e., taking into account the constructive/destructive interference) of the far-field scattered radiation. Dependent scattering has been previously studied analytically by considering the second mechanism only. Dependent absorption, which is due to the former, has not been considered in the literature even though absorption is more important than scattering in the extinction of radiation by small (Rayleigh) absorbing particles.

Introduction

Modern engineering technology is replete with systems in which thermal radiation is a dominant mode of energy transfer. Many systems within this category contain particulates that actively participate in the radiative transfer processes. Some examples that involve highly concentrated small particles are fluidized and packed-bed combustors, packed-bed catalytic reactors, microsphere insulations, combustors with deposited soot on the walls, and furnaces laden with agglomerated particles. In these systems the scattering and absorption of thermal radiation by particles plays an important role in the overall energy transfer, and its understanding is central to the prediction and evaluation of system performance.

Independent scattering is the commonly used assumption whereby each particle in a densely packed system acts independently in the absorption and scattering of radiation, unaffected by the presence of other particles. By this consideration the energy scattered (or absorbed) by a system of particles is the algebraic sum of the energy scattered (or absorbed) by each particle. The radiative characteristics of the assembly are obtained by summing up the characteristics of each isolated particle (Mie theory), which are readily available from literature (Kerker, 1961; Bohren and Huffman, 1983).

When the particles are densely packed the above assumption of independent scattering and absorption breaks down, as indicated by the experimental studies, some of which are referenced here (Hottel et al., 1971; Brewster and Tien, 1982; Yamada et al., 1986). This is due to two fundamental mechanisms. The first mechanism is the near-field interparticle effect, where the internal field of each particle is affected by the presence of the others. Consequently this modifies the amount of radiation absorbed as well as the amount of radiation scattered by each particle. The second is that of coherent addition (i.e., taking into account the constructive/destructive interference) of the scattered radiation by each particle in the far field, which is manifested by a change in the total scattered field. The second mechanism and its effect on the scattering of radiation by dense homogeneous systems has been studied analytically by various researchers (Debye, 1925; Twersky, 1975; Cartigny et al., 1986) and has been reviewed recently by Tien and Drolen (1987). A regime map, based primarily on experimental data, indicating the regions where these mechanisms lead to a significant deviation from the independent scattering assumption is also presented for nonabsorbing particles (Brewster and Tien, 1982; Tien and Drolen, 1987).

Both of the above-stated mechanisms are taken into account by solving exactly the electromagnetic equations for two particles (Hunka and Mei, 1981), and for assemblies of Rayleigh particles (i.e., whose diameters are small compared to the wavelength) (Jones, 1979a, 1979b). These exact solutions have to be numerically evaluated at the expense of immense computational effort, and are not conducive to obtaining the general radiative characteristics for randomly packed particulate systems typical in engineering applications. In addition, these results pertain to configurations of particles that are fixed relative to the incident radiation and require a knowledge of the exact position of each particle in the system.

Most small particles commonly encountered in engineering practice, such as soot, fly-ash, and other combustion products, have a significantly large index of absorption. The scattering efficiency of these small particles, whose diameters are smaller than the wavelength, is proportional to the fourth power of the ratio of the diameter to the wavelength, whereas the absorption efficiency is proportional to the first power (Kerker, 1961; Bohren and Huffman, 1983). Thus absorption has a greater impact on the radiative transfer through such particulate systems as compared to the scattering. However, the previous analyses of dense homogeneous particulate systems have not considered the dependent aspects of absorption (Tien and Drolen, 1987) or have presented exact solutions (Jones, 1979a, 1979b) that are not adaptable for predicting general absorption and scattering characteristics.

This study presents a complete model for predicting the absorption and the scattering characteristics of homogeneous dense particulate systems by including both mechanisms of dependent effects previously mentioned. The near-field interaction between closely packed Rayleigh particles is examined by solving the integral equations that describe the electric field in the particulate medium (Saxon, 1973). The solutions are generalized for random homogeneous clouds by a spatial averaging process and by using statistical distributions for the number density of the particles. Utilizing scattering analysis that accounts for the coherent addition of the scattered radiation in the far field (Tien and Drolen, 1987), a complete model

[1]Present address: Lawrence Berkeley Laboratory, Berkeley, CA 94720.

Contributed by the Heat Transfer Division and presented at the 24th National Heat Transfer Conference, Pittsburgh, Pennsylvania, August 9–12, 1987. Manuscript received by the Heat Transfer Division May 3, 1988. Keywords: Packed and Fluidized Beds, Radiation, Sprays/Droplets.

for dependent scattering and absorption is developed. Dependent extinction is then evaluated from the sum of the corresponding scattering and absorption quantities.

Theoretical Model

Under consideration is a homogeneous system of randomly positioned and uniformly distributed spheres dispersed in a dielectric medium. The particles are of a uniform diameter D and are small so that they lie in the Rayleigh scattering regime, i.e., $\alpha << 1$, where α, defined as $\pi D/\lambda$, is the size parameter of the spheres and λ is the wavelength of the incident radiation. The Rayleigh regime encompasses many types of particle frequently found in engineering systems, such as soot and combustion products in flames and smoke layers, microspheres in insulations, and other small particles especially at long wavelength (i.e., infrared) applications. The spheres may be absorbing, but with a moderate index of absorption κ in order to satisfy the Rayleigh–Debye scattering condition: $2\alpha|m-1| << 1$, where m is the complex refractive index of the particles represented by $n+i\kappa$, and n is the index of refraction. The dielectric matrix has a refractive index of unity. The above condition ensures that the phase shift across the particle is negligible and the internal field of each particle is approximately constant.

The incident radiation is assumed to be a plane wave propagating in the positive z direction, as shown in Fig. 1. The incident electric field vector $\mathbf{E}_{inc}$ is assumed proportional to $\exp(ikz - i\omega t)$, where k $(=2\pi/\lambda)$ is the propagation constant, ω $(=2\pi\nu)$ is the angular frequency, ν is the frequency of the incident radiation, and t is time. The incident field is taken to be unpolarized, representative of thermal radiation in engineering systems such as natural light.

The internal field of each particle in the system is evaluated

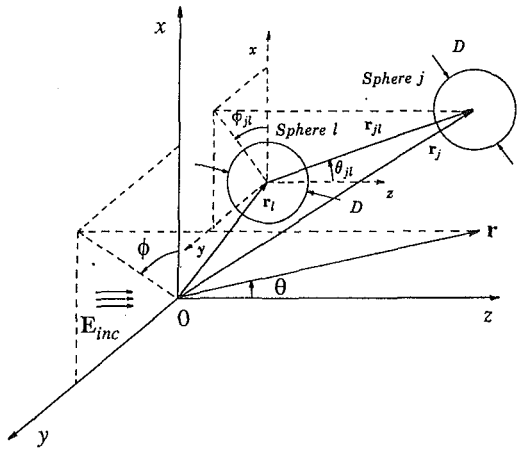

Fig. 1 Coordinate system

from the integral equation given below for the electric field $\mathbf{E}$ at a point $\mathbf{r}$ in space (Saxon, 1973):

$$\mathbf{E}(\mathbf{r}) = \mathbf{E}_{inc}(\mathbf{r}) + k^2 \sum_{j=1}^{N} \int_{V_j} \mathbf{E}(\mathbf{r}_j')(\epsilon - 1) G(\mathbf{r}, \mathbf{r}_j') dV_j'$$

$$+ \sum_{j=1}^{N} \int_{V_j} [\nabla_j(\nabla_j \cdot \mathbf{E}(\mathbf{r}_j')(\epsilon - 1))] G(\mathbf{r}, \mathbf{r}_j') dV_j' \quad (1)$$

where N is the total number of particles, $\mathbf{r}_j'$ defines a location within the jth particle, $\epsilon = m^2$, and $G(\mathbf{r}, \mathbf{r}_j')$ is a tensor spherical Green's function. Using the assumption of uniform internal field within each particle j, $\mathbf{E}(\mathbf{r}_j)$ can be taken out of the in-

Nomenclature

a, a', b, c = elements of tensor $\mathbf{T}_{ij}$
A = complex number, equation (10)
d, e = elements of tensor $\mathbf{T}_{ij}$
D = diameter of the particles
$\mathbf{e}$ = unit vector
$\mathbf{E}$ = electric field vector
f_v = solid volume fraction $= 4N\pi(D/2)^3/3V$
$F(\theta)$ = form factor to account for coherent addition of intensities, equation (16)
$g(R)$ = radial distribution of number density, normalized by N/V
$G(\mathbf{r}, \mathbf{r}_j)$ = Green's function in spherical geometry
$h_n^{(m)}$ = spherical Bessel functions
$H(\beta)$ = $3(\sin\beta - \beta\cos\beta)/\beta^3$
i = $\sqrt{-1}$
I = scattered intensity, energy/steradian/projected area
I_0 = intensity of incident radiation
k = propagation constant $= 2\pi/\lambda$
L = length of the one-dimensional medium
m = complex refractive index $= n + i\kappa$
n = index of refraction
N = number of particles
$P_n^{(m)}$ = Legendre function
q = radiative flux
Q = efficiency
$\mathbf{r}$ = radial vector
R = ratio of radial distance to diameter $= r/D$
t = time
T = temperature
$\mathbf{T}_{ij}$ = tensor defined by equation (3)
V = volume
x, y, z = Cartesian coordinates
α = six parameter $= \pi D/\lambda$
β = $4\alpha \sin(\theta/2)$
γ = function defined by equation (20)
ϵ = relative dielectric constant, m^2
ζ = complex correction factor, equation (13)
θ = polar angle
κ = index of absorption
λ = wavelength of incident radiation
Λ = function defined in Table 3
ν = frequency of incident radiation
Ξ = function defined in Table 3
τ = optical depth
ϕ = azimuthal angle
Φ = scattering phase function
χ = parameter in liquid model
ω = angular frequency $= 2\pi\nu$

Subscripts

a = absorption
D = dependent effects
e = extinction
inc = incident radiation
$indep$ = independent theory
j, l = particle identification
L = length of one-dimensional medium
M = Mie theory for one particle
N = N particles
s = scattering

Superscripts

$\bar{}$ = averaged over solid angle

tegrals in equation (1) and the following equation for the internal field of the lth particle is obtained (Jones, 1979a):

$$\left[\mathbf{E}(\mathbf{r}_l)-\frac{i}{3}\left(\frac{\epsilon-1}{\epsilon+2}\right)\alpha^3\sum_{\substack{j=1\\ j\neq 1}}^{N}\mathbf{T}_{jl}\cdot\mathbf{E}(\mathbf{r}_j)\right]=\frac{3}{\epsilon+2}\,\mathbf{E}_{inc}(\mathbf{r}_l),$$

$$l=1,\ \ldots,\ N \tag{2}$$

The cartesian tensor $\mathbf{T}_{jl}$ has the following form:

$$\mathbf{T}_{jl}=\begin{bmatrix} a & b & c\\ b & a' & d\\ c & d & e\end{bmatrix} \tag{3}$$

with

$$\begin{aligned}
a&=-h_0^{(1)}(kr_{jl})-h_2^{(1)}(kr_{jl})[P_2(\cos\theta_{jl})\\
&\quad-0.5\cos(2\phi_{jl})P_2^{(2)}(\cos\theta_{jl})]\\
a'&=-h_0^{(1)}(kr_{jl})-h_2^{(1)}(kr_{jl})[P_2(\cos\theta_{jl})\\
&\quad+0.5\cos(2\phi_{jl})P_2^{(2)}(\cos\theta_{jl})]\\
b&=0.5h_2^{(1)}(kr_{jl})\sin(2\phi_{jl})P_2^{(2)}(\cos\theta_{jl})\\
c&=-h_2^{(1)}(kr_{jl})\cos(\phi_{jl})P_2^{(1)}(\cos\theta_{jl})\\
d&=-h_2^{(1)}(kr_{jl})\sin(\phi_{jl})P_2^{(1)}(\cos\theta_{jl})\\
e&=2h_2^{(1)}(kr_{jl})P_2^{(1)}(\cos\theta_{jl})
\end{aligned} \tag{4}$$

where $h_m^{(n)}$ and $P_m^{(n)}$ are the spherical Bessel functions and the associated Legendre functions, respectively, and θ and ϕ are the polar and azimuthal angles. The subscript jl indicates the relative angle between particles j and l (Fig. 1). Equation (2) represents a system of $3N$ linear algebraic equations for the $3N$ unknown electric field Cartesian components. For a system of particles where N is extremely large, the resulting system of equations is impossible to solve by existing techniques. The evaluation of the components of $\mathbf{T}_{jl}$ for every pair of particles in the particulate system is also a task of immense proportions. Furthermore, the vector position of each particle has to be specified.

The mathematical intransigence of the set of equations described above is eased with the introduction of the following approximation. Noting that the incident field is proportional to $\exp(ikz)$ and that the fields within the particles are assumed uniform, the internal fields of the secondary particles j in equation (2) may be related to that of the primary particle l under consideration by the leading order approximation

$$\mathbf{E}(\mathbf{r}_j)=\exp(ik(z_j-z_l))\mathbf{E}(\mathbf{r}_l) \tag{5}$$

Physically, the above approximation inplies that the magnitudes of the internal fields of the *secondary* scatterers j are taken to be the same as that of the *primary* particle l under consideration, and that these internal fields have a phase difference equal to the instantaneous phase difference of the incident radiation striking the respective particles. This is a reasonable approximation since in a dense randomly packed isotropic medium no particle is uniquely defined in terms of its electromagnetic interactions with the rest of the system. Each particle has similar interactions with the surrounding medium and hence it is expected that their internal fields are similar in magnitude. The above is different from the Rayleigh-Gans-Debye or Born approximation (Bohren and Huffman, 1983), which takes the internal field of each particle to be identically proportional to the local incident field, i.e., neglects the near-field effects, and can be obtained by neglecting the second term on the left side of equation (2). Substituting equations (5) into equation (2) yields

$$\left[\mathbf{I}-\frac{i}{3}\left(\frac{\epsilon-1}{\epsilon+2}\right)\alpha^3\sum_{\substack{j=1\\ j\neq 1}}^{N}\exp(ik(z_j-z_l))\mathbf{T}_{jl}\right]\cdot\mathbf{E}(\mathbf{r}_l)=\frac{3}{\epsilon+2}\,\mathbf{E}_{inc}(\mathbf{r}_l),\qquad l=1,\ \ldots,\ N, \tag{6}$$

where $\mathbf{I}$ is the identity tensor.

Even though equation (6) has alleviated the need to solve large systems of linear equations, it remains complicated due to the dot-product that interrelates each Cartesian component of $\mathbf{E}(\mathbf{r}_l)$ to the other two. Equation (6) is a system of three linear equations for three unknown Cartesian components of $\mathbf{E}(\mathbf{r}_l)$. The solution of the equation still requires a knowledge of the position vectors of the various particles in space and is not suitable for analyzing random systems with a large number of particles. This complexity is made tractable by using the center of the lth particle as the reference and assuming the angular positions of the other spheres j to be random in space. This is incorporated into the above by averaging $\mathbf{T}_{jl}$ over all directions:

$$\bar{\mathbf{T}}_{jl}=\frac{1}{4\pi}\int_{\phi_{jl}=0}^{2\pi}\int_{\theta_{jl}=0}^{\pi}\exp(ikr_{jl}\cos\theta_{jl})\mathbf{T}_{jl}\sin\theta_{jl}d\theta_{jl}d\phi_{jl} \tag{7}$$

where the bar above indicates averaged over solid angle. The geometry from Fig. 1 has been used in equation (7) to note that $(z_j-z_l)=(\mathbf{r}_j-\mathbf{r}_l)\cdot\mathbf{e}_z=r_{jl}\cos\theta_{jl}$. From equations (3) and (4) the above averaging process yields $\bar{b}=\bar{c}=\bar{d}=0$, and

$$\begin{aligned}
\bar{a}=\bar{a}'&=-h_0^{(1)}(kr_{jl})\left[\frac{\sin(kr_{jl})}{kr_{jl}}\right]\\
&\quad-h_2^{(1)}(kr_{jl})\left[\frac{\sin(kr_{jl})}{kr_{jl}}+3\frac{\cos(kr_{jl})}{(kr_{jl})^2}-3\frac{\sin(kr_{jl})}{(kr_{jl})^3}\right]
\end{aligned} \tag{8}$$

Since $\bar{b}=\bar{c}=\bar{d}=0$, and the z component of the incident electric field vector $\mathbf{E}_{inc}(\mathbf{r}_l)$ is zero, the x and y components of $\mathbf{E}(\mathbf{r}_l)$ are now decoupled in equation (6) and the z component of $\mathbf{E}(\mathbf{r}_l)$ vanishes. This is a very significant result since it allows the dot-product on the left side to be replaced by an algebraic multiplication and the identity tensor to be replaced by unity. Also $\bar{e}$ can be dropped from further considerations, resulting in

$$\left[1-\frac{i}{3}\left(\frac{\epsilon-1}{\epsilon+2}\right)\alpha^3\sum_{\substack{j=1\\ j\neq 1}}^{N}\bar{a}(kr_{jl})\right]\mathbf{E}(\mathbf{r}_l)=\frac{3}{\epsilon+2}\,\mathbf{E}_{inc}(\mathbf{r}_l),\qquad l=1,\ \ldots,\ N. \tag{9}$$

The above is a simple scalar equation that permits the Cartesian components of the electric internal field to be determined without solving linear algebraic equations. However, information about the radial separation between pairs of particles is still needed to solve equation (9). This is simplified by introducing statistical pair-distribution functions. Under the assumption of a continuous and infinite distribution of particles in the cloud, the summation in equation (9) is replaced by an integral using a statistical number density distribution function $g(r)$ as a weighting function, i.e., by defining

$$A=\frac{N}{V}\,4\pi\int_0^{\infty}r^2\bar{a}(kr)g(r)dr=24f_v\int_0^{\infty}\bar{a}(2\alpha R)g(R)R^2dR \tag{10}$$

where f_v is the solid volume fraction, R is the nondimensional radial distance r/D, and g is the ratio of the number of particles per unit volume at a radial distance r from the center of the reference particle l to the average number density N/V. The distribution function g obeys the normalization

$$\frac{N}{V}\int_V g(r)dV \approx 24f_v\int_0^\infty g(R)R^2dR = N \tag{11}$$

Using the definitions of spherical Bessel functions, equation (8) and (10) are combined to yield

$$A = 24f_v\int_0^\infty R^2\left[i\frac{\sin(2\alpha R)}{(2\alpha R)^2} + \left\{\frac{i}{2\alpha R}\left(\frac{3}{(2\alpha R)^2}-1\right) + \frac{3}{(2\alpha R)^2}\right\}\times\left\{\frac{\sin(2\alpha R)}{2\alpha R} + 3\frac{\cos(2\alpha R)}{(2\alpha R)^2} - 3\frac{\sin(2\alpha R)}{(2\alpha R)^3}\right\}\right] g(R)\exp(i2\alpha R)dR \tag{12}$$

where $g(R)=0$ for $0\le R<1$, and $g(R)\to 1$ as $R\to\infty$.

Defining a factor ζ as

$$\zeta = \left[1 - \frac{i}{3}\left(\frac{\epsilon-1}{\epsilon+2}\right)\alpha^3 A\right]^{-1} \tag{13}$$

and using equation (10), equation (9) is reduced to

$$\mathbf{E}(\mathbf{r}_l) = \zeta\frac{3}{\epsilon+2}\mathbf{E}_{inc}(\mathbf{r}_l) \tag{14}$$

where l is any particle in the cloud. Thus modeling the homogeneous particulate system as a random statistical distribution of particles has reduced the complicated system of linear equations to a linear scalar equation. This facilitates the computation of the general radiative characteristics of the system without having to know the exact geometric structure of the particulate medium. Since ζ is a complex correction factor that is multiplied to the internal field predicted by the Mie theory to obtain the internal field that accounts for the interparticle effects, all subsequent scattered fields are similarly modified. The scattering intensity, which is proportional to the square of the magnitude of the electric vector of the scattered field, is modified to include the near-field interparticle effects by a multiplication of $|\zeta|^2$.

A scattering analysis recently presented (Cartigny et al., 1986; Tien and Drolen, 1987), along with equation (14), permits the scattering intensity I_{DN} from a cloud of N particles to be derived as

$$I_{DN}(\theta) = N|\zeta|^2 F(\theta) I_M(\theta) \tag{15}$$

where I_M is the intensity of Mie scattering from a single isolated sphere and $F(\theta)$ is a form factor that accounts for the coherent addition (i.e., taking into account the phase differences) of the scattered radiation in the far field. The representative volume containing N particles is assumed small enough that the far-field scattered radiation is devoid of any multiple scattering components and the single-scatter phase differences are preserved, and yet large enough for the dependent effects to be accurately modeled. The representation of $F(\theta)$ is as follows (Tien and Drolen, 1987):

$$F(\theta) = 1 + 24f_v\int_0^\infty R^2[g(R)-1]\frac{\sin(\beta R)}{\beta R}dR \tag{16}$$

where $\beta = 4\alpha\sin(\theta/2)$. Angular averaging of the positions of the particles and the assumption of a continuous statistical distribution of particles are used to obtain the above equation for a homogeneous particulate system. Coherent addition of radiation is always present in the far field, but for particles that are randomly positioned with large interparticle clearance (greater than 0.5λ) $F(\theta)\to 1$ (Tien and Drolen, 1987).

The dependent extinction and scattering efficiencies, Q_{eD} and Q_{sD}, for Rayleigh particles are obtained from the above by following a derivation from the scattering and extinction fundamentals (Bohren and Huffman, 1983; Kumar, 1987; Kumar and Tien, 1989), which yields

$$Q_{aD} = 4\alpha\mathrm{Im}\left(\zeta\frac{\epsilon-1}{\epsilon+2}\right) \tag{17}$$

$$Q_{sD} = \frac{8}{3}\alpha^4\left|\frac{\epsilon-1}{\epsilon+2}\right|^2|\zeta|^2\gamma = Q_{sM}|\zeta|^2\gamma \tag{18}$$

$$Q_{eD} = Q_{aD} + Q_{sD} \tag{19}$$

where

$$\gamma = \frac{1}{4\pi}\int_{\phi=0}^{2\pi}\int_{\theta=0}^{\pi} F(\theta)\Phi_M(\theta)\sin\theta d\theta d\phi \tag{20}$$

and Φ_M is the Mie scattering phase function, which for the Rayleigh particles under consideration is given by

$$\Phi_M(\theta) = \frac{3}{4}(1+\cos^2\theta) \tag{21}$$

The dependent scattering phase function is obtained from its basic definition (Kerker, 1961; Bohren and Huffman, 1983)

$$\Phi_D(\theta) = \frac{4\pi}{Q_{sD}}\frac{I_{DN}(\theta)}{NI_0} \tag{22}$$

Using a similar definition of $\Phi_M(\theta)$ and the expression of $I_{DN}(\theta)$ from equation (15), the above equation is simplified to

$$\Phi_D(\theta) = \frac{Q_{sM}}{Q_{sD}}F(\theta)\Phi_M(\theta) = \frac{F(\theta)\Phi_M(\theta)}{\gamma} \tag{23}$$

The near-field interparticle effects do not modify the dependent scattering phase function, as is evident from the above. This follows from the definition of the phase function, which is the ratio of the energy scattered to the isotropically scattered energy; the factor $|\zeta|^2$ cancels out.

The radiative properties of single isolated Rayleigh particles, and hence of corresponding particulate systems in the independent scattering/absorption regime, are functions of the refractive index and size parameter. To account for the dependent effects, the present model requires additionally the value of the volume fraction and an appropriate distribution function. Details of the geometric structure within the particulate system are not of importance and the resulting formulation is very easy to use. This is demonstrated in the following sections.

Applications

The analytical model developed presents simple expressions to account for the interparticle effects on the radiative characteristics of spherical particles in a densely packed system. The application of this model is contingent on the selection of an appropriate distribution function $g(R)$. Accurate statistical distributions that are functions of the volume fraction and the size of the particles have been presented in the literature, such as that by Percus and Yevick (1958). The drawback of such a representation is that it has to be evaluated numerically for most cases and does not yield closed-form solutions. Since this study focuses on understanding the fundamentals of the dependent effects in a particulate system, three simple distributions are considered that enable closed-form solutions to be obtained. They are the gas model, the packed-sphere model (Cartigny et al., 1986), and the liquid model (Drolen and Tien, 1987), which are sketched in Fig. 2.

The gas model, which is more accurate for low volume fractions ($f_v<0.1$), has the following form:

$$g(R) = \begin{cases} 0 & R<1 \\ 1 & R>1 \end{cases} \tag{24}$$

This distribution function indicates that no neighboring particle exists within one particle diameter of the central scatterer

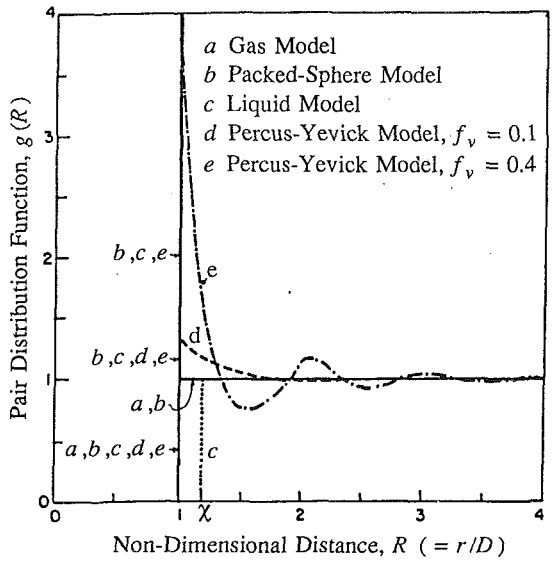

Fig. 2 Statistical pair distribution functions

Table 1 Expressions for ζ for Rayleigh particles

$g(R)$	ζ
Gas model	$\left[1 - \frac{\varepsilon-1}{\varepsilon+2} f_v(1 + 1.6\alpha^2)\right]^{-1}$
Packed-sphere model	$\left[1 - \frac{\varepsilon-1}{\varepsilon+2} f_v(1 + 0.7134\alpha^2)\right]^{-1}$
Liquid model	$\left[1 - \frac{\varepsilon-1}{\varepsilon+2} f_v(1 + 1.6\alpha^2(\chi^2 - 0.5541))\right]^{-1}$

Table 2 Expressions for $F(\theta)$

$g(R)$	$F(\theta)$
Gas model	$1 - 8f_v H(\beta)$
Packed-sphere model	$1 - 8f_v[H(\beta) - 0.831(\sin\beta)/\beta]$
Liquid model	$1 - 8f_v[\chi^3 H(\chi\beta) - 0.831(\sin\beta)/\beta]$
Percus-Yevick model	$(1 - f_v)^4/(1 + 2f_v)^2$, $\alpha \to 0$
$\beta = 4\alpha\sin(\theta/2)$	
$H(\beta) = 3(\sin\beta - \beta\cos\beta)/\beta^3$ $\approx 1 - \beta^2/10$, $\theta \to 0$, $\alpha \to 0$	

and outside this diameter the likelihood of finding another particle is uniform. The number of density of the particles at any radial distance greater than D is constant and is equal to N/V. The packed-sphere model attempts to account for a higher particle number density close to the central particle by introducing a Dirac delta function at $R = 1$. Otherwise it is the same as the gas model. The packed-sphere model is more accurate at higher volume fractions ($f_v > 0.1$) and is given by

$$g(R) = \begin{cases} 0 & R < 1 \\ 1 & R > 1 \end{cases}, \quad \lim_{\delta \to 0} \int_{1-\delta}^{1+\delta} R^2 g(R) dR = \frac{1}{3}\left[1 - \frac{3}{4\rho\sqrt{2}}\right] \tag{25}$$

Table 3 Expressions for γ using Rayleigh phase functions

$g(R)$	γ
Gas model	$1 - 8f_v\Lambda(4\alpha)$
Packed-sphere model	$1 - 8f_v[\Lambda(4\alpha) - 0.831\Xi(4\alpha)]$
Liquid model	$1.0 - 8f_v[\chi^3\Lambda(\chi 4\alpha) - 0.831\Xi(4\alpha)]$
Percus-Yevick model	$(1 - f_v)^4/(1 + 2f_v)^2$, $\alpha \to 0$
$\Lambda(\xi) = \frac{9}{\xi^2}\left[\frac{\sin\xi}{\xi}\left(-1 + \frac{16}{\xi^2}\right) + \frac{\cos\xi}{\xi^2}\left(-4 + \frac{16}{\xi^2}\right) + \left(1 - \frac{4}{\xi^2} - \frac{16}{\xi^4}\right)\right]$	
$\Xi(\xi) = \frac{3}{\xi^2}\left[\frac{\sin\xi}{\xi}\left(4 - \frac{48}{\xi^2}\right) + \cos\xi\left(-1 + \frac{20}{\xi^2} - \frac{48}{\xi^4}\right) + \left(1 + \frac{4}{\xi^2} + \frac{48}{\xi^4}\right)\right]$	

Table 4 Expressions for γ for Rayleigh particles

$g(R)$	γ
Gas model	$1 - 8f_v(1 - 0.8\alpha^2)$
Packed-sphere model	$1 - 8f_v(0.169 + 0.308\alpha^2)$
Liquid model	$1 - 8f_v\left[(\chi^3 - 0.831) - \alpha^2(0.8\chi^5 - 1.108)\right]$
Percus-Yevick model	$(1 - f_v)^4/(1 + 2f_v)^2$, $\alpha \to 0$

Experimental measurements of $g(R)$ for various liquid indicate that they can be modeled by the following distribution, known as the liquid model:

$$g(R) = \begin{cases} 0, & R < 1, \quad 1 < R < \chi \\ 1, & R > \chi \end{cases},$$

$$\lim_{\delta \to 0} \int_{1-\delta}^{1+\delta} R^2 g(R) dR = \frac{1}{3}\left[1 - \frac{3}{4\pi\sqrt{2}}\right] \tag{26}$$

where $\chi = 1.18$ to match X-ray scattering data. It has also been correlated as

$$\chi = 1 + 0.5\exp(-f_v/0.15) \tag{27}$$

by Drolen and Tien (1987) to match the experimental scattering efficiency data of Yamada et al. (1986). The combination of the delta function at $R = 1$ and the void between $R = 1$ and $R = \chi$ attempts to capture the oscillatory behavior of the true experimental $g(R)$ of liquids.

The distribution function of Percus and Yevick (1958) is more realistic than any of those listed above. It has to be numerically evaluated and has a sharp peak at $R = 1$ for high f_v as does the packed-sphere model, approaches the gas model at low f_v, and has the oscillatory behavior that the liquid model approximates. Thus it incorporates the behavior of each of the simpler models. Even though the results of the Percus-Yevick distribution match the experimental data of purely scattering media accurately (Drolen et al., 1987), it is not considered in this study because it does not provide closed-form solutions. Moreover, the results of the other models described above are within a few percent of the experiments cited.

The expressions for A and ζ are analytically obtained via equations (12) and (13) using the three distributions under consideration. After tedious algebraic manipulations, and using the Rayleigh assumption of $\alpha << 1$ to retain only the leading order terms in the expansion of the trigonometric functions in the final step of the evaluations leads to the expressions presented in Table 1. It is noted that if the second-order term is neglected by virtue of the Rayleigh scattering

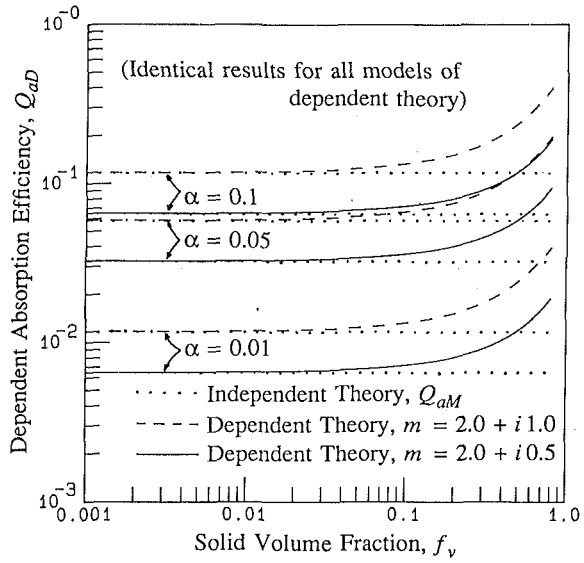

Fig. 3 Dependent absorption efficiency of particles in a homogeneous medium

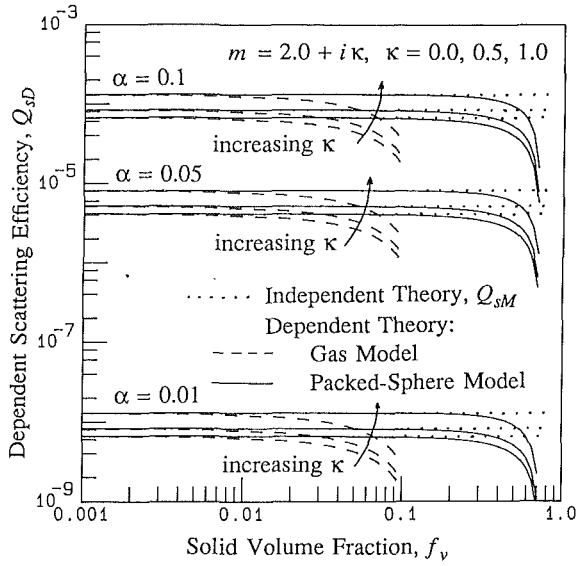

Fig. 5 Dependent scattering efficiency of particles in a homogeneous medium

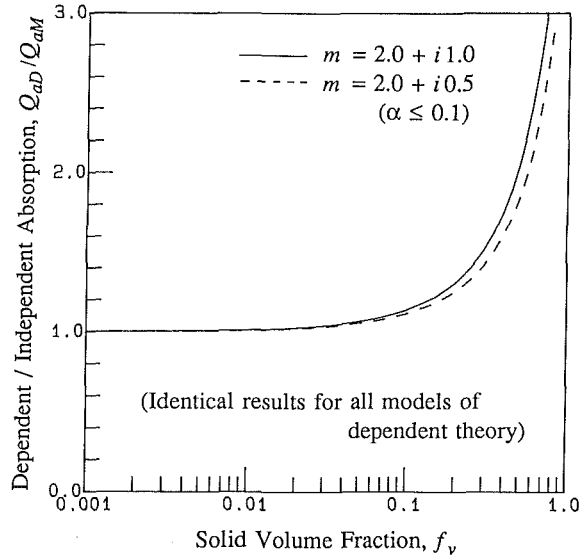

Fig. 4 Ratio of dependent to independent absorption efficiencies

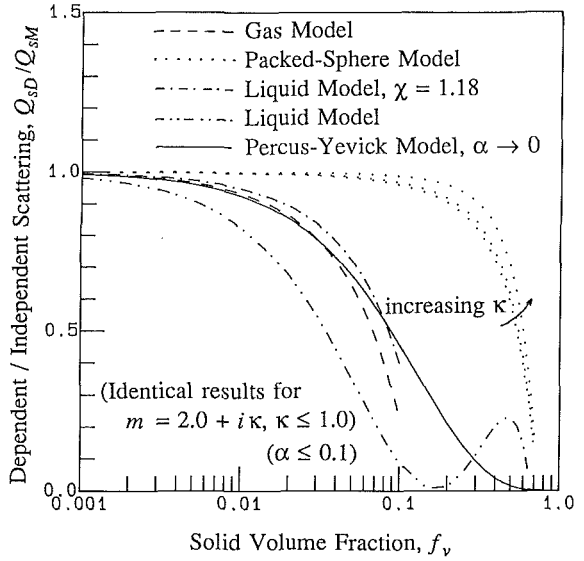

Fig. 6 Ratio of dependent to independent scattering efficiencies

assumption, then the expressions for ζ resulting from either model become identical. The closed-form representations of the form factor are presented in Table 2. Using the phase function for Rayleigh scattering, equation (21), the expressions for γ as presented in Table 3 are obtained. Expressions in Table 4 are derived from those in Table 3 by retaining only the leading order terms for small α. The right-hand side of the expressions become negative for the gas model if f_v is larger than 0.125 for $\alpha << 1$. This leads to an erroneous negative value of Q_{sD}. Due to this consideration, and the fact that the gas model is accurate for small volume fractions, the corresponding expression for γ should not be used if f_v is greater than 0.1.

In the limiting case of $f_v \to 0$ the effects of interparticle interactions vanish, as is mathematically observed from the right-hand sides of the expressions in Tables 1 through 4. Physically this is expected since small f_v implies that particles are spaced far apart and the resulting interparticle interactions in the near field are negligible. Coherent addition of scattered radiation in the far field is also negligible due to the large spacing between particles and the randomness of their positions in the particulate system. Another limiting case is that of nonabsorbing particles obtained by letting $\kappa \to 0$. In this case it is seen that the values of the absorption efficiencies go to zero.

Numerical Results

Radiative Properties. The simple closed-form analytical expressions for the scattering and absorption efficiencies of densely packed systems, obtained in the previous sections, are illustrated by considering a specific case. A particulate medium consisting of spherical soot particles that satisfy both the Rayleigh and the Rayleigh–Debye conditions is selected. Two values of the refractive index are chosen to represent soot in hydrocarbon flames (Lee and Tien, 1981): $m = 2.0 + i0.5$ in visible range and $m = 2.0 + i1.0$ in the infrared. Figures 3 and 4 present the values of the dependent absorption efficiencies that are computed using the present formulation and Figs. 5 and 6 present the dependent scattering. A reference case for scattering efficiencies of corresponding nonabsorbing particles with the same value of n (= 2.0) is also included. It is evident from these graphs that the attenuation of radiation by absorption dominates over that by scattering in such systems

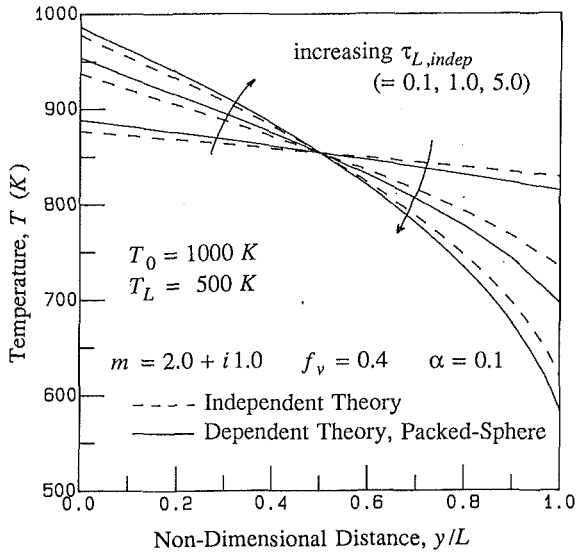

Fig. 7 Temperature distribution in a planar medium in radiative equilibrium

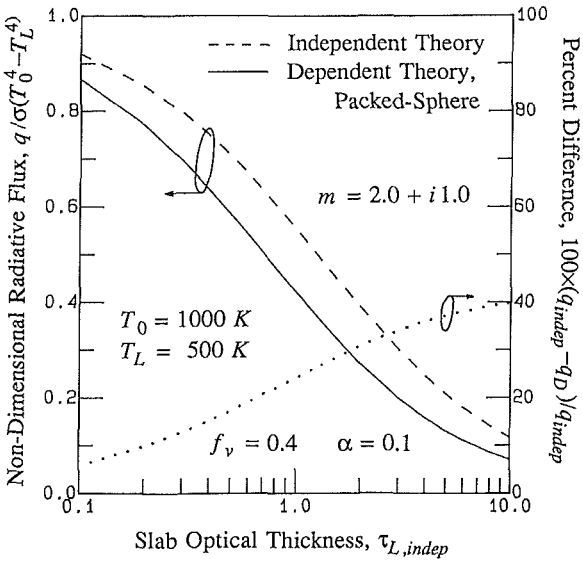

Fig. 8 Radiative flux in a planar medium in radiative equilibrium

since the magnitudes of the absorption efficiencies are relatively large as compared to those of scattering.

The absorption efficiency increases as the spacing between particles decreases (i.e., f_v increases) while the scattering efficiency exhibits a decline. The total extinction, being the sum of absorption and scattering, also increases since the system is absorption dominated. The dependent absorption efficiencies computed by using any of the statistical distributions mentioned previously are graphically identical since the difference is only in the third or fourth significant digits. An increase of approximately 5 percent in the absorption efficiency is observed for the cases considered at about a volume fraction of 0.06. The gas model yields negative scattering efficiency values at large volume fractions and should not be used if f_v is greater than 0.1. The packed-sphere model suffers from no such drawbacks. Even though the magnitudes of the scattering efficiencies depend on κ (Fig. 5), the ratio of the dependent scattering efficiency to the independent is rather insensitive to the value of κ as seen from Fig. 6. The absorption efficiency depends strongly on the value of κ and is zero for $\kappa = 0$.

It should be noted that though the packed-sphere model yields more reasonable results than the gas model and the liquid model, this in itself does not justify using the packed-sphere model as a predictive tool without experimental verification. The fact that the packed-sphere model gives correct limiting behavior is built into its representation of the distribution function. Similarly, the incorrect result at large f_v obtained by using the gas model is inherent in the corresponding assumed form of $g(R)$. The liquid model with $\chi = 1.18$ is marginally better than the gas model, whereas that with χ from equation (27) gives physically unreasonable results (nonmonotonic behavior with increasing solid volume fraction). The distribution function $g(R)$ is to be selected on the basis of experimental data, as for instance it has been experimentally demonstrated (Drolen et al., 1987) that the Percus-Yevick model yields an accurate representation of the coherent addition of scattered radiation in the far field.

Radiative Transfer. To examine the influence of the dependent effects on the transport of radiative energy, a gray plane-parallel homogeneous slab of length L bounded by black surfaces at temperatures $T_0 = 1000$ K and $T_L = 500$ K is considered. The medium is taken to be in radiative equilibrium. The particles are monodispersed in diameter with an effective size parameter of 0.1. The refractive index of particles is $m = 2.0 + i1.0$ representative of soot in the infrared. The system is a representation of deposited layers of soot on walls of combustion systems.

The temperature distribution for a volume fraction of 0.4, obtained by the method of Kumar et al. (1988), is presented in Fig. 7 for three different optical thicknesses of the slab. For this set of operating conditions the ratio of the optical thickness based on dependent packed-sphere extinction theory to that based on the independent is approximately 1.76. The larger optical thickness corresponding to the dependent case pushes the temperature profile toward a more optically dense one with less steep gradients at the boundaries. Figure 8 presents the heat flux in the medium as a function of the optical thickness of the slab. The radiative flux is much lower for the dependent case because of the corresponding higher optical density and is reduced by as much as 40 percent at an optical thickness $\tau_{L,indep}$ (based on independent extinction coefficient) of 10.0.

Conclusion

Absorption of radiation is the dominant mechanism of radiation extinction by small absorbing particles in the Rayleigh regime. The evaluation of radiative transfer in such systems is thus more sensitive to the variations in the absorption characteristics than those in the scattering. Changes in the absorption properties of particles in a dense homogeneous particulate medium due to interparticle interactions have not been studied in the literature. This study presents an analytical model to account for the modification of the absorption and scattering properties by these dependent effects. The resulting expressions are simple to use and require a knowledge of the refractive index m, size parameter α, and the volume fractions f_v. Details of the internal geometric structure of the particulate medium are not required and an appropriate statistical particle distribution function $g(R)$ is to be selected.

Another consideration is whether ignoring the dependent effects in absorption while only accounting for those in scattering is sufficient when analyzing transport of radiation. This is important because previous studies in the literature, reviewed by Tien and Drolen (1987), have only examined dependent scattering. The present results indicate that for absorbing systems the deviation of the radiative flux from independent theory by considering only dependent scattering is insignificant. Dependent scattering would have a higher impact if the particles were weakly absorbing, and would be very important

if they were nonabsorbing. Dependent effects introduce an increase in the absorption and a decrease in the scattering of energy. For highly absorbing particles this leads to a net increase in extinction, and for nonabsorbing particles a net decrease. Since most engineering systems, especially combustion systems, are highly absorbing, ignoring the dependent effects will overpredict the radiative flux.

References

Bohren, C. F., and Huffman, D. R., 1983, *Absorption and Scattering of Light by Small Particles*, Wiley, New York.

Brewster, M. Q., and Tien, C. L., 1982, "Radiative Transfer in Packed Fluidized-Beds: Dependent Versus Independent Scattering," ASME JOURNAL OF HEAT TRANSFER, Vol. 104, pp. 573-579.

Cartigny, J. D., Yamada, Y., and Tien, C. L., 1986, "Radiative Transfer With Dependent Scattering by Particles: Part 1—Theoretical Investigation," ASME JOURNAL OF HEAT TRANSFER, Vol. 108, pp. 608-613.

Debye, P., 1925, "Note on the Scattering of X-Rays," *Journal of Mathematical Physics*, Vol. 4, pp. 133-147.

Drolen, B. L., and Tien, C. L., 1987, "Independent and Dependent Scattering in Packed-Sphere Systems," *Journal of Thermophysics and Heat Transfer*, Vol. 1, pp. 63-68.

Drolen, B. L., Kumar, S., and Tien, C. L., 1987, "Experiments on Dependent Scattering of Radiation," *AIAA 22nd Thermophysics Conference (Honolulu)*, June 8-10, Paper No. 87-1485.

Hottel, H. C., Sarofim, A. F., Dalzell, W. H., and Vasalos, I. A., 1971, "Optical Properties of Coatings. Effect of Pigment Concentration," *AIAA Journal*, Vol. 9, pp. 1895-1898.

Hunka, J. F., and Mei, K. K., 1981, "Electromagnetic Scattering by Two Bodies of Revolution," *Electromagnetics*, Vol. 1, pp. 329-347.

Jones, A. R., 1979a, "Electromagnetic Wave Scattering by Assemblies of Particles in the Rayleigh Approximation," *Proceedings of the Royal Society of London*, Vol. A.366, pp. 111-127 (corrections in Vol. A.375, pp. 453-454).

Jones, A. R., 1979b, "Scattering Efficiency Factors for Agglomerates of Small Spheres," *Journal of Physics D: Applied Physics*, Vol. 12, pp. 1661-1672.

Kerker, M., 1961, *The Scattering of Light and Other Electromagnetic Radiation*, Academic Press, New York.

Kumar, S., 1987, "Thermal Radiation in Particulate Systems," Ph.D. Dissertation, Department of Mechanical Engineering, University of California at Berkeley.

Kumar, S., and Tien, C. L., 1987, "Dependent Scattering and Absorption of Radiation by Small Particles," *Proceedings, 24th National Heat Transfer Conference*, ASME HTD-Vol. 72, A. M. Smith and T. F. Smith, eds., pp. 1-7.

Kumar, S., and Tien, C. L., 1989, "Effective Diameter of Agglomerates for Radiative Extinction and Scattering," *Combustion Science and Technology*, Vol. 66, pp. 199-216.

Kumar, S., Majumdar, A., and Tien, C. L., 1988, "The Differential-Discrete-Ordinate Method for Solving the General Equation of Radiative Transfer," *Proceedings, 25th National Heat Transfer Conference*, ASME HTD-Vol. 96, H. R. Jacobs, ed., pp. 179-185.

Lee, S. C., and Tien, C. L., 1981, "Optical Constants of Soot in Hydrocarbon Flames," *Proceedings, Eighteenth Symposium (International) on Combustion*, The Combustion Institute, Pittsburgh, pp. 1159-1166.

Percus, J. K., and Yevick, G. J., 1958, "Analysis of Classical Statistical Mechanics by Means of Collective Coordinates," *Physics Review*, Vol. 110, pp. 1-13.

Saxon, D. S., 1973, "Lectures on the Scattering of Light," *UCLA International Conference on Radiation and Remote Probing of Atmosphere*, J. G. Kurigan, ed., pp. 227-308.

Tien, C. L., and Drolen, B. L., 1987, "Thermal Radiation in Particulate Media with Dependent and Independent Scattering," *Annual Review of Numerical Fluid Mechanics and Heat Transfer*, Vol. 1, pp. 1-32.

Twersky, V., 1975, "Transparency of Pair-Correlated, Random Distributions of Small Scatterers, With Applications to the Cornea," *Journal of Optical Society of America*, Vol. 65, pp. 524-530.

Yamada, Y., Cartigny, J. D., and Tien, C. L., 1986, "Radiative Transfer With Dependent Scattering by Particles: Part 2—Experimental Investigation," ASME JOURNAL OF HEAT TRANSFER, Vol. 108, pp. 614-618.

Transient Plume Influence in Measurement of Convective Heat Release Rates of Fast-Growing Fires Using a Large-Scale Fire Products Collector

Hong-Zeng Yu
Factory Mutual Research Corporation,
Norwood, MA 02062

A theory for strongly buoyant transient plumes was used to determine whether the convective heat flow measured by a large-scale Fire Products Collector (FPC) could approximate the instantaneous convective heat release rate generated by fast-growing fires. The theory was confirmed by the plume data of rack storage fires obtained in this study. The theory provides a scheme for deriving the convective heat release rate generated at the fire source from the convective heat flow measured by the FPC.

Introduction

The large-scale Fire Products Collector (FPC) has been widely used to measure the convective heat release rate of fire (Heskestad, 1981; Babrauskas, 1984). The collection hood of the FPC is positioned above the fuel array to collect fire products to measure convective heat release rate and other fire properties. Under some circumstances, because of the constraints of the test facility or the necessity of investigation of plume development, the collection hood is located high above the fuel array. As a result of this high elevation, the heat release rate measured by the FPC tends to lag behind the actual heat release rate generated at the fire source. For steady or slowly developing fires, the lag may not pose a problem to measurements. However, for fast-growing fires, especially in the initial period when the plume gas velocity is low, the lag may cause a significant discrepancy between the measured and the actual heat release rates.

For heterogeneous solid fuels, the actual heat release rate at the fire source is usually an unknown quantity. Hence, the degree of measurement discrepancy cannot be readily determined by comparing the actual heat release rate generated at the source with that measured by the FPC. The objective of this paper is to quantify the effect of measurement lag caused by the transient plume flow based on a transient plume theory presented here. The theory will be formulated and validated by the plume data of rack-storage fires. It will be demonstrated that, using the relationship established from the theory, the actual convective heat release rate at the fire source can be derived from the convective heat flow measured by the FPC.

Transient Plume Theory

A theory for strongly buoyant, transient plumes has been developed to investigate the transport of plume gases from the fire source to an elevation above the source. The present theoretical work is an extension of the weak plume theory described by Delichatsios (1979). For strong plumes, the density difference between the plume gases and the ambient air is significant. For weak plumes, this difference is negligible in the plume modeling, except for buoyancy considerations.

An integral model has been employed to deal with the strongly buoyant, transient plume. The principal assumptions are: axisymmetric flow with no swirl, homogeneous and stagnant surroundings, negligible kinetic and potential energies, ideal gas, and point heat source. For strong plumes, the entrainment rate of ambient air into the plume has been found to be proportional to the square root of the product of ambient air density and flow momentum (Ricou and Spalding, 1961; Morton, 1965). Therefore, the conservation equations for mass, momentum, and energy are

$$\frac{\partial}{\partial t}\int_0^\infty \rho r\partial r + \frac{\partial}{\partial Z}\int_0^\infty u\rho r\partial r = K\left(\frac{\rho_\infty}{2\pi}\int_0^\infty \rho u^2 r\partial r\right)^{1/2} \quad (1)$$

$$\frac{\partial}{\partial t}\int_0^\infty \rho u r\partial r + \frac{\partial}{\partial Z}\int_0^\infty \rho u^2 r\partial r = \int_0^\infty (\rho_\infty - \rho) g r\partial r \quad (2)$$

$$\frac{\partial}{\partial t}\int_0^\infty \rho (T - T_\infty) r\partial r + \frac{\partial}{\partial Z}\int_0^\infty \rho u (T - T_\infty) r\partial r = 0 \quad (3)$$

where r is the radial distance measured from the plume centerline, Z is the vertical distance measured from the point source, and K is the entrainment coefficient. Other variables are listed in the Nomenclature.

Defining a new radial coordinate, $r' = [2\int_0^r (\rho/\rho_\infty) r\partial r]^{1/2}$, and assuming Gaussian flow profiles in the r' coordinate, equations (1) through (3) can be written in the form of constant density flow

$$\frac{\partial}{\partial t}(b^2) + \frac{1}{2}\frac{\partial}{\partial Z}(b^2 u_\phi) = \frac{K}{4}\frac{2}{\pi} b u_\phi \quad (4)$$

$$\frac{\partial}{\partial t}(b^2 u_\phi) + \frac{1}{2}\frac{\partial}{\partial Z}(b^2 u_\phi^2) = \frac{1}{\beta^2} b^2 \delta_\phi \quad (5)$$

$$\frac{\partial}{\partial t}(b^2 \delta_\phi) + \frac{\beta^2}{1+\beta^2}\frac{\partial}{\partial Z}(b^2 u_\phi \delta_\phi) = 0 \quad (6)$$

where the subscript ϕ denotes the centerline values. In equations (4) and (5), $\delta_\phi = g\,(T_\phi - T_\infty)/T_\infty$, β is the ratio of the velocity profile width to the temperature profile width, and b is the half-width of the velocity profile measured from the centerline to the radial distance, where $u/u_\phi = 1/e$ in the r' coordinate.

The flow front of the transient plume moves farther away from the plume source as time passes. Nondimensional analysis suggests that equations (4)–(6) have similarity solutions if the vertical distance between the plume front and the

Contributed by the Heat Transfer Division for publication in the JOURNAL OF HEAT TRANSFER. Manuscript received by the Heat Transfer Division October 11, 1988; revision received June 22, 1989. Keywords: Fire/Flames, Plumes, Transient and Unsteady Heat Transfer.

plume source has a power-law dependence with time. Introducing scaling parameters of $Z_0=\alpha\, t^k$, $u_o=\alpha\, k\, t^{k-1}$, and $a_o=\alpha\, k(k-1)t^{k-2}$ for length, velocity, and buoyancy, respectively, equations (4)–(6) are nondimensionalized in the following expressions:

$$2F_2^2-\eta\frac{\partial}{\partial\eta}F_2^2+\frac{1}{2}\frac{\partial}{\partial\eta}(F_1F_2^2)=\frac{K}{4}\frac{2}{\pi}F_1F_2 \tag{7}$$

$$(3k-1)F_1F_2^2-k\,\eta\frac{\partial}{\partial\eta}(F_1F_2^2)+\frac{1}{2}k\frac{\partial}{\partial\eta}(F_1^2F_2^2)=\frac{k-1}{\beta^2}F_2^2F_3 \tag{8}$$

$$(3k-2)\,F_2^2F_3-k\eta\frac{\partial}{\partial\eta}(F_2^2F_3)+\frac{\beta^2}{1+\beta^2}k\frac{\partial}{\partial\eta}(F_1F_2^2F_3)=0 \tag{9}$$

where $F_1=u_\phi/u_o$, $F_2=b/Z_o$, $F_3=\delta_\phi/a_o$, and $\eta=\alpha^{-1}Z\,t^{-k}$. The values of α and k are positive constants.

Under the assumption of point heat source, equations (7)–(9) cannot be solved readily because the starting values of F_1 and F_3 are not finite at the source. However, in the plume adjacent to the source, the flow is expected to be close to quasi-steady flow, which corresponds to the instantaneous heat release rate at the source. Therefore, if F_1, F_2, and F_3 are normalized by their respective quasi-steady values, equations (7)–(9) become solvable after the normalization because the starting values of the normalized dependent variables are equal to one at the source.

In the plume where a quasi-steady condition applies, the instantaneous heat release rate at the source can be calculated from

$$Q_c=2\pi\int_0^\infty \rho u(T-T_\infty)C_p\, r\, \partial r \tag{10}$$

Based on the definitions of Z_o, u_o, a_o, F_1, F_2, and F_3, it can be shown that power-law heat sources are essential in order to have similarity solutions. This has been indicated by Delichatsios (1979) for the case of weak plumes. If the power-law heat source is represented by $Q_c=\gamma\, t^p$, from equation (10), it can be shown that

$p=4k-3$, and

$$\gamma=\pi\, T_\infty\, \rho_\infty\, C_p\, F_1\, F_2^2\, F_3\, \alpha^4\, k^2(k-1)/g/(1+\beta^2)$$

If a quasi-steady-state condition applies, the terms underlined in equations (7)–(9) are retained. The normalized width, velocity, and buoyancy force of the quasi-steady plume with respect to Z_o, u_o, and a_o are

$$B=\frac{3K}{5}\sqrt{\frac{2}{\pi}}\,\eta$$

$$U=\left[\frac{25}{3}\frac{g}{T_\infty\rho_\infty C_p}\frac{\gamma(1+\beta^2)}{K^2\,\alpha^4\,\beta^2\,k^3}\right]^{1/3}\eta^{-1/3}$$

and

$$\Delta=\frac{2}{3k(k-1)}\left[\frac{25}{3}\frac{g}{T_\infty\,\rho_\infty\,C_p}\frac{\beta\,\gamma(1+\beta^2)}{K^2\alpha^4}\right]^{2/3}\eta^{-5/3}$$

respectively.

Defining $f_1=F_1/U$, $f_2=F_2/B$, and $f_3=F_3/\Delta$, equations (7)–(9) can be written as

$$4\;yf_2\frac{df_1}{dy}+4\,y\left[2f_1-\frac{4k}{p}y\right]\frac{df_2}{dy}=5f_1(1-f_2) \tag{11}$$

$$4\frac{k}{p}y^2\frac{df_1}{dy}+4y\left(1-2\frac{k}{p}y\right)\frac{f_1}{f_2}\frac{df_2}{dy}=-3f_1{}^2-2f_3+5\frac{f_1{}^2}{f_2}+yf_1 \tag{12}$$

$$2\left(\frac{\beta^2}{1+\beta^2}\right)\frac{df_1}{dy}+\frac{4}{f_2}\left(\frac{\beta^2}{1+\beta^2}f_1-\frac{k}{p}y\right)\frac{df_2}{dy}+\frac{2}{f_3}\left(\frac{\beta^2}{1+\beta^2}f_1-\frac{k}{p}y\right)\frac{df_3}{dy}=-1 \tag{13}$$

where

$$y=p\eta^{4/3}\Big/\left[\frac{25}{3}\frac{g}{T_\infty\,\rho_\infty\,C_p}\frac{\gamma(1+\beta^2)}{K^2\alpha^4\beta^2}\right]^{1/3}$$

The starting conditions are $f_1=1$, $f_2=1$, and $f_3=1$ at $y=0$.

As indicated by Delichatsios (1979), it can be shown that $y=(dQ_c/dt/Q_c)\;(Z/u_{\phi,s})$. The parameter y is an indicator of the plume transience. The transience becomes relatively significant if the fire growth rate (dQ_c/dt) increases, or the

Nomenclature

a_0 = a scaling parameter for plume buoyancy force
B = normalized flow width of a quasi-steady plume
b = plume width in r' coordinate
C_p = air specific heat
F_1 = normalized centerline velocity of a transient plume
F_2 = normalized width of a transient plume
F_3 = normalized centerline buoyancy force of a transient plume
f_1 = $F_1/U_{\phi,s}$
f_2 = F_2/B
f_3 = F_3/Δ
g = gravitational acceleration
H = distance between FPC and top of fuel array
H_o = elevation of plume virtual origin
K = entrainment constant
k = $(p+3)/4$
P = power index of a power-law fire
Q_c = convective heat release rate at the fire source
Q_y = convective heat flow measured by the FPC
RTI = thermocouple response time index
r = radial coordinate
r' = transformed radial coordinate
T = absolute gas temperature
t = time
U = normalized centerline velocity of a quasi-steady plume
u = centerline velocity of a transient plume
u_0 = a scaling parameter for plume velocity
y = plume transience parameter
Z = vertical coordinate
Z_0 = a scaling parameter for length
α = a constant in the scaling parameters
β = ratio of velocity profile width to temperature profile width
γ = coefficient of power-law equation
Δ = normalized centerline buoyancy force of a quasi-steady plume
δ = centerline buoyancy force of a transient plume
η = similarity variable
ρ = air density

Subscripts

s = quasi-steady values
TC = thermocouple measurements
ϕ = plume centerline
∞ = ambient

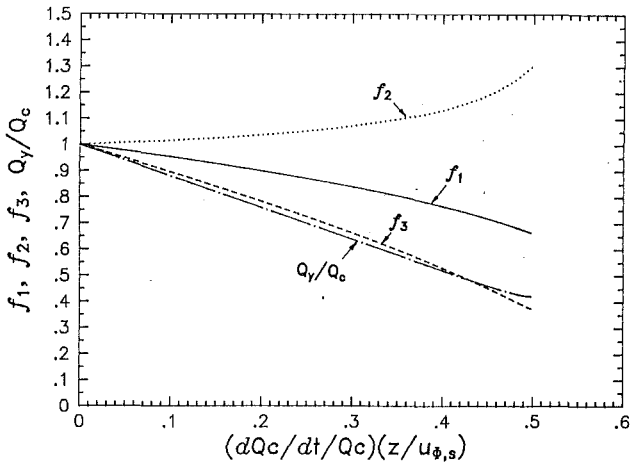

Fig. 1 Theoretical values of the following normalized properties of a strongly buoyant, transient plume: centerline velocity f_1, flow width f_2, centerline temperature f_3, and convective heat flow Q_y/Q_c, for $P=3$ and $\beta=0.85$

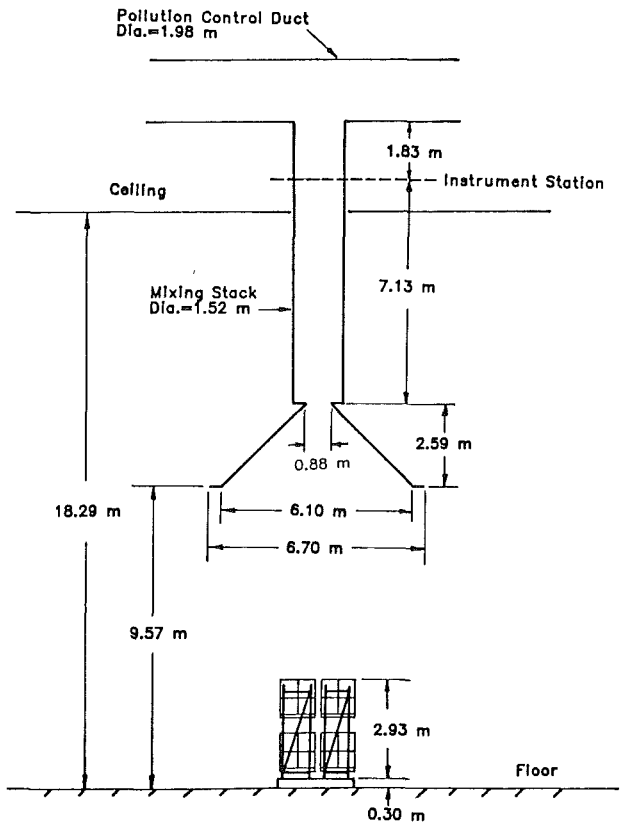

Fig. 2 The Fire Products Collector

relative elevation (Z) is farther from the source. It can also be shown that the convective heat flow at a value of y is $Q_y = f_1 f_2^2 f_3 Q_c$.

A rational extrapolation procedure (Fox, 1971) was used to integrate equations (11)–(13). Figure 1 presents the calculated f_1, f_2, f_3, and Q_y/Q_c versus y for $p=3$ and $\beta=0.85$, which pertains to the rack-storage fires conducted in this study. A mathematical singularity can be found present at $y=0.51$ for equations (11)–(13). Physically, this singularity corresponds to the plume front where the flow jump occurs. For a growing fire, as shown in Fig. 1, the plume progressively deviates from quasi-steady state as the transience parameter y increases. At $y=0.5$, the convective heat flow is only about 40 percent of the convective heat released at the source at the same time. It will be demonstrated later that the instantaneous value of Q_c can be derived from the measured Q_y by using the relationships shown in Fig. 1.

Experimental Setup

Four rack-storage fire tests were conducted under the large-scale FPC (10 MW capacity) located at the FMRC Test Center at West Gloucester, RI (Heskestad, 1981). The overall dimensions of the building are 61 m × 76 m, with two floor-to-ceiling heights of 9.14 m and 18.28 m. The FPC is located at the 18.28 m ceiling height site.

Fuel Array. The fuel consisted of polystyrene cups packaged in compartmented, single-wall corrugated paper cartons; each carton measured 0.53 m × 0.53 m × 0.51 m high and contained 125 compartments in a 5 × 5 × 5 array. Vertical and horizontal cradboard dividers 0.4 mm thick were used to form the compartments, each of which contained a single 473 ml cup. Eight cartons were placed on a wood pallet forming a stack of two cartons wide by two cartons deep by two cartons high, defined as a pallet load. For each pallet load, the weight of the polystyrene cups was 29.28 kg; the weight of empty cartons with dividers was 21.84 kg, while the weight of the wood pallets ranged from 23.1 to 24.1 kg. Detailed illustrations of the wood pallet and a pallet load of fuel were presented by Yu in another report (1988).

The fuel arrays tested were two pallet loads wide and two pallet loads deep. Two storage heights were employed, corresponding to two and three tiers of storage. A double-row steel rack was used to hold the pallet loads of fuel. An example of the arrangement of pallet loads in a steel rack was illustrated by Yu and Kung (1984). The pallet loads were separated by 0.15-m vertical flues; the height of each tier of the steel rack was 1.52 m. The vertical distance measured from the bottom of the steel rack to the top of the fuel array was 2.93 m for two-tier-high storage, and 4.48 m for three-tier storage. The entire fuel array was placed on a 0.3-m-high platform that was leveled on the floor. Four fire tests were conducted: Tests 1 and 2 are for the two-tier fuel array; Tests 3 and 4 are for the three-tier fuel array.

Instrumentation. In this study, the FPC was used to measure convective heat flow at 9.57 m above the floor; thermocouples and bidirectional velocity probes were used to measure plume gas temperatures and velocities under the FPC.

Figure 2 illustrates the shape and dimensions of the FPC and its relationship to the floor and ceiling of the test site. The FPC is a 1.52-m-dia vertical stainless steel stack connected to a large collection hood of 6.10 m at its widest. The gas flow inside the FPC was induced by the blower of the building pollution-control system. The instrumentation station was located 7.13 m downstream of the orifice. The gas transport time from the intake of the hood to the instrumentation station was less than 0.3 s. At this instrumentation station the convective heat flow was measured. Heskestad (1981) describes this FPC is detail.

The plume gas temperatures and velocities were measured at 7.62 m and 8.84 m above the floor. At 8.84 m above the floor, 13 thermocouples and 5 bidirectional velocity probes were installed to measure the temperature and velocity profiles. With the central thermocouple being located on the centerline of the FPC and fuel array, the thermocouples and velocity probes were aligned with the two orthogonally crossing vertical flues of the fuel array. The positions of these thermocouples and velocity probes with respect to the vertical centerline are shown in Fig. 3. At 7.62 m above the floor, only one thermocouple and one velocity probe were used to measure centerline plume temperatures and velocities. All thermocouples were fabricated from 30-gage, inconel-sheathed,

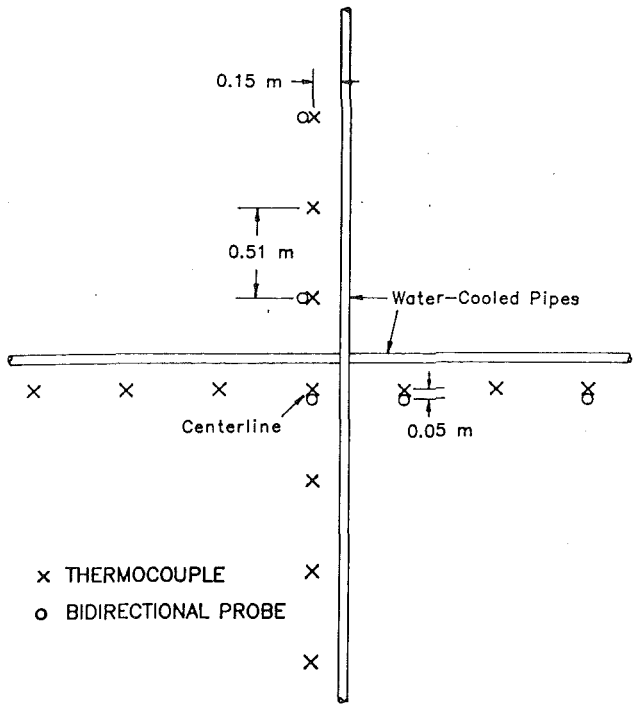

Fig. 3 Layouts of thermocouples and bidirectional velocity probes at 8.84 m above the floor

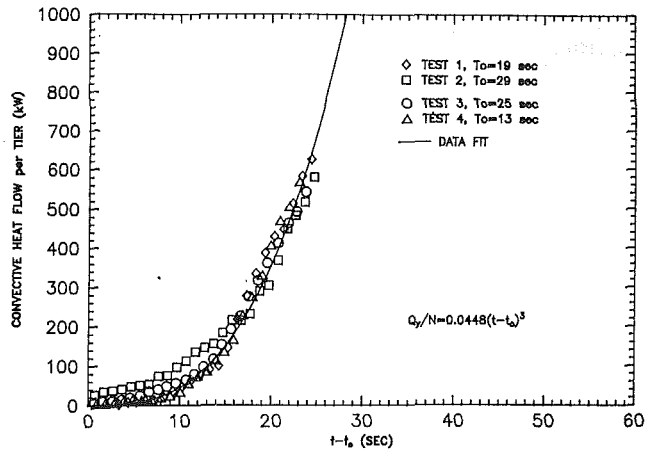

Fig. 4 The plume convective heat flow measured by the Fire Products Collector

chromel-alumel thermocouple wire. The thermocouple signals were conditioned using thermocouple signal conditioners (Analog Devices, 3B37 K-type signal conditioner). The thermocouple beads were of 0.66 mm diameter and had a time constant of 1.9 s at 2.5 m/s gas velocity. Differential pressure transducers (Setra Model 261, ±12.7 mm water full range) were used to measure the pressure differentials of individual bidirectional velocity probes. With this transducer, it was possible to measure velocities reliably down to 0.5 m/s with a response time of about 50 ms.

All the data channels were monitored using a DEC PDP 11/23 data acquisition system. Every second the system scanned the data channels once and recorded the readings on a magnetic disk.

Test Procedure. Before flow was initiated in the FPC the baseline signals were recorded for 60 s. Subsequently, the blower was turned on and the flow inside the stack stabilized within 60 s. At 120 s from the start of data recording, the fuel array was ignited.

The ignition source consisted of four cellucotton rolls (0.08 m diameter, 0.08 m long), each soaked with 120 ml gasoline and wrapped in a polyethylene bag. The cellucotton rolls were placed near the center flue space of the fuel array at the bottom of the pallet loads of the lowest tier. A propane torch was used to ignite the rolls.

During the test, all doors and windows communicating with the test volume were closed.

Experimental Results and Analysis

For the four fire tests conducted in this study, there was always an incipient period after ignition. After the incipient period, the fire growth could be approximated by a power-law equation. Only the power-law fire growth period was investigated in this study, which started at the end of the incipient period and lasted for about 25 s (see Fig. 4). The fire plume generated in this period was highly transient under the FPC. Consequently, the delay of FPC measurement in this power-law fire growth period caused by plume gas transport from the fire source to the FPC might be significant. After the power-law fire growth period, the plume convective heat flow increases at slower rates (Yu, 1988). Therefore, the transience of the subsequent plume flow is less significant than that in the power-law fire growth period.

Data Analysis. A time-averaging process was applied to the convective heat flows measured by the FPC. Since the data fluctuations ranged from 1 s to 3 s, a five-point (4 s) rolling averaging scheme was employed. The processed convective heat flows for the four fire tests in the initial fire growth period are presented in Fig. 4. In this figure, the ratios of the measured convective heat flow versus the number of tiers of fuel array are plotted against the time lapse from the end of the fire growth incipient period (t_o). After the incipient period, the convective heat flow per tier could be approximated by a power-law equation. In this study, the ends of individual incipient periods were determined by plotting the convective heat flow per tier versus time in thet log-log coordinates. As shown in Fig. 4, the heat flows in the period of 25 s after the incipient period can be represented by a power-law equation of the third power

$$Q_y = 0.0448\, N(t-t_o)^3 \quad \text{for} \quad t-t_o > 0 \text{ s} \tag{14}$$

where Q_y (kW) is the convective heat flow measured by the FPC and N is the number of tiers of fuel array.

To correct the measurement delay caused by the relatively slow response of thermocouples, the relationship (Heskestad and Smith, 1980)

$$T = T_{TC} + \frac{\text{RTI}}{u^{1/2}} \frac{dT_{TC}}{dt} \tag{15}$$

was employed. In equation (15), T_{TC} is the measured plume temperature, T is the actual plume temperature, and RTI (time constant $\times u^{1/2}$) is the response time index of the thermocouple, which remains relatively constant in a gas stream for a temperature range of ambient to 400°C. The RTI value for thermocouples used in this study was 3 $(\text{m}\cdot\text{s})^{1/2}$. The corrected plume centerline temperatures were used to compare with the predictions of the transient plume theory.

The data reduction of gas velocity was based on the corrected gas temperature. Since the velocity fluctuation frequencies were comparable to those of the convective heat flow measurements, the five-point rolling averaging scheme was also applied to the gas velocity data.

Comparison Between Measurements and Theoretical Predictions of Transient Plumes. In the investigation period, the gas temperature and velocity distributions at 8.84 m above the floor were well represented by Gaussian distributions for

Table 1 Starting times and corresponding Q_y to integrate equations (17) and (18)

Test No.	Starting time for integration (end time of investigation period) (s)	Q_y (kW)
1	42.3	1240
2	54.6	1334
3	47.7	1499
4	38.0	1790

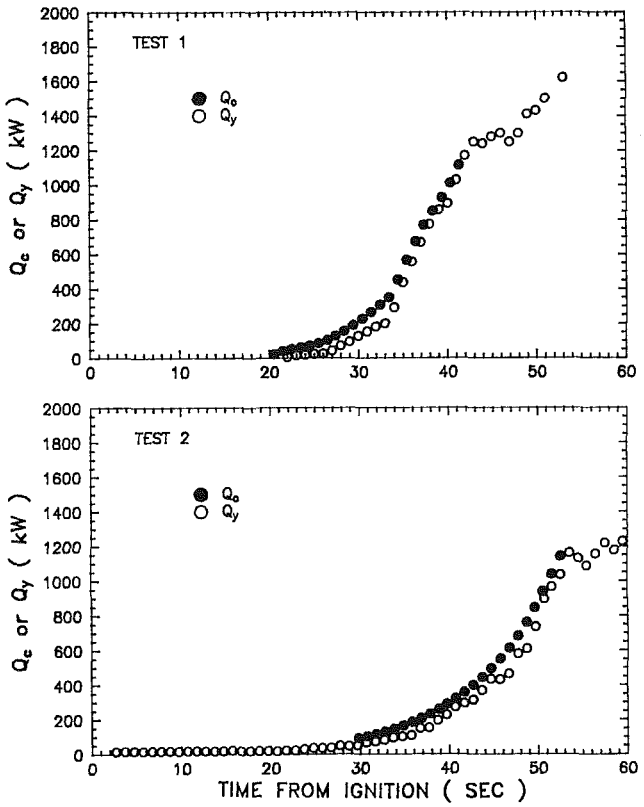

Fig. 5 The measured plume convective heat flow Q_y and the calculated fire convective heat release rate Q_c for two-tier rack-storage fuel arrays

two-tier (Tests 1 and 2) and three-tier (Tests 3 and 4) fuel arrays. In this period, the ratio of the velocity profile width to the temperature profile width ranged from 0.7 to 1 for Tests 1-4. Assuming that the convective heat release rate at the fire source has a third-power dependence with time and employing the width ratio of 0.85 (average of 0.7 and 1.0), the variations of plume velocity width, centerline temperature, centerline velocity, and convective heat flow with respect to the parameter y may be represented theoretically by the relationships shown in Fig. 1.

Based on Fig. 1, the relationship between Q_y and Q_c can be approximated by

$$\frac{Q_y}{Q_c} = 1 - 1.202 \frac{1}{Q_c} \frac{dQ_c}{dt} \frac{Z}{u_{\phi,s}} \quad \text{for } 0 \le y \le 0.5 \qquad (16)$$

In equation (16), $Z = H - H_o$, where H is the vertical distance between the FPC and the top of fuel array, and H_o is the elevation of the vertical origin of the plume relative to the top of fuel array. From Yu and Kung (1984), the virtual origin elevation is

$$\underset{(\mathrm{m})}{H_o} = -1.6 + 0.094 \underset{(\mathrm{kW})}{Q_c^{0.4}}$$

for two-tier fuel arrays, and

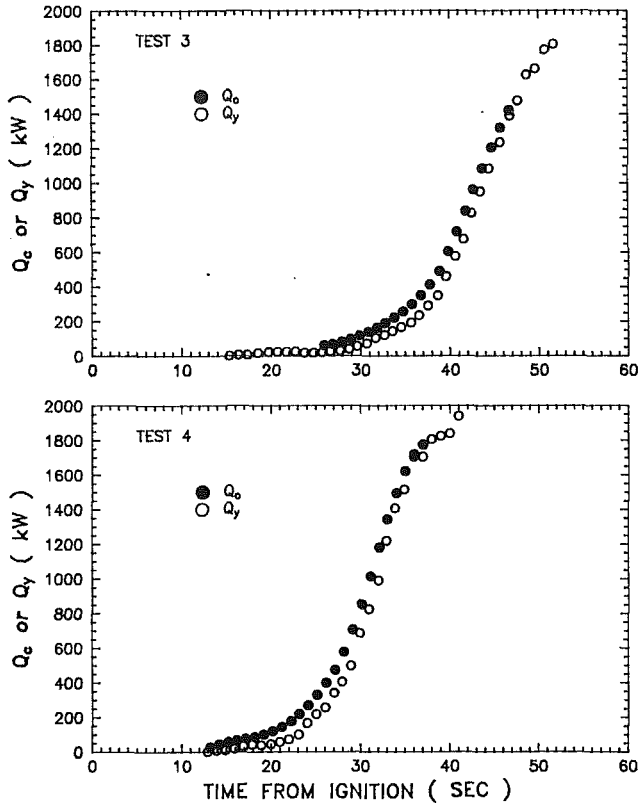

Fig. 6 The measured plume convective heat flow Q_y and the calculated fire convective heat release rate Q_c for three-tier rack-storage fuel arrays

$$\underset{(\mathrm{m})}{H_o} = -2.4 + 0.095 \underset{(\mathrm{kW})}{Q_c^{0.4}}$$

for three-tier fuel arrays.

The centerline velocity of quasi-steady plumes can be calculated from (Yu and Kung, 1984)

$$\underset{(\mathrm{m/s})}{u_{\phi,s}} = 1.287 \; \underset{(\mathrm{m})}{Z^{-1/3}} \underset{(\mathrm{kW})}{Q_c^{1/3}}$$

Substituting the above three equations, equation (16) can be written for the elevation at the bottom of the FPC (9.57 m above the floor) as

$$\frac{dQ_c}{dt} = 1.07 \; Q_c^{1/3} (Q_c - Q_y) (7.94 - 0.094 \; Q_c^{0.4})^{-4/3} \qquad (17)$$

for two-tier fuel arrays;

$$\frac{dQ_c}{dt} = 1.07 \; Q_c^{1/3} (Q_c - Q_y) (7.19 - 0.095 \; Q_c^{0.4})^{-4/3} \qquad (18)$$

for three-tier fuel arrays, where Q_c and Q_y are in kW.

At the end of the investigation period (see Table 1), the plume centerline velocity at 8.84 m above the floor (0.73 m below the FPC) reached 10 m/s. Due to the high gas velocity and small value of $dQ_c/dt/Q_c$, the value of the plume transience parameter y at the FPC level is close to zero at the end of the investigation period. Therefore, it is reasonable to make the approximation that the plume reaches quasi-steady state at the end of the investigation periods up to the elevation of the FPC, i.e., the convective heat flow measured by the FPC, Q_y, is close to the convective heat release rate at the fire source, Q_c. Taking $dQ_y/dt = dQ_c/dt$ at the end of the investigation periods, equations (17) and (18) can be integrated backward with respect to time to obtain Q_c. The corresponding convective heat release rates used to initiate the integration are tabulated in Table 1. The results for two-tier and three-tier fuel arrays are presented in Figs. 5 and 6, respectively. It can

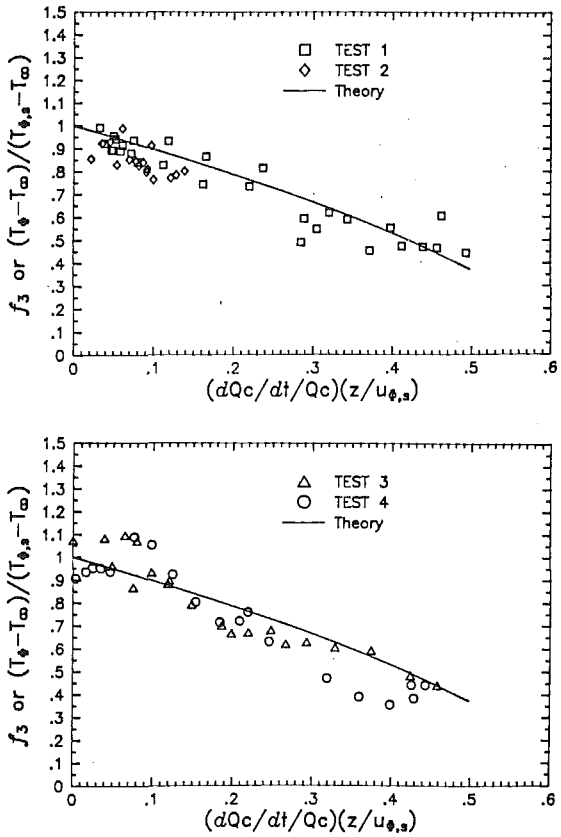

Fig. 7 Comparison between the theoretical results and the experimental data of normalized plume centerline temperature for two-tier (above) and three-tier (below) fuel arrays

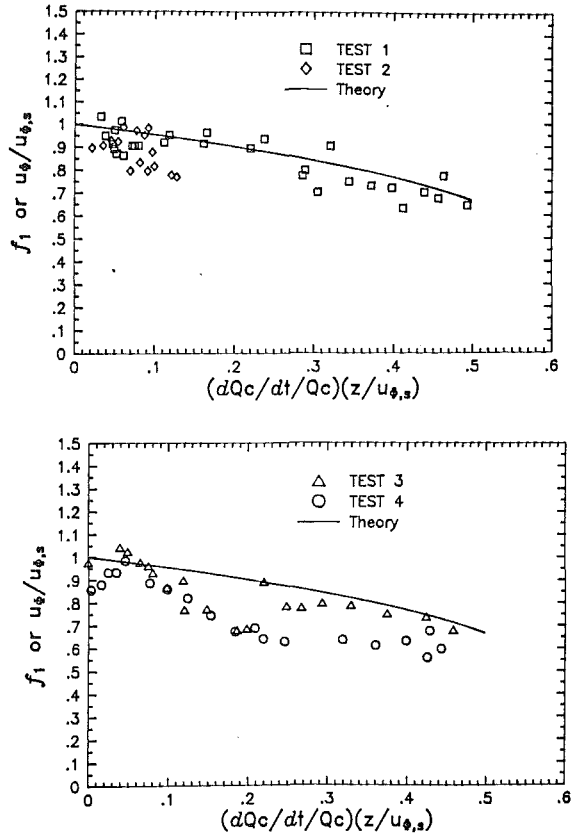

Fig. 8 Comparison between the theoretical results and the experimental data of normalized plume centerline velocity for two-tier (above) and three-tier (below) fuel arrays

be shown that the Q_c values can also be approximated by a power-law equation of the third power.

Based on the definitions of F_1, F_3, U, and Δ, it can be shown that $f_1 = u_\phi/u_{\phi,s}$ and $f_3 = (T_\phi - T_\infty)/(T_{\phi,s} - T_\infty)$. The values of $u_{\phi,s}$ and $T_{\phi,s}$ represent the centerline velocity and temperature of quasi-steady plumes, which can be calculated by using the correlations presented by Yu and Kung (1984).

The ratios of $(T_\phi - T_\infty)$ versus $(T_{\phi,s} - T_\infty)$ of two-tier and three-tier fuel arrays are presented in Fig. 7, while the ratios of u_ϕ versus $u_{\phi,s}$ are shown in Fig. 8. The results indicate reasonably good agreements between the theoretical predictions and experimental data for two-tier and three-tier fuel arrays.

Based on the above results, we may conclude that equation (16) can be used to derive the convective heat release rate at the fire source from the convective heat flow measured by the FPC under the present test conditions. For two-tier and three-tier fuel arrays, the maximum difference between Q_y and Q_c in the investigation period is less than 160 kW (see Figs. 5 and 6). The theory is expected to apply to other fuel arrays provided that the fire growth has a power-law dependence with time.

Summary and Conclusions

A theory for strongly buoyant and transient plumes was used to investigate the transport of plume gases from the fire source to the elevation of the large-scale Fire Products Collector. For power-law fires, the degree of plume transience could be determined by a parameter, $y = (dQ_c/dt/Q_c)\ (Z/u_{\phi,s})$. This parameter accounts for the fire growth rate and plume elevation relative to the fire source. The greater the y value, the more transient is the plume. The theory was confirmed by the plume data obtained in this work. The theory provided a relationship between the convective heat release rate generated at the fire source and the convective heat flow measured above the fire source.

References

Babrauskas, V., 1984, "Upholstered Furniture Room Fires—Measurements, Comparison With Furniture Calorimeter Data and Flashover Predictions," *J. of Fire Sciences*, Vol. 2, pp. 5–19.

Delichatsios, M. A., 1979, "Time Similarity Analysis of Unsteady Buoyant Plumes in Neutral Surroundings," *Journal of Fluid Mechanics*, Vol. 93, pp. 241–250.

Fox, P. A., 1971, "DESUB: Integration of a First-Order System of Ordinary Differential Equations," *Mathematical Software*, J. R. Rice, ed., Academic Press, New York.

Heskestad, G., 1981, "A Fire Products Collector for Calorimetry Into the MW Range," FMRC Technical Report, J.I. OC2E1.RA, Factory Mutual Research Corporation, Norwood, MA.

Heskestad, G., and Smith, H. F., 1980, "Plunge Test for Determination of Sprinkler Sensitivity," FMRC Technical Report, J.I. 3A1E2.RR, Factory Mutual Research Corporation, Norwood, MA.

Morton, B. R., 1965, "Modeling Fire Plumes," *Tenth Symposium (International) on Combustion*, The Combustion Institute, Pittsburgh, PA, pp. 973–982.

Ricou, F. P., and Spalding, D. B., 1961, "Measurements of Entrainment by Axisymmetrical Turbulent Jets," *Journal of Fluid Mechanics*, Vol. 11, pp. 21–32.

Yu, H.-Z., 1988, "RDD Test Protocol for Early Suppression Fast Response Sprinkler Applications," FMRC Technical Report, J.I. On1JO.RA(1), Factory Mutual Research Corporation, Norwood, MA.

Yu, H.-Z., and Kung, H.-C., 1984, "Strong Buoyant Plumes of Growing Rack Storage Fires," *Twentieth Symposium (International) on Combustion*, The Combustion Institute, Pittsburgh, PA, pp. 1547–1554.

Yu, H.-Z., 1988, "Transient Plume Influence in Measurement of Effective Convective Heats of Rack Storage Fires," FMRC Technical Report, J.I. ON1JO.RA(2), Factory Mutual Research Corporation, Norwood, MA.

The Effect of Heat Transfer on Coal Devolatilization

J.-T. Yang
Associate Professor.

G.-G. Wang
Graduate Student.

Department of Power Mechanical Engineering,
National Tsing Hua University,
Hsinchu, Taiwan

This study investigates the heat transfer effect on the transient behavior of preheating, ignition, and combustion of a single coal particle pyrolyzed in a hot convective environment. The theoretical model covers two aspects: (1) heat and mass transfer and pyrolysis within the particle, (2) thermal radiation, diffusion, and combustion of the reactive gases and air outside of the particle. Semenov's criteria are adopted to define ignition and a modified model derived from droplet combustion is used to estimate the flame radius and temperature. Distributions of temperature, species concentrations, and combustion rate are solved simultaneously. The prediction is verified by a set of experimental data.

Introduction

The coal devolatilization process is the principal research topic related to coal combustion, gasification, and liquefaction. It involves complex interactions of heat and mass transfer, and chemical reaction mechanisms; therefore a huge amount of experimental exploration has been conducted to dig out certain dominating principles of this complexity. Nevertheless, to establish a useful theoretical model to compare and combine with the experimental approaches should be an effective and time-saving approach for the analysis of the devolatilization process.

Many early studies on coal devolatilization emphasized the chemical reaction mechanisms (Anthony and Howard, 1976; Solomon and Hamblen, 1983) and pulverized coal devolatilization (Phuoc and Durbetaki, 1987; Smith and Smoot, 1980). Among the mechanism models, the parallel first-order reaction mechanism proposed by Ubhayakar et al. (1976) has been widely adopted. However, the effect of heat and mass transport on devolatilization of large coal particles has not yet been extensively explored. On experimental aspect, Essenhigh (1985) was the first to measure the effects of coal type and particle size on combustion time and average reaction rate of large coal particles. It is suggested that for particles larger than 0.3 mm in diameter, heat transfer is the main controlling factor. Ragland and Yang (1985) performed a systematic experimental investigation to determine the influences of temperature, oxygen concentration, particle size, and coal type on the transient combustion behavior of millimeter-sized particles. They provided valuable combustion data for large coal particles in convective flow, but further efforts are needed on theoretical interpretation of pyrolysis. On the aspect of heat and mass transfer, Bliek et al. (1985) emphasized the model of intraparticle transport analysis and used the TGA experiment to check their prediction. They did not include the flame effect in the model. Kansa and Perlee (1980) established a comprehensive coal dust combustion model. Their approach to the solid portion is similar to this work, but it assumes that the radiation source, the flame, is at a fixed position, and the coal dusts flow toward it. Maloney and Jenkins (1984) tried to combine heat transfer, mass transfer, and reaction mechanism in the model of pyrolysis, but the results did not clearly indicate the influence of each individual factor. Agarwal et al. (1984) concentrated on the effects of convection and Biot number in fluidized bed combustion with the assumption that the coal particles were nonporous. The predicted trend was consistent with Essenhigh's data; however, the model only added an artificial factor of the effect of radiation, and the impervious particle assumption might not be suitable for the case of low rank coal, which has higher porosity. Phuoc and Durbetaki (1987) examined the combined effect of heat transfer, mass transfer, and kinetics on a small single coal particle undergoing pyrolysis. They treated the coal particle being pyrolyzed in the inert and stagnant environment as an isothermal system and neglected thermal radiation. All these works either did not consider ignition and the effect of flame on pyrolysis, or were restricted to pulverized coal, or needed more in-depth analysis on the heat and mass transfer of large coal particle devolatilization.

In the present work, a mathematical model is developed to simulate the pyrolysis behavior of a coal particle burned under the effects of forced convection in a hot air stream, furnace wall radiation, and a diffusion flame. The whole combustion process is divided into three parts: preheating, ignition, and combustion. An experimental setup is also designed to assist the analysis. This study focuses on some of the major aspects of heat transfer. These include the influences of furnace wall radiation, convection between the coal particle and the free-stream air, convection between the flame and the free-stream air, conduction through the gaseous phase to the coal particle surface, and flame radiation, on heat and mass transfer. The propagation of the reaction zone inside the particle and the rate-controlling factors are also discussed in this paper.

Model Formulation

The schematic representations of the problem are shown in Fig. 1. When the coal particle is put into the furnace, it is heated by the furnace wall radiation and convection from the hot air stream and then it starts to pyrolyze. As the ignition criteria are fulfilled, the particle ignites. The diffusion flame develops around the particle and then the pyrolyzed vapor reacts under the influences of flame radiation, conduction, and wall radiation until all the volatile content is completely consumed. The model is categorized into five distinct zones, as depicted in Fig. 1(A). The solid phase consists of an unreacted core, a pyrolyzing zone, and a charred zone. The thermal energy is transferred from the particle surface into the pyrolyzing zone, and then proceeds from the zone into the unreacted core. The gaseous phase contains the pyrolyzed vapor and hot air, which are separated by the infinitely thin diffusion flame, as illustrated in Fig. 1(A). Before ignition the flame does not exit and the gas phase has only one zone, as shown in Fig. 1(*B*).

In the present model, the single coal particle is assumed to be composed of nonpyrolyzing char and volatile matter. Upon heating, the volatile matter pyrolyzes and diffuses out to the particle surface through the porous part of the particle. The two-competitive-reaction mechanism (Ubhayakar et al., 1976) is chosen for the pyrolysis reaction. Local thermal equilibrium is assumed inside the particle. In the gaseous phase, the pyrolyzed vapor diffuses outward. The oxygen in the air dif-

Contributed by the Heat Transfer Division for publication in the JOURNAL OF HEAT TRANSFER. Manuscript received by the Heat Transfer Division June 7, 1988; revisions received December 1988 and February 1989. Keywords: Combustion, Forced Convection, Transient and Unsteady Heat Transfer.

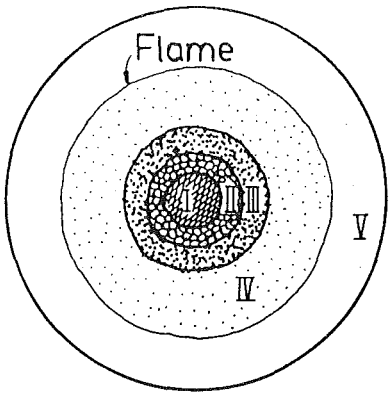

(A)

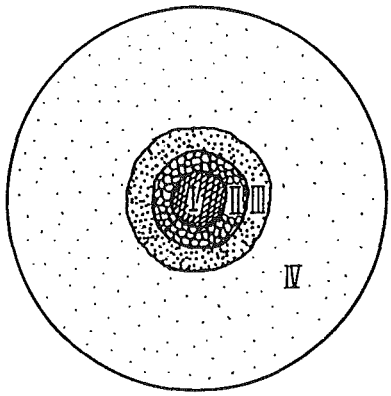

(B)

Fig. 1 Physical configuration of the model: (A) combustion process, (I) unreacted core, (II) pyrolysis zone, (III) charred zone, (IV) reactive gases, (V) hot air; (B) gasification process, (I) unreacted core, (II) pyrolysis zone, (II) charred zone, (IV) mixing zone of reactive gases and air

fuses in the opposite direction and thus forms a thin diffusion flame, once the Semenov ignition criteria are met. Mass diffusion and thermal diffusion in this zone can be treated as quasi-steady compared to the conversion rate of the solid phase.

Region I, Region II, and Region III. The continuity equations for solid and gaseous parts of the coal particle are

$$\frac{\partial}{\partial t}(\epsilon\rho_g) + \nabla\cdot(\rho_g U) = \dot{R}_g \tag{1}$$

$$\frac{\partial}{\partial t}((1-\epsilon)\rho_s) = \dot{R}_s \tag{2}$$

$$\dot{R}_g = -\dot{R}_s \tag{3}$$

The superficial velocity U is defined as the local average velocity of gas through the area of the control volume; the porosity ϵ is defined as the ratio of void in the particle to the total volume. The porosity increases as the volatile matter pyrolyzes. The relation between porosity and volatile matter mass ratio is

$$\epsilon = \epsilon^o + \frac{V^o_{VM}}{V_{\text{coal}}}\left(1 - \frac{VM}{VM^o}\right) \tag{4}$$

The pyrolysis reaction rate is calculated according to the two-competitive-reaction mechanism as

$$\dot{R}_s = -C_1 A_{p1}(\rho_{\text{coal}} - \rho_{ch})\exp(-E_{a1}/R_u T) - C_2 A_{p2}(\rho_{\text{coal}} - \rho_{ch})\exp(-E_{a2}/R_u T) \tag{5}$$

The momentum equation is simplified to Darcy's equation, which only contains the viscous term and the diffusion term, given as

$$\frac{\mu U}{\kappa} + \nabla P = 0 \tag{6}$$

In the equation, κ is the permeability of the coal particle. The pore radius within the coal particle is very small (0.1–10 μm) and the superficial velocity is not high, so the inertial and body force terms are much less than the viscous term, and thus can be neglected.

The relation among density, pressure, and temperature is described as

$$P = \rho_g R T \tag{7}$$

The energy equation, which includes the energy accumulated in both the solid and the gas, conductive heat transfer, the enthalpy flow through the gaseous part, the flow work, and the heat released from chemical reactions, is given as

Nomenclature

A = area, m^2
A_{p1}, A_{p2} = prefactor, 1/s
C_g = heat capacity of the gases, kcal/(kg·K)
C_1, C_2 = stoichiometric factors
D = gas phase diffusivity, m^2/s
d = diameter, m
E_{a1}, E_{a2} = activation energy, kcal/mole
$\hat{F}$ = view factor
FC = fixed carbon mass ratio
ΔH = enthalpy of combustion, kcal
Δh = heat of reaction, kcal/kg
h_{cov} = heat transfer coefficient, W/(m^2·K)
h_g = enthalpy of gas, kcal/kg
h_R = heat released from pyrolysis, kcal/kg
h_s = enthalpy of solid, kcal/kg
k = thermal conductivity, W/(m·K)
m = mass, kg
$\dot{m}''$ = mass flux of fuel or oxygen, kg/(m^2·s)
$\dot{m}'''$ = mass consumption or generation rate, kg/(s·m^3)
Nu = Nusselt number
P = pressure, N/m^2
Pr = Prandtl number
$Q_{\text{gene, f}}$ = flame combustion heat generation, W
$Q_{\text{gene, o}}$ = surrounding reaction heat generation, W
$Q_{\text{loss, f}}$ = flame heat loss, W
$Q_{\text{loss, o}}$ = surrounding heat loss, W
$q''_{\text{cond, fs}}$ = flame to coal surface conduction heat transfer, W/m^2
$q''_{\text{conv, fo}}$ = flame to surrounding convection heat transfer, W/m^2
$q''_{\text{conv, os}}$ = coal surface to surrounding convection heat transfer, W/m^2
$q''_{\text{rad, fs}}$ = flame to coal surface radiation heat transfer, W/m^2
$q''_{\text{rad, fw}}$ = flame to furnace of wall radiation heat transfer, W/m^2

$$\frac{\partial}{\partial t}(\epsilon\rho_g h_g + (1-\epsilon)\rho_s h_s) - \frac{1}{r^2}\frac{\partial}{\partial r} r^2 k \frac{\partial T}{\partial r} + \frac{1}{r^2}\frac{\partial}{\partial r}(r^2 \rho_g U h_g) - \frac{\partial(\epsilon P)}{\partial t} + h_R \frac{\partial}{\partial t}((1-\epsilon)\rho_s) = 0 \quad (8)$$

where h_g, h_s, and h_R are the enthalpy of the gas, the enthalpy of the solid, and heat released per unit mass of volatile matter, respectively. The conductivity is calculated from the following equation:

$$k = \epsilon k_g + (1-\epsilon)k_s \quad (9)$$

The thermal conductivity, heat capacity, and density of gas are estimated as properties of air.

Combining equations (2) and (5) gives the relation among porosity, volatile matter mass ratio, and temperature as

$$\frac{\partial}{\partial t}((1-\epsilon)VM) = (1-\epsilon^o)(-C_1 A_{p1} VM \exp(-E_{a1}/R_u T) - C_2 A_{p2} VM \exp(-E_{a2}/R_u T)) \quad (10)$$

The initial conditions are

$$T(r, 0) = 300 \text{ K} \quad (11a)$$

$$P(r, 0) = 101{,}325 \text{ N/m}^2 \quad (11b)$$

$$U(r, 0) = 0 \text{ m/s} \quad (11c)$$

$$\epsilon(r, 0) = \epsilon^o = 0.15 \quad (11d)$$

$$VM(r, 0) = VM^o = 0.5 \quad (11e)$$

and the boundary conditions are

$$\frac{\partial T}{\partial r}(0, t) = 0 \quad (12a)$$

$$\frac{\partial P}{\partial r}(0, t) = 0 \quad (12b)$$

$$U(0, t) = 0 \quad (12c)$$

Other boundary conditions for the energy equation are listed below.

(*A*) *Pre-ignition Stage:*

$$k\frac{\partial T}{\partial r}(r_s, t < t_{ig}) = q''_{\text{rad, ws}} + q''_{\text{conv, os}} \quad (13)$$

(*B*) *Combustion Stage:*

$$k\frac{\partial T}{\partial r}(r_s, t > t_{ig}) = (1-\alpha_f) q''_{\text{rad, ws}} + \alpha_f q''_{\text{rad, fs}} + q''_{\text{cond, fs}} \quad (14)$$

where

$$q''_{\text{rad, ws}} = \sum_{i=1}^{3} \alpha_s \alpha_i \sigma \hat{F}_{si}(T_i^4 - T_s^4) \quad (15)$$

$$q''_{\text{conv, os}} = h_{\text{cov}}(T_o - T_s) \quad (16)$$

$$q''_{\text{rad, fs}} = \alpha_f \alpha_s \sigma \hat{F}_{sf}(T_f^4 - T_s^4) \quad (17)$$

$$q''_{\text{cond, fs}} = k_g(T_f - T_s)/(r_s - (r_s/r_f)) \quad (18)$$

In the equations, $\hat{F}$ is the total exchange factor (Beckman, 1971) and all of the surface are assumed to be grey.

Since the enveloping flame blocks the free air stream from the burning praticle, the transpiration effect is not significant and the heat transfer coefficient h_{cov} is given by the Ranz–Marshall equation (Faeth, 1977)

$$\text{Nu} = \frac{h_{\text{cov}}\, d}{k} = 2 + 0.6\ \text{Re}^{1/2}\text{Pr}^{1/3} \quad (19)$$

The ignition condition is judged by the Semenov criteria (Lerment and Yip, 1984), which are

$$Q_{\text{gene, o}} > Q_{\text{loss, o}} \quad (20)$$

$$\frac{dQ_{\text{gene,o}}}{dT} > \frac{dQ_{\text{loss, o}}}{dT} \quad (21)$$

where

$$Q_{\text{gene, o}} = (Q^0_{\text{com}}{}_{298} + \Delta H^{\text{Product}}_{T_o - 298} - \Delta H^{\text{Reactant}}_{T_o - 298})/\Delta t \quad (22)$$

$$Q_{\text{loss, o}} = h_{\text{cov}} A_s (T_o - T_s) \quad (23)$$

The flame temperature is then estimated from

$$Q_{\text{gene, f}} = Q_{\text{loss, f}} = f(T_f) \quad (24)$$

where

$$Q_{\text{gene, f}} = (Q^0_{\text{com}}{}_{298} + \Delta H^{\text{Product}}_{T_f - 298} - \Delta H^{\text{Reactant}}_{T_f - 298})/\Delta t \quad (25)$$

$$Q_{\text{loss, f}} = A_f q''_{\text{rad, fw}} + A_s q''_{\text{rad, fs}} + A_f q''_{\text{conv, fo}} + 4\pi r_s^2 q''_{\text{cond, fs}} \quad (26)$$

$$q''_{\text{rad, fw}} = \sum_{i=1}^{3} \alpha_f \alpha_i \sigma \hat{F}_{fi}(T_f^4 - T_i^4) \quad (27)$$

$$q''_{\text{conv, fo}} = h_{\text{cov}}(T_f - T_o) \quad (28)$$

Nomenclature (cont.)

$q''_{\text{rad, ws}}$ = furnace wall to coal surface radiation heat transfer, W/m^2
q''' = heat consumption or generation of gas phase reaction, W/m^3
$\dot{R}$ = reaction rate, kg/(s·m^3)
R = gas constant, kcal/(kg·K)
R_u = universal gas constant, kcal/(mole·K)
Re = Reynolds number
r = radius, m
r_f = flame radius, m
r_s = coal particle radius, m
T = temperature, K
t = time, s
U = superficial velocity, m/s
u = velocity, m/s
V = volume, m^3
V_{coal} = volume of coal particle, m^3
VM = volatile matter mass ratio
Y = mole fraction
α = absorptivity, thermal diffusivity, m^2/s
β = stoichiometric ratio
ϵ = porosity
κ = permeability, Dracy = cp·cm^2/(atm·s)
μ = viscosity, cp
ρ = density, kg/m^3
ρ_{coal} = density of coal, kg/m^3
σ = Stefan–Boltzmann constant

Superscript

o = initial value

Subscripts

ch = char
F = fuel
FR = fuel interior
f = flame
g = gas
i = furnace wall position
ig = ignition
0 = oxygen
o = surrounding
P = product
s = solid
∞ = at infinity

Table 1 Thermal properties of coal and input parameters for the model (Howard, 1981; Ubhayakar, 1976; Lerment and Yip, 1984)

Bituminous coal	
ρ_{coal}, kg/m³	1785
α_f	0.0, 0.1, 0.5
h_R, cal/kg	1
κ, Darcy	0.15
k_s, W/(m·K)	0.25
k_g	air
Cp_s, kJ/(kg·K)	$(-0.218+0.0038T-0.0176T^2)$ x FC $+(0.88+0.0033T)$ x VM
Cp_g	air
FC	0.5
A_{p1}, 1/s	3.7×10^5
E_{a1}, kcal/mol	17.6
C_1	0.3
A_{p2}, 1/s	1.46×10^{13}
E_{a2}, kcal/mol	60.0
C_2	1.0

Table 2 Properties of coal and related parameters used for experimental verification

ρ_{coal}	1375 kg/m³
Proximate Analysis	
Moisture (a.r.)	1.6 %
V.M. (d.a.f.)	28.8 %
F.C. (d.a.f.)	56.9 %
Ash (a.r.)	12.7 %
Ultimate analysis (% d.a.f.)	
Carbon	68.17
Oxygen	11.99
Hydrogen	4.10
Nitrogen	1.06
Sulfur	0.41

Region IV and Region V. The species equation is

$$\rho_g D_i \frac{d}{dr}\left(r^2 \frac{dY_i}{dr}\right) - \frac{d}{dr}(\dot{m}'' r^2) Y_i + r^2 \dot{m}_i''' = 0 \tag{29}$$

where $i = F, 0$. The energy equation is

$$k_g \frac{d}{dr}\left(r^2 \frac{dT}{dr}\right) - C_g \frac{d}{dr}(\dot{m}'' r^2) T + r^2 q''' = 0 \tag{30}$$

$$\dot{m}'' r^2 = \dot{m}_s'' r_s^2 \tag{31}$$

$$\dot{m}_s'' = \frac{4}{3} \pi r_s^3 \dot{R}_g / 4\pi r_s^2 \tag{32}$$

with the boundary conditions

$$Y_{FR} = 1 \tag{33a}$$

$$T(r_s) = T_s \tag{33b}$$

$$Y_{F\infty} = 0 \tag{34a}$$

$$Y_{0\infty} = 0.232 \tag{34b}$$

$$T_\infty = T_o \tag{34c}$$

We examine the reaction as β grams fuel react with 1 gram oxygen and produces $(1+\beta)$ grams product and $(\beta \Delta h)$ calorie heat

$$\beta F + 0 \rightarrow (1+\beta) P + \beta \Delta h \tag{35}$$

and

$$-\frac{\dot{m}_F'''}{\beta} = -\dot{m}_0''' = \frac{\dot{m}_P'''}{1+\beta} = \frac{q'''}{\beta \Delta h} \tag{36}$$

$$\dot{m}_s'' Y_{FR} = \dot{m}_s'' Y_{Fs} - \rho_g D_F \frac{dY_F}{dr}\bigg|_s + \beta \rho_g D_0 \frac{dY_0}{dr}\bigg|_s \tag{37}$$

According to equation (29) and assuming Le = 1, $\alpha_g = D_F = D_o$

$$\rho_g \alpha_g \frac{d}{dr} r^2 \frac{d}{dr}(Y_F - \beta Y_0) - \frac{d}{dr}(\dot{m}'' r^2)(Y_F - \beta Y_0) + r^2(\dot{m}_F''' - \beta \dot{m}_0''') = 0 \tag{38}$$

Let

$$b = ((Y_F - Y_{F\infty}) - \beta(Y_0 - Y_{0\infty}))/(Y_{Fs} - Y_{FR}) \tag{39}$$

Applying equation (36), the last term of equation (38) can be cancelled and equation (38) becomes

$$\rho_g \alpha_g \frac{d}{dr} r^2 \frac{db}{dr} - \frac{d}{dr}(\dot{m}'' r^2 b) = 0 \tag{40}$$

Equation (37) can be rearranged to

$$\rho_g \alpha_g \frac{db}{dr}\bigg|_s = \dot{m}_s'' \tag{41}$$

We integrate equation (40) twice with the boundary conditions (equations (41) and (34*a*, *b*))

$$\dot{m}_s'' r_s^2 / (\rho_g \alpha_g r) = \ln((b_\infty - b_s + 1)/(b - b_s + 1)) \tag{42}$$

when $r = r_f$, $Y_F = \beta Y_0$, therefore

$$b_f = (\beta Y_{0\infty} - Y_{F\infty})/(Y_{Fs} - Y_{FR}) \tag{43}$$

with the infinitely thin flame approximation

$$Y_0(r_s) = Y_{0s} = 0 \tag{44}$$

Substitution of equation (43) into equation (42) with equation (44) gives the flame radius as

$$r_f = \dot{m}_s'' r_s^2 / (\rho_g \alpha_g \ln(1 + \beta Y_{0\infty}/Y_{FR})) \tag{45}$$

The continuity equations, momentum equation, and energy equation are solved simultaneously through an implicit finite difference scheme. Since radiation is involved in this problem the governing equations are nonlinear and coupled together, and the pyrolysis rate of coal, the flame radius, and the flame temperature are solved iteratively at each time step once the enveloped flame is formed, and only until all of the three terms are converged will it proceed to the next time step. Two varieties of coal, one in the theoretical model and the other for experimental verification, are used. The properties and their related parameters are listed in Tables 1 and 2.

Experimental Design

The experimental setup is shown in Fig. 2. Air is heated by a 5-kW ceramic heater, flows upward through several regulating screens, and then enters the 6-cm-dia, 30-cm-long pyrex cylindrical test section to burn the coal particle. The coal particle is hung at 20 cm below the top surface of the furnace. The coal particle is attached with a piece of 0.3-mm-dia wire to a 2-mm-dia quartz rod, which is connected to an Ohaus Galaxy-120 electronic balance with 1 mg resolution. The drag force exerted on the particle is first measured as the difference between the weight readings as the air flow is swiftly switched off and

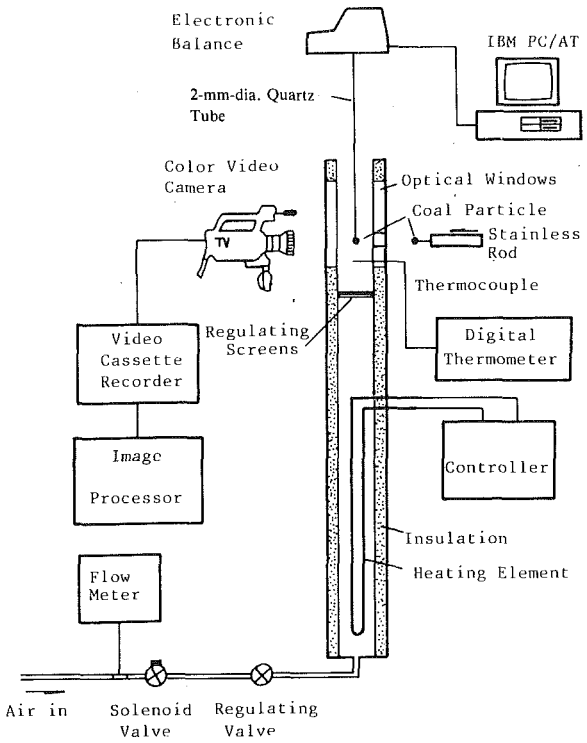

Fig. 2 Experimental apparatus

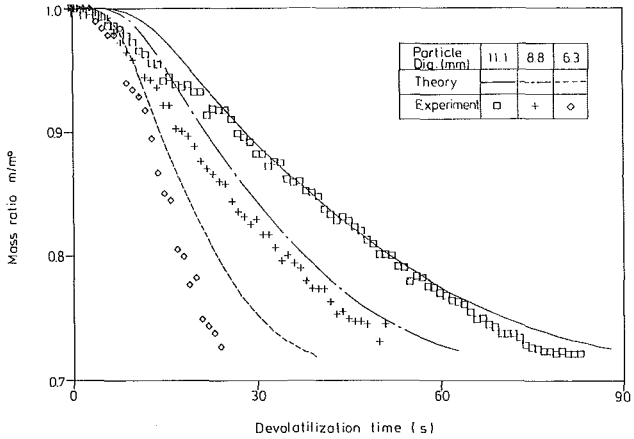

Fig. 3 Effect of particle diameter on transient mass conversion ratio ($T = 1073$ K, $u_\infty = 0.3$ m/s, $VM^o = 0.288$)

on by controlling the solenoid valve. The drag force is then subtracted from the measurement of weight change of the coal particle during devolatilization. All these data are recorded in a microcomputer once every 0.5 s. In order to reduce the installation time of the coal sample and thus to obtain accurate data of the ignition delay time, a hole is drilled on the pyrex wall and the individual coal particle is fixed at the front of a 2-cm-dia stainless steel tube and is put into the test section for testing. In addition, two 5 cm by 20 cm optical windows are set in the test section and through them the devolatilization phenomenon is observed and recorded. The coal sample used for model verification in Figs. 3–6 is provided by the China Steel Company in Taiwan and the related properties are listed in Table 2.

Results and Discussion

General Results. Typical results for the effect of particle size at 1073 K on transient mass burning ratio are shown in Fig. 3. The prediction agrees well with the experimental data

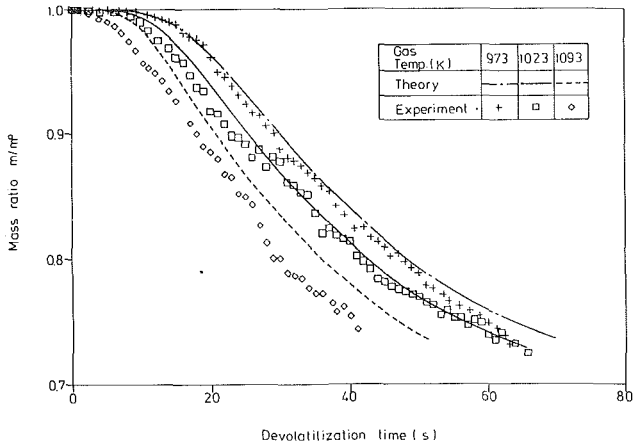

Fig. 4 Effect of air temperature on transient mass conversion ratio ($d = 8.8$ mm, $u_\infty = 0.3$ m/s, $VM^o = 0.288$)

of bituminous coal. The effect of temperature of 8.8-mm-dia particles is shown in Fig. 4. It is clear that the model predictions are fairly reasonable except at the end of the devolatilization. It was found through experiments that at the final stage the pyrolyzing coal particle began to generate several cracks and kept enlarging, which enhanced the burning rate and therefore made the data deviate from the predicted curve. Figures 5 and 6 are the comparisons of ignition delay and other characteristic times between the experiment and the model prediction. In the figures t_5, t_{50}, and t_{95} are the times at which 5, 50, and 95 percent of the volatile matter is left, respectively. Except at a few points the model is verified rather well by the experiment. It is judged that at low temperature, such as the case of 973 K, the pyrolyzed vapor will be blown downstream before ignition until significant energy is built up. Therefore the measured ignition time is much longer. In addition, this one-dimensional model may have to be verified if the Reynolds number is higher than 40, because the symmetric enveloping flame assumption, then, will deviate from the reality.

When the devolatilization process goes on in a low-temperature environment or for small particles, the process is usually controlled by chemical kinetics. Figure 7 shows that for a 0.2-mm-dia coal particle burned at 1200 K air flow, the mass conversion takes place homogeneously throughout the whole particle and the dominating mechanism is chemical kinetics. On the other hand, for the 11.8-mm-dia particle the thermal energy diffuses only a short distance within the particle in each time step and the devolatilization process is controlled by heat transfer. This makes a fairly narrow reaction zone, which moves layer by layer into the unreacted core as time goes by. Figure 8 shows that the influence of chemical kinetics is gradually surpassed by the diffusional effect as the air temperature rises from 900 K to 1500 K.

Heat Transfer. Hot air is one of the main heat sources for coal devolatilization. Figure 9 shows that higher air stream temperature causes less ignition delay time, less devolatilization time, but higher surface temperature at ignition. It is well understood that raising the Reynolds number will enhance the heating rate to the particle, and therefore result in a higher surface temperature at ignition, as indicated in Fig. 10. Similarly, the surface temperature at ignition at 1200 K is found to be higher than that at 900 K. In addition, the ignition delay time shortens with the increase of the Reynolds number but the total devolatilization time remains almost constant. More energy is carried away from the flame due to the convective heat transfer at higher Reynolds number and hence the flame temperature is reduced, as depicted in Fig. 11. However, since the flame emissivity is usually less than 0.1, its effect on the total burning rate becomes negligible for Reynolds

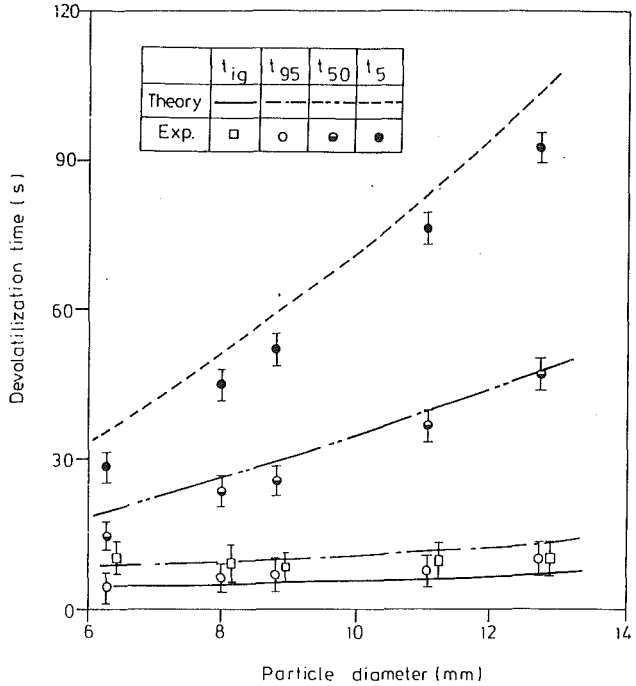

Fig. 5 Variation of devolatilization time with initial particle diameter ($T = 1073$ K, $u_\infty = 0.3$ m/s, $VM^o = 0.288$)

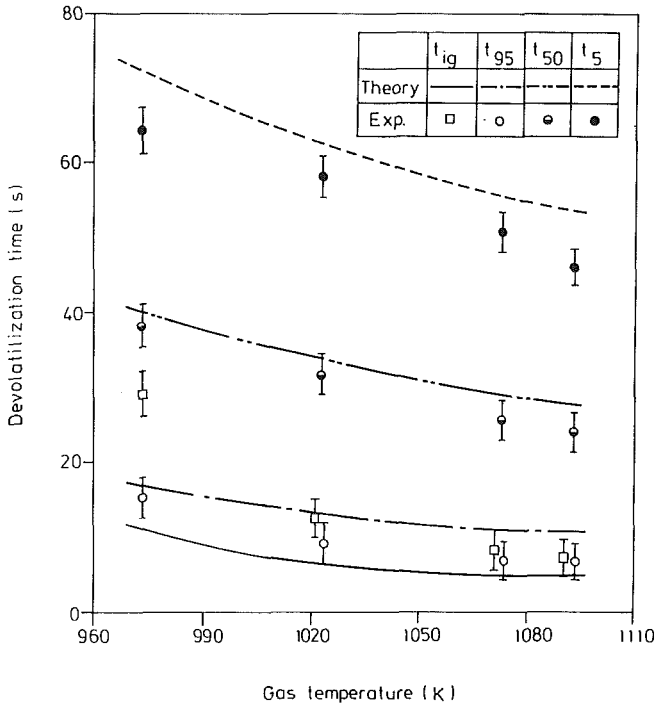

Fig. 6 Variation of devolatilization time with air temperature ($d = 8.8$ mm, $u_\infty = 0.3$ m/s, $VM^o = 0.288$)

numbers between 15 and 1.5 (corresponding to the relative velocities of 0.46 m/s and 0.05 m/s) at 1200 K.

Figure 12 illustrates the effect of the particle size on the devolatilization characteristics of air at 1200 K. Since the convective heat transfer coefficient is inversely proportional to the particle diameter, the ignition delay time and the devolatilization time both increase as the particle size increases.

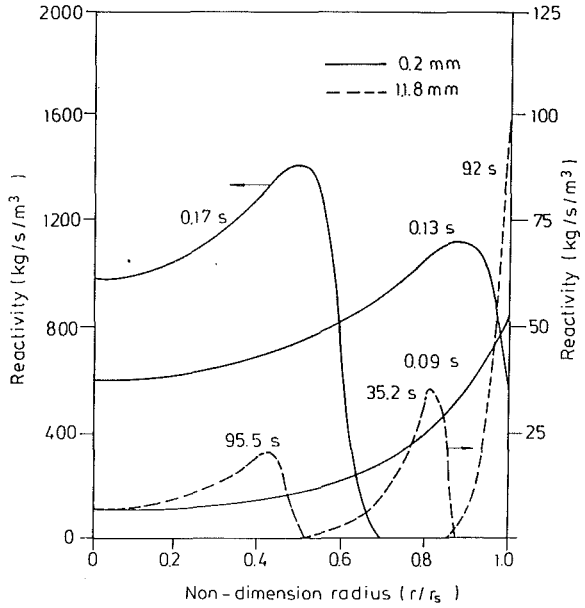

Fig. 7 Radial variation of reactivity in the particle with various particle sizes ($T = 1200$ K, $\alpha_f = 0.1$)

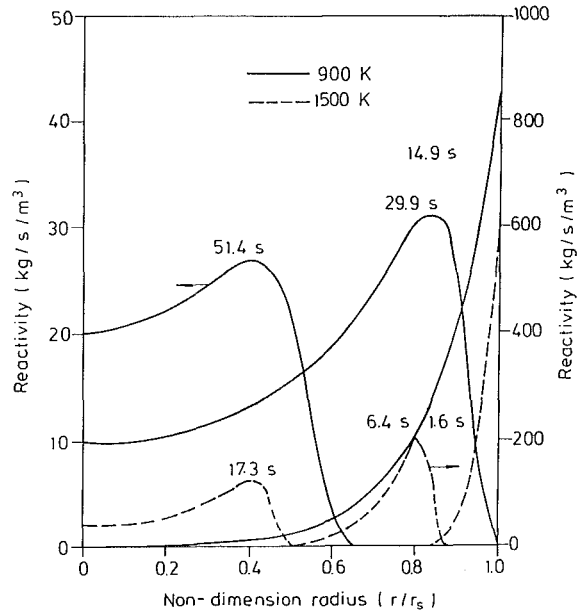

Fig. 8 Effect of temperature on radial variation of reactivity ($d = 5.3$ mm, $\alpha_f = 0.1$)

This study estimates that when the surrounding air is under 1200 K, 70–90 percent of heat generated at the flame front is lost to the air flow, and the flame temperature right after ignition is only between 1300 K and 1500 K. The contribution of radiation and convection can relatively be split into 70 percent/30 percent, and 10 percent/90 percent for 11.8-mm-dia and 0.2-mm-dia particles, respectively, prior to ignition, as shown in Figs. 13 and 14. The percentages split among flame radiation, wall radiation, and gaseous conduction after ignition are 15 percent/75 percent/10 percent and 6 percent/4 percent/90 percent for the cases of 11.8-mm-dia and 0.2-mm-dia, respectively. Furnace wall radiation is found to be the main heat source through the pre-ignition and devolatilization stages for 11.8-mm-dia particles. However, convection and conduction, respectively, are the major factors before and after ignition for smaller particles.

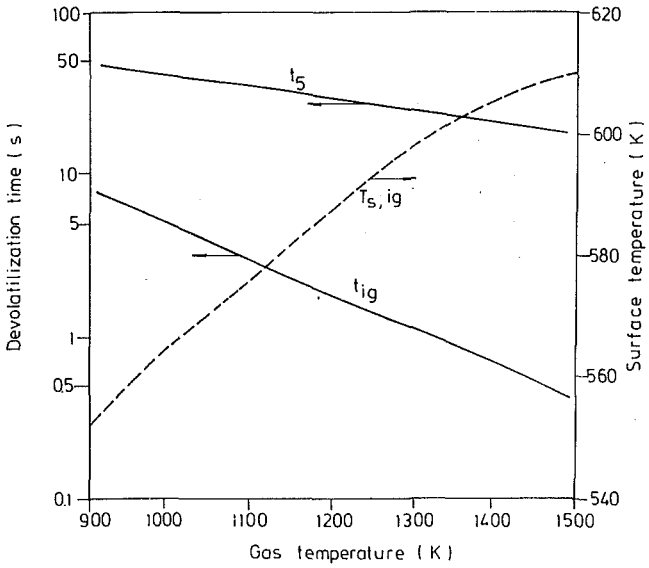

Fig. 9 Effect of air temperature on the devolatilization characteristics ($d = 5.3$ mm, $\alpha_f = 0.1$)

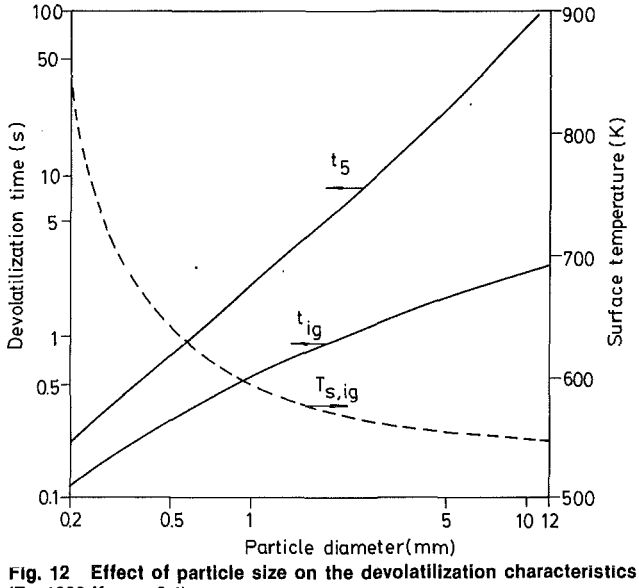

Fig. 12 Effect of particle size on the devolatilization characteristics ($T = 1200$ K, $\alpha_f = 0.1$)

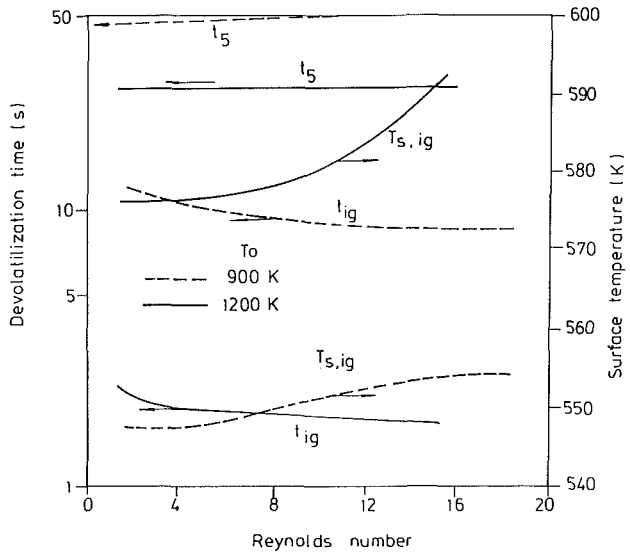

Fig. 10 Effect of Reynolds number on the devolatilization characteristics ($d = 5.3$ mm, $\alpha_f = 0.1$)

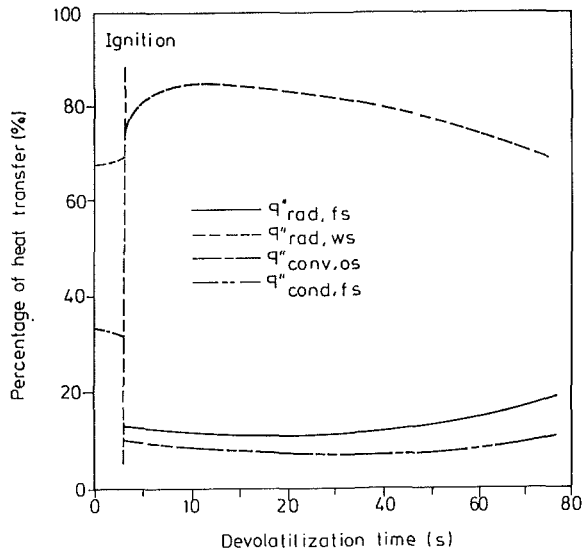

Fig. 13 Ratios of different heat transfer modes ($T = 1200$ K, $d = 11.8$ mm, $\alpha_f = 0.1$)

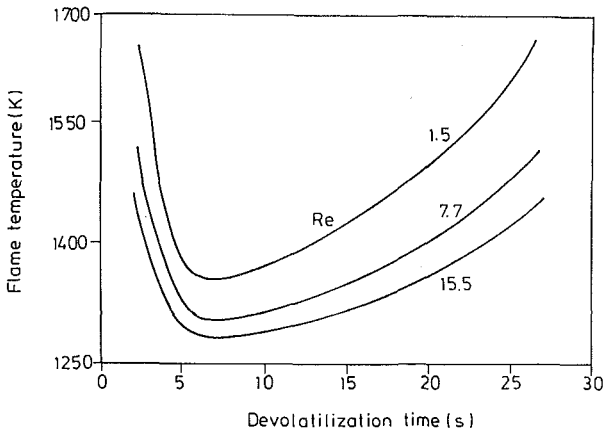

Fig. 11 Effect of Reynolds number on flame temperature ($T = 1200$ K, $d = 5.3$ mm, $\alpha_f = 0.1$)

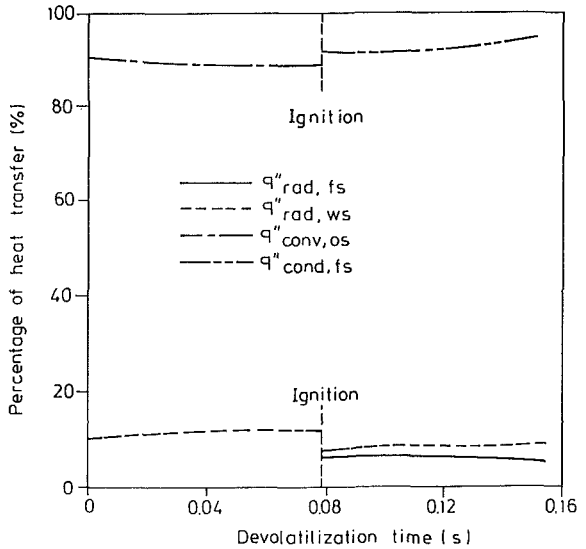

Fig. 14 Ratios of different heat transfer modes ($T = 1200$ K, $d = 0.2$ mm, $\alpha_f = 0.1$)

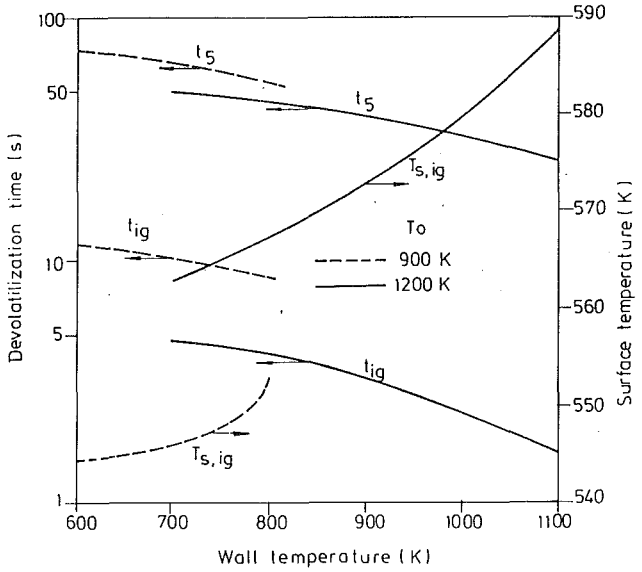

Fig. 15 Effect of the furnace wall temperature on the devolatilization characteristics ($d = 5.3$ mm)

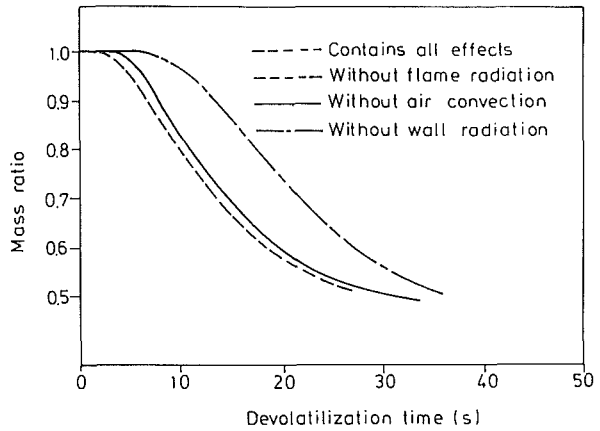

Fig. 16 Effect of heat transfer mode on transient mass burning ratio ($T = 1200$ K, $d = 5.3$ mm, $\alpha_f = 0.1$)

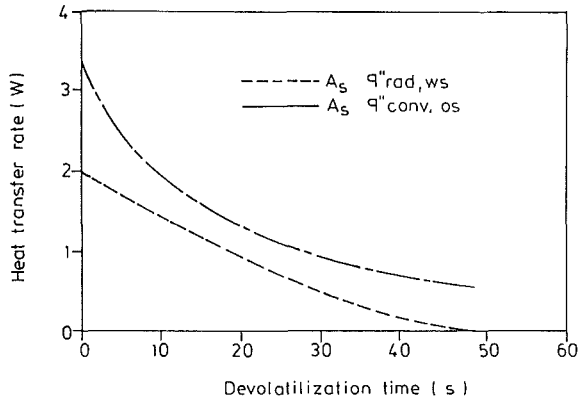

Fig. 17 Various heat transfer rates of gasification ($T = 900$ K, $d = 5.3$ mm)

The influence of furnace wall radiation has also been analyzed by separately setting the wall temperature to be 100 K to 400 K below the air temperature, which is 1200 K. The results are shown in Fig. 15. It is obvious that the effect of wall radiation is significant. With higher wall temperature the ignition delay is shorter, the total pyrolysis rate is faster, and the flame temperature is higher after the flame has developed. In addition to accelerating ignition, higher wall radiation also

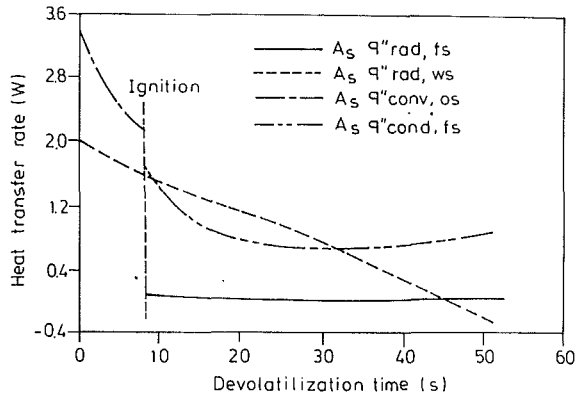

Fig. 18 Various heat tranafer rates of combustion ($T = 900$ K, $d = 5.3$ mm, $\alpha_f = 0.1$)

Table 3 Characteristic times under the influence of different heat transfer modes ($d = 5.3$ mm, $\alpha_f = 0.1$)

Temp. (K)	Air convec.	Wall radia.	Flame radia.	t_{95} (s)	t_{50} (s)	t_5 (s)	t_{ig} (s)
900	X	X	X	14.95	29.91	51.80	8.46
900	X	X	–	14.96	29.55	50.82	8.46
900	X	–	–	24.36	47.30	71.24	14.96
900	–	X	X	27.30	41.71	63.21	21.50
900	X	–	X	21.82	38.60	57.62	14.30
1200	X	X	X	4.86	12.69	26.94	1.70
1200	X	X	–	4.82	12.46	26.56	1.70
1200	X	–	–	13.82	29.90	48.31	6.27
1200	–	X	X	6.28	13.95	28.11	7.67
1200	X	–	X	10.65	21.40	35.12	5.35

Table 4 Characteristic times under the influence of flame emissivities ($d = 5.3$ mm)

Temp. (K)	α_f	t_{95} (s)	t_{50} (s)	t_5 (s)	t_{95-50} (s)	t_{50-5} (s)	$\frac{t_{95-50}}{t_{50-5}}$	t_{ig} (s)
900	0.1	21.8	38.6	57.6	16.8	19.0	0.883	14.3
900	0.5	18.3	27.8	40.5	9.5	12.7	0.744	14.3
1200	0.1	10.7	21.4	35.1	10.7	13.7	0.774	5.4
1200	0.5	7.4	13.3	22.1	5.9	8.8	0.659	5.4

enhances heating rate near the particle surface. This consequently increases the influence of the diffusion factors.

The relative roles of wall radiation and convection are also compared by separately taking out of the model the convective term, the wall radiation term, and the flame radiation term. Figure 16 clearly shows that without considering flame radiation, the transient mass ratio curve for 1200 K air follows the curve for the general case very closely. When the wall radiation is left out the curve shifts far away from the general case, whereas the deviation is only moderate when the convection is excluded. Further comparison information is also listed in Table 3. The deviation of combustion time (t_5) is 22 and 11 percent by omitting the terms of convection and wall radiation, respectively, in air flow at 900 K. The corresponding deviations at 1200 K are 4 and 30 percent, respectively. It is then judged that the wall radiation is the major factor at higher temperature air flow, while both the radiation and the convection are important at lower air temperatures for 5.3 mm coal particles.

Another conclusion from Table 3 is that convection seems to be slightly more important than radiation for ignition of solid fuels. For an air temperature of 1200 K, the ignition delay will increase 6 s when the convection term is left out, while the corresponding increase for neglecting radiation is 3.6 s.

The effect of flame radiation is investigated by altering the flame emissivity from 0.1 to 0.5. The results are listed in Table 4. At higher flame emissivity the radiation energy to the particle surface is higher. In the mean time, the heat loss from the flame to the wall also increases and thus reduces the flame temperature. This will actually decrease the flame radiation heat and conduction heat to the particle surface. Since the variation of flame temperature is not significant, the net heat transfer rate to the particle is increased and the devolatilization time is reduced to 30 percent at 900 K and 37 percent at 1200 K as the flame emissivity changes from 0.1 to 0.5.

If the volatile content is pyrolyzed in the inert environment, there will be no flame and the volatile content of the coal particle is consumed by pure gasification. The main heat transfer mode of gasification will be convection, as demonstrated in Fig. 17. The corresponding case of devolatilization is illustrated in Fig. 18. Because the flame temperature is not high, the total heat transfer rate is less than that of the gasification case, and consequently the devolatilization time is shorter. Nevertheless, if the air flow velocity is reduced to 1/10, then the devolatilization rate is certainly faster than the gasification rate.

Conclusions

In the present work a combustion model is developed and related experiments are conducted to study the devolatilization process and combustion characteristics of a single coal particle burned in a hot convective environment. Although the one-dimensional approach is adopted, the predicted trends are quite reasonable if the Reynolds number is less than 40 and the predicted characteristic times agree with the experimental data. The results show that heat and mass transfer is as important as chemical reaction for coal devolatilization. However, for millimeter-sized coal particles burned in a higher temperature environment, the process tends to be controlled more by the diffusional factors. The effect of chemical reactions is significant if the particle diameter is less than 0.5 mm.

The analysis also gives a clear indication that the furnace wall radiation is a major heat transfer source throughout the combustion process when the particle size is relatively large. For small size particles, the dominating factors are convection and conduction, respectively, before and after ignition. Although it is difficult to determine the value of flame emissivity, the predicted results show that the enveloping flame radiation will be a significant factor only when there is no wall radiation or when the Reynolds number is very low. When the flow rate is high enough, the flame temperature will be reduced and consequently the total combustion time will be longer than that of gasification case.

Acknowledgments

The work was supported by the National Science Council of Taiwan under Contract No. NSC76-0401-E007-15. The authors wish to thank Mr. Hsin-Min Law for the assistance in carrying out the experiments and the China Steel Corporation for providing the coal samples and conducting the ultimate analysis and the proximate analysis.

References

Agarwal, P. K., Genetti, W. E., and Lee, Y. Y., 1984, "Model for Devolatilization of Coal Particles in Fludized Beds," *J. Fuel*, Vol. 63, pp. 1157–1165.

Anthony, D. B., and Howard, J. B., 1976, "Coal Devolatilization and Hydrogasification," *J. AIChE*, Vol. 22, pp. 625–656.

Beckman, W. A., 1971, "The Solution of Heat Transfer Problem on a Digital Computer," *Solar Energy*, Vol. 13, pp. 293–300.

Bliek, A., van Poelje, W. E., van Swaaij, W. P. M., and van Beckum, F. P. H., 1985, "Effects of Intraparticle Heat and Mass Transfer During Devolatilization of a Single Coal Particle," *J. AIChE*, Vol. 31, pp. 1666–1681.

Essenhigh, R. H., 1981, "Fundamentals of Coal Combustion," in: *Chemistry of Coal Utilization*, Second Supp. Vol., M. A. Elliott, ed., Wiley, New York, pp. 1153–1312.

Faeth, G. M., 1977, "Current Status of Droplet and Liquid Combustion," *Prog. Energy Combust. Sci.*, Vol. 3, pp. 191–224.

Kansa, E. J., and Perlee, H. E., 1980, "A Transient Dust-Flame Model: Application to Coal Dust Flames," *Combustion and Flame*, Vol. 38, pp. 17–36.

Lerment, J. C., and Yip, S., 1984, "A Generalized Semenov Model for Thermal Ignition in Nonuniform Temperature Systems," *Combustion and Flame*, Vol. 57, pp. 41–54.

Maloney, D. J., and Jenkins, R. G., 1984, "Coupled Heat and Mass Transport and Chemical Kinetic Rate Limitations During Coal Rapid Pyrolysis," *20th Sym. (Int.) on Combustion*, pp. 1435–1443.

Phuoc, T. X., and Durbetaki, P., 1987, "Heat and Mass Transfer Analysis of a Coal Particle Undergoing Pyrolysis," *Int. J. Heat Mass Transfer*, Vol. 30, pp. 2331–2339.

Ragland, K. W., and Yang, J. T., 1985, "Combustion of Millimeter-Sized Coal Particles in Convective Flow," *Combustion and Flame*, Vol. 60, pp. 285–297.

Smith, P. J., and Smoot, L. D., 1980, "One-Dimensional Model for Pulverized Coal Combustion and Gasification," *Combustion Science and Technology*, Vol. 23, pp. 17–31.

Solomon, P. R., and Hamblen, D. G., 1983, "Finding Orders in Coal Pyrolysis Kinetics," *Prog. Energy Combust. Sci.*, Vol. 9, pp. 323–361.

Ubhayakar, S. K., Stickler, D. B., von Rosenberg, C. W., Jr., and Gannon, R. E., 1976, "Rapid Devolatilization of Pulverized Coal in Hot Combustion Gases," *16th Sym. (Int.) on Combustion*, pp. 427–436.

Thermal Analysis of Hydrogen Combustion in a 1/4-Scale Boiling Water Reactor Containment Building

E. A. Ural
Mem. ASME

F. Tamanini

Factory Mutual Research Corporation,
Norwood, MA 02062

A mathematical model has been developed for the analysis of hydrogen combustion in boiling water reactor containment buildings. The overall phenomenon is similar to that observed in enclosure fires with the major differences being: (1) The containment building is hermetically sealed, and (2) diffusion flames form above a water pool at the bottom of the containment, through which hydrogen is released. The calculated results are compared with data obtained in tests performed in a 1/4-scale model of the containment building. The zone modeling approach, which was used in these calculations, has been demonstrated to be suitable for application to the combustion dynamics produced by the hydrogen flames in containment volumes.

1 Introduction

The accident at the Three Mile Island Nuclear Power Station showed that large amounts of hydrogen can be released in the containment area of a nuclear reactor during certain types of degraded-core accidents. In response to this concern, the operators of nuclear power plants have considered different methods for avoiding the accidental formation of flammable hydrogen/air mixtures in large portions of the containment volume. The concept of controlled burning was eventually selected for implementation in a group of large-volume (greater than 42,500 m^3, 1.5 million ft^3) containment buildings, which includes boiling-water-reactor (BWR) Mark III designs. With this approach, glow plug igniters, which are installed throughout the containment volume, are activated in the case of hydrogen release during a degraded-core accident for the purpose of causing localized early combustion of small gas accumulations.

While it was originally postulated that a succession of volume burns (small deflagrations) would be the combustion mode resulting during continuous hydrogen injection in the containment, the establishment of diffusion flames near the injection sites appeared likely, following initial light-off, for situations where the injection rate is sufficiently high. In order to evaluate the combustion phenomenon, in particular with regard to the thermal environment produced by nonpremixed burning, a group of utilities, the Hydrogen Control Owners Group (HCOG), has sponsored a test program in a 1/4-scale facility simulating a Mark III containment. As a parallel effort to the experimental program, HCOG has also supported the analytical work described in the present paper, whose goal is to provide a quantitative estimate of the energy exchanges resulting from hydrogen combustion in the containment volume. The approach in modeling has been similar to the zone models for enclosure fires as opposed to more detailed field models (e.g., Travis, 1984).

This paper discusses the current status of the model by showing comparisons between predictions and experimental data. Since it is outside the scope of this paper, the experimental test facility and instrumentation are described only to the extent necessary to provide adequate background to the discussion of the theoretical model.

Contributed by the Heat Transfer Division and presented at the 2nd ASME-JSME Thermal Engineering Joint Conference, Honolulu, Hawaii, March 1987. Manuscript received by the Heat Transfer Division February 4, 1988. Keywords: Combustion, Fire/Flames, Modeling and Scaling.

2 Experimental Program

Since the dynamics of the low-momentum hydrogen flames existing in the containment is controlled by buoyancy, the Froude modeling technique was used as the basis for the design of the experiment (Tamanini, 1983). This approach, which has been validated by several applications to problems of fires in enclosures, is expected to provide an accurate representation of turbulent entrainment, flow circulation, and flame geometry, with accurate mapping of gas temperatures and scaling of gas velocities, at least away from walls. On the other hand, heat fluxes to solid surfaces are expected to depart from perfect scaling. The goal of the analytical effort is to determine the effect of imperfect scaling of these heat fluxes on the extrapolation of test results from the model to full scale. The scope of this paper, however, is limited to comparison of test results with the model predictions for model validation.

The test enclosure, which is designed to operate at pressures up to 275 kPa above ambient, consists of a steel outer tank 9.6 m in diameter by 15.1 m high, containing a smaller steel tank 6.3 m in diameter by 7.0 m high. Two orthogonal vertical cross sections of the facility are shown in Fig. 1. The space between the two tanks is the test volume, which contains grated or solid floors and other large blockages simulating the obstructions that exist in the actual containments. The surfaces of the two cylindrical tanks, as well as those of the enclosed volumes exposed to the test volume, are covered with

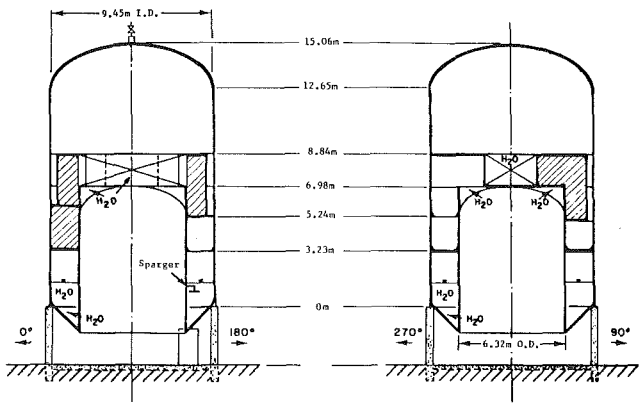

Fig. 1 Elevation views of the 1/4-scale facility

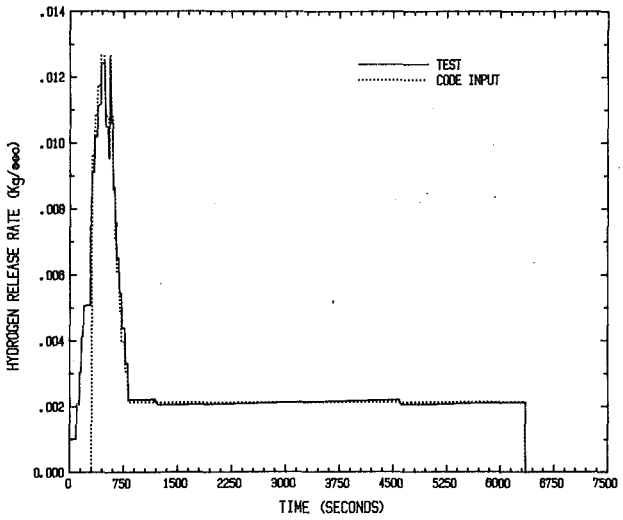

Fig. 2 Total hydrogen release rate

layers (7.6 or 11 cm thick) of refractory insulation, which simulate the concrete surfaces in the actual containment. There are five levels of flooring in the test volume made up of grating, grating covered with metal plates, or insulation. The lower portion of the gap between the two tanks is filled with about 1.4 to 1.8 m of water to simulate the suppression pool of the actual plants. Hydrogen and steam are released through vent holes on the surface of the inner tank or through nine spargers submerged in the suppression pool near the inner wall. Each sparger has four horizontal perforated arms extending 38 cm in four perpendicular directions. Hydrogen and a hydrogen/steam mixture are injected at rates representative of conditions of degraded-core accident scenarios.

Hydrogen and steam flow control valves are activated by programmable flow control mechanisms, which can follow preassigned release histories. Core heatup and degradation have been modeled by HCOG and release histories of hydrogen and steam have been calculated. Figure 2 shows one such release as used in Test P-07. These are the total flow rates through nine spargers in the 1/4-scale facility, which are Froude scaled from the full-scale values.

The facility is equipped with over 120 gas thermocouples distributed throughout the test volume. Several of the thermocouples are mounted on the surface of insulation or on grates. Five total and five radiant heat flux gages are mounted near the suppression pool. In addition, five video cameras sensitive to visible/near-IR light provide video records of the hydrogen flames. During a test, gas samples are drawn continuously from 21 different locations in the test volume and are analyzed to determine hydrogen and oxygen concentrations. Bidirectional velocity probes have also been installed in order to characterize the global circulation patterns. Two pressure transducers record the containment pressure while several types of calorimeter have been used to make calorimetric measurements. Additional instrumentation is used to determine process parameters such as hydrogen and steam flow rates and temperatures.

Fifty-six automotive glow plug igniters are installed throughout the test volume providing the means of ignition when hydrogen accumulates to flammable levels during the test.

Experiments are started by the initiation of hydrogen and steam injection with the glow plug igniters already energized. Ignition typically takes place relatively early in the release history when a flammable mixture forms around one of the lowest level igniters. At the time of ignition and during combustion, hydrogen accumulation at higher elevations is relatively low, with the dry basis mole fraction of the order of 1 percent. Ignition is accompanied by a very mild deflagration involving a small fraction of the test volume within the annular space between the suppression pool and the first floor above it. Following this initial transient, standing diffusion flames become established on the pool surface. The ignition process, although seen in video monitors and heard through the test volume microphone, does not produce a detectable sudden rise on the pressure trace.

The base of each diffusion flame is located within the inner half of the gap between the inner and outer walls on the pool surface with an area of the order of the square of the sparger diameter. At the peak of the release rate history shown in Fig. 2, the flames have an L/D ratio of approximately unity, which decreases with decreasing hydrogen flow rate. At lower hydrogen release rates, combustion takes a more intermittent appearance with individual flamelets flickering over the pool surface.

At high hydrogen release rates, the flames are observed to be leaning toward the inner wall; at lower flow rates the inner portion of the flames still appears to be attracted by the inner wall, while the outer portion seems unaffected by the presence of the wall.

3 Mathematical Model Description

The approach (Ural and Tamanini, 1986) has been to mate a global model for the containment atmosphere with a flame/plume model for the hydrogen diffusion flames. The global model treats the entire containment atmosphere as a single volume to calculate gas pressure and background parameters such as ambient temperature and composition needed for the diffusion flame model. The flame/plume model treats the diffusion flames and plumes to calculate the gas temperature and heat flux distributions and the associated heat sinks needed in the global model. Heat transfer calculations in both the global model and flame/plume model are based on surface temperatures calculated with the surface heat up wall models.

All the exposed surfaces in the test volume are categorized and lumped into three separate surface models, each of which is characterized by a single temperature varying in time. The "outer wall" model accounts for all the exposed surfaces of the outer shell. The remaining exposed refractory surfaces are lumped into an "inner wall" model. All exposed steel in the containment, referred to here as "equipment," is treated as a single mass with a uniform temperature.

3.1 Flame/Plume Model. Since the spargers are very close to the inner wall and the flames have been observed to lean toward the inner wall (at least at high release rates), the plumes have been conceived as attaching to the inner wall and are modeled as two-dimensional wall plumes of width equal to the sparger diameter. As the plumes rise, they are allowed to grow only in the direction normal to the inner wall. The velocity and temperature fields are described by linearizing wall plume correlations found in the literature (Liburdy et al., 1979) and are given by

$$u_p\left(\frac{\rho C_p}{g\beta Q_z}\right)^{1/3} = 3.0\left(1-\frac{y}{0.17z}\right) \quad (1)$$

$$g\beta z\Delta T_p\left(\frac{\rho C_p}{g\beta Q_z}\right)^{2/3} = 5.9\left(1-\frac{y}{0.17z}\right) \quad (2)$$

where Q_z is the convective energy of the plume per unit width at elevation z. At the top of the inner wall these plumes are truncated and are assumed to mix instantaneously with the background gas. The plume correlations are used down to the flame tip, which is calculated as the height at which the peak

plume temperature rise given by equation (2) equals 820 K. This turbulent buoyant diffusion flame temperature rise is 40.6 percent of the adiabatic flame temperature for a stoichiometric hydrogen/air mixture. The figure of 40.6 percent was obtained by analysis of data for hydrocarbon diffusion flames (Hasemi and Tokunaga, 1984). The temperature in the flame region is assumed to be uniform.

In the calculations, the plume convective energy Q_z decreases as the plume rises and is adjusted for thermal losses at three elevations, i.e., flame tip, lowest floor level, and the top of the inner wall. Between these elevations Q_z is treated as constant.

The plumes lose heat to the inner wall and to equipment via convection. The heat transfer coefficient h_{iw} for convection from the plume to the inner wall is calculated using the experimental correlation (Ahmad and Faeth, 1979)

$$q''_w = h_{iw}\Delta T_p = 1.9\ \mathrm{Pr}^{-2/3}\frac{Q_z}{z}\left(\frac{g\beta z^3 Q_z \mathrm{Pr}}{\rho_\infty C_p \nu_\infty^3}\right)^{-0.095} \tag{3}$$

which was obtained with the wall and ambient temperatures approximately equal. In the present case, when these temperatures may be different, a linear correction has been made for the temperature differential. It should be noted that the heat transfer coefficient and the gas temperature in equation (3) both vary with elevation and are integrated from the flame tip to the top of the inner wall over the area touched by the plumes.

The equipment is assumed to consist of horizontal cylinders uniformly distributed in the annular region between the inner and outer walls above the lowest floor. The heat transfer coefficient for plume convection is calculated locally using the turbulent forced convection correlation (Kreith, 1976) for crossflow over tube bundles:

$$\mathrm{Nu}_{eq} = 0.33\ \mathrm{Pr}^{1/3}\mathrm{Re}_{eq}^{0.6} \tag{4}$$

which is based on tube diameter, taken here as the characteristic dimension of steel equipment and structures in the annular region. The total rate of heat loss from the plumes to the equipment is calculated by integrating over the equipment surface intercepted by the plumes the product of the local heat transfer coefficient and the temperature difference between gas and equipment.

The flames are allowed to lose heat by convection to the inner wall and to the suppression pool surface, and by radiation to the inner wall and the outer wall.

Flame convection to the inner wall and to the suppression pool is evaluated using a uniform heat transfer coefficient equal to the value given by equation (3) at the flame tip and the difference between the flame temperature and the appropriate surface temperature. The heat exchange areas for each flame for the inner wall and for the pool surface, respectively, are taken as: a rectangle defined by the sparger diameter and the flame height, and the sparger diameter squared. The pool heat losses calculated this way become an increasing fraction of the heat release rate when the latter is decreasing. Based on experimental evidence (Corlett, 1965), this fraction is not allowed to exceed 25 percent.

The radiant heat loss from the flames is conventionally expressed as a constant fraction χ_R of heat release rate. For hydrogen diffusion flames in air, χ_R values were measured by Fishburne and Pergament (1979) to be between 0.09 and 0.15, typically increasing with decreasing Froude number. Since the Froude numbers in the present facility are well below those of Fishburne and Pergament (1984), the highest value of 0.15 was adopted for χ_R in the analysis. Although the value of χ_R is expected to change with the ambient oxygen concentration, there do not appear to be any published data for hydrogen diffusion flames under vitiated conditions. Based on the observations in the tests that the diffusion flames become less emissive as oxygen is depleted, a linear relationship between χ_R and the oxygen mole fraction, χ_{02}, has been assumed so that χ_R is 0.15 when χ_{02} is 21 percent and is zero when the oxygen mole fraction drops to 5 percent, which is also taken as the flame quenching criterion.

Based on a simple estimation (Ural and Tamanini, 1986) of view factors of inner and outer walls from the sparger axis, 35.1 percent of the radiant energy is assumed to be absorbed by the inner wall, whereas the rest is assumed to go in the direction of the outer wall. The transmittance of the background gas for the latter radiation was estimated to be 90 percent using the total transmittance model of Grosshandler (1980). The remaining 10 percent of the radiation toward the outer wall is absorbed by the background gas.

3.2 Global Model. The global model keeps track of the energy and mass exchanges across the test volume boundaries and calculates the instantaneous values of the parameters needed for the flame/plume model, such as the background pressure, temperature, and composition, as well as the wall surface temperatures.

The global energy balance is written as

$$\frac{d}{dt}(Mu) = \dot{m}_{\mathrm{H}_2}\,\bar{h}_{\mathrm{H}_2} + \dot{m}_A\,\bar{h}_A - \dot{m}_c\,h_s(T_\infty) - \dot{Q}_L \tag{5}$$

where $\dot{m}_{\mathrm{H}_2}$ is the rate of hydrogen release, and $\dot{m}_A$ is the rate of air addition ($\dot{m}_A$ would be zero in an actual plant but is present in the 1/4-scale facility due to purge of the video camera enclosures). The rate of steam condensation on all the solid surfaces is expressed by $\dot{m}_c$, which can be negative if the conditions are favorable for evaporation, as will be discussed later. All the heat losses from the test volume are lumped into the last term in equation (5). It should be noted that no steam injection term appears in equation (5), since most of the steam injected along with hydrogen is stripped from the mixture when bubbling through the suppression pool.

The velocity probes located inside the test volume indicated tangential and vertical gas velocities near the outer wall of the order of 1 m/s at high hydrogen release rates. Based on this observation, an average gas velocity was imposed on the background gas model, which is calculated by dividing the plume mass flow rate at the top of the inner wall by the background gas density and available cross-sectional area at this elevation. The available cross-sectional area was taken simply as one half of the annular area not occupied by the plumes. The background gas velocity calculated this way was 1.1 m/s at the peak hydrogen release rate. This global circulation is expected to minimize the stratification effects while increasing the heat losses from the background gas.

Preliminary analysis has indicated that these low background velocities would not affect the natural convection to the inner and outer walls while they significantly enhance the convection to equipment. Therefore, convection from the background gas to the inner and outer walls is estimated using the turbulent natural convection correlation (Kreith, 1976) for vertical flat plates

$$\mathrm{Nu}_w = 0.13\ (\mathrm{PrGr}_w)^{1/3} \tag{6}$$

which results in a heat transfer coefficient independent of scale.

The equipment is represented as uniformly distributed horizontal cylinders. The heat transfer coefficient is calculated using the combined convection correlation of Moffat and Kays (1984)

$$\mathrm{Nu}_{eq} = (\mathrm{Nu}_{\mathrm{NC}}^{3.2} + \mathrm{Nu}_{\mathrm{FC}}^{3.2})^{1/3.2} \tag{7}$$

where

$$\mathrm{Nu}_{\mathrm{NC}} = \begin{cases} 0.47\ (\mathrm{PrGr})^{1/4} & \mathrm{PrGr} < 10^9 \\ 0.10\ (\mathrm{PrGr})^{1/3} & \mathrm{PrGr} > 10^9 \end{cases} \tag{8}$$

Table 1 Input parameters for test volume description

Free volume	617.5	m^3
Outer wall surface	421.5	m^2
Inner wall surface	235.	m^2
Inner and outer wall $(k\rho c)^{1/2}$	1.61	$kWs^{1/2}/m^2K$
Steel equipment mass	10,829	kg
Steel, specific heat	0.46	kJ/kg K
Annulus equipment surface	170.8	m^2
Dome equipment surface	192.	m^2
Equipment characteristic dimension	0.019	m
Outer wall radius	4.72	m
Inner wall radius	3.16	m
Sparger arm length	0.381	m
Sparger axis radius	3.54	m
Lowest floor elevation from pool surface	1.83	m
Inner wall elevation from pool surface	5.58	m

is the natural convection component (Rohsenow and Harnett, 1973), and

$$\mathrm{Nu}_{\mathrm{FC}} = (0.4\,\mathrm{Re}^{0.5} + 0.06\,\mathrm{Re}^{0.67})\,\mathrm{Pr}^{0.4} \tag{9}$$

is the forced convection component (Kreith, 1976).

In estimating the condensation mass flux, condensation in the presence of noncondensable gas has been considered (Spalding, 1963)

$$\dot{m}_c'' = \frac{\mu_{\mathrm{ref}}}{L}\,\frac{\mathrm{Nu}}{\mathrm{Pr}^{1/3}\mathrm{Sc}^{2/3}}\,\frac{\ln(1+B)}{B}\,(Y_\infty - Y_w) \tag{10}$$

where $B = -(Y_\infty - Y_w)/(1 - Y_w)$; Y_∞ is the mass fraction of steam in the background gas; and Y_w is the mass fraction of steam corresponding to the saturation pressure at the appropriate wall temperature. Based on experimental observation, the solid surfaces are assumed to be covered with a sufficient water film so that, when $\dot{m}_c''$ calculated by equation (10) becomes negative, evaporation is allowed. On the other hand, the water film is assumed to be sufficiently thin that its thermal resistance may be ignored.

In terms of the global heat balance, steam condensation/evaporation is sensed as enthalpy removal/addition as expressed in equation (5), while the energy associated with steam going from background gas temperature to water at the surface temperature is deposited on the appropriate wall surface.

Another condensation mechanism incorporated into the model is the homogeneous condensation that occurs when the background gas temperature drops below the saturation temperature associated with the steam content. At that time, a sufficient amount of steam is allowed to condense so that the background gas at the end of the time step is saturated, and the associated phase-change energy is deposited in the background gas.

The net radiant heat going into surface i is expressed as

$$A_i \tilde{q}_i'' = A_i \sigma(\epsilon_g T_\infty^4 - \epsilon_i T_i^4) + \sum_{j=i}^{3} \sigma A_j \tau_{ji} F_{ji} \epsilon_j T_j^4 \tag{11}$$

where ϵ_g is the background gas emissivity calculated (Modak, 1979) as a function of steam partial pressure, gas temperature, total pressure, and mean beam length. For the sake of simplicity, the surface emissivity ϵ_i, and the average transmissivities τ_{ji}, are taken as equal to ϵ_g and $(1-\epsilon_g)$, respectively. The exchange factors F_{ji} are estimated using simple geometric and heat balance arguments (see Ural and Tamanini, 1986).

Different heat-up models are used for equipment, and for inner and outer walls due to their different natures.

The equipment mostly consists of steel grating and sheet metal plates with small thermal characteristic dimensions so that temperature gradients can be ignored. Therefore, equipment surface temperature is expressed as

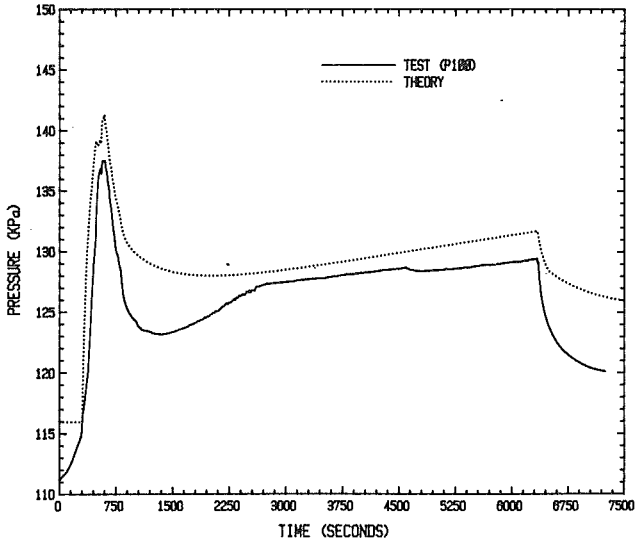

Fig. 3 Measured and calculated containment pressure

$$M_{eq} C_{eq} \frac{dT_{eq}}{dt} = \dot{Q}_{eq} \tag{12}$$

where $\dot{Q}_{eq}$ is the total rate of energy absorbed by the equipment, both from background gas and from plumes.

The inner and outer walls, on the other hand, are covered with thick layers of insulation with relatively low thermal conductivity so that a semi-infinite solid model (Carslaw and Jaeger, 1959) is used

$$T_w = T_{w_o} + \frac{1}{\sqrt{\pi k_c \rho_c C_c}} \int_0^t q_w''(t-\tau)\frac{d\tau}{\tau^{1/2}} \tag{13}$$

where q_w'' is the average heat flux incident on the appropriate wall.

3.3 Key Input Parameters. The hydrogen release history, input into the code as shown in Fig. 2 by a dotted line, is adjusted to start at the time of the experimentally observed light-off. As seen in the figure, small quantities of hydrogen injected prior to ignition, and after the flames are extinguished, which amount to a few volume percent average, are ignored in the analysis. Furthermore, as indicated previously, the possibility of steam bypass through the suppression pool is ignored.

The calculations are started with all temperatures being equal to 301 K with the initial pressure at 116 kPa. The initial mixture is taken as air with 3 mole percent steam, which is a slightly superheated state.

The parameters describing the test volume have been determined by careful evaluation of the facility drawings and are summarized in Table 1.

4 Discussion of Results

The mathematical model described in Section 3 was run to simulate Test P-07 performed in the 1/4-scale facility; the model results are compared with data from the test in the following discussion. In accordance with the model formulation comparisons are made with parameters in two categories: (1) global parameters, and (2) local parameters.

4.1 Comparison With Global Parameters. Global parameters pertain to the average values for the bulk of the test volume. Under the slow burn conditions observed in the tests, the most readily measured indicator of the average state of the test volume is the containment pressure. The measured and calculated containment pressures are shown in Fig. 3. The theory seems to overpredict the peak overpressure by 17 percent. The discrepancy increases to as high as 78 percent after

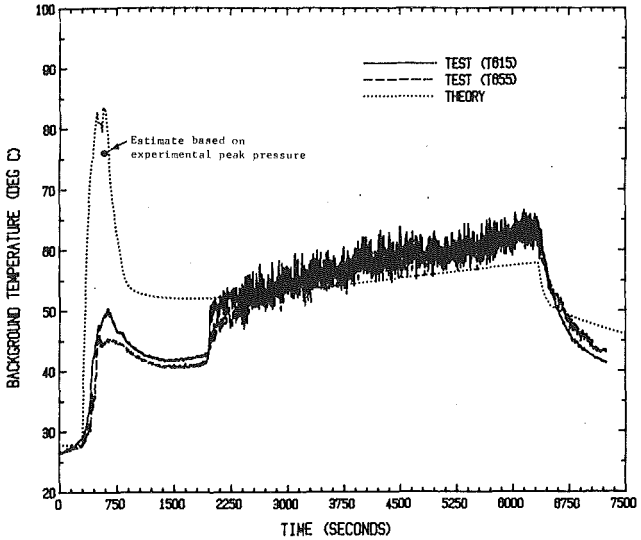

Fig. 4 Measured and calculated background gas temperatures

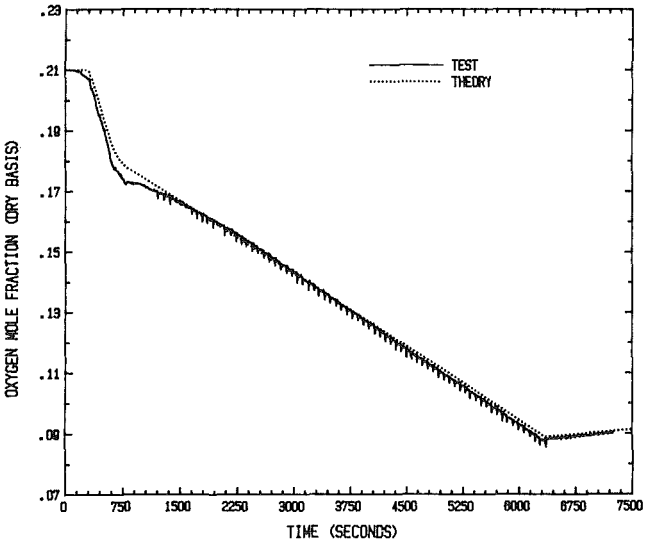

Fig. 5 Measured and calculated background oxygen concentration

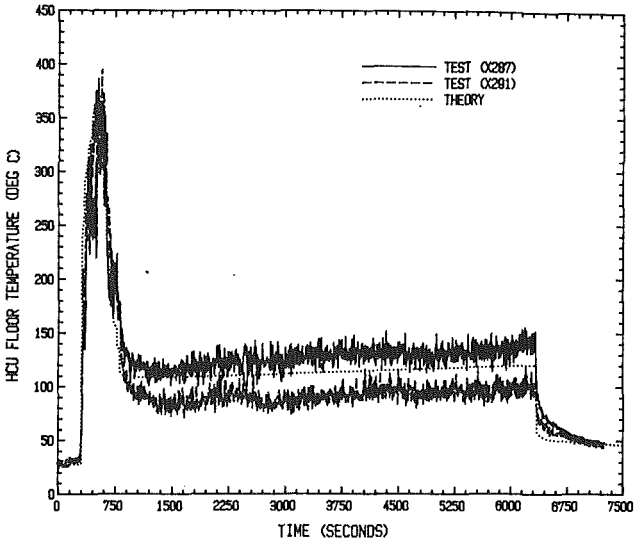

Fig. 6 Measured and calculated peak temperature at the lowest floor elevation

the peak, at a time when partial extinction of the flames was observed in the test. This temporary extinguishment is not simulated by the model.

The calculated background gas temperature is shown by the dotted line in Fig. 4. Also shown in this plot are the temperature measurements from two thermocouples, T615 (1.83 m, 45 deg, 12.80 m)[1] and T655 (3.96 m, 225 deg, 10.67 m) both located in the dome region. The model appears to be substantially overestimating the background gas temperature during the early portions of the transient. This was attributed to water film covering most of the thermocouple beads, which prevented the thermocouples from following the gas temperature (as also suggested by the lack of fluctuations) until this film was completely evaporated. This appears to be indeed the case since the experimental and theoretical pressures displayed a better agreement than the background gas temperatures in this period. Furthermore, the peak value of average gas temperature deduced from the experimental peak pressure rise is in good agreement with the predicted peak temperature (cf Fig. 4). The agreement between experiment and theory is reasonable for the later position of the transient.

The calculated dry-basis oxygen mole fraction is shown in Fig. 5. Also shown in this plot are the data from oxygen analyzer 0001, which provide a multiplexed signal from 12 different sampling points mostly away from the hydrogen release sites in the test volume. This should provide a good indication of containment averaged oxygen concentration. The calculated and measured rates of global oxygen consumption match closely.

4.2 Comparison With Local Parameters. The local parameters are more important in terms of describing the severity of the environment for equipment survivability analysis, yet more difficult to compare with data from the theoretical standpoint. The most severe thermal environment is obviously low in the containment near the diffusion flames. In actual reactors, some of the critical equipment that is expected to survive the diffusion flames is located on or above the lowest floor, which is at the 3.23 m elevation in the 1/4-scale facility.

The peak floor temperature calculated at 1.83 m above the suppression pool level is shown with a dotted line in Fig. 6. The plot also includes the data from thermocouples T287 (3.35 m, 326.3 deg, 3.41 m) and X291 (3.57 m, 330 deg, 3.41 m) in Test P-07. These thermocouples recorded the highest temperatures among all the thermocouples located at the 3.41 m elevation mainly due to the effect of the corner formed by the inner wall and the vertical surface of an enclosed volume and due to three active spargers (at azimuths 315 deg, 330 deg, 345 deg) concentrated in this chimney. Therefore, the remarkable agreement seen in Fig. 6 may be fortuitous, in view of the approximate character of the model, for predicting local parameters. While the model is not intended to be a predictive tool for calculating the local temperatures, it is expected to provide reasonable estimates of the relationship between lowest floor peak gas temperatures for the 1/4-scale facility and actual containment. However, due caution must be exercised even for the latter, because of the uncertainties associated with the individual submodels.

Comparisons of the calculated and measured heat fluxes are difficult because of the location and orientation of the heat flux gages. For example, in simulating Test S-05.1, the model predicted 30 kW/m^2 convective and 15 kW/m^2 radiative peak heat flux to the inner wall from the flames. However, in Test S-05.1, none of the heat flux gages were engulfed in flames. In a different test with higher hydrogen release rate the inner wall heat flux gage No. 176 (3.16 m, 315 deg, 2.13 m) was engulfed

[1] Cylindrical coordinates given as (radius, azimuth, elevation).

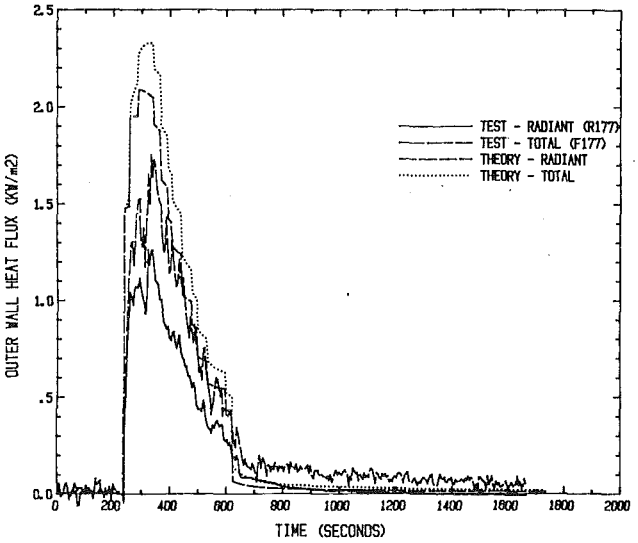

Fig. 7 Measured and calculated heat fluxes for the outer wall heat flux gages (test S-05.1)

in flames and indicated radiant and total heat fluxes up to 30 kW/m^2 and 53 kW/m^2, respectively.

The radiant and total heat flux data from the outer wall gage No. 177 (4.72 m, 315 deg, 2.13 m) for Test S-05.1 are plotted in Fig. 7. The heat flux gages are normally kept at elevated temperature in order to prevent condensation on them. This temperature difference from the rest of the containment results in negative offset of the output, which was taken out in Fig. 7. Also shown in Fig. 7 with a dotted line is the calculated radiant heat flux to the outer wall at the location of the heat flux gage, consisting of background and flame radiation. The latter is calculated approximately by assuming that three flames are seen by the heat flux gage as point sources located on the corresponding sparger axes at the elevation of the radiometer, which is assumed to have a Lambertian sensitivity. The convective component of the calculated total heat flux curve shown in Fig. 7 is taken only as the background convection; and condensation is not included due to the elevated temperature of the heat flux gage.

5 Conclusions

The model overestimates the pressure rise by 10 to 20 percent except for a period when temporary quenching of flames was observed in the experiments. The agreement between the calculated and measured background gas temperatures was reasonable, given the level of sophistication of the model.

The peak gas temperature calculated at the lowest floor elevation has matched the highest temperatures measured at this elevation rather remarkably. However, it should be kept in mind that the model predicts the peak temperatures to be at the interface of the plumes with the inner wall, and these temperatures are equal for each plume at a given elevation. The experimental data, on the other hand, show that the location and the value of peak gas temperature at a given elevation are strongly affected by sparger configuration, global circulation pattern, and local flow confinement effects.

At the time of peak background temperature, the model predicts that 31 percent of the energy released by combustion is lost directly by the flames: 1/3 by radiation and 2/3 by convection. Convection is responsible for 20 percent of the loss of the combustion energy from the plume region. The rest of the energy, 49 percent, is lost by the background gas with the largest contributor being convective heat loss to equipment (28 percent of combustion energy).

Comparisons with two other tests have indicated that even better agreement between the experiment and theory could be achieved by increasing the direct heat losses from the flames while reducing the background gas heat transfer to equipment. However, these improvements could not be justified at the present time due to scarcity of pertinent data.

Acknowledgments

This work was sponsored by the Hydrogen Control Owners Group (HCOG) through EPRI Contract Y101-1. The authors are grateful to John Hosler, EPRI Contract Manager, for his strong interest in the work and continuous encouragement. Dr. Robert G. Zalosh of FMRC led the development of an earlier version of the model and has provided continuous guidance in all phases of this project. The authors also gratefully acknowledge the advice provided through several discussions by Drs. Ronald Alpert, Michael Delichatsios, John de Ris, Gunnar Heskestad, and Hong-Zeng You of FMRC.

References

Ahmad, T., and Faeth, J. M., 1979, "Turbulent Wall Fires," *Seventeenth Symposium (International) on Combustion*, The Combustion Institute, pp. 1149-1160.

Carslaw, H. S., and Jaeger, J. C., 1959, *Conduction of Heat in Solids*, Oxford University Press, United Kingdom, p. 76.

Corlett, R. C., 1965, "Heat Transfer Data Summary—Pool Burning Study," Eng. Sci. Lab. Tech. Rept. No. 19, Div. of Eng. and Applied Sci., Harvard University, Cambridge, MA.

Fishburne, E. S., and Pergament, H. S., 1979, "The Dynamics and Radiant Intensity of Large Hydrogen Flames," *Seventeenth Symposium (International) on Combustion*, The Combustion Institute, pp. 1063-1074.

Grosshandler, W. L., 1980, "Radiative Heat Transfer in Nonhomogeneous Gases: A Simplified Approach," *Int. J. Heat and Mass Transfer*, Vol. 23, pp. 1447-1459.

Hasemi, Y., and Tokunaga, T., 1984, "Some Experimental Aspects of Turbulent Diffusion Flames and Buoyant Plumes From Fire Sources Against a Wall and in Corners of Walls," *Comb. Sci. and Tech.*, Vol. 40, pp. 1-17.

Kreith, F., 1976, *Principles of Heat Transfer*, 3rd ed., Intext, New York, pp. 420-423.

Liburdy, J. A., Groff, E. G., and Faeth, G. M., 1979, "Structure of a Turbulent Thermal Plume Rising Along an Isothermal Wall," ASME JOURNAL OF HEAT TRANSFER, Vol. 101, pp. 249-255.

Modak, A. T., 1979, "Radiation From Products of Combustion," *Fire Research*, Vol. 1, pp. 339-361.

Moffat, R. J., and Kays, W. M., 1984, "Review of Turbulent-Boundary-Layer Heat Transfer Research at Stanford 1958-1983," *Advances in Heat Transfer*, Academic Press, Vol. 16, pp. 241-365.

Rohsenow, W. M., and Harnett, eds., 1973, *Handbook of Heat Transfer*, McGraw-Hill, New York, pp. 6-15.

Spalding, D. B., 1963, *Convective Mass Transfer*, McGraw-Hill, New York, pp. 156-164.

Tamanini, F., 1983, "Reduced-Scale Modeling of Diffusion Flames in Enclosures (The Case of Hydrogen Burning in the Mark III Containment)," Report No. J.I.0H5R8.RK, Factory Mutual Research Corporation, Norwood, MA.

Travis, J. R., 1984, *Designing for Hydrogen in Nuclear Power Plants*, K. K. Niyogi, and M. D. Bernstein, eds., ASME, New York, p. 87.

Ural, E. A., and Tamanini, F., 1986, "Thermal Analysis of Hydrogen Diffusion Flames in BWR Mark III Containments and a 1/4 Scale Model," Report No. J.I.0J3R0.RK, Factory Mutual Research Corporation, Norwood, MA.

Experimental Study of Surfactant Effects on Pool Boiling Heat Transfer

Ying Liang Tzan
Graduate Student.

Yu Min Yang
Associate Professor.

Department of Chemical Engineering,
National Cheng Kung University,
Tainan, Taiwan 70101

In the first part of this work, nucleate boiling of aqueous solutions of sodium lauryl sulfate (SLS) over relatively wide ranges of concentration and heat flux was carried out in a pool boiling apparatus. The experimental results show that a small amount of surface active additive makes the nucleate boiling heat transfer coefficient h *considerably higher, and that there is an optimum additive concentration for higher heat fluxes. Beyond this optimum point, further increase in additive concentration makes* h *lower. In the second part of this work, nucleate boiling heat transfer rate for n-propanol–water binary mixtures with various amounts of sodium lauryl sulfate were measured in the same pool boiling apparatus. The importance of the mass diffusion effect, which is caused by preferential evaporation of the more volatile component at the vapor–liquid interface on the boiling of the binary mixture, has been confirmed. However, it is shown that the effect exerted by the addition of a surfactant dominates over the mass diffusion effect in dilute binary mixtures.*

Introduction

Water. Small amounts of certain surfactants in aqueous solution have been known to enhance the rate of nucleate boiling heat transfer of water significantly (Frost and Kippenhan, 1967); Jontz and Myers, 1960; Morgan et al., 1949; Roll and Myers, 1964; Shah and Darby, 1973; Shibayama et al., 1980; Stroebe et al., 1939; Yang and Maa, 1983). Because the concentration is usually very low, the addition of surfactants to water causes no significant change in physical properties except that the surface tension is depressed considerably. Since surface tension is an important theoretical parameter affecting nucleation in a boiling liquid, it is desirable to establish a quantitative relationship between the depression in surface tension of a solution and the increase in the rate of heat transfer in the nucleate boiling region.

A number of studies have been made in the past to relate the nucleate boiling heat transfer coefficient to the surface tension of a boiling liquid. Besides the well-known semitheoretical approaches (such as those of Rohsenow, Forster and Zuber, and others), which dealt tacitly with a single component, two experimental approaches have been used. Some authors carried out their experiments using various pure liquids of different surface tension, and the others used surface active additives to change the surface tension of the boiling liquid. The nucleate boiling heat transfer coefficient is related to the surface tension of the liquid by the equation

$$h = (\text{const})\sigma^n \tag{1}$$

At least a dozen n values have been published in the literature, ranging from -3.3 to 1.275 (Yang, 1983).

It is evident that the influence of surfactant additives on boiling heat transfer is neither simple nor direct. In other words, one cannot expect that a solution of surface active solute will boil in the same way as a pure liquid with the same surface tension value. Therefore, past boiling heat transfer correlations for surfactant solutions in the literature, as expressed in the form of equation (1), cannot be very meaningful. While surfactant additives generally depress surface tension, the primary effect may well be due to other factors that may be independent of, or at best only indirectly related to, changes in surface tension.

In a theoretical investigation of the stability of shallow pools of dilute surfactant solutions heated from below, Palmer and Berg (1972) defined several dimensionless groups for describing their systems. The relevant dimensionless group to this work is the elasticity number E_l, which represents the effectiveness of the solute in generating surface restoring forces. Shah and Darby (1973) demonstrated that the effect of surfactant additives on the evaporating heat transfer coefficient for vertical film flow over a flat plate could be attributed to foaming, and explained in terms of the Gibbs film elasticity. It should be noted that the solutions they tested were very dilute (≤ 50 ppm) and the heat fluxes they considered were low (< 150 kW/m^2). Yang and Maa (1983) attributed the surfactant effect on the enhancement of pool boiling heat transfer coefficients to the "Marangoni effect" (Scriven and Sternling, 1960), which implies that depletion of the adsorbed additive molecules at the vapor–liquid interface due to expansion of the vapor bubble may cause the surface tension to increase locally. The vapor bubbles are thus stabilized and the bubble–bubble and bubble–heating surface interactions become quite different from that of a pure liquid.

Binary Mixtures. Boiling of mixtures is involved in many industrial processes and is an attractive subject for heat transfer research. For nucleate pool boiling in a binary mixture, it is well known (Collier, 1981; Shock, 1982; Thome and Shock, 1984; Van Stralen and Cole, 1979; Tzan and Yang, 1988) that the heat transfer coefficient and bubble departure diameter are lower than that in a pure fluid of identical physical properties. Many authors have explained this reduction in heat transfer coefficient by a local depletion of the more volatile component at the vapor–liquid interface. This causes the local saturation temperature to be greater than that in the bulk fluid. The superheat available for heat transfer is therefore less than what it would be for a pure fluid. The bubble growth rates are consequently reduced and so are the heat transfer coefficients. This mass diffusion effect, which represents the extra mass diffusion resistance due to the concentration gradient caused by the preferential evaporation of the more volatile component, can be expressed by (Calus and Leonidopoulos, 1974)

Contributed by the Heat Transfer Division for publication in the JOURNAL OF HEAT TRANSFER. Manuscript received by the Heat Transfer Division August 24, 1988. Keywords: Augmentation and Enhancement, Boiling, Phase-Change Phenomena.

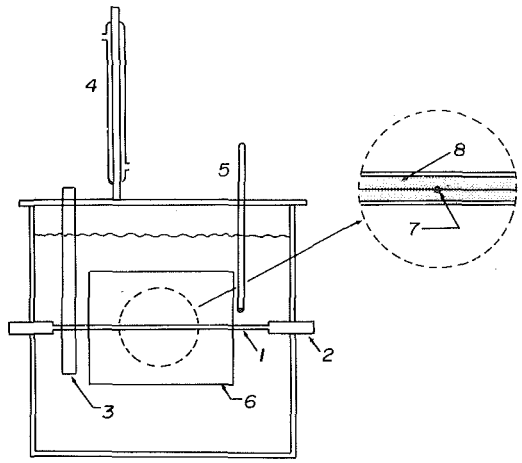

Fig. 1 The pool boiling apparatus: (1) heating element; (2) nickel-coated copper tube; (3) supplementary heater; (4) reflux condenser; (5) mercury thermometer; (6) view window; (7) thermocouple junction; (8) silicon carbide powder

$$F=(x-y)\left(\frac{\alpha}{D}\right)^{0.5}\left(\frac{C_{PL}}{h_{LG}}\right)\left(\frac{dT}{dx}\right) \tag{2}$$

Small amounts of a certain surfactant in aqueous solution have been known significantly to enhance the rate of nucleate boiling heat transfer of water as mentioned above. Nevertheless, the effect of surfactant additive on boiling characteristics of binary mixtures has not been studied systematically.

The objectives of this work are to determine experimentally the influence of a surfactant additive upon the nucleate boiling heat transfer coefficient of water and *n*-propanol-water binary mixtures over relatively wide ranges of concentration and heat flux in a small pool.

Experimental Apparatus and Procedure

Figure 1 shows the pool boiling apparatus used in this work. An electric heating element is made of a seamless stainless steel tube (3.35 mm o.d, 2.80 mm i.d., and 98.0 mm long) packed with silicon carbide powder. The surface of the heating element is polished by No. 1200 sandpaper and both ends are welded to 9 mm o.d. nickel-coated thick-walled copper tubes. The junction of a chromel/alumel thermocouple is placed at the central position in the powder. Because the heating element is sufficiently thin and long, heat conduction in the axial direction can be neglected. The thermocouple actually measures an average temperature of the inner tube wall. The heat flux released from the heating element to the surrounding liquid is controlled by adjusting the current supplied by a rectifier with a capacity of 20 V and 500 A; the outer tube surface temperature can be computed from the inner tube surface temperature and the heat flux values (Yang, 1983). The pool is insulated but some heat loss was noticeable. A supplementary heater is installed for the purposes of bringing up the temperature of the liquid pool at the beginning of the experiment and maintaining it at the boiling point of the test fluid during the period of operation. In order to avoid the influence of heat flow from the supplementary heater on the experimental results, it was surrounded by a glass tube to guide the fluid flow. The pool temperature is measured by a calibrated thermometer. A reflux condenser is provided for condensing the vapor generated in the pool. Because the liquid level above the heating element is sufficiently high, the return of subcooled condensate has little effect on the experimental results. Boiling on the surface of the heating element can be illuminated, observed, and photographed through view windows on the front and rear side of this apparatus.

The additive used in this work is sodium lauryl sulfate (SLS, $C_{12}H_{25}NaSO_4$). It is a water soluble, anionic surface active agent. *n*-Propanol, which is soluble in water, was chosen as the organic component of the binary mixture. Eight mixtures—including 5 wt %, 10 wt %, 20 wt %, 45 wt %, 60 wt %, 71.7 wt %, and 80 wt % *n*-propanol—were studied.

Because the boiling heat transfer rate is very sensitive to the state of the heating surface, boiling of pure water was carried out until the reproducibility of the boiling curve became very good before the beginning of each set of experiments with the addition of various amounts of additive. After the last experiment of each set, another run using pure water was also made to check whether there is any significant change of the condition of the heating surface during this set of experiments.

In this work, the surface tensions of water and binary mixtures with various amounts of surfactant additive at the boiling point were determined by the capillary rise method under atmospheric pressure.

Results and Discussion

The surface tension data determined at the boiling point for various additive concentrations are shown in Fig. 2. The surface tension is depressed considerably for water and binary mixtures of 5 wt % and 10 wt % *n*-propanol. For the mixtures with concentrations greater than 10 wt % *n*-propanol, as the *n*-propanol concentration is increased, the addition of SLS causes less and less change in surface tension. It is worthwhile to note that there was no measurable change in the bubble point temperature with increasing surfactant concentration in the experiments.

Figure 3 shows the reproducibility of the boiling data of pure water. The heavily shaded area represents the region covering 28 data points of four runs for pure water. They are the first, the last, and two intermediate runs in a series of runs for water of various surfactant concentrations. This shows that no serious change of surface condition of the heating element occurs when a series of experiments is carried out. The

Nomenclature

C = bulk concentration of solute, ppm
C_{PL} = specific heat of liquid, J kg^{-1} K^{-1}
D = diffusion coefficient in the bulk, m^2 s^{-1}
E_l = elasticity number
F = function defined by equation (2)
h = boiling heat transfer coefficient, kW m^{-2} K^{-1}
h' = boiling heat transfer coefficient of pure water, kW m^{-2} K^{-1}
h_{LG} = latent heat of evaporation, J kg^{-1}
j = mass flux $= q/h_{LG}$, kg m^{-2} s^{-1}
n = constant
q = heat flux, kW m^{-2}
T = temperature, K
ΔT = superheat, K
x = mass fraction of lighter component in the liquid phase
y = mass fraction of lighter component in the vapor phase
α = thermal diffusivity, m^2 s^{-1}
σ = surface tension, N m^{-1}

Subscripts

I = ideal
az = azeotrope

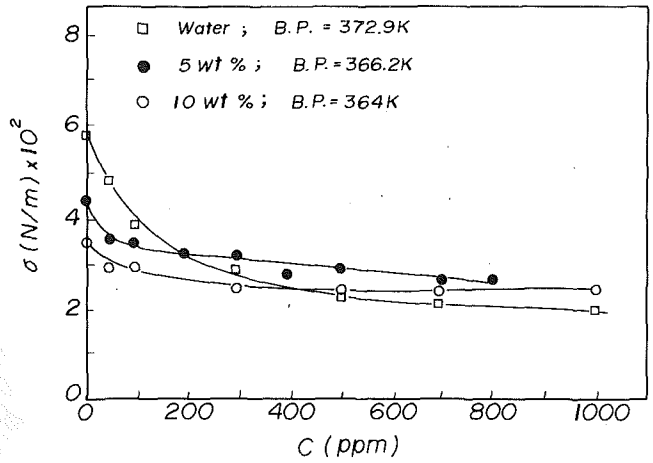

Fig. 2 Surface tension at the boiling point as a function of surfactant concentration

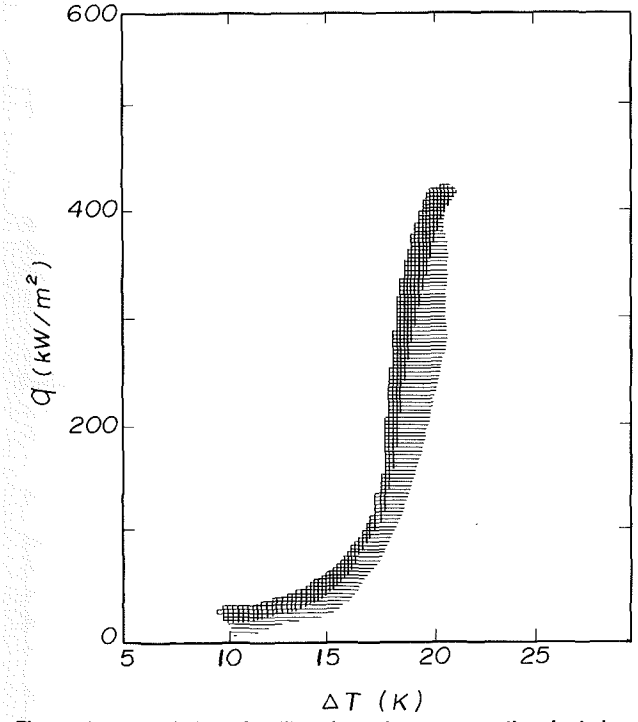

Fig. 3 Reproducibility of boiling data of pure water; the shaded area represents the region of data

shaded area represents the region covering 77 data points of 11 boiling curves for pure water. These are the boiling curves for the first, the last, and nine intermediate runs in a series of experimental runs for water and binary mixtures with various surfactant concentrations. In view of the long-term operation of the same boiling surface, the reproducibility is thought to be quite good.

The appearance of boiling of water containing surfactant is considerably different from that of pure water. As shown in the photographs of Fig. 4, the surfactant makes the number of vapor bubbles on the heating surface much larger, the size of the bubble smaller, and the coalescence of the bubbles more difficult.

Figure 5 shows a set of decreasing legs of boiling curves for water containing SLS of various concentrations. When the heat flux is relatively low, the boiling curve shifts leftward as the concentration of SLS is increased. When the heat flux increases, the boiling curves for higher SLS concentration incline rightward and approach the curve for pure water. The in-

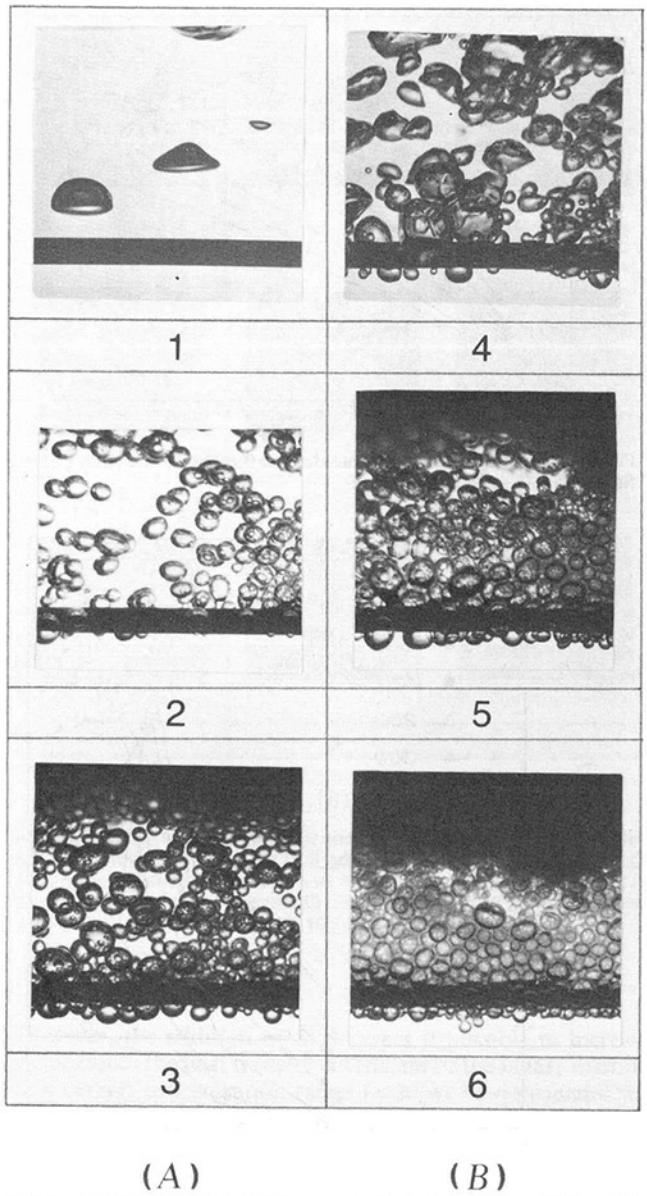

Fig. 4 Boiling behavior of aqueous surfactant solutions: (A) $q = 89$ kW/m^2, (1) 0 ppm, (2) 500 ppm, (3) 1000 ppm; (B) $q = 229$ kW/m^2, (4) 0 ppm, (5) 500 ppm, (6) 1000 ppm

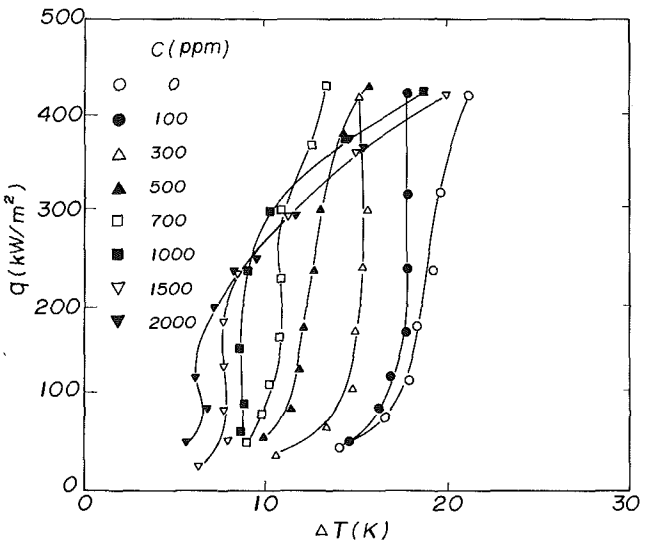

Fig. 5 Boiling curves of aqueous solution of SLS

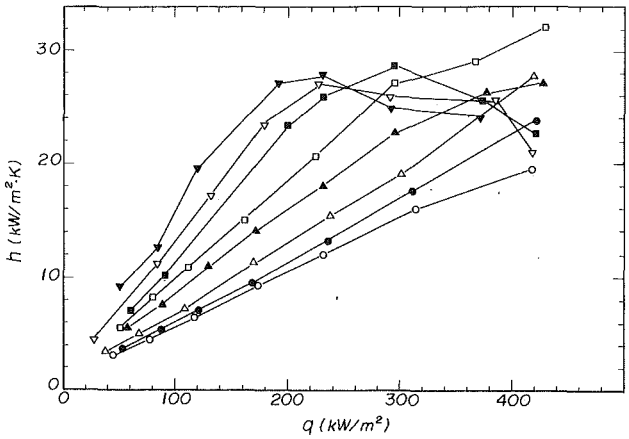

Fig. 6 Nucleate boiling heat transfer coefficient as a function of heat flux; symbols as in Fig. 5.

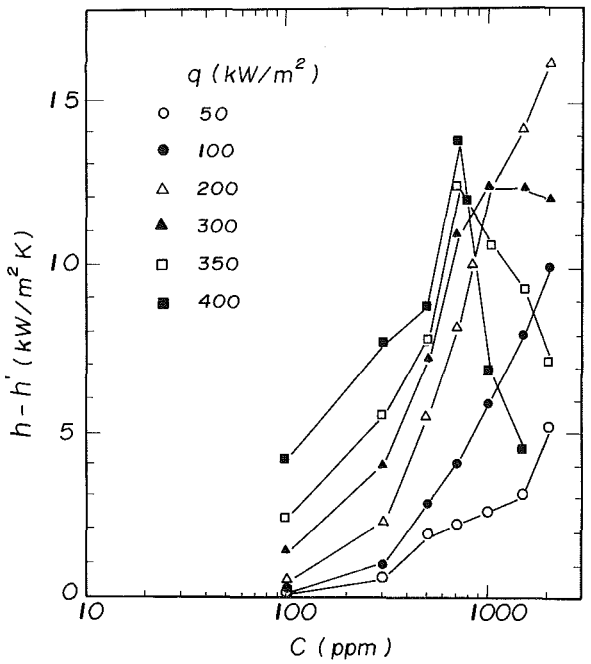

Fig. 7 ($h-h'$) as a function of concentration for an aqueous solution of SLS

fluence of heat flux and additive concentration on the nucleate boiling heat transfer rate of SLS solutions is more evident if the experimental data in Fig. 5 are expressed as a plot of heat transfer coefficient versus heat flux, as shown in Fig. 6. The heat transfer coefficient is increased as the heat flux and concentration are increased except when the heat flux level is higher than about 200 kW/m^2, and the concentration of solutions is higher than 700 ppm. Of these two trends, the former is consistent with most results observed previously (e.g., Shah and Darby, 1973; Yang and Maa, 1983). The latter has seldom been reported. This may be attributed to the fact that the solution tested was usually too dilute and/or the heat flux level conducted was too low in most of the past experiments reported in the literature.

The improvement of the heat transfer coefficient by the addition of a surface active agent can be expressed by the difference, $h-h'$, where h and h' are the boiling heat transfer coefficients for the cases of surfactant solutions and pure water, respectively. Figure 7 shows ($h-h'$) as functions of additive concentration with heat flux as a parameter. With increasing heat flux the existence of a maximum on the ($h-h'$)

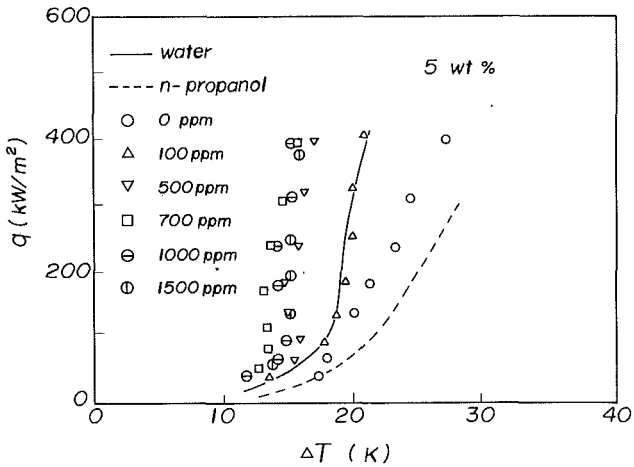

Fig. 8 Pool boiling data: 5 wt % *n*-propanol

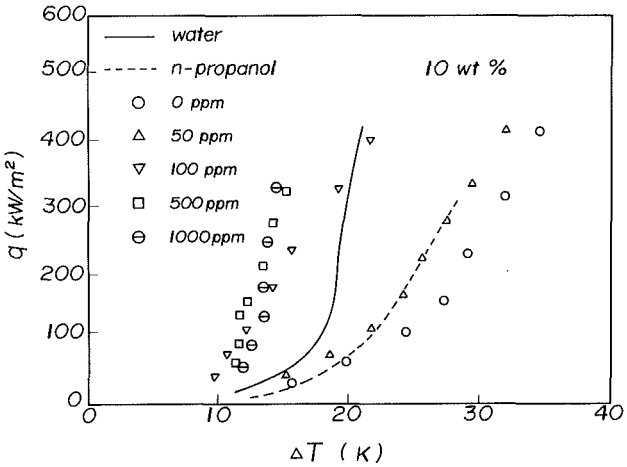

Fig. 9 Pool boiling data: 10 wt % *n*-propanol

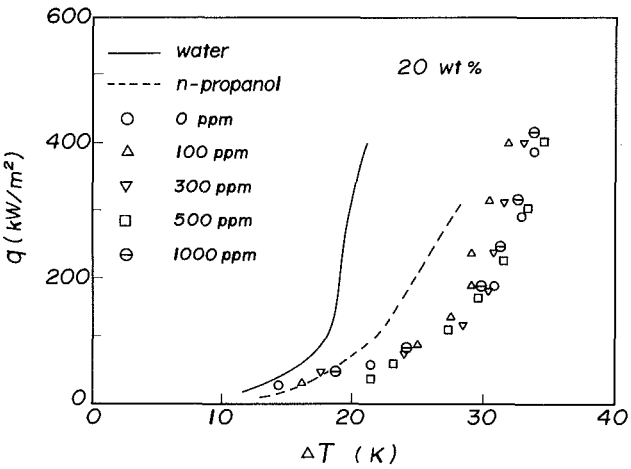

Fig. 10 Pool boiling data: 20 wt % *n*-propanol

curve is more evident, and the concentrations at the position of these maxima shift to the left.

Figures 8–10 show the boiling curves of water and *n*-propanol and three sets of boiling data for binary mixtures of 5 wt %, 10 wt %, and 20 wt % *n*-propanol, respectively, with various amounts of surfactant. It should be noted that SLS is soluble in all of the binary mixtures studied in this work, except for pure *n*-propanol, in which it is insoluble.

Figure 8 shows the effect of surface active additive on the boiling heat transfer rate of mixture of 5 wt % *n*-propanol. The data of the binary mixture without surface active additive lie between the boiling curves of water and *n*-propanol. As the

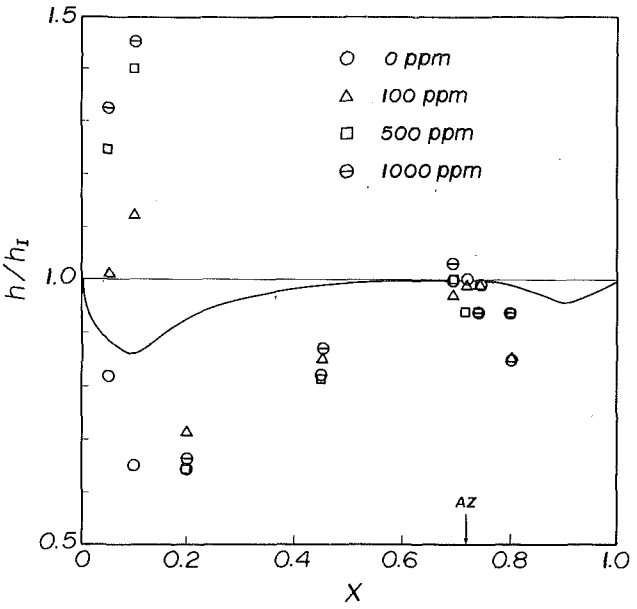

Fig. 11 Effect of SLS additive on the normalized heat transfer coefficient of a binary mixture: — equation (5); $q = 300$ kW/m^2

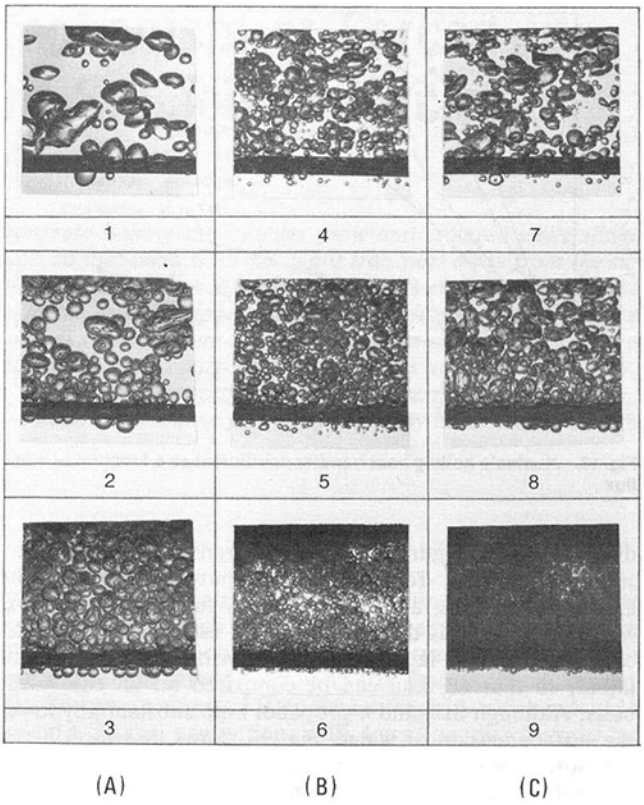

Fig. 12 Boiling behavior of water and binary mixture with SLS additive; $q = 175$ kW/m^2 (A) water with SLS additives, (1) 0 ppm, (2) 500 ppm, (3) 1000 ppm; (B) binary mixture of 5 wt % *n*-propanol with SLS additive; (4) 0 ppm, (5) 100 ppm, (6) 500 ppm; (C) binary mixture of 10 wt % *n*-propanol with SLS additive; (7) 0 ppm, (8) 100 ppm, (9) 1000 ppm

amount of surface active additive increases, the boiling heat transfer rate is enhanced with a nonlinear trend. For the mixture with surfactant additive greater than 100 ppm, the boiling heat transfer rate is even greater than that of water. Similar results can be found in Fig. 9 for a mixture of 10 wt % *n*-propanol, except that the data of the binary mixture without surface active additive lie to the right of the boiling curve of pure *n*-propanol. The trend of the enhancement of nucleate boiling heat transfer coefficient for 5 wt % and 10 wt % *n*-propanol mixtures at higher surfactant concentrations with increasing heat flux is similar to that of water but less profound.

Figure 10 shows that surface active additive has relatively little effect on the boiling characteristics of the binary mixture of 20 wt % *n*-propanol. The boiling heat transfer rate of these solutions can never exceed that of water. This is also true for the binary mixtures of 45 wt %, 69 wt %, 71.7 wt %, and 80 wt % *n*-propanol.

Figure 11 shows the normalized experimental heat transfer coefficient h/h_I, as a function of concentration of the binary mixture with the amount of SLS added as a parameter. The normalized experimental heat transfer coefficient is defined as

$$\frac{h}{h_I} = \frac{\Delta T_I}{\Delta T} \tag{3}$$

where, on the left side of the azeotrope

$$\Delta T_I = \left(\frac{x}{x_{az}}\right)\Delta T_{az} + \left(\frac{x_{az} - x}{x_{az}}\right)\Delta T_{x=0} \tag{4}$$

is the ideal wall superheat at constant heat flux. A similar expression is used for the right side of the azeotrope.

Figure 11 also demonstrates a comparison between the normalized heat transfer coefficient of binary mixtures and the predicted values by

$$\frac{h}{h_I} = \frac{\Delta T_I}{\Delta T_I(1+F)} = \frac{1}{1+F} \tag{5}$$

This equation is based on the model accounting for the mass diffusion effect on boiling heat transfer of the binary mixture. Although equation (5) drastically underpredicts the experimental values, it is evident that this equation demonstrates the trend of the experimental data of binary mixtures. However, the addition of SLS makes it possible to increase significantly the heat transfer coefficient of the binary mixture in a certain concentration range (<20 wt % *n*-propanol for the case of *n*-propanol–water mixtures). It is postulated that the interfacial effect caused by the addition of surfactant does dominate over the mass diffusion effect of binary mixture in this concentration range. On the other hand, SLS has an insignificant effect on the boiling characteristics of binary mixtures containing at least 20 wt % *n*-propanol. This may be due to the fact that SLS also has an insignificant effect on the surface tension of these mixtures.

The addition of a small amount of SLS makes the boiling behavior quite different from that of pure water and the binary mixtures without the surface active additive. This is shown in the photographs of Fig. 12. The surface active additive reduced significantly the tendency of coalescence between vapor bubbles. These bubbles are smaller in size but larger in number than the cases of pure water and the binary mixture with zero additive concentration. They tend to stay on the heating surface in a relatively orderly manner. For binary mixtures of concentration greater than 10 wt %, however, the addition of SLS causes no significant change in boiling behavior.

From equation (2), it is clear that the mass diffusion effect is a unique characterisitic of liquid mixtures. There is no room for the extra mass diffusion resistance to occur in single-component liquids. For *n*-propanol–water binary mixtures, the value of the function F is always positive but with $y = x$. The mass diffusion effect is null for the mixture at an azeotropic composition of 71.7 wt % *n*-propanol. It is of much significance to compare the boiling characteristics of liquids under the conditions without the presence of the mass

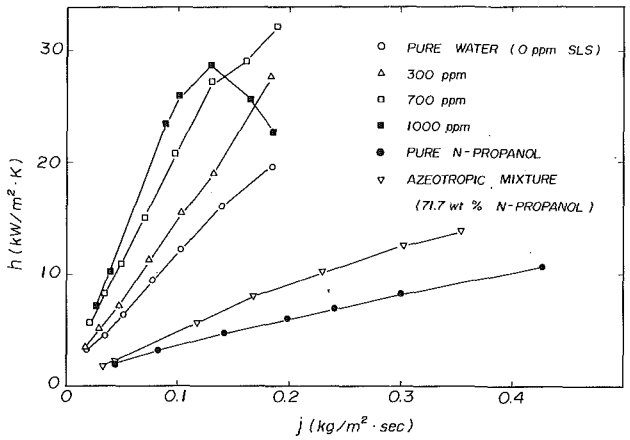

Fig. 13 Nucleate boiling heat transfer coefficient as a function of mass flux

diffusion effect. Figure 13 shows heat transfer coefficient versus mass flux, j, for pure water, pure n-propanol, the azeotropic mixture, and three aqueous surfactant solutions. Mass flux, which is defined as q/h_{LG}, is chosen to take account of different latent heats of vaporization for different liquid, so that all data can be compared on an equivalent basis. Although SLS and n-propanol both substantially lower the surface tension of water, Fig. 13 shows that n-propanol deteriorates while SLS enhances (with a nonlinear trend) boiling heat transfer of water. Regarding the effect of surface tension on nucleate boiling, these data illustrate how complex the issue is. Further study is desirable.

Conclusions

Pool boiling experiments were carried out for relatively wide ranges of surfactant concentration and heat flux. The results verify again that a small amount of surface active additive makes the nucleate boiling heat transfer coefficient of water considerably higher. It was also found that there is an optimum additive concentration for high heat flux. Beyond this optimum point, further increase in additive concentration makes the boiling heat transfer coefficient lower.

Nucleate pool boiling experiments on n-propanol–water mixtures confirm the importance of mass diffusion effect on the boiling heat transfer of binary systems. The experimental data for the binary mixtures of this system with various amounts of SLS give the first evidence of surfactant effect on binary mixture. It is shown that the surfactant effect dominates over the mass diffusion effect in dilute mixtures.

Acknowledgments

This study was supported by the National Science Council of Taiwan through grant No. NSC 75-0402-E006-06. Professor Jer Ru Maa is gratefully acknowledged for his helpful discussions.

References

Calus, W. F., and Leonidopoulos, D. J., 1974, "Pool Boiling-Binary Liquid Mixtures," *International Journal of Heat and Mass Transfer*, Vol. 17, pp. 249–256.

Collier, J. G., 1981, *Convective Boiling and Condensation*, 2nd ed., McGraw-Hill, New York.

Frost, W., and Kippenhan, C. J., 1967, "Bubble Growth and Heat Transfer Mechanisms in the Forced Convection Boiling of Water Containing a Surface Active Agent," *International Journal of Heat and Mass Transfer*, Vol. 10, pp. 931–949.

Jontz, P. D., and Myers, J. E., 1960, "The Effect of Dynamic Surface Tension on Nucleate Boiling Coefficients," *AIChE Journal*, Vol. 6, No. 1, pp. 34–38.

Morgan, A. I., Bromley, L. A., and Wilke, C. R., 1949, "Effect of Surface Tension on Heat Transfer in Boiling," *Industrial and Engineering Chemistry*, Vol. 41, No. 12, pp. 2767–2769.

Palmer, H. J., and Berg, J. C., 1972, "Hydrodynamic Stability of Surfactant Solutions Heated From Below," *Journal of Fluid Mechanics*, Vol. 51, pp. 385–402.

Roll, J. B., and Myers, J. E., 1964, "The Effect of Surface Tension on Factors in Boiling Heat Transfer," *AIChE Journal*, Vol. 10, No. 4, pp. 530–534.

Scriven, L. E., and Sternling, C. V., 1960, "The Marangoni Effects," *Nature*, Vol. 187, No. 4733, pp. 186–188.

Shah, B. H., and Darby, R., 1973, "The Effect of Surfactant on Evaporative Heat Transfer in Vertical Film Flow," *International Journal of Heat and Mass Transfer*, Vol. 16, pp. 1889–1903.

Shibayama, S., Katsuta, M., Suzuki, K., Kurose, T., and Hatano, Y., 1980, "A Study on Boiling Heat Transfer in a Thin Liquid Film," *Heat Transfer (Japan Research)*, Vol. 9, No. 4, pp. 12–40.

Shock, R. A. W., 1982, "Boiling in Multicomponent Fluids," *Multiphase Science and Technology*, Vol. 1, G. F. Hewitt, J. M. Delhaye, and N. Zuber, eds., Hemisphere, New York.

Stroebe, G. W., Baker, E. M., and Badger, W. L., 1939, "Boiling-Film Heat Transfer Coefficients in a Long-Tube Vertical Evaporator," *Industrial and Engineering Chemistry*, Vol. 31, No. 2, pp. 200–206.

Thome, J. R., and Shock, R. A. W., 1984, "Boiling of Multicomponent Liquid Mixtures," *Advances in Heat Transfer*, Vol. 16, J. P. Harnett and T. F. Irvine, Jr., eds., Academic Press, New York.

Tzan, Y. L., and Yang, Y. M., 1988, "Pool Boiling of Binary Mixtures," *Chemical Engineering Communications*, Vol. 66, pp. 71–82.

Van Stralen, S. J. D., and Cole, R., 1979, *Boiling Phenomena*, Hemisphere, New York.

Yang, Y. M., and Maa, J. R., 1983, "Pool Boiling of Dilute Surfactant Solutions," ASME JOURNAL OF HEAT TRANSFER, Vol. 105, pp. 190–192.

Yang, Y. M., 1983, "Surface Effects and Boiling Heat Transfer," Ph.D. Thesis, National Cheng Kung University, Tainan, Taiwan.

On the Mechanism of Forced-Convection Subcooled Nucleate Boiling

G. Tsung-Chang
Graduate Student.

S. G. Bankoff
W. P. Murphy Professor.
Fellow ASME

Chemical Engineering Department,
Northwestern University,
Evanston, IL 60208-3120

In highly subcooled nucleate boiling the bubbles grow and collapse while sliding along the heated surface, so that there is no net vapor transport away from the surface. A long-standing question exists as to whether conduction and convection between the bubbles, or latent heat transport through the bubbles, is the dominant heat transfer mechanism. It is shown here by simple calculations that the sliding of the bubble results in augmentation of microlayer evaporation under the bubble by a factor of two or more over a stationary bubble with a continuous microlayer. It appears therefore that the latent heat transport mechanism may be dominant at large bulk subcoolings.

I Introduction

When a subcooled liquid flows past a heated solid surface, a dramatic increase in the heat transfer rate at the solid surface is observed if boiling commences. Gunther (1950) (see also Gunther and Kreith, 1950), in an early investigation connected with the cooling of liquid rocket nozzle throats, showed that heat transfer coefficients of the order of 10^2 kW/m^2 K were attainable in subcooled convective nucleate boiling of water in small-diameter tubes at high velocities. These values are two orders of magnitude greater than those measured in ordinary convective heat transfer. The immediate question that comes to mind is: How and why does the presence of vapor bubbles at the solid surface affect the heat transfer rate so strongly? This is a fundamental problem, which underlies many engineering applications, such as the design of high-performance nuclear reactors and liquid-cooled rocket engines.

Two major mechanisms were discussed at an early conference (Bankoff et al., 1956) aimed at understanding these results. The first mechanism, which had been suggested earlier by Gunther and Kreith (1950), is based on the additional turbulent mixing, or microconvection, that is achieved near the surface between the growing and collapsing bubbles. The second mechanism, discussed at the same conference by Snyder and also by Bankoff, focuses on latent heat transport through the bubble. When a vapor bubble grows on a solid surface, a thin liquid viscous layer, called a microlayer, must be formed beneath the bubble in order to satisfy the no-slip boundary condition at the solid surface. The top of the bubble quickly grows beyond the thermal layer into the cool liquid. Latent heat is transported through the bubble, with the microlayer evaporating simultaneously as condensation occurs over the cold polar cap.

The subcooled nucleate boiling experiments by Gunther (1950) and Gunther and Kreith (1950) were remarkable, in that they showed highly similar behavior in diverse geometries; this behavior was completely different from ordinary nucleate boiling. Gunther and Kreith (1950) employed a flat horizontal strip heater in a stationary pool of subcooled water, while Gunther (1950) investigated forced-convection boiling in a transparent channel at high coolant velocities. In contrast to saturated nucleate boiling, where essentially all the heat leaves the wall as latent heat carried by departing bubbles, the surface boiling activity in these experiments consisted of small hemispherical vapor bubbles, which grew and collapsed while always remaining attached to the heating surface. The frequencies were as high as 10^3 Hz when the subcooling was more than 55 K. Furthermore, vigorous convective motions were observed, even in the pool boiling experiments. Strong tangential flows were observed from the heater strip, which induced a reverse thermal convection, with downflow directly over the heater. As the subcooling was reduced, this effect weakened, and eventually reverted to the usual upflow pattern above the heat surface. This reverse convective effect suggests that at high pool subcoolings the region above the heater is locally a low-pressure region, induced by the rapid rate of condensation in the growing and collapsing bubbles.

Bankoff and Mikesell (1959), Bankoff (1959), Bankoff and Mason (1962), and later Snyder and Robin (1969) and Robin and Snyder (1970a, 1970b), examined the latent heat transport mechanism in more detail, and concluded that it could be a very significant, and even dominant, fraction of the total heat transfer. On the other hand, Plesset and Prosperetti (1978), based on an analysis of microlayer evaporation (Mixon et al., 1960; Cooper and Lloyd, 1969; Sharp, 1964), came to the conclusion that in Gunther's experiment latent heat transport amounted to a small fraction of the total heat transfer per bubble. The internal bubble pressure, needed for a kinetic theory estimate of the net evaporation rate from the microlayer, was obtained directly from the observed bubble radius–time curves, assuming purely radial liquid flow around the bubble. Bankoff and Mikesell (1959) had earlier shown, by a similar analysis, that for these symmetrically growing and collapsing bubbles, the internal bubble pressure was nearly constant in time. The restraining pressure difference was about 4 kPa, which, from kinetic theory and assuming an accommodation coefficient of unity, amounts to a condensing heat flux of 8.5 MW/m^2. Because of the enormous population of tiny bubbles ($R_{max} \leq 0.4$ mm), only a rough approximation to the bubble number density and fraction of the surface covered by bubbles was possible. Using the figure of 10 percent coverage visually observed by Gunther for a liquid bulk subcooling for 67 K and velocity of 3.25 m/s, the lower-bound condensation rate on the curved bubble surfaces amounted to about 40 percent of the total heat flux, with a heat transfer coefficient of 0.13 MW/m^{2}K. Later experiments by Bankoff and Mason (1962) and Robin and Snyder (1970a), in which a metered steam flow was injected into a turbulent stream of cold water, showed that the single-bubble surface heat transfer coefficients could be about 0.5 to 1 MW/m^{2}K. Hence the latent heat transport mechanism would account for all of the wall heat transfer if the same heat transfer coefficients were realized in the Gunther experiments. We note that the growth

Contributed by the Heat Transfer Division for publication in the JOURNAL OF HEAT TRANSFER. Manuscript received by the Heat Transfer Division November 13, 1987. Keywords: Boiling, Forced Convection, Phase-Change Phenomena.

and collapse history of a Rayleigh bubble is determined by the (constant) restraining pressure difference, and the initial impulse wrench. The latter is determined by the local thickness of the superheated viscous sublayer in which the bubble originates. This thickness is a stochastic variable, so that the maximum bubble radius is also stochastic. At any instant many bubbles will be smaller than the effective resolution, so that the coverage may be considerably underestimated. On the other hand, the Bankhoff and Mason experiment involved a single bubble growing and collapsing in place at a pinhole in the metal wall, and hence did not take into account interference effects of an array of bubbles on the wall. We note that turbulent flat-plate boundary layer calculations (Tsung-Chang, 1987) show that the thickness of the superheated liquid layer on the wall is about 1 μm for the Gunther data, so that nearly all the bubble surface is a condensing surface.

Koffman (1983) and Koffman and Plesset (1983) provided additional evidence by measuring the microlayer liquid evaporation in the pool boiling of water on a tin-oxide surface at a low subcooling (5.7°C) and heat flux (0.0265 MW/m^2 as compared to 3.3 MW/m^2 in the Gunther and Kreith, 1950, experiment). Koffman concluded from numerical integration of his microlayer data that, for the data of Gunther and Kreith, microlayer evaporation could account for about 40 percent of the total heat transfer.

More recently, Del Valle and Kenning (1985) performed forced-convection subcooled nucleate boiling experiments under conditions similar to those of Gunther (1950) (water velocity 1.7 ms, 84 K subcooling, heat flux 3.44 to 4.67 MW/m^2), but with rather different results. Gunther reported that the bubbles grew and collapsed at the wall while sliding at about 0.8 free-stream velocity, while Del Valle and Kenning stated that the vast majority of bubbles grew and collapsed at their own nucleation sites. The reasons for this discrepancy are unknown. Differences in wall thickness, surface finish, wall shear stress, and/or heated length may be involved. Del Valle and Kenning further introduce a third heat transfer mechanism, in addition to microconvection between the bubbles and latent heat transport within the bubbles. This consists of transient conduction within the maximum projected bubble area and surrounding areas of influence. This is hard to quantify, since the liquid returning to wet a previously dry or microlayer-covered area under the bubble is in continuous contact with steam. Hence its surface temperature will be that of the steam, and the boundary layer thickness is unknown. Other experimental bubble data in subcooled flow boiling have been presented by Treshchev (1969), Tolubinsky and Kostanchuk (1970), and Ünal (1976).

Plesset and Prosperetti (1978) came to the conclusion that latent heat transport may be significant in saturated, or slightly subcooled, boiling, but decreases in significance as the subcooling is increased, owing to the shorted exposure times. This may be due, in part, to the above-mentioned difficulty in obtaining accurate bubble number densities at high subcoolings. In addition, the effect of bubbles sliding along the wall, while growing and collapsing under the influence of the local bulk stream velocity, has not heretofore been taken into account. This has the effect of exposing fresh microlayer surface to the vapor more rapidly than with a stationary bubble. Furthermore, thin evaporating liquid films are subject to instabilities and rupture in times of order 10^{-6} ms (Williams and Davis, 1982; Burelbach et al., 1988) so that a moving dry spot under the bubble can be anticipated. Since the contact line represents both a force and temperature singularity (Dussan and Davis, 1974; Davis, 1983), one can expect an additional correction to the evaporative flux. The purpose of this is to examine both of these effects in a simple manner. It is found that the corrections, taken together with the uncertainty in the measured bubble number densities in the Gunther (1950) experiments, are sufficient to assure that latent heat transport is a significant, and probably dominant, fraction of the total surface transfer in highly subcooled nucleate boiling.

II Analysis

We now examine the effects of bubble sliding and dryout in order to show the augmentation of the evaporation mechanism. The experimental data of Gunther (1950) and Gunther and Kreith (1950) for highly subcooled nucleate boiling of water are used in the calculations. Tables 1 and 2 contain some data from their experiments, which will be used later.

Bubble Sliding Effects. If the microlayer is assumed to be a stagnant layer at the wall temperature on formation, the evaporation rate at any time after exposure of an area element is given by the solution of the semi-infinite slab conduction problem

$$\dot{q} = -k\frac{\partial T}{\partial z}\bigg|_{z=0} = \frac{k\Delta t}{\sqrt{\pi a t}} = \dot{m}_e \Delta h_v \tag{1}$$

where $\Delta T = T_w - T_{\text{sat}}$, $\dot{m}_e$ is the evaporative mass flux, and Δh_v is the latent heat. Here the motion of the boundary due to evaporation has been ignored. If this effect is taken into account it will serve to increase the heat flux.

In order to estimate the sliding effect on heat transfer, consider a hemispherical bubble with constant radius R_b and a step-function lifetime. If the bubble moves with constant velocity U in the x direction, the travel path of the bubble base during its lifetime can be as shown in Fig. 1. Let t_1 be the time when the small element at (x, y) is exposed to the bubble base, and t_2 be the time when it is covered by liquid again. Then the

Nomenclature

a = thermal diffusivity
Δh_v = latent heat of evaporation
J = net mass flux
k = thermal conductivity
$\dot{m}_e$ = evaporative mass flux
p_i = internal pressure
P = system pressure
p^e = equilibrium pressure
q = heat flow rate
$\dot{q}$ = heat flux
Q = total heat flow during bubble lifetime
R, R_b = bubble radius
R_G = gas constant
R_m = maximum radius of bubble
t = time
t_b = bubble lifetime
t_e = exposure time
t_g = bubble growth time
t_m = time of maximum bubble radius
T_b = bubble wall temperature
T_{liq} = bulk temperature of the subcooled liquid
T_{sat} = saturation temperature
T_w = solid wall temperature
ΔT = difference between the solid wall temperature and the saturation temperatures
U = sliding velocity of bubble
U_∞ = free-stream velocity
α = accommodation coefficient for condensation or evaporation
γ = ratio of stationary to sliding bubble heat transfer, equation (8)
δ = microlayer thickness
θ_o = contact angle
ν = liquid kinematic viscosity
ρ = liquid density
σ = surface tension
$\tau = t/t_m$ = dimensionless time

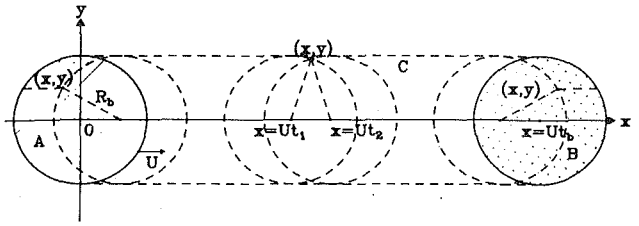

Fig. 1 Traveling path of a bubble with constant radius during entire lifetime

total exposure time, t_e, for the small element should be equal to $(t_2 - t_1)$, and the total heat transfer through the bubble base during the whole lifetime will be

$$Q = \int_y \int_x \int_0^{t_e} \frac{k\Delta t}{\sqrt{\pi a}} \frac{1}{\sqrt{t_e}} dt_e dx dy \tag{2}$$

As shown in Fig. 1, for a small element at (x, y) in the shaded area A

$$t_e = \frac{\sqrt{R_b^2 - y^2} + x}{U}$$

Thus

$$Q_A = \frac{2k\Delta T}{\sqrt{\pi a}} \int_0^{R_b} \int_{-\sqrt{R_b^2-y^2}}^{\sqrt{R_b^2-y^2}} \int_0^{\frac{\sqrt{R_b^2-y^2}+x}{U}} \frac{1}{\sqrt{t_e}} dt_e dx dy$$

$$= \frac{8\sqrt{2}k\Delta T}{3\sqrt{\pi a}} \frac{R_b^{5/2}}{\sqrt{U}} B\left(\frac{7}{4}, \frac{1}{2}\right) \tag{3}$$

where $B(7/4, 1/2)$ is the beta function. For the small element (x, y) in the dotted area B shown in Fig. 1

$$t_1 = \frac{x - \sqrt{R_b^2 - y^2}}{U}$$

$$t_2 = t_b$$

Hence

$$Q_B = \frac{2k\Delta T}{\sqrt{\pi a}} \int_0^{R_b} \int_{Ut_b - \sqrt{R_b^2-y^2}}^{UT_b + \sqrt{R_b^2-y^2}} \int_0^{t_b} \frac{-x - \sqrt{R_b^2-y^2}}{U} \frac{1}{\sqrt{t_e}} dt_e dx dy$$

$$= \frac{8\sqrt{2}k\Delta T}{3\sqrt{\pi a}} \frac{R_b^{5/2}}{\sqrt{U}} B\left(\frac{7}{4}, \frac{1}{2}\right) \tag{4}$$

For the small element (x, y) in area C, i.e., in an area other than A and B

$$t_1 = \frac{x - \sqrt{R_b^2 - y^2}}{U}$$

$$t_2 = \frac{x + \sqrt{R_b^2 - y^2}}{U}$$

Thus

$$Q_C = \frac{2k\Delta T}{\sqrt{\pi a}} \int_0^{R_b} \int_{\sqrt{R_b^2-y^2}}^{Ut_b - \sqrt{R_b^2-y^2}} \int_0^{\frac{2\sqrt{R_b^2-y^2}}{U}} \frac{1}{\sqrt{t_e}} dt_e dx dy$$

$$= \frac{4\sqrt{2}k\Delta T}{\sqrt{\pi a}} \frac{R_b^{5/2}}{\sqrt{U}} \left[\frac{Ut_b}{2R_b} B\left(\frac{5}{4}, \frac{1}{2}\right) - B\left(\frac{7}{4}, \frac{1}{2}\right)\right]$$

Table 1 Experimental data of Gunther (1950) used in this work

No. of Experiment	1	2	3
Free-stream velocity, U_∞ (m/s)	3	3	3
Maximum bubble radius, R_m (cm)	0.038	0.044	0.051
Lifetime of bubble, t_b (μs)	300	450	600
Subcooling, $\Delta T_{sub} = T_{sat} - T_{liq}$ (°C)	72	50	33

Table 2 Experimental information used in the calculation of the condensation rate

System pressure, $P = 28.8$ in. Hg
Bulk liquid temperature, $T_\infty = 26.7$°C
Liquid temperature at the wall, $T_w = 137.8$°C
Saturation temperature at P, $T_{sat} = 98.9$°C
Length of heating metal strip, $d = 6.35$ cm
Kinematic viscosity of liquid, $\nu = 2.99 + 10^{-3}$ cm^2/s
Free-stream velocity, $U_\infty = 3$ m/s
Maximum bubble radius, $R_m = 0.038$ cm
Lifetime of bubble, $t_b = 300$ s
Population of bubbles, $N = 9 \times 10^8$ bubbles/m^2 s
Heat flux, $q/A = 4.5 \times 10^3$ kW/m^2

Hence the total heat flow during the lifetime of a bubble is

$$Q_{sliding} = Q_A + Q_B + Q_C$$

$$= \frac{4\sqrt{2}k\Delta T}{\sqrt{\pi a}} \frac{R_b^{5/2}}{\sqrt{U}} \left[\frac{Ut_b}{2R_b} B\left(\frac{5}{4}, \frac{1}{2}\right) - \frac{1}{3} B\left(\frac{7}{4}, \frac{1}{2}\right)\right]$$

For comparison, similar calculations can be made for a stationary bubble, i.e.,

$$Q_{stationary} = \frac{2k\Delta T}{\sqrt{\pi a}} \int_0^{R_b} \int_{-\sqrt{R_b^2-y^2}}^{\sqrt{R_b^2-y^2}} \int_0^{t_b} \frac{1}{\sqrt{t_e}} dt_e dx dy$$

where t_e is independent of the position (x, y). Therefore

$$Q_{stationary} = \frac{2\sqrt{\pi}k\Delta T}{\sqrt{a}} R_b^2 t_b^{1/2} \tag{7}$$

The ratio of the total heat flows through the moving and stationary bubbles is thus approximated by

$$\gamma \triangleq \frac{Q_{stationary}}{Q_{sliding}}$$

$$= \frac{\sqrt{2}}{4} \frac{1}{\left(\frac{Ut_b}{2R_b}\right) B\left(\frac{5}{4}, \frac{1}{2}\right) - \frac{1}{3} B\left(\frac{7}{4}, \frac{1}{2}\right)} \left(\frac{Ut_b}{R_b}\right)^{1/2}$$

$$= \frac{1}{2.472\left(\frac{Ut_b}{R_b}\right) - 1.356} \left(\frac{Ut_b}{R_b}\right)^{1/2} \tag{8}$$

In the limiting case, $U \to 0$, the ratio defined in equation (8) should be equal to 1. It is then found that $(Ut_b/R_b) \to 0.94$.

In the experiments of Gunther (1950), the maximum bubble radius R_m ranged from 0.4 to 0.5 mm and t_b ranged from 300 to 600 μs for 72 K to 33 K bulk liquid subcooling and 3 m/s free-stream velocity U_∞. Bankoff and Mikesell (1959) noted the surprising symmetry of the growth and collapse radius-time curves for these bubbles, and concluded that a fairly constant negative pressure difference existed between the bubble interior and its surrounding during most of its lifetime. A good approximation for the radius-time curve is a simple quadratic relation

$$\frac{R_m - R(t)}{R_m} = (1 - \tau)^2 \tag{9}$$

where $\tau = t/t_m$. If R_b is taken to be the average bubble radius during its lifetime

$$R_b = \frac{\int_0^{t_b} R(t)dt}{\int_0^{t_b} dt} = \frac{2}{3}R_m \tag{11}$$

and $U = 0.8\ U_\infty$, then the heat flow ratio γ ranges from 0.22 to 0.31, based on Gunther's (1950) data.

Another estimate of the slding effects can be made by employing the symmetric bubble radius–time curves suggested by Bankoff and Mikesell (1959) instead of the constant-radius and step-function lifetime assumption. If the bubble radius follows the quadratic relation (equation (9)), the heat flux at the base of a stationary bubble is given by

$$\dot{q}_{\text{stationary}}(r,\ t) = \frac{k\Delta T}{\sqrt{\pi a t_m}} \frac{1}{\sqrt{\tau_e}} \tag{12}$$

From equation (9), the time corresponding to a radius R can be expressed as

$$\tau = 1 \pm \left(1 - \frac{R}{R_m}\right)^{1/2} \tag{13}$$

where "$-$" is the growth period, "$+$" for the collapse period. The exposure time for a small element at (r, θ) is then given by

$$\begin{aligned} \tau_e &= \frac{t_e}{t_m} = \tau_R - \tau_r \\ &= \left(1 - \frac{r}{R_m}\right)^{1/2} \pm \left(1 - \frac{R}{R_m}\right)^{1/2} \\ &= \left(1 - \frac{r}{R_m}\right)^{1/2} - (1 - \tau) \end{aligned} \tag{14}$$

The heat flow rate through the base of a bubble is given as

$$\begin{aligned} q_{\text{stationary}} &= \int_0^{2\pi} \int_0^{R} \dot{q} r dr d\theta \\ &= \frac{4\pi^{1/2} k\Delta T}{(at_m)^{1/2}} R_m^2 \tau^{3/2} \left(\frac{32}{35}\tau^2 - \frac{16}{5}\tau + \frac{8}{3}\right) \end{aligned} \tag{15}$$

Hence the total heat flow during the lifetime of a bubble is

$$\begin{aligned} Q_{\text{stationary}} &= \int_0^{t_b} q(t)dt = t_m \int_0^2 q(\tau)d\tau \\ &= 1.1493 \frac{\sqrt{\pi} k\Delta T}{\sqrt{a}} R_m^2 t_m^{1/2} \end{aligned} \tag{16}$$

For the case of sliding bubbles, the exposure time for each small element in the base of the bubble depends not only on the sliding velocity, but also on the growth rate. Since the intention of this investigation is to examine the sliding effects in a simple manner, the exposure time is approximated by

$$t_e = \frac{(L/2 - x)}{U} \tag{17}$$

where L is the length of a square that has the same area as the bubble base (Fig. 2). Thus

$$\begin{aligned} L^2(t) &= \pi R^2(t) \\ &= \pi R_m^2 [1 - (1 - \tau)^2]^2 \end{aligned} \tag{18}$$

The heat flow rate through the bubble base is

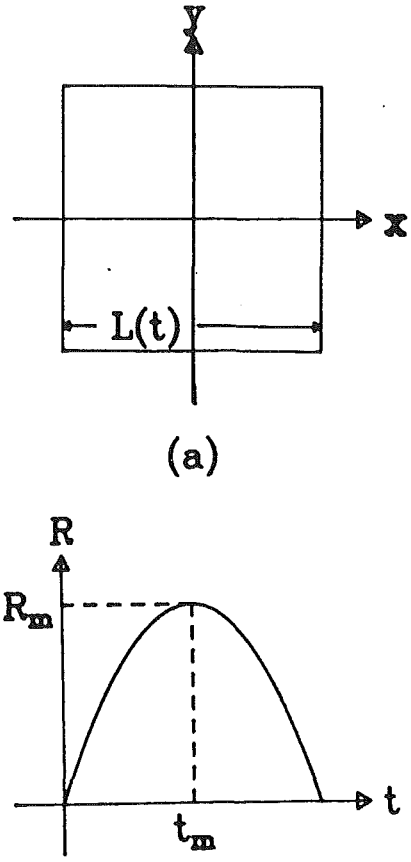

Fig. 2 A simple sketch of the contact region

$$\begin{aligned} q_{\text{sliding}} &= 2\int_{-L/2}^{L/2} \int_0^{L/2} \dot{q} dy dx \\ &= \frac{2k\Delta T U^{1/2}}{(\pi a)^{1/2}} [L(t)]^{3/2} \end{aligned} \tag{19}$$

and the total heat flow during the lifetime of a bubble is

$$\begin{aligned} Q_{\text{sliding}} &= \int_0^{t_b} q_{\text{sliding}}(t)dt \\ &= \frac{3\pi^{5/4} k\Delta T}{4a^{1/2}} U^{1/2} R_m^{3/2} t_m \end{aligned} \tag{20}$$

The ratio of the total heat flows through the moving and stationary bubbles is then

$$\gamma = \frac{Q_{\text{stationary}}}{Q_{\text{sliding}}} = 0.6494 \left(\frac{R_m}{Ut_m}\right)^{1/2} \tag{21}$$

This ratio ranges from 0.54 to 0.66, accordinng to Gunther's data.

Equation (21) is a crude, but conservative, estimate. In equation (17), the exposure time is obtained by only considering the sliding motion in the x direction. If the growth rate of the bubble radius had been taken into account, the exposure time would have been smaller. Also, when the growth rate of the bubble radius is greater than the sliding velocity, some portion of the solid surface will be re-covered by the bubble base. For that part of surface, the exposure time is even less.

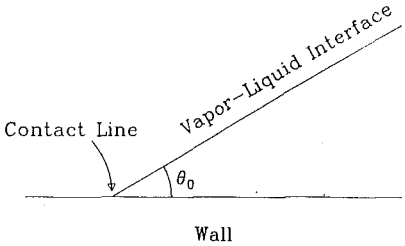

Fig. 3 Hemispherical bubble with quadratic radius-time relation: *(a)* square with same area as the base of the bubble; *(b)* bubble radius versus time

Contact Line Effects. Apart from the reduced exposure time of the bubble base microlayer owing to sliding along the heated wall in highly subcooled nucleate boiling, another effect may be important with engineering surfaces, such as stainless steel in water. This is the possible existence of a moving contact line under the bubble as a result of instability and dryout of the microlayer under evaporation. For film thicknesses less than about 100 nm, a horizontal liquid film becomes unstable under the influence of van der Waals forces (Sheludko, 1967), and ruptures very rapidly, as shown by the analysis of Williams and Davis (1987), for an isothermal film, and Bankoff and Davis (1982, 1987) and Burelbach et al. (1988), for an evaporating film. According to the analysis of Cooper and Lloyd (1969), the local thickness of the microlayer is proportional to the square root of the time of its uncovering since the beginning of bubble growth. Hence the central region of the microlayer will rupture in times of order 1 μs (Burelbach et al., 1988), provided that the wall is only partially wetted (contact angle > 0 deg). Engineering surfaces, such as stainless steel, commonly exhibit contact angles of 40 deg or more. The existence of a contact line in an evaporating system implies a temperature singularity, as will be shown below. This is confirmed by the measurements of Cooper and Lloyd (1969) and Sharp (1964), who found large cooling effects shortly after the bubble boundary passed over thermocouples mounted just below the microlayer. We note that this is contrary to the model of Plesset and Prosperetti (1978). They assumed a continuous microlayer of uniform thickness such that temperature variations owing to evaporation never reach the solid wall beneath during the bubble lifetime.

It is, of course, physically unrealistic that a temperature singularity exists over a finite time, since the solid wall is cooled by the large heat fluxes in the neighborhood of the contact line. Furthermore, owing to the large evaporation rates in that neighborhood, there is a significant departure from vapor-liquid equilibrium, and hence in the interface temperature from the saturation temperature. These effects are difficult to calculate, and we content ourselves with demonstrating the existence of a logarithmic singularity in the total heat flux under the assumptions of uniform wall temperature and saturation temperature at the vapor-liquid interface. For a nonmetallic liquid evaporating on a hot metallic wall, this model is particularly pertinent.

The singularity at the contact line can be illustrated further. Figure 3 shows a simple diagrammatic representation for the contact region of a bubble. When the contact angle θ_o equals zero, the wall is well wetted. For the case of a stationary bubble, if all local liquid motions are neglected, the steady-state energy equation describing the liquid in the wedge region is

$$\frac{1}{r}\frac{\partial}{\partial r}\left(r\frac{\partial T}{\partial r}\right)+\frac{1}{r^2}\frac{\partial^2 T}{\partial \theta^2}=0 \tag{22}$$

with boundary conditions

$$T=T_w \qquad \text{at } \theta=0$$

$$T=T_{\text{sat}} \qquad \text{at } \theta=\theta_o \tag{23}$$

We note that the temperature at $r=0$ is undefined. The solution of this standard problem by conformal mapping, or by inspection, shows that the radial lines are isotherms. Hence, the local heat flux through the bubble wall at distance r from the contact line is

$$q=-\frac{k}{r}\frac{\partial T}{\partial \theta}\bigg|_{\theta_o}=\frac{k(T_w-T_{\text{sat}})}{\theta_o}\frac{1}{r} \tag{24}$$

This shows that a logarithmic singularity exists in the neighborhood of the contact line in the evaporation rate. A more complete analysis would require a two-region solution of the potential problem in order to remove the logarithmic singularity, together with consideration of liquid–vapor nonequilibrium close to the apparent singularity.

IV Conclusions

We have thus shown that the sliding of a bubble while attached to the solid wall in highly subcooled nucleate boiling results in a significant augmentation of microlayer evaporation. Since simplified models are used, it is difficult to assign a definite improvement factor, but the calculations indicate an increase by a factor at least two, and possibly much more, over a nonsliding bubble with a continuous microlayer. Koffman (1983) has estimated, based on Gunther (1950) and his own data, that about 40 percent of the total heat transfer during subcooled nucleate boiling can be attributed to microlayer evaporation. If we apply the above improvement factor, it becomes clear that the latent heat mechanism dominates, or is at least important, in nucleate boiling with large bulk subcoolings. This is then consistent with the very large heat transfer coefficients measured by Bankoff and Mason (1962) at the surface of small, growing and collapsing bubbles obtained by injecting steam through a small pinhole into a turbulent cold water stream.

References

Bankoff, S. G., Colahan, W. J., Jr., and Bartz, D. R., 1956, "Summary of Conference of Bubble Dynamics and Boiling Heat Transfer Held at the Jet Propulsion Laboratory," Memo No. 20-137, Jet Propulsion Laboratory, Pasadena, CA.

Bankoff, S. G., 1959, "On the Mechanism of Subcooled Nucleate Boiling," Jet Propulsion Lab. Memo 30-38.

Bankoff, S. G., and Mikesell, R. D., 1959, "Bubble Growth Rates in Highly Subcooled Nucleate Boiling," *Chem. Eng. Progress Symposium Series*, Vol. 55, No. 29, pp. 95-102.

Bankoff, S. G., 1961, "On the Mechanism of Subcooled Nucleate Boiling, Parts 1 and 2," *Chem. Eng. Progr. Symposium Series*, No. 32, Vol. 57, pp. 156-163; 164-172.

Bankoff, S. G., 1962, "A Note on Latent Heat Transport in Nucleate Boiling," *AIChE J.*, Vol. 8, pp. 63-65.

Bankoff, S. G., and Mason, J. P., 1962, "Heat Transfer From the Surface of a Steam Bubble in Turbulent Subcooled Liquid Stream," *AIChE J.*, Vol. 8, pp. 30-33.

Bankoff, S. G., and Davis, S. H., 1987, "Stability of Thin Films," presented at the 6th International Physicochemical Hydrodynamics Conference, Oxford, United Kingdom.

Burelbach, J. P., Bankoff, S. G., and Davis, S. H., 1988, "Nonlinear Stability of Evaporating/Condensing Liquid Films," *J. Fluid Mech.*, Vol. 195, pp. 463-494.

Cooper, M. G., and Lloyd, A. J. P., 1969, "The Microlayer in Nucleate Pool Boiling," *Int. J. Heat Mass Transfer*, Vol. 12, pp. 895-913.

Davis, S. H., 1983, "Contact-Line Problems in Fluid Mechanics," ASME *Journal of Applied Mechanics*, Vol. 50, pp. 977-982.

Dussan, E. B., V, and Davis, S. H., 1974, "On the Motion of a Fluid-Fluid Interface Along a Solid Surface," *J. Fluid Mech.*, Part 1, Vol. 65, pp. 71-95.

Gunther, F. C., 1950, "Photographic Study of Surface-Boiling Heat Transfer to Water With Forced Convection," Jet Propulsion Laboratory, Pasadena, CA, Progress Report No. 4-120; also *Trans. ASME*, Vol. 73, 1951, pp. 115-124.

Gunther, F. C., and Kreith, F., 1950, "Photographic Study of Bubble Formation in Heat Transfer to Subcooled Water," Jet Propulsion Laboratory, Pasadena, CA, Progress Report No. 4-75.

Jawurek, H. H., 1969, "Simultaneous Determination of Microlayer Geometry and Bubble Growth in Nucleate Boiling," *Int. J. Heat Mass Transfer*, Vol. 12, pp. 843-848.

Koffman, L. D., 1983, "Microlayer Evaporation in Subcooled Nucleate Boil-

ing," presented at the Third Multiphase Flow and Heat Transfer Symposium-Workshop, Miami Beach, FL.

Koffman, L. D., and Plesset, M. S., 1983, "Experimental Observations of the Microlayer in Vapor Bubble Growth on a Heated Solid," ASME JOURNAL OF HEAT TRANSFER, Vol. 105, pp. 625–632.

Mixon, R. O., Jr., Chon, W. Y., and Beatty K. O., Jr., 1960, "The Effect of Electrolytic Gas Evolution on Heat Transfer," *Chem. Eng. Progr. Symposium Series*, No. 30, Vol. 56, pp. 75–81.

Plesset, M. S., and Prosperetti, A., 1978, "The Contribution of Latent Heat Transport in Subcooled Nucleate Boiling," *Int. J. Heat Mass Transfer*, Vol. 21, pp. 725–734.

Robin, T. T., and Snyder, N. W., 1970a, "Bubble Dynamics in Subcooled Nucleate Boiling Based on the Mass Transfer Mechanism," *Int. J. Heat Mass Transfer*, Vol. 13, pp. 305–318.

Robin, T. T., and Snyder, N. W., 1970b, "Theoretical Analysis of Bubble Dynamics for an Artificially Produced Vapor Bubble in a Turbulent Stream," *Int. J. Heat Mass Transfer*, Vol. 13, pp. 523–536.

Sharp, R. R., 1964, "The Nature of Liquid Film Evaporation During Nucleate Boiling," NASA TN D-1997.

Sheludko, A., 1967, "Thin Liquid Films," *Adv. Colloid Interface Sci.*, Vol. 1, No. 4, pp. 391–464.

Snyder, N. W., and Robin, T. T., 1969, "Mass-Transfer Model in Subcooled Nucleate Boiling," ASME JOURNAL OF HEAT TRANSFER, Vol. 91, pp. 404–412.

Voutsinos, C. M., and Judd, R. L., 1975, "Laser Interferometric Investigation of the Microlayer Evaporation Phenomenon," ASME JOURNAL OF HEAT TRANSFER, Vol. 97, pp. 88–92.

Williams, M. B., and Davis, S. H., 1982, "Nonlinear Theory of Film Rupture," *J. Colloid Interface Sci.*, Vol. 90, No. 1, pp. 220–228.

A General Correlation for Saturated Two-Phase Flow Boiling Heat Transfer Inside Horizontal and Vertical Tubes

S. G. Kandlikar[1]
Mechanical Engineering Department,
Rochester Institute of Technology,
Rochester, NY 14623-0887

A simple correlation was developed earlier by Kandlikar (1983) for predicting saturated flow boiling heat transfer coefficients inside horizontal and vertical tubes. It was based on a model utilizing the contributions due to nucleate boiling and convective mechanisms. It incorporated a fluid-dependent parameter F_{fl} in the nucleate boiling term. The predictive ability of the correlation for different refrigerants was confirmed by comparing it with the recent data on R-113 by Jensen and Bensler (1986) and Khanpara et al. (1986). In the present work, the earlier correlation is further refined by expanding the data base to 5246 data points from 24 experimental investigations with ten fluids. The proposed correlation, equations (4) and (5), along with the constants given in Tables 3 and 4, gives a mean deviation of 15.9 percent with water data, and 18.8 percent with all refrigerant data, and it also predicts the correct h_{TP} versus x trend as verified with water and R-113 data. Additional testing with recent R-22 and R-113 data yielded the lowest mean deviations among correlations tested. The proposed correlation can be extended to other fluids by evaluating the fluid-dependent parameter F_{fl} for that fluid from its flow boiling or pool boiling data.

Introduction

The importance of accurately predicting saturated flow boiling heat transfer coefficients has been well recognized, as seen from a large number of analytical and experimental investigations conducted in the last 10–15 years. A knowledge of these coefficients and their parametric behavior can reduce the cost and avoid the drastic results due to underdesign or overdesign of evaporators, boilers, and other two-phase process equipments. A general flow boiling correlation can satisfy these requirements, and it can further assist in establishing the effects of different parameters leading to a better understanding of the flow boiling phenomenon.

An additional role of a general correlation is seen in the investigations on augmentation of flow boiling heat transfer. In order to establish the enhancement factors with different enhancement devices such as surface treatments, twisted tapes and helical inserts, microfin surfaces, or additives, it is necessary to estimate accurately the baseline performance with the smooth tubes. Conducting the experiments with smooth tubes with the exact same conditions as in the enhanced tube experiments is rather difficult. Instead, the experiments may be replaced by a general flow boiling correlation to predict the baseline performance. However, the researchers may want to verify the validity of the correlation for their experimental conditions by conducting a few tests.

After establishing a need for a general correlation, the available correlations are reviewed in the following sections. The objectives for the present work are then stated. This is followed by a description of the correlation development, results and discussion, and the concluding remarks.

Previous Work

Research in the flow boiling area has been directed toward gaining a fundamental understanding of the flow boiling phenomenon as well as toward obtaining experimental results that may be employed in equipment design. The fundamental studies clearly brought out the complexities of the flow boiling mechanisms (see Collier, 1981, for a comprehensive survey). Some of the major complexities involved are: bubble growth and departure behavior in the flow field of a two-phase mixture, distribution of the two phases relative to each other and relative to the tube wall (flow pattern and entrainment effects), departure from thermodynamic equilibrium at local conditions, characteristics of the heat transfer surface, and the effects of fluid properties. A realistic comprehensive model addressing these complexities has not yet been developed for use by equipment designers.

The experimental studies on two-phase flow boiling provided the actual values of heat transfer coefficients for a number of fluids under specific ranges of operating conditions. These form the basis for developing and testing any correlation. In order to develop a general correlation, it is essential to have an extensive data base covering different fluids with a wide range of operating conditions such as mass flux, heat flux, pressure, quality, and tube diameter. In the absence of a comprehensive data bank in the literature, every researcher in this field has to undertake this task before beginning any correlation work.

There are a large number of saturated flow boiling correlations (well over 30) available in the literature. Some of the well-known correlations were summarized by Kandlikar (1983). The flow boiling correlations in general may be classified into two categories. Under the first category, the correlations are developed by experimental investigators to represent their own data, and in some instances, a few other data sources with the same fluid. After ascertaining the accuracy of the experiments conducted, these individual correlations may be used by the designer within the same range of parameters. The correlations under the second category are developed on the basis of a larger number of data sets involving a number of fluids over a wide range of parameters. These correlations are more valuable since they represent a larger

[1]Current address: Visiting Scientist, Mechanical Engineering Department, Massachusetts Institute of Technology, Cambridge, MA 02139.

Contributed by the Heat Transfer Division and presented at the ASME Winter Annual Meeting, Boston, Massachusetts, November 29–December 2, 1987. Manuscript received by the Heat Transfer Division September 8, 1987. Keywords: Boiling, Multiphase Flows, Phase-Change Phenomena.

Table 1 Some important correlations for flow boiling heat transfer inside tubes

Investigator	Details	Correlation	Comments
1. Chen (1966)	Vertical flow; water, methanol, cyclohexane, pentane; 600 data points	$h_{TP} = h_{mac} + h_{mic}$ $h_{mac} = h_{Dittus\text{-}Boelter} \times F$ $h_{mic} = h_{Forster\text{-}Zuber} \times S$ F and S functions of Re_l and X_{tt}	Mean deviations of 12% with data of six investigators. Used extensively. Large deviations observed with recent data on refrigerants.
2. Shah (1982)	Vertical and horizontal flow; water, R-11, R-12, R-22, R-113, cyclohexane; 800 data points.	Originally given in a chart form by Shah (1976). Equations fitted as: $h_{TP} = h_{TP}(Co, Bo, Fr_{lo})$	90% data falls within 30 percent. Recommended by Collier (1980). Large deviations with some recent experimental data.
3. Bjorge, Hall and Rohsenow (1982)	Vertical flow; water; 8 data sets.	High quality region, (x>0.05): $q = q_{FC} + q_B - q_{Bi}$ Low quality region, (x<0.05): $q = [q_{FC}^2 + (q_B - q_{Bi})^2]^{0.5}$	Mean deviations of 15 percent against 17.4 percent with the Chen correlation. Equations using superposition technique. Provides insight into flow boiling mechanism.
4. Kandlikar (1983)	Vertical and horizontal flow; water, R-11, R-12, R-114, nitrogen, neon; 1100 data points.	$\frac{h_{TP}}{h_l} = D_1 (Co)^{D_2} (25\ Fr_{lo})^{D_5} + D_3 (Bo)^{D_4} (25\ Fr_{lo})^{D_6}$	Mean deviations of 17.1 percent against 38 percent with the Shah correlation. A fluid dependent parameter F_{fl} introduced.
5. Gungor and Winterton (1986)	Vertical and horizontal flow; water, R-11, R-12, R-22, R-113, R-114, ethylene glycol; 3600 data points.	$h_{TP} = E\ h_l + S\ h_{pool}$ E and S are functions of Bo, X_{tt}, and Fr_{lo}.	Mean deviation of 19.7 percent with all data tested.
6. Gungor and Winterton (1987)	Same as Gungor and Winterton (1986).	$\frac{h_{TP}}{h_l} = 1 + 3000\ Bo^{0.86} + [x/(1-x)]^{0.75} (\rho_l/\rho_g)^{0.41}$ Fr_{lo} correction for horizontal tube	Correlation is simplified as compared to their (1986) correlation. Agreement with data is also slightly improved

data base and cover a much broader range of operating conditions.

Table 1 gives six important correlations available in the literature. The widely used correlation by Chen (1966), #1 in Table 1, was developed on the basis of six different data sources. It offered a relatively simple additive form of nucleate boiling and convective terms. Many later experimental studies such as those of Anderson et al. (1966), Chaddock

Nomenclature

Bo = boiling number $= q/(Gi_{lg})$
c_p = specific heat, J/kgK
Co = convection number $= \left(\frac{1-x}{x}\right)^{0.8} \left(\frac{\rho_g}{\rho_l}\right)^{0.5}$
C_1–C_6 = constants in equations (1)–(4)
D_1–D_6 = constants in Kandlikar (1983) correlation, Table 1
D = inside diameter of tube, m
F = forced convection correction factor used in Chen (1966) correlation, Table 1
F_{fl} = fluid-dependent parameter in equations (2)–(4) given in Table 4; also used in Kandlikar (1983) correlation, Table 1
$F_{\text{pool boiling}}$ = pool boiling multiplication factor in Forster–Zuber correlation used by Jallouk (1975), Table 1
Fr_{lo} = Froude number with all flow as liquid $= G^2/(\rho_l^2 gD)$
G = mass flux, kg/m^{2}s
g = acceleration due to gravity, m/s^2
h = heat transfer coefficient, W/m^2°C
i_{lg} = latent heat of vaporization, J/kg
k = thermal conductivity, W/m°C
m = constant
N = number of data points
n = constant
Pr = Prandtl number $= c_p\mu/k$
q = heat flux, W/m^2
Re_l = liquid Reynolds number $= GD(1-x)/\mu_l$
S = suppression factor, used by Chen (1966), and Gungor and Winterton (1986), different expressions
ΔT = temperature difference between wall and fluid, °C
X_{tt} = Martinelli parameter $= \left(\frac{1-x}{x}\right)^{0.9} \left(\frac{\rho_g}{\rho_l}\right)^{0.5} \left(\frac{\mu_l}{\mu_g}\right)^{0.1}$
x = dryness fraction
μ = dynamic viscosity, Ns/m^2
ρ = density, kg/m^3
σ = surface tension, N/m

Subscripts

B = nucleate boiling
Bi = onset of nucleate boiling
conv = convection
exp = experimental
FC = forced convection
g = vapor
l = liquid
lg = latent
mac = macroconvection
mic = microconvection
nucl = nucleate boiling
pred = predicted
sat = saturation
TP = two-phase

and Noerager (1966), Jallouk (1974), and Mohr and Runge (1977) have indicated that this correlation tends to overpredict the effect of nucleation, thereby resulting in large deviations. Further refinements in Chen's correlation were directed at predicting the nucleate boiling component with other pool boiling correlations. Jallouk incorporated the Rohsenow (1952) pool boiling correlation, while the Cooper (1984) correlation was used by Gungor and Winterton (1986). Efforts were also directed at correlating the enhancement factor F and the suppression factor S in the Chen correlation to a number of operating and system variables, e.g., Ross (1985) and Bennett and Chen (1980).

Shah (1976) proposed a correlation in graphic form using the boiling number, Bo and the convection number Co. He proposed replacement of the Martinelli parameter X_{tt} with the convection number Co, since the viscosity ratio was found to have no significant influence. A total of 800 data points was used in the correlation development. In a later paper, listed as #2 in Table 1, Shah (1982) presented equations to fit his earlier chart correlation. The Shah correlation is currently the most widely accepted one, and is recommended by Collier (1981).

Bjorge et al. (1982) developed a correlation, #3 in Table 1, to cover the subcooled and the high-quality regions with water as a test fluid. They employed the Colburn (1933) equation for single-phase convection, the Mikic–Rohsenow (1969) correlation for the nucleate boiling contribution, and the procedure of Bergles and Rohsenow (1964) for the wall superheat at the incipience of boiling. In the high-quality region, the correlation of Traviss et al. (1972) for annular flow condensation was slightly modified after testing it against nonnucleating forced convection boiling data. Bjorge et al.'s final correlation could correlate the water data derived from eight different sources better than the Chen correlation (13.9 percent against 17.4 percent). The basic heat transfer model of Bjorge et al. was employed by Yilmaz and Westwater (1980) to study the effect of velocity on the nucleate boiling and flow boiling mechanisms of R-113 flowing outside a circular tube in crossflow.

Kandlikar and Thakur (1982) proposed an additive correlation with nucleate boiling and convective contributions. The same data sets used by Shah (1976) were employed in the development of the correlation. The mean deviation with the data was 13.7 percent. The model was further refined by Kandlikar (1983), listed as #4 in Table 1, to include the effects of different fluids through a fluid-dependent parameter F_{fl} introduced in the nucleate boiling term. The values of F_{fl} for R-11, R-12, R-114, nitrogen, and neon were recommended on the basis of the respective flow boiling data. Considerable improvement was observed with all data over the Shah correlation. In order to extend the correlation to new fluids, Kandlikar described a scheme to determine F_{fl} using available flow boiling data. In the absence of any flow boiling data, F_{fl} could be estimated as the multiplier needed in the Forster and Zuber (1955) correlation to correlate the pool boiling data for that fluid. On the basis of Jallouk's (1974) data on pool boiling, an F_{fl} value of 1.240 was predicted for R-113.

Khanpara et al. (1986) compared their plain tube data for R-113 with correlations by Shah (1982), Pujol and Stenning (1969), and Kandlikar (1983). The Kandlikar correlation along with the suggested F_{fl} value of 1.240 resulted in the best agreement (± 20 percent) with their plain tube data, although no R-113 flow boiling data were employed in the development of the correlation. Estimating the F_{fl} value for R-113 from flow boiling data would further improve the agreement. This confirmed the validity of the scheme proposed by Kandlikar (1983) to extend the correlation to new fluids.

The correlation proposed by Gungor and Winterton (1986), listed as #5 in Table 1, is a modification of the Chen correlation, and is developed using 3700 data points. The enhancement factor F is replaced by E, which is dependent on the boiling number Bo and the Martinelli parameter X_{tt}. The suppression factor S is correlated as a function of X_{tt} and liquid Reynolds number Re_l. The Forster and Zuber (1955) pool boiling correlation was replaced by the Cooper (1984) correlation. A more recent correlation proposed by Gungor and Winterton (1987), #6 in Table 1, is based on the similar nondimensional parameters as used by Shah (1982) and Kandlikar (1983). A constant term representing the liquid-only heat transfer coefficient is added to the usual nucleate boiling and convective boiling terms. The mean deviation with 1701 points for refrigerants was 21.3 percent, while 1891 data points for water were correlated with a mean deviation of 21.2 percent. The comparison of different correlations presented in their work included the Kandlikar and Thakur (1981) correlation.

Objectives of the Present Work

After reviewing the literature for available correlations and models describing the flow boiling mechanism, it was clear that the ability of a correlation to apply to new fluids is an important feature. Equally important are the ability to correlate additional data with any test fluids used in the correlation development, and the ability to predict correctly the dependency of heat transfer coefficient on various system parameters. The Kandlikar (1983) correlation was able to correlate the data better than the Shah (1982) correlation, and was able to be extended to new fluids. This correlation was based on only 1100 data points, while a larger data base seemed necessary to arrive at a general correlation. To meet these needs, it was decided to conduct the following work:

- Develop a large data bank of at least 5000 data points for a number of fluids during flow boiling in plain circular tubes.
- Investigate the form of correlation by studying the effects of including various parameters in the Kandlikar (1983) correlation, and carry out further refinements.
- Compare the results with the other correlations listed in Table 1.
- Compare the correlations directly with the experimental data points to study the influence of different parameters.

Correlation Development

Data Base. As a first step in the development of the correlation, data on 24 experimental investigations were obtained and stored as data files in a computer. Table 2 shows the details of each data set representing a total of 5246 data points. This is one of the largest data banks developed for two-phase correlation work. The individual data sets have been carefully studied, and wherever possible, the raw data from the experimental results were used in the reduction of the data to a standard format. The experimental procedure employed in each investigation was studied to examine the accuracy of the data. Some of the commonly noted sources of errors were: (*i*) errors in the determination of quality using heat balance on long preheated sections with heat losses; (*ii*) absence of simultaneous measurement of pressure and wall temperature at any section along the test section resulting in errors in local saturation temperature; (*iii*) very low temperature difference between wall and fluid, as compared to the accuracy of the temperature measurement, resulting in large errors in heat transfer coefficient calculations, (*iv*) errors or discrepancies in property equations used in the data reduction by the investigators while reporting data; (*v*) presence of oil in the refrigerant flowing through the test section; and (*vi*) errors due to peculiar conditions existing in the test section entry region, such as a sharp bend or flow disturbance due to probes, in general classified under history of flow.

A number of early investigations reported the average heat transfer coefficient over the evaporator length. In some cases,

Table 2 Details of the data sources used in the correlation development

Data set	Ori	D mm	N	G kg/m^{2}s	q x 10^3 W/m^2	X	ΔT deg C	Co	Bo x 10^4	Fr	p bar
Water											
1. Mumm (1954)	Hor	11.8	158	339-1383	157-247	0.005-0.563	4.4-63.9	0.04-3.03	0.53-10.9	1.14-19.07	3.1-13.8
2. Perroud et al. (1960)	Ver	5	41	1249-8179	540-2280	0.098-0.699	4.5-17.5	0.102-1.07	0.063-5.35	-	3.2-64.2
3. Sani (1960)	Ver	18.3	38	248-1031	43-157	0.019-0.143	1.6-6.3	0.109-0.62	0.236-1.77	-	1.1-2.7
4. Wright (1961)	Ver	12,. 18.3	136	434-2434	4.7-277	0.001-0.124	2.2-82.4	0.13-12.80	0.03-12.8	-	1.1-23.2
5. Morzov (1969)	Ver	32	171	773-1634	116-515	0.004-0.342	0.31-13.1	0.045-3.20	4.5-17.1	-	31.0-41.0
6. Stone (1971)	Ver	12.2	71	67-596	44-933	0.005-0.570	6.4-23.1	0.02-1.79	0.93-15.1	-	1.0-2.4
7. Bennett (1976)	Ver	20.4	257	115-981	136-581	0.005-0.196	3.9-24.6	0.11-2.56	0.06-20.4	-	2.0
8. Kenning, Cooper (1987)	Ver	9.6	471	123-630	52-417	0.004-0.671	1.3-24.5	0.02-2.60	0.39-11.3	-	1.6-5.9
R-11											
9. Chawla (1966)	Hor	6,14, 25	503	13-252	1.2-93	0.1-0.95	1.3-22.4	0.005-0.34	0.53-28.6	0.0002-0.47	0.4-0.9
10. Riedel, Purcupile (1971)	Hor	6.66, 18.85	85	1472-4579	60-92.8	0.002-0.21	2.6-13.5	0.69-23.90	1.3-2.89	7.7-75.2	5.6-9.1
11. Bandel (1973)	Hor	14	167	106-727	0.9-92.9	0.09-0.82	0.08-15.6	0.015-0.312	0.09-20.0	0.36-16.6	0.6
R-12											
12. Riedel, Purcupile (1971)	Hor	6.66, 18.85	92	1440-4479	22-80	0.001-0.2	2.1-10.2	0.65-43.60	1.1-2.8	6.6-69.2	6.9-7.0
13. Rhee (1972)	Hor	18.85	157	242-1915	0.3-80	0.017-0.987	1.1-15.7	0.006-4.10	0.03-9.4	0.2-12.0	7.3-10.3
14. Bandel (1973)	Hor	20	54	104-441	2-70	0.5	1.0-11.8	0.12	0.07-3.82	0.04-0.73	3.0-3.2
15. Kaufman (1974)	Ver	20.5	98	658-4850	9.5-111	0.017-0.209	1.1-7.6	0.69-11.10	0.24-5.0	-	10.9-29.1
R-13B1											
16. Ross (1985)	Hor	9	160	353-1220	10-51.3	0.01-0.6	1.4-13.9	0.046-7.10	1.38-8.7	0.43-5.52	5.7-7.0
R-22											
17. Chaddock, Brunemann (1967)	Hor	11.68	22	113-474	2.0-70.6	0.203-0.676	0.8-7.6	0.08-0.464	0.22-6.38	0.07-1.27	7.0
18. Zuber (1967)	Ver	10.16	230	84-867	4.1-70.6	0.002-0.592	1.2-7.2	0.12-20.8	1.37-10.9	-	5.7,10.8
19. Steiner (1984)	Hor	20	74	80-800	5-70	0.02-0.43	1.0-8.0	0.18-20.3	2.1-10.0	0.14-4.72	5.9
R-113											
20. Jensen (1986)	Ver	8.1	1264	165-1523	6.7-51.1	0.001-0.71	0.6-16.1	0.004-52.1	0.035-12.65	-	2.7-8.2
R-114											
21. Jallouk (1974)	Ver	20	347	157-1313	0.8-82.1	0.017-0.71	2.2-18.4	0.08-5.72	0.05-24.02	-	4.4-14.8
R-152											
22. Ross (1985)	Hor	9	374	140-713	4.7-89.9	0.01-0.86	1.1-14.7	0.03-5.72	0.46-9.78	0.23-5.82	1.2-2.4
Neon											
23. Mohr, Runge (1977)	Hor	4,6	143	77-131	0.4-49	0.12-0.95	0.04-1.67	0.01-0.52	0.32-46.5	0.1-0.31	1.3-1.6
Nitrogen											
24. Steiner, Schlunder (1977)	Hor	14	133	40-450	0.3-40	0.1-0.95	0.15-3.51	0.02-1.96	0.049-34.4	0.03-4.17	4.9-15.8

the entry to the evaporator was at qualities below 0.1, and the exit was almost saturated vapor. Taking the h_{TP} and x values at average test conditions is inappropriate and results in an inaccurate h_{TP}–x relationship in a correlation. For this reason, nine such data sets utilized by Shah in his correlation development have not been included in the present study. These are: Bryan and Quaint (1951), Yodder and Dodge (1951), and Bryan and Siegel (1955) for R-11; Ashley (1942), Johnston and Chaddock (1964), and Chaddock and Noerager (1966) for R-12; and Pierre (1957), Johnston and Chaddock (1964), and Anderson et al. (1966) for R-22.

Although the accuracy of each data set employed in the present work is different, and is difficult to ascertain, it is estimated that most of these data sources are free from gross errors. A few data sets that yielded very large errors with all correlations were investigated further. After evaluating possible sources of errors, these sets were not used in the determination of the fluid-dependent parameter for that fluid. It should also be emphasized that some important parameters such as the history of flow and tube surface characteristics are not quantified and may partly be responsible for the differences between two data sets with the same fluid.

Table 3 Constants in the proposed correlation, equation (4)

Constant	Convective region	Nucleate boiling region
C_1	1.1360	0.6683
C_2	-0.9	-0.2
C_3	667.2	1058.0
C_4	0.7	0.7
C_5*	0.3	0.3

*C_5=0 for vertical tubes, and for horizontal tubes with Fr_l>0.04.

Correlation for Vertical Flow With Water. The correlation given by Kandlikar (1983), #4 in Table 2, was used as the basis for the present correlation development. The starting point was the vertical-flow data for water. The two-phase flow boiling heat transfer coefficient, h_{TP} was expressed as the sum of the convective and the nucleate boiling terms, given by

$$h_{TP} = C_1 Co^{C_2} h_l + C_3 Bo^{C_4} h_l \quad (1)$$

convective boiling term + nucleate boiling term

where h_{TP} = two-phase heat transfer coefficient; C_1-C_4 = constants to be determined; Co = convection number; Bo = boiling number; and h_l = single-phase heat transfer coefficient with only the liquid fraction flowing in the tube. In the present work, the Dittus-Boelter equation is used to calculate h_l.

The effort was now directed toward obtaining the best values of C_2 and C_4, which would result in the lowest mean error with all the vertical-flow data sets with water. The exponents C_2 and C_4 were systematically varied over a wide range. For every set of C_2 and C_4 values, corresponding coefficients, C_1 and C_3 were evaluated using a least-squares program with the vertical-flow data for water. The mean error for each data set was also calculated. Initially, the data was divided into two regions as follows:

$Co < 0.65$–convective boiling region

$Co > 0.65$–nucleate boiling region

In the convective boiling region, the heat transfer is predominantly by a convective mechanism. Similarly, in the nucleate boiling region, the heat transfer is predominantly by nucleate boiling mechanism. Influence of heat flux is particularly different in the two regions, as will be discussed later.

The above procedure of separating the two regions results in a discontinuity at $Co = 0.65$. It is present in the Shah correlation. This discontinuity is eliminated here by allowing the transition from one region to another at the intersection of the respective correlations.

At this point, the form of correlation was extensively tested for any effects such as the enhancement factor F or the suppression factor S used in the Chen correlation. This involved modification of the base correlation, equation (1), by incorporating one or more multiplication factors at a time in the convective and nucleate boiling terms. Some of the multiplication factors used in the convective term are: Bo^m, $(x/(1-x))^m$, x^m, and Re_l^m. Similarly, the multiplication factors used in the nucleate boiling term are: Co^m, $Co^m Bo^n$, X_{tt}^m, $(x/(1-x))^m$, x^m, Re_l^m, and (convective term)^m. The exponents m and n were varied over a wide range from -2.0 to $+2.0$. For every case, the coefficients C_1 and C_3 were evaluated using the available data sets in the least-square routine.

In every case with an additional multiplication factor in the convective or in the nucleate boiling term, the mean deviation was higher than the base correlation. The form of correlation suggested by Gungor and Winterton (1987), (h_{TP}/h_l = 1 + convective boiling term + nucleate boiling term), was also tried without any improvement. In most cases, the resulting mean error was significantly higher than the corresponding mean error with equation (1). This confirmed the adequacy of the present model in representing the two mechanisms over a wide range of operating conditions.

Fluid-Dependent Parameter for Other Fluids. The correlation was then extended to other fluids by incorporating a fluid-dependent parameter F_{fl}. Equation (1) is rewritten in a slightly different form, and F_{fl} is included in the second term as follows:

$$\frac{h_{TP}}{h_l} = C_1 Co^{C_2} + C_3 Bo^{C_4} F_{fl} \quad (2)$$

For each fluid, the value of F_{fl} was varied over a range from 0.5 to 5.0. For each F_{fl} value, the mean deviations were obtained for each data set of that fluid. The F_{fl} value that resulted in the lowest combined mean error for all data sets for that fluid under both regions, convective and nucleate boiling, was finally selected.

Froude Number Effect in Horizontal Flow. The influence of stratification at low flow rates in horizontal tubes was correlated by introducing the Froude number in the nucleate boiling in the convective boiling terms as follows:

$$\frac{h_{TP}}{h_l} = C_1 Co^{C_2} (25 \mathrm{Fr}_{lo})^{C_5} + C_3 Bo^{C_4} (25 \mathrm{Fr}_{lo})^{C_6} F_{fl} \quad (3)$$

C_5 and C_6 were systematically varied and the mean deviations for all the data sets for all fluids with $Fr_{lo} < 0.04$ were evaluated. The limiting value of 0.04 was also varied and the mean deviation for each data set was obtained by adjusting the constant 25 accordingly to yield (constant × limiting value) = 1. The limiting value of 0.04 was found to be most suitable with all the horizontal-flow data sets. The entire process from the beginning was repeated to include the horizontal-flow data points with $Fr_{lo} > 0.04$ along with the vertical-flow data sets for evaluating the constants.

Final Form of the Proposed Correlation. The final form of the equation obtained in this analysis is

$$\frac{h_{TP}}{h_l} = C_1 Co^{C_2} (25 \mathrm{Fr}_{lo})^{C_5} + C_3 Bo^{C_4} F_{fl} \quad (4)$$

The single-phase liquid-only heat transfer coefficient h_l is given by

$$h_l = 0.023 \, \mathrm{Re}_l^{0.8} \mathrm{Pr}_l^{0.4} (k_l/D) \quad (5)$$

The values of constants C_1-C_5 are given in Table 3. The constant C_6 in equationn (3) was found to be zero, and therefore the Froude number multiplier in the nucleate boiling term in equation (4) is missing. Also, for vertical flow, and for horizontal flow with $Fr_{lo} > 0.04$, the Froude number multiplier in the convective boiling term in equation (4) becomes unity. The two sets of values given in Table 3 correspond to the convective boiling and nucleate boiling regions, respectively. The heat transfer coefficient at any given condition is evaluated using the two sets of constants for the two regions, and since the transition from one region to another occurs at the intersection of the respective correlations, the higher of the two heat transfer coefficient values represents the predicted value from the proposed correlation. This method provides a continuity between the convective and nucleate boiling regions.

Table 4 Fluid dependent parameter F_{fl} in the proposed correlation, equation (4)

Fluid	F_{fl}
Water	1.00
R-11	1.30
R-12	1.50
R-13B1	1.31
R-22	2.20
R-113	1.30
R-114	1.24
R-152a	1.10
Nitrogen	4.70
Neon	3.50

Table 4 gives the values of the fluid-dependent parameters F_{fl} for water, R-11, R-12, R-13B1, R-22, R-113, R-114, R-152a, nitrogen, and neon. For other fluids not covered here, the scheme suggested by Kandlikar (1983), and described in the literature review section above, may be employed to calculate F_{fl}.

All the fluid properties required in the data reduction and the development of the correlation were evaluated using the *ASHRAE Handbook* (1985), *ASHRAE Thermophysical Properties* (1976), Reynolds (1979), and the surface tension properties published by DuPont. The equation for the vapor pressure for R-113 was derived from Mastroianni et al. (1978).

Results and Discussion

In this section, the results of the correlation development and some comparisons among different correlations are presented. A total of six correlations are compared with the experimental data for their accuracy of prediction, and their ability to depict correctly the trend of h_{TP} versus x.

Nucleate Boiling Term. The constant C_4 in the proposed correlation, equation (4), is the exponent to the boiling number ($Bo = q/(Gi_{lg})$) in the nucleate boiling term, and is seen to be 0.7 for both convective and nucleate boiling regions. The dependence of the nucleate boiling contribution on heat flux q is therefore proportional to $q^{0.7}$. The underlying mechanism for the nucleate boiling in two-phase flow can be related to the pool boiling, and it seems reasonable to expect similar dependence on q in both cases. The dependence of the heat transfer coefficient on q in pool boiling can be expressed as

$$h \propto q^n$$

The value of the exponent n is 0.7 as given by two correlations recommended in the *Heat Exchanger Design Handbook* (1983), one by Borishanski (1969) and the other by Ratiani and Shekriladze (1972). Rohsenow's pool boiling correlation yields n equal to 0.67. Thus it is seen that the nucleate boiling term shows dependence on q similar to the case of pool boiling.

Convective Boiling Term. The dependence of the convective boiling term on quality is investigated in the two regions. In the convective boiling region, the exponent of Co is -0.9, and along with the $Re_l^{0.8}$ in the h_l expression, the convective boiling term varies as $x^{0.72}(1-x)^{0.08}$. However, this dependence should not be viewed in isolation, since the nucleate boiling contribution varies as $(1-x)^{0.8}$. Combining these two contributions may result in a different dependent of h_{TP} on x depending on the fluid and other system and operating parameters.

The exponent of Co in the nucleate boiling region is -0.2, which is much weaker than the value -0.891 found in the earlier work by Kandlikar (1983). The main reason for this is that very few data points in this region were used in the earlier work. This weak dependence on Co is to be expected in the nucleate boiling region where convection is not the dominant mechanism of heat transfer. As Bo increases, the percentage contribution due to convective boiling decreases. At high heat fluxes the heat transfer is predominantly by the nucleate boiling mechanism. However, at low heat flux values, the convective contribution may be quite significant. The proposed correlation is able to cover both these cases.

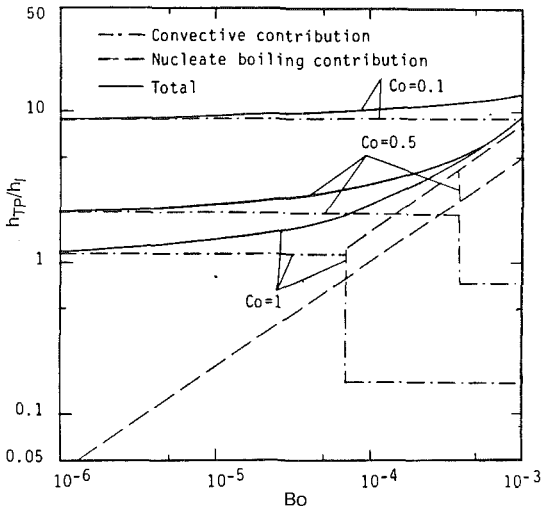

Fig. 1 Variation of h_{TP}/h_l with Bo in the proposed correlation, equations (4) and (5)

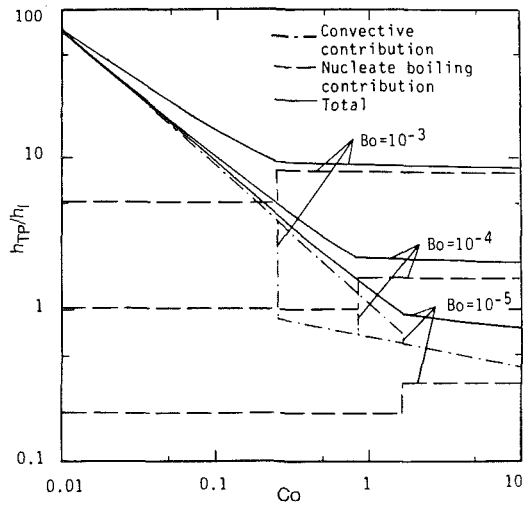

Fig. 2 Variation of h_{TP}/h_l with Co in the proposed correlation, equations (4) and (5)

Influence of Bo and Co. The contributions of convective boiling and nucleate boiling multipliers to h_l are shown in Figs. 1 and 2. These figures show the dependence of the ratio h_{TP}/h_l on Co and Bo, and not the actual variation of h_{TP}. Figure 1 shows the variation of h_{TP}/h_l with Bo for three values of Co: 0.1, 0.4, and 1.0. The contribution of the two mechanisms is also shown. The two regions are identified by a step change in the contributions of each mechanism. Note however that there is no step change in the sum of the two contributions. At lower values of Bo, the heat transfer is predominantly convective and the influence of Bo is relatively small. As Bo increases at a constant Co value, the convective contribution remains constant, but the nucleate boiling com-

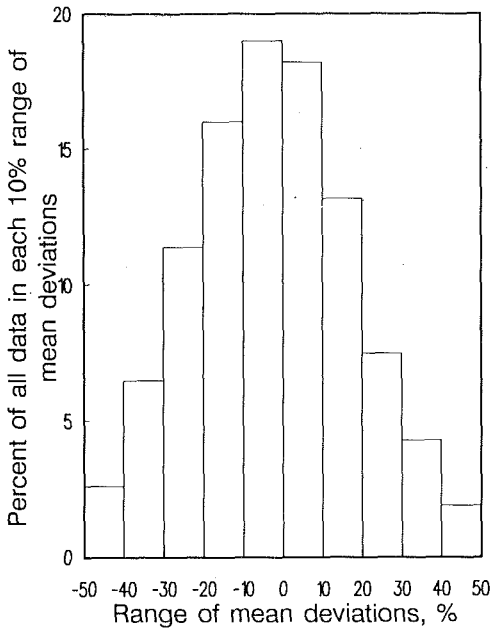

Fig. 3 Histogram of mean errors for all data with the proposed correlation, equations (4) and (5)

ponent first increases slowly, and then rapidly until the convective contribution becomes relatively insignificant in the nucleate boiling dominant region.

Similarly, the variation of h_{TP}/h_l with Co is plotted in Fig. 2 for three values of Bo: 10^{-5}, 10^{-4}, and 10^{-3}. Smaller values of Co represent the convective boiling dominant region. Here the influence of Bo tends to be smaller and all the Bo curves tend to merge into a single line. However at higher values of Co, the heat transfer is nucleate boiling dominant and the influence of Co becomes quite small.

A comprehensive figure showing the comparison of the proposed correlation with all data points would prove to be of little value due to the large number of data points involved. Instead, a histogram showing the percentages of number of points in every 10 percent mean deviation range is plotted in Fig. 3. The x axis gives the mean deviation range such as -50 to -40, -40 to -30, -30 to -20, and so on up to $+40$ to $+50$ percent error. The percentages of data points falling in each of these ranges are shown as vertical boxes in each region. Thus it can be seen that 66 percent of all data points fall within ± 20 percent, while 86 percent fall within ± 30 percent.

Comparison of Correlations. A comparison of the proposed correlation with five other correlations listed in Table 1 is made for all the 24 data sets used in this investigation. Table 5 gives the mean deviations between the experimental and predicted values from each correlation for water, seven refrigerants, and two cryogenic fluds. Since the data were stored with heat flux as a parameter, an iteration scheme was needed with the Chen (1966) and Bjorge et al. (1982) correlations.

As can be seen from Table 5, the proposed correlation from the present work yields the lowest values of mean deviations for water, all refrigerants, and cryogenic fluids. In the case of water, all the correlations perform quite well. In particular, the horizontal-flow data of Mumm are correlated by all correlations to within 15 percent except by the Chen correlation. For the vertical-flow data for water, large errors are noted. Bartoletti et al.'s (1964) high-pressure water data for 5 and 9-mm tubes could not be correlated by any of the correlations, all of them underpredicting by about 30–35 percent. Further evaluation of these data is needed; they were therefore not included in the data bank and the comparison reported in Table

Table 5 Comparison of correlations with experimental data

Fluid	Mean Deviations, percent					
	Present work	Shah (1982)	Gungor and Winterton (1987)	Gungor and Winterton (1986)	Chen (1966)	Bjorge, Hall and Rohsenow (1982)
Water						
Vertical	16.2	18.7	19.2	21.6	31.0	31.2
Horizontal	13.0	12.0	14.6	14.8	20.2	12.3
All water	15.9	17.9	18.5	20.7	29.6	24.6
Refrigerants						
R-11	16.9	17.6	20.7	25.8	42.4	30.5
R-12	23.3	34.8	27.2	30.7	74.0	64.0
R-1381	15.4	19.7	20.6	16.5	59.2	79.6
R-22	16.1	39.1	34.2	39.9	44.3	63.2
R-113	20.6	23.7	24.9	22.0	25.2	26.2
R-114	22.8	25.7	22.4	22.8	35.1	36.1
R-152A	16.3	19.9	18.1	23.8	60.2	83.1
All Refrigerants	18.8	25.8	24.0	25.9	48.6	54.7
Cryogenic fluids						
Nitrogen	19.3	57.3	45.8	*	*	*
Neon	18.7	46.9	43.5	*	*	*

* Errors could not be computed due to insufficient data

5. Unusually large deviations were noted for Wright's data with the Bjorge et al. correlation, and are not included in the reported mean deviations for that correlation in Table 5. Another important observation was made that Kenning and Cooper's data for vertical flow were correlated to within 15 percent by all correlations. From the description given by the investigators on the experimental apparatus and measurement techniques, their data set seems to be of very high accuracy.

For all refrigerants combined, the mean deviation is 18.8 percent with the proposed correlation, while it is above 24 percent with the other correlations. The errors with some refrigerants, e.g., R-22, are quite high with other correlations. This clearly indicates a need for a fluid-dependent parameter in the correlating scheme.

Another equally important factor in the comparison of the correlations is their ability to predict correct parametric trends among the important system variables. The basic trend of h_{TP} versus x was compared from different correlations against the systematic data available for R-113 and water. Figures 4 and 5 show the comparison of the correlations with the experimental data points from Jensen and Bensler (1986) at two system pressures of 5.5 bar and 2.7 bar with R-113. A decreasing trend of h_{TP} with x in the entire x range is seen for this data set. A similar trend has been observed with some other refrigerant data. This trend is quite different from a more accepted trend of constant h_{TP} at low x followed by increasing h_{TP} at higher x observed for water. The proposed correlation correctly predicts the decreasing trend of h_{TP} with x for R-113. At lower x values, corresponding to the nucleate boiling region, the experimental h_{TP} values are seen to be higher than those at higher qualities corresponding to the convective region. The proposed correlation shows a similar trend, with higher h_{TP} values at low x, and a rapidly decreasing trend with x at lower qualities, followed by a gradual descent at higher x values. Both the Gungor and Winterton correlations predict a monotonously decreasing trend, which fails to account for the considerably higher h_{TP} values at lower x. The Shah correlation predicts a complex trend due to a number of step variations present in it. The Chen and the Bjorge et al. correlations predict an ever-increasing trend of h_{TP} with x, which is quite opposite to the trend seen from the experimental data points.

The fluid-dependent parameter B_M in the Bjorge et al. correlation was set at 1.89 E-14 in the above comparisons. Setting

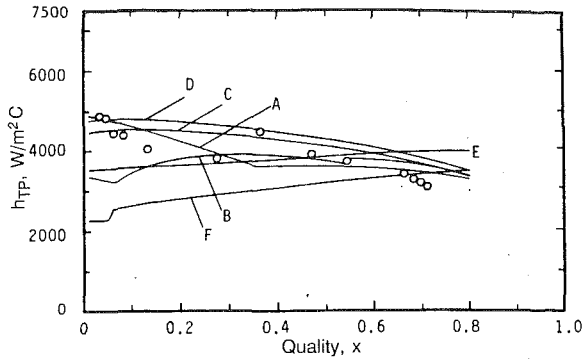

Fig. 4 Comparison of h_{TP} versus x for the Jensen and Bensler (1986) R-113 data and six correlations; $G = 637$ kg/m^{2}s, $q = 51{,}000$ W/m^2, $T_{sat} = 110°C$, $D = 0.81$ cm: (A) proposed correlation, equations (4) and (5); (B) Shah (1982); (C) Gungor and Winterton (1987); (D) Gungor and Winterton (1986); (E) Chen (1966); (F) Bjorge et al. (1982), o —data points

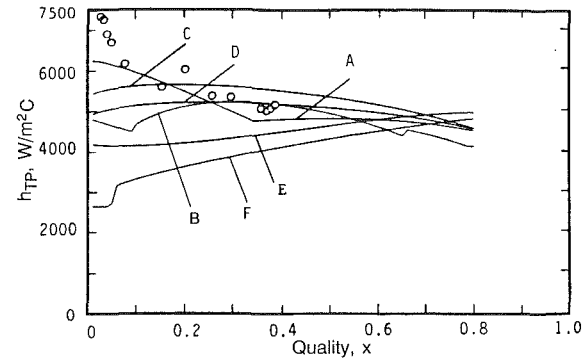

Fig. 5 Comparison of h_{TP} versus x for the Jensen and Bensler (1986) R-113 data and six correlations; $G = 295$ kg/m^{2}s, $q = 49{,}000$ W/m^2, $T_{sat} = 81°C$, $D = 0.81$ cm: (A) proposed correlation, equations (4) and (5); (B) Shah (1982); (C) Gungor and Winterton (1987); (D) Gungor and Winterton (1986); (E) Chen (1966); (F) Bjorge et al. (1982), o —data points

B_M at 1.03 E-13 in the correlation as suggested by Mikic and Rohsenow (1969) would improve the agreement with the data for refrigerants.

A similar comparison for water data from Cooper and Kenning (1986) for two system pressures of 1.638 and 1.974 bar is shown in Fig. 6. Here again the agreement between the predicted and the experimental values is excellent with the proposed correlation. The Shah correlation does quite well with water data. Both the Gungor and Winterton correlations and the Chen correlation slightly underpredict the heat transfer coefficient for this data set, while the Bjorge et al. correlation predicts an unusual rapidly increasing trend at higher x values.

The inability of the other correlations to predict the h_{TP}–x trend correctly is due to two reasons. Firstly, the form of the correlation may not be appropriate, e.g., the Gungor and Winterton (1987) correlation has h_l as an additive term, which severely affects the h_{TP}–x trend in the nucleate boiling region. Secondly, the other correlations, including those of Shah and Chen, have utilized average heat transfer coefficient data in their development, and therefore are unable to reflect the correct trend due to the averaging effects.

As is clear from the preceding discussion on Figs. 4–6, the proposed correlation is able to predict the increasing h_{TP} versus x trend for water, as well as a decreasing trend with R-113 for the given set of operating conditions. This has been made possible by the choice of an appropriate form of correlation, and the introduction of the fluid-dependent parameter F_{fl}, which is able to account for the different nucleate boiling behaviors of different fluids.

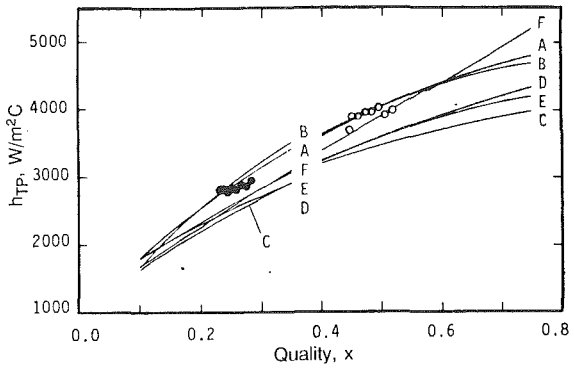

Fig. 6 Comparison of h_{TP} versus x for Kenning and Cooper's (1986) water data and six correlations; o $G = 203$ kg/m^{2}s, $q = 213{,}000$ W/m^2, $T_{sat} = 120°C$, $D = 0.96$ cm; • $G = 202$ kg/m^{2}s, $q = 142{,}000$ W/m^2, $T_{sat} = 114°C$, $D = 0.96$ cm; (A) proposed correlation, equations (4) and (5); (B) Shah (1982); (C) Gungor and Winterton (1987); (D) Gungor and Winterton (1986); (E) Chen (1966), (F) Bjorge et al. (1982)

A further comparison of the parametric dependence predicted by different correlations is presented by Kandlikar (1988). In that work, it is shown that Collier's flow boiling map is inadequate to represent the parametric trends for refrigerants, and suitable modifications are suggested.

Klimenko's Correlation. Klimenko (1988) recently proposed a flow boiling correlation that incorporates the wall thermal conductivity effect. In the nucleate boiling region, there are no flow effects included, while in the convective boiling region, h_{TP} is assumed to be independent of the tube diameter and the dependence on G and x is assumed to be proportional to $[G(1+x(\rho_l/\rho_g)]^{0.6}$. This yields an increasing h_{TP} versus x trend for all fluids, contrary to the observations made in the present study. Klimenko considered many earlier data sets with average coefficients and discarded more than half the data points in each set as being unacceptable. None of the recent local data on refrigerants were utilized. Klimenko also concludes that the Chen correlation is better than the Shah correlation, which again is contrary to the present findings.

Cryogenic Fluids. In the present study, only one data source each for nitrogen and neon was utilized in evaluating the respective fluid-dependent parameter F_{fl}, which is found to be 4.7 for nitrogen and 3.5 for neon. These values are quite large compared to those for water and the refrigerants. This prompted a further investigation on the correlations and experimental data sets pertaining to cryogenic fluids.

Klimenko (1982) presented a correlation specifically developed for cryogenic fluids on the basis of nine sets for hydrogen, neon, and nitrogen. He cites a lack of detailed information as a major problem in evaluating the accuracy of the experimental data sets. About 50 percent of the data from four sets was discarded in accordance with the "principle of maximum representativeness." No further details were given by Klimenko regarding the data selection process. The remaining data were correlated by a scheme similar to that developed for refrigerants (Klimenko, 1988), in which the wall thermal capacity was found to be an important correlating parameter. Deev et al. (1984) compared Klimenko's correlation with his own data and six other data sets for nitrogen. Deev et al.'s data along with four other data sets were correlated by Klimenko's correlation to within ±20 percent. However, data of Ronzhin and Usyukin (1968) and Steiner and Schlunder (1976) gave deviations in excess of −50 to +100 percent.

Shah (1984) compiled twelve experimental data sets for helium, hydrogen, neon, nitrogen, and argon, and compared them with his correlation and Klimenko's (1982) correlation. He observed no systematic dependence of the heat transfer coefficient on the wall thermal capacity contrary to

Klimenko's observation. The comparison of mean deviations for the twelve data sets shows that Shah's correlation gives better results than Klimenko's correlation. However, the mean deviations for some of the data sets are quite large, e.g., Muller et al.'s (1983) data for nitrogen at reduced pressures of 0.6 and 0.8: 59 percent; Steiner and Schlunder's (1977) data for nitrogen: 59 percent; Mohr and Runge's (1977) data for neon: 49 percent; and Ogato and Sato's data for helium: 37 percent. It may be noted that Shah utilized all the data points in each set while comparing the correlations.

As seen from the above discussion, the data for cryogenic fluids could not be correlated well with any available correlation. The main problem seems to lie in determining the accuracy of the data sets. As pointed out earlier, the major sources of error seem to be: low temperature differences with cryogenic fluids, inaccurate estimates of heat losses from the test section, and difficulties in obtaining local measurements. Under these circumstances, the development of a general correlation for cryogenic fluids may have to wait until reliable experimental data are available for different cryogenic fluids. The fluid-dependent parameter in the proposed correlation may then be derived from the reliable data sets.

Additional Remarks. Further comparison of different correlations was made with Khanpara's (1986) recent R-22 and R-113 data in 8.71-mm-dia horizontal tubes, made available by Prof. A. E. Bergles of Rensselaer Polytechnic Institute, Troy, NY. These data are believed to be very accurate since great care was taken in eliminating any entrance effects, and in reducing other experimental uncertainties. There are 100 data points for R-22 and 110 data points for R-113, covering both the nucleate boiling and convective regions. The mean percent deviations with the different correlations for R-22 and R-113, respectively, are: present study—15.2 and 20.8; Shah—36.1 and 22.3; Gungor and Winterton (1986)—39.4 and 26.2; Winterton (1987)—31.3 and 21.1; Bjorge et al.—43.8 and 51.3; and Chen—47.9 and 56.9. Since these data sets were not used in any of the correlation development, including the present one, they should serve as a fair comparison of different correlations. As seen from this comparison, the proposed correlation gives the lowest mean deviations for both R-22 and R-113.

A comment regarding the simplicity and ease of use of these correlations is appropriate. The correlations of Shah, and Gungor and Winterton (1986, 1987), and the proposed correlation are explicit in terms of heat flux, and require only the quality, mass flux, heat flux, and tube diameter as input operating variables. The fluid properties required are liquid thermal conductivity, liquid specific heat, liquid and vapor phase densities, liquid viscosity, and the latent heat of vaporization. Other correlations by Chen, and Bjorge et al., are explicit in terms of the temperature difference between the wall and the fluid saturation temperature, and require a number of additional properties including surface tension, vapor viscosity, and vapor pressure equation.

It is expected that the values of F_{fl} for different fluids recommended in this paper may undergo further refinements as more reliable data become available for each fluid. It may also be possible to accommodate the surface condition variation through this parameter, and extend it to enhanced surfaces.

Conclusions

A total of 5246 data points for water, R-11, R-12, R13-B1, R-22, R-113, R-114, R-152a, nitrogen, and neon have been compiled from 24 experimental investigations on saturated flow boiling inside vertical and horizontal tubes. A correlation is developed from these data sets using an additive model and a fluid-dependent parameter F_{fl}. This correlation results in a mean deviation of 15.9 percent with water data, and 18.8 percent with all refrigerant data combined. The corresponding figures are 17.9 percent and 25.8 percent with the Shah (1982) correlation, and 18.5 percent and 24.0 percent with the Gungor and Winterton (1987) correlation. The proposed correlation gives a continuous variation of heat transfer coefficient along an evaporator tube and agrees with the trends of h_{TP} versus x as seen from the experimental data for water and R-113.

References

Ashley, C. M., 1942, "The Heat Transfer of Evaporating Freon," *American Society of Refrigerating Engineers Journal*, Feb., pp. 89–95.

Anderson, S. W., Rich, D. G., and Geary, D. F., 1966, "Evaporation of R22 in a Horizontal 3/4 in. OD Tube," *ASHRAE Transactions*, Vol. 72, pp. 28–41.

ASHRAE, 1976, *Thermophysical Properties of Refrigerants*, ASHRAE, New York.

Bandel, J., 1973, "Druckverlust und Wärmeübergang bei der Verdampfung siedender Kaltemittel im durchströmten waagerechten Rohr," Ph.D. dissertation, Universität Karlsruhe, Federal Republic of Germany.

Bartoletti, S., Lombardi, C., and Silvestri, M., 1964, "Heat Transfer to Stream–Water Mixtures," Report R-78, Research Contract between Euratom and Centro Informazioni Studi Esperienzo, Milan, Italy.

Bennett, D. L., 1976, "A Study of Internal Forced Convective Boiling Heat Transfer for Binary Mixtures," Ph.D. dissertation, Lehigh University, PA.

Bennett, D. L., and Chen, J. C., 1980, "Forced Convective Boiling in Vertical Tubes for Saturated Pure Components and Binary Mixtures," *AIChE Journal*, Vol. 26, pp. 454–461.

Bergles, A. E., and Rohsenow, W. M., 1964, "The Determination of Forced Convection Surface Boiling Heat Transfer," ASME JOURNAL OF HEAT TRANSFER, Vol. 86, pp. 365–372.

Bjorge, R. W., Hall, G. R., and Rohsenow, W. M., 1982, "Correlation of Forced Convection Boiling Heat Transfer Data," *International Journal of Heat and Mass Transfer*, Vol. 25, No. 6, pp. 753–757.

Borishanski, V. M., 1969, "Correlation of the Effect of Pressure on the Critical Heat Flux and Heat Transfer Rates Using the Theory of Thermodynamic Similarity," in: *Problems of Heat Transfer and Hydraulics of Two-Phase Media*, Z. Z. Kutateladze, ed., Pergamon, Oxford, United Kingdom, pp. 16–37.

Bryan, W. L., and Quaint, G. W., 1951, "Heat Transfer Coefficients in Horizontal Tube Evaporators," *Regrigerating Engineering*, Vol. 59, No. 1, pp. 67–72.

Bryan, W. L., and Siegel, L. G., 1955, "Heat Transfer Coefficients in Horizontal Tube Evaporators," *Refrigerating Engineering*, Vol. 63, No. 5, pp. 36–45, 120.

Chaddock, J. B., and Brunemann, H., 1967, "Forced Convection Boiling of Refrigerants in Horizontal Tubes," Report No. HL-113, School of Engineering, Duke University.

Chaddock, J. B., and Noerager, J. A., 1966, "Evaporation of R-12 in Horizontal Tube With Constant Heat Flux," *ASHRAE Transactions*, Vol. 72, Part I, pp. 99–103.

Chawla, J. M., 1967, "Wärmeübergang und Druckabfall in waagrechten Rohren bei der Strömung von verdampfenden Kältemitteln," *VDI-Forschungsheft*, No. 523.

Chen, J. C., 1966, "A Correlation for Boiling Heat Transfer to Saturated Fluids in Convective Flow," *Industrial and Engineering Chemistry, Process Design and Development*, Vol. 5, No. 3, pp. 322–329.

Colburn, A. P., 1933, "A Method of Correlating Forced Convection Heat Transfer Data and a Comparison With Fluid Friction," reprinted in: *International Journal of Heat and Mass Transfer*, Vol. 7, 1964, pp. 1359–1384.

Collier, J. G., 1981, *Convective Boiling and Condensation*, 2nd ed., McGraw-Hill, New York.

Cooper, M. G., 1984, "Saturation Nucleate Pool Boiling," 1st U.K. National Conference on Heat Transfer, Vol. 2, pp. 785–793 (Industrial and Chemical Engineering Symposium Series No. 86).

Deev, V. I., Arkhipov, V. V., and Novikov, V. N., 1984, "Heat Transfer With Boiling of Nitrogen Under Conditions of Forced Motion," *Thermal Engineering*, Vol. 31, pp. 143–146.

E. I. DuPont de Nemors and Co. 1967, "Surface Tension of the Freon Compounds," DuPont Technical Bulletin D-27.

Forster, H. K., and Zuber, N., 1955, "Dynamics of Vapor Bubbles and Boiling Heat Transfer," *Journal of AIChE*, Vol. 1, pp. 531–535.

Gungor, K. E., and Winterton, R. H. S., 1986, "A General Correlation for Flow Boiling in Tubes and Annuli," *International Journal of Heat and Mass Transfer*, Vol. 29, No. 3, pp. 351–358.

Gungor, K. E., and Winterton, R. H. S., 1987, "Simplified General Correlation for Saturated Flow Boiling and Comparisons of Correlations With Data," *The Canadian Journal of Chemical Engineering*, Vol. 65, No. 1, pp. 148–156.

Heat Exchanger Design Handbook, 1983, Section 2.7.2, Hemisphere Publishing Corporation, New York.

Jallouk, P. A., 1974, "Two-Phase Flow Pressure Drop and Heat Transfer Characteristics of Refrigerants in Vertical Tubes," Ph.D. Dissertation, University of Tennessee, Knoxville, TN.

Jensen, M. K., and Bensler, H. P., 1986, "Saturated Forced Convective Boiling Heat Transfer With Twisted-Tape Inserts," ASME JOURNAL OF HEAT TRANSFER, Vol. 108, pp. 93-99.

Johnston, R. C., and Chaddock, J. B., 1964, "Heat Transfer and Pressure Drop of Refrigerants Evaporating in Horizontal Tubes," *ASHRAE Transactions*, Vol. 70, pp. 163-172.

Kandlikar, S. G., and Thakur, B. K., 1982, "A New Correlation for Heat Transfer During Flow Boiling," *Proceedings, 16th Southeastern Seminar on Thermal Sciences*, Miami, FL.

Kandlikar, S. G., 1983, "An Improved Correlation for Predicting Two-Phase Flow Boiling Heat Transfer Coefficient in Horizontal and Vertical Tubes," in: *Heat Exchangers for Two-Phase Flow Applications*, ASME, New York.

Kandlikar, S. G., 1988, "A Parametric Study of Saturated Flow Boiling Heat Transfer Inside Horizontal and Vertical Tubes," presented at the First World Conference on Experimental Heat Transfer, Fluid Mechanics and Thermodynamics, Dubrovnik, Yugoslavia.

Kaufmann, W. D., 1974, "Untersuchung des Wärmeübergangs und des Druckverlustes der zweiphasenströmung con R-12 im senkrechte Rohr," Swiss Tech. University, dissertation No. 5169, Zurich, Switzerland.

Kenning, D. B. R., and Cooper, M. G., Jan. 1986, *Personal Communication*.

Khanpara, J. C., 1986, "Augmentation of In-Tube Evaporation and Condensation With Micro-fin Tubes Using R-113 and R-22," Ph.D. dissertation, Iowa State University, Ames, IA.

Khanpara, J. C., Bergles, A. E., and Pate, M. B., 1986, "Augmentation of R-113 In-Tube Evaporation With Micro-fin Tubes," ASHRAE Paper No. PO-86-11, No. 3.

Klimenko, V., 1982, "Heat Transfer Intensity at Forced Flow Boiling of Cryogenic Liquids in Tubes," *Cryogenics*, Vol. 22, pp. 569-576.

Klimenko, V. V., 1988, "A Generalized Correlation for Two-Phase Forced Flow Heat Transfer," *International Journal of Heat and Mass Transfer*, Vol. 31, No. 3, pp. 541-552.

Mastroianni, M. J., Stah, R. F., and Sheldon, P. N., 1978, "Physical and Thermodynamic Properties of 1, 1,2-Trifluorotrichloroethane (R-113)," *ACS Journal of Chemical and Engineering Data*, Vol. 23, No. 2, pp. 113-118.

Mikic, B. B., and Rohsenow, W. M., 1969, "A New Correlation of Pool Boiling Data Including the Effect of Heating Surface Characteristics," ASME JOURNAL OF HEAT TRANSFER, Vol. 91, p. 245.

Mohr, V., and Runge, R., 1977, "Forced Convection Boiling of Neon in Horizontal Tubes," *Heat Transfer in Boiling*, E. Hahne, and U. Grigull, eds., Hemisphere Publishing Corporation, New York.

Morzov, V. G., 1969, "Heat Transfer During the Boiling of Water in Tubes," in: *Convective Heat Transfer in Two Phase and One Phase Flows*, V. M. Borishanskii and I. I. Paleev, eds., Israel Program for Scientific Translations Ltd., pp. 106-114.

Muller, H., Bonn, W., and Steiner, D., 1983, "Heat Transfer and Critical Heat Flux at Flow Boiling of Nitrogen and Argon Within a Horizontal Tube," in: *Heat Exchangers*, J. Taborek, G. F. Hewitt, and N. Afgan, eds., Hemisphere Publishing Corp., Washington, DC, pp. 233-250.

Mumm, J. F., 1954, "Heat Transfer to Boiling Water Forced Through a Uniformly Heated Tube," Report No. ANL-5276, Argonne National Laboratory, Argonnne, IL.

Ogato, H., and Sato, S., 1974, "Forced Convection Heat Transfer to Boiling Helium in a Tube," *Cryogenics*, Vol. 14, pp. 375-380.

Perroud, P., de la Harpe, A., and Rebiere, J., 1960, "Experimental Investigation of the Coefficient of Heat Transfer, Critical Heat Flux and Pressure Drop of Water Steam Mixtures in Turbulent Flow in a Vertical Tube," Grenoble Center for Nuclear Studies, Physico-Chemical and Low-Temperature Laboratory, Report CEA No. 1853.

Pierre, B., 1957, "The Coefficient of Heat Transfer for Boiling Freon-12 in Horizontal Tubes," *Heating and Air Treatment Engineer*, Dec., pp. 302-310.

Pujol, L., and Stenning, A. H., 1969, "Effect of Flow Directions on the Boiling Heat Transfer Coefficients in Vertical Tubes," *Cocurrent Gas-Liquid Flow*, A. A. Rhodes, and B. B. Scott, eds., Plenum Press, New York, pp. 401-453.

Ratiani, G. V., and Shekriladze, I. G., 1972, "Study of the Process of Fully Developed Boiling of Liquids," *Heat Transfer—Soviet Research*, Vol. 4, No. 4, pp. 126-141.

Reynolds, W. C., 1979, *Thermodynamic Properties in SI*, Stanford University, Stanford, CA.

Rhee, B. W., 1972, "Heat Transfer to Boiling Refrigerants R-12 and R-22 Flowing Inside a Plain Copper Tube," Ph.D. dissertation, The University of Michigan, Ann Arbor, MI.

Riedel, K., and Purcupile, J. C., 1971, "Experimental and Analytical Investigation—Boiling Heat Transfer in Evaporator Tubes—Horizontal Flow," report prepared under NSF Grant 257, CMV No. 1-55307, Carnegie-Mellon University, Pittsburgh, PA.

Rohsenow, W. M., 1952, "A Method of Correlating Heat Transfer Data for Surface Boiling of Liquids," *Transactions of ASME*, Vol. 74, pp. 969-975.

Ronzhin, L. P., and Usyukin, I. P., 1968, "Experimental Investigation of Nitrogen Boiling Under Conditions of Forced Motion in a Horizontal Tube," *Kislorodnaya Promyshlennost*, Vol. 2, pp. 25-33.

Ross, H. D., 1985, "An Investigation of Horizontal Flow Boiling of Pure and Mixed Refrigerants," Ph.D. dissertation, University of Maryland.

Sani, R. L., 1960, "Downflow Boiling and Non-boiling Heat Transfer in a Uniformly Heated Tube," M.S. thesis, UCRL-9023, University of California at Berkeley.

Shah, M. M., 1976, "A New Correlation for Heat Transfer During Boiling Flow Through Pipes," *ASHRAE Transactions*, Vol. 82, Part II, pp. 66-86.

Shah, M. M., 1982, "Chart Correlation for Saturated Boiling Heat Transfer: Equations and Further Study," *ASHRAE Transactions*, Vol. 88, Part I, pp. 185-196.

Shah, M. M., 1984, "Prediction of Heat Transfer During Boiling of Cryogenic Fluids Flowing in Tubes," *Cryogenics*, Vol. 24, pp. 231-236.

Steiner, D., 1984, Personal Communication.

Steiner, D., and Schlunder, E. U., 1977, "Heat Transfer and Pressure Drop for Boiling Nitrogen Flowing in a Horizontal Tube," *Heat Transfer in Boiling*, E. Hahne, and U. Grigull, eds., Hemisphere Publishing Corporation, New York.

Stone, J. R., 1971, "Subcooled and Net Boiling Heat Transfer to Low Pressure Water in Electrically Heated Tubes," NASA TN D-6402, NASA Lewis Research Center, Cleveland, OH.

Traviss, D. P., Rohsenow, W. M., and Baron, A. B., 1972, "Forced Convection Condensation Inside Tubes: A Heat Transfer Equation for Design," ASHRAE Reprint No. 2272 RP-63.

Wright, R. M., 1961, "Downflow Forced Convection Boiling of Water in Uniformly Heated Tubes," UCRL Report 9744, University of California at Berkeley.

Yilmaz, S., and Westwater, J. W., 1980, "Effect of Velocity on Heat Transfer to Boiling Freon-113," ASME JOURNAL OF HEAT TRANSFER, Vol. 20, pp. 26-31.

Zuber, N., Staub, F. W., Bijwaard, G., and Kroger, P. G., 1967, "Steady State and Transient Void Fraction in Two-Phase Flow Systems," General Electric Company, Report No. GEAP-5417.

Film Condensation of R-11 Vapor on Single Horizontal Enhanced Condenser Tubes

S. P. Sukhatme

B. S. Jagadish

P. Prabhakaran

Department of Mechanical Engineering,
Indian Institute of Technology,
Powai, Bombay 400076, India

The heat transfer performance of R-11 vapor condensing on single horizontal trapezodially shaped integral-fin tubes has been investigated by systematically varying the fin density, the semi-vertex angle, and the fin height. For the nine copper tubes tested, the best performance has been obtained with a tube having a fin density of 1417 fpm, a semi-vertex angle of 10 deg, and a fin height of 1.22 mm. This tube has yielded a maximum value of the heat transfer coefficient of 16,500 W/m² K at a ΔT of about 3 K, corresponding to an enhancement ratio of 10.3. The performance of the tube has been further improved by fabricating from it "specially enhanced" tubes having axial grooves of varying height. An enhancement ratio of 12.3 has been obtained with this type of tube.

Introduction

The use of integral-fin tubes is the most commonly employed enhancement technique for horizontal tube surface condensers. The fins usually have a two-dimensional trapezoidal or rectangular cross section as shown in Fig. 1. In the last few years, some specially enhanced three-dimensional surfaces have also been developed. Two such surfaces are also shown in Fig. 1.

One of the first experimental studies of condensation on integral-fin tubes with a rectangular cross-section was made by Beatty and Katz (1948). Based on their data, they developed an equation by applying Nusselt's equations for film condensation on a smooth horizontal tube and a vertical plate to the horizontal portion between the fins and to the short vertical fin surfaces respectively.

A method using surface tension forces to enhance film condensation was proposed for the first time by Gregorig (1954). His "fluted tube" consisted of grooved surfaces that were not very different from integral fins with a trapezoidal cross section. Although studies by Katz and Geist (1948), and Pearson and Withers (1969), have supported the prediction of the Beatty–Katz equation, later studies have shown that this equation does not predict the values of the heat transfer coefficient for many situations. Webb et al. (1982) have shown that this is due to the fact that very often surface tension rather than gravity controls the condensate flow over the fin surface and significant condensate flooding occurs between the fins in the lower portion of the tube circumference.

In the last two decades, a number of theoretical and experimental investigations have been carried out by various investigators. Comprehensive theoretical models have been developed by Karkhu and Borovkov (1971), Webb et al. (1985), Adamek (1985), and Honda and Nozu (1987). Generally the analysis has been carried out by dividing the tube surface into three regions; (*i*) The unflooded crest region where a very thin condensate film occurs due to surface tension driven forces, (*ii*) the unflooded valley region, which serves essentially as a condensate drainage channel, and (*iii*) the flooded bottom region caused by liquid retention between the fins.

The research on the experimental side can be broadly classified into two categories: that on high surface tension fluids, and that on low surface tension fluids. The use of integral-fin tubes with a high surface tension working fluid (e.g., steam) was restricted, until recently, due to the severity of condensate flooding between the fins. Recent systematic investigations by Yau et al. (1985), Wanniarachchi et al. (1986), and Marto et al. (1986) have optimized the fin density, fin shape, and size used when steam is the working fluid. Some experimental studies have also been reported for low surface tension fluids such as fluorocarbon refrigerants. Carnavos (1980), Rudy (1982), and Furukawa Electric (1981) have reported experimental studies using R-11 as the working fluid. However, systematic studies on the effect of fin density and fin geometry on the condensing performance of a low surface tension fluid have not been reported.

In the present paper, we report the results of experimental studies of heat transfer during film condensation of R-11 vapor on single horizontal trapezoidally shaped integral-fin tubes by systematically varying the fin density, the semi-vertex angle, and the fin height. The experimental results are compared with the theoretical models. Data on some specially enhanced tubes are also reported.

Experimental Setup and Procedure

Experimental Setup. The experimental setup (Fig. 2) con-

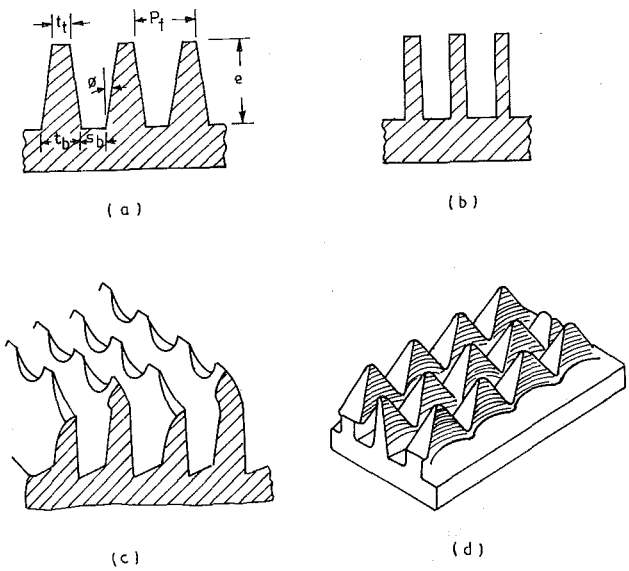

Fig. 1 Enhanced surface condenser tubes. Integral fins, two-dimensional: (a) trapezoidal cross section and (b) rectangular cross section. Specially enhanced, three-dimensional: (c) Thermoexcel-C and (d) Everfin-Δ.

Contributed by the Heat Transfer Division for publication in the JOURNAL OF HEAT TRANSFER. Manuscript received by the Heat Transfer Division October 2, 1987. Keywords: Condensation, Multiphase Flows.

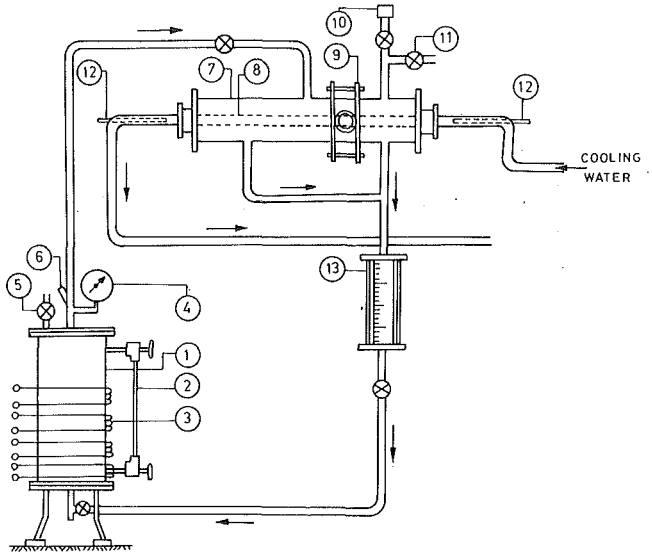

Fig. 2 Schematic diagram of experimental setup: (1) refrigerant-11 boiler, (2) liquid level indicator, (3) heaters, (4) pressure gauge, (5) charging connection, (6) thermocouple, (7) test section, (8) condenser tube, (9) sight glass assembly, (10) pressure transducer, (11) flushing vent, (12) thermopile pocket, and (13) condensate measuring tube

sisted essentially of a boiler (1), a test section (7), a working fluid circulating loop, and a cooling water circulating loop. The test section consisted of a horizontal cylindrical brass shell (0.095 m diameter and 0.5 m long) in which the copper condenser tube (8) to be tested (average outer diameter 0.0242 m and average inner diameter 0.0156 m) was fitted co-axially. The end plates of the shell were made of fiber-reinforced bakelite plates in order to reduce the heat flow between the condenser tube and the brass shell. These plates were held together with check nuts screwed on the condenser tube. A sight glass assembly (9) was provided on the test section shell in order to view the condensation over a part of the tube. A traveling microscope was mounted on the sight glass assembly to measure the extent of condensate flooding taking place between the fins.

Calibrated 36 SWG copper-constantan thermocouples were used to measure the vapor temperature in the annular space between the tube and the shell, and the wall temperatures in the condenser tube. A calibrated digital pressure transducer (10) was mounted on the condenser shell in order to measure the vapor pressure in the test section. The surface temperatures of the condenser tubes were measured at five equidistant locations along the length and at three locations

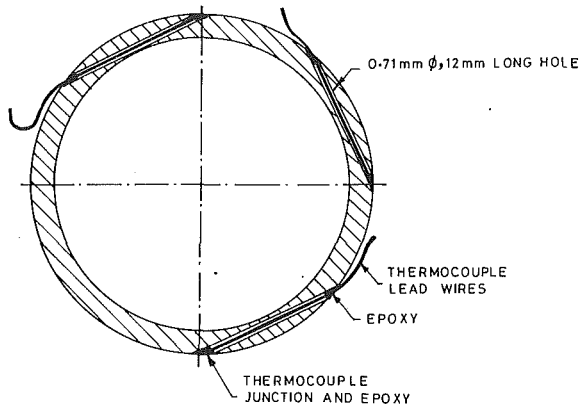

Fig. 3 Details of positioning of thermocouples in condenser tube wall

(the top, bottom, and midplane) at each section. All thermocouple junctions were embedded close to the outer surface of the tube wall and the lead wires taken through small holes (0.71 mm diameter) drilled tangentially in the wall of the tube as shown in Fig. 3. The length of the holes through which the lead wires were taken was about 12 mm and the hole ends were properly sealed with epoxy adhesive. Any possible error due to conduction along the thermocouple lead wires was thus essentially eliminated. A multimeter having a resolution of 1 μV was used to measure the thermocouple emfs. More details are given by Prabhakaran (1987).

The boiler was a vertical cylindrical shell made of mild steel. It had an inner diameter of 0.154 m and a height of 0.30 m. The level of liquid in the boiler was indicated by a pyrex glass level indicator (2). Four heating coils (3) each having a capacity of 2.25 kW were wound around the boiler shell. A stabilized power supply was given to each of the heating elements. A 0.0174 m diameter copper tube was used to connect the boiler to the test section, while a 0.019 m diameter return line was provided for connecting the test section to the boiler. A graduated condensate measuring tube (13) made of pyrex glass having a diameter of 0.033 m was provided in the return line. In order to determine the rate of condensation, a manually operated valve just after the measuring tube was closed and the rise in level of the condensate in the tube over a small interval of time was measured.

The cooling water circulating loop consisted of a water storage tank, a centrifugal pump, two rotameters in parallel, and lines from the storage tank to the condenser tube and back. Calibrated rotameters were used to measure the cooling water flow rate. A five-junction thermopile was provided at

Nomenclature

A_f = actual fin surface area, m^2
A_o = outside area of finned tube over fin $= \pi d_o l$, m^2
d_i = inner diameter of tube, m
d_o = outer diameter of tube to fin tip, m
e = height of fin, m
e_a = height of axial groove in specially enhanced tube, m
$\bar{h}$ = average heat transfer coefficient predicted by various models, W/m^{2}K: subscripts: A = Adamek, HN = Honda and Nozu, KB = Karkhu and Borovkov, WRK = Webb, Rudy, and Kedzierski
$\bar{h}_e$ = average heat transfer coefficient from experiment, W/m^{2}K
l = length of condenser tube, m
P_f = fin pitch, m
P_{fa} = pitch of axial grooves, m
$\dot{Q}_a$ = average heat transfer rate $= (\dot{Q}_c + \dot{Q}_{cw})/2$, W
$\dot{Q}_c$ = heat transfer rate from condensate, W
$\dot{Q}_{cw}$ = heat transfer rate to cooling water, W
s_b = distance between adjacent fins at base, m
s_{ba} = width of axial groove at base, m
s_{ta} = width of axial groove at tip, m
t_b = fin thickness at base of fin, m
t_t = fin thickness at tip of fin, m
$\bar{T}_v$ = average vapor temperature, K
$\bar{T}_w$ = average wall temperature of condenser tube, K
ΔT = difference between average vapor temperature and average wall temperature $= \bar{T}_v - \bar{T}_w$, K
ϕ = fin semi-vertex angle, deg
ϕ_a = semi-vertex angle of axial groove, deg

Table 1 Geometric specifications of integral-fin tubes

Tube	Tube specification		Fin specification							Area ratio A_f/A_o
	d_o, mm	d_i, mm	Fin density, fpm	P_f, mm	e, mm	ϕ, deg	t_t, mm	t_b, mm	s_b, mm	
1	24.10	15.50	945	1.06	0.69	30	0.13	0.93	0.13	3.16
2	24.05	15.50	1417	0.71	0.46	30	0.09	0.62	0.09	3.20
3	24.10	15.70	1890	0.53	0.34	30	0.07	0.46	0.07	3.18
4	23.54	15.50	2205	0.45	0.29	30	0.06	0.39	0.06	3.18
5	24.00	15.70	1417	0.71	0.46	20	0.09	0.42	0.29	3.24
6	24.36	15.60	1417	0.71	0.46	10	0.09	0.25	0.46	3.35
7	24.00	15.70	1417	0.71	0.71	10	0.09	0.34	0.37	4.58
8	24.60	15.60	1417	0.71	0.92	10	0.09	0.41	0.30	5.62
9	25.00	15.70	1417	0.71	1.22	10	0.09	0.52	0.19	7.05

Table 2 Geometric specifications of axially cut grooves in specially enhanced tubes (The specially enhanced tubes were made from Tube 9. There were 80 longitudinal/axial grooves in each tube.)

Tube	P_{fa}, mm	e_a, mm	ϕ_a, deg	s_{ta}, mm	s_{ba}, mm
10	1.00	0.70	10	0.35	0.10
11	1.00	0.90	10	0.42	0.10
12	1.00	1.22	10	0.53	0.10

the inlet and outlet of the condenser tube in order to measure the rise in temperature of the cooling water.

Experimental Procedure and Data Reduction. Initially the experimental setup was evacuated by connecting a vacuum pump to the vent line (11) provided at the top of the condenser shell. The boiler was then charged with R-11 liquid. First, experiments were conducted to check the heat loss from the test setup, which was well insulated with about 5 cm of fiberglass wool. The tests showed that the insulation provided was adequate and that the heat loss was negligible. Then the amount of noncondensable gases present in the test loop was reduced to a negligible value by repeated purging. This was achieved as follows: For a given heat input to the boiler and a given cooling water flow rate, readings were taken at steady state. The flushing vent above the test section was then opened for a brief period to allow the escape of noncondensable gases (if any) along with pure vapor. The system was again allowed to reach steady state and the readings taken. This process was repeated a number of times over a period of a day or two until repetitive sets of steady-state readings were obtained.

The experimental procedure adopted was first to adjust the flow rate of water and then the heat supplied to preselected values and allow the system to come to steady state. A guideline for adjusting these quantities was that the temperature rise of the cooling water was about 10 percent of ΔT. This resulted in an axial wall temperature variation, which was small relative to the value of ΔT. Measurements generally showed that this variation was essentially linear. The circumferential wall temperature variation was about 0.7 K at a ΔT of 3 K and about 1 K at a ΔT of 7 K.

The average heat transfer coefficient ($\bar{h}_e$) was calculated using the expression

$$\bar{h}_e = \frac{\dot{Q}_a}{A_o \Delta T} = \frac{(\dot{Q}_{cw} + \dot{Q}_c)/2}{\pi d_o l (\bar{T}_v - \bar{T}_w)} \quad (1)$$

The mean heat transfer rate ($\dot{Q}_a$) was the average of the values obtained by two methods, the heat gained by the cooling water and the heat of condensation obtained by measuring the rate of condensation and multiplying by the latent heat. The data for a test were accepted only if the heat transfer rates calculated by the two methods agreed to within 8 percent of each other. The outside area of the bare tube (A_o) from which the fins were cut was used as the reference area. The ΔT used in computing the average heat transfer coefficient was the difference between the average temperature of the vapor and the average wall temperature, the latter taking into consideration the circumferential and axial variation. As a check, the vapor temperature in the shell was compared with the saturation temperature corresponding to the measured vapor pressure. The comparison showed that the two values always agreed within 0.2 K.

An uncertainty analysis along the lines suggested by Kline and McClintock (1953) showed that the uncertainty due to measurement errors in the determination of $\dot{Q}_{cw}$ and $\dot{Q}_c$ was about 4 and 1.5 percent, respectively. With the additional check of ensuring that the values of $\dot{Q}_{cw}$ and $\dot{Q}_c$ were always within 8 percent, it is likely that the uncertainty in the value of $\dot{Q}_a$ was at most about 4 percent. This uncertainty coupled with an estimated uncertainty of ± 0.25 K in the value of ΔT yielded an uncertainty of about 9 percent in the value of $\bar{h}_e$ at a ΔT of 3 K and an uncertainty of about 5 percent at a ΔT of 7 K.

Results and Discussion

Tests Conducted. Three sets of experiments involving nine integral-fin tubes[1] (Tubes 1–9) and one set of experiments involving three specially enhanced tubes (Tubes 10–12) were carried out. The geometric specifications of the tubes are given in Tables 1 and 2. Preliminary tests were first carried out on a smooth tube. It was found that the experimental values were a little less than the theoretical values given by the Nusselt prediction (Fig. 4). At ΔT greater than 4 K, the experimental values agreed to within 5 percent of the Nusselt prediction, while at smaller ΔT around 3 K, the agreement was within 15 percent. Overall, the smooth tube data can be considered to be in reasonably good agreement with the theory. As a check, the heat transfer coefficients on the condensing side were also obtained from the experimental data without using the wall temperature measurements. This was done by assuming the validity of the Dittus–Boelter correlation for the water side and subtracting the water side thermal resistance from the overall resistance. It was found that the values of the condensing side heat transfer coefficient obtained in this manner agreed very well with the experimental values for the smooth tube presented in Fig. 4.

The three sets of experiments on Tubes 1–9 were conducted to study the effect of fin density, fin semi-vertex angle, and fin

[1] The term "integral-fin tube" is used throughout this paper to denote a two-dimensional surface. On the other hand, the term "specially enhanced tube" is used to denote a three-dimensional surface.

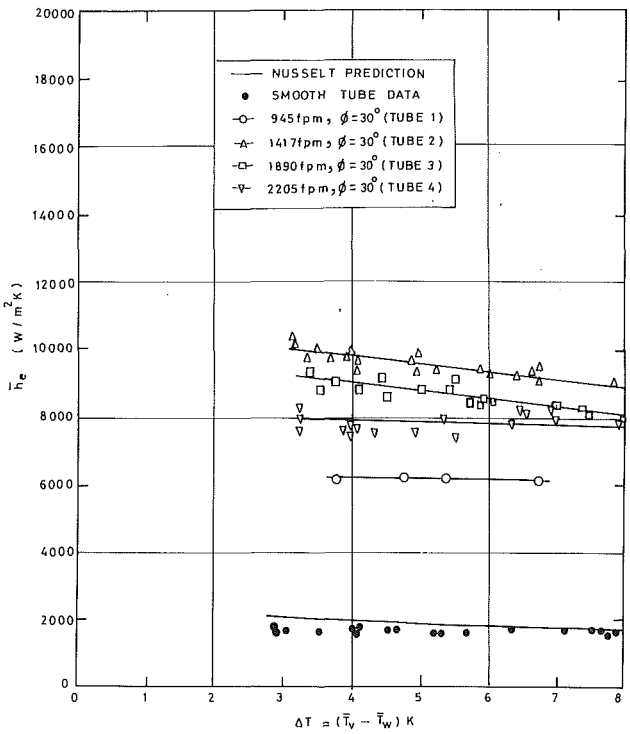

Fig. 4 Variation of $\bar{h}_e$ with ΔT for integral-fin tubes 1–4

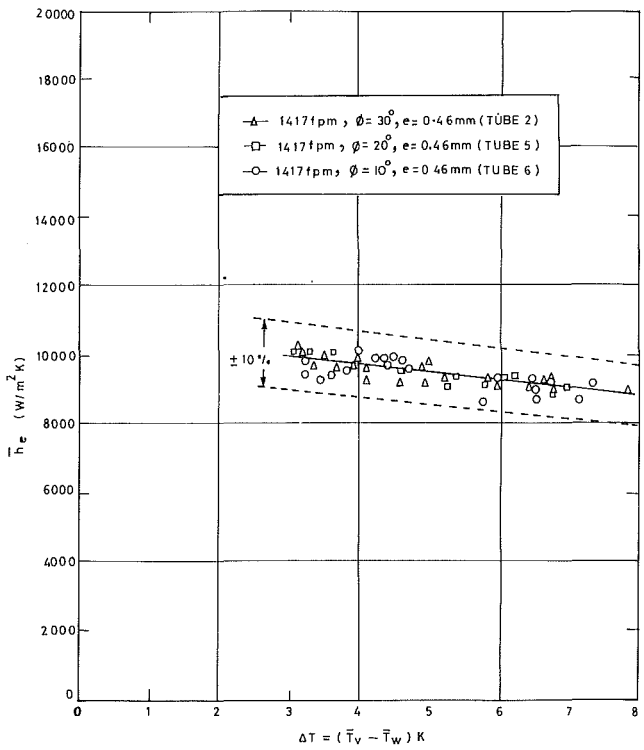

Fig. 5 Variation of $\bar{h}_e$ with ΔT for integral-fin tubes 2, 5, and 6

height. Tubes 1–4 constituted the first set, wherein the fin density was varied from 945 to 1417 to 1890 and finally to 2205 fins per meter (fpm). The fins were cut as American Standard Screw threads with a semi-vertex angle of 30 deg. Because of the fixed value of the semi-vertex angle, the fin height for this set varied from 0.69 mm to 0.29 mm. The second set consisted of testing Tubes 5 and 6 and comparing the data with those obtained for Tube 2 in order to study the effect of semi-vertex angle on performance. The semi-vertex angle was varied from 30 deg (Tube 2) to 20 deg (Tube 5) and finally to 10 deg (Tube 6), keeping the fin density and fin height at 1417 fpm and 0.46 mm, respectively. In the third set of experiments involving Tubes 7–9, the fin height was increased from 0.71 mm (Tube 7) to 0.92 mm (Tube 8) and finally to 1.22 mm (Tube 9). The fin density and fin semi-vertex angle were kept constant at 1417 fpm and 10 deg, respectively, for this set.

Finally, three specially enhanced tubes were made by cutting trapezoidally shaped grooves axially along the length of the integral-fin tube (Tube 9). The trapezoidal groove cut axially had a semi-vertex angle of 10 deg and a groove root width of 0.1 mm. Eighty grooves with a pitch of 1 mm were cut and the groove height was increased from 0.7 (Tube 10) to 0.9 (Tube 11) and finally to 1.22 mm, thereby increasing the groove width at the tip from 0.35 to 0.42 to 0.53 mm. The axially cut grooves give three-dimensional pyramidal shaped low fins on all the tubes. It is felt that with such shapes the surface tension pull would be in two directions rather than one, thereby yielding thinner condensate films on the crests.

The test runs were carried out for heat transfer rates ranging from 266 to 4480 W; vapor pressure varying from 150 to 250 kN/m² (abs), and ΔT varying from 3 to 8 K.

Integral-Fin Tubes. Figure 4 shows the variation of the average heat transfer coefficients ($\bar{h}_e$) with ΔT for Tubes 1–4. For each of Tubes 1–4, it is observed that the value of the heat transfer coefficient decreases a little or stays nearly constant with increasing values of ΔT. This variation is essentially similar to that obtained in previous investigations. The best performance is obtained for a fin density of 1417 fpm (Tube 2). It may be noted however that this performance is to be attributed to both the fin density and the fin height as both are varied in this set.

Since previous investigators have also obtained superior performances with a fin density around 1400 fpm, it was decided to conduct further experimentation only with a fin density of 1417 fpm. Thus in the second set of experiments, the semi-vertex angle was reduced first to 20 deg and then to 10 deg (Tubes 5 and 6), with the other parameters held constant. The data obtained with these tubes are plotted in Fig. 5 along with the data of Tube 2. It is seen that there is no significant effect of semi-vertex angle on $\bar{h}_e$. Although there is some scatter, the data for all three tubes lie in one band of ± 10 percent around the mean. This observation is somewhat similar to that made by Marto et al. (1986) with steam.

With a smaller semi-vertex angle, it is possible to have fins with larger height. In the third set of experiments, it was therefore decided to increase the height of the fins of Tube 6 in steps. The data obtained with these tubes along with the data of Tube 6 are plotted in Fig. 6. It is seen that there is a very strong effect of increasing height, the performance improving with each successive cut. The best performance is obtained for Tube 9 with the largest height of 1.22 mm in this set. It yields a maximum value of $\bar{h}_e$ of 16,500 W/m² K at a ΔT of about 3 K corresponding to an enhancement ratio of about 10.3 on the smooth tube value. Tubes with fin heights greater than 1.22 mm could not be made due to fabrication difficulties. If this had been possible, it is likely that an optimum height would have been determined.

It is worth noting that for the data presented for the three sets of experiments, the ratio of fin to bare tube area (A_f/A_o) has varied from 3.16 to 7.05 (see Table 1). The enhancement ratio in each case is greater than the area ratio. Thus it is clear that both surface tension and an increase in surface area have contributed to the improvement in performance.

Finally approximate comparisons are made with the data of previous investigators. Exact comparisons are not possible because of differences in the geometries of tubes tested. The data obtained with Tube 8 are presented in Fig. 7 along with

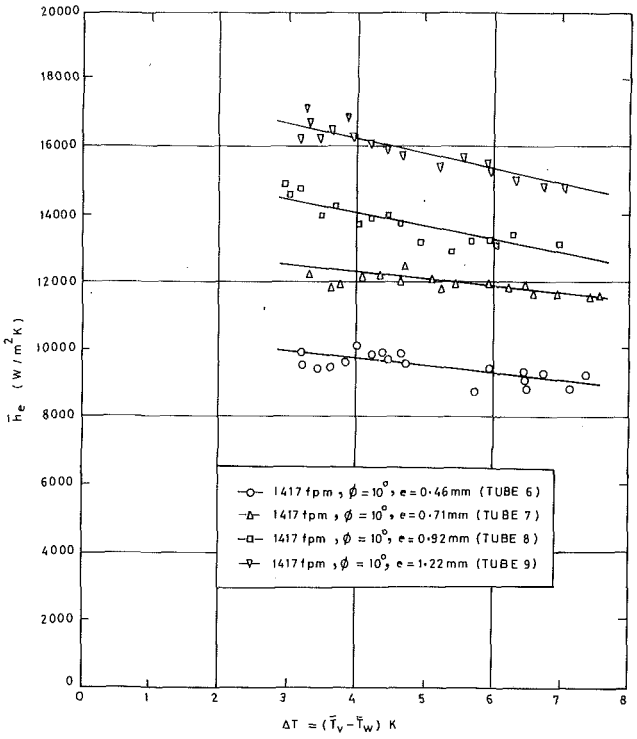

Fig. 6 Variation of $\bar{h}_e$ with ΔT for integral-fin tubes 6-9

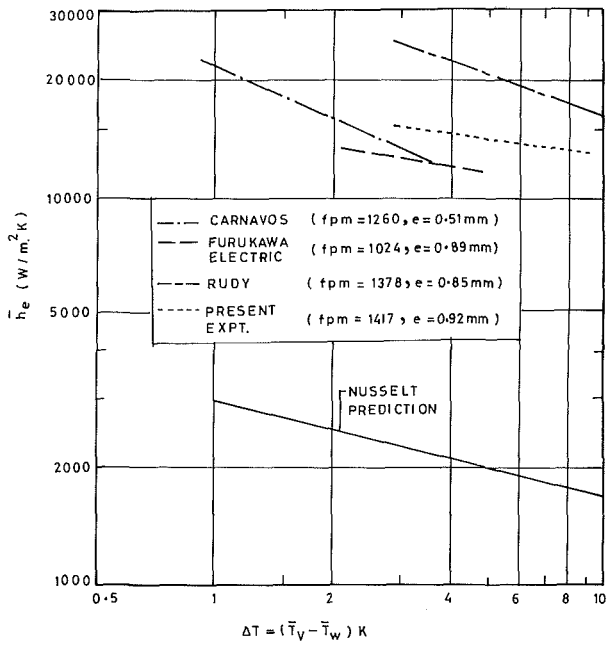

Fig. 7 Comparison of experimental results obtained on integral-fin tube 8 with previous investigations

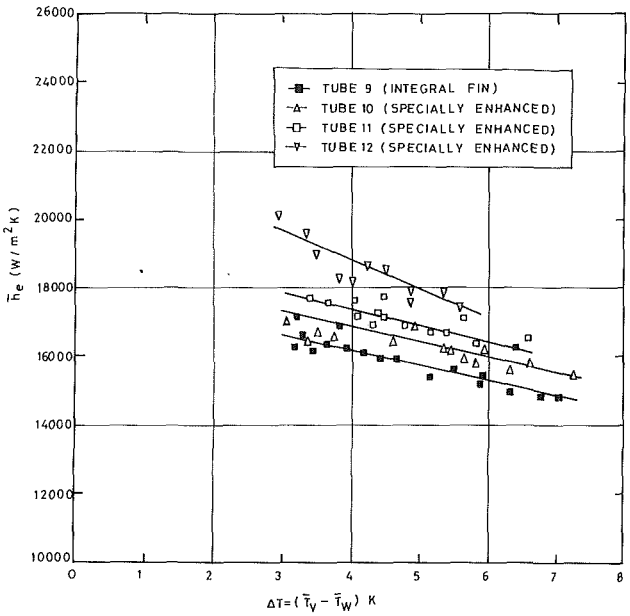

Fig. 8 Comparison of performance of specially enhanced tubes 10-12 with integral-fin tube 9

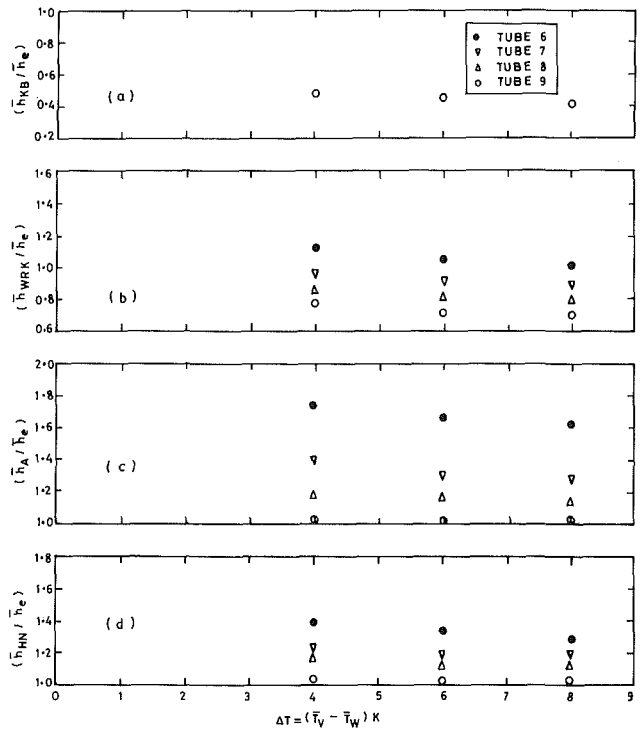

Fig. 9 Comparison of present experimental results with various theoretical models

the R-11 data of Carnavos (1980), Furukawa Electric (1981), and Rudy (1982). It is seen that the present data are of comparable magnitude and lie between the data reported by Rudy and those reported by Furukawa Electric Co.

Specially Enhanced Tubes. Figure 8 shows the results of the experimental investigations on the three specially enhanced condenser tubes (Tubes 10–12). For comparison, the data of Tube 9 are also presented. It can be seen that the maximum value of the heat transfer coefficient increases from 16,500 to 17,400 W/m^2 K at a ΔT of about 3 K when grooves of 0.7 mm are cut in Tube 9. It increases further from 17,400 to 17,800 W/m^2 K when the groove height is increased from 0.7 to 0.9 mm, and from 17,800 to 19,800 W/m^2 K when the height is increased from 0.9 to 1.22 mm. Thus Tube 12 gives a 20 percent increase in $\bar{h}_e$ over the best integral-fin tube (Tube 9). This corresponds to an enhancement ratio of 12.3 on the smooth tube value.

Condensate Flooding Angle. The condensate flooding angle was determined for one integral-fin tube (Tube 8) and all three specially enhanced tubes by measuring the vertical height from the bottom to the point on the fins where complete flooding occurs. For all the tubes, the flooding angle was

found to be essentially independent of the rate of condensation. For Tube 8, an average value of 47.6 deg was obtained, which agreed closely with the values calculated from the theoretical formulae suggested by Honda et al. (1983) and Rudy and Webb (1985). For Tubes 10–12, the flooding angle was found to be almost the same. An average value of 37.5 deg was obtained, which is about 20 percent less than that for Tube 8. This is obviously one of the factors contributing to the improved performance of the specially enhanced tubes.

Comparison With Theoretical Models. Finally the experimental results are compared with the values predicted by the theoretical models of Karkhu and Borovkov (1971), Webb et al. (1985), Adamek (1985), and Honda and Nozu (1987). The comparison is shown in Fig. 9 for $\Delta T = 4$, 6, and 8 K. The results obtained for Tubes 6–9 are used for the purpose.

The range of applicability of the model of Karkhu and Borovkov is restricted. In the present situation, a comparison is possible only with the data for Tube 9. Figure 9(*a*) gives the variation of $(\bar{h}_{KB}/\bar{h}_e)$ with ΔT for this case. It is seen that the model underpredicts the value of the heat transfer coefficient considerably. The values predicted range from 40 to 60 percent of the experimentally measured values.

In order to apply the method suggested by Webb et al., it is first necessary to characterize the condensing surface by a parameter ζ. The method for calculating the value of ζ is not very precise. However, the range of values of ζ for the trapezoidally shaped fins of Tubes 6–9 is likely to be from -0.8 to -1.0. The calculations are therefore done by selecting a probable value of -0.95. The results are presented in Fig. 9(*b*) for Tubes 6–9. It can be seen that for Tube 9, the model underpredicts the values by about 30 percent. However, for Tubes 6–8, the predicted values agree within 25 percent with the experimental results. It should be noted that the predicted value of $\bar{h}_{WRK}$ is sensitive to changes in the value of ζ.

The comparison with the model of Adamek is shown in Fig. 9(*c*). It is seen that the model overpredicts the value of the heat transfer coefficient by about 40 percent for Tubes 7–9. In the case of Tube 6, the overprediction is even more.

The Honda and Nozu model is the latest of the predictive models. From Fig. 9(*d*), it can be seen that this model predicts values within 25 percent of the experimental data for Tubes 7–9 and within 40 percent of the data for Tube 6.

Thus of the four models available, the ones of Webb et al. and Honda and Nozu appear to be the better.

Conclusions

1 The experiments on integral-fin tubes have shown that the value of $\bar{h}_e$ depends on the fin density and fin height, but is not significantly affected by changes in the semi-vertex angle. The best performance has been obtained with Tube 9, which has yielded a maximum value of $\bar{h}_e$ of 16,500 W/m^2 K at a ΔT of about 3 K, corresponding to an enhancement ratio of 10.3.

2 Of the specially enhanced tubes, Tube 12 was found to give the best performance. It yielded a maximum value of $\bar{h}_e$ of 19,800 W/m^2 K at a ΔT of about 3 K, corresponding to an enhancement ratio of 12.3.

3 The experimental results on integral-fin tubes have been compared with the available predictive models. The models of Webb et al. and Honda and Nozu agree best with the present experimental results.

Acknowledgments

The authors express their gratitude to the Council of Scientific and Industrial Research, New Delhi, for supporting this research work.

References

Adamek, T., 1985, "Analytical Model of Film Condensation on Integral-Fin Tubes," *Wärme- und Stoffübertragung*, Vol. 19, No. 2, pp. 145–157.

Beatty, K. O., and Katz, D. L., 1948, "Condensation of Vapours on Outside of Finned Tubes," *Chemical Engineering Progress*, Vol. 44, No. 1, pp. 55–70.

Carnavos, T. C., 1980, "An Experimental Study: Condensing R-11 on Augmented Tubes," ASME Paper No. 80-HT-54, pp. 54–60.

Furukawa Electric, 1981, Technical Commercial Literature, Tokyo, Japan.

Gregorig, R., 1954, "Hautkondensation on feingewellten Oberflachen bei Berucksichtigung der Oberflachenspannungen," *Zeitchrift für Angewandte Mathematik und Physik*, Vol. 5, p. 36.

Honda, H., Nozu, S., and Mitzumori, K., 1983, "Augmentation of Condensation on Horizontal Finned Tubes by Attaching a Porous Drainage Plate," *Proceedings, ASME-JSME Thermal Engineering Joint Conference*, Honolulu, HI, Vol. 3, pp. 289–295.

Honda, H., and Nozu, S., 1987, "A Prediction Method for Heat Transfer During Film Condensation on Horizontal Low Integral-Fin Tubes," ASME JOURNAL OF HEAT TRANSFER, Vol. 109, No. 1, pp. 218–225.

Katz, D. L., and Geist, J. M., 1948, "Condensation of Six Finned Tubes in a Vertical Row," *Trans. ASME*, Vol. 70, pp. 907–914.

Karkhu, V. A., and Borovkov, V. P., 1971, "Film Condensation of Vapour at Finely-Finned Horizontal Tubes," *Heat Transfer, Soviet Research*, Vol. 3, No. 2, pp. 183–191.

Kline, S. J., and McClintock, F. A., 1953, "Describing Uncertainties in Single-Sample Experiments," *Mechanical Engineering*, Vol. 75, pp. 3–8.

Marto, P. J., Mitrou, E., Wanniarachchi, A. S., and Rose, J. W., 1986, "Film Condensation of Steam on Horizontal Finned Tubes: Effect of Fin Shape," *Proceedings, 8th International Heat Transfer Conference*, Vol. 4, pp. 1695–1700.

Pearson, J. F., and Withers, J. G., 1969, "New Finned Tube Configuration Improves Refrigerant Condensing," *ASHRAE Journal*, Vol. 11, pp. 77–82.

Prabhakaran, P., 1987, "Heat Transfer During Film Condensation of R-11 Vapour on Single Horizontal Enhanced Condenser Tubes," Ph.D. Thesis, Mechanical Engineering Dept., Indian Institute of Technology, Bombay, India.

Rudy, T. M., 1982, "A Theoretical and Experimental Study of Condensation on Single Integral-Fin Tubes," Ph.D. Thesis, Mechanical Engineering Dept., The Pennsylvania State University, University Park, PA.

Rudy, T. M., and Webb, R. L., 1985, "An Analytical Model to Predict Condensate Retention on Horizontal Integral-Fin Tubes," ASME JOURNAL OF HEAT TRANSFER, Vol. 107, pp. 361–365.

Webb, R. L., Keswani, S. T., and Rudy, T. M., 1982, "Investigations of Surface Tension and Gravity Effects in Film Condensation," *Proceedings, 7th International Heat Transfer Conference*, pp. 175–180.

Webb, R. L., Rudy, T. M., and Kedzierski, M. A., 1985, "Prediction of the Condensation Coefficient on Horizontal Integral-Fin Tubes," ASME JOURNAL OF HEAT TRANSFER, Vol. 107, pp. 255–270.

Wanniarachchi, A. S., Marto, P. J., and Rose, J. W., 1986, "Film Condensation of Steam on Horizontal Finned Tubes: Effect of Fin Spacing," ASME JOURNAL OF HEAT TRANSFER, Vol. 108, No. 4, pp. 960–965.

Yau, K. K., Cooper, J. R., and Rose, J. W., 1985, "Effect of Fin Spacing on the Performance of Horizontal Integral-Fin Condenser Tubes," ASME JOURNAL OF HEAT TRANSFER, Vol. 107, pp. 377–383.

O. A. Plumb

D. B. Burnett

A. Shekarriz

Department of Mechanical and Materials Engineering,
Washington State University,
Pullman, WA 99164-2920

Film Condensation on a Vertical Flat Plate in a Packed Bed

Film condensation on a vertical isothermal surface submerged in a packed bed was examined experimentally. Results are presented for packed beds consisting of glass beads ranging from 350 μm to 5000 μm in diameter. The condensing fluid was saturated R-11. The experimental results are compared with the theoretical results of Cheng (1981) and White and Tien (1987a). The experimental results are in poor agreement with the Cheng (1981) theory due to the effects of surface tension and variable porosity near the surface. The experimental results are in qualitative agreement with White and Tien (1987a) theory, which accounts for the wall effects. The results indicate that an improved theory that accounts for surface tension is necessary in order to achieve quantitative agreement with the experimental data.

Introduction

Condensation in porous media occurs in a large number of geophysical situations and engineering applications. The particular case of film condensation occurs in heat pipe wicks, geothermal reservoirs, packed bed reactors, and during certain scenarios involving water encroachment near nuclear waste repositories. An understanding of the physical phenomena that affect the condensation rate as well as the ability to predict heat transfer rates during condensation is critical to the understanding and prediction of the overall system performance in these applications.

The problem to be considered is illustrated schematically in Fig. 1. There are several physical phenomena that may have a significant influence on the heat transfer rate. The flow in the liquid film may be either Darcian or non-Darcian, depending upon the magnitude of the Reynolds number based on the pore or particle diameter. Furthermore, there are several possible wall effects that may be important. For granular porous media adjacent to a smooth wall the porosity and hence the permeability and effective thermal conductivity may vary in a fashion that is not well defined. The liquid film may be either thicker or thinner than the grain diameter leading to different approaches to the analysis of the flow in the film. The analyst is also faced with the decision as to whether or not to include the no-slip condition on the liquid velocity at the wall by using the Darcy–Brinkman extension of Darcy's law. Finally, the issue of surface tension or capillary effects has received very little attention.

The first analysis of this problem by Cheng (1981) presents similar solutions for a constant property porous medium assuming Darcy flow. The effect of the no-slip boundary condition, non-Darcy flow, and wall effects on properties have been considered more recently by Kaviany (1986) and White and Tien (1987a). Capillary effects have been analyzed by Plumb (1984) and by Shekarriz and Plumb (1986). Most recently, the first experimental work on film condensation in porous media was reported by White and Tien (1987b). These experiments were conducted using packed beds of spheres and sand as well as foametal and polyurethane foam. The former was used to examine the case of variable porosity near the wall and the latter to examine the constant porosity porous medium.

The work presented here focuses on the packed bed or variable porosity case. The validation of analytical studies mentioned and the identification of conditions under which capillary effects might become important were of primary interest. It may be worth noting that the results of White and Tien (1987a, 1987b) appeared after our study was completed.

Contributed by the Heat Transfer Division and presented at the ASME/AIChE National Heat Transfer Conference, Houston, Texas, July 24–27, 1988. Manuscript received by the Heat Transfer Division March 24, 1988. Keywords: Condensation, Packed and Fluidized Beds, Porous Media.

Theoretical Results

Previous theoretical results, which will be compared with our experimental results, are summarized below. For film condensation on a vertical isothermal surface the results of Cheng (1981), which assume constant properties and Darcy flow, result in the following:

$$\frac{\mathrm{Nu}_x\sqrt{2\mathrm{Ja}}}{\sqrt{\mathrm{Ra}_x}}=\left[1+\frac{2\mathrm{Ja}}{\pi}\right]^{1/2} \tag{1}$$

Since our experiment is designed to measure the overall Nusselt number as opposed to the local Nusselt number, the integrated form of equation (1) is of interest

$$\mathrm{Nu}_L\sqrt{\frac{2\mathrm{Ja}}{1+2\mathrm{Ja}/\pi}}=\sqrt{2\mathrm{Ra}_L} \tag{2}$$

For a packed bed with experimental variation in porosity running from unity at the wall to the porosity of the bed several particle diameters away from the wall, White and Tien (1987b) give the following approximation to their theoretical results:

$$\mathrm{Nu}_x\left(\frac{\mathrm{Ja}}{\mathrm{Ra}_x}\right)\left(\frac{x}{D}\right)\sim 0.56\left[\frac{x^2}{D^2}\,\frac{\mathrm{Ja}}{\mathrm{Ra}_x}\right]^{0.6} \tag{3}$$

From equation (3) the overall Nusselt number can be shown to be

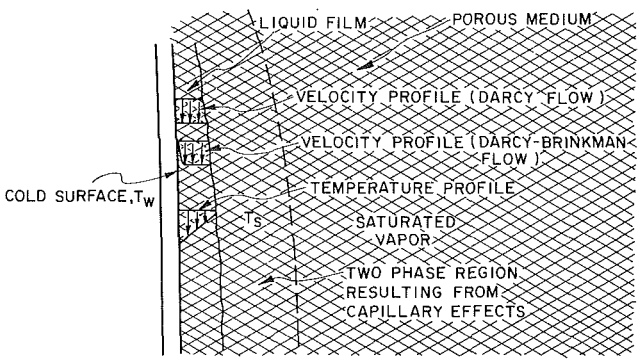

Fig. 1 Film condensation on a vertical surface in a packed bed

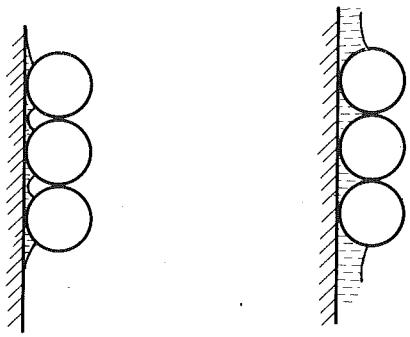

Fig. 2 (*a*) Liquid film thickness much less than bead radius causes liquid holdup due to surface tension; (*b*) a thicker liquid film results in less holdup

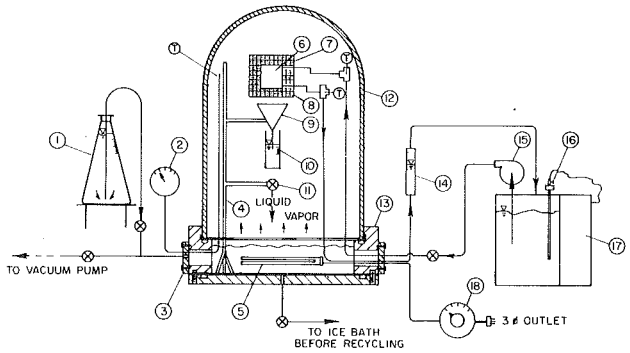

Fig. 3 Schematic diagram of the experimental apparatus. Components are: (1) R-11 container, (2) dial pressure gage, (3) inlet/outlet port, (4) support, (5) immersion heater, (6) condenser, (7) glass beads, (8) wire mesh screen, (9) funnel, (10) measuring cup, (11) solenoid valve, (12) glass bell jar, (13) aluminum base, (14) rotometer, (15) pump, (16) thermoregulator, (17) constant-temperature bath, and (18) power station.

$$\mathrm{Nu}_L\left(\frac{L}{D}\right)\left(\frac{\mathrm{Ja}}{\mathrm{Ra}_L}\right)\sim 0.93\left[\left(\frac{L^2}{D^2}\right)\frac{\mathrm{Ja}}{\mathrm{Ra}_L}\right]^{0.6} \tag{4}$$

One would expect capillary or surface tension effects to enter in two different ways. First, if the liquid film thickness is much less than the particle diameter, it would be expected that surface tension will hold up liquid, as illustrated in Fig. 2. This liquid hold up would cause the heat transfer or condensation rate to be decreased because of the greater average film thickness. If the film thickness is greater than the particle diameter, there exists the potential to transport liquid normal to the surface via capillary action. This effect is analyzed by Plumb (1984) and Plumb and Shekarriz (1986). They demonstrate that capillary transport can act to thin the liquid film and hence increase the condensation rate. However, the analysis neglects the effect of the counterflow of vapor toward the liquid film and is therefore not conclusive.

Experimental Apparatus and Procedure

The test apparatus is schematically illustrated in Fig. 3. The experimental setup may be broken into four main subsystems: (1) an evacuation/pressurization system to minimize noncondensible gases and isolate the test section from the environment, (2) a cooling system to supply and maintain a constant temperature cooling liquid to the condenser, (3) a boiling system for vaporization of the working fluid, and (4) a measurement system, for measuring desired temperatures, pressures, and mass condensation rate.

The evacuation/pressurization system included an octagonal aluminum base with eight inlet/outlet ports, a 6.3 mm (1/4 in.) thick glass bell jar measuring 305 mm (12 in.) in diameter at the base by 457 mm (18 in.) in height, two longitudinal straps to secure the bell jar to the base, and a vacuum pump. O-rings were used at the contact surfaces between the ports and the base and the bell jar and the base to minimize leakage. System components routed through the ports were sealed either by an appropriate tube or pipe fitting or by application of a nitrite-based adhesive. The glass bell jar was chosen to allow full observation of the experiments.

The cooling system was composed of a 450-W constant temperature bath with a thermoregulator, a 62-W centrifugal pump, and a rotometer to measure coolant flow rate. Copper tubing was used to connect the cooling system to the condenser. Cooling liquid flowed through the copper condenser in a labyrinth fashion to create as uniform a surface temperature as possible. The condenser measured 7.6 cm (3.0 in.) in length by 5.7 cm (2.25 in.) in width by 2.5 cm (1.0 in.) in thickness. Except for the front and back surfaces, the condenser was insulated with 2.5 cm (1.0 in.) thick nylon. All connecting tubes and cooling lines were insulated with a fiberglass-based insulation tape.

The temperature difference between the inlet and outlet cooling liquid was measured using a differential thermocouple and a potentiometer accurate to ± 0.025°C. This difference was less than 1°C for all tests reported. Surface temperature was measured directly by a copper-constantan thermocouple embedded on the surface inside a 1.6 mm (1/16 in.) deep hole. Three thermocouples were placed on the outside edge of the condenser to measure variations in surface temperature. These temperatures did not vary by more than 1°C, which allowed for measurement of the surface temperature by the single

Nomenclature

C_P = specific heat, J/kg-K
D = bead diameter, m
g = gravitational acceleration, m/s^2
h = heat transfer coefficient, W/m^2-K
h_{fg} = latent heat of vaporization, J/kg
Ja = Jacob number $= C_{pl}(T_{\mathrm{SAT}}-T_w)/h_{fg}$
k = effective thermal conductivity, W/m-K
K = permeability, m^2
L = length of condenser surface, m
m = condensation rate, kg/s
Nu = Nusselt number $= hL/k$
Ra = Darcy–Rayleigh number $= gKL(\rho_l-\rho_v)/\mu\alpha$
T_W = surface temperature, K
T_{SAT} = saturation temperature, K
x = streamwise coordinate (vertical), m
α = effective thermal diffusivity, m^2/s
μ = dynamic viscosity of liquid, kg/m-s
ρ = density, kg/m^3
ϕ = porosity

Subscripts

l = liquid phase
L = based on L
s = solid phase
v = vapor phase
x = based on x

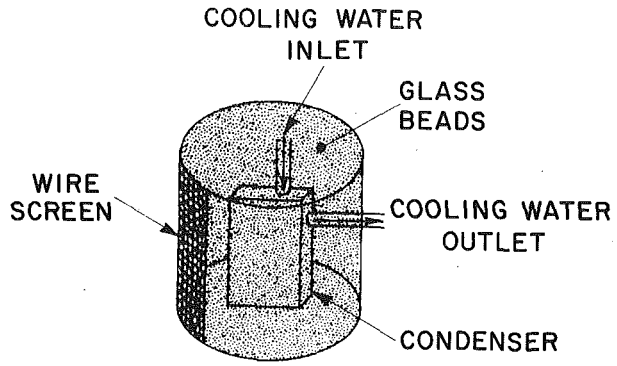

Fig. 4 Schematic of condenser in packed bed

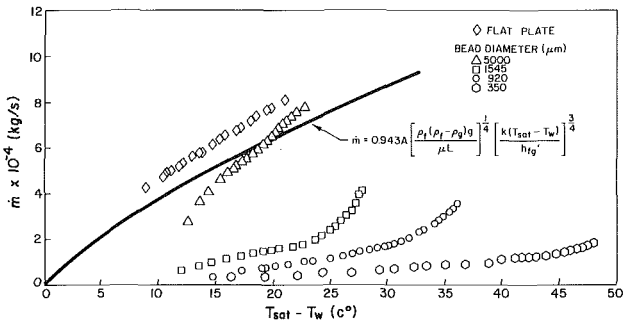

Fig. 5 Experimental results for packed bed and the vertical surface in the absence of the packed bed

embedded thermocouple. In addition, four thermocouples were positioned in the packed bed. These thermocouples were intended to assist in determining the location of the liquid–vapor interface and establish the existence of the two-phase region resulting from surface tension effects. Two thermocouples and a pressure gage were used to determine the saturation temperature in the chamber. A 10-channel digital thermometer was used in conjunction with the thermocouples to yield actual temperature measurements.

An evacuation-injection procedure was used to initiate the experiment. The system was evacuated to approximately 3 torr (0.1 in. Hg) absolute pressure. Refrigerant 11 (R-11) was injected into the system until the system pressure increased to about 500 torr (20 in. Hg) absolute. The injection process was stopped and the system was again evacuated. The advantage of evacuating, injecting R-11, then evacuating again is to considerably reduce the amount of noncondensible gases. The mass of noncondensible gases was calculated based on the above-measured pressures and found to be less than 0.01 percent, which is sufficiently small to insure a negligible effect on condensation rate.

Once the system was fully evacuated, R-11 was injected again. Enough R-11 was injected to cover the heating coils of a 2-kW immersion heater placed near the base of the system. When the pressure reached approximately 1 atm absolute, condensation was initiated by allowing the cooling fluid to pass through the condenser. Condensate was collected in a 100 ml nylon cup. The cup incorporated a graduated viewing glass and could be emptied by use of a solenoid valve. Condensation rates were determined by measuring the time it took to collect 100 ± 3 ml of condensate.

Experiments were conducted using glass beads 350, 920, 1545, and 5000 μm in diameter. The beads were randomly packed in a cylindrical container approximately 18 cm (7 in.) in diameter and 23 cm (9 in.) high fabricated from a fine mesh screen as shown in Fig. 4. Values of the permeability were 7.5×10^{-11}m^2, 3.5×10^{-10}m^2, 1.2×10^{-9}m^2, and 2×10^{-8}m^2, respectively. These values were measured experimentally in a constant head permeameter except for the 350 μm beads. In this case the permeability was determined by extrapolating the plot of permeability versus particle diameter obtained from the measurement on the larger three bead sizes. The results are consistent with those presented in Bear (1972) in that permeability is proportional to the square of particle diameter. In all cases the porosity of the beds was approximately 0.35, which is typical for randomly packed spheres. The 5000 μm beads varied in size by ± 100 μm. The 1545 μm beads varied in size from 1410–1680 μm. The 920 μm beads varied in size from 840–1000 μm and the 350 μm size beads varied in size from 280 to 420 μm. Only the 1545 μm beads had a significant amount of beads that were not spherical in shape.

Experimental Results

An experiment was first run in the absence of a packed bed to ensure that the results obtained were consistent with the Nusselt analysis and previous experimental studies of film condensation from a vertical isothermal surface. Liquid properties were calculated using the average of the measured wall and saturated temperatures. These results are shown in dimensional form in Fig. 5. The film Reynolds number for the data reported falls in the range of 15 to 50. The data are consistent with previous experimental studies in that the condensation rate exceeds the Nusselt theory by approximately 20 percent (Lienhard, 1987). The solid line in Fig. 5 represents the Nusselt theory (Lienhard, 1987). The results were both steady and repeatable.

Dimensional results for condensation rate as a function of wall subcooling are shown in Fig. 5 for all four bead sizes. For the 5000 μm beads the experimental results increase approximately as the degree of subcooling to the first power, as opposed to the Nusselt theory, which predicts the 3/4 power. In this case the film thickness as predicted from the Cheng (1981) theory is roughly two orders of magnitude smaller than the particle diameter. Hence, we expect liquid holdup due to surface tension as illustrated in Fig. 2 to be evident. The experimental results are consistent with this argument in that at the lower condensation rates the data fall below the Nusselt theory and at high condensation rates they approach the results for a continuous fluid. The results for the smaller three bead sizes all show a different trend. At lower condensation rates, corresponding to low wall subcooling, the data indicate the condensation rate is approximately proportional to temperature different to the 1/2 power as predicted by the Cheng (1981) theory. In all cases, at a high temperature difference the results show a distinct increase in condensation rate above the 1/2 power relationship. Inertial effects are ruled out since calculations indicate the flow to be well within the Darcy regime. We hypothesize that this is the point at which the liquid film thickness is of the same magnitude as the bead diameter and capillary transport away from the surface is taking place. However, for the smaller beads with lower permeability the film thickness should be greater. Thus, one would expect the capillary transport to occur at lower subcooling for smaller beads. We can only speculate with regard to reasons for this apparent contradiction. It is possible that for the lower permeabilities and a thick liquid film the capillary effects are less pronounced because the low permeability is inhibiting the flow of vapor toward the condenser surface and the surface tension driven flow of liquid away from the surface.

The thermocouples that were located in the packed bed always indicated that saturation temperature, except for one that was very close to the surface. This thermocouple indicated subcooled liquid at high condensation rates, which is

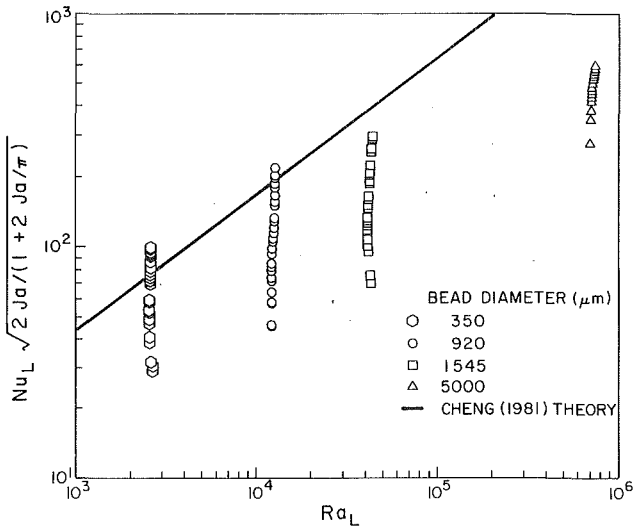

Fig. 6 Dimensionless overall condensation rate as a function of the Darcy-Rayleigh number

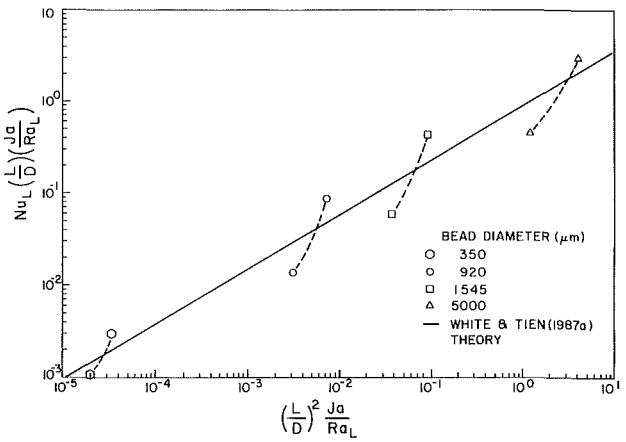

Fig. 7 Comparison of experimental results with the White and Tien theory

to be expected. No correspondence between these thermocouple readings and the change in slope of the experimental results shown in Fig. 5 was detected.

The experimental results are plotted in dimensionless form for comparison with the Cheng theory (1981) in Fig. 6. The effective thermal conductivity utilized in putting the data in this format was estimated using

$$k = \phi k_l + (1-\phi)k_s \tag{5}$$

Although this is an approximation, it has been shown to be a good approximation (Nozad, 1983) when the properties of the solid and liquid phases do not differ by more than an order of magnitude, as is the case with R-11 and glass beads. The porosity was assumed to be 35 percent, which is appropriate for a packed bed of uniform spheres. Since the experimental data represent only four permeabilities, only four Rayleigh numbers between 10^3 and 10^6 result. The experimental results for the overall heat transfer fall below those predicted by the Cheng theory except for the two smaller bead sizes at high wall subcooling. The agreement improves at lower Rayleigh numbers the results clearly indicate the importance of an additional parameter or parameters. We assume that these parameters should be indicative of surface tension effects and wall effects. For small film thicknesses the ratio of film thickness to bead diameter may be of importance, whereas at larger film thicknesses the ratio of capillary (imbibition) forces to gravitational (drainage) forces should be of importance. Various attempts to rescale the data with a third parameter, such as the ratio of film thickness to bead diameter, were unsuccessful. It should also be pointed out that the Cheng (1981) theory does not asymptotically approach the Nusselt theory as the permeability becomes large. The Cheng (1981) theory, in fact, yields a higher condensation rate. This is because Darcy's law does not approach Navier-Stokes as the permeability becomes large. Hence, for the large-diameter beads, even if the film thickness was greater than the bead diameter, good agreement between the Cheng (1981) theory and the experimental result might not be expected.

Figure 7 compares our experimental results with the theory of White and Tien (1987a) given by equation (4). For the purpose of illustration we have plotted only the extreme data points. We note that the White and Tien (1987b) data fall in a broad band below the theoretical result (by as much as 50 percent) and better fit a 0.65 power law. In the White and Tien study the condenser wall was cooled thermoelectrically using the Peltier effect. Ten thermoelectric devices were used and controlled so that local heat transfer coefficients could be measured. The test section was 30 cm high and 1.6 cm square and completely filled with the packing material (glass beads or coarse sand). Hence the vapor flow to the top end of the condenser section had to traverse the entire packed bed before condensing. This, coupled with the relatively small cross-sectional area (1.6 cm square), may account for the experimental data falling below that reported in this study. It is also worth noting that for film condensation in the absence of a porous medium the majority of their results fall on or below the Nusselt theory, even for film Reynolds numbers as high as 25, while in this study the results fall above the Nusselt theory. White and Tien (1987b) report only local results; thus a direct plot of their results on Fig. 7 is not possible. Our data for all four bead sizes span the White and Tien theory. At low wall subcooling and hence, small film thickness, the data fall below the theory, persumably due to liquid holdup resulting from surface tension. For high wall subcooling the experimental results fall above the theory. We are tempted to argue again that this is a result of surface tension or capillary effects due to imbibition of liquid away from the wall and subsequent drainage in a two-phase region, as proposed by Plumb (1984). However, the same trend is evident for all four bead sizes, and in the case of the 5000 μm beads the estimated film thickness is nearly two orders of magnitude smaller than the bead size. In this case neither the Cheng (1981) theory or the White and Tien (1987a) theory should be expected to be appropriate.

Conclusions

Experiments were conducted to measure the condensation rate during film condensation on a vertical surface in a packed bed. The results are compared with the Cheng (1981) theory and the White and Tien (1987a) theory. Although the results are in qualitative agreement with the latter theory, the data indicate that the theory requires an additional parameter, presumably indicative of the effects of surface tension.

For large-diameter glass beads when the liquid film is less than the bead diameter in thickness, surface tension effects decrease the heat transfer by holding up liquid and creating a locally thickened film. This effect is most pronounced when the film is very thin compared to the bead diameter. For cases where the liquid film thickness is greater than the bead diameter, capillary transport of liquid away from the film can enhance the heat transfer. This effect was more pronounced and occurred at a lower temperature difference for higher permeability packed beds.

Acknowledgments

The authors would like to acknowledge the support of the National Science Foundation under grant No. CBT-84-18497. The critical comments of the reviewers were extremely helpful in preparing the final manuscript.

References

Bear, J., 1972, *Dynamics of Fluids in Porous Media*, America Elsevier Pub. Co., New York.

Cheng, P., 1981, "Film Condensation Along an Inclined Surface in a Porous Medium," *Int. J. Heat Mass Transfer*, Vol. 24, pp. 983–990.

Kaviany, M., 1986, "Boundary Layer Treatment of Film Condensation in the Presence of a Solid Matrix," *Int. J. Heat Mass Transfer*, Vol. 29, pp. 951–954.

Lienhard, J. H., 1987, *A Heat Transfer Textbook*, 2nd ed., Prentice-Hall, Inc., New Jersey, pp. 391–402.

Nozad, I., 1983, "Effective Thermal Conductivities for Two- and Three-Phase Systems: A Theoretical and Experimental Study," Ph.D. Thesis, Chemical Engineerinng Department, University of California, Davis.

Plumb, O. A., 1984, "Capillary Effects of Film Condensation in Porous Media," presented at the 19th AIAA Thermophysics Conference, Snowmass, CO.

Shekarriz, A., and Plumb, O. A., 1986, "A Theoretical Study of Filmwise Condensation Using Porous Fins," ASME Paper No. 86-HT-31.

White, S. M., and Tien, C. L., 1987a, "Analysis of Laminar Film Condensation in a Porous Medium," *Proc. of the 1987 ASME–JSME Thermal Engineering Joint Conference*, Honolulu, HI, Vol. 2, pp. 401–406.

White, S. M., and Tien, C. L., 1987b, "An Experimental Investigation of Film Condensation in Porous Structures," *Proc. of the 6th International Heat Pipe Conference*, Grenoble, France.

H. M. Paynter
Thermodynamics Research Center,
Texas A&M University,
College Station, TX 77843

E. P. Fahrenthold

G. Y. Masada

Department of Mechanical Engineering,
University of Texas,
Austin, TX 78712

Simple Pressure and Energy State Equations for Lennard-Jones (12,6) Fluid

A recently published (Paynter, 1985, 1988) simple veridical equation of state represents a direct extension and generalization of the classical van der Waals equation, yet at the same time remains consistent with modern nonanalytical expansions about the critical point. With the use of this particular equation of state, compact expressions are here obtained for the pressure and configurational energy of the Lennard-Jones (12, 6) fluid, together with a saturation curve and other coexistence properties.

1 Introduction

The Lennard-Jones (LJ) fluid has been widely studied both by theoretical and by computer simulation methods. While known to represent no real intermolecular potential, it nevertheless provides a convenient model for testing theories purporting to relate molecular properties to bulk fluid properties. For perturbation theories a reasonably accurate equation of state (EOS) for the Helmholtz free energy is required over a sufficiently wide range of densities and temperatures. Thanks to the efforts of many investigators over the last three decades the existing Monte Carlo/molecular dynamics (MC/MD) simulation data are now adequate for such a synoptic representation.

Nicolas et al. (1979) provided an equation of state (EOS) for a Lennard-Jones fluid. This work adopted a multiparameter expansion to represent the equilibrium data in a form suitable only for computer-based models. In contrast, we have adopted a simpler EOS (Paynter, 1985, 1988) capable of yielding better fits at low temperature/high density and at high temperature/low density while at the same time remaining consistent with virial coefficients, and incorporating a *nonclassical* critical region, here defined as a nonanalytic critical isotherm. This approach takes cognizance of a program by Wagner and others at Bochum (Ewers and Wagner, 1979) as well as being guided by the results of Haar and coworkers (Harr and Shenker, 1970, 1971; Kohler and Haar, 1981) and of Hall and Hacker (1982, 1983) and Hacker and Hall (1985).

The particular set of results presented has been calibrated in terms of the best current estimates of the critical constants (P_c, ρ_c, T_c, Z_c) while providing reasonable fits to the second, third, and fourth virial coefficients as analytically derived by Barker and colleagues (Barker and Monaghan, 1962; Barker et al., 1966).

2 Scaled Variables

The LJ (12, 6) fluid is characterized by the intermolecular repulsion-attraction potential

$$u/\epsilon = 4[(\sigma/r)^{12} - (\sigma/r)^6] \tag{1}$$

Extensive experimental data are now available for this artificial model fluid based upon many MC/MD computer simulations, each employing N particles within a unit cell volume V.

It is customary to nondimensionalize all such resullts by utilizing as scaling parameters the molecular diameter, σ, and the energy depth ϵ, together with the Boltzman constant k. Resulting normed variables are then conventionally defined as

$$T^* = (k/\epsilon)T = 1/(\beta\epsilon) \tag{2}$$

$$\rho^* = (N\sigma^3)/V \tag{3}$$

$$P^* = (\sigma^3/\epsilon)P \tag{4}$$

$$U^* = U/(N\epsilon) \tag{5}$$

For any such fixed intermolecular potential the resultant scaled critical constants P_c^*, ρ_c^*, T_c^* must necessarily be fixed numbers, as is also the case for the critical compressibility (Z_c) and the Riedel parameter (ψ_c), where

$$Z_c = P_c^*/(\rho_c^* T_c^*) \tag{6}$$

$$\psi_c = [d(\ln P_v^*)/d(\ln T^*)]\,|_{T^* = T_c^*} \tag{7}$$

with P_v^* the vapor pressure.

3 Virial Coefficients

Equilibrium properties of the LJ fluid can be obtained from the Helmholtz energy function A, expressed in terms of number density (ρ^*) and absolute temperature ($T^* = 1/\tau^*$), and taken here as the dimensionless Massieu potential $J = \beta A = A/(kT)$.

Then given J, one can obtain the compressibility factor Z as

$$Z = P^*/(\rho^* T^*) = \rho^* \partial J/\partial \rho^* = 1 + \sum_{k=2}^{\infty} B_k(T)\rho^{k-1} = 1 + B\rho + C\rho^2 + D\rho^3 + \ldots \tag{8}$$

where B_k is the kth virial coefficient, depending only upon temperature. The existence of this virial expansion implies that J itself can be correspondingly expanded in the form

$$J = J_o(\tau) + \sum_{k=2}^{\infty} B_k(\tau)\rho^{k-1}/(k-1) \tag{9}$$

With J dimensionless, it is convenient also to use the dimensionless measures B_k^*, τ^*, and ρ^*. Thus given J we obtain the general results

$$Z = \rho^*[\partial J/\partial \rho^*] = 1 + \sum_{k=2}^{\infty} B_k^*(\tau^*)(\rho^*)^{k-1} \tag{10}$$

$$U^* = \partial J/\partial \tau^* = \sum_{k=2}^{\infty} [dB_k^*(\tau^*)/d\tau^*](\rho^*)^{k-1}/(k-1) \tag{11}$$

Our approach here is to *fit* the EOS parameters from the $P^*(\rho^*, \tau^*)$ data and then to *predict* the U^* values as a validation check.

Contributed by the Heat Transfer Division and presented at the Tenth Symposium on Thermophysical Properties, Gaithersburg, Maryland, June 20-23, 1988. Manuscript received by the Heat Transfer Division November 23, 1988. Keywords: Thermophysical Properties.

From Lebowitz (1969) we know that

$$B_{i+1}(\tau) = \tau^{i/4} \sum_{j=0}^{\infty} b_{ij} \tau^{j/2} \tag{12}$$

with the particular results

$$B(\tau) = \tau^{1/4} \sum_{j=0}^{\infty} b_j \tau^{j/2} \tag{13}$$

$$C(\tau) = \tau^{1/2} \sum_{j=0}^{\infty} c_j \tau^{j/2} \tag{14}$$

$$D(\tau) = \tau^{3/4} \sum_{j=0}^{\infty} d_j \tau^{j/2} \tag{15}$$

While these series are only weakly convergent at lower temperatures, nevertheless, Hirschfelder et al. (1954), Barker and Monaghan (1962), and Barker et al. (1966) have been able to exploit these series for the lower virial coefficients, while Hansen (1970) and Ashurst (1976, 1977) have employed the Lebowitz expansions for the free energy at high temperatures.

Recognizing the singular role played by $B(\tau)$, we adopted the following form for $B^*(T^*)$ for the LJ (12, 6) fluid:

$$B^* = (\tau^*)^{\mu} (b_o + b_1 X) \tag{16}$$

$$X = \exp[\gamma_1 (\tau^*)^{1/2} + \gamma_2 \tau^*] \tag{17}$$

This particular form for B^* was chosen because it could meet several significant conditions:

(1) It yields exact results for the square well fluid (SWF) at all temperatures, with zero values for μ and γ_1;

(2) It converges to exact results for the LJ (12, 6) fluid at high temperatures with $\mu = 1/4$ and with suitably constrained values for the remaining constants b_o, b_1, γ_1, γ_2.

Regression constants determined in this study for correlations of the second, third, and fourth virial coefficients are provided in Appendices A and B. The parameters adopted for B^* are

$$\gamma_1 = 0.8690486 \tag{18}$$

$$\gamma_2 = 0.20 \tag{19}$$

$$b_o = 7.429586 \tag{20}$$

$$b_1 = -4.412604 \tag{21}$$

These parameters produce an accurate four-parameter model for $B^*(T^*)$.

Having so fitted B^*, the transformed temperature variable X is then frozen in form, and the following expressions are assumed for the third and fourth virial coefficients:

$$C^* = (2\pi/3)^2 (\tau^*)^{1/2} (c_o + c_1 X + c_2 X^2 + c_3 X^3) \tag{22}$$

$$D^* = (2\pi/3)^3 (\tau^*)^{3/4} (d_o + d_1 X + d_2 X^2 + d_3 X^3 + d_4 X^4 + d_5 X^5 + d_6 X^6) \tag{32}$$

These forms are known to yield exact results for the SWF (Hirshfelder et al., 1954) by letting the exponents on τ^* vanish; they yield excellent approximations to the LJ coefficients with up to four precision points for C^*, and seven for D^*. The coefficients c_i and d_i are given in Appendix A. However, an efficient EOS will employ fewer parameters; these formal expansions are most useful as interpolating devices and as analytical probes.

4 Extended Virial Coefficients

Given MC and MD simulation data along any isotherm $\tau = \tau_o$ in the form of $Z = Z(\rho, \tau_o)$, together with the value of $B^* = B^*(\tau_o)$, corresponding sets of values $Y_x(\rho)$ can be found where

$$Y_x = [(Z-1)/\rho^* - B^*]/\rho^* \tag{24}$$

By further partitioning all such data into values corresponding to densities respectively below and above critical density, values for $Y_<(\rho^* < \rho_c^*)$ and $Y_>(\rho^* > \rho_c^*)$ can be grouped together, where the subscripts "<" and ">" refer, respectively, to values below and above critical density. In this way the pairs $[C_<, D_<]$ and $[C_>, D_>]$ can be found by linear regression of the expressions

$$Y_< = C_< + D_< \rho^* \tag{25}$$

$$Y_> = C_> + D_> \rho^* \tag{26}$$

If the data for subcritical and supercritical densities are separately processed it is found that $C_<$ approximates C^* and $D_<$ approximates D^*; in contrast, $C_>$ and $D_>$ bear no simple relation to C^* and D^*. This suggests that while we recognize the inability of $C_< \cong C^*$ and $D_< \cong D^*$ to represent high-density properties, we continue to exploit the "fourth-order" character of the isotherms. This can be accomplished simply by *defining* a set of *extended* virial coefficients in the fashion (for $k > 2$)

$$B_{kx} = B_{k<} F + B_{k>} [1 - F] \tag{27}$$

where F is an appropriate switching function. Consistent with the classical Benedict-Webb-Rubin EOS (Cooper and Goldfrank, 1967) as well as with the Nicolas et al. (1979) EOS for the LJ fluid this function has been taken as

$$F(\rho_r) = \exp(-\gamma \rho^2) \cong \exp[(\rho/\rho_c)^2 \ln(1/2)] \tag{28}$$

Fitted values of $C_> = B_{3>}$ and $D_> = B_{4>}$ are given in Appendix B, as well as correlations of these coefficients with B^*.

5 Hall Plots of Isochores

It is well known that isochores of P versus T and of P/T versus $1/T$ are nearly linear; however, even this residual curvature is largely eliminated when P/T (or alternatively the compressibility factor $Z = PV/kNT$) is plotted against the second virial coefficient B, instead of against $1/T$. This noteworthy fact was beneficially utilized by Hall and Hacker (1982, 1983) who made extensive use of the variable $X_H = (B_c - B)/B_c$, with B_c the value of B at the critical temperature $T = T_c$. When this observation is then combined with the earlier cited results of Haar and collaborators, particularly in a critically expanded form (Paynter, 1988), it becomes clear that much of the information content in any EOS is contained in the detailed structure of $B(T)$.

The approximate location of the critical point is clearly evident in any form of Hall plot, with the "fan" of isochores in the neighborhood of $\rho^* \cong 0.3$ "radiating" about the critical point. Once the virial coefficient $B_c^* = B^*(T_c^*)$ has been reasonably determined, one can then obtain directly the Y-intercept values, Y_{BC}, on a translated vertical axis corresponding to

$$X^c = B^* - B_c^* \tag{29}$$

and thus determine a new origin through an *inferred* critical point so as to obtain

$$Y^c = (Z-1)/\rho^* - (Z^c - 1)/\rho^* = Y_{BO} - Y_{BC} \tag{30}$$

where $Z^c = Z(T_c^*)$ is the critical isotherm for the compressibility factor.

Thus by combining the results of Haar and co-workers and Hall and Hacker we can anticipate that for *any* pure substance a plot of the transformed variables

$$Y_H = (Z - Z^c)/\rho \tag{31}$$

$$X_H = B - B^c \tag{32}$$

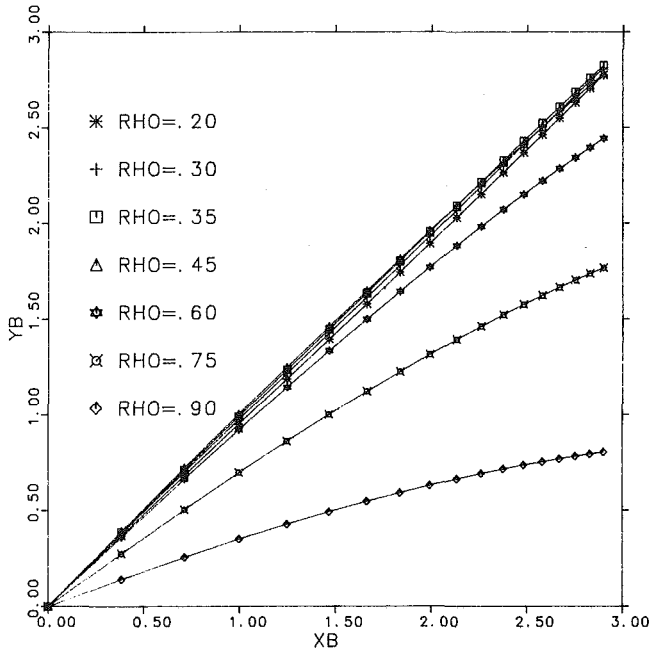

Fig. 1(a) Hall plot of $Y_B = (Z - Z^C)/\rho^*$ versus $X_B = B^*(T^*) - B^*(T_c^*)$ for Lennard-Jones fluid, in the form of isochores at temperatures above the critical temperatures ($T^* > 1.30$); markers represent data calculated using the virial coefficient correlations described in sections 3 and 4

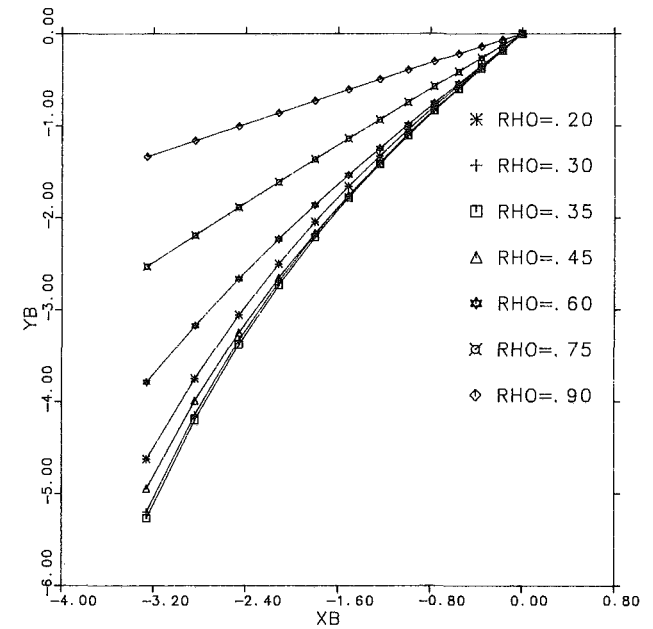

Fig. 1(b) Hall plot of $Y_B = (Z - Z^C)/\rho^*$ versus $X_B = B^*(T^*) - B^*(T_c^*)$ for Lennard-Jones fluid, in the form of isochores at temperatures below the critical temperatures ($T^* < 1.30$); markers represent data calculated using the virial coefficient correlations described in sections 3 and 4

will always yield a family of nearly linear curves, all passing through an origin at the critical point and whose slopes are all less then, but of the order of, unity. Indeed for the classical van der Waals equation and for many of its extensions and generalizations this family collapses to a single line of unity slope.

We have exploited this substantial simplification by correlating and so plotting for the LJ (12, 6) fluid the quantity

$$Y_B = (Z - Z^c)/\rho^* \tag{33}$$

against $X_B = \Delta_c B^* = B^*(T^*) - B^*(T_c^*)$. Figure 1 ($a$) shows such representative isochores above the critical temperature, while Fig. 1 (b) depicts these same isochores below the critical temperature. These results suggest that the dominant effect of C^* and D^* is simply to reduce the isochoric slope; the task is then to determine this slope in terms of density, as in Section 7, below.

6 Critical Isotherm

The above procedure indicates how the compressibility factor along the critical isotherm $Z^c = Z(\rho^*)$ can be estimated directly from the raw experimental data. On the other hand, the previously cited references (Paynter, 1985, 1988) gave a *canonical form* for the critical isotherm as

$$Z^c = Z_c[1 + (\rho_r - 1)^3 M]/\rho_r \tag{34}$$

where $\rho_r = \rho/\rho_c$ and $Z_c = P_c V_c/kNT_c$. Fluid models having a *classical* critical region (e.g., van der Waals fluid) would have $M = 1 + m(\rho_r)$, while *nonclassical* and generally *nonanalytical* critical domains can be represented by $M = |\rho - 1|^{\delta - 3}[1 + m(\rho_r)]$; clearly the classical situation corresponds to a critical exponent $\delta = 3$.

In all cases, the modulus function m can be represented similar to the virial coefficients, namely

$$m = m_< F + m_>[1 - F] = m_> + [m_< - m_>]F \tag{35}$$

Consistent with classical models and virial expansions we can again take $F = \exp(-\gamma\rho_r^2)$ and $m_< = \sum_{k=1}^{\infty} m_{k<}\rho_r^k$; $m_> = \sum_{k=1}^{\infty} m_{k>}\rho_r^k$.

For the LJ data it is found that $\delta \cong 4$ and all m coefficients are negligible except for $m_{1<} = 1.0$ and $m_{2>} = 0.15$. Thus we obtain

$$m = [m_1\rho_r]F + [m_2\rho_r^2][1 - F] \tag{36}$$

and finally

$$Z^c = (1/3)\{1 + [(\rho_r - 1)^3 |\rho_r - 1|][1 + m]\}/\rho_r \tag{37}$$

In contrast to the earlier Nicolas et al. (1979) EOS, which assumed a classical critical region (with $T_c^* = 1.35$, $\rho_c^* = 0.35$, $P_c^* = 0.142$) we have fitted our EOS to a nonclassical critical domain with the adopted critical constants

$$T_c^* = 1.30 \tag{38}$$

$$\rho_c^* = 0.30 \tag{39}$$

$$P_c^* = 0.13 \tag{40}$$

resulting in the values

$$\text{Critical compressibility factor: } Z_c = 1/3 \tag{41}$$

$$\text{Riedel parameter: } \psi_c = 6.1 \tag{42}$$

7 Simplified EOS

The previous sections have suggested that most of the information content in any EOS is contained in the detailed structure of two particular functions:

(1) the second virial coefficient $B^*(\tau^*)$ and

(2) the compressibility factor $Z^c(\rho^*)$ along the critical isotherm $T^* = T_c^*$.

Thus one direct generalization of the classical van der Waals EOS takes the form

$$Z - Z^c = \rho^*(B^* - B_c^*) \tag{43}$$

$$\Delta Z = \rho^* \Delta B^* \tag{44}$$

which we have designated the critically expanded Haar-Shenker-Kohler equation of state. The Hall plot for this simplest EOS reduces to a single line while the LJ fluid produces a *family* of lines, whose slope at the critically expanded origin may be expressed as

$$K = \Delta Z/(\rho^* \Delta B^*) = K(\rho^*) = \left[1 + \sum_{i=1}^{\infty} i k_i (\rho^*)^i\right] \quad (45)$$

Then using the previously described extended virial coefficients together with the available MC/MD data along isochores allowed determination of the slope coefficients as follows:

$$k_1 = -0.815 \quad (46)$$

$$k_2 = 2.193 \quad (47)$$

$$k_3 = -2.58 \quad (48)$$

$$k_4 = 1.257 \quad (49)$$

In this way we obtain an efficient EOS, realizing a factor of two improvement in the number of fitted coefficients as compared to Nicolas et al. (1979). All the needed properties can be determined directly; for example:

$$\text{Massieu potential: } J = J^c + \Delta B^* \rho^* \left[1 + \sum_{i=1}^{\infty} k_i (\rho^*)^i\right] \quad (50)$$

$$\text{Compressibility factor: } Z = Z^c + \Delta B^* \rho^* \left[1 + \sum_{i=1}^{\infty} i k_i (\rho^*)^i\right] \quad (51)$$

Chemical potential: $G = J + Z = J^c + Z^c + \Delta B^* \rho^*$

$$\left[1 + \sum_{i=1}^{\infty} (i+1) k_i (\rho^*)^i\right] \quad (52)$$

8 Coexistence Data

Having determined EOS expressions for the chemical potential $J + Z \equiv G(\rho^*, T^*)$ and for $P^*/T^* \equiv Q(\rho^*, T^*)$, we may then determine precise coexistence properties for values of $T^* < T_c^*$ by simply enforcing the constraints

$$G_v = G_l \text{ and } Q_v = Q_l \text{ for } \rho_c^* > \rho_v^* \text{ and } \rho_l^* > \rho_c^* \quad (53)$$

Table 1 supplies orthobaric densities and the corresponding saturation pressures. The three right-most columns of this table give corresponding values of the conventional reduced correlations

$$(\rho_{lr} - \rho_{vr})/(1 - T_r)^{1/3} \quad (54)$$

$$(\rho_{lr} + \rho_{vr} - 2)/(1 - T_r) \quad (55)$$

$$[\ln(P_r/T_r)]/(1 - T_r) \quad (56)$$

where

$$P_r = P^*/P_c^* \quad (57)$$

$$T_r = T^*/T_c^* \quad (58)$$

$$\rho_{lr} = \rho_l^*/\rho_c^*; \quad \rho_{vr} = \rho_v^*/\rho_c^* \quad (59)$$

9 Internal Energy

Given the previously determined $J(\rho^*, \tau^*)$ we may now calculate the scaled internal energy $U^* = U/(N\epsilon)$ directly in the fashion

$$U^* = \partial J/\partial \tau^* = (3/2)T^* + U_E^* \quad (60)$$

where the excess energy U_E^* is then found to be

$$U_E^* = \sum_{k=2}^{\infty} [dB_{kx}^*/d\tau^*][(\rho^*)^{k-1}/(k-1)] \quad (61)$$

with B_{kx}^* the extended virial coefficients. A simpler expression results upon using the approximation to J developed in section 7. In this case we write

Table 1 Coexistence data: saturation pressures and orthobaric densities

T^*	P_v^*	ρ_v^*	ρ_l^*	$\frac{(\rho_{lr} - \rho_{vr})}{(1-T_r)^{1/3}}$	$\frac{(\rho_{lr}+\rho_{vr}-2)}{(1-T_r)}$	$\frac{\lvert\ln(P_r/T_r)\rvert}{(1-T_r)}$
0.70	.0016	.0023	.8467	3.6420	1.7979	8.2215
0.75	.0027	.0037	.8259	3.6507	1.8087	7.8431
0.80	.0045	.0058	.8041	3.6592	1.8194	7.4791
0.85	.0072	.0088	.7813	3.6672	1.8306	7.1367
0.90	.0111	.0131	.7571	3.6738	1.8437	6.8035
0.95	.0167	.0189	.7315	3.6781	1.8620	6.4734
1.00	.0242	.0269	.7038	3.6788	1.8878	6.1566
1.05	.0341	.0374	.6738	3.6753	1.9270	5.8542
1.10	.0466	.0512	.6405	3.6655	1.9860	5.5654
1.15	.0624	.0696	.6026	3.6489	2.0847	5.2888
1.20	.0816	.0949	.5571	3.6222	2.2540	5.0232
1.25	.1041	.1335	.4960	3.5796	2.5603	4.7763
1.275	.1164	.1653	.4489	3.5288	2.4529	4.6719

$$U_E^* = [dB^*/d\tau^*]\left[1 + \sum_{i=1}^{4} k_i (\rho^*)^i\right]\rho^* \quad (62)$$

The last calculation can still be further simplified by utilizing the strong linear correlation between $dB^*/d\tau^*$ and B^*, itself, which then results in a final approximation

$$U_E^* \approx [0.6\,B^* - 6][1 - (\rho^{*3})/3]\rho^* \quad (63)$$

where we have also employed a comparable approximation for $K(\rho^*)$.

10 Conclusion

With improved computer capabilities, it can be expected that increasing amounts of MC/MD simulation data will be made available to researchers interested in relating molecular and continuum properties for artificial fluids. This will increase the need for systematic analysis and interpretation of the growing body of simulation data derived from these computer-based models.

Despite the simplicity of the LJ fluid interaction potential and the extent to which it has been studied previously, we have shown that significant improvements on existing EOS correlations for this model fluid may yet be obtained, using expansions based upon a nonanalytical critical isotherm. In this regard classical virial coefficient correlations only serve an intermediate data reduction function.

Acknowledgments

This work was supported in part by a Program Development Fund Grant provided by the Department of Mechanical Engineering at the University of Texas at Austin. The authors would like to thank the members of the Thermodynamics Research Center at Texas A&M University for their comments and suggestions on some of the work reported here.

References

Ashurst, W. T., 1976, "Equilibrium and Transport Estimates for Hydrogen and Helium via Lennard-Jones Fluid," Report No. SAND76-8710, Sandia Labs, Livermore, CA.

Ashurst, W. T., 1977, "Equilibrium and Transport Estimates for Hydrogen and Helium via Lennard-Jones Fluid," *Proceedings of the Seventh Symposium on Thermophysical Properties*, pp. 431–436.

Barker, J. A., Leonard, P. J., and Pompe, A., 1966, "Fifth Virial Coefficients," *Journal of Chemical Physics*, Vol. 44, No. 11, pp. 4206–4211.

Barker, J. A., and Monaghan, J. J., 1962, "Fourth Virial Coefficients for the 12-6 Potential," *Journal of Chemical Physics*, Vol. 36, No. 10, pp. 2564–2571.

Cooper, H. W., and Goldfrank, J. C., 1967, "B-W-R Constants and New Correlations," *Hydrocarbon Processing*, Vol. 46, No. 12.

Ewers, J., and Wagner, W., 1979, "A Method for Optimizing the Structure of Equations of State and Its Application to an Equation of State for Oxygen," *Proceedings of the Eighth Thermophysical Properties Symposium*, pp. 78–87.

Haar, L., and Shenker, S. H., 1971, "Equation of State for Dense Gases," *Journal of Chemical Physics*, Vol. 55, No. 10, pp. 4951–4958.

Haar, L., and Shenker, S. H., 1970, "A Phenomenological Equation of State," *Proceedings of the Fifth Symposium on Thermophysical Properties*, pp. 223–226.

Hacker, B. A., and Hall, C. K., 1985, "Second Virial Coefficient as a Corresponding States Temperature Variable for Pure Fluids: A Universal Satura-

tion Curve," *Industrial and Engineering Chemistry Fundamentals*, Vol. 24, pp. 262–265.

Hall, C. K., and Hacker, B. A., 1982, "On the Second Virial Coefficient as a Corresponding-States Variable for Mixtures," presented at the AIChE Annual Meeting, Los Angeles, CA.

Hall, C. K., and Hacker, B. A., 1983, "Corresponding States Theories for Chain Molecules," in: *Chemical Engineering at Supercritical Fluid Conditions*, M. E. Paulaitis, J. M. L. Penninger, R. D. Gray, Jr., and P. Davidson, eds., Ann Arbor Science Publishers, Ann Arbor, MI, Chap. 16.

Hansen, J. P., 1970, "Phase Transition of the Lennard-Jones System. II. High-Temperature Limit," *Physical Review A*, Vol. 2, No. 1, pp. 221–230.

Hirschfelder, J. O., Curtiss, C. F., and Bird, R. B., 1954, *Molecular Theory of Gases and Liquids*, Wiley, New York.

Kohler, F., and Haar, L., 1981, "A New Representation for Thermodynamic Properties of a Fluid," *Journal of Chemical Physics*, Vol. 75, No. 1, pp. 388–394.

Lebowitz, J. L., 1969, "Analytical Properties of Systems With Lennard-Jones Type Potentials," *Physics Letters*, Vol. 28A, No. 9, pp. 596–597.

Nicolas, J. J., Gubbins, K. E., Streett, W. B., and Tildesley, D. J., 1979, "Equation of State for Lennard-Jones Fluid," *Molecular Physics*, Vol. 37, No. 5, pp. 1429–1454.

Paynter, H. M., 1985, "Simple Veridical State Equations for Thermofluid Simulation: Generalization and Improvements Upon Van der Waals," ASME *Journal of Dynamic Systems, Measurement, and Control*, Vol. 107, pp. 233–234.

Paynter, H. M., 1988, "Critically-Expanded Haar–Shenker–Kohler State Relations for Thermofluid Dynamics and Control," presented at the ASME Winter Annual Meeting, Chicago, IL, Paper No. 88-WA/DSC-20.

APPENDIX A

Low-Density Virial Coefficients

The following regression constants were determined for the low-density virial coefficient correlations outlined in section 3; these correspond to $0.6 \le T^* \le 20$.

$\gamma_1 = 0.8690486$; $\gamma_2 = 0.20$; $b_o = 7.429586$; $b_1 = -4.412604$

$c_o = 10.74218$ $c_1 = -14.31667$ $c_2 = 6.63002$
$c_3 = -1.005855$ $d_o = -5.424577$ $d_1 = 10.01665$
$d_2 = -2.496062$ $d_3 = -2.160515$ $d_4 = 0.3019563$
$d_5 = 0.4921982$ $d_6 = -0.1218598$

APPENDIX B

High-Density Virial Coefficients

The following regression constants were determined for the high-density virial coefficient correlations outlined in section 4:

T^*	$C_>$	$D_>$
0.551	+39.777	-20.848
0.634	+12.032	+ 2.883
0.720	- 0.963	+14.316
0.810	- 4.443	+16.527
0.902	- 6.135	+17.377
0.977	- 4.846	+15.196
1.060	- 3.794	+13.255
1.080	- 2.556	+11.387
1.135	- 2.361	+10.975
1.150	- 2.142	+10.373
1.200	- 3.953	+12.866
1.235	- 1.785	+ 9.831
2.740	- 1.178	+ 7.782
4.000	+ 1.305	+ 3.473
20.00	+ 0.739	+ 1.980

These coefficients were then correlated with B^* over the range $0.634 \le T^* \le 20.0$ in the form

$$C_> = c_{0>} + c_{1>} B^* + c_{2>} (B^*)^2 + c_{3>} (B^*)^3$$

$$D_> = d_{0>} + d_{1>} B^* + d_{2>} (B^*)^2 + d_{3>} (B^*)^3$$

for use in succeeding calculations. Values of the regression coefficients are as follows:

$c_{0>} = 0.6986445$; $c_{1>} = -0.2432811$; $c_{2>} = -0.4565959$;

$c_{3>} = -0.04372434$ $d_{0>} = -0.86698936$;

$d_{1>} = 0.42074018$; $d_{2>} = 0.042401312$; $d_{3>} = 4.0872970$

Journal of Heat Transfer

Technical Notes

This section contains shorter technical papers. These shorter papers will be subjected to the same review process as that for full papers.

Heat Transfer Measurements in Incompressible Turbulent Flat Plate Boundary Layers With Step Wall Temperature Boundary Conditions

R. P. Taylor,[1,2] P. H. Love,[1,3] H. W. Coleman,[1,4] and M. H. Hosni[1,3]

Introduction

This paper presents heat transfer data for the case of incompressible turbulent boundary layer flow of air over a smooth flat plate with an unheated starting length followed by a heated region with constant wall temperature. This problem is one of the fundamental problems of convective heat transfer. Under the assumption of incompressible flow with constant fluid properties, the boundary layer momentum and energy equations become uncoupled and, in addition, the energy equation becomes linear. Therefore, the problem of heat transfer in the boundary layer with an arbitrary surface temperature is amenable to solution by superposition. The simplest boundary condition for which solutions can serve as the kernel of this superposition is the step wall temperature. As shown by Reynolds et al. (1958), the heat transfer solution for complicated wall temperature distributions can be reduced to rather simple quadrature by using superposition with the step wall temperature solution.

To the authors' knowledge the only systematic experimental studies of the step wall temperature boundary condition in turbulent flat plate boundary layers are the limited ($Re_x < 800{,}000$) work of Scesa (1951) and the definitive work of Reynolds et al. (1958). Reynolds et al. presented 18 experimental runs with streamwise Reynolds numbers Re_x ranging from 100,000 to 3,500,000, and Reynolds numbers based on unheated length Re_ϕ ranging from 500,000 to 3,000,000. The experiments presented in this paper are an extension of those experiments. Data are presented for six experimental cases with values of Re_x ranging from 100,000 to 10,000,000 and values of Re_ϕ ranging from 600,000 to 5,600,000.

Experiments

The experiments were performed in the Turbulent Heat Transfer Test Facility at Mississippi State University. A description of the facility and its qualification is presented by Coleman et al. (1988). This closed-loop air tunnel has a free-stream velocity range of 6 to 67 m/s. The air temperature is controlled with a heat exchanger and cooling water loop. The air flow is conditioned by a system of honeycomb and screens. The thermal boundary condition is set by computer control of the electrical power to each of the 24 individual plates, which make up the bottom surface of the nominally 0.1 m high by 0.5 m wide by 2.4 m long test section. Each aluminum plate (about 10 mm thick by 0.1 m in the flow direction) is heated uniformly from below by a custom-manufactured, rubber-encased electric heater pad. Design computations showed that, with this configuration, a plate can be considered to be at a uniform temperature. The top wall of the test section can be adjusted to maintain a constant free-stream velocity. The boundary layer is tripped with a 1 mm high by 12 mm wide wooden strip, which is located immediately in front of the test surface at the nozzle exit.

Measurements in the nozzle exit plane showed the free-stream turbulent intensity to be less than 0.3 percent and the mean velocity to be uniform within about 0.5 percent. Measurements 1.1 m downstream of the nozzle exit showed the spanwise variation of momentum thickness to be less than ± 5 percent. Profiles of mean temperature and velocity were in good agreement with the usual "laws-of-the-wall." Stanton number data for the baseline uniform temperature cases were in excellent agreement with the data of Reynolds et al. (1958), which is the definitive data set on which the usual Stanton number correlations are based (Kays and Crawford, 1980, for example). The current data fall within the data scatter of this definitive data set.

The data reduction expression for the Stanton number is

$$\mathrm{St} = \frac{W - q_r - q_c}{A\rho c_p u_\infty (t_w - T_\infty)} \tag{1}$$

The plate power W is measured with a precision wattmeter. The radiation loss q_r, and the conduction losses q_c, are estimated based on the data from the qualification tests (Coleman et al., 1988). Typical values for q_r/W and q_c/W are 1 percent and 0.5 percent, respectively. The plate area A is measured directly. The density ρ and specific heat c_p are determined from property data for moist air using the measured values of barometric pressure and wet and dry bulb temperatures in the tunnel. The free-stream velocity u_∞ is measured using a pitot probe and specially calibrated differential pressure transducers. The test plate temperatures t_w are measured using specially calibrated thermistors. The free-stream recovery temperature is measured with a specially calibrated thermistor probe, and the free-stream total temperature T_∞ is then computed using a recovery factor of 0.86 (Eckert and Goldstein, 1976). All fluid properties are evaluated at the free-stream static temperature. The uncertainty in the Stanton number was estimated by Coleman et al.

[1]Thermal & Fluid Dynamics Laboratory, Mechanical and Nuclear Engineering Department, Mississippi State University, MS 39762.

[2]Associate Professor.

[3]Graduate Research Assistant.

[4]Professor.

Contributed by the Heat Transfer Division for publication in the JOURNAL OF HEAT TRANSFER. Manuscript received by the Heat Transfer Division October 21, 1988. Keywords: Forced Convection.

Table 1 Data for a nominal free-stream velocity of 28 m/s

		u_∞ = 27.9 m/s				T_∞ = 26.5°C	u_∞ = 28.0 m/s				T_∞ = 26.3°C	u_∞ = 28.0 m/s				T_∞ = 26.2°C	u_∞ = 27.9 m/s				T_∞ = 25.9°C
P#	x(m)	t_w(C)	Re_x X10^{-6}	St X10^3	U%		t_w(C)	Re_x X10^{-6}	St X10^3	U%		t_w(C)	Re_x X10^{-6}	St X10^3	U%		t_w(C)	Re_x X10^{-6}	St X10^3	U%	
1	0.05	43.9	0.09	3.70	---	*	26.3	....	....	...		26.0	....	....	...		25.8	....	....	...	
2	0.15	44.3	0.27	2.75	1.6		27.0	....	....	...		26.2	....	....	...		26.0	....	....	...	
3	0.25	43.7	0.45	2.29	1.6		30.3	....	....	...		26.3	....	....	...		26.0	....	....	...	
4	0.36	44.1	0.62	2.25	1.6		44.0	0.63	3.90	---	*	26.4	....	....	...		26.2	....	....	...	
5	0.46	44.1	0.80	2.06	1.6		43.9	0.81	2.45	1.6		26.6	....	....	...		26.2	....	....	...	
6	0.56	44.1	0.98	2.00	1.6		44.1	0.99	2.32	1.6		26.9	....	....	...		26.3	....	....	...	
7	0.66	43.8	1.16	1.89	1.6		43.6	1.17	2.15	1.6		28.0	....	....	...	*	26.3	....	....	...	
8	0.76	43.9	1.33	1.86	1.6		43.7	1.35	2.08	1.6		44.0	1.35	3.27	---	*	26.3	....	....	...	
9	0.86	44.0	1.51	1.82	1.6		43.8	1.53	1.99	1.6		44.1	1.53	2.43	1.6		26.4	....	....	...	
10	0.97	44.0	1.69	1.77	1.6		43.9	1.71	1.92	1.6		44.1	1.71	2.25	1.6		26.4	....	....	...	
11	1.07	44.0	1.87	1.75	1.7		43.8	1.89	1.87	1.6		44.1	1.89	2.15	1.6		26.6	....	....	...	
12	1.17	44.0	2.05	1.70	1.7		43.9	2.07	1.82	1.7		44.2	2.07	2.08	1.6		27.4	....	....	...	
13	1.27	44.0	2.22	1.68	1.7		43.8	2.25	1.77	1.7		43.8	2.25	1.93	1.6		30.3	....	....	...	*
14	1.37	44.0	2.40	1.66	1.7		43.9	2.43	1.74	1.7		44.1	2.43	1.95	1.6		44.3	2.42	3.41	---	*
15	1.47	44.0	2.58	1.65	1.7		43.9	2.61	1.72	1.7		43.9	2.61	1.87	1.6		44.4	2.60	2.27	1.6	
16	1.57	44.0	2.76	1.62	1.7		43.8	2.79	1.69	1.7		44.0	2.79	1.85	1.6		44.2	2.78	2.13	1.6	
17	1.68	44.0	2.94	1.61	1.7		43.8	2.97	1.68	1.7		44.0	2.97	1.82	1.6		44.2	2.96	2.05	1.6	
18	1.78	44.0	3.11	1.61	1.7		43.8	3.15	1.65	1.7		44.0	3.15	1.79	1.6		44.3	3.14	1.99	1.6	
19	1.88	44.0	3.29	1.57	1.7		43.7	3.33	1.63	1.7		44.0	3.33	1.75	1.7		44.3	3.32	1.94	1.6	
20	1.98	44.0	3.47	1.57	1.7		43.8	3.52	1.62	1.7		43.9	3.51	1.72	1.7		44.3	3.50	1.87	1.7	
21	2.08	44.0	3.65	1.57	1.8		43.8	3.70	1.60	1.8		43.9	3.69	1.69	1.7		44.4	3.68	1.84	1.7	
22	2.18	44.0	3.83	1.53	1.9		43.7	3.88	1.57	1.9		43.9	3.87	1.66	1.9		44.4	3.86	1.80	1.8	
23	2.29	43.9	4.00	1.50	2.2		43.8	4.06	1.54	2.2		43.9	4.05	1.63	2.1		44.3	4.04	1.73	2.1	
24	2.39	43.9	4.18	1.55	---	*	43.8	4.24	1.58	---	*	43.9	4.23	1.66	---	*	44.3	4.22	1.77	---	*

* End effects are not included in the data reduction or the estimates of the uncertainty.

Table 2 Data for a nominal free-stream velocity of 67 m/s

		u_∞ = 66.9 m/s				T_∞ = 32.9°C	u_∞ = 67.3 m/s				T_∞ = 32.5°C	u_∞ = 67.5 m/s				T_∞ = 32.3°C	u_∞ = 66.9 m/s				T_∞ = 31.8°C
P#	x(m)	t_w(C)	Re_x X10^{-6}	St X10^3	U%		t_w(C)	Re_x X10^{-6}	St X10^3	U%		t_w(C)	Re_x X10^{-6}	St X10^3	U%		t_w(C)	Re_x X10^{-6}	St X10^3	U%	
1	0.05	44.3	0.21	3.19	---	*	32.1	....	....	...		31.7	....	....	...		31.4	....	....	...	
2	0.15	44.3	0.64	2.22	2.6		32.4	....	....	...		31.9	....	....	...		31.8	....	....	...	
3	0.25	44.1	1.07	1.97	2.6		32.5	....	....	...		32.1	....	....	...		31.9	....	....	...	
4	0.36	44.2	1.50	1.84	2.6		32.7	....	....	...		32.1	....	....	...		31.9	....	....	...	
5	0.46	44.2	1.93	1.74	2.7		34.0	....	....	...	*	32.2	....	....	...		32.0	....	....	...	
6	0.56	44.2	2.36	1.66	2.7		43.9	2.33	2.74	---	*	32.2	....	....	...		32.0	....	....	...	
7	0.66	44.2	2.78	1.63	2.7		44.1	2.76	2.04	2.7		32.3	....	....	...		32.0	....	....	...	
8	0.76	44.2	3.21	1.59	2.7		44.1	3.19	1.90	2.7		33.3	....	....	...	*	32.1	....	....	...	
9	0.86	44.2	3.64	1.55	2.7		44.1	3.61	1.79	2.7		43.9	3.64	2.60	---	*	32.1	....	....	...	
10	0.97	44.2	4.07	1.51	2.7		44.1	4.04	1.73	2.7		44.0	4.05	2.00	2.6		32.1	....	....	...	
11	1.07	44.2	4.50	1.50	2.6		44.1	4.46	1.69	2.6		43.9	4.48	1.89	2.6		32.1	....	....	...	
12	1.17	44.2	4.93	1.47	2.6		44.1	4.89	1.63	2.6		43.8	4.91	1.78	2.6		32.2	....	....	...	
13	1.27	44.2	5.36	1.45	2.6		44.1	5.31	1.60	2.6		43.9	5.34	1.74	2.6		33.3	....	....	...	*
14	1.37	44.1	5.78	1.42	2.7		44.1	5.74	1.57	2.6		43.9	5.76	1.69	2.6		44.0	5.77	2.48	---	*
15	1.47	44.1	6.21	1.44	2.7		44.0	6.16	1.55	2.7		43.8	6.19	1.66	2.6		44.2	6.20	1.91	2.5	
16	1.57	44.2	6.64	1.41	2.7		44.0	6.59	1.53	2.7		43.9	6.62	1.63	2.6		44.2	6.63	1.80	2.5	
17	1.68	44.1	7.07	1.41	2.7		44.1	7.01	1.52	2.7		43.9	7.04	1.63	2.6		44.2	7.05	1.75	2.5	
18	1.78	44.1	7.50	1.41	2.7		44.1	7.44	1.50	2.7		44.0	7.47	1.60	2.6		44.1	7.48	1.69	2.5	
19	1.88	44.2	7.93	1.40	2.6		44.1	7.86	1.49	2.6		43.8	7.90	1.56	2.6		44.0	7.91	1.66	2.5	
20	1.98	44.2	8.35	1.40	2.6		44.1	8.29	1.47	2.6		43.8	8.33	1.55	2.6		44.1	8.34	1.63	2.5	
21	2.08	44.1	8.78	1.36	2.6		44.0	8.72	1.45	2.6		43.8	8.75	1.53	2.6		44.0	8.76	1.59	2.5	
22	2.18	44.2	9.21	1.37	2.6		44.1	9.14	1.44	2.6		43.8	9.18	1.51	2.5		44.0	9.19	1.56	2.5	
23	2.29	44.2	9.64	1.33	2.6		44.1	9.57	1.40	2.6		43.8	9.61	1.47	2.6		44.1	9.62	1.52	2.4	
24	2.39	44.2	10.0	1.36	---	*	44.0	9.99	1.43	---	*	43.8	10.04	1.50	---	*	44.1	10.00	1.54	---	*

* End effects are not included in the data reduction or the estimates of the uncertainty.

(1988) based on the ANSI/ASME Standard on Measurement Uncertainty. The estimated uncertainties are presented in Tables 1 and 2.

For the experimental results and all computations, the origin of the momentum boundary layer was taken to be the nozzle exit, and the origin of the thermal boundary layer was taken to be the start of the heated surface. The authors decided not to include any virtual origin estimates in the data presentation or computations.

Theory

The solution of the unheated starting length problem is here divided into two classes: (1) the solution of the integral boundary layer equations and (2) the finite difference solution of the partial differential equations of the boundary layer. For the integral solution, we follow the procedure of Reynolds et al. (1958). The details of this solution are readily available (Kays and Crawford, 1980), and only the result is given here. Using the 1/7 power law approximation of the velocity and temperature profiles, they established that for an unheated starting length ϕ, the local Stanton number can be expressed as

$$\frac{\mathrm{St}(\phi; x)}{\mathrm{St}_t(x)} = \left[1 - \left(\frac{\phi}{x}\right)^{0.9}\right]^{-1/9} \tag{2}$$

where $\mathrm{St}_t(x)$ is the constant wall temperature Stanton number.

The finite difference solution of the incompressible boundary layer equations is now routine. Cebeci and Bradshaw (1984) present a complete discussion of these solutions. The solutions presented in this paper are based on a mixing length turbulence model with van Driest damping and a constant turbulent Prandtl number, $\mathrm{Pr}_t = 0.9$. For all computations in this paper the BLACOMP code as verified by Gatlin (1983) is used. The particular details of the solutions presented here can be found in Love et al. (1988). As was the case with the experimental data reduction, all fluid properties are assumed to be constant and are evaluated at the free-stream static temperature.

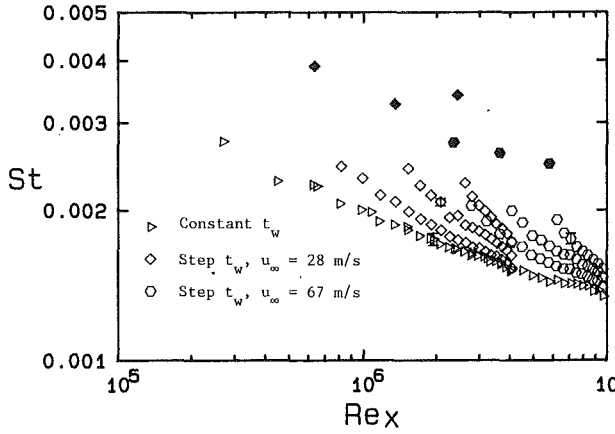

Fig. 1 Summary of the Stanton number data for the constant wall temperature and the unheated starting length cases. The solid symbol indicates the first heated plate.

Results

Stanton number measurements were made at nominal free-stream velocities of 28 m/s and 67 m/s. Three unheated starting length cases were run at each velocity. The lengths of the unheated regions were chosen so that an appropriate spread in Reynolds numbers, Re_ϕ, was obtained. The results of these experiments are presented in Tables 1 and 2. The uncertainty for each Stanton number, U, is presented as a percentage of the Stanton number value. As indicated in the tables, the end effects of the first heated plate and the last plate are not accounted for in the data reduction. These plates act in effect as guard heaters for the other heated plates. Inspection of the tables reveals that for the step wall temperature cases there is some heat leakage into the unheated plates and the step temperature boundary condition is not clean. However, both the integral and numerical solutions assume a clean, sharp step in wall temperature.

Figure 1 shows a summary of the Stanton number data for a constant wall temperature boundary condition and the unheated starting length cases for $u_\infty = 28$ m/s and $u_\infty = 67$ m/s. The first heated plate is highlighted in each case by plotting its data point as a solid symbol. Data from the last plate are not plotted for any case. The figure shows that a step in wall temperature has a large effect on the Stanton number in the heated region near the step. But as the thermal boundary layer develops, the Stanton numbers approach the results for the constant wall temperature boundary layers. The starting lengths were chosen so that the last case at $u_\infty = 28$ m/s and the first case at $u_\infty = 67$ m/s had approximately the same value of Re_ϕ. Based on the data of Reynolds et al., the results of these two cases should coincide when plotted as St versus Re_x. The figure shows that this is true for the present results.

Figure 2 shows a comparison of the results of the experiments with the integral solution in equation (2), dashed lines, and with the finite difference solutions, solid lines, for $u_\infty = 28$ m/s. Figure 3 shows the same comparison for $u_\infty = 67$ m/s. The results are presented in terms of $\mathrm{St}/\mathrm{St}_t$ for a direct comparison of equation (2). The St_t data were used to nor-

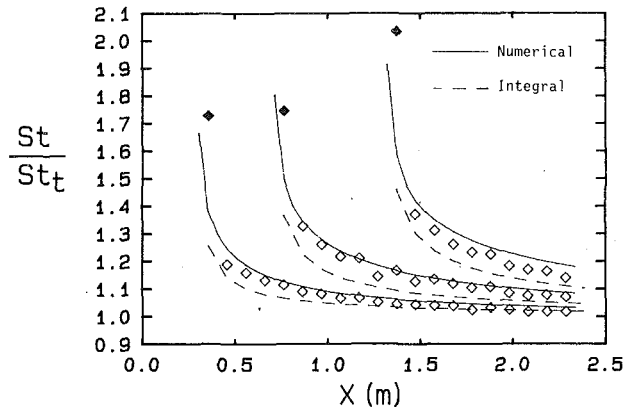

Fig. 2 Comparison of the data with the solutions for $u_\infty = 28$ m/s. The solid symbol indicates the first heated plate.

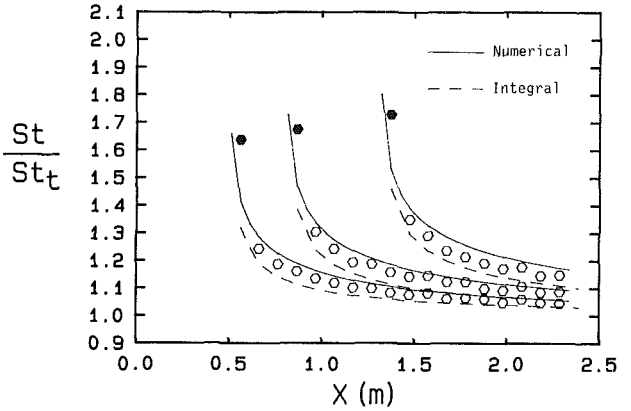

Fig. 3 Comparison of the data with the solutions for $u_\infty = 67$ m/s. The solid symbol indicates the first heated plate.

malize the St data, and the finite difference solutions for constant wall temperature St_t were used to normalize the finite difference solutions St. The figures show that both the finite difference and integral solutions are in very good agreement with the data in all cases. The integral solutions are consistently low by a small amount in the region of the step in wall temperature. Some disagreement should be expected since the 1/7 power law approximation for the temperature profiles was used in the integral solution. Thus the integral solution is an asymptotic case where the thermal boundary layer has had a chance to develop well. From the comparisons in the figures, it can be concluded that equation (2) is still appropriate for values of $Re_x \rightarrow 10^7$.

Acknowledgments

This work was supported by the U. S. Air Force Office of Scientific Research (Research Grant No. AFOSR-86-0178). The interest and encouragement of Dr. Jim Wilson and Capt. Hank Helin are gratefully acknowledged. The experimental apparatus was acquired under Grant No. AFOSR-85-0075.

References

Cebeci, T., and Bradshaw, P., 1984, *Physical and Computational Aspects of Convective Heat Transfer*, Springer-Verlag, New York.

Coleman, H. W., Hosni, M. H., Taylor, R. P., and Brown, G. B., 1988, "Smooth Wall Qualification of a Turbulent Heat Transfer Test Facility," TFD-88-2, Mechanical and Nuclear Engineering Department, Mississippi State University.

Eckert, R. G., and Goldstein, R. J., 1976, *Measurements in Heat Transfer*, 2nd ed., McGraw-Hill, New York.

Gatlin, B., 1983, "An Instructional Computer Program for Computing the Steady, Compressible, Turbulent Flow of an Arbitrary Fluid Near a Smooth Wall," MS Thesis, Mechanical and Nuclear Engineering Department, Mississippi State University.

Kays, W. M., and Crawford, M. E., 1980, *Convective Heat and Mass Transfer*, McGraw-Hill, New York.

Love, P., Taylor, R. P., Coleman, H. W., and Hosni, M. H., 1988, "Effects of Thermal Boundary Condition on Heat Transfer in the Turbulent Incompressible Flat Plate Boundary Layer," TFD-88-3, Mechanical and Nuclear Engineering Department, Mississippi State University.

Reynolds, W. C., Kays, W. M., and Kline, S. J., 1958, "Heat Transfer in the Turbulent Incompressible Boundary Layer, Parts I, II, and III," NASA Memos 12-1-58W, 12-2-58W, and 12-3-58W.

Scesa, S., 1951, "Experimental Investigation of Convective Heat Transfer to Air From a Flat Plate With a Stepwise Discontinuous Surface Temperature," MS Thesis, University of California.

Heat Transfer Measurements in Turbulent Liquid Flow Through a Vertical Annular Channel

A. Hasan,[1] R. P. Roy,[1] and S. P. Kalra[2]

Nomenclature

D_h = hydraulic diameter
Gr = Grashof number
h = heat transfer coefficient, defined in equation (1)
k_f = liquid thermal conductivity
L = axial distance from beginning of heating
Nu = Nusselt number $= hD_h/k_f$
q''_{w_i} = heat flux at inner wall
r = radial coordinate
Re = Reynolds number
R_i = inner radius of annulus
R_o = outer radius of annulus
R^* = nondimensional radial coordinate $= (r-R_i)/(R_o-R_i)$
t = liquid temperature fluctuation $= T-\bar{T}$
$\bar{T}$, $\bar{T}_{in}$ = mean temperature, mean inlet temperature
T^* = nondimensional temperature $= (\bar{T}-\bar{T}_{in})k_f/q''_{w_i}D_h$
z = axial coordinate

Introduction

A number of experimental studies have been reported on heat transfer in turbulent liquid flow through heated annuli (e.g., Heikal et al., 1976, in air; Müller-Steinhagen et al., 1986, in liquid heptane; Petukhov and Roizen, 1964, in gas; and Roy et al., 1986, in liquid Refrigerant-113). A more comprehensive list of references can be found from Gnielinski (1983).

The experimental work reported here is a continuation of an earlier study (Roy et al., 1986) of turbulent liquid flow through a vertical concentric annulus with the inner wall heated (constant heat flux) and the outer wall insulated. The measurements have been made in a region where the velocity and temperature fields are expected to be fully developed. For the experiments reported here, the effect of free convection may be neglected since the ratio Gr/Re^2 is much less than unity even at the lowest Reynolds number.

[1]Department of Mechanical and Aerospace Engineering, Arizona State University, Tempe, AZ 85287-6106.

[2]Electric Power Research Institute, Palo Alto, CA 94304.

Contributed by the Heat Transfer Division for publication in the JOURNAL OF HEAT TRANSFER. Manuscript received by the Heat Transfer Division June 20, 1988; revision received July 5, 1989. Keywords: Forced Convection, Turbulence.

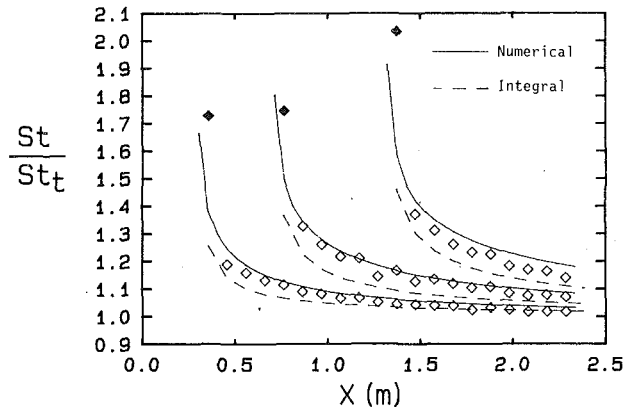

Fig. 2 Comparison of the data with the solutions for $u_\infty = 28$ m/s. The solid symbol indicates the first heated plate.

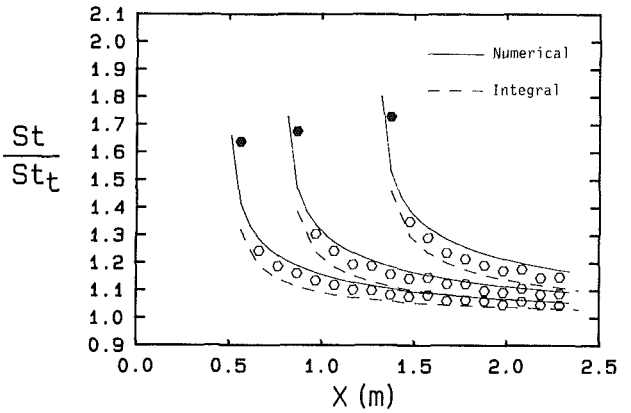

Fig. 3 Comparison of the data with the solutions for $u_\infty = 67$ m/s. The solid symbol indicates the first heated plate.

malize the St data, and the finite difference solutions for constant wall temperature St_t were used to normalize the finite difference solutions St. The figures show that both the finite difference and integral solutions are in very good agreement with the data in all cases. The integral solutions are consistently low by a small amount in the region of the step in wall temperature. Some disagreement should be expected since the 1/7 power law approximation for the temperature profiles was used in the integral solution. Thus the integral solution is an asymptotic case where the thermal boundary layer has had a chance to develop well. From the comparisons in the figures, it can be concluded that equation (2) is still appropriate for values of $Re_x \rightarrow 10^7$.

Acknowledgments

This work was supported by the U. S. Air Force Office of Scientific Research (Research Grant No. AFOSR-86-0178). The interest and encouragement of Dr. Jim Wilson and Capt. Hank Helin are gratefully acknowledged. The experimental apparatus was acquired under Grant No. AFOSR-85-0075.

References

Cebeci, T., and Bradshaw, P., 1984, *Physical and Computational Aspects of Convective Heat Transfer*, Springer-Verlag, New York.

Coleman, H. W., Hosni, M. H., Taylor, R. P., and Brown, G. B., 1988, "Smooth Wall Qualification of a Turbulent Heat Transfer Test Facility," TFD-88-2, Mechanical and Nuclear Engineering Department, Mississippi State University.

Eckert, R. G., and Goldstein, R. J., 1976, *Measurements in Heat Transfer*, 2nd ed., McGraw-Hill, New York.

Gatlin, B., 1983, "An Instructional Computer Program for Computing the Steady, Compressible, Turbulent Flow of an Arbitrary Fluid Near a Smooth Wall," MS Thesis, Mechanical and Nuclear Engineering Department, Mississippi State University.

Kays, W. M., and Crawford, M. E., 1980, *Convective Heat and Mass Transfer*, McGraw-Hill, New York.

Love, P., Taylor, R. P., Coleman, H. W., and Hosni, M. H., 1988, "Effects of Thermal Boundary Condition on Heat Transfer in the Turbulent Incompressible Flat Plate Boundary Layer," TFD-88-3, Mechanical and Nuclear Engineering Department, Mississippi State University.

Reynolds, W. C., Kays, W. M., and Kline, S. J., 1958, "Heat Transfer in the Turbulent Incompressible Boundary Layer, Parts I, II, and III," NASA Memos 12-1-58W, 12-2-58W, and 12-3-58W.

Scesa, S., 1951, "Experimental Investigation of Convective Heat Transfer to Air From a Flat Plate With a Stepwise Discontinuous Surface Temperature," MS Thesis, University of California.

Heat Transfer Measurements in Turbulent Liquid Flow Through a Vertical Annular Channel

A. Hasan,[1] R. P. Roy,[1] and S. P. Kalra[2]

Nomenclature

D_h = hydraulic diameter
Gr = Grashof number
h = heat transfer coefficient, defined in equation (1)
k_f = liquid thermal conductivity
L = axial distance from beginning of heating
Nu = Nusselt number $= hD_h/k_f$
q''_{w_i} = heat flux at inner wall
r = radial coordinate
Re = Reynolds number
R_i = inner radius of annulus
R_o = outer radius of annulus
R^* = nondimensional radial coordinate $= (r - R_i)/(R_o - R_i)$
t = liquid temperature fluctuation $= T - \bar{T}$
$\bar{T}$, $\bar{T}_{in}$ = mean temperature, mean inlet temperature
T^* = nondimensional temperature $= (\bar{T} - \bar{T}_{in})k_f/q''_{w_i}D_h$
z = axial coordinate

Introduction

A number of experimental studies have been reported on heat transfer in turbulent liquid flow through heated annuli (e.g., Heikal et al., 1976, in air; Müller-Steinhagen et al., 1986, in liquid heptane; Petukhov and Roizen, 1964, in gas; and Roy et al., 1986, in liquid Refrigerant-113). A more comprehensive list of references can be found from Gnielinski (1983).

The experimental work reported here is a continuation of an earlier study (Roy et al., 1986) of turbulent liquid flow through a vertical concentric annulus with the inner wall heated (constant heat flux) and the outer wall insulated. The measurements have been made in a region where the velocity and temperature fields are expected to be fully developed. For the experiments reported here, the effect of free convection may be neglected since the ratio Gr/Re^2 is much less than unity even at the lowest Reynolds number.

[1]Department of Mechanical and Aerospace Engineering, Arizona State University, Tempe, AZ 85287-6106.
[2]Electric Power Research Institute, Palo Alto, CA 94304.

Contributed by the Heat Transfer Division for publication in the JOURNAL OF HEAT TRANSFER. Manuscript received by the Heat Transfer Division June 20, 1988; revision received July 5, 1989. Keywords: Forced Convection, Turbulence.

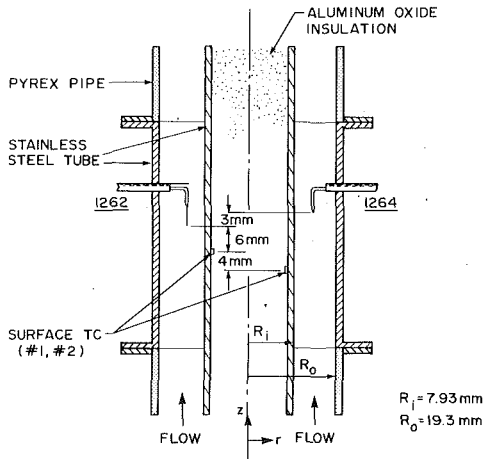

Fig. 1 The annular test section

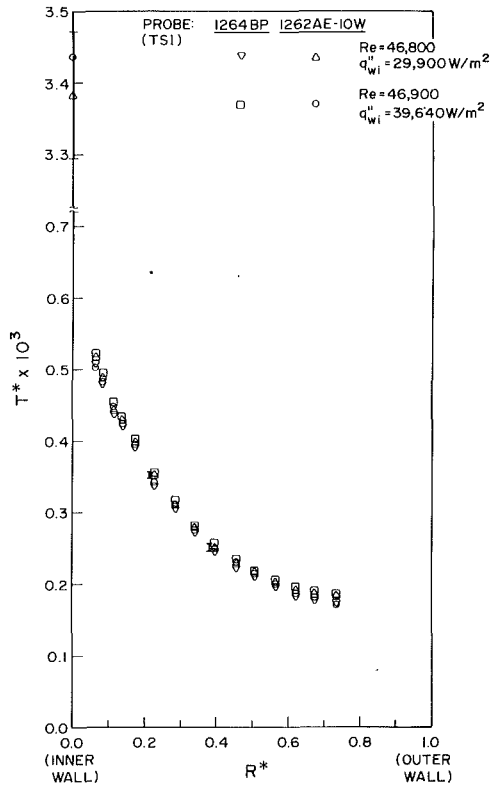

Fig. 2 Mean temperature profiles

Experimental Apparatus

The experiment rig, which uses liquid Refrigerant-113 as the working fluid, has been described elsewhere (Jain and Roy, 1983). Only the new annular test section will be briefly described here.

(A) Test Section. As shown in Fig. 1, the annular test section was comprised of an outer pyrex pipe of 38.6-mm i.d. and an inner section of a thin-walled (1.25-mm wall) seamless 304 stainless steel tube of 15.9-mm o.d. The test section was 3.66 m long, and heat could be supplied to the upper 2.75 m by resistively heating (by d-c) the stainless steel tube. The temperature field measurement plane was approximately 86 hydraulic diameters downstream of the beginning of heated length. Concentricity of the test section was maintained by four support vane assemblies, each assembly consisting of four 9 mm long and 1 mm thick vanes in an **X** configuration, carefully welded to the inner tube at approximately equal axial spacings. The nearest vane assembly upstream of the measurement plane was about 32 hydraulic diameters away.

The stainless steel tube was filled with aluminum oxide powder insulation. The outer pipe was insulated with 50-mm-thick jacketed fiberglass wool.

The wall heat flux during any experiment was calculated by multiplying the measured voltage drop across the heater tube by the current passing through the tube (also measured) and then dividing the product by the tube surface area. Heat balance calculations based on the liquid mass flow rate through the test section and the rise in its mixed-mean temperature always accounted for the heat generated in the tube wall to within ± 2 percent.

(B) Temperature Measurement Instrumentation. Radial distribution of the mean liquid temperature at diametrically opposite locations in the test section was measured by (*i*) a specially made miniature conical hot-film probe (TSI 1264 BP, 30 deg tip angle, no quartz coating on the platinum film), and (*ii*) a miniature cylindrical hot-film probe (TSI 1262AE-10W, 25-μm diameter, with quartz coating on the platinum film, 51-μm sensing length oriented perpendicular to the r–z plane, Fig. 1). Each probe was operated in conjunction with a constant current thermometry module (TSI 1040). The slight difference in the liquid temperature due to the axial spacing of about 3 mm between the two sensors was calculated and found to be well within the experimental uncertainty.

The radial distribution of the liquid temperature fluctuation intensity was obtained only by means of the cylindrical hot-film probe, since its frequency response was significantly better (flat to at least 100 Hz) than the conical probe.

The heated wall temperature was measured by means of two copper-constantan thermocouples (Omega, foil thickness $\simeq 0.012$ mm) mounted (baked on with Omegabond epoxy) at diametrically opposite locations on the inner wall of the stainless steel tube at about the same axial location as the hot-film probes (see Fig. 1). The thin layer of epoxy electrically insulated the thermocouple from the tube (this was verified by measuring the resistance between them). The average of the two surface temperature measurements was taken to be the (axially) local tube inner wall temperature. The tube outer wall (i.e., the annulus heated wall) temperature was then determined analytically by a steady-state heat conduction analysis.

In order to account for the slight mismatch (a few mm, see Fig. 1) between the axial positions of the hot-film sensors and the wall thermocouples, a correction to the mixed-mean liquid temperature used in determining the heat transfer coefficient was calculated, only to find that the associated error in the measured heat transfer coefficient was less than 0.1 percent, which is well within the experimental uncertainty.

The TSI 1262 probe was equipped with a protective pin, which extended radially 250 μm beyond the sensor. This helped verify the location of the inner (heated) wall relative to the sensor. As for the TSI 1264 probe, its stem could be brought to touch the inner wall to verify the sensor location. The uncertainty associated with the positioning of the two hot-film sensors by their respective probe traversing mechanisms was ± 25 μm.

(C) Temperature Calibration. Each hot-film sensor was calibrated in situ by increasing the temperature of the liquid entering the test section in stages by means of a preheater located upstream. The test section itself was unheated. Outputs of the surface thermocouples were also compared with known surface temperatures in this manner.

Results and Discussion

(A) Mean Temperature Profiles. Figure 2 shows the radial profiles of the nondimensional mean liquid temperature, T^*, for two wall heat fluxes and a Reynolds

number of approximately 47,000. Measurements due to both sensors (i.e., diametrically opposite profiles) are shown. The corresponding wall temperatures are also shown. Representative uncertainty bars are shown as well.[3] The data shown are typical of those at other heat fluxes and Reynolds numbers for which experiments were conducted.

(B) Temperature Fluctuation Intensity Profiles. In our earlier paper we reported on the dependence of the temperature fluctuation intensity on the magnitude of the wall heat flux. At a given Reynolds number, the intensity was seen to increase with an increase in the wall heat flux, especially in the proximity of the heated wall. Also noted in the Reynolds number range of 35,000 – 50,000 was a flattening trend in the magnitude of the intensity as the heated wall was approached.

Figure 3 shows data from some recent experiments conducted to explore the behavior of liquid temperature fluctuation intensity distribution over a somewhat wider range of Reynolds number. Five radial profiles are shown. For four of these, the wall heat flux is approximately 29,400 W/m^2 and the Reynolds number ranges from about 26,000 to 47,000. In the fifth case, the Reynolds number is 18,000 and the wall heat flux 17,000 W/m^2.[4] Two features are noteworthy:

(*i*) At any specific wall heat flux, as the Reynolds number is increased, the temperature fluctuation intensity decreases. This is especially noticeable near the heated wall. A qualitative explanation may be that as the Reynolds number increases at a given heat flux the temperature differential between the wall and the liquid decreases, causing the fluctuation intensity to decrease;

(*ii*) As the Reynolds number decreases, the flattening trend in the intensity profile in the vicinity of the heated wall is reduced significantly. In fact, at the lowest Reynolds number studied by us, i.e., 18,000, there is essentially no flattening.

Such a flattening trend has not been observed in turbulent liquid flow through heated pipes (e.g., Burchill, 1970). This trend thus appears to be a feature of higher Reynolds number turbulent flow through annuli.

It has been suggested (Hojstrup et al., 1976) that the prongs in anemometer probes may attenuate the ambient temperature fluctuations sensed. A later series of measurements we took with a fast microthermocouple (time constant $\approx$ 5 ms) indicated that this is indeed true. Although all the features of the temperature fluctuations described in the preceding paragraphs were still maintained, it is possible that the attenuation of the intensity near the heated wall could have been as much as 15 percent at the lower Reynolds numbers. This attenuation effect was found to decrease with increasing Reynolds number.

(C) Comparison With Heat Transfer Correlations. Figure 4 is a log-log plot of the (Nusselt No.)/(Prandtl No.)$^{0.4}$ ratio versus Reynolds number for our experiments. The liquid properties necessary for the calculation of these numbers were evaluated at the prevalent mixed mean temperature. The wall heat transfer coefficient h is defined as

$$h \triangleq \frac{q''_{w_i}}{\bar{T}_{\text{wall}} - \bar{T}_{\text{mixed mean}}} \tag{1}$$

where $T_{\text{mixed mean}}$, the mixed mean liquid temperature, is calculated from the measured mean liquid temperature radial distribution and the mean axial velocity radial distribution. The latter distribution was reported in our earlier study (Roy et al., 1986).

[3] The experimental uncertainties were estimated by the method of Kline and McClintock (1953).

[4] It was necessary to reduce the wall heat flux substantially in this case in order to prevent the onset of nucleate boiling at the wall.

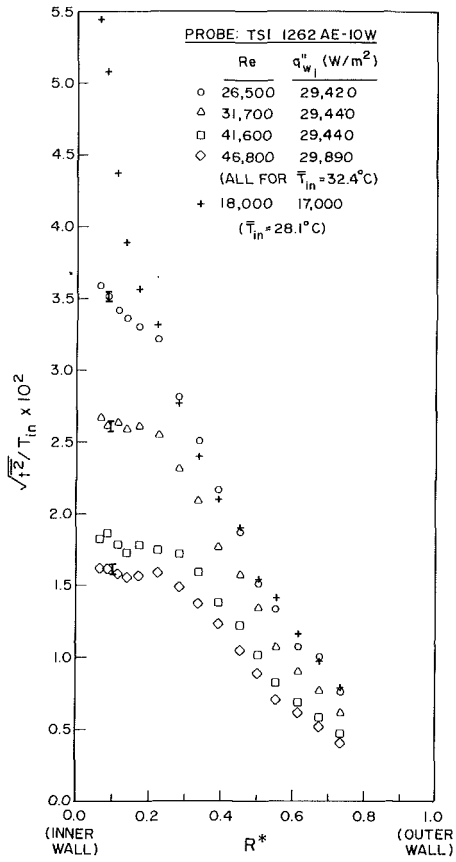

Fig. 3 Temperature fluctuation intensity profiles

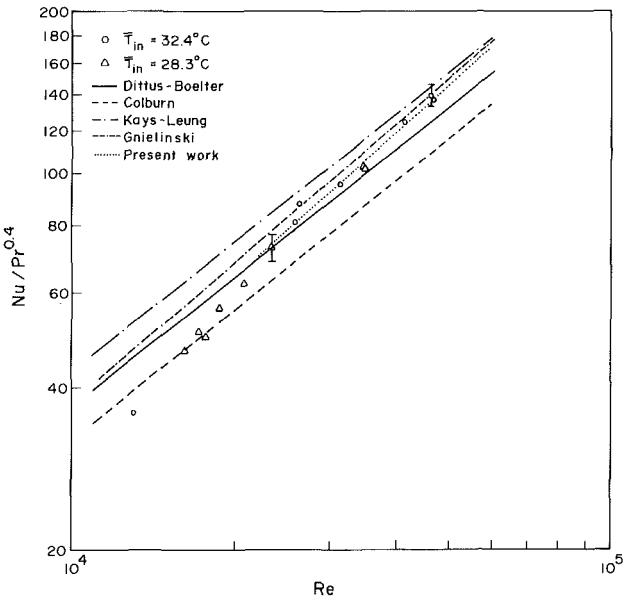

Fig. 4 Relationship between Nusselt, Prandtl, and Reynolds numbers

The following turbulent flow relations are also plotted in Fig. 4 for comparison purposes:

(*i*) the Dittus–Boelter correlation;

(*ii*) the Colburn correlation (accounting for the fact that the exponent on the Prandtl number is 1/3);

(*iii*) results of the Kays and Leung (1962) analysis;

(*iv*) the relationship for annuli with inner wall heated and the outer wall insulated reported by Gnielinski (1983):

$$\mathrm{Nu} = \left(\frac{\mathrm{Pr}}{\mathrm{Pr}_{\mathrm{wall}}}\right)^{0.11} \cdot \frac{(f/8)(\mathrm{Re}-1000)\mathrm{Pr}}{1+12.7\sqrt{f/8}(\mathrm{Pr}^{2/3}-1)} \cdot \left[1+\left(\frac{d_h}{L}\right)^{2/3}\right] \cdot \left[0.86\left(\frac{R_i}{R_o}\right)^{-0.16}\right] \quad (2)$$

where $f=(1.82\log_{10}\mathrm{Re}-1.64)^{-2}$.

Neither the Dittus-Boelter and Colburn correlations nor the Kays-Leung analysis compare consistently well with our experimental data. The Gnielinski correlation does better however, especially at higher Reynolds numbers. It appears from a study of our data that the Reynolds number exponent in the Nu-Pr-Re relationship has two different values in the Reynolds number range investigated. It may be suggested that transition to fully turbulent flow occurs in the Reynolds number range studied (about 10,000-50,000) and only beyond the upper limit can the heat transfer data be expected to compare well with appropriate turbulent flow relations. A best fit of our data in the Reynolds number range of 23,000-47,000 is given by

$$\mathrm{Nu} = 0.0106\ \mathrm{Re}^{0.88}\ \mathrm{Pr}^{0.4} \quad (3)$$

and is shown in Fig. 4.

It has been suggested earlier (Petukhov and Roizen, 1964) that for an annular channel with the inner wall heated and the outer wall insulated, the influence of the inner and outer radii can be accounted for by the equation

$$\frac{\mathrm{Nu}}{\mathrm{Nu}_{\mathrm{pipe}}} = 0.86\left(\frac{R_i}{R_o}\right)^{-0.16} \quad (4)$$

where $\mathrm{Nu}_{\mathrm{pipe}}$ is calculated from, for example, the Dittus-Boelter correlation on the basis of the hydraulic diameter of the annulus. Note that the right-hand side of equation (4) appears as a factor in the relation given in equation (2). For our channel, this factor is equal to 0.99, yielding a correction that is well within the experimental uncertainty.

Concluding Remarks

Both the wall heat flux and Reynolds number have significant influences on the magnitude of the temperature fluctuation intensity and its radial distribution in turbulent liquid flow through vertical annuli. Some interesting trends have been identified.

For the Reynolds number range investigated in this work, the Nusselt No.-Prandtl No.-Reynolds No. relationship for the measured data does not follow the fully turbulent flow correlations of Dittus-Boelter and Colburn. The same conclusion appears to hold for the Kays-Leung analysis. Agreement with the relation suggested by Gnielinski is better, especially at the higher Reynolds number values. A best-fit relation for the Reynolds number range of 23,000-47,000 is suggested.

Acknowledgments

Partial support of this work by Electric Power Research Institute, Nuclear Power Division, is gratefully acknowledged.

References

Burchill, W. E., 1970, "Statistical Properties of Velocity and Temperature in Isothermal and Nonisothermal Pipe Flow," Ph.D. Thesis, University of Illinois.

Gnielinski, V., 1983, "Forced Convection in Ducts," *Heat Exchanger Design Handbook*, Vol. 2, Chap. 2.5.1, Hemisphere Publishing Corp., Washington, DC.

Heikal, M. R. F., Walklate, P. J., and Hatton, A. P., 1976, "The Effect of Free Stream Turbulence Level on the Flow and Heat Transfer in the Entrance Region of an Annulus," *International Journal of Heat and Mass Transfer*, Vol. 20, pp. 763-771.

Jain, P. K., and Roy, R. P., 1983, "Stochastic Characteristics of Vapor Fraction and Wall Pressure Fluctuations in Boiling Flow," *International Journal of Multiphase Flow*, Vol. 9, No. 5, pp. 463-489.

Hojstrup, J., Rasmussen, K., and Larsen, S. E., 1976, "Dynamic Calibration of Temperature Wires in Still Air," *Disa Information*, No. 20, pp. 22-30.

Kays, W. M., and Leung, E. Y., 1963, "Heat Transfer in Annular Passages: Hydrodynamically Developed Turbulent Flow With Arbitrarily Prescribed Heat Flux," *International Journal of Heat and Mass Transfer*, Vol. 6, pp. 537-557.

Kline, S. J., and McClintock, F. A., 1953, "The Description of Uncertainties in Single Sample Experiments," *Mechanical Engineering*, Vol. 75, pp. 3-9.

Müller-Steinhagen, H., Epstein, N., and Watkinson, A. P., 1986, "Subcooled Boiling and Convective Heat Transfer for Heptane Flowing Inside an Annulus and Past a Coiled Wire: Part I—Experimental Results," ASME JOURNAL OF HEAT TRANSFER, Vol. 108, pp. 922-927; "Part II—Correlation of Data," pp. 928-933.

Petukhov, B. S., and Roizen, L. I., 1964, "Generalized Relationships for Heat Transfer in a Turbulent Flow of Gas in Tubes of Annular Section," *High Temperature*, Vol. 2, pp. 65-68.

Roy, R. P., Krishnan, V. S., and Raman, A., 1986, "Measurement in Turbulent Liquid Flow Through a Vertical Concentric Annular Channel," ASME JOURNAL OF HEAT TRANSFER, Vol. 108, pp. 199-202.

Buoyancy Effects on Laminar Forced Convection in the Thermal Entrance Region of Horizontal Rectangular Channels

F. C. Chou[1] and G. J. Hwang[2]

Introduction

Buoyancy effects on laminar forced convection in the thermal entrance region of a horizontal square channel for $\mathrm{Pr}=0.7$, 1, 2, 5, 10, and 100 and $\mathrm{Ra}=10^4$, 3×10^4, 6×10^4, and 10^5 have been studied by Chou and Hwang (1987) using a vorticity-velocity method. However, the mixed convection in horizontal rectangular channels with width-to-height aspect ratios other than one is also important in engineering applications (Shah and London, 1974). The flow and heat transfer characteristics may be significantly influenced by the aspect ratio.

Laminar mixed convection in the hydrodynamically and thermally fully developed flow has been investigated by Cheng and Hwang (1969) and Chou and Hwang (1984) in horizontal rectangular channels with aspect ratios $\gamma=0.2$, 0.5, 1, 2, and 5. However, the buoyancy effects on the laminar forced convection in the thermal entrance flow are also very significant. This problem had been studied in rectangular channels with uniform wall heat flux with $\gamma=0.2$, 0.5, 1, 2, and 5 by Cheng et al. (1972). Laminar mixed convection in the thermal entrance region of tubes has been studied previously (Cheng and Ou, 1974; Hwang and Lin, 1985), but the results are applicable only to fluids with large Prandtl numbers. Other references concerning studies on the mixed convection problem in rectangular channels have been quoted in Shah and London (1978).

A relatively novel vorticity-velocity formulation of the Navier-Stokes equations and the related numerical scheme were developed by Chou and Hwang (1987) to study the laminar mixed convection in the thermal entrance region of a square duct for moderate and small Prandtl number fluids. The purpose of the present investigation is to extend the previous work to channels of aspect ratios $\gamma=0.2$, 0.5, 2, and 5 to examine the effect of aspect ratio on the flow and heat transfer characteristics. Primitive variable calculations are widely used when solving three-dimensional flows, but difficulties occur with the boundary conditions for the pressure equations (Kim and Moin, 1985). The advantage of using the vorticity-velocity formulation had also been evaluated by Farouk and Fusegi (1986).

[1]Department of Mechanical Engineering, National Central University, Chung-li, Taiwan 32054.

[2]Department of Power Mechanical Engineering, National Tsing-Hua University, Hsinchu, Taiwan 30043; Mem. ASME.

Contributed by the Heat Transfer Division and presented at the ASME National Heat Transfer Conference, Houston, Texas, July 24-27, 1988. Manuscript received by the Heat Transfer Division March 22, 1988. Keywords: Mixed Convection.

$$\mathrm{Nu} = \left(\frac{\mathrm{Pr}}{\mathrm{Pr}_{\mathrm{wall}}}\right)^{0.11} \cdot \frac{(f/8)(\mathrm{Re}-1000)\mathrm{Pr}}{1+12.7\sqrt{f/8}(\mathrm{Pr}^{2/3}-1)} \cdot \left[1+\left(\frac{d_h}{L}\right)^{2/3}\right] \cdot \left[0.86\left(\frac{R_i}{R_o}\right)^{-0.16}\right] \quad (2)$$

where $f=(1.82\log_{10}\mathrm{Re}-1.64)^{-2}$.

Neither the Dittus-Boelter and Colburn correlations nor the Kays-Leung analysis compare consistently well with our experimental data. The Gnielinski correlation does better however, especially at higher Reynolds numbers. It appears from a study of our data that the Reynolds number exponent in the Nu-Pr-Re relationship has two different values in the Reynolds number range investigated. It may be suggested that transition to fully turbulent flow occurs in the Reynolds number range studied (about 10,000-50,000) and only beyond the upper limit can the heat transfer data be expected to compare well with appropriate turbulent flow relations. A best fit of our data in the Reynolds number range of 23,000-47,000 is given by

$$\mathrm{Nu} = 0.0106\ \mathrm{Re}^{0.88}\ \mathrm{Pr}^{0.4} \quad (3)$$

and is shown in Fig. 4.

It has been suggested earlier (Petukhov and Roizen, 1964) that for an annular channel with the inner wall heated and the outer wall insulated, the influence of the inner and outer radii can be accounted for by the equation

$$\frac{\mathrm{Nu}}{\mathrm{Nu}_{\mathrm{pipe}}} = 0.86\left(\frac{R_i}{R_o}\right)^{-0.16} \quad (4)$$

where $\mathrm{Nu}_{\mathrm{pipe}}$ is calculated from, for example, the Dittus-Boelter correlation on the basis of the hydraulic diameter of the annulus. Note that the right-hand side of equation (4) appears as a factor in the relation given in equation (2). For our channel, this factor is equal to 0.99, yielding a correction that is well within the experimental uncertainty.

Concluding Remarks

Both the wall heat flux and Reynolds number have significant influences on the magnitude of the temperature fluctuation intensity and its radial distribution in turbulent liquid flow through vertical annuli. Some interesting trends have been identified.

For the Reynolds number range investigated in this work, the Nusselt No.-Prandtl No.-Reynolds No. relationship for the measured data does not follow the fully turbulent flow correlations of Dittus-Boelter and Colburn. The same conclusion appears to hold for the Kays-Leung analysis. Agreement with the relation suggested by Gnielinski is better, especially at the higher Reynolds number values. A best-fit relation for the Reynolds number range of 23,000-47,000 is suggested.

Acknowledgments

Partial support of this work by Electric Power Research Institute, Nuclear Power Division, is gratefully acknowledged.

References

Burchill, W. E., 1970, "Statistical Properties of Velocity and Temperature in Isothermal and Nonisothermal Pipe Flow," Ph.D. Thesis, University of Illinois.

Gnielinski, V., 1983, "Forced Convection in Ducts," *Heat Exchanger Design Handbook*, Vol. 2, Chap. 2.5.1, Hemisphere Publishing Corp., Washington, DC.

Heikal, M. R. F., Walklate, P. J., and Hatton, A. P., 1976, "The Effect of Free Stream Turbulence Level on the Flow and Heat Transfer in the Entrance Region of an Annulus," *International Journal of Heat and Mass Transfer*, Vol. 20, pp. 763-771.

Jain, P. K., and Roy, R. P., 1983, "Stochastic Characteristics of Vapor Fraction and Wall Pressure Fluctuations in Boiling Flow," *International Journal of Multiphase Flow*, Vol. 9, No. 5, pp. 463-489.

Hojstrup, J., Rasmussen, K., and Larsen, S. E., 1976, "Dynamic Calibration of Temperature Wires in Still Air," *Disa Information*, No. 20, pp. 22-30.

Kays, W. M., and Leung, E. Y., 1963, "Heat Transfer in Annular Passages: Hydrodynamically Developed Turbulent Flow With Arbitrarily Prescribed Heat Flux," *International Journal of Heat and Mass Transfer*, Vol. 6, pp. 537-557.

Kline, S. J., and McClintock, F. A., 1953, "The Description of Uncertainties in Single Sample Experiments," *Mechanical Engineering*, Vol. 75, pp. 3-9.

Müller-Steinhagen, H., Epstein, N., and Watkinson, A. P., 1986, "Subcooled Boiling and Convective Heat Transfer for Heptane Flowing Inside an Annulus and Past a Coiled Wire: Part I—Experimental Results," ASME JOURNAL OF HEAT TRANSFER, Vol. 108, pp. 922-927; "Part II—Correlation of Data," pp. 928-933.

Petukhov, B. S., and Roizen, L. I., 1964, "Generalized Relationships for Heat Transfer in a Turbulent Flow of Gas in Tubes of Annular Section," *High Temperature*, Vol. 2, pp. 65-68.

Roy, R. P., Krishnan, V. S., and Raman, A., 1986, "Measurement in Turbulent Liquid Flow Through a Vertical Concentric Annular Channel," ASME JOURNAL OF HEAT TRANSFER, Vol. 108, pp. 199-202.

Buoyancy Effects on Laminar Forced Convection in the Thermal Entrance Region of Horizontal Rectangular Channels

F. C. Chou[1] and G. J. Hwang[2]

Introduction

Buoyancy effects on laminar forced convection in the thermal entrance region of a horizontal square channel for $\mathrm{Pr}=0.7$, 1, 2, 5, 10, and 100 and $\mathrm{Ra}=10^4$, 3×10^4, 6×10^4, and 10^5 have been studied by Chou and Hwang (1987) using a vorticity-velocity method. However, the mixed convection in horizontal rectangular channels with width-to-height aspect ratios other than one is also important in engineering applications (Shah and London, 1974). The flow and heat transfer characteristics may be significantly influenced by the aspect ratio.

Laminar mixed convection in the hydrodynamically and thermally fully developed flow has been investigated by Cheng and Hwang (1969) and Chou and Hwang (1984) in horizontal rectangular channels with aspect ratios $\gamma=0.2$, 0.5, 1, 2, and 5. However, the buoyancy effects on the laminar forced convection in the thermal entrance flow are also very significant. This problem had been studied in rectangular channels with uniform wall heat flux with $\gamma=0.2$, 0.5, 1, 2, and 5 by Cheng et al. (1972). Laminar mixed convection in the thermal entrance region of tubes has been studied previously (Cheng and Ou, 1974; Hwang and Lin, 1985), but the results are applicable only to fluids with large Prandtl numbers. Other references concerning studies on the mixed convection problem in rectangular channels have been quoted in Shah and London (1978).

A relatively novel vorticity-velocity formulation of the Navier-Stokes equations and the related numerical scheme were developed by Chou and Hwang (1987) to study the laminar mixed convection in the thermal entrance region of a square duct for moderate and small Prandtl number fluids. The purpose of the present investigation is to extend the previous work to channels of aspect ratios $\gamma=0.2$, 0.5, 2, and 5 to examine the effect of aspect ratio on the flow and heat transfer characteristics. Primitive variable calculations are widely used when solving three-dimensional flows, but difficulties occur with the boundary conditions for the pressure equations (Kim and Moin, 1985). The advantage of using the vorticity-velocity formulation had also been evaluated by Farouk and Fusegi (1986).

[1]Department of Mechanical Engineering, National Central University, Chung-li, Taiwan 32054.

[2]Department of Power Mechanical Engineering, National Tsing-Hua University, Hsinchu, Taiwan 30043; Mem. ASME.

Contributed by the Heat Transfer Division and presented at the ASME National Heat Transfer Conference, Houston, Texas, July 24-27, 1988. Manuscript received by the Heat Transfer Division March 22, 1988. Keywords: Mixed Convection.

Theoretical Analysis

The problem considered is a steady laminar viscous flow in a horizontal rectangular channel. A uniform wall heat flux is imposed on all the walls of the channel at $Z>0$. A fully developed velocity profile W_f is assumed for the upstream boundary condition. In the thermal entrance region the axial velocity is considered to be composed of two parts, one due to the fully developed flow, say W_f, and one induced by the buoyancy effect, say W. Symmetric counterrotating vortices are then induced by the buoyancy force near the vertical walls and the convective heat transfer coefficient is greatly enhanced over that of pure force convection. The Boussinesq approximation is used to characterize the buoyancy effect. The axial diffusion effect is neglected by using the high Peclet number assumption as employed in previous works of Cheng and his co-workers, Hong et al. (1974), Patankar and Spalding (1972), Ramakrishna et al. (1982), and Abou-Ellail and Morcos (1983). It had been noted by Ozisik (1985) that in general the effect of axial conduction in the fluid is negligible for $\mathrm{Pe}>50$, and $\mathrm{Re}<2000$ is the condition necessary for the existence of laminar flow. Therefore, the approximate range of Reynolds number is about $70<\mathrm{Re}<2000$ for the laminar flows of $\mathrm{Pr}=0.7$ and 5 considered in the present work. The viscous dissipation and compressibility effects in the energy equation will be neglected. Under the foregoing assumptions and introducing the following dimensionless variables and parameters:

$$x=X/\mathrm{De},\quad y=Y/\mathrm{De},\quad z=Z/(\mathrm{PrReDe}),$$

$$u=U/U_c,\quad v=V/U_c,\quad w_f=W_f/\overline{W}_f,\quad w=W/(\mathrm{Ra}\overline{W}_f)$$

$$p=P/[\rho U_c\nu/\mathrm{De}],\quad \theta=(T-T_{in})/\theta_c,\quad \mathrm{Gr}=g\beta\theta_c De^3/\nu^2,$$

$$\mathrm{Pr}=\nu/\alpha,\quad \mathrm{Ra}=\mathrm{PrGr},\quad \mathrm{Re}=\overline{W}_f\mathrm{De}/\nu,\quad \mathrm{Pe}=\mathrm{PrRe} \tag{1}$$

where $\mathrm{De}=4A/S$, $U_c=\mathrm{Gr}\nu/\mathrm{De}$, $\theta_c=q_w\mathrm{De}/k$, and T_{in} is the uniform fluid temperature at the entrance, the following governing equations can be obtained as in Chou and Hwang (1987):

$$\nabla^2 u=\frac{\partial\xi}{\partial y}-\frac{\partial^2 w}{\partial x\partial z} \tag{2}$$

$$\nabla^2 v=-\frac{\partial\xi}{\partial x}-\frac{\partial^2 w}{\partial y\partial z} \tag{3}$$

$$\mathrm{Gr}\left(u\frac{\partial\xi}{\partial x}+v\frac{\partial\xi}{\partial y}+w\frac{\partial\xi}{\partial z}+\frac{\partial u}{\partial x}\xi+\frac{\partial v}{\partial y}\xi+\frac{\partial w}{\partial y}\frac{\partial u}{\partial z}-\frac{\partial w}{\partial x}\frac{\partial v}{\partial z}\right)+\frac{1}{\mathrm{Pr}}\left(\frac{\partial w_f}{\partial y}\frac{\partial u}{\partial z}-\frac{\partial w_f}{\partial x}\frac{\partial v}{\partial z}+w_f\frac{\partial\xi}{\partial z}\right)=\nabla^2\xi-\frac{\partial\theta}{\partial x} \tag{4}$$

$$\mathrm{Gr}\left(u\frac{\partial w}{\partial x}+v\frac{\partial w}{\partial y}+w\frac{\partial w}{\partial z}\right)+\frac{1}{\mathrm{Pr}}\left(u\frac{\partial w_f}{\partial x}+v\frac{\partial w_f}{\partial y}+w_f\frac{\partial w}{\partial z}\right)=-\frac{1}{\mathrm{Pe}^2}\frac{\partial p}{\partial z}+\nabla^2 w \tag{5}$$

$$\nabla^2 w_f=C \tag{6}$$

$$\mathrm{Ra}\left(u\frac{\partial\theta}{\partial x}+v\frac{\partial\theta}{\partial y}+w\frac{\partial\theta}{\partial z}\right)+w_f\frac{\partial\theta}{\partial z}=\nabla^2\theta \tag{7}$$

where $\xi=\partial u/\partial y-\partial v/\partial x$ is the axial vorticity, $\nabla^2=\partial^2/\partial x^2+\partial^2/\partial y^2$, and $C=(\mathrm{De}^2/\mu\overline{W}_f)\,\partial P_f/\partial Z=\text{const}$. A large Prandtl number assumption is frequently used (Cheng et al., 1972; Hong et al., 1974; Cheng and Ou, 1974; Ou et al., 1974; Ou and Cheng, 1977) to neglect the convective terms in the momentum equations and the numerical computation is thus drastically simplified. That simplification is not made in the present study. The vorticity-velocity method developed by Chou and Hwang (1987) is employed to overcome the complexities in the computation of the three-dimensional fluid flow.

Table 1 Values of fRe and Nu for fully developed laminar flow in rectangular channels (Shah and London, 1978)

Aspect ratio, γ	1	0.5, 2	0.2,5
fRe	14.227	15.548	19.071
Nu	3.091	3.02	2.93

Because of symmetry, it suffices to solve the problem in half of the rectangular region. The boundary conditions are

$$u=v=w_f=w=0 \text{ and } \partial\theta/\partial n=1 \text{ at walls}$$

$$u=\partial v/\partial x=\partial w/\partial x=\partial w_f/\partial x=\partial\theta/\partial x=0$$

$$\text{at symmetry plane } x=(1/\gamma+1)/4 \tag{8}$$

$$u=v=w=\xi=\theta=0 \text{ at entrance } z=0$$

where $\gamma=a/b$ is the aspect ratio of the rectangular channel. Then equations (2)-(7) and boundary conditions (8) can be solved for u, v, w, w_f, ξ, and θ by using the numerical technique described in Chou and Hwang (1987).

After the developing velocity and temperature fields along the axial direction are obtained, the computation of the local friction factor and the local Nusselt number are of practical interest. Following the usual definitions, the expression for the product of the friction factor and the Reynolds number $f\cdot\mathrm{Re}$ and the Nusselt number Nu can be written based on the overall force balance for an axial length dZ and the temperature gradient at the wall. The results are

$$(f\mathrm{Re})_0=2\bar{\tau}_w/(\rho\bar{W}_f^2)\cdot(\mathrm{De}\bar{W}_f/\nu)=-\mathrm{De}^2(\partial P_f/\partial Z)/(2\rho\nu\bar{W}_f) \tag{9}$$

$$f\mathrm{Re}/(f\mathrm{Re})_0=1+(\partial P/\partial Z)/(\partial P_f/\partial Z)=1-\mathrm{Ra}\cdot f_1(z)/C \tag{10}$$

$$\mathrm{Nu}=\bar{h}\mathrm{De}/k_f=1/(\bar{\theta}_w-\theta_b) \tag{11}$$

where the subscript 0 denotes the quantity for pure forced convection, θ_b is the local mixed-mean (bulk) fluid temperature, $f_1(z)=-(\partial P/\partial z)/\mathrm{Pe}^2$ is the dimensionless pressure term in the axial momentum equation (5), and $\bar{h}$ is the arithmetic average of the convective heat transfer coefficient on the walls of the channel. Although the Nusselt number may also be obtained by considering overall energy balance for the axial length, only the value of Nu in equation (11) is used in the present study because of better accuracy.

By numerical experiments, the axial step size Δz is selected depending on the magnitude of the Prandtl number and Rayleigh number. In the present study, Δz ranges from 10^{-4} to 4×10^{-4}. A larger Δz can be used for the lower value of Rayleigh number. In the case of high Rayleigh number and small Prandtl number, a small Δz was chosen. The cross-sectional mesh sizes ($M\times N$) of 16×80, 16×64, 30×30, and 40×16 are used for the aspect ratios $\gamma=0.2$, 0.5, 2 and 5. The required computer time for one set of Pr, Ra, and γ was approximately 800-1600 s on a CYBER-172 system.

Results and Discussion

Although not shown, a numerical experiment has been made in a manner similar to that of Chou and Hwang (1987) to ensure the independence of the computed numerical values on the mesh size $M\times N$ and axial step size Δz.

The buoyancy effect on the flow characteristics of the system is usually presented by the friction factor ratio

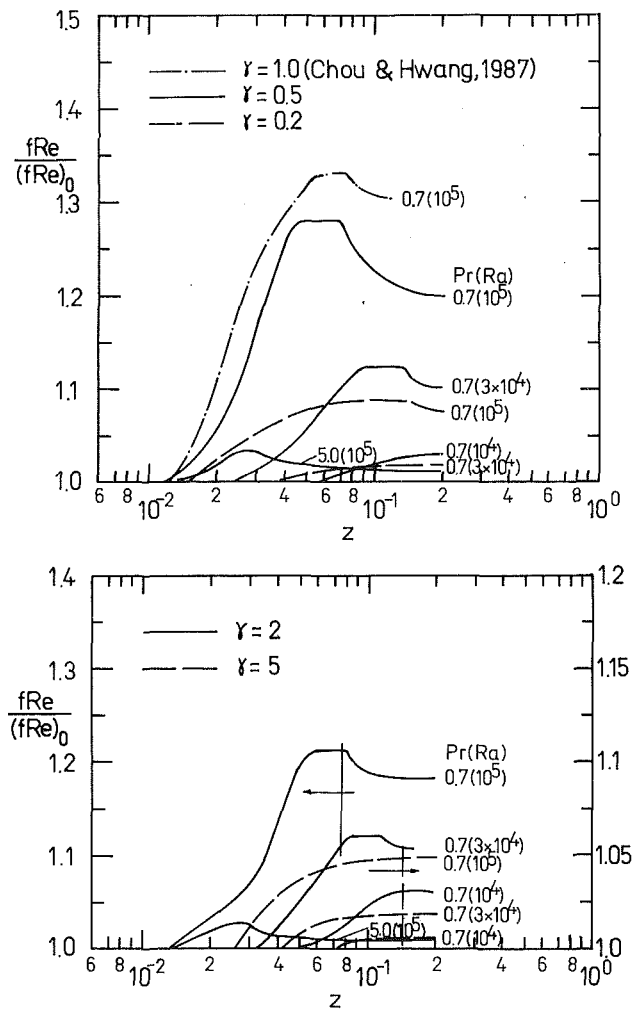

Fig. 1 Local friction factor versus z for (a) $\gamma = 0.2$ and 0.5, and (b) $\gamma = 2$ and 5

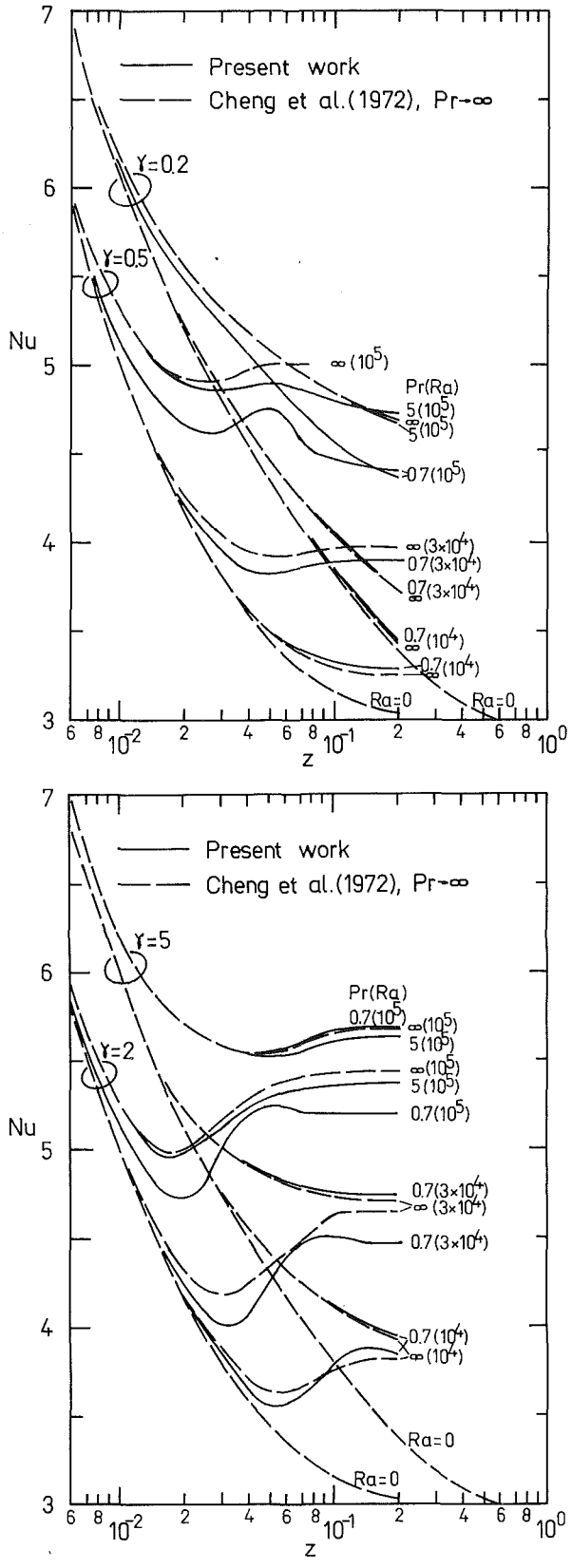

Fig. 2 Local Nusselt number versus z for (a) $\gamma = 0.2$ and 0.5, and (b) $\gamma = 2$ and 5

$fRe/(fRe)_0$, where the subscript 0 denotes the quantity for fully developed pure forced convection. The values of fRe and Nu for fully developed laminar flow in rectangular channels are shown in Table 1. Figures 1(*a*) and 1(*b*) show the variation of $fRe/(fRe)_0$ versus dimensionless axial length z for the cases of $\gamma = 0.2$ and 0.5, and $\gamma = 2$ and 5, respectively, with parameters $Pr = 0.7$ and $Ra = 10^4$, 3×10^4, and 10^5. The variation of the local friction factor ratio along the channel shows that the buoyancy effect is negligible up to a certain axial position z where the value of $fRe/(fRe)_0$ departs from unity. With further examination, one can observe that the axial position z is dependent mainly on the magnitude of the Rayleigh number and almost independent of the value of Pr. In other words, the curves having same value of Ra branch out from the line of $fRe/(fRe)_0 = 1.0$ at almost the same axial position. Then, after reaching maximum values, the curves rapidly approach the limiting values with fully developed velocity profiles. This phenomenon was also noted by Chou and Hwang (1987). Furthermore, the curves with higher Pr fall below those of lower Pr for the same value of Ra. The curves of higher Ra lie above those of lower Ra for the same value of Pr. It is also noted that for the same or even slightly higher values of Gr (= Ra/Pr), the curves with higher values of Pr give lower values of $fRe/(fRe)_0$ in the region at $z > 0.1$ in comparison with lower values of Pr.

A comparison between the results in Fig. 1(*a*) for $\gamma = 0.2$, 0.5, and 1 shows that the entry length is shortened by the increasing aspect ratio. The curves of higher aspect ratio ($\gamma = 0.5$) fall above those of $\gamma = 0.2$ for the same values of Ra and Pr. The trends are reversed in Fig 1(*b*) for $\gamma = 2$ and 5. The curves with aspect ratio $\gamma = 2$ have shorter entry lengths and lie above those of $\gamma = 5$ for the same values of Ra and Pr. A further comparison of the results in Figs. 1(*a*) and 1(*b*) reveals

that the curve of $Pr(Ra) = 0.7(10^5)$ for $\gamma = 1$ falls above those of $Pr(Ra) = 0.7(10^5)$ for aspect ratios other than 1 because of stronger secondary flow intensity.

The numerical results of the buoyancy effect on the local Nusselt number in the thermal entrance region of the horizontal channels with aspect ratios $\gamma = 0.2$ and 0.5, and $\gamma = 2$ and 5 are shown in Figs. 2(*a*) and 2(*b*). The results of Cheng et al. (1972), shown by dashed lines, based on the large Prandtl number assumption ($Pr \to \infty$), are also shown for comparison. The asymptotic value of Nu for pure forced convection at $z \to \infty$ are 3.02 for $\gamma = 0.5$ and 2, and 2.93 for $\gamma = 0.2$ and 5(Shah and London, 1978). The variation in the local Nusselt number along the channel axis z shows that the buoyancy effect is negligible up to a certain axial distance from the entrance depending mainly on the magnitude of Rayleigh number and the Prandtl number. The curve of local Nusselt number is seen to deviate from the curve with $Ra = 0$ as a result of the development of the secondary flow induced by buoyancy, and finally approaches an asymptotic value when the temperature profile becomes fully developed. For some curves, especially for the cases of $\gamma = 0.5$ and 2, a minimum-maximum local Nusselt number exists. The occurrence of the minimum Nusselt number is a result of combined entrance and natural convection effects as already explained by Cheng et al. (1972). Longitudinal oscillations in the Nusselt number were also reported by Knox and Incropera (1986) for the mixed convection in horizontal channels. In the present work, a comparison between the locations in the axial length z of the maximum local $f\mathrm{Re}/(f\mathrm{Re})_0$ and Nu for each set of parameters Ra, Pr, and γ, one can conclude that the maximum local Nusselt number is seen to be a result of the maximum intensity of secondary flow, which is represented by the maximum local $f\mathrm{Re}/(f\mathrm{Re})_0$.

A further comparison among the results Figs. 2(*a*) and 2(*b*) for $\gamma = 0.2$, 0.5, 2, and 5 shows that the effect of aspect ratio on the local Nusselt number variation is appreciable. Similar to the effect on the variation of local $f\mathrm{Re}/(f\mathrm{Re})_0$, the entry length is shorter in channels with aspect ratios close to 1, say 2 and 0.5, because of lower flow resistance. For the curves of fixed Ra and Pr, the asymptotic values of local Nusselt number Nu are seen to increase monotonically with the increase in aspect ratio.

One can also observe that the difference between the curves of $Pr = 0.7$, $Ra = 10^5$ and $Pr = 5$, $Ra = 10^5$ for $\gamma = 0.2$, 0.5, 2, and 5 decreases as the aspect ratio γ increases from 0.2 to 5. Prandtl number does affect the Nusselt number variation especially in channels of small aspect ratio. The Rayleigh number has a major effect on the heat transfer rate in the channel for all aspect ratios.

Acknowledgments

This work was supported by the National Science Council of Taiwan under Grant No. NSC75-0401-E007-01.

References

Abou-Ellail, M. M. M., and Morcos, S. M., 1983, "Buoyancy Effects in the Entrance Region of Horizontal Rectangular Channels," ASME JOURNAL OF HEAT TRANSFER, Vol. 104, pp. 924-928.

Cheng, K. C., and Hwang, G. J., 1969, "Numerical Solution for Combined Free and Forced Laminar Convection in Horizontal Rectangular Channels," ASME JOURNAL OF HEAT TRANSFER, Vol. 91, pp. 59-66.

Cheng, K. C., Hong, S. W., and Hwang, G. J., 1972, "Buoyancy Effects on Laminar Heat Transfer in the Thermal Entrance Region of Horizontal Rectangular Channels With Uniform Wall Heat Flux for Large Prandtl Number Fluid," *International Journal of Heat and Mass Transfer*, Vol. 15, pp. 1819-1836.

Cheng, K. C., and Ou, J. W., 1974, "Free Convection Effects on Graetz Problem for Large Prandtl Number Fluids in Horizontal Tubes With Uniform Wall Heat Flux," *Proceedings, 5th International Heat Transfer Conference*, Vol. 3, pp. 159-163.

Chou, F. C., and Hwang, G. J., 1984, "Combined Free and Forced Laminar Convection in Horizontal Rectangular Channels for High ReRa," *Canadian Journal of Chemical Engineering*, Vol. 62, pp. 830-836.

Chou, F. C., and Hwang, G. J., 1987, "Vorticity-Velocity Method for Graetz Problem With the Effect of Natural Convection in a Horizontal Rectangular Channel With Uniform Wall Heat Flux," ASME JOURNAL OF HEAT TRANSFER, Vol. 109, pp. 704-710.

Farouk, B., and Fusegi, T., 1986, "Predictions of Fluid and Heat Transfer Problems by the Vorticity-Velocity Formulation of the Navier-Stokes Equations," *Journal of Computational Physics*, Vol. 65, pp. 227-243.

Hieber, C. A., and Sreenivasan, S. K., 1974, "Natural Convection Effects on Graetz Problem in Horizontal Isothermal Tubes," *International Journal of Heat and Mass Transfer*, Vol. 17, pp. 1337-1348.

Hong, S. W., Morcos, S. M., and Bergles, A. E., 1974, "Analytical and Experimental Results for Combined Forced and Free Laminar Convection in Horizontal Tubes," *Proceedings, 5th International Heat Transfer Conference*, Vol. 3, pp. 154-158.

Hwang, G. J., and Lin, M. J., 1985, "Natural Convection Effects on Laminar Heat Transfer in the Thermal Entrance Region of Horizontal Isothermal Tube," *Journal of Chinese Institute of Engineers*, Vol. 8, pp. 343-355.

Kim, J., and Moin, M., 1985, "Application of Fractional Step Method to Incompressible Navier-Stokes Equation," *Journal of Computational Physics*, Vol. 59, pp. 308-323.

Knox, A. L., and Incropera, F. L., 1986, "Mixed Convection Flow and Heat Transfer in the Entry Region of a Horizontal Rectangular Duct," ASME Paper No. 86-HT-18.

Ou, J. W., Cheng, K. C., and Lin, R. C., 1974, "Natural Convection Effects on Graetz Problem in Horizontal Rectangular Channels With Uniform Wall Temperature for Large Pr," *International Journal of Heat and Mass Transfer*, Vol. 17, pp. 835-843.

Ou, J. W., and Cheng, K. C., 1977, "Natural Convection Effects on Graetz Problem in Horizontal Isothermal Tubes," *International Journal of Heat and Mass Transfer*, Vol. 20, pp. 953-960.

Ozisik, M. N., 1985, *Heat Transfer, A Basic Approach*, McGraw-Hill, New York.

Patankar, S. V., and Spalding, D. B., 1972, "A Calculation Procedure for Heat and Mass Transfer in Three Dimensional Parabolic Flows," *International Journal of Heat and Mass Transfer*, Vol. 15, pp. 1787-1806.

Ramakrishna, K., Rubin, S. G., and Khosla, P. K., 1982, "Laminar Natural Convection Along Vertical Square Ducts," *Numerical Heat Transfer*, Vol. 5, pp. 59-79.

Shah, R. H., and London, A. L., 1974, "Thermal Boundary Conditions and Some Solutions for Laminar Duct Flow Forced Convection," ASME JOURNAL OF HEAT TRANSFER, Vol. 96, pp. 159-165.

Shah, R. H., and London, A. L., 1978, *Laminar Flow Forced Convection in Ducts*, Academic Press, New York.

Oscillatory Natural Convection in Rectangular Enclosures Filled With Mercury

Y. Kamotani[1] and T. Sahraoui[1]

Introduction

Lately, natural convection in low Prandtl number (Pr) fluids has gained importance because of growing interest in the transport phenomena in crystal growth processes (Ostrach, 1983). It is known that some of the undesirable striations encountered in crystals grown from the melt are caused by thermal instabilities associated with natural convection in the melt. Several investigators in the past studied, theoretically as well as experimentally, natural convection in shallow rectangular enclosures with low Pr fluids, and found that the flow became oscillatory under certain conditions (e. g., Hurle et al., 1974; Gill, 1974; Hart, 1972, 1983; Kuo et al., 1986). The theoretical studies considered only very shallow and very wide enclosures. In a typical crystal growth configuration the container aspect ratio Ar (depth/length ratio) is not very small (typically 0.1 to 1) nor is the width ratio Wr (width/depth ratio) very large (typically 1 to 10), so the instability is expected to be influenced by the parameters Ar and Wr. Thus

[1]Department of Mechanical and Aerospace Engineering, Case Western Reserve University, Cleveland, OH 44106.

Contributed by the Heat Transfer Division and presented at the ASME/JSME Thermal Engineering Joint Conference, Honolulu, Hawaii, March 1987. Manuscript received by the Heat Transfer Division October 21, 1987. Keywords: Enclosure Flows, Flow Instability, Natural Convection.

that the curve of $Pr(Ra) = 0.7(10^5)$ for $\gamma = 1$ falls above those of $Pr(Ra) = 0.7(10^5)$ for aspect ratios other than 1 because of stronger secondary flow intensity.

The numerical results of the buoyancy effect on the local Nusselt number in the thermal entrance region of the horizontal channels with aspect ratios $\gamma = 0.2$ and 0.5, and $\gamma = 2$ and 5 are shown in Figs. 2(*a*) and 2(*b*). The results of Cheng et al. (1972), shown by dashed lines, based on the large Prandtl number assumption ($Pr \to \infty$), are also shown for comparison. The asymptotic value of Nu for pure forced convection at $z \to \infty$ are 3.02 for $\gamma = 0.5$ and 2, and 2.93 for $\gamma = 0.2$ and 5(Shah and London, 1978). The variation in the local Nusselt number along the channel axis z shows that the buoyancy effect is negligible up to a certain axial distance from the entrance depending mainly on the magnitude of Rayleigh number and the Prandtl number. The curve of local Nusselt number is seen to deviate from the curve with $Ra = 0$ as a result of the development of the secondary flow induced by buoyancy, and finally approaches an asymptotic value when the temperature profile becomes fully developed. For some curves, especially for the cases of $\gamma = 0.5$ and 2, a minimum-maximum local Nusselt number exists. The occurrence of the minimum Nusselt number is a result of combined entrance and natural convection effects as already explained by Cheng et al. (1972). Longitudinal oscillations in the Nusselt number were also reported by Knox and Incropera (1986) for the mixed convection in horizontal channels. In the present work, a comparison between the locations in the axial length z of the maximum local $f\mathrm{Re}/(f\mathrm{Re})_0$ and Nu for each set of parameters Ra, Pr, and γ, one can conclude that the maximum local Nusselt number is seen to be a result of the maximum intensity of secondary flow, which is represented by the maximum local $f\mathrm{Re}/(f\mathrm{Re})_0$.

A further comparison among the results Figs. 2(*a*) and 2(*b*) for $\gamma = 0.2$, 0.5, 2, and 5 shows that the effect of aspect ratio on the local Nusselt number variation is appreciable. Similar to the effect on the variation of local $f\mathrm{Re}/(f\mathrm{Re})_0$, the entry length is shorter in channels with aspect ratios close to 1, say 2 and 0.5, because of lower flow resistance. For the curves of fixed Ra and Pr, the asymptotic values of local Nusselt number Nu are seen to increase monotonically with the increase in aspect ratio.

One can also observe that the difference between the curves of $Pr = 0.7$, $Ra = 10^5$ and $Pr = 5$, $Ra = 10^5$ for $\gamma = 0.2$, 0.5, 2, and 5 decreases as the aspect ratio γ increases from 0.2 to 5. Prandtl number does affect the Nusselt number variation especially in channels of small aspect ratio. The Rayleigh number has a major effect on the heat transfer rate in the channel for all aspect ratios.

Acknowledgments

This work was supported by the National Science Council of Taiwan under Grant No. NSC75-0401-E007-01.

References

Abou-Ellail, M. M. M., and Morcos, S. M., 1983, "Buoyancy Effects in the Entrance Region of Horizontal Rectangular Channels," ASME JOURNAL OF HEAT TRANSFER, Vol. 104, pp. 924–928.

Cheng, K. C., and Hwang, G. J., 1969, "Numerical Solution for Combined Free and Forced Laminar Convection in Horizontal Rectangular Channels," ASME JOURNAL OF HEAT TRANSFER, Vol. 91, pp. 59–66.

Cheng, K. C., Hong, S. W., and Hwang, G. J., 1972, "Buoyancy Effects on Laminar Heat Transfer in the Thermal Entrance Region of Horizontal Rectangular Channels With Uniform Wall Heat Flux for Large Prandtl Number Fluid," *International Journal of Heat and Mass Transfer*, Vol. 15, pp. 1819–1836.

Cheng, K. C., and Ou, J. W., 1974, "Free Convection Effects on Graetz Problem for Large Prandtl Number Fluids in Horizontal Tubes With Uniform Wall Heat Flux," *Proceedings, 5th International Heat Transfer Conference*, Vol. 3, pp. 159–163.

Chou, F. C., and Hwang, G. J., 1984, "Combined Free and Forced Laminar Convection in Horizontal Rectangular Channels for High ReRa," *Canadian Journal of Chemical Engineering*, Vol. 62, pp. 830–836.

Chou, F. C., and Hwang, G. J., 1987, "Vorticity-Velocity Method for Graetz Problem With the Effect of Natural Convection in a Horizontal Rectangular Channel With Uniform Wall Heat Flux," ASME JOURNAL OF HEAT TRANSFER, Vol. 109, pp. 704–710.

Farouk, B., and Fusegi, T., 1986, "Predictions of Fluid and Heat Transfer Problems by the Vorticity-Velocity Formulation of the Navier-Stokes Equations," *Journal of Computational Physics*, Vol. 65, pp. 227–243.

Hieber, C. A., and Sreenivasan, S. K., 1974, "Natural Convection Effects on Graetz Problem in Horizontal Isothermal Tubes," *International Journal of Heat and Mass Transfer*, Vol. 17, pp. 1337–1348.

Hong, S. W., Morcos, S. M., and Bergles, A. E., 1974, "Analytical and Experimental Results for Combined Forced and Free Laminar Convection in Horizontal Tubes," *Proceedings, 5th International Heat Transfer Conference*, Vol. 3, pp. 154–158.

Hwang, G. J., and Lin, M. J., 1985, "Natural Convection Effects on Laminar Heat Transfer in the Thermal Entrance Region of Horizontal Isothermal Tube," *Journal of Chinese Institute of Engineers*, Vol. 8, pp. 343–355.

Kim, J., and Moin, M., 1985, "Application of Fractional Step Method to Incompressible Navier-Stokes Equation," *Journal of Computational Physics*, Vol. 59, pp. 308–323.

Knox, A. L., and Incropera, F. L., 1986, "Mixed Convection Flow and Heat Transfer in the Entry Region of a Horizontal Rectangular Duct," ASME Paper No. 86-HT-18.

Ou, J. W., Cheng, K. C., and Lin, R. C., 1974, "Natural Convection Effects on Graetz Problem in Horizontal Rectangular Channels With Uniform Wall Temperature for Large Pr," *International Journal of Heat and Mass Transfer*, Vol. 17, pp. 835–843.

Ou, J. W., and Cheng, K. C., 1977, "Natural Convection Effects on Graetz Problem in Horizontal Isothermal Tubes," *International Journal of Heat and Mass Transfer*, Vol. 20, pp. 953–960.

Ozisik, M. N., 1985, *Heat Transfer, A Basic Approach*, McGraw-Hill, New York.

Patankar, S. V., and Spalding, D. B., 1972, "A Calculation Procedure for Heat and Mass Transfer in Three Dimensional Parabolic Flows," *International Journal of Heat and Mass Transfer*, Vol. 15, pp. 1787–1806.

Ramakrishna, K., Rubin, S. G., and Khosla, P. K., 1982, "Laminar Natural Convection Along Vertical Square Ducts," *Numerical Heat Transfer*, Vol. 5, pp. 59–79.

Shah, R. H., and London, A. L., 1974, "Thermal Boundary Conditions and Some Solutions for Laminar Duct Flow Forced Convection," ASME JOURNAL OF HEAT TRANSFER, Vol. 96, pp. 159–165.

Shah, R. H., and London, A. L., 1978, *Laminar Flow Forced Convection in Ducts*, Academic Press, New York.

Oscillatory Natural Convection in Rectangular Enclosures Filled With Mercury

Y. Kamotani[1] and T. Sahraoui[1]

Introduction

Lately, natural convection in low Prandtl number (Pr) fluids has gained importance because of growing interest in the transport phenomena in crystal growth processes (Ostrach, 1983). It is known that some of the undesirable striations encountered in crystals grown from the melt are caused by thermal instabilities associated with natural convection in the melt. Several investigators in the past studied, theoretically as well as experimentally, natural convection in shallow rectangular enclosures with low Pr fluids, and found that the flow became oscillatory under certain conditions (e. g., Hurle et al., 1974; Gill, 1974; Hart, 1972, 1983; Kuo et al., 1986). The theoretical studies considered only very shallow and very wide enclosures. In a typical crystal growth configuration the container aspect ratio Ar (depth/length ratio) is not very small (typically 0.1 to 1) nor is the width ratio Wr (width/depth ratio) very large (typically 1 to 10), so the instability is expected to be influenced by the parameters Ar and Wr. Thus

[1]Department of Mechanical and Aerospace Engineering, Case Western Reserve University, Cleveland, OH 44106.

Contributed by the Heat Transfer Division and presented at the ASME/JSME Thermal Engineering Joint Conference, Honolulu, Hawaii, March 1987. Manuscript received by the Heat Transfer Division October 21, 1987. Keywords: Enclosure Flows, Flow Instability, Natural Convection.

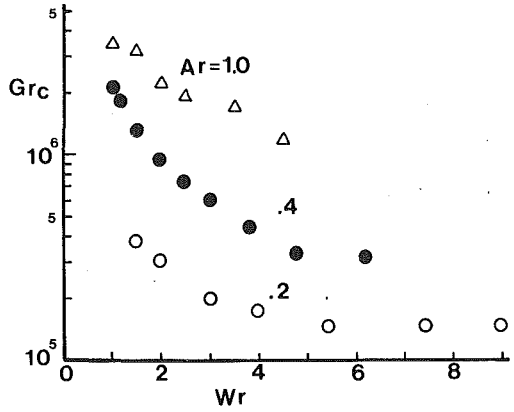

Fig. 1 Critical Grashof number as a function of *Wr*

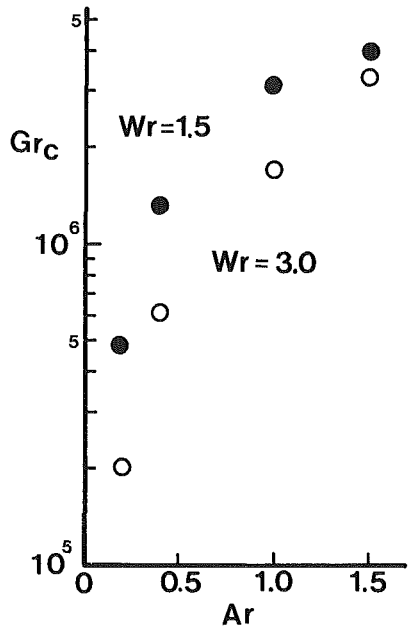

Fig. 2 Critical Grashof number as a function of *Ar*

the objective of the present work is to investigate experimentally the effects of *Ar* and *Wr* on the onset of thermal instability and the oscillation phenomenon. Mercury is used as the test fluid. The ranges of *Ar* and *Wr* in the present work are wider than those in the work by Hurle et al. (1974). The present work is partially based on the work by Sahraoui (1986).

Test Apparatus and Procedure

The test cell is a horizontally placed rectangular enclosure with variable depth, width, and length (distance between the vertical hot and cold end walls). The hot and cold end walls are water jackets made of copper with water from constant temperature baths running through them. The position of one of the end walls can be changed. The side and top walls of the test cell are made of 6.4-mm-thick plexiglass and the bottom wall is made of 17.5-mm-thick plexiglass. Since the thermal conductivity of mercury is 45 times that of plexiglass, the plexiglass walls are considered to be thermally insulated walls. The top plate has several small holes through which to insert a thermocouple probe into the test section. With the present system L (length) can be changed from 1 to 10 cm, W (width) up to 5 cm, and H (depth) up to 5 cm.

A thermocouple probe (0.2 mm dia) is used to measure temperature distribution in the test fluid. To detect

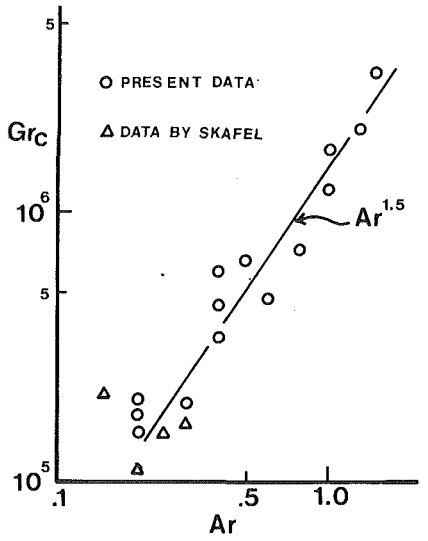

Fig. 3 Correlation of Gr_c with *Ar* for large *Wr*

temperature oscillations in the fluid the thermocouple output is amplified (10–1000 times) and fed to a rms meter or to an oscilloscope. To determine the onset of instability, the hot wall temperature is increased stepwise with a 0.2–1.0°C increment in each step. At each setting, the temperatures of the end walls are measured after they become steady and the output from the thermocouple probe placed inside the fluid is recorded. The measured temperature difference between the hot and cold walls (ΔT) is estimated to be accurate within 3 percent of ΔT. The onset of oscillation is reproducible within 15 percent of ΔT_c (critical temperature difference).

Results and Discussion

The important dimensionless parameters in the problem are: Grashof number Gr (based on H), Pr, Ar, and Wr. The Pr of mercury is 0.02. The Grashof number based on ΔT_c is the critical Grashof number Gr_c. The Gr in the present experiment is larger than 10^5. The past theoretical stability work considered only very shallow enclosures in which the flow streamlines are parallel in the core region (the region away from the hot and cold end regions) with a linear, stratified temperature gradient (the so-called core-driven flow regime). In the ranges of parameters studied herein the temperature measurement shows that there exist boundary layers along the hot and cold walls and the fluid temperature changes sharply in the end regions with much smaller temperature gradients in the core (the boundary layer flow regime). Therefore the stability criteria obtained by Hart (1983) and Gill (1974) are not applicable in the present experiment.

The effect of Wr on Gr_c is shown in Fig. 1. For a given Ar, Gr_c decreases with increasing Wr. The figure suggests that Gr_c becomes constant beyond about $Wr = 5$. The past analyses on the instability showed that longitudinal rolls appear in the enclosure after the onset of instability, the strength of which varies sinusoidally with time. Our oscillation phase study shows that only one roll is present in the range of Wr studied herein. If it can be assumed that Gr_c becomes minimum when the container is wide enough to accommodate at least one most unstable roll, the size of the most unstable roll is considered to be about $5H$ in contrast to $4.4H$ predicted for an infinitely wide container (Hart, 1983).

The effect of Ar on Gr_c is shown in Fig. 2. For a given Wr, Gr_c increases sharply with increasing Ar probably due to the fact that the viscous effect of the end walls on the roll increases. It is interesting to note that the oscillation occurs

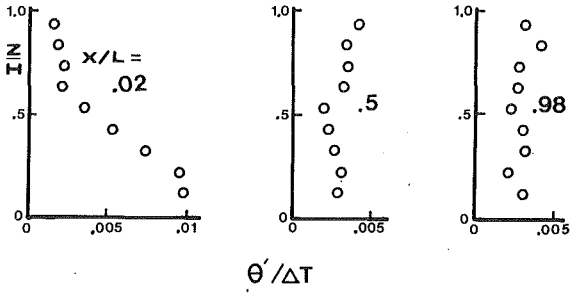

Fig. 4 Temperature oscillation amplitude variation with location for $Gr = 8 \times 10^7$, $Ar = 0.3$, and $Wr = 0.8$ (θ' = rms oscillation level, X = horizontal distance from cold end wall, Z = vertical distance from bottom wall)

even when $Ar > 1$, although the oscillation pattern is not very sinusoidal. Figure 2 also shows that the effect of Wr on Gr_c becomes smaller as Ar increases.

It is useful to attempt to correlate the experimental data of Gr_c obtained in the present work as well as in the past work. It turns out it is not possible to correlate Gr_c with both Ar and Wr, but if we accept an error of about 30 percent to obtain a rough criterion of the instability, the effect of Ar on Gr_c is more dominant than that of Wr as long as $Wr > 3$. For this reason the values of Gr_c are correlated with Ar in the range $Wr > 3$ in Fig. 3. The data taken by Skafel (reported by Gill, 1974) are also shown. Although Skafel's data are scattered, they generally agree with the present data. The trend in the figure indicates that Gr_c is nearly proportional to $Ar^{1.5}$. In terms of dimensional variables, ΔT_c is proportional to $(HL)^{-1.5}$, which means H and L are equally important for the instability.

Once the flow becomes unstable, the entire flow field oscillates, but the oscillation amplitude varies within the container. As Fig. 4 shows, the oscillation level is highest near the bottom of the cold wall. In some cases the oscillation level is found to be relatively high also near the top of the hot wall. Thus the oscillation level is high in the regions where the temperature gradients are relatively large. The fact that the oscillation level is high near the end walls is considered to be detrimental to crystal growth processes.

Conclusion

The results of the above experiment on oscillatory natural convection in mercury-filled rectangular enclosures show that the instability is influenced by the container aspect ratio and the width ratio. The flow becomes more resistant to oscillation as the aspect ratio is increased. For a given aspect ratio the critical temperature difference is minimum when the container width is about 5 times the depth. The oscillation level is relatively high near the end walls.

References

Gill, A. E., 1974, "A Theory of Thermal Oscillations in Liquid Metals," *Journal of Fluid Mechanics*, Vol. 64, Part 3, pp. 577–588.

Hart, J., 1972, "Stability of Thin Non-rotating Hadley Cells," *Journal of Atmospheric Science*, Vol. 29, pp. 687–697.

Hart, J., 1983, "A Note on the Stability of Low-Prandtl-Number Hadley Circulations," *Journal of Fluid Mechanics*, Vol. 132, pp. 271–281.

Hurle, D. T. J., Jakeman, E., and Johnson, C. P., 1974, "Convective Temperature Oscillations in Molten Gallium," *Journal of Fluid Mechanics*, Vol. 64, Part 3, pp. 565–576.

Kuo, H. P., Korpela, S. A., Chait, A., and Marcus, P. S., 1986, "Stability of Natural Convection in a Shallow Cavity," *Proceedings, 8th International Heat Tranfser Conference*, Hemisphere Publishing Corp., Washington, DC, Vol. 4, pp. 1539–1544.

Ostrach, S., 1983, "Fluid Mechanics in Crystal Growth, The 1982 Freeman Scholar Lecture," ASME *Journal of Fluids Engineering*, Vol. 105, pp. 5–10.

Sahraoui, T., 1986, "Oscillatory Natural Convection in Shallow Rectangular Enclosures Filled With Mercury," M. S. Thesis, Case Western Reserve University, Cleveland, OH.

Measurement of Liquid Film Thickness During Passage of Bubbles in a Vertical Rectangular Channel

M. Monde[1]

Introduction

Heat transfer is markedly enhanced when bubbles generated on a heated surface pass through the narrow space under conditions of bubble or slug flow (Ishibashi and Nishikawa, 1969; Monde and Kusuda, 1988). In boiling on a horizontal tube bundle (Nakashima, 1978; Fujita et al., 1986), the heat transfer is enhanced in a certain range of heat flux by vapor bubbles. It is pointed out by Monde (1988) and Nakashima (1978) that a remaining liquid film, which is created when a bubble passes through, plays an essential role in heat transfer enhancement. Therefore, knowledge of the liquid film thickness is necessary to elucidate the mechanism of enhancement due to the passing bubbles. The thickness of the liquid film, however, seems to remain unknown except for some special cases: bubbles in a capillary tube (Marchessault and Mason, 1960), in a vertical tube sealed at one end (Bretherton, 1960), and in a vertical tube in which a bubble rises at terminal velocity (Street and Tek, 1965), transient voiding of a liquid-filled channel (Oezgu and Chen, 1976), and slug expulsion (Fauske et al., 1970).

The present paper measures the liquid film thickness remaining on the wall when a bubble rises in a vertical rectangular channel.

Experimental Apparatus and Procedure

The entire experimental system consists of four main portions: a test section where the heat is transferred from a heating material mounted into a narrow space of 2 mm wide to the test liquid, equipment for forcibly injecting an air bubble into the narrow space, an electrical system for heating both the heating material and the test liquid, and equipment to measure the temperature and the heat rate of the heating material. This system is the same as that employed in the experiment of Monde and Kusuda (1988), except for the injection equipment. The injection equipment will be explained here.

Figure 1 shows the main part of the experimental apparatus. Air at room temperature is injected into the narrow space at a designated period of 0.1 to 1.0 s within a scatter of ± 3 percent by controlling the frequency of a solenoid valve ⑩ connected with a frequency controller. The length of the air bubble can be controlled to be equal to 0.01, 0.02, and 0.03 m within a scatter of ± 5 percent by adjusting the pressure of the air line with a decompressing valve. The range of the period was determined from the following points: first, the limitation of the frequency response of the solenoid valve, and second, the stability of the frequency controller. A conducting copper block is connected to each end of a stainless steel foil 50 μm thick and this foil (0.01 m long and 0.02 m wide), being directly heated by a direct current, works as the heating material. This foil is brazed onto the copper block to reduce the electrical contact resistance, so that more than 97 percent of the electrical input can be consumed properly in this foil. This fact was checked by comparing the calculated resistance of this foil with the measured resistance calculated by measuring both voltage drop and current. The commercial stainless steel foil was used in this experiment without any processing of the surface except for cleaning it with acetone and then pure water. The reverse side of the foil was fastened by a binding agent

[1]Department of Mechanical Engineering, Saga University, Japan 840.

Contributed by the Heat Transfer Division for publication in the JOURNAL OF HEAT TRANSFER. Manuscript received by the Heat Transfer Division April 26, 1988. Keywords: Measurement Techniques, Multiphase Flows, Phase-Change Phenomena.

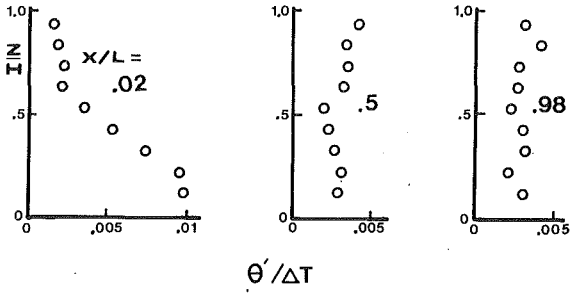

Fig. 4 Temperature oscillation amplitude variation with location for $Gr = 8 \times 10^7$, $Ar = 0.3$, and $Wr = 0.8$ (θ' = rms oscillation level, X = horizontal distance from cold end wall, Z = vertical distance from bottom wall)

even when $Ar > 1$, although the oscillation pattern is not very sinusoidal. Figure 2 also shows that the effect of Wr on Gr_c becomes smaller as Ar increases.

It is useful to attempt to correlate the experimental data of Gr_c obtained in the present work as well as in the past work. It turns out it is not possible to correlate Gr_c with both Ar and Wr, but if we accept an error of about 30 percent to obtain a rough criterion of the instability, the effect of Ar on Gr_c is more dominant than that of Wr as long as $Wr > 3$. For this reason the values of Gr_c are correlated with Ar in the range $Wr > 3$ in Fig. 3. The data taken by Skafel (reported by Gill, 1974) are also shown. Although Skafel's data are scattered, they generally agree with the present data. The trend in the figure indicates that Gr_c is nearly proportional to $Ar^{1.5}$. In terms of dimensional variables, ΔT_c is proportional to $(HL)^{-1.5}$, which means H and L are equally important for the instability.

Once the flow becomes unstable, the entire flow field oscillates, but the oscillation amplitude varies within the container. As Fig. 4 shows, the oscillation level is highest near the bottom of the cold wall. In some cases the oscillation level is found to be relatively high also near the top of the hot wall. Thus the oscillation level is high in the regions where the temperature gradients are relatively large. The fact that the oscillation level is high near the end walls is considered to be detrimental to crystal growth processes.

Conclusion

The results of the above experiment on oscillatory natural convection in mercury-filled rectangular enclosures show that the instability is influenced by the container aspect ratio and the width ratio. The flow becomes more resistant to oscillation as the aspect ratio is increased. For a given aspect ratio the critical temperature difference is minimum when the container width is about 5 times the depth. The oscillation level is relatively high near the end walls.

References

Gill, A. E., 1974, "A Theory of Thermal Oscillations in Liquid Metals," *Journal of Fluid Mechanics*, Vol. 64, Part 3, pp. 577–588.

Hart, J., 1972, "Stability of Thin Non-rotating Hadley Cells," *Journal of Atmospheric Science*, Vol. 29, pp. 687–697.

Hart, J., 1983, "A Note on the Stability of Low-Prandtl-Number Hadley Circulations," *Journal of Fluid Mechanics*, Vol. 132, pp. 271–281.

Hurle, D. T. J., Jakeman, E., and Johnson, C. P., 1974, "Convective Temperature Oscillations in Molten Gallium," *Journal of Fluid Mechanics*, Vol. 64, Part 3, pp. 565–576.

Kuo, H. P., Korpela, S. A., Chait, A., and Marcus, P. S., 1986, "Stability of Natural Convection in a Shallow Cavity," *Proceedings, 8th International Heat Tranfser Conference*, Hemisphere Publishing Corp., Washington, DC, Vol. 4, pp. 1539–1544.

Ostrach, S., 1983, "Fluid Mechanics in Crystal Growth, The 1982 Freeman Scholar Lecture," ASME *Journal of Fluids Engineering*, Vol. 105, pp. 5–10.

Sahraoui, T., 1986, "Oscillatory Natural Convection in Shallow Rectangular Enclosures Filled With Mercury," M. S. Thesis, Case Western Reserve University, Cleveland, OH.

Measurement of Liquid Film Thickness During Passage of Bubbles in a Vertical Rectangular Channel

M. Monde[1]

Introduction

Heat transfer is markedly enhanced when bubbles generated on a heated surface pass through the narrow space under conditions of bubble or slug flow (Ishibashi and Nishikawa, 1969; Monde and Kusuda, 1988). In boiling on a horizontal tube bundle (Nakashima, 1978; Fujita et al., 1986), the heat transfer is enhanced in a certain range of heat flux by vapor bubbles. It is pointed out by Monde (1988) and Nakashima (1978) that a remaining liquid film, which is created when a bubble passes through, plays an essential role in heat transfer enhancement. Therefore, knowledge of the liquid film thickness is necessary to elucidate the mechanism of enhancement due to the passing bubbles. The thickness of the liquid film, however, seems to remain unknown except for some special cases: bubbles in a capillary tube (Marchessault and Mason, 1960), in a vertical tube sealed at one end (Bretherton, 1960), and in a vertical tube in which a bubble rises at terminal velocity (Street and Tek, 1965), transient voiding of a liquid-filled channel (Oezgu and Chen, 1976), and slug expulsion (Fauske et al., 1970).

The present paper measures the liquid film thickness remaining on the wall when a bubble rises in a vertical rectangular channel.

Experimental Apparatus and Procedure

The entire experimental system consists of four main portions: a test section where the heat is transferred from a heating material mounted into a narrow space of 2 mm wide to the test liquid, equipment for forcibly injecting an air bubble into the narrow space, an electrical system for heating both the heating material and the test liquid, and equipment to measure the temperature and the heat rate of the heating material. This system is the same as that employed in the experiment of Monde and Kusuda (1988), except for the injection equipment. The injection equipment will be explained here.

Figure 1 shows the main part of the experimental apparatus. Air at room temperature is injected into the narrow space at a designated period of 0.1 to 1.0 s within a scatter of ± 3 percent by controlling the frequency of a solenoid valve ⑩ connected with a frequency controller. The length of the air bubble can be controlled to be equal to 0.01, 0.02, and 0.03 m within a scatter of ± 5 percent by adjusting the pressure of the air line with a decompressing valve. The range of the period was determined from the following points: first, the limitation of the frequency response of the solenoid valve, and second, the stability of the frequency controller. A conducting copper block is connected to each end of a stainless steel foil 50 μm thick and this foil (0.01 m long and 0.02 m wide), being directly heated by a direct current, works as the heating material. This foil is brazed onto the copper block to reduce the electrical contact resistance, so that more than 97 percent of the electrical input can be consumed properly in this foil. This fact was checked by comparing the calculated resistance of this foil with the measured resistance calculated by measuring both voltage drop and current. The commercial stainless steel foil was used in this experiment without any processing of the surface except for cleaning it with acetone and then pure water. The reverse side of the foil was fastened by a binding agent

[1]Department of Mechanical Engineering, Saga University, Japan 840.

Contributed by the Heat Transfer Division for publication in the JOURNAL OF HEAT TRANSFER. Manuscript received by the Heat Transfer Division April 26, 1988. Keywords: Measurement Techniques, Multiphase Flows, Phase-Change Phenomena.

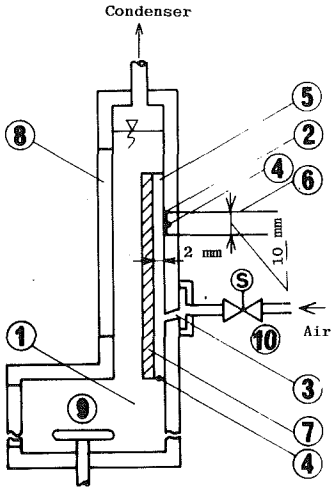

1. Heating apparatus
2. Heated material
3. Nozzle
4. Thermocouple
5. Spacer
6. Electrode
7. Glass plate
8. Window
9. Auxiliary
10. Solenoid valve

Fig. 1 Essential part of the experimental apparatus

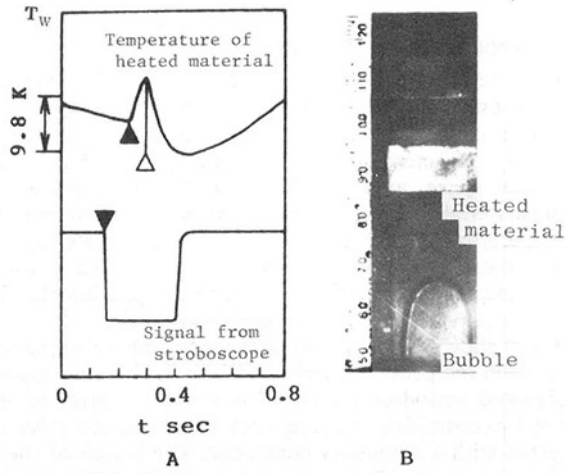

Fig. 2 Transient temperature of the heated material and position of the passing bubble (q_w = 1.2 × 10⁵ W/m², T_o = 1.0 s, l_b = 0.03 m, and T_b = 30°C)

to a bakelite block for thermal insulation. This foil was set up at the position of 0.15 m from the entrance of the narrow space. The clearance of the narrow space was built by attaching 2-mm glass spacers to both sides of the narrow space.

A Joule-heat from the heating material is determined by assuming the thermal energy to be equal to the electric input. The local temperature of the heating material T_w was measured by a chromel-alumel thermocouple 50 μm in diameter spot-welded to the center of the back side of the foil. The heat loss through the thermocouple lead was reduced by giving the lead near the foil the shape of a fork. It should be noted that the temperature difference between both sides of this foil was about 0.1 K at a Joule heat of 20 W generated in the foil, corresponding to a heat flux of 10^5 W/m² on the assumption that the back side is completely insulated. The variation of the temperature of the heating material was recorded by an electromagnetic oscillograph having a frequency response of 300 Hz and a sensitivity of 0.1 K. The relationship between the temperature change of the heating material and the position of the bubble can be measured by synchronizing the electromagnetic oscillograph to a 35-mm still camera connected with a stroboscope. The temperature of the test liquid measured at the entrance of the narrow space was kept at 303 K (30°C) and 333 K (60°C), with a temperature fluctuation of 0.1 K, by using an auxiliary heater.

Experimental Results: Transient Temperatures of the Heated Material During the Passage of a Bubble

Figure 2 shows a typical transient temperature response at a heat flux of 1.2 × 10^5 W/m² for a period of 1.0 s related to the position of the bubble. The time, indicated with the mark ▲ in Fig. 2, at which the bubble just arrives at the heating material, can be calculated from the rising velocity of the bubble (Monde and Kusuda, 1988) and the position of the bubble at the timing mark ▼. The symbol △ in Fig. 2 gives the time at which the bubble just leaves the heating material.

From the curve of the transient temperature measured under the conditions shown in Fig. 2, we notice that the temperature of the heating material rises rapidly immediately after the bubble reaches it, and then continues to increase until the bubble passes over it. This is due to the fact that most of the heat from the heating material is stored as sensible heat in the residual liquid on it, because no evaporation would occur on the interface appearing during the passage of the bubble. It should be noted that when the temperature of the residual liquid continues to rise and approaches the saturation temperature, part of the heat is transported by latent heat due to evaporation on the interface.

The temperature, and the time derivative of the temperature at a fixed time, can be measured from the transient temperature curve as shown in Fig. 2 by the following procedure. The original chart, on which the transient temperature is measured, first is optically enlarged about seven times to read the scale easily. It is necessary to add that noise with a frequency of 60 Hz, induced by an electric unit, is superimposed on the transient temperatures in the original chart, and its level is less than 0.2 K. This noise, however, can be skillfully eliminated by sampling the values of the transient temperature on a mesh, overlapped on the chart, with a frequency of 60 Hz and by smoothly connecting these values on it since the same level of noise would appear on it. The temperatures at five different points around a fixed time t_o from the time when the temperature starts rising are measured, yielding the time derivative of the temperature at that time as follows:

$$\frac{dT_w(t_o)}{dt} = \frac{4}{7}\left[\frac{1}{\Delta t}(T_w(t_o+\Delta t) - T_w(t_o)) + \frac{1}{4\,\Delta t}(T_w(t_o+\Delta t) - T_w(t_o-\Delta t)) + \frac{1}{16\,\Delta t}(T_w(t_o+2\Delta t) - T_w(t_o-2\Delta t))\right] \quad (1)$$

where Δt is 0.0025 or 0.005 s, corresponding to t_o = 0.01 or 0.02 s, respectively. Equation (1) can make a reduction of an error with smoothing and using weighted factors in approximating a derivative with a finite difference method. The error in this way is about $(2/7)\Delta t(d^2T_w/dt^2)$ compared with $0.5\Delta t(d^2T_w/dt^2)$ in an ordinary finite difference, namely $(T_w(t_o+\Delta t) - T_w(t_o))/\Delta t$. In addition, the uncertainty of $dT_w(t_o)/dt$ calculated mainly depends on the temperature difference and time interval Δt. The reduction in the error of $dT_w(t_o)/dt$ was attained by making the time interval Δt smaller and then the temperature difference larger. This is, however, contradictory, and it is impossible to satisfy both conditions. Therefore, Δt = 0.0025 or 0.005 is chosen such that $(T_w(t_o+\Delta t) - T_w(t_o))$ becomes larger than about 1 K. As a result, the uncertainty may become less than 10 percent. Figure 3 shows the time derivative $dT_w(t_o)/dt$ plotted against the heat flux for the period of the passing bubble. The scattering of $dT_w(t_o)/dt$ in Fig. 3 is mainly attributed to the uncertainty of

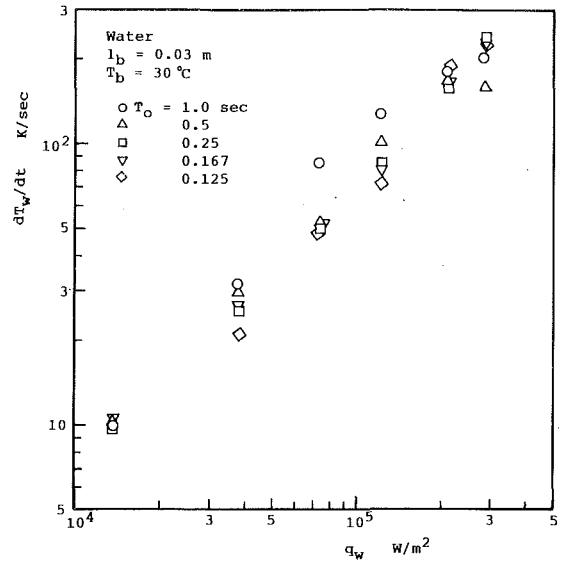

Fig. 3 Relationship between time derivative of the heated material temperature and the heat flux

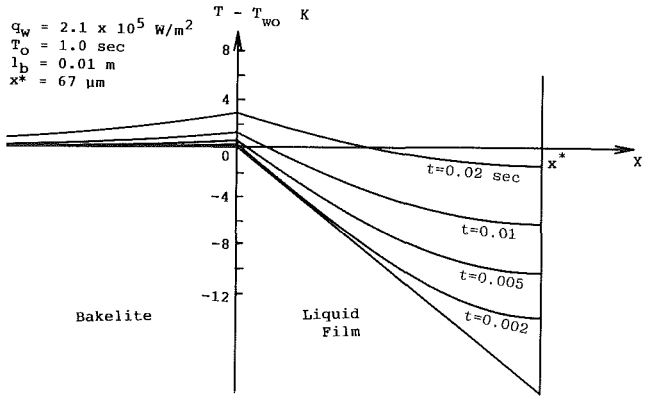

Fig. 4 Temperature profile in the liquid film and the bakelite for the case of q_w = 2.1 x 10^5 W/m^2, T_o = 1.0 s, and l_b = 0.01 m

$(T_w(t_o+\Delta t) - T_w(t_o))$, and to the scatter of the bubble length as well as the period.

Prediction of Film Thickness

To calculate the film thickness from the transient temperature curves as shown in Fig. 2, we introduce the following assumptions as first approximations.

1 Heat flows in the liquid film and the bakelite are given by one-dimensional heat conduction. The convective effect in the liquid film is ignored because the liquid film is created by suddenly cutting off a nearly fully developed velocity boundary layer with the bubble, which leaves it very thin.

2 The temperature in the stainless steel foil is uniform over its width since its thermal diffusivity is about thirty times as large as that of water. In addition, it is very difficult to measure the temperature gradient in the foil. As a result, it was assumed that the temperature of the foil was equal to the transient temperature in Fig. 2.

3 The transient temperature is approximated by a polynomial of second order with $T_w(t_o)$ and $dT_w(t_o)/dt$ as

$$T_w(t) - T_w(0) = A\,t^2 + Bt \tag{2}$$

where

$$A = (dT_w(t_o)/dt)/t_o - (T_w(t_o) - T_w(0))/t_o^2$$

$$B = -(dT_w(t_o)/dt) + 2(T_w(t_o) - T_w(0))/t_o$$

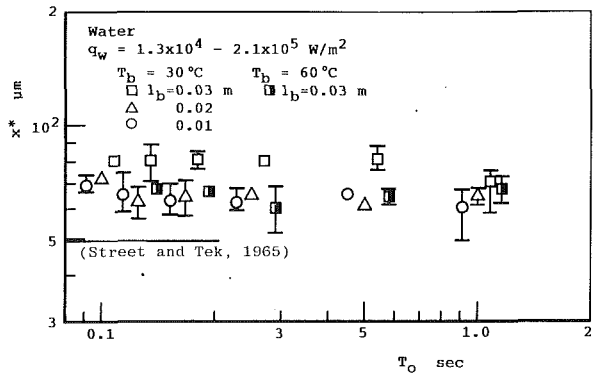

Fig. 5 Thickness of the liquid film versus period of the passing bubble

The constants A and B in equation (2) are given from the measurement of the transient temperature.

4 The initial temperature profile in the thin liquid film may be approximated as

$$T(x) = T_w(0) - (q_w/\lambda)x, \qquad 0<x<x^* \tag{3}$$

since the temperature profile in the liquid, which is formed on the foil during one cycle, is suddenly cut off at $x = x^*$ very near the foil by the passing bubble (Monde, 1988). In addition, as dT_w/dt is negligibly small just before the passing bubble reaches the foil, q_w may be nearly equal to the actual heat flux on the foil surface.

5 The 10-mm-thick bakelite used to reduce the heat loss is semi-infinite, since the heat cannot penetrate the other end in the short time of t_o = 0.02 s.

On the basis of these assumptions, one can obtain the temperature profiles in the thin liquid film and the bakelite under the conditions prescribed by equations (2) and (3) by using the Laplace transformation (Carslaw and Jaeger, 1959) when the thin film appears during the passage of the bubble. The heat flux at both surfaces of the foil can be easily derived from the temperature profiles obtained as

$$q_l = q_w - 2\,q_w \sum_0^\infty (-1)^n \operatorname{erfc}\frac{(2n+1)x^*}{2\sqrt{at}} + \frac{2\lambda}{a}\sqrt{at}B\left[\frac{1}{\sqrt{\pi}} + 2\sum_1^\infty (-1)^n \left(\frac{1}{\sqrt{\pi}} e^{-n^2x^{*2}/at} - \frac{n\,x^*}{\sqrt{at}}\operatorname{erfc}\frac{nx^*}{\sqrt{at}}\right)\right] + \frac{16\lambda A\sqrt{at^3}}{a}\left(\frac{1}{\sqrt{\pi}} + \sum_1^\infty (-1)^n\, i^3\operatorname{erfc}\frac{n\,x^*}{\sqrt{at}}\right) \tag{4}$$

$$q_b = \frac{2B}{\sqrt{\pi}}\sqrt{(\rho c\lambda)_b t} + \frac{8\,A\sqrt{(\rho c\lambda)_b t^3}}{3\sqrt{\pi}} \tag{5}$$

where q_1 and q_b are the surface heat fluxes for the liquid film and the bakelite, ρ, c, λ, and a are density, specific heat, thermal conductivity, and thermal diffusivity, and x^* and t are the film thickness and the time.

In addition, the heat balance in the foil may be expressed

$$Q_s = Q_j - Q_l - Q_b \tag{6}$$

where $Q_s = \int_0^t (\rho c\delta)_s\,(dT_w/dt)\,dt$, $Q_j = q_w\,t$, $Q_l = \int_0^t q_l\,dt$, and $Q_b = \int_0^t q_b\,dt$; Q_j is a Joule heat generated in the foil, Q_s is an internal energy of the foil, and Q_l and Q_b are the heat transfer rates per unit area from both ends of the foil to the liquid and the bakelite.

The liquid film thickness can be implicitly determined from equation (6), with equations (4) and (5), by numerical methods, because of the difficulty of performing the integration. The

value of the film thickness can be determined by an iterative substitution of a value into x^* in equation (4) until the difference between both sides of equation (6) becomes a minimum for fixed values of A, B, and q_w measured. Figure 4 shows, as an example, a transient temperature profile in the liquid film and the bakelite calculated from equations (4) and (5) after determining the thickness x^*.

Figure 5 shows the liquid film thickness determined by the abovementioned procedure against the period of the passing bubble with different lengths. In Fig. 5, a light solid line is the prediction of Street and Tek (1965) for a limiting thickness given by a balance of wall shear and gravity forces in a vertical tube. It was corrected for a rectangular channel by using hydraulic diameter.

From Fig. 5, it can be seen that most of the values of the liquid film thickness range from 60 to 80 μm over the whole experimental range of $q_w = 1.3 \times 10^4$–2.8×10^5 W/m^2, $T_o = 0.1$–1.0 s, and $l_b = 0.01$, 0.02, and 0.03 m. The scattering of the data seems to be attributed to the uncertainty of the measurements, especially $dT_w(t_o)/dt$, because $dT_w(t_o)/dt$ plays an essential role in equation (2) and the error included in $dT_w(t_o)/dt$ propagates in the iteration of equations (4), (5), and (6). Therefore, these data are statistically processed to give $x^* = 71.7$ μm as a mean and $\sigma_x = 1.38$ as the standard deviation. It should be mentioned that under the condition of $q_w = 3.7 \times 10^4$ W/m^2, $T_o = 1.0$ s, and $l_b = 0.03$ m, 10.0 percent of the Joule heat Q_j is consumed as Q_s, 86.3 percent as Q_l, and 3.7 percent as Q_b.

Finally, it may be of interest to note that the film thickness $x^* = 34$ μm for a space of 2 mm, irrespective of volume and frequency of injected air bubbles, although the uncertainty of measurements and situations of their experiments are unknown (Nishikawa et al., 1984).

Conclusions

To measure the liquid film thickness remaining on the wall during the passage of a bubble in a vertical rectangular channel, an experiment has been carried out by injecting air bubbles with lengths of 0.01, 0.02, and 0.03 m at periods of 0.1 to 1.0 s into it. The thickness ranged from 60 to 80 μm. It was independent of the bubble length and the period of the passing bubble over the whole experimental range. The mean value of the thickness was 72 μm.

References

Bretherton, F. P., 1961, "The Motion of Long Bubbles in Tubes," *J. Fluid Mechanics*, Vol. 10, pp. 166–188.

Carslaw, H. S., and Jaeger, J. C., 1959, *Conduction of Heat in Solids*, Oxford University Press, United Kingdom.

Fauske, H. K., Ford, W. D., and Grolmes, M. A., 1970, "Liquid Film Thickness for Slug Expulsion," *Trans. ANS.*, Vol. 13, pp. 646–647.

Fujita, Y., Ohta, H., Hidaka, S., and Nisikawa, K., 1986, "Nucleate Boiling Heat Transfer on Horizontal Tubes in Bundles," *Heat Transfer 86*, Vol. 5, pp. 2131–2136.

Ishibashi, E., and Nishikawa, K., 1969, "Saturated Boiling Heat Transfer in Narrow Space," *Int. J. Heat Mass Transfer*, Vol. 12, pp. 863–894.

Marchessault, R. N., and Mason, S. G., 1960, "Flow of Entrapped Bubbles Through a Capillary," *Ind. Engng. Chem.*, Vol. 52, pp. 79–84.

Monde, M., 1988, "Characteristic of Heat Transfer Enhancement Due to Bubbles Passing Through a Narrow Vertical Channel," ASME JOURNAL OF HEAT TRANSFER, Vol. 110, pp. 1016–1019.

Monde, M., and Kusuda, H., 1988, "Enhancement of Heat Transfer Due to Bubbles Passing Through a Narrow Vertical Rectangular Channel," *Proc. of 1st World Conf. on Experimental Heat Transfer, Fluid Mechanics and Thermodynamics*, Dubrovnik, Yugoslavia, pp. 1459–1465.

Nakashima, K., 1978, "Boiling Heat Transfer Outside Horizontal Multitube Bundle," *Trans. of JSME*, Vol. 42, pp. 1047–1057.

Nishikawa, K., Fujita, Y., Uchida, S., and Ohta, H., 1984, "Effect of Surface Configuration on Nucleate Boiling Heat Transfer," *Int. J. Heat Mass Transfer*, Vol. 27, pp. 1559–1571.

Oezgu, M. R., and Chen, J. C., 1976, "Local Film Thickness During Transient Voiding of a Liquid-Filled Channel," ASME JOURNAL OF HEAT TRANSFER, Vol. 98, pp. 159–165.

Street, J. R., and Tek, M. R., 1965, "Dynamics of Bullet Shaped Bubbles Encountered in Vertical Gas Liquid Slug Flow," *AIChE Journal*, Vol. 11, pp. 644–650.

An Experimental Study in Nucleate Boiling Heat Transfer From a Sphere

D. Dix[1] and J. Orozco[1]

Nomenclature

A = area
c_p = specific heat
k = thermal conductivity
m = sphere mass
q' = heat flux
q = heat rate
q'_{mb} = Moissis–Berenson transition flux
r = sphere radius
t = time
T = temperature
$\Delta T_v = T_w - T_{sat}$
$\Delta T_b = T_{sat} - T_l$
α = thermal diffusivity
θ = angle measured from the forward stagnation point
ρ = density
ϕ = azimuthal angle

Superscript

n = time step in finite difference analysis

Subscripts

b = boiling
c = conduction
i = inner
l = liquid
o = outer
sat = saturation
v = vapor
w = wall

Introduction

A systematic investigation of the effects of the orientation and dimensions of the heated surface on the nucleate boiling regime was presented by Van Stralen and Sluyter (1969). The behavior of water and some aqueous binary systems was studied on electrically heated platinum wires, both for saturated pool boiling and for surface boiling. Their findings showed that the peak flux density for the platinum wire in the horizontal position was 45 percent higher than the corresponding value for the wire in the vertical position. They also found that the boiling fluxes in the region of isolated bubbles were always higher for the horizontal wire. They attributed this effect not only to an increased maximal bubble population (the main cause), but also partly to a higher convective contribution. The smaller number of active sites for the vertical position was believed to be caused by a premature onset of film boiling in the upper part of the wire, due to the formation of large vapor slugs. In this case, the coalescing bubbles originated from nuclei that were distributed over the entire heating surface. This behavior differed from that on a horizontal wire, where bubble coalescence was generally restricted to nearby nuclei.

Recently, the issue of the influence of surface orientation on

[1]Department of Mechanical Engineering, University of Illinois at Chicago, Chicago, IL 60680.

Contributed by the Heat Transfer Division for publication in the JOURNAL OF HEAT TRANSFER. Manuscript received by the Heat Transfer Division June 13, 1988. Keywords: Boiling, Flow Visualization, Instrumentation.

value of the film thickness can be determined by an iterative substitution of a value into x^* in equation (4) until the difference between both sides of equation (6) becomes a minimum for fixed values of A, B, and q_w measured. Figure 4 shows, as an example, a transient temperature profile in the liquid film and the bakelite calculated from equations (4) and (5) after determining the thickness x^*.

Figure 5 shows the liquid film thickness determined by the abovementioned procedure against the period of the passing bubble with different lengths. In Fig. 5, a light solid line is the prediction of Street and Tek (1965) for a limiting thickness given by a balance of wall shear and gravity forces in a vertical tube. It was corrected for a rectangular channel by using hydraulic diameter.

From Fig. 5, it can be seen that most of the values of the liquid film thickness range from 60 to 80 μm over the whole experimental range of $q_w = 1.3 \times 10^4$–2.8×10^5 W/m^2, $T_o = 0.1$–1.0 s, and $l_b = 0.01$, 0.02, and 0.03 m. The scattering of the data seems to be attributed to the uncertainty of the measurements, especially $dT_w(t_o)/dt$, because $dT_w(t_o)/dt$ plays an essential role in equation (2) and the error included in $dT_w(t_o)/dt$ propagates in the iteration of equations (4), (5), and (6). Therefore, these data are statistically processed to give $x^* = 71.7$ μm as a mean and $\sigma_x = 1.38$ as the standard deviation. It should be mentioned that under the condition of $q_w = 3.7 \times 10^4$ W/m^2, $T_o = 1.0$ s, and $l_b = 0.03$ m, 10.0 percent of the Joule heat Q_j is consumed as Q_s, 86.3 percent as Q_l, and 3.7 percent as Q_b.

Finally, it may be of interest to note that the film thickness $x^* = 34$ μm for a space of 2 mm, irrespective of volume and frequency of injected air bubbles, although the uncertainty of measurements and situations of their experiments are unknown (Nishikawa et al., 1984).

Conclusions

To measure the liquid film thickness remaining on the wall during the passage of a bubble in a vertical rectangular channel, an experiment has been carried out by injecting air bubbles with lengths of 0.01, 0.02, and 0.03 m at periods of 0.1 to 1.0 s into it. The thickness ranged from 60 to 80 μm. It was independent of the bubble length and the period of the passing bubble over the whole experimental range. The mean value of the thickness was 72 μm.

References

Bretherton, F. P., 1961, "The Motion of Long Bubbles in Tubes," *J. Fluid Mechanics*, Vol. 10, pp. 166–188.

Carslaw, H. S., and Jaeger, J. C., 1959, *Conduction of Heat in Solids*, Oxford University Press, United Kingdom.

Fauske, H. K., Ford, W. D., and Grolmes, M. A., 1970, "Liquid Film Thickness for Slug Expulsion," *Trans. ANS.*, Vol. 13, pp. 646–647.

Fujita, Y., Ohta, H., Hidaka, S., and Nisikawa, K., 1986, "Nucleate Boiling Heat Transfer on Horizontal Tubes in Bundles," *Heat Transfer 86*, Vol. 5, pp. 2131–2136.

Ishibashi, E., and Nishikawa, K., 1969, "Saturated Boiling Heat Transfer in Narrow Space," *Int. J. Heat Mass Transfer*, Vol. 12, pp. 863–894.

Marchessault, R. N., and Mason, S. G., 1960, "Flow of Entrapped Bubbles Through a Capillary," *Ind. Engng. Chem.*, Vol. 52, pp. 79–84.

Monde, M., 1988, "Characteristic of Heat Transfer Enhancement Due to Bubbles Passing Through a Narrow Vertical Channel," ASME JOURNAL OF HEAT TRANSFER, Vol. 110, pp. 1016–1019.

Monde, M., and Kusuda, H., 1988, "Enhancement of Heat Transfer Due to Bubbles Passing Through a Narrow Vertical Rectangular Channel," *Proc. of 1st World Conf. on Experimental Heat Transfer, Fluid Mechanics and Thermodynamics*, Dubrovnik, Yugoslavia, pp. 1459–1465.

Nakashima, K., 1978, "Boiling Heat Transfer Outside Horizontal Multitube Bundle," *Trans. of JSME*, Vol. 42, pp. 1047–1057.

Nishikawa, K., Fujita, Y., Uchida, S., and Ohta, H., 1984, "Effect of Surface Configuration on Nucleate Boiling Heat Transfer," *Int. J. Heat Mass Transfer*, Vol. 27, pp. 1559–1571.

Oezgu, M. R., and Chen, J. C., 1976, "Local Film Thickness During Transient Voiding of a Liquid-Filled Channel," ASME JOURNAL OF HEAT TRANSFER, Vol. 98, pp. 159–165.

Street, J. R., and Tek, M. R., 1965, "Dynamics of Bullet Shaped Bubbles Encountered in Vertical Gas Liquid Slug Flow," *AIChE Journal*, Vol. 11, pp. 644–650.

An Experimental Study in Nucleate Boiling Heat Transfer From a Sphere

D. Dix[1] and J. Orozco[1]

Nomenclature

A = area
c_p = specific heat
k = thermal conductivity
m = sphere mass
q' = heat flux
q = heat rate
q'_{mb} = Moissis–Berenson transition flux
r = sphere radius
t = time
T = temperature
ΔT_v = $T_w - T_{sat}$
ΔT_b = $T_{sat} - T_l$
α = thermal diffusivity
θ = angle measured from the forward stagnation point
ρ = density
ϕ = azimuthal angle

Superscript

n = time step in finite difference analysis

Subscripts

b = boiling
c = conduction
i = inner
l = liquid
o = outer
sat = saturation
v = vapor
w = wall

Introduction

A systematic investigation of the effects of the orientation and dimensions of the heated surface on the nucleate boiling regime was presented by Van Stralen and Sluyter (1969). The behavior of water and some aqueous binary systems was studied on electrically heated platinum wires, both for saturated pool boiling and for surface boiling. Their findings showed that the peak flux density for the platinum wire in the horizontal position was 45 percent higher than the corresponding value for the wire in the vertical position. They also found that the boiling fluxes in the region of isolated bubbles were always higher for the horizontal wire. They attributed this effect not only to an increased maximal bubble population (the main cause), but also partly to a higher convective contribution. The smaller number of active sites for the vertical position was believed to be caused by a premature onset of film boiling in the upper part of the wire, due to the formation of large vapor slugs. In this case, the coalescing bubbles originated from nuclei that were distributed over the entire heating surface. This behavior differed from that on a horizontal wire, where bubble coalescence was generally restricted to nearby nuclei.

Recently, the issue of the influence of surface orientation on

[1]Department of Mechanical Engineering, University of Illinois at Chicago, Chicago, IL 60680.

Contributed by the Heat Transfer Division for publication in the JOURNAL OF HEAT TRANSFER. Manuscript received by the Heat Transfer Division June 13, 1988. Keywords: Boiling, Flow Visualization, Instrumentation.

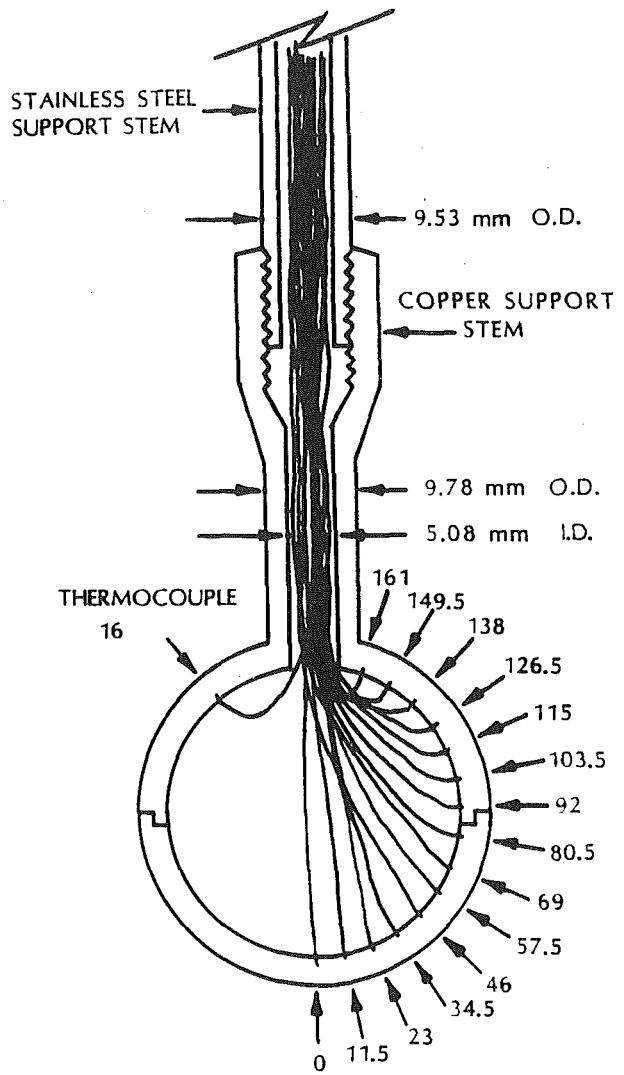

Fig. 1 Hollow copper sphere and thermocouples

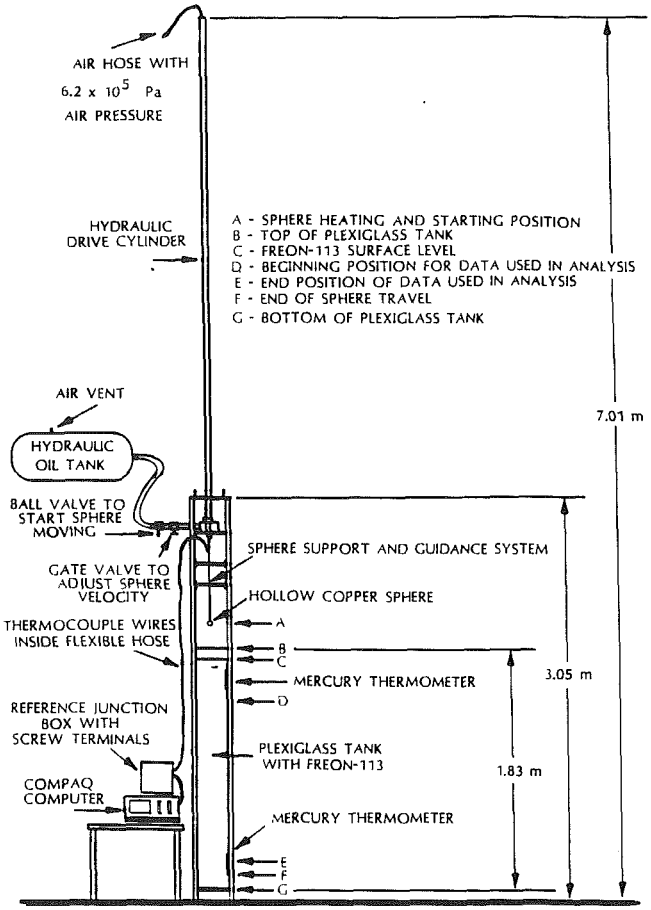

Fig. 2 Test fixture, front view

the nucleate boiling process was addressed by Nishikawa et al. (1983). Their experiments showed that for a flat plate oriented at an angle that varied between 0 and 175 deg from a horizontal, upward-facing position, the orientation of the heating surface strongly affected q_b' (the boiling flux) when q_b' was low, but had no effect when q_b' was high.

Based on the experimental data of Nishikawa et al. and the hydrodynamics of nucleate boiling, Lienhard (1985) concluded that in the regime of isolated bubbles the heat removal was gravity dependent, and that it was gravity independent in the regime of slugs and columns. He also pointed out that the transition between an orientation-dependent and an orientation-independent regime was predicted by the Moissis–Berenson equation (1963).

Subramanian and Witte (1987) examined the quenching of a 2.54-cm hollow copper sphere in methanol and water. Their results showed that temperature variation was insignificant for film boiling. However, a significant variation in both surface temperature and heat rate occurred around the sphere during transition/nucleate boiling. Ungar and Eichhorn (1982) and Irving and Westwater (1986) also obtained nonuniform boiling regimes while quenching spheres of several diameters.

It is customary when using the transient quenching method of obtaining boiling curves for spheres, q_b' versus ΔT_v, to make temperature measurements at selected locations, usually two or three locations. In addition, the data reduction generally involves the use of a polynomial curve-fit for either the temperature or the heat rate variation around the surface of the sphere. However, this technique of data reduction could lead to erroneous computation of heat rates when the polynomial selected does not yield the correct values of temperature at every point along the heated surface. The accuracy of the polynomial is usually improved by increasing the number of temperature measurements.

The purpose of this work is to report experimental measurements of boiling fluxes in both pool and forced convection from a 3.84-cm copper sphere instrumented with 16 copper-constantan thermocouples. The experiments were conducted in Freon-113 using a quenching technique. The sphere, with surfaces of every orientation, allowed us to investigate the effect of surface orientation on the boiling process. Our findings for the sphere are compared with those of Nishikawa for flat plates and those of Van Stralen for wires.

Experimental Arrangement

A 3.84-cm hollow copper sphere with an average wall thickness of 0.28 cm was used for both the pool and flow-boiling experiments. The hollow copper sphere was machined in two hollow hemispheres from a 5.00-cm copper bar. Prior to press fitting the sphere together, 16 30-gage copper-constantan thermocouples were mechanically pinned to the inner surface of the sphere. Figure 1 shows the hollow copper sphere and the location of the thermocouples.

The tank holding Freon-113, made from 127-cm-thick plexiglass, was 3.05 m tall with a cross section of 25.4 cm by 25.4 cm. The tank was filled with 108 liters of Freon-113. The liquid temperature was monitored with two mercury thermometers submerged in the tank as shown in Fig. 2. The

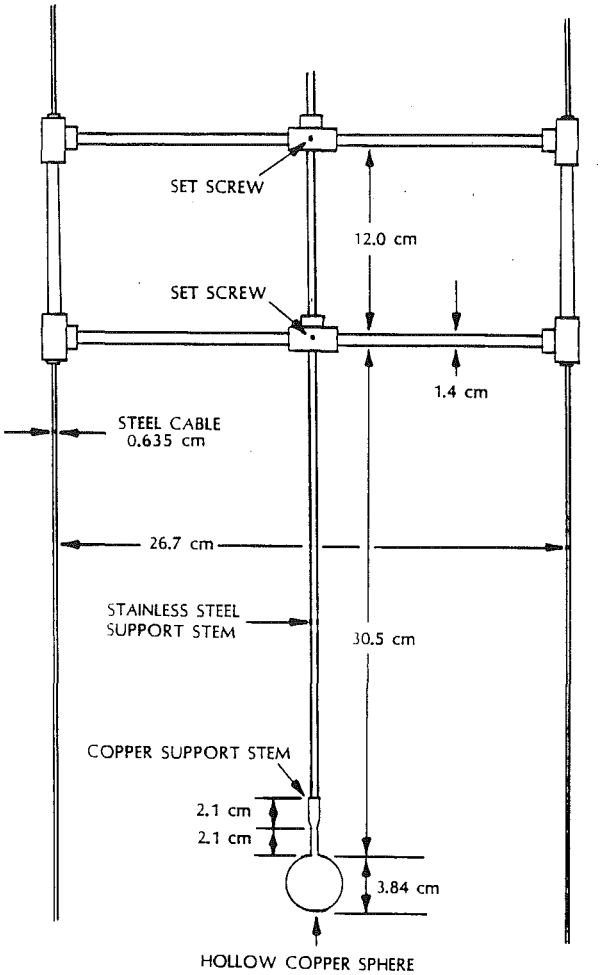

Fig. 3 Sphere support and guidance system

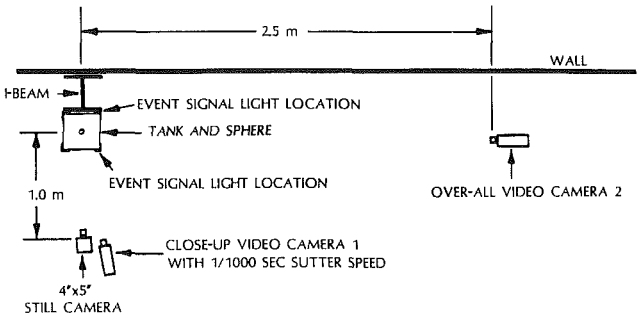

Fig. 4 Video and still camera positions

Freon-113 temperature was controlled with a hot water copper tubing exchanger located at the bottom of the plexiglass tank. For both the pool and flow boiling experiments, the sphere was heated to the required temperature by means of a gas-fueled calorimeter.

For the forced convection experiments the sphere was quenched in Freon-113, which was propelled into the tank by a 4.00-m-long, double-acting, hydraulic cylinder. When the cylinder was pressurized on the top with compressed air regulated to 6.2×10^5 Pa, hydraulic oil was forced out of the bottom of the cylinder; it then traveled through a gate valve, a ball valve, and into a holding tank. The valves were used to regulate the flow of oil and, therefore, control the speed of the sphere. The copper sphere was supported by a 1.00-cm stainless steel tube, which screwed into the short copper stem

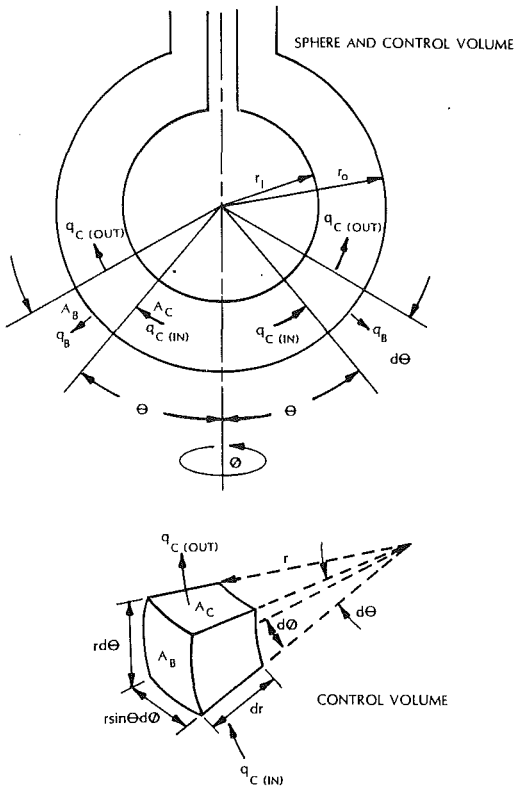

Fig. 5 Control volume

at the rear of the copper sphere. The sphere and stem were guided into the tank by a support system sliding on two cables as illustrated in Fig. 3. The pool boiling experiments were recorded with a close-up camera. Two video cameras were used to record all forced convection tests. The position of each camera is presented in Fig. 4. A Panasonic WVD-5000, equipped with a high-speed, 1/1000 second shutter speed, was used for all the close-up video recordings. The high-speed shutter was effective in providing clear, stop-action video pictures. A JVC model KY-310V camera was used for the overall video. Both cameras recorded 30 frames per second. In addition to the video cameras, a large format, Crown Graphic Special, 10.16 cm by 12.70 cm view camera with a Schneider-Kreuznach 135 mm f/5.6 lens and Polaroid 545 film holder was used to record sphere–vapor interaction in great detail. A studio lighting strobe, Novatron 440 HDX, was synchronized to the camera shutter. Photographs were taken at 1/500 second on Polaroid type-55 Land film. Due to the type of camera used, only one photograph per test was taken.

Temperature measurements were recorded at 16 locations on the inside of the hollow copper sphere. The data acquisition was accomplished with a Compaq computer. Two Data Translation boards, DT2813, with DT707 screw terminals were used to record the millivolt output from each thermocouple. Thermocouples were sampled sequentially at the rate of 50 measurements per second. An event signal and two LED lights were used to correlate the computer data with the visual results of the video and still cameras. When the event signal switch was activated, it lit two LEDs and sent a 2.70 mV signal to the computer. The two LED lights were also visible to each video camera. The event signal was activated during each forced convection test. This provided accurate correlation of sphere temperature and heat flux to visual observations of the boiling process during each test. Sphere velocities were determined with the aid of the overall video camera.

Data Reduction

Significant temperature variation occurred around the sur-

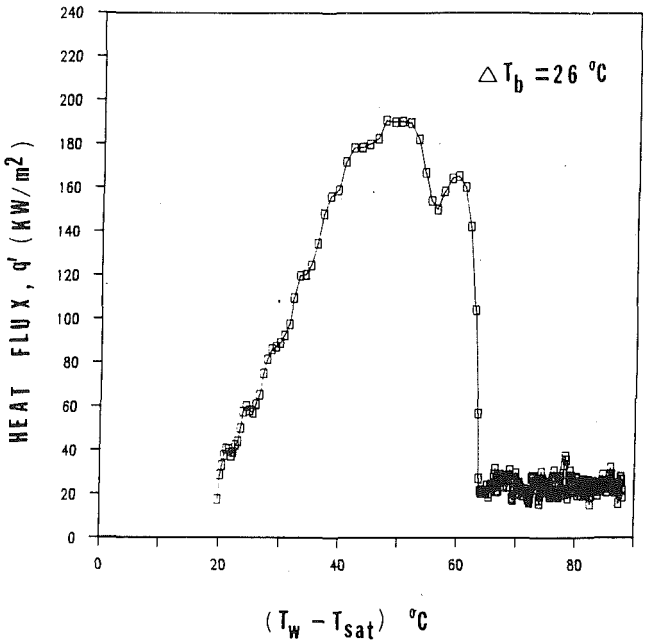

Fig. 6 Boiling flux at the 0 deg position

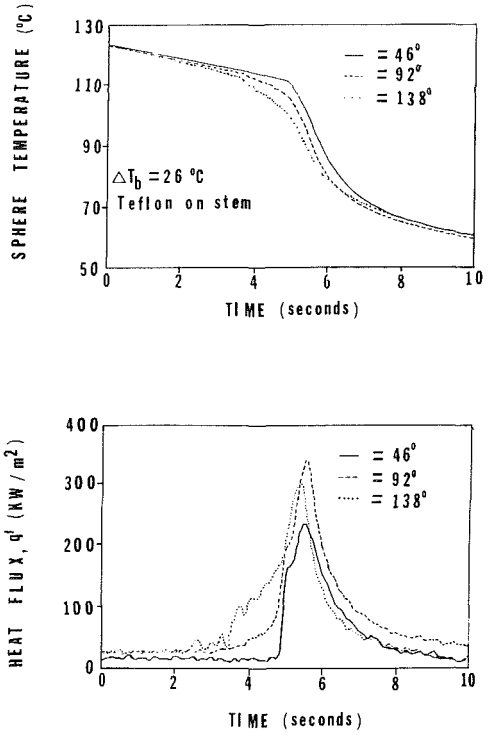

Fig. 7 Time history of temperature and heat flux for test 57

face of the sphere during the boiling process. Thus, the T-t data had to be reduced so as to account for T and q_b' variation with angular location. To solve for the sphere boiling flux, an energy balance was conducted on the control volume shown in Fig. 5. Neglecting the effect of thermal radiation and of convection between the air inside the sphere and the sphere's inside surface, the energy balance yields

$$(m_s c_p)\frac{\partial T_w}{\partial t} = q_{c,\theta} - q_{c,\theta+\Delta\theta} - q_{b,\theta} \tag{1}$$

where

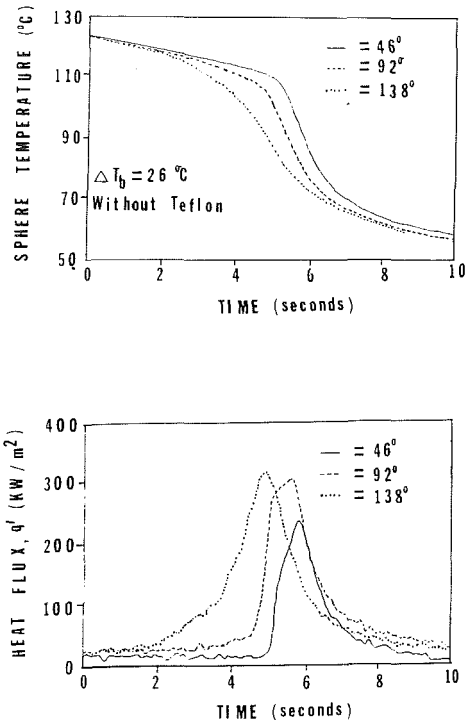

Fig. 8 Time history of temperature and heat flux for test 58

$(m_s c_p)\dfrac{\partial T_w}{\partial t}$ = transient experienced by the sphere mass

$q_{c,\theta}$ and $q_{c,\theta+\Delta\theta}$ = conduction heat rates at the θ and $\theta+\Delta\theta$ locations

$q_{b,\theta}$ = boiling heat rate from the surface of the control volume at the θ location.

Substituting the corresponding expressions for $q_{c,\theta}$, $q_{c,\theta+\Delta\theta}$, and q_b into equation (1) yields the following equation for the energy balance:

$$q_b' = k\left(\frac{\partial^2 T_w}{\partial\theta^2}\cot\theta\,\frac{\partial T_w}{\partial\theta}\right)\left(\frac{r_o - r_i}{r_o r_i}\right) - \rho c_p\frac{\partial T_w}{\partial t}(r_o - r_i) \tag{2}$$

Substitution of the temperature measurements in equation (2) allows the computation of boiling fluxes in all regimes. To this effect, equation (2) is converted to a finite-difference equation. Using an explicit formulation that is second-order accurate in θ and first-order accurate in t, equation (2) becomes

$$q_{b,\theta}' = C_1\left[\frac{T_{w,\theta+\Delta\theta}^n - T_{w,\theta}^n + T_{w,\theta-\Delta\theta}^n}{(\Delta\theta)^2} + \cot\theta\,\frac{T_{w,\theta+\Delta\theta}^n - T_{w,\theta-\Delta\theta}^n}{(2\Delta\theta)}\right] - C_2\left[\frac{T_{w,\theta}^{n+1} - T_{w,\theta}^{n-1}}{(2\Delta t)}\right] \tag{3}$$

where

$$C_1 = k_s\left(\frac{r_o - r_i}{r_o r_i}\right) \tag{4}$$

and

$$C_2 = (\rho c_p)_s\,(r_o - r_i) \tag{5}$$

An example of the computed boiling flux is presented in Fig. 6 for $\theta = 0$.

Reproducibility between experimental data performed at the same conditions was quite good, with deviations of only a few percent between comparable data. The uncertainty in the heat transfer measurements was due to temperature recording

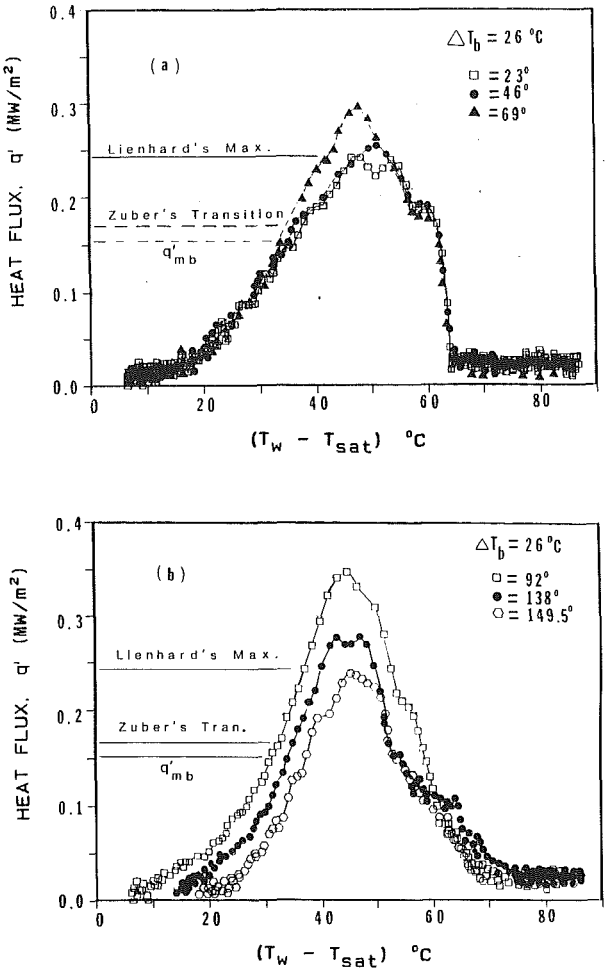

Fig. 9 Boiling fluxes at selected location on the sphere lower and upper halves

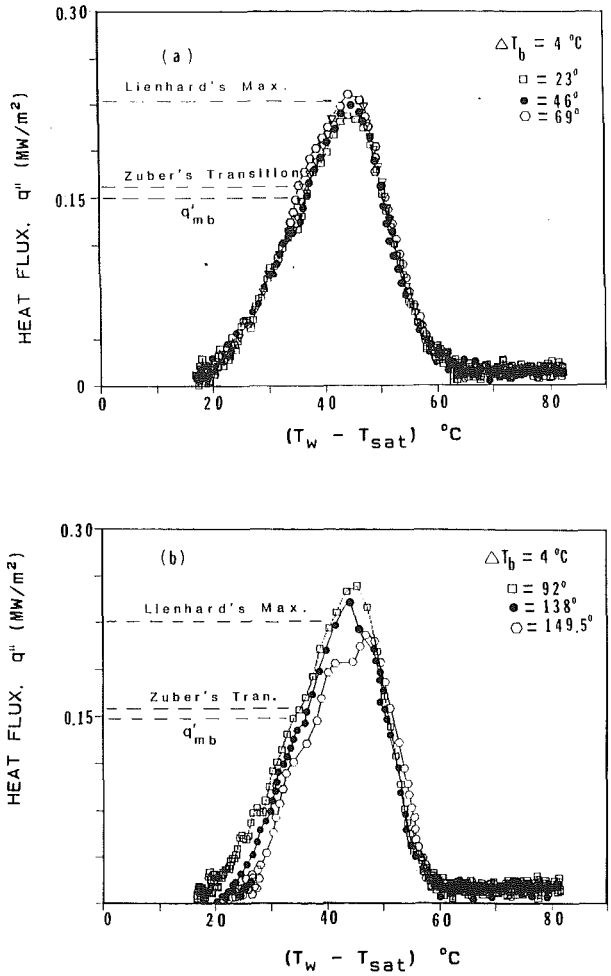

Fig. 10 Boiling fluxes for Freon-113 near saturation

errors. A detailed uncertainty analysis indicated that the maximum expected uncertainty of ±10 percent would occur in the nucleate boiling regime.

Discussion of Results

Twenty pool boiling experiments were conducted in Freon-113 at 20–45°C. The forced convection experiments were conducted in the same temperature range for sphere velocities below 0.8 m/s. The relatively low velocity range for the forced convection experiments was the result of the quenching technique used. For velocities higher than 0.8 m/s the duration of the experiments in the nucleate boiling range was very short, therefore limiting the acquisition of temperature measurements.

Figure 7 illustrates the general nature of the T–t history and the fluxes calculated for the thermocouples located at the 46, 92, and 138 deg locations for 21°C Freon-113 in pool boiling. All pool boiling tests were conducted with the bottom of the sphere immersed 16 cm below the liquid surface. It is worth mentioning that the support stem was studied for its effects as a cooling fin on the sphere. Tests were run with the stem wrapped with teflon tape. Video recordings of the boiling process revealed that without teflon the collapse of film boiling started on the stem, traveled down to the back of the sphere, and then around the sphere to the front stagnation point. With teflon wrapped on the stem, the vapor film collapse occurred all over the sphere almost simultaneously. A comparison between Figs. 7 and 8 shows that the teflon wrapping minimized the difference in temperature between the front and back of the sphere and that the peak heat fluxes occurred almost simultaneously. The peak heat fluxes in test 58, Fig. 7, occurred 1 to 1.5 s apart.

Figure 9(a) displays the heat transfer results for various angular positions on the lower half of the sphere. Contrary to the findings of Nishikawa et al., the experimental results showed that the nucleate boiling flux was independent of angular position for $\Delta T_v < 40$°C; however, our results compare favorably to those obtained by Irving and Westwater (1986) for the quenching of a 10.16-cm aluminum sphere. Variation of the boiling flux with angular position was observed in the neighborhood of the higher maximum heat flux. An increase in angular position brought about a maximum heat flux. The heat transfer results for some angular positions on the sphere's upper half are presented in Fig. 9(b). The measurements revealed that the peak heat flux as well as the lower part of the nucleate boiling regime continued to be dependent on an angular location. The data indicated good agreement with the Ded and Lienhard (1982) theory for peak heat flux only for the lower half of the sphere. A comparison between Figs. 9 and 10 indicates that an increase in liquid temperature results in lower heat rates at all points on the surface of the sphere.

Complete boiling curves were obtained in forced convection for relatively low sphere velocities (less than 0.8 m/s). In this velocity range the effect of orientation on the boiling process was negligible; however, higher boiling fluxes were obtained in forced convection. Figure 11 shows the boiling fluxes obtained for a sphere velocity of 0.5 m/s.

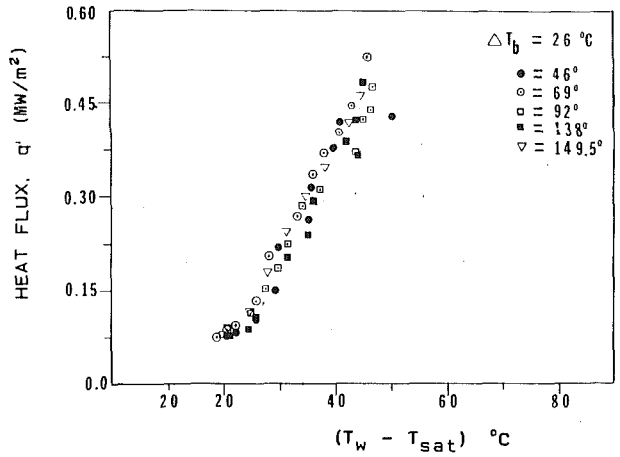

Fig. 11 Forced convection fluxes for a sphere velocity of 0.5 m/s

Conclusions

The major findings in this study are:

1 The pool boiling experimental data show that in the region of isolated bubbles, the boiling fluxes are surface orientation independent on the lower half of the sphere. This finding is contrary to the results of Nishikawa et al. The data also indicate that variation of boiling flux with orientation occurs only above the Moissis–Berenson transition and the Lienhard's theory for peak heat flux is in good agreement with the computed fluxes for the sphere lower half.

2 The pool boiling fluxes are surface orientation dependent on the upper half of the sphere and the peak heat fluxes deviate from Lienhard's predicted maximum.

3 The behavior of the pool boiling process could be explained in terms of Van Stralen's observations. On the lower half of the sphere, in the region of columns and jets, the interaction between vapor slugs is enhanced by the curvature of the sphere. This interaction leads to a smaller maximal number of active nucleic sites and consequently to lower orientation-dependent peak fluxes. However, the boiling fluxes do not decrease in the θ direction because, unlike Van Stralen's heated wires, the sphere has a boiling area that increases with θ on the lower half of the sphere. On the upper half of the sphere, surface orientation plays no role in the interaction between vapor jets, thus maximizing the number of nucleic sites.

4 The nucleate boiling fluxes are not affected by surface orientation in forced convection. However, this conclusion is based on experimental data at low sphere velocity.

Acknowledgments

This research was supported in part by a grant from Amoco Research, and by the National Science Foundation through grant No. CBT-880898.

References

Ded, J. S., and Lienhard, J. H., 1972, "The Peak Pool Boiling Heat Flux From a Sphere," *AIChE J.*, Vol. 18, No. 2, p. 373.

Dix, D. E., 1988, "Heat Transfer From a Sphere in Pool and Forced Convection of Subcooled Freon-113," MS Thesis, Department of Mechanical Engineering, University of Illinois at Chicago, Chicago, IL.

Irving, M. E., and Westwater, J. W., 1986, "Limitations for Obtaining Boiling Curves by the Quenching Method With Sphere," *Proc. Eighth Int. Heat Transfer Conference*, Vol. 4, pp. 2061–2065.

Lienhard, J. H., 1985, "On the Two Regimes of Nucleate Boiling," ASME JOURNAL OF HEAT TRANSFER, Vol. 107, pp. 262–264.

Moissis, R., and Berenson, P. J., 1963, "On the Hydrodynamic Transitions in Nucleate Boiling," ASME JOURNAL OF HEAT TRANSFER, Vol. 85, pp. 221–229.

Nishikawa, K., Fujita, Y., Uchida, S., and Ohta, H., 1983, "Effect of Heating Surface Orientation on Nucleate Boiling Heat Transfer," *Proc. ASME-JSME Thermal Engineering Joint Conference*, Honolulu, HI, Mar. 20–24, 1983, Vol. 1, ASME, New York, pp. 129–136.

Subramanian, S., and Witte, L. C., 1987, "Quenching of a Hollow Sphere," ASME JOURNAL OF HEAT TRANSFER, Vol. 109, pp. 262–264.

Ungar, E., and Eichhorn, R., 1982, "Local Surface Boiling Heat Transfer From a Submerged Sphere," ASME Paper No 82-HT-27.

Van Stralen, S. J. D., and Sluyter, W. M., 1969, "Investigations on the Critical Heat Flux of Pure Liquids and Mixtures Under Various Conditions," *International Journal Heat and Mass Transfer*, Vol. 12, pp. 1353–1384.

Liquid–Solid Contact in Pool Film Boiling From a Cylinder

K.-H. Chang[1] and L. C. Witte[2]

Introduction

In film boiling, liquid is separated from the heating surface by the formation of a continuous vapor film. But some experiments have shown evidence of intermittent liquid–solid contact as shown by photographs and signal traces when boiling conditions are near the minimum film boiling point. These works include Bradfield (1966), Yao and Henry (1978), Lee et al. (1982, 1985), Dhuga and Winterton (1985), and Neti et al. (1986). Therefore, it appears that the vapor film may become unstable at a heat flux and wall superheat higher than those at the minimum point.

The wavy nature of the liquid–vapor interface during the vapor removal process in pool film boiling from a flat heating surface can induce the liquid to contact the heating surface, as pointed out by Witte et al. (1983). As a bubble departs from the vapor film, the liquid can rush toward the surface and momentarily wet the local portion of the heating surface below the breakaway point. The vapor film is re-established after the brief contact to separate the liquid from the surface. Pool boiling from cylinders and spheres also exhibits this type of vapor removal, in which the wavy interface occurs at the top of the body.

The detection of liquid–solid contact in film boiling requires very delicate preparation of the heating surface. Electrical conductance probes, microthermocouples, fiber-optic probes, and electrical impedance methods have been used to measure the contact. Technical restrictions have required that almost all the studies measuring liquid–solid contact be limited to a flat heater geometry.

Obviously if liquid–solid contact occurs during film boiling from flat heating surfaces, the contact phenomenon should also be found in geometries other than flat heaters. The similarity between a large cylinder and a flat plate in many boiling situations makes one believe that there are similarities between the two geometries regarding contact behavior. Little work has been done to provide quantitative liquid–solid contact information on cylindrical and spherical heating surfaces.

The present study investigated the possibility of such contact in pool film boiling from a cylindrical heater with concentration on the low heat flux and low wall superheat conditions of film boiling. The measurement of contact was carried out by using a microthermocouple probe with its thermo-junction flush with the heater surface. Surface temperature depressions caused by liquid–solid contacts were obtained through the rapid response of the probe coupled to a data acquisition system. The contact parameters at varying boiling conditions were found from the history of the temperature depressions.

[1]Design Engineer, Imo Delaval, Inc., Los Angeles, CA.

[2]Professor and Chairman, Department of Mechanical Engineering, University of Houston, Houston, TX 77204-4792; Fellow ASME.

Contributed by the Heat Transfer Division for publication in the JOURNAL OF HEAT TRANSFER. Manuscript received by the Heat Transfer Division January 6, 1989. Keywords: Boiling, Measurement Techniques, Phase Change Phenomena.

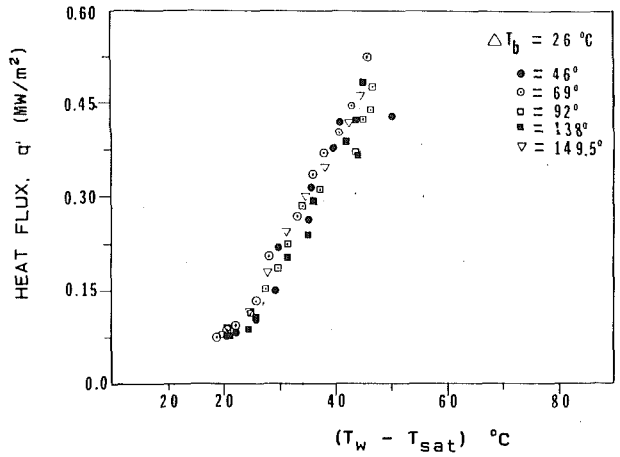

Fig. 11 Forced convection fluxes for a sphere velocity of 0.5 m/s

Conclusions

The major findings in this study are:

1 The pool boiling experimental data show that in the region of isolated bubbles, the boiling fluxes are surface orientation independent on the lower half of the sphere. This finding is contrary to the results of Nishikawa et al. The data also indicate that variation of boiling flux with orientation occurs only above the Moissis–Berenson transition and the Lienhard's theory for peak heat flux is in good agreement with the computed fluxes for the sphere lower half.

2 The pool boiling fluxes are surface orientation dependent on the upper half of the sphere and the peak heat fluxes deviate from Lienhard's predicted maximum.

3 The behavior of the pool boiling process could be explained in terms of Van Stralen's observations. On the lower half of the sphere, in the region of columns and jets, the interaction between vapor slugs is enhanced by the curvature of the sphere. This interaction leads to a smaller maximal number of active nucleic sites and consequently to lower orientation-dependent peak fluxes. However, the boiling fluxes do not decrease in the θ direction because, unlike Van Stralen's heated wires, the sphere has a boiling area that increases with θ on the lower half of the sphere. On the upper half of the sphere, surface orientation plays no role in the interaction between vapor jets, thus maximizing the number of nucleic sites.

4 The nucleate boiling fluxes are not affected by surface orientation in forced convection. However, this conclusion is based on experimental data at low sphere velocity.

Acknowledgments

This research was supported in part by a grant from Amoco Research, and by the National Science Foundation through grant No. CBT-880898.

References

Ded, J. S., and Lienhard, J. H., 1972, "The Peak Pool Boiling Heat Flux From a Sphere," *AIChE J.*, Vol. 18, No. 2, p. 373.

Dix, D. E., 1988, "Heat Transfer From a Sphere in Pool and Forced Convection of Subcooled Freon-113," MS Thesis, Department of Mechanical Engineering, University of Illinois at Chicago, Chicago, IL.

Irving, M. E., and Westwater, J. W., 1986, "Limitations for Obtaining Boiling Curves by the Quenching Method With Sphere," *Proc. Eighth Int. Heat Transfer Conference*, Vol. 4, pp. 2061–2065.

Lienhard, J. H., 1985, "On the Two Regimes of Nucleate Boiling," ASME JOURNAL OF HEAT TRANSFER, Vol. 107, pp. 262–264.

Moissis, R., and Berenson, P. J., 1963, "On the Hydrodynamic Transitions in Nucleate Boiling," ASME JOURNAL OF HEAT TRANSFER, Vol. 85, pp. 221–229.

Nishikawa, K., Fujita, Y., Uchida, S., and Ohta, H., 1983, "Effect of Heating Surface Orientation on Nucleate Boiling Heat Transfer," *Proc. ASME-JSME Thermal Engineering Joint Conference*, Honolulu, HI, Mar. 20–24, 1983, Vol. 1, ASME, New York, pp. 129–136.

Subramanian, S., and Witte, L. C., 1987, "Quenching of a Hollow Sphere," ASME JOURNAL OF HEAT TRANSFER, Vol. 109, pp. 262–264.

Ungar, E., and Eichhorn, R., 1982, "Local Surface Boiling Heat Transfer From a Submerged Sphere," ASME Paper No 82-HT-27.

Van Stralen, S. J. D., and Sluyter, W. M., 1969, "Investigations on the Critical Heat Flux of Pure Liquids and Mixtures Under Various Conditions," *International Journal Heat and Mass Transfer*, Vol. 12, pp. 1353–1384.

Liquid–Solid Contact in Pool Film Boiling From a Cylinder

K.-H. Chang[1] and L. C. Witte[2]

Introduction

In film boiling, liquid is separated from the heating surface by the formation of a continuous vapor film. But some experiments have shown evidence of intermittent liquid–solid contact as shown by photographs and signal traces when boiling conditions are near the minimum film boiling point. These works include Bradfield (1966), Yao and Henry (1978), Lee et al. (1982, 1985), Dhuga and Winterton (1985), and Neti et al. (1986). Therefore, it appears that the vapor film may become unstable at a heat flux and wall superheat higher than those at the minimum point.

The wavy nature of the liquid–vapor interface during the vapor removal process in pool film boiling from a flat heating surface can induce the liquid to contact the heating surface, as pointed out by Witte et al. (1983). As a bubble departs from the vapor film, the liquid can rush toward the surface and momentarily wet the local portion of the heating surface below the breakaway point. The vapor film is re-established after the brief contact to separate the liquid from the surface. Pool boiling from cylinders and spheres also exhibits this type of vapor removal, in which the wavy interface occurs at the top of the body.

The detection of liquid–solid contact in film boiling requires very delicate preparation of the heating surface. Electrical conductance probes, microthermocouples, fiber-optic probes, and electrical impedance methods have been used to measure the contact. Technical restrictions have required that almost all the studies measuring liquid–solid contact be limited to a flat heater geometry.

Obviously if liquid–solid contact occurs during film boiling from flat heating surfaces, the contact phenomenon should also be found in geometries other than flat heaters. The similarity between a large cylinder and a flat plate in many boiling situations makes one believe that there are similarities between the two geometries regarding contact behavior. Little work has been done to provide quantitative liquid–solid contact information on cylindrical and spherical heating surfaces.

The present study investigated the possibility of such contact in pool film boiling from a cylindrical heater with concentration on the low heat flux and low wall superheat conditions of film boiling. The measurement of contact was carried out by using a microthermocouple probe with its thermo-junction flush with the heater surface. Surface temperature depressions caused by liquid–solid contacts were obtained through the rapid response of the probe coupled to a data acquisition system. The contact parameters at varying boiling conditions were found from the history of the temperature depressions.

[1]Design Engineer, Imo Delaval, Inc., Los Angeles, CA.

[2]Professor and Chairman, Department of Mechanical Engineering, University of Houston, Houston, TX 77204-4792; Fellow ASME.

Contributed by the Heat Transfer Division for publication in the JOURNAL OF HEAT TRANSFER. Manuscript received by the Heat Transfer Division January 6, 1989. Keywords: Boiling, Measurement Techniques, Phase Change Phenomena.

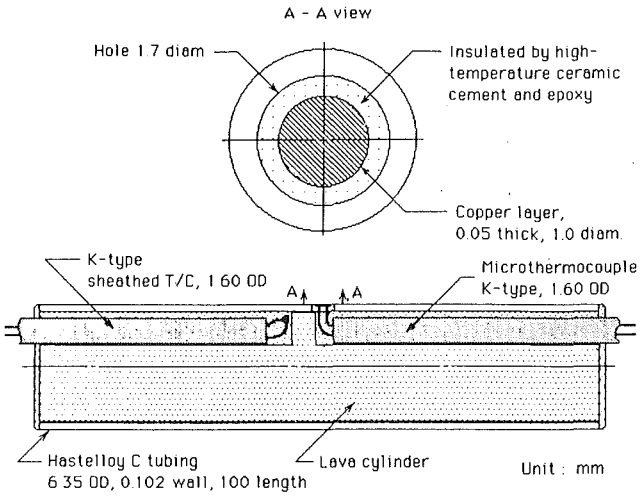

Fig. 1 A microthermocouple probe installed in the cylindrical heater

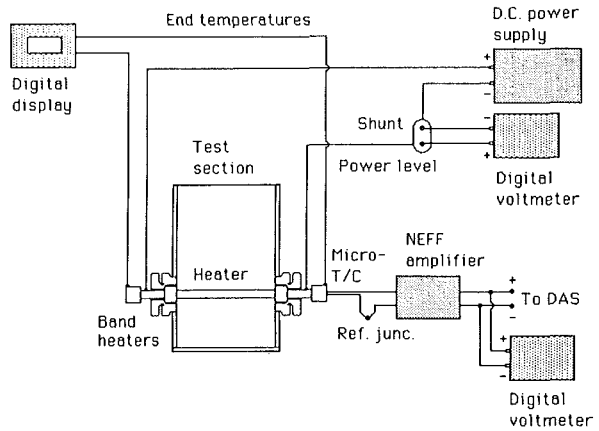

Fig. 2 Schematic diagram of the experimental measurement system

Experimental Apparatus

Experiments were done with a thin-walled Hastelloy C cylindrical heater of 6.35-mm o.d., 0.102-mm wall thickness, and 100-mm length with a lava insert for structural rigidity. A chromel/alumel microthermocouple probe was installed near the midpoint of the heater as shown in Fig. 1. A groove in the lava insert provided space for the 1.60-mm o.d. Inconel sheathed microthermocouple of 0.4-mm wires to be laid into it. The wires were brought out to the surface through a 1.7-mm hole drilled into the heater. The wires and the sheath were surrounded by high-temperature ceramic cement, which electrically insulated the probe from the heater.

A 0.05-mm-thick, 1-mm circular copper layer was electrochemically plated over the wires to form a fast-response thermo-junction. The copper layer was also insulated from the heater surface with high-temperature epoxy surrounding it. After the epoxy was cured, the copper layer and the epoxy were then polished to be flush with the heater surface. The response time of the junction was estimated to be 0.9 ms. The microthermocouple probe/heater is discussed in detail by Chang (1987) and Chang and Witte (1988).

Another identical thermocouple with an ordinary bead was installed from the other end of the heater to measure the average temperature of the heater assembly. The output of this thermocouple was used to verify that the surface temperature fluctuated around an average value for the heater.

The schematic diagram of the experimental measurement system is shown in Fig. 2. The cylindrical heater was placed inside a Plexiglas container 80 mm × 80 mm and 125 mm high. Brass/Teflon buses and Teflon bushings were used to support the heater. The front faces of the buses and bushings were flush with the inside wall of the container. The Brass/Teflon buses were designed to create uniform film boiling at low heat flux and wall superheat, and their design is described by Chang et al. (1988).

Insulated guard heaters were installed on the ends of the buses to counteract axial heat loss along the heater surface. They were 25.4-mm-dia band heaters rated at 150 watts. Thermocouples were installed under these heaters on the bus surfaces. The buses were connected to a regulated d.c. power supply of 15 volts and 100 amperes maximum capacity. The voltage output of the microthermocouple probe was recorded by a DEC Micro-11 computer through an A/D converter and a Neff preamplifier. The details of the data acquisition system are given by Chang (1987). An uncertainty analysis (see Chang, 1987) showed that the temperature uncertainty was less than about 0.25°C while the uncertainty in the heat flux was about 3 percent.

Pool boiling experiments were performed by first heating the heater in air to a temperature higher than what was estimated to be the minimum film boiling temperature. Freon-11 liquid was then gently introduced into the container while the power was increased to maintain film boiling. This procedure involved partial quenching as the liquid contacted and immersed the heater. Since heat was being generated continuously in the thin-walled heater, steady-state film boiling could be achieved. This procedure circumvented the need to drive the heater past the maximum heat flux point prior to entry into film boiling. It was also desirable to avoid the possibility of burning out the thin thermo-junction when directly passing through the maximum point using resistance heating.

The power to the heater was lowered after the probe output was recorded for several seconds at a steady-state condition. This was repeated at about 10°C increments in ΔT_w until the transition to nucleate boiling began. ΔT_w is defined as $(T_w - T_{sat})$, where T_w is the probe temperature and T_{sat} is the liquid boiling temperature. The cylindrical heater was rotated to different angular positions to find the angular dependence of liquid–solid contact. The experiments were carried out at atmospheric pressure with saturated Freon-11.

Experimental Results and Discussion

The thermo-junction was first rotated to the 180-deg position measured from the bottom of the cylindrical heater. Samples of the probe output in pool film boiling are shown in Fig. 3. These outputs represent the rapid changes of the heater surface temperature with the heater surface maintained at a time-average of $\Delta T_w = 179°C$, 139°C, and 115°C with Freon-11 liquid wetting the heater surface intermittently. In Fig. 3(*a*), where $\Delta T_w = 179°C$, the surface temperature fluctuations were small except for one temperature depression of 4.4°C. When the wall superheat was decreased to 139°C as shown in Fig. 3(*b*), more temperature fluctuations were observed, which reveals that liquid–solid contact is more active at lower ΔT_w.

The time duration of liquid–solid contact, t_c, was found as shown on Fig. 3(*c*). It represents the time over which energy is rapidly taken from the probe, thus reducing its temperature (shown as an emf output in this case). The ΔT_c is the temperature depression that occurs as a result of the liquid–solid contact. An example is also shown on Fig. 3(*c*).

With decreasing ΔT_w, the temperature depressions became larger and the time duration of the contacts became longer as well. The temperature fluctuations were quite dramatic at $\Delta T_w = 115°C$, as seen in Fig. 3(*c*). This boiling condition is very close to the minimum film boiling point. With a little further decrease of ΔT_w, the vapor film collapsed, starting from the bottom and proceeding to the top of the cylindrical heater.

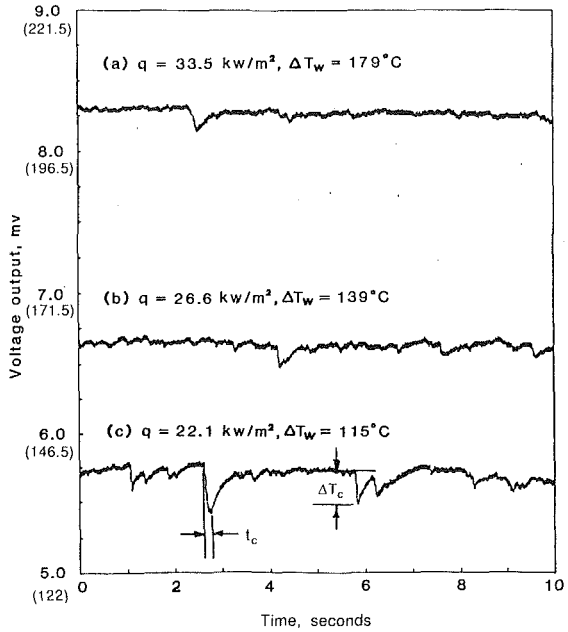

Fig. 3 Probe output in Freon-11 pool film boiling from a 6.35-mm cylinder with probe at 180 deg position (number in parentheses indicate temperature in °C)

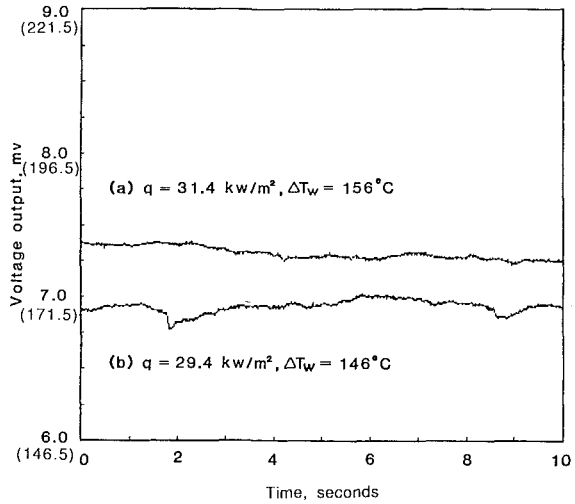

Fig. 4 Probe output in Freon-11 pool film boiling from a 6.35-mm cylinder with probe at 110 deg position (numbers in parentheses indicate temperature in °C)

The microthermocouple probe also detected liquid–solid contact at the position of 110 deg. As can be seen in Fig. 4, the surface temperature fluctuations were much less than those with the probe at the 180-deg position. The temperature depressions and time durations were smaller in magnitude than the previous case. The vapor film collapsed near $\Delta T_w = 143°C$, which was higher than that when the probe was at 180 deg.

When the probe was at the 0-deg point (or facing down), few liquid–solid contacts were found before the vapor film collapsed, as shown in Fig. 5. However, there was a large temperature depression prior to the transition to nucleate boiling. This indicates that if there is a contact in the neighborhood of the probe, the arrangement of the probe material may form a local cold spot on the heater surface and the contact can lead to the breakdown of the vapor film.

Our measurements showed that liquid–solid contact was more likely to occur at the top than at the bottom of the heater. Its extent intensified with a decrease in wall superheat.

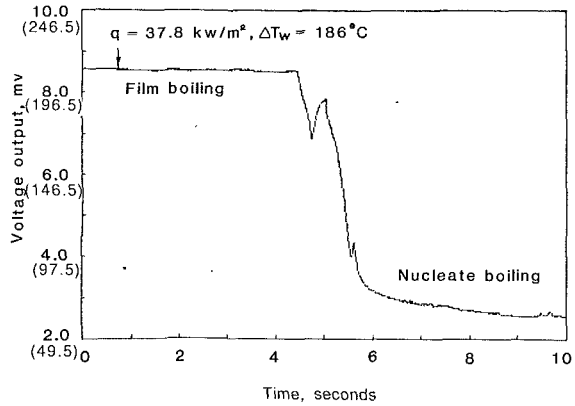

Fig. 5 Probe output in Freon-11 pool film boiling from a 6.35-mm cylinder with probe at 0 deg position (numbers in parentheses indicate temperature in °C)

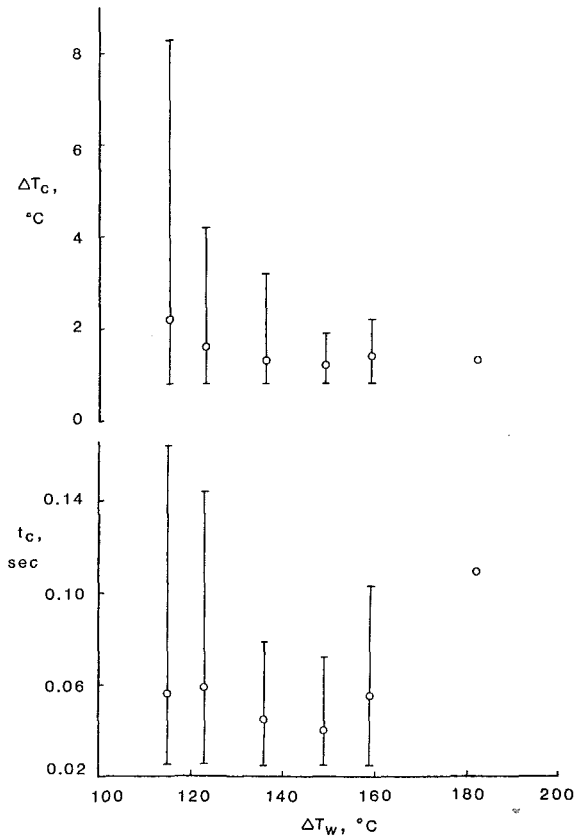

Fig. 6 Liquid–solid contact data of Freon-11 pool film boiling from a 6.35-mm cylinder probe at 180 deg position

If a contact was large enough that the surface temperature could not recover before another large contact occurred, then the vapor film broke down with a transition to nucleate boiling.

The liquid–solid contact data with the probe at 180 deg were used to find essential information about such contacts, i.e., the relationships between temperature depression, time duration, and wall superheat. Figure 6 shows the dependencies of the temperature depression, ΔT_c, and the duration of contact, t_c, on wall superheat, ΔT_w. The average values of the contact data along with their range of variation (represented by the bars) are shown in Fig. 6. The variations of ΔT_c and t_c are well outside their estimated accuracies, which are 0.25°C and 0.005 s, respectively. The average temperature depression and time duration did not increase much with decreasing wall superheat. However, the upper limit changed substantially

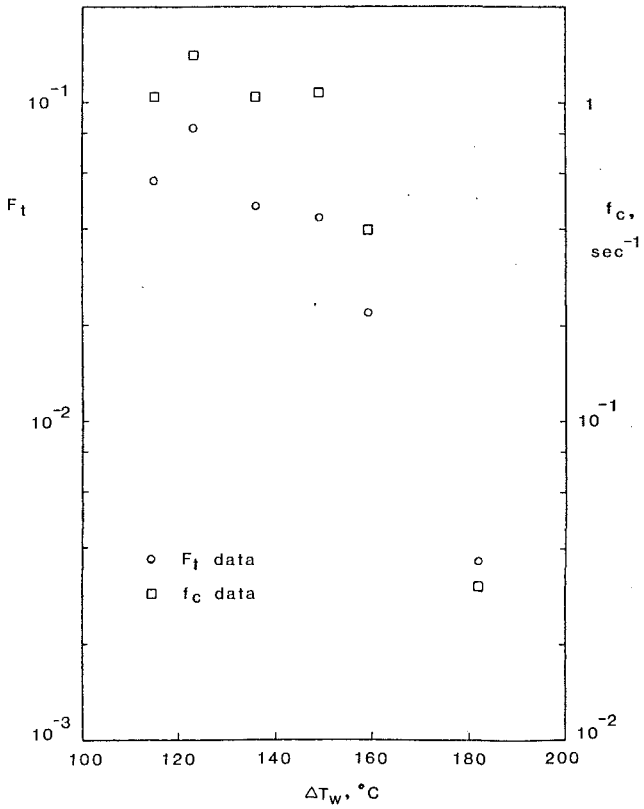

Fig. 7 Time fraction and contact frequency of Freon-11 pool film boiling from a 6.35-mm cylinder with probe at 180 deg position

with wall superheat. Note that the temperature depression and time duration are related to each other; that is, a large temperature depression was always accompanied by a long time duration during a liquid-solid contact.

Another parameter that could be obtained from the time duration data was the time fraction of liquid-solid contact. The time fraction F_t represents the ratio of the summation of the time that liquid contacted the solid surface to the total sampling time, which was 50 s for most experiments. The time fraction with the probe located at 180 deg is shown in Fig. 7 as a function of wall superheat. The average contact frequency was determined by summing the numbers of measurable contacts and dividing by the sum time (~ 50 s). The average contact frequency f_c is also included in Fig. 7. Both the time fraction and contact frequency increased dramatically with decreasing wall superheat. The time fraction was about 0.0035 at $\Delta T_w = 181°C$, it increased to 0.02 at $\Delta T_w = 159°C$, and it reached 0.08 at $\Delta T_w = 123°C$. It should go beyond 0.1 and approach 1.0 in transition and nucleate boiling.

Most of the experimental data for liquid-solid contact in pool film boiling from flat heaters show very small time or area fractions in film boiling, with the order less than 10^{-2} s. The studies of Lee et al. (1985) and Dhuga and Winterton (1985) covered only the transition and nucleate boiling regimes, while Neti et al. (1986) did not distinguish film boiling data from those in transition boiling. The fraction data of Yao and Henry (1978) were defined in a different manner with the maximal value larger than 1.0, which makes a direct comparison impossible.

In general, the time fraction measurements of the present study agreed with other contact data. Liquid-solid contact clearly exists in the low heat flux film boiling regime. Some unstable vapor films with intermittent breakdowns were observed during the experiments. The vapor removal process from the top of the cylindrical heater seemed to contribute most to the contact in pool boiling from the cylindrical heater. The heater surface at other angular locations shows insignificant liquid-solid contact in film boiling. However, initial contacts on the liquid-solid probe when it was located at zero degrees led to immediate transition to nucleate boiling, as explained earlier.

Acknowledgments

The experimental work was performed when the first author was a research assistant supported by NSF Grant No. MEA-8411894. The assistance of S. Sankaran is appreciated.

References

Bradfield, W. S., 1966, "Liquid-Solid Contact in Stable Film Boiling," *Industrial and Engineering Chemistry-Fundamentals*, Vol. 5, No. 2, pp. 200–204.

Chang, K.-H., 1987, "The Instability of Vapor Films in Flow Boiling From Cylinders," Ph.D. Dissertation, University of Houston, TX.

Chang, K.-H., and Witte, L. C., 1988a, "Liquid-Solid Contact During Flow Boiling From Freon-11," *Proceedings of the 1988 National Heat Transfer Conference*, Houston, TX, ASME HTD-96, Vol. 2, pp. 659–665.

Chang, K.-H., Witte, L. C., and Sankaran, S., 1988b, "The Influence of End Conditions on Minimum Film Boiling From a Cylinder," *Proceedings of the 1988 National Heat Transfer Conference*, Houston, TX, ASME HTD-96, Vol. 2, pp. 385–388.

Dhuga, D. S., and Winterton, R. H. S., 1985, "Measurement of Surface Contact in Transition Boiling," *Int. J. Heat Mass Transfer*, Vol. 28, No. 10, pp. 1869–1880.

Lee, L., Chen, J. C., and Nelson, R. A., 1982, "Surface Probe for Measurement of Liquid Contact in Film and Transition Boiling on High-Temperature Surface," *Rev. of Sci. Instr.*, Vol. 53, No. 9, pp. 1472–1476.

Lee, L. Y. W., Chen, J. C., and Nelson, R. A., 1985, "Liquid-Solid Contact Measurement Using a Surface Thermocouple Temperature Probe in Atmospheric Pool Boiling Water," *Int. J. Heat Mass Transfer*, Vol. 28, No. 8, pp. 1415–1423.

Neti, S., Butrie, T. J., and Chen, J. C., 1986, "Fiber-Optic Liquid Contact Measurement in Pool Boiling," *Rev. of Sci. Instr.*, Vol. 57, No. 12, pp. 3043–3047.

Witte, L. C., Orozco, J., and Chang, K.-H., 1983, "On the Role of Liquid-Solid Contact in Subcooled Flow Film Boiling From Submerged Bodies," *Interfacial Transport Phenomena*, ASME HTD-Vol. 23, pp. 67–74.

Yao, S. C., and Henry, R. E., 1978, "An Investigation of the Minimum Film Boiling Temperature on Horizontal Surfaces," ASME JOURNAL OF HEAT TRANSFER, Vol. 100, pp. 260–267.